NASA SP-194

LIQUID PROPELLANT ROCKET COMBUSTION INSTABILITY

NATIONAL AERONAUTICS AND SPACE ADMINISTRATION

NASA SP–194

LIQUID PROPELLANT ROCKET COMBUSTION INSTABILITY

Editor
DAVID T. HARRJE
Princeton University

Associate Editor
FREDERICK H. REARDON
Sacramento State College

Scientific and Technical Information Office 1972
NATIONAL AERONAUTICS AND SPACE ADMINISTRATION
Washington, D.C.

For sale by the Superintendent of Documents,
U.S. Government Printing Office, Washington, D.C. 20402
Price$5.50
Library of Congress Catalog Card Number 70–170324
Stock number 3300–0450

PREFACE

This reference book originated in the concern of a number of engineers engaged in the solution of problems of combustion instability for more effective communication between the various workers in this field. In December 1962 an ad hoc working group was formed by the JANNAF Interagency Propulsion Committee (then the Interagency Chemical Rocket Propulsion Group, ICRPG) to study the extent of combustion instability problems in liquid propellant rocket engines and to make recommendations as to their solution. This ad hoc group urged that a more permanent working group be established to promote an integrated research and technology plan, which could provide stability design criteria, and to promote a better exchange of technical information among scientists and engineers interested in combustion instability in liquid propellant rockets. The ICRPG formed a Working Group on Liquid Propellant Combustion Instability in January 1964. Beginning that year, annual conferences have been held by the Working Group. These conferences, the proceedings of which are published promptly in the form of expanded abstracts (with illustrations), have proven to be extremely effective in enhancing the exchange of up-to-date information.

It was recognized from the beginning, however, that much of the theoretical and experimental combustion instability information was scattered in numerous progress reports and technical papers in various journals and conference proceedings. In its first year, the Working Group recommended the preparation of a book that would help to train new workers in the field, as well as providing a reference for others. In 1964 a reference book committee was appointed by the Working Group to outline the content. At the 1965 Working Group meeting, the committee presented its recommended reference book outline, and means of implementing the writing and publication of the book were discussed. Further deliberations by the committee during 1966 resulted in the recommendation that a prime contract be given to a general editor, someone well acquainted with the combustion instability field, who could subcontract the variety of subject matter to a number of specialized authors. This recommendation was adopted by the Working Group; work was initiated in 1967 under a NASA contract with Princeton University, with Richard J. Priem, of the NASA-Lewis Research Center, as contract monitor. Funds for the contract were provided by NASA, the Air Force, the Army, and the Navy. The excellence of the work done by the Reference Book Committee is evidenced by the fact that their suggested outline has been rather closely followed.

It is hoped that this reference book will prove to be useful to all workers in the liquid propellant combustion instability field, whether they are engaged in research, design, or development. The philosophy followed in compiling this book is that the prime importance is to provide the main outline of the most significant developments, both theoretical and experimental, with emphasis on fundamental principles and relationships between alternative approaches. For detailed information, the reader is supplied with an extensive list of references, which should help guard against rapid obsolescence of the reference book, a danger faced by any text in a fast-developing field.

There are four main parts to the book: (1) background information, including an introduction to the phenomenon of combustion instability and a discussion of pertinent aspects of the combustion and flow processes that take place in a liquid propellant rocket engine (Chs. 1 to 3), (2) analytical models of both low and high frequency instability, with the theoretical basis of each model given first and the use of the models in design and development following in a separate chapter (Chs. 4 to 6), (3) a practical guide for designers, including aspects of excitation and damping, with experiential information integrated as much as possible with the results of theoretical studies (Chs. 7 and 8), and (4) experimental aspects of the study of combustion instability, that is, techniques used to identify and investigate oscillatory processes in both research and developmental hardware, and methods of rating the stability of a given engine (Chs. 9 and 10).

The reference book is designed to allow the reader to *quickly* look up information on combustion instability and related topics. The detailed index provided by the authors and editors as well as the extensive table of contents should greatly aid the reader in this respect. The General Nomenclature, supplemented by specialized nomenclature when required, should provide the required information to interpret the equations accurately. Each equation, figure, and table is uniquely numbered by section to avoid confusion.

We are greatly indebted to the many authors and reviewers (whose names are listed elsewhere in the book) for the generally high quality of their manuscripts and their cooperativeness during the editorial process. Special thanks go to Robert J. Hefner and L. Paul Combs, who took responsibility for compiling Chapters 9 and 10, respectively, and to Owen W. Dykema, who edited Section 7.4.

The Editors

David T. Harrje
Frederick H. Reardon

CONTENTS

CHAPTER PAGE

CHAPTER PAGE

CHAPTER PAGE

EDITORS, AUTHORS, AND REVIEWERS

Abbe, Charles J. Captain, USAF Formerly: Senior Project Engineer Air Force Rocket Propulsion Lab.	Contributor, Sects. 6.4.3, 7.4.2, and 7.4.3 Reviewer, Chapter 4
Agosta, Vito D. Professor of Aerospace Engineering Aerospace Engineering and Applied Mechanics Polytechnic Institute of Brooklyn	Author, Sects. 3.5.2.1 to 3.5.2.3
Bastress, E. Karl Director, Applied Sciences Group Northern Research and Engineering Corp.	Author, Sects. 4.4.2 and 6.6
Bickford, Landis L. Supervisor, Control Dynamics Aerojet Liquid Rocket Company	Author, Sects. 5.5.3, 6.2.3.4, 7.5.2, and 7.5.3
Bloomer, Harry E. Aerospace Engineer V/STOL and Noise Division NASA-Lewis Research Center	Author, Sect. 10.3
Bracco, Frediano V. Member of the Research Staff Dept. of Aerospace and Mechanical Sciences Princeton University	Author, Sect. 7.2.4 Reviewer, Chapter 4
Breen, Ben P. Vice President KVB Engineering	Contributor, Sect. 6.4.3
Burge, Harland L. Manager, Applied Technology Dept. TRW Systems	Contributor, Sect. 7.4.5
Campbell, David T. Manager, Propulsion Technology Advanced Programs Rocketdyne	Contributor, Sects. 4.3.1 and 6.4.1 to 6.4.3 Reviewer, Chapter 2
Campbell, John, Jr. Manager, Production Thrust Chamber Unit Engineering Dept. Rocketdyne	Contributor, Sect. 7.4.4

Carpenter, Thomas W. Assistant Professor Aeronautical Dept. California State Polytechnic College	Reviewer, Chapter 2
Chew, Thomas J. C. Senior Project Engineer Air Force Rocket Propulsion Laboratory	Reviewer, Chapter 10
Clayton, Richard M. Member of the Technical Staff Liquid Propulsion Section Jet Propulsion Laboratory	Author, Sect. 7.2.6 Contributor, Sect. 7.6 Reviewer, Chapter 10
Clinger, Eugene C. Engineering Manager Liquid Rocket Division Rocketdyne	Contributor, Sect. 7.4.3
Combs, L. Paul Member of the Technical Staff Advanced Programs Rocketdyne	Editor, Chapter 10 Author, Sects. 10.1 to 10.4 and 10.7 Reviewer, Chapter 9
Coultas, Thomas A. Program Manager Combustion and Materials Technology Advanced Programs Rocketdyne	Author, Sects. 1.2.1 to 1.2.3, 7.2.3, 8.3.6, 8.5.3, 9.2.2, 9.4.1, 9.4.2, and 9.4.3.2
Crocco, Luigi Robert H. Goddard Professor of Aerospace Propulsion Aerospace and Mechanical Sciences Dept. Princeton University	Author, Sects. 4.2 and 5.3.2
Culick, Fred E. C. Associate Professor of Engineering Mechanical Engineering Dept. California Institute of Technology	Author, Sect. 4.5
Dobbins, Richard A. Professor of Engineering Division of Engineering Brown University	Author, Sect. 8.5.2
Dykema, Owen W. Member of the Technical Staff Applied Mechanics Division The Aerospace Corporation	Editor, Section 7.4 Author, Sects. 1.2.4, 4.4.1.3, 6.5.2, 7.4, 7.4.1, and 7.4.6 Reviewer, Chapter 3
Erbs, Joseph E. Project Engineer, Lance Liquid Rocket Division Rocketdyne	Reviewer, Chapter 7

Faeth, Gerard M. Associate Professor Mechanical Engineering Dept. Pennsylvania State University	Reviewer, Chapter 2
Fairchild, David A. Engineering Manager, Mechanical Design Aerojet Liquid Rocket Co.	Author, Sect. 10.5
Feiler, Charles E. Head, Acoustics Section V/STOL and Noise Division NASA-Lewis Research Center	Author, Sects. 4.4.1.2 and 6.5.1
Fenwick, James R. Member of the Technical Staff Liquid Rocket Division Rocketdyne	Author, Sects. 3.2, 5.4.3, and 7.5.1 Contributor, Sect. 3.3.1
Ford, Wayne M. Member of the Technical Staff Advanced Programs Rocketdyne	Author, Sects. 9.4.1 and 9.6.4
Garrison, Gary D. Assistant Project Engineer Florida Research and Development Center Pratt and Whitney Aircraft Co.	Author, Sects. 8.3.4 and 8.3.5
Goelz, Ralph R. Aerospace Engineer Chemical Rocket Division NASA-Lewis Research Center	Contributor, Sect. 8.5.1
Groeneweg, John F. Aerospace Engineer V/STOL and Noise Division NASA-Lewis Research Center	Author, Sect. 2.2.4
Hammer, Sandford S. Associate Professor Engineering Sciences Dept. Hofstra University	Reviewer, Chapter 4
Harris, George H. Operations Research Analyst Management Sciences Division Arthur D. Little, Inc.	Author, Sects. 4.4.2 and 6.6
Harrje, David T. Senior Research Engineer and Lecturer Dept. of Aerospace and Mechanical Sciences Princeton University	Editor, Reference Book Editor, Chapters 1, 2, 7, and 8 Author, Sects. 1.3, 1.4, 3.3.1, 3.3.2, 7.1, 7.2.4, 8.5.1, 10.3, and 10.6.2 to 10.6.4 Contributor, Sects. 7.4.2 and 7.4.3

Hefner, Robert J. Director of Engineering Consumer Products Group Bell and Howell Company Formerly: Manager, Combustion Dynamics Dept. Liquid Rocket Operations Aerojet-General Corp.	Editor, Chapter 9 Author, Sects. 9.1, 9.2.1, 9.2.3, 9.3.3, 9.3.5, 9.4.1, 9.6.1, 9.6.2, 9.7.1, 10.2, 10.3, and 10.7 Contributor, Sect. 8.5.1 Reviewer, Chapter 10
Heidmann, Marcus F. Research Scientist Chemical Rocket Division NASA-Lewis Research Center	Author, Sects. 4.4.1.2, 6.5.1, and 10.4 Reviewer, Chapter 7
Hewitt, Ross A. Engineering Specialist Combustion Dynamics Dept. Aerojet Liquid Rocket Company	Reviewer, Chapter 3
Howells, Edgar Senior Engineer Research and Development McGraw-Edison Power Systems Division Formerly: Member of the Combustion Devices Group Bell Aerospace Company	Author, Sect. 9.5
Kesselring, Robert C. Member of the Technical Staff Advanced Programs Rocketdyne	Author, Sects. 9.2.2, 9.4.2, 9.4.4.1, and 9.4.4.3
Kosvic, Thomas C. Test Engineer KVB Engineering	Contributor, Sect. 4.3.2
Lazar, Robert S. Project Engineer Naval Underwater Systems Center	Reviewer, Chapter 1
Leeper, Charles K. Assistant General Manager Research and Engineering Aerojet Nuclear Company	Author, Sects. 4.4.1.4 and 6.5.3
Levine, Robert S. Staff Scientist Space Technology Division NASA—Langley Research Center	Reviewer, Chapter 1
Lewis, J. Dudley Superintendent, Liquid Engines Division Rocket Propulsion Establishment Great Britain	Author, Sects. 2.3.3 and 2.3.4

Lovingham, Joseph J. Director of Engineering The McIntire Company Formerly: Chief, Systems Engineering Reaction Motors Division Thiokol Chemical Corporation	Contributor, Sect. 7.4.5
Lytle, Archie D. Principal Engineer Bell Aerospace Company	Author, Sect. 5.6
Masters, Arthur I. Senior Assistant Project Engineer Florida Research and Development Center Pratt & Whitney Aircraft Company	Contributor, Sect. 7.4.4
Matthews, Birch J. Member of the Technical Staff TRW Systems	Author, Sect. 9.4.5
McBride, James M. Supervisor Combustion Dynamics Aerojet Liquid Rocket Company	Author, Sects. 8.2.2 and 8.2.3 Contributor, Sect. 7.4.2
Miller, Irwin Senior Staff Manager Management Sciences Division A. D. Little Co.	Author, Sects. 4.4.2 and 6.6
Miller, Joseph Manager, Propulsion Systems Engineering Dept. TRW Systems	Reviewer, Chapter 5
Mitchell, Charles E. Assistant Professor Dept. of Mechanical Engineering Colorado State University	Reviewer, Chapter 7
Monteil, Vernon H. Manager, Booster Propulsion Applied Mechanics Division The Aerospace Corporation	Author, Sect. 1.2.4
Morgan, C. Joe Aerospace Engineer Chemical Rocket Division NASA-Lewis Research Center	Reviewer, Chapter 8
Nestlerode, James A. Member of the Technical Staff Liquid Rocket Division Rocketdyne	Author, Sects. 3.2, 5.4.3, and 7.5.1 Contributor, Sect. 3.3.1 Reviewer, Chapter 6

Nicholls, J. A. Professor Dept. of Aerospace Engineering The University of Michigan	Author, Sects. 3.3.3, 3.4.3.2, and 3.4.4.3
Oberg, Carl L. Manager, Combustion Advanced Programs Rocketdyne	Author, Sects. 8.3.6 and 8.5.3
Osborn, John R. Professor of Mechanical Engineering Purdue University	Author, Sect. 7.2.5 Reviewer, Chapter 9
Phillips, Bert R. Aerospace Engineer Chemical Rocket Division NASA-Lewis Research Center	Author, Sects. 8.3.2 and 8.3.3
Powell, Walter B. Member of the Technical Staff Liquid Propulsion Section Jet Propulsion Laboratory	Author, Sect. 1.1.3
Priem, Richard J. Head, Rocket Combustion Section Chemical Rocket Division NASA-Lewis Research Center	Contract Monitor on Reference Book Author, Sects. 4.3, 6.4, and 6.7
Proffitt, Robert L. Principal Scientist, Mechanics and Optics Research Division Rocketdyne	Author, Sect. 9.4.3.2
Ranger, Arthur A. Assistant Professor School of Aeronautics, Astronautics, and Engineering Sciences Purdue University	Reviewer, Chapter 3
Reardon, Frederick H. Associate Professor of Mechanical Engineering Sacramento State College	Associate Editor, Reference Book Editor, Chapters 3, 4, 5, 6 Author, Sects. 3.3.1, 3.3.2, 3.4.4.1, 3.4.4.2, 3.5.3.3, 5.1, 5.2, 5.3.1, 5.4.1, 5.4.2, 5.5.1, 5.5.2, 6.1, 6.3, 6.7, 7.3, and 8.2.1
Rice, Edward J. Aerospace Engineer V/STOL and Noise Division NASA-Lewis Research Center	Author, Sect. 2.2.3

Richmond, Robert J. Technical Assistant Propulsion and Power Branch Astronautics Laboratory Marshall Space Flight Center	Author, Sects. 1.1.1 and 1.1.2
Rogero, Steve Senior Research Engineer Instrumentation Section Jet Propulsion Laboratory	Author, Sect. 9.3.3
Rosner, Daniel E. Associate Professor Dept. of Engineering and Applied Science Yale University and Consultant to Aerochem Research Laboratories	Author, Sect. 2.4
Rupe, Jack H. Research Group Supervisor Liquid Propulsion Section Jet Propulsion Laboratory	Author, Sects. 2.2.1, 2.3.1, and 2.3.2
Sack, Larry E. Member of the Technical Staff Liquid Rocket Division Rocketdyne	Author, Sects. 3.2, 5.4.3, and 7.5.1 Contributor, Sect. 3.3.1
Sanscrainte, Willard A. Technical Director of Advanced Agena Rocket Engines Bell Aerospace Company	Reviewer, Chapter 9
Senneff, John M. Assistant Chief Engineer Combustion Devices Bell Aerospace Company	Author, Sects. 8.3.6 and 10.2 Contributor, Sects. 7.4.2 and 8.5.1 Reviewer, Chapter 8
Sirignano, William A. Associate Professor Dept. of Aerospace and Mechanical Sciences Princeton University	Author, Sects. 3.5.1, 3.5.2.4, 3.5.3.1, 3.5.3.2, 3.6, 4.1, 8.1, and 8.4.1 Reviewer, Chapter 8
Smith, Allan J. Jr. Research Engineer Georgia Institute of Technology Formerly: Design Engineer Aerojet-General Corp.	Author, Sects. 7.2.1 and 8.4.4 Contributor, Sects. 7.4.2 and 7.6 Reviewer, Chapter 6
Sokolowski, Daniel E. Aerospace Engineer Chemical Rocket Division NASA-Lewis Research Center	Author, Sect. 10.6.1 Reviewer, Chapter 5

Strahle, Warren C. Associate Professor of Aerospace Engineering Georgia Institute of Technology Formerly: Member of the Professional Staff Science and Technology Division Institute for Defense Analyses	Author, Sects. 3.1, 3.4.1, 3.4.2, and 3.4.3.1 Reviewer, Chapter 4
Szuch, John R. Project Engineer Advanced Systems Division NASA-Lewis Research Center	Author, Sects. 5.2, 5.5.1, 5.5.2, 5.6, 6.2.1, 6.2.2, 6.2.3.1 to 6.2.3.3, and 6.2.4
Thibodaux, Joseph G. Jr. Chief, Propulsion and Power Division NASA-Manned Spacecraft Center	Reviewer, Chapter 1
Tonon, Thomas S. NASA Fellow Dept. of Aerospace and Mechanical Sciences Princeton University	Author, Sects. 8.3.1.2 and 8.3.1.3
Valentine, Ralph S. Director, Engineering Research Dept. Atlantic Research Corporation	Author, Sects. 2.5 and 9.6.3
Van Huff, Norman E. Manager, Design and Analysis Dept. Engineering Aerojet Liquid Rocket Company	Author, Sect. 9.6.5
Van Wyk, Rod Manager, System Analysis Section Winchester Group Research Olin Corporation	Contributor, Sect. 4.3.2
Varma, Ashok K. Guggenheim Fellow Dept. of Aerospace and Mechanical Sciences Princeton University	Author, Sect. 8.4.5 Reviewer, Chapter 6
Vincent, Joseph Member of the Technical Staff Liquid Rocket Division Rocketdyne	Author, Sect. 10.5
Wanhainen, John P. Aerospace Engineer Chemical Rocket Division NASA-Lewis Research Center	Author, Sect. 8.4.2 Contributor, Sect. 7.4.4
Waugh, Richard C. Engineering Specialist Combustion Dynamics Dept. Aerojet Liquid Rocket Co.	Reviewer, Chapter 5

Wesley, Robert D.
Section Supervisor, Experimental Instrumentation
Aerojet Nuclear Company

Author, Sects. 9.3.1 to 9.3.5, 9.4.3.1, 9.4.3.3, and 9.6.1

Wieber, Paul R.
Aerospace Research Engineer
Physics and Chemistry Division
NASA-Lewis Research Center

Author, Sect. 9.6.6

Williams, Forman A.
Professor of Aerospace Engineering
Dept. of Aerospace and Mechanical Engineering Sciences
University of California, San Diego

Author, Sect. 2.1

Wood, Leroy M.
Research Engineer
Propellants and Combustion Technology
Bell Aerospace Company

Author, Sect. 9.4.4.2

Wuerker, Ralph F.
Member of the Technical Staff
TRW Systems

Author, Sect. 9.4.5

Zinn, Ben T.
Professor of Aerospace Engineering
Georgia Institute of Technology

Author, Sects. 7.2.2, 8.3.1, 8.3.1.1, and 8.4.3

CHAPTER 1

Introduction

The subject of this reference book is combustion instability as associated with liquid propellant rocket engines. Before the details of unstable combustion can be properly discussed, however, the reader should have some knowledge of the liquid rocket engine systems involved, and the associated performance parameters, as well as the combustion instability phenomenon itself. An understanding and knowledge of the past accomplishments and the present status of the problem should also prove helpful. It is the purpose of this introductory chapter to meet these needs.

Subsequent chapters will treat much of this introductory material in far greater detail—exploring the mechanisms of instability, mathematical approaches for solutions of specific problems, application of solutions to actual engines, experimental measurements, and stability rating techniques to name only a few of the subject areas discussed at length. However, other portions of this chapter, such as the engine systems and performance parameters, will not be treated again but will be only referenced. Even with the material that is discussed later, the emphasis given by each author to what he deems to be the most important aspects of the subject most likely will receive a somewhat different emphasis in the chapters that follow. For this reason, the reader with a particular need should evaluate the overall assessments discussed here with the more specific information that follows in the subsequent chapters.

1.1 LIQUID ROCKET ENGINE SYSTEMS

1.1.1 Conventional Engines*

Liquid rocket engine systems can be classified into two broad categories, pressure-fed and pump-fed. In general, these systems are not used interchangeably for the same application. Pressure-fed designs are preferred for reaction control and space propulsion systems where thrust and chamber pressure are low and where emphasis is on simplicity for multiple restart capability. Pump-fed engines are used for high thrust, high chamber pressure applications typical of the booster and upper stages of launch vehicles where long durations are common. The propellant tanks, although large, can be kept light because their strength must provide only for structural rigidity and a pressure sufficient to provide the proper net positive suction head (NPSH) to the pump. The more complex start transient can be tolerated because of a limited necessity for restarting the engine.

Although there are numerous possible propellant combinations,[483] three are basic to conventional engines in current use. They are classified as earth storable, cryogenic and cryogenic-storable. *Earth storable* implies that the propellant is in the liquid state at standard conditions of temperature and pressure. Propellants which are gases at standard conditions, but through chilling have been liquified, are known as *cryogenic* propellants. Insulated containers are required for their storage and unless cooling is provided, boiloff losses are inevitable. *Cryogenic-storable* combinations consist of one cryogenic and one storable propellant.

The common storable combination consists of nitrogen tetroxide for the oxidizer and a blend of 50 percent hydrazine and 50 percent unsymmetrical dimethylhydrazine (UDMH) for the fuel (the blended fuel is known as 50–50, or Aerozine 50 and will be referred to as A-50). Monomethylhydrazine (MMH) is sometimes substituted for the A-50. These storable com-

* R. J. Richmond, Author.

binations are hypergolic (i.e., combustion occurs from a spontaneous reaction as the propellants come in contact) and thus find wide application in space propulsion systems where restarts are necessary. Apollo spacecraft use a number of rocket engines that employ these propellant combinations in pressure-fed systems. Military pump-fed systems also use storables based on "instant readiness" (no last minute tank filling as would be required with cryogenics because of boiloff losses).

Currently, the most widely used cryogenic combination consists of liquid oxygen for the oxidizer and liquid hydrogen for the fuel. This combination requires an ignition source such as a spark arrangement. The performance of this propellant combination is the highest of those under discussion. A typical engine using these propellants is the pump-fed J-2 engine on the Apollo V system. Long term storage of liquid hydrogen requires special insulation and careful design because of the low temperatures involved (−423.3° F).

The cryogenic-storable combination in wide use is liquid oxygen and RP-1 (a fine cut of kerosene). This combination is used in a number of booster engines—typical is the pump-fed F-1 engine of the Apollo V launch vehicle. The propellant combination provides good performance combined with extremely low cost. Ignition is accomplished by igniter fluids such as triethylaluminum (TEA or TEAL), triethylborane (TEB), or mixtures (TEA/TEB) which are hypergolic with the oxygen.

In future space engines another propellant classification is becoming more prominent. Known as *space-storables*, these propellants are cryogenics which under the space environment may be stored for sufficient periods to fill the role of current earth storables but with added performance potential. Some typical examples are the light hydrocarbon fuels such as methane used with fluorinated oxidizers (FLOX or OF_2).

Common to conventional engines in current use is a thrust chamber assembly (TCA) as shown in Fig. 1.1.1a. The typical components are labeled and include the injector (which contains fuel and oxidizer orifices to introduce the propellants into the chamber), the manifolds for the propellants, the combustion chamber where the propellants are reacted and which extends to the inlet of the de Laval nozzle (combustion instability occurs within the combustion chamber), combustion instability damping devices such as the baffle and acoustic liner, and the de Laval nozzle which converts the thermal energy of the heated combustion products to kinetic energy of the exhaust jet.

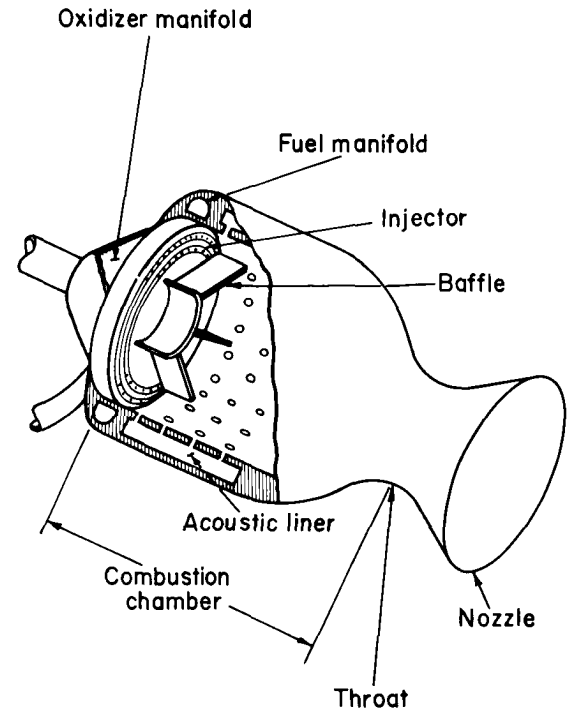

FIGURE 1.1.1a.—Typical components of a thrust chamber assembly.

1.1.1.1 Pressure-fed engines.—The thrust levels of pressure-fed engines in current use range from about 5 to 22,000 pounds. Their propellant flow systems are extremely simple. Basic components consist of a propellant valve, injector, combustion chamber, and nozzle. The propellant valve admits the propellant to the combustion chamber through the injector which mixes and atomizes the propellant prior to reaction. The shape of the combustion chamber is normally a right circular cylinder to which is attached a converging-diverging nozzle (de Laval type). A typical schematic of a pressure-fed engine is shown in Fig. 1.1.1b. This represents the Apollo Service Propulsion System (SPS) which is used to propel

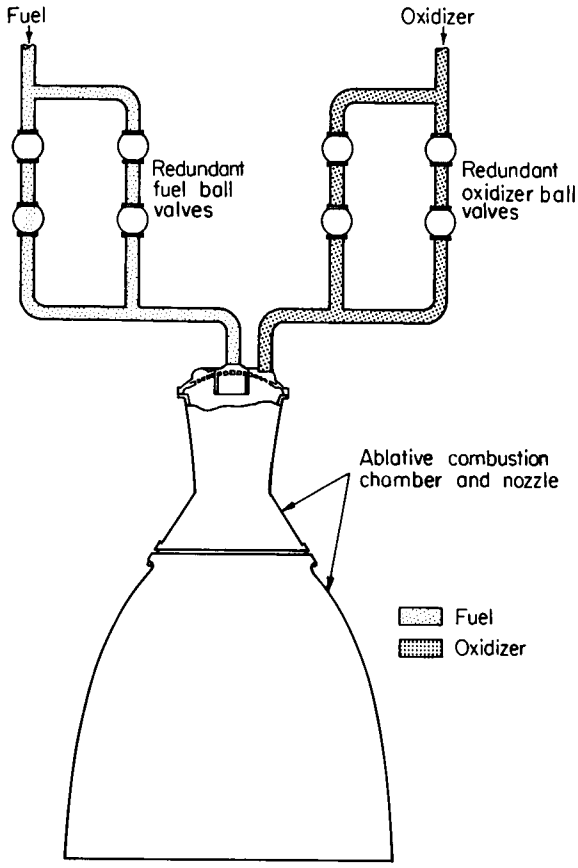

FIGURE 1.1.1b.—Service propulsion system propellant flow schematic.

the command and lunar modules into lunar orbit and the command module back to earth.

The feed system for supplying propellant to the engine consists of the propellant tanks, feed lines, and prevalves in the propellant lines (the latter are usually located at the base of the tank for positive containment of the propellant prior to engine start). It is common for the inlet of the main propellant valve to be considered the feed system–engine interface. The propellants are forced from the propellant tanks into the combustion chamber by means of gas pressure in the tank ullage space above the liquid propellant surface. There are several methods for providing this pressurizing gas; however, the most common is the stored gas technique using helium in high pressure vessels. Pressurizing gas is admitted to the propellant tank ullage space through a line containing a number of pressure regulators and valves. Since the thrust level is directly proportional to the ullage pressure for pressure-fed systems, sophisticated pressure control is required to achieve and maintain the desired thrust. In contrast, the thrust level of pump-fed systems is insensitive to normal tolerances in tank pressure. (See Ref. 593, pp. 173–263 for a detailed discussion of pressurization systems.)

Since the propellant tanks must contain pressure equal to the chamber pressure, the total pressure losses in the flow system and the dynamic head associated with the propellant injection velocity, they must be of rather heavy construction compared to tanks for pump-fed systems. Therefore, pressure-fed systems are attractive for low chamber pressure applications. Typical of such chamber pressures is the current range from about 100 to 120 psia. With respect to weight, as chamber pressure is increased beyond this range, pump-fed systems become more attractive. In order to minimize tank weight, great emphasis is placed on minimizing the pressure drop across the feed line, propellant valve, and injector. A further reduction in tank pressure is realized by substituting ablative combustion chambers and nozzles for regeneratively cooled components, thereby avoiding the pressure drop associated with the regenerative cooling passages.

Pressure-fed systems, as any other rocket engine system, are susceptible to combustion instability of the low, intermediate or high frequency types. The various forms of instability are discussed in Sect. 1.2. It is sufficient to remark here that if pressure-fed systems seek to minimize tank weight via reductions of pressure drop, specifically, the injector pressure drop, then low frequency instability becomes a particular problem. Here the coupling is between the feed system and the combustion process in the engine. More will be said on this subject in subsequent chapters.

1.1.1.2 Pump-fed engines.—Pump-fed engines are used for high thrust, high chamber pressure applications. Those in current use have thrust levels ranging from about 16,000 to 1,500,000 pounds at chamber pressures from about 300 to 1000 psia. The systems contain the same components as the pressure-fed designs plus turbo-

pump and gas generator subsystems for pumping the propellant into the combustion chamber. The typical pump-fed system operates on the high pressure ratio, low mass flow parallel* turbine cycle. The engine-feed system interface is at the turbopump inlet flanges.

In the feed system portion of the design, one important consideration is to minimize the tank weight. The tank must be strong enough to provide only structural rigidity and pressure sufficient to maintain the required NPSH; the latter factor is important in pump design and considerable effort is devoted to minimizing NPSH during engine development. In some cases effort has been so successful in this regard that structural, rather than pressure considerations, govern the tank weight.

The turbopump subsystem (which is considered part of the engine) consists of two pumps (usually centrifugal), a turbine, and in some cases a gearbox (now considered obsolete) mated together to form a complete unit. The energy to drive the turbine is supplied by the gas generator subsystem consisting of a propellant valve, injector and combustion chamber. Propellant is tapped from the turbopump discharge lines, injected into the combustor through the gas generator injector, chemically reacted and converted to gas. The gas is expanded through the turbine which drives the pumps. Since the operating temperature limit of current turbine materials is about 1500° F, the gas generator is operated with excess fuel to avoid exceeding this limit. A schematic of the F-1 engine, a typical pump-fed system is shown in Fig. 1.1.1c.

Since the gas generator is a combustion device, similar in some respects to the main combustor and with many of the same inherent combustion problems, a brief discussion is warranted here. The valve which controls the flow to the combustor is normally mounted on the injector which in turn is mounted on the combustor body. This assembly is mounted directly on the turbine manifold by means of a short duct. Since the gas generator must provide gases at low temperature to be compatible with the turbine, cooling of the combustor body is not required. The gas generator has no throat; however, the turbine nozzles through which the gas is injected into the turbine normally operate in a choked condition. Therefore, the gas generator, turbine manifold, and nozzle assembly can be treated by the same analytical methods as the main combustion chamber.

Ideally, the gas generator should supply a completely reacted gas of uniform temperature to the turbine. Combustion must be stable to avoid vibration and pressure oscillations. Uniform temperature is necessary to avoid local hot spots which could overheat regions of the combustor body or the turbine manifold. A completely reacted gas at the turbine manifold inlet is necessary for efficient turbine operation. If the gas is not completely reacted at that point, the reaction continues with rising temperatures as the gas travels through the manifold. This is known as gas generator "afterburning." The gas that travels the farthest before entering the nozzles is usually the hottest while that which enters the nozzles almost immediately is the coolest. This results in the turbine operating at a lower average temperature than necessary. The injector has the largest effect on the uniformity and degree of reaction attained, but the configuration of the combustor body also is influential. The volume of the combustor body must be large enough to provide adequate stay-time for the reaction to be completed. In order to minimize the stay-time and hence combustor size, mixing is enhanced mechanically by using L-shaped combustor bodies along with choke rings and screens. Afterburning problems have been experienced primarily with the LOX/RP-1 propellant combination. (See Ref. 593, pp. 273–304 for a more detailed discussion of pump-fed systems.)

The main chamber and gas generator are susceptible to the same types of combustion instability mentioned in connection with the pressure-fed systems. Low frequency instability or chugging can occur when the combustion dynamics are in resonance with the engine-feed system dynamics. Normally the feed system upstream of the pumps is not considered in the analysis of chugging because of the isolation due to the pumps. However, recent evidence has become available which shows that this is not necessarily the case. Consequently, pump-fed engines

* The word "parallel" refers to the fact that in this cycle the turbine is in parallel with the main combustion chamber.

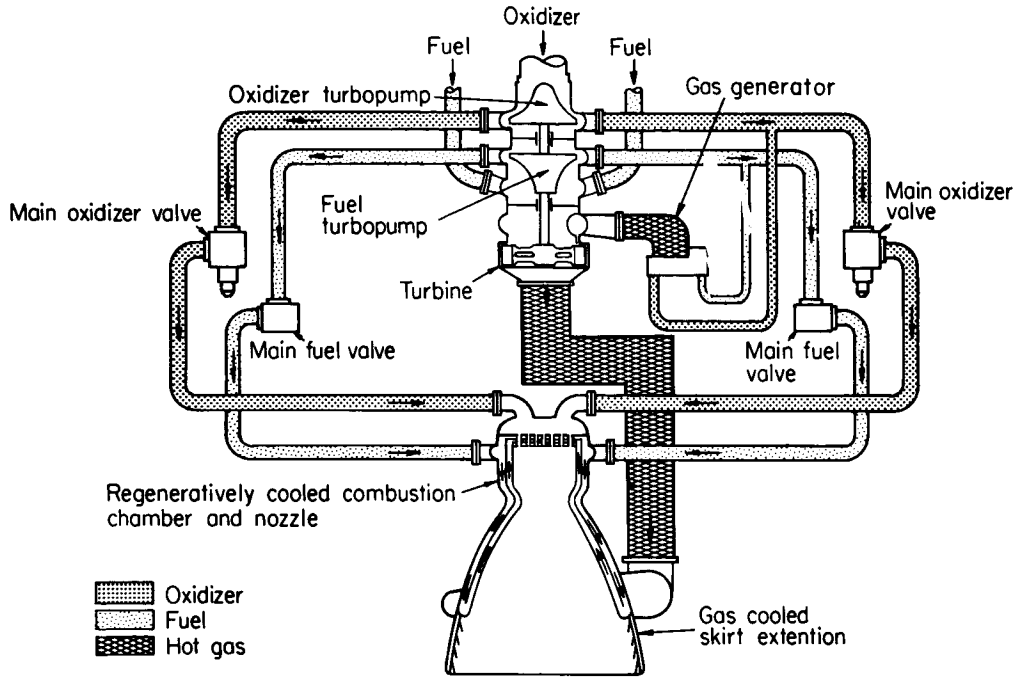

FIGURE 1.1.1c.—F-1 engine propellant schematic.

as well as pressure-fed engines must be considered in combination with their ultimate feed systems before their low frequency stability can be assessed. The combustion process could also couple with the blade wake frequency of the turbopumps. However, this rarely occurs because the blade wake frequency usually is not matched to either the low or high frequency dynamics of the combustion process. The blade wake frequency refers to the pressure pulses present in the engine feed lines due to the turbopump impellers and is defined as the product of the pump speed and the number of impeller blades. High frequency or acoustic instability can also occur.

1.1.2 Advanced Engines

The preceding section discussed the two basic conventional engine systems. This section presents two advanced systems being considered for future applications. These are the aerospike and staged combustion systems. These systems, as well as the conventional pump-fed systems, operate on two basic power cycles which can be categorized in terms of the turbine used. These are the high pressure ratio, low mass flow, parallel turbine and the low pressure ratio, high mass flow, series* turbine cycles. There are several variations of these two cycles.[395] The conventional pump-fed system discussed previously is an example of a high pressure ratio, low mass flow, parallel turbine cycle. A variation of this is the so called tap-off cycle which taps gas from the main combustion chamber to drive the turbine, thus eliminating the gas generator subsystem.

1.1.2.1 Aerospike engine.—One advanced engine concept under investigation is the toroidal aerodynamic spike or simply aerospike engine.[3] A schematic of a possible system designed to operate at 1500 psia chamber pressure is shown in Fig. 1.1.2a. Gas tapped from the main combustion chamber drives high pressure ratio, low mass flow, parallel turbines which puts this engine in the same general cycle class as the conventional engine. The aerospike differs from the conventional engine in the configuration of the nozzle and combustion chamber. The combustion

* The series turbine cycle uses a turbine in series with the main combustion chamber.

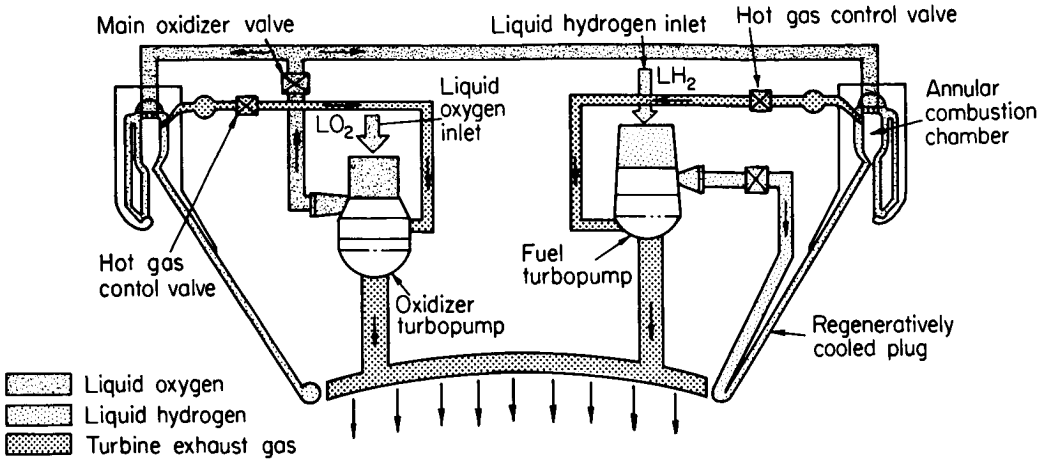

FIGURE 1.1.2a.—Aerodynamic spike engine propellant flow schematic.

chamber is toroidal in shape, rather than cylindrical, and instead of a conventional bell nozzle, the combustion chamber discharges the exhaust gases onto a regeneratively cooled, truncated plug nozzle. The turbine drive gases, after expanding through the turbine, are discharged through the base of the plug to increase the base pressure and nozzle performance.

The advantages of the aerospike engine are that the nozzle provides continuous optimum expansion to the local ambient pressure throughout its trajectory. The outer boundary of the exhaust jet is a freely expanding jet which adjusts to the ambient pressure field. This results in a higher total integrated impulse over the vehicle flight path. In addition, the combination of the toroidal combustor and the aerodynamic spike nozzle results in a compact short-length engine. Additional discussion of the aerospike engine is presented in Ref. 368, pp. 10–15.

The aerospike engine is susceptible to the same types of combustion instability as the engines previously discussed. In addition to the low and high frequency instability encountered in conventional systems, the aerospike engine by virtue of the long path around its annular combustion chamber can encounter acoustic instability at frequencies low enough to couple with the feed system. This is sometimes referred to as the "racetrack" mode. It is similar to the coupling of acoustic modes with the feed system of large conventional engines. In practice this may not be a serious problem because structural requirements probably will result in circumferential partitioning of the combustion chamber. Therefore, each partitioned section might act as an individual combustion chamber whose dimensions would not permit acoustic frequencies low enough to couple with the feed system.

1.1.2.2 Staged combustion engine.— Another advanced engine concept being investigated for future application is the staged-combustion system[68,69] employing a conventional bell nozzle with an extendible skirt. The skirt is extended at upper altitude to improve the nozzle performance. This engine operates on the cycle which uses the low pressure ratio, high mass flow series turbine. This is sometimes called the staged-combustion topping cycle. A schematic of a proposed system is shown in Fig. 1.1.2b. This system differs from the conventional system in both cycle and configuration. The engine consists of a primary combustion chamber, turbopump and turbine assembly, secondary combustion chamber and bell nozzle with skirt. The total fuel used by the engine is pumped into the primary combustion chamber where it is combined with a small fraction of the oxidizer to produce a low temperature (1500° F) fuel-rich gas. This gas is then expanded through a low pressure ratio, high mass flow turbine which drives the turbopumps. It leaves the turbine and enters the secondary combustor where it is combined with the remaining oxidizer at the optimum mixture ratio prior to expansion through the bell nozzle.

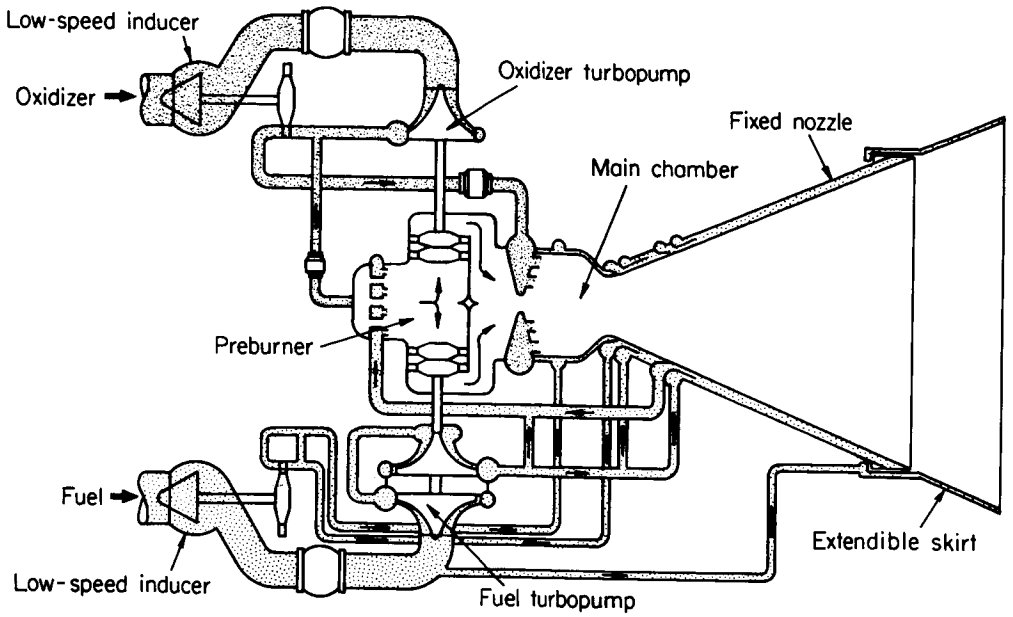

FIGURE 1.1.2b.—Staged combustion engine propellant flow schematic.

Staged combustion systems currently under consideration operate at chamber pressures up to 6000 psi for the primary combustor and at 3000 psi and above for the secondary combustor. Due to these high pressures, regenerative cooling of the secondary combustion chamber and throat requires special consideration. To accomplish this, combustion chambers must be constructed from materials with thermal conductivities much higher than those in current use. Transpiration cooling, a technique of passing a controlled amount of fuel through the chamber walls, is an alternate cooling technique. It is not as desirable as regenerative cooling because of the performance loss associated with poor combustion of the cooling fuel after it enters the combustion chamber. Transpiration cooling, therefore, would be used only in the critical areas of the throat and combustion chamber. The major portion of the nozzle downstream of the throat where the heat flux is lower would be regeneratively cooled as is the current practice.

The advantages of the staged combustion system are that its cycle is more efficient than the high pressure ratio, low mass flow parallel turbine cycle because all the propellant which drives the turbines is ultimately burned at optimum mixture ratio and expanded through the nozzle. The high chamber pressure permits increased specific impulse because larger nozzle expansion ratios can be used without corresponding increases in the physical size of the nozzle exit. The extendible skirt improves the performance further (at altitude) by providing additional expansion ratio.

Combustion instability can also occur in staged combustion systems. Both the primary and secondary combustors can encounter high and low frequency combustion instability. In addition, complex interactions can occur between the primary and secondary combustors, the primary combustor and the feed system, and the secondary combustor and the oxidizer feed system.

1.1.3 Performance Parameters*

The following nomenclature pertains to Sect. 1.1.3:

F	Thrust
g_c	Gravitational constant
r	Nozzle radius (perpendicular to axis)
α	Streamline angle, measured from axis
δ^*	Boundary-layer displacement thickness

* W. B. Powell, Author.

η_{ER} Energy-release efficiency,

$$\frac{I_{sp} \text{ with actual energy release}}{I_{sp} \text{ with } 100\% \text{ energy release}}$$

θ^* Boundary-layer momentum thickness

Subscripts:

a	Ambient
e	Nozzle exit
o	Stagnation
vac	Vacuum
1, 2, i	Stream tube indexes

Superscript:

( )′	Potential flow nozzle contour

1.1.3.1 External performance parameters.—A rocket motor is characterized to a great extent by the propellant mass flow which it consumes and the thrust which it produces, and, to a lesser extent, by the size, shape, and area ratio of the exhaust nozzle, and by the pressure in the combustion chamber.

The fundamental rocket motor performance parameter is the *vacuum specific impulse* ($I_{sp_{vac}}$), or pounds-force thrust, in a vacuum environment, per pound-mass per second of propellant flow. Vacuum specific impulse completely determines vehicle performance in space flight applications. Further, for a given propellant and nozzle shape, vacuum specific impulse is quite insensitive to small changes in combustion chamber pressure, the size of the rocket motor, the propellant mass flow rate, or the thrust level.

A second rocket thrust chamber parameter, the *characteristic velocity* (c^*), correlates propellant mass flow. Experimental evaluation and correlation of the characteristic velocity requires use of the stagnation pressure in the combustion chamber; this is a quantity which cannot be measured directly, and which in many cases has no single unique value. Thus the characteristic velocity cannot be defined or measured as accurately as can the vacuum specific impulse. However, the characteristic velocity, even with an uncertainty of several percent, can be a useful parameter for sizing propulsion system components. To achieve the required thrust the propellant mass flow rate can typically be adjusted over a larger range than the uncertainty in the characteristic velocity by simple mechanical means, and without any change in the characteristic velocity or the vacuum specific impulse.

The external characteristics and performance parameters of the rocket motor are illustrated and defined in Fig. 1.1.3a, along with an indication of the accuracy which is acceptable in each. Typical values of the vacuum specific impulse and the characteristic velocity can be seen in Table 1.1.3a.

1.1.3.2 Internal processes in rocket thrust chambers.—If the performance of a real rocket motor is to be analyzed and predicted, it is necessary at the start to have a complete inventory of the processes and parameters which influence the performance. Next it is necessary to have realistic and workable analytical models for these processes, and the requisite physical data as input. Finally, it is necessary to combine the treatment of the separate processes so as to consider all the processes and their interactions concurrently. It is not sufficient to calculate the performance of an idealized reference model and then to subtract supposedly linearly independent increments of performance corresponding to the separate recognized sources of loss. It is not sufficient because there are important interactions between

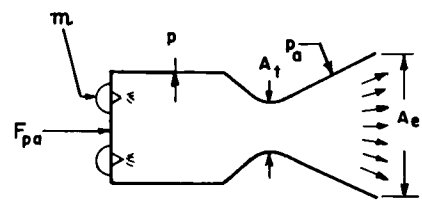

$$F_{vac} = F_{p_a} + p_a A_e$$

$$I_{sp_{vac}} = \frac{F_{vac}}{\dot{m}}, \ (\pm 1/2\ \%)$$

$$c^* = \frac{p_o A_t g_c}{\dot{m}}, \ (\pm 4\ \%)$$

Measured data

F_{pa}

$\dot{m}$

p_a

A_e

A_t

$p \rightarrow p_o$ Approx.

FIGURE 1.1.3a.—External performance characteristics of rocket motor (where the vacuum thrust is F_{vac}).

TABLE 1.1.3a.—EXAMPLES OF PERFORMANCE CORRELATION AND PREDICTION

System	Low area ratio			High area ratio			O/F	c*, ft/sec
	ϵ	$I_{sp_{vac}}$, (lbf-sec)/lbm	η_{ER}	ϵ	$I_{sp_{vac}}$, (lbf-sec)/lbm			
		Experimental			Experimental	Predicted		
F_2/H_2 $P_o=50$ psia $F=1200$ lbf	[a]1.9	343	1.00	[a]60	417	428.7	12.0	7850
$N_2O_4/A-50$ $P_o=100$ psia $F=1000$ lbf	1.0	209.6	.98	[a]60	307	311.6	1.8	5550
$N_2O_4/A-50$ $P_o=105$ psia $F=8000$ lbf	1.0	211.1	.99	[b]40	313.2	316.1	2.0	5310
$N_2O_4/A-50$ $P_o=97$ psia $F=20{,}000$ lbf	1.5	231.3	.97	[b]62.5	313.5	318.4	1.6	5490

[a] 15° Conical nozzle.
[b] Contoured nozzle (or bell nozzle).

the several processes which occur in a real rocket motor.

The internal processes which accompany the production of thrust by a rocket motor are not as evident as are the external characteristics, nor are they as yet completely understood. The principal internal processes in a conventional rocket motor are shown on Fig. 1.1.3b and are listed on Table 1.1.3b. Each of these processes has associated with it a loss in performance (compared to the ideal one-dimensional isentropic equilibrium performance); approximate percentage magnitudes of the loss in specific impulse corresponding to each of the processes are also shown on Table 1.1.3b. While these identified processes are of primary importance in the analysis of steady-state performance of rocket motors, some of them are also known to be important in the analysis and prediction of combustion instability.

A description of the listed liquid propellant rocket motor internal processes and a discussion of their principal interactions follow:

NONUNIFORM MIXTURE RATIO DISTRIBUTION: Propellant is injected into the motor at the upstream end of the combustion chamber. Often a low mixture ratio region is deliberately produced near the wall of the thrust chamber in order to reduce the severity of the environment to which the thrust chamber is exposed. Additionally, the injector propellant manifolding and the orifice pattern may be such that there are variations in both local mixture ratio and local density of mass injection across the face of the injector, superimposed on any deliberately created distribution (see Sect. 2.3).

These propellant mass and mixture ratio distributions are best identified by non-reactive fluid simulant flow tests, wherein the spray down-

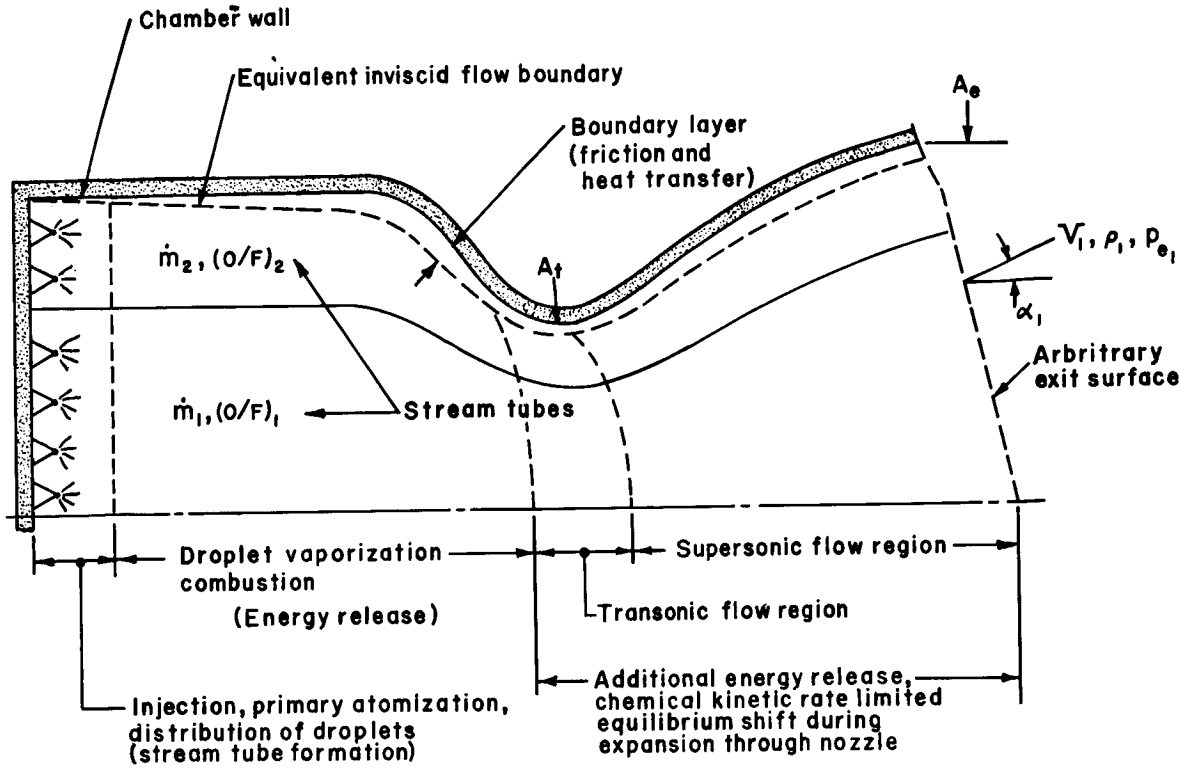

$$F_{vac} = \int_s \dot{m}_i V_i \cos\alpha_i + \int p_{e_i} dA_{e_i}$$

FIGURE 1.1.3b.—Internal processes in the real rocket motor.

stream of the injector face is sampled.* Alternatively, a careful analysis based on the hydraulic flow characteristics of the injector propellant passages and orifices can give a useful indication of the delivered distributions.

It has been found that regions of identifiable mass and mixture ratio which are larger than a typical molecular mixing distance (about $\frac{1}{2}$ inch) tend to maintain their separate identity as they react and progress through the thrust chamber and nozzle.

Thus the rocket motor can be idealized as a group of separate, non-mixing, rocket motors (stream tubes) operating in parallel, and constrained to coexist within the overall chamber and nozzle contour.

As a first order approximation, the performance of the stream tube rocket motor is the mass-averaged performance of each of its stream tubes, each presumed to expand through a nozzle having the shape and exit area ratio of the overall nozzle. The net effect of the variation in mixture ratio from stream tube to stream tube is a decrease in performance compared to the performance that would have been obtained at a uniform average mixture ratio.

TWO-DIMENSIONAL NOZZLE FLOW: The two-dimensional shape of the de Laval nozzle affects the flow in two ways. Near the throat, curving of the flow distorts the pressure distribution, leading to curved constant-pressure surfaces. This causes a decrease in the mass flow through the nozzle, compared to one-dimensional sonic flow through the geometrical throat area; and the divergence of the exit flow results in a loss of axial momentum, and thus a loss in specific impulse.

* However, it is recognized that the chemical reaction can alter the non-reactive-fluid spray distributions.

TABLE 1.1.3b.—REAL ROCKET MOTOR PROCESSES AND LOSSES

Process	Typical loss percent
Nonuniform mixture ratio distribution (stream tubes)	0 to 5
Incomplete energy release	1 to 5
Multi-phase flow (solid particles)	Not treated here
Two-dimensional flow (curvature and divergence)	0.1 to 3
Finite reaction rates (kinetics)	0.1 to 10
Boundary layer (friction and heat transfer)	0.5 to 5

Various approaches to determining the effect of throat curvature on the pressure distribution in the transonic flow field and on the mass flow through the nozzle are given in the literature. When two or more stream tubes coexist in a given nozzle flow, additional constraints, beyond the fundamental assumption that the static pressure is everywhere continuous, are needed to define the sonic surface and to determine the relative flow areas occupied by the stream tubes in the region of the nozzle throat.

Kliegel and Quan[409] have presented an analysis of the flow of two concentric stream tubes within a rocket nozzle. Propellant injection conditions were not specified. They concluded that the sonic surfaces of the stream tubes must lie on a common constant-pressure surface, since this condition maximizes the total mass flow through the throat.

Norton[519b] studied the flow of multiple stream tubes through a nozzle with the injection conditions (mass, momentum, energy) specified for each stream tube, and found that the sonic surface was, in general, discontinuous.

In either case, if the properties of the gases in two stream tubes differ, then the stagnation pressures of the two stream tubes differ. This causes the difficulty, which was mentioned earlier, in the definition and evaluation of the characteristic velocity.

The development of the supersonic flow field and the divergence of the exit flow are determined by the shape of the two-dimensional nozzle downstream of the throat. The supersonic flow for an inviscid fluid can be developed by a method-of-characteristics calculation, using as a starting point a transonic solution such as that mentioned above. Such a calculation gives the pressure on the surface of the nozzle downstream of the starting line, and/or the pressure, density, velocity, and direction of flow through any chosen nozzle exit surface. The total thrust of the nozzle determined from either the starting line pressure and axial momentum flux plus the axial component of the surface pressure forces in the supersonic region of the nozzle, or from the exit surface pressure and axial momentum flux, is the same, and reflects the loss in axial momentum due to divergence of the exit flow.

FINITE REACTION RATES: The gases in the combustion chamber of a rocket motor are generally at a high enough temperature that some dissociation of molecular species has taken place. As the hot gases expand through the nozzle, the pressure and temperature decrease. At the reduced pressure and temperature, the dissociated species tend to recombine, and to liberate energy as they do so. However, these recombination reactions are rate-limited, and are only partly completed during transit through a typical rocket nozzle. With a knowledge of the rate constants for the particular reactions involved, and a specific nozzle size or time scale, the kinetic effects can be incorporated in the nozzle flow and performance calculation. The effect is always a decrease in the otherwise attainable performance.

MULTI-PHASE FLOW: Some propellants yield combustion products which contain solid particles in the combustion chamber, or which form condensed species during expansion through the nozzle. The magnitude of the effect of solid particle flow on the rocket motor performance depends on the state and number of the particles as well as on their drag and heat transfer coefficients. The two-phase flow process effects on performance are complex, and the basic data needed to analyze the process is difficult to obtain. Some existing computer programs approximate the effect of two-phase flow in one-dimensional nozzles, but no two-dimensional treatment is available at the present time. For these reasons no estimate of the magnitude of the two-phase flow loss is given in Table 1.1.3b.

INCOMPLETE ENERGY RELEASE: Atomization, mixing, evaporation, and reaction of the injected propellant do not occur instantaneously or completely in a rocket motor. Typically, most of the combustion is completed within the combustion chamber, before the products of combustion enter the nozzle convergence section. Some droplets may evaporate and some reaction may occur during transit through the nozzle.* However, some propellant droplets may not evaporate within the confines of the thrust chamber, and some evaporated molecules may not find "partners" with which they can react. The result in either case is an energy deficiency and a small change in the composition and properties of the combustion products, with a reduction in the realized performance.

A distinction should be made between the stream tube process and the incomplete energy release process. A stream tube is a macroscopic region of uniform mixture ratio, distinguishable from other macroscopic regions having other uniform mixture ratios. Energy release efficiency is a measure of the completeness of the reaction within a stream tube; it is related to the degree of mixing and vaporization of the drops produced by the individual injector elements and to the microscale processes by which molecules mix and react.

The real distributed energy release process has not been completely described and modeled as yet, although some analytical and experimental investigations are under way and others have been proposed.

In the absence of a capability of analytically describing the energy release process and predicting its effect on performance, an empirical interim model and procedure[23] has been found useful. Incomplete energy release is modeled analytically by reducing the total energy of the system through a reduction in the stagnation enthalpy. Prior to expansion, 100% of the propellant is presumed to be in thermodynamic equilibrium at the reduced enthalpy level. The chemical and fluid dynamic calculations are then made in their usual manner. The calculated performance is reduced as a result of the lower energy available to the expansion process. The reduced enthalpy also provides a different base condition from which the kinetic loss is reckoned. This empirical single-parameter model was selected for interim use because it is simple and unambiguous.

While this simplified energy release model cannot exactly duplicate the effect of the real distributed energy release process, it has proven, empirically, to give useful overall performance correlations and extrapolations when used with several conventional propellant systems.

BOUNDARY LAYER FRICTION AND HEAT TRANSFER: The effect of surface friction and of heat transfer from the combustion gases to the wall is confined to a relatively thin layer of gases next to the wall. The core of the gas flow can be considered to be remote from viscous or heat transfer effects.

The influence of the boundary layer on rocket motor performance is given by a model which replaces the real flow with an equivalent completely inviscid and isentropic potential flow. A displacement thickness, δ^*, is evaluated which defines the size and shape of the potential flow nozzle with respect to the real nozzle, so that the mass flow through the potential flow nozzle is the same as that through the real nozzle. This is shown in Fig. 1.1.3c. The excess momentum flux through the equivalent potential flow nozzle over the momentum flux of the real flow is given by a momentum thickness, θ, of the potential flow, such that an annular layer of the potential flow of thickness θ has this amount of momentum. Then, as shown on Fig. 1.1.3c, the thrust of the real motor is obtained by correcting the thrust of the equivalent potential flow motor for the excess momentum flux and for the exit pressure acting on the displacement thickness. The propellant mass flow as computed for the throat of the equivalent potential flow motor is used with the calculated real motor thrust to obtain the specific impulse. The derivation of the expressions for the displacement and momentum thicknesses from the basic heat transfer, friction, and fluid flow relationships is given by Elliott, Bartz, and Silver[241] and by Alber[60].

A unique feature of the treatment by Elliott, Bartz, and Silver is the simultaneous solution

* A study by Mitchell[491] has shown that combustion in the supersonic portion of the nozzle flow, even at high area ratio, can still contribute to performance.

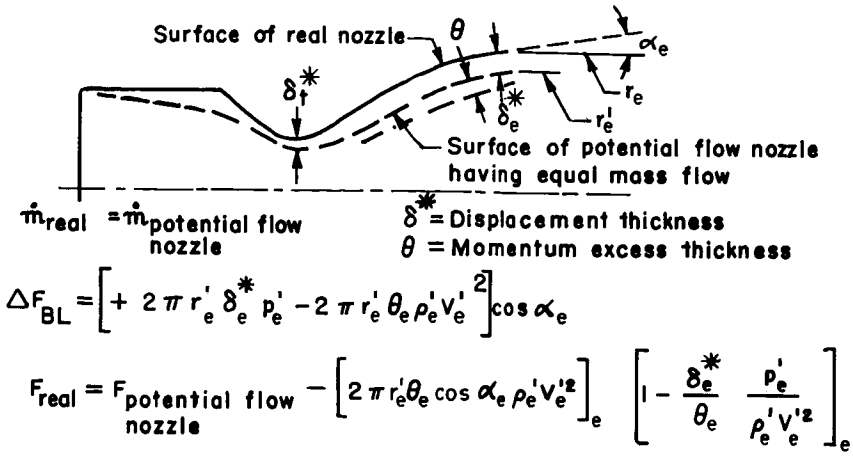

FIGURE 1.1.3c.—Boundary layer model and performance correction.

of the integral momentum and energy equations for the thin boundary layer. This results in the losses due to heat transfer to the wall appearing indirectly, as part of the total boundary layer loss, rather than appearing separately, as in earlier boundary layer treatments. Thus all interactions between shear drag and heat loss from the gases are taken care of within the boundary layer model. Alber[60] takes an overall look at this approach to the evaluation of the boundary layer losses and shows that the displacement thickness-momentum thickness approach is exactly equivalent to a correct accounting of the axial component of the pressure forces acting on the interior of the nozzle.

INTERACTIONS BETWEEN PROCESSES: In principle, each process occurring in the real thrust chamber interacts with each other process. These interactions must be accounted for in a valid performance calculation procedure. Some of the more important of these interactions are discussed here in general terms:

(1) *The effect of incomplete energy release on kinetic losses and on the nozzle expansion process.* Incomplete evaporation, mixing, and reaction result in a loss of energy and a change in the composition of the combustion products, compared to complete reaction. The temperature of the gases entering the expansion nozzle is reduced, and associated with this is a reduction in the fraction of dissociated species present. While that part of the total loss directly ascribable to kinetics may decrease, the net effect of incomplete energy release and kinetics is a decrease in the vacuum specific impulse. Further, due to the thermodynamic nature of the nozzle expansion process, the percentage performance loss for a given energy deficiency increases with the nozzle area ratio, and the magnitude of this effect increases with increasing energy loss.

(2) *The effect of two-dimensional flow on kinetic and other losses.* Two-dimensional flow affects the magnitude and rate of change of the properties of the expanding gas. Small nozzles and nozzles having small radius of curvature throats and/or high expansion angles just downstream of the throat may expand the combustion gases so rapidly that there is not enough time for rate-limited equilibrium shifts to occur. Nozzle contour curvature, located near the exit of a "bell" nozzle, can cause local changes in pressure, density, velocity, and direction which enter into calculation of the boundary layer loss and the divergence loss.

(3) *The effect of nonuniform mass and mixture ratio distribution on kinetic losses.* Stream tubes having different mixture ratios will produce combustion gases having different properties and temperatures, and thus the kinetic losses will be different in each stream tube.

(4) *The effects of incomplete energy release, kinetics, stream tube flow, and two-dimensional flow on the boundary layer loss.* The properties used in calculating the boundary layer corrections are those of the stream tube closest to the wall. The properties of the gases in this stream tube

are determined by the local mixture ratio and by the energy release, kinetics, and two-dimensional interaction effects.

1.1.3.3 Real rocket performance calculations.— Calculation of the performance of a real rocket motor must be based on an integrated physical model that is a composite of models describing each of the physical processes or effects occurring in the real rocket motor. Separate inputs should define each effect, and the calculated performance should reflect the result of all interactions.

If all of the real rocket motor processes are identified and appropriately modeled, and if the input information is available to accurately specify each process or loss, then the computed performance will be identical to the performance of the real rocket motor as measured on a test stand (presuming accuracy of the test data).

In practice, this degree of perfection has not yet been achieved. Some processes have still not been adequately modeled, some needed physical data are not as yet known with sufficient accuracy, and present computational procedures are limited.

Because of these present limitations, the capability to predict the performance of the general case of a real rocket motor does not now exist. However, a practical methodology for correlating and predicting the performance of a useful class of rocket motors has been developed by the Performance Standardization Working Group* of the ICRPG[23, 555b]. This class of rocket motors is limited to those that

a. Use propellants whose combustion products are entirely gas phase, with no solid particles. (Currently only the chemical elements C, H, O, Cl, F, and N can be handled.)
b. Are large enough so that the flow is not dominated by viscous effects (i.e., above about 100 lbf thrust)
c. Have conventional de Laval nozzles
d. Have conventional upstream-end propellant injection techniques; no mass addition in the supersonic region
e. Are in steady-state operation

These restrictions correspond to the capabilities of existing computer programs, and to processes which are relatively well understood. Despite these seeming limitations, there is a wide and important field of applicability for the developed performance calculation capability; i.e., most rocket motors used for space propulsion applications use propellants composed of the six listed elements, produce more than 100 lbf thrust, and have de Laval nozzles.

The rocket motor performance calculation capability developed by the Performance Standardization Working Group is based on two computer programs and on the use of the empirical model for the incomplete energy release process, (discussed under Sect. 1.1.3.2). The two computer programs were selected by the Working Group from among all those that were available to it in June 1967. These computer programs, selected on the basis of technical validity, computation time, documentation, and other factors[60], have since been modified and improved to meet the needs of a standardized performance calculation and prediction procedure and to be compatible with each other, and have been made available as reference programs.[17,22,23,44,45] (These and other related computer programs can be obtained through CPIA (Chemical Propulsion Information Agency), The Johns Hopkins University, 8621 Georgia Avenue, Silver Springs Maryland 20910.)

1.2 COMBUSTION INSTABILITY*

Combustion instability problems have been experienced during nearly every rocket engine development program. Since these problems severely impair the operation of the engine and vehicle system, there is considerable incentive to seek an understanding of this undesirable phenomenon. Combustion instability results from coupling between the combustion and the fluid dynamics of the system. Through this coupling, oscillatory energy is supplied by the combustion

* The Performance Standardization Working Group of the Interagency Chemical Rocket Propulsion Group was organized in 1965 and has functioned through its three committees; Overall Concepts, Theoretical Methods, and Experimental Measurements. The ICRPG Performance Evaluation Manual for Liquid Propellant Rocket Engines[23] is the product of joint efforts of the Overall Concepts and the Theoretical Methods committees.

* T. A. Coultas, Author, Sects. 1.2.1 to 1.2.3.

to sustain the oscillations. Only if the damping processes present in the system are sufficiently large to dissipate the oscillatory energy more rapidly than it is supplied, will the oscillations decay. Thus, combustion instability may be prevented by either increasing the damping or decreasing the coupling with the driving forces.

Several distinct types of instability have been observed and their physical manifestations have caused a variety of picturesque names to be generated for each of them. A common trait is that all types of combustion instability are characterized by chamber pressure oscillations, although the frequency and amplitude of these oscillations and their external manifestations normally vary with the type of instability.

Oscillatory operation of a rocket engine is undesirable for many reasons. One of the most important of these effects is the severe vibration. Vibration levels in excess of 1000 g have been experienced. Such vibration levels can impair the operation of sensitive guidance components and have severe effects upon payloads and even relatively massive structural members. Another severe effect is the grossly increased heat transfer due to the oscillatory operation. This increase is often sufficient to melt and destroy portions of the rocket system. Other less drastic effects include decreased performance, uncontrolled impulse, variation in thrust vector, and the effects of oscillatory propellant flow rates.

1.2.1 Physical Manifestations

Combustion instability is manifested in many ways. The most satisfactory method of detection and study of combustion instability is the measurement of chamber pressure (see Sect. 9.3). Pressure measurements made in the propellant feed system show similar oscillations, and in some cases the amplitude measured here may be greater than that measured in the combustion chamber. In the combustion chamber, frequencies from less than 100 to over 15,000 hertz have been measured at amplitudes of from 10 to 1000 percent of steady-state chamber pressure. In addition to pressure measurements, instabilities are often shown by means of vibration measurements. The very high vibration levels often measured have given rise to the term "rough combustion," meaning in that case unstable combustion. Vibration measurements often do not correlate well with the corresponding chamber pressure measurements. Frequently, however, there will be similarities in frequency as well as in severity or amplitude (see Sect. 9.5).

Temperature and heat transfer monitoring has also been successful in indicating the onset of combustion instability. Thermocouples buried in the chamber wall respond to the rapid increase in wall temperature. Faster response is afforded by measuring the transducer coolant or the local regenerative coolant temperature changes (see Sect. 9.6.5).

Combustion instability also causes oscillations of the axial position of the Mach diamonds in the exhaust plume and this can be detected by high speed photography. The oscillations of the Mach diamonds will usually correspond in frequency to the chamber pressure oscillations. Monitoring of the luminosity variations from the exhaust plume is another optical technique sometimes used. These variations in luminosity may be very weak. For instance, it has been estimated for one case that the relative amplitude of brightness oscillations in the plume would be only 0.1 percent of the relative oscillations in chamber pressure (optical measurements are discussed in Sect. 9.4). Flow rate variations and thrust variations have also been observed as an indication of combustion instability.

1.2.1.1 Damage.—In addition to the destructive vibration, thrust magnitude and direction vibrations, and uncontrolled impulse caused by an oscillating system, combustion instabilities may result in extensive damage to the thrust chamber and injector itself. High frequency instabilities result in grossly increased convective heat transfer coefficients in the chamber walls. With the prevalent tangential mode instabilities this increase occurs at all axial positions in the chamber. Since the heat transfer rate is normally highest near the nozzle throat, this is a very sensitive location. In one rocket engine development program it was found that combustion instability caused the nozzle to be neatly severed at the throat and dropped into the exhaust flame deflector. In another program, where considerable unreacted oxidizer was present near the injector, together with the maximum tangential mode

amplitude, increased heat transfer rates resulted in chemically burning the thrust chamber at that location. This can become a chain reaction, burning not only the chamber and the injector, but propellant lines and thrust stand structure as well.

Combustion instability is not always so dramatically destructive. Lower frequency modes of instability may do no damage at all. Even some high frequency instabilities are nondestructive if the injector and thrust chamber are satisfactorily cooled and sufficiently strong. In fact, at high frequencies, a quite sophisticated set of instrumentation is often required to determine if the combustion is unstable. At very high frequencies, the amplitude of the oscillations may be quite low and the damage incurred negligible over the short periods of times (3 to 4 seconds) typically used to obtain performance data.

1.2.1.2 Effect on combustion efficiency.—The apparent performance of a particular rocket system may either increase or decrease during a combustion instability. At high frequencies, the high transverse pressure and velocity gradients enhance both factors which control the steady-state rocket engine performance. These factors are mixing (distribution), and vaporization of the propellants. In engines where either of these factors has not been very thoroughly optimized for steady-state operation, it might be expected that the performance would increase during an instability. In contrast, for the case of an optimally designed injector configuration displacement of the propellants may actually result in a performance loss. Considerable design efforts are usually put forth to assure that the propellant mixture ratio is made as uniform as possible at each point on the injector face. In spite of these efforts, however, combustion may occur locally at mixture ratios considerably off design or optimum value, particularly for propellants which vaporize at grossly different rates. It has been found that if the propellants have not been properly distributed within about an inch downstream of the injector, any transverse mixture ratio variations tend to persist, since gas phase mixing is exceedingly slow. In the presence of a strong acoustic field, however, the gas-phase mixing is considerably enhanced, minimizing this source of inefficiency.

Effort is also expended to assure that the propellants will be atomized into droplets sufficiently small that they will be completely vaporized in the chamber prior to expansion through the nozzle. Propellant vaporization is governed by heat and mass transfer between the propellant droplets and the hot combustion gases. Additional convective effects generated by the acoustic or oscillatory pressure field will enhance the combustion efficiency by accelerating the vaporization of the propellants. In spite of these factors, which sometimes increase the combustion efficiency, other effects of combustion instability may override them and decrease the apparent or overall combustion efficiency.

The presence of low frequency or longitudinal mode high frequency oscillations may result in a decided increase in the axial mixture ratio variations. This is particularly true with injectors having unequal injection pressure drops across the two propellant systems. Here, a temporarily lowered chamber pressure will cause a much larger quantity of one propellant to be injected during the low pressure portion of the cycle than of the other propellant. Thus, alternatively high and low mixture ratio injection rates will result in wide variations in mixture ratio along the length of the chamber, resulting in poor performance. Further, the grossly increased injection rates during the low pressure part of the cycle can result in a portion of both propellants being exhausted from the chamber unburned. Thus, even though the mixing and vaporization may be very complete during one portion of the cycle, (high chamber pressure and low injection rate) the chamber is flooded during the low chamber pressure portion of the cycle. Other less important losses occurring during combustion instability include increased heat transfer and friction.

As a rule of thumb, it may be stated that high frequency instabilities tend to increase the combustion efficiency if the combustor is not initially a high performer, while low frequency oscillations tend to decrease performance.

1.2.2 Classification

Several different classes of instability have been identified and studied experimentally. Usually the instability driving mechanisms differ among the classes such that different methods are re-

quired to control or eliminate the instability. Historically, instabilities have been classified by their frequency range, but there is not a sharp dividing line between the so-called low, intermediate and high frequency classes. Classification of combustion instability, merely by its frequency, has led to much confusion. It would appear that a better method would relate the classes of instability to their effects, the most important coupling mechanisms, and to the devices used to eliminate them.

1.2.2.1 Low frequency, chug.—Of the various types of combustion instability the low-frequency type, or chug, also called putt-putt, groaning, and motor-boating, is perhaps the easiest to handle both from an analytical and experimental or developmental standpoint (see Chapters 5 and 6). It is generally accepted that the frequency range which might be encountered in the chugging mode is less than several hundred hertz. In this frequency range, the wavelength is usually much larger than characteristic dimensions of either the chamber or the feed system. In some cases, however, there may be wave motion in the propellant feed lines. This instability usually begins with a low amplitude, sinusoidal wave shape, growing in a linear fashion to higher amplitude.

Analytically, the chamber may be simulated by a lumped volume element, the combustion represented by a simple, constant time delay and the propellant feed system resistance neglected, although feed system inertance and capacitance may become important in the analysis. The combustion time delay is defined as the time required for the liquid propellant to enter the chamber, travel at injection velocity to an impingement point, then be totally vaporized and burned. Usually an empirical average can be found for each propellant. A value which has often been used is simply the liquid flight time from injector face to impingement point, usually for the least volatile of the propellants since this constitutes a major portion of the total time lag. Methods of elimination of chug instabilities include: increasing the pressure drop in the injector, increasing fluid inertance (i.e., longer L/D in the injector or feed system), decreasing chamber volume, etc. Attempts to change the time delay have met with mixed success. These changes, even if successful in eliminating chug, may decrease the system performance or bring about a high frequency instability.

Other low frequency instabilities have been caused by coupling of the combustion process with the injector structure. The injector may act as a diaphragm and oscillate in an "oil can" mode. This can cause nonuniform propellant injection and atomization which results in a low frequency instability. Still other cases can allow coupling between the combustion, or chamber pressure, and the structural system. One instance was found where pressure oscillations in the propellant contained in the regenerative cooling jacket were being caused by chamber pressure perturbations flexing the jacket wall structure with the resultant coupling causing a low frequency instability. Another rocket system instability, of very low frequency (order of a few hertz), is caused by propellant flow rate oscillations which result from pump amplification of the fluctuations of the pump inlet pressure (the pump inlet pressure variations are due to the g-loading of the liquid column extending back to the tank). Although this "pogo" instability is driven by thrust modulations that are transferred to the structure, the combustion is perturbed so slowly as to remain essentially steady and hence this is not generally considered a combustion instability.

1.2.2.2 High frequency instability—The most destructive type of instability is referred to as high frequency instability, resonant combustion, or acoustic instability. The latter is a generic term derived from the observed correspondence in frequency and phase between experimentally observed chamber pressure oscillations and those calculated for the acoustic resonances of the chamber (see Chapters 4 and 6). Both axial (longitudinal) and transverse (radial and tangential) modes are included in this terminology. High frequency instability has also been called by such names as "screaming," "squealing," "organing," "screeching," and just plain "rough." It is generally conceded that the effect of the propellant feed system is usually unimportant in the study of high frequency instability. The frequencies are often so high as to preclude coup-

ling with the relatively sluggish feed system. It should be noted, however, that in large combustion chambers the fundamental acoustic frequency may be so low that the feed system can easily couple. Combinations of resonant combustion and chug instability have also been observed. In some cases the elimination of the chug by feed system changes has also resulted in elimination of the resonant combustion. In other cases, the opposite has been true.

An oscillatory source of energy is required for sustaining an instability. For high frequency instabilities, this energy must come from the propellant combustion and is usually only weakly dependent upon the feed system. Further, the sustaining energy addition must be properly time-phased with respect to the oscillating pressure. In most high frequency instabilities the coupling appears to be direct. Each wave affects the propellant combustion strongly enough so that sustaining energy is added directly to that wave (i.e., within a time no longer than $\frac{1}{2}$ the period). Effects of secondary importance can come from transient change in propellant injection rates, in propellant impingement and atomization characteristics and from residual effects from one cycle influencing the amplification of the next. In general, however, these simply affect the equilibrium amplitude of the instability.

SUSTAINING MECHANISMS: Sustaining mechanisms which have been proposed for high frequency include: loss of ignition, sensitive chemical preparation time, physical time delays, detonation processes, pressure or temperature sensitive chemical kinetics, the "exploding" of droplets heated to above their critical temperature and pressure and the shattering and mixing of the streams, fans, or drops by the gas particle motion. These are only a few of the more recurrent explanations which are advanced to explain the sustained combustion instabilities. Many of these will be discussed in detail in later chapters.

METHODS OF ELIMINATION: Two fundamental methods of eliminating high-frequency combustion chamber instability have been employed: (1) making changes in the propellant spray combustion field or in the pressure wave character* so that the combustion response to the wave motion releases less oscillatory energy than that required for sustaining the oscillations; and (2) making changes in the dynamic energy losses or damping so that they exceed the energy gains from the combustion response (see Chapters 7 and 8). Into the first category fall the very common developmental attempts to achieve stability by varying the injector hole pattern, hole size, pressure drop, etc.

Of the thousands of postulates or design criteria for achieving combustion stability, the following is an example of an injector design rule that has worked out quite well. In nearly every case, "the stability of a rocket engine will be improved if the two phases, i.e., liquid and combustion gases, move at grossly different axial velocities." This rule of thumb indicates that if the most volatile propellant is injected at higher velocity, the engine will become more stable. Also, if the less volatile propellant is injected at lower velocities, further increases in stability will be found. This "relative velocity" criterion is probably responsible for the generally observed good stability characteristics of engines using gaseous hydrogen fuel. Like all generalizations in the study of combustion instability, there have been exceptions to the rule and certain limits must be set. Often it is not practical for performance, compatibility, or other system reasons to increase the relative injection velocities (see Sect. 7.4).

The predominant effect of combustion chamber baffles places them in this first category as well, because their stabilizing influence primarily results from simultaneously increased resonant frequency (i.e., a shift to higher modes) and lowered acoustic displacement of the combustion gases within a baffle compartment. Some of their effectiveness may also stem from disruption of wave propagation and droplet shattering. In addition, there may be some effect of the baffles in energy dissipation due to vortex shedding, but the extent of this contribution to effectiveness of baffles is not currently known.

Although it is known that engines may be stabilized by the use of baffles on the injector face, less well-defined criteria exist for defining how many baffles are required, i.e., the necessary baffle spacing, or baffle length required to achieve

* Frequency or wave shape alterations may be accomplished through changes of the chamber geometry.

dynamic stability in the engine (see Sects. 3.5.3.3 and 8.2). Although some empirical rules have been developed which seem applicable to some propellant combinations over narrow ranges of injector variation, these rules are based only upon experience. When they fail in practice they must be replaced by other rules which accommodate the most recent failures of the old ones. Generally, it has been thought that if a baffle is made long enough to "shield" the region in the chamber wherein the major portion of the combustion occurs, and if the baffle spacing is such that the baffle cavity frequency is above about 5000 Hz, the engine would be stable. Unfortunately, there is much evidence which contradicts this rule. In one case it was found that longer baffles made the engine even more unstable. In most cases, however, it has been found that if the baffles are made long enough, and if they are spaced closely enough, the engine will stabilize.

Baffles are not generally regarded as a panacea for promoting combustion stability. Even if sufficient and proper baffles did assure stability, it would still be desirable to minimize the length and number of baffles used. The presence of baffles on the injector face represent a discontinuity in the most important combustion region. It has been shown that baffles can have significant and deleterious effects on both combustion efficiency, and the effectiveness of nozzle thrust-vector-control injection*. Furthermore, as the baffle length is increased, the heat losses from the combustion gases can become large enough to lower combustion efficiency, and the heat loads to the baffles may become prohibitive. Thus, it is desirable from the standpoint of cost, complexity, performance, thermal compatibility and thrust vector control to minimize the number and length of baffles used in a combustion chamber to achieve dynamic combustion stability.

In the second category fall various types of damping devices. Items of this nature have been noted to be effective when metal-walled combustion chambers were replaced with ablative chambers (Sect. 8.5.1) or lined with Helmholtz or other types of acoustic absorbers (Sect. 8.2). Acoustic absorbers are also often considered to be a panacea. It is noted that if "enough" highly absorbing resonators are inserted into a chamber, it will be stable. Similar to the case of baffles, questions remain as to the correct design criteria, and together with other operational factors it is desirable to minimize the use of acoustic absorbers. It has also been found that the inclusion of particulate matter into the combustion gas acts as an absorbing device by dissipation of oscillatory energy through frictional processes associated with particle drag. This damping method has been widely acclaimed as the solution to high frequency instability problems in solid propellant motors (see Sect. 8.5.2).

1.2.2.3 Intermediate frequency, buzz.—Between the two extreme types of combustion instability is the intermediate frequency. It is unfortunate, but most of the combustion instabilities which are not obviously either low or high-frequency are lumped into this intermediate category. This propensity is so strong that often many chugging instabilities at higher than usual frequency are referred to as buzz (see Chapters 5 and 6).

The beginning of an intermediate frequency instability usual y shows a growing coherence of the combustion noise at a particular frequency with slowly increasing amplitude. There is usually wave motion in the propellant feed system. Although there may be wave motion in the chamber, the phase and frequency does not usually correspond to an acoustic mode. If chug and buzz-types are to be distinguished, it is by spatial chamber pressure variations present during buzz instability. The pressure wave shape is very nearly sinusoidal and one or both of the propellant feed systems may be highly coupled. Buzz-type instabilities are not particularly damaging if they remain at low amplitude, but may degrade performance, total impulse or thrust vector. In some cases the amplitude increases to the point of triggering a high frequency mode.

In very large chambers there may be wave motion which approximates that of acoustic instability. In one buzz instability the amplitude and phase relationships in the combustion chamber were the same as for a first tangential acoustic mode, but the frequency was 20 to 30 percent

* This effectiveness loss is because of mixture ratio effects associated with the baffle which persists into the nozzle.

lower than had previously been observed for this mode. This particular instability was cured by the use of quarter-wave tubes placed on the propellant feed system. Some instances of longitudinal high-frequency instability, although by definition an acoustic mode, probably should be called buzz. This is because this acoustic instability has the linear buzz characteristics, is usually feed system coupled, and may be eliminated by feed system rather than combustion changes.

A type of instability which also falls into the intermediate category is the so-called "entropy wave." Here axial mixture ratio gradients passing the sonic plane in the nozzle may emit a pressure wave which travels upstream toward the injector. The reflected wave influences the mixture ratio and hence travels back downstream as an entropy discontinuity at the gas velocity. The overall effect is that of an intermediate frequency oscillation.

Buzz is often encountered in development programs on engines which are designed to throttle over a wide thrust range. It is almost axiomatic that if the throttling range is to be very wide, buzz or chug will be encountered at some thrust condition. This is because the combustion is given a continuously varying set of conditions; e.g., velocity of propellants, impingement time, atomization effectiveness, etc. It is nearly certain that at least one condition will be found which is favorable for coupling with wave motion in the propellant feed system. This is particularly true if the engine is fairly large, allowing many possible resonances in manifolds, domes, feed lines and other parts of the feed system.

This type of instability has been noted on many engines which were designed to be throttled. Not only will the engine buzz at some operating condition, but often these oscillations will increase in amplitude sufficiently to initiate a high frequency instability.

1.2.3 Initiation of Combustion Instability

In addition to the characteristics of the fully-developed instability discussed in the previous section, the manner in which the instability starts can also furnish an important clue to the diagnostician. Knowledge of how the instability began may be as important as its mode, frequency and amplitude. The combustion chamber may be either triggered unstable by some artificial disturbance or the instability may develop spontaneously.

The initiation of an acoustic instability is frequently a nonlinear phenomenon; that is, there may be a threshold value of perturbation amplitude above which a sustained instability is caused, and below which the perturbation will damp. Thus a single pressure disturbance can be amplified and result in sustained combustion instability. A rocket engine's inherent stability determines its ability to absorb large disturbances and yet return to its steady-state operation. This was the impetus for combustion stability rating devices which provide artificial disturbances to a combustion chamber (see Chapter 10).

Prior to the introduction of stability rating devices, a rocket engine's inherent stability was determined by reliance upon the occurrence of spontaneous stability. This required very many tests and one system was deemed more stable than another if, in many tests, the superior system exhibited fewer occurrences of combustion instability. In other cases, the operational conditions were varied from the nominal. The system which remained stable through the widest excursion of operating conditions such as mixture ratio, chamber pressure, fuel temperature, etc., was alleged to be the more stable.

The technique of relying upon spontaneously occurring combustion instability was desirable in that the rating found was clearly associated with naturally occurring disturbances and the combustion was not changed because of the insertion of foreign rating devices into the system. However, using that approach, either a very large number of tests was required for rating, or the rating obtained might not be typical of the occasional large trigger source (for instance, a hard start). Furthermore, there was no method for determining the size of perturbation to which the system would be stable. If the rating was obtained by changing the operating conditions, it may have been obtained at conditions remote from actual operating conditions. At the off-nominal conditions there might be completely different driving and damping mechanisms present than at the desired operating conditions. Because of these severe limitations, combustion stability

rating devices have been developed to perturb stable, steady-state combustion upon demand, and thus eliminate some of the disadvantages of the naturally occurring instability rating approach.

Rating devices have helped to shorten the development cycle of rocket engines. Prior to extensive use of these devices it was possible to arrive at the flight test stage and encounter small system changes which gave perturbations sufficiently different than those previously experienced so as to cause a sustained instability.

In addition to the methods of initiation, the beginning of the combustion instability is quite different for the two cases. The fully-developed instability may be remarkably similar even though this initiation stage is distinctly different. These characteristics are contrasted by a variety of name pairs; such as, sinusoidal versus steep-fronted waves, spontaneous versus triggered or pulsed, small amplitude versus finite amplitude, and more generally, linear versus nonlinear. This latter distinction is derived from the type of analysis which is believed applicable to the mathematical modeling of at least the onset of these instabilities. Because of this fundamental difference in the initiation characteristics, two rather distinct schools of thought have developed (see Chapter 4).

Linear instabilities are nearly always considered to be spontaneous, but devices have been constructed which sometimes can enhance the occurrence of linear instabilities. Nonlinear instabilities, on the other hand, are always triggered by a finite disturbance. The disturbance may occur naturally, or may be artificially triggered by a combustion stability rating device.

1.2.3.1 Spontaneously initiated linear instability.—Spontaneous instabilities require no initial disturbance, but rather grow out of the noise inherent in the combustion process. If an engine is to experience a linear instability, it might be expected to begin immediately upon reaching normal operating conditions, since no trigger is required. However, variations in test conditions as well as the closeness to a stability boundary could delay that occurrence somewhat. It would appear that if an engine has experienced an instability of this type, it should yield to a linear or small perturbation analysis at the stability boundary.

Pressure perturbations on the order of a few percent of the steady-state chamber pressure and exhibiting a sinusoidal shape are deemed linear. Transition to a distorted wave shape and amplitudes increased to above ten percent of chamber pressure imply a nonlinear regime has been reached. Should this latter wave shape be present from the onset of resonant combustion then a nonlinear analysis is required.

All classes of combustion instability are distinguished from random turbulent fluctuations or combustion noise by coherence of a particular frequency or set of frequencies and in most cases by a much greater amplitude. Turbulent or random chamber pressure oscillations in rocket engines may have amplitudes on the order of one to three percent. It should be noted that these "random" oscillations, when spectrally analyzed, show many preferred frequencies. These frequencies, even in a stably operating system, can usually be attributed to some system characteristics such as pump speed, propellant feed line length or combustion chamber dimensions.

The lower frequency instabilities such as chug and buzz, and even most longitudinal mode high-frequency instabilities, were historically found to be linearly initiated. The high frequency nonlinear instabilities were not generally recognized. This was probably due to the relatively crude pressure transducers which were available at the time and the absence of rating devices. Further, the early engines were usually characterized by low injection density and were prone to a linear, or slowly building instability. Exceptions to this may have been found on some start sequences which resulted in a finite perturbation or "hard start."

Linear, low-frequency instabilities acting as triggers for high frequency instabilities are often prevalent during engine start-up. As noted, an engine operating over a wide range of thrusts, flowrates, and chamber pressures is much more likely to experience an intermediate frequency instability. Thus, if an engine's start transient is very gradual, i.e., full thrust is achieved only after several seconds, some set of operating conditions is likely to be prone to a linear buzz or chug instability. This linear instability can grow

and trigger resonant combustion. To prevent this occurrence upon engine start, the start sequence is typically shortened to a few milliseconds (while still avoiding overshoot or hard start). In this manner, the linear growth of any oscillations is curtailed since the "sensitive" portion of the start is quickly passed through.

1.2.3.2 Induced or nonlinear combustion instability.—It would appear that most of the combustion instabilities which are encountered today are initiated by finite disturbances. These finite disturbances may take the form of several types of natural disturbances or artificial triggers which are used to determine dynamic stability of an engine system.

The naturally occurring disturbances have acquired the descriptive names of "spikes" and "pops." Although there is no universal agreement in the rocket industry, it is generally conceded that a "spike" is a significant chamber over-pressure upon ignition of the engine. A "pop" is defined as a similar over-pressure, but occurring spontaneously during mainstage operation (i.e., operation at nominal chamber pressure).

For many years the sources of pops and spikes were the subject of intensive research during rocket engine development programs. In more recent years, however, the source of the disturbance has become of less interest due to the development of stability rating devices. Engine systems which have withstood a variety of artificial combustion perturbations and quickly returned to stable operating conditions have been assumed to damp natural perturbations rapidly. This has been found to be the case in many engine systems and natural perturbations have thus been rendered innocuous, although wherever possible the sources of such disturbances are still removed.

Under conditions of high altitude operation, hypergolic bipropellant combinations may characteristically start with an extremely high chamber pressure spike. This spike may be attributed to the explosion/deflagration of the propellants collected in the thrust chamber and/or accumulated on its walls during the period of ignition delay. These chamber pressure spikes may be of sufficient magnitude to result in destructive thrust chamber failure, or adversely affect the guidance sensor systems. Further, for small engines used for intermittent operation, the resultant thrust or total impulse is severely altered from that of a smooth start. For larger engines, this ignition spike can result in a trigger for sustained resonant combustion which may cause subsequent hardware destruction.

NATURALLY OCCURRING TRIGGERS: Hypergolic liquid bipropellant rocket engines may operate over a wide range of conditions, ranging from a highly pulsed mode of operation to long duration firings. In either situation, the ignition and start transients must be compatible with the propulsion system. For example, high pressure spikes resulting from explosions of accumulated propellants may result in the complete failure of a radiation cooled chamber.

Propellants are said to be "beneficially hypergolic" if the chemical reaction initiated by contact of the two propellants is sufficiently energetic to establish steady-state combustion with a smooth pressure buildup in a specified period of time. Because of low chemical reactivity, the chemical reaction may build up slowly for a period of time allowing unreacted propellant accumulation to occur in the chamber. This period of time may result in undesirable spiking when true ignition actually occurs because the propagation flame front passes through premixed propellants and builds into a detonation wave. Much of the experience with spiking is clouded by instrumental problems. Very sophisticated and high frequency response instrumentation is required to make a careful study of spiking.[431] A typical spike pressure amplitude may be ten times steady-state chamber pressures, but with pulse duration of only a few microseconds. This spike may either decay in a single cycle or show linear damping, lasting through several cycles of an acoustic mode of the chamber. High frequency instability following a spike will usually, but not always, damp very quickly as steady-state operating conditions are approached.

Pops are not usually severely damaging to combustion chambers, but like spikes they can severely disrupt either programed impulse or delicate portions of missile systems. They are also natural triggers for high-frequency instabilities. Pops are most often noticed in medium to large-sized rocket engines and are not limited to

hypergolic propellants. Neither a comprehensive knowledge of the source of pops nor information on wave growth thresholds are known. Some pops are thought to be caused by leaks in the injector. It is possible that these leaks lead to liquid propellant flowing in an uncontrolled manner across the injector face, collecting in pockets, and (without the necessity of oxidizer being present in the case of monopropellants such as hydrazine) exploding. Likewise, initiating disturbances could be caused by a collection of storable propellants in cracks or crevices where detonation of hydrazine (for example) is enhanced by partial confinement as well as catalytic effects of and heat transfer from solid surfaces.

Accumulation of hydrazine in pressure pickup ports has been detected by chemical analysis after firing of N_2O_4/50% hydrazine–50% UDMH propellants. Apparently, the UDMH was selectively distilled away. Explosive decomposition of film coolant, the possibility of a noise pulse of unusual amplitude from the combustion zone, and disturbances in the feed system are all possible sources of pops. Probably many disturbances occur that are too weak to cause pops.

ARTIFICIAL TRIGGERS: To avoid the many tests which may be required to determine stability by relying upon natural triggers, stability rating devices have been developed. Although many types have been employed, three techniques are most often used to perturb combustion systems. These are the (inert) gas pulse, the pulse gun and the nondirectional bomb. The first seems to act as a velocity perturbation to the combustion processes, while the pulse gun and bomb give both a pressure and velocity perturbation. These devices give perturbations of a finite size (10 to 500 percent of chamber pressure). Thus the triggered instability is nonlinear and is best described by the nonlinear theory.

The gas pulse used on engines employing LOX and RP-1 propellants was found effective in producing perturbations which triggered sustained instability. Recently, however, the gas pulse has been utilized on storable propellants such as N_2O_4 and 50% hydrazine and 50% UDMH with practically imperceptible effect upon the combustion. With the RP-1/LOX propellants the gas pulse was successfully used to determine a most sensitive combustion region.

The pulse gun, as the name implies, is a device which resembles a gun. It consists of a breech into which an explosive (or powder) is placed, usually in a conventional cartridge case, a firing mechanism, a barrel, and usually a diaphragm to protect the explosive from the direct rocket chamber environment. Like the gas pulse, the pulse gun barrel is usually attached to the rocket chamber such that the pulse is fired tangential to the chamber, but it too may be oriented in any direction. This device fires upon command to the firing mechanism which may be a mechanical detonator to initiate the main charge. The explosive charge in a pulse gun may vary from 3 or 4 grains of gun powder to over 100 grains of high explosive. To some degree, the overpressure in the chamber caused by the pulse gun is related to the charge size but the relationship with sustained instability may not be so direct.

The explosive bomb consists of three major parts. There is the explosive itself, usually a high explosive such as RDX, some sort of a detonator which may be either initiated thermally by the rocket gases or may be exploded electrically from an external signal. Lastly, there is a case which insulates the explosive charge and its detonator from the environment of the rocket chamber and furnishes some degree of containment for the explosive. Like the pulse gun, explosive charges from 2 to 100 grains are typically used. Unlike the pulse gun and gas pulse, the bomb is usually mounted inside the chamber and is not restricted to a wall location. The perturbation from a bomb is less directional than the pulse gun; both can give chamber pressure perturbations of 10 to 500 percent.

The presence of these devices may introduce spurious effects on combustion. It has been found that even though most of the bomb case is expelled after the bomb detonates, the bomb disturbs the combustion prior to detonation and the small case residual may have an effect. The pulse gun and gas pulse also introduce an additional cavity into the chamber which may result in acoustic interaction.

1.2.4 Dynamic Stability*

The ultimate objective of any rocket engine

* V. H. Monteil and O. W. Dykema, Authors.

development program is the successful flight. Since large costs, important program objectives and, in some cases men's lives are involved in each flight, considerable efforts to guarantee the success of the flight are justified. In the area of combustion stability, this means the attainment of high confidence, prior to conducting any flight, that the engine will not sustain damage during the flight because of combustion instability. Both theory and experiment indicate that a condition referred to as *dynamic stability* will yield the necessary high degree of confidence which will result in the engine performing stably.

1.2.4.1 Dynamic versus statistical stability.— In most cases, the coupled combustion gas dynamic system of a liquid rocket engine appears to be nonlinear and requires some kind of trigger, natural or artificial, to initiate a high frequency, high amplitude, damaging chamber pressure oscillation. As a result, a great deal of effort is expended in attempting to determine what type and magnitude of triggers might occur in flight and in evaluating engine stability with artificial triggers of the assumed type. Many cases have occurred, however, where no apparent trigger can be observed, and the oscillation appears simply to grow, out of combustion noise, to some limit cycle amplitude. It is apparent in these cases that a trigger was not observable either because the available instrumentation was not adequate to detect it or the system simply became linearly unstable and no trigger was involved. The role of a trigger clearly is irrelevant in a linearly unstable system.

The concept of dynamic stability on the other hand, avoids any consideration of the possible types and magnitudes of naturally occurring triggers. *Dynamic stability is concerned only with the response of the system subsequent to transients in system operation and requires that the system return to normal operation after any and all transients.* The particular artificial transient which might be used to evaluate the system stability need not have a direct relation to naturally occurring disturbances. The significant factor in dynamic stability is the behavior of the system once the initial disturbance is removed. Although dynamic stability is largely concerned with nonlinear stability, confidence is also obtained in the linear stability of the system. Control system theory[217] defines a nonlinear system as stable if the transients, resulting from a change of any kind in the system operation, die out or if the amplitudes of subsequent sustained oscillations are *sufficiently small.* This definition implies that the change in system operation can be of any kind and can be artificial or natural. The stability of the nonlinear system is defined only by the system behavior subsequent to the transient. A dynamically stable nonlinear system *cannot sustain* high amplitude, damaging oscillations and will always return to acceptable operation regardless of the transients which might occur.

The value of dynamic stability lies in the definition of the kind of steady-state operation that the system can sustain. In a nonlinear system, large perturbations of steady-state operating conditions may be required to gain confidence that the system cannot sustain damaging operation. An unstable linear system, however, does not require a large system transient for oscillation growth. If the steady-state operating conditions become such that the system becomes linearly unstable, the instability will be immediately apparent. Unfortunately, not all of the operating conditions, which may control linear stability, are known. Thus, a system naturally stable (no artificial perturbations) under many operating conditions in a number of tests may still develop a destructive instability under apparently the identical operating conditions incurred in later tests.

In summary, the concept of dynamic stability involves the use of the system response to evaluate the stability of a system. To evaluate dynamic stability the system is driven, by any means, into high amplitude oscillations. If the oscillations subsequently decay rapidly to steady-state combustion, then it is apparent that no high amplitude, damaging, limit cycle oscillation (nonlinear) exists (at least within the range of the system disturbance). A rocket engine which has demonstrated this response over the range of operating conditions expected in flight should always remain stable in flight, even under rather wide excursions and abnormal transients.

Another approach to gain some confidence in the stability of an engine is based on conducting a large number of stable tests and flights. This

confidence is called *statistical stability*. Statistical stability indicates only that instabilities have occurred rarely, or never, under the operating conditions tested. This does not rule out the possibility that the system can sustain a nonlinear instability but may only indicate that the natural occurrence of a destabilizing trigger is rare. It also does not indicate a broad range of stability outside of the range of hardware and operating conditions tested.

There are engines that are known to be nonlinearly unstable, but have demonstrated a reasonably good record of stable combustion in flight. Confidence that these systems will not encounter a damaging instability depends entirely on the vast background of test data which indicates that as long as the engine operates in a known region of test experience, there is a low probability that instability will result. Any small change in hardware and/or nominal operating conditions can invalidate this vast background of supporting data and may result in instability and/or require the generation of an equally vast background of data with the new system to regain an equal confidence level.

There are many examples in the history of liquid rocket engine development programs where a thrust chamber assembly which has exhibited statistical stability for a large number of tests suddenly begins to self-trigger high frequency combustion instability in a high percentage of tests. The cause of the radical change in stability (if the cause can even be found) is often a small change in hardware or operating conditions which, it was thought, would have little or no effect on stability. When this change in stability occurs far along in a vehicle development program, when all hardware and operating conditions of the vehicle/propulsion systems are "frozen," the cost in terms of money and flight program delays required to correct this problem can be disastrous. Not only must the stability be improved, but the effects of the necessary changes (usually to the injector) on the rest of the propulsion system and vehicle must also be evaluated and changes made where necessary. Once the redesign is made, the data on performance, compatibility and reliability compiled from previous component, system and flight testing are no longer applicable to the new system. Therefore either a second extensive component and system demonstration program must be run or subsequent vehicles must be flown with decreased confidence in the predicted performance and reliability of the vehicle. The loss of even one vehicle during a flight program because of unknown reliability of some components or system is sufficiently expensive to justify extensive efforts to assure the highest possible confidence in the reliability of all components and systems prior to demonstration testing and flight. The development of an engine to satisfy the dynamic stability criteria has been shown to be a means of assuring high confidence in the stable operation of the engine.

Probably the most vivid demonstration of the above discussion lies in the Atlas program. The Atlas booster injector was extensively tested and qualified at both the component and engine system levels prior to its first flight. The thrust chamber assembly exhibited stable combustion and an incidence rate of instability of approximately one percent. Despite this low probability of unstable operation, two successive Atlas vehicles developed spontaneous instabilities on the launch pad which resulted in a complete failure of the missions. As a result, a time consuming and expensive development effort had to be conducted (in the middle of the flight program) to assure stable operation. A 14-month special program was necessary to develop a baffled injector, to demonstrate dynamic stability, and to re-demonstrate engine system operation, reliability and compatibility with the new injector. The Atlas booster with the dynamically stable, baffled injector has never exhibited a combustion instability in hundreds of subsequent tests and flights. Similarly, subsequent programs such as the F-1, and Titan III, Stages I and II, have developed dynamically stable injectors and have encountered no incidences of combustion instability in many hundreds of subsequent tests. Furthermore, these engines have sustained malfunctions such as baffle and chamber failures, foreign objects in the feed systems and extreme excursions in operating conditions, yet these abnormal conditions have not resulted in combustion instabilities. These same conditions might well have caused combustion instability in statistically stable engines.

1.2.4.2 Dynamic stability in engine development programs.—Unfortunately, in the majority of past rocket engine development programs, combustion stability was defined as a requirement late in the program, and in some instances, after flight testing had begun. In these cases the engine components were in an advanced state of development, and the engine system had been extensively tested before the dynamic stability requirements were imposed. This had the effect of severely restricting design freedom in the stability effort. Typical restrictions in past programs included requirements to maintain combustion chamber dimensions, propellant system hydraulic resistances, injector element type, chamber heat flux, and engine performance. Under these restrictions a simple mechanical damping device, the baffle evolved. Baffles could be mounted on existing injectors and thus solve the stability problem with minimum effort and time. These early injectors relied primarily on baffles (generally consisting of an even number of blades extending radially from a central hub) to stabilize the combustion. Later systems, with greater freedom, employed baffles (generally an odd number of blades) in conjunction with modifications of the combustion process through the use of larger injector orifices (see Sects. 3.5.3.3 and 8.2 for details).

The prohibitive expense involved when major, developed vehicle components must be changed to solve a stability problem clearly point up the need for early development of dynamic stability. Early development of dynamic stability, demonstrated by rigorous pulse testing, assures a broad framework of stability within which other aspects of the vehicle may be developed with confidence.

Statistical stability cannot be developed early since it requires a large number of tests on the final prototype hardware. It is exactly this aspect of statistical stability which sets the stage for costly time-consuming, difficult re-development programs to obtain stability after all other development is complete. All engine components must be completely developed before a meaningful statistical stability statement can be made. This approach often results in the acceptance of whatever degree of stability which results at the end of a development program.

In contrast with statistical stability, the concept of dynamic stability faces the problem squarely and develops the desired stability early in a program. When the need for high confidence in the stable operation of an engine is recognized in the preliminary planning stage, a decision can be made to satisfy simultaneously dynamic stability, performance and compatibility from the very start of engine development. Theories and experimental evidence indicate that all of the variables of injector design, chamber configuration, and operating conditions affect combustion stability, performance, heat transfer, and durability. If all these aspects of chamber design are considered simultaneously and early in the development program, not only can a more optimum solution for the total design be reached, but each individual problem area can be solved more quickly and surely.

For example, the large thrust-per-element (LTE) injector design approach is often considered as a solution for combustion stability. Since an increase in thrust per element usually results in increased mean spray droplet size, one might expect a corresponding loss in performance. If a solution for an existing combustion instability problem is being sought far downstream in a development program, little can be done to avoid this performance loss and the loss either must be accepted or the LTE solution for stability cannot be used. If, however, a stable system is being sought at the outset of a development program, then a small increase in the combustion chamber stay time (chamber length or contraction ratio) may restore the performance with very little real penalty to the thrust chamber design.

1.2.4.3 Demonstrating dynamic stability in engine development programs.—Perhaps one of the most difficult problems encountered in early engine stability programs was that of measuring the relative stability of any new injector design. It is obvious that an ideal evaluation of the stability of the system could be obtained if every possible mode or mechanism of instability could be artificially excited to produce clearly defined oscillations. The driving force could then be removed to determine if the system would return to normal acceptable operation, or if it would sustain oscillations of some objectionable

magnitude. Implementation of this concept, however, is difficult. At first the modes or mechanisms of instability were only vaguely theorized and methods of introducing any sort of planned disturbance in the system were nonexistent. However, it was obvious that a part of the nonlinear feedback system of a hot firing thrust chamber is the oscillation of the combustor gases in the various acoustic modes of the chamber. Thus it appeared that the most convenient method of evaluating the stability of an engine under development was to force the chamber pressure into oscillation, and to observe the subsequent response. This method makes the implicit assumption that an artificial disturbance of chamber pressure is a direct means of triggering a nonlinearly unstable system. In order to gain the maximum confidence in the stability of an engine rated by this method, allowances must be made for possible shortcomings of driving just the chamber pressure. One approach would be to produce very high amplitude chamber pressure oscillations, over a broad frequency spectrum. A few attempts to drive the system with a sinusoidal oscillation proved that the energy requirements for such a system were far beyond that attainable with any existing or contemplated driving devices. The most direct alternative method of performing this operation subjects the chamber to a very short duration pulse of sufficient amplitude to excite any or all of the acoustic modes. This pulse could be provided only with some sort of explosive device.

Two types of explosive pulsing techniques have been used for stability rating of rocket engines. These are the pulse gun and the non-directional bomb. Both were described in Sect. 1.2.3 in connection with nonlinear combustion instability. A more detailed discussion of explosive pulsing techniques can be found in Chapter 10. The majority of engine development programs concerned with dynamic stability have used bombs to generate the explosive pulses and thus further discussion in this section will be limited to bombs.

For demonstration of dynamic stability in an engine development program, it is necessary to define the pulse in some terms which will yield consistent results. Pulse overpressure levels and bomb size have been used as criteria. The levels cited as overpressure criteria usually vary from 50 to 100 percent of chamber pressure. An overpressure criterion usually does not yield consistent results because both the true magnitude as well as the recorded indication of the overpressure depend strongly on many unknown and uncontrolled variables. The problem of measuring shock-type pressure waves has been pursued for many years. Instruments which are able to react rapidly to a step change in pressure level are notoriously poor in measuring the absolute level of the step change itself. Careful calibrations of many commercial high frequency pressure transducers in a shock tube by investigators at JPL[597] have shown overshoot from 56 to as high as 260 percent of the true step change in pressure. Variations of this type are amplified by the sensitivity of the transducer to vibration, partially recessed mounting, the type of transducer, the signal conditioning, and the recording system (see Sect. 9.3). All of these problems make it extremely difficult to be sure that an adequate pulse was supplied and, therefore, whether dynamic stability was adequately demonstrated.

In the transmission of the pulse from the charge to the measuring instrument, distance is an important factor. Normally in a gaseous medium, for a given charge size, the local pressure level will be proportional to the inverse of the distance from the charge for the three-dimensional case. In a chamber filled with droplets, which cause "diffusion" of a pressure wave, the pressure decays much more rapidly. On the other hand, it has been observed that the chamber reaction zone may respond violently even to small pulses, producing overpressures which are many times greater than that produced by the same explosive charge in a pressurized, passive chamber. This combustion zone response to the pulse is known to be affected by the magnitude of the pressure pulse and the local combustion conditions. Thus the actual overpressure that a transducer will record varies widely depending on the location of the instrument relative to the charge, and on the response of the intervening combustion zone.

Because of the difficulty of reproducibly generating and measuring overpressure levels, many engine development programs have used an explosive pulse charge size criterion to demonstrate

dynamic stability. One obvious upper limit to the charge size on a given engine is excessive structural damage. For solid wall thrust chambers of the Atlas and Titan types a 200 grain charge appears to be near the structural limit. After repeated pulse testing with 200 grain charges some minor bolt stretching and baffle cracking have occurred.

Another limit on charge size is the effect of the pulse on propellant flow rates into the chamber. An excessively large pulse may change the flow rates sufficiently that the new operating conditions are quite different from those which one wishes to test for stability. During the short period before the desired flows are re-established the amplitude of the pulse induced chamber pressure oscillations may be greatly reduced. The degree to which flows are changed by the pulse, and the time before nominal flow are re-established are functions of the particular chamber and feed system under test and few generalizations can be made with respect to a limit on bomb size. There have been cases where a large charge will not induce instability while a smaller one will induce it (see Sect. 10.2.4.1). This has been attributed to the effect of the large pulse on the propellant flow rates. A simple test series, with a range of charge sizes, can be run to establish that there is no charge size, small or large, which can initiate instability in the engine.

The location of these charges in the chamber should be such that the charge is most likely to initiate oscillations in the preferred and/or damaging modes of the chamber. Theory and experiment indicate that the transverse modes are both the most probable and damaging. The best charge location to initiate oscillations in all transverse modes simultaneously is near the injector and near the chamber wall. Here again an anomaly apparently exists, as in the case of the effect of charge size on propellant flows. A few isolated cases have been reported where an engine can be triggered by a bomb located near the throat, but not by the same bomb, under the same conditions, from any other location. Again, the bomb location in the corner between the injector and the wall should still be considered the the prime location to demonstrate dynamic stability and a few tests should be made to eliminate the possibility of any location anomaly.

As a result of the above discussion, a reasonable test program can be established to adequately demonstrate dynamic stability and establish confidence that an engine will not self-ignite instability in flight. A typical dynamic stability criterion intended for this purpose is outlined below. The general approach followed in this criterion is to strive to develop dynamic stability early in a program, with a few candidate injectors. These tests are designed to screen out unstable configurations and to establish the dynamically stable candidate. Use of bombs as large as are feasible, and the location near the injector face and the wall is the approach often employed for this initial screening. The possibilities of flow stoppage and/or a more sensitive charge size or location are evaluated with the selected candidate. Development of performance and compatibility may proceed using the most stable candidate injector. The stability of the final prototype configuration is then evaluated over the limits of the anticipated flight operating conditions. A final test of stability in the engine, with small bombs to limit hardware damage, evaluates possible flight-configured engine system effects of stability. Criteria very similar to this have been followed successfully for Stages I and II on Titan III and Agena. Much of this type of stability testing has also been accomplished on the Atlas, Thor, H-1 and F-1 engines. The following is an example of dynamic stability criteria for a large engine:

I. General Criterion
An injector shall be considered dynamically stable if the amplitudes of driven oscillations resulting from all of the required explosive pulse tests attenuate to 5 percent of mean chamber pressure within 40 milliseconds.

II. Explosive
The explosive shall be composition C-4 or a commercially available RDX equivalent.

III. Bomb Locations
Bombs shall be located at each of three positions as specified below:
A. Radially between the wall and the mid-radius of the chamber and axially

not further from the injector than one-quarter of the distance from the injector to the throat.

B. Radially between the wall and the mid-radius of the chamber and axially in the convergent nozzle section.

C. Radially on the centerline of the chamber and axially not further from the injector than one quarter of the distance from the injector to the throat.

IV. Test Conditions
Pulsing shall be accomplished at 5 conditions of chamber pressure and mixture ratio in steady-state operation. The maximum and minimum test conditions are defined as the estimated extremes of operation in flight.

V. Hardware
Pulse tests shall be conducted in solid wall (or water-cooled) combustion chambers, except for engine pulse tests which shall be conducted on flight-configured hardware.

VI. Required Explosive Pulse Tests
The required explosive pulse tests are listed in the following table:

Test	Bomb size, grains	Location	Test conditions		Hardware
			Chamber pressure	Mixture ratio	
Initial screening of candidate injectors (each injector type)					
1	200	A	Nom.	Nom.	Solid wall
2	200	A	Min.	Max.	Solid wall
Candidate injector evaluation (at least one injector)					
1	25	A	Nom.	Nom.	Solid wall
2	50	A	Nom.	Nom.	Solid wall
3	100	A	Nom.	Nom.	Solid wall
4	200	A	Nom.	Nom.	Solid wall
5	200	B	Nom.	Nom.	Solid wall
6	200	C	Nom.	Nom.	Solid wall
Prototype verification (each of two injectors)					
1	200	A	Nom.	Nom.	Solid wall
2	200	A	Max.	Max.	Solid wall
3	200	A	Min.	Min.	Solid wall
4	200	A	Max.	Min.	Solid wall
5	200	A	Min.	Max.	Solid wall
Engine verification (each of two engines)					
1	50	A	Nom.	Nom.	Flight-configured

1.3 HISTORICAL SURVEY*

In the history of liquid propellant rocket development the point where combustion instability became important was where these phenomena were first recognized as being responsible for rocket failures. Combustion-oriented oscillations in pressure could easily go undetected using the steady-state instrumentation that was standard in the 1950 era and before. When combustion instability amplitudes were sufficiently high to generate audible signals, the chance for detection of the instability was enhanced.

The recognition of different classes of oscillation, with different responsible mechanisms, was also an important milestone in the 1950 era. Two theoretical papers were a direct result of interest generated by a Bureau of Aeronautics symposium on the subject of combustion instability in liquid propellant rocket motors (Naval Research Laboratory December 7–8, 1950). One analysis by Summerfield[673] considered the effect of both inertia in liquid propellant feed lines and combustion chamber capacitance with a constant combustion time lag, and was applied to low frequency instability. Crocco[173] advanced the concept of the pressure dependence of the time lag, which was applied to low frequency phenomena in monopropellant and bipropellant motors, and high frequency instability with combustion concentrated near the injector face. This is not to say these Princeton professors were the first authors dealing with the subject, since Gunder and Friant[300] had provided early insight to the problem and the time lag theory apparently had been suggested by the Von Karman group at JPL in the late 1940's.

Experimental investigations of combustion instability were in the early stages at a number of industry, government, and university laboratories in the early 1950's. For example, the use of observation windows as a means to study combustion phenomena were used by Altseimer[65] at Aerojet for steady-state observations, and by Berman et al.[95,96] at General Electric to observe unsteady phenomena. Later these techniques were extended by Ellis and Pickford[242] at Aerojet to include instability observation via circumferential as well as axial slits. Levine and Lawhead and their associates at Rocketdyne developed a two-dimensional motor in which the entire cross section (in the form of a 2-D strip) of a high-thrust chamber could be observed and where attention could be concentrated on the important combustion phenomena immediately downstream of the injector.† Still later, Rossman et al.[606] at Bell Aerosystems used the window principle for studies of the droplets that were generated in the actual combustion environment. One of the early studies that utilized such observation techniques, together with pressure instrumentation, was conducted by Tischler et al.[462] at NACA Lewis Research Center. That study pointed out the complex situation of combined modes since two types of wave motion were clearly shown in combination.

Other investigators were also involved in the improvement of the instability recognition and observation techniques. The combined efforts of researchers at Princeton, MIT, and NACA Lewis resulted in the Li-Liu differential pressure transducer.[449] This strain gauge-type pickup with a water-cooled catenary diaphragm was the forerunner of later miniaturized versions using the strain gauge concept. Industrial development of the capacitance-type pressure transducers, which have proved even more successful over the years in combustion research, were also in an embryo stage during the early 1950's with higher frequency, more rugged, smaller versions to come. The piezoelectric-type transducer, which has gained wide usage in the past few years, did not contribute to these early studies.

Another experimental research that was being carried out during this early era involved basic measurements of the fundamental times associated with the combustion process to test the sensitive time lag theory. Information on chamber behavior was being sought by varying fuel and oxidizer flow rates sinusoidally, and then measuring the resultant fluctuations in chamber pressure. This technique did provide basic information on the total time lag[469] (see Sect. 6.2.2) which had significance for low-frequency instability. However, in order to check the high

* D. T. Harrje, Author, with contributions from the ICRPG Working Group on Liquid Rocket Combustion Instability.

† See Sect. 9.2.2 for details.

frequency mode theory, frequency limitations of the apparatus necessitated replacement by a stability-limits-testing technique that was used by Grey and Harrje[180] in 1958 at Princeton to confirm the sensitive time lag theory as applied to the longitudinal mode. This was achieved by holding the combustion process constant and varying the chamber length (hence the frequency). Similar techniques were applied by Harrje and Reardon[187] via a sector motor to confirm the transverse mode behavior two years later.

In late 1958 a widely publicized disagreement occurred between Zucrow-Osborn,[774] and Crocco.[174] The point in question involved the results of the tests just mentioned, which indicated a definite time lag behavior, and those results from gas rocket studies at Purdue which argued against the necessity of a time lag. Several years passed before the theory of Sirignano[646] and the experiments of Glassman et al.[113] involving the wave shape and the importance of the Arrhenius rate function in gas-rocket-type combustors helped to clarify the differences between the two combustion devices.

During the 1950's and early 1960's the AFOSR Contractors Meetings provided the forum for most liquid rocket instability discussions just as today the ICRPG serves this need. One constant point of discussion was whether nonlinear or linear theoretical analysis should be used for the high-frequency instability problem. Torda,[697] then at Brooklyn Polytechnic Institute, was one early advocate of the nonlinear approach. Priem and others later supplied the concepts applied to rocket engines. The subject of nonlinear theory will be discussed more fully in a moment.

While arguments as to the best way to proceed theoretically on the instability problem were in progress, the question remaining in the background was how much was really known about steady-state combustion. Along these lines information on the factors influencing mass and mixture ratio, injector element design, and other propellant flow phenomena were being studied by Rupe[615] and others at JPL. Related studies were being conducted by Heidmann,[336] Ingebo,[375] Morrell,[499] Priem[559] and others at Lewis Research Center. These studies formed the background for the Priem-Heidmann propellant vaporization model[564] which relates the propellant properties to the chamber length required for efficient steady-state combustion. A similar model was later developed by Lambiris, Combs and Levine[421] at Rocketdyne to better describe combustion phenomena as encountered in large engines. The use of streak photography, variable-length testing, static pressure profiles and shock tracers have all added to our knowledge of the axial steady-state combustion profile. Taking these rocket combustion studies up to the present, it now appears possible to check out the validity of various combustion mechanisms by a "direct" method.[114]

Before leaving the subject of injection studies, which were often directly related to the combustion processes, some specific topics should be cited. Included in the group were studies of spray fluctuation, impingement angle, liquid phase mixing, dynamic characteristics, drop-size distribution, spatial characteristics, droplet breakup, etc.

The steady-state model developed at Lewis Research Center was followed in 1962 by a nonlinear theory using a one-dimensional model to predict combustion instability limits. Priem and Guentert[563] were the originators of this theoretical approach which is described in Chapter 4. The model uses various mechanisms from the injection-combustion studies just discussed. A disturbance is inserted into each model and the computer is used to evaluate whether stability or instability results.

Considering the actual rocket hardware, although a relatively large thrust United States liquid rocket engine was available in the early 1950's (i.e., the Redstone), the era of the large engine was really closer to 1960. A number of engines in the 100 to 200 thousand-pound thrust class had been developed by that time and the greater than million-pound thrust designs were being studied (F-1 and M-1). Large engine feed system associated instability had already been experienced and solved for the case of the Redstone engine. The approach followed for high frequency instability was that incidences could be eliminated with controlled start sequencing (to avoid triggering such modes), and by careful selection of injection patterns and types, e.g., LOX/hydrocarbon injectors avoided unlike impingement injector designs which were more

susceptible to spontaneous resonant combustion.

Life with this approach was hazardous as was shown by two Atlas mishaps described in Sect. 1.2.4.1. Thus in 1961 the Atlas booster[493] became the first production engine to adopt a different stability approach—use of a baffle so as to avoid both spontaneous and triggered forms of resonant combustion.

Techniques to control combustion instability using baffles were first used in 1954 by Male and Kerslake[461] at NACA Lewis. Numerous studies at Aerojet, Rocketdyne, and Princeton also helped to point out the benefits and limitations of the baffle approach. As explained in Sect. 8.2, the mechanisms by which stability is accomplished using the baffle are still not completely clear—indeed more than one mechanism is probably responsible. The criticality of injection conditions near the baffle was found to be especially important in establishing the desired damping.

A few years after the addition of the baffle to the Atlas engine there was strong sentiment that further instability research was unnecessary since the high-frequency problem had been solved. This same argument was used again a few years later for the acoustic liner approach to instability suppression. Unfortunately, it has not turned out to be that simple for either device to achieve universal stability and both devices have preferred applications.

Liner design* has had the advantage of a reasonable theoretical base, particularly with recent additions that treat nonlinear effects. However it has been found that typically the design problem is made difficult by the actual chamber environments that are present. Experimental studies in liner design for rocket motors were initiated by Blackman and Lewis in the early 1960's at Pratt & Whitney. That work has been extended by Garrison. Other experimental work has been principally conducted by Phillips at NASA Lewis, Oberg at Rocketdyne, and Harrje at Princeton. The theory of resonators as related to combustion applications was clarified by the work of Ingard. Nonlinear theoretical extensions using the jet-flow model were done by Sirignano.

Both baffles and liners have been receiving much attention in recent years because of the ability to damp transverse modes. However, the design of the subsonic portion of the nozzle is also important for stability. The majority of nozzle studies† have been theoretical, with Crocco, Culick, Reardon, Sirignano, and Zinn the principal contributors. The nozzle may serve as the main damping source for longitudinal mode or may provide slight amplifications in certain transverse mode situations. Only in the longitudinal case have experiments been made.

The merits of being able to determine the relative stability of candidate injector designs by rating devices were discussed at length in Sect. 1.2.4.1 and the details of the techniques can be found in Chapter 10. These techniques were under development in the late 1950's primarily at Aerojet and Rocketdyne. Stemming from such studies a 220-grain bomb was developed for the Atlas MA-5 dynamic stability verification in 1961.[493] Studies of stability rating techniques using bombs, pulse guns and gas injection have been conducted more recently (1965–1968) by Combs et al. at Rocketdyne as well as at other organizations. Evaluation of the techniques was the prime purpose of the studies as discussed in Chapter 10. The rating techniques are the standard means of evaluating dynamic stability, for example, the Titan IIIM Stage I baffled injector was designed for dynamic stability and was proved successful from the first test (1964). Two programs that have yielded a great deal of information on the development problems in achieving dynamic stability were the F-1 program[20] conducted at Rocketdyne and the GEMSIP program[11] at Aerojet. An ad hoc committee formed for the F-1 problem played an important role of transmitting information to and from both of those programs.

To achieve dynamic stability more than damping devices and rating techniques were required; predictions of the stability limits were necessary. Reardon's empirical correlations[650] based upon the Crocco sensitive time lag theory were applied to the design of various engines. Modifications of the Priem theory by Dynamic Science and Rocketdyne proved helpful in other design ap-

* See Sect. 8.3 for individual references.

† See Sect. 3.6 for individual references.

plications.[91,136] Another correlation approach conceived in the early 60's by Dykema[238] also allowed stability predictions to be made on new hardware designs. This later approach is based on droplet parameters controlling the response, a subject which was further studied by Strahle[665] at Princeton. In another analysis with the emphasis on understanding the conditions conducive to instability in LOX/LH_2 engines, Feiler and Heidmann[260] formulated a response model which has proven quite successful.

Chapters 4 and 6 supply the background and application data on these approaches. In addition to NASA's interest, AFRPL has been deeply involved in this important aspect of designing for stable operation through in-house testing efforts, extension of computer programs for the Priem approach[136] and encouragement in the publication of a manual on how to apply the sensitive time lag theory.[650]

Damping devices have not been necessary in all rocket motors to achieve the desired stability for manned flight. One example is the Agena engine with a successful history of 250 launches, over 350 space firings and nearly 3000 ground tests which have demonstrated that a reliable system can be maintained without producing disturbances frequently assumed to a general condition of rocket engine combustion. The variable-thrust TRW LM ascent engine has met all the dynamic stability criteria without requiring damping devices. The merits of the later injector design approach together with a competitive Rocketdyne module design (see Sect. 7.4.5) are currently being tested on larger diameter hardware where the stability demands are more difficult to meet.

Designs of recent years have extended engine operation to higher pressures, above the critical conditions of the propellants. Experimental programs have been evaluating these effects on stability. Such studies have been active at Aerojet, Rocketdyne, Penn State, Illinois Institute of Technology, and elsewhere.

It has not been only the newer ranges of pressure operation that have required additional study. The effect of reactive jets of the hypergolic propellants which cause the jets to deflect rather than mix has also received recent attention at JPL[364] and Dynamic Science.[777] The criticality of the impingement processes has been studied by a new approach at JPL[618] and offers an explanation for the popping phenomena (Sect. 7.6).

The advent of the laser and the ability to overpower combustion light has encouraged renewed study of the difficult problem of droplet measurements both cold and hot. Weurker et al.* at TRW have been the leaders in this area. Use of improved paraffin droplet techniques has also shown considerable promise in the study of droplet distributions (Dickerson et al.[224] at Rocketdyne).

Another area of recent interest has involved further development of damping devices. Rocketdyne has concentrated on the use of slots in the injector face, often in conjunction with baffles, a design which was used for the LM ascent engine.[522] A similar approach involved the use, at Bell Aerosystems, of a toroidal cavity resonator with apertures extending into the chamber at the injector-chamber interface. This design proved completely successful on the PBPS axial engine. Similar designs had also shown considerable promise in the Bell LM ascent engine development. In an even more recent program, Aerojet and Aerospace have been performing tests on a relatively small number of damping devices placed across an injector face. As few as three Helmholtz resonators[324] placed in the walls of research chambers at Princeton had indicated a marked stability improvement—preferred conditions were those in which a short baffle limited the frequency spectrum with damping accomplished by the resonators.

The nature of the tangential mode is still not completely clear. Tests in recent years by Clayton[151] at JPL have revealed shock-type waves in 11-inch diameter hardware. Other observations in similar diameter hardware have revealed the peaked Maslin and Moore wave predictions. Phase differences have also been shown where the wave leads near the nozzle entrance in the JPL study whereas it leads near the injector based on the measurements of others. Explanations have been offered which involve detonation-like processes,[48] however, the frequency has been shown to be limited in all cases to that

* See Sect. 9.4.5 for references.

predicted from acoustic theory. These wave data are necessary if the proper theoretical analysis is to be applied. Wave growth studies have been made by Agosta in the past and remain a subject of active interest.

In this review of the history of combustion instability the emphasis, following a brief discussion of the earlier works, was to concentrate on the high frequency modes or resonant combustion. While resonant combustion is perhaps the most dramatic way to destroy an engine (burnout in a matter of milliseconds) problems in both low and intermediate frequency instability have plagued many engine development programs. The early monograph by Crocco and Cheng[179] served a need in clarifying the basic mechanisms associated with low frequency instability. An active program of research into low frequency phenomena has been maintained for many years at NASA Lewis with Wenzel, Szuch, Dorsch, Priem* and others participating. Studies in this area are still in progress though they are few in number.

Intermediate frequency instability has had the most uneven history. Often the receptacle for those unstable phenomena which could not be readily explained by the high and low frequency theory, much uncertainty continues to exist as to the importance of this type oscillation. Scala in 1956 analyzed entropy wave-type instability but, as explained by Crocco in Sect. 5.3.2, this instability is relatively rare in a pure form. In the past few years, Fenwick et al. at Rocketdyne, McCormack at Dartmouth and investigators at Princeton have looked at the bunching effects and the basic jet frequencies as responsible mechanisms for intermediate frequency phenomena.† Many of these jet characteristics had been observed in earlier investigations. The Rocketdyne analysis was used with success in solutions of some H-1 development problems of buzz in 1966.

1.4 CURRENT STATUS‡

Combustion instability research and development has led a somewhat clouded history. Unlike performance, which has always received its proper share of attention, instability has often in the past been something that was only spoken of in guarded terms—certainly it was not to be advertised. In recent years this state of affairs has vastly improved and frank and open discussions of current instability problems have taken place and even are part of the annual ICRPG Combustion Conferences.

A factor in determining the heartbeat of current research into combustion instability phenomena is the status of engine development programs. Currently liquid rocket development programs are at a very low ebb; hence the concern for the health of the associated instability research. Will the answers be ready when the next generation of engines are developed? This cyclic tendency is not unique to the rocket field nor has it failed to be felt before in instability research. Just prior to the advent of Sputnik (1957 era) marked one previous low point. Another hesitation occurred with the development and use of the baffle on large engines, in the early 1960's. However, reoccurring engine problems on various thrust units subsequently spurred even more work in these areas of research and development.

To summarize the status of the instability problem as of today it is necessary to subdivide the problem into several principal categories: (1) the understanding of the processes fundamental to liquid rockets such as atomization, mixing, vaporization, chemical kinetics, etc., (2) the application of instability theory to hardware design primarily as a guide in predicting stability trends, (3) the application of damping devices such as baffles, liners, slots, etc., which do not attempt to alter the combustion but rather seek to absorb energy or restrict wave motion, (4) the ability to detect the phenomena of combustion instability, and (5) the development of techniques to rate liquid rocket engines for stability.

Progress in category one, the fundamentals of liquid rocket combustion processes, has been understandably slow. This is because of the extreme difficulty in attempting to observe and measure these physical and chemical processes which often take place simultaneously at high speed and in environments that rule out conven-

* See Chapter 5 for individual references.

† See Sect. 3.3 for individual references.

‡ D. T. Harrje, Author, with contributions from the ICRPG Working Group on Liquid Rocket Combustion Instability.

tional instrumentation. An example of such difficulties are the studies of unsteady droplet burning rates (as discussed in Sect. 3.4.2) where direct observation is often impossible, especially if one wishes to closely simulate the actual environments encountered in high injection density, high chamber pressure rocket combustors. Hence simulation must be attempted by other means such as scaling, substitution of propellants (for such improvements as optical clarity), laboratory evaluation of only a portion of the processes involved, etc.

Perhaps it will never be possible to solve the combustion instability problem by the direct approach of attempting to understand in sufficient detail the steps through which an element of propellant passes from its point of injection into the combustor until it is converted into combustion products. However, this basic effort needs to be continued because knowledge of how the physical and chemical processes are influenced by injector element design and operating conditions, and how they are altered by factors such as pressure and velocity perturbations is essential to the successful application of instability theory. Should the key be found in these fundamental studies the dividends would be tremendous—think what it would mean to be able to directly predict stability from parameters such as droplet size (primarily a function of the injection orifice diameters and differential pressure) and the unsteady burning rate factors (from a knowledge of propellant choice, injection density, axial and transverse combustion distribution, etc.).

In category two, the theories as currently used act more to indicate trends and thus point the way to logically move in achieving stability. Correlations using the theories as outlined in Chapters 4, 5 and 6 can all point to considerable successes in this regard. Through refinements in our knowledge via the more fundamental studies, future theoretical models hopefully will improve these stability correlations. We have moved a long way from the dark days of the early fifties. Incorporation of nonlinear effects, with the resultant clarification of phenomena that previously were poorly understood, is one milestone along the road. Computer developments and mathematical advances have provided powerful tools to the theoretician in his battle with the instability problem. Unfortunately, because of such factors, a crash program to devise the ultimate theory has never been feasible—constant reevaluation of the current tools available and how they relate current knowledge of the actual rocket combustion instability requires both time and patience.

Before leaving the subject of theory status, mention should be made of low and intermediate frequency theory as well as that pertaining to resonant combustion. Although often regarded as a problem substantially less difficult, instability in the low and intermediate ranges continues to appear in a surprising number of engine development programs. Often this is due not to the lack of theory or the inability to analyze the problem but rather because of the numerous factors that can influence the occurrence of these instabilities and new parameters that enter the picture because of different operating regimes. A recent example is the problem associated with pressurization gases that dissolve in the propellants causing enhancement of lower frequency oscillations. Further study is currently being carried out to provide the proper model. Another example is the spray bunching phenomenon associated with intermediate frequency oscillations. Studies in that case have yielded important insight so that problems of that type could be overcome.

In category three, immediate solutions to the instability problem are being sought using damping devices. Success has been achieved in almost every case. Progress to date has also been good in understanding how these devices function, particularly in the case of liners where theoretical models have kept pace with the applications. Based on usage, certainly baffle proponents need to make few apologies. Even without a good theoretical base, experimentation with the controlling design parameters has achieved a high degree of success. Were it not for the heat transfer penalties and the design complications, the quest for alternate solutions would have gained little impetus. Recently more effort has been directed toward better explaining the fluid mechanical role played by baffles so that less empiricism will be required in future applications.

With regard to liners and the closely related acoustic slots, application has been rather limited

although the tests that were performed have been generally quite encouraging. As mentioned in the previous section, limited liner concepts and slots have been successfully applied to developed hardware. In most applications it is required that the gas properties (speed of sound based on temperature, molecular weight, and ratio of specific heats) possess a degree of uniformity so that the theory may be successfully applied. The trend in optimization is to choose the best location for these damping devices so that designs can be minimized in size, complexity and cost. Acoustic liners for ablative chambers is one approach being investigated. The theory of acoustic slots, nonlinear regimes of operation, and optimum configuration based upon fundamental flow considerations are typical of other areas of study.

The last two status categories are concerned with detection and rating combustion instability incidences. Detection has vastly improved over the years. Where there were at one time problems in evaluating instability occurrences at relatively low frequency, today measurements at tens of thousands of cycles per second have been achieved, thus allowing not only better high frequency measurements, but accurate recording of shock-type wave forms as well. One of the principal factors in this success is the wide use of relatively small piezoelectric transducers with ablative protection, helium or water cooling. This together with tape recording advances (flat response to 80 kHz or better is now possible) has allowed these and other miniaturized probes to make unsteady pressure measurements that were previously impossible. Although further improvements in pressure measurements will undoubtedly take place in the future, the current status is extremely good.

In those applications where chamber pressure measurements still are not feasible (e.g., certain flight-weight hardware) other primarily optical techniques, often using recent advances in technology, have been used with considerable success. These approaches are described in Sect. 9.4.

Last of the categories is the status of rating methods to ascertain the tendency toward combustion instability of an engine. Stability rating techniques have improved over the years to a point that rating of combustors over a wide thrust range can be achieved with a high degree of confidence. Problems may still exist in the very low thrust range where the rating technique may alter the normal combustion environment or provide a source for damping after the disturbance has been generated (the physical size of the bomb can be the problem in the first instance, the port of the pulse gun the cause in the second). However, these are the exceptions rather than the rule and the ability to rate engines for stability has become quite refined as discussed in connection with Dynamic Stability (Sect. 1.2.4) and Stability Rating (Chapter 10).

Thus it might be said at this time that a good working balance has been achieved between the theoretician and experimentalist, the development engineer and the researcher in the field of combustion instability. Each group has made a contribution toward the goal of providing stable combustors and in the understanding of the controlling factors. Not all the problems have been solved but steady progress has been made on all fronts. Future needs will require new insight; however, the immediate problem of engine stabilization has been achieved in almost every case. Alternate approaches have evolved so that important factors such as performance, chamber compatibility, and stability can exist in harmony.

CHAPTER 2

Steady-State Processes

2.1 GENERAL DESCRIPTION OF COMBUSTION AND FLOW PROCESSES*

In a very general sense, the character of the time-dependent perturbations that can exist in a system depends on the steady-state properties of the unperturbed system. Therefore, every aspect of the steady-state combustion and flow processes in liquid propellant rocket motors is potentially relevant to combustion instability. For this reason, it is important to have as thorough a knowledge as possible of steady-state motor processes before undertaking a study of combustion instability. Five textbooks can be recommended as sources for background material: Ref. 63, Ref. 78 (especially Ch. 7), Ref. 536 (especially Ch. 26), Ref. 535 (especially Ch. 3), and Ref. 740 (especially Ch. 11).

A complete knowledge of the sequence of events that occurs in a steadily operating liquid propellant rocket motor has never been attained. Liquid propellant combustion processes are quite complicated and defy precise analytical description. A host of comprehensible subprocesses are of direct relevance to the overall combustion sequence as shown in Fig. 2.3.3a. It is details of these subprocesses to which subsequent sections of this chapter are devoted. In the present section, we shall attempt to discuss how these subprocesses might be integrated into a description of the overall process. The integration is necessarily imprecise; except for the simplest models, it consists merely of patchwork.

2.1.1 Overall Description

As a brief introduction to the kinds of combustion and flow processes that occur in liquid propellant rocket motors, it can be stated first that the propellants are usually injected from a distributing manifold (Sect. 2.2.1) through orifices into the combustion chamber in the form of liquid jets (Sect. 2.2.2). In some manner, the jets must atomize, i.e., break up into small droplets, and the droplets must vaporize. Atomization is often achieved by causing two (doublet) or three (triplet) streams of like (or sometimes unlike) liquids to impinge;* impinging jets produce thin liquid sheets or fans which disintegrate rapidly, first into ligaments and then into droplets (Sect. 2.2.3). Except in monopropellant systems, the reactive fuel and oxidizer vapors must intermix (Sect. 2.3.3.3). The mixed vapors react, and finally the hot product gases flow out of the combustion chamber through a choked nozzle.

Numerous variations of this sequence of events can occur. For example, with some injector designs the liquid propellants may be partially or totally mixed, atomized or vaporized before they enter the combustion chamber, by contouring the internal injector geometry suitably, by injecting gases into injector passages in a controlled manner, or by other methods (Sect. 2.3.3.1). Some propellants (monopropellants and bipropellant components with monopropellant characteristics) may experience appreciable condensed-phase combustion reactions before mixing or vaporizing; in other systems liquid-phase mixing may occur and give rise to condensed-phase or surface reactions. Heterogeneous reactions may also be of importance in the absence of liquid-phase mixing, particularly for hypergolic propellant combinations which ignite spontaneously upon contact,

* F. A. Williams, Author.

* Other techniques that have been used for liquid/liquid systems include showerhead, splash-plate and swirl atomizers. Gas/liquid injectors often employ coaxial elements where liquid in the central jet is sheared by a surrounding annular gas. Impinging gas and liquid jets are also used.

and notably at interfaces between impinging fuel and oxidizer jets or fans. Thorough gas-phase mixing of fuel and oxidizer may not be achieved, either by accident or by design (Sect. 2.5), e.g., poor mixing occurs near the chamber walls when fuel-rich streams are intentionally sprayed there for purposes of cooling. Condensed phases may be present in the equilibrium mixture of combustion products when utilization is made of propellants containing either metals (which produce refractory oxides) or substantial amounts of carbon (which itself condenses). There are regions in many motors, especially between spray fans, where reaction products recirculate back to the vicinity of the injector instead of proceeding directly to the nozzle, with the result that a fraction of the gases remains in the combustion chamber for a long time (Sect. 2.3.4). A number of examples may be cited of chambers which operate at pressure levels above the critical point of one or more of the liquid propellants;[601] under these conditions the sharp distinction between liquid and gas disappears and the usual descriptions of atomization and vaporization processes require modification (Sect. 2.4.2.2).

This list of complications, illustrating the nonsystematic ways in which departures from the normal combustion sequence often occur, could be extended farther. However, it is less instructive to pursue a discussion of complications than to elaborate further on simpler models for the combustion sequences. The present paragraph serves as a warning not to apply existing models universally.

The following nomenclature pertains to Sect. 2.1:

A, n	Constants in vaporization rate expression, Eq. 2.1.5–1
a, b, α, β	Constants in size distribution function, Eq. 2.1.6–1
$\mathfrak{B}$	Pre-exponential (frequency) factor in reaction rate
D_I	First Damköhler number
E_{act}	Activation energy
$\mathbf{F}_j$	Drag force per unit mass on drop of kind j
$G(r_L)$	Drop size distribution function
g_j	Number of drops of kind j per unit volume
H_j	Total (thermal+chemical) enthalpy added to gas from drop of kind j per unit mass of drop vaporized
k	Specific reaction rate constant
$\dot{m}_j$	Time rate of increase in mass of drop of kind j
Q_j	Number of drops of kind j produced per unit volume, per unit mass range, per unit time
$\mathbf{q}$	Heat flux vector
$\mathfrak{R}$	Gas constant per unit mass
$\mathfrak{R}^o$	Universal gas constant
$\mathbf{U}_i$	Diffusion velocity of species i
$\mathbf{V}_{Lj}$	Velocity of drop of kind j
$\mathfrak{w}_i$	Mass rate of production of species i by gas-phase reactions
$\mathbf{x}$	Position of drop in chamber
η_c	Combustion efficiency
τ_c	Overall conversion time
τ_r	Residence time
Ω_{ij}	Mass of species i added to gas by a vaporizing drop of kind j per unit mass of drop vaporized

Subscripts:

i	Index denoting chemical species: $i=1, \ldots, N$
j	Index denoting droplet kind; $j=1, \ldots, M$ (e.g., fuel, oxidizer)

2.1.2 Conversion Time and Residence Time

A helpful crutch in considering the complex sequence of combustion processes is to ascribe to the propellant combination an overall conversion time τ_c, which is the time required, from the instant of injection, for a representative element of propellant to produce equilibrium combustion products. Sophisticated variants of this conversion time appear in the "time-lag" descriptions of combustion instability[179] (Sect. 4.2). In discussions of steady-state motor operation, it is relevant to compare τ_c with the residence time τ_r of a representative element of propellant in the chamber. Obviously the optimum motor design is achieved when the first Damköhler number[213] $D_I \equiv \tau_r/\tau_c$ is unity, since for $D_I<1$ the residence time is too short for the conversion processes to be completed in the chamber, whereas for $D_I>1$ the excessive chamber volume may cause flow friction and

weight penalties. The description of the steady-state combustion sequence, which arises from the τ_c and τ_r concepts, is ill-defined and physically unsatisfying because nothing is said about the history of events that occur during the interval τ_c, thereby making it impossible, in general, to compute either τ_c or τ_r in a simple way. One must introduce simplifying hypotheses concerning processes that occur during τ_c for these concepts to become useful. Some simplified models lend themselves naturally to description in terms of τ_c, while others do not.

2.1.3 Characteristic Length and Characteristic Velocity

One useful simplifying assumption is that injected propellants vaporize very rapidly, since then both τ_c and τ_r can be investigated by considering only gas-phase processes. Under this condition, if the material in the combustion chamber is approximated as an ideal gas, with gas constant $\mathfrak{R}$ and specific heat ratio γ, at stagnation conditions, then τ_r is simply related to the chamber temperature T_c and to the characteristic length L^* of the motor (the ratio of the chamber volume to the throat area). This correspondence can be seen by first noting that τ_r is the ratio of the mass contained in the chamber to the mass per second flowing out the nozzle, then using the well-known isentropic formula relating the mass flow through a choked nozzle to stagnation conditions; the result is[78]

$$\tau_r = L^*(\gamma\mathfrak{R}T_c)^{-1/2}\left(\frac{\gamma+1}{2}\right)^{\gamma+1/2(\gamma-1)}$$

$$= \frac{L^*}{\gamma c^*}\left(\frac{\gamma+1}{2}\right)^{\gamma+1/\gamma-1} \qquad (2.1.3\text{–}1)$$

where the characteristic velocity c^* (the product of chamber pressure and throat area divided by the mass flow rate) has been introduced in the last expression. This result for τ_r enables one to interpret the Damköhler criterion for optimum motor design in terms of an optimum characteristic length L^*. Irrespective of the validity of the assumption of short condensed-phase residence times, it may be stated that experimentally, optimum values for L^* are observed to exist and to vary appreciably with propellant combination, injector design, etc.; they typically lie in the range 10 to 70 inches.

2.1.4 Gas-Phase Processes

Additional hypotheses concerning the nature of the gas-phase conversion processes are needed for obtaining a correspondingly simple expression for τ_c. If it is assumed (in addition to instantaneous vaporization) that gas-phase mixing processes are also rapid, so that the gases in the chamber are essentially premixed combustibles, then τ_c is determined by the chemical kinetics (both mechanisms and rates) of the gas-phase reactions. For example, approximating the gas-phase reactions as a one-step, first-order process with specific reaction rate constant

$$k = \mathfrak{B}\exp(-E_{act}/\mathfrak{R}^\circ T_c) \qquad (2.1.4\text{–}1)$$

(where $\mathfrak{B}$ is the frequency factor, E_{act} is the activation energy and $\mathfrak{R}^\circ$ is the universal gas constant), one finds by solving the elementary first-order chemical kinetic equation that the ratio of the mass of reactants present at time t to the mass of reactants present at the time of injection (t=0), a ratio which clearly equals the combustion efficiency η_c of a chamber with residence time t, is given by

$$\eta_c = 1 - e^{-kt} \qquad (2.1.4\text{–}2)$$

Strictly speaking, this result yields an infinite chemical conversion time τ_c (a property shared by many widely differing models, which makes it more appropriate to discuss the results of such models in terms of η_c rather than L^*), but combustion will be reasonably complete (e.g., $\eta_c = 0.99$) in a time that is expressible in terms of the parameters $\mathfrak{B}$, E_{act} and T_c; e.g.,

$$\tau_c \approx 4.61\mathfrak{B}^{-1}\exp(E_{act}/\mathfrak{R}^\circ T_c) \qquad (2.1.4\text{–}3)$$

since $\ln(1-0.99) = -4.61$. This result provides an illustration of how, with a sufficient number of assumptions, the conversion time can be related to parameters of a more fundamental nature.

Much more can be said about gas-phase chemical kinetics, about gas-phase mixing and about models that disregard the presence of condensed phases in the chamber. The best description of premixed gas-phase kinetics depends intimately on the propellant combination; for some propellants

(e.g., hydrogen-oxygen) the kinetics are understood well,[122] while for others practically no information exists. It generally is found that the gas-phase reaction time decreases when either the chamber temperature or the chamber pressure is increased.

Descriptions of gas-phase mixing processes (Sect. 2.3.3.3) depend strongly on chamber shape and on injection-pattern geometry; relevant molecular transport properties are typically known more accurately than chemical kinetic parameters, but turbulent mixing processes, which generally occur in motors, are difficult to describe properly.[536,740] Mixing-process models for rocket combustion have not received much attention and deserve to be studied further.

One-dimensional models for premixed gas flow in constant-area motors, accounting for nonzero Mach numbers in the chamber through relevant mass, momentum and energy conservation equations, can be formulated in terms of the algebraic equations of "diabatic" flow (constant-area flow with heat addition). Such models can be extended to variable-area chambers and in particular to throatless chambers which produce supersonic flow through thermal choking (e.g., purely diverging reactors); the description then involves obtaining solutions to ordinary differential equations.[289,748]

Instead of dwelling further on these and other elaborations of descriptions of gas-phase processes, we shall proceed to discuss models that consider condensed phases. One reason for doing so is that for most rocket motors the conversion time τ_c is appreciably longer than would be expected on the basis of gas-phase chemical kinetics alone; thus, if gas-phase processes are dominant, mixing must be of importance.

2.1.5 Condensed-Phase and Gasification Processes

A straightforward extension of the preceding ideas is to assume that τ_c is the sum of two terms, a time lag associated with condensed-phase processes and a time lag associated with gas-phase processes.[78] It can be argued approximately and qualitatively that the *rates* of the condensed-phase processes are likely to be relatively unaffected by the chamber pressure, whereas the rates of the gas-phase processes are pressure dependent, generally increasing as pressure increases. This causes the ratio of the condensed-phase to gas-phase τ_c contributions to increase as the chamber pressure is increased, and it also provides a basis for introducing a "pressure-sensitive time lag" into descriptions of combustion instability[179] (Sect. 4.2). Since this division of the conversion time is rather imprecise, it is instructive to consider condensed-phase models which are more explicit, less phenomenological and more mechanistic.

Aside from descriptions dealing with homogeneous condensed-phase chemical kinetics, the simplest model that focuses attention on the condensed phase was stated first by Probert.[568] It is assumed that the liquid propellant jets break up instantaneously into droplets and that gases evolved from droplets by vaporization, mix and react instantaneously to produce equilibrium combustion products. The droplets are assumed to move at a velocity V_L in the direction of the chamber axis, and the rate of vaporization of these droplets is taken to control the conversion time. Thus, the model is essentially one of spray combustion or spray evaporation.

A number of different choices are possible for describing the spray vaporization processes. For monopropellant systems it may be assumed that the chemical heat release occurs in the spherically symmetrical gas flow region near each droplet. Then monopropellant droplet combustion theories (Sect. 2.4.3) should be used for describing the vaporization rates. If it is assumed that the chemical heat release occurs in gas regions far removed from each droplet, in that case simple vaporization theories (Sect. 2.4.1) should be used for describing the vaporization rates.

In bipropellant systems (Sect. 2.4.2) there is a great variety of limiting cases. If one of the propellants is much more volatile than the other, then it is reasonable to assume that the volatile propellant vaporizes instantaneously after injection and that the spray model refers to vaporization of the less volatile constituent. In bipropellants utilizing liquid oxygen and hydrocarbon fuels, it can usually be assumed that the oxidizer vaporizes instantaneously, while for hydrogen-oxygen systems the hydrogen can often be assumed to be gaseous at the injector exit.[440] When one of the propellants vaporizes quickly, the vaporization rate of the less volatile constituent can be described on the basis of the theory of

burning of a fuel droplet in an oxidizing atmosphere (or of an oxidizing droplet in a fuel atmosphere, as the case may be) (Sect. 2.4.2). Alternatively, if chemical reaction times are long compared with the time for an element of vapor to diffuse away from the vicinity of a droplet (but still short compared with the time for the droplet to vaporize), the droplet vaporization rates can be described on the basis of the theory of nonreactive droplet vaporization (Sect. 2.4.1). If both propellants are of comparable volatility, then spray descriptions can be developed for which condensed phases of two different chemical types are taken into account.[740] Droplet vaporization during the heat-up period can also be analyzed.

Whatever description is adopted for the vaporization process, analysis of this process yields an expression for the time rate of change of droplet radius r_L, which can usually be approximated reasonably well* by an equation of the form[740]

$$\frac{dr_L}{dt} = -Ar_L^{-n} \qquad (2.1.5\text{–}1)$$

where the value of A which is independent of r_L, depends on local gas-phase and droplet properties and where the constant n generally lies in the range $0 \leq n \leq 1$.

2.1.6 Spray Combustion

In order to complete the description of a spray combustion model, one might assume for simplicity that at any given axial position in the chamber all droplets are of the same size (i.e., that the spray is monodisperse). It is obviously more realistic to account for differences in the diameters of the various droplets, but the system is so complex that this can be done only statistically. Thus, it is convenient in such models to introduce a droplet size distribution function $G(r_L)$, such that $G(r_L)dr_L$ is the probable number of droplets with radius between r_L and r_L+dr_L. A four-parameter functional form for $G(r_L)$, capable of correlating experimentally measured size distributions, is[743]

$$G(r_L) = br_L^{\beta} \exp(-ar_L^{\alpha}) \qquad (2.1.6\text{–}1)$$

where a, b, α and β are constants. Other functional forms have also been used (Sect. 2.2.4).

A partial differential equation with independent variables r_L and t (or r_L and the axial coordinate x) can be written for the time (or space) evolution of the distribution function G. This equation has been referred to as the spray equation. If the values of the constants a, b, α and β are assumed to be known from measured atomizer characteristics, and if the quantities V_L, A, and n are treated as known constants, then the spray equation can be solved for the spatial development of G in the combustion chamber. From this solution, one can calculate η_c for a chamber of a specified length, thereby obtaining a rather detailed description of the combustion processes implied by the spray combustion model. It is found that, for a given chamber length, large vaporization rates (large A), small droplets (small r_L), small injection velocities (small V_L) and spray distributions that are as nearly monodisperse as possible, all favor high combustion efficiency.[740]

This relatively simple type of spray combustion model is amenable to improvement by taking into account the effect of the spray on the gas phase. It is not proper to specify V_L and A in advance; instead, these quantities will vary with axial distance in a manner dictated by mass, momentum and energy conservation for the two-phase system in one-dimensional flow. We shall not delve now into the details or results of the improved analyses, except to say that it becomes desirable to account for differences between droplet and gas velocities, so that droplet drag coefficients become relevant parameters.† Studies of the coupling between the gas phase and the spray have led to a considerable amount of information on propellant vaporization as a design criterion for rocket-engine combustion chambers.‡ The primary fallacy in these descriptions probably is the assumption of one dimensionality; if this assumption is deleted, then it becomes exceedingly difficult to develop a comprehensible, detailed description of spray combustion.

A few calculations have been made for sophisti-

* This relationship, as usually derived, does not consider forced convection or droplet stripping. However, these processes can be correlated approximately by the same equation with a suitable relative velocity dependence in A.

† See Refs. 53, 535, 656, 660 and 745 and see Sects. 2.3.3.2 and 2.4.1 for drag coefficients.

‡ See Refs. 117, 132, 343, 369, 373, 420, 557, 558, 559, 564, 565, 651, 738 and Sect. 7.2.4.

cated spray combustion models in which properties are not invariant in planes normal to the motor axis.* The choice of the transverse variations is based on the droplet distributions expected to be produced by atomizers that have particular relative geometrical positions, consistent with some simple injector designs. Cold-flow measurements of spray characteristics can help in providing upstream boundary conditions and in extending the calculations to include a wider class of injectors.[356] Electronic digital computers are used in the calculations, and it is difficult to draw generally valid conclusions from the results. Faced with such complexities in attempts to develop improved theoretical descriptions of the complete combustion sequence, one is motivated to seek guidance from laboratory experiments on rocket motors.

2.1.7 Experimental Observations†

The most revealing laboratory experiments that have been reported consist of observations made by Levine and coworkers on two-dimensional motors with transparent walls.[420,421,424,440] Both streak photography and high-speed cinematography have been employed. The natural luminosity of the combustion process has been observed, and strong backlighting has been used in an effort to make condensed phases visible. Many measurements were made with liquid oxygen as the oxidizer and alcohol as the fuel, since this combination facilitates observation in some respects. However, a number of observations were reported on liquid oxygen and hydrocarbon fuels such as kerosene, on liquid oxygen and gaseous or liquid hydrogen, and on storable hypergolic combinations such as nitrogen tetroxide and unsymmetrical dimethyl hydrazine.

These experiments show highly heterogeneous conditions in the combustion chamber and do not appear to conform to the assumption of one-dimensional flow. The streak photographs are interpretable in terms of the presence of droplets of differing sizes moving with differing velocities; slopes of streak traces can be correlated with velocities ranging from those expected for the largest droplets to those expected for the gas.[420] The motion pictures show axial striations of luminosity extending downstream from the like-on-like doublet fans, sometimes beyond the throat of the nozzle.[440] They indicate that intense heat release occurs where the fuel and oxidizer fans first meet and that the more volatile propellant often vaporizes quickly, producing a downstream region in which droplets of the less volatile propellant (e.g., hydrocarbon fuel in hydrocarbon-liquid oxygen systems) burn in the gaseous atmosphere provided by the volatile constituent. Downstream intensity peaks coincide with the axes of the fans of the less volatile propellant, thereby providing support for the use of droplet combustion models in downstream regions. It was inferred qualitatively from these studies that the upstream jet-impingement and fan-intersection regions are of critical importance to phenomena of combustion instability.[440] Processes occurring in these regions are certainly the most complex and the least understood of the processes occurring anywhere in the chamber. Thus, it is likely to be quite difficult to develop adequate analytical descriptions of the steady-state combustion and flow processes that are most relevant to combustion instability.

2.1.8 Elaboration on Description of Spray-Combustion Models

In spite of this unfavorable outlook, analytical work is continuing on the development of steady-state spray-combustion models, with the specific objective of obtaining models that will be useful in calculations of combustion instability (Sects. 4.3 and 7.2.4). It is therefore of interest here to look more closely at the bases of these models and at how subsequent material in Chapter 2 bears on their development.

Models for steady-state combustion of a spray generally begin with the assumption that the spray is a dilute collection of spherical droplets. The term "dilute" means that the volume occupied by condensed material can be neglected in comparison with the volume occupied by gas—an excellent approximation except possibly in the immediate vicinity of the injector. In hypothesizing that droplets are spherical, consideration of the injection process and of most atomization

* See Refs. 165, 166, 356, 421 and Sects. 2.3 and 2.5.
† See also Sects. 2.3.3.2, 2.3.3.3 and 2.3.4.

processes is ruled out. Thus the information in Sects. 2.2.1, 2.2.2 and 2.2.3 affects spray combustion theories only through upstream boundary conditions.* An exception to this statement is that atomization through aerodynamic shattering and atomization or coalescence through interdroplet collisions, can sometimes be included as break-up or coalescence criteria, by assuming that the interaction time is short enough for the consequent droplet deformations to be negligible; thus, material in Sect. 2.2.3 sometimes appears directly in spray combustion models (Sect. 4.3.1.3).

If $\mathbf{V}_{Lj}$ denotes the velocity of a j droplet of mass m, then counting droplets of kind j leads to the steady-state spray equation

$$\frac{\partial}{\partial m}(\dot{m}_j g_j) + \nabla \cdot (\mathbf{V}_{Lj} g_j) = Q_j \qquad j = 1, \ldots, M \quad (2.1.8\text{–}1)$$

Here the size distribution function $g_j(m, \mathbf{x})$, defined as the number of droplets of kind j per unit volume at position $\mathbf{x}$ per unit range of mass about m, possesses an m dependence that can be described by formulas inferred from either Eq. (2.1.6–1) or equations appearing in Sect. 2.2.4 (which contains additional information on distribution functions). The quantity $\dot{m}_j(m, \mathbf{x})$ is the time rate of increase in mass of a droplet of kind j and mass m at position $\mathbf{x}$; its approximate functional dependence on m can be inferred easily from Eq. (2.1.5–1). A more elaborate form indicating the dependence on droplet and gas properties is given in full in Sect. 2.4. The source term Q_j represents the number of droplets of kind j per unit volume per unit range of m produced per unit time by shattering, droplet collisions, etc.; the information in Sect. 2.2.3 must be used in obtaining Q_j. There are M different kinds of droplets (fuel, oxidizer) in the system.

Conservation of chemical species i in the gas can be expressed, for steady flow of a dilute spray, as

$$\nabla \cdot [\rho(\mathbf{V} + \mathbf{U}_i) Y_i] = \mathfrak{w}_i - \sum_{j=1}^{M} \int_0^\infty \dot{m}_j \Omega_{ij} g_j dm \qquad i = 1, \ldots, N \quad (2.1.8\text{–}2)$$

Here ρ is the gas density, $\mathbf{V}$ is the gas velocity, Y_i is the mass fraction of chemical species i in the gas, $\mathbf{U}_i$ is the diffusion velocity for species i, $\mathfrak{w}_i$ is the mass rate of production of species i in the gas phase by homogeneous chemical reactions, and there are N different gaseous species in the system. The quantity Ω_{ij} is defined as the mass of chemical species i added to the gas by a vaporizing droplet of kind j per unit mass of droplet vaporized. The introduction of Ω_{ij} affords the option of either considering simple vaporization (in which case, for the example of a fuel droplet, Ω_{ij} would be unity when i denotes fuel and zero otherwise) followed by homogeneous combustion, which is accounted for through $\mathfrak{w}_i$, or hypothesizing the existence of a diffusion flame in the thin boundary layer surrounding the droplet (in which case, for the example of a fuel droplet, Ω_{ij} would be zero when i denotes fuel, negative when i denotes oxidizer, and positive when i denotes reaction products, with the values of Ω_{ij} for oxidizer and products determined by the stoichiometry of the diffusion flame). The material in Sect. 2.4 is relevant to the determination of Ω_{ij}.

Overall mass conservation for the gas can be obtained by summing Eq. (2.1.8–2) over all species N. Since conservation of mass in the gasification process implies

$$\sum_{i=1}^{N} \Omega_{ij} = 1 \qquad j = 1, \ldots, M$$

since conservation of mass in homogeneous chemical reactions implies

$$\sum_{i=1}^{N} \mathfrak{w}_i = 0$$

and since the definition of diffusion velocities implies

$$\sum_{i=1}^{N} Y_i \mathbf{U}_i = 0$$

we find (using $\sum_{i=1}^{N} Y_i = 1$) that

$$\nabla \cdot (\rho \mathbf{V}) = -\sum_{j=1}^{M} \int_0^\infty \dot{m}_j g_j dm \quad (2.1.8\text{–}3)$$

The derivation demonstrates that Eq. (2.1.8–3) is contained in the set (2.1.8–2).

* Aid in establishing upstream boundary conditions can be gleaned from Sects. 2.3.1, 2.3.2, 2.3.3.1 and 2.3.4 as well as 2.2.1, 2.2.2 and 2.2.3.

To derive an equation for conservation of momentum of the gas, it is reasonable for dilute sprays in rocket motors to assume that forces experienced by droplets consist solely of aerodynamic forces (skin-friction and separation drag) exerted by the gas. If $\mathbf{F}_j(m, \mathbf{x})$ denotes the drag force per unit mass (i.e., acceleration) exerted on a droplet of kind j by the gas, then the steady-state momentum conservation equation for the gas can be reasoned to be

$$\rho\mathbf{V}\cdot\nabla\mathbf{V} = -\nabla p - \nabla\cdot\mathfrak{T} - \sum_{j=1}^{M}\int_0^\infty m\mathbf{F}_j g_j dm - \sum_{j=1}^{M}\int_0^\infty \dot{m}_j(\mathbf{V}_{Lj}-\mathbf{V})g_j dm \qquad (2.1.8\text{–}4)$$

where p is the hydrostatic pressure, $\mathfrak{T}$ is the viscous stress tensor of the gas, and the last term accounts for the momentum carried to the gas by the material that vaporizes from the droplets. Information appearing in Sects. 2.3.3.2 and 2.4.1 is useful for obtaining $\mathbf{F}_j$ in terms of droplet and gas properties. The steady-state motion of the droplets is described by the equations

$$\dot{m}_j \frac{\partial}{\partial m}\mathbf{V}_{Lj} + \mathbf{V}_{Lj}\cdot\nabla\mathbf{V}_{Lj} = \mathbf{F}_j \qquad j = 1, \ldots, M \qquad (2.1.8\text{–}5)$$

in which the first term accounts for the possibility that the droplet velocity is size dependent.

In terms of the total (thermal plus chemical) enthalpy per unit mass for the gas h and the gas-phase heat flux vector $\mathbf{q}$, which includes energy transfer by heat conduction, diffusion and radiation, the steady-state equation for conservation of energy for the gas can be written as

$$\nabla\cdot[\rho\mathbf{V}(h+V^2/2)] = -\nabla\cdot\mathbf{q} - \nabla\cdot(\mathfrak{T}\cdot\mathbf{V}) - \sum_{j=1}^{M}\int_0^\infty m(\mathbf{F}_j\cdot\mathbf{V}_{Lj})g_j dm - \sum_{j=1}^{M}\int_0^\infty \dot{m}_j(H_j + V^2_{Lj}/2)g_j dm \qquad (2.1.8\text{–}6)$$

where $V^2 \equiv \mathbf{V}\cdot\mathbf{V}$ and $V_{Lj}^2 \equiv \mathbf{V}_{Lj}\cdot\mathbf{V}_{Lj}$. The last two terms account for the work done on the gas by the droplets and the energy added to the gas by the material vaporizing from the droplets. The quantity H_j is defined as total (thermal plus chemical) enthalpy added to the gas from a droplet of kind j per unit mass of droplet vaporized. Its value depends on processes occurring in the boundary layer adjacent to a droplet and can be inferred from discussion given in Sect. 2.4. Applying energy conservation across the boundary layer, one finds that H_j is the total enthalpy leaving the surface of a droplet of kind j per unit mass vaporized and therefore energy conservation for the droplet can be expressed as

$$\dot{m}_j \frac{\partial}{\partial m}(m h_j) + \mathbf{V}_{Lj}\cdot\nabla(m h_j) = \dot{m}_j H_j \qquad j = 1, \ldots, M \qquad (2.1.8\text{–}7)$$

where $h_j(m, \mathbf{x})$ is the total (thermal plus chemical) enthalpy per unit mass for a droplet of kind j.

Equations (2.1.8–1) through (2.1.8–7) can be viewed as 5M+N+4 equations in the 5M+N+4 unknowns g_j, (ρY_i), $\mathbf{V}$, $\mathbf{V}_{Lj}$, h and h_j. When expressions for gas-phase transport fluxes* $(U_i, \mathfrak{T}, \mathbf{q})$, homogeneous reaction rates† $(\mathfrak{w}_i)$, thermodynamic properties (p, ...) and droplet behavior $(\dot{m}_j, Q_j, \Omega_{ij}, \mathbf{F}_j, H_j$ as obtained from Sects. 2.2.3, 2.3.3.2 and 2.4) are appended to the set, and when upstream spray distribution functions and a sufficient number of other upstream boundary conditions and boundary conditions at the chamber side-walls are known, then in principle a complete description of the spray combustion process can be obtained from these equations. To develop such solutions is the fundamental objective of steady-state theories for spray combustion.

Since it is clear that the system of equations is complicated, solutions have been obtained only by introducing further simplifications. Except for the studies mentioned at the end of Sect. 2.1.6, the first simplifying assumption always has been one-dimensional flow. This reduces the number of independent variables from four (m and $\mathbf{x}$) to two (m and x). Next, unless one introduces highly simplifying assumptions concerning the fluid mechanics,[740] the usual practice has been to eliminate m as a variable by considering only monodisperse

* These quantities generally have been neglected entirely since typically they are small in the core flow.

† Only occasionally have these been included.

sprays,[656,660,738] by introducing a small number (2 to 5) of discrete droplet sizes,[558,559,564,565] or by accounting for a size distribution in a somewhat ad hoc manner.[745] The result is a set of ordinary differential equations in x which at least can be programmed for computer solution.

After reducing the system to ordinary differential equations, investigators have adopted two paths to obtain solutions. One group has simplified further until it becomes possible to obtain analytical solutions.[53,656,660,740,745] Another group has programmed the system for solution by digital computer.* The first approach leads rapidly to some general conclusions such as those cited in Sect. 2.1.6. The second approach affords the possibility of simultaneously including a greater number of phenomena. The second approach has produced a number of rather general conclusions for specific propellant combinations. These include[421]

a. A uniformly-distributed, one-dimensional treatment of the injection region is unrealistic.
b. Calculation of droplet acceleration in a high-velocity, combustion gas stream must include the influence of droplet deformation on the aerodynamic drag coefficient.
c. The effects of forced convection on heat and mass transfer processes must not be neglected.
d. Droplet breakup processes must be considered, particularly if combustion chamber length for attaining high efficiency is to be computed.
e. The combustion rates of monodisperse sprays compare well with the combustion rates of corresponding polydisperse sprays. If the largest droplets' velocities are of interest, however, the monodisperse spray model does not supply that information and cannot be used.
f. Both fuel and oxidizer sprays should be considered, particularly if details in the injection region are to be computed.
g. The changes of chamber pressure with combustion progress and gas acceleration are easily incorporated in a model for machine solution, and should not be neglected.

* Refs. include 132, 420, 557, 558, 559, 564, 565 and 738.

The applicability of the results to real rocket motors should always be judged through comparison with quantitative and qualitative observations such as those reported in Sects. 2.3 and 2.5.

2.2 INJECTION AND ATOMIZATION

2.2.1 Manifold Flow*

In all but the very simplest of injection schemes, such as a single element, it is necessary (or convenient) to distribute the propellant to the injection orifices by means of a manifold. In most current schemes this manifold consists of a number of connected passages fed by the single outlet of a shutoff valve, and terminating in the orifice array.

Consider first the case where the injector consists of a large number of relatively small orifices. The mass and mixture ratio distributions (Sects. 2.3.1 and 2.3.2) may then be characterized on a scale defined by the flow from the individual orifices, assuming the interaction of jets and sprays is unimportant for this situation. Here the manifold design, based on distribution capability, plays a dominant role in determining the essential features of the early reaction region in the chamber. If the manifolding results in a poor distribution of propellants; performance, chamber capability and even stability can be adversely affected. For such situations it is essential that the overall discharge coefficient from valve exit to orifice exit be matched (or controlled in a specified way if the discharge from individual orifices is not intended to be uniform) so as to provide the desired local flow.

As the scale of the element increases, the mass and mixture ratio distributions within individual elements are detectable in the overall combustion process.† Under these circumstances, the interaction between manifold flows and jet properties must be taken into account. The turbulence within the manifold and, in particular, the local velocities in the vicinity of the orifice entrance (e.g., the so-called cross-velocity), can directly influence the stability (both spatial and temporal), contiguous-

* J. H. Rupe, Author.

† Note that changes in combustion length can mask such effects.

ness, and symmetry of the effluent jets.[705] As these jet properties are degraded by adverse conditions within the manifold, the mass and mixture ratio distributions associated with each element become ill-defined, unsteady, and nonreproducible. This results in the initial conditions for the so-called steady-state combustion process also becoming indeterminate. Thus, it is seen that in addition to the process of propellant distribution, the manifold also has a role in determining the flow properties within the orifice itself and at the orifice exit. Although the orifice configuration[613,616] (Sect. 2.2.2) can be utilized in certain instances to relax such manifold requirements as low cross-velocity at the orifice inlet, the available compromises (e.g., an orifice more than 10 diameters long) are often unacceptable since they are believed by some designers to introduce insurmountable difficulties in fabrication.

In addition to the requirements that the manifold provide the essential control of mass distribution–either uniquely when jet properties are inconsequential or in conjunction with the orifice geometry when jet properties are a factor—it is also necessary to consider the absolute magnitude of the pressure loss sustained in the manifold itself and the absolute volumes contained within the flow passages. These are not free variables since they are, in general, elements of a flow system and must be considered from that viewpoint. Unfortunately, specific guidelines for manifold design have not as yet been elucidated; however, it seems safe to assume that the objectives of small volumes and low pressure losses are both desirable but often incompatible. Under steady-state conditions, manifold volume has little significance and hence can be increased to produce relatively quiescent conditions at the orifice entry and thus maximize jet stability. Conversely, the problems associated with flow transients at engine startup and shutdown, and propellant holdup in the manifolds are aggravated as the volumes increase.

The manifold problem can be treated to a first order analytic approximation by calculation of the equivalent hydraulic resistances of each passage. This basic concept is illustrated in most texts on hydraulics (see Refs. 234, 621, 709). This approach is clearly an iterative procedure that must account for the interaction of all flow elements. However, such analyses tend to degenerate rapidly through a series of compromises that are required to facilitate manifold fabrication. Thus, the manifold design is dominated by empiricism with consideration given to minimizing pressure drop, cross-velocities, and dead spots. The problem has received only superficial documentation in the open literature (for example, Ref. 705).

2.2.2 Jet Properties*

Insofar as liquid propellant rocket injectors are concerned, the term "jet" refers to the effluent flow from an injector orifice. In most cases of practical interest the jet is in the liquid phase† and is conceived as a steady, continuous stream that is aligned along a particular reference line relative to the exit orifice geometry, and exhibits a marked density discontinuity with its surroundings. Although many geometrical variations are possible, the one receiving wide acceptance is the "cylindrical" jet. This jet is characterized by an axis of symmetry, a free boundary, and a velocity profile within the flow. The extent to which these conceptual qualities are realized is to a large measure dependent upon the extent to which the flow within the cylindrical portion of the orifice can eliminate the deleterious effects introduced by the hydrodynamics of the manifold flow and the transition acceleration from the manifold to flow within the orifice boundaries.

The orifice configurations that are most common in rocket injectors are quite similar to those that have been utilized for many years in control and/or measurement devices.[464] This family of orifice configurations is illustrated in Fig. 2.2.2a and the essential features of each are as follows: (a) represents the conventional sharp edged orifice, (b) is a rounded or contour approach orifice, (c) is a higher L/D, square-edged orifice, which produces a cylindrical jet as in (a) and (b), while (d) is that same orifice where the jet has

* J. H. Rupe, Author.

† A notable exception is hydrogen, which in most cases is injected into an environment above its critical pressure so that the only possible distinction between liquid or gas is based on whether or not the temperature is less than or greater than the critical temperature. Other exceptions are found in the high chamber pressure designs receiving attention currently.

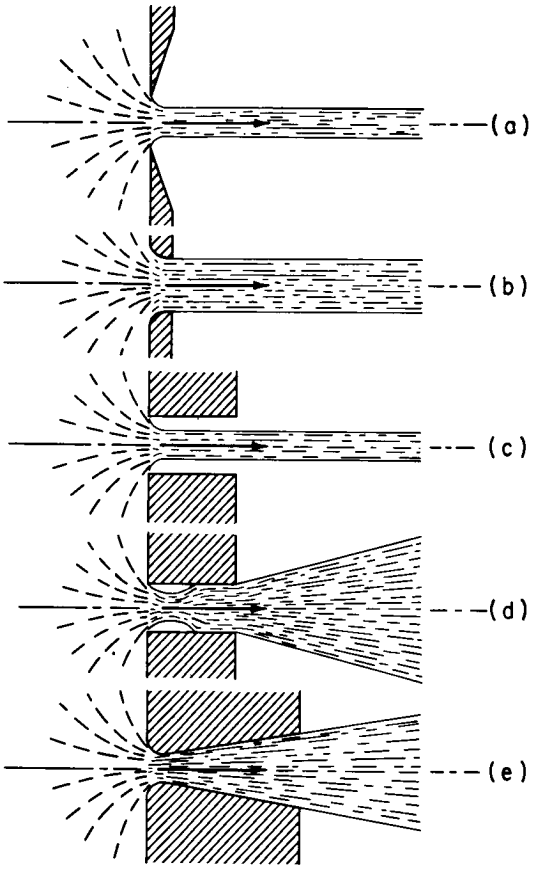

FIGURE 2.2.2a.—Jets emanating from several typical orifice configurations.

reattached to the orifice wall, and finally (e) represents a venturi orifice.

For the sharp-edged orifice flow conditions of (a) and (c) the discharge coefficient C_d lies between 0.6 and 0.7.* In (d), the flow reattaches to the wall allowing the orifice to flow "full." The result is agitated and divergent flow at the exit (bushy or broomy flow), and the discharge coefficient rises to between 0.8 and 0.85. A still higher C_d is achieved with (b) when the contour is not too abrupt and L/D is small ($\approx$0.25 to 0.5), i.e., for a good, smooth, rounded orifice $C_d \approx 0.97$. For the best designs $C_d = 0.99$, while with poor curvature, cross currents and resultant contraction the discharge coefficient may be as low as 0.90.[464]

In the case of the venturi orifice (e) both divergence angle and length affect the ability of the orifice to flow full.[464] Chamber conditions are also very important in determining flow in the divergent section; especially when this orifice is operated as a cavitating venturi[181] to limit communication from chamber to feed system. The discharge coefficient is therefore also easily altered.[464]

It is interesting to note that modern rocket injector designs are still dominated by the configuration exemplified by (c) and (d) and hence are characterized by the flow properties just described. The transition between flow condition (c) and (d) is known as "hydraulic flip" and is sensitive to injection pressure, orifice length/diameter ratio, orifice entrance configuration, and the fluid properties.

In an effort to delineate bounds on operating conditions for which hydraulic flip would occur, Northrup studied the phenomenon in 1951.[519] This work was extended by Wright[761] who attempted to determine the effect of cross-velocities on the separation conditions. In some very recent studies[383] these experiments were verified and an analytic model was developed as a tool to aid in predicting the conditions for which separation might occur. The interrelated effects of orifice L/D ratio, manifold cross-velocities and pressure drop on the discharge coefficient of typical orifices (and of the hysteresis effect exhibited) are illustrated in Figure 2.2.2b from the work of Northrup.[3, 519a, 318]

Clearly this concern with dual flow configurations is related to the generally recognized need to control discharge coefficients and maintain the stability and direction of the jet configuration as well. This is critical in those instances where the secondary flows become important, as exemplified in the sprays of impinging jets.

Correlations relating spray properties to the degradation of jet properties have not yet been devised. However some insight into the magnitude of these effects is given in Ref. 617 where it is shown that mass distributions in sprays of "well-controlled" impinging doublets exhibit gross variations when the velocity profiles are not identical. Similar illustrative experiments are described in

* A procedure for determining the discharge coefficients for "non-cavitating" flows through short, sharp-edged orifices has been developed by Hall,[304] who showed reasonable agreement with experimental measurements for that particular flow regime.

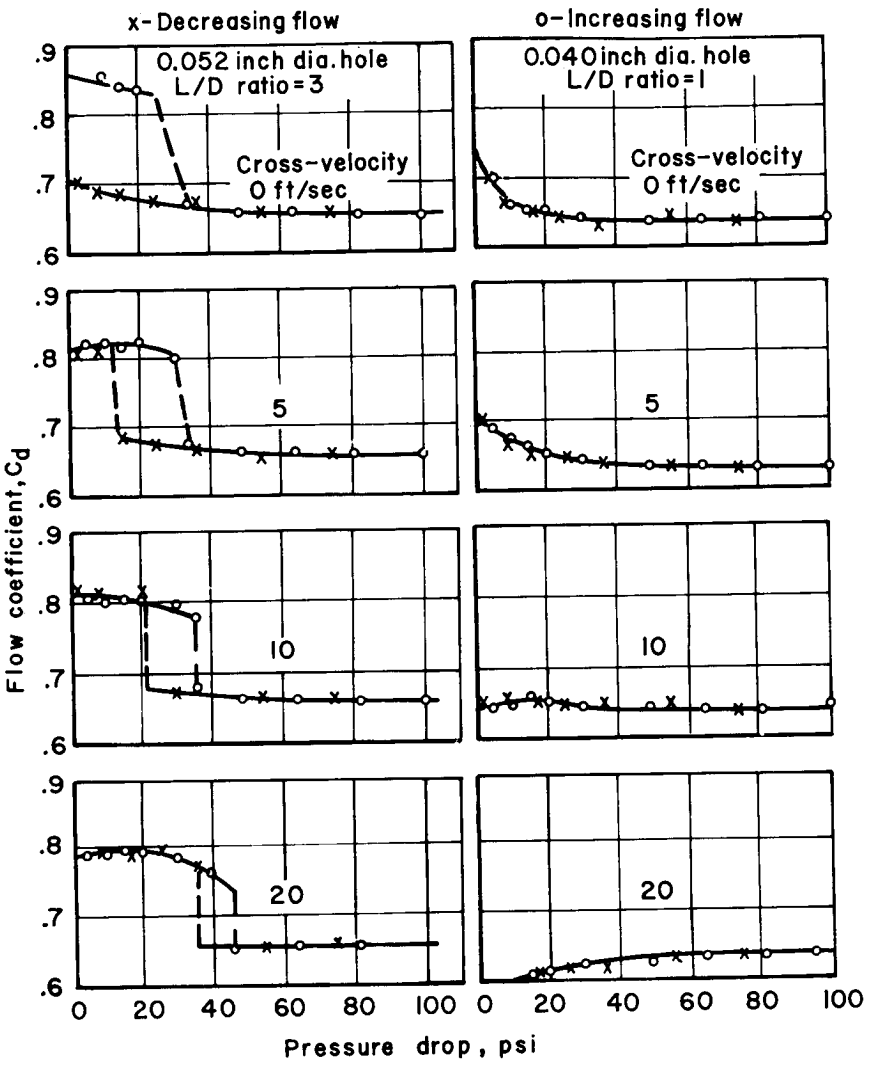

FIGURE 2.2.2b.—Typical variation of flow coefficient vs pressure drop at different cross-velocities for orifices with and without flow discontinuities.

Ref. 288 where truly identical jets whose centerlines were misaligned in a predetermined fashion were utilized to form a series of sprays and the resulting mass and mixture ratio distributions were determined. When taken together the results show that relatively small changes in direction and/or momentum (or its distribution within the jet) will produce marked changes in the properties of the sprays that are formed. Thus, it must be concluded that control of mass and mixture ratio distributions on a scale that is determined by the discrete properties associated with a given element must stem from adequate control of jet properties.

The detailed properties of a family of jet flows have been presented in some detail in Ref. 616. However, these studies failed to generalize on the relationship between orifice configuration and manifold disturbances to the resulting jet properties. Thus, although definitive information on steady jets formed by particular orifice geometries is available, the coupling between jet properties (as determined by injector design) and the consequent steady-state combustion environment has yet to be elucidated.

Although this chapter is primarily concerned with the steady-state properties of the injec-

tion/combustion process, it should be clear from the above that the attainment of truly steady jets is dependent upon conformance to at least one of two essential criteria; i.e., "quiescent manifolds" or "near fully-developed-flows at orifice exits." Since common practice does not satisfy either of these criteria, then it must also be concluded that in most instances the early combustion region is only quasi-steady and it is this quasi-steady environment that is perturbed by and ultimately coupled to the combustion chamber dynamics. The fact that variations in combustion chamber conditions, (e.g., pressure, vibration, etc.) can perturb these quasi-steady injection properties in a significant manner, not necessarily related to combustion or combustion instability, can introduce considerable difficulty in correlating unsteady "combustion" observations.

2.2.3 Mechanisms of Atomization*

The following nomenclature pertains to Sect. 2.2.3:

A_k	Coefficients in disturbance function series
C_d	Discharge coefficient
$f(x, r, \theta, t)$	Disturbance function
g	Spatial distribution of disturbance function
k	Transverse wave number
L_b	Breakup length
l_w	Wavelength
n	Longitudinal wave number, $2\pi/l_w$
s	Complex disturbance growth rate, $\lambda+i\omega$
t_b	Breakup time
t_{sep}	Time for separation of fluid from jet, fastest-growing disturbance
y	Thickness of annulus, coaxial injector element
λ	Growth rate of disturbance
ν	Kinematic viscosity
ω	Disturbance frequency
Subscript:	
max	Conditions associated with fastest-growing disturbance

* E. J. Rice, Author.

For proper combustion it is necessary to atomize the propellants and thereby provide a great increase in liquid surface area to accelerate burning. Hopefully, in this process the appropriate distribution of the propellants will be maintained so as to achieve the desired mixing. Atomization involves the breakup of liquid jets and/or sheets. In this section the processes involved in liquid stream and drop breakup are discussed with a brief review presented of the analytical treatments available to describe the simpler breakup mechanisms.

Several breakup mechanisms may be important in the atomization process with the mechanism dependent upon the type of injector. A highly idealized version of the atomization process may be described as follows: the liquid is ejected from an orifice as a jet, as a sheet, or as two or more jets which may impinge to form a sheet. Disturbances are present in the liquid which deform the surface. Typical disturbances include jet turbulence, gas bubble formation, injector orifice imperfections, aerodynamic effects from ambient gas, or injector vibration. Forces due to surface tension, or more importantly to aerodynamic pressure caused by a relative velocity difference between the fluid and the ambient gas, act upon the surface deformations causing them to grow. If growth is sufficient, the jet or sheet may be severed or at least an element of fluid may be ripped from the liquid surface. The severed fluid may form a drop or may form an unstable ligament which will later break up into drops and finally, if the aerodynamic force on the drops is sufficiently large, the drops can be shattered into smaller drops.

For some simple breakup mechanisms theoretical treatment has been successful. In the following sections the general analytical approach and its application to some simple breakup models are discussed.

2.2.3.1 *Liquid surface instability.*—A stable, steady flow system is assumed to exist as a liquid jet or sheet. Superimposed upon this stable system is an assumed disturbance of the form

$$f(x, r, \theta, t) = e^{st}g(x, r, \theta) \qquad (2.2.3\text{–}1)$$

where x, r, θ are the spatial coordinates, t is time, and s may be a complex number ($s=\lambda+i\omega$).

The nonlinear equations of mass, momentum, or energy conservation are linearized by assuming the disturbance is small compared with the stable system dimensions (jet or sheet). These perturbation-type equations are then substituted into the appropriate conservation equations. This results in differential equations in the spatial disturbance function $g(x, r, \theta)$. Solutions for the spatial disturbance function are then sought which will satisfy liquid surface boundary conditions. The boundary condition may be expressed as a surface pressure which can include surface tension, shear stress, and aerodynamic pressure. The spatial disturbance function g may include the velocity potential function, and/or the stream function, or just the disturbance amplitude function, depending upon the approach used.

If the solution yields a positive real part of the complex growth rate (s in Eq. (2.2.3–1)) the disturbance will grow and thus be unstable. The disturbance wavelength for maximum instability is then found. This may be determined from maximum disturbance growth rate or else from maximum disturbance growth, if the rate is a function of time. The predominant disturbance wavelength then allows inferences about drop size, breakup length, and breakup time.

Several limitations to the theoretical analysis should be realized. First, the disturbance amplitude is assumed small to linearize the differential equations of motion. At breakup, the disturbance may approach or exceed the fluid system dimensions (e.g., jet diameter) and thus the linearized equations may not be valid. Second, to obtain closed form or explicit solutions an assumption of either very long or short wavelength disturbances must be made which means the solution is not necessarily valid except over a limited wavelength range. Third, in determining the predominant disturbance wavelength it is usually assumed that disturbances of all wavelengths initially have the same amplitude. This may be violated due to such phenomena as a nonuniform turbulence spectrum, cyclic flow oscillation or separation at a boundary, or perhaps a mechanical oscillation of the orifices.

Another limitation to theoretical breakup analysis involves the overlapping of competing breakup mechanisms. For instance, theoretical breakup analysis is successful in predicting drop size for low velocity jets where capillary forces are predominant. At high jet velocities jet turbulence and aerodynamic forces are controlling. In the transition region theoretical breakup analysis is of little use since both mechanisms are of comparable importance.

The failure to predict drop size distributions is a further limitation to the theoretical approach. In some limiting cases average drop sizes are predicted but not distributions. Drop size distributions must be determined experimentally and the dependence upon system properties must be empirically correlated. This will be dealt with in Sect. 2.2.4.

In spite of all its limitations, theoretical analysis of liquid jet and sheet breakup provides much useful information in several limiting cases. The following sections will discuss the results of some of these analyses.

2.2.3.2 *Liquid jet breakup, low velocity.*—The breakup of a liquid jet at low velocity cannot be truly called atomization since an increase of surface area does not result. However, it is an interesting limiting case and has been used to produce sprays of uniform drop size.[206]

Rayleigh[578] first derived the equation for the stability of a non-viscous jet subjected only to surface tension forces. Weber[723] extended the analysis by including the jet viscosity. Both analyses were for the case of symmetrical disturbances on the jet surface (see Fig. 2.2.3a).

Rayleigh's[578] analysis yielded the following relationship between the wavelength of the disturbance which will exhibit the maximum growth rate (real part of s in Eq. (2.2.3–1)) and the jet radius:

$$l_{w_{max}} = 9.02 r_j \qquad (2.2.3\text{–}2)$$

For comparison, Weber's[723] analysis, which included the liquid viscosity, yielded

$$l_{w_{max}} = 8.89 r_j \left(1 + \frac{3\mu_L}{\sqrt{2 r_j \rho_L S}}\right)^{1/2} \qquad (2.2.3\text{–}3)$$

with the maximum growth rate given by

$$\lambda_{max} = \left[\sqrt{\frac{8\rho_L r_j^3}{S}} + \frac{6\mu_L r_j}{S}\right]^{-1} \qquad (2.2.3\text{–}4)$$

The slight difference between Eqs. (2.2.3–2) and (–3) with $\mu_L = 0$ is due to the approximation of

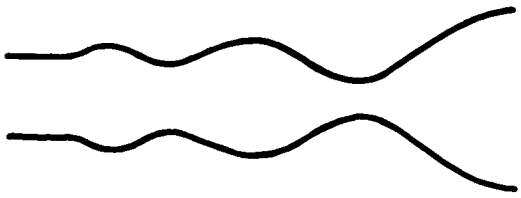

FIGURE 2.2.3a.—Symmetric disturbance.

Bessel functions in the derivation leading to Eq. (2.2.3–3). The following inferences as to breakup time, breakup length, and drop size are given for the results of Weber. The parallel set due to Eq. (2.2.3–2) can be obtained with only small differences by setting viscosity equal to zero. The breakup time for the jet can be estimated by

$$t_b \approx \frac{1}{\lambda_{max}} = \sqrt{\frac{8\rho_L r_j^3}{\mathcal{S}}} + \frac{6\mu_L r_j}{\mathcal{S}} \qquad (2.2.3\text{–}5)$$

and the breakup length is then:

$$L_b \approx V_j t_b \qquad (2.2.3\text{–}6)$$

With the assumption that the jet breaks at one wavelength interval and this forms one drop, a mass balance yields the following for the drop size:

$$d_L = 1.88 d_j \left[1 + \frac{3\mu_L}{\sqrt{\rho_L \mathcal{S} d_j}}\right]^{1/6} \qquad (2.2.3\text{–}7)$$

From Eqs. (2.2.3–5) and (–7) it is seen that high surface tension ($\mathcal{S}$) causes more rapid jet breakup, while for low viscosity fluids the drop size is independent of $\mathcal{S}$ and depends only upon jet diameter, d_j. For viscous fluids the breakup time and the drop size are seen to increase.

Equations (2.2.3–2) through (–7) are valid only for disturbances whose wavelengths are greater than the jet circumference ($l_w > \pi d_j$). For this case the surface tension is the driving force causing the instability, and the viscous terms represent damping forces. The jet tends toward a configuration with less surface area and thus less surface energy. Short wavelength disturbances ($l_w < \pi d_j$) represent stable configurations since the surface area is increased. The surface tension is thus a restoring force tending to maintain the jet's original shape.

Levich[439] provides an excellent discussion of the stability of a low velocity liquid jet subjected to arbitrary deformations with large wavelengths. He considers the solution for an arbitrary disturbance (f) of the form

$$f = \sum_k A_k e^{inx+st} \cos(k\theta) \qquad (2.2.3\text{–}8)$$

where $k = 0, 1, 2, \ldots$. The equation for the growth rate is

$$s = \lambda + i\omega = -\nu n^2 + \sqrt{(\nu n^2)^2 + \frac{\mathcal{S} n^2}{2\rho_L r_j}(1 - k^2 - n^2 r_j^2)} \qquad (2.2.3\text{–}9)$$

Examination of Eq. (2.2.3–9) suggests that

$$k^2 < 1 - (n r_j)^2 \qquad (2.2.3\text{–}10)$$

is a necessary condition for λ to be positive. Now $n r_j = 2\pi r_j / l_w$ is a small number because of the long wavelength consideration. Thus, instability results only with $k = 0$. This is the axisymmetric case as seen in Eq. (2.2.3–8) and shown in Fig. 2.2.3a.

For $k = 1$ (stable) the disturbance is such that the jet cross-section remains circular but is displaced from the undisturbed jet axis. This type of disturbance is shown in Fig. 2.2.3b.

A low velocity jet thus breaks up only from axisymmetric disturbances whose wavelength is greater than the jet circumference.

2.2.3.3 *Liquid jet breakup, high velocity.*—The more interesting (and complicated) case of breakup with high jet velocity can result in true atomization with the production of very small drops and a large increase in liquid surface area. High jet velocity in this case really means a *high relative velocity* between the jet and its surrounding atmosphere. This can be accomplished by injecting a high velocity jet into a low velocity atmosphere or by surrounding the jet with a high velocity gas. The main distinction between this case and the previously discussed low velocity jet is that aerodynamic forces must now be considered acting on the jet surface.

FIGURE 2.2.3b.—Asymmetric sinuous disturbance.

Weber[723] considered the case of jet breakup with atmospheric effects. The results of his analysis show the disturbance maximum growth rate (λ_{max}) to increase and to shift to shorter wavelength with increasing relative velocity. This would indicate a faster disintegration of the jet and reduced drop size. For more detail on Weber's[723] results see Ref. 24, p. 1–40.

Due to the complicated nature of the equations when aerodynamic effects are considered, Levich[439] separated the analysis into four limiting cases. He considered long and short wavelength disturbances for both high and low viscosity fluids. The following is a summary of that analysis.

For short wavelength disturbances and low liquid viscosity, the following expression was obtained for the wave growth rate:

$$s=\sqrt{\frac{n^2}{\rho_L}\left[\rho(\Delta V)^2-\mathcal{S}n\right]} \qquad (2.2.3\text{–}11)$$

Thus, s can be real for

$$l_w \geq \frac{2\pi\mathcal{S}}{\rho(\Delta V)^2} \qquad (2.2.3\text{–}12)$$

For very high relative velocities extremely short wavelength disturbances can be unstable. It should be recalled that for low velocities only disturbances with wavelengths larger than the jet circumference were unstable. If the drop size produced is of the order of magnitude of the disturbance wavelength, high velocity jets can produce very small drops in comparison to low velocity jets.

In contrast to low velocity jets the separation of fluid from the jet surface, due to short wavelength disturbances, does not sever the jet. Final breakup of the jet is produced by the cumulative effect of separation of small quantities of fluid. The time for separation of the fastest growing wavelength is

$$t_{sep} \approx \frac{\mathcal{S}}{(\Delta V)^3}\sqrt{\frac{\rho_L}{\rho^3}} \qquad (2.2.3\text{–}13)$$

while the breakup time for the jet is

$$t_b \approx \frac{r_j}{\Delta V}\sqrt{\frac{\rho_L}{\rho}} \qquad (2.2.3\text{–}14)$$

Equation (2.2.3–14) was derived using an energy balance involving the energy transferred to the jet by the surrounding gas, energy consumed in liquid surface increase, and energy dissipation in the jet. From Eqs. (2.2.3–13) and (–14) it is seen that, at high relative velocities, the time for separation of individual drops is much less than the time for complete breakup of the jet. The atomization of the jet thus commences almost immediately upon injection into the atmosphere and continues throughout the jet length.

For high viscosity fluids Levich[439] shows that

$$\lambda \approx \frac{\rho(\Delta V)^2-\mathcal{S}n}{\rho_L \nu} \qquad (2.2.3\text{–}15)$$

Thus higher growth rate disturbances are obtained for long wavelengths (smaller n). He also shows that the time for jet breakup t_b increases without bound with increasing viscosity, and thus concludes that small drops (from small l_w) cannot be produced by viscous jets.

Considering the case of long wavelength disturbances on the surface of a high velocity jet, with an arbitrary disturbance as in Eq. (2.2.3–8) and for small fluid viscosity, the disturbance growth rate was shown[439] to be

$$s=\sqrt{\frac{-\rho n^4 r_j^2(\Delta V)^2 \ln\left(\frac{nr_j}{2}\right)}{2\rho_L}+\frac{\mathcal{S}n^2}{2\rho_L r_j}(1-k^2-n^2r_j^2)} \qquad (2.2.3\text{–}16)$$

where growth rate is real for

$$k^2 \leq 1-(nr_j)^2+\frac{\rho n^2 r_j^3(\Delta V)^2 \ln\left(\frac{l_w}{\pi r_j}\right)}{\mathcal{S}} \qquad (2.2.3\text{–}17)$$

Thus, for large relative velocity, values of k greater than zero can produce instability. It should be recalled that for low jet velocity instability resulted only with a symmetrical disturbance (k=0). An inspection of Eq. (2.2.3–16) reveals that even though a sinuous disturbance (k=1, see Fig. 2.2.3b) may grow, the symmetrical disturbance (k=0, see Fig. 2.2.3a) will grow faster and should thus dominate the jet breakup.

At sufficiently high velocities the second term in Eq. (2.2.3–16) can be omitted and thus

$$s=n^2 r_j \Delta V\sqrt{\frac{\rho}{2\rho_L}}\ln\left(\frac{l_w}{\pi r_j}\right) \qquad (2.2.3\text{–}18)$$

which shows the disturbance will grow for long

wavelength ($l_w > \pi r_j$). In Eq. (2.2.3–18) the type of disturbance* ($k = 0, 1, 2, \ldots$) no longer appears. All types thus grow equally fast.

Levich shows the time for jet breakup of low viscosity, high velocity jets to be

$$t_b \approx \frac{r_j}{\Delta V}\sqrt{\frac{\rho_L}{\rho}} \qquad (2.2.3\text{–}19)$$

A comparison of Equations (2.2.3–19) and (–14) shows that the breakup times are of the same order of magnitude. This implies that, for a high velocity jet of low viscosity, small drop size atomization and large drop size fragmentation have probabilities equal in order of magnitude.

For long wavelength disturbances on a high velocity, high viscosity jet, the growth rate was shown[439] to be

$$s \approx \frac{\rho(\Delta V)^2(nr_j)^2}{4\mu_L}\ln\left(\frac{l_w}{\pi r_j}\right) \qquad (2.2.3\text{–}20)$$

the jet breakup time to be

$$t_b = \frac{5\mu_L}{\rho(\Delta V)^2} \qquad (2.2.3\text{–}21)$$

and the wavelength for maximum growth rate to be

$$l_{w_{max}} = 6r_j \qquad (2.2.3\text{–}22)$$

High viscosity thus reduces the disturbance growth rate and increases the time for jet breakup (and thus the breakup length). Large drops due to jet fragmentation are produced with very viscous jets. A number of experimental studies have provided further information on high relative velocity breakup. These include publications by Ingebo,[379] Clark[146] and Morrell.[500,501]

2.2.3.4 *Summary of jet breakup results.*—This section provides a brief review of the more important conclusions obtained from the theoretical jet breakup discussion in Sects. 2.2.3.2 and 3. Equation numbers are given for reference back to these previous sections.

Low velocity jets break up by fragmentation due to the growth of symmetrical waves on the jet surface. The diameter of the resulting drops is about twice the jet diameter for low viscosity fluids. Fluid viscosity increases the drop size and jet breakup length (see Eqs. (2.2.3–5), (–6) and (–7)).

At intermediate jet-gas relative velocities, where aerodynamic forces must be considered, short wavelength disturbances are unstable for low viscosity fluids. This results in formation of small drops which are shed from the jet surface. Long wavelength disturbances are also unstable with the symmetrical case having the fastest growth rate. For sufficiently high relative velocities the sinuous and higher order transverse† disturbances can become unstable. These would result in jet fragmentation forming large drops (see Eqs. (2.2.3–12) and (–16)).

For very high jet velocities small droplet shedding from the jet surface continues but the character of long wavelength disturbances changes. All transverse and symmetrical disturbances grow equally fast. Sinuous or higher order transverse disturbances may cause jet fragmentation with the formation of large drops (see Eq. (2.2.3–18)).

Increasing fluid viscosity reduces the fluid shedding from the jet surface and increases the drop size for that fluid which is severed. High viscosity fluid jets break up due to long wavelength fragmentation with resultant large drop sizes (see Eq. (2.2.3–15) and (–20)).

Some support for the theoretical results is obtained from the experimental observations on jet breakup given by Grant and Middleman.[296] At low jet velocities they observed symmetrical wave breakup. Higher velocities caused the appearance of transverse waves which damped and symmetrical waves continued to break the jet. A further increase in jet velocity produced jet breakup by transverse waves. For even higher velocities, and a turbulent jet, surface atomization prevailed.

2.2.3.5 *Surface breakup*—The theoretical jet breakup models reviewed in Sections 2.2.3.2 and 3 considered the deviation, due to a disturbance of a liquid jet from its original cylindrical geometry.

* Also see Eq. (2.2.3–8).

† This should not be confused with transverse acoustic modes of instability in a combustion chamber. The definition implied here derives from Eq. (2.2.3–8) and defines the jet cross-section shape under the influence of the disturbance.

A low viscosity jet, under the influence of a high relative velocity gas environment, forms short wavelength surface disturbances which are independent of jet diameter (see Eq. 2.2.3–12). In the following analysis a simplified approach ignoring the actual jet geometry is thus used.

Mayer[470] considered the case of wind-induced capillary waves on a flat, deep liquid surface. He assumed that when a wave grows to an amplitude comparable to its wavelength, the wave crest severs and forms droplets of size proportional to the wavelength. A functional form for the drop size distribution generated by the wave breakup was obtained which enabled the derivation of an average drop size given by

$$d_L = 9\pi(16)^{1/3} B \left(\frac{\mu_L \sqrt{S/\rho_L}}{\rho(\Delta V)^2}\right)^{2/3} \qquad (2.2.3\text{–}23)$$

where $B \approx 0.3$. Excellent agreement was shown between this theoretical drop size[470] and empirical correlations of jet breakup in high speed gas streams obtained by Weiss and Worsham.[724]

Adelberg[49,50,51] has extended Mayer's analysis to include the effect of fluid acceleration on the surface disturbance wave speed. He shows that these acceleration waves (as distinguished from capillary waves of Mayer's analysis) are controlling if the jet is experiencing a large acceleration.

An empirical correlation on the mass median drop size produced by a concentric tube injector was presented in Ref. 352. The correlation, considering only those parameters actually varied, can be reduced to

$$d_L \sim \frac{V_j}{\Delta V} \sqrt{\frac{d_j^3}{y}} \qquad (2.2.3\text{–}24)$$

where y is the gas annulus thickness. The exponent on ΔV is seen to agree well with that of Eq. (2.2.3–23) (i.e., -1 versus $-\frac{4}{3}$).

The conditions in a concentric tube injector differ from those assumed by Mayer in the following ways. A thin annulus of gas of high velocity is injected concentrically around a liquid jet of low velocity. The high velocity gas stream mixes with the surrounding gas environment. When this mixing region has penetrated to the liquid jet, the liquid jet thereafter experiences a decelerating gas environment. A thinner gas annulus decreases the length of the high gas velocity region. A higher liquid velocity results in more rapid escape from the high gas velocity region. A larger liquid jet diameter reduces the fraction of liquid atomized by high gas velocity surface stripping. Mayer's analysis assumes a steady velocity difference between the gas and the liquid, thereby eliminating the separate effects of liquid and gas velocities and the finite quantity of high velocity gas available for surface atomization. The importance of finite liquid jet diameter is discussed, but it does not appear in Mayer's analysis.

The qualitative discussion of the concentric tube injector was presented here since, with proper simplifying assumptions, the system may be amenable to analytical treatment.

2.2.3.6 *Liquid sheet breakup.*—Dombrowski and Johns[230] considered the stability of asymmetric waves (see Fig. 2.2.3b) on a viscous liquid sheet under the influence of aerodynamic forces caused by a steady cocurrent gas flow. They obtained wave number and growth rate expressions which are viscous effect multipliers of the inviscid solutions of Squire.[664] Also they allowed the sheet thickness to vary with time (following the fluid particles).

The drop size produced by the breakup of a radially flowing liquid sheet (sheet thickness varies inversely with distance) was obtained in the following manner. When the disturbance with the wavelength for greatest total growth (not necessarily greatest growth rate) reaches a critical amplitude, the wave breaks at the crests and troughs. Wave fragments of one-half wavelength are formed which contract into ligaments. The ligaments are assumed to break into drops according to Weber's criterion (Eq. 2.2.3–7).

The resultant drop size expression of Dombrowski and Johns[230] is quite lengthy and the reader is referred to the source for the details. However, the following should be noted here. In Ref. 230 the theoretical drop size (after adjustment by a suitable constant) was compared to that obtained experimentally from fan sprays and the agreement was favorable. The effect of the spray variables upon drop size depends upon which of four domains is dominant. These four domains can be defined by whether or not the viscosity is effective in the sheet breaking into ligaments

and in the ligaments breaking into drops. The limits on the exponents for the two extremes of low and high viscosity are: viscosity 0 to $\frac{7}{20}$, surface tension $+\frac{1}{3}$ to $-\frac{1}{12}$, relative velocity $-\frac{2}{3}$ to $\approx -\frac{1}{6}$, liquid density $-\frac{1}{6}$ to $\approx -\frac{1}{3}$, and gas density $-\frac{1}{6}$ to $\approx -\frac{1}{12}$.

It may be possible to utilize the analysis of Dombrowski and Johns[230] to obtain theoretical drop size expressions for other atomization devices besides fan sprays. However, the sheet thickness as a function of time must be known. Perhaps the excellent analysis of Hasson and Peck[326] can provide the starting point for impinging jet injectors and the water bell analysis of Taylor[683] for swirl atomizers.

Spray formation from impinging liquid jets results from breakup of the resulting liquid sheets. The empirical dropsize correlation by Ingebo[375] is one which has been used often for the common case of impinging liquid jets. More recent dropsize correlations have been obtained by Dickerson,[224] using a molten wax technique. In the latter work spray size distributions for various types of impinging jet elements were empirically correlated in terms of orifice sizes and injection velocities. Work with liquid sheet breakup in a unique injector design is being conducted by Riebling.[592]

2.2.3.7 *Secondary drop breakup.*—A liquid drop removed from a sheet or jet may be exposed to the aerodynamic pressure effect of a high relative gas velocity. If this pressure is sufficiently large to overcome the restoring force of the drop surface tension, the drop will disintegrate into smaller droplets. The Weber number[357] defined as

$$\mathrm{We} = \frac{\rho(\Delta V)^2 d_L}{2\mathcal{S}} \qquad (2.2.3\text{–}25)$$

is considered as an effective indicator of the necessary gas dynamic environment for secondary breakup.

Hinze[357] has analyzed the forced deformation of a liquid sphere under the influence of the pressure distribution caused by turbulent gas flow around the sphere. He considered the two cases of a suddenly applied steady velocity and a gradually increasing velocity as may occur with falling raindrops. His results are presented as the deviation of the liquid surface from the original sphere at the stagnation point. Hinze concludes that a drop will shatter if the surface deformation at the stagnation point is roughly equal to the drop radius. This occurs if the Weber number exceeds six for a low viscosity drop and ten for a high viscosity drop in the case of a suddenly applied steady gas velocity.

If the result is rounded off and the surface deformation is equal to the drop radius, the drop breakup time can be estimated by

$$t_b \approx \frac{d_L}{2(\Delta V)} \sqrt{\frac{\rho_L}{\rho}} \qquad (2.2.3\text{–}26)$$

for a low viscosity drop with a suddenly applied steady gas velocity.

It has been pointed out[357] that in the actual atomization process, a newly formed drop is not subjected to a steady relative gas velocity. The drag force between the gas and the liquid will reduce the relative velocity. If the drop breakup time is sufficiently large, the Weber number may be reduced below critical before the drop shatters.

Photographs of drop breakup with a suddenly imposed gas velocity were presented by Rabin, Schallenmuller, and Lawhead.[569] Two types of drop breakup were shown, shear- and bag-type breakup. With both types the drop is first flattened. If bag-type breakup occurs the center of the disk blows out into a bag which breaks into very small droplets while the ring breaks into much larger drops. With shear-type breakup the edges of the flattened drop are sheared into sheets and ligaments which then break into drops. In Refs. 210 and 515 the drop breakup time was experimentally shown to be of the same form as (but ten times the value of) Eq. (2.2.3–26). Additional references on secondary droplet breakup include Refs. 222, 223 and 755.

2.2.4 Spray Description*

The final form of the liquid phase in the chain of events leading to combustion is often a collection of roughly spherical droplets called a spray.† A common objective of experimental droplet measurements and atomization analyses is a

* J. F. Groeneweg, Author.

† For some cryogenic propellants, such as liquid oxygen, this concept of a spray may be inadequate since substantial phase change may occur while the liquid is in ligament or jet form.

description of the spray which allows the prediction of droplet propagation within the combustion chamber and, ultimately, the energy release profile (see Sects. 2.4 and 7.2.4). The purpose of this section is to outline the type of information necessary for spray description and to briefly review the existing level of knowledge of steady-state spray properties.

The basic factor influencing all approaches to spray description is summed up by the statement that spray formation is a random process. Fixing all injection parameters which can be controlled such as flow rates, fluid properties and injection geometry does not produce drops of a single size traveling at the same velocity at a particular position. The fact that droplet births are distributed throughout a region of space and are the result of fluctuating gas-liquid interactions means that a statistical treatment is required.

The following nomenclature pertains to Sect. 2.2.4:

D_L	Drop diameter
D_{jk}	Generalized mean drop diameter
D_m	Mass median drop diameter
D_{30}	Volume mean drop diameter
D_{max}	Maximum drop diameter
D_{32}	Volume-surface (Sauter) mean drop diameter
$f(D_L, \mathbf{V}_L, \mathbf{x}, t)$	Spray density distribution
f_s	Spatial drop size distribution
$\mathbf{f}_F$	Flux drop size distribution
g	General drop number distribution
$\mathbf{x}$	Drop position
$\alpha, \beta, \delta, \eta, \kappa, \psi$	Parameters in empirical distribution functions

A basis for spray description is provided by the concept of a spray density function, $f(D_L, \mathbf{V}_L, \mathbf{x}, t)$, which specifies the number of drops in the ranges of dD_L, $d\mathbf{V}_L$, and $d\mathbf{x}$, about the size, D_L, velocity $\mathbf{V}_L$, and position $\mathbf{x}$ at a time t. This function theoretically represents the results of a spray sampling operation in which sample size approaches infinity while increments in droplet properties, ΔD_L, $\Delta \mathbf{V}_L$ and $\Delta \mathbf{x}$ (the category sizes considered) approach zero. A theoretical prediction of f from a knowledge of injection parameters does not now exist (Sect. 2.2.3) so experimental estimates of f must be used. Statistical uncertainty is reduced as sampling effort increases. While the time variable is not a consideration in this section because only steady-state conditions are considered, unsteady behavior is of interest for instability analysis (Sect. 3.3). Conservation equations may be written for f,[743] and are the basis of predicting downstream behavior based on the specification of an initial density function at formation.

The function f could be considered to depend on other variables than those listed above, such as temperature, however, existing knowledge of even velocity and position dependence is scarce. Drop sizes have received most of the emphasis in both experiment and analysis. However, detailed measurements[299] have shown that, even immediately after formation at a particular position, drops of a given size move with different velocities indicating that velocity should be treated on an equal statistical basis with drop size. Spray properties are also strong functions of position[277, 589] due to droplet-gas transport processes. From an analytical viewpoint the key positions are those where spray formation has just been completed since they locate the initial conditions required for analysis.

The bulk of existing spray data is composed of various types of drop size distributions and mean drop sizes. Analytical representations of these quantities are obtained by various integrations of f over the droplet variables. Integration over a particular droplet variable reduces the amount of information available and ignores the distributed nature of the variable in favor of the simplification realized by dealing with a mean value. The remainder of this section ignores time dependence since only steady-state conditions are considered, and spatial dependence is implicit.

Two general types of drop size distribution data are available corresponding to two kinds of sampling methods used. They are the spatial distribution f_s, and the flux (temporal) distribution $\mathbf{f}_F$ given by

$$f_s = \int f \, d\mathbf{V}_L \qquad (2.2.4\text{-}1)$$

$$\mathbf{f}_F = \int \mathbf{V}_L f \, d\mathbf{V}_L \qquad (2.2.4\text{-}2)$$

Spatial distributions representing the number of

drops per unit volume per unit size are estimated from instantaneous samples of the droplet population in a given spray volume; e.g., high-speed photography. Flux distributions which specify the number of drops per unit size crossing a unit area per unit time are estimated by collecting a sample of all drops passing a plane in the spray during a known sampling time; e.g., frozen wax[224,724] or immiscible fluid collection cell methods.[465] The distinction between f_s and $\mathbf{f}_F$ is usually ignored in the literature, but differences between the two can be large depending on the distribution of drop velocities.[299] In the remainder of this section the symbol g will be used to refer to size distributions in general without regard to type. Size distributions are usually normalized to make the integral over all sizes equal to one. In that case, any physical magnitudes of liquid concentrations or fluxes are lost unless they are purposely specified as the normalization factor.

Data which result from individual measurements of diameter produce a number distribution of the type shown schematically in Fig. 2.2.4. Uncertainties are greatest at very small sizes where measurement resolution is limiting and at very large sizes where measured frequencies are particularly sensitive to sample size. Mass distributions obtained by weighting the ordinates of the number distribution by D_L^3 are a useful form which often allows reasonable extrapolations to be made at the size extremes. The particular examples shown in Fig. 2.2.4 each have a single

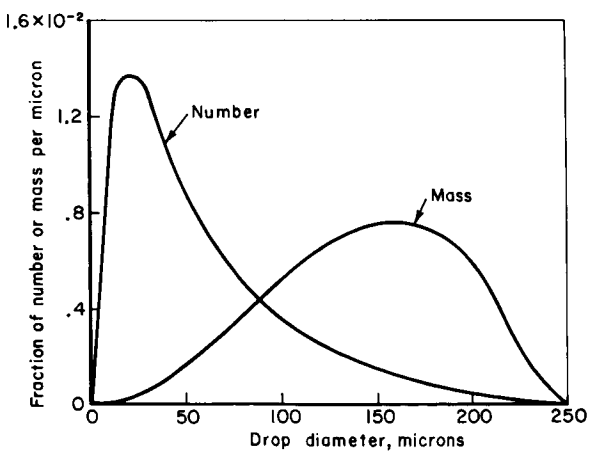

FIGURE 2.2.4.—Typical drop size distributions.

peak (unimodal), but some experimenters have found definite bimodal characteristics.[101,218,299,339]

Partial characterization of distributions is furnished by various mean sizes. A general set of means is defined by[507]

$$(D_{jk})^{j-k} = \frac{\int (D_L)^j g \, dD_L}{\int (D_L)^k g \, dD_L} \qquad (2.2.4\text{–}3)$$

where g is a number distribution and the integration is over the complete range of sizes. If $k=0$ the denominator simply assures normalization. Two commonly used means are the volume mean, D_{30}, and the volume-surface (Sauter) mean, D_{32}. Two additional parameters used to characterize distributions are the mass median, D_m, and a maximum drop size, D_{max}.

Since a theoretical prediction of the form of g is lacking, a variety of empirical forms have been used to fit size distribution data. The equations are basically of two types:

$$g(D_L) \sim D_L^{\alpha} \exp\left(-\beta D_L^{\kappa}\right) \qquad (2.2.4\text{–}4)$$

$$g(D_L) \sim \exp\left(-\tfrac{1}{2}y^2\right) \qquad (2.2.4\text{–}5)$$

with

$$y = \delta \ln\left(\frac{D_L}{D_m}\right) \qquad (2.2.4\text{–}5a)$$

or

$$y = \psi \ln\left(\frac{\eta D_L}{D_{max} - D_L}\right) \qquad (2.2.4\text{–}5b)$$

where α, β, δ, η, κ and ψ are parameters. The first, Eq. (2.2.4–4), may be called a generalized gamma function,[450] and specialized conditions on the parameters lead to forms having names such as Nukiyama-Tanasawa and Rosin-Rammler. The second group consists of logarithmic transformations of the normal distribution,[390] Eq. (2.2.4–5). Equation (2.2.4–5a) gives the log-normal distribution whose range extends to infinite sizes while the upper limit form, Eq. (2.2.4–5b), provides for a maximum size. For any particular case of Eqs. (2.2.4–4) to (–5), the means given by Eq. (2.2.4–3) may be calculated as functions of the distribution parameters.[97,507] Mass medians are usually determined from a cumulative plot and maximum size from either

the largest observed or a drop stability criterion (Sect. 2.2.3).

A comprehensive empirical approach would be to choose a distribution equation capable of fitting the data and to correlate its parameters with injection conditions. The labor of such an approach has limited the number of such attempts and their scope. For example, the parameters in Nukijama-Tanasawa forms of Eq. (2.2.4–4) have been correlated for impinging jets[224,375] and cross-current injection[379] in air streams; and the parameters in the upper-limit form of Eq. (2.2.4–5) have been correlated for a swirl atomizer[589] and a collection of size data from several injector types.[506] In the absence of parameter correlations, distribution equations are fitted to specific data sets or the distribution data are simply plotted and tabulated.[101,277,339] Direct measurements of spray characteristics in a rocket combustion environment[377,378,373] are scarce because of the associated experimental difficulties. Indirectly, distribution characteristics based on the log-normal form have been inferred from an analysis of rocket performance based on a vaporization model.[564]

Other than size distributions, most of the existing data is in the form of mean, median, or maximum drop sizes. In principle, an infinite number of means given by Eq. (2.2.4–3) are equivalent to the specification of the distribution. In practice, investigators have usually only measured and correlated one or two size indicators for a given set of conditions. A sampling of the literature (see Table 2.2.4) confirms the intuitive trends of drop sizes which vary directly with orifice size, liquid viscosity, and surface tension; and inversely with relative velocity between the gas and liquid. Additional information for impinging jet arrangements may be found in Refs. 224 and 375. Maximum drop diameters measured for injection into a cocurrent gas flow have been found to depend on the acceleration or deceleration of the gas stream in addition to the liquid and gas velocities.[376] The dependence of size on gas density cannot be approximated by a simple exponent since a switch in dependence from inverse to direct is observed as gas density increases.[218,229] Specific injector types and their relation to droplet sizes are discussed in Sect. 7.4.

In summary, spray description requires a statistical treatment, and the concept of the spray density function furnishes a basis for analysis. Spray data available as input to this model are

TABLE 2.2.4—VALUES OF EXPONENTS SPECIFYING THE DEPENDENCE OF DROP SIZE ON INJECTION VARIABLES[a]

Conditions	Drop size correlated	Orifice diameter	Surface tension	Liquid viscosity	Liquid density	Velocity[b]	Ref.
Single jet crosscurrent injection into heated air	D_{30} D_{max}	$\frac{1}{2}$ 0.42	$\frac{1}{4}$ 0.29	$\frac{1}{4}$ 0.29	$-\frac{1}{4}$ −0.29	$-\frac{3}{4}$(g) −0.87(g)	379
Single jet, costream and contrastream injection into heated air	D_m	$\frac{1}{6}$	[c]$5/12$	$\frac{1}{3}$	[c]$-\frac{5}{6}$	$-4/3$(r)	724
Correlation for pressure, swirl and impinging jets	D_{32} D_{max}	0.65 .52	0.20 .18	0.35 .48	−0.35 −.48	−0.55(r) −.66(r)	506
Swirl nozzle injection into stagnant gas	D_{32}	0.53	0.21	0	−0.48	−0.50(L)	219

[a] For example, $D_{30} = d_i^{1/2} S^{1/4} \mu_L^{1/4} \rho_L^{1/4} V^{-3/4}$.
[b] g, gas; L, liquid; r, relative.
[c] Not varied in experiment.

mainly limited to specific size distributions or correlations of mean sizes with injection conditions.

2.3 SPATIAL DISTRIBUTION OF PROPELLANTS

The following nomenclature pertains to Sect. 2.3:

C	Concentration of gaseous propellant
E_m	Mixing efficiency factor, defined in Eq. (2.3.3–1)
F(C)	Concentration distribution function
G	Local flow rate per unit area
g	Spreading factor
K_A	Sampling area correction factor
M_j	Momentum ratio function, defined in Eq. (2.3.3–2)
$\dot{m}$	Local total mass flow rate, $\dot{m}_1+\dot{m}_2$
n	Number of samples with $\phi<\phi_T$
n′	Number of samples with $\phi>\phi_T$
p, q, A	Constants in F(C) expression, Eq. (2.3.3–8)
S_t	Lagrangian scale of turbulence
v_{rms}	Root-mean-square lateral velocity
W	Point-source strength
α	Impingement angle
$\beta(p, q)$	Beta function
ϕ	Mass flux fraction, $\dot{m}_1/(\dot{m}_1+\dot{m}_2)$
Ψ	Ripple factor, C_{min}/C_{max}

Subscripts:

T	Overall or total spray conditions
1, 2	Indices specifying propellant components (e.g., oxidizer and fuel)

2.3.1 Mass Flux Distribution*

The mass flux distribution in the transverse plane is of considerable interest in liquid rocket engine design. If a uniform mass flux distribution is to be achieved by the time the nozzle throat is reached, i.e., all propellants to be burned prior to that location (thus providing uniform product temperature and density), then considerable attention must be given to the initial mass flux distribution achieved at (or near) the injector. Although the initial mass flux distribution can be somewhat less than uniform, such nonuniformities cannot exceed the capabilities of secondary mixing† (primarily diffusion in a smoothly operating combustion chamber) if the desired throat condition is to be met. The problem in general is to achieve (other factors being equal) a uniform mass flux throughout the throat cross section with a minimum chamber length.

The initial propellant distributions produced by real injectors are basically three-dimensional arrays of droplets formed from ligaments emanating from many sources. The complexity of such systems imposes the necessity of reducing these more-or-less known properties of a single spray to the desired mass flux distribution thru some arbitrary or intuitive artifice.

In certain analyses[544,421,164] the discrete properties of the individual elements are reduced to an assumed uniform (or other prescribed) distribution of particles of known size near the injector face so that the droplet-gas interaction process can be described. Although this process results in a tractable combustion model, the contribution of the injector (to the extent that it does not satisfy the assumption) with regard to mass flux distribution is lost.

An alternate approach[613] emphasizes the contribution of individual elements as determined from measurements on non-reactive sprays. Such measurements serve to define, strictly from geometrical considerations, the mass flux distribution at the axial station where the boundary enclosing some 95% of the total mass flux for the element is a proportionate share of the chamber cross section. At that station the radial component of velocity is presumed to go to zero—hence a mass flux for the bounded surface can be specified.

In the case of elements composed of identical like-on-like impinging jets, these distributions can be characterized to a reasonable approximation by a two-dimensional Gaussian distribution within essentially elliptical boundaries. This is the general description that is utilized by Reardon et al.[583] in portraying the element orientations for like-

* J. H. Rupe, Author of Sects. 2.3.1 and 2.3.2.

† The discussion here will concentrate on designs which seek to achieve uniform mass flux across the injector face. The use of nonuniform mass flux distributions for purposes such as: improved stability, modified heat transfer, specialized research modeling, etc., encourages other mixing phenomena which include recirculation and radial winds. These are discussed in Sects. 2.3.3, 2.3.4, 7.2.5, 8.5.3 and 9.2.2.

doublet sprays from which interactions and/or coupling effects with combustion chamber dynamics are inferred. This representation is specifically appropriate for the distributions produced by doublets comprised of identical jets.

On the other hand, for non-identical jets (including like-jets of differing momenta) the mass distributions resulting from impingement are symmetrical only about the plane including the jet centerlines. The phenomenon is illustrated in Fig. 2.3.1a where the normalized mass flux for two different element configurations are portrayed.[613] It is noted that only in one of these cases are the jets identical. As the jet momenta diverge from a ratio of unity, the resultant becomes increasingly non-planar and hence can make a unique contribution to the overall mass flux distribution.

This concept of an element mass distribution being utilized to form a composite for a complete injector is illustrated in Fig. 2.3.1b[613] which portrays the mass distribution for an injector consisting of 6 elements. It should be noted that in the actual "model" (of which this is a reproduction) the absolute magnitude of mass flux is proportional to the density of the photographic negative, which can be used to provide a quantitative description of the mass flux distribution at the model plane. A computer model has recently been developed[356] to describe the three-dimensional spray mass flux patterns formed by arrays of injector elements as in a complete injector. The model uses empirical cold flow data[613,356] to characterize the contributions from individual elements. Collisions of spray droplets from adjacent elements are considered on a probability basis. Development injectors, as well as research injectors, are now characterized by similar methods.[224,258] Normally full injectors are tested rather than individual elements in order to characterize, non-reactively, the element-element interactions.

2.3.2 Mixture Ratio Distribution

Of the several parameters that serve to characterize the combustion process in a liquid propellant rocket engine, the mixture ratio distribution* is certainly one of the most important. The performance level that is achieved,[703,145,271] the compatibility of the gas side boundary flows[609,168] with the wall, as well as the stability of the combustion process[583] are intimately related to this parameter. Although it is undoubtedly true that there is no one particular mixture ratio distribution that is best for all possible requirements, the intuitive arguments for achieving a specified distribution in a controlled and reproducible manner are rather overwhelming. Also as is the case with mass flux distribution (Sect. 2.3.1), it is logical from the standpoint of performance to strive for a uniform distribution at the nozzle throat, and to accomplish this objective with the minimum possible chamber length. Since the modification of an initial mixture ratio distribution by secondary mixing processes (Sect. 2.3.3) is a relatively ineffectual process,[168,318] it is apparent that the injection scheme must play the most important role in the determination of this chamber property.

Attempts to measure mixture ratio distributions in actual rocket engines by direct sampling techniques date back at least twenty years.[73,125,448] However, until the advent of the high speed mass spectrometer, these studies were necessarily limited due to the extreme severity of the environment being sampled and the dependence of a composition determination upon an inferential relationship with, for example, temperature.[73] The additional complications arising from slow sampling rates and the necessity for direct analysis of the sampled gases precluded the wide acceptance of such techniques. However, several new efforts[628,758] that utilize high speed mass spectrometers for real time analysis of local combustion products show promise of yielding the much needed information. No data have been published to date but the apparatus and techniques are in the advanced stage of development.

In lieu of a direct measurement of mixture ratio distribution and/or a correlation with injector geometries, there are several alternate procedures that have been devised to describe this parameter. One method uses the flow rate from individual

* It should of course be recognized that the description of mixture ratio serves only to separate the mass flux distributions of the individual propellants. Obviously an equivalent representation would be to specify the individual mass flux distributions rather than their quotient so that the discussions relating to scale of the element and secondary mixing are equally applicable here.

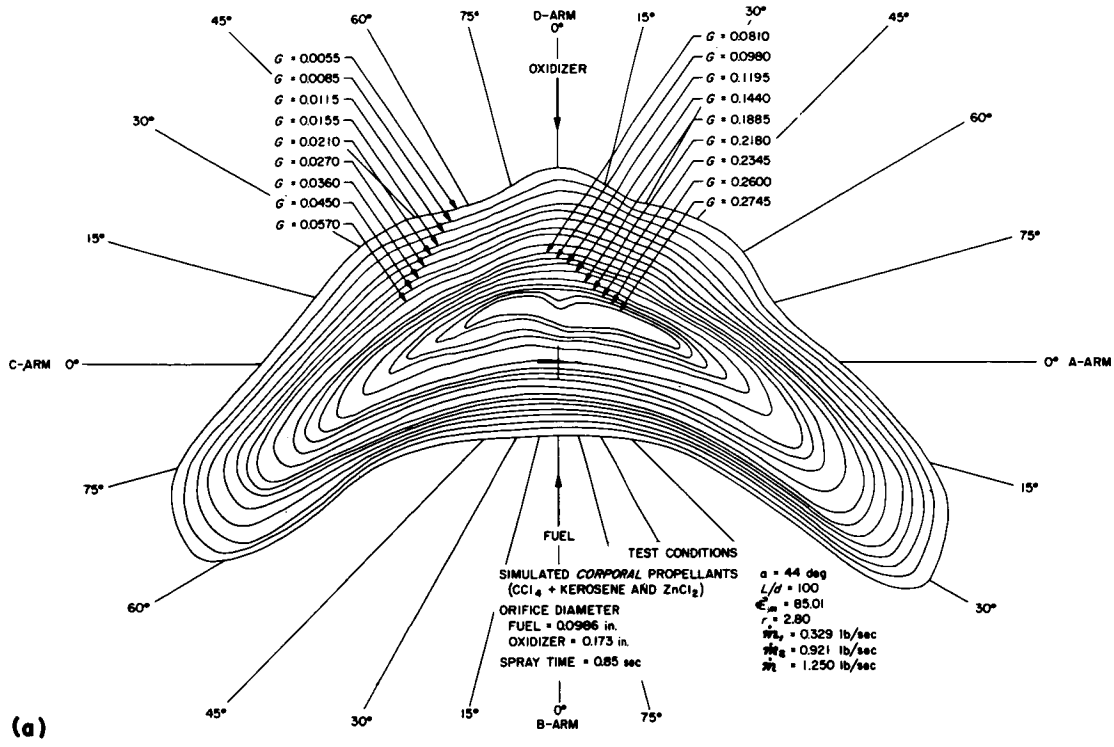

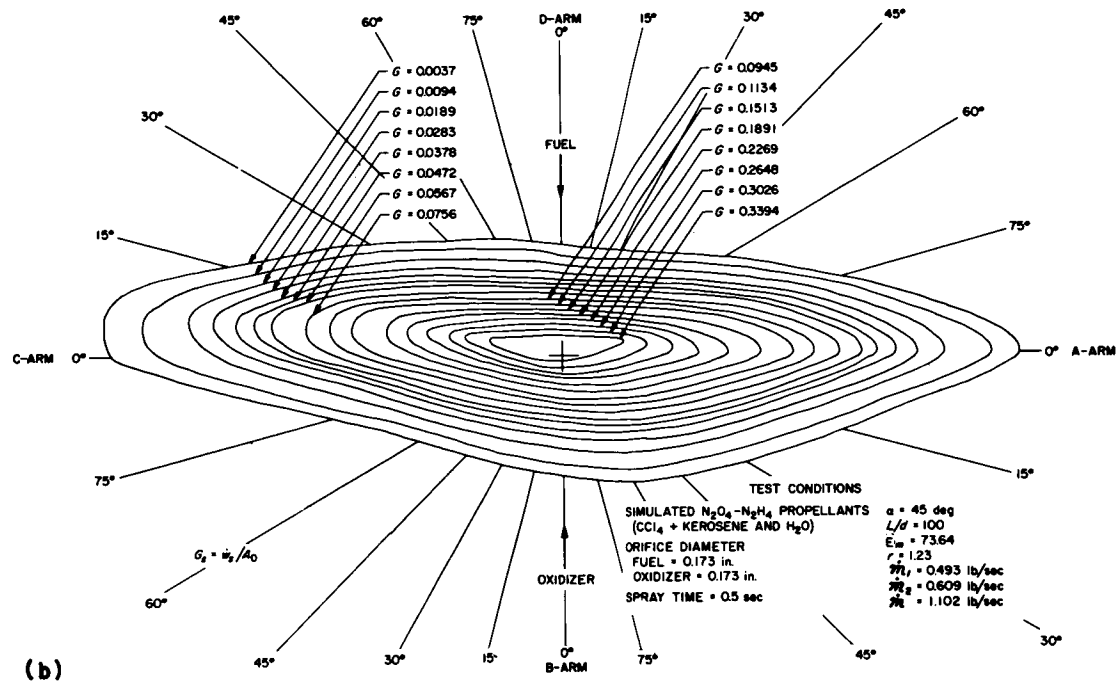

(a) On a spherical surface for nonsimilar jets.
(b) On a spherical surface for similar jets.
FIGURE 2.3.1a.—Mass flux distributions for typical doublet elements.

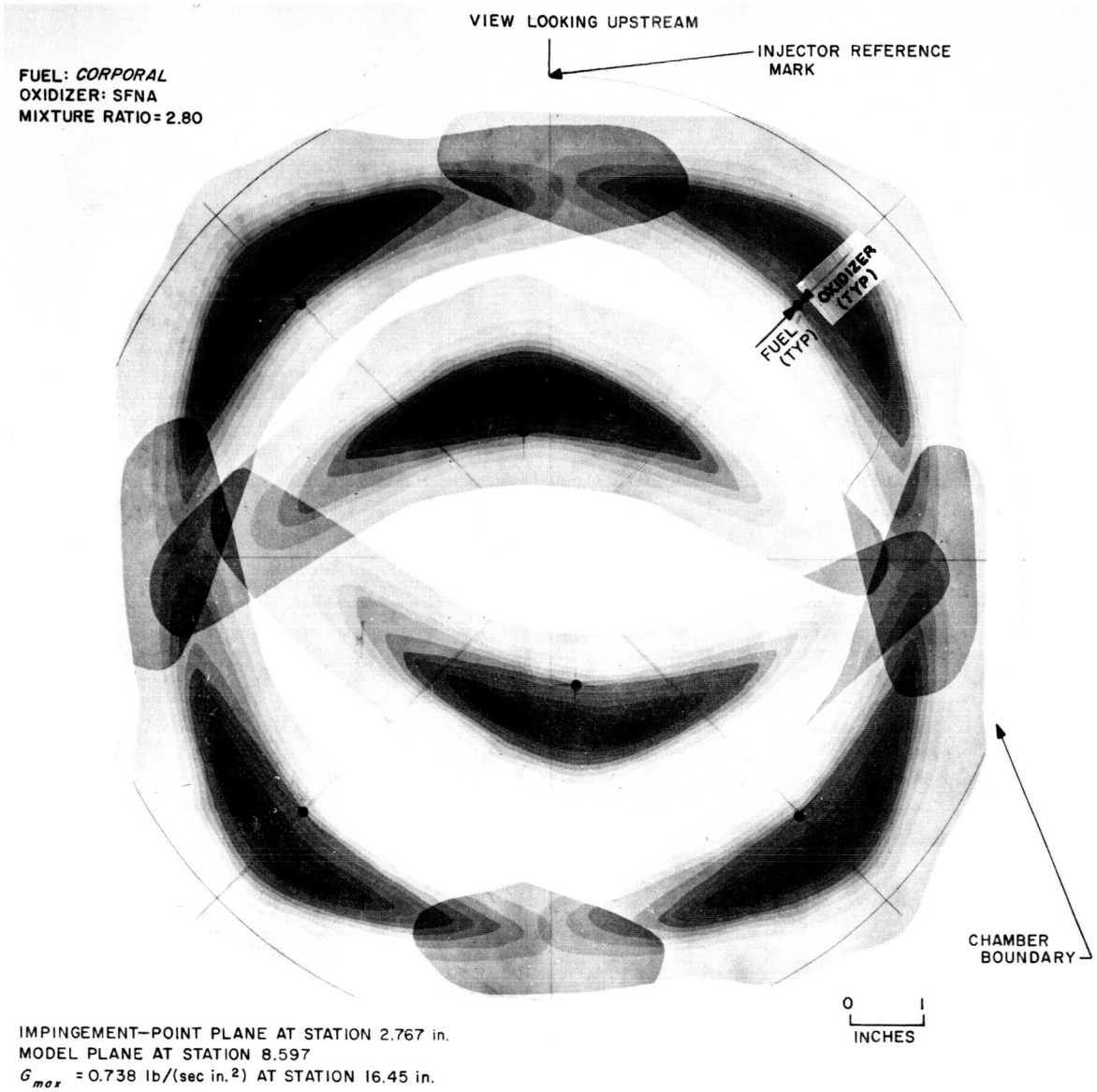

FIGURE 2.3.1b.—Mass flux distribution for a six-element array of unlike doublets.

orifices (based in general on an extrapolation from non-reactive calibration fluids to propellants), while a second utilizes experimental measurements of mixture ratio distributions within sprays formed by elements or entire injectors but with non-reactive fluid. In at least one case[705] the mixture ratio has been inferred from the erosion pattern on an ablative wall. Another technique using thermocouple rake measurements of the sprays formed by propellants (and pseudopropellants) injected at different temperature levels has also been successful in the measurement of mixture ratio gradients.[102]

The flow rate method is the most common means to estimate local mixture ratio but necessarily results in an arbitrary definition of the region of the chamber that is characterized by the stated value. Conn et al.[168] imply a circular section while Harrje[583] prefers an ellipse. Each of these is undoubtedly a valid representation when the scale of the element is small. On the other hand, when the distribution within the element

becomes significant, then a procedure that defines local properties becomes more meaningful. The results obtained with one such procedure[613] are illustrated in Fig. 2.3.2 where the mixture ratio distribution for two typical doublet elements are superimposed upon their mass flux distributions (the same mass flux distributions shown in Fig. 2.3.1a). It is particularly interesting to note that regions of relatively nonuniform mixture ratios (associated with significant mass fluxes) dominate these distributions even though the mixing efficiencies characterizing the entire sprays were relatively high.

For cases of no element–element interaction a composite array of such elements would yield a mixture ratio distribution analogous to the one shown in Fig. 2.3.1b and these distributions would then provide the appropriate initial conditions required for the analysis of steady-state combustion.[554,762] The mathematical model[356] previously mentioned in connection with spray mass flux likewise describes mixture ratio distributions for liquid-liquid propellant systems. In effect, this model represents a numerical means of describing information such as shown in Fig. 2.3.1b, with additional (analytical) predictions as to how this mixture ratio pattern would vary with axial location. Allowance is taken for inter-element droplet collisions, but not for gross distortion of spray patterns by adjacent elements.

Extensive current application of the technique originally advocated by Rupe[613] to describe mixture ratio distribution of full (liquid-liquid) injectors has provided empirical verification of the general validity of this method in application to performance analysis.[224,258] In some cases, however, element-to-element interaction substantially distorts the distribution that would be anticipated by simple superposition of individual element patterns.

In at least one instance[617] detailed measurements on nonreactive sprays have been used to determine a single quantity, i.e., a mixing efficiency, to represent the degree of uniformity of mixture ratio and to utilize this parameter* to define a correlation with element configuration that in turn provided a so-called "uniformity criterion."[612] This criterion has been used to improve rocket combustor performance.[145,610]

These sampling techniques have also been useful in characterizing mixture ratio distributions of other element types[244,591] as well as complete injectors, and to show that uniformity of mixture ratio is indeed a prerequisite to high performance.[389,609]

It should be noted that the properties deduced from nonreactive sprays of unlike doublets have restricted applicability for highly reactive propellants[135b,246,389,415,777] due to a phenomenon referred to as reactive stream separation. For certain propellants and for specific element types (e.g. unlike doublets) preliminary bounds for this occurrence have been established in terms of operating pressure, jet velocities and diameters, propellant temperatures, and propellant reactivity.[415,430] However, it seems clear that these gross effects should be taken into account when prescribing the size of the element for which the initial mass and mixture distributions of unlike impinging hypergolic elements are presumed known.[389,619]

Although the analogous problem of combustion effects on the mixture ratio and mass distributions of elements composed of like-on-like sprays have not been studied extensively and therefore have not as yet been quantitatively described, it would seem reasonable to assume that similar effects may appear if fuel and oxidizer from closely spaced adjacent elements come into intimate contact prior to full atomization into spray droplets. Thus it is seen that the mixture ratio distributions associated with highly reactive (hypergolic) systems require further elucidation.

2.3.3 Mixing Processes†

Before detailed consideration is given to the mechanism and characteristics of the various mixing processes which occur and play an important role in rocket engine combustion, it is pertinent to review briefly their overall significance and relative importance.[159,355,269]

* The parametric relationship for maximized mixing uniformity as applied to unlike doublets is discussed in Sect. 2.3.3.1, see Eq. 2.3.3–2. The modified versions of that relationship for other unlike element types are discussed in Refs. 244 and 591.

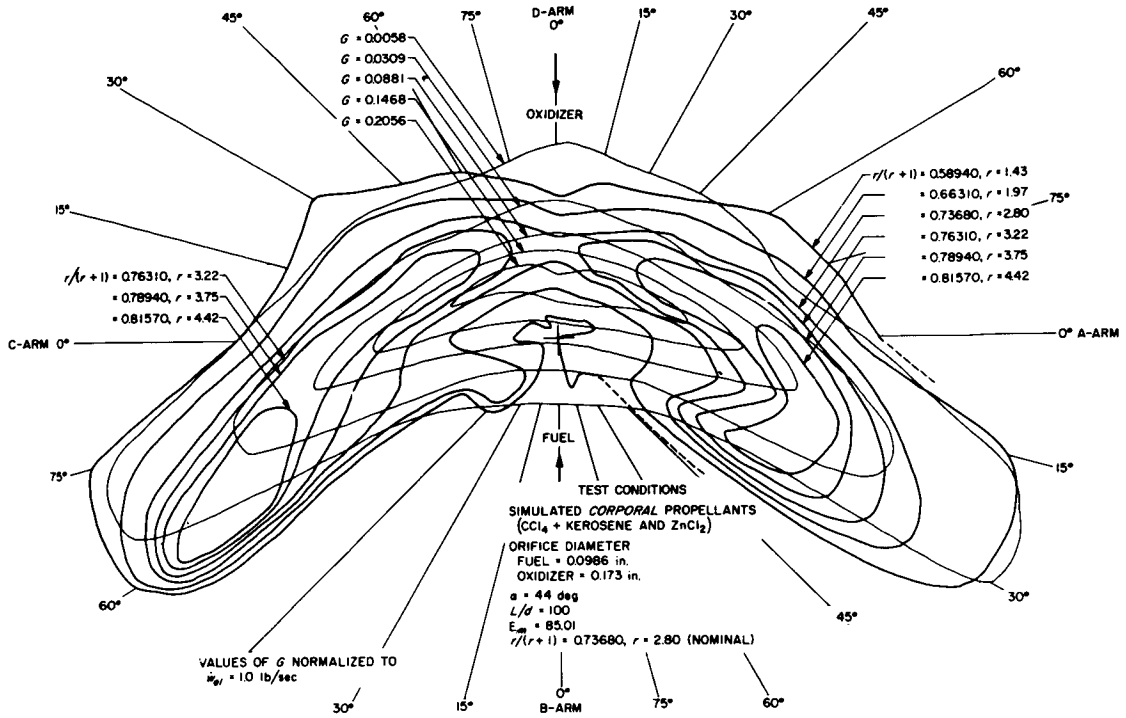

(a)

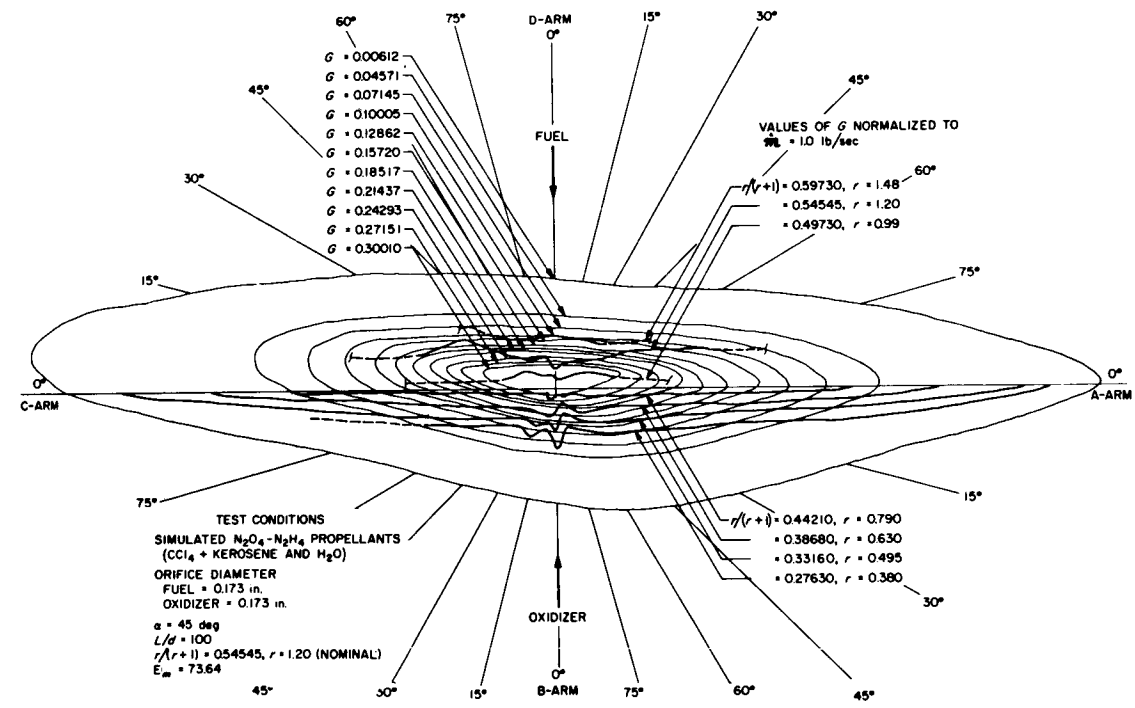

(b)

(a) On a plane surface for nonsimilar jets.
(b) On a plane surface for similar jets.
FIGURE 2.3.2.—Mixture ratio distributions for typical unlike double elements.

It has long been recognized from practical design requirements that chemical kinetic processes, based on pre-mixed vapor-phase reactants, are neither rate controlling nor do they exert a dominant influence upon combustion characteristics in most liquid bipropellant rocket engines during steady-state operation. It may be noted that monopropellant combustion is far more susceptible to control by kinetic effects. In common with other high intensity systems, bipropellant rocket combustion performance is largely determined by a complex network of interdependent physical processes as are indicated schematically in Fig. 2.3.3a. This diagram illustrates the general case and it will be appreciated that under any given set of operating conditions, propellant combination, or injector design configuration some of the reaction paths may assume greater or lesser importance and may even be absent altogether. Nevertheless, it can be seen that for all bipropellant combinations and at every selected operating condition, adequate mixing of fuel with oxidant is an essential criterion for the attainment of efficient combustion, i.e., maximum heat release in minimum volume.

As indicated in Fig. 2.3.3a, it is possible for propellant mixing in the rocket engine to occur under one, or more, of the following three conditions:

1. in the liquid phase
2. by droplet transport in a heterogeneous environment
3. in the vapor-phase

By comparison with combustion systems for air-breathing engines, the rocket has the advantage of being able to utilize liquid-phase mixing under prescribed circumstances, whereas the higher gas temperatures of the rocket usually prevent all but rudimentary attempts at enhancement and control by aerodynamic methods. Other practical considerations apart from combustion efficiency may also impose design constraints especially affecting the injector configuration. For example, although rapid mixing in the liquid and vapor-phases is a prerequisite of good performance, at the same time there is often a requirement to inhibit mixing processes in the boundary layer in order to reduce heat transfer rates to acceptable values by film cooling or other means.

Therefore, in the following discussion of mixing processes under rocket combustion conditions in the three categories enumerated above, it is important to recognize the complexity involved and that any theoretical or experimental appraisal of one process in isolation is virtually impossible to achieve in practice.

2.3.3.1 *Liquid phase mixing.*—There are obvious attractions in attempting to achieve a high proportion of oxidant/fuel mixing in the liquid phase, since this technique offers the greatest prospect of exercising design control where it is likely to be most effective, at the source of the ensuing chain of combustion processes. Although several attempts to obtain liquid-liquid mixing before injection have been reported, these have usually been unsuccessful owing to the onset of uncontrolled reactions during transient off-design operation caused by the high sensitivity of the premixed propellants. Consequently, attention has been directed mainly towards methods of liquid phase mixing within the combustion chamber itself. Exceptions to this generalization are provided by design solutions of the "recessed-cup" and similar types where mixing and often partial-reaction take place in small pre-combustion chambers on the injector face. In practice, liquid phase mixing has been found to enhance the rates of heat release and combustion efficiencies with some hypergolic propellant combinations*; whereas, with non-hypergolic propellants there has often been a tendency to provoke unstable combustion.[539, 318, 446]

So far, no authoritative theoretical model has been derived to describe liquid phase mixing processes, especially those in the presence of highly exothermic chemical reactions, produced by typical injection systems. Instead, there have been a considerable number of experimental investigations, among which those at the Jet Propulsion Laboratory (e.g., Refs. 617, 612, 615 and 244) are of particular significance. These studies have provided quantitative data and empirical correlations under nonreactive or essentially isothermal conditions and attempts have been made to relate these to measurements of the overall combustion

* Reacting stream separation[246, 389, 415] may preclude liquid phase mixing for common hypergolic propellant combinations under certain operating conditions.

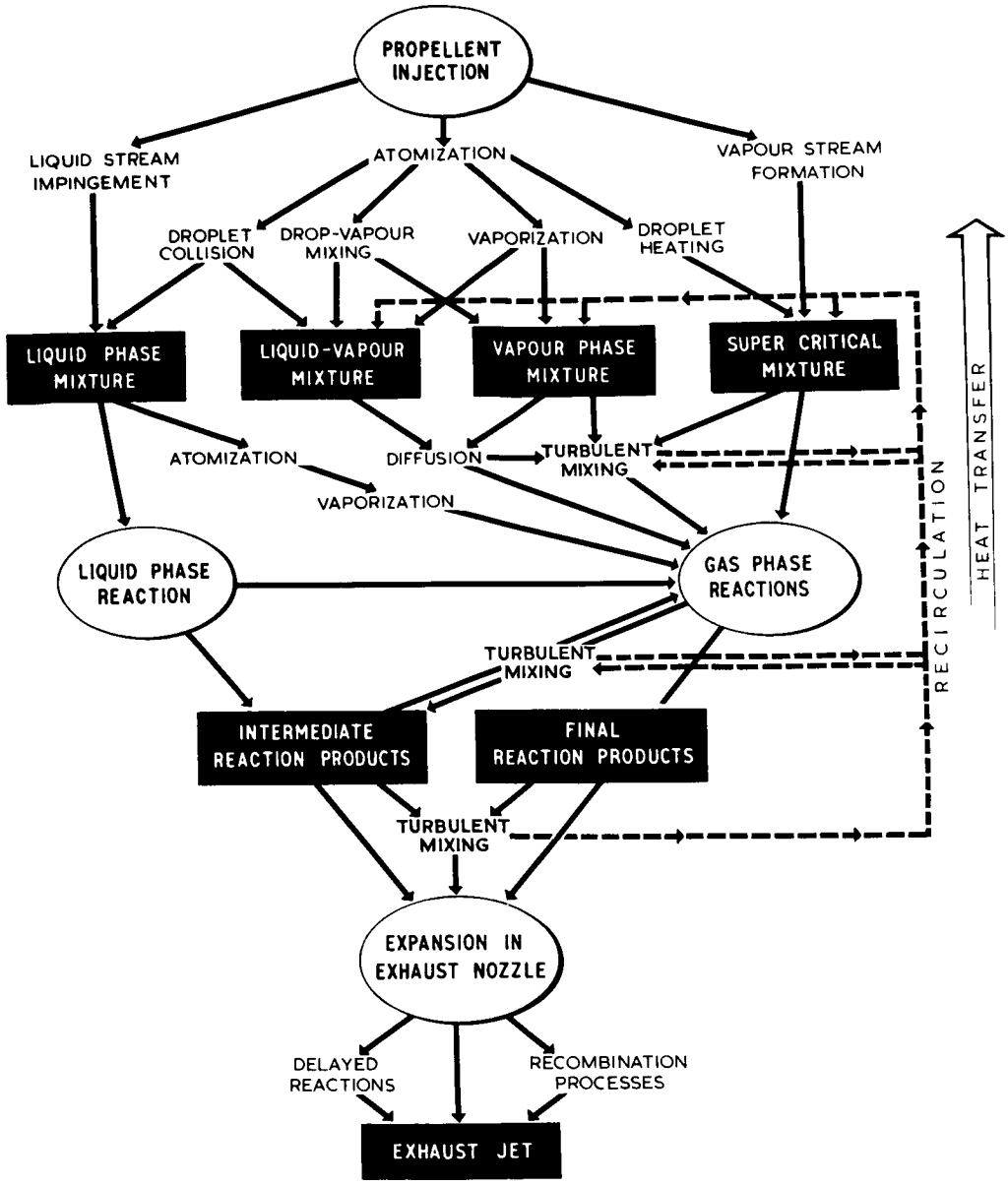

FIGURE 2.3.3a.—Combustion and allied processes in liquid propellant rocket engines.

performance and to qualitative visual observations of the flame shape or intensity.

Propellant mixing can be produced by a wide variety of injector designs, the most common of which include

(a) impinging jet; whereby single or multiple plain cylindrical streams of each propellant converge at a common point in free space near the face of the injector

(b) impinging sheet; these are similar to impinging jets except that propellants are formed into thin sheets by fan sprays or other methods before converging upon each other

(c) splash plate; propellants are injected through plain jets to impinge on suitably positioned plate. Some liquid phase mixing

occurs on the surface during film formation

(d) vortex; plain jets of one propellant impinge on a cylindrical surface film of the second, thus providing a low resultant axial momentum

Typical mixing and resultant flow patterns produced by representative impinging-jet, splash plate and vortex injectors are illustrated in Fig. 2.3.3b derived from Refs. 246 and 111. Liquid phase mixing can be seen to be confined to a very small volume and its effectiveness is known to depend on the destruction of the oncoming fluid momentum in a regular and controlled manner; hence the advantages of surface impingement techniques which do not depend on close design tolerances and are least prone to flow disturbances.

The wide variety and range of complexity of injector designs has made the analysis and interpretation of experimental results very difficult to present in any general manner. However, limited comparisons have been possible by the adoption of a mixing efficiency factor, E_m,[617] defined as

$$E_m = 100\left\{1-\left[\sum_0^n \frac{K_A \dot{m}(\phi_T-\phi)}{\dot{m}_T\phi_T} + \sum_0^{n'} \frac{K_A \dot{m}(\phi_T-\phi)}{\dot{m}_T(\phi_T-1)}\right]\right\} \quad (2.3.3\text{–}1)$$

where

n	number of samples with $\phi<\phi_T$
n′	number of samples with $\phi>\phi_T$
K_A	factor for sampling area correction defined as the ratio of the area of equivalent spherical surface represented by the sample to the cross sectional area of the sample tube
$\dot{m}$	local mass flow rate of the spray
$\dot{m}_T$	overall mass flow rate of total spray or component stream

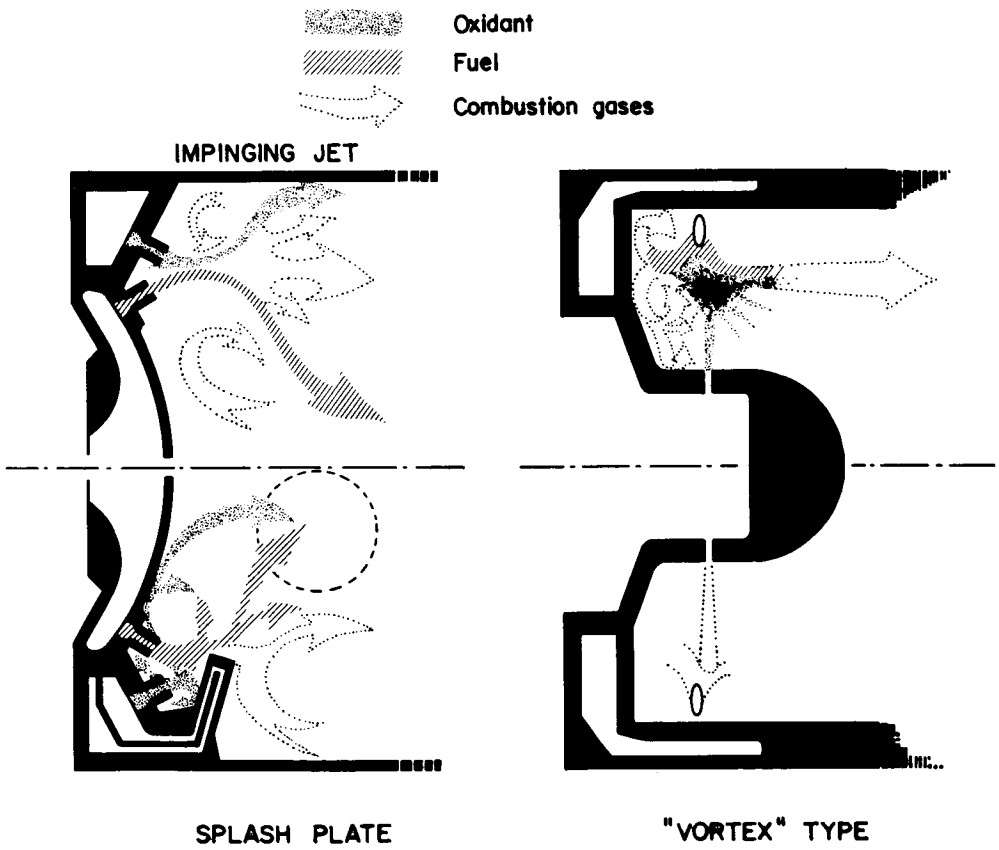

FIGURE 2.3.3b.—Relative locations of fuel, oxidizer and combustion gases associated with splash plate and vortex-type injectors.

ϕ local mass flux fraction $= \dot{m}_1/(\dot{m}_1+\dot{m}_2)$

ϕ_T overall mass flux fraction $= \dot{m}_{T_1}(\dot{m}_{T_2}+\dot{m}_{T_2})$

and subscripts 1 and 2 are used to identify the two components (e.g. oxidant and fuel).

This mixing factor, based on the variation of local mixture ratio and weighted in accordance with the proportion of the spray represented by each sample, has been used by various workers to compare sprays produced by differing injector configurations and operating conditions, and is generally preferred to other expressions relating the distribution of samples about a mean value. For example, in the simplest case of the impingement of two unlike jets in free space it has been possible to show[612,615] that for a range of geometrical and operating conditions the mixture distributions are dependent on stream momenta. At any given condition the most uniform mixture distribution (i.e. E_m was a maximum) was obtained with equal momenta in the two jets, i.e.,

$$\rho_1 u_1^2 d_1 = \rho_2 u_2^2 d_2$$

or

$$M_j = \left[1+\frac{\rho_1 u_1^2 d_1}{\rho_2 u_2^2 d_2}\right]^{-1} = 0.5 \qquad (2.3.3\text{–}2)$$

in which ρ is the fluid density, u the axial injection velocity, and d the jet diameter; while M_j is a convenient expression for representing large variations in momentum ratio. A typical correlation, from Ref. 615, obtained from experimental studies of a simple unlike doublet system with an impingement angle of 60°, is shown in Fig. 2.3.3c. Similar trends of variation in mixing efficiency with liquid stream momenta have also been observed for coplanar triplet injectors[111] and concave surface deflectors.[592,252] These and other similar investigations have also shown the dependence of mass flux distribution (spray patternation) and in some cases of spray quality (drop-size and drop-size distribution), on injector geometry and jet momenta. In addition, there is evidence[237] under nonreacting conditions, that the miscibility of the two fluids has little or no effect upon the mixing efficiency and distribution of fluid components.

Cold flow tests with effectively inert fluids, similar to those described above, are capable of simulating the liquid-phase mixing behavior at practical combustion conditions, provided mixing rates are large compared with chemical reaction rates[246]; for example, when using stabilized fuming nitric acid and various alcohols or kerosene/amine mixtures. Conversely, with propellant combinations which give rise to rapid liquid phase reactions (e.g., oxidizers such as chlorine trifluoride or nitrogen tetroxide with mixed hydrazine derivative fuels) the impingement mechanism can be strongly influenced. Photographic studies[246] have shown violent evolution of gases at the impingement interface sufficient to blow apart, or separate, the streams of fuel and oxidizer and thus inhibit further mixing and atomization. With such systems it is, therefore, probable that the uniformity of mixture distribution is not only dependent on the ratio of the momenta in the two streams but also on the relative momentum between them. Highly reactive propellant combinations, however, can be made to give good combustion efficiencies by design features which nullify the disrupting influence of gas evolution i.e., the use of multiple interlacing injection elements or such devices as the recessed-cup injector.

Injector designs like the splash plate and vortex, which lead to liquid phase mixing on a solid surface, have the advantage of avoiding the necessity for accurate alignment inherent in impinging systems and to some extent mitigate against the effects of spontaneous reaction. How-

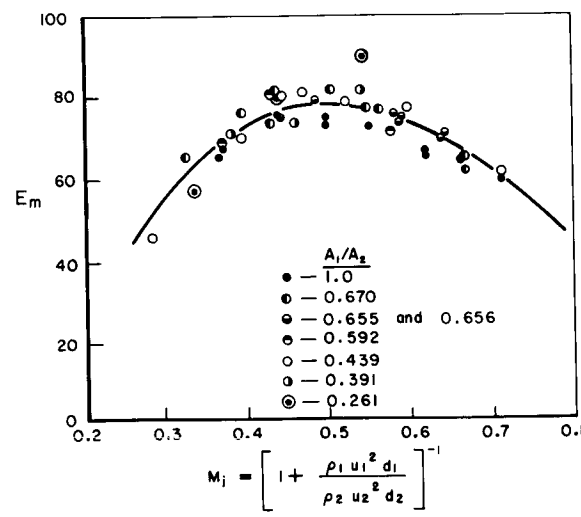

FIGURE 2.3.3c.—A correlation of the dynamic characteristics of free liquid jets and E_m for an impingement angle of 60°.

ever, these designs lend themselves to an infinite variety of geometrical configurations, scale effect and operating criteria with the result that no effective characterization of their design features has been possible up to the present time. Nevertheless, a number of qualitative design rules of an ad hoc nature have been accumulated for particular systems as a result of intensive development experience. A typical procedure is the following: during the development of an injection system, several design configurations are subjected to cold flow mixture and mass distribution measurements over a range of operating conditions. Selected configurations are then subjected to open burner tests for photographic recordings to be made of the flow patterns and flame shape, then finally to detailed determination of their combustion performance and heat transfer properties under normal rocket engine conditions.[111] By this means it has been possible to formulate empirical design rules on the effects produced by changes in stream momenta, impingement position, injector geometry, etc., for the particular systems studied. Some of the rules may be of more general application.

Unfortunately, this comparatively tedious and costly approach* is likely to remain for some time the best available method for the acquisition of detailed knowledge on any given type of injector, where complex liquid and gas phase mixing processes are involved. The desirable alternative, a comprehensive theoretical model of the various chemical and fluid dynamic processes, is unlikely to be realized until a better understanding of the fundamental mechanisms has been achieved.

2.3.3.2 *Droplet transport.*—The initial combustion characteristics of most liquid-fueled high-intensity systems depend largely on the related processes of atomization and spray mixing originating at the injector. This is especially true of the liquid bipropellant rocket engine where the injection process is employed both as a means of imparting a large surface area to the liquid volume for vaporization purposes and for encouraging spray dispersion as an aid to the mixing of fuel with oxidant, see Fig. 2.3.3a. Previously discussed methods of propellant injection which provide intentional liquid stream impingement as a primary mixing device may still rely on spray mixing as a secondary process, see Fig. 2.3.3b. In addition, for many injectors (e.g., like-impinging), each propellant is atomized independently through a multiplicity of separate injector elements so there is no direct liquid mixing. Primary mixing of propellants then takes place through intermingling between unlike sprays as a result of (1) natural expansion in the spatial distributions, (2) droplet dispersion by turbulent eddy diffusion in the surrounding gas and (3) forced mixing by deliberate spray impingement.

As in the case of vaporization rate predictions, an intimate knowledge of the initial spray characteristics is an essential prerequisite of any attempt to predict and understand the subsequent droplet mixing processes. Numerous experimental determinations of the spray properties under cold-flow conditions have been reported in the literature (see Sect. 2.2.3 and 2.2.4) for atomizers of the types used as injector elements in rocket engine applications. These studies have included measurements of the drop-size distributions, mass-flux distributions (patternation) and velocity distributions near the point of spray formation for a variety of injector element designs and scales with a range of fluid properties, ambient densities and operating conditions. In many instances it has been possible to correlate results satisfactorily by empirical, or semiempirical, relationships for a particular range of circumstances and these relationships are of use in theoretical models of spray combustion processes.

Both vaporization and mixing processes in sprays are then dependent on the ballistics and trajectories of individual drops, or groups of droplets, which may be determined from empirically derived drag coefficients, C_D, using an expression of the form[740]

$$\frac{dV_L}{dt} = 0.75 \frac{C_D \rho \Delta V \, |\Delta V|}{\rho_L d_L} \qquad (2.3.3\text{–}3)$$

in which ΔV is the relative velocity between droplets of diameter d_L and liquid density ρ_L, and surrounding gas of density ρ. In practice it has been found that the drag coefficients of liquid droplets, especially under evaporating conditions and high Reynolds number, depart markedly from

* Even this approach is much less costly than hot firings.

those derived for solid spheres, i.e. Stokes Law in which

$$C_D = 24Re^{-1} \qquad (2.3.3\text{–}4)$$

where Re is the Reynolds number based on droplet diameter, relative droplet to gas velocity and the appropriate gas properties. Correlations which allow both for liquid evaporation[374] and for droplet distortion at high relative velocities[569] with burning and non-burning fuel droplets are

$$\left.\begin{aligned} C_D &= 27Re^{-0.84} & 0<Re<80 \\ &= 0.271Re^{0.217} & 80<Re<10^4 \\ &= 2 & Re>10^4 \end{aligned}\right\} \qquad (2.3.3\text{–}5)$$

The importance of recognizing the effects of evaporation and drop distortion, implicit in these correlations of C_D with Re, has been demonstrated[419] in a comparison of experimentally determined burning rates with theoretical predictions for droplet evaporation under typical rocket combustion conditions.

It is now theoretically possible by statistical methods to provide a comprehensive model for the subsequent droplet transportation mechanism[743] and thus derive a complete distribution of mass and composition within the combustion chamber, including the probability of droplet collisions producing either agglomeration or liquid phase reactions. However, the complexity of the problem has, so far, defied rigorous analysis and in practice numerical solutions have only been obtained after drastic, or perhaps oversimplification of the mathematical expressions and the physical model. Instead, the majority of work on spray mixing under rocket combustion conditions has been by inferential observations based on the flame patterns produced in semi-transparent chambers (e.g., Refs. 246, 111, 419 and 421) and on direct measurements of composition or temperature profiles.[445]

Small-scale studies of single and multiple fuel sprays under simulated rocket combustion conditions[445] have shown that nonuniform mixture distributions in the combustion products could be related to cold-flow measurements of mass-flux distribution. The technique has also been used to demonstrate that the additive effects of adjacent sprays of the same component, measured under cold-flow conditions, are reproduced in the combustion product distributions.

In addition to the time-averaged spatial distribution and propellant mixing processes attributed to the liquid injection mechanism; it may also be necessary to consider temporal variations in mass-flux, and hence in mixing, caused by periodic disruption of the liquid streams during the atomization process.[446, 341] Small-scale combustion studies have confirmed the presence of these periodic variations in terms of light emission and temperature at a point, and good correlation has been obtained with measured frequencies. It may be noted that these periodic fluctuations in mixture ratio also give rise to apparent anomalies in the composition of gases sampled from the combustion zone which suggest unrealistic departures from chemical equilibrium among the sampled constituents.[200]

Finally, a simplified analytical treatment of forced mixing between unlike sprays has been considered in the formulation of a semi-empirical combustion model[421] based on the use of adjacent sprays of fuel and oxidizer produced by impinging jet "like-on-like" injection elements. Mixing was assumed to take place instantaneously at the boundaries of "wedge" shaped regions containing fuel or oxidant sprays whose configurations were determined from cold flow experiments. A comparison with experiments in a two-dimensional combustion chamber showed that the theoretical model, which included spray mixing as a rate controlling process near the injector face, was better able to describe the measured velocity distributions than one where vaporization alone was considered.

None of the studies of spray mixing and droplet transport processes, whether theoretical or experimental in nature, have yet considered adequately the effects of operation at high pressures when the critical temperature of either, or both, droplet systems could be exceeded.

2.3.3.3 *Vapor mixing.*—It has long been recognized from high-speed motion and streak photography that some nonuniformity in gas composition and temperature distributions persist throughout the rocket combustion chamber and into the expansion nozzle despite efforts to promote fuel and oxidant mixing in the liquid phase by direct impingement or spray interpenetration. Moreover, these striations in mixture strength

have been demonstrated to continue far beyond the point at which vaporization processes were complete,[445] so that final mixing of the propellants was taking place through turbulent diffusion processes in the vapor phase. In practical systems where it becomes possible to achieve good atomization, for example by the use of blast atomizers* with oxygen/hydrogen or H.T.P.†/hydrocarbon propellant combinations, it is probable that vapor phase turbulent mixing becomes the dominant rate-controlling mechanism in the steady-state combustion process. Although a high degree of turbulent mixing is clearly desirable if high performance is to be achieved; there is also evidence that excessive mixing is unnecessary and can, under certain circumstances, degrade the combustion efficiency.[214]

Turbulent mixing between gas streams has received considerable attention in connection with air-breathing combustion systems of all types and an extensive coverage of the subject is available in the published literature. Less attention has been paid to this topic under rocket combustion conditions; but a theoretical analysis becomes feasible if the intensity and scale of the turbulence are known, together with the configuration and aerodynamic properties of the gaseous sources. A further assumption has to be made, or empirical data have to be used, on the influence that combustion can have on physical properties and on the turbulent intensity. Although it has been postulated that discrepancies between theoretical and measured flame propagation rates were due to "flame generated turbulence"[397] and this concept has received wide acceptance, serious doubts about its validity have recently been expressed.[437]

A simple analytical treatment[100] of turbulent mixing under rocket combustion conditions was based on equations developed for the injection of gas from a point source into a uniformly turbulent gas stream in the absence of chemical reactions. Molecular diffusion processes were ignored and solutions obtained at various locations downstream from the point sources by assuming values for the scale and intensity of main stream turbulence. Results of this analysis were presented in terms of a "ripple factor," Ψ, defined as the ratio of the minimum to the maximum concentrations across any given plane normal to the direction of flow. This ripple factor was found to depend on the ratio of downstream length to the separation distance between sources and on the intensity, but not the scale, of turbulence. For the selected values of separation distance and turbulence intensity it was concluded that turbulent mixing rates were large (at least in the principal combustion zone) compared with those of vaporization and, therefore, that the latter process was dominantly rate-controlling.

Experimental studies of vapor phase mixing under rocket combustion conditions have used direct gas sampling methods,[445,447] the addition of a tracer,[350] or spectroscopic measurements[129] to evaluate changes of composition profiles along the length of the chamber. In the particular case of oxygen/hydrogen combustion with concentric jet injection systems, radiation measurements[129] confirmed that turbulent mixing controlled the extent of reaction if liquid oxygen was injected through a central jet surrounded by an annular stream of gaseous hydrogen. However, if the propellant streams were interchanged, a condition which might be expected to enhance mixing near the injector by expansion of the gaseous core, it was found that propellant vaporization appeared to become rate controlling. A similar result was obtained by assessing the variation in combustion efficiency with chamber length[349] and this trend has also been observed by other workers at differing engine scales.

The influence of turbulent mixing on combustion performance has been analyzed[351] using as a basis the earlier analytical treatment of the decay of concentration profiles.[100] Numerical solutions for eight propellant combinations and a range of chamber geometries were expressed in terms of a mixing parameter, TL/S, the product of turbulence intensity and the ratio of chamber length to injector element spacing. Reasonable correlation was established with experimental measurements and this "mixing model" enabled conclusions to be reached on the effects of maldistribution on

* Blast atomizers may be defined as those in which the primary source of energy for liquid breakup is derived from a suitably oriented jet of gas, usually at high-velocity.

† H.T.P. (High Test Peroxide). Concentrated solutions of hydrogen peroxide in water, (usually 85 to 100 weight percent hydrogen peroxide) which are used either as a monopropellant or as an oxidizer in a bipropellant system for rocket propulsion applications.

combustion performance and optimum performance mixture ratio. However, an apparently anomalous result was the decrease of turbulence intensity along the chamber axis, from values as high as 10 percent near the injector to about 2 percent 8 inches downstream.

More recently, as part of an analysis of convective heat transfer within the combustion chamber, a better description of experimental results on turbulent mixing processes has been achieved.[531] In this theoretical model it is assumed that the root mean square lateral velocity, and not the turbulence intensity, remains constant throughout the chamber length. Thus, as combustion takes place and the mean axial velocity increases, the turbulent intensity will fall away in a manner closely similar to measured observations. The same basic mixing theory as that developed for hydrocarbon/air combustion[637] was used to predict the concentration, C, derived from a point source of strength, W, at a radius, r, from the longitudinal axis of the source, given by

$$C = \frac{W}{4\pi g} \cdot \exp\left(-r^2/4g\right) \qquad (2.3.3\text{–}6)$$

in which g is a spreading factor defined by

$$g = S_t V_{rms} t + S_t^2[\exp\left(-V_{rms} t/S_t\right) - 1] \qquad (2.3.3\text{–}7)$$

where S_t is the Lagrangian scale of turbulence, V_{rms} the root mean square lateral velocity, and t the time after injection. The adoption of a constant value of r.m.s. lateral velocity, V_{rms}, has been found by computation to lead to a final turbulence intensity of the order of 1.5 percent with complete combustion and thus is in good agreement with experimental observations.

Most experimental and theoretical studies of vapor phase mixing have been concerned with changes in composition, which may be described in terms of mixture strength profiles, over sections of the combustion chamber normal to the direction of gas flow. However, nonuniformities may also be present in an axial direction which give rise to random, or periodic, fluctuations in composition about a mean value at any given point. It has already been mentioned that these fluctuations can originate from the spray breakup mechanism (see Sect. 2.3.3.2), but they can also be caused by gas dynamic processes near the injector face, e.g., vortex generation and nonuniform recirculation. Under rocket combustion conditions the "pockets" of gas flowing past a point can vary in composition between the extremes of pure fuel and pure oxidant and it has been found[200] that these variations about the mean value were best described by the beta-distribution function, F(C), given by

$$F(C) = AC^{p-1}(1-C)^{q-1} \qquad (2.3.3\text{–}8)$$

$$\text{for } 0 < C < 1$$

where p and q are constants limited to positive values and A is a normalization constant defined as

$$A^{-1} = \int_0^1 C^{p-1}(1-C)^{q-1} dC \qquad (2.3.3\text{–}9)$$

$$= \beta(1, p, q)$$

in which the concentration, C, is expressed as the ratio of oxidant-equivalent moles of fuel to the total oxidant equivalent moles of both fuel and oxidant, i.e., $C = (2n_C + \frac{1}{2}n_H)/(2n_C + \frac{1}{2}n_H + n_O)$. This analysis was successful in explaining apparent departures from chemical equilibrium in samples collected over finite time intervals.[447] Moreover, as a corollary, it was concluded that conventional gas sampling methods and a complete chemical analysis could be used to assess the magnitude of mixture ratio fluctuations at a point.

2.3.4 Recirculation

The significance of recirculation as a flame-holding, or piloting, mechanism in air-breathing combustion systems of all types is well known and has been the subject of a number of investigations reported in the published literature. These have ranged from aerodynamic studies of the conditions under which recirculating flows and vortices can become established in confined ducts, usually of very simple geometrical shape, to assessments of the effects of recirculation and entrainment on the mixing between coaxial streams. Experiments have been carried out both with reacting and non-reacting constituents and, although much of the work is not strictly applicable to rocket conditions, many useful qualitative observations and generalizations emerge.[205,77,84]

In the liquid propellant rocket engine, gaseous recirculation phenomena are normally confined to

a narrow region of the combustion chamber near the injector where they can be induced by entrainment and momentum exchange between the injected propellants and the surrounding gas. These entrainment effects give rise to high local turbulence[77] and a reverse flow of gas which, depending on its source, consists either of cool unburned propellant vapor or of hot combustion products. Moreover, the recirculation flow patterns may be localized around each individual injector element, or else may be of larger scale giving rise to "cross winds" over appreciable areas of the surface of the injector. Recirculation can, therefore, be either beneficial or detrimental to the stable combustion processes and reliable operation of the engine according to the scale and intensity of the flow, also depending on the composition and temperature of the gases taking part.

When injector designs and the rates of chemical reaction are such that only cold unreacted propellant vapors form the recirculating flow, it has been stated[159] that the resultant eddy can have but little effect on the combustion process. While this may be substantially true for highly localized effects in which the injected stream only entrains its own vapor; other evidence is available to indicate that if unlike vapors become entrained then mixing is improved and there is an increase in the initial rate of heat release.

In the case of recirculation of combustion products, there are claimed to be three independent ways in which they can assist combustion.[159] First, they are able to provide a continuous heat source for ignition purposes and, if not balanced in composition, are capable of further reaction with the propellant vapors. Secondly, they enable combustion processes to be brought into the "core" of each spray system. Finally, the resultant evolution of gaseous combustion products within the sprays may accelerate the spatial expansion process, thereby leading to more rapid spray mixing. Nevertheless, despite this awareness of its beneficial effects as a flame piloting mechanism, there has apparently only been one instance, in a thermal ignition H.T.P./kerosene rocket engine, where deliberate design provision was made to make use of this phenomenon. On the other hand, an excessive reverse flow of hot combustion products can have detrimental effects in causing overheating of the face of the injector,[116] which can be clearly identified with local flow patterns and velocities.

Most experimental investigations of recirculation under rocket combustion conditions have been by qualitative observations, using high-speed photographic techniques, as part of more general studies of the flame patterns in transparent combustion chambers. Moreover, few attempts have been made to confine attention to the recirculation zone itself in order to relate spray geometry or propellant momenta to the resulting flow regimes.[201,275] One detailed study of recirculation as a flame piloting mechanism[689] did, however, investigate in a systematic manner the significance of selected design and operational variables on the overall performance of the system. In this essentially experimental program, the effects of basic chamber geometry and propellant properties, including mixture ratio, were assessed in terms of mixing profiles derived from gas sampling and analysis, both for reacting and non-reactive conditions. Nevertheless, further work of this nature is needed before reliable generalizations can be made and the importance of recirculation in the more general context of vapor-phase mixing can be established.

In addition, limited studies of the flow regime near the injector face have been made using flow visualization techniques similar to those developed for application to air-breathing combustion systems. Of these, possibly the most interesting is that in which the phase change produced by flash vaporization is used to simulate the density changes under combustion conditions,[360] although it is evident that considerable development of this technique is necessary before it can be regarded as being of general usefulness.

The importance of the momenta of the injected propellants in determining the nature of the recirculation has been demonstrated experimentally[526] by subjecting a typical impinging jet injector to a wide range of differential pressure (i.e., mixture ratio) conditions at a constant chamber pressure. Temperature measurements at selected points on the surface of the injector showed the anticipated approximate relationship with the gas temperature and mixture ratio as long as the total momentum of the oxidant flow exceeded that of the fuel. A complete reversal of this trend was observed at very fuel-rich mixture

conditions as fuel momentum became dominant, Fig. 2.3.4, when surface temperatures rose rapidly despite the continuing fall in the mean combustion temperature. Further evidence from these investigations showed that when oxidant momentum dominated the recirculation process the reverse flow was fuel-rich in composition, but the converse was true when the fuel sprays provided the main entrainment mechanism.

Therefore, empirical work has shown that recirculation can provide an important contribution to the stability and intensity of the combustion process in the injection region. Although no clear proof exists, it is also logical to assume that disturbances in the recirculating flow regime can produce related variations in the heat release rate in the primary mixing region and thus establish a possible driving mechanism for combustion instability.

2.4 LIQUID DROPLET VAPORIZATION AND COMBUSTION*

Far from literally *atomizing* (or "molecularizing") liquid propellants, rocket motor injectors produce nonuniform sprays of droplets with the median size typically containing some 10^{15} molecules/droplet. Owing to low liquid phase diffusion rates and temperatures this initial state of molecular aggregation is ordinarily incompatible with high volumetric chemical reaction rates. Hence rapid droplet *vaporization* is essential to compact and efficient combustion. The combustion behavior of such sprays is indeed a statistical consequence of the vaporization/combustion behavior of its interacting individual droplets, each of which finds itself in a rather extreme and time-varying local environment (even during stable combustion). In this section, we briefly discuss the results of fundamental research on individual droplet vaporization, with emphasis on the significant effects of localized *gas phase* chemical reaction in augmenting the vaporization rates of monopropellant and bipropellant droplets (fuel in oxidizer vapor or vice versa). While some overlap is inevitable, attention will be directed at important experimental and theoretical developments since the comprehensive reviews of Spalding,[661] Wise and Agoston,[752] F. A. Williams[740] and A. Williams.[741]

The following nomenclature pertains to Sect. 2.4:

a	Stoichiometric coefficient
B	Dimensionless interfacial mass transfer rate (transfer number)
$\mathfrak{B}$	Pre-exponential factor
b	Stoichiometric coefficient
C	Constant in Eq. (2.4.1–8)
C_D	Drag coefficient
D_I	First Damköhler number
$\mathfrak{D}$	Fick binary diffusion coefficient
d_L	Droplet diameter
E_{act}	Overall activation energy of homogeneous reaction
h_c	Heat of vapor phase combustion per unit mass of oxidizer (Sect. 2.4.2) or of fuel (Sect. 2.4.3)
k	Reaction rate constant
Le	Lewis number, Pr/Sc
$\dot{m}''$	Mass flux per unit area, $\equiv \dot{m}/\pi r_L^2$
n	Overall reaction order, $\alpha+\beta$
Pe	Peclet number, Re·Pr, based on d_L
r_{eq}	Equivalent initial release radius at prevailing pressure (supercritical combustion)
$\mathfrak{r}_{st}$	Stoichiometric oxidizer/fuel mass ratio
S_u	Laminar flame speed with respect to unburned gas
V_∞	Relative velocity (absolute value) between droplet and gas, $\lvert V-V_d \rvert$
α	Reaction order with respect to oxidizer vapor
β	Reaction order with respect to fuel vapor
κ	Apparent evaporation coefficient, $-d(d_L^2)/dt$
ν	Kinematic viscosity, μ/ρ
τ	Dimensionless time, $\mathfrak{D}t/r_{eff}^2$
χ	Stoichiometry parameter, $(Y_{OX,\infty}/Y_{F,L})/\mathfrak{r}_{st}$

Abbreviations:

bp	Boiling point
B-S	Burke-Schumann
DS	Distributed-source
fct( )	Function of ( )
LOX	Liquid oxygen [O_2(L)]
PS	Point-source
QS	Quasi-steady

* D. E. Rosner, Author.

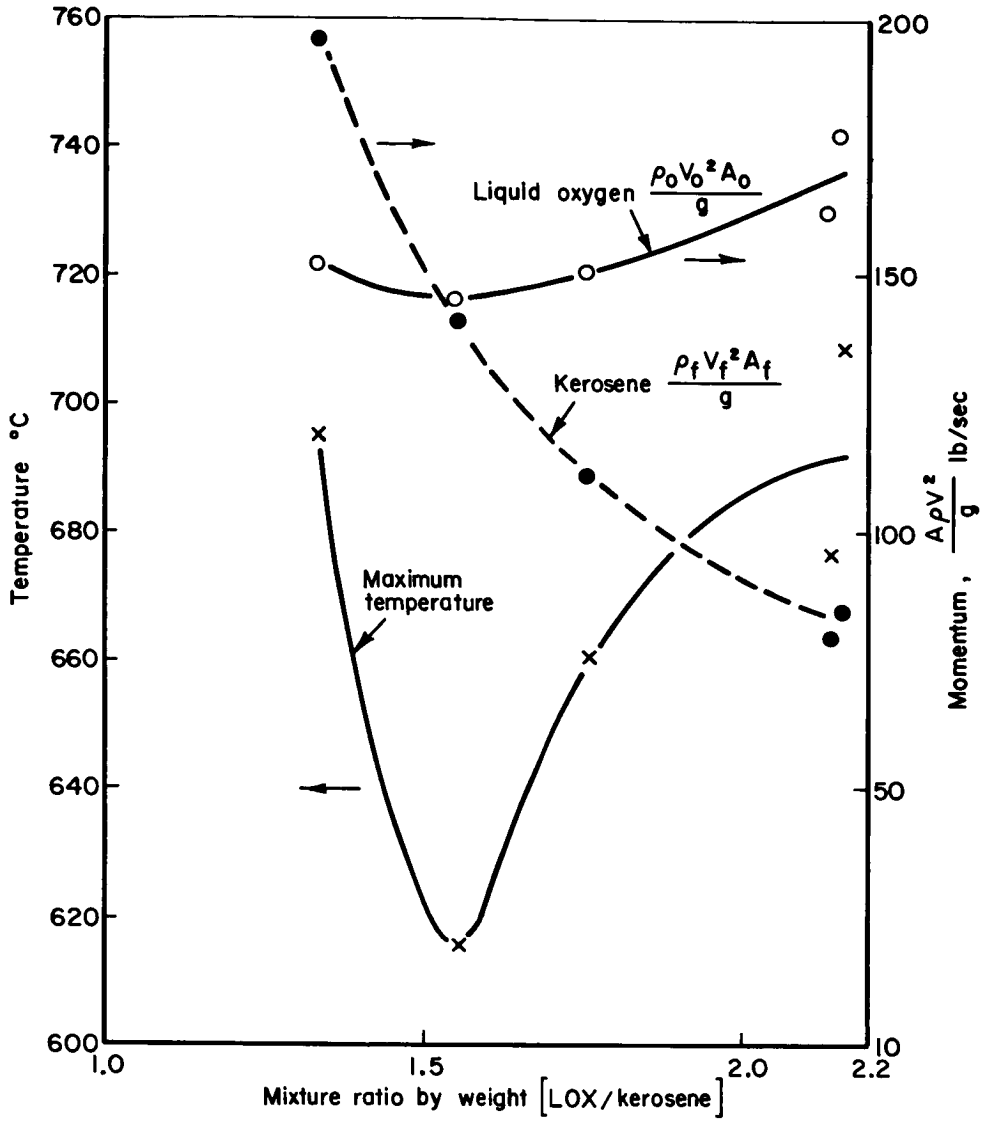

FIGURE 2.3.4.—The influence of liquid propellant momentum on injector face temperature.

(g)	Gas
(L)	Liquid
μ	Micron (10^{-6} m)
$(\bar{\ })$	Average value of ( )
[ ]	Concentration
Subscripts:	
ad	Adiabatic
AE	Auto-extinction
AI	Auto-ignition
bp	Boiling point
BO	Blow-off
cr	At critical point
comb	With combustion
d	Droplet
D	Pertaining to diffusion
eff	Effective
eq	Local equilibrium
ext	At extinction
H	Pertaining to heat conduction
max	Maximum (B-S limit)
P	Product
u	Unburned mixture

v	Vapor
vap	Vaporization
w	At wall (vaporizing surface)
wb	Wet-bulb
∞	At infinity (far from droplet)

To fix ideas it is useful to examine the experimentally observed behavior of an isolated fuel droplet when suddenly confronted with a stagnant, hot oxidizer (containing) gas (see Figs. 2.4a and 2.4b). Such experiments[518] typically involve photographically following the rate of diameter decrease of a fuel droplet suspended on a thermocouple junction. One notes the existence of the following distinct regimes: (1) transient heat-up interval during which the droplet surface temperature rises to the (nonreactive) "wet bulb" temperature with some change in droplet diameter, d_L (2) a vaporization period during which d_L^2 decreases linearly with time with the droplet temperature remaining nearly constant, and (3) an "augmented" vaporization period (d_L^2 again linear in time) associated with the presence of a diffusion flame surrounding the droplet. Heat generated by the localized *gas phase* reaction of fuel vapor and ambient oxidizer drives the surface temperature up to near the fuel boiling point, and sustains the enhanced vaporization rate until droplet consumption or extinction.

While such laboratory experiments can provide valuable insight into the possible life-history of a droplet in a rocket motor combustion chamber, *direct* use of these data is precluded by the vast gap in environmental conditions (pressure level, droplet size, relative flow velocities, turbulence level) ordinarily separating well-defined laboratory experiments from rocket chamber conditions. For this reason considerable attention has properly been focused on acquiring an *understanding* of the physical and chemical phenomena governing each stage in the droplet lifetime. In the absence of such understanding it would clearly be impossible to (1) generalize (correlate) the results of available experiments, (2) reliably extrapolate the results to environmental conditions anticipated in rocket combustion chambers, and (3) correct for artifacts of the experimental configuration. Even in the presence of such understanding, however, the application of such fundamental data on droplet behavior to rocket motors continues to tax the ingenuity of designers.

While radically new experimental techniques have apparently not been introduced, methods used successfully in the past have been extended to provide interesting new data on the drag coefficients of vaporizing and burning bipropellant droplets, vaporization and burning times for

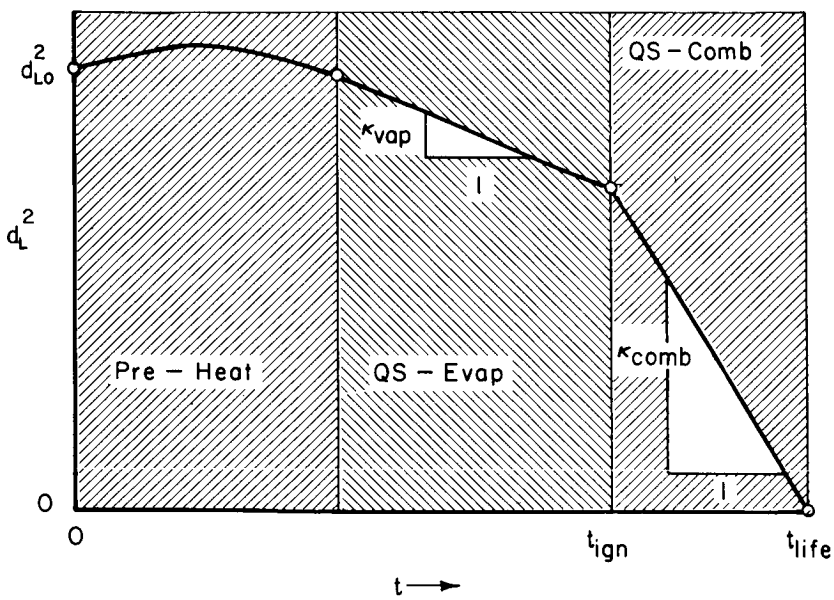

FIGURE 2.4a.—Square of droplet diameter versus time; fuel droplet placed in hot stagnant oxidizer-containing gas.

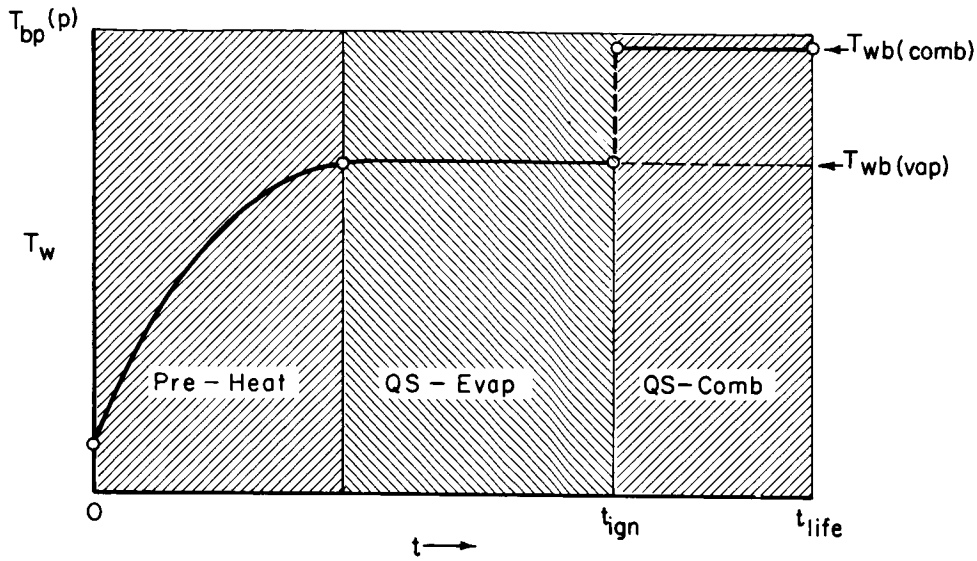

FIGURE 2.4b.—Droplet surface temperature versus time; fuel droplet placed in hot stagnant oxidizer-containing gas.

bipropellants at extremely high (supercritical) pressures, and monopropellant burning rates and flame structure (in ambient environments which react with the primary decomposition products of the droplet). Previous theoretical models of the combustion of bipropellant and monopropellant droplets have been considerably extended, in part with the help of new mathematical techniques and/or approximations. These extensions are of three types: i.e., those which (1) increase the accuracy of absolute predictions (burning rate, flame shape, etc.), (2) extend the domain of applicability of previous results (e.g., to higher pressure levels, incipient forced convection), and (3) enable a qualitative understanding of the effects of physical and chemical kinetic parameters (e.g., on flame zone structure, burning rate, environmental conditions enabling droplet ignition or leading to extinction, etc.). As a byproduct, this work has delineated the limitations of previous theoretical models of droplet burning, and highlighted aspects of droplet burning having direct relevance to rocket motor combustion instability. In what follows we outline these advances against the voluminous background of previously available droplet results.

2.4.1 Droplet Heat-Up and Vaporization

Combustion chamber "stay-times" must be long enough to ensure that unconsumed droplets do not emerge. Accordingly, several authors have considered the design consequences of deliberately simplified one-dimensional steady flow models in which propellant vaporization is the rate-controlling process. In the most complete numerical study of this type,[565] it is assumed that (1) all droplets in the initial spray have the same initial velocity and never shatter or coalesce, and (2) properties of the bulk gas flow (resulting from propellant vaporization) correspond to instantaneous stoichiometric combustion. The results of *single* drop studies play an important role in such models since the initial spray distribution is represented by several different groups of drop sizes (each containing a fixed percent of the initial mass of the spray) whose histories are then computed from the laws governing droplet heat transfer, mass transfer and drag.

Most experimental droplet evaporation studies have been carried out using the above-mentioned "captive droplet" technique (e.g., $\geq 500\mu$ droplet suspended on one (or more) thermocouple junction(s) or a silica filament), in which forced convection or natural convection flows of hot gases augment the droplet vaporization rate. Smaller droplets can be accommodated using "free-flight" techniques in which droplets are projected,[363] or fall freely through hot gases

produced by a furnace or flame.[240,757] In the latter case drag measurements can also be obtained for vaporizing droplets by simultaneously recording droplet position-time data.[240] As noted below, this information is required to predict droplet trajectories, instantaneous velocity lags (between local gas and droplet) and, hence, instantaneous vaporization rates in combustors.

Experimental studies on single-component droplets have led to the following important observations and conclusions,[112,248,249,302,562] which form the basis of the quantitative model outlined below: (1) in a quiescent environment the time to achieve the droplet wet bulb temperature is proportional to $d_{L,0}^2$ and can be an appreciable portion of the total vaporization time, (2) owing either to small droplet size, or internal circulation within large droplets, actual drop temperature histories are well represented by neglecting internal temperature gradients* (compared to external gradients; i.e., the "infinite liquid thermal conductivity approximation"), (3) for droplets of high volatility the unidirectional mass transport process causes the heat transfer, mass transfer, and drag coefficients to fall below those appropriate to solid (nonvaporizing) spheres at the same Reynolds number, (4) despite the transient nature of the droplet heat/mass transfer problem, step-by-step application of relations strictly derived for steady state conditions usually leads to accurate predictions†, (5) after the droplet temperature reaches the "wet bulb" temperature (i.e., when heat transferred from the hot gas environment is used almost exclusively to vaporize liquid) the droplet surface area decreases nearly linearly with time (see Fig. 2.4a)‡ corresponding to a mass rate of volatilization, $\dot{m}$, decreasing nearly linearly with instantaneous droplet diameter.

Several alternative, but essentially equivalent, quantitative formulations of the above-mentioned phenomena have been reported. Our choice here is based on conciseness and ease of generalizing the results to cases in which combustion occurs. In each case one considers a *single* droplet, and expresses the facts that: (1) the time rate of change of its energy content is equal to the instantaneous difference between the convective heat input and the heat required for surface vaporization, (2) the time rate of change of droplet mass is governed by the rate at which its vapors can diffuse away through the background gas, and (3) the product of instantaneous droplet mass and acceleration is equal to the net aerodynamic (drag) force acting on the droplet. Explicitly, the resulting coupled equations governing heat transfer, mass transfer and drag for a quasi-spherical droplet of instantaneous diameter $d_L(=2r_L)$ are, respectively,

$$\frac{d}{dt}\left[\left(\tfrac{4}{3}\pi r_L^3\right)\rho_L c_L T_L\right] = (4\pi r_L^2)\frac{Nu_H}{d_L}\bar{\mathfrak{K}}(T_\infty - T_L) - (4\pi r_L^2)\dot{m}''h_v \quad (2.4.1\text{–}1)$$

$$-\frac{1}{(4\pi r_L^2)}\frac{d}{dt}\left(\tfrac{4}{3}\pi r_L^3\rho_L\right) \equiv \dot{m}'' = \overline{\mathfrak{D}\rho}\frac{Nu_D}{d_L}\left(\frac{Y_{v,w}-Y_{v,\infty}}{1-Y_{v,w}}\right) \quad (2.4.1\text{–}2)$$

$$\rho_L\left(\tfrac{4}{3}\pi r_L^3\right)\frac{dV_d}{dt} = \tfrac{1}{2}\bar{\rho}(V-V_d)\,|V-V_d|\,(\pi r_L^2)C_D \quad (2.4.1\text{–}3)$$

Here the station subscripts L, w, ∞ refer respectively to the liquid, the gas/vapor mixture at the liquid/gas interface ($T_w = T_L$), and the ambient stream ("far" from the droplet); the remaining symbols are defined in the Nomenclature. The subscript d (Eq. (2.4.1–3)) refers to the droplet, unsubscripted variables pertain to the gas, $|V-V_d| = V_\infty$ being the instantaneous absolute value of the relative velocity between droplet and gas. The dimensionless heat transfer, mass transfer, and drag coefficients Nu_H, Nu_D, and C_D appearing (and essentially *defined*) in Eqs. (2.4.1–1, –2, and –3) depend not only on the

* Internal absorption of IR radiation can produce unusual temperature profiles within droplets (see, e.g., H. C. Hottel et al.[363]), however, calculations indicate that this effect is probably negligible in most rocket motors and industrial furnaces. It is also clear that the present discussion does not apply to droplets capable of undergoing exothermic *liquid phase* reaction.

† Limitations of this "quasi-steady" (QS) approximation will be discussed later on.

‡ Systematic departures from the "d^2-law" occur in the presence of non-negligible convective contributions (free or forced), since convection causes diameter-dependent heat transfer augmentation.

local Reynolds number* $Re \equiv V_\infty d_L/\bar{\nu}$, but also on the dimensionless mass transfer rate per unit area†:

$$B \equiv \frac{\dot{m}'' d_L}{\bar{\mathfrak{D}}\rho Nu_D} = \frac{Y_{v,w} - Y_{v,\infty}}{1 - Y_{v,w}} \quad (2.4.1\text{–}4)$$

Physically, this is largely due to distortion of the radial profiles of vapor mass fraction Y_v, temperature, T, and tangential velocity due to convective transport associated with the radial mass transfer from the droplet. Thus, the simplest possible forced convection correlations which include these essential phenomena would be of the form‡ $Nu_H(Re, Pr, B)$, $Nu_D(Re, Sc, B)$, and $C_D(Re, B)$, where property values are introduced as some suitable "mean" condition representative of the local environment within the boundary layer (see below).

Before presenting recent experimental and theoretical results for the dimensionless transfer coefficients, some comment is in order on the (frequently invoked) simplifications arising when (1) the convective heating of the droplet and evaporative cooling are nearly in balance (i.e., when $T_L \rightarrow T_{L,wb}$), and (2) $Le \approx 1$. Then Eqs. (2.4.1–1) and (2.4.1–2) can be combined to provide a simple implicit equation for $T_{L,wb}$,[661] viz:

$$B_{vap,wb} \equiv \frac{Y_{v,eq}(T_{L,wb}) - Y_{v,\infty}}{1 - Y_{v,eq}(T_{L,wb})}$$

$$= \frac{\bar{c}_p(T_\infty - T_{L,wb})}{h_v(T_L, wb)} \quad (2.4.1\text{–}5)$$

where we have introduced the assumption of local equilibrium at the gas/liquid interface, viz. $Y_{v,w} = Y_{v,eq}(T_L)$. Once solved for $T_{L,wb}$, the value of $Y_{v,eq}(T_{L,wb})$ can be inserted in Eq. (2.4.1–2) to provide the quasi-steady vaporization rate during the period $T_L \approx T_{L,wb}$ (see Fig. 2.4b). In the extreme case in which T_∞ greatly exceeds the *boiling point* of the liquid,* examination of Eq. (2.4.1–5) reveals $T_{L,wb} \rightarrow T_{bp}$, hence

$$B_{vap} \approx \frac{\bar{c}_p(T_\infty - T_{bp})}{h_v} \quad (2.4.1\text{–}6)$$

This limiting result, when combined with the appropriate Nu(Re, Pr, B) relation, enables $\dot{m}''$ to be calculated without the need to explicitly consider the vapor diffusion equation. For this reason, this extreme is (somewhat misleadingly) called "heat transfer controlled."

Early work on droplet vaporization in forced convection environments was based on "synthesized" correlations of the separable form:[657,661]

$$Nu(Re, Pr, B) = \frac{\ln(1+B)}{B} Nu_{B=0}(Re, Pr) \quad (2.4.1\text{–}7)$$

where, $Nu_{B=0}(Re, Pr)$ constitutes the corresponding *solid* sphere Nusselt number, commonly taken as†

$$Nu_{B=0}(Re, Pr) = 2(1 + CRe^{1/2}Pr^{1/3}) \quad (2.4.1\text{–}8)$$

However, the logarithmic "driving force" $\ln(1+B)$ is known to be exact‡ only in the stagnant limit ($Re \rightarrow 0$, $Nu_{B=0} \rightarrow 2$). Moreover, available constant property solutions to the conservation equations indicate that (1) the $\ln(1+B)$ driving force overestimates laminar flow mass transfer rates at high Reynolds number and large B, (2) except as an empirical approximation, it is unlikely that the transfer coefficients can be written in the separable form fct(B)·fct(Re, Pr) at all Reynolds numbers, and (3)

* The Grashof number must be considered in the presence of appreciable bouyancy.

† Sometimes referred to as the "transfer number."[661] The second part of Eq. 2.4.1–4 follows from a mass balance at the liquid/vapor interface by invoking the conditions of (1) no vapor phase chemical reaction, (2) Fick's law of diffusion, and (3) ambient ("foreign") gas impenetrability into the droplet.

‡ In the absence of gas phase chemical reaction, the differential equations governing heat and mass transport are similar, leading to the expectation that Nu_H (Re, Pr, B) and Nu_D (Re, Sc, B) will have similar functional forms. For gas mixtures relevant to combustion the diffusivity ratio $\bar{\mathfrak{D}}/[\bar{\mathfrak{K}}/(\rho\, c_p)]$ (or Lewis number, $Le \equiv Pr/Sc$) is frequently near unity, in which case $Nu_H \approx Nu_D$.

* This is defined by $p_{v,eq}(T_{bp}) = p$, where p is the prevailing total pressure.

† This semi-theoretical form has been suggested by Frössling,[280] Ranz and Marshall,[577] and, most recently, Lee and Ryley.[435] Recommended values for the constant C are 0.276, 0.30 and 0.37, respectively.

‡ The (implicit) law $Nu/Nu_{B=0} = [\ln(1+B)/B]$ is equivalent to the (explicit) law[99] (utilized by Priem,[562] El Wakil et al.[248,249]) $Nu/Nu_{B=0} = B'/[\exp(B') - 1]$, where $B' \equiv \dot{m}'' d_L/(\bar{\mathfrak{D}}\rho\ Nu_{B=0})$

even in the absence of mass transfer Eq. (2.4.1–8) overestimates the incipient effects of small forced convection when ($Re<1$).*

Despite these "theoretical" objections, experimental correlations of the above-mentioned separable form have proven reasonably successful and, although there is a need for simple design formulae, few practical alternatives have been suggested. The meaning of "reasonably successful" can be judged from the recent experimental work of Eisenklam et al.,[240] who photographed 25–2000μ droplets of six distinct liquids falling freely through unheated air. Figure 2.4.1a shows heat transfer coefficients† inferred from observed evaporation coefficients κ_{vap} [where $\kappa_{vap} \equiv -d(d_L^2)/dt$] during the $T_L \approx T_{L,wb}$ portion of the free-fall. These authors state that the use of $[\ln(1+B)]/B$ in the ordinate was somewhat less successful than $(1+B)^{-1}$, again suggesting that the driving force $\ln(1+B)$ somewhat underestimates the "blowing effect" (thereby overestimating mass transfer rates) when laminar forced convection is significant.‡

Corresponding drag coefficient data, correlated in the same way, are shown in Fig. 2.4.1b. Here the "standard sphere drag" curve is $C_D(Re)$ for solid inert spheres ($B=0$). With regard to the drag on bluff objects it should be commented that the reduction factor $[\ln(1+B)]/B$ has no theoretical basis, even in the Stokes flow limit: $Re \ll 1$. A self-consistent formalism for calculating the correction to the Stokes drag law for a vaporizing spherical droplet with no internal circulation has recently been outlined by Fendell et al.[266] who have calculated the reduction in $C_D \cdot Re$ for several illustrative cases. Unfortunately, however, simple closed-form corrections do

* Improved semi-empirical forms of Eq. 2.4.1–8 can be developed for small Peclet numbers ($Pe = Re \cdot Pr$) and $B = 0$ based on the fact that the proper small Pe behavior has been shown[47] to be $Nu = 2[1+(1/4)(Pe)+\cdots]$, with the next term being of order $Pe^2 \ln Pe$.

† In the presence of appreciable property variations (due to any cause) a "correlation" is of no use if an author has not carefully stated the conditions under which property values are to be (or have been) inserted. In Fig. 2.4.1a, based on the work of Eisenklam et al.[240] all property values are those of the surrounding medium (air) evaluated at the temperature $\frac{1}{2}(T_{L,wb}+T_\infty)$.

‡ However, a driving force like $B/(1+B)$ would appear to be unreasonable on theoretical grounds when $B \to \infty$ since there is no evidence that transfer rates would become *independent* of B at sufficiently large B. The maximum value of B_{vap} in the experiments of Eisenklam et al.[240] was 3.

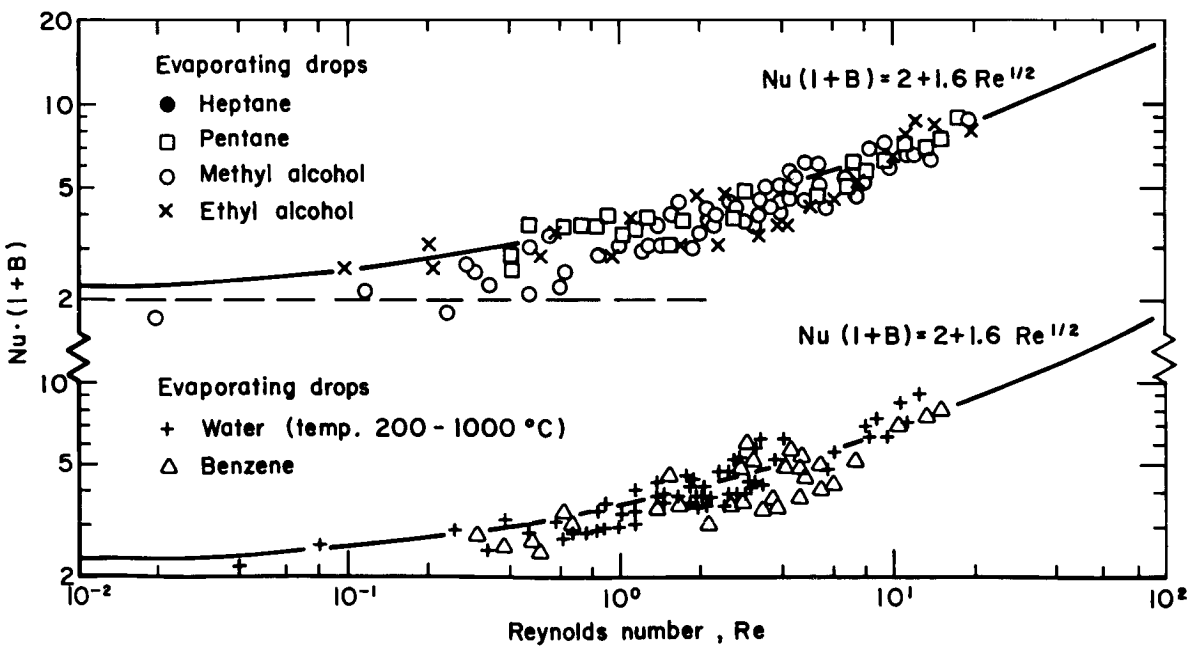

FIGURE 2.4.1a.—Correlation of heat transfer data for a vaporizing droplet (after Eisenklam et al.[240]).

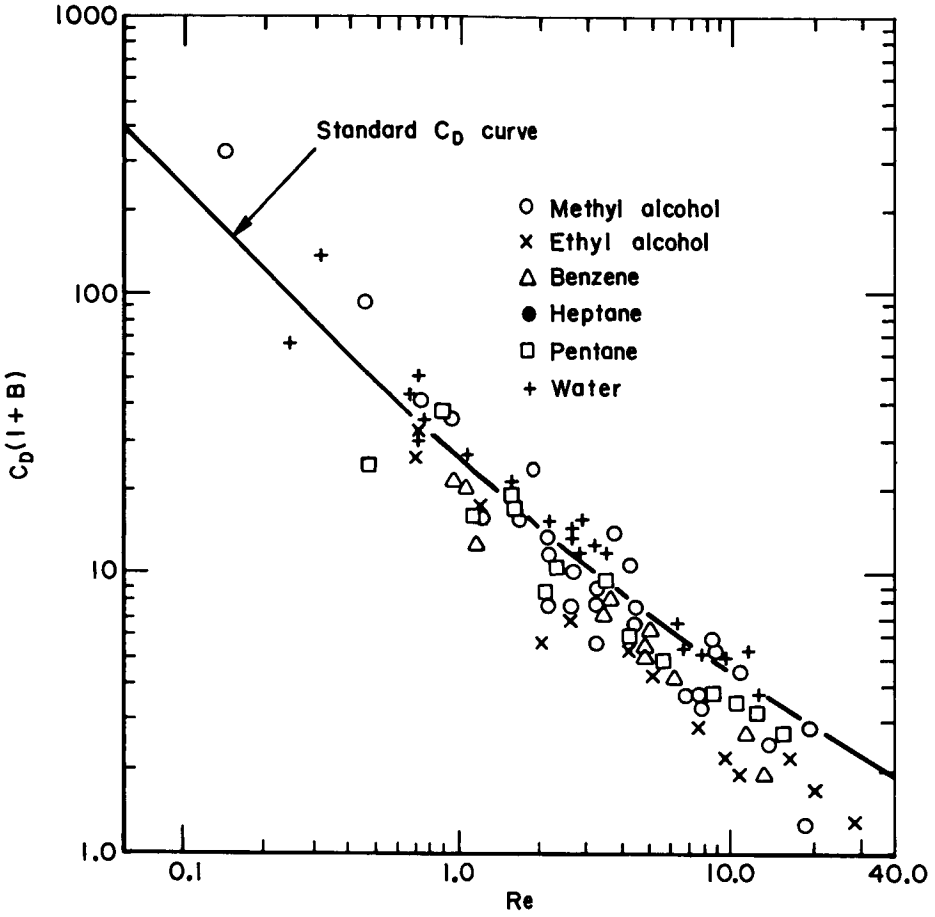

FIGURE 2.4.1b.—Correlation of drag data for a vaporizing droplet (after Eisenklam et al.[240]).

not emerge, hence additional computations will be required to establish trends.

Before considering extreme conditions which tax the validity of Eqs. (2.4.1-1, 2, 3), it is instructive to briefly examine the simplest possible case, viz, the evaporation constant for a small droplet preheated to near the wet bulb temperature, suddenly placed in a high temperature stagnant gas. Then, for $Le \approx 1$, the previous "quasi-steady" equations yield[661]

$$\kappa_{vap} = \frac{d_{L,0}^2}{t_{vap}}$$

$$= \frac{8}{\rho_L}\left(\frac{\bar{\mathfrak{K}}}{\bar{c}_p}\right) \ln\left[1 + \frac{\bar{c}_p(T_\infty - T_{bp})}{h_v}\right] \quad (2.4.1\text{-}9)$$

This equation quantitatively expresses the often verified behavior that the time, t_{vap}, required to completely vaporize a droplet in a particular high temperature environment: (1) increases as the square of the initial droplet diameter, (2) diminishes for fuels of high volatility (low T_{bp}, low latent heat), and (3) depends only weakly on the prevailing pressure level.*

It is now appropriate to consider several circumstances in which the previous equations fail to apply—circumstances which, it turns out, are often intimately connected with unstable rocket motor combustion. Thus, essential modifications are to be expected when either (1) parameters or boundary conditions (p, $Y_{v,\infty}$, T_∞, V_∞, . . .)

* In Eq. (2.4.1-9) only T_{bp} and h_v noticeably depend on pressure level. However, these effects are slight (at pressures well below the critical pressure of the fuel), act in opposing directions, and appear within the logarithmic term.

undergo appreciable percentage changes in times not large compared with $r_L^2/\overline{\mathfrak{D}}$, (2) the droplet temperature is driven up to near the thermodynamic critical temperature† of the liquid, or (3) exothermic chemical reaction (either vapor decomposition, or fuel vapor/oxidizer vapor combustion) occurs sufficiently close to the droplet surface to augment the heat transfer rate and, hence, vaporization rate (see Fig. 2.4.1a). Items (1) and (2) both violate the fundamental quasi-steady assumption underlying Eqs. 2.4.1–1, –2, and –3 according to which a truly transient, moving boundary problem (e.g., a shrinking droplet) has been approximated by an "equivalent" steady problem with radial mass transport.[740] Item (2) is intimately related to this approximation since the radial interface velocity cannot be neglected (compared to the radial *gas* velocity at $r = r_L$) when the liquid density is not much greater than the prevailing gas mixture density.[742,434] On the face of it this conclusion would appear to cast doubt on calculations of the type reported by Wieber,[738] who used equations essentially equivalent to (2.4.1–1, 2, 3) to show that at supercritical pressures* heptane and oxygen droplets can attain their critical temperatures following injection into 2780° K gas. However, it is interesting to note that during transient heat-up an evaporating droplet can actually *expand* due to decreasing liquid density (see Eq. 2.4.1–2)‡ as, in fact, Wieber's calculations reveal. In such cases the absolute interface velocity need not be large as $\rho_L \rightarrow \rho_w$, hence the accuracy of the QS approximation may not degenerate badly.§

† At the critical temperature of a substance, parent "liquid" and the "vapor" with which it is in equilibrium are equally dense—hence the two phases become indistinguishable. As a consequence, both the latent heat of vaporization and surface tension vanish as $T_L \rightarrow T_{cr}$. The equilibrium "vapor" pressure at T_{cr} is called the critical pressure, p_{cr} (see Sect. 2.4.2).

* The critical pressure itself can be exceeded without significant departures from the QS/finite latent heat droplet model. What is relevant is the *supercritical* pressure level at which no subcritical *wet bulb* temperature (satisfying Eq. 2.4.1–5) exists.[601]

‡ Only when $\rho_L = \text{const.}$ does Eq. (2.4.1–2) specialize to the frequently used form $-\rho_L(dr_L/dt) = \dot{m}''$.

§ A more quantitative statement must await additional calculations and/or measurements.

Since some droplets can apparently reach their critical points prior to significant fractional vaporization loss or velocity equilibration, it is likely that droplet distortion, shattering and, ultimately, simple vapor/gas diffusion will then govern the rate of mixing. This class of "near-critical" phenomena may bear directly upon high pressure rocket motor combustion instability, in view of the greatly increased pressure dependence of the "droplet" vaporization rates in this region. Analogous remarks apply to droplet *combustion* at supercritical pressures (see Sect. 2.4.2).

The problem of enhanced droplet vaporization rates in the presence of localized exothermic chemical reaction (within the droplet boundary layer; see Fig. 2.4a) is taken up in Sect. 2.4.2, however it is appropriate to raise here two related questions: (a) Under what set of environmental conditions is ignition ultimately possible (for a particular droplet)? (b) How long will it take before ignition occurs? The latter question is closely related to the transient heat-up/vaporization calculations already outlined. Indeed Williams[742] has shown that the so-called droplet "ignition-delay" is usually of the same order of magnitude as the time to attain the wet-bulb temperature. However, t_{ign} for a particular fuel may display (1) a dependence on oxidizer mass fraction $Y_{OX,\infty}$ in the surroundings, (2) a sensitivity to ignition-promoting additives and (3) can be appreciably *shorter* than the time to achieve $T_L \approx T_{L,wb}$. Accordingly, one alternative approach for estimating a lower limit to t_{ign} is to estimate the time required to first form a locally combustible mixture (T, Y_F, Y_{OX} combination)* within the droplet boundary layer. Priem et al.,[562] and El Wakil and Abdou,[247] who have made such calculations, term this the *physical ignition delay.* To obtain the *total* ignition delay one must generally add on a *chemical ignition delay,* i.e., the time required from the beginning of perceptible homogeneous reaction to the establishment of the envelope diffusion flame. Unfortunately, reliable estimates of the chemical ignition delay cannot be

* For this purpose it is often helpful to note that for $Le \approx 1$ the following simple interrelation between Y_{OX}, Y_F, T exists within the boundary layer:

$$\frac{T - T_\infty}{T_W - T_\infty} = \frac{Y_{OX,\infty} - Y_{OX}}{Y_{OX,\infty} - Y_{OX,W}} = \frac{Y_F - Y_{F,\infty}}{Y_{F,W} - Y_{F,\infty}}$$

made based on presently available data and theory.

2.4.2 Bipropellant Droplet Combustion

An important consequence of spray size distributions and unequal droplet evaporation rates for combustion chambers is that a fuel droplet can find itself in an oxidizer-rich vapor (or vice versa). This introduces the possibility of localized exothermic *vapor phase* chemical reaction, with attendant increases in the heat feedback and hence vaporization rates of individual droplets (see Fig. 2.4a–b). To answer the question of whether such processes play an important role in determining bipropellant spray combustion efficiency, space requirements, and stability, it is necessary to first consider the laws governing such "heterogeneous combustion," the possible vaporization rate augmentations due to gas phase combustion in the droplet boundary layer or wake, and the dependence of these vaporization rate augmentation phenomena on liquid/vapor properties and environmental conditions.

In addition to obvious modifications of the suspended drop and falling drop techniques already mentioned, a fruitful experimental method for elucidating steady "burning" rates of individual droplets (with and without convective flow) and reaction zone structure has been the "simulated-captive droplet" technique, in which a wetted porous sphere plays the role of the droplet* (see Fig. 2.4.2a).[57,753] Such experiments are carried out by feeding liquid reactant into the sphere at the rate determined (upon ignition) by the physical and chemical parameters of a system under study—the major assumption being that simulation of *internal* droplet phenomena (circulation heat conduction/radiative heat absorption/emission) is not essential to model steady state droplet combustion. While practical considerations have limited this technique to sphere diameters above about 2000μ, much of the experimental data on isolated "droplets" (discussed below) has been obtained with its aid.

Controlled droplet combustion experimentation has led to the establishment of the following important facts and patterns.† (1) Combustion in the immediate vicinity of a droplet can be of two general types, depending primarily on the relative velocity V_∞ between gas and droplet. At low V_∞ one observes distorted "envelope" flames characterized by a contiguous vapor phase diffusion flame zone wrapped around (but not contacting) the droplet. In this envelope flame, vapors emanating from the fuel droplet react with oxygen diffusing inward from the environment providing a localized source of heat and reaction products. At larger V_∞ the quasi-steady state configuration becomes that of a "flame-holding" droplet supplying fuel vapor into its wake, where combustion then occurs due to mixing with ambient gas. Ultimately, at sufficiently large V_∞, "blow off" (complete extinction) occurs. (2) In the envelope flame regime, for nearly stagnant conditions, d_L^2 again decreases linearly with time,* however, the *apparent* evaporation coefficient (i.e., the combustion constant κ_{comb}) exceeds κ_{vap} (for the same environmental conditions) by a factor depending primarily on the heats of combustion and vaporization, ambient temperature level and ambient oxidizer mass fraction. (3) Droplet burning rates are remarkably insensitive to the fuel chemistry (structure) and pressure level,‡ suggesting rate control due to physical processes (diffusion/heat transport) rather than chemical kinetic factors. (4) The drag on a burning droplet (with either envelope or wake flame) is significantly less than that on a solid sphere of the same size in the same environment, and (5) quasi-steady state droplet combustion is not possible for all combinations of ambient oxidizer mass fraction, temperature, pressure level and droplet size (e.g., in a gas mixture of particular composition and temperature, combustion cannot be achieved if the pressure levels and/or droplet diameters are too small).

---

* Some of the earliest heterogeneous combustion data were obtained using a simple variant of the simulated drop technique, viz. fuel-wetted, fabric-covered solid (nonporous) spheres.[659]

† References include 57, 58, 240, 290, 292, 293, 303, 363, 518, 658, 680, 753 and 756. For a recent review and bibliography see Ref. 741.

* Again this implies that the instantaneous mass vaporization rate, $\dot{m}$, varies nearly linearly with droplet diameter.

‡ This is for $p \ll p_{cr}$ (see Ref. 124); phenomena peculiar to $p > p_{cr}$ will be dealt with later on in the present section.

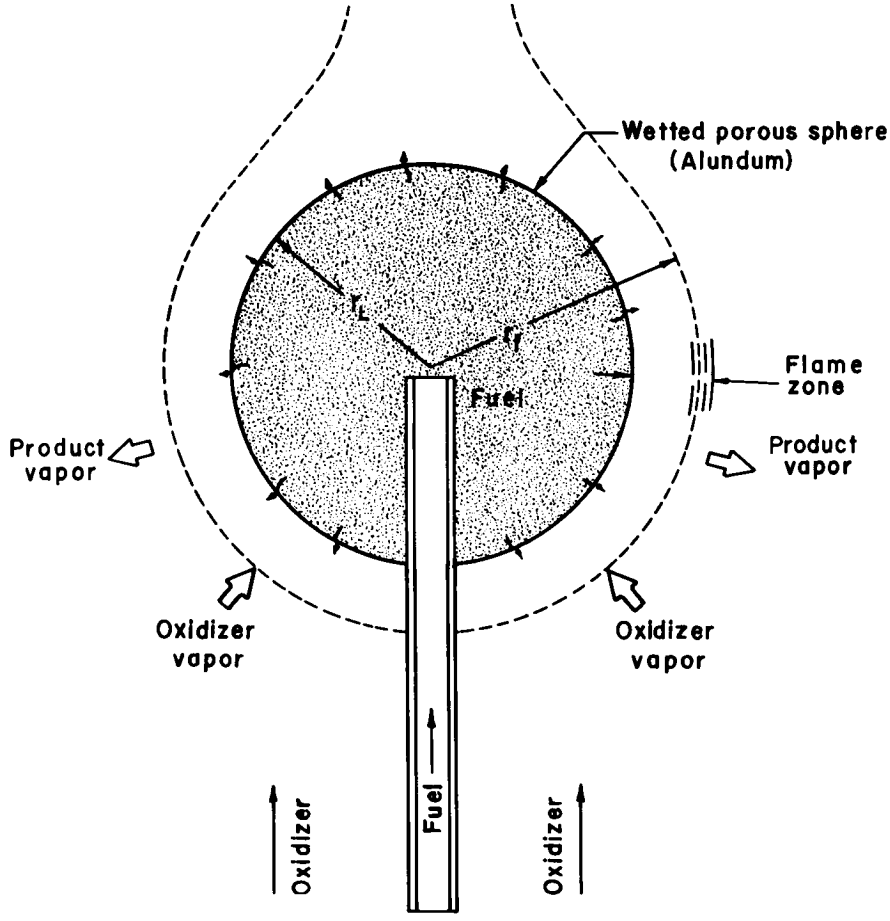

FIGURE 2.4.2a.—Fuel-fed porous sphere technique for simulating droplet combustion (after Wise, Lorell, and Wood[763]).

2.4.2.1 *Envelope flame model for subcritical pressures—theory and experiment.*—As a starting point in the iterative process of building a theory compatible with the above-mentioned facts, consideration was focused on the simplest case of a spherically symmetric system—i.e., a fuel droplet suspended in an unbounded oxidizer containing gas mixture with no free or forced convective distortion of the composition and temperature profiles in the vicinity of the droplet. Upon ignition, the droplet supplies fuel vapor which meets and reacts with oxidizer vapors in a narrow gas phase diffusion flame zone concentric with (enveloping) the droplet surface (Godsave,[290] Spalding[658] et al.). In this quasi-steady model (see Fig. 2.4.2b)* flame zone radial position and the fuel vaporization rate adjust themselves to be compatible with the requirement that the conductive heat feedback from the vapor phase diffusion flame be adequate to supply the latent heat of vaporization at the droplet surface. Without making any restrictive assumptions concerning the vapor phase flame zone structure, when Le = 1 and constant mean thermodynamic transport properties are assumed, it can be shown from the governing conservation equations that a linear combination of temperature and oxidizer mass fraction satisfies a boundary value problem identical to that governing the corresponding

* In this figure, and in the following discussion, the droplet is considered to be fuel, and the surroundings contain oxidizer. However, the treatment clearly applies equally well to the converse case.

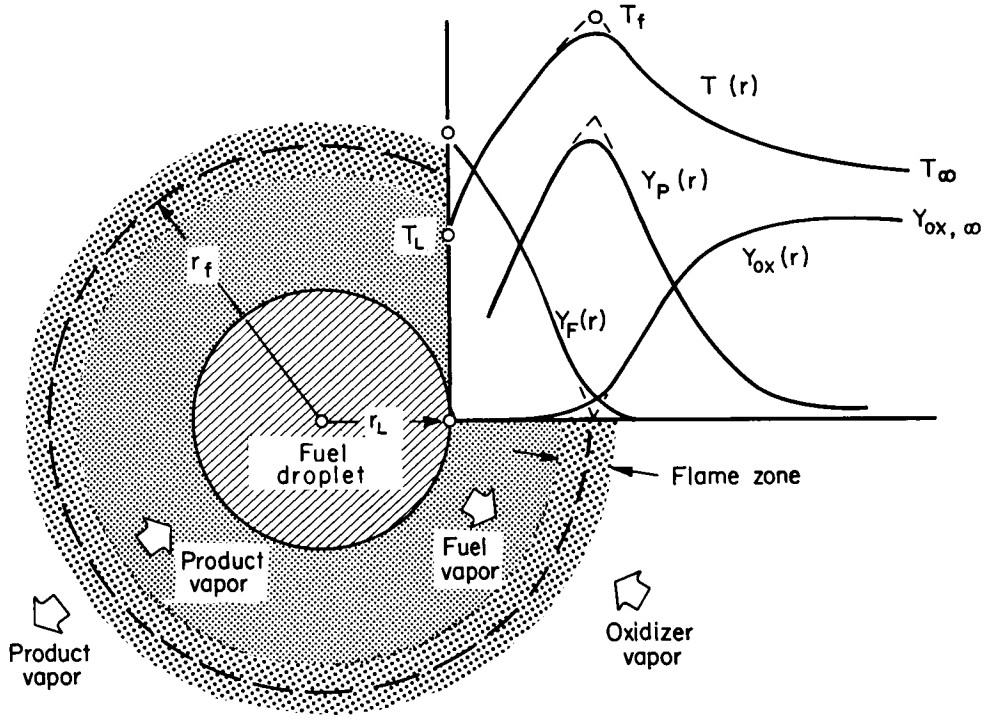

FIGURE 2.4.2b.—Diffusion flame model of subcritical pressure bipropellant droplet combustion in the absence of convective distortion.

pure droplet vaporization problem. In this way, one can immediately write the quasi-steady mass burning rate in the general form.[740]

$$\dot{m}=4\pi r_L\left(\frac{\bar{\mathfrak{K}}}{\bar{c}_p}\right)\ln\left[1+\frac{\bar{c}_p(T_\infty-T_w)+(Y_{ox,\infty}-Y_{ox,w})h_c}{h_v+Y_{ox,w}h_c}\right] \tag{2.4.2–1}$$

Here h_c is the heat released (*per unit mass of oxidizer consumed*) in the *vapor phase* reaction between fuel and oxidizer. While (as indicated above) Eq. (2.4.2–1) applies regardless of the distribution of chemical heat release within the droplet boundary layer, in the absence of additional information its quantitative use is limited to the case when the homogeneous chemical reaction rates are adequate to prevent oxidizer from "fighting its way" to the surface, i.e., when $Y_{ox,w}=0$. Then Eq. (2.4.2–1) becomes identical to the expression for steady-state droplet vaporization (in the absence of chemical reaction) provided one replaces $B_{vap}=\bar{c}_p\cdot(T_\infty-T_w)/h_v$ with†

$$B_{comb}=\frac{\bar{c}_p(T_\infty-T_w)}{h_v}+\frac{Y_{ox,\infty}h_c}{h_v} \tag{2.4.2–2}$$

Fortunately, when combustion occurs the assumption $T_w\approx T_{bp}(p)$ can be justified even in unheated surroundings,[742] hence all quantities in Eqs. (2.4.2–1, –2) are estimable. As an important immediate consequence, Eqs. (2.4.1–9) and (2.4.2–2) show that in a stagnant environment the enhancement in apparent vaporization constant $[-d(d_L^2)/dt]$ due to combustion (see Fig. 2.4a) is approximately:

$$\frac{\kappa_{comb}}{\kappa_{vap}}\approx\frac{\ln(1+B_{comb})}{\ln(1+B_{vap})} \tag{2.4.2–3}$$

which indeed exhibits the experimentally observed

† An interesting (but rarely stated) interpretation of this Le = 1 result is that the evaporation rate of an *ignited* droplet in oxidizer-containing gas at temperature T_∞ is the same as the evaporation rate of a *noncombusting* droplet (of the same size) in combustion products of final temperature $T_\infty+(Y_{ox\infty}h_c/\bar{c}_p)$.

trends with T_∞, $Y_{OX,\infty}$, h_c and h_v. This simple treatment also rationalizes the observed insensitivity of burning rates to chemical factors and pressure level, since $\ln(1+B_{comb})$ does not show order-of-magnitude changes for a wide class of organic fuels in oxygen-containing gases, moreover $\ln(1+B_{comb})$ exhibits only a weak dependence on pressure level (for reasons identical to those already discussed for B_{vap})*.

Before discussing chemical kinetic phenomena, ignition and extinction, it is appropriate to stress here that even in the absence of effects peculiar to particular experimental conditions (e.g., natural convection around large droplets at high pressures) the previous expressions often provide only a guide to orders-of-magnitude and trends. This is due principally to the extreme property variations,[399] and departures from unit Lewis number which can occur in real cases† (e.g., oxygen droplets burning in a hydrogen environment).[399,361] For this reason several methods of accounting for property variations have been suggested; however, useful results usually require simplifying the kinetic model to the extent that all chemical reaction is considered confined to a flame sheet of negligible radial thickness. In this extreme, sometimes called the Burke-Schumann[128] limit,‡ oxidizer and fuel vapor do not co-exist (intermix)—instead, both concentrations vanish at the flame sheet, with their gradients standing in the stoichiometric ratio to one another (see dashed contours, Fig. 2.4.2b). As will be noted below, this thin-flame limit is not merely an irrational computational approximation—it represents a self-consistent asymptotic limit* [for the cases of very large (a) bimolecular forward rate constant), (b) pressure level and/or, (c) droplet size] from which the maximum possible (diffusion limited) droplet burning rate, $\dot{m}_{max}$, can be predicted.

To embrace the fact that droplet combustion simply does not occur for all combinations of droplet size and environmental conditions (p, $Y_{OX,\infty}$, T_∞) it is necessary to explicitly introduce chemical kinetic limitations into the envelope flame model. Despite the resulting complexity, only by these means does it appear to be possible to decide whether (a) the lower limit $\dot{m}_{vap}$ (no chemical reaction) or the upper limit $\dot{m}_{max}$ (flame sheet envelope) is more appropriate in a particular set of circumstances, or (b) neither limit yields a sufficiently accurate prediction. Even if a detailed knowledge of the (multi-step, branching chain) chemical kinetics of fuel vapor/oxidizer vapor systems of practical interest were available, specific numerical predictions would be costly and tedious, hence a great deal of semi-quantitative and qualitative information has recently been gleaned from simplified† but general theoretical treatments[263,398,452,682] of evaporation as enhanced by single step irreversible vapor phase reactions of the form: $aOX+bF \xrightarrow{k}$ products. In these treatments the reaction rate (per unit volume) is assumed to be of the mass-action form: rate $\propto k(T)\cdot[OX]^\alpha[F]^\beta$, which defines the *forward rate constant* $k(T)$ (usually taken to have an Arrhenius temperature dependence, i.e., $\mathfrak{B}\exp(-E_{act}/\mathfrak{R}T)$) and the *individual reaction orders* α, β. If $T_{f,ad}$, is the adiabatic flame temperature for the ambient gas/fuel combination, and n is the *overall order* ($n=\alpha+\beta$) then inspection of the governing conservation equations indicates that the normalized magnitude of the combustion-enhanced vaporization rate should be of the general form:

* Early measurements on large captive droplets[292,303] and porous spheres[57] in nearly quiescent oxidizing environments revealed more sensitive pressure dependencies than expected from $h_v(p)$ and $T_{bp}(p)$. However, these departures from the simple theory were shown to be compatible with induced (natural convection) flows which distort the quasi-steady flame shape and augment heat/mass transfer rates.

† However, Eq. (2.4.2–1), together with a reasonable choice of mean properties, *has* provided remarkably successful absolute predictions of κ_{comb} for hydrocarbon/air systems; see, e.g., Refs. 293, 292. Recent computer solutions of the transient variable property burning equations (in the thin-flame limit) suggest that this agreement only occurs after an initial transient which is not short compared to the total droplet lifetime [see Kotaki, S. and Okazaki, T., Int. J. Heat Mass Transfer, Vol. 12, pp. 395–609, 1969, and Nuruzzaman, A. S. M., and Beer, J. M., Comb. Sci. Tech., pp. 17–24, 1971].

‡ After the investigators who first applied "flame-sheet" concepts (in 1928) to treat steady-state diffusion flame shapes in ducts.

* See Refs. 261, 263, 279, 398, 452 and 682.

† Full advantage is usually taken of the $Le=1$ (or "Schvab-Zeldovich") approximation which enables first integrals (algebraic interrelations between $Y_F(r)$, $Y_{OX}(r)$, $Y_p(r)$, $T(r)$) to be used to reduce the overall coupled problem to the integration of one highly nonlinear ordinary differential equation.

$$\frac{\dot{m}-\dot{m}_{vap}}{\dot{m}_{max}-\dot{m}_{vap}} = \text{fct}\ (D_I) \qquad (2.4.2\text{–}4)$$

where D_I represents the appropriate* *Damköhler number* (ratio of characteristic diffusion time to chemical reaction time), given by

$$D_I \equiv \frac{k(T_{f,ad})}{4\mathfrak{D}_\infty \rho_\infty}\left(\frac{aM_{OX}+bM_F}{M_{OX}{}^\alpha M_F{}^\beta}\right)\rho_\infty{}^n d_L{}^2 \qquad (2.4.2\text{–}5)$$

and fct (D_I) has the limits fct $(0)=0$, fct $(\infty)=1$. The behavior of $\dot{m}$ for large but finite D_I has been investigated by the method of matched asymptotic expansions, which (in the present application) offers a systematic technique for obtaining corrections to $\dot{m}_{max}$ to account for incipient flame zone broadening.* Coupled with a regular parameter perturbation for $D_I \ll 1$† and numerical methods for intermediate D_I, it is possible to obtain the behavior of fct (D_I) in Eq. (2.4.2–4). To bring out the implications of these theoretical studies for practical systems the resulting behavior is shown on log scale in Figs. 2.4.2c, d in the form of the enhancement ratio $\dot{m}/\dot{m}_{vap}$ vs‡ $p^{n/2}d_L$, implying that such parameters as ambient oxidizer concentration, temperature level, fuel identity, etc., are held constant.

Two qualitatively different types of behavior are obtained,[263] depending primarily on the ratio $E_{act}/\mathfrak{R}T_{f,act}$. When this ratio is sufficiently small (as for vapor phase reactions of very low activation energy) then $\dot{m}/\dot{m}_{vap}$ vs. $p^{n/2}d_L$ is single-valued (monotonic), i.e., one and only one quasi-steady burning rate between $\dot{m}_{vap}$ and $\dot{m}_{max}$ exists at each value of $p^{n/2}d_L$. However, in the more frequently encountered case (large activation energy) $\dot{m}/\dot{m}_{vap}$ vs. $p^{n/2}d_L$ reveals a domain of multiple-valued (non-unique or non-monotonic) behavior,[263] within which (in particular) *both* high $\dot{m}$ (near equilibrium) and low $\dot{m}$ (near inert) solutions* exist for a particular $p^{n/2}d_L$. This situation is quite reminiscent of earlier work on the combustion of carbon (a true *heterogeneous* reaction) wherein it was shown that "ignition" and "extinction" correspond to the system suddenly jumping from the lower branch to the upper branch and vice versa. To fix ideas, consider the near equilibrium combustion of a large (captive) droplet at high pressure. As the pressure level is continually reduced only slight departures† from $\dot{m}_{max}$ will be observed. However, these departures will increase until point AE is attained (Fig. 2.4.2d). At only slightly lower pressure levels "low pressure extinction" (*a*uto-*e*xtinction) will occur, i.e., the only "available" quasi-steady state will be that corresponding to only slight (usually negligible) combustion enhancement.‡ Similar comments apply for extinction due to the droplet size becoming insufficient (at constant pressure level). Analogy with previous ignition studies would also suggest that droplets originally vaporizing in accord with the "near-inert" branch will "spontaneously ignite" (*a*uto-*i*gnite) when the pressure level brings $p^{n/2}d_L$ above $(p^{n/2}d_L)_{AI}$. In this way, the domains of possible droplet combustion receive their explanation in terms of the relevant gas phase kinetics, within the confines of a quasi-steady spherically symmetric theory. Even for this simplified kinetic scheme, however, extensive computations and parametric studies would be required to map out similar curves for various ambient temperatures and oxidizer levels.

* The appropriate Damköhler numbers for the near frozen (virtually no reaction) expansion is similar to Eq. 2.4.2–4 but based on k evaluated at $T_{L,wb}$ or T_∞, whichever is higher. For droplets in a *convective* environment the characteristic diffusion time will be shortened, hence, if all other things were equal, D_I would be reduced appreciably due to relative motion between droplet and gas. In practice convection produces flame distortion and ultimately, flame "blowoff" (see Fig. 2.4.2e and accompanying discussion).

† Slight reversibility (large but finite equilibrium constant), also produces flame zone broadening, and the effects can be treated by similar mathematical techniques.[144,263]

‡ This abscissa is proportional to $D_I{}^{1/2}$ for a particular system (in view of the pressure dependence of the diffusion coefficient). When the overall order is 2, the abscissa becomes simply the pressure-diameter product.

* In all cases of this type examined theoretically to date, the intermediate (3rd eligible steady state) is statically unstable and hence should be physically unrealizable.

† The effects of incipient flame zone broadening on the burning rate have been shown[398] to be intimately connected with the reaction order, α, and are extremely small when $\alpha \leq 1$.

‡ Tarifa[680] has presented data on the dependence of κ_{comb} on pd_L for gasoline, and $p^{0.55}d_L$ for kerosene. Also included are data on the pressure dependence of the minimum droplet diameter allowing combustion (for kerosene, gasoline, n-heptane and ethyl alcohol).

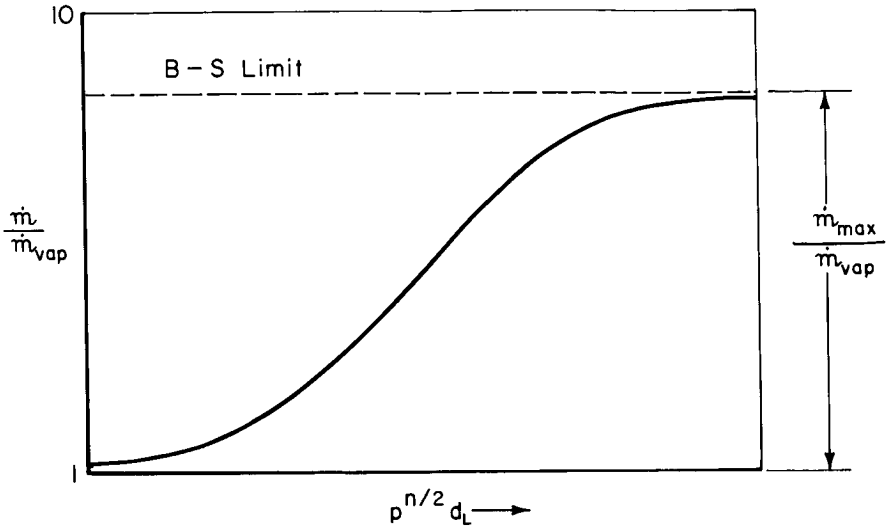

FIGURE 2.4.2c.—Homogeneous chemical kinetic effects on quasi-steady droplet combustion rates; single-valued case (low activation energy).

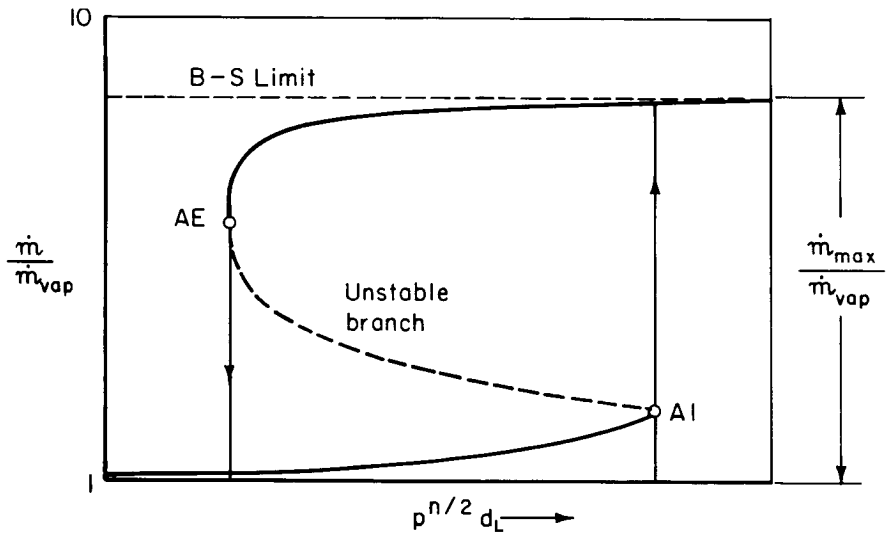

FIGURE 2.4.2d.—Homogeneous chemical kinetic effects on quasi-steady droplet combustion rates; multiple-valued case[263] exhibiting auto-ignition and auto-extinction (high activation energy).

This, together with the realization that only trends are usually sought, has motivated the development and exploitation of less rigorous, but more computationally convenient approximate methods. In one of these, due to Peskin and Wise,[546] the nonlinearity of the Arrhenius temperature dependence is retained but the chemical reactions are artificially confined to a zone of negligible radial thickness (a "modified flame surface"). The quasi-steady, constant property, coupled *linear** differential equations governing flame location, temperature and composition

* In this model the nonlinearity is artificially removed from the differential equations and placed in the boundary conditions on each zone.

profiles, and burning rate, $\dot{m}$, are then solved, leading to implicit but closed-form transcendental relations between $\dot{m}$, D_I and the parameters of the problem. Peskin et al.[545] have used these results to illustrate the existence of auto-ignition and auto-extinction ambient temperatures and their dependence on ambient oxidizer mass fraction† at constant pd_L, however at this time the available body of such information is limited, as are relevant experimental data.‡

Droplet ignition, quasi-steady burning rates, and extinction in practical combustors are strongly influenced by forced convection (due to instantaneous droplet-gas velocity lags) and turbulence (intensity/scale), neither of which can be included in simple spherico-symmetric theoretical models. While progress in these difficult areas (together with the ancillary question of the drag on burning droplets) has been largely as a result of direct experimentation, several recent theoretical analyses have shed light on qualitative aspects of these effects.

As a practical expedient, there is still no alternative but to assume that forced convection* augments the quasi-steady burning rate $\dot{m}_{max}$ and vaporization rate, $\dot{m}_{vap}$, by the same factor (see Eq. 2.4.2–8)† provided the extinction criterion (see below) is not contravened.‡ This appears to be rigorously true at very low values of Re·Pr, (at which the semi-empirical Frössling form of $Nu_{B=0}(Re)$ breaks down) since Fendell et al.[267] have shown that, for constant property creeping flow around a small vaporizing/burning sphere:

$$\dot{m}_{max} \approx (\dot{m}_{max})_{Re=0} \cdot [1 + \tfrac{1}{4}(Re \cdot Sc) + \cdots] \tag{2.4.2–6}$$

which is precisely the result that would be anticipated for nonreactive mass transfer from a sphere in the absence of appreciable interfacial velocities.[47] At higher Reynolds numbers theoretical analyses become intractable, but then available experimental data[57] supports the empirical use of a Frössling-type correlation,* as in the non-burning case.

Experimental data on the drag on burning droplets, either in the regime of envelope flames or wake flames, reveal drag *reductions* when compared with the drag expected from solid spheres in the same fluid dynamic environments. In addition to the data reviewed by Wise and Agoston,[752] Eisenklam et al.[240] have recently reported drag coefficients for droplets of methyl alcohol, ethyl alcohol, benzene, heptane and pentane freely falling in heated air. For a particular choice of mean properties used,† and in the envelope flame regime, these authors report a correlation of the same form as for non-burning droplets (see Fig. 2.4.1b), viz:

† Interestingly enough, it is found that as the ambient oxygen concentration is reduced (1) ignition and extinction temperatures approach one another, and (2) differences between $\dot{m}$ on the near equilibrium and near frozen branches diminish. Eventually the double-valued region disappears, hence below this value of $Y_{ox,\infty}$ ignition/extinction (as defined here) should not occur (see Fig. 2.4.2c).

‡ Despite the fact that the combustion of large droplets at near atmospheric pressure is nearly diffusion-limited, Wood et al.[757] have shown that flame inhibitors (e.g., CF_3Br) added to air can cause the extinction of ethanol combustion. Typically, extinction occurs without much "warning," i.e., the value of $\dot{m}$ at incipient extinction is not significantly lower than $\dot{m}$ in the absence of inhibitor. Bipropellant droplet theory, as outlined in the present section, shows that for sufficiently large $p^{n/2}d_L$ it is hopeless to search for "burning rate catalysts." It is interesting to contrast this situation to that of monopropellant burning (Sect. 2.4.3).

* Though a great deal of work has been done on *natural convection*-induced distortion of flame shapes and augmentation of burning rates (owing to its importance in many laboratory studies on droplet burning in quiescent environments), we focus attention here on *forced convection* phenomena, since they are likely to be of greater relevance to actual combustor environments.

† Departures from this form of correlation in the work of Eisenklam et al.[240] may only be apparent, i.e., a consequence of their calculation procedure for Nu. A more general definition than their Eq. (1) would have been $Nu = (\frac{1}{4})(\bar{c}_p/\bar{\mathfrak{R}})(\rho_L/B)\kappa$. Recorrelation of their envelope flame data (for heptane, pentane, methyl alcohol and ethyl alcohol) on this basis is suggested.

‡ Once the flame no longer envelops the sphere, the heat transfer to the sphere abruptly drops, with the result that values of $\dot{m}$ in the wake flame region can be reduced to values only somewhat larger than $\dot{m}_{vap}$ (see Fig. 2.4.2e).[412,753]

* See previous footnote with regard to the data of Eisenklam et al.

† Consult Ref. 240 for details; e.g., the mean gas density was (somewhat arbitrarily) taken as $\frac{1}{4}[\rho_F(T_{bp}) + 2\rho_\infty(T_{f,ad}) + \rho_\infty(T_{bp})]$.

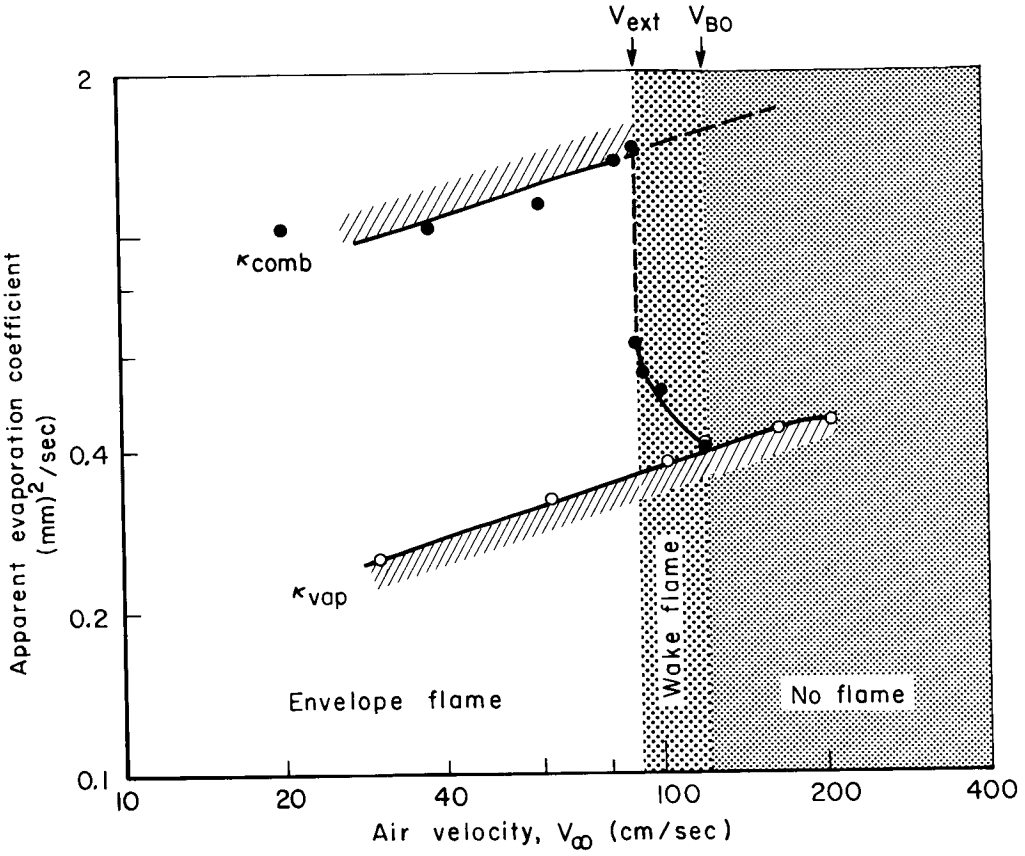

FIGURE 2.4.2c.—Apparent evaporation coefficients for cetane with envelope flame, wake flame, and following blow-off (after Kumagai[412]).

$$C_D(\mathrm{Re}, B) = \frac{1}{1+B} C_{D,B=0}(\mathrm{Re}) \qquad (2.4.2\text{–}7)$$

again suggesting a reduction factor (due to interfacial mass transfer) comparable to that for heat and mass transfer coefficients (see Fig. 2.4.2a). The role of variable properties must be considered with special care for reported drag coefficients. For example, when C_D and Re are based upon *upstream* gas properties, the data points fall very close to the "standard drag curve" (i.e., appear independent of B_{comb}). In this connection, it should be remarked that Fendell et al.[267] have reported the surprising result that a *constant property* flame sheet model in the creeping flow regime can yield drag coefficients in *excess* of the Stokes value. Whether this is an artifact of the constant property model, or a realistic consequence of peripherally nonuniform vapor injection at large Sc but low Reynolds numbers, remains to be seen.

The relative velocity V_{ext} at which flame extinction occurs on the upstream portion of a droplet has been experimentally studied using captive droplets. While available measurements cover only a narrow range of fuel/oxidizer combinations and environmental parameters, they generally support the semi-quantitative treatment of Zeldovich[767] and Spalding,[661] according to which there is a finite upper limit (set by homogeneous chemical kinetics) to the flux of fuel vapor that can be consumed by a diffusion flame zone.* From this point of view, the effect of increased relative velocity is to continuously increase the fuel flux "imposed" on the flame; this results in an increased flame zone thickness necessary to consume the fuel and depressed maximum temperatures—ultimately producing

* This upper limit being of the same order of magnitude as the fuel mass flux in a *premixed* stoichiometric flame at the same pressure level.

localized extinction. For a laminar flow stagnation point the theory predicts that V_{ext} should depend linearly on d_L (i.e., there should exist a *critical velocity gradient*),† a trend which has been observed in some,[482,659] but not all,[57,700] experiments. For specific fuel/oxidizer systems, only limited data are available for

$$(V_\infty/d_L)_{ext} = \text{fct}\ (T_\infty, Y_{OX,\infty}, p, \text{turbulence intensity/scale}) \tag{2.4.2-8}$$

however the theoretical approaches outlined earlier, when extended to include convection, should be capable of modeling this class of phenomena. Indeed Peskin and Yeh[547] have reported qualitative agreement between $(V/d_L)_{ext}$ as predicted for a modified flame surface/creeping flow theory and the observations of Ref. 482 on $(V/d_L)_{ext}$ for kerosene and ethyl alcohol in air.

Only limited data are available on droplet burning rates and extinction phenomena in flows containing periodic (e.g., sound field) or random (i.e., turbulent) disturbances. With regard to time averaged burning rates, significant enhancements have been reported for periodic disturbances‡ but no observable enhancements were reported in the turbulent case.[57] However, increased turbulence intensity significantly reduces V_{ext}, especially when the scale of the turbulence is comparable to the near-extinction flame "stand off" distance.[57]

2.4.2.2 *Envelope flame model for supercritical pressures—theory and experiment.*—Calculations relevant to rocket motors (and diesel engines) reveal that droplets injected into a chamber maintained at a pressure, p, sufficiently greater than the liquid's *critical pressure,** p_{cr}, can be heated to their critical temperature, T_{cr}, *before completely vaporizing.*[738] Since the latent heat of vaporization and surface tension vanish at T_{cr}, this means that the subsequent combustion of such a "droplet" (fuel pocket)† should be qualitatively, as well as quantitatively, different from that already described. That this will not be a rare situation can be seen from Table 2.4.2, which collects thermodynamic critical state data for several common fuels and oxidizers.

If the gas in the spherical pocket‡ does not react with its surroundings, then the time required for it to disappear by molecular interdiffusion can be estimated from available solutions to the transient diffusion equation in spherical coordinates. If combustion occurs at the "interface" between fuel vapor and oxidizer (containing) vapor then the time to consume the fuel will be shortened, but still limited by molecular diffusion processes (i.e., the rate fuel and oxidizer vapors can diffuse toward one another through the product gas generated at the reaction zone). Since the pressure levels of interest here are large, this suggests transient application of the envelope flame sheet concept. Such a treatment is particularly straightforward if one makes the rather extreme assumption of a *constant density* field, thereby ruling out radially symmetric *convective* transport. Spalding[662] presented simple closed-form results for the flame-history and burning time by regarding the fuel pocket as the result of an instantaneous (at $t=0$) *point source* (PS).* Rosner[601] presented closed-form results for finite-size ("distributed" at $t=0$) sources (DS), suggesting that this model should be more accurate when the stoichiometry favors short burning

† For large kerosene "droplets" in 293 K air, $(V_\infty/d_L)_{ext}$ is about 10^2 sec^{-1}. However, much larger values are required at higher ambient temperatures.

‡ It appears however, that the value of $(\kappa_{comb})_{avg}$ cannot exceed some limit, no matter how violent the oxidizing gas vibrations may be.[413] Phase lags between $\dot{m}(t)$, $\dot{m}_{comb}(t)$ and $p(t)$, $V_\infty(t)$ are currently under theoretical investigation, owing to their relevance to the combustion instability problem (see Sect. 3.4.2).

* There is a region of *super*critical pressures ($p > p_{cr}$) in which the wet bulb temperature will be *sub*critical ($T_{L,wb} < T_{cr}$). This region is narrowed considerably in the presence of an envelope flame.

† Again, these remarks apply equally well to an oxidizer pocket in a hot fuel vapor surroundings.

‡ Droplet breakup (prior to $T_L \rightarrow T_{cr}$) and fuel pocket distortion due to velocity lags ($V_\infty \neq 0$), which would considerably shorten the combustion time, are not considered here. Effects due to high turbulence intensity, and fuel vapor *pyrolysis* at high pressures and temperatures[434] have not yet been accurately assessed, and are likewise omitted here.

* Chervinsky[137b] has recently generalized Spalding's PS treatment by allowing for self-induced radial convection, subject only to the restriction $\rho T = \text{const} = \rho_\infty T_\infty$.

TABLE 2.4.2.—CRITICAL CONDITIONS FOR SOME FUELS AND OXIDIZERS[543]

Substance	p_{cr}, atm	T_{cr}, °K
Hydrogen (H_2)	12.8	33.3
Kerosene ($C_{12.5}H_{24}$)	26	662
Ethanol (C_2H_5OH)	63.1	516.3
Ammonia (NH_3)	111.5	405.6
Hydrazine (N_2H_4)	145	653.2
Fluorine (F_2)	25	118.2
Oxygen (O_2)	49.7	154.4
Nitrogen tetroxide (N_2O_4)	100	431.2

times. Both treatments lead to important conclusions that the burning time for a fuel pocket should increase with (1) pressure (as $p^{1/3}$), (2) initial fuel pocket mass (as $m^{2/3}$), and (3) nearness of ambient gas composition to that of the products of stoichiometric combustion. The last two conclusions apply also to *droplet* combustion at $p < p_{cr}$*, however the first conclusion is in sharp contrast to subcritical pressure behavior (where, it will be recalled that, if anything, higher pressures *shortened* burning times).

The time evolution of fuel, oxidizer and product profiles for the DS model[600] can be appreciated by referring to Fig. 2.4.2f. Here τ is the dimensionless time, $\mathfrak{D}t/r_{eff}^2$, and r_{eff} is the radius that a pure fuel vapor sphere would attain if it included the total amount of fuel released and had the same density as the surrounding gas. According to these models, the dimensionless time required to consume all fuel originally present, designated τ_b, depends only on the stoichiometry of the system. If the latter is specified by $\chi \equiv (Y_{OX,\infty}/Y_{F,L})/\mathfrak{r}_{st}$ where $\mathfrak{r}_{st}$ is the stoichiometric oxidizer/fuel mass ratio, then the predicted $\tau_b(\chi)$ relationships are as shown in Fig. 2.4.2g, taken from Ref. 601. The coordinates of Fig. 2.4.2g are chosen such that the point source relation

$$\tau_b(\mathrm{PS}) = (4\pi)^{-1}\{[3/(4\pi)]\cdot[\chi/(1+\chi)]\}^{-2/3} \tag{2.4.2-9}$$

reduces to a straight line. The distributed source (DS) model leads to the inverted result [easily solved for $\chi(\tau_b)$]:

$$\chi/(1+\chi) = \mathrm{erf}\,[1/(2\tau_b^{1/2})] - [1/(\pi\tau_b)^{1/2}]\exp[-1/(4\tau_b)] \tag{2.4.2-10}$$

Note that the PS model always overestimates burning time, the departures exceeding 10 percent for χ above about 10^{-1}.

In experiments designed to check the accuracy of these models, Faeth et al.[256] ignited 600 to 1000μ n-decane droplets ($p_{cr} = 20.7$ atm) in a freely-falling pressure vessel* containing O_2/N_2 mixtures. Maximum flame radii and burning times were then photographically inferred in the supercritical pressure range up to 136 atm., and in the composition range: air–pure oxygen. Estimated burning times in air (normalized to the burning time at $p = 1$ atm) are shown in Fig. 2.4.2h, together with the DS-model prediction at supercritical pressures.† The effects of oxygen enrichment in the surrounding environment were also well represented by the PS and DS theories, the latter being somewhat more accurate at the highest value of χ possible for the n-decane/oxygen system ($\chi = 0.32$). These trends, together with reasonable predictions of maximum flame radius,‡ suggest that "droplet" combustion at supercritical pressures can indeed be regarded as a transient, diffusion-limited vapor phase process; however additional data and more general and detailed theoretical treatments will no doubt be required for application for rocket motor design.

* Thus, the desirability of fine subdivision (atomization) remains unaltered, and the effects of combustion disappear as $Y_{OX,\infty} \to 0$.

* Especially at these high density levels, free-fall is essential to prevent (1) extensive flame distortion due to natural convection, and (2) loss of the suspended "droplet" when the surface tension vanishes.

† The band is due to uncertainties in assumed property values.

‡ In contrast to quasi-steady *droplet* combustion theories (in which the predicted flame radius r_f shrinks monotonically with time, in direct proportion to r_L), the transient "chemical release" theories of supercritical pressure combustion predict that the flame radius initially increases, passes through a maximum at about τ_b/e and then collapses to zero at τ_b. It is interesting to note here that one of the greatest weaknesses of QS *droplet* combustion theory (discussed earlier in this section) was its inability to accurately predict flame radii in the Burke-Schumann (flame sheet) limit.

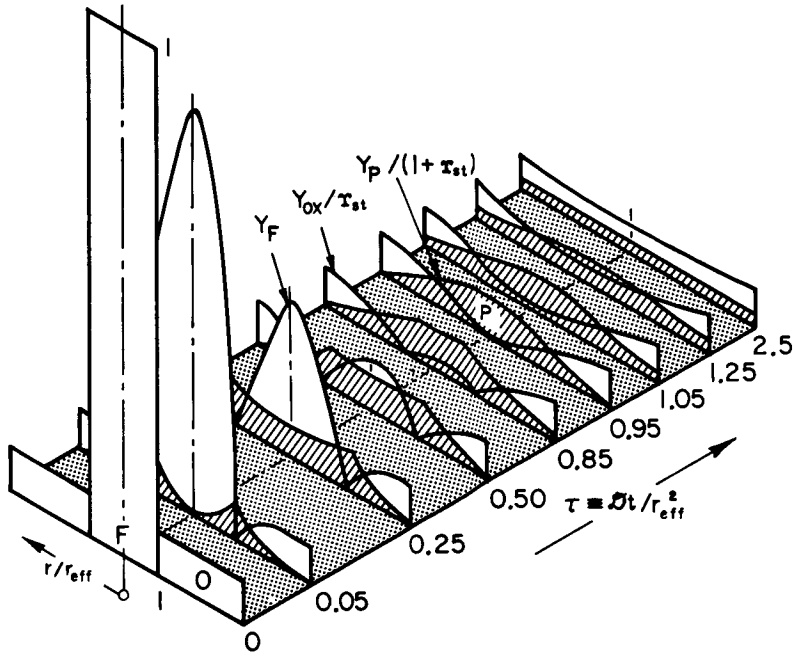

FIGURE 2.4.2f.—Time evolution of fuel, oxidizer and product concentrations according to the distributed source (DS) chemical release model of "droplet" combustion at supercritical pressures; $\chi = 10^{-1}$ (after Rosner[600]).

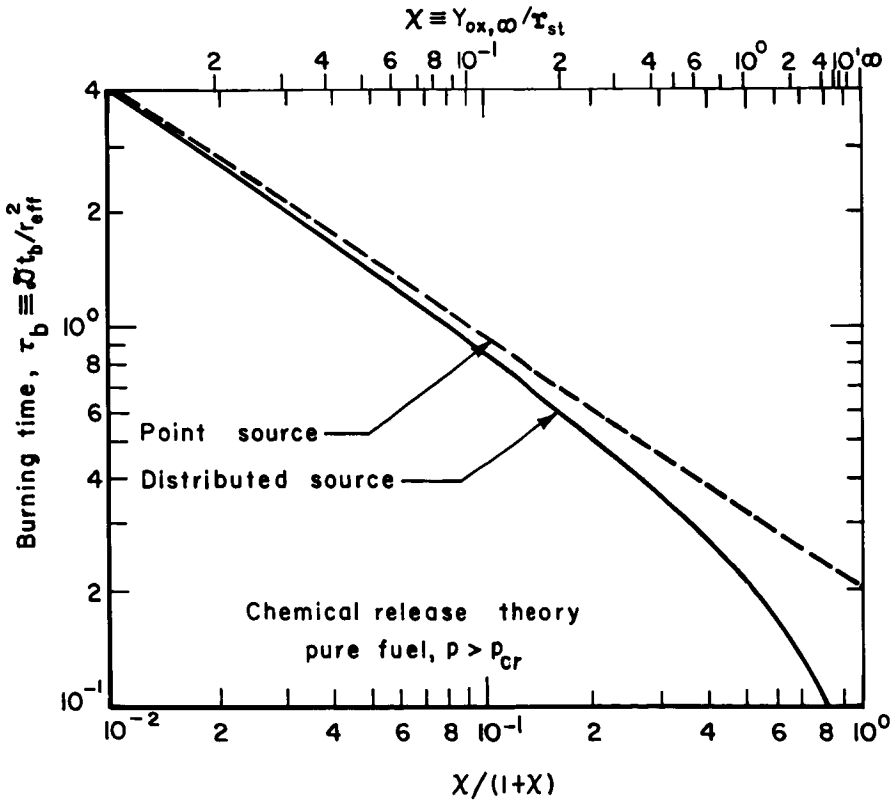

FIGURE 2.4.2g.—Dimensionless time to complete combustion; comparison of the point source (PS) and distributed source (DS) models of "droplet" combustion at supercritical pressures (after Rosner[601]).

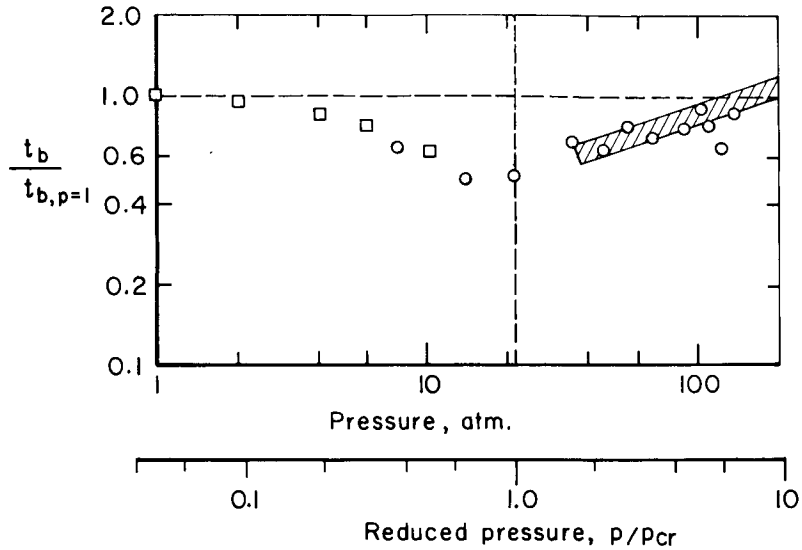

FIGURE 2.4.2h.—Observed time required to complete combustion (normalized by the p = 1 atm. value) versus pressure level; *n*-decane in air (⊡ Hall and Diederichsen[303]; ⊙ Faeth et al.[256]; shaded line (of slope ⅓) is theoretical prediction).

It seems likely that these conclusions will have important implications with regard to combustion instability at high pressure levels (see Refs. 601, 662, 738 and Sect. 3.4.4.2). Indeed, a recent combustion instability analysis[136] incorporating a supercritical pressure envelope flame model has predicted significant alterations in stability limits.

2.4.3 Monopropellant Droplet Combustion

Liquids whose vapors are thermodynamically capable of exothermic chemical reaction are called *monopropellants* or said to have "monopropellant capability." In liquid *bipropellant* rocket motors the fuel (e.g., hydrazine) or oxidizer (e.g., ozone) may *individually* have this capability, hence their gasification rates can be enhanced by the heat feedback resulting from localized vapor phase decomposition*, even in the absence of diffusion-limited chemical reaction with surrounding vapors of oxidizer or fuel. Consequently, combustor efficiency, space requirements and stability cannot be accurately assessed without considering singular features of the gasification of such metastable liquids.

When compared with previously discussed bipropellant droplet combustion, experiments on captive[118,239,257,429,682] or simulated[79,353,604] monopropellant droplets have indeed revealed increased sensitivity of droplet gasification rate $\dot{m}$ to (1) droplet diameter, in many cases approximating $\dot{m} \sim d_L^2$ (corresponding to a *linear* diameter-time curve for captive droplets decomposing in a stagnant atmosphere), (2) pressure level, even at pressure levels far lower than the critical pressure of the fuel, and (3) fuel additives (catalysts, inhibitors) and impurities. Moreover, the absolute value of $\dot{m}$ can exceed that pertaining to simple vaporization into a product gas environment maintained at the adiabatic decomposition temperature. At present, well-defined experimental data on monopropellant droplets (e.g., ignition, extinction, flow rate effects, drag) are far more limited than for bipropellants. However, many of the above-mentioned trends can be rationalized in terms of quasi-steady diffusion theory, coupled with homogeneous chemical kinetics. For reasons which will become evident below, our discussion is

* Not all monopropellants are single metastable compounds. Some are physical solutions, synthesized using oxidizer and fuel constituents [e.g., $NH_3(L)/NH_4NO_3(L)$, $CH_3NO_3(L)/CH_3OH(L)$], whose mixture ratio (or "oxygen balance") can be varied at will.[64] However, for purposes of discussion, we will merely refer to monopropellant "fuel" decomposition (even if the liquid is not in itself a usable monopropellant, or the reaction is not a simple decomposition). As before, most of the discussion applies equally well to *oxidizer* droplets having some "monopropellant capability."

divided into two parts, depending upon the absence or presence of an outer diffusion flame involving ambient oxidizer.

2.4.3.1 *Monopropellant droplet decomposition in an atmosphere comprised solely of inert gases or decomposition products—theory and experiment.*—In the absence of a surrounding oxidizing gas, the simplest model capable of embracing the above-mentioned phenomena is sketched in Fig. 2.4.3a. Here, heat generated by the spherically symmetrical *premixed* vapor phase decomposition flame zone is conducted back to the spherical fuel droplet to sustain the quasi-steady vaporization rate $\dot{m}$. In this model, pursued independently by Lorell and Wise,[455] Spalding and Jain,[663] Williams,[747] Tarifa et al.,[682] Rosser and Peskin[604] and Fendell,[262,264,265] the enhancement in vaporization rate evidently depends on the radial location of the vapor decomposition flame zone, which now cannot be determined based only on considerations of radial diffusion (independently of the decomposition *kinetics*). Not surprisingly, mathematical treatments of this problem closely resemble those of premixed *gas* laminar flame theory,[740] with modifications being required to account for (1) spherical geometry and (2) the role of the droplet as a "flame holder" at the so-called "cold boundary." Common to all available treatments are the important assumptions that (1) the propellant reversibily vaporizes* at the surface $r = r_L$ (in accord with a Clausius-Clapeyron type law) to yield decomposable vapors, (2) decomposition *products* (which back-diffuse) are insoluble in the liquid fuel, and (3) nonconductive heat transfer mechanisms (e.g., radiation) are negligible. As in the case of laminar flame theory, it is possible to formulate and numerically solve the multicomponent, variable property conservation equations in the presence of specified chain-branching reactions. However, greater insight has resulted from analytical treatments of deliberately simplified chemical/transport models. Apart from the ubiquitous $Le = 1$ and constant property approxi-

* Apart from this boundary condition, the monopropellant droplet problem is also the spherical analog of the burning of homogeneous solid propellants which irreversibly gasify. However, this difference in boundary conditions is responsible for markedly different high pressure behavior.

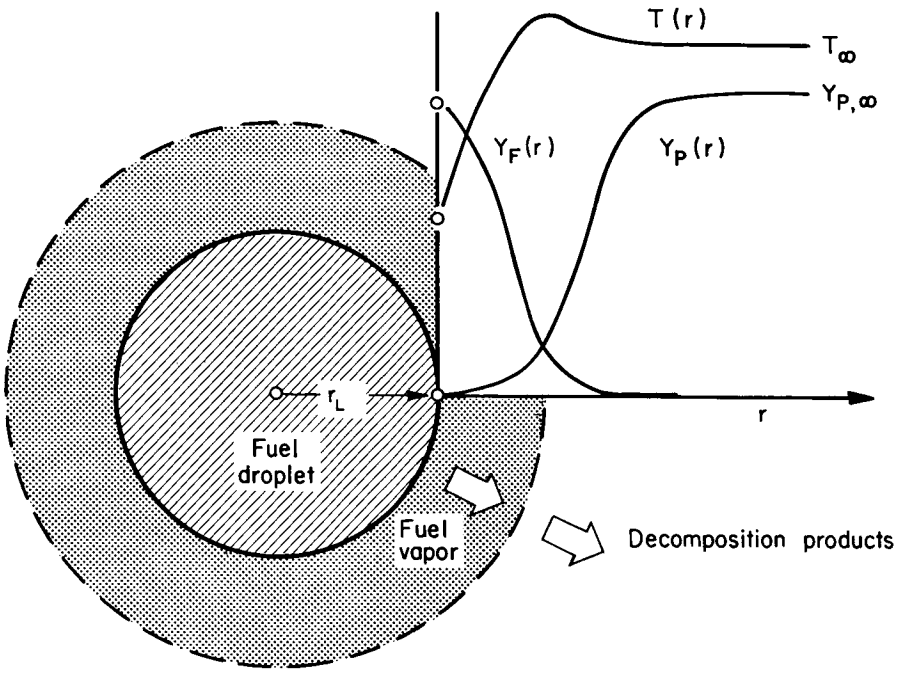

FIGURE 2.4.3a.—Premixed decomposition flame model of subcritical pressure monopropellant gasification in the absence of convective distortion.

mations, two types of chemical kinetic models have proven especially fruitful, and are briefly outlined below.‡

FLAME SHEET MODEL (Spalding and Jain,[663] Jain[387]): If the activation energy, E_{act} (for the vapor decomposition reaction) and pressure level, p, are sufficiently high*, then the thickness of the decomposition zone will be small compared to its radius of curvature. This being the case, the simplicity of the thin-flame (or "flame sheet") concept in bipropellant combustion can also be exploited here (i.e., zones on both sides of the flame sheet become chemically "source-free") but without suppressing the fundamental influence of chemical kinetics (now embedded in a flame speed parameter, often available from direct experimentation with gases). The result for gasification rate enhancement, $\dot{m}/\dot{m}_{vap}$ in the adiabatic case (i.e., a droplet surrounded by its own decomposition products at the adiabatic decomposition temperature) is particularly simple and instructive[663]:

$$\frac{\dot{m}}{\dot{m}_{vap}} = \{1+\tfrac{1}{2}[D_I^{1/2}-(D_I+4D_I^{1/2})^{1/2}]\}^{-1} \tag{2.4.3-1}$$

where

$$D_I^{1/2} \equiv (\rho_u S_u)/\dot{m}_{vap}''$$

and

$\rho_u S_u \equiv$ mass burning velocity for a plane adiabatic† flame (proportional to $[k(T_{f,ad})p^n]^{1/2}$).

This relation, shown plotted in Fig. 2.4.3b, immediately reveals that (1) the effect of chemical reaction is always to increase the burning rate as compared with a chemically stable droplet with the same physical properties; (2) in the limit if $D_I \to 0$ (which corresponds to slow kinetics, low pressure and/or small droplet diameter), $\dot{m} \to \dot{m}_{vap}$ and hence increases linearly with diameter, and logarithmically with the value of $1+B_{vap}$ (as previously discussed, Sect. 2.4.1); and (3) in the limit if $D_I \to \infty$ (which corresponds to rapid kinetics, high pressure and/or large droplet diameter*) $\dot{m} \to 4\pi r_L^2 \cdot (\rho_u S_u)$ and hence increases with droplet *area*, and (pressure level)$^{n/2}$, and becomes independent of B_{vap}. This simple model is therefore in qualitative accord with each of the experimental observations outlined above, with the sensitivity to additives and impurities following from the strong dependence of $\dot{m}$ on gas phase kinetics ($\dot{m} \sim [k(T_{f,ad})]^{1/2}$) at large values of $p^{n/2}d_L$. In the absence of relevant flame speed data, absolute values of $\rho_u S_u$ (and hence $\dot{m}$) can often be estimated in terms of gas phase rate data (e.g., using Spalding's "centroid method").[740] By combining available information for ethyl nitrate, propyl nitrate, hydrazine and nitromethane, Spalding and Jain[663] have given the estimates of B_{vap} and $D_I^{1/2}/r_L$ which are collected in Table 2.4.3. The applicability of this treatment has been extended by Jain[387] to include the frequently encountered non-adiabatic case,† i.e., $T_\infty \gtrless T_{f,ad}$. The relevant flame speed then differs from the adiabatic flame speed, but the correction can be rationally estimated in terms of the imposed enthalpy gradient and the activation energy of the homogeneous decomposition reaction. Using exact numerical integrations for a simple class of k(T) functions, Jain[387] has further shown that thin-flame theory only slightly overestimates $\dot{m}$, especially for large values of E_{act}, D_I, and B_{vap}.

FIRST ORDER (n=1), CONSTANT k MODELS (Rosser and Peskin,[604] Fendell[262,264,265]): Linearized models of monopropellant decomposition, resulting from the assumptions of first order kinetics with a temperature independent rate constant, lead to analytic predictions without

‡ Of course, additional approximations (not discussed here) have been introduced and successfully used to obtain numerical results (see, e.g., the "profile method" exploited by Tarifa et al.[682] in multicomponent systems).

* For the decomposition reaction of useful monopropellants E_{act} is necessarily high since the monopropellant must be safely stored (prior to its use), but rapidly decomposed at high temperatures (to yield compact combustors).

† The unburned gas temperature and composition corresponds to the total enthalpy of the composition products far from the droplet.

* It is interesting to contrast this behavior to that of bipropellant droplets, viz. monopropellants are influenced by chemical kinetics when k, p and d are *large*, whereas bipropellants (provided ignition has occurred) are influenced by chemical kinetics when k, p and d_L are *small* (cf. Figs. 2.4.2c, d and 2.4.3b).

† Results confirm the expectation that monopropellant decomposition rates are far more sensitive to T_∞ than bipropellant combustion rates. (See discussion of extinction, below.)

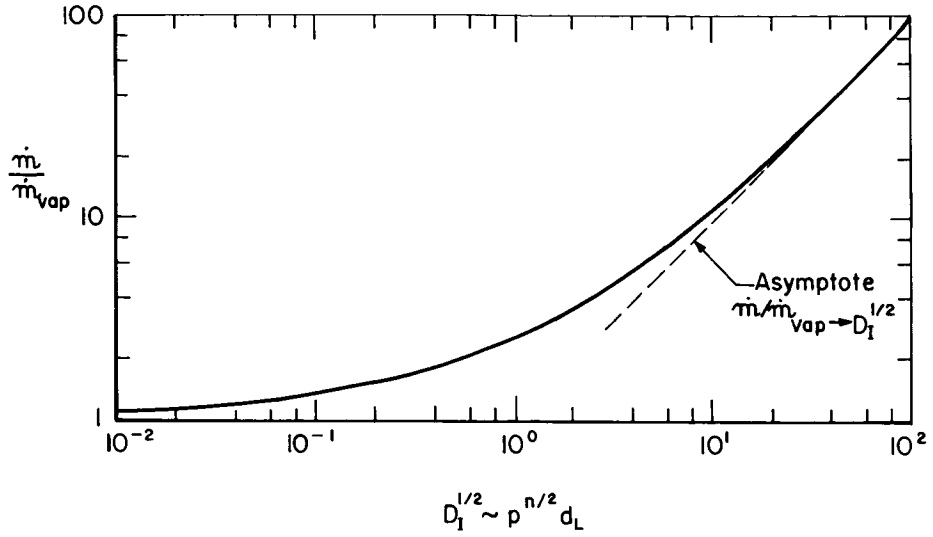

FIGURE 2.4.3b.—Effect of exothermic chemical decomposition on the gasification rate of monopropellant droplets surrounded by motionless decomposition products at the adiabatic decomposition temperature (after Spalding and Jain[663]).

a priori restrictions on flame zone thickness. Using matched asymptotic expansion methods, Fendell[262,264,265] (1965) has shown that for this model the incipient effects of chemical decomposition can be represented by the series:

$$\frac{\dot{m}}{\dot{m}_{vap}} = 1 + \left(\frac{kr_L^2}{\bar{\mathfrak{D}}}\right)^{1/2} \cdot \frac{(h_c/h_v)}{1+B_{vap}} + \cdots \quad (2.4.3\text{–}2)$$

which predicts slightly smaller enhancements than thin-flame theory when $kr_L^2/\bar{\mathfrak{D}}$ is small but nonzero. In the opposite extreme $kr_L^2/\bar{\mathfrak{D}} \gg 1$ this expansion method[264] as well as an alternative approximation method[604] leads to asymptotic behavior of the form

$$\frac{\dot{m}}{\dot{m}_{vap}} = \left(\frac{kr_L^2}{\bar{\mathfrak{D}}}\right)^{1/2} \cdot \frac{\text{fct}\ (h_c/h_v)}{\ln\ (1+B_{vap})} \quad (2.4.3\text{–}3)$$

in qualitative agreement with the thin flame model.*

Virtually no systematic experiments on monopropellant decomposition rate and drag in forced convection environments have been reported, however the effects of incipient forced convection have recently been predicted by Faeth[254] and Fendell,[262] using quite different approximation methods. At the outset, it seems clear that the influence on $\dot{m}$ should depend markedly† on the kinetic parameter D_I. This is due to the fact that incipient forced convection should have little effect on the evaporation rate when the decomposition flame is well embedded within the boundary layer (large D_I). On the other hand, when the decomposition kinetics are sufficiently slow the flame will be too far from the droplet, hence $\dot{m}$ should approach $\dot{m}_{vap}(\text{Re})$. It is thus the intermediate case, occurring when $(kr_L^2/\bar{\mathfrak{D}})^{1/2}$ and Re are of the same order of magnitude, which requires detailed treatment. Interestingly enough, Fendell's calculations[262] for this case reveal that Eq. (2.4.3–3) overestimates $(\dot{m}/\dot{m}_{vap})-1$ by less than 30 percent when $(kr_L^2/\bar{\mathfrak{D}})^{1/2}$ and Re are comparable and Re is small but nonzero.‡ Faeth's computations[254] for adiabatic monopropellant decomposition indi-

* However, in the limit: $kr_L^2/\bar{\mathfrak{D}} >> 1$, when $h_c > h_L$. Fendell[262,264,265] derives an alternative solution (reported to be equally compatible with the governing equations and boundary conditions) which indicates that $\dot{m}/\dot{m}_{vap}$ approaches (from above!) an asymptotic limit depending only on h_c/h_v and B_{vap}. The significance of this apparent non-uniqueness is not clear.

† In contrast to the bipropellant case in which both $\dot{m}_{vap}$ and $\dot{m}_{max}$ are affected by convection in a similar way.

‡ The $\dot{m}_{vap}$ in Eq. (2.4.3) is then interpreted as $\dot{m}_{vap}{}_{\cdot Re=0}$ $[1+\frac{1}{4}(\text{Re})(\text{Pr})+\cdots]$.

TABLE 2.4.3.—THERMODYNAMIC AND KINETIC PARAMETERS FOR THIN-FLAME THEORY OF ADIABATIC MONOPROPELLANT DROPLET BURNING[663]

Pressure, atm	Ethyl nitrate		Propyl nitrate		Hydrazine		Nitromethane	
	B_{vap}	$D_I^{1/2}/r_L$, cm^{-1} (a)	B_{vap}	$D_I^{1/2}/r_L$, cm^{-1}	B_{vap}	$D_I^{1/2}/r_L$, cm^{-1}	B_{vap}	$D_I^{1/2}/r_L$, cm^{-1}
1	6.73	15.6	1.86	9.5	2.63	85.3	5.56	4.4
10	5.50	171	1.52	124	2.29	294	4.64	48.2
20	5.06	355	1.51	250	2.20	421	4.36	99.3
40	4.80	867	1.42	520	2.08	618	4.03	206
60	4.49	1010	1.37	800	2.08	771	3.88	316

[a] Values rounded to three significant figures.

cate that the coupled region is fortunately rather narrow, suggesting the simple estimation procedure*

$$\dot{m} \cong \begin{cases} \dot{m}_{Re=0} \text{ for Re such that } \dot{m}_{Re=0} > \dot{m}_{vap}(Re) \\ \dot{m}_{vap}(Re) \text{ for Re such that } \dot{m}_{vap}(Re) > \dot{m}_{Re=0} \end{cases} \tag{2.4.3–4}$$

which noticeably underestimates $\dot{m}$ only at Reynolds numbers such that $\dot{m}_{vap}(Re) \approx \dot{m}_{Re=0}$. Here $\dot{m}_{Re=0}$ is the chemically enhanced vaporization rate as calculated from the theory of monopropellant decomposition in a stagnant atmosphere. The situation is more complex in the nonadiabatic case, for when $T_\infty < T_{f,ad}$ convection has two opposing effects. At first convection causes increased heat loss from the flame zone, suppressing the decomposition reaction. This can outweigh the increase in transfer rates normally expected in nonreactive convective situations, leading to a region of *decreasing* $\dot{m}$ with increasing Reynolds number. Under these circumstances Eq. (2.4.3–4) *over-estimates* decomposition rates for Reynolds numbers approaching $(kr_L^2/\bar{\mathfrak{D}})^{1/2}$.

Little work has been reported on the ignition and extinction behavior of monopropellant droplets in stagnant and convective environments. Jain's[387] prediction that for sufficiently cold environments, steady burning is not possible unless D_I is sufficiently large,† is certainly compatible with the observation that monopropellant burning frequently cannot be sustained unless some oxidizer is added to the ambient environment (discussed below) especially at low pressures. With regard to the ignition transient, even under environmental conditions such that quasi-steady decomposition with $T_L \approx T_{bp}$ is ultimately possible, complete droplet consumption may occur before this QS stage is reached[257]; suggesting that appreciable decomposition can occur at temperatures well below the prevailing boiling point, especially at high pressure levels. In these same experiments "ignition" of the decomposition reaction was observed to occur well before the nonreactive "wet bulb" temperature was reached, again especially at elevated pressures (i.e., high values of $T_{L,wb}$). Thus, it appears that a greater degree of gasification occurs during the heat-up period of monopropellants than is normally the case for bipropellants (see Sect. 2.4.1). To predict the droplet mass history therefore requires quasi-steady gasification rate calculations carried out with $T_L < T_{L,wb}$ [hence $Y_{F,w} < Y_{F,eq}(T_{L,wb})$] in the simultaneous presence of gas phase decom-

* Equivalent to that adopted by Beltran[89] et al. for estimating the effects of enhanced hydrazine gasification rates on rocket motor efficiency and instability (see next subsection).

† Corollary results for the dependence of droplet size at extinction on an activation energy parameter have been reported by Jain and Ramani.[388] If the temperature sensitivity of the decomposition reaction rate is sufficiently weak, stable "burning" appears to be possible however small the droplet.

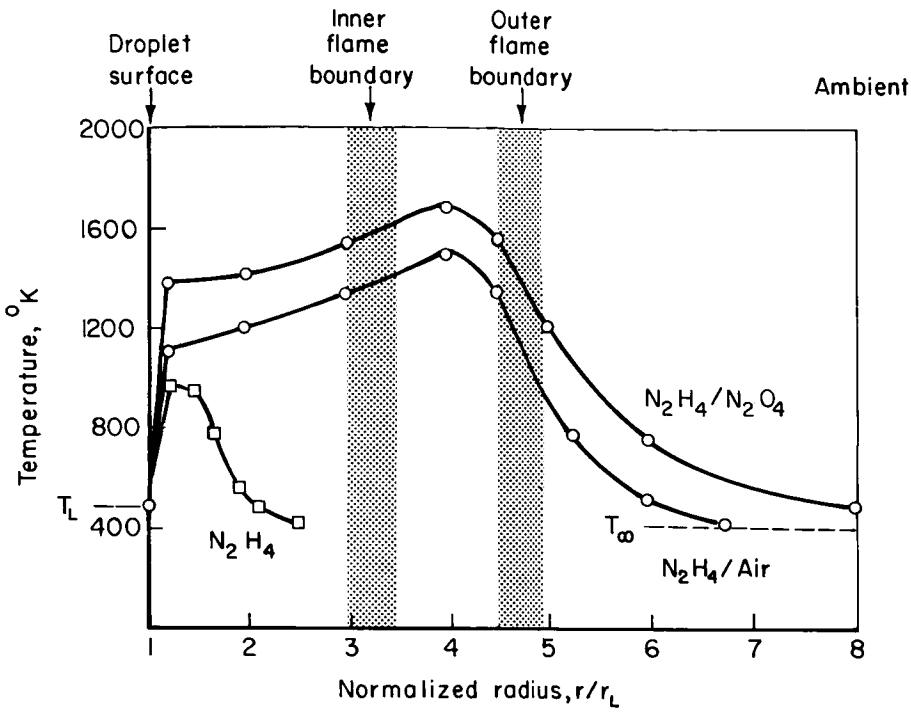

FIGURE 2.4.3c.—Observed radial temperature profiles for a hydrazine droplet decomposing in an inert atmosphere, in air, and in nitrogen tetroxide (after Hersh et al.[353]).

position and forced convection. Calculations of this type[253] reveal strong effects of convection on $\dot{m}$ in the presence of rapid chemical decomposition [even under conditions such that the Reynolds number effect would ultimately be negligible (when $T_{F,w} < Y_{F,eq}(T_{L,wb})$); see Eq. 2.4.3–4].

2.4.3.2 *Monopropellant droplet fuel decomposition in an oxidizing atmosphere—theory and experiment.*—In a bipropellant system such as hydrazine/liquid oxygen the gasification rate of a hydrazine droplet can be simultaneously influenced by exothermic fuel decomposition *and* localized reaction of fuel-like decomposition products with the surrounding oxygen-rich vapors. Indeed, captive droplet experiments by Dykema and Green,[239] Lawver[429] and Hersh et al.[353] have revealed (1) hydrazine gasification rate enhancements in O_2 and NO_2/N_2O_4 containing vapors,* and (2) the existence of a "dual"-envelope flame. The thermal effects of the outer diffusion flame are evident in the thermocouple traverses of Hersh et al.[353] (1967), represented in Fig. 2.4.3c for hydrazine decomposition in nitrogen, air, and nitrogen tetroxide. As anticipated, increased ambient oxidizer concentration increases: (1) peak diffusion flame temperature, (2) peak decomposition flame temperature, (3) thermal gradients near the droplet surface, and hence quasi-steady gasification rates. Under such conditions the burning rate dependence on pressure level, droplet size and impurity or additive level can exhibit some characteristics of bipropellant droplet flames [e.g., linear d_L^2 vs. t behavior, indicating $\dot{m} \sim d$] some characteristics of monopropellant flames (increased sensitivity to pressure level and impurity/additives) and often "hybrid" characteristics [e.g., intermediate pressure dependencies (see Rosser and Peskin[604])].

Pending much-needed additional research on dual-flame combustion, many ad hoc estimates (of unknown accuracy) have been made by

* Several investigators have reported difficulties in stabilizing monopropellant decomposition burning in the absence of ambient oxidizer (especially at low pressures and ambient temperatures). Hence the outer diffusion flame plays a role in many available studies of "monopropellant" combustion.

invoking selected results already discussed for simpler limiting cases.* For quiescent systems, burning rate estimates are usually made by assuming the role of the outer diffusion flame is merely to raise the effective value of T_∞—otherwise the burning rate is that of a monopropellant decomposing in an inert environment. In convective flow environments Beltran et al.[89] employ this "effective T_∞" approach only if the boundary layer thickness (inferred from the instantaneous value of Nu(Re, B, Pr)) exceeds the estimated standoff distance of the decomposition flame (assumed independent of Re). At relative velocities such that this inequality breaks down, only single-flame theory is applied, much in the spirit of Eqs. (2.4.3–4). Interestingly enough, when this computational scheme is used together with the Priem-Heidmann[565,564] technique for estimating combustor efficiencies (based on liquid propellant gasification as the rate limiting step), the N_2H_4/LOX system no longer appears so anomalous, i.e., decomposition and/or combustion-enhanced gasification apparently account for the high combustor efficiencies previously observed with this propellant combination.[89]

2.5 FLOW PROCESSES†

2.5.1 Core Flow

2.5.1.1 *Effects of injector design.*—The steady-state gas dynamic flow pattern within a rocket thrust chamber is determined primarily by the injector design. If combustion instability occurs, the relatively definable pattern is obliterated and replaced by a gas dynamic environment which is usually highly turbulent and erosive. Since there are few practical applications for a rocket engine whose normal mode of operation is unstable, there is little value in considering instability as a steady-state characteristic. Here we shall consider only the characteristics of steady-state operation in stable systems. It is noted however, that the steady-state gas dynamic pattern in a thrust chamber is closely related to the probability of an instability occurring. That is, the mass and mixture ratio distribution and the energy release profile generated as the steady-state flow field in a thrust chamber are also the determinants of the stability margin.

For element-type injectors associated with axisymmetric cylindrical or conical chambers, it may be said that the location of an element of fluid near the injector face† uniquely determines the location of that element of fluid at the nozzle exit. It has been shown[318,246,619,554] that flow in a rocket chamber may be characterized by stream tubes as outlined in Sect. 1.1.3 (see Fig. 1.1.3b). Each stream tube exhibits a particular mass flow, mixture ratio and energy release profile determined by the injector design characteristics. Within a stream tube, the gas properties are considered to be homogeneous at any axial station. This is reasonable, as the flow is highly turbulent within a given stream tube.

The stream tube concept of core flow is consistent with the highly turbulent flow in rocket chambers for the following reason: the dimension of turbulence is typically very much smaller than the diameter of the chamber. For example, calculations of the Prandtl mixing length[632] for chamber flow generally shows the typical dimension of turbulence to be on the order of 0.5 inch, much smaller than most chamber diameters. Thus virtually complete mixing will occur within a stream tube, but overall area mixing will not occur.

For convenience one would not wish to choose a stream tube smaller than one element. However, based on the work of Rupe (see Sect. 2.3.2) mixture ratio nonuniformities have been shown to exist with elements of 100 lbs. thrust. Also, recent investigations[356,224] have shown the importance of intermixing of spray fans from adjacent elements. Thus the distinction must be drawn between spray interdispersion, which is important, and gas stream mixing, which apparently has no great influence in most practical rocket motors. There-

* In contrast, Fendell,[265] again using the method of matched asymptotic expansions, has undertaken a systematic cataloging of enhanced vaporization behavior for those cases in which monopropellant decomposition must precede the diffusion flame reaction. As might be anticipated from the previous sections, the magnitudes of *two* distinct Damköhler numbers are found to govern the behavior of such systems.

† R. S. Valentine, Author.

† Beyond the axial location where the sprays are formed i.e., where radial winds or intense recirculation, if present, are no longer a factor.

fore the majority of rocket engines, with thrust per element on the order of 50 to 500 lbf, exhibit the tendency to provide unmixed areas within the spray fan of a single element. However, even with these nonuniformities, the choice of a single element stream tube, often approaching the 0.5 inch size, generally provides a reasonable basis for performance calculations.

For very large thrust per element systems (over 1000 lb F/E) the composition of the element must be analyzed further. Conversely, low thrust per element engines (less than 1 lb F/E) will show relatively complete mixing over a span of several elements. Thrust chambers less than one inch in diameter may be considered as comprising only a single homogeneous stream tube in the steady-state core flow field.

Even though chamber core flow may be reasonably characterized by stream tubes, this does not imply that flow in the chamber is always axial. There are, of course, interactions between the stream tubes resulting from chemical and gas dynamic gradients. For example, two adjacent stream tubes of identical mixture ratio and energy release profile would not be inclined to interact chemically. However, two adjacent stream tubes of widely differing mixture ratio would tend to react at the interface creating additional turbulence and intermixing between the contents of both stream tubes. The difference in mixture ratio could occur either as a result of hydraulic distribution behind the injector face or because of different types of elements exhibiting different energy release profiles. The former case could be intentional, such as boundary cooling wherein adjacent rows of elements have different mixture ratios, or could result from injector manifold maldistribution. An example of the latter would be adjacent location of two types of element with identical mass flow and overall mixture ratio. If one were, say, a two-oxidizer-on-one-fuel triplet, and the other a four-oxidizer-on-one-fuel pentad, it is clear that oxidizer droplet size and vaporization rates would differ. Thus, at a given axial station, the mixture ratio of the vaporized propellants in each stream tube might be significantly different.

Gas dynamic factors affecting interactions between stream tubes could result from pattern voids or varying energy release profiles between stream tubes. Pattern voids occur either by imperfect mass distribution at the injector face or because, barriers such as baffles, interfere with even mass distribution. The result of voids is lateral flow towards the vacant areas. In severe cases this lateral motion may result in some mixing between stream tubes. There are also generally adverse wall effects associated with strong lateral flows, so this is never a desirable case.

Stream tube divergence and displacement may also occur as a result of an uneven energy release profile. A combination of short impinging and long impinging elements on the same injector will often produce this phenomenon. The short impinging elements react rapidly, with the energy release resulting in expansion of the affected stream tubes into the entire available flow area. When the long impinging elements react, the hot gases formed at that point then force the previously generated gases back into their original positions with corresponding lateral motion. In some cases these lateral flows can be damaging. For example, consider an injector with short impinging outer elements and long impinging inner elements. The outer elements react first, driving hot gases into the center as the effluent from the inner elements is still largely unvaporized. Later the inner elements react driving gases outward toward the wall. When combined with the convergence of the chamber as the throat is approached, these outward flows often create an erosive atmosphere which results in severe streaking near the throat. In this situation, the chamber is often undamaged near the injector face.

Many rocket engines have been developed using vortex or swirl cup concepts. These systems have generally been relatively high performing, and can be compatible with the chamber, if carefully designed. Compatibility is not much more difficult to attain in such a system than with conventional elements as all of the induced lateral flow is in the same direction. Cooling of the chamber tends to be more difficult with swirling core flow, as the boundary layer thickness is reduced and heat transfer coefficients are generally higher as a result of the greater velocity past the wall. Compatibility becomes a serious problem however, if the lateral flows are opposed, and can concentrate at specific points around the circumference

of the chamber. This generally results in chamber streaking or burnout and is most often noted near the injector face.

Momentum of the injector element effluent streams can also contribute to lateral flow, either intentionally or unintentionally. An engine operating at off-design conditions will often have element effluents in which the resultant momentum vector is non-axial. Cases have been noted[168] in which a change in operating conditions to a cooler combustion temperature and less corrosive reaction products have resulted in marked decrease in duration capability. This effect can be directly related to lateral flows of erosive gases resulting from an unfavorable change in resultant momentum vectors.

Lateral flow can be used to good advantage by the injector designer who is unable to achieve even mass distribution because mechanical obstructions prevent proper element location. The elements may be located as nearly as physically possible to the desired area, then the effluents may be directed into the void area by adjustment of the momentum level and resultant direction.

2.5.1.2 *Mechanical turbulence generation.*—It has often been observed that low performing thrust chambers may be improved by artificial inducement of turbulence and lateral flow in the core. Common methods of inducing lateral flow include vortex or swirl elements, canted baffles and adjustments to the wall contour. As an example, a thrust chamber with an energy release efficiency of 80% achieved a 12% increase in performance when a ring shaped baffle was installed in the chamber a few inches downstream of the injector (this "enzian ring" baffle extends from the wall).

It is important to note that mechanical turbulence generation will probably only result in better performance in systems which are basically low performing initially. An injector/chamber combination, which has even mass and mixture ratio distributions and elements which generate small enough droplets to insure that vaporization is completed in the available length, will probably not gain but rather will lose performance as a result of induced lateral flow. Furthermore, injector/chamber compatibility is far more difficult to attain in the presence of lateral core flows. The flow obstructions themselves are very susceptible to thermal or erosive damage and are rarely satisfactory except for very short durations in high energy rockets. They do, however, find successful application in low flame temperature gas generators.

2.5.2 Boundary Flow

2.5.2.1 *Film or boundary coolant.*—Control of the chemical composition and temperature of the steady-state boundary flow is almost universally used as a means for cooling thrust chambers. Virtually all practical systems operate at combustion temperatures far greater than any known material can withstand. Often, the wall must also be protected against chemical attack from highly corrosive components of the combusting gases.

The degree of need for boundary flow as a device for wall protection is directly related to the injector core design. The existence of strong lateral flows generated as described in the preceding section may require massive amounts of film coolant to offset potential damage. Conversely, even mass and mixture ratio distribution and evenly distributed energy release will minimize the need for film or boundary coolant.

Film and boundary coolant are generally applied evenly around the periphery of the injector. This is not necessarily the best practice. To minimize the need for boundary protection, coolant should be concentrated at critical zones—those where lateral flows or adverse chemical concentrations would tend to attack the wall.

Cases have been observed in which the use of evenly distributed film coolant has actually had an adverse effect. For example, if fuel coolant should come in contact with an oxidizer-rich stream tube of the core flow, the resulting reaction right at the wall can create high temperature turbulent gas flow which will disrupt the boundary layer and permit corrosive and erosive gas streams to contact the wall.

Injectors with face baffles to prevent combustion instability generally require film coolant at the point where the baffle approaches the chamber wall. Usually, the baffle is thick enough to create a void which is filled at the baffle tip by lateral gas flows. Often, opposing gas flows concentrate at this point, and hence the most common location for chamber damage is downstream of

the baffle tips (if a sufficient gap exists between the baffle and chamber wall the same damage can occur at that location). While this effect can be minimized by careful design, it is at this location that boundary flow control is most needed.

2.5.2.2 *Wall effects.*—Protection of the chamber wall or of baffles if they are present, is the primary reason for applying boundary flow control. As discussed previously, most wall or baffle damage results from imperfections in the core flow which sweep away the boundary layer and expose the wall to attack. The type of attack varies from single critical areas to generalized attack when protection is uniformly insufficient. It is always true that chambers fail at a single point—that point at which the susceptibility of the wall and the severity of the contained gases combine to provide the worst environment.

Baffles are generally attacked at the tips, at points where cooling is a minimum or external forces are highest or both. Chamber walls usually exhibit some indications of localized streaking, or in the case of regenerative chambers, specific tubes which are more prone to burnout than others. The streaks often indicate the direction of gas dynamic motion within the chamber. For example, often the protected zones under film coolant orifices may be seen to cant toward zones where voids are being filled by lateral flows such as downstream of the baffles.

Where strong but evenly distributed radial outflows exist, or where evenly distributed adverse chemical species are present, the chamber may exhibit general roughness from the erosive or corrosive attack. In some cases, the flow pattern is such that a deep gouge may appear at one or more locations, usually near the injector face. This is indicative of a strong local condition which attacks the wall, then is dissipated downstream by the boundary protective flow. Such gouges would become streaks in the absence of the protective flow.

2.5.2.3 *Off-design operation.*—Changes in operating conditions or increased cooling requirements are sometimes imposed upon engine systems after design is complete and frozen. These systems are then called upon to operate under circumstances other than those for which they were designed. This happens commonly, as few designers are capable of determining in advance precisely what minimum cooling requirements will be or, to a lesser extent, the mixture ratio at which performance will be optimized.

Off-design operation means that flow in the injector manifolds will not be as designed, with higher velocities and pressure drops in some channels, lower in others. The element resultant momentum vectors which would normally have been designed to be axial originally, may deviate a great deal from axial.

These changes require corresponding adjustments of boundary flow protection in order to maintain the highest performance consistent with durability. In general, a change to off-design operation will result in lower performance and poorer compatibility than would be exhibited by an injector designed specifically for the new conditions.

The following is an example of the cost in performance of off-design operation. A particular thrust chamber was designed to operate with no film coolant, and was found to be incompatible with the chamber over the required duration. As a result, film coolant was added until the injector/chamber met minimum compatibility requirements. This required 20% of the fuel as film coolant, and resulted in a performance loss of about 4%. It was subsequently found that a similar injector designed for 6% fuel film cooling was compatible, and exhibited only a 1% performance loss over the uncooled case. Thus, the difference in boundary flow requirements of 14% of the fuel could be attributed to the effects of operating at an off-design condition.

2.5.3 Energy Release Distribution

2.5.3.1 *Element design.*—Energy release occurs as the result of contact between fuel and oxidizer within the combustion chamber. As described previously, the energy release profile is determined by the element design, with stream tubes formed by different types of elements exhibiting differing rates of combustion, dependent primarily upon droplet size distribution, propellant volatility, and gas-spray relative velocity. The overall energy release efficiency is determined by the percentage of the propellant that is able to vaporize and burn in the available combustion

length. Thus, a few inefficient stream tubes can reduce the overall energy release efficiency below acceptable limits.

If an injector with an even mass distribution has elements which are all identical in mass flow, mixture ratio, and design, then the energy release will proceed evenly in all stream tubes. If the elements are very efficient with respect to atomization of propellants, and generate a very small droplet size distribution, most of the energy release will take place within a very short distance from the injector face. This system will generally exhibit excellent performance and compatibility characteristics but will have a tendency to be unstable. Thus, from the standpoint of stability, it is generally good to have wide distribution of energy release, axially, circumferentially and radially. It becomes clear that a practical engine must represent a balance between the factors affecting performance, compatibility and stability. The balance depends upon mission requirements. Manned systems generally must be dynamically stable, with performance being of secondary importance, whereas unmanned systems with high performance requirements must sometimes accept lower stability margins.

Energy release distribution is affected primarily by initial drop size distribution.[564] Droplet size is determined by the size and type of element, design characteristics of the element and propellant properties. As described in Sect. 2.2, atomization is most commonly obtained by momentum effects in impinging liquid streams, stripping of liquid jets or sheets due to shear from local gas-liquid relative velocities, swirl induced by orifice pressure drop, or combinations of these. With hypergolic propellants, an additional phenomenon occurs which affects droplet size and in turn energy release distribution. This phenomenon, reactive stream separation,[246, 389, 415] results from the rapid interface reaction that occurs when hypergolic droplets come in contact with one another.

2.5.3.2 *Combustion volume and length effects.*— In liquid rockets the characteristic length, L*, is an almost meaningless parameter since volume comparisons are implied (see Sect. 2.1.3). L* requirements to achieve a given energy release efficiency are related primarily to the injector and chamber design characteristics and to a lesser extent to propellant properties. For example, equivalent energy release efficiencies have been attained in an L* of 5 to 10 inches with a very fine element pattern as have been achieved with an L* of 30 to 40 inches with coarser elements. Some cases have even been observed in which a reduction of L* has led to higher energy release efficiency with the same injector. This can occur when L* is reduced by lowering the contraction ratio, A_c/A_t, thus increasing the gas velocity past the vaporizing droplets†. In contrast, any reduction in L* which results from reduced combustion length, L, will invariably result in reduced energy release.

When combustion is above about 95% complete, droplet vaporization may cease to be the predominant factor in further energy release. Kinetic factors and mixing efficiency may then become limiting. At this point however, combustion is at a state of completion such that there is little impact upon combustion stability regardless of the distribution.

In systems of low energy release efficiency, the combustion front is distributed over a wide axial distance. In these systems, combustion may continue on into the expansion nozzle. Generally these systems are not unstable because of the low combustion rate at any given axial station. No instance has been recorded in which nozzle combustion has had any affect upon combustion stability.

† For chamber contraction ratios less than about two, the high chamber gas velocities may cause secondary atomization of large droplets with dramatic increases in energy release rates as compared to chambers with larger A_c/A_t.

CHAPTER 3

Dynamics of Combustion and Flow Processes

3.1 INTRODUCTION*

Although the preceding chapter is concerned with steady-state descriptions of the combustion and flow processes that take place in a liquid propellant rocket engine, dynamics are actually considered there also. For example, liquid particle trajectories involve an inertia lag between the drag force and the change of velocity. The distinction to be made here is that the term "dynamics" is used to refer to unsteadiness viewed in an Eulerian sense. In a frame of reference fixed to the rocket engine, the processes of Chapter 2 appear time-independent. The existence of such a stable steady state is taken from experimental evidence. However, it is also known that under certain conditions an engine does not possess this steady state. The various fluid mechanical and particle dynamics processes may then behave differently from the steady-state descriptions of the previous chapter.

Such behavioral differences usually occur when time rates of storage of mass, species, momentum, and energy with an Eulerian control volume become important. For example, the application of a pressure difference across an injector does not cause an immediate velocity response of the liquid propellant. There is a period of acceleration (i.e., a time rate of storage of momentum) before the steady state is reached. The compressibility of the chamber gases or feed line liquids allows for the existence of wave motions (time rate of storage of mass). Such wave motions can cause unsteadiness in the combustion process by many mechanisms. For example, if the diffusion field surrounding a vaporizing droplet is exposed to a time-varying free stream, heat transfer and species diffusion processes will not respond in phase with the local conditions but will possess phase lags.

Storage rates do not have to occur on the microscopic scale to be important. Low frequency instability can be caused by differences in injection, burning, and discharge rates when viewing the entire engine as the system. Here, phase differences may occur by consideration of only the "steady-state" process descriptions of the preceding chapter. In a Lagrangian sense there is a time delay between injection and burning of a fluid element that is important in the descriptions of various phase relations in an Eulerian view.

Because the investigation of periodic phenomena is obviously of interest to stability analysis, much of the following work is devoted to periodic descriptions, characterized by a circular frequency ω. This frequency defines a characteristic cycle time against which other process times may be compared. If the period is much longer than some characteristic time of the process under consideration, the process is said to behave in a "quasi-steady" manner with respect to the oscillation. For example, if the chamber pressure at a point oscillates slowly with respect to the wave propagation time in the chamber, the wave motion effects may be disregarded, and the pressure is determined by quasi-steady chamber mass conservation. Also, if the gas field surrounding a vaporizing droplet is undergoing oscillations that are slow compared to gas-phase diffusion in the vapor film around the droplet, this diffusion process behaves quasi-steadily with respect to the oscillation. In this quasi-steady limit, which has practical value for some processes, many of the descriptions of the previous chapter may apply directly to the oscillating system. However, in the more interesting cases, new techniques of treatment are required because the unsteadiness plays an essential role.

* W. C. Strahle, Author.

The concept of a single circular frequency breaks down in certain instances. If shock waves occur, for example, the combustion process encounters a succession of step functions. In a Fourier sense many frequencies are present. There can be no quasi-steady behavior because there are always components of the wave with sufficiently high frequencies. In any event, extreme caution is required in the use of quasi-steady considerations when unsteadiness occurs somewhere in the system. There are so many process times operative in a rocket system that it is easily possible to have essential unsteadiness with respect to several processes but quasi-steady behavior with respect to others. Because of this complexity it is sometimes difficult to reconcile results of different workers on what appears to be the same problem.

This chapter summarizes the state of knowledge of unsteady behavior of feed system flow, atomization, combustion, and wave propagation processes. The treatments of these topics make use of the usual distinctions of engineering systems. That is, consideration is given to linear and nonlinear behavior, lumped or distributed parameter systems, and quasi-steady or unsteady behavior. Presumably, perfect knowledge of all pertinent processes would allow a comprehensive description of unsteady behavior of the rocket system by an appropriate patching of the elemental processes. Such syntheses are discussed in Chapters 4 and 5, but it will be apparent that the knowledge of the elements is insufficient to expect much success without a good deal of empiricism introduced in the synthesis procedures. Whereas the gas dynamics and feed system dynamics are relatively well understood, the injection and combustion processes are not. In Chapter 2, it is indicated that under certain restrictions the steady-state description of injection and combustion is well in hand. However, the actual structure of the steady-state is not understood in sufficient detail to form a basis for unsteady analysis. There are, of course certain problems in wave propagation that have escaped solution, but the pacing item appears to be the injection and combustion processes.

3.2 FLOW IN PROPELLANT FEED SYSTEMS*

High performance rocket engine systems are usually achieved by minimizing feed system losses, thereby minimizing the overall thrust/weight ratio. However, the losses introduced by orifices, high-pressure-drop injectors, etc., provide one of the most direct methods of obtaining dynamic stability in the lower frequency range. Thus, there must often be a tradeoff between the static and dynamic performance of the system. Occasionally a feed system may be tuned to force a stable coupling with the combustion process by use of passive systems (e.g., quarter-wave tubes, Helmholtz or Quincke resonators) that introduce a resonance out of phase with an otherwise unstable system resonance. Hopefully, when both feed system and combustion dynamics are more thoroughly understood, stable systems will be a matter of standard design practice. For the present, analytical methods are helpful in (1) estimating the dynamics of the coupled feed system, (2) providing a method for understanding test data, and (3) providing a "logical" test facility where, after correlation with test data, the effects of system changes may be evaluated.

Evaluating the dynamics of a feed system requires an extension of steady-state calculations to include inertance and capacitance effects. The inertance is the tendency of the fluid to resist flow rate changes due to pressure forces. Similarly, the capacitance is the tendency to resist pressure changes, despite changes in flow rate. Both the inertance and capacitance effects are time-dependent and enable a fluid system to exhibit preferred or characteristic frequencies. These frequencies are analogous to those exhibited by a vibrating string, or more closely, an organ pipe. This section describes this "acoustic" behavior and then discusses methods of formulating and studying the dynamics of a propellant feed system.

The following nomenclature pertains to Sect. 3.2:

A_{jk}	Normalization coefficient
a	Diameter of plane duct blockage (see Fig. 3.2.2d)
b_o	Orifice radius
f	Friction factor
k_o	Orifice inertance correction coefficient

* J. A. Nestlerode, J. R. Fenwick, and L. E. Sack, Authors.

$\mathcal{L}'$	Inertance of elbow associated with distance along centerline
$\mathcal{L}''$	Inertance of elbow due to curvature
l_o	Orifice length
l_w	Wavelength
$\tilde{m}_j$	Normalized flow rate for mode j
R_t	Tip radius of pump impeller
S	Peripheral area of pump impeller
ν_j	Damping coefficient for j-th mode
Φ	Pump flow coefficient
ϕ	Turning angle of elbow
Ψ	Pump head coefficient
Ω	Pump impeller rotational speed

Subscripts:

ar	Anti-resonance
j	Fourier mode index
k	Location index
l	Feed line
r	Resonance

3.2.1 Feed System Acoustics

Long feed lines tend to exhibit so-called "standing" waves, which result from the superposition of incident and reflected traveling waves. Standing wave patterns have spatially fixed points of maximum and minimum pressure (and velocity) fluctuation, termed antinodes and nodes, respectively. For low velocity flow, the standing wave frequencies may be calculated from fluid properties and feed system characteristics by the well-known relationship

$$l_w f = a \qquad (3.2.1\text{–}1)$$

where l_w is the wavelength, f is the frequency, and a is the sound velocity in the fluid. To relate to a characteristic feed system dimension requires some insight into the nature of standing waves. Fig. 3.2.1 shows a possible standing wave in a line connecting a tank and a downstream constriction. For a standing wave, a velocity node is a pressure antinode, and vice versa. The tank represents a large capacitance, and so maintains relatively constant pressure despite flow fluctuations. On the other hand, the constriction has a high inertance and will attempt to maintain constant flow despite pressure fluctuations. For the wave shown in Fig. 3.2.1, only $\frac{3}{4}$ of a complete wavelength appears, or $l_w = \frac{4}{3}l$. This mode would be referred to as the second closed-open acoustic mode of the duct; the fundamental mode would have $l_w = 4l$. Any mode compatible with the boundary or end conditions can be expected. Hence, from a determination of the end conditions the standing-wave resonances can be predicted. A troublesome frequency may be eliminated by placing a restrictive or capacitive device at the proper location.

The other basic type of resonance is that of the classical Helmholtz resonator, in which a large-capacitance element is coupled directly to a relatively short element of large inertance. In mechanical terms, the inertance element may be thought of as a mass and the capacitive element as a spring. The coupled system has a natural frequency given by

$$f = \frac{a}{2\pi}\sqrt{\frac{A}{l\mathcal{V}}} \qquad (3.2.1\text{–}2)$$

where $\mathcal{V}$ is the volume of the capacitive element and l is the effective length and A the cross sectional area of the inertance element. For the idealized Helmholtz resonator, harmonics do not occur.

By a cursory inspection of a given propellant feed system, with the concepts of Helmholtz and standing-wave resonators in mind, estimates of natural frequencies and, therefore, of probable frequencies of potential feed-coupled instabilities are revealed. For systems in which nodes or antinodes are not obvious because of more complex geometry or many interrelated components, it becomes necessary to use equations of a more general form.

3.2.2 Component Dynamics

3.2.2.1 *Lumped-parameter approach.*—In general, a fluid system can be simulated by an equivalent resistance, capacitance, and inductance network. In the lumped-parameter approach the system is divided into many small "lumps" of resistance, capacitance, and inductance, so that the system is governed by a set of simultaneous, ordinary differential equations rather than by partial differential equations. The analytical description may be made as accurate as desired in the frequency domain by choosing a sufficient number of lumps. A useful procedure is to determine the wavelength of the highest frequency of

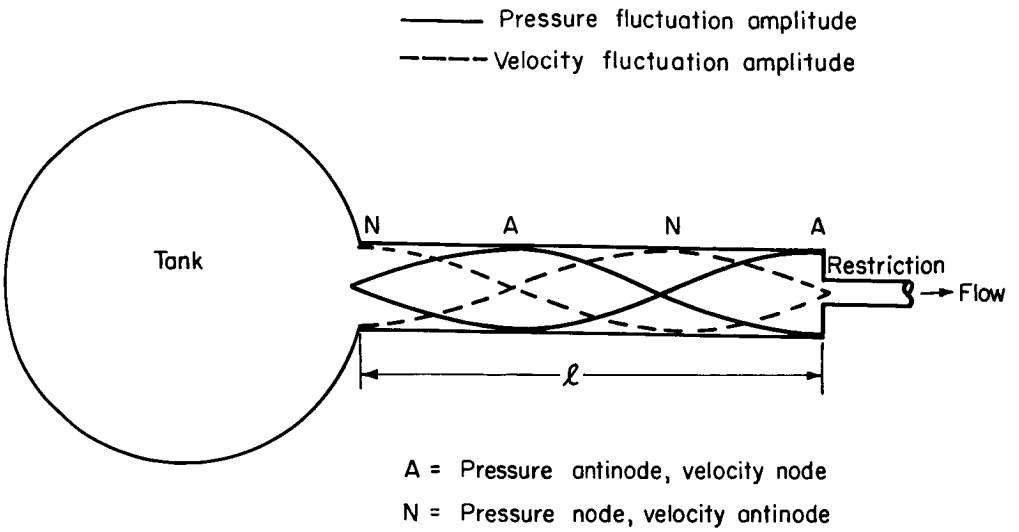

FIGURE 3.2.1.—Possible standing wave in a feed line.

interest from Eq. (3.2.1–1) and then to use no fewer than eight lumps per wavelength.

The most common elements encountered in feed systems are uniform flow passages. For such a feed line section (Fig. 3.2.2a) a generally accepted representation for pressure loss is

$$p_1 - p_2 = \mathcal{R}\dot{m}^2 \qquad (3.2.2\text{–}1)$$

where the resistance $\mathcal{R}$ is related to the friction factor $\mathfrak{f}$ by

$$\mathcal{R} = \frac{\mathfrak{f}l}{2\rho DA^2} \qquad (3.2.2\text{–}2)$$

When the time variation of the fluid variables is considered, there are additional contributions to the flow and pressure terms. First, consider inertia alone, i.e., the acceleration of a fluid column, Newton's second law gives

$$p_1 - p_2 = \left(\frac{l}{A}\right)\frac{d\dot{m}}{dt} = \mathcal{L}\frac{d\dot{m}}{dt} \qquad (3.2.2\text{–}3)$$

where $\mathcal{L}$ is the fluid inertance.

The remaining fundamental dynamic term is the fluid capacitance, a measure of the compressibility of the fluid, which is the change in the mass m of fluid stored in an elemental volume v for a unit change in the pressure in the volume, i.e.,

$$\mathcal{C} = \frac{\partial m}{\partial p}$$

From Fig. 3.2.2b, it can be seen that

$$m = \int (\dot{m}_1 - \dot{m}_2)\,dt$$

Thus

$$p = \frac{1}{\mathcal{C}}\int (\dot{m}_1 - \dot{m}_2)\,dt \qquad (3.2.2\text{–}4)$$

or

$$\dot{m}_1 - \dot{m}_2 = \mathcal{C}\frac{dp}{dt}$$

where the capacitance $\mathcal{C}$ is related to the bulk modulus K of the fluid by

$$\mathcal{C} = \rho\frac{\mathcal{V}}{K} \qquad (3.2.2\text{–}5)$$

The representation of a feed system must include not only the relatively uniform feed lines,

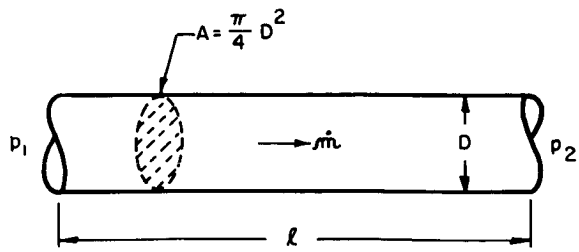

FIGURE 3.2.2a.—Section of feed line for derivation of lumped resistance and inertance relation.

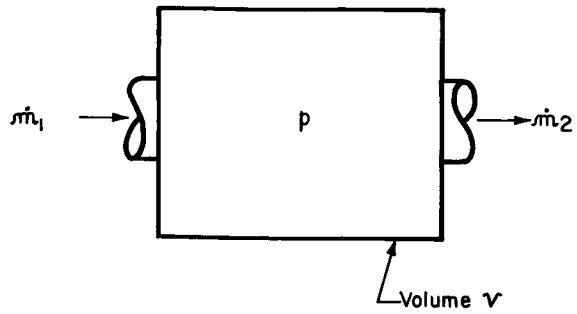

FIGURE 3.2.2b.—Elemental volume for derivation of lumped capacitance relation.

but also system elements such as elbows, valves, orifices, tapered sections, and pumps. Such elements, which are characterized by three-dimensional flow fields, may influence, or may even control, both the static and dynamic behavior of the feed system. Even though one-dimensional flow is usually assumed for low and intermediate frequency problems, it is the three-dimensional nature of these elements that influences the one-dimensional dynamics. For example, a very short orifice clearly has resistance. Moreover, because of the characteristic pattern of the flow through the orifice, an effective inertance is present that is greater than can be accounted for by the orifice length alone. Similarly, the three dimensional flow within a centrifugal pump results in local cavitation, with a resulting significant local decrease in the bulk modulus.

In evaluating the effective inertance of a component, the theoretical and experimental work of Jackson[385] is of particular value. In this work, elbows, duct blockage, orifices, and tapered sections were investigated. In the following paragraphs, it is assumed that the resistance of each component is readily obtainable by analytical or empirical techniques.

ELBOWS: The inertance of an elbow can be regarded as the sum of two contributions: (1) that associated with the distance along the centerline ($\mathcal{L}'$) and (2) the additional inertance due to curvature ($\mathcal{L}''$). Fig. 3.2.2c shows $\mathcal{L}''$ values for both curved and mitered configurations. For curved elbows of large radius ratio the curvature inertance $\mathcal{L}''$ is negligible. On the other hand, for mitered elbows, the curvature inertance ($\mathcal{L}''$) is a larger part of the total inertance.

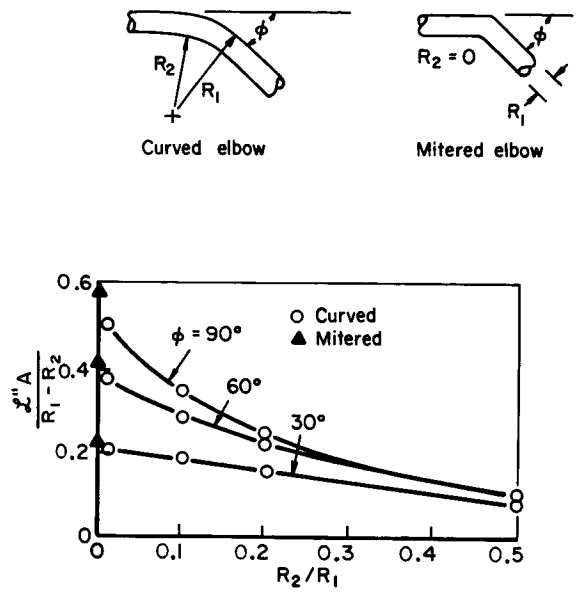

FIGURE 3.2.2c.—Inertance $\mathcal{L}''$ due to duct curvature.

DUCT BLOCKAGE: When a plane barrier is placed in a duct, the inertance contribution of the blockage has been shown by Jackson[385] to be as in Fig. 3.2.2d.

ORIFICES: For low velocity flow ($V < \omega l_o$) through orifices with small length-to-diameter ratio, the inertance is given by[702]

$$\mathcal{L} = \frac{l_o}{\pi b_o^2}\left(1 + 1.7\frac{b_o}{l_o}\right) \qquad (3.2.2\text{–}6a)$$

where b_o is the orifice radius and l_o is the orifice length. At higher velocities $\mathcal{L}$ decreases until

$$\mathcal{L} = \frac{3}{8}\frac{l_o}{\pi b_o^2}\left(1 + 1.7\frac{b_o}{l_o}\right) \qquad (3.2.2\text{–}6b)$$

at a Reynolds number of about 2000. To account for wall effects, Eq. (3.2.2–6) can be modified[108] to

$$\mathcal{L} = \frac{3}{8}\frac{l_o}{\pi b_o^2}\left(1 + 1.7k_o\frac{b_o}{l_o}\right) \qquad (3.2.2\text{–}7)$$

where the coefficient k_o is given by

$$k_o = 1 - \frac{2b_o}{D} \qquad (3.2.2\text{–}8a)$$

or if the feed line diameter D is less than about 2 centimeters,

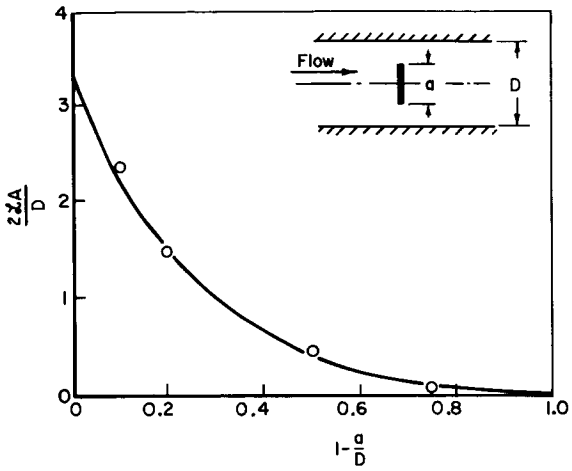

FIGURE 3.2.2d.—Inertance due to duct blockage.

$$k_o = 1 - \frac{2b_o}{D}\left[0.245(3+\sqrt{b_o})\right]^{1/3} \quad (3.2.2\text{–}8b)$$

where b_o is in centimeters.

PUMPS: The proper treatment of pumps requires more than just the simulation of the head-flow relationships. The capacitance and inertance can be equally important, particularly in the high-speed pumps used in rocket engine systems. The capacitance of a pump is larger than that predicted by Eq. (3.2.2–5) because of the cavitation that normally occurs. The author is unaware of any technique other than testing that is presently available for determining the effective capacitance of a pump. The inertance of a centrifugal pump can be estimated from the empirical equation

$$\mathcal{L} = \frac{R_t}{3S\Phi^2} = \frac{\Delta p}{3\Phi\Psi\dot{m}\Omega} \quad (3.2.2\text{–}9)$$

where R_t is the tip radius, S is the impeller peripheral area, Φ is the flow coefficient, Ψ is the head coefficient, and Ω is the impeller rotational speed.

SUMMARY: In a lumped-parameter analysis, the procedure is to define the maximum frequency required and then to write the ordinary differential equations for the pressure within the elements and the flow between elements. Application of boundary conditions such as tank pressure or chamber pressure relations enables simultaneous solution of the equations. The obvious drawback of the lumped-parameter approach is that the number of equations increases rapidly for frequencies upward of 100 Hz. For such situations there are other methods of solution that are more tractable.

3.2.2.2 *Continuous-parameter approach.*—The continuous-parameter feed line description is based on the one-dimensional wave equation (water hammer equation).[43,103,453] The compressibility of a small element of liquid is expressed as

$$\frac{\partial p}{\partial t} = \frac{K_L}{\rho_L A_l}\frac{\partial \dot{m}}{\partial x} \quad (3.2.2\text{–}10)$$

and the inertia of the element is expressed as

$$\frac{\partial p}{\partial x} = \frac{1}{A_l}\frac{\partial \dot{m}}{\partial t} \quad (3.2.2\text{–}11)$$

Eqs. (3.2.2–10) and (3.2.2–11) may be solved in many ways, but for simulation purposes, two representations are most useful. Both are solutions for time-varying pressure and flow rate at two stations along a length of feed line (Fig. 3.2.2e):

$$p_2(t) = -\frac{a_L}{A_l}\dot{m}_2(t) + 2p_1(t-t_l) + \frac{a_L}{A_l}\dot{m}_2(t-2t_l) - p_2(t-2t_l) \quad (3.2.2\text{–}12a)$$

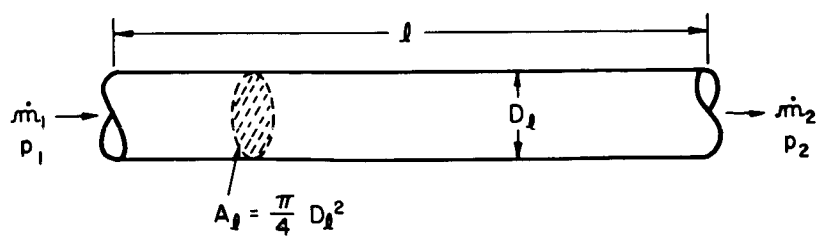

FIGURE 3.2.2e.—Section of feed line for derivation of continuous-parameter relations.

$$\frac{a_L}{A_l}\dot{m}_1(t)=p_1(t)+2\frac{a_L}{A_l}\dot{m}_2(t-t_l)$$

$$-p_1(t-2t_l)-\frac{a_L}{A_l}\dot{m}_1(t-2t_l) \qquad (3.2.2\text{–}12b)$$

or

$$p_2(t)+\frac{a_L}{A_l}\dot{m}_2(t)=p_1(t-t_l)+\frac{a_L}{A_l}\dot{m}_1(t-t_l) \qquad (3.2.2\text{–}13a)$$

$$p_1(t)-\frac{a_L}{A_l}\dot{m}_1(t)=p_2(t-t_l)-\frac{a_L}{A_l}\dot{m}_2(t-t_l) \qquad (3.2.2\text{–}13b)$$

where $a_L^2=K_L/\rho_L$ and $t_l=l/a_L$. From these equation pairs (representing a four-terminal network), the Laplace transforms may be written

$$p_2[1+\exp(-2t_l s)]$$

$$=-\frac{a_L}{A_l}\dot{m}_2[1-\exp(-2t_l s(]+2p_1\exp(-t_l s) \qquad (3.2.2\text{–}14a)$$

$$\frac{a_L}{A_l}\dot{m}_1[1+\exp(-2t_l s)]$$

$$=p_1[1-\exp(-2t_l s)]+\frac{2a_L}{A_l}\dot{m}_2\exp(-t_l s) \qquad (3.2.2\text{–}14b)$$

or

$$p_2+\frac{a_L}{A_l}\dot{m}_2=\left(p_1+\frac{a_L}{A_l}\dot{m}_1\right)\exp(-t_l s) \qquad (3.2.2\text{–}15a)$$

$$p_1-\frac{a_L}{A_l}\dot{m}_1=\left(p_2-\frac{a_L}{A_l}\dot{m}_2\right)\exp(-t_l s) \qquad (3.2.2\text{–}15b)$$

The description of the flow dynamics is completed by specifying two boundary conditions. In a complex feed system, with several distinct sections of feed line, the boundary conditions often take the form of matching conditions at the places where the line sections are connected to each other or to other system components (Sect. 5.4.2). The boundary conditions determine the resonances of the feed line. For example, a line connecting a large tank and a closed end has resonances at frequencies given by

$$\omega_r=\frac{k_r\pi}{2t_l} \qquad k_r=1, 3, 5, \cdots$$

Anti-resonances occur at

$$\omega_{ar}=\frac{k_{ar}\pi}{t_l} \qquad k_{ar}=0, 1, 2, 3 \cdots$$

If the closed end is replaced by an orifice, the resonances will still be apparent, but they will not be conservative and will be changed in frequency unless a pressure anti-node (flow node) occurs at the orifice. Fig. 3.2.2f illustrates the damping effect of an orifice in a fluid line.

The equations presented in this section are valid for a lossless line. With a pressure loss included, the pressure resonances are damped, since any pressure fluctuation results in a change in orifice flow rate and hence an energy loss. Correspondingly, the anti-resonance is conservative since input flow is of such phase that it exactly matches flowrate in the pipe and no pressure fluctuation takes place across the orifice. Thus, with damping present, the resonant frequencies are slightly reduced whereas the anti-resonant frequencies remain fixed.

3.2.2.3 *Modal techniques.*—Lumped-parameter analyses have been shown to be extremely flexible and powerful; they also maintain a physical significance in the time domain. However, complex systems often become difficult to evaluate in the frequency domain and require a large amount of computer equipment. To minimize computer requirements, system frequency response is often compromised. Distributed-parameter techniques have extended frequency-response capability but become difficult to handle when nonuniform systems or time-varying nonlinearities are encountered. Modal analysis is an additional technique that often has advantages over either the lumped- or distributed-parameter methods.

Although modal techniques have had standard acceptance in treating mechanical and structural vibrations, they have not been used generally to simulate fluid systems. The basis of modal analysis is the concept of characterizing a system, or obtaining a solution, as a function of boundary

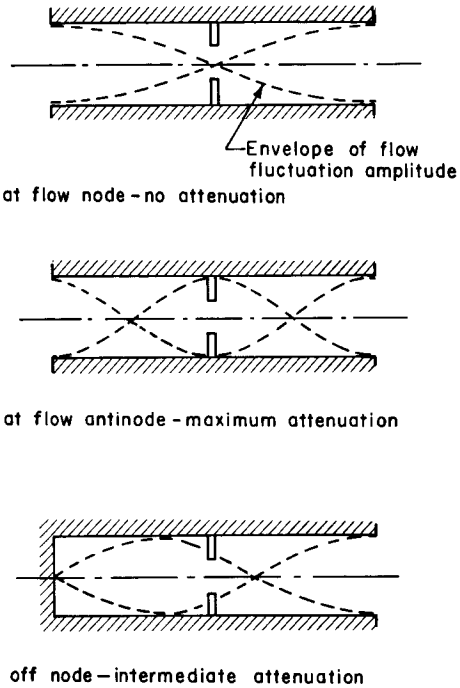

FIGURE 3.2.2f.—Damping effect of an orifice in a fluid line.

variables in terms of a Fourier series of frequency-dependent terms. A detailed discussion of modal analysis, including a mathematical development of the solution, is given in Ref. 139. Only a brief summary is given here.

The flow rate $\dot{m}_k$ at any location k in a feed system is written as

$$\dot{m}_k = \sum_{j=0}^{\infty} \dot{m}_{jk} \qquad (3.2.2\text{–}16)$$

where the index j denotes a Fourier mode having a characteristic frequency ω_j. For a uniform area flow passage

$$\omega_j = \frac{j\pi a_L}{l} \qquad (3.2.2\text{–}17)$$

A normalized flow rate for mode j is defined by

$$\tilde{m}_j = \frac{s \sum_{k=0}^{N} A_{jk} p_k(s)}{s^2 + 2\nu_j s + \omega_j^2} = \frac{\dot{m}_{jk}}{A_{jk}} \qquad (3.2.2\text{–}18)$$

where p_k is a boundary or input pressure at location k, the A_{jk} are normalization coefficients, and s is the complex Laplace transform operator. The damping coefficient ν_j introduces losses. The steady-state coefficient ν_o is used to satisfy pressure drop conditions; the values of the high-frequency damping coefficients ν_j are usually not well known, but reasonable values are 0.03 to 0.05, unless a concentrated resistance is present. Once a solution is obtained in terms of the Laplace variable, the solution in the time domain can be obtained by performing the inverse transformation.

The normal disadvantages of an infinite-series solution are not present with the modal analysis since truncating the series only limits the frequency response of the solution to a definable frequency range. Thus, the frequency response of the solution can be tailored to the requirements of the analysis. An additional advantage of the modal technique is that the form of the solution is the same regardless of the complexity of the system or the method used to evaluate the Fourier coefficients. A system can be described in as fine detail as desired, using such conventional methods as finite difference nets. Once a finite difference model is formulated (a model that might be too large to be mechanized to give a transient solution on the computer), conventional eigenvalue techniques can be used to obtain the Fourier coefficients. Thus, the modal analysis allows use of the powerful finite difference techniques but does not require the solution of the finite difference net as part of a larger system, nor does it require the solution for internal coordinates. Therefore, it is like most distributed-parameter approaches in that an input-output solution is obtained.

3.2.3 System Response

The purpose of a feed system description is, of course, to provide a boundary condition for the analysis of the combustion and flow in the thrust chamber. Three approaches are used to describe the effect of the feed system. The simplest and most commonly used approach is that of a limiting condition, such as constant injection pressure or constant injection flow. If the engine operation is not strongly dependent on the feed system behavior, then such a simple approach is justified. However, in many cases more information is needed. A second approach is to use a feed system transfer function derived by combining the linearized equations for the feed system components. Using this approach the engine problem may be solved in either the time or frequency

domain. The third approach involves the solution of the nonlinear differential equations in the time domain. This technique may be necessary if wide-range operation of the system is required or if limit-cycle* operation is to be studied. Of the three approaches, the linear approximation is generally the most useful.

The feed system transfer function is derived from the set of equations for the components by writing each variable as the sum of a steady-state value and a perturbation. Subtraction of the steady-state equations gives a set of relations among the perturbations. These relations are then Laplace-transformed. Finally, using substitution to eliminate variables, a feed system transfer function

$$G(s) = \frac{\dot{m}_i'(s)}{\Delta p'(s)}$$

is obtained. By setting $s = i\omega$, the vector relation $G(\omega)$ between pressure and mass flow rate oscillations can be determined. Usually, this type of frequency response function is sufficient for engine stability studies.

Since the substitution process to obtain $G(s)$ is quite tedious for complex feed systems, it is standard practice to assemble the linear equations on a computer and then to determine $G(\omega)$ for the desired frequency range. Using a digital computer, this determination involves the solution of a matrix of equations with complex coefficients. On an analog computer, a sinusoidal voltage representing $\Delta p'$ is applied and the amplitude and phase of the voltage representing $\dot{m}_i'$ are measured. Curve-fitting techniques have been developed to allow the frequency response thus determined to be represented analytically by a ratio of polynomials.[453]

In choosing the frequency response requirements for components of a finite difference model, it is desirable to use mathematical descriptions that are valid from zero (steady-state) to a frequency well above (usually about 10 times) the frequency range of interest. A benefit of using such component transfer functions is that when many transfer functions are mathematically joined the steady-state gain ratio is a very convenient check. Furthermore, a thorough understanding of dynamic coupling effects at lower frequencies often allows a better understanding of the higher frequency effects.

In attempting to study the characteristics of an engine system, the frequency domain techniques have, as discussed above, particular advantages and disadvantages. Alternatives to the frequency domain studies are the less sophisticated time domain response studies. Time domain analysis makes up for the inability to use classical stability criteria by providing not only an extremely powerful analytical tool, but also a practical method of incorporating multiple and massive nonlinearities, and allows correlation with actual transient or limit-cycle test data.

The significance of being able to correlate analytical results with engine system data cannot be overemphasized. The importance of such correlation is twofold: (1) to verify the validity of the model, and (2) to convince others who are unfamiliar with analytical models (but who must accept and use the model results) that the model really represents the actual engine system. Fundamental to correlating with most engine system limit-cycle data is the necessity to include multiple, time-dependent nonlinearities. Most time-dependent analytical models allow the inclusion of any definable nonlinearity.

Another, and certainly not insignificant, advantage of time domain analyses is that they lend themselves to analog simulation. Analog techniques are of particular value when iteration, survey, optimization, or real-time data-input studies are to be made. In addition, the output recorders are often identical to those used to display engine test data, allowing an excellent visual correlation between analysis and experiment.

At times it is necessary to define the effect of feed system response on an apparent transverse mode of combustion instability. A mathematical model of the feed system can be developed that allows a detailed representation of complex injector passageways and also allows for the distribution of oscillatory chamber pressure across the face of the injector. Such a feed system model utilizes the matrix representation of n-port networks to combine the linearized equations describing the interconnection of manifolds, channels, coolant tubes, and injection orifices.[98,720]

* That is, oscillation at some relatively constant amplitude.

As an example, a feed system model using 28-port fuel and oxidizer networks is illustrated in Figs. 3.2.3a and 3.2.3b. In this example, the injector face has been divided into seven regions (Fig. 3.2.3c). The injector networks can be split into sub-networks to match the measured pressure data. The overall fuel network shown in Fig. 3.2.3a is split into two sub-networks, one representing the injector face circuit and the other, the chamber coolant circuit. A useful division for the oxidizer injector is shown in Fig. 3.2.3b.

3.2.4 Comparison of Analysis and Experiment

An effective example of the agreement between analysis and experiment was provided by the occurrence of a feed-system-coupled oscillation during development of the F-1 engine.[509] Four aspects of this oscillation were significant: (1)

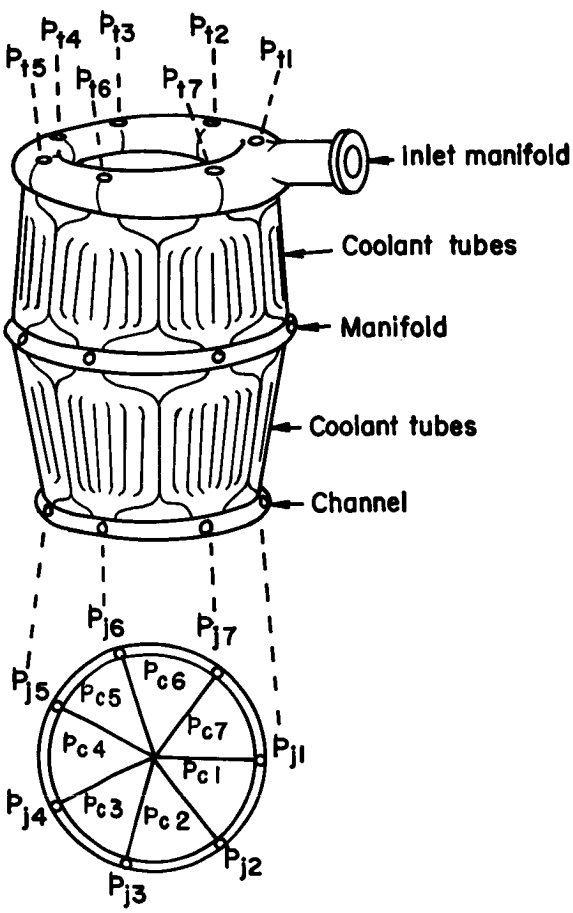

FIGURE 3.2.3a.—Fuel injector network.

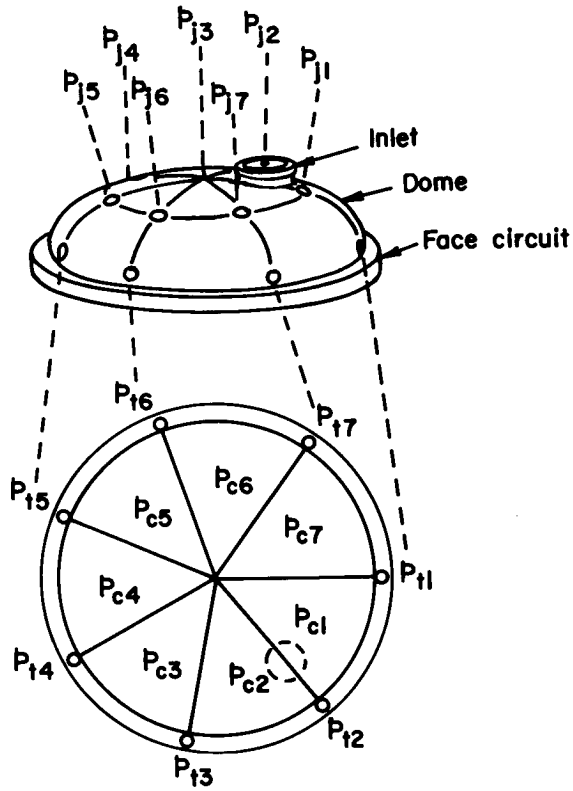

FIGURE 3.2.3b.—Oxidizer injector network.

the system was physically large enough to accommodate a large number of measurements throughout the feed system, and the existence of the measurements did not affect the system, (2) the application of suppression devices was entirely successful, (3) the analysis was further confirmed by laboratory-scale acoustic modeling techniques, and (4) it was demonstrated that harmonics at least as high as the sixth may be sources of troublesome frequencies.

A schematic of the F-1 thrust chamber test facility is shown in Fig. 3.2.4a. Oscillations at 420 Hz were noted in the LO_2 inlet and chamber, but not at the splitter. A mathematical analysis of the feed system indicated many possible natural resonant frequencies and overtones, among which a standing wave between the splitter and the chamber had a sixth acoustic-mode resonance at 420 Hz. In addition, that particular resonance had a pressure node at the splitter, in agreement with the test data.

To confirm the existence of a sixth-mode resonance in a complex feed system, a Plexiglas

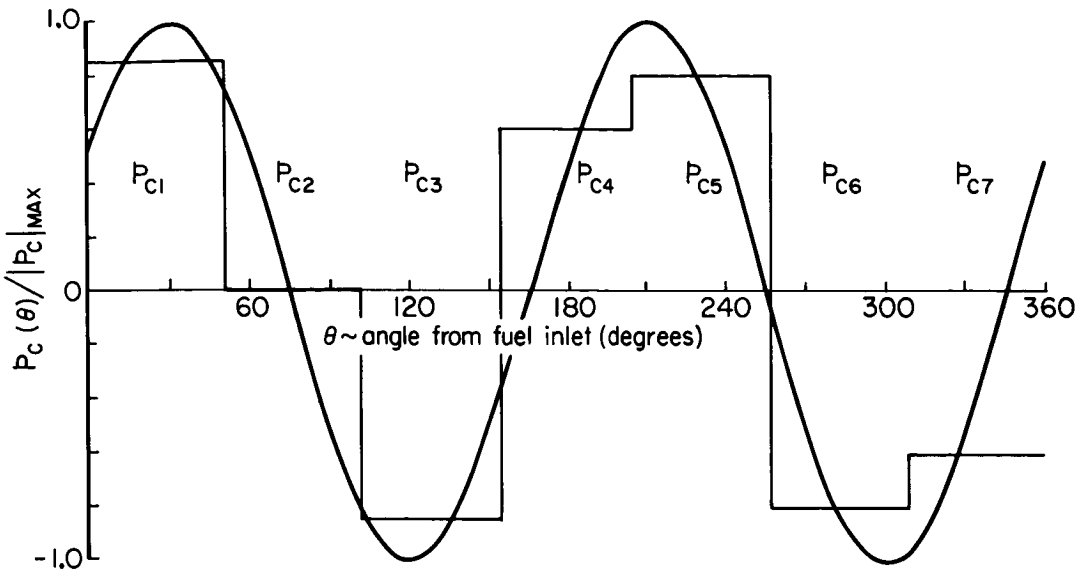

FIGURE 3.2.3c.—Approximation of circumferential pressure distribution by seven constant-pressure regions.

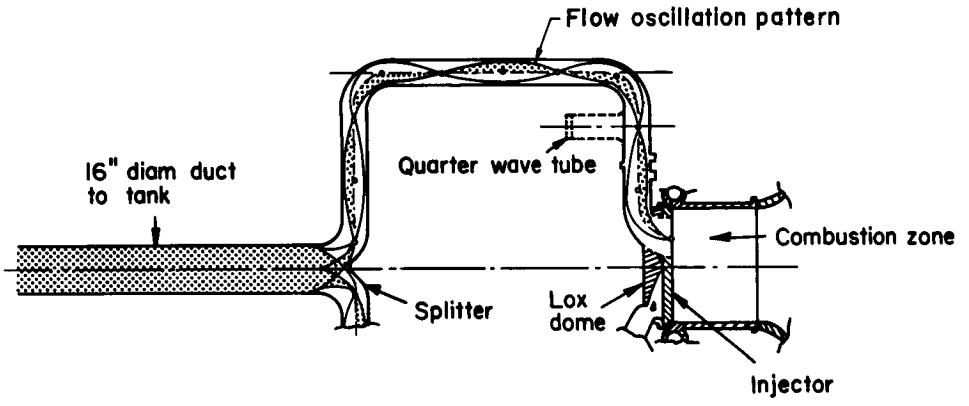

FIGURE 3.2.4a.—Schematic of F-1 thrust chamber feed system showing observed wave pattern.

scale model was built. When excited with an acoustic driver in the chamber, the model showed all the pressure node and antinode characteristics of a sixth-mode oscillation between the chamber and splitter. A traverse of the frequency spectrum clearly exhibited the sixth-mode (Fig. 3.2.4b). Additional measurements on the actual thrust chamber test stand further confirmed the mode identification.

To suppress the oscillations a side-branch quarter-wave-tube resonator was placed at the location of a pressure antinode in the feed system. According to theory, such a device should split the resonance into two resonances of lesser magnitude. This prediction was confirmed on the acoustic model. Fig. 3.2.4c shows the frequency spectrum obtained with a quarter-wave-length resonator in each leg of the inlet ducting. With resonators installed on the test stand, several hundred hot-firing tests, some with hardware that had previously exhibited the oscillations, were conducted with no occurrence of the 420 Hz oscillation.

3.3 INJECTION PROCESSES

Except for a few rather widely scattered investigations, the consideration of the dynamic

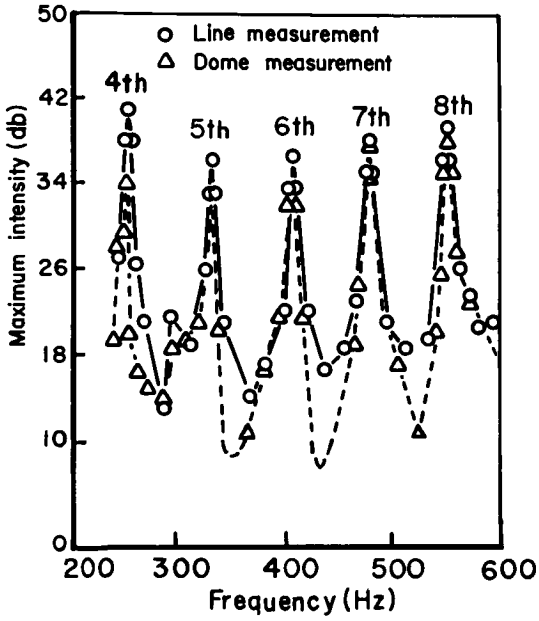

FIGURE 3.2.4b.—Spectral characteristics of feed system model without resonators.

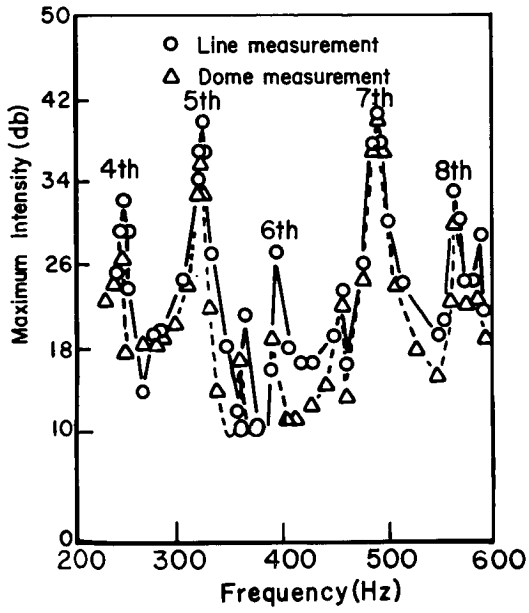

FIGURE 3.2.4c.—Spectral characteristics of feed system model with quarter-wave tubes.

aspects of liquid propellant injection processes is a recent development. Early studies of low frequency instability concentrated on injection rate oscillations as the controlling mechanism. When attention shifted to the high frequency problem, the injection rate was assumed to be constant and droplet burning processes were identified as the controlling factors. It is now generally recognized that the intermediate processes of atomization and mixing, which serve to prepare the injected propellants for combustion, can be of great importance in both low and high frequency instability. It is also clear that these intermediate processes may provide a significant coupling between injection rate oscillations and droplet burning dynamics.

The emphasis in this section is on the character of the injection sprays rather than on the mass flux variation, which was discussed in Sect. 3.2. Consideration is given to the effects of oscillatory conditions on drop size as well as the spatial distributions of mass and mixture ratio, both as mean and fluctuating quantities. The discussion is divided into three parts. First, the effects of upstream conditions on the formation of propellant sprays are reviewed. These conditions include flow rate oscillations, hydraulic flip, and injector vibration. In the second part, the emphasis is placed on the response of the injection sprays to pressure and velocity oscillations in the combustion chamber. Consideration is given to the displacement and breakup of jets and sprays as well as to the mixing of the propellants, both in liquid and vapor phases. Attention is restricted to small perturbations from the mean operating conditions. The final part of this section deals with the effects of shock waves on the breakup of liquid jets and drops.

It should be noted that the coupling of these processes with the combustion and flow conditions in the chamber to form a closed feedback loop is not considered in this section. That discussion is deferred to Chapters 4 and 5, in which complete theoretical models of instability are presented.

The following nomenclature pertains to Sect. 3.3:

C_D	Drag coefficient
d_{Lo}	Initial drop or jet diameter
d_s	Effective spray width
$\tilde{f}$	Instantaneous burning rate
k	Liquid-gas momentum exchange coefficient
l	Velocity interaction index
q	Dynamic pressure

T_b	Dimensionless droplet breakup time, $=\tau_b\sqrt{\beta}$
X_s	Spacing between fuel and oxidizer sprays
Y_{OX}	Mass fraction of oxidizer in spray
β	Gas/liquid density ratio
δ	Displacement
η	Gas/liquid viscosity ratio
τ_b	Dimensionless droplet breakup time, $V(t_b/d_L)$
τ_c	Characteristic combustion time
τ_x	Time required for a fluid particle to travel from injector face to a distance x downstream
τ_y	Relaxation time for droplet burning process

Subscripts:

d	Threshold level for nonlinear mixing
s	Saturation level, nonlinear mixing

3.3.1 Effects of Upstream Conditions*

The effects on injection streams of upstream disturbances can take several forms. One form is a bunching of the propellants at a location downstream of the injector, the so-called "klystron" effect. Another change in the character of the injected propellants can take place via "hydraulic flip," that is, the shifting from a cylindrical jet to a bushy jet and vice versa. A marked increase in the jet velocity can cause increased aerodynamic breakup as well as altering that portion of the droplet generation associated with ligament breakup. At the other extreme (i.e., a sharp decrease in jet velocity following a feed system disturbance) flow rates can be effectively stopped, necessitating what is essentially a restart of the engine.[154]

3.3.1.1 *Flow rate oscillations.*—The klystron effect has been studied by several investigators.[475,268] Sinusoidal flow variations can be converted to sharply spiked waveforms at downstream locations by this mechanism, which may thus be a source of low and intermediate frequency instability.[268] The axial flow variations in the spray are very similar to the naturally occurring "Christmas tree" or "pagoda" effect common to impinging-jet injectors (Fig. 3.3.1a).[341,344] Close correspondence of these natural variations to intermediate frequency instabilities has been shown in hot firings; chamber pressure fluctuations were also correlated with the spray oscillations.[749]

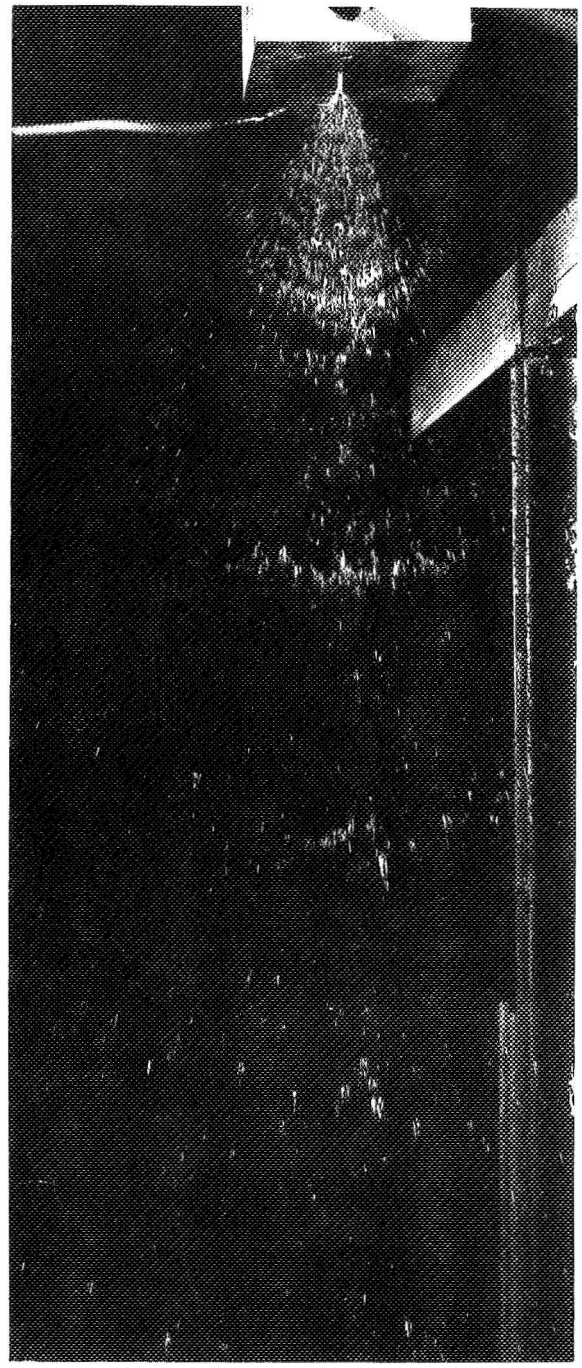

FIGURE 3.3.1a.—Klystron effect, impinging jets.

* D. T. Harrje and F. H. Reardon, Authors, with contributions from J. A. Nestlerode, J. R. Fenwick, and L. E. Sack.

A simplified illustration of the unsteady injection process is shown in Fig. 3.3.1b. Because the faster fluid particles overtake the slower ones, at some axial station the maximum-velocity particles will theoretically be at the same location as the minimum-velocity particles. Continuity considerations dictate that the fluid originally between the maximum- and minimum-velocity particles should still be approximately between them. Hence the fluid appears to have "clumped." The klystron effect has been well established in electrical systems and is commonly used to provide amplification of high frequency signals. Experiments have indicated the applicability of this effect to fluid systems.[268] The photograph of a single jet in Fig. 3.3.1c shows the severe clumping illustrated schematically in Fig. 3.3.1b. The occurrence of the klystron effect with impinging jets is shown in Fig. 3.3.1a. The development of a single clump is shown in Fig. 3.3.1d.

The flow rate at any axial distance x from the injector is[268]

$$\dot{m}(x, t) = \left\{ \frac{\dot{m}_i}{1-\tau_x \underline{\dot{m}}(\ddot{m}_i/\dot{m}_i^2)} + \sum_{j=1}^{\infty} \left[\frac{\underline{\dot{m}}-\dot{m}_i}{\dot{m}_i} \bar{\tau}_x \right]^j \frac{d^j}{dt^j} \left[\frac{\dot{m}_i}{1-\tau_x(\underline{\dot{m}}\ddot{m}_i/\dot{m}_i^2)} \right] \right\}_{t-\bar{\tau}_x} \quad (3.3.1\text{–}1)$$

where $\ddot{m}_i = d\dot{m}_i/dt$ and τ_x is the time required for a fluid particle to travel from the injector to station x. Eq. (3.3.1–1) is valid for $\tau_x \underline{\dot{m}}(\ddot{m}_i/\dot{m}_i^2) < 1.0$. The derivative terms, produced by variations in τ_x, tend to "time-squeeze" the wave form. In a closed-loop system simulation, at least the first derivative term should be used to minimize flow rate errors, although assuming a constant τ_x leads to the simpler expression

$$\dot{m}(x, t) = \left[\frac{\dot{m}_i}{1-\tau_x \underline{\dot{m}}(\ddot{m}_i/\dot{m}_i^2)} \right]_{t-\bar{\tau}_x} \quad (3.3.1\text{–}2)$$

Typical wave shapes resulting from Eqs. (3.3.1–1) and (3.3.1–2) are compared to that for the pure time delay, $\dot{m}(x, t) = \dot{m}_i(t-\bar{\tau}_x)$, in Fig. 3.3.1e.

Eq. (3.3.1–1) may be linearized by assuming that both $\underline{\dot{m}} - \dot{m}_i$ and $\ddot{m}_i$ approach zero. Thus,

$$\frac{\dot{m}'(x, t)}{\underline{\dot{m}}} = \frac{\dot{m}_i(t-\bar{\tau}_x)}{\underline{\dot{m}}_i} + \bar{\tau}_x \frac{d}{dt}\left(\frac{\dot{m}_i}{\underline{\dot{m}}_i}\right)_{t-\bar{\tau}_x} \quad (3.3.1\text{–}3)$$

or in Laplace notation

$$\frac{\dot{m}(x, s)}{\underline{\dot{m}}} = \exp(-\bar{\tau}_x s)(1+\bar{\tau}_x s)\frac{\dot{m}_i(s)}{\underline{\dot{m}}_i} \quad (3.3.1\text{–}4)$$

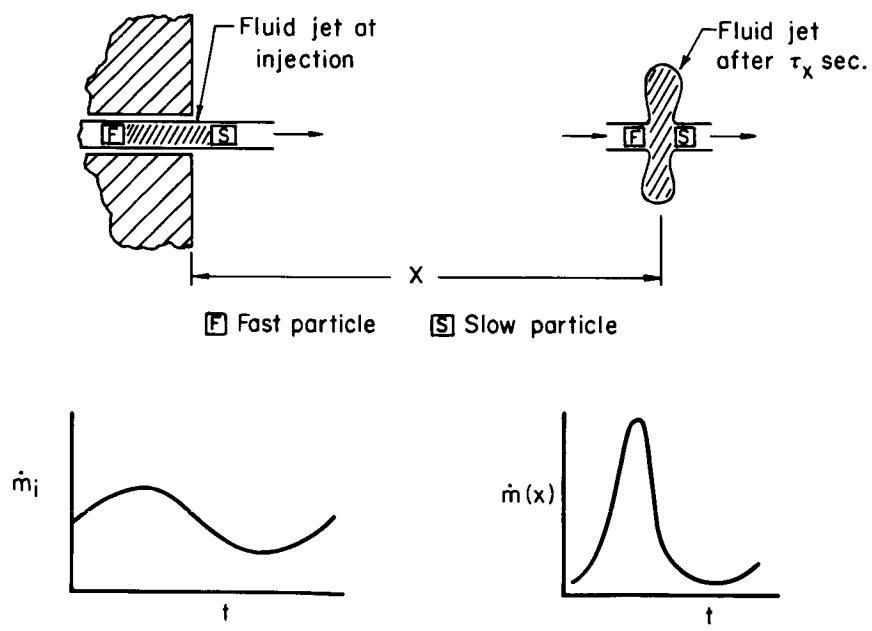

FIGURE 3.3.1b.—Schematic illustration of unsteady injection showing the klystron effect.

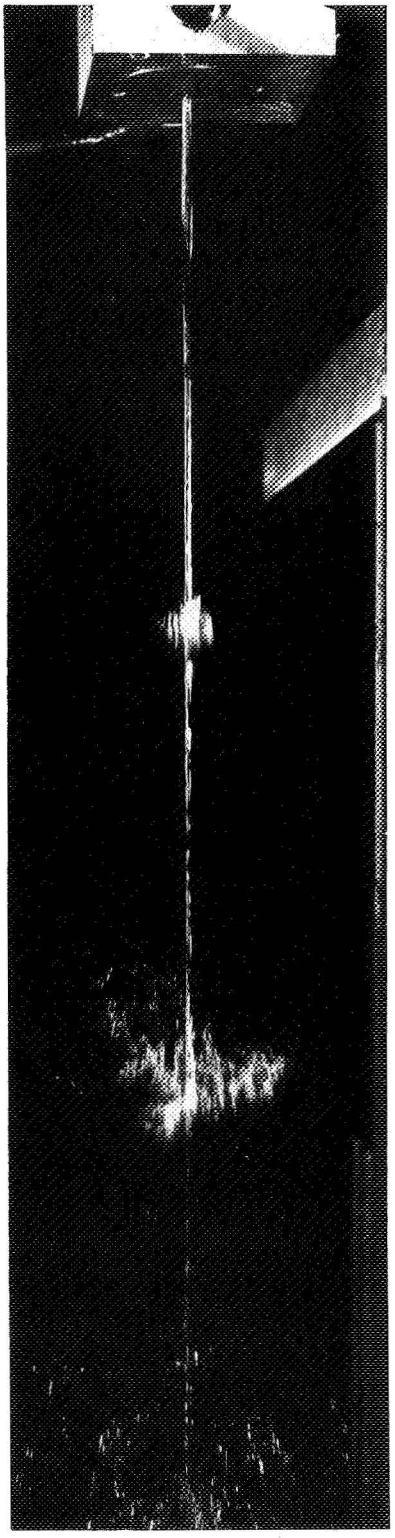

FIGURE 3.3.1c.—Klystron effect, single vertical jet.

Eq. (3.3.1–4) indicates the potential of the klystron effect for up to 90° phase lead relative to the pure time delay, as well as amplification, not present with a simple time delay mechanism. The Bode diagram of Fig. 3.3.1f illustrates the gain and phase characteristics for the klystron and time delay mechanisms.

The sharp, pulse-type flow variations resulting from klystron amplification can explain the saw-tooth waves seen in injector-end chamber pressure during "chug" and "buzz" instabilities. Low amplitude, low frequency oscillations with such amplification could result in periodic bursts of chamber acoustic resonances. Such a phenomenon has been observed in what has been called "resurging."[272]

3.3.1.2 *Hydraulic flip.*—The change in the character of injected streams known as "hydraulic flip" has been suggested as a possible cause of the undesirable combustion phenomenon of "popping."[704] Hydraulic flip is discussed in some detail in Sect. 2.2.2. It has been postulated that operation of an injector in the transition region between cylindrical and bushy liquid streams produces local pressure disturbances. These disturbances propagate through pockets of unburned propellant and are amplified into steep-fronted waves. Since hydraulic flip occurs only in certain ranges of injector pressure drop,[3,519] injector design modifications that removed the injector operation from the critical pressure drop ranges proved successful.[704] However, really definitive tests have not been made, so that the influence of hydraulic flip remains somewhat conjectural.

3.3.1.3 *Injector vibration.*—The actual mechanical vibration of the injector face or the coupling of structural vibrations through intermediate flow components, such as the coolant tubes of a tubular-wall chamber, can also result in significant variations in the propellant injection sprays, and so be responsible for unstable operation.[272] A clumping effect similar to that of the klystron mechanism has been produced experimentally at frequencies as high as 4500 Hz.[475] Carried to the extreme, this mechanism resembles the technique used to generate droplets of known size by means of vibrating orifices.[513,511]

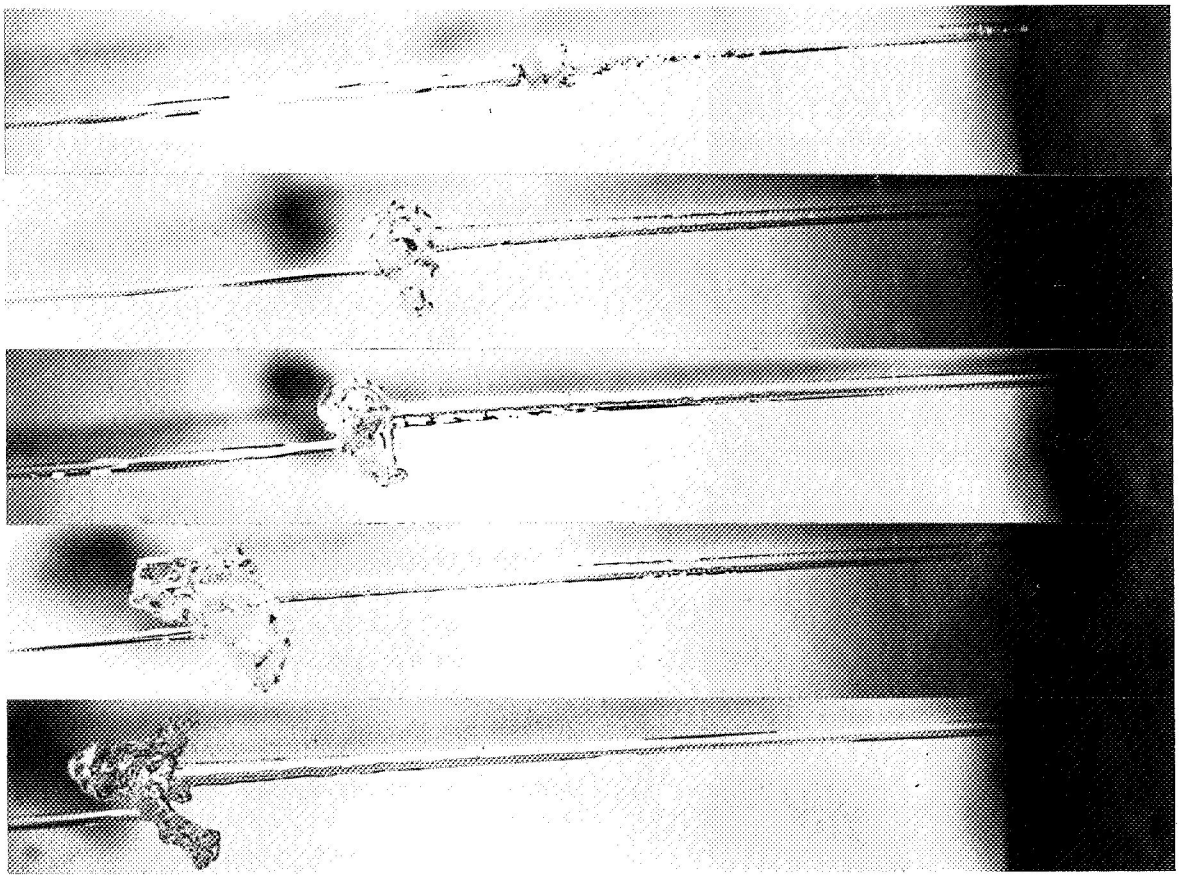

FIGURE 3.3.1d.—Development of a "clump" in a horizontal jet.

3.3.2 Effects of Small Perturbations in Chamber Conditions*

Even if the flow rate is constant, the injection sprays are affected in various ways by oscillating chamber conditions. Therefore, the rate of delivery of prepared propellants to the combustion zone is not constant, but oscillates in response to the pressure and velocity oscillations of the gases filling the combustion chamber. In addition, because of the nonlinearities associated with many of the atomization and mixing processes, oscillatory operation may result in the alteration of the mean characteristics of the sprays from steady state. For purposes of discussion, the non-steady effects considered in this section can be divided into two groups, viz., effects associated with atomization and jet breakup, and effects related to mixing.

3.3.2.1 *Atomization and jet breakup.*—Very little quantitative data is available on the effects of an oscillating environment on the droplet size distribution of typical injection sprays. In one study, oscillations with pressure amplitudes of 5% of the mean values produced no noticeable changes.[287] Oscillations were provided at higher levels in several investigations. However, the emphasis was placed on determining the effect on the jets themselves, rather than on measurements of the droplet spray resulting from jet impingement.[587]

3.3.2.2 *Mixing.*—Some stratification exists in the spray produced by any liquid propellant injector.[613,653] As the droplets of each propellant

* F. H. Reardon and D. T. Harrje, Authors.

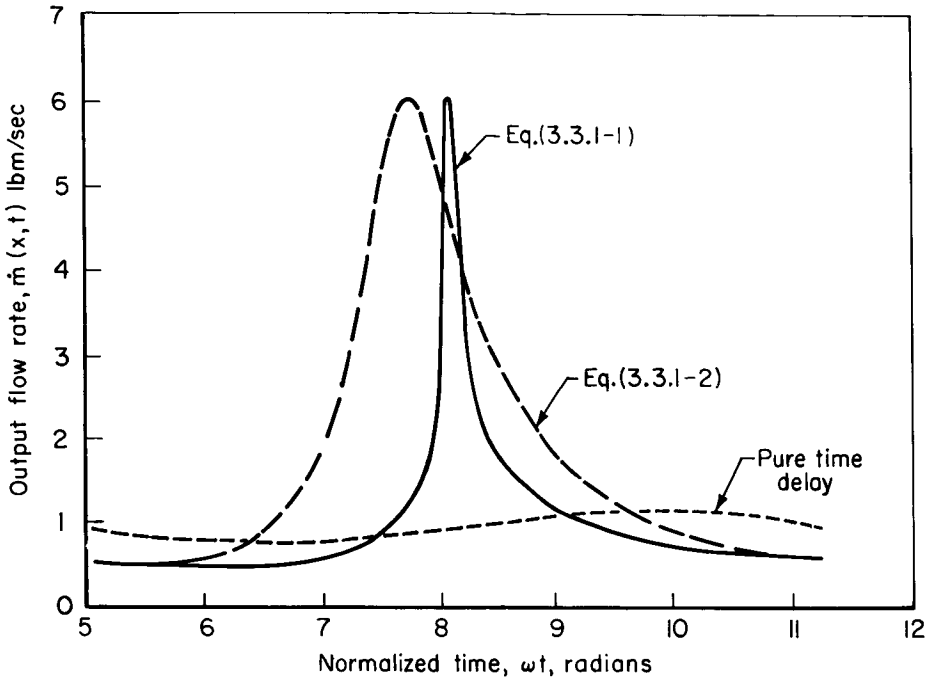

FIGURE 3.3.1e.—Comparison of wave shapes for sinusoidal injection rate variation $\dot{m}_i = 1 - 0.16 \sin 5t$ (lbm/sec); mean transport time $\tau_x = 1.0$ sec.

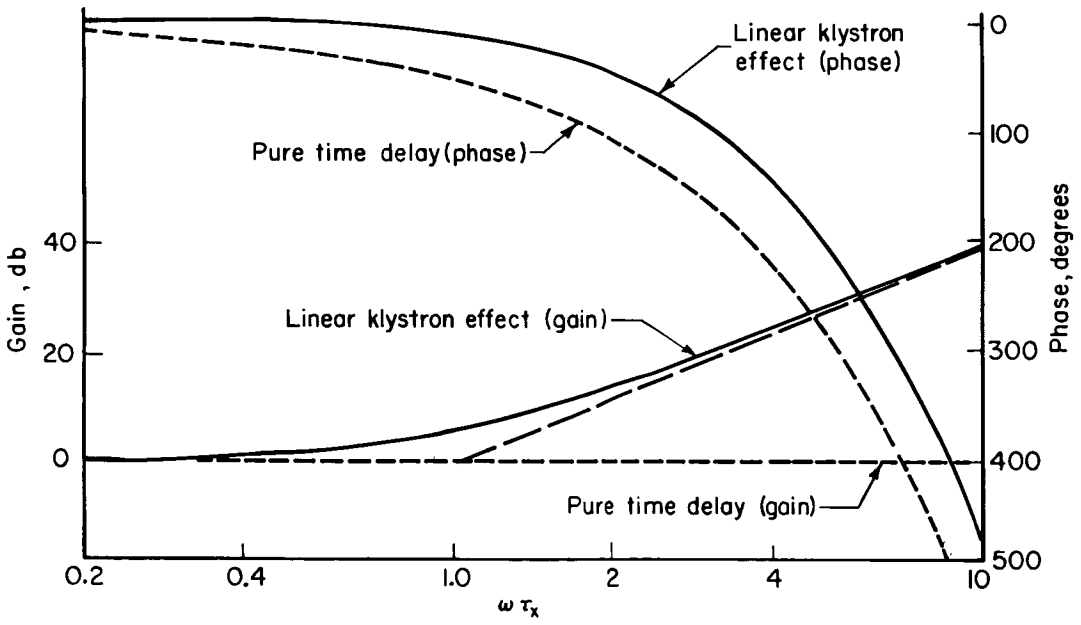

FIGURE 3.3.1f.—Bode diagram for linearized klystron effect and pure time delay.

evaporate, the vapor must diffuse away and mix with the vapor of the other propellant in the right proportion for chemical reaction. The burning rate of a given droplet will, therefore, be a function of the mixture ratio of the vapor surrounding it. Because of the stratification of the liquid spray,

there will be mixture ratio gradients in the vapor. If a transverse acoustic field is imposed on such a spray, the vapor will be displaced relative to the droplet, causing mixture ratio oscillations in the vicinity of each vaporizing droplet. Hence, there will be an oscillation in the burning rate, which can couple with the acoustic field to produce instability. Experimental results showing the importance of this mechanism have been obtained by several investigators.[441, 542, 582]

A linearized model of the above mechanism can be developed by considering the effects of small transverse velocity perturbations on the spray formed by an unlike-impinging doublet injector element with nonhypergolic propellants.[583] At any given axial station, such a spray will consist of liquid droplets, vapors, and gaseous combustion products. As indicated schematically in Fig. 3.3.2a, the stratification will be approximately symmetrical about the line of centers of the doublet orifices. The exact shape of the lines of constant oxidizer mass fraction Y_{OX} depends, of course, on the injector design, operating conditions, and propellant characteristics. Also, because of turbulence in the combustion chamber, the Y_{OX} contours shown in Fig. 3.3.2a represent only a mean condition.

Consider first a fuel droplet, which will be in an oxidant-deficient region of the spray. A velocity perturbation V′ that increases the oxidizer mass fraction in the vicinity of the droplet will increase the burning rate of the droplet. Since the velocity perturbations in an acoustic field change direction cyclically, the burning rate of the droplet will oscillate with the frequency of the applied acoustic field. For a small velocity perturbation $\mathbf{V}'e^{i\omega t}$, the instantaneous burning rate $\tilde{f}$ can be written as

$$\tilde{f}=\bar{f}(1+\boldsymbol{l}\cdot\mathbf{V}'e^{i\omega t}) \qquad (3.3.2\text{–}1)$$

where $\boldsymbol{l}$ is a "velocity interaction index" vector (see Sect. 4.2), which has the same direction as the gradient of Y_{OX}.

Clearly, the effects of a given velocity perturbation will be opposite for oxidizer and fuel droplets, since an increase in oxidizer fraction corresponds to a fuel fraction decrease. Thus, the effects of the same velocity perturbation will tend to cancel, unless the propellants have significantly different vaporization rates. In the latter case, at any axial station there will be a greater number of droplets of the less-volatile propellant, and summation of the velocity effect over all of the droplets in the spray will result in a net contribution to the burning rate.

An expression for the velocity interaction index can be obtained as follows. From Eq. (3.3.2–1),

$$\boldsymbol{l}\cdot\mathbf{V}'e^{i\omega t}=\frac{\tilde{f}-\bar{f}}{\bar{f}}$$

and considering that only Y_{OX} variations affect the rate $\tilde{f}$

$$\frac{\tilde{f}-\bar{f}}{\bar{f}}=\frac{1}{\bar{f}}\left(\frac{\partial\tilde{f}}{\partial Y_{OX}}\right)Y_{OX}'e^{i\omega t}=\frac{\tilde{f}_y}{\bar{f}}\,Y_{OX}'e^{i\omega t}$$

The local oxidizer fraction oscillates because of the relative motion of the vapor with respect to the liquid droplet, hence

$$Y_{OX}'=-\frac{1}{i\omega}(\mathbf{V}'-\mathbf{V}_L')\cdot\nabla\bar{Y}_{OX}$$

and the liquid velocity perturbation is approximately

$$\mathbf{V}_L'=\frac{k}{i\omega}\mathbf{V}'$$

where k is a drag coefficient (Sect. 4.1). Therefore,

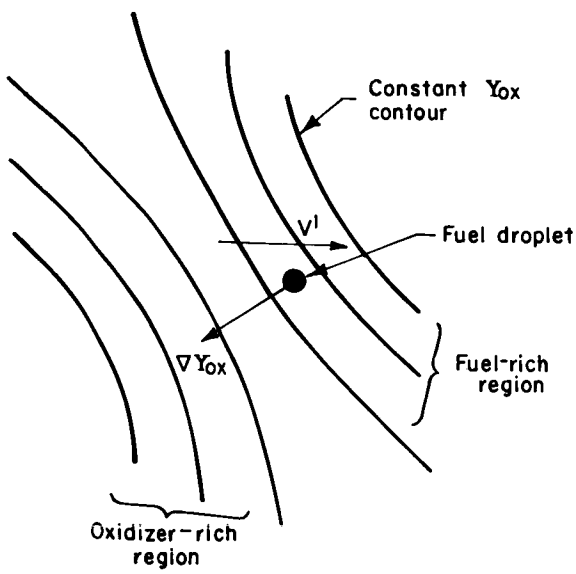

FIGURE 3.3.2a.—Schematic illustration of the stratification in the spray produced by an unlike-impinging doublet.

$$\boldsymbol{l} = -\frac{\left(1-\frac{k}{\mathrm{i}\omega}\right)\tilde{f}_y}{\mathrm{i}\omega\bar{f}}\nabla\bar{Y}_{OX} \qquad (3.3.2\text{–}2)$$

The proportionality factor $\tilde{f}_y$ is a dynamic function of the droplet and vapor characteristics, not necessarily the same as that obtained by steady-state analysis or experiment. One simple formulation that has some physical justification is

$$\tilde{f}_y = \bar{f}_y \exp\left(-\mathrm{i}\omega\tau_y\right)$$

where τ_y is a relaxation time for the droplet burning process. Inserting this formulation into Eq. (3.3.2–2) gives

$$l = \frac{\bar{f}_y}{\omega\bar{f}}\left(1-\frac{k}{\mathrm{i}\omega}\right)\exp\left[-\mathrm{i}\omega\left(\tau_y-\frac{\pi}{z}\right)\right]\nabla\bar{Y}_{OX} \qquad (3.3.2\text{–}3)$$

Assuming further that the combustion response peaks at a certain resonant frequency $\omega_r = \pi/\tau_c$, where τ_c is a characteristic combustion time (Sect. 4.2.1.1), an effective value of $\boldsymbol{l}$ is obtained by setting $\omega = \omega_r$ in Eq. (3.3.2–3). Thus

$$\boldsymbol{l} = \frac{\tau_c\bar{f}_y}{\pi\bar{f}}\left(1-\frac{k\tau_c}{\mathrm{i}\pi}\right)\exp\left[-\mathrm{i}\pi\left(\frac{1}{2}-\frac{\tau_y}{\tau_c}\right)\right]\nabla\bar{Y}_{OX} \qquad (3.3.2\text{–}4)$$

The quantity of interest in practical cases is a mean value $\boldsymbol{l}_m$ of the velocity interaction index that characterizes the entire spray. This, of course, should be obtained by averaging over all of the droplets of the controlling propellant in the spray. However, it is also instructive to proceed by defining an effective spray width d_s such that

$$\frac{1}{d_s} = \left[\frac{\bar{f}_y}{\bar{f}}\nabla\bar{Y}_{OX}\right]_{mean}$$

Then the magnitude of the mean velocity index can be expressed as

$$|\,l_m\,| = \frac{\tau_c}{\pi d_s}\left(1+\mathrm{i}\frac{k\tau_c}{\pi}\right)\exp\left[-\mathrm{i}\pi\left(\frac{1}{2}-\frac{\tau_y}{\tau_c}\right)\right] \qquad (3.3.2\text{–}5)$$

and its direction is the same as that of the mean Y_{OX} gradient.

Several observations can be made about Eq. (3.3.2–5). First, the drag coefficient k is generally quite small, of $0(0.1)$, and decreases with increasing droplet size. Very small droplets follow the gas motion closely, so that this displacement mechanism is significant only for the larger droplets. It is expected also that this mechanism is most effective near the injector face, where there are more large droplets.

A second observation is that in order for the velocity interaction index to be real, that is, for the combustion response to be in phase with the velocity perturbation, as assumed in Ref. 582, the relaxation time τ_y must be about one-half of the characteristic combustion time τ_c. On the other hand, if the relaxation time is very small, the combustion response will be in phase with the displacement, and a real-valued displacement index $\mathbf{m} = \mathrm{i}\omega\mathbf{l}$ can be used in Eq. (3.3.2–1).

The characteristic combustion time τ_c can be identified with the sensitive time lag defined by Crocco (Sect. 4.2.1). Then the velocity or displacement sensitivity of the combustion process might be expected to increase with increasing injection orifice size (Sect. 6.3.3). However, the effective spray width is also likely to increase with orifice size. At present, the dependence of the index $\boldsymbol{l}$ (or $\mathbf{m}$) on design and operational factors has not yet been determined. However, on the basis of experimental stability limits, for moderate orifice size (0.080 in.), and the propellant combination LOX/ethanol, Smith and Reardon[650] estimated the magnitude of $\boldsymbol{l}$ to be in the range 1 to 4, in good agreement with Eq. (3.3.2–5), which can thus be used to obtain a rough magnitude of the velocity index.

The linearized analysis given in the preceding discussion will not be valid for all types of injection pattern. In many cases, the only significant mixing effects are definitely nonlinear in character. For example, although approximately linear velocity effects can be expected for a like-on-like injector pattern if the spacing between unlike spray fans is sufficiently small, for typical designs the spacing is large enough that nonlinear effects must be taken into consideration.

Qualitatively, the nature of the nonlinear displacement sensitivity of a like-on-like injector pattern can be seen by considering an isolated element, consisting of one pair of oxidizer orifices and one pair of fuel orifices (Fig. 3.3.2b). For concreteness, suppose that the oxidizer vaporizes

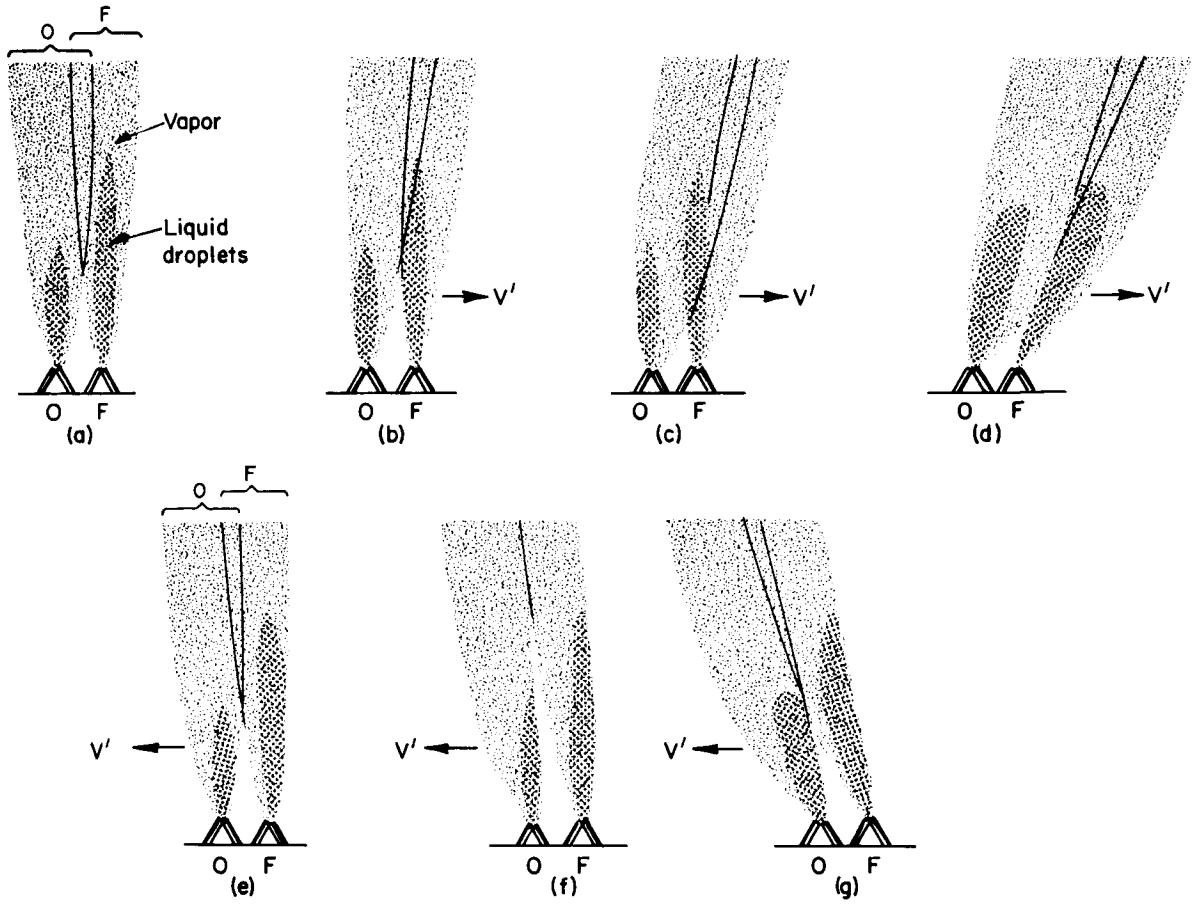

(a) Steady state. (b) Small amplitude. (c) Moderate amplitude. (d) Very large amplitude. (e) Small amplitude. (f) Moderate amplitude. (g) Very large amplitude.

FIGURE 3.3.2b.—Nonlinear velocity (displacement) effect, with like-on-like injection element.

more rapidly than the fuel, and that the velocity perturbation is parallel to the lines of centers of the orifice pairs. Since most of the mass in the liquid phase is concentrated near the axis of each spray fan, a small transverse velocity perturbation will produce no appreciable effect on the burning rate.

For a moderate perturbation in the O→F direction, the oxidizer vapor will be displaced into the region of highest fuel droplet concentration, producing an increase in the burning rate. However, a very large velocity perturbation will disrupt the fuel spray, displacing it in the direction of the velocity, that is, away from the oxidizer. Thus, the burning rate enhancement due to displacement of oxidizer vapor will be limited.*

For velocity perturbations in the F→O direction, small amplitudes will again have little effect, other than to move the combustion zone in the downstream direction. Larger amplitudes will cause separation of the oxidizer vapor from the fuel, resulting in a sharp reduction in the burning rate. Again a limiting influence will be operative for very large amplitudes in that the fuel spray will be broken up and displaced along with the oxidizer spray.

Thus, the response function of a like-on-like injector element can be approximated by a combination of deadband and saturation, as

* This is one possible explanation of the "over-bombing" effect discussed in Chapter 10.

illustrated in Fig. 3.3.2c, although complete symmetry is not likely. The presence of adjacent elements will modify the response function, probably eliminating the saturation effect for O→F velocities and adding such an effect for F→O velocities, as shown by the broken line in Fig. 3.3.2c.

Recent studies of hypergolic propellant combinations[252,415] have indicated that under certain conditions the rapid liquid-phase reactions produce vapor pockets that keep the unlike liquids apart and so inhibit the mixing that would otherwise occur with unlike-impinging injection elements. On this basis, it is not to be expected that such injectors will exhibit the linear displacement effects with hypergolic propellants that have been observed with nonhypergolic propellants. When injection stream separation occurs, the combustion response to transverse velocity perturbations should be similar to that of like-on-like injection, as discussed above.

Quantitative specification of the nonlinear velocity (displacement) sensitivity cannot be accomplished without detailed and systematic studies of spray combustion. However, some rough estimates are possible on the basis of existing knowledge. Considering the like-on-like injection element of Fig. 3.3.2b, if the spacing between fuel and oxidizer sprays is denoted by x_s, then the displacement δ_d' of the oxidizer vapor necessary to produce an appreciable change in the combustion rate should be on the order of $x_s/2$. The corresponding velocity perturbation is

$$V_d' \approx \omega\delta_d' \approx \frac{\pi x_s}{2\tau_c} \qquad (3.3.2\text{–}6)$$

The point at which saturation effects begin is more difficult to estimate. Assuming the breakup of the fuel spray to be the controlling event, as discussed previously, the experimental results of Clark[146] can be used to estimate the perturbation level for saturation effects in terms of velocity or displacement perturbations:

$$V_s' \approx \frac{d_F}{\tau_c}\sqrt{\frac{\rho_L}{\rho}}\,; \qquad \delta_s' \approx \frac{V_s'}{\omega} \approx \frac{d_F}{\pi}\sqrt{\frac{\rho_L}{\rho}} \qquad (3.3.2\text{–}7)$$

where d_F is the width of the fuel spray.* The

* It should be noted that Clark studied only cylindrical liquid jets, not the sprays formed by impinging jets. However, the authors are unaware of comparable experiments performed on sprays that can serve to determine whether Eq. (3.3.2–7) is a valid extrapolation of Clark's results.

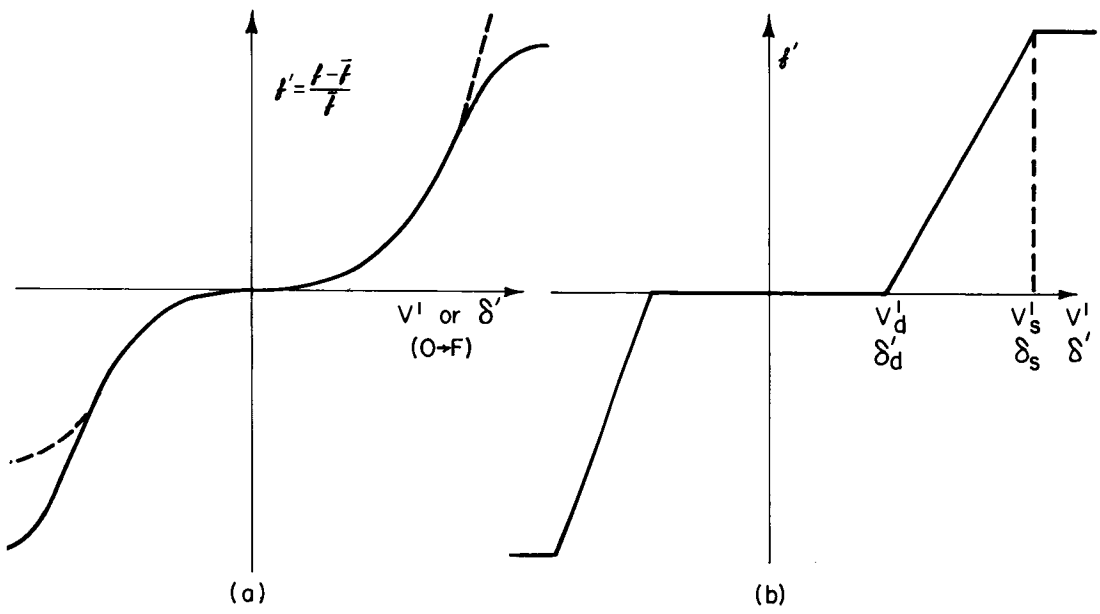

(a) Actual (solid curve denotes isolated element; dashed curve denotes adjacent elements present).

(b) Approximate deadband-saturation model.

FIGURE 3.3.2c.—Burning rate perturbation for like-on-like element.

final parameter required to specify the combustion response for this deadband-saturation model is the slope of the combustion response function for $V_d' < V' < V_s' (\delta_d' < \delta < \delta_s')$. This slope should be approximately the same as that for the linear displacement model, or

$$\frac{d\tilde{f}'}{dV'} \approx \frac{\tau_c}{\pi d_F}; \qquad \frac{d\tilde{f}'}{d\delta'} \approx \frac{1}{d_F} \qquad (3.3.2\text{–}8)$$

As discussed previously, the choice between the velocity and displacement formulations given in Eqs. (3.3.2–6) to (3.3.2–8) depends on whether the combustion response is in phase with the velocity perturbation or with the displacement perturbation.

3.3.3 Stream and Droplet Breakup by Shock Waves*

When shock waves are present in a droplet combustion field, a large pressure distribution is established about each droplet, the droplet deforms, there is a shearing force at the periphery of the drop, and internal motion and surface tension come into play. Under certain conditions the droplet (or jet) may be broken up mechanically at a rate greater than the vaporization rate, so that a different characteristic time for the conversion of liquid to vapor is experienced. Thus, the presence of shock waves can lead to changes in the spatial energy release patterns and characteristic times such that there is a distinct change in the stability behavior of the combustor.

The discussion in this section is not intended to be an all-inclusive review of the subject, but rather is aimed at putting the problem into perspective in terms of the application to rocket combustion.

Consider a spherical droplet, or cylindrical jet of liquid, initially at rest, that is suddenly impacted by a shock wave. The shock induces a flow behind it that may be subsonic or supersonic; in the latter case there will also be a bow shock (Fig. 3.3.3). Most of the discussion following is concerned with the droplet case, but the difference between drop and jet breakup is small and will be pointed out later. It is desired to determine the rate of conversion of the original drop into smaller

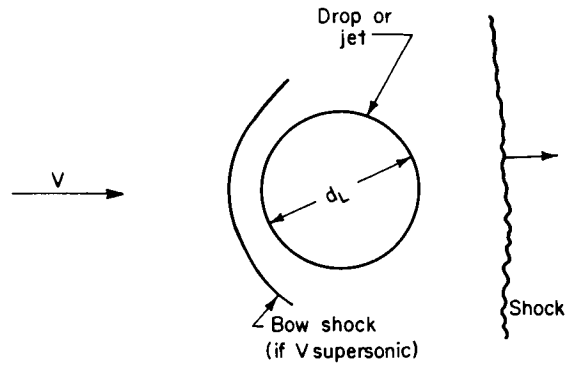

FIGURE 3.3.3.—Liquid drop or jet in a uniform stream.

drops, the total breakup time, the motion of the parent drop, and the nature of the secondary drops. A complete analytical treatment of this problem, including the details of drop deformation and internal motion, has never been made. Accordingly, it is necessary to resort to dimensional analysis, experimental observations, and approximate theories.

The results of many experimental studies* indicate that the influence of the incident shock, the internal motion of the liquid, and the increased vaporization rate due to the temperature increase across the shock are sufficiently small to be neglected. The fact that the shock plays no role other than inducing the flow implies that the relative flow between the drop and gas is the important consideration and not how the flow was generated.

Subject to the above simplifications, and considering a perfect gas, dimensional analysis yields the following functional relationship:

$$\tau_b = \tau_b(\mathrm{We}, \mathrm{Re}, \mathfrak{M}, \beta, \eta) \qquad (3.3.3\text{–}1)$$

where

$$\tau_b = \frac{V t_b}{d_{Lo}} \qquad \text{dimensionless breakup time}$$

$$\mathrm{We} = \frac{\rho V^2 d_{Lo}}{2 S_L} \qquad \text{Weber number}$$

$$\mathrm{Re} = \frac{\rho V d_{Lo}}{\mu} \qquad \text{Reynolds number} \qquad (3.3.3\text{–}2)$$

* J. A. Nicholls, Author.

* Cited in the text following.

$\mathfrak{M} = \frac{V}{a}$ Mach number

$\beta = \frac{\rho}{\rho_L}$ density ratio

$\eta = \frac{\mu}{\mu_L}$ viscosity ratio

The exact form of Eq. (3.3.3–1) must be determined from experimental investigations.

In shock tube studies with relatively weak shocks, it was noted that for flow conditions below a certain critical Weber number the drop did not break up but rather translated with the flow and gradually vaporized.[315,314] For water and methyl alcohol the critical Weber number ranged from 3.6 to 8.4, but higher values were required for very viscous liquids. For We slightly greater than critical the drop disintegrated in the "bag" mode. In this mode the increased pressure near the forward stagnation point forces the central portion to "inflate" in the downstream direction in the form of a bag. This blown up portion is gradually sheared off from an outer rim and forms a number of smaller drops. Obviously, surface tension is of importance in this mode. For We substantially greater than critical the disintegration was of the "stripping" mode. The stripping mode is characterized by liquid shearing (or stripping) off the periphery of the drop; surface tension is unimportant.

In another study,[569] a Reynolds number effect on the critical Weber number was determined, with the empirical correlation

$$We_{crit}/(Re_{crit})^{1/2} = \text{constant} \qquad (3.3.3\text{–}3)$$

where the constant equaled about 0.5 for nonburning drops. It was shown that the form of Eq. (3.3.3–3) is consistent with a boundary layer stripping analysis of breakup. Burning drops broke up at lower dynamic pressures, presumably due to lowered surface tension. The correlation at the critical condition for burning drops was not as good as that for nonburning drops, which was attributed to uncertainty in the proper value of surface tension.

When one considers the elevated pressures and temperatures in rocket combustors and typical drop or jet sizes, one finds that the critical conditions for breakup can be exceeded by very weak shock waves. Thus, it is to be expected that the stripping mode of breakup will be more pertinent than the bag mode in rocket applications. Furthermore, the drop breakup time in the bag mode will usually be longer than the residence time in the chamber and hence not as influential for instability. Most of the remaining discussion, then, will be devoted to the stripping mode of breakup.

Shock tube investigations* have shown the following relation for breakup time for the stripping mode:

$$t_b \sim \frac{d_{Lo}}{V}\sqrt{\frac{\rho_L}{\rho}} \quad \text{or} \quad t_b \sim d_{Lo}\sqrt{\frac{\rho_L}{q}} \qquad (3.3.3\text{–}4)$$

where q is the dynamic pressure. If a new dimensionless breakup time, $T_b = \sqrt{\beta}\tau_b$, is introduced, Eq. (3.3.3–4) becomes simply

$$T_b = \text{constant} \qquad (3.3.3\text{–}5)$$

This correlation shows that Re, η, and We are unimportant in the case of the stripping mode. Moreover, the shock itself, as well as internal motion in the drop and the vaporization rate are also unimportant. Similar results have been obtained for liquid jets.[146,501] The same correlation has been found to hold for both burning and nonburning drops.[384,569]

Several approximate theoretical analyses† using varied approaches have led to relations similar to Eq. (3.3.3–5). However, a theoretical analysis that treated the breakup as stemming from the generation and shedding of capillary waves[222] did not lead to Eq. (3.3.3–5), or the expected limiting behavior but did appear to give reasonable agreement with experiment. It is not clear at present whether capillary or boundary layer stripping is the predominant mechanism.

It must be pointed out that the breakup time is not unambiguous, and different investigators use different breakup criteria. This fact must, of course, be taken into account in comparing results. Nicholson and Hill[517] obtained $T_b \approx 3.5$, whereas Jaarsma and Derksen[384] reported $T_b \approx 4.5$, and Ranger[575] found $T_b \approx 4$ for low subsonic Mach numbers, increasing to about 5.5 at $M = 1$, then

* References 250, 384, 517, 569, 576, 598, and 755.
† References 146, 133, 500, 575, and 755.

decreasing towards 4 at supersonic velocities. This increase in T_b in the transonic range is similar to the behavior of the drag coefficient. In view of this result, it is instructive to review some experimental determinations of drag coefficients for drops undergoing stripping breakup. Ranger and Nicholls[576] found that such drops followed very nearly a parabolic trajectory in the x,t plane. From Newton's law, the acceleration of a spherical drop is

$$\frac{d^2x}{dt^2} = \frac{3}{4}\frac{C_D}{d_L}\frac{\rho}{\rho_L}(V-V_L)^2 \qquad (3.3.3\text{–}6)$$

Since a parabolic trajectory implies constant acceleration, the distance traveled by the drop before breakup is given by

$$X_b = \frac{x_b}{d_{Lo}} = \frac{3}{8}C_{Do}T_b^2 \qquad (3.3.3\text{–}7)$$

where C_{Do} is the drag coefficient based on initial drop conditions. Ranger and Nicholls found $C_{Do} \approx 3.0$, whereas Jaarsma and Derksen reported $C_{Do} \approx 2.5$, for burning and nonburning drops. Somewhat lower values were obtained by Rabin, et al.[569]

For liquid jets, similar results have been reported,[146,501] with dimensionless breakup time T_b determined to be in the range 3.2 to 3.9. However, these values may be somewhat low because of the method of determining T_b, viz, the continuity of electrical current through the jet. Povinelli[555] obtained the empirical displacement expression

$$\frac{x}{d_{Lo}} = 0.7\left(\frac{\sqrt{\beta}V_o}{d_{Lo}}t\right)^2 \qquad (3.3.3\text{–}8)$$

from tests with many different liquids. From such data a value of 2.2 for the drag coefficient is obtained.

In summary, if $We(Re)^{-1/2} \gg 0.5$ for a given flow condition, the drop or jet will break up by a stripping mechanism. In this case, for incompressible flow, a simple but useful relation for engineering purposes is $T_b = 4$. In the transonic flow range this value of breakup time may increase by almost 50%. For those cases where $We(Re)^{-1/2}$ is closer to 0.5 and the bag mode, or a combination of the bag and stripping modes, is experienced, the reader is referred to the work of Wolfe and Anderson.[755]

3.4 COMBUSTION PROCESSES

Attention is focused in this section on processes that are important in controlling the high frequency type of combustion instability, since the considerations of Chapter 2 are directly applicable to low and intermediate frequency cases (see Sect. 5.2).

The following nomenclature pertains to Sect. 3.4:

A	Constant in Nusselt number correlation
B	Response function coefficient, Eq. (3.4.2–4)
b	Normalized slope of vapor-pressure curve
$g(\omega_3)$	Frequency dependence of heat flux to droplet
$\dot{m}_b$	Droplet burning rate
m_L	Droplet mass
n	Exponent in Nusselt number correlation
$\mathcal{P}$	"Open-loop" combustion response function (complex)
$\mathcal{P}_R$	Real part of $\mathcal{P}$
q_L	Heat flux to droplet
$t_1, \ldots t_5$	Characteristic times of droplet burning, defined in Table 3.4.2a
t_i	Instant of injection
$t-t_i$	Time elapsed from injection
T_L	Droplet surface temperature
T_∞	Temperature of atmosphere surrounding droplet
Y_{FL}	Fuel mass fraction at droplet surface
τ_l	Droplet lifetime

3.4.1 Controlling Processes*

There is limited evidence that the mechanism for high frequency combustion instability lies in the vaporization and combustion processes. Droplet burning in an actual combustor is recognized as a highly complex phenomenon, consisting of many concurrent as well as sequential processes. The burning also interacts with the droplet drag and the consequent drop flight history. However, it appears that the drag perturbations have a minor effect on stability criteria. In any event, significant differences

* W. C. Strahle, Author.

between the unsteady and steady states enter into descriptions of the combustion process. Even for the limited class of systems controlled by subcritical vaporization in the steady state, assurance is impossible that the considerations of Sect. 2.4 may be carried over into the unsteady state.

Most work on unsteady combustion has centered about the subcritical* droplet burning process because of its success in predicting steady performance (see Chapter 2). However, many diagnostic experiments giving the theoretician information on the detailed structure of the steady state have not been performed. It has therefore been necessary to proceed by assumption. Unknown factors include the degree of circulation within a droplet, the structure of the wake, the role of free stream turbulence and droplet interference effects, and the droplet flame structure. All of these affect any theoretical formulation of the unsteady state. The problem is that usual high frequency cycle times may be of the same order as the delay time between vaporization of a fluid element and its combustion. The important quantity entering stability criteria is the combustion rate, which is not, in general, instantaneously the same as the vaporization rate.[178]

In spite of the difficulties, there is evidence that for many systems the droplet burning process is controlling (see Sects. 4.3 and 4.4). It is therefore worthwhile to investigate the models that have been proposed for unsteady droplet burning. Only the burning process itself is considered here; the inclusion into rocket system analysis is covered in Chapter 4. There are also some mechanisms which have been advanced that do not treat the burning process in detail but are capable of incorporation into stability analysis on a heuristic basis.[583,179,260] Since these mechanisms do not rest on complete and detailed treatments of the burning process, they are discussed in Sect. 4.2 and 4.4 in connection with high frequency stability analysis methods.

3.4.2 Linear, Nonsteady Drop and Spray Burning

The study of burning under the influence of small amplitude disturbances in ambient gas is a logical starting point for understanding the unsteady burning phenomena. Attention is restricted here to liquid elements vaporizing in a subcritical state, so that a well-defined liquid state exists surrounded by a gas phase diffusion field. The gas at large distances from the liquid-gas interface is assumed to be undergoing small oscillations which, in the frame of reference of the liquid, may be decomposed into one or several frequencies. Since linearity is assumed, it is permissible to consider the response of the burning process to one frequency at a time, the final result being obtained by superposition. It is assumed that the liquid is spherical and that its geometrical shape is invariant with time.

3.4.2.1 *The frequency spectrum.*—The gas phase oscillation is considered to be the forcing oscillation and the objective is to determine the behavior of the vaporization or burning process under the influence of this oscillation. In other words, the "open-loop" response of the burning process is required. The frequency response will not depart from quasi-steady form unless the cycle time of the forcing oscillation becomes commensurate with some characteristic time of the burning process. Therefore, it is useful to examine and order the times which are characteristic of droplet burning.

Five characteristic times are of interest: a droplet lifetime t_1, a liquid thermal inertia time t_2, a liquid thermal diffusion time t_3, a gas-phase diffusion time for a locally stagnant gas field t_4, and a forced-convection gas-phase diffusion time t_5. These characteristic times are defined in Table 3.4.2a; numerical limits are specified on the basis of property data.[471,29] Liquid hydrogen has been excluded as a propellant. As defined in Table 3.4.2a, the times are heat transfer oriented, but can be converted to mass or vorticity transfer times by use of appropriate Prandtl or Schmidt numbers. It should be kept in mind that these times are dimensional groupings that order the appropriate process times; they should not be confused with precise estimates of the actual process times. For example, the grouping denoted droplet lifetime is a term to which the actual lifetime is proportional, but the true droplet lifetime depends on the precise nature of the convective field and the values of other physical

* That is, at a pressure below the critical pressure of the propellant.

parameters. It is conceivable that a turbulent process controls the gas phase diffusion time in the droplet wake. To account for this in Table 3.4.2a, the effective thermal conductivity has arbitrarily been increased by a factor of 10 for the upper limit estimate. No estimate of chemical kinetic times has been made since it is usually assumed that they are short compared to all the listed times.* Because of the wide latitude taken in the construction of Table 3.4.2a, it is best to consider the middle decade of the time range as most representative.

As the frequency increases (beginning from zero) the first effect should be interaction with the droplet lifetime t_1. That is, when the cycle time becomes commensurate with t_1 there will be important unsteady interaction with the decreasing droplet size. When the cycle time becomes of the order of the liquid thermal inertia time t_2, the droplet temperature cannot perfectly follow that demanded by a quasi-steady treatment with respect to this process. When the cycle time becomes commensurate with the liquid heat transfer diffusion time t_3, a thermal wave appears in the liquid. Continuing in this manner, one can proceed to the high frequency limiting behavior with respect to all processes. For precise estimates, however, it is necessary to investigate more details, just as in a linear mass-spring-damper system a resonance develops when the forcing frequency becomes commensurate with the natural frequency, but the exact frequency of resonance depends on the amount of damping. Detailed theories giving the relations between cycle time and process times are discussed later in this section. Here it is of interest to state the magnitudes of the frequency-time product where important unsteady interaction occurs:

$$\omega t_1 \sim 20$$
$$\omega t_2 \sim 100$$
$$\omega t_3 \sim 1000$$
$$\omega t_4 \sim 5$$
$$\omega t_5 \sim 5$$

These estimates come from numerical calculations based on the various theories investigated later in the section. The large magnitude of ωt_1 is due to the fact that the actual lifetime is quite a bit smaller than the dimensional grouping. The second and third products are large because of the strong role played by the derivative of the vapor pressure with respect to temperature in governing mass and heat transfer processes.

The frequency ranges for unsteady interaction, based on the data of Table 3.4.2a and the ωt products given above, are listed in Table 3.4.2b. Of interest is the fact that all five processes can exhibit unsteady behavior within the range of frequencies that is characteristic of high frequency combustion instability. There has been, however, no comprehensive study which has included all processes. At most, two have been treated at a time.

Consideration of the five characteristic times defined in Table 3.4.2a shows that they all scale with droplet radius r_L raised to a power between 3/2 and 2. This leads to an interesting independence: regardless of which theory may be correct, the scaling rules, at least with regard to drop size, are roughly the same.

3.4.2.2 *Response functions.*—In the linear stability theory a quantity of interest to be obtained from droplet burning theory is the open-loop response function

$$\mathcal{P}_R = \mathcal{R}e\left[\frac{\dot{m}_b'(x, y, z, t)\,p(x, y, z)}{p'(x, y, z, t)\,\dot{m}_b(x, y, z)}\right] \quad (3.4.2\text{–}1)$$

Here p' and $\dot{m}_b'$ are the instantaneous perturbations of the pressure and burning rate from their respective steady state values $\bar{p}$ and $\dot{m}_b$, and $\mathcal{R}e$ denotes the real part.* For instability, $\mathcal{P}_R$ must be positive and of order unity at a chamber position where the pressure is varying. In this section the response function will be presented as derived from several droplet burning theories. Since there is not enough space to present all parametric results, the reader is referred to the literature cited below for detailed effects. The results presented here are, however, representative of practical rocket parameters.

Unsteadiness with respect to droplet lifetime

* However, a theory has appeared in the literature based on chemical kinetics as the controlling mechanism for instability.[203] The assumption may bear a reexamination in the future.

* For a precise formulation of $\mathcal{P}_R$ together with a magnitude estimate and the manipulation of Eq. (3.4.2–1) into a form appropriate for stability criteria, see Ch. 4.

TABLE 3.4.2a.—CHARACTERISTIC TIMES OF THE DROPLET BURNING PROCESS

Raw data	Definition	Time range, sec
$50 \leq r_L \leq 200$ microns $2.2\times10^5 \leq \frac{\rho_L c_L}{\mathfrak{K}} \leq 11\times10^5 \frac{\text{sec}}{\text{ft}^2}$	Droplet lifetime: $t_1 \equiv \frac{\rho_L c_p r_L^2}{\mathfrak{K}}$	2.6×10^{-3} to 6.5
$9.4 \leq \rho_L c_L \leq 50.3 \frac{\text{Btu}}{(°\text{R})(\text{ft}^3)}$	Liquid thermal inertia: $t_2 \equiv \frac{\rho_L c_L r_L^2}{\mathfrak{K}}$	0.52×10^{-2} to 8.8
$15.6 \leq \rho_L \leq 125 \frac{\text{lbm}}{\text{ft}^3}$ $0.03 \leq \rho \leq 0.4 \frac{\text{lbm}}{\text{ft}^3}$	Liquid thermal diffusion: $t_3 \equiv \frac{\rho_L c_L r_L^2}{\mathfrak{K}_L}$	6.8×10^{-4} to 5.4×10^{-1}
$0.28\times10^{-5} \leq \mathfrak{K} \leq 5.2\times10^{-5} \frac{\text{Btu}}{(°\text{R})\ (\text{sec-ft})}$ $0.94\times10^{-5} \leq \mu \leq 5.4\times10^{-5} \frac{\text{lb}}{\text{ft-sec}}$	Gas phase diffusion (film thickness$\sim r_L$): $t_4 \equiv \frac{\rho c_p r_L^2}{\mathfrak{K}}$	1.7×10^{-6} to 2.1×10^{-2}
$10 \leq \text{Re} \leq 100$ $\text{Pr} \approx 1$	Gas phase diffusion $\left(\text{film thickness} \sim \frac{r_L}{\text{Re}^{1/2}}\right)$: $t_5 \equiv \frac{\rho c_p r_L^2}{\mathfrak{K}\text{Re}}$	1.7×10^{-7} to 2.1×10^{-3}

and liquid inertia, with all other processes considered fast compared to these, forms the basis for analyses by Heidmann and Wieber[346] and Tang and Crocco.[192] The assumption is made that burning coincides with vaporization. In the frequency range of interest this is justifiable if, on the average, the fluid burns within a thin leading edge boundary layer or in a turbulent near wake. By neglecting the liquid thermal diffusion time effects (the thermal wave) the droplet temperature is at any instant considered uniform, but varying with time. In the opinion of the author, both of these assumptions are open to question,[654] and necessary diagnostic experiments are needed.

The characteristics of the unsteady droplet burning process are examined here by an analysis similar to those of Heidmann and Tang, but with

TABLE 3.4.2b.—FREQUENCY RANGES FOR UNSTEADY INTERACTION

Process	Frequency	Range, Hz
Droplet lifetime	ω_1	0.49 to 1200
Liquid thermal inertia	ω_2	18 to 3100
Liquid thermal diffusion	ω_3	290 to 2.3×10^5
Gas phase diffusion (stagnant field or wake)	ω_4	38 to 4.7×10^5
Gas phase diffusion (forced convection)	ω_5	380 to 4.7×10^6
Combustion instability		500 to 3×10^4

some differences. The purpose is to show, within the framework of a single model, the characteristics of previous analyses as well as to indicate another effect not heretofore shown in the literature. First, the Nusselt numbers for heat and mass transfer are taken in an approximate, high Reynolds number form:

$$\mathrm{Nu}=A\left(\frac{r_L}{r_{Lo}}\right)^{1/2}\left(\frac{p}{\bar{p}}\right)^n \qquad (3.4.2\text{–}2)$$

where the constants A and n are chosen to best fit the actual form.* The second difference is that the mean drop size is taken as constant throughout its lifetime, with fluid supplied from a source in the center until all the original mass of the drop has been vaporized. Third, the perturbation heat transfer to the drop is obtained from the spherically-symmetric heat equation, assuming no internal convection and a uniform temperature in the steady state. The heat flux is given by

$$q_L'=\mathfrak{R}_L\cdot 4\pi r_L T_L' g(\omega_3) \qquad (3.4.2\text{–}3)$$

where

$$\omega_3=\frac{\omega\rho_L c_L r_L^2}{\mathfrak{R}_L}$$

$$g(\omega_3)=(i\omega_3)^{1/2}\coth(i\omega_3)^{1/2}-1$$

* The effects of velocity perturbations are inherently nonlinear for transverse oscillations and are often minor for axial oscillations and thus have been omitted from this expression.

Here T_L' is the perturbation of droplet surface temperature. Fourth, the thermal conductivity varies as the first power of temperature, and the Prandtl and Schmidt numbers are unity.

Under the constraint that the injected drop size is a constant the following response function may be developed by standard perturbation methods:

$$\mathcal{P}_R=B\left[\frac{i\omega/\alpha}{(i\omega/\alpha)+1}+\frac{\exp\{[(i\omega/\alpha)+1]\alpha(t_i-t)\}}{(i\omega/\alpha)+1}\right] \qquad (3.4.2\text{–}4a)$$

where

$$B=n+\frac{\gamma-1}{\gamma}-a\frac{Y_{F_L}'}{p'};$$

$$\alpha=\frac{1}{2\tau_l};$$

$$a=-\frac{A}{\beta(1-\bar{Y}_{F_L})}$$

$$\beta=A\ln\left(\frac{1}{1-\bar{Y}_{F_L}}\right)=A\ln\left[1+\frac{c_p(\bar{T}_\infty-\bar{T}_L)}{h_v}\right]$$

$$\frac{Y_{F_L}'}{p'}=\frac{-c\bar{Y}_{F_L}+\dfrac{\gamma-1}{\gamma}\dfrac{\bar{T}_\infty}{\beta}\left(\dfrac{\partial\beta}{\partial\bar{T}_\infty}\right)b}{c-ba};$$

$$b=-\frac{\bar{T}_L}{\bar{p}}\frac{dp_v}{dT_L} \qquad (3.4.2\text{–}4b)$$

$$c=\frac{\bar{T}_L}{\beta}\frac{d\beta}{dT_L}-\frac{\mathfrak{R}_L}{\mathfrak{R}}\frac{c_p\bar{T}_L}{\beta h_v}A\bar{Y}_{F_L}g(\omega_3);$$

$$\omega_3=\frac{3}{2}\beta\frac{c_L}{c_p}\frac{\mathfrak{R}_L}{\mathfrak{R}}\frac{\omega}{\alpha}$$

In Eqs. (3.4.2–4), γ is the ratio of specific heats of the gas, τ_l is the droplet lifetime, defined in the above sense, and $t-t_i$ is the elapsed time from injection.

As $\omega/\alpha\rightarrow\infty$, that is, as the cycle time becomes short compared to the lifetime, the expression in brackets in Eq. (3.4.2–4a) approaches unity. Heidmann's analysis does not contain the second term in brackets because the constraint on injected drop size was not imposed in that theory.

It should be noted that $|t_i - t| < \tau_l$. When averaged over the chamber volume (i.e., over droplets in different stages of their lifetime) an effective (average) value of $\alpha(t_i - t)$ results that is appropriate for chamber stability criteria.

As $\omega/\alpha \to 0$, the response function of Eq. (3.4.2–4a) does not vanish as determined by Heidmann, but remains finite, as in Tang's numerical study. This behavior is due solely to the constraint on the injected drop size. Physically, even though all propellant is consumed in a time short compared with a cycle time, there is still a nonvanishing perturbation in burning rate because the droplet burns faster at high pressure.

The term B contains all the processes related to unsteady heat transfer to the droplet, which are dependent on ω_3. As $\mathfrak{K}_L \to \infty$ (essentially the Heidmann-Tang assumption) the results become similar to those of Heidmann and Tang since Eq. (3.4.2–3) becomes

$$q_L' = T_L' \rho_L c_L \cdot \tfrac{4}{3}\pi r_L^3 \cdot i\omega = m_L c_L \frac{dT_L}{dt}$$

and is a pure heat capacitance effect.

Fig. 3.4.2a shows four response curves calculated by use of Eq. (3.4.2–4). The shapes of these curves indicate that essentially the same controlling physics are contained in Eq. (3.4.2–4) as in the Heidmann and Tang models, as may be seen by comparison in the top part of Fig. 3.4.2b. The main difference when comparable assumptions are used is that the peak in the present model is too broad. This is evidently a consequence of the constant size assumption. Curve A, for which $\mathfrak{K}_L/\mathfrak{K} = 100$, closely resembles Tang's results. The rise in the curve is due to interaction with the lifetime; the decay begins when the heat capacitance effect takes over. Heidmann's curve is also similar except for the zero frequency limit. At the injection station (i.e., $\alpha(t - t_i) = 0$) the response curve for this case follows curve B and then breaks to curve A. Averaged over the chamber the response curve would still have a peak in the vicinity of $\omega_3 = 100$, which, for $t_3 = 10^{-2}$ sec (Table 3.4.2a), corresponds to 200 Hz.

For the opposite limit of no internal circulation curves B and C are obtained. In the case of internal circulation the peak is broader than for curve A, and the quasi-steady behavior holds quite far out in the frequency range. Thus, the true state of affairs with regard to the liquid circulation can have a large influence on the results, which indicates that some diagnostic experiments are needed.

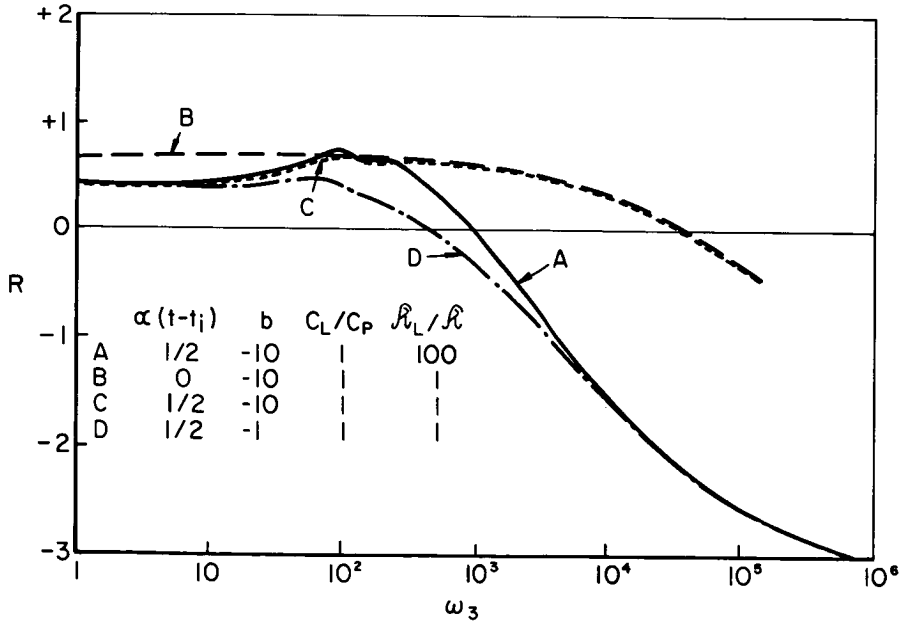

FIGURE 3.4.2a.—Vaporization-rate frequency response functions under various assumptions concerning heat transfer to the liquid, from Eq. (3.4.2–4), with $A = 3.0$, $n = 0.5$, $\gamma = 1.2$, $c_p T_\infty / h_v = 10$, and $T_\infty / T_L = 10$.

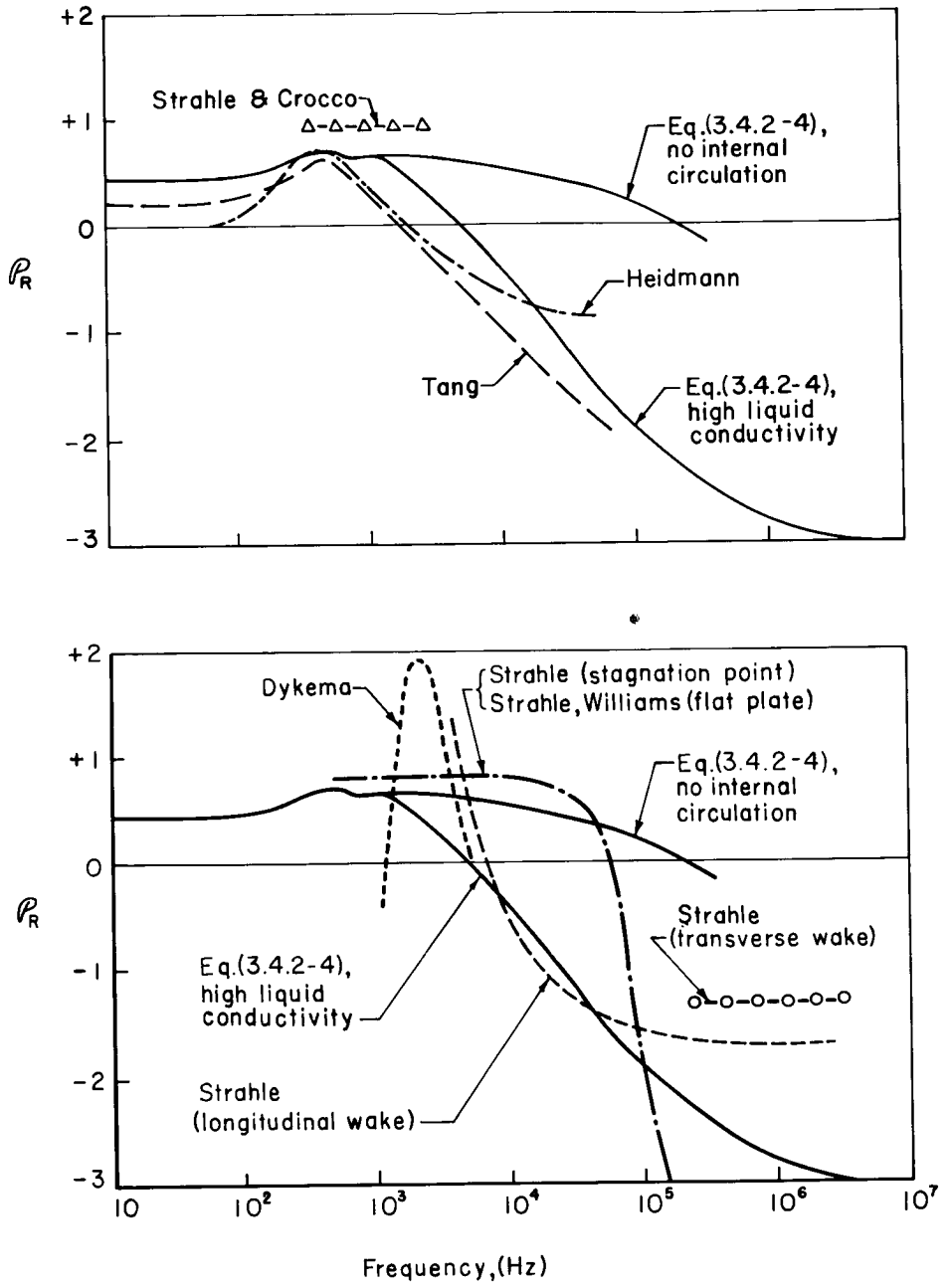

FIGURE 3.4.2b.—Compilation of burning-rate frequency response functions.

Regardless of the nature of the assumptions the heat transfer process is highly delayed in becoming effective. Normally, it would be expected that this process would play a strong role at $\omega_3 \approx 1$, but because of the large slope of the vapor-pressure curve of the liquid propellant it does not become effective until higher frequencies. To illustrate this point, curve D is drawn for the unrealistic case of $b = -1$. Usually $b \approx -10$, so that only small temperature variations are required in the liquid to accommodate the mass transfer equation.

Curves A and C are shown in the top part of Fig. 3.4.2b (for $t_3 = 3.2 \times 10^{-2}$ sec), together with results of Heidmann and Tang. A peak value, obtained by Strahle and Crocco,[671] is also indicated. This peak was obtained by assuming oscillations fast with respect to lifetime but slow with respect to all other processes. Essentially, it is the factor B in Eq. (3.4.2–4a) with $\omega_3 = 0$.

Dykema[235] was the first to discover a response peak in the proper frequency range on the basis of a simplified sphericosymmetric droplet burning model. The assumptions essentially amount to fast oscillations with respect to the liquid processes and lifetime (t_1, t_2, and t_3) and oscillations commensurate with t_4. Because spherical symmetry was considered, t_5 did not enter. A typical response function for this model is shown in the bottom part of Fig. 3.4.2b. It is of sufficient magnitude to drive instability as observed; the analytical details are presented in Sect. 4.4.1.3. A fundamental assumption is that the flame position is constant while the ambient gas is oscillating. Strahle[665] has found that some artifice of this type is necessary to obtain any solution to the spherically symmetric, time-dependent problem. However, it is also known that the flame movement in a well-posed problem can have an influence on the response function.

Actually, even if a flame can be held within the leading-edge boundary layer of a drop, most combustion[665] must still take place in the wake in the usual high-convection field found in combustion chambers. With this in mind, Strahle[669, 666] considered both longitudinal and transverse waves acting upon an overventilated diffusion flame in accordance with the experimental observations of Kumagai and Kimura.[414] The process time of interest is the gas phase diffusion time t_4, the same as for sphericosymmetric burning because the transverse wake scale is the same as the droplet size. In the high frequency limit, which was all that was treated, the wake behavior becomes independent of conditions near the liquid and all other process times are unimportant.

The longitudinal wake analysis is the more satisfactory since the side of approach to the high frequency limit can be seen in the bottom part of Fig. 3.4.2b. However, the analytical procedure allows no estimate of the lowest frequency at which the result is valid; certainly the upward trend cannot continue. Eventually, as the frequency is reduced, the curve must tend toward the low frequency results of Heidmann and Tang, since at sufficiently low frequency, combustion will closely follow vaporization within a cycle time. It is not known whether a response peak develops. The treatment of transverse waves was useful in that it showed that the same physics were involved at the high frequency limit as with longitudinal waves. However, the side of approach to the limit could not be extracted because of a peculiarity in the steady-state flame structure and the occurrence of displacement effects.[666]

While discussing analyses in the frequency range dominated by gas phase diffusion time t_4 it is worth noting that no unsteady treatment of low-Reynolds-number droplet burning has appeared. In this case the problem is nearly sphericosymmetric but, because convection is present, the difficulty in Dykema's work would not arise. The results would be of value near the point where $V_{gas} - V_{liquid} = 0$. Such a treatment would also remove a singularity that appears in the analysis if Nu is chosen in the usual convective form (Sect. 2.4). That is, the $Re^{1/2}$-law must fail near $Re = 0$.

For large Reynolds numbers (say $Re > 10$), Strahle[667, 670] and Williams[744] have considered longitudinal-sound-wave perturbations acting on the leading edge of a burning droplet. A collapsed flame zone was assumed to exist in the interior of the leading edge boundary layer. Strahle considered both the stagnation point and a flat plate. Williams considered only the flat plate but carried the treatment into a wider frequency range than Strahle and also made a wider parametric survey of results. With his solution technique, Williams was not able to extract the burning rate perturbation, which was the result of Strahle's analysis. Instead, Williams introduced an admittance concept that has been shown[178] to yield essentially the same results as the flame burning rate. For practical rocket parameters the admittance and burning rate behavior appear comparable for both the flat plate treatment and the stagnation point treatment. A typical stagnation-point curve near a velocity node is presented in the bottom part of Fig. 3.4.2b.

There are three difficulties with the results of these treatments. First, only shallow response

peaks, if any, occur. Second, the break from quasi-steady behavior occurs at such a large frequency that no influence on stability is expected. Only near the point of relative velocity reversal in a high Reynolds number environment is the frequency in the proper range. This restrictive set of conditions holds for such a short fraction of a droplet lifetime as to have no meaning when considering chamber averages. Third, the important assumption is made that the liquid temperature is constant in time, which from the treatment above means that there is no internal droplet circulation and the partial pressure-temperature slope (b) is sufficiently large. Thus, the cycle time is considered short with respect to t_1 and t_2, commensurate with t_5, and long compared to t_3. This can only be reasonable near the relative velocity reversal point. The break in the curve at rather large values of ωt_5 instead of at lower values could not be anticipated without construction of the theory; in fact, this is the major contribution of these theories. A useful treatment that has not yet been made would be the inclusion of a more realistic liquid state with a leading edge boundary layer behaving quasi-steadily with respect to t_5. It can be shown that such an analysis does not necessarily produce a curve of the form of the tailoff portion of the Heidmann and Tang curves.

The preceding discussion has shown that there are wide differences between the results of the various theories of unsteady droplet burning. In spite of the divergent theoretical results and the absence of proper experiments, three observations can be made: (1) Regardless of the choice of the mechanism, all droplet burning theories show a decoupling of the combustion and acoustic processes at large enough frequency; the item missing is a proper description of the low frequency cutoff. (2) It is this author's opinion that a promising prospect is in further work with respect to t_4, with inclusion of the effects due to interactions with t_1, t_2, and t_3. (3) Diagnostic experiments on the structure of the droplet burning process are needed.

The success of droplet burning theories in correctly predicting the mechanism of high frequency instability is consequently limited; however, there is a large body of evidence which indicates that, if the theoretician were to search diligently enough (with a model including sufficient real-life complexity), a mechanism could be found for the support of high frequency oscillations with the framework of the droplet burning process. The body of evidence is that of the correlation of the observed frequency of oscillation with parameters affecting droplet size (see Sects. 6.3.3, 6.5.2, and Refs. 235, 347). Furthermore, the scaling of frequency with approximately the square of droplet radius is observed. One is hard-pressed to find any mechanism other than droplet burning that would scale results in this manner.

Thus, the value of the droplet burning theories is to present a scaling rule. If one assumes the existence of a response curve with the proper peak that is a universal curve when plotted against ωr_L^2, then this curve can be used to investigate effects of parameter changes on system behavior. The difficulty is that the precise shape of the curve cannot reasonably be expected to be universal; it must depend on fuel type, operating conditions, etc., in some manner, as yet unknown. Thus, whereas effects of droplet size can be investigated in a reasonable way, changes in droplet size are usually produced at the expense of other changes in operating conditions, the effects of which cannot be explained theoretically.

3.4.3 Nonlinear Drop and Spray Burning

3.4.3.1 *Vaporization**.—The only truly nonlinear work concerning the details of the vaporization process is that by Heidmann and Wieber.[347] Other studies, which consider the rocket system interacting with the vaporization process, are reported in the following chapter. Presumably, these systems analyses show the same effects as the Heidmann-Wieber study since the equations are similar. However, this is speculation, since there also are some differences.

Heidmann and Wieber considered the effect of a transverse wave of linear form but finite magnitude on the vaporization process. Combustion was assumed to be instantaneous following vaporization. Thus, no restrictive assumptions concerning the lack of a heat-up period or modification of the convective effect in the Nusselt

* W. C. Strahle, Author.

number were necessary. A response function, equivalent to Eq. (3.4.2–1) averaged over the chamber, was evaluated, but it was done with a numerical technique that is not necessarily equivalent to that usually used in analytical stability criteria. Although it is an intuitively attractive procedure, there is a question about its accuracy in the low frequency limit.

The primary assumption was that the liquid temperature was uniform but time-varying, to which the objections of Sect. 3.4.2.2 may again be raised. Actually, this numerical study preceded the analytical study and the results are qualitatively the same (see Fig. 3.4.2b). The calculated response function was correlated with the ratio of the cycle time to the half-lifetime of the droplets.* The results are interesting because of the existence of the response peak, which occurs usually at the lower end of the range of interest to instability. Some success in its use has been reported.[347]

3.4.3.2 *Effects of shock waves*†.—The combustion characteristics of jets and sprays may be substantially changed in the presence of shock waves. If a shock passes through a combustion field it will cause temperature and pressure increases as well as a gaseous flow immediately behind the shock. The temperature increase will tend to increase the vaporization rate, but this effect may be overshadowed by the aerodynamic breakup of the drops or jets. The latter mechanism is discussed in Sect. 3.3.3, where it is pointed out that under rocket combustor conditions even weak shocks can lead to the onset of drop breakup via the stripping mode.

Williams[746] treated such a problem in an analytical study of the structure of heterogeneous detonation. Subject to the limitation of uniform drop size and no aerodynamic drop shattering, he concluded that the extended reaction zone, due to the relatively slow vaporization process, would lead to large wall losses and hence preclude detonation. In such a case the energy release by combustion would not reinforce the shock, and hence the shock would gradually dissipate. However, if the drops were sufficiently small (less than about 10 microns), the spray detonation would be essentially the same as a gaseous detonation. Under rocket motor conditions the situation will be favorable to a strong interaction of combustion and shock in that there will always be some small drops present and, further, shattering can easily become influential.

Experimental work on the interaction of shock waves and combustion includes the studies of Rabin, et al.,[569] discussed in Sect. 3.3.3. Additional shock tube studies were made by Webber,[722] who noted spontaneous explosion when fine sprays and sprays of a volatile fuel were subjected to shock waves. In an extension of this work, Cramer[171] passed a shock wave through a DECH (diethylcyclohexane, a very non-volatile fuel) spray in an oxygen atmosphere. A steep-fronted, high-velocity wave resulted, which was described as "detonation-like."

A systematic investigation of two-phase detonation by Dabora, Ragland, and Nicholls[207–210, 570, 572] showed conclusively that aerodynamic shattering plays a major role and, in fact, is the main determinant of the overall reaction zone length. Thus the results presented in Sect. 3.3.3 are applicable in fixing the combustion time behind shocks. It was also shown that two-phase Chapman-Jouget detonations could be maintained even though the reaction zone was as long as two feet, with the attendant high heat transfer and frictional losses. The larger drop sizes led to greater reaction zone lengths (since breakup time is proportional to drop size), greater losses, and hence to lower propagation velocities for the same mixture ratio. At the lower velocities, where the temperatures behind the shock were lower, the combustion was observed to be delayed until the droplet wake region, where the sheared-off microdroplets reacted explosively. Local shocks were formed which overtook the main shock and reinforced it, thus providing the mechanism to sustain the wave. At higher wave velocities, and hence higher post-shock temperatures, burning occurred earlier, possibly at the stagnation point of the drop.

Jaarsma and Derksen[384] found that the burning time of DECH drops subjected to shock waves corresponded to the breakup time. This time was two orders of magnitude shorter than a calculated

* In view of the remarks of Sect. 3.4.2, it could also have been correlated with ωt_2.

† J. A. Nicholls, Author of Sects. 3.4.3.2 and 3.4.4.3.

burning time due to forced convection if no shattering occurred. They also observed that burning drops could be extinguished by passage of a shock when the partial pressure of the oxygen in the combustion field was relatively low.

3.4.4 Special Effects

The preceding sections have neglected certain aspects of liquid propellant combustion that may be of considerable importance in unsteady rocket operation. Some of these special effects are considered in this section; however, very little fundamental research has been done, particularly on the unsteady behavior.

3.4.4.1 *Monopropellant fuel.*—Certain fuels of practical importance, such as hydrazine, UDMH, MMH, or blends of these, can support either decomposition or oxidation flames, or both, depending on local oxidizer concentration and convective conditions within the combustion chamber (see Sect. 2.4.3). The addition of exothermic decomposition to the droplet burning processes enhances the burning rate and hence leads to shorter droplet lifetimes.[353] This effect is particularly significant for low values of the droplet Reynolds number based on the relative velocity between the liquid and gas. Unfortunately, only a steady-state analytical model has been constructed.[140] Definitive conclusions regarding the influence of exothermic fuel decomposition on unsteady burning cannot be drawn at this time.

3.4.4.2 *Supercritical chamber pressure.*—When a liquid propellant is sprayed into an atmosphere that is at a pressure greater than the critical pressure of the propellant, the combustion dynamics cannot be expected to be the same as the subcritical dynamics discussed in Sect. 3.4.2. Although some experimental and theoretical efforts have been made on the steady-state problem (Sect. 2.4.2.2), unsteady effects have not yet been considered.* In fact, the steady state is not sufficiently well understood to provide a proper foundation for dynamics investigations. There are some indications that high-pressure pyrolysis effects are of greater importance than supercritical phenomena and that conventional droplet burning concepts are not applicable at very high pressures.[434]

3.4.4.3 *Liquid films on surfaces.*—Liquid propellants may impinge on surfaces inside the combustor, either as coolants for chamber walls or baffles or because of misdirected injector sprays. The question thus arises as to whether such a liquid film can lead to a combustion-supported shock, or "detonation-like" wave (see Sect. 3.4.3.2).

Shock tube experiments have been reported in which thin layers of lubricating oil, grease, or carbon black, once ignited, led to accelerating combustion fronts and eventually to sustained detonation.[294,454] The detonation velocity was somewhat periodic; secondary shocks were observed that overtook the main shock and caused it to accelerate. The main shock slowed gradually after each collision until the next secondary shock overtook it.[570]

In an analytical study, Ragland[571] used laminar boundary layer theory to assess the vaporization and combustion rate of the liquid layer behind the main shock front. Combining these results with the experimental data, and recognizing that in the real case the boundary layer would undoubtedly be turbulent, he concluded that vaporization of the liquid layer is the major rate-controlling mechanism for film detonation. This result is in contrast to the liquid drop case in which aerodynamic shattering is rate-controlling (Sect. 3.4.3.2).

3.5 WAVE PROPAGATION IN COMBUSTION CHAMBERS

Wave motion of the gases in the combustion chamber is an important factor in intermediate and high frequency instability. The nature of this wave motion is discussed in this section, however, coupling with the combustion process is reserved for Chapter 4. Mathematical and experimental studies are presented, and the relationships between wave pattern and chamber geometry are described. The combustion chamber is here

* However, high frequency instability has been observed in tests of rocket combustors at supercritical chamber pressures (see Sect. 7.4.2).

defined as extending from the injector face to the entrance of the nozzle; unsteady nozzle flow is considered in Sect. 3.6.

For convenience, the discussion is divided into three parts. Linear wave motions, considered in the first part, are those in which the wave shape is essentially sinusoidal. The amplitudes of oscillation here are small enough that wave distortion has not occurred. The second section, on nonlinear wave motion, considers the effects of large amplitudes and the resulting wave distortion. Finally, the other causes of wave distortion and weakening, such as liquid and solid particle drag, acoustic linears, and injector-face baffles, are described.

3.5.1 Linear Wave Motion*

The following nomenclature pertains to Sect. 3.5.1 (see also Sect. 4.1.2):

B	Annular chamber transverse distribution constant
$\mathcal{E}$	Nozzle admittance coefficient (complex)
I	Inhomogeneous term in wave equation
I_{mn}	Term in eigenfunction expansion of I
$L_{\nu m}$	Associated Legendre function of first kind
m, n	Eigenfunction indices for rectangular chamber
$\mathcal{Y}$	Admittance of acoustic liner
β	Half-angle of conical chamber
κ	Ratio of height to width of rectangular chamber
ν, m	Eigenfunction indices for conical chamber
ν, η	Eigenfunction indices for circular cylindrical chamber
$\rho_L{}^\circ$	Mass of liquid per unit chamber volume
Σ_{mn}	Term in eigenfunction expansion of entropy perturbation
ϕ	Angle-coordinate in spherical coordinate system
χ	Transverse eigenvalue: $\chi^2 = m^2 + n^2$ for rectangular chamber; $\chi = s_{\nu\eta}$ for circular chamber
χ^*	Transverse eigenvalue for rigid, impervious chamber walls
$\psi_{\nu,\eta}$	Transverse distribution function for perturbations in circular cylindrical chamber

* W. A. Sirignano, Author.

3.5.1.1 *General considerations.*—High frequency and intermediate frequency combustion instability in a liquid propellant rocket motor involves wave motion in the combustion chamber and in the exhaust nozzle. A disturbance of the flow, at any point in the chamber or nozzle, would propagate as a wave away from that point. The boundary conditions on the wave motion are prescribed according to the chamber, injector, and nozzle shapes. These boundary conditions are physical constraints on the wave motion and lead to certain *discrete* modes of oscillation. That is, only certain frequencies and wave patterns are allowable. In theory these are infinite in number; although only the lower-frequency modes appear in practice. These frequencies and wave patterns are, in mathematical terms, eigenvalues and eigenfunctions. When they occur in combustion chambers they are analogous to frequencies and wave patterns for the classical problems of vibrating strings and membranes (of finite dimensions), and of organ-pipe and closed chamber oscillations. In fact, the rocket combustion chamber may be considered (for the purpose of physical insight) as a modification of a closed chamber having certain complicating features: a through-flow, two-phase flow with combustion and droplet drag; and the presence of an injector at one end and an exhaust nozzle at the other end. Also, acoustic absorption devices may be placed along the walls or at the injector face.

It is now clear how the wave patterns and frequencies in the rocket motor may be considered as distortions of the wave patterns and frequencies in the closed chamber case. These distortions, of course, are due to the complicating features just listed. If these distortions are small, the model can be analyzed by an iterative approach, in which these complicating features are neglected in the first step. Then the first approximation to the solution for the rocket chamber wave patterns and frequencies are equivalent to the closed chamber solutions. These solutions are given in standard acoustics texts[495,579] but will also be reproduced later in this section. The complicating features account for energy removal from and energy addition to the oscillating gases in the chambers. Essentially, the amplitude of the oscillation is determined by the condition of equilibrium; that is, in equilibrium, the amount of energy removed

from the chamber oscillation equals the amount added to the chamber oscillation (per unit time). Whenever the amount added is greater (less) than the amount removed, the amplitude grows (decays) until an equilibrium is reached. For stable engines, this equilibrium only occurs at zero amplitude while for unstable engines, it occurs at some finite amplitude.

The magnitude of this finite amplitude can only be determined by a nonlinear theory of some sort. There is some advantage, however, to a linear theory in which the amplitude is considered to be very small and quantities which are quadratic in the amplitude, or smaller, are neglected. It is simpler to develop a linear theory than a more general nonlinear theory since so much more is known about linear differential equations than nonlinear differential equations. The linear theory is sufficient to analyze the onset of spontaneous instability since it predicts when small perturbations grow, remain neutral, or decay. On the other hand, a nonlinear theory is required to predict the transient behavior and the limit cycle if the small perturbation grows. Wave steepening and shock formation are nonlinear effects which obviously are neglected in a linear theory. Thus, a nonlinear theory is required to predict accurately the wave shapes for pressures and velocity. Furthermore, in cases where instability does not occur spontaneously but must be triggered by some finite-amplitude perturbation, only a nonlinear theory could predict the onset of instability.

A linear analysis can, however, accurately show various features of the oscillations, at least in a qualitative manner, if not always a quantitative manner. For example, the effects of the nozzle and chamber geometries, the effect of the combustion distribution, the effect of droplet drag, and the effect of acoustic liners can be predicted with a large degree of confidence. The natural frequencies of oscillation can be predicted with extreme accuracy.

There exist a number of linear analyses of longitudinal oscillations in cylindrical chambers[178, 179, 180] and of three-dimensional oscillations in circular cylindrical chambers.* The approach taken in this section is essentially equivalent to these analyses, which consider small amplitude oscillations and a low mean-flow Mach number. However, the discussion here is somewhat more general; annular chambers, conical chambers, and rectangular cross-section chambers are also considered. The annular and conical chambers are of practical importance; the rectangular cross sections have been useful for certain diagnostic experiments (Sect. 9.2). In addition the present analysis considers the effect of acoustic liners.

The conservation equations governing the unsteady flow in a rocket combustion chamber are presented in Sect. 4.1. By appropriate differentiations and combinations, there is obtained the wave equation for the pressure oscillations

$$\frac{1}{\gamma}\left[\frac{\partial^2 p}{\partial t^2} - a^2\nabla^2 p\right] = a^2\frac{\partial M}{\partial t} - a^2\nabla\cdot[\mathbf{F}+M\mathbf{V}-\nabla\cdot\rho\mathbf{V}\mathbf{V}] + (\gamma-1)\frac{\partial}{\partial t}[G-\mathbf{V}\cdot\mathbf{F}] - \frac{\partial}{\partial t}[p\mathbf{V}\cdot\nabla\sigma] + \frac{\partial p}{\partial t}\frac{\partial a^2}{\partial t} \tag{3.5.1-1}$$

where a is the sonic velocity, ρ is the density, σ is the entropy, and $\mathbf{V}$ is the velocity, all for the gas phase; M is the burning rate, or rate of generation of gas; $\mathbf{F}$ is the force per unit volume exerted on the gas because of momentum exchange with the liquid phase; G is a combination of energy release rate due to chemical reaction and phase change and of the rate of energy exchange between the two phases. In Eq. (3.5.1–1) the following nondimensionalizing scheme has been used: thermodynamic properties are nondimensionalized with respect to their steady-state stagnation values,* the velocities are nondimensionalized with respect to the steady-state stagnation sonic velocity, the burning rate M by the product of the stagnation density and the sonic velocity divided by the characteristic length of the combustor, the time t by the characteristic length divided by the stagnation speed of sound, and the spatial coordinates by the characteristic length.

* See References 178, 187, 203, 582, 583 and 630.

* When terms of the order of the Mach number squared are neglected, these values are uniform throughout the chamber.

For a linear analysis, each dependent variable can be considered to be the sum of a steady-state part and a perturbation, e.g.,

$$p=\bar{p}+p'e^{st}$$

Squares and products of perturbations are considered to be negligibly small. Also, $\bar{\mathbf{V}}$, $\bar{\mathbf{V}}_L$, k, $\bar{M}$, and M' may be considered as sufficiently small so that their squares and products may be neglected. Assuming that the burning rate equals the vaporization rate, the energy release term E in Eq. (4.1.2–7) may be combined with the liquid internal energy. It can be shown that the following approximations are then valid:

$$(\mathbf{F}+M\mathbf{V})'\approx -k\bar{\rho}_L{}^{\circ}\mathbf{V}'$$

$$(G-\mathbf{V}\cdot\mathbf{F})'\approx G'\approx -\bar{M}h_s'\approx -\frac{\bar{M}}{\gamma}p'$$

With these simplifications, Eq. (3.5.1–1) gives

$$\bar{p}=\text{constant}$$

for the steady state and

$$\frac{1}{\gamma}[s^2p'-\nabla^2p']=sM'+\nabla\cdot[k\bar{\rho}_L{}^{\circ}\mathbf{V}'+\nabla\cdot\bar{\mathbf{V}}\mathbf{V}'+\nabla\cdot\mathbf{V}'\bar{\mathbf{V}}]-\frac{\gamma-1}{\gamma}s\bar{M}p'-s[\bar{\mathbf{V}}\cdot\nabla\sigma'] \qquad (3.5.1\text{–}2)$$

for the perturbations, where k is a liquid-gas momentum interchange coefficient and $\rho_L{}^{\circ}$ is the mass of liquid per unit chamber volume.

It is convenient to use Cartesian coordinates (x, y, z) for chambers with rectangular cross sections, cylindrical coordinates (x, r, θ) for chambers with circular cross sections, and spherical coordinates (r, ϕ, θ) for conical chambers. In the case of a conical chamber, it is assumed that the injector face is a portion of a spherical surface whose center corresponds to the apex of the cone. The velocity components (for any coordinate system) are denoted by u, v, and w.

The right-hand side of Eq. (3.5.1–2) is of the order of the mean-flow Mach number. Neglecting terms of the order of Mach number squared compared to unity, it can be shown that

$$\frac{1}{\gamma}[s^2p'-\nabla^2p']=sM'-\frac{k\bar{\rho}_L{}^{\circ}sp'}{\gamma}-\frac{(\gamma-1)}{\gamma}s\bar{M}p'-s\bar{u}\frac{\partial\sigma'}{\partial x_1}+2\frac{d\bar{u}}{dx_1}\frac{\partial u'}{\partial x_1}-2\bar{u}\frac{s}{\gamma}\frac{\partial p'}{\partial x_1}+2u'\frac{d^2\bar{u}}{dx_1{}^2}-2\frac{s}{\gamma}\frac{d\bar{u}}{dx_1}p'+\Omega\equiv I \qquad (3.5.1\text{–}3)$$

where $x_1=x$ and $\Omega=0$ for Cartesian and cylindrical coordinates and $x_1=r$ and

$$\Omega=-\frac{3s}{\gamma}p'\frac{\bar{u}}{r}+2u'\frac{d}{dr}\left(\frac{\bar{u}}{r}\right)+\frac{d\bar{u}}{dr}\left[\frac{2u'}{r}+\frac{v'\cot\phi}{r}\right]+\bar{u}\left[2\frac{\partial}{\partial r}\left(\frac{u'}{r}\right)+\cot\phi\frac{\partial}{\partial r}\left(\frac{v'}{r}\right)\right]+\frac{\bar{u}}{r}\left[-\frac{\partial u'}{\partial r}-\frac{2u'}{r}-\frac{v'}{r}\cot\phi\right] \qquad (3.5.1\text{–}3a)$$

for spherical coordinates.

Further developments of the equations and their ultimate solution is made by means of either eigenfunction expansions or a Green's function. The details of either approach depends upon the particular boundary conditions or, in other words, the geometry of the combustion chamber.

3.5.1.2 *Application to specific hardware geometries.*—The method of eigenfunction expansions will be employed here.* Only the leading term in the eigenfunction expansion is of interest to us, since it is the main factor in determining the stability and the frequency of the oscillation. Also, in small amplitude oscillatory situations without shockwaves, this term predominates and accurately predicts the wave shape.

For rectangular cross sections, the transverse eigenfunctions are sinusoidal and the expansions are

* On the other hand, Culick[351] has made use of a Green's function in solving this type of problem.

$$
\begin{aligned}
p' &= P_{mn}(x)\cos(my+\delta_1)\cos(nz+\delta_2)+\cdots\\
u' &= U_{mn}(x)\cos(my+\delta_1)\cos(nz+\delta_2)+\cdots\\
v' &= V_{mn}(x)\sin(my+\delta_1)\cos(nz+\delta_2)+\cdots\\
w' &= W_{mn}(x)\cos(my+\delta_1)\sin(nz+\delta_2)+\cdots\\
\sigma' &= \Sigma_{mn}(x)\cos(my+\delta_1)\cos(nz+\delta_2)+\cdots\\
M' &= M_{mn}(x)\cos(my+\delta_1)\cos(nz+\delta_2)+\cdots\\
I &= I_{mn}(x)\cos(my+\delta_1)\cos(nz+\delta_2)+\cdots
\end{aligned}
\tag{3.5.1–4}
$$

where Eq. (3.5.1–3) and (–4) may be considered to yield

$$
\begin{aligned}
I_{mn} = sM_{mn} &- \frac{k\rho_L{}^{\circ}s}{\gamma}P_{mn} - \frac{\gamma-1}{\gamma}sP_{mn}\frac{d\bar{u}}{dx}\\
&- s\bar{u}\frac{d\Sigma_{mn}}{dx} + 2\frac{d\bar{u}}{dx}\frac{dU_{mn}}{dx}\\
&- 2\bar{u}\frac{s}{\gamma}\frac{dP_{mn}}{dx} + 2\frac{d^2\bar{u}}{dx^2}U_{mn} - 2\frac{s}{\gamma}\frac{d\bar{u}}{dx}P_{mn}
\end{aligned}
\tag{3.5.1–5}
$$

These expansions are chosen so that the system is separable. In the above relations, x, y and z should be considered quantities nondimensionalized by the chamber width.

Eqs. (3.5.1–4) and (–5) may now be combined to yield the differential equation

$$
\frac{1}{\gamma}\frac{d^2P_{mn}}{dx^2} - \frac{1}{\gamma}(s^2+\chi^2)P_{mn} = -I_{mn} \tag{3.5.1–6}
$$

where

$$
\chi^2 = m^2+n^2
$$

The boundary conditions at the chamber walls determine m and n. If κ is the ratio of chamber height to width, and m^* and $n^*\kappa$ are each considered to be zero or any integer times π, we have, for unlined chambers, that the normal velocity at the chamber walls is zero. Therefore

$$
\delta_1 = 0; \qquad \delta_2 = 0
$$

$$
m = m^*; \qquad n = n^*
$$

or the eigenvalue

$$
\chi^2 = m^{*2}+n^{*2} = \chi^{*2}
$$

However, for lined† chambers with the admittance coefficient, $L = L_r + iL_i$, it can be shown that

$$
\delta_1 = -\frac{\gamma s\mathcal{Y}}{m^*}; \qquad \delta_2 = -\frac{\gamma s\mathcal{Y}}{n^*\kappa}
$$

$$
\chi = \chi^* + \frac{2\mathcal{Y}\gamma s}{\chi^*}\left(\frac{1+\kappa}{\kappa}\right) \equiv \chi^* + \chi^{(1)} \tag{3.5.1–7}
$$

For longitudinal modes, $m^* = n^* = 0$ but with liners there would still be transverse motion.

A similar eigenfunction expansion can be made for circular cross-sectional chambers. Annular chambers as well as "full" chambers may be considered with the following:

$$
\begin{aligned}
p' &= P_{\nu\eta}(x)\psi_{\nu\eta}(r)e^{i\nu\theta}+\cdots\\
u' &= U_{\nu\eta}(x)\psi_{\nu\eta}(r)e^{i\nu\theta}+\cdots\\
v' &= V_{\nu\eta}(x)\frac{d\psi_{\nu\eta}}{dr}(r)e^{i\nu\theta}+\cdots\\
w' &= W_{\nu\eta}(x)\frac{\psi_{\nu\eta}(r)}{r}e^{i\nu\theta}+\cdots\\
\sigma' &= \Sigma_{\nu\eta}(x)\psi_{\nu\eta}(r)e^{i\nu\theta}+\cdots\\
M' &= M_{\nu\eta}(x)\psi_{\nu\eta}(r)e^{i\nu\theta}+\cdots\\
I &= I_{\nu\eta}(x)\psi_{\nu\eta}(r)e^{i\nu\theta}+\cdots
\end{aligned}
\tag{3.5.1–8}
$$

These expressions correspond to spinning modes but standing modes may be obtained in a trivial manner by a linear combination of two modes spinning in opposite directions.

In Eq. (3.5.1–8), the radial eigenfunctions are linear combinations of the Bessel functions so that

$$
\psi_{\nu\eta}(r) = J_\nu(s_{\nu\eta}r) + BY_\nu(s_{\nu\eta}r)
$$

where B is a nonzero constant for annular chambers and is zero for "full" chambers. r and x are nondimensionalized by the outside wall radius.

Combination of Eqs. (3.5.1–3) and (–8) yields the relation for $I_{\nu\eta}(x)$. This relation is given by Eq. (3.5.1–5) if m and n are replaced by ν and η, respectively. Furthermore, Eqs. (3.5.1–3) and (–8) can yield a differential equation for $P_{\nu\eta}(x)$ which is identical to Eq. (3.5.1–6) if m and n are replaced by ν and η and

$$
\chi = s_{\nu\eta}
$$

† All four walls are considered to be acoustically lined here, but other cases could be considered.

ν is always zero or an integer to maintain continuity. Consider first the full circular chamber boundary condition. For unlined chambers, the normal velocity at the wall is zero so that $s_{\nu\eta}=s_{\nu\eta}^*$ which is a solution of

$$J_\nu'(s_{\nu\eta}^*)=0$$

See Table 3.5.1 for the roots of this equation. On the other hand, for lined chambers, it can be shown that

$$s_{\nu\eta}\approx s_{\nu\eta}^*+\frac{\gamma s}{s_{\nu\eta}^*}\frac{\mathcal{Y}}{1-\left(\frac{\nu}{s_{\nu\eta}^*}\right)^2}\equiv\chi^*+\chi^{(1)} \qquad (3.5.1\text{–}9)$$

Again, L is a liner admittance coefficient.

In the unlined annular chamber where ξ is the ratio of the inner wall radius to the outer wall radius, we find that $s_{\nu\eta}=s_{\nu\eta}^*$ which is a root of

$$\frac{dJ_\nu}{dr}(s_{\nu\eta}^*)\frac{dY_\nu}{dr}(s_{\nu\eta}^*\xi)-\frac{dJ_\nu}{dr}(s_{\nu\eta}^*\xi)\frac{dY_\nu}{dr}(s_{\nu\eta}^*)=0$$

Roots of this equation have been calculated in Ref. 120. In addition, we find that $B=B^*$ where

$$B^*=-\frac{dJ_\nu}{dr}(s_{\nu\eta}^*\xi)\Big/\frac{dY_\nu}{dr}(s_{\nu\eta}^*\xi)$$

TABLE 3.5.1.—ROOTS OF $\frac{dJ_\nu}{dr}(s_{\nu\eta})=0$

$\left(\text{Frequency } f=\frac{s_{\nu\eta}\bar{a}_c}{2\pi r_c}\right)$

ν	η	$s_{\nu\eta}$	Transverse character of mode
1	1	1.8413	First tangential
2	1	3.0543	Second tangential
0	2	3.8317	First radial
3	1	4.2012	Third tangential
0	3	7.0156	Second radial
1	2	5.3313	Combined first tangential and first radial
1	3	8.5263	Combined first tangential and second radial
2	2	6.7060	Combined second tangential and first radial

These conditions imply that the radial velocity is zero at both the inner and outer walls.

With an acoustic liner on both chamber walls, it follows that

$$s_{\nu\eta}=s_{\nu\eta}^*+\frac{\gamma s\mathcal{Y}}{s_{\nu\eta}^*}\frac{f(s_{\nu\eta}^*)-f(s_{\nu\eta}^*\xi)}{\left[\left(\frac{\nu}{s_{\nu\eta}^*}\right)^2-1\right]f(s_{\nu\eta}^*\xi)-\xi\left[\left(\frac{\nu}{s_{\nu\eta}^*\xi}\right)^2-1\right]f(s_{\nu\eta}^*)}$$

$$\equiv\chi^*+\chi^{(1)} \qquad (3.5.1\text{–}10)$$

and

$$B=B^*+\frac{\gamma s\mathcal{Y}}{s_{\nu\eta}^*}\frac{\left(\frac{\nu}{s_{\nu\eta}^*}\right)^2\left(\frac{1}{\xi}-1\right)+(1-\xi)}{\left[\left(\frac{\nu}{s_{\nu\eta}^*}\right)^2-1\right]f(s_{\nu\eta}^*\xi)-\xi\left[\left(\frac{\nu}{s_{\nu\eta}^*\xi}\right)^2-1\right]f(s_{\nu\eta}^*)}$$

where

$$f(x)\equiv Y_\nu'(x)/[J_\nu(x)+B^*Y_\nu(x)]$$

Again, for longitudinal modes there will be radial motion in the presence of acoustic liners.

So, it is seen that the governing equations for the longitudinal variations can be reduced to a similar form for rectangular and circular (including annular) cross-sectional geometries. It is reasonable to assume that this is possible for all cylindrical geometries, no matter what the cross-sectional shape is. Subscripts are omitted in the following discussion, so that it may be understood that the analysis has some generality.

It is convenient to write the variables as the sum of two terms: one of order unity (zero superscript) and the other of the order of the mean flow Mach number (unity superscript). That is,

$$\begin{aligned} P&=P^{(0)}+P^{(1)}\\ U&=U^{(0)}+U^{(1)}\\ M&=M^{(1)}\\ \Sigma&=\Sigma^{(1)}\\ s&=s^{(0)}+s^{(1)}\end{aligned} \qquad (3.5.1\text{–}11)$$

The mass source and entropy perturbations must be of the order of the Mach number since they disappear as the mean flow disappears. It is also assumed that all liner and nozzle admittance terms are of the order of the mean flow Mach number.

Now, Eqs. (3.5.1–5), (–6), (–7) (or (–9) or (–10)), and (–11) yield after separation according to order in Mach number

$$\frac{1}{\gamma}\frac{d^2P^{(0)}}{dx^2}-\left[\frac{(s^{(0)})^2+(\chi^*)^2}{\gamma}\right]P^{(0)}=0 \qquad (3.5.1\text{–}12)$$

$$\frac{1}{\gamma}\frac{d^2P^{(1)}}{dx^2}-\left[\frac{(s^{(0)})^2+(\chi^*)^2}{\gamma}\right]P^{(1)}$$

$$=\frac{2s^{(0)}s^{(1)}}{\gamma}P^{(0)}+\frac{2\chi^*\chi^{(1)}}{\gamma}P^{(0)}-s^{(0)}M^{(0)}$$

$$+\frac{k\rho_L{}^{\circ}s^{(0)}}{\gamma}P^{(0)}+\frac{\gamma+1}{\gamma}s^{(0)}\frac{d\bar{u}}{ux}P^{(0)}+s^{(0)}\bar{u}\frac{d\Sigma^{(1)}}{dx}$$

$$-2\frac{d\bar{u}}{dx}\frac{dU^{(0)}}{dx}+2\bar{u}\frac{s^{(0)}}{\gamma}\frac{dP^{(0)}}{dx}-2\frac{d^2\bar{u}}{dx^2}U^{(0)}$$

$$+\frac{2s^{(0)}}{\gamma}\frac{d\bar{u}}{dx}P^{(0)} \qquad (3.5.1\text{–}13)$$

The longitudinal velocity disappears at the injector face so that the boundary conditions there become after some manipulation with the momentum equation

$$\frac{dP^{(0)}}{dx}=0 \quad \text{at} \quad x=0 \qquad (3.5.1\text{–}14)$$

and

$$\frac{dP^{(1)}}{dx}=0 \quad \text{at} \quad x=0 \qquad (3.5.1\text{–}15)$$

Similarly, the nozzle boundary conditions are considered as discussed in Sect. 3.6, so that

$$\frac{dP^{(0)}}{dx}=0 \quad \text{at} \quad x=x_e \qquad (3.5.1\text{–}16)$$

and

$$\frac{dP^{(1)}}{dx}=s^{(0)}\mathcal{E}P^{(0)}-\gamma\bar{u}_e\frac{dU^{(0)}}{dx} \quad \text{at} \quad x=x_e \qquad (3.5.1\text{–}17)$$

It follows then from Eqs. (3.5.1–12), (–14) and (–16) that

$$P^{(0)}=\cos\sqrt{(\omega^{(0)})^2-(\chi^*)^2}\,x \qquad (3.5.1\text{–}18)$$

where $s^{(0)}=i\omega^{(0)}$. Obviously, since the system is homogeneous, any arbitrary constant multiplied by the above solution is still a solution so that the amplitude is not determined by a linear analysis. From momentum considerations, it can be shown that

$$U^{(0)}=\frac{\sqrt{(\omega^{(0)})^2-(\chi^*)^2}}{\gamma i\omega^{(0)}}\sin\sqrt{(\omega^{(0)})^2-(\chi^*)^2}\,x \qquad (3.5.1\text{–}19)$$

Furthermore, it can be shown that the transverse velocity component has a longitudinal variation which is in phase with the longitudinal variation of the pressure dependence. In Eqs. (3.5.1–18) and (–19), the frequency is found to be

$$\omega^{(0)}=\sqrt{(\chi^*)^2+\frac{\pi^2j^2}{x_e{}^2}} \qquad j=0,1,2,\ldots$$

The nature of the linear oscillations is seen from Eqs. (3.5.1–4), (–7), (–18), and (–19). In general, undulatory functions such as sinusoidal and Bessel functions describe the amplitude as a function of position in the chamber. The presence of the chamber walls, the injector, and the nozzle tend to prevent travelling waves but allow standing waves. That is, only standing waves may occur in the longitudinal direction for any chamber, in the radial direction for circular chambers, and in both transverse directions for rectangular chambers.* This occurs because a velocity node must be placed at the chamber walls and at the injector-face. Also, the nozzle entrance has small longitudinal velocity variations, so that to lowest order, it is a node. Travelling (spinning) waves occur only in the tangential direction for circular chambers; however, the presence of injector-face baffles will inhibit these modes, allowing only standing modes.

At times, the argument of the trigonometric functions in Eqs. (3.5.1–18) and (–19) may become small imaginary numbers. It is convenient to use the hyperbolic cosine and sine functions in that case.

It must be remembered that the waveforms predicted by a linear analysis can be grossly in

* It is possible to obtain transverse travelling modes chambers with square cross-sections.

error for large amplitude oscillations, especially if shockwaves form.

It can be shown that Eqs. (3.5.1–13), (–15) and (–17) imply after substitution by (–18) and (–19) that

$$As^{(1)}x_e-\mathcal{E}+A\frac{\chi^*}{i\omega^{(0)}}\chi^{(1)}x_e-\gamma\int_0^{x_e}M^{(1)}\cos\pi j\frac{x}{x_e}dx$$

$$+\int_0^{x_e}k\bar{\rho}_L{}^\circ\cos^2\pi j\frac{x}{x_e}dx$$

$$+(\gamma+1)\int_0^{x_e}\frac{d\bar{u}}{dx}\cos^2\pi j\frac{x}{x_e}dx$$

$$+2\frac{\pi^2j^2}{x_e{}^2(\omega^{(0)})^2}\int_0^{x_e}\frac{d\bar{u}}{dx}\cos^2\pi j\frac{x}{x_e}dx$$

$$-\frac{\pi j}{x_e}\int_0^{x_e}\bar{u}\sin 2\pi j\frac{x}{x_e}dx$$

$$+\frac{\pi j}{x_e(\omega^{(0)})^2}\int_0^{x_e}\frac{d^2\bar{u}}{dx^2}\sin 2\pi j\frac{x}{x_e}dx=0 \quad (3.5.1\text{–}20)$$

where $A=A(j)$. For purely transverse modes $A=A(0)=2$ while for mixed modes or purely longitudinal ($j=1, 2$, etc.), $A=1$. Eq. (3.5.1–20) may be interpreted as a complex relation or two real relations which determine $s^{(1)}=\lambda^{(1)}+i\omega^{(1)}$. $\omega^{(1)}$ is a modification (of the order of the Mach number) of the frequency, but more importantly, the sign of $\lambda^{(1)}$ determines the stability. For $\lambda^{(1)}$ positive, the oscillation amplitude grows with time and instability occurs, while for $\lambda^{(1)}$ negative, the amplitude decays and, therefore, stability occurs. Neutral stability occurs with $\lambda^{(1)}=0$. The effect of entropy waves for sufficiently well distributed combustion can be shown to be negligible so that entropy waves are neglected in Eq. (3.5.1–20).

Separation of the real and imaginary parts of Eq. (3.5.1–20) and simplification by means of integration of parts yields:

$$A\lambda^{(1)}x_e=\mathcal{E}_r-\frac{A\chi^*}{\omega^{(0)}}x_e\chi_i{}^{(1)}+\gamma\int_0^{x_e}M_r{}^{(1)}\cos\pi j\frac{x}{x_e}dx$$

$$-\frac{1}{2}\int_0^{x_e}k\bar{\rho}_L{}^\circ\left(1+\cos 2\pi j\frac{x}{x_e}\right)dx$$

$$-(\gamma+1)\bar{u}_e+\left(\frac{j\pi}{\omega^{(0)}x_e}\right)^2\bar{u}_e$$

$$-\frac{j\pi}{x_e}\left[\gamma-2\left(\frac{\pi j}{x_e\omega^{(0)}}\right)^2\right]\int_0^{x_e}\bar{u}\sin 2j\pi\frac{x}{x_e}dx \quad (3.5.1\text{–}21)$$

and

$$A\omega^{(1)}x_e=\mathcal{E}_i+\frac{A\chi^*}{\omega^{(0)}}x_e\chi_r{}^{(1)}+\gamma\int_0^{x_e}M_i{}^{(1)}\cos\pi j\frac{x}{x_e}dx \quad (3.5.1\text{–}22)$$

The first term on the right-hand-side of Eq. (3.5.1–21) is the real part of the nozzle admittance coefficient. For longitudinal modes, it is negative and therefore represents a stabilizing factor. However, for first tangential mode oscillations, it surprisingly is positive indicating that the nozzle has a destabilizing effect for that mode. Calculations (see Sect. 3.6 and Sect. 8.4.3) indicate that $\mathcal{E}_r$ can be of the order of the Mach number in certain cases. In those cases, the effect of the nozzle is important compared to other effects to be discussed. In other cases, calculations show that this term is of higher order and has, therefore, a negligible effect upon the stability (except in marginal situations). In general, the significant changes in the engine stability characteristics of an engine which can be achieved through modifications of the nozzle design cannot be neglected.

The second term which represents the damping effect of acoustic liners can be the largest stabilizing factor with proper design. Further discussion of this term is contained in Sect. 3.5.3.2. Also, acoustic liner operation is discussed in Sect. 8.3.

The third term on the right-hand-side of Eq. (3.5.1–21) represents the driving mechanism provided by the combustion process. This destabilizing term contains the burning rate perturbation which is discussed in Sections 3.4, 4.2.1.2, and 4.3.1.3. The fourth term, representing droplet drag, has a stabilizing effect and is discussed further in Section 3.5.3.1.

For longitudinal modes of oscillation $\omega^{(0)}=j\pi/x$ and the last three terms of Eq. (3.5.1–21) combine to yield the negative (stabilizing) quantity

$$-\gamma\bar{u}_e-\omega^{(0)}(\gamma-2)\int_0^{x_e}\bar{u}\sin 2\omega^{(0)}x dx$$

This implies that distribution of combustion tends to stabilize the longitudinal modes. For purely transverse modes $j=0$ and these last three terms are simply $-(\gamma+1)\bar{u}_e$ which is a stabilizing quantity independent of combustion distribution. These terms are most important as stabilizing quantities; usually, only the acoustic liner term is more important.

Eq. (3.5.1–22) gives the frequency correction due to the nozzle, liner, and combustion process. This equation is weakly coupled to Eq. (3.5.1–21) since the frequency appears implicitly in the arguments of the nozzle and liner admittance coefficients. It should also appear in the combustion response term. If in the range of interest $\mathcal{E}_r$, L_r, and the combustion response terms are not strong functions of the frequency ω, we may set $\omega=\omega^{(0)}$ in Eq. (3.5.1–21) which would uncouple the two equations with no loss of accuracy. If any of them are strong functions, the two equations should be solved simultaneously.

The question arises as to whether Eqs. (3.5.1–21) and (3.5.1–22) apply to transverse modes in the limiting case of concentrated combustion, since a different result has been obtained for this case.[771] The differences in the analytical procedures are discussed in some detail in Ref. 650. Isentropic oscillations are assumed in Ref. 771, and the change in velocity which a particle undergoes as it changes phase is not taken into account. This velocity change provides an important damping effect. Therefore, the implication is that Eqs. (3.5.1–21) and (3.5.1–22) should be used even in the concentrated combustion case for transverse modes and that these relations were not obtained in Ref. 771 only because certain physical effects were neglected. This discrepancy does not occur in the concentrated combustion case for longitudinal mode oscillations because the combustion zone is a velocity node (to lowest order) and the change in velocity of a particle changing phase is of higher order.

Other than this discrepancy, and the one in the droplet drag term discussed in Sect. 3.5.3.1, Eqs. (3.5.1–21) and (–22) can be shown to be in agreement with previously published stability relations which result from linear analyses. That is, any other differences can be shown to be of higher order or else due to the more general nature of the present discussion.

It is interesting to note that the same stability relation applies for various cylindrical configurations: rectangular cross-sections, circular cross-sections, and circular annular cross-sections. There will be the same effect of combustion distribution droplet drag nozzle entrance Mach number, combustion response, frequency, and ratio of specific heats in the various configurations. However, the actual values of the nozzle admittance and acoustic liner terms would differ from one configuration to another. Again, it could be speculated that Eqs. (3.5.1–21) and (–22) might apply to all cylindrical chambers, no matter what the cross-sectional shape.

It is expected that the stability relations for chambers of varying cross-sectional area would differ from Eqs. (3.5.1–21) and (–22). It is still to be determined exactly what effect area change might have. There seem to be two approaches to the solution of this problem. One is to consider the case of small area change as a small perturbation to the cylindrical case. The other approach which applies only for conical chambers involves the use of spherical coordinates as discussed earlier.

For conical chambers, the lowest order approximation to the pressure perturbation is given by

$$P_{\nu m}(r)L_{\nu m}(\cos\phi)e^{i\nu\theta}e^{st}$$

where ν is an integer (or zero) and $L_{\nu m}$ is a Legendre's associated function of the first kind. m is determined by the relation of zero normal velocity at the wall or $L'(\cos\beta)=0$ where β is the half-angle of the converging chamber.

It can be shown that

$$P_{\nu m}(r)=\frac{1}{\sqrt{r}}J_{(m+1/2)}(\omega^{(0)}r)+B\frac{1}{\sqrt{r}}J_{-(m+1/2)}(\omega^{(0)}r)$$

where J is a Bessel function of the first kind and $\omega^{(0)}$ and B are determined by boundary conditions at the injector and nozzle entrance. The above relation applies strictly to a spinning wave but the standing wave is obtained in a trivial manner by the summation of two spinning waves travelling in opposite directions.

Thus, for conical chambers, the amplitude variation is described by sinusoidal, Bessel, and associated Legendre functions. As with the cylindrical chambers, travelling modes will occur in the azimuthal direction.

3.5.2 Nonlinear Wave Motion

The following nomenclature pertains to Sect. 3.5.2:

r_p Base pressure ratio for wave reflection
δ_r Radial gas displacement
δ_t Tangential gas displacement
ϵ Perturbation amplitude parameter

3.5.2.1 *Introduction.**—Random pressure waves, generated by a variety of processes or events, can propagate through the reacting mixture in a combustion chamber and with time can reduce to modes of resonance dictated by the rocket chamber geometry and the wave forcing function.† The existence of resonance is dependent on whether the wave-energy accumulative processes are greater than the dissipative processes. The history of the wave shape and structure is determined not only by the gas dynamics of the reacting medium, but also by the initial wave shape, the characteristics of the chamber boundaries, the unsteady behavior of the mass and concomitant energy sources, and the dissipative and dispersive processes that occur.[308,481]

The wave motion in a combustion chamber can be described by the conservation equations for gas-liquid flow that include mass and drag source and heat sink terms (Sect. 4.1.2). The wave forcing function comprises the mass source terms and their derivatives. Such a mass source term (M) should include the position- and time-dependent behavior of all of the propellant particles in the chamber. A major simplification is achieved by considering M to be the product of three functions: (1) the initial propellant spray distribution function across the injector face based on the injector design and hydrodynamics (Sect. 2.3), (2) a distribution function that gives the particle sizes at any location in the chamber,[308,740] and (3) a function that expresses the time-dependent behavior of a mass source in a time-dependent environment (Sect. 3.4).

A characteristic time for the wave motion is the wave period; for the particle, the characteristic time is the relaxation time for the process describing the particle behavior, e.g., evaporation, chemical kinetics, viscous mixing, etc. These processes produce wave distortion due to absorption and dispersion effects. The relaxation processes are usually of short time duration compared to the wave period and are determined in a Lagrangian frame of reference with respect to the particle. Thus, it is necessary to generate short-term solutions of the differential equations describing the relaxation processes.

At the present time, computer capability does not exist to solve the general case of wave development from initiation to steady-state oscillation. In view of this situation, the problem can be divided into two parts: (1) the initial wave development, and (2) the steady-state wave propagation.

In the following discussion, the wave behavior for the longitudinal and tangential modes are considered separately. Wave behavior observed from experimental data as well as the equations that model the behavior are discussed.

3.5.2.2 *Longitudinal modes.**—Coupling between the mechanical energy in a pressure wave and the available thermal energy in a gas volume element during a fluctuation in heat release is based on the Rayleigh criterion.[143,142] Included in this concept is the wave shape and velocity as well as the rate processes occurring in the reacting gases. Thus, the wave shape assumes an important role in that it determines the wave residence time in a reacting-gas volume element.

A significant property of longitudinal wave propagation is coalescence. For example, consider a burning droplet disturbed by a passing wave. Due to the change in droplet burning rate, wavelets are generated[141] which coalesce as they propagate and ultimately overtake the initial wave that caused the disturbance, thereby causing wave amplification. In addition, as a wave propagates in a gas it deforms. A compression wave in decelerating flow steepens; an expansion wave in accelerating flow broadens. A compression wave in accelerating flow and an expansion wave in decelerating flow may steepen or broaden depending on the magnitude of the wave slope and the velocity gradient in the fluid flow.[641] Because of wave deformation, the wave residence time is continuously changing as the wave propagates

* V. D. Agosta, Author Sects. 3.5.2.1 3.5.2.2 and 3.5.2.3.

† "Wave forcing function," "resonance," and "mode" are acoustic terminology and are borrowed in the absence of suitable terminology for the nonlinear case.

through a chamber. The energy in the wave is a function of its velocity and wave shape. Thus, the effective amplitude and wavelength, i.e., the wave slope, determines the nature of the energy or mass coupling to the propagating wave.

The velocity gradient is related to the pressure gradient, which can be determined readily from pressure measurements along the length of the combustor. Typical measurements[308] are shown in Fig. 3.5.2a. In general, it is found that steeper pressure gradients occur for injectors that promote rapid jet breakup and intimate mixing of propellants.[544] Thus, a compression wave that starts at the injector may steepen or broaden, but on reflection from the nozzle will always steepen (Fig. 3.5.2b).[306] Fig. 3.5.2c shows an x, t plot of such a wave; several patterns of behavior are observed. In the case shown, the wave slope broadened from 32 to 30 psi/in. as the wave propagated down the chamber. On reflection from the nozzle, it steepened from 17 to 105 psi/in. After reflection from the injector face, the wave first broadened from 75 to 63 psi/in. and then steepened to 95 psi/in. It was noted that these events were not repeated on the two succeeding downstream passes. The wave amplitude decreased from 70 psi to 55 psi on the downstream traverse and increased from 60 to 193 psi as the wave moved upstream. The measured frequency indicated that the wave was at all times propagating at the local velocity of sound relative to the mean gas flow. In such a situation the frequency is equal to the product of the "organ pipe" resonant frequency and a Mach number factor:[56]

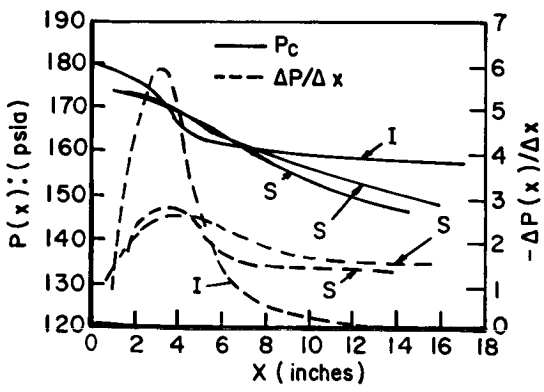

FIGURE 3.5.2a.—Experimental distributions of pressure and axial pressure gradient for showerhead (S) and impinging (I) injectors.

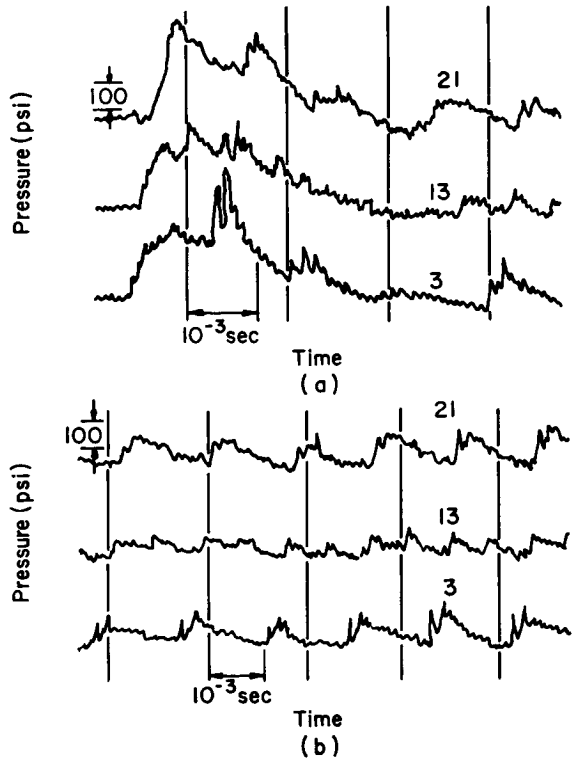

(a) Initial wave.
(b) Initiated oscillations.

FIGURE 3.5.2b.—Wave shapes observed in a 2-inch-diameter, 24-inch-long combustor with a contraction ratio of 1.5. (Propellants, LO_2/JP-5A; transducers located at 3, 13, and 21 in. from injector face.)

$$f=\frac{j\bar{c}}{2x_e}\left[1-\left(\frac{\bar{u}}{\bar{a}}\right)^2\right] \qquad j=1, 2, \ldots \qquad (3.5.2\text{–}1)$$

where x_e is the effective length of the chamber (including an appropriate correction for the effect of the exhaust nozzle), $\bar{u}$ and $\bar{a}$ are mean values of the fluid and sonic velocities, respectively.

From Fig. 3.5.2b it can be seen that after the first group of waves (initiated by a modified shock tube) attenuated, a similar behavior occurred spontaneously. In one pass through the chamber the wave amplitude increased to over 100 psi, and was added to an increasing base pressure.* This wave also damped out, and again spontaneous wave behavior occurred, but without

* The term "base pressure" refers to the local pressure just ahead of the wave.

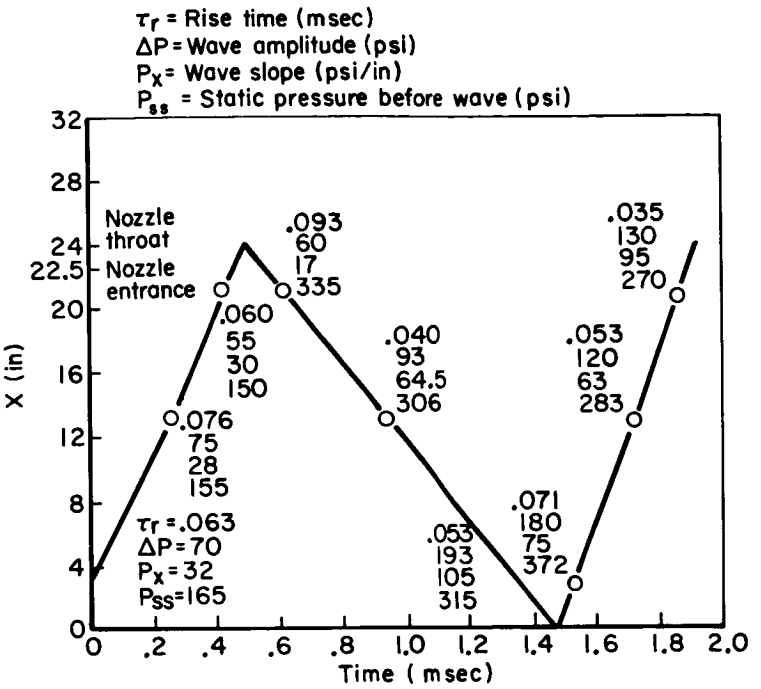

FIGURE 3.5.2c.—Propagation of longitudinal wave in combustor of Fig. 3.5.2b.

the increase in base pressure as the wave built up to about 100 psi amplitude in one pass. The time interval between these events was about equal to the propellant fill time of the combustion chamber.

Experimental data (Fig. 3.5.2d) using different injectors indicated that wave steepening occurred with showerhead injectors ($\Delta p/\Delta x<3$), and wave broadening was obtained with impinging injectors ($\Delta p/\Delta x>4$).[307] It was found that the base pressure amplification was inversely proportional to both the chamber length and maximum slope of the steady-state pressure profile, as shown in Fig. 3.5.2e. The amount of wave-initiated evaporation, coalescence, and subsequent increase in base pressure was greater with showerhead injectors than with impinging injectors.

If one considers the interaction of a wave with a burning propellant, then the change in wave pressure causes a change in the entropy of the products of combustion. From a gas dynamic point of view, these entropy waves appear as contact surfaces that move downstream at the local gas velocity.[54]

Another pattern of wave behavior in the longitudinal mode is one in which the amplitude of oscillation increases past the linear regime to substantial values so that shock waves occur in the system.[143,646] Several shock development mechanisms have been proposed. According to one mechanism, shock waves develop from wave coalescence; that is, the wave front steepens, the aft end broadens, and the wave amplitude increases. In theoretical analyses the existence of shock waves is ascertained from the intersection of wave characteristics of the same family. At present, numerical methods are being developed to determine the existence and formation of shock waves.[480,496] Alternatively, it is suggested that the superposition of low- and high-frequency wave trains that propagate in a combustion chamber produce a progressive wave amplification followed by a sudden damping. It is found experimentally that for low wave amplitudes the pressure oscillations are more-or-less sinusoidal and the frequency is well defined. As the chamber length is increased, harmonics are found to occur, thus distorting the wave forms. Finally, pressure peaks of very short duration but of high amplitude may appear with a concomitant increase in frequency.[78]

In summary, longitudinal wave propagation in

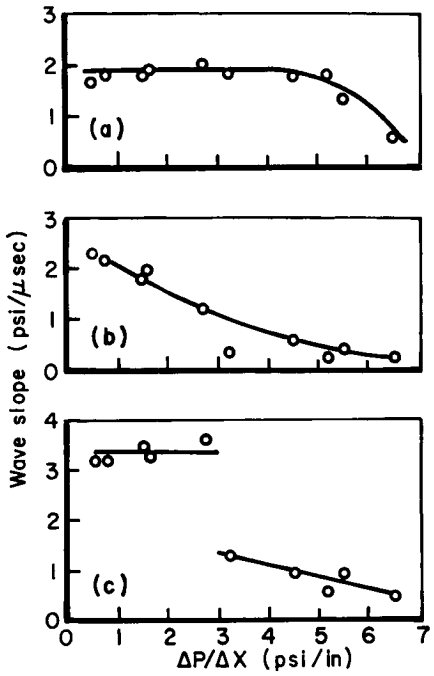

(a) Incident wave at injector.
(b) Incident wave at nozzle.
(c) Reflected wave at injector.

FIGURE 3.5.2d.—Relation of wave slope to maximum pressure gradient (steady state).

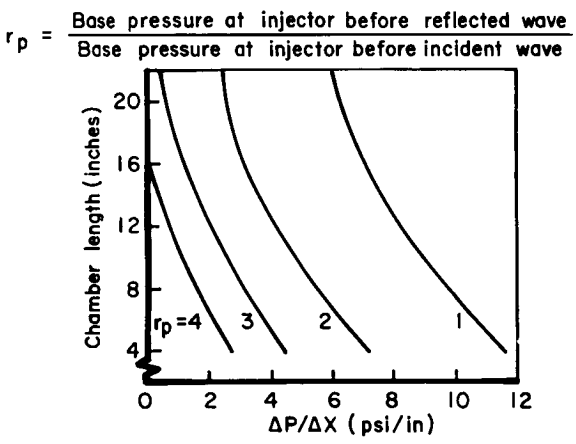

FIGURE 3.5.2e.—Base pressure amplification.

a liquid propellant rocket combustion chamber exhibits the following behavior. The wave amplitude growth may go through a linear regime or spontaneously begin in the nonlinear regime. The resonant frequency is decreased by mean flow effects; no true standing wave occurs in the chamber. Wave deformation occurs due to (1) wave coalescence of a fluid dynamic nature, and (2) absorption and dispersion because of relaxation processes. Since the chamber is filled with liquid propellant particles, a low frequency variation in base pressure may occur which is related to the propellant fill time of the chamber. Large amplitude waves may be of a continuous structure and thus propagate at the local velocity of sound, or they may be discontinuous and propagate at shock wave velocities. Finally, no truly one-dimensional waves can exist in an interacting gas-particle-filled cavity due to the generation of wavelets produced by the interaction.

3.5.2.3 *Transverse modes.*—Detonation-like behavior is not uncommon in the tangential modes of instability. In some cases, wave pressure ratios of 15 and wave velocities approaching Mach 6 with respect to the reactants are encountered.[143] With respect to the combustion gases, wave velocities near Mach 1.84—the value determined from solutions of the linear wave equation—are observed. In Fig. 3.5.2f some nonlinear characteristics of tangential waves are shown: (1) the extreme wave amplitude, (2) the steep wave fronts, and (3) the ragged waveform behind the wave front. Any explanation of the nature of these features at this time can only be conjecture.

The wave front shape of a spinning tangential wave is illustrated in Fig. 3.5.2g. The data, taken with an 11 inch diameter combustor in which a bomb was used to initiate oscillations, show several general properties. It appears that a single equivalent wave surface is formed. The wave pressure amplitude is greatest at the periphery and decreases toward the chamber axis and toward the nozzle. The wave front near the chamber axis and near the nozzle precedes the wave front at the wall near the injector end. Moreover, the wave front does not appear to be normal to any wall surface. From Fig. 3.5.2f it can be seen that at low pressure amplitudes, which appear at the nozzle end of the chamber, the waveform is sinusoidal, whereas at the larger pressure amplitudes the wave fronts become quite steep and are followed by a strong damping.

It is observed from theoretical and experimental data that wave amplitudes are increased by the presence of mass and energy sources, which re-

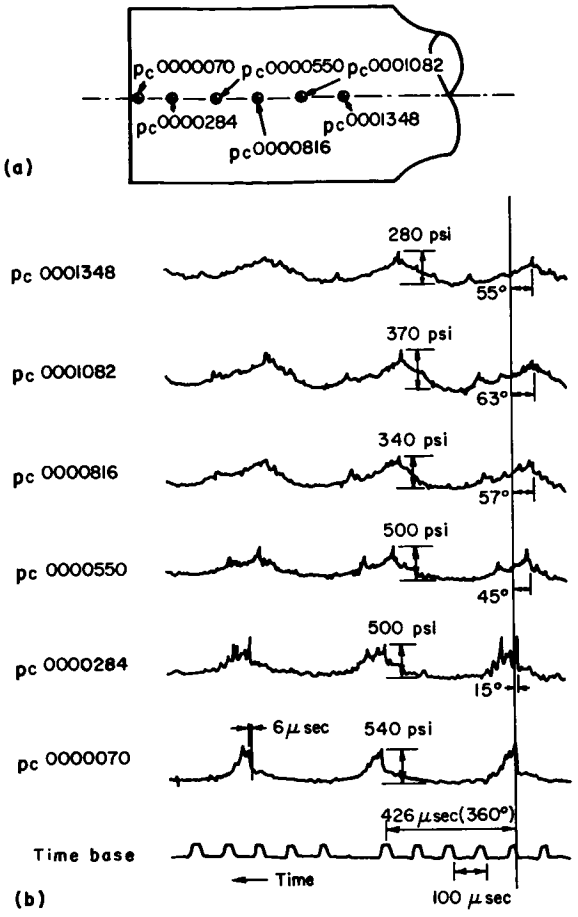

(a) Transducer locations.
(b) Wave shapes 25 milliseconds after bomb pulse.
FIGURE 3.5.2f.—Experimental tangential wave shapes.

spond to the fluctuations in chamber conditions induced by the pressure waves. As noted previously, the source strength depends on the propellant injection distribution as well as on the dynamic response of the combustion process. For transverse modes, the injection distribution is one of the most important factors influencing the wave-combustion interaction. In addition, centrifugal effects produced by the rotating gases during the spinning tangential mode account in part for the high pressure amplitude.

The generation of the ragged waveform behind the wave front can be due to several factors. One of these is the wavelets that result from changes in mass and/or energy source strengths, which have been suggested both from theoretical and experimental observations (Sect. 3.4.3.2). These wavelets interact with the wave front and with the chamber walls, producing raggedness of the waveform. Another factor is the asymmetry of the wave motion. That is, if the wave is not a pure spinning tangential mode, reflections from the chamber walls occur. Graphical construction of waveforms in which reflections from a cylindrical wall occur contain many features similar to those observed experimentally.

The remaining nonlinear effect is the occurrence of the steep wave front. There are several processes, both gas dynamic and chemical in origin, that can account for such a characteristic. Wave deformation of a gas dynamic origin is produced by the coupling of centrifugal effects with density gradients that may occur in a wave. The more dense parts of the wave experience larger centrifugal forces and thus larger pressure amplitudes accrue than for the case where centrifugal effects are negligible or where density gradients are small. For two-phase flow the centrifugal effects may cause the particles to move toward the periphery of the chamber. Hence zones of intense chemical reaction can be formed that can be coupled to the natural modes of wave behavior in the chamber. Chemical reaction processes produce dispersion, which may take the form of generating a precursor moving at the frozen speed of sound followed by a wave train near the equilibrium speed of sound, i.e., a wave broadening process. On the other hand, where the reaction time approaches the characteristic time for the wave, efficient coupling between the wave train and the chemical energy may occur to produce detonation-like behavior.[636] Finally, wave coalescence due to droplet burning may occur, thereby steepening passing waves.

3.5.2.4 *Nonlinear transverse gas displacement.**— The gases in the rocket combustion will not be homocompositional since mixture ratio is not uniform throughout the chamber. Under pressure oscillations, the vaporized propellant will undergo velocity and, therefore, displacement oscillations. Here, of course, the liquid propellants would not be displaced as much as the gaseous propellants and, to the first approximation, may be considered

* W. A. Sirignano, Author.

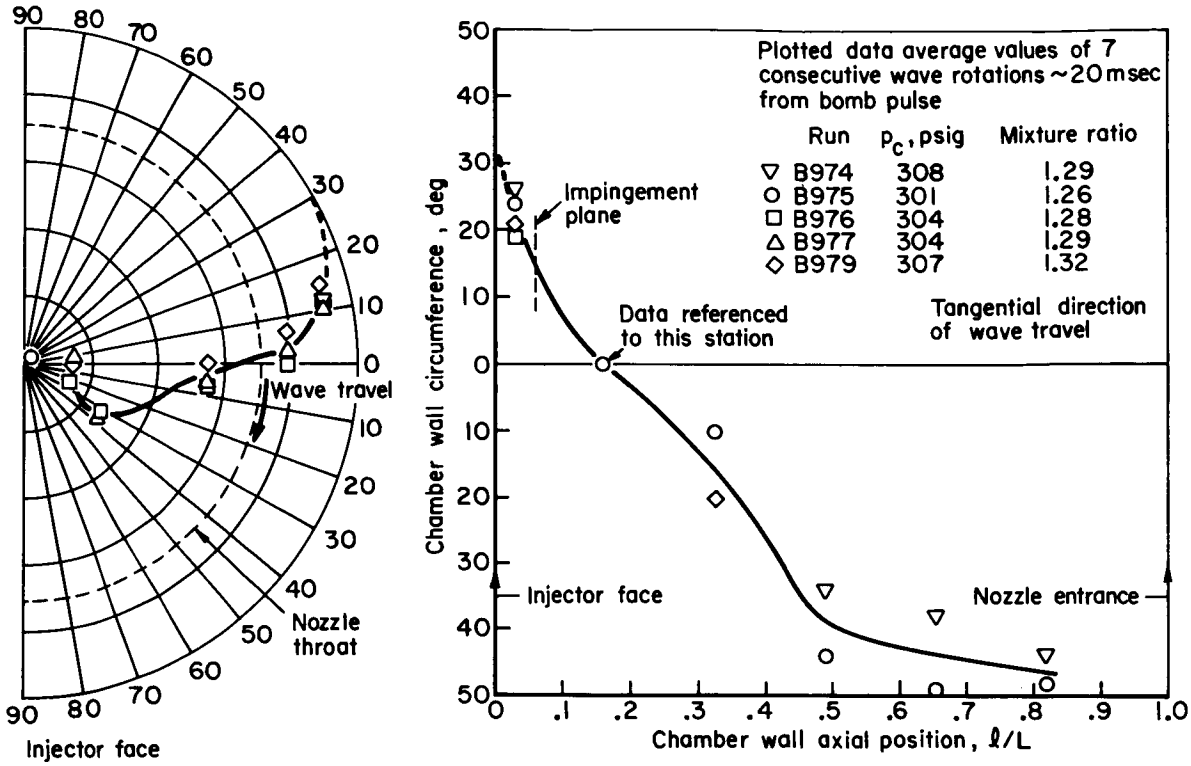

FIGURE 3.5.2g.—Shape of wave front; spinning tangential wave.

as stationary. Then, if these are transverse oscillations, the vaporized propellant would move in and out of regions of different mixture ratios. This could have a significant effect upon the combustion response.

A certain amount of theoretical and experimental work on the combustion response due to linear displacement effects has been performed.[583] Here the n, τ theory was modified to consider not only the pressure sensitivity of the combustion process but also the velocity and displacement sensitivity. An additional study of the nonlinear displacement, but without consideration of the feedback on the combustion process was made.[186]

In the latter study, combustion and mean flow effects were neglected and the approach of Maslen and Moore[466] was employed to determine the pressure and velocity solutions. That is, the nonlinear, two-dimensional wave equation was solved up to and including second order in an amplitude parameter ϵ. In particular, the first tangential spinning and standing modes were considered.

From these velocities, the gas particle displacement was determined by integration. Typical results are shown in Figs. 3.5.2h and i. For the spinning wave case (Fig. 3.5.2h), the trajectories are seen to be nearly elliptical orbits (the deviation from ellipses are second-order effects). In that figure, δ_r is the radial displacement, δ_t is the tangential displacement, and r is the mean radial location of the particle. All quantities are nondimensionalized by the chamber radius. The ratio of the semi-minor axis to the semi-major axis decreases in a continuous manner from unity at the center of the chamber to zero at the outer wall. The angular position in the chamber produces only a phase shift and does not change the orbit shape. The orbit is symmetric with respect to the δ_r-axis only. Note that the maximum displacement increases as the radius decreases.

For the standing wave case (Fig. 3.5.2i), the particle paths consist of motion back-and-forth along a curvilinear trajectory. There is a strong dependence on the angle θ as well as on the radius r. Since the linear approximation gives straight-line trajectories, it is obvious that non-

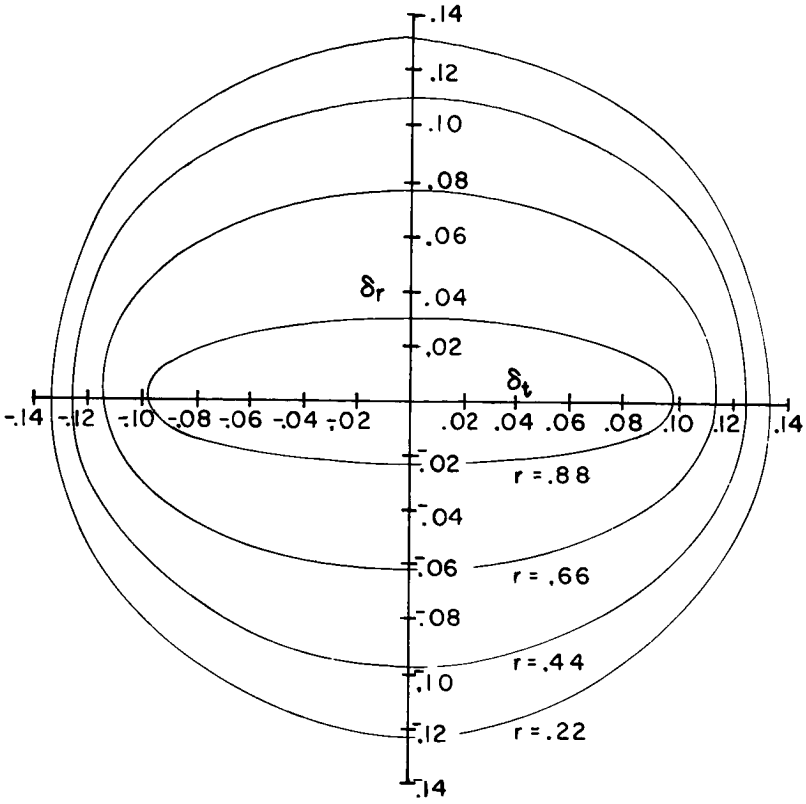

FIGURE 3.5.2h.—Typical traveling wave displacement, where $\epsilon = 0.5$.

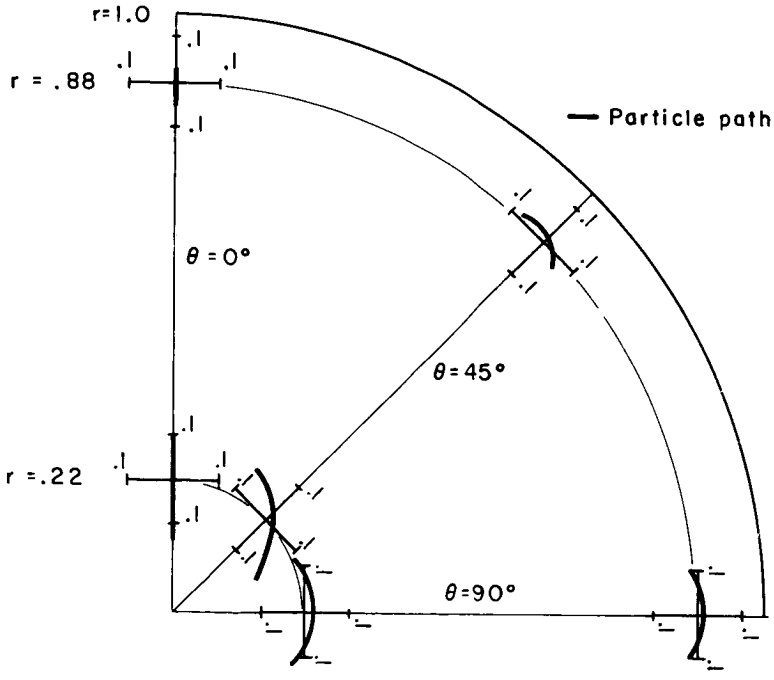

FIGURE 3.5.2i.—Typical standing wave displacement, where $\epsilon = 0.5$.

linear effects are reasonably severe for the standing wave, more so than for the spinning wave. Since a double symmetry exists, only one quarter of the chamber is shown in Fig. 3.5.2i.

A more recent study[190] shows that certain nonlinear terms were neglected in the original work and the particle paths in the spinning wave case are not exactly closed. Rather, a second order streaming, in the direction of wave travel, occurs. The streaming, superimposed upon the closed orbit motion, results in a looping motion. This occurs in the irrotational case and differs from the streaming due to viscosity studied by Maslen and Moore.[466] It is shown further that a net angular momentum exists with the spinning wave, implying that the gas field must experience a net torque in order to initiate the spinning wave.

3.5.3 Damping Effects

The following nomenclature pertains to Sect. 3.5.3 (see also Sect. 3.5.1):

a	Fractional open area of liner
χ	Transverse eigenvalue for lined chamber
χ^*	Transverse eigenvalue for rigid, impervious chamber walls

3.5.3.1 *Liquid and solid particle drag.**—Liquid droplets are always present in liquid-propellant rocket motors and are moving at some relative velocity to the surrounding gases. This velocity difference allows a flow of a viscous fluid over the droplet and results in a drag force. This drag force is also present under oscillatory conditions and results in a loss of energy from the oscillating gases. The effect of this drag, then, is to stabilize the oscillation. The mathematical representation of this drag and its effect upon stability is given by a linearized analysis in Sect. 3.5.1.

It is seen from Eq. (3.5.1–21) that the amplification factor $\lambda^{(1)}$ is decreased by the negative quantity

$$-\frac{1}{2Ax_e}\int_0^{x_e} k\bar{\rho}_L{}^\circ\left(1+\cos\frac{2j\pi x}{x_e}\right)dx$$

due to the droplet drag effect. The negative value, of course, implies damping, rather than amplification, due to this drag effect. Eq. (3.5.1–22) shows that droplet drag has no effect upon the frequency.

There is a difference between the droplet drag effect predicted previously in Refs. 178, 187, 582, and 583 and that predicted here. In those papers, a complex k_t is defined which replaces the k used here. The necessity of introducing this quantity was caused by an improper ordering of the equations and it is claimed the present results in this article are correct. Perhaps these present results are also more intuitively appealing in that they predict the droplet drag has only a damping effect and does not affect the frequency while the previous references predict an effect upon the frequency.

For purely transverse modes ($j=0$), the damping added by droplet drag becomes

$$\frac{1}{2x_e}\int_0^{x_e} k\bar{\rho}_L{}^\circ\,dx$$

On the other hand, for purely longitudinal or mixed modes with the combustion concentrated near the injector face, the damping will become exactly twice the above value. Axial spreading of the combustion zone tends to reduce the damping. However, this spreading may not be undesirable since Eq. (3.5.1–21) shows that it also decreased the combustion response term.

An estimate of k can be made by considering the drag of a spherical body. Then

$$k=\frac{3}{4}\frac{\mu C_D \mathrm{Re}}{d_L{}^2\rho_L}$$

where C_D is the drag coefficient, d_L is the droplet diameter, ρ_L is the density of the liquid, μ is the gas viscosity, and Re is the Reynolds number based on the gas properties and the relative velocity.

Any solid particles formed as combustion products would, of course, produce the same effect as liquid particles. The only difference between the drag of the two types of particles would be due to internal circulation and distortion of the shape in the liquid case. Very small liquid droplets would be expected to act as solid particles since surface tension and liquid viscous forces would dominate inertial forces as the droplet size becomes very small.

* W. A. Sirignano, Author Sects. 3.5.3.1 and 3.5.3.2.

3.5.3.2 *Acoustic liners and nonrigid walls.*— Acoustic liners and nonrigid walls have a damping effect because they allow a normal velocity at the wall which has a component in phase with the pressure oscillation. This means that work is done over each cycle in moving the fluid back and forth at the boundary. The work is equal to the energy dissipated due to jet formation and friction. In the case of an acoustic liner, jet formation is the more important effect by at least an order of magnitude.

The effect of liners and nonrigid walls is conveniently given by an admittance coefficient $\mathcal{Y}$:

$$\mathcal{Y}=\mathcal{Y}_R+i\mathcal{Y}_I=\left.\frac{v'}{p'}\right|_{\text{wall}} \qquad (3.5.3\text{–}1)$$

This boundary condition is a relationship between the pressure and the average normal velocity. The averaging is performed on a length scale that is large compared to the distance between liner orifice centers but small compared to the chamber dimensions and, therefore, to the wavelength. The boundary condition given by Eq. (3.5.3–5) introduces two effects on the eigenvalue χ: (1) an imaginary term is added, which means that a damping effect is present due to the dissipation in the liner flow, and (2) the real part is modified, indicating a modification of the natural frequency $\omega^{(0)}$.

Denoting the eigenvalue for rigid, impervious (unlined) walls by χ^*, for the lined or nonrigid wall, since the effects are of the order of the mean flow Mach number, $\chi=\chi^*+\chi^{(1)}$. The correction term depends on the chamber geometry and on the extent of the liner. Assuming that the lining is uniform along all chamber walls and extends from the injector to the nozzle entrance, the following results are obtained:

(1) rectangular chamber $(\chi^{*2}=m^{*2}+n^{*2})$:

$$\chi^{(1)}=\frac{2\gamma s^{(0)}\mathcal{Y}}{(m^2+n^2)^{1/2}}\left(\frac{1+\chi}{\chi}\right) \qquad (3.5.3\text{–}2)$$

(2) circular chamber $(\chi^*=s_{\nu\eta}^*)$:

$$\chi^{(1)}=\frac{\gamma s^{(0)}\mathcal{Y}}{s_{\nu\eta}^*}\,\frac{1}{1-\left(\dfrac{\nu}{s_{\nu\eta}^*}\right)^2} \qquad (3.5.3\text{–}3)$$

(3) circular-annular chamber $(\chi^*=s_{\nu\eta})$:

$$\chi^{(1)}=\frac{\gamma s^{(0)}\mathcal{Y}}{s_{\nu\eta}^*}\cdot\frac{f(s_{\nu\eta}^*)-f(s_{\nu\eta}^*\xi)}{\left[\left(\dfrac{\nu}{s_{\nu\eta}^*}\right)^2-1\right]f(s_{\nu\eta}^*\xi)-\xi\left[\left(\dfrac{\nu}{s_{\nu\eta}^*\xi}\right)^2-1\right]f(s_{\nu\eta}^*)} \qquad (3.5.3\text{–}4)$$

where

$$f(\phi)=\frac{Y_\nu'(\phi)}{J_\nu(\phi)+B^*Y_\nu(\phi)} \qquad (3.5.3\text{–}5)$$

The effects of the wall admittance on the real and imaginary parts of $s^{(1)}$ are then found to be

$$\lambda^{(1)}=\lambda^{(1)}\mathcal{Y}_{=0}-\frac{\chi^*}{\omega^{(0)}}\cdot\chi_I^{(1)} \qquad (3.5.3\text{–}6)$$

$$\omega^{(1)}=\omega^{(1)}\mathcal{Y}_{=0}+\frac{\chi^*}{\omega^{(0)}}\cdot\chi_R^{(0)} \qquad (3.5.3\text{–}7)$$

where $\chi_R^{(1)}$ and $\chi_I^{(1)}$ are the real and imaginary parts of $\chi^{(1)}$, from the appropriate equation given above. Since $s^{(0)}=i\omega^{(0)}$ the real part $\mathcal{Y}_R$ of the wall admittance will appear in the $\lambda^{(1)}$ relation and hence determine the stability. The imaginary part $\mathcal{Y}_I$ determines the frequency modification.

No theory exists for calculating the admittance coefficient of a nonrigid wall. A significant amount of theory does exist, however, for the admittance of acoustic liners. At the resonant point (where the natural frequency of the liner equals the frequency of the chamber oscillations) the real part of the liner admittance coefficient can be approximated[644] by

$$\mathcal{Y}_R=\frac{\sqrt{3\pi}a}{2\sqrt{\gamma\epsilon}} \qquad (3.5.3\text{–}8)$$

where ϵ is the mean-to-peak pressure amplitude divided by the mean pressure, a is the fractional open area of the liner surface.

As an example, consider $\epsilon=0.1$, $a=0.025$, $\gamma=1.2$, first tangential mode operation in a circular chamber ($\nu=1$, $s_{\nu\eta}=1.84$), chamber radius equal to chamber length, and $\bar{u}_e=0.1$. The liner damping term in Eq. (3.5.3–12a) is equal to 0.38, and is substantially larger than the damping term $(\gamma+1)\bar{u}_e$ which equals 0.22. The ratio of the liner damping term to the latter term decreases monotonically with increasing mean flow velocity and amplitude of oscillation. If ϵ were 0.4 or $\bar{u}_e=0.2$, this ratio would be halved. This example illustrates

the fact that liners are more effective for lower Mach number chambers. Also, they are more effective against spontaneous instability than against triggered instability. The effectiveness of the liner increases in direct proportion to the ratio of the lined surface area to the cross-sectional area. In circular chambers, since $\nu/s_{\nu\eta} \rightarrow 1$ as $\nu \rightarrow \infty$, liners are most effective for the high transverse modes.

3.5.3.3 *Injector-face baffles.**—Transverse wave motion in a combustion chamber can be damped by baffles on the injector face. A typical baffle configuration is shown in Fig. 3.5.3a. The blades are usually planar and the hub cylindrical, and all surfaces are parallel to the chamber axis to minimize interference with the mean flow. Many different baffle configurations have been designed and tested; several are illustrated in Fig. 3.5.3b. Most large liquid rocket engines have made use of baffles to prevent the occurrence of transverse-mode combustion instability.[11,156,215,331]

Because of the complex nature of the oscillation patterns in a baffled combustion chamber, the effects of the baffles on the wave motion are not fully understood. However, two effects have been identified as being important in the suppression of combustion instability: (1) the modification of the acoustic resonance properties of the combustion chamber, and (2) the alteration of the oscillatory flow patterns in the vicinity of the injector face. A third effect, which has not yet been investigated in detail, is (3) the dissipation resulting from the formation and destruction of vortices in the cavities between baffle blades.

The acoustic resonance characteristics of a typical combustion chamber, with and without baffles, are shown in Fig. 3.5.3c. In these amplitude-frequency plots, obtained by methods discussed in Sect. 9.6.6, the peaks correspond to the acoustic modes of the chamber. In general, the higher peaks are associated with the more strongly resonant modes, which have the lower damping rates. The effect of the baffle is seen to be twofold: (1) the frequencies of the lower-order transverse modes are reduced, and (2) the peak amplitudes of the same modes are lowered, that is, the damping rates of those modes are increased. It should be noted that the longitudinal modes are not affected,* and neither are the higher-order transverse modes that are compatible with the baffle configuration. In the case shown in Fig. 3.5.3c, the third tangential mode (3T) is compatible with the six-blade baffle, whereas the first radial (1R) is not, because of the hub.

It has been shown that the amount of the frequency shift and the increase in the damping rate both increase with increasing baffle length, as illustrated in Fig. 3.5.3d.[11,331] An approximate acoustical analysis, presented in detail in Sect. 8.2.1, indicates that the chamber length and diameter and the nozzle admittance (see Sect. 3.6) are also important factors in determining the amount of baffle damping. Since the analysis assumes a large number of blades, such that only axial oscillations are possible in the baffle cavities, it cannot predict the damping of modes that are nearly compatible with baffle configuration. In such cases, it can usually be expected that the damping in the baffled and unbaffled chambers will be about the same. An example of this is shown in Fig. 3.5.3d. As illustrated in Fig. 3.5.3e, the baffle blades of the "compatible baffle" approximate the streamlines of the first tangential standing mode, imposed in the acoustic tests represented in Fig. 3.5.3d.

Although it is convenient to discuss the resonances of a baffled chamber in terms of the acoustic modes of the chamber without baffles, it must be remembered, as Wieber[737] has pointed out, that the correspondence exists only in an approximate, gross sense. Complications enter also through the interaction of the different resonance characteristics of the baffle cavities and the unbaffled part of the chamber. For example, in an engine that had a baffle consisting of a central hub with radial blades extending outward from the hub, a coupling was established between a longitudinal mode in the baffle cavities and the first radial mode in the unbaffled part of the chamber. As a result, the radial mode frequency was reduced to the extent that it matched the resonant frequency of the combustion process, thus producing instability.[11]

Of equal importance to the problem of com-

* F. H. Reardon, Author.

* Careful measurements show that there is a frequency shift for longitudinal modes, due to the decreased cross-sectional area in the baffle part of the chamber.[11]

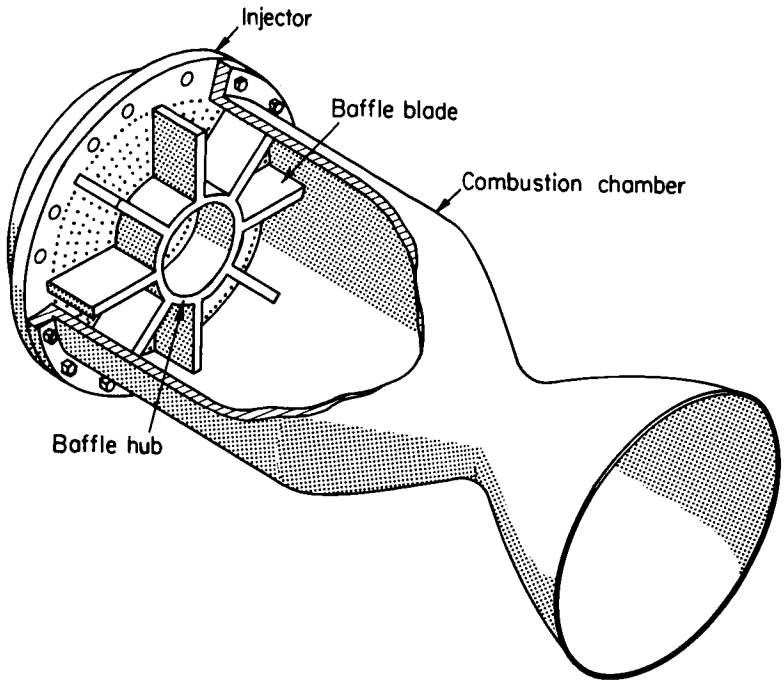

FIGURE 3.5.3a.—Cutaway sketch of combustion chamber showing injector-face baffle.

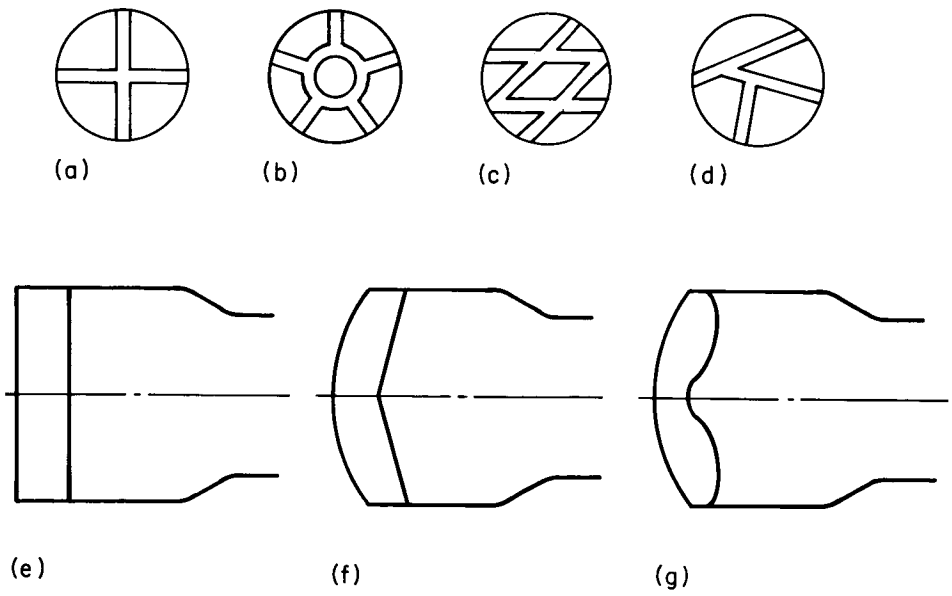

(a) Radial blades; no hub.
(b) Radial blades; with hub.
(c) Diagonal blades, or "eggcrate."
(d) Irregular blade arrangement.
(e) Rectangular blade on planar injector face.
(f) "Parallel" blade; dished injector face.
(g) "Wing" blade; dished injector face.

FIGURE 3.5.3b.—Typical baffle configurations.

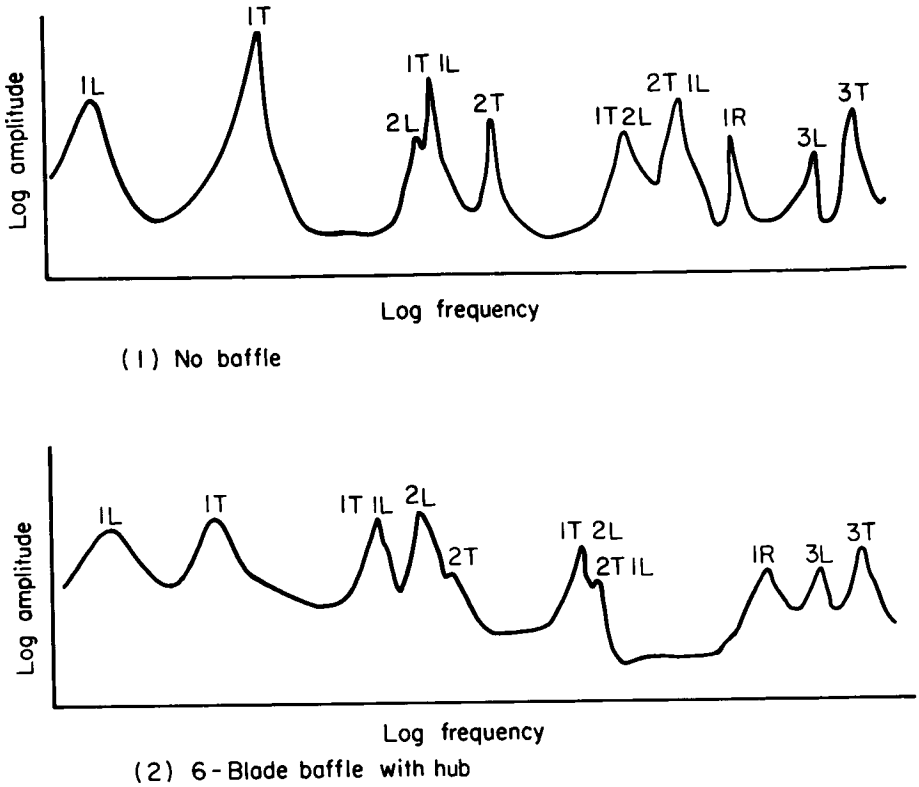

FIGURE 3.5.3c.—Acoustic resonance characteristics of typical combustion chamber, with and without baffles. Modal pattern identified for each resonance (L, longitudinal; T, tangential; R, radial).

bustion instability are the oscillatory flow patterns that can lead to an oscillating energy release rate, and thus contribute directly to the excitation of instability. In particular, the early experiments of Levine and Bambanek[441] and Reardon[582] demonstrated that transverse velocity components, associated with transverse modes of oscillation, have a strong effect on the combustion process. This effect is especially great in the region near the injector face, where there are large temperature and concentration gradients, and for the spinning forms of tangential modes.* It is clear that within the baffle cavities the transverse flow patterns are quite different from those in an unbaffled chamber. Since there is a velocity node at each baffle surface, the magnitude of the velocity oscillations is greatly reduced, effectively eliminating this type of excitation.

* For further discussion of these effects, see Sections 2.3, 3.3, 3.4, and 4.2.

The spatial region in which the baffle effectively inhibits transverse flow depends on the length of the blades, but also on the blade spacing and the wave pattern of the mode induced in the unbaffled part of the chamber. Although the flow in the baffle cavities has not yet been explored in detail, the general picture has been established by several independent investigations. In the development of baffles for the second stage engine of the Gemini launch vehicle, it was found that the size of the perturbation required to trigger instability increased as the number of blades was increased, with the baffle length held constant.[331] Similar results, in which the minimum baffle length required for stability increased as the baffle blade spacing was increased, were reported by Hannum and Scott.[312] These indirect observations of the baffle blocking effects have been confirmed by the direct measurements of Crocco, et al. of the breakup of a freon jet subjected to transverse nitrogen pulses.[190]

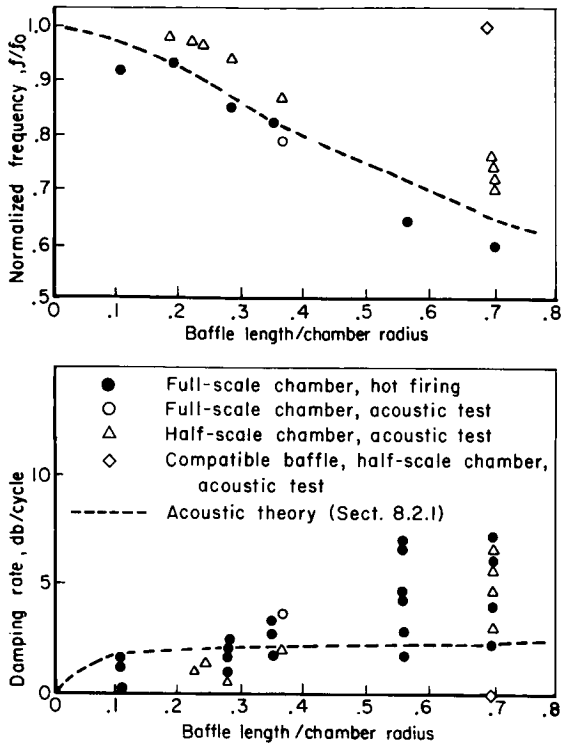

FIGURE 3.5.3d.—Effect of baffle length on oscillation frequency and damping rate (adapted from Refs. 11 and 331).

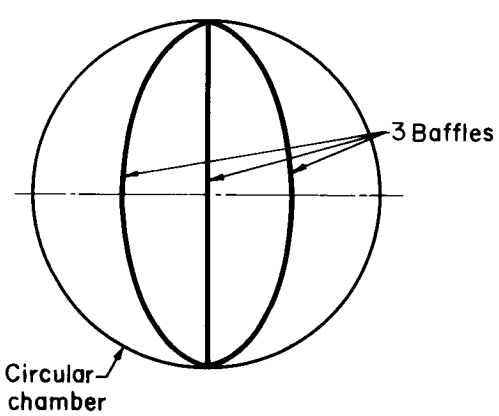

FIGURE 3.5.3e.—"Compatible baffle" configuration.

Investigations of the steady flow past cavities and around blunt obstacles indicate that a complex vortex motion is set up within the cavity, consisting of a primary vortex approximately centered in the cavity, with secondary vortices at the corners.* In the case of oscillatory flow past a baffle cavity, it is to be expected that such vortices are also present, but unsteady in time, the direction of rotation alternating in response to the flow past the baffle. Such creation and destruction of vortices may provide a source of energy dissipation that is significant in certain cases. Further research is necessary to establish the validity of this conclusion.

3.6 UNSTEADY FLOW IN EXHAUST NOZZLES†

For a proper understanding of the nature of wave motion in a combustion chamber it is important to know the behavior of the flow in the exhaust nozzle under oscillatory conditions. In particular, it is necessary to determine how a wave generated in the combustion chamber is partially reflected and partially transmitted at the entrance of the nozzle. In mathematical terms, it is necessary to know the boundary condition imposed by the nozzle on the oscillatory flow in the combustion chamber. This boundary condition takes the form of an admittance relation between the various perturbations (e.g., pressure, velocity, entropy). If the perturbations are sufficiently small, so that the problem can be linearized, the admittance equation must also be linear. For large-amplitude oscillations, nonlinear effects must be taken into consideration.

If the flow in the nozzle is supercritical (as is normally the case in rocket engines), for sufficiently small oscillations the supersonic portion of the nozzle has no effect on the chamber conditions. Downstream of the throat the oscillations must always propagate downstream and cannot interfere with the flow upstream. Hence the logical choice for the surface on which a boundary condition is specified would be the surface where the sonic velocity is achieved, that is, for small oscillations about an approximately one-dimensional flow, the throat itself. It has been shown[179] that the proper boundary condition at the throat is that the solution remains regular there, even though a singularity tends to result from the inability of the disturbances to propagate upstream from the supersonic to the subsonic region.

In practice, it is useful to divide the chamber

* References include 11, 594, 698, 725 and 751.

† W. A. Sirignano, Author.

plus nozzle into two parts: the combustion chamber, extending from the injector to the nozzle entrance, where the combustion processes take place but the mean flow Mach number is relatively low; and the nozzle, where no combustion occurs but the mean Mach number increases to unity. The result of this subdivision is to move the boundary of the combustion chamber from the throat up to the nozzle entrance, where the appropriate boundary condition can be obtained by studying the oscillatory behavior of the nozzle by itself. The admittance equation is obtained from the condition of non-singularity at the throat.

The following nomenclature pertains to Sect. 3.6 (see also Sect. 4.2.2):

$\mathcal{A}$, $\mathcal{B}$, $\mathcal{E}$, $\mathcal{C}$	Nozzle admittance coefficients
f_1, f_2, f_3	
g, h, j, k	Auxiliary functions
$\hat{F}^{(1)}$, $\hat{F}^{(2)}$	
k	Scale factor for nozzle shape
P	Axial dependence of pressure perturbation
R	Radius of curvature at throat (conical nozzle)
U, V, W	Axial dependencies of velocity perturbations
α	Admittance coefficient for isentropic, irrotational or longitudinal oscillations
ζ°	Auxiliary function
θ_1	Semi-angle of conical nozzle
χ	Velocity gradient at throat
Σ	Axial dependence of entropy perturbation
Φ	Function related to axial velocity perturbation
ϕ	Velocity potential
ϕ°	Velocity potential, normalized
ψ	Stream function

3.6.1 Linear Nozzle Admittance Equation

Only a brief discussion of the analysis leading to the admittance equation can be given here. For details of the mathematical development, the reader should consult Ref. 196.

To simplify the analysis, the steady-state flow is considered to be one-dimensional, although the perturbed flow may be three-dimensional. The combustion process is assumed to be completed before the flow enters the nozzle so that there are no energy or mass sources in the nozzle. However, allowance is made for the occurrence of entropy and vorticity waves in the nozzle due to the combustion in the chamber. For an axisymmetric nozzle, a convenient coordinate system is that which employs the values of the velocity potential ϕ and stream function ψ of the steady-state flow in addition to the azimuthal angle θ (Fig. 3.6.1). Since the value of the stream function is a constant at the nozzle walls where the boundary conditions are applied, separation of variables is allowed. Culick[202] did not use this coordinate transformation and was forced to a more cumbersome analysis. Two dimensional nozzles have also been analyzed; the treatment is parallel to the axisymmetric case and will not be given here.

Under the assumption of small amplitudes, the perturbations are governed by linear, partial differential equations. These equations are separated on the assumption that the nozzle is sufficiently long that the cosine of the semi-angle of convergence may be approximated by unity. As a result, the time and azimuthal dependencies are given by sinusoidal functions. The radial* dependencies are expressed in terms of Bessel functions of the first kind, just as in the circular cylindrical chamber analysis (Sect. 3.5.1.2). The axial dependencies are related to the solution of a second-order, linear, ordinary differential equation with complex coefficients:

$$\bar{u}^2(\bar{a}^2-\bar{u}^2)\frac{d^2\Phi}{d\phi^2}-\bar{u}^2\left(\frac{1}{\bar{a}^2}\frac{d\bar{u}^2}{d\phi}+2i\omega\right)$$
$$+\left[\omega^2-i\omega\left(\frac{\gamma-1}{2}\right)\frac{\bar{u}^2}{\bar{a}^2}\frac{d\bar{u}^2}{d\phi}-s_{\nu\eta}{}^2\bar{\rho}\bar{u}\bar{a}^2\right]\Phi$$
$$=-\bar{a}^2f_0(\phi)[C_1F^{(1)}(\phi)+C_2F^{(2)}(\phi)] \quad (3.6.1\text{–}1)$$

where Φ is related to the axial velocity perturbation, $\bar{u}$ and $\bar{a}$ are the steady-state gas and sonic velocities (nondimensionalized by the sonic velocity at the throat $\bar{a}_{th}$), ω is the angular frequency of oscillation (nondimensionalized by $\bar{a}_{th}$ and the throat radius r_{th}), and $s_{\nu\eta}$ is the eigenvalue for the particular mode of oscillation. This equation is

* The radial coordinate r is related in a simple manner to the steady-state stream function under the assumptions of the analysis. Similarly, the axial coordinate x is related to the steady-state velocity potential.

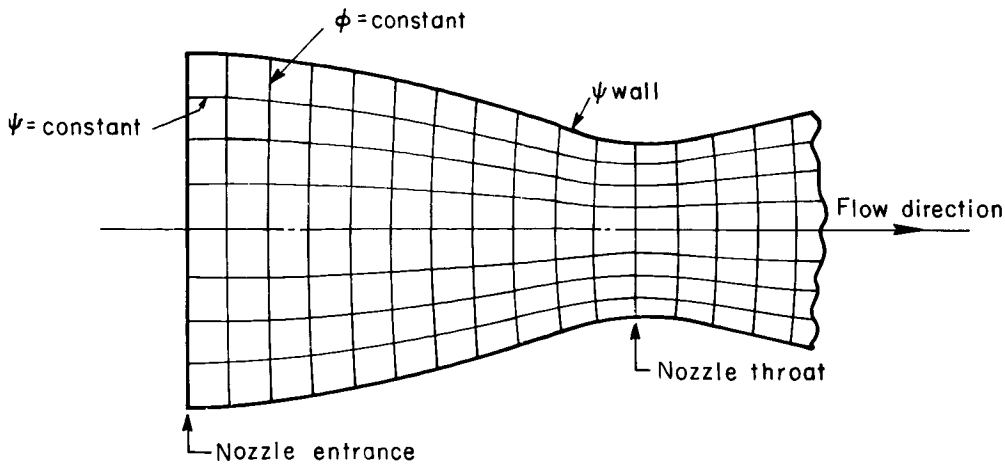

FIGURE 3.6.1.—Coordinate system used for the solution of the oscillatory nozzle flow.

singular at the throat; one of the homogeneous solutions will be regular there and the other one will be singular. Discarding the singular solution has been demonstrated to be equivalent to disallowing perturbations to propagate upstream from the supersonic portion of the nozzle.[179] The solution of Eq. (3.6.1–1) can only be obtained in exact form by numerical integration.

The linear admittance condition can be written as

$$U+\mathcal{A}P+\mathcal{B}V+\mathcal{C}\Sigma=0 \qquad (3.6.1\text{–}2)$$

where U, P, V, and Σ are the axial dependencies of the nondimensional perturbations of axial velocity, pressure, radial velocity, and entropy, respectively. The admittance coefficients $\mathcal{A}$, $\mathcal{B}$, and $\mathcal{C}$ are given by

$$\mathcal{A}=\frac{1}{\gamma}\left(\frac{\gamma+1}{2}\right)^{(\gamma+1)/2(\gamma-1)}\frac{\bar{u}}{(\bar{a})^{2/(\gamma-1}}\times\left[\frac{\bar{a}^2f_1-\zeta^\circ}{\bar{u}^2(\bar{a}^2f_1-\zeta^\circ)-\dfrac{i\omega^\circ}{2}}\right] \qquad (3.6.1\text{–}3)$$

$$\mathcal{B}=\frac{i\omega^\circ\chi\bar{u}^{1/2}}{(\bar{a})^{1/(\gamma-1)}}\left[\frac{\bar{a}^2f_1}{\bar{u}^2(\bar{a}^2f_1-\zeta^\circ)-\dfrac{i\omega^\circ}{2}}\right] \qquad (3.6.1\text{–}4)$$

$$\mathcal{C}=\left(\frac{2}{\gamma+1}\right)^{1/2}\bar{u}\bar{a}^2\times\left[\frac{\left(\dfrac{1-\bar{u}^2}{2}\right)f_1-\dfrac{i\omega f_2}{2}+f_3\zeta^\circ}{\bar{u}^2(\bar{a}^2f_1-\zeta^\circ)-\dfrac{i\omega^\circ}{2}}\right] \qquad (3.6.1\text{–}5)$$

The admittance coefficients are complex numbers because the auxiliary functions $f_3\zeta^\circ$, f_1, f_2, and f_3 are complex. To determine the variation of the flow property perturbations throughout the nozzle, it would be necessary to integrate the second-order equation for Φ, Eq. (3.6.1–1). However, since the interest normally lies in the prediction of overall stability characteristics and not in the details of the flow itself, such an approach is not necessary. The auxiliary functions satisfy first-order equations obtained by reduction of Eq. (3.6.1–1):

$$\frac{d\zeta^\circ}{d\phi^\circ}+\zeta^{\circ 2}=(\dot{g}+ih)\zeta^\circ-(j+ik) \qquad (3.6.1\text{–}6)$$

$$\frac{d}{d\phi^\circ}[(1-\bar{u}^2)f_m]+\left\{\zeta^\circ-i\omega^\circ\left[\frac{1}{2\bar{u}^2}+\frac{2}{(\gamma+1)(1-\bar{u}^2)}\right]\right\}\times[(1-\bar{u}^2)f_m]=\frac{2}{\gamma+1}\hat{F}^{(m)};\qquad m=1,2 \qquad (3.6.1\text{–}7)$$

$$\frac{d}{d\phi^\circ}(\bar{a}^2f_3)-\frac{i\omega^\circ}{2\bar{u}^2}(\bar{a}^2f_3)=\frac{1}{2}\frac{d\bar{u}^2}{d\phi^\circ} \qquad (3.6.1\text{–}8)$$

where

$$\mathcal{J}=\left(\frac{\gamma+1}{2}\right)\frac{\bar{u}^2}{\bar{a}^2}\frac{d\bar{u}^2}{d\phi^\circ}$$

$$h=\omega^\circ\bar{u}^2$$

$$j=\left(\frac{\omega^{\circ 2}}{4}\right)\frac{s^\circ{}_{\nu\eta}{}^2\bar{u}(\bar{a})^{2/(\gamma-1)}}{4}$$

$$k=-\left(\frac{\gamma-1}{4}\right)\frac{\bar{u}^2}{\bar{a}^2}\frac{d\bar{u}^2}{d\phi^\circ}\,\omega^\circ$$

$$\hat{F}^{(1)}=\frac{s^\circ{}_{\nu\eta}{}^2(\bar{a})^{2/(\gamma-1)}}{4\bar{u}}$$

$$\hat{F}^{(2)}=\frac{df_3}{d\phi^\circ}+\frac{s^\circ{}_{\nu\eta}{}^2\bar{u}(\bar{a})^{2/(\gamma-1)}}{2i\omega}\left(\frac{1-\bar{u}^2}{2\bar{u}^2}+\frac{\bar{a}^2}{\bar{u}^2}f_3\right)$$

$$\omega^\circ=\frac{\omega}{\chi}$$

$$s^\circ{}_{\nu\eta}=\frac{s_{\nu\eta}}{\chi}$$

$$\chi=\left(\frac{d\bar{u}}{dx}\right)_{th}$$

$$\phi^\circ=2\chi(\phi-\phi_{th})=2\chi\int_0^x\bar{u}\,dx' \qquad (3.6.1\text{–}9)$$

The admittance coefficients for a given nozzle geometry can thus be calculated as functions of the velocity potential ϕ°, which can readily be converted to the axial coordinate x or the local, mean-flow Mach number $(\bar{u}/\bar{a})$. That is, when the admittance coefficients at the nozzle entrance are desired, the axial coordinate at the entrance or the entrance Mach number must be known before the admittance coefficients can be determined.

3.6.2 Calculation of Admittance Coefficients

Eq. (3.6.1–6) is a complex Riccati equation and can only be solved by numerical integration. Once this is done the linear, first-order equations for f_1, f_2, and f_3 can be solved obtaining the standard integral forms. However, rather than evaluating the integral solutions numerically, it is more convenient to solve all four complex (or eight real) equations simultaneously by numerical integration.

In addition to the admittance coefficients $\mathcal{A}$, $\mathcal{B}$, and $\mathcal{G}$ defined in Sect. 3.6.1, two other complex admittance coefficients are useful and have been calculated. One of these coefficients is

$$\alpha=-\left(\frac{\gamma+1}{2}\right)^{(\gamma+1)/2(\gamma-1)}\left[\frac{\bar{u}}{(\bar{a})^{2/(\gamma-1)}}\cdot\frac{\zeta^\circ}{\bar{u}^2\zeta^\circ+\dfrac{i\omega^\circ}{2}}\right] \qquad (3.6.2\text{–}1)$$

which is the admittance coefficient to be used in the relation

$$U=\frac{\alpha}{\gamma}P$$

in the absence of vorticity and entropy perturbations. When $s_{\nu\eta}=0$, α is also the admittance coefficient for isentropic longitudinal oscillations.

The other special coefficient is

$$\mathcal{E}=\gamma\mathcal{A}-\frac{\mathcal{B}}{i\omega_c} \qquad (3.6.2\text{–}2)$$

where ω_c is the nondimensional frequency appropriate to chamber oscillations (i.e., reference quantities are stagnation speed of sound and nozzle entrance radius). The combined admittance coefficient $\mathcal{E}$ is important in transverse-mode combustion instability applications (Sect. 4.2.2). For low Mach numbers, α and $-\mathcal{E}$ are approximately equal. That is, at low mean-flow Mach numbers $\mathcal{E}$ becomes very nearly independent of f_1 even though $\mathcal{A}$ and $\mathcal{B}$ are dependent on it.

The steady-state velocity profile $\bar{u}(\phi)$ must be determined for the given geometry of the convergent part of the nozzle. A first-order differential equation governs $\bar{u}$, and this equation can be solved simultaneously with the equations for ζ°, f_1, f_2, and f_3. The most systematic and comprehensive calculations of nozzle admittance coefficients[196] have been performed for a nozzle with the generatrix shaped as a circular arc with radius of curvature R near the throat and with a smooth transition to a conical nozzle of semi-angle θ_1 in the remainder of the convergent portion. The value $\gamma=1.2$ was used; ω values were in the range 0 to 10 and $s_{\nu\eta}$ values were in the range 0 to 9. For each combination of ω and $s_{\nu\eta}$, the system was integrated along the nozzle length beginning at the throat and extending to the point where the Mach number is 0.05. The solutions were

determined at certain specified values of Mach number by interpolation and then the admittance coefficients were calculated at these specified points.

In using these results, one would take the values of the admittance coefficients at the Mach number equal to the entrance Mach number of the particular nozzle of interest. Thus, by the method used in Ref. 196, one integration was able to provide information for an infinity of contraction ratios. Of course, the calculations were made for a conical nozzle joined directly to a cylindrical chamber, whereas in practice a smooth transition would occur between the conical and cylindrical portions. However, an exact calculation of this actual situation would require one integration for each contraction ratio; the approximation employed in Ref. 196 represented a large time-saving technique. An alternative approach has also been used; that is, the calculation of admittance coefficients has been incorporated into the chamber stability analysis.[650]

One of the most interesting results is that the nozzle may have a destabilizing effect on the transverse modes of oscillation. This is indicated by negative values of the real part of α or positive values of the real part of $\mathcal{E}$. Negative α_R and positive $\mathcal{E}_R$ generally occur in the range of "purely" transverse modes, where ω_c is close to $s_{\nu\eta}$. For such modes the nozzle would have a destabilizing effect. On the other hand, for longitudinal modes and those mixed modes where the longitudinal dimensions are most significant in determining the frequency ($\omega_c \gg s_{\nu\eta}$), α_R is positive and $\mathcal{E}_R$ is negative, so that the nozzle has a damping effect on the oscillations.

The admittance coefficient $\mathcal{C}$ is generally quite small compared to the coefficients $\mathcal{A}$ and $\mathcal{B}$. This result and the fact that the amplitude of the entropy oscillation is small compared to the amplitude of the pressure and velocity oscillations in most situations of physical interest mean that usually Eq. (3.6.1–2) may be simplified to

$$U+\mathcal{A}P+\mathcal{B}V=0 \qquad (3.6.2\text{–}3)$$

It should be noted that $\mathcal{B}=0$ whenever $s_{\nu\eta}=0$. Furthermore, f_1 also equals zero, and it follows that $-\alpha/\gamma$ and $\mathcal{A}$ are identical in that case.

Figures 3.6.2a through 3.6.2d show results of the numerical integration for a sample case

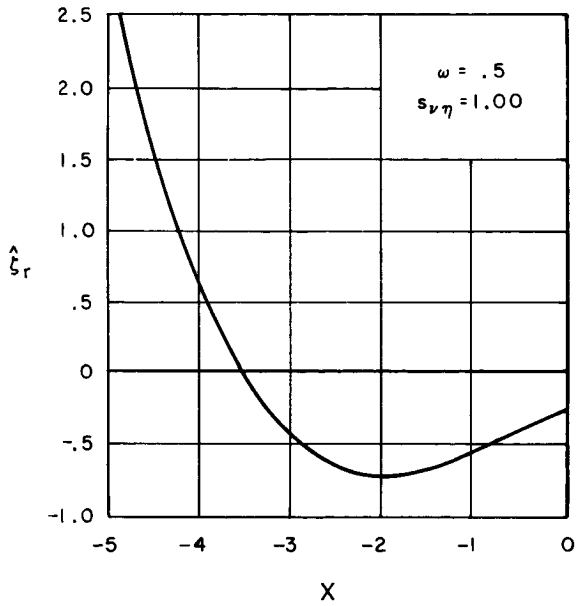

FIGURE 3.6.2a.—Real part of ζ° versus axial distance.

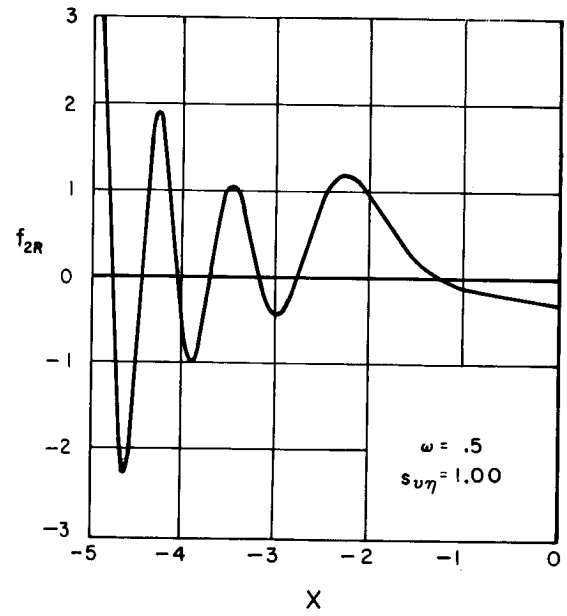

FIGURE 3.6.2b.—Real part of f_{2R} versus axial distance.

($\omega=0.5$, $s_{\nu\eta}=1.0$). Fig. 3.6.2a, in which ζ°_R is plotted against axial distance, shows a gradual change in ζ°_R due to the relatively long pressure wavelength. Fig. 3.6.2b shows f_{2R} to be undulating*

* As used here, "undulation" pertains to spatial variations, whereas "oscillation" is used for temporal variations.

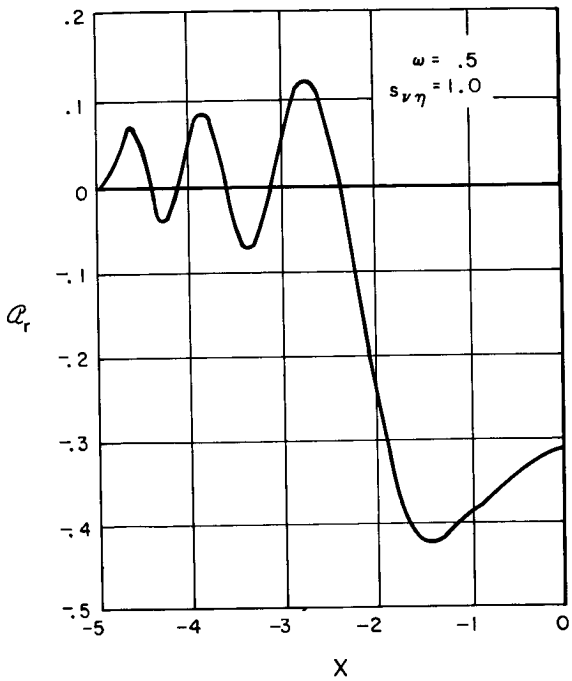

FIGURE 3.6.2c.—Real part of pressure admittance coefficient versus axial distance.

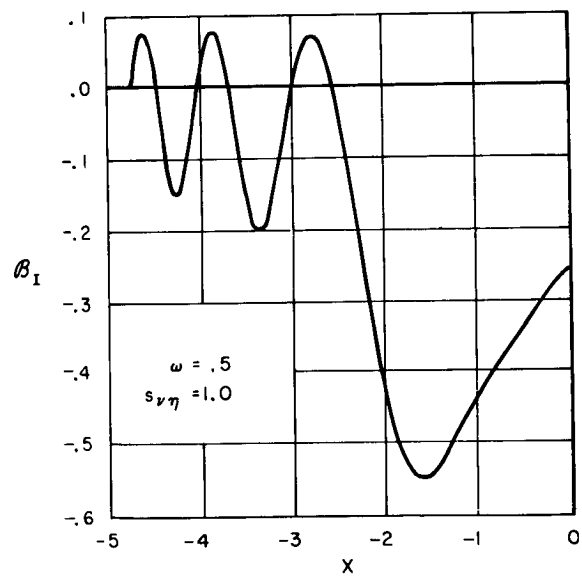

FIGURE 3.6.2d.—Imaginary part of radial velocity admittance coefficient versus axial distance.

rapidly due to the relatively small entropy and vorticity wavelengths. It should be noted that pressure waves propagate with the speed of sound whereas entropy and vorticity waves propagate with the subsonic gas velocity. Figs. 3.6.2c and 3.6.2d show the admittance coefficients $\mathcal{A}_R$ and $\mathcal{B}_I$ (which are the most pertinent from a stability viewpoint) plotted against axial distance. Superimposed on a gradual change due to the pressure waves there is a rapid undulation due to the entropy and vorticity waves. At higher frequencies the oscillations become more severe since the undulations in the admittance coefficients also occur due to pressure waves. The undulations due to entropy and vorticity waves become still more rapid.

A limited number of calculations have been performed wherein the throat wall curvature, the cone angle, and the ratio of specific heats have been changed. It was found that changing γ from the standard value of 1.2 to 1.4 generally produced a change in the admittance coefficients of only a few percent. The other two parameters affected the results more significantly.

Calculations were made with $R=3.0$ (compared to $R=2.0$ in the standard cases) and $\theta_1=30°$, and also with $R=2.0$ and $\theta_1=15°$ ($\theta_1=30°$ in the standard cases). When R was changed and θ_1 left constant, the results changed most significantly in the high Mach number range near the throat. A slight increase in $\mathcal{E}_R$ and $\mathcal{E}_I$ was observed with increasing R, but only for the smaller values of $s_{\nu\eta}$ (corresponding to lower-order modes). Further upstream, in the low Mach number range, the difference between the $R=2$ and $R=3$ cases was smaller. On the basis of this small amount of evidence, it seems that far away from the throat the results do not depend very strongly on the particulars of the nozzle shape at the throat.

When θ_1 was changed and R left constant, the solution near the throat did not change, of course. Only in the conical part of the nozzle was a change produced. Decreasing the angle θ_1 produced small increases in $\mathcal{E}_R$ and $\mathcal{E}_I$ for purely transverse modes. For combined longitudinal-transverse modes $\mathcal{E}_R$ became more negative for smaller θ_1. Again, significant effects were obtained only for small $s_{\nu\eta}$.

It should be noted that the results of the calculations for the standard three-dimensional axisymmetric nozzle may be scaled for use with certain annular nozzles. The major restriction is that the inner wall of the annular nozzle must have the same shape as a stream tube contour in the

three-dimensional nozzle. This implies that the two nozzle flows are identical in the steady state (that is, of course, only in the common region where both flows exist). Also, under the long-nozzle, one dimensional steady-state flow assumption this means that the ratio of the outer wall radius to the inner wall radius is constant along the convergent section of the nozzle.

The equations for the annular nozzle may be separated in the same manner and the same differential equations remain to be integrated as in the three dimensional case. However, now $s_{\nu\eta}$ is determined by the equation

$$\frac{dJ_\nu}{dx}(x)\frac{dY_\nu}{dx}(\xi x)-\frac{dJ_\nu}{dx}(\xi x)\frac{dY_\nu}{dx}(x)=0$$

where J_ν and Y_ν are Bessel functions of the first kind and second kind, respectively, and ξ is the ratio of the inner to outer wall diameter (ν is an integer, here). So using the proper value of $s_{\nu\eta}$, the results of the three dimensional nozzle calculations for both admittances and flow properties may be used for the annular nozzle. The values of $s_{\nu\eta}$ for various annuli may be found in Ref. 120.*

The admittance coefficients for a whole family of nozzles may be obtained by scaling the results calculated for a particular reference nozzle. If k is the scale factor and if a nozzle has a velocity distribution

$$\bar{u}(x)=\bar{u}_{ref}(kx)$$

then the admittance coefficients for this nozzle have been found[196] to be given by the following formulas

$$\mathcal{A}(\bar{u},\omega,s_{\nu\eta})=\mathcal{A}_{ref}\left(\bar{u},\frac{\omega}{k},\frac{s_{\nu\eta}}{k}\right)$$

$$\mathcal{B}(\bar{u},\omega,s_{\nu\eta})=k\mathcal{B}_{ref}\left(\bar{u},\frac{\omega}{k},\frac{s_{\nu\eta}}{k}\right)$$

$$\mathcal{C}(\bar{u},\omega,s_{\nu\eta})=\mathcal{C}_{ref}\left(\bar{u},\frac{\omega}{k},\frac{s_{\nu\eta}}{k}\right)$$

$$\mathcal{E}(\bar{u},\omega,s_{\nu\eta})=\mathcal{E}_{ref}\left(\bar{u},\frac{\omega}{k},\frac{s_{\nu\eta}}{k}\right)$$

$$\alpha(\bar{u},\omega,s_{\nu\eta})=\alpha_{ref}\left(\bar{u},\frac{\omega}{k},\frac{s_{\nu\eta}}{k}\right)$$

A scale transformation of this type is merely a linear deformation of the nozzle walls in the axial direction. Scaling in the radial direction is trivial since all lengths have been nondimensionalized with respect to the throat radius.

3.6.3 Experimental Verification

Verification of the linearized nozzle theory has been obtained for longitudinal mode oscillations; no verification, however, has been attempted for transverse oscillations or nonlinear longitudinal oscillations.

The earliest measurements by Lambiris[418] were successful in demonstrating that the oscillatory behavior in a constant section duct joined to a choked nozzle would be accurately predicted if the nozzle boundary condition were applied at the nozzle entrance. This demonstration was not completely satisfactory since it was indirect and many other factors affect the flow in the duct. Crocco, Monti, and Grey[195] later performed a more satisfactory experiment whereby the oscillatory flow properties at the nozzle entrance were measured with a pressure transducer and a hot-wire anemometer. From these measurements, admittance coefficients were calculated and compared with the theoretical predictions.

Overall accuracies were limited by turbulence noise and the generation of higher harmonics; however, the theory and experiment were in fundamental agreement. The data reduction required a relationship between pressure and density. The isentropic assumption was found to be improper but a more general polytropic relationship produced a good fit between theory and experiment.

3.6.4 Nonlinear Effects

The linearized analysis which has been performed applies to small-amplitude oscillations and is most useful in the treatment of spontaneous instabilities. It can be used in the prediction of the stability of the steady-state operation and, if the regime oscillation in the unstable situation has a small amplitude, it can be used to predict some characteristics of the oscillation. However, if the oscillation does not initiate spontaneously but

* In the reference, β is defined as the reciprocal of our ξ; therefore their value of $s_{\nu\eta}$ must be multiplied by their β to obtain our value of $s_{\nu\eta}$.

instead requires a finite-size disturbance to the steady-state operation in order to excite an oscillation, the linearized analysis is not sufficient. Also, if the regime oscillation does not have a small amplitude (as is often the case), the linearized analysis does not accurately predict all of the characteristics of the oscillations. In these situations, a nonlinear analysis is better suited on the basis of accuracy.

The analysis of the axisymmetric nozzle was extended to include nonlinear effects by Zinn.[771] A perturbation series was employed whereby the perturbation parameter was a measure of the amplitude. Of course, the first order solution is identical to the linearized solution discussed in previous sections. The second and third order solutions, which represent nonlinear effects, were obtained by the technique of eigenfunction expansion. The nonlinear case differs from the linear case in that the nonlinear standing and travelling waves in the tangential mode must be treated separately; the standing wave cannot be considered as the superposition of two travelling waves. Calculations were made only in the irrotational case although the analysis is more general.

Zinn treated the problem in such a manner that left the nozzle oscillation problem coupled to the chamber oscillation problem. A preferred method which uncouples the numerical integration of the nozzle equations from the chamber flow has been suggested.[196]

3.6.5 Other Effects

The effects of condensed phases and combustion in the nozzle upon the oscillatory behavior of the nozzle have always been neglected under the assumption that in a well-designed motor essentially all of the combustion occurs prior to the nozzle entrance. In the absence of any theoretical prediction or experimental evidence, one can only be guided by intuition. It would be expected that the presence of a condensed phase in the nozzle flow would result in a stabilizing effect since droplet or particle drag implies a loss in momentum for the gases. Also, the presence of energy addition due to combustion would have a destabilizing effect if the energy were added in phase with the oscillations. These are the same effects that would occur in a constant diameter motor. It is not clear how these opposite effects will modify the oscillatory behavior when combined.

CHAPTER 4

Analytical Models of High Frequency Combustion Instability

4.1 INTRODUCTION*

4.1.1 Scope of Current Analytical Models

The task of achieving a quantitative knowledge of the unsteady behavior of the phenomena taking place in a liquid propellant rocket combustion chamber is indeed a formidable one. In the last few years substantial advances have been made in the formulation of analytical models of high frequency combustion instability. However, the mathematical difficulties are such that solutions are difficult to obtain, even with the simplest models. As a result, the ultimate goal of establishing quantitative connections between the observed instability phenomena and the basic physicochemical and geometrical elements of the combustion process is still far from being reached.

The unsteady operation of a combustor can be divided into two parts, the interaction of which is somewhat analogous to that of the forward and feedback loops of a servo system. The first part involves the oscillatory behavior of the combustion processes, such as liquid propellant injection, atomization, and vaporization and mass and thermal diffusion and chemical reaction in the flame region. The second part involves the oscillations of the two-phase flow that is confined by the combustion chamber walls. This confinement leads to the existence of certain natural modes of oscillation that resemble the acoustic modes of the chamber. These modes may be described as longitudinal, transverse, or combined (i.e., longitudinal-transverse) on the basis of the orientation of the oscillation relative to the axis of the combustor.

The dynamics of the component processes involved in high frequency combustion instability are discussed in some detail in Chapter 3. The emphasis here is on the interaction between combustion and wave processes that results in oscillatory operation of the combustor. At present, there are two types of approach that predominate. The first (chronologically) is that employing the sensitive time lag concept set forth by Crocco.[179] The second type of analysis involves the study of certain combustion mechanisms and modified equations of gas motion as posed by Priem and Guentert.[563] In addition to these more-or-less comprehensive theories, there have been studies concentrated on the response characteristics of one or more combustion processes, as well as empirical and semi-empirical similarity approaches. These various types of analyses are presented in this chapter. The discussion of their application to engine design and development is deferred to Chapter 6.

The approach of Crocco and his collaborators is based on the consideration that there exists a characteristic time (a relaxation time) for the combustion mechanism. Therefore, the combustion process does not respond immediately to perturbations in pressure, temperature, and velocity, but instead the response occurs after a time lag. This time lag is represented by a certain analytical form discussed in Sect. 4.2. This is a heuristic approach since the combustion mechanism itself is not analyzed to determine its dynamic response. Instead, certain relations are postulated that contain what is intuitively believed to be the proper qualitative characteristics of the dynamic response. Experiments have indicated that the quantitative behavior is also well characterized, at least in the linear case.[180, 583] Because of the time lag in the combustion response, instability is more probable in certain frequency ranges, where the period of oscillation and the characteristic time of the combustion process are commensurate.

* W. A. Sirignano, Author.

The Priem approach, on the other hand, is based on the examination of actual combustion mechanisms. So far, only quasi-steady analyses have been performed; therefore, no time lag exists and the combustion response is instantaneous. Obviously, no frequency dependence occurs with this type of response. Initial efforts were concerned with vaporization and chemical kinetics as rate-controlling processes.[556] More recently, other effects, such as atomization and jet breakup, vortex flow in the chamber, and droplet motion, have been included in the theoretical model.[91,136]

There are other differences between the Crocco and Priem approaches than those involving the treatment of the combustion processes. In the development of the sensitive time lag theory, both longitudinal[179,488,645] and transverse modes[187,583,630,771] have been considered. The transverse mode analyses introduce two additional space dimensions; the longitudinal analyses require the study of shock-wave oscillations. Two different mathematical techniques have been used: (a) small perturbation analysis,[179,187,583,630] in which the equations are linearized, allowing the study of the stability of steady-state operation, and (b) nonlinear analysis,[645,488,771] valid for finite amplitudes that are not too large, yielding limit-cycle solutions. In addition, the time lag theory includes a careful analysis of the effects of the injector-face boundary conditions and the oscillatory flow in the nozzle on the solution in the combustion chamber.

Most of the analyses that follow the approach of Priem have considered a one-dimensional model of the tangential mode of oscillation, with amplitudes of any size. No restrictions are made on the amplitude because numerical integration is used and the nonlinearity offers no special difficulty as it would in an analytical approach. When attention is confined to thin, circular annuli, it is clear that radial and longitudinal wave motion cannot be considered. Also, in this approach the radial motion associated with tangential waves has been neglected. Solutions for these thin annuli have been combined into quasi-three-dimensional models. With the isolation of each thin annulus, the effect of any boundary conditions at the nozzle, injector face, or chamber walls is not considered. Rather, certain assumptions are employed in order to solve the equations. These assumptions have not been justified by any mathematical limiting processes, but by the simplifications that they produce.

The response function models of the instability phenomenon, discussed in Sect. 4.4, differ from the Crocco and Priem models in that certain aspects of the problem, such as the combustion process, are emphasized, and the coupled problem is not treated. Also included in Sect. 4.4 is a discussion of similarity methods, which have been employed in the attempt to circumvent the complexities of the comprehensive mathematical analysis.

4.1.2 General Conservation Equations

The conservation equations for the two-phase flow in the combustion chamber will now be written, assuming that most of the chamber volume is occupied by gases and a smaller portion is occupied by liquids, mainly in droplet form. A control volume is chosen that contains gases and many droplets, and each liquid and gas property is represented by an average value taken over the volume. As the volume shrinks to a point, it is assumed that both liquids and gases exist at that point.

The following nomenclature pertains to Sect. 4.1.2:

E	Energy release rate per unit volume due to chemical reaction and phase change
F	Force per unit volume exerted on gas by liquid
G	Combined energy release rate defined in Eq. (4.1.2–6)
k	Momentum interchange coefficient, defined in Eq. (4.1.2–3)
$\rho_L{}^\circ$	Mass of liquid per unit chamber volume

The conservation of mass implies that the net mass leaving the liquid phase must equal the net mass entering the gas phase. Using the subscript L to indicate liquid quantities and the absence of subscripts to indicate gas quantities, this statement may be represented by

$$\frac{\partial \rho}{\partial t}+\nabla\cdot\rho\mathbf{V}=\frac{\partial \rho_L}{\partial t}-\nabla\cdot\rho_L{}^\circ\mathbf{V}_L\equiv M \quad (4.1.2\text{–}1)$$

The quantity M has the role of the mass source in the continuity equation for the gas flow. It

should be noted that $\rho_L{}^\circ$ is the mass of liquid per unit chamber volume (mass concentration) rather than liquid density.

For most applications, the gases may be taken to be inviscid, except as they exchange momentum with the liquid phase. Therefore, the conservation of momentum for the two-phase flow implies that

$$\frac{\partial(\rho\mathbf{V})}{\partial t}+\nabla\cdot\rho\mathbf{V}\mathbf{V}+\nabla p=-\frac{\partial\rho_L{}^\circ\mathbf{V}_L}{\partial t}-\nabla\cdot\rho_L{}^\circ\mathbf{V}_L\mathbf{V}_L$$

which may be combined with Eq. (4.1.2–1) to yield

$$\rho\frac{\partial\mathbf{V}}{\partial t}+\rho\mathbf{V}\cdot\nabla\mathbf{V}+\nabla p$$

$$=M(\mathbf{V}_L-\mathbf{V})-\rho_L{}^\circ\frac{\partial\mathbf{V}_L}{\partial t}-\rho_L{}^\circ\mathbf{V}_L\cdot\nabla\mathbf{V}_L$$

$$\equiv\mathbf{F} \qquad (4.1.2\text{–}2)$$

In this equation, $\mathbf{F}$ is the force per unit volume exerted on the gas due to momentum exchange with the liquid phase. If the relative velocity between liquid and gas is sufficiently small, low Reynolds number flow occurs and

$$\frac{\partial\mathbf{V}_L}{\partial t}+\mathbf{V}_L\cdot\nabla\mathbf{V}_L=k(\mathbf{V}-\mathbf{V}_L) \qquad (4.1.2\text{–}3)$$

where k is independent of velocity and may be determined exactly (following Stokes) for certain shapes in laminar flow. In turbulent situations, it may be considered as an empirical factor. Since k depends upon droplet radius, which varies with droplet location in the chamber, it actually is a variable. However, for simplicity, an average value is often taken. Obviously, the choice of this average can significantly affect the results. From Eqs. (4.1.2–2) and (–3) it is seen that

$$\mathbf{F}=(M+k\rho_L{}^\circ)(\mathbf{V}_L-\mathbf{V}) \qquad (4.1.2\text{–}4)$$

The conservation of energy states that

$$\frac{\partial}{\partial t}(\rho e_s)+\nabla\cdot(\rho e_s\mathbf{V})+\frac{\partial}{\partial t}(\rho_L{}^\circ e_{Ls})$$

$$+\nabla\cdot(\rho_L{}^\circ e_{Ls}\mathbf{V}_L)+\nabla\cdot p\mathbf{V}=E \qquad (4.1.2\text{–}5)$$

where E is the energy released per unit time per unit volume due to chemical reaction and change of phase. Exothermic reactions have a positive contribution to E whereas endothermic reactions (including vaporization) have a negative contribution. By definition,

$$e_s=e+\tfrac{1}{2}\mathbf{V}\cdot\mathbf{V}$$

Combination of Eqs. (4.1.2–1) and (–5), together with the definition of the stagnation enthalpy,

$$h_s=e_s+\frac{p}{\rho}$$

yields another form of the energy equation

$$\rho\frac{\partial h_s}{\partial t}+\rho\mathbf{V}\cdot\nabla h_s-\frac{\partial p}{\partial t}=E-\rho_L{}^\circ\frac{\partial e_{Ls}}{\partial t}-\rho_L{}^\circ\mathbf{V}_L\cdot\nabla e_{Ls}$$

$$+M(e_{Ls}-h_s)\equiv G \qquad (4.1.2\text{–}6)$$

where G is a combination of energy release rate due to chemical reaction and phase change and a rate of energy exchange between the two phases.

Equation (4.1.2–3) may be used to show that

$$\frac{\partial e_{Ls}}{\partial t}+\mathbf{V}_L\cdot\nabla e_{Ls}=\frac{\partial e_L}{\partial t}+\mathbf{V}_L\cdot\nabla e_L+k\mathbf{V}_L\cdot(\mathbf{V}-\mathbf{V}_L)$$

If the droplet temperature varies only slightly through most of the droplet lifetime and both liquid and gas velocities are small compared to the speed of sound in the gas, the above terms may be neglected, so that

$$G\approx E+M(e_{Ls}-h_s) \qquad (4.1.2\text{–}7)$$

Certain other interesting relations may be derived that govern the generation of entropy and vorticity. One might expect that, since terms representing viscosity and thermal diffusion have been neglected in the equations given here, the generation of vorticity and entropy due to these effects must have been neglected also. This is not the case; the terms representing momentum and energy exchange between the phases do produce generation of entropy and vorticity. Therefore, the effects of viscosity and thermal diffusion in the gas film surrounding the droplets and in the wake following the droplet have been included in the conservation equations in an implicit manner. In particular, the curl operation on Eq. (4.1.2–2) divided by the gas density yields

$$\frac{\partial\boldsymbol{\zeta}}{\partial t}+\mathbf{V}\cdot\nabla\boldsymbol{\zeta}-\boldsymbol{\zeta}\cdot\nabla\mathbf{V}+\boldsymbol{\zeta}(\nabla\cdot\mathbf{V})+\nabla\left(\frac{1}{\rho}\right)\times\nabla p=\nabla\times\frac{\mathbf{F}}{\rho}$$

$$(4.1.2\text{–}8)$$

where the vorticity ζ is defined as curl $\mathbf{V}$. Since there is no basis for assuming that $\mathbf{F}/\rho$ is the gradient of some scalar function, a nonzero $\mathbf{F}$ leads to the generation of vorticity since

$$\frac{\partial \zeta}{\partial t}+\mathbf{V}\cdot\nabla\zeta\neq 0$$

even if the initial vorticity were zero and the density were represented as a function of pressure only. The laws of thermodynamics together with Eqs. (4.1.2–1), (–2) and (–6) result in

$$\rho T\left(\frac{\partial \sigma}{\partial t}+\mathbf{V}\cdot\nabla\sigma\right)=G-\mathbf{V}\cdot\mathbf{F} \quad (4.1.2\text{–}9)$$

from which it is seen that the entropy change in the gas is caused by energy release in the combustion process and by energy exchange with the liquid phase, including work done in momentum exchange. Normally, the energy release in the combustion process is the most important phenomenon which generates vorticity and entropy.

4.2 THE SENSITIVE TIME LAG THEORY*

4.2.1 Basic Concepts

The Sensitive Time Lag Theory was originally formulated with the sole intent of gaining an insight into the essential features of the phenomenon of high frequency combustion instability. However, it was found that analyses based on the theory were able to predict accurately the quantitative behavior of combustion systems in quite a few cases. As a result, the mathematical developments and engineering applications have been extended far beyond those that were expected from this simple, heuristic approach. In this section, the main features of the time lag concept and theoretical approach are summarized. The linearized analysis is presented in Sect. 4.2.2; methods of solving the nonlinear problem are discussed in Sect. 4.2.3.

The following nomenclature pertains to Sect. 4.2.1 (see also Sect. 4.1.2):

A_i	Injection port area (per unit injector surface area)
$\mathbf{D}$	Droplet drag term, $k\rho_L(\mathbf{V}-\mathbf{V}_L)$
$E_{\grave{a}}$	Level of intermediate process accumulation in definition of time lag
$\tilde{f}$	Rate of intermediate processes
L	Chamber length
m	Displacement sensitivity index
n	Interaction index
δ	Gas displacement
μ°	Injection density
τ	Variable part of total time lag, "sensitive time lag"
τ_T	Total combustion time lag

Subscripts:

r	Radial direction
θ	Tangential direction

4.2.1.1 *The sensitive time lag.*—Suppose that it is possible to follow a small parcel of propellant as it undergoes the series of transformations necessary to take it from its initial liquid conditions to its final merging into the gases of complete combustion. In the course of these transformations its presence in the chamber is felt through the momentum and energy exchanges with the rest of the material filling the chamber. With respect to combustion instability, the most important are the energy exchanges, particularly in the form of work (originating in the chemical energy of the propellants) developed against, or absorbed from, the surrounding gases. Since the work exchanges increase with the volume of the propellant parcel, its contribution to the general picture will become especially important toward the end of the transformation into combustion gases.

At this point, the simplifying assumption can be made that this transformation is discontinuous. That is, it can be assumed that the whole gasification process, from the liquid propellant to the final combustion products, is collapsed into a single instant. Then the only information needed to describe the process is the time and location corresponding to the gasification of each parcel. The fact that the gas generation is assumed to be a discontinuous process does not imply that the combustion is not distributed throughout the chamber volume, since the time and location of the gasification of various propellant parcels will, in general, be significantly diversified. A useful consequence of this assumption is that the material filling the chamber consists only of gases of complete combustion and of ungasified liquid

* L. Crocco, Author.

propellants, the intermediate substances occupying a negligible fraction of the volume. Neglecting also the volume of the liquid phase, there results the simplified picture of a chamber filled with gases of complete combustion continuously generated throughout the volume by gas sources, and continuously exhausted through the nozzle. The strength of the gas sources may be variable in time, in response to time-varying conditions in the chamber, thus providing a feedback mechanism for the occurrence of combustion instability.

Since the location of the propellant parcel at the time of gasification can be related to the time through the knowledge of droplet motion, only the time really needs to be known, for instance in the form of a time delay from injection to gasification of each parcel. This time delay τ_T must be different for different parcels, but it also must be a function of time in the case that chamber conditions are varying. To obtain a quantitative representation of the response of the combustion time delay to varying chamber conditions, one can reason in the following way.* The gasification takes place because certain intermediate processes have accumulated to the proper level. Denote the gasification instant for a given parcel by t, and consider the parcel at an instant t_1 such that

$$t-\tau_T<t_1<t$$

The process accumulation condition can be written as

$$\int_{t-\tau_T}^{t} \tilde{f}\,dt_1=E_{\acute{a}} \qquad (4.2.1\text{–}1)$$

where $\tilde{f}$ indicates the time rate at which the relevant process is accumulated and $E_{\acute{a}}$ is the level required for gasification. In general, $\tilde{f}$ depends on the instantaneous ambient conditions and on the particular phase of the time delay through which the propellant is passing. However, the simplifying assumption can be made that $\tilde{f}$ remains unchanged during the first phase of the time delay and that only during the last phase, of duration τ, it is uniformly sensitive to chamber conditions. Concentrating for the moment only on the effects of the ambient pressure, an "interaction index" n can be defined by

$$n=\left(\frac{\partial \ln \tilde{f}}{\partial \ln p}\right)$$

which is constant during the "sensitive time lag" τ. Then, when chamber conditions are varying,*

$$\tilde{f}=\bar{f}\left[1+n\,\frac{(p-\bar{p})}{\bar{p}}\right] \qquad (4.2.1\text{–}2)$$

so that Eq. (4.2.1–1) can be written

$$\int_{t-\tau_T}^{t-\tau} \bar{f}\,dt_1+n\int_{t-\tau}^{t} \bar{f}\,\frac{(p-\bar{p})}{\bar{p}}\,dt_1=\int_{t-\bar{\tau}_T}^{t} \bar{f}\,dt_1$$

Making the further assumption that $\bar{f}$ is constant during τ, it is possible to relate the sensitive time lag to the pressure by

$$\tau-\bar{\tau}=-n\int_{t-\bar{\tau}}^{t} \frac{p-\bar{p}}{\bar{p}}\,dt_1 \qquad (4.2.1\text{–}3)$$

The knowledge of the sensitive time lag τ allows the determination of the combustion rate. The propellant gasified in the volume element under consideration during the time interval dt is Mdt. This same amount was injected during the interval $d(t-\tau)$. Assuming that the injection rate is unaffected by the chamber conditions,

$$M\,dt=\bar{M}\,d(t-\tau)$$

Hence,

$$M-\bar{M}=-\bar{M}\left(\frac{\partial\tau}{\partial t}\right)$$

Therefore, assuming that the spatial displacement of the propellant during τ can be neglected, differentiation of Eq. (4.2.1–3) gives

$$\frac{M-\bar{M}}{\bar{M}}=-\left(\frac{\partial\tau}{\partial t}\right)=+n\,\frac{p(t)-p(t-\bar{\tau})}{\bar{p}} \qquad (4.2.1\text{–}4)$$

This method of expressing the pressure sensitivity can be applied to other variables as well. Temperature oscillations can in many cases be correlated with pressure oscillations and need not be treated separately. Rather, the interaction index n is defined to include the effects of both pressure and temperature. This is not the case for velocity or displacement sensitivity, which may also be important, especially for transverse modes. Such sensitivity results from the mixture

* For a detailed discussion and a critical evaluation of this reasoning process see Ref. 176 and for additional background see Ref. 179.

* A bar over a quantity indicates that it is evaluated at the mean, or steady-state, conditions.

ratio nonuniformities that commonly exist in practical engines, and are most severe near the injector face.[582,583] The expression for $\tilde{f}$ can be extended to cover displacement sensitivity by adding a linear sensitivity to the radial displacement δ_r and one to the circumferential displacement δ_θ in the form

$$\frac{\tilde{f}}{\bar{f}}=1+n\frac{(p-\bar{p})}{\bar{p}}+m_r\delta_r+m_\theta\delta_\theta \quad (4.2.1\text{–}2a)$$

with constant m_r and m_θ, and assuming a common sensitive time lag. However, one could also make the simpler assumption that the variation of the mixture ratio resulting from the displacement produces an immediate variation in the burning rate, without the time lag behavior.[583] In any case, the linearization of the displacement sensitivity is only valid if the mixture ratio is stratified in the proper fashion. In general this is not true and nonlinear displacement effects must be expected.

Even when only pressure sensitivity is considered, the above formulation is based on several restrictive assumptions. A more sophisticated formulation is presented in Ref. 176; it is shown that a simple representation of the type of Eq. (4.2.1–4), illustrated in Fig. 4.2.1 for a sinusoidal pressure oscillation, may generally be used only near the energy feedback peaks. Also interesting to notice is the fact that whereas Eq. (4.2.1–4) predicts, (as can be seen from the figure) an infinite array of peaks at frequencies such that $\omega\bar{\tau}$ varies by multiples of 2π, the more sophisticated formulation predicts only one peak at one frequency, in agreement with the great majority of experimental results. An exception, however, is provided by the multiple peaks observed by McBride and Veglia,[474] results which are in harmony with the predictions of the more restrictive formulation presented here.

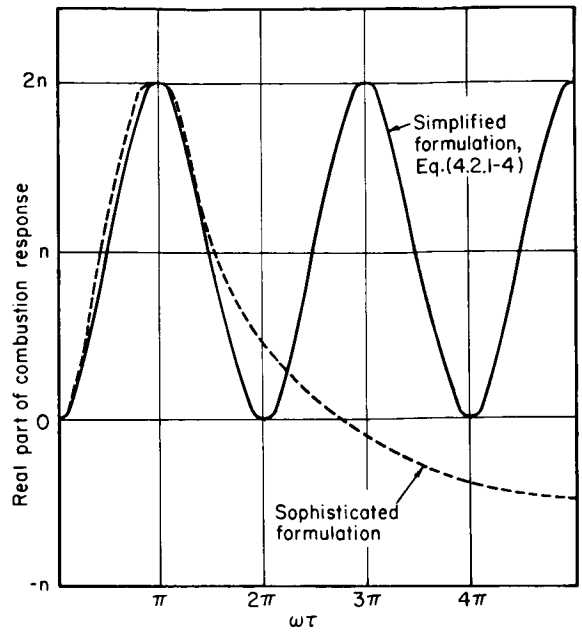

FIGURE 4.2.1.—Response of pressure-sensitive combustion process to a sinusoidal chamber pressure oscillation: comparison of Eq. (4.2.1–4) and sophisticated formulation (ref. 176).

4.2.1.2 *Theoretical approach.*—Formulating the unsteady behavior of a combustion system in precise mathematical terms is a task of great difficulty because of the complexity of the phenomena taking place in the combustion chamber and resulting in the final outflow of combustion gases through the nozzle. The liquid propellants must undergo atomization, heating, evaporation, mixing, and chemical reaction before the formation of the final products of combustion is achieved. Added to the heterogeneity of the flow is the complication of nonuniformity, resulting from the fact that the propellants are not premixed but are injected separately from a number of discrete ports. The mixing process, which must in the end reduce this nonuniformity to an acceptable level, strongly depends on the turbulence level, which is, in turn, determined in a very elusive way by the combustion process itself. The turbulence probably is also related to the intensity of the recirculation currents produced by the heterogeneity and nonuniformity of the flow. Interference with the combustion process may result from the application of film cooling, necessary in most high thrust engines to reduce the level of the heat flux to the walls. Another complication comes from the unsteady behavior of the exhaust nozzle. Even if the combustion is completed before its entrance, the unsteady exhaust flow may be substantially different from steady, one-dimensional flow.

Although qualitative ideas about these phenomena may be gained without difficulty, the task of reaching a quantitative knowledge of them

and of their relative importance under unsteady conditions, is far from being completed. Substantial advances are being made in this direction; however, the importance of finding an engineering solution to the problem of combustion instability justifies the use of a less fundamental, semi-empirical approach.

In the analysis presented here it is assumed that the combustion chamber is filled with the gases of complete combustion and droplets of unreacted propellants, which act as gas sources. The combustion gases are assumed to be homocompositional, inviscid (except for the existence of a droplet drag), and thermally and calorically perfect. The liquid phase is assumed to be well dispersed throughout the chamber, and the variations of its energy e_{Ls} (internal plus kinetic energy) are neglected. It would be possible, of course, to take into account the heat exchanges with the droplets, which may in some cases play an appreciable role.

Although it is possible to carry out the analysis starting from the conservation equations in integral form,[178] with certain simplifications in the order of magnitude considerations, in this discussion the more common differential forms will be used, as in most of the published analyses.[179,187,582,583,630] The equations will be written in nondimensional form. Pressure, density, temperature, enthalpy, and sonic velocity are normalized in such a way that they are unity in a chosen reference state, viz, the state of the gas at the injector face in steady conditions. Hence, the equation of state is

$$p = \rho T \qquad (4.2.1\text{–}5)$$

The velocities are divided by the reference sonic velocity, the dimensions by a chosen reference length,* and the time by the same reference length divided by the reference sonic velocity. Using this nondimensionalization scheme, the conservation equations, Eqs. (4.1.2–1), (4.1.2–2), (4.1.2–3) and (4.1.2–5) are

$$\frac{\partial \rho}{\partial t} + \nabla \cdot (\rho \mathbf{V}) = -\frac{\partial \rho_L{}^\circ}{\partial t} - \nabla \cdot (\rho_L{}^\circ \mathbf{V}_L) = M \qquad (4.2.1\text{–}6)$$

$$\rho \frac{\partial \mathbf{V}}{\partial t} + \rho \mathbf{V} \cdot \nabla \mathbf{V} + \frac{\nabla p}{\gamma} = M(\mathbf{V}_L - \mathbf{V}) - \mathbf{D} \qquad (4.2.1\text{–}7)$$

$$\rho_L \frac{\partial \mathbf{V}_L}{\partial t} + \rho_L \mathbf{V}_L \cdot \nabla \mathbf{V}_L = \mathbf{D} = k\rho_L{}^\circ (\mathbf{V} - \mathbf{V}_L) \qquad (4.2.1\text{–}8)$$

$$\frac{\partial}{\partial t}(\rho e_s) + \nabla \cdot (\rho h_s \mathbf{V}) = M e_{Ls} \qquad (4.2.1\text{–}9)$$

In these equations, the strength of the gas source has been divided by the product of the reference density, reference sound velocity, and the reciprocal of the reference length; $\rho_L{}^\circ$ is not liquid density, but rather the mass of liquid per unit volume, divided by the reference density; and the internal energy is defined so as to include the chemical energy. Because of the scheme used to nondimensionalize, the stagnation energy is

$$e_s = e + \frac{\gamma - 1}{2} V^2$$

The energy equation can be simplified by noting that the normalized enthalpy coincides with the normalized temperature and the internal energy (normalized by the reference enthalpy) is equal to T/γ. Also, by virtue of the simplifying assumption already discussed, the liquid energy e_{Ls} has the constant value of unity, i.e.,*

$$e_{Ls} = \bar{e}_{Ls} = \bar{h}_s = \bar{T} + \frac{\gamma - 1}{2} \bar{V}^2 = 1$$

Thus, the energy equation becomes

$$\frac{\partial}{\partial t}\left(\rho T_s - \frac{\gamma - 1}{\gamma} p\right) + \nabla \cdot (\rho T_s \mathbf{V}) = M \qquad (4.2.1\text{–}10)$$

where

$$T_s = T + \frac{\gamma - 1}{2} V^2$$

A comment on the droplet drag is in order here. A momentum equation for the liquid phase could be written to include the drag on a droplet in terms of the local Reynolds number, the relative velocity, the drop size, with also a drop size distribution characterizing the whole liquid spray. However, in this heuristic model it is not desirable to introduce such additional complications. For

* For longitudinal modes the reference length is usually the cylindrical chamber length, whereas for transverse modes the chamber radius is used.

* Recent results suggest that e_{Ls} can be different from 1; see Sect. 7.2.4.

this reason, the more convenient formulation of Eq. (4.2.1–8) is chosen, with the assumption that the coefficient k is substantially smaller than unity.[178,179]

To complete the mathematical model, appropriate boundary conditions must be stated for both the liquid and gaseous phases. For the liquid phase, assuming that the injection process is unaffected by the chamber oscillations,* it is sufficient to assign the injection velocity u_{Li}, and the injection density $\mu^\circ = A_i \rho_L u_{Li} = \rho_{Li}{}^\circ u_{Li}$, where A_i represents the injection port area per unit injector surface area and ρ_L is the normalized liquid density.

For the gaseous phase, the condition at the solid surfaces is the vanishing of the normal velocity component. More subtle is the condition concerning the exhaust flow. The proper place to prescribe that boundary condition is the sonic throat, since perturbations downstream of that surface cannot influence the upstream flow. In practice, however, it is useful to divide the upstream region into two parts: (a) the combustion chamber (down to the nozzle entrance) where the processes of combustion take place and the Mach number is relatively low, and (b) the nozzle (down to the throat) where no combustion is assumed to take place but the Mach number grows to unity. The study of the oscillatory behavior in the latter part is a problem of transonic gas dynamics, which may be solved separately to obtain a relation between flow perturbations at the nozzle entrance, the so-called admittance condition (Sect. 3.6). This admittance condition is then used as the boundary condition for the combustion chamber flow, to be applied at the nozzle entrance.

STEADY STATE: The conservation equations apply, of course, also to the steady-state problem when the time derivatives are suppressed. Even for this simplified system of equations a closed-form integration is generally impossible. However, the solution becomes simple if the chamber is assumed to be cylindrical and if the flow in the chamber and nozzle can be considered to be one-dimensional. The latter is a reasonable assumption when, on the one hand, the injection conditions are sufficiently close to being uniform and, on the other hand, the convergence of the nozzle is not too strong. Assuming, then, that the steady-state flow is one-dimensional, $\bar{\mathbf{V}}$ and $\bar{\mathbf{V}}_L$ are reduced to their axial components $\bar{u}$ and $\bar{u}_L$ and one obtains

$$\bar{\rho}\bar{u} = \rho_{Li}{}^\circ u_{Li} - \bar{\rho}_L{}^\circ \bar{u}_L = \int_0^x \bar{M}\, dx' \qquad (4.2.1\text{–}11)$$

$$\frac{\bar{p}-1}{\gamma} = \rho_{Li}{}^\circ u_{Li}{}^2 - \bar{\rho}_L{}^\circ \bar{u}_L{}^2 - \bar{\rho}\bar{u}^2$$

$$= \rho_{Li}{}^\circ u_{Li}(u_{Li} - \bar{u}_L) + \bar{\rho}\bar{u}(\bar{u}_L - \bar{u}) \qquad (4.2.1\text{–}12)$$

$$\frac{\bar{p}}{\bar{\rho}} = \bar{T} = 1 - \frac{\gamma-1}{2}\bar{u}^2 \qquad (4.2.1\text{–}13)$$

These four equations, plus the differential equation

$$\bar{u}_L \frac{d\bar{u}_L}{dx} = k(\bar{u} - \bar{u}_L) \qquad (4.2.1\text{–}14)$$

obtained from Eq. (4.2.1–8) under the present assumptions, are sufficient to determine the five steady-state variables $\bar{\rho}$, $\bar{u}$, $\bar{\rho}_L{}^\circ$, $\bar{u}_L$, and $\bar{p}$ if $\bar{M}$ is a known function of the same quantities, as it would be for a mechanistic model. On the contrary, for the heuristic model under discussion here, the function $\bar{M}$ is not prescribed. Rather, it is assumed that the steady-state processes result in a certain $\bar{u}(x)$, which is assigned. In this case the integration of Eq. (4.2.1–14) can be carried out independently of the other equations. Once $\bar{u}_L(x)$ is known, one obtains

$$\bar{\rho} = \frac{\bar{p}}{1 - \frac{\gamma-1}{2}\bar{u}^2} = \frac{1 + \gamma\rho_{Li}{}^\circ u_{Li}(u_{Li} - \bar{u}_L)}{1 + \frac{\gamma+1}{2}\bar{u}^2 - \gamma\bar{u}_L\bar{u}}$$

$$\bar{\rho}_L{}^\circ = \frac{\rho_{Li}{}^\circ u_{Li} - \bar{\rho}\bar{u}}{\bar{u}_L} \qquad (4.2.1\text{–}15)$$

and $\bar{M}$ can be determined by differentiation of $\bar{\rho}\bar{u}$.

The assumption that k is small has already been stated. Equation (4.2.1–14) shows what this assumption means in terms of droplet penetration. Taking $\bar{u} = 0$ and integrating, it is seen that $\bar{u}_L$ drops from u_{Li} to zero in a distance (called the penetration distance) equal to u_{Li}/k. Hence the penetration distance is of order unity (comparable to the reference length) if k is of a magnitude close to u_{Li}, which is generally a small quantity.

* This is not a necessary assumption, it is used here to simplify the presentation of the theory. The analysis by Waugh[720] indicates how injection effects can be included.

STABILITY ANALYSIS: In order to study the oscillatory behavior of the system, each dependent variable is split into its steady part, considered above, and an oscillatory perturbation, the behavior of which is to be determined and provides the key to the problem of instability. The discussion in the section following (4.2.2) will be concerned with the problem of "linear instability" in which any perturbation, no matter how small, is amplified with time if the combustor is unstable. Expressions will be derived that relate the combustion and flow parameters at the boundary between stable and unstable operation. The case of "nonlinear instability," in which only perturbations above a certain magnitude are amplified while below it they are damped, will be discussed in Sect. 4.2.3.

4.2.2 Linear Theory

To consider only the conditions under which linear instability can appear, without being concerned about the final situation created by the amplification, it can be assumed that the perturbation magnitudes are infinitesimally small. This limitation has the great advantage that in the mathematical developments one must keep only the terms that are linear in the perturbations, whereas terms containing powers or products of perturbations, being infinitesimal of a higher order, can be dropped. As a result, the relations between the perturbations, unlike the original equations, are linear.

The most important consequence of the linearity is that the principle of superposition can be applied, since the sum of two solutions of the equations is also a solution. This allows, for instance, the decomposition of an oscillation into its Fourier components, each one of a different frequency. Each Fourier component satisfies an equation that is independent of those satisfied by the other components. The study of the equation will reveal whether or not the corresponding component is unstable. If it is, the whole oscillation will be amplified with time regardless of the behavior of the other components. Hence the study of stability can be performed on the individual components rather than on the most general type of oscillation.

The following nomenclature pertains to Sect. 4.2.2 (see also Sects. 4.1.2 and 4.2.1):

$A_{\nu\eta}, B_{\nu\eta}, C_{\nu\eta}$	Eigenfunction expansion coefficients
$\mathcal{A}, \mathcal{B}, \mathcal{C}$	Nozzle admittance coefficients
B	Constant in radial distribution function for annular chamber
$\mathcal{F}_r, \mathcal{F}_\theta$	Combustion response functions for transverse gas displacement oscillations
G_R	Function defined in Eq. (4.2.2–23a)
j	Index for longitudinal modes; $j = 0, 1, 2, \ldots$
l_r, l_θ	Transverse velocity sensitivity indices
$M_{\nu\eta}$	Eigenfunction coefficient for burning rate M'
$\tilde{m}_r, \tilde{m}_\theta$	Mean values of displacement sensitivity indices
$\mathcal{P}$	Combustion response function for pressure oscillations
P	Axial dependence of pressure perturbation
P_{00}	Maximum amplitude of pressure perturbation
$s_{\nu\eta}$	Transverse mode eigenvalue
U, V, W	Axial dependencies of velocity perturbations
$\mathbf{W}$	Dyadic defined in Eq. (4.2.2–14)
$\mathbf{X}, \mathbf{Y}, \mathbf{Z}$	Functions defined in Eq. (4.2.2–14)
α_c	Included angle between walls of sector chamber
η	Integer index denoting number of nodal circles of a transverse acoustic mode
Θ_ν	Azimuthal (circumferential) distribution of pressure perturbations in circular chamber
ν	Index denoting number of nodal diameters of transverse acoustic mode
$\Psi_{\nu\eta}$	Radial distribution of pressure perturbations in circular chamber
Subscripts:	
eff	Effective
p, q	Indices in transverse eigenfunction expansions
ν, η	Indices denoting a particular transverse mode

0, 1, 2, . . . Indices denoting terms in series expressions

To study damped or amplified oscillations, the time dependence of the perturbations must be exponential, rather than harmonic, as in Fourier analysis, that is, each perturbation amplitude is multiplied by exp(st), where

$$s=\lambda+i\omega$$

ω being the angular frequency and λ the amplification coefficient, both of which are nondimensional (the normalization factor is the reciprocal of the normalization factor of the time).

Accordingly, the pressure perturbation is defined by

$$p=\bar{p}+\mathcal{R}e(p'e^{st}) \qquad (4.2.2\text{–}1)$$

in which p' is the complex amplitude of the perturbation, that is, a quantity such that the real part of $p'\exp(st)$ represents the actual instantaneous perturbation. Similar equations define the perturbations of all other quantities, scalar or vectorial. The complex amplitudes thus defined are functions of the location alone.

4.2.2.1 *Governing equations.*—Substitution of the expressions like Eq. (4.2.2–1) into Eq. (4.2.1–6) produces, after subtraction of the corresponding steady equations, the following equations of continuity:

$$s\rho'+\bar{\rho}\nabla\cdot\mathbf{V}'+\mathbf{V}'\cdot\nabla\bar{\rho}=M'-\nabla\cdot(\rho'\bar{\mathbf{V}}) \qquad (4.2.2\text{–}2)$$

$$s\rho_L'+\nabla\cdot(\bar{\mathbf{V}}_L\rho_L^{\circ\prime})=-M'-\nabla\cdot(\bar{\rho}_L^{\circ}\mathbf{V}_L') \qquad (4.2.2\text{–}3)$$

Similarly, the momentum equations are obtained from Eq. (4.2.1–7) and Eq. (4.2.1–8) as

$$s(\bar{\rho}\mathbf{V}'+\bar{\mathbf{V}}\rho')+\frac{\nabla p'}{\gamma}=-s(\bar{\rho}_L^{\circ}\mathbf{V}_L'+\bar{\mathbf{V}}_L\rho_L^{\circ\prime})$$
$$-\nabla\cdot(2\bar{\rho}\bar{\mathbf{V}}\mathbf{V}'+2\bar{\rho}_L^{\circ}\bar{\mathbf{V}}_L\mathbf{V}_L'+\bar{\mathbf{V}}\bar{\mathbf{V}}\rho'+\bar{\mathbf{V}}_L\bar{\mathbf{V}}_L\rho_L^{\circ\prime}) \qquad (4.2.2\text{–}4)$$

$$s\mathbf{V}_L'+(\bar{\mathbf{V}}_L\cdot\nabla)\mathbf{V}_L'+(\mathbf{V}_L'\cdot\nabla)\bar{\mathbf{V}}_L=k(\mathbf{V}'-\mathbf{V}_L') \qquad (4.2.2\text{–}5)$$

Finally, multiplying Eq. (4.2.1–6) by $\bar{T}_s$ (which equals 1, as Eq. (4.2.1–13) shows) and subtracting it from Eq. (4.2.1–10) gives

$$s\left(\bar{\rho}T_s'-\frac{\gamma-1}{\gamma}p'\right)+\nabla\cdot(\bar{\rho}\bar{\mathbf{V}}T_s')=0 \qquad (4.2.2\text{–}6)$$

with

$$T_s'=T'+(\gamma-1)\bar{\mathbf{V}}\cdot\mathbf{V}'$$

It is convenient at this point to introduce the normalized entropy σ, defined as the entropy variation from the reference state divided by c_p. The relation between pressure, entropy, and density is

$$\rho=p^{1/\gamma}e^{-\sigma} \qquad (4.2.2\text{–}7)$$

Eq. (4.2.1–5) and (4.2.2.–7) yield the perturbation equations

$$\bar{\rho}T'-\frac{\gamma-1}{\gamma}p'=\bar{p}\sigma'=\frac{p'}{\gamma}-\bar{T}\rho' \qquad (4.2.2\text{–}8)$$

which can be introduced into Eq. (4.2.2–6) to give the following form of the energy equation:

$$s[\bar{p}\sigma'+(\gamma-1)\bar{\rho}\bar{\mathbf{V}}\cdot\mathbf{V}']$$
$$+\nabla\cdot\{\bar{\mathbf{V}}[\bar{p}\sigma'+(\gamma-1)\bar{\rho}\bar{\mathbf{V}}\cdot\mathbf{V}']\}$$
$$=-\frac{\gamma-1}{\gamma}\nabla\cdot(\bar{\mathbf{V}}p') \qquad (4.2.2\text{–}9)$$

The set of perturbation equations is completed by rewriting Eq. (4.2.1–4) in the form

$$M'=n[1-\exp(-s\bar{\tau})]\bar{M}\frac{p'}{\bar{p}}=\mathcal{P}\bar{M}\frac{p'}{\bar{p}} \qquad (4.2.2\text{–}10)$$

which is applicable when only pressure sensitivity needs to be considered. For the more general case in which displacement effects must also be included, Eq. (4.2.2–10) is replaced by

$$M'=\bar{M}(\mathcal{P}p'/\bar{p}+\mathcal{F}_r\delta_r'+\mathcal{F}_\theta\delta_\theta') \qquad (4.2.2\text{–}10a)$$

where

$$\mathcal{F}_r=m_r[1-\exp(-s\bar{\tau})];$$
$$\mathcal{F}_\theta=m_\theta[1-\exp(-s\bar{\tau})] \qquad (4.2.2\text{–}11)$$

4.2.2.2 *Method of solution.*—The system of perturbation equations governing the oscillatory flow in the combustion chamber consists of Eqs. (4.2.2–2), (–3), (–4), (–5), (–8), (–9), and (–10). This complicated system can be solved using the following technique. First, use Eq. (4.2.2–8) to eliminate the entropy perturbation σ' from the energy equation, Eq. (4.2.2–9), writing the latter in the form

$$s\left(\rho'-\frac{p'}{\gamma}\right)=s[(1-\bar{T})\rho'+(\gamma-1)\bar{p}\bar{\mathbf{V}}\cdot\mathbf{V}']$$

$$+\nabla\cdot\{\bar{\mathbf{V}}[p'-\bar{T}\rho'+(\gamma-1)\bar{p}\bar{\mathbf{V}}\cdot\mathbf{V}']\} \tag{4.2.2–12}$$

Next, use Eq. (4.2.2–12) to eliminate ρ' in favor of p' on the L.H.S. of Eq. (4.2.2–2) and (–4), which then can be arranged as

$$\frac{sp'}{\gamma}+\nabla\cdot\mathbf{V}'=-sX+\nabla\cdot\mathbf{Y}+M'$$

$$s\mathbf{V}'+\frac{\Delta p'}{\gamma}=-s\mathbf{Z}-\nabla\cdot\mathbf{W} \tag{4.2.2–13}$$

where

$$X=(\gamma-1)\bar{p}\bar{\mathbf{V}}\cdot\mathbf{V}'+(1-\bar{T})\rho'$$

$$\mathbf{Y}=-\bar{\mathbf{V}}p'+(1-\bar{\rho})\mathbf{V}'-(\gamma-1)\bar{\rho}\bar{\mathbf{V}}(\bar{\mathbf{V}}'\cdot\mathbf{V})-(1-\bar{T})\bar{\mathbf{V}}\rho'$$

$$\mathbf{Z}=\bar{\mathbf{V}}\rho'+\bar{\rho}_L{}^{\circ}\mathbf{V}_L'+\bar{\mathbf{V}}_L\rho_L{}^{\circ\prime}-(1-\bar{\rho})\mathbf{V}'$$

$$\mathbf{W}=2\bar{\rho}\bar{\mathbf{V}}\mathbf{V}'+2\bar{\rho}_L{}^{\circ}\bar{\mathbf{V}}_L\mathbf{V}_L'+\bar{\mathbf{V}}\bar{\mathbf{V}}\rho'+\bar{\mathbf{V}}_L\bar{\mathbf{V}}_L\rho_L' \tag{4.2.2–14}$$

In Eq. (4.2.2–14) $\mathbf{W}$ is a dyadic,[504] but $\nabla\cdot\mathbf{W}$ is a vector, and can be calculated by applying the rule

$$\nabla\cdot(\mathbf{AB})=(\mathbf{A}\cdot\nabla)\mathbf{B}+\mathbf{B}(\nabla\cdot\mathbf{A})$$

where $\mathbf{A}$ and $\mathbf{B}$ are two vectors into which $\mathbf{W}$ can be split.

The form of the system of Eq. (4.2.2–13) allows an easy series solution when the gas and droplet velocities are substantially smaller than the sonic velocity, that is, when $\bar{u}$ and $\bar{u}_L$ (and, of course, the nozzle entrance velocity $\bar{u}_e$) are small compared to unity. In this case, it can be seen from Eq. (4.2.1–12) and (–13) that $\bar{p}-1$, $1-\bar{T}$, and $1-\bar{\rho}$ are small quantities of $\mathcal{O}(\bar{u}_e^2)$, and $\bar{M}$ is of $\mathcal{O}(\bar{u}_e)$, provided that $d\bar{u}/dx$ is of $\mathcal{O}(\bar{u}_e)$, that is, if the combustion is well spread out axially. In this case inspection of Eq. (4.2.2–14) shows that all terms on the R.H.S. of Eq. (4.2.2–13) are of $\mathcal{O}(\bar{u}_e)$ or higher when compared to the perturbations. As a result, one can solve the equations by expanding the quantities in series, e.g.,

$$p'=p_0+p_1+p_2+\cdots$$

$$\mathbf{V}'=\mathbf{V}_0+\mathbf{V}_1+\mathbf{V}_2+\cdots$$

where p_1/p_0 and V_1/V_0 are of $\mathcal{O}(\bar{u}_e)$, p_2/p_0 and V_2/V_0 are of $\mathcal{O}(\bar{u}_e^2)$, etc.

Introducing such series expansions into Eq. (4.2.2–13), it is found that the first two terms are given by

$$\frac{sp_0}{\gamma}+\nabla\cdot\mathbf{V}_0=0$$

$$s\mathbf{V}_0+\frac{\nabla p_0}{\gamma}=0 \tag{4.2.2–15}$$

and

$$\frac{sp_1}{\gamma}+\nabla\cdot\mathbf{V}_1=-sX_1+\nabla\cdot\mathbf{Y}_1+M_1$$

$$s\mathbf{V}_1+\frac{\nabla p_1}{\gamma}=-s\mathbf{Z}_1-\nabla\cdot\mathbf{W}_1 \tag{4.2.2–16}$$

where the subscript 1 applied to the quantities on the R.H.S. means that all terms of order higher than $\mathcal{O}(\bar{u}_e)$ have been suppressed from these expressions. The relevant forms of these quantities are[178, 179, 582]

$$X_1=(\gamma-1)\bar{u}u_0$$

$$\mathbf{Y}_1=-\mathbf{V}p_0$$

$$\mathbf{Z}_1=\frac{\bar{\mathbf{V}}p_0}{\gamma}+\bar{\rho}_L\mathbf{V}_{L1}$$

$$\mathbf{W}_1=2\bar{\mathbf{V}}\mathbf{V}_0 \tag{4.2.2–17}$$

The following items should be observed with regard to Eq. (4.2.2–17): The only component of $\bar{\mathbf{V}}$ is the axial component $\bar{u}$. The perturbation ρ_L' only enters in higher order terms and so does not need to be computed. However, $\mathbf{V}_L'$ is needed; its lowest order term $\mathbf{V}_{L1}$ can be obtained from Eq. (4.2.2–5). In the expression for $\mathbf{Z}_1$, ρ_0 has been replaced by p_0/γ. Now from Eq. (4.2.2–8), ρ' and p' are related to σ', which can be obtained, independently of the series expansion, from Eq. (4.2.2–9), with the result

$$\sigma'=-\frac{(\gamma-1)\bar{\rho}\bar{u}u'}{\bar{p}}-\frac{(\gamma-1)}{\gamma\bar{u}\bar{p}}\int_0^x\left(p'\frac{d\bar{u}}{dx'}+\bar{u}\frac{\partial p'}{\partial x'}\right)\exp\left[-s\int_{x'}^x\frac{dx''}{\bar{u}(x'')}\right]dx' \tag{4.2.2–18}$$

It can be shown that if $d\bar{u}/dx$ is of $\mathcal{O}(\bar{u}_e)$ the integral term is, like the other term, of $\mathcal{O}(\bar{u}_e)$ compared to the perturbations. Then the first non-zero term in the series expansion for σ' is σ_1. Hence, Eq. (4.2.2–8) gives $\rho_0=p_0/\gamma$.

A different result is obtained for the σ' series

if the combustion is rather concentrated, so that $d\bar{u}/dx$ is of $\mathcal{O}(1)$ or larger. In that case, the integral term of Eq. (4.2.2–18) is of $\mathcal{O}(1)$, and the σ_0 term is not zero. However, because of its oscillatory character, the contribution of the σ_0 term that would appear in $\mathbf{Z}_1$ is only of $\mathcal{O}(\bar{u}_e^2)$ in the final solution of Eq. (4.2.2–16) and hence can be neglected. This result applies also to the other terms that have been disregarded in Eq. (4.2.2–17), which thus remain valid even if the combustion is concentrated.

The zeroth-order equations, Eq. (4.2.2–15), are the equations of acoustics. Upon elimination of $\mathbf{V}_0$ they result in the wave equation

$$\nabla^2 p_0 + s^2 p_0 = 0 \qquad (4.2.2\text{–}19)$$

written in terms of the complex frequency s. Particular solutions of this equation are known; once expressions for p_0 and $\mathbf{V}_0$ are obtained, they can be inserted into Eq. (4.2.2–17) and then Eq. (4.2.2–16) can be solved. One can require that the zeroth-order solutions p_0 and $\mathbf{V}_0$ satisfy the boundary conditions, in which case they are eigenfunctions and exist only for well defined values s_0 of s, called eigenvalues. Alternatively, one can apply to the zeroth-order solution all the boundary conditions except the nozzle admittance conditions, in which case s remains undefined. In this procedure, the complete boundary conditions are applied only to the combinations p_0+p_1, $\mathbf{V}_0+\mathbf{V}_1$, after which s will be determined. This second procedure is preferable for the actual evaluation of the stability conditions. However, the first procedure allows a simpler discussion,[178] and so will be followed here.

Since the boundary conditions are to be applied separately to the zeroth-order solution, it is necessary to expand s in a series,

$$s = s_0 + s_1 + \cdots$$

because, in general, s does not agree with the eigenvalue s_0. The zeroth-order equations are then written in the same form as Eq. (4.2.2–15) but with s_0 in place of s. The first-order equations then become

$$\frac{s_0 p_1}{\gamma} + \nabla\cdot\mathbf{V}_1 = -s_0 X_1 + \nabla\cdot\mathbf{Y}_1 + M_1 - \frac{s_1 p_0}{\gamma}$$

$$s_0\mathbf{V}_1 + \frac{\nabla p_1}{\gamma} = -s_0\mathbf{Z}_1 - \nabla\cdot\mathbf{W}_1 - s_1\mathbf{V}_0 \qquad (4.2.2\text{–}16a)$$

where the quantities on the R.H.S. are still defined by Eq. (4.2.2–17). Since the solutions are somewhat different for longitudinal and transverse modes, these are taken up separately in the next two sections.

4.2.2.3 *Longitudinal mode solution.*—For purely longitudinal oscillations the zeroth-order equations are

$$\frac{s_0 p_0}{\gamma} + \frac{du_0}{dx} = 0$$

$$s_0 u_0 + \frac{d}{dx}\left(\frac{p_0}{\gamma}\right) = 0$$

Their solution is a neutral oscillation with

$$p_0 = P_{00}\cos\omega_0 x$$

$$u_0 = -i\frac{P_{00}}{\gamma}\sin\omega_0 x$$

$$s_0 = i\omega_0 = ij(\pi/L) \qquad (4.2.2\text{–}20)$$

The eigenvalue s_0 is always imaginary. Its value is determined from the requirement that u_0 vanish not only at the injector face, $x=0$, but also at the nozzle entrance, $x=L$. The integer j characterizes the mode of oscillation and represents the number of pressure nodal sections. P_{00} is the maximum amplitude of the pressure perturbation.

The first-order correction u_1 is found from Eq. (4.2.2–16a)

$$\frac{\gamma u_1(x)}{P_{00}} = \gamma(\mathcal{P}-1)\cos\omega_0 x$$
$$-\mathcal{P}\gamma\omega_0\int_0^x \bar{u}(x')\sin\omega_0(x-2x')\,dx'$$
$$+\omega_0\int_0^x \bar{u}(x')[\sin\omega_0 x$$
$$-(2-\gamma)\sin\omega_0(x-2x')]\,dx'$$
$$-\frac{k}{2}\int_0^x \bar{\rho}_L^{\circ}(x')[\cos\omega_0 x$$
$$-\cos\omega_0(x-2x')]\,dx' - s_1 x\cos\omega_0 x \qquad (4.2.2\text{–}21)$$

where $\mathcal{P}$ is defined by Eq. (4.2.2–10). This expression for u_1 can be inserted into the first-order nozzle admittance condition,*

$$u_1(L) = -\mathcal{A}p_0(L) \qquad (4.2.2\text{–}22)$$

The admittance coefficient $\mathcal{A}$ is complex, as is the combustion response factor $\mathcal{P}$. For use in Eq. (4.2.2–22) both of these quantities are evaluated at $s = s_0 = i\omega_0$. Since Eq. (4.2.2–22) is a complex equation, it can be used to determine the real and imaginary parts of $s_1 = \lambda_1 + i\omega_1$. The value of ω_1 provides the frequency change with respect to the acoustic frequency ω_0, and the value of λ_1 the amplification coefficient, since $\lambda_0 = 0$. The sign of λ_1 establishes whether the operation is stable ($\lambda_1 < 0$) or unstable ($\lambda_1 > 0$). The stability boundary, which divides regions of stable operation from those of unstable operation, is obtained by setting $\lambda_1 = 0$, with the result

$$n(1 - \cos \omega_0\bar{\tau}) = G_R \qquad (4.2.2\text{–}23)$$

where

$$G_R = \frac{\gamma(\bar{u}_e - \mathcal{A}_R) - (2-\gamma)\omega_0 \int_0^L \bar{u} \sin 2\omega_0 x dx + \frac{k}{2}\int_0^L \bar{\rho}_L{}^\circ (1 - 2\cos 2\omega_0 x) dx}{\gamma\left(\bar{u}_e + \omega_0 \int_0^L \bar{u} \sin 2\omega_0 x \, dx\right)} \qquad (4.2.2\text{–}23a)$$

Fig. 4.2.2.a illustrates the consequences of Eq. (4.2.2–23) and the regions in which $\lambda_1 \gtrless 0$. The abscissa is the ratio of the sensitive time lag to the oscillation period $t_w = 2\pi/\omega_0$. The maximum tendency to instability takes place when $\bar{\tau}$ contains an integral number of periods plus a half-period, according to the simple formulation of the n, τ model under discussion here. If the more sophisticated treatment[176] mentioned in Sect. 4.2.1.1 were used, only the stability boundary curve with the minimum at $\bar{\tau}/t_w = 0.5$ would be obtained from Eq. (4.2.2–23). Concentrating on this lowest-frequency loop, it can be seen first of all that n/G_R must be greater than 0.5 for instability to be possible, and the larger G_R is, the larger n must be. Hence, terms producing an increase of G_R are stabilizing. It is clear, therefore, that the term in k, representing the effect of the droplet drag, is stabilizing. Since $\mathcal{A}_R$ is generally negative, the effect of the nozzle is also stabilizing, with a longer nozzle producing greater damping.

Even if $n/G_R > 0.5$, unstable operation occurs only when $\omega_0\bar{\tau}$ is in a certain range. That is, for a given value of $\bar{\tau}$, there is an ω_0-range corresponding to instability, which means, according to Eq. (4.2.2–20), that j/L must be in the corresponding range. If there is an integer j for which this is true, the combustion will be unstable in the corresponding mode. The order of the possible mode increases with L, as illustrated by the experimental results shown in Fig. 4.2.2b. Similarly, for a given mode (value of j) instability is only possible over a certain range of length for a given pair of values of n and $\bar{\tau}$. This theoretical result, which can be seen in Fig. 4.2.2c, provides also the basis for the experimental determination of the empirical coefficients n and $\bar{\tau}$. The method, which is described in detail in Ref. 180, involves the measurement of stability limits* in terms of the chamber length and operating parameters. By measuring also the oscillation frequency near the lower stability limit (smaller L), it was possible to obtain a direct experimental verification of the theory.[180] That is, inserting the measured frequency and length of the lower stability limit into Eq. (4.2.2–23), the values of n and $\bar{\tau}$ were calculated as functions of mixture ratio and chamber pressure. Then these n, $\bar{\tau}$ values were used in Eq. (4.2.2–23) to predict the frequency and length at the upper limit. The good agreement obtained is shown in Fig. 4.2.2d.

It is clear from Eq. (4.2.2–23) that n_M, the minimum value of the interaction index for which

* For consistency with the assumption $u_0(L) = 0$, the admittance coefficient $\mathcal{A}$ should be of $\mathcal{O}(\bar{u}_E)$. Actually it is found that, although in some cases $\mathcal{A}$ is quite small, in many cases it is of $\mathcal{O}(1)$. This is the reason that for accurate calculations it is better to apply the nozzle condition in the form $u_0(L) + u_1(L) = \mathcal{A}(\omega)p_0(L)$, as mentioned in Sect. 4.2.2.2, reserving the present procedure only for the purpose of qualitative discussion.

* When instability regimes overlap a frequency problem in interpretation is present; the wave characteristics and a knowledge of boundary shape (based on nonoverlapping regimes) are helpful in this interpretation.

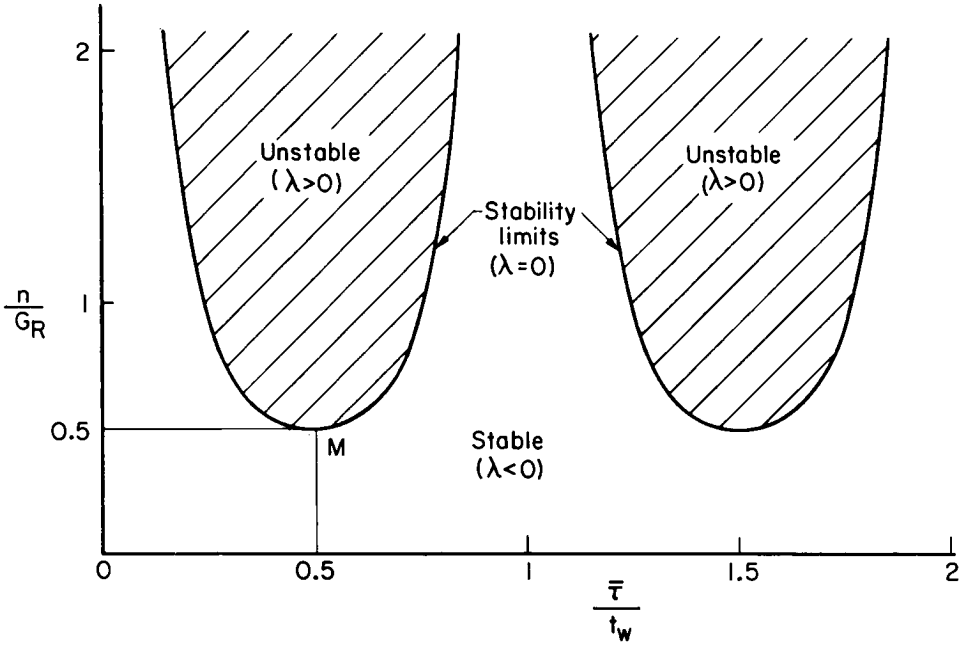

FIGURE 4.2.2a.—Typical stability limits determined from Eq. (4.2.2–23).

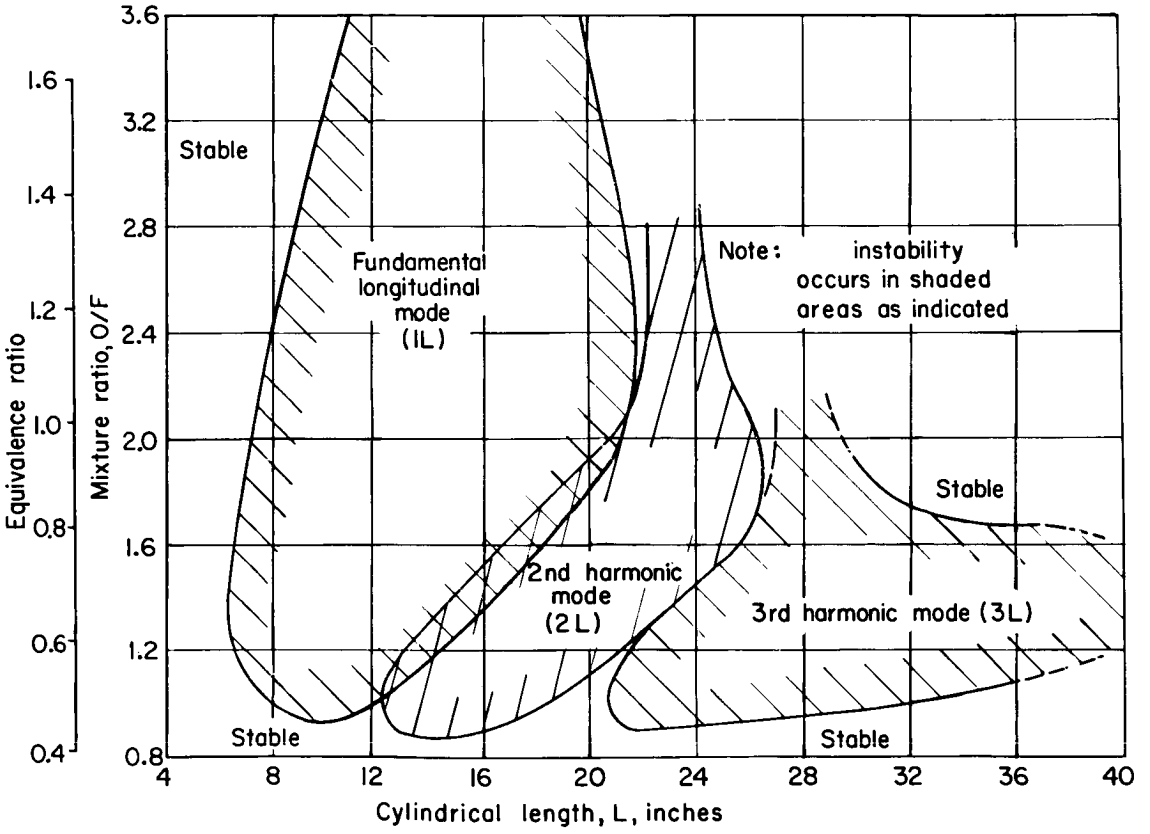

FIGURE 4.2.2b.—Experimental stability limits obtained with the Princeton University variable-length combustor. Propellants, LOX/ethanol; chamber pressure, 300 psia; S: = 0.05.

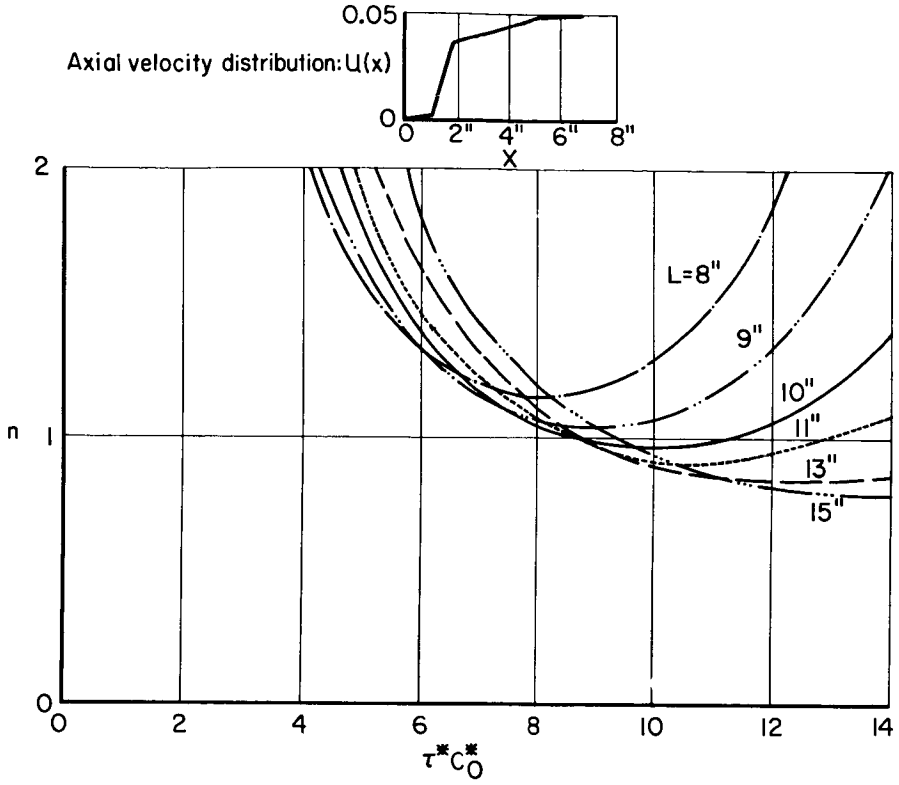

FIGURE 4.2.2c.—Effect of chamber length on stability limits for first longitudinal mode.

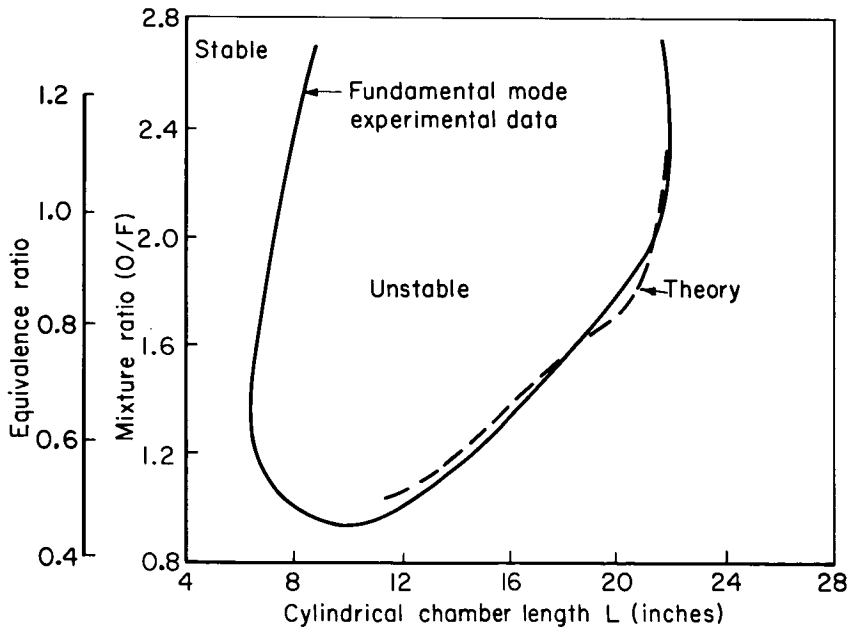

FIGURE 4.2.2d.—Comparison of experimental and theoretical stability limits. Experimental conditions same as Fig. 4.2.2b; theoretical upper limit determined from experimental measurements at lower limit.

instability is possible ($n_M = \frac{1}{2}G_R$), is dependent on the axial distribution of combustion, represented by $\bar{u}(x)$. Increasing the axial spreading of the combustion increases n_M (Fig. 4.2.2e) and so is stabilizing. Since the frequency also enters the combustion distribution terms of Eq. (4.2.2–23a) the effect of the shape of $\bar{u}(x)$ changes from mode to mode. As shown in Fig. 4.2.2e, the maximum stability of the first longitudinal mode is obtained (for linear $u(x)$) when the combustion is spread over about 80% of the chamber length, whereas the greatest stability of the second mode occurs when the combustion is spread over about 40% of the chamber length. Another source of the different stability behavior of the two modes is the nozzle admittance coefficient $\mathcal{A}_R$. In addition, for $j > 1$, the value of $\omega_0 L$ becomes large compared to unity, and the treatment developed in this section

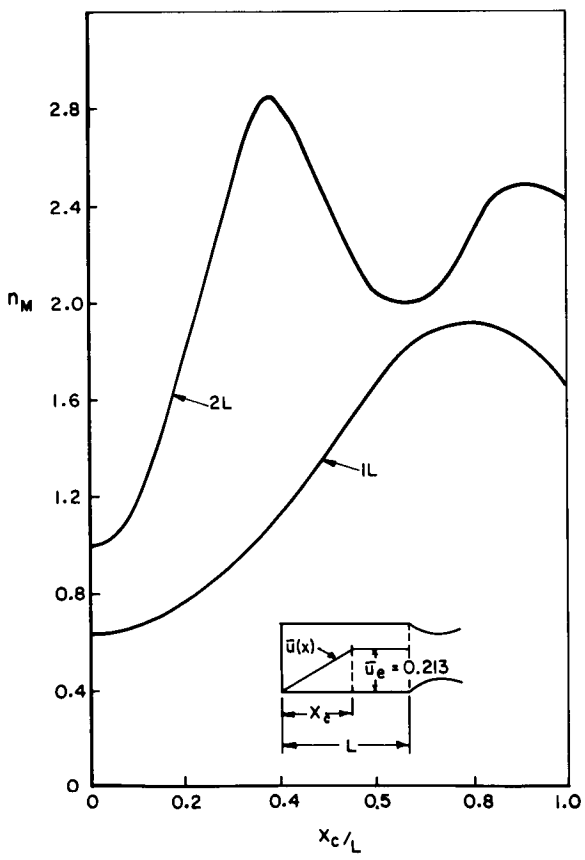

FIGURE 4.2.2e.—Effect of axial combustion distribution on minimum point of stability limit curve; first (1L) and second (2L) longitudinal modes.

must be replaced with a more sophisticated one.[179] An extensive discussion of the low-Mach-number theory, including the effects of a $\bar{\tau}$ variation from one propellant element to another, is given in Ref. 179.

Recent attention has been given to the effects of large chamber Mach numbers on the stability of the longitudinal modes.[190] Typical results are shown in Fig. 4.2.2f, in which stability limits for the first and second modes are given for two values of the Mach number and for short and long exhaust nozzles. Earlier, low-Mach-number analyses[179] showed that increasing the length of the subsonic portion of the exhaust nozzle is stabilizing, increasing the value of n_M and reducing the frequency, in addition. As shown by curves (a) and (b) of Fig. 4.2.2f, the effect of increasing the nozzle length is to shift the stability limit curve on the n, τ diagram up and to the right, although the shift in the τ-direction is much smaller than the shift in the n-direction. For high chamber Mach numbers, curves (c) and (d), the stabilizing effect of lengthening the nozzle is much smaller than for low Mach numbers, and the τ-shift is comparable to the n-shift. For a given nozzle length, increasing the chamber Mach number is destabilizing, although the effect is not very large for a short nozzle (Fig. 4.2.2f). In addition to the decrease in n_M, there is a large shift of the instability region to larger values of τ, with a correspondingly large decrease in the oscillation frequency. The latter effect results, of course, from the fact that the small perturbations considered in the linear theory travel at sonic velocity with respect to the mean gas flow in the chamber, so that the frequency of the first longitudinal mode is given approximately by $(a_m/2L_{eff})(1-u_m^2)$, where L_{eff} is the effective length of the chamber (including a part of the subsonic portion of the nozzle), a_m is the mean sonic velocity, and u_m is the mean Mach number. It is interesting to note that even for nonlinear waves, experimental frequencies are in good agreement with the theoretical predictions.[55]

4.2.2.4 *Transverse mode solution.*—In the case of transverse mode oscillations in a cylindrical chamber, the reference length is taken as the chamber radius, and the transverse coordinates are the azimuthal angle θ and the normalized

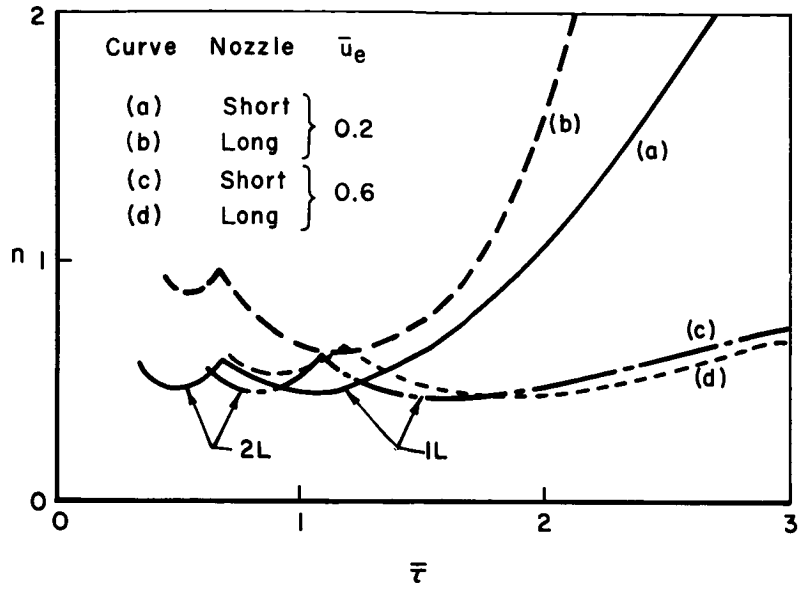

FIGURE 4.2.2f.—Stability limits for first (1L) and second (2L) longitudinal modes. Combustion concentrated at injector end of chamber.

radius r. The velocity components in the x, r, and θ directions are u, v, and w, respectively. The zeroth-order equations for this case are

$$\frac{s_0 p_0}{\gamma} + \frac{\partial u_0}{\partial x} + \frac{1}{r}\frac{\partial (r v_0)}{\partial r} + \frac{1}{r}\frac{\partial w_0}{\partial \theta} = 0$$

$$s_0 u_0 + \frac{1}{\gamma}\frac{\partial p_0}{\partial x} = s_0 v_0 + \frac{1}{\gamma}\frac{\partial p_0}{\partial r} = s_0 w_0 + \frac{1}{\gamma r}\frac{\partial p_0}{\partial \theta} = 0 \qquad (4.2.2\text{–}24)$$

For purely transverse (i.e., independent of x) oscillations, the acoustic solution is

$$p_0 = P_{00}\Psi_{\nu\eta}(r)\,\Theta_\nu(\theta)$$

$$u_0 = 0$$

$$v_0 = -\frac{P_{00}}{\gamma s_0}\frac{d\Psi_{\nu\eta}}{dr}\Theta_\nu \qquad (4.2.2\text{–}25)$$

$$w_0 = -\frac{P_{00}}{\gamma s_0}\frac{\Psi_{\nu\eta}}{r}\frac{d\Theta_\nu}{d\theta}$$

where Θ_ν is either of the expressions

$$\exp(\pm i\nu\theta)$$

corresponding to waves spinning in the negative or positive direction, or any combination of the two, such as $\sin \nu\theta$ or $\cos \nu\theta$, corresponding to standing modes, with the integer ν representing the number of nodal diameters of the particular mode. The radial dependence is given by the Bessel function $\Psi_{\nu\eta} = J_\nu(s_{\nu\eta} r)$ where $s_{\nu\eta}$ is any root of the equation*

$$\frac{dJ_\nu}{dZ}(Z) = 0$$

There are an infinite number of such roots, distinguished by the integral index η, such that $\eta - 1$ is the number of nodal circles of the solution. Finally, the eigenvalue s_0 is

$$s_0 = i\omega_0 = i s_{\nu\eta}$$

The first-order corrections are obtained from

* For an annular chamber, the radial dependence must include both Bessel functions, viz, $\Psi_{\nu\eta} = J_\nu(s_{\nu\eta} r) + BY_\nu(s_{\nu\eta} r)$ where $s_{\nu\eta}$ is a root of the equation

$$\frac{dJ_\nu}{dZ}(Z)\frac{dY_\nu}{dZ}(\xi Z) - \frac{dJ_\nu}{dZ}(\xi Z)\frac{dY_\nu}{dZ}(Z) = 0$$

in which $\xi = r_i/r_0$ is the ratio of the inner radius to the outer radius of the chamber. The constant B is determined from the condition

$$\frac{dJ_\nu}{dZ}(s_{\nu\eta}) + B\frac{dY_\nu}{dZ}(s_{\nu\eta}) = 0$$

Eq. (4.2.2–16a). When the combustion response is given by Eq. (4.2.2–10) that is, when only pressure-sensitivity is considered, the variables are immediately separated by taking

$$\begin{aligned} p_1 &= P_1(x)\Psi_{\nu\eta}(r)\Theta_\nu(\theta) \\ u_1 &= U_1(x)\Psi_{\nu\eta}(r)\Theta_\nu(\theta) \\ v_1 &= V_1(x)(d\Psi_{\nu\eta}/dr)\Theta_\nu(\theta) \\ w_1 &= W_1(x)(\Psi_{\nu\eta}/r)(d\Theta_\nu/d\theta) \end{aligned} \qquad (4.2.2\text{–}26)$$

thus converting Eq. (4.2.2–16a) into a set of ordinary differential equations for P_1, U_1, V_1, and W_1. However, when Eq. (4.2.2–10a) is used for the combustion response, to take into account the effects of displacement sensitivity, the variables are not immediately separable, and only become so by expanding both the perturbations and the combustion response terms in doubly infinite series of the eigenfunctions $\Psi_{pq}(r)$ and $\Theta_p(\theta)$. For stability, it has been shown that only the term corresponding to $p=\nu$, $q=\eta$ is important.[582] Actually, only the following expression for U_1, obtained by integrating the appropriate differential equation, is needed for the stability analysis:

$$U_1(x) = \int_0^x M_{\nu\eta}dx - \frac{P_{00}}{\gamma}\left[(\gamma+1)\bar{u}(x) + k\int_0^x \bar{\rho}_L{}^\circ dx' + 2s_1 x\right] \qquad (4.2.2\text{–}27)$$

In Eq. (4.2.2–27) $M_{\nu\eta}$ is the $p=\nu$, $q=\eta$ coefficient of the eigenfunction expansion of M_1.

As in the longitudinal case, the above expression for U_1, evaluated at $x=L$, is inserted into the nozzle admittance condition. Taking into account the fact that the effects of entropy are small at these frequencies (as in the longitudinal case), this gives

$$U_1(L) = -\mathcal{A}(s_{\nu\eta})P_{00} + \mathcal{B}(s_{\nu\eta})\frac{P_{00}}{i\gamma s_{\nu\eta}} = \mathcal{E}(s_{\nu\eta})\frac{P_{00}}{\gamma} \qquad (4.2.2\text{–}28)$$

For the purpose of this discussion, it is assumed that the admittance coefficients $\mathcal{A}$ and $\mathcal{B}$ and the combined coefficient $\mathcal{E}=\mathcal{E}_R+i\mathcal{E}_I$ are of $\mathcal{O}(\bar{u}_e)$, which is generally true. However, for more accurate calculations it is preferable to follow the alternate procedure discussed in Sect. 4.2.2.3.

Setting the amplification coefficient $\lambda_1=0$ to obtain the equation for the stability boundary yields Eq. (4.2.2–23) again, except that G_R is now defined by

$$G_R = 1 + \frac{1}{\gamma} - \frac{\mathcal{E}_R}{\gamma\bar{u}_e} + \frac{k}{\gamma\bar{u}_e}\int_0^L \bar{\rho}_L{}^\circ dx \qquad (4.2.2\text{–}29)$$

when only pressure sensitivity is considered. For any given mode, the general picture of the stability boundary, and the stable and unstable regions of operation given in Fig. 4.2.2a still holds. More accurate calculations for the first three transverse modes are shown in Fig. 4.2.2g, in which the strong overlapping of the instability regions can be seen.

Examination of Eq. (4.2.2–29) reveals that the droplet drag effect is stabilizing, as it was for the longitudinal modes (see discussion following Eq. (4.2.2–23)). Nozzle admittance calculations[582, 196] have shown that $\mathcal{E}_r$ is generally small and positive (Sect. 3.6). Therefore, the nozzle is slightly destabilizing. Although in the longitudinal case the nozzle can supply an appreciable amount of damping, no damping can be expected from it in

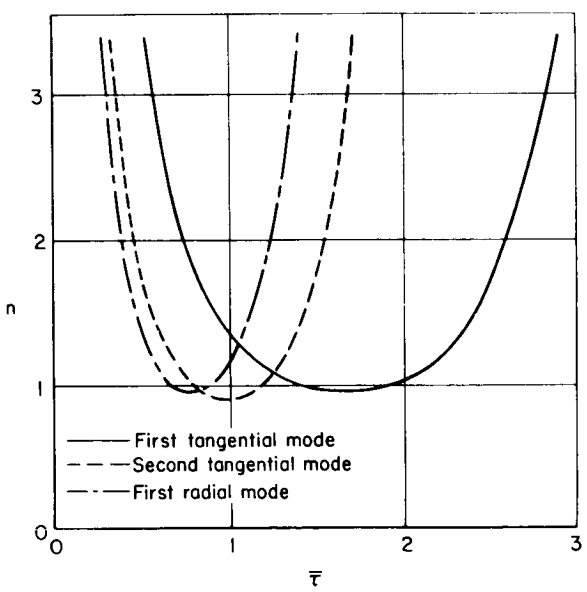

FIGURE 4.2.2g.—Theoretical stability limits for the three lowest-order transverse modes. Uniform injection; $\bar{u}_e=0.10$.

the purely transverse case. Fortunately, the first two terms of G_R contribute strong damping effects. These terms can be traced back to the original equations to determine the physical nature of these effects. The first term comes from the necessity of supplying extra "pumping work" when the gases are produced at a pressure different from the steady pressure. The second term is due to the necessity of supplying to the gas produced the proper transverse momentum. These two effects, in the absence of artificial means of damping, are the major sources of damping in transverse modes.

The effects of several design parameters are shown by the stability limit curves of Fig. 4.2.2h.[190] It can be seen that increasing the chamber Mach number and concentrating the combustion near the injector face are both destabilizing. However, whereas increasing the Mach number shifts the instability zone to larger τ, concentrating the combustion has a small effect in the opposite direction. The effect of chamber length is dependent on both the chamber Mach number and the axial distribution of combustion. As shown in Fig. 4.2.2h(b), increasing the length is stabilizing for low Mach number but is destabilizing for high Mach number, when the combustion is spread axially. Zinn[769] has obtained the same results for combustion concentrated at the injector except that the magnitude of the length effect is much reduced for the case of concentrated combustion. In Ref. 7 it is shown that either spreading the combustion or moving a concentrated front away from the injector is stabilizing, with the effect being larger for shorter chambers.

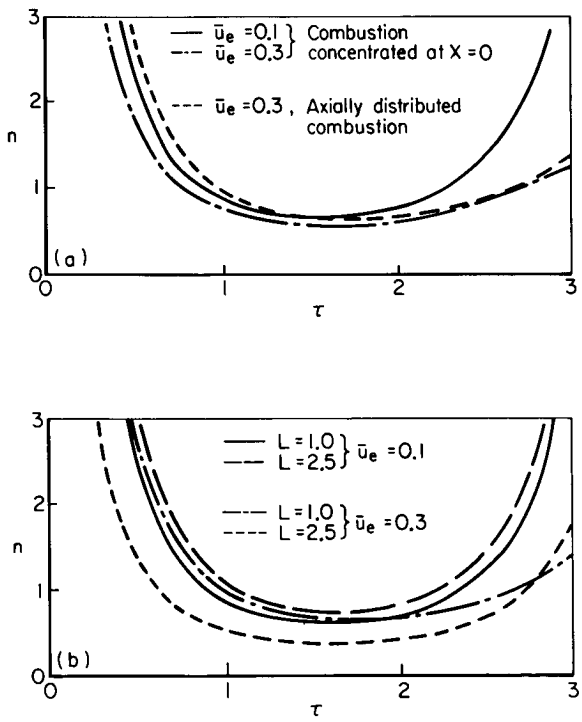

(a) Effects of chamber Mach number and axial combustion distribution. L = 1.

(b) Effects of chamber length. Combustion spread axially.

FIGURE 4.2.2h.—Parametric studies of first tangential mode stability limits.

Up to this point, the propellant injection distribution has been assumed to be practically uniform. However, sometimes it is not feasible or, possibly, not desirable to design for uniform injection. In such cases, the injection density $\mu^\circ = \rho_{Li}{}^\circ u_{Li}$ is an assigned function of r and θ.† The mean injection density $\mu^\circ{}_m$ can be obtained from

$$\mu^\circ{}_m = \frac{1}{\pi}\int_0^1\int_0^{2\pi} \mu^\circ(r,\theta)\,r\,dr\,d\theta$$

and, assuming the combustion density to coincide with the injection density, the combustion response perturbation can be obtained by multiplying Eq. (4.2.2–10) or (–10a) by $\mu^\circ/\mu^\circ{}_m$. Then even in the absence of displacement sensitivity it is necessary to expand M_1 in a series of eigenfunctions. For pure pressure sensitivity the stability boundary is still described by Eq. (4.2.2–23) with G_R given by

$$G_R = \frac{1}{A_{\nu\eta}}\left[1 + \frac{1}{\gamma} - \frac{\varepsilon_r}{\gamma\bar{u}_e} + \frac{k}{\gamma\bar{u}_e}\int_0^L \rho_L{}^\circ dx\right]$$

where

$$A_{\nu\eta} = \frac{\int_0^1\int_0^{2\pi} \mu^\circ p_0 p_0{}^* r\,dr\,d\theta}{\mu^\circ{}_m \int_0^1\int_0^{2\pi} p_0 p_0{}^* r\,dr\,d\theta} \qquad (4.2.2\text{–}30)$$

with the asterisk denoting the complex conjugate.

† This is, of course, inconsistent with the assumption of one-dimensional steady flow, but an inconsistency that must be accepted in view of the difficulties involved in a three-dimensional steady-state analysis.

Fig. 4.2.2i shows the values of $A_{\nu\eta}$ for the first three transverse modes, calculated for the extreme case of combustion concentrated on a single circle of radius r_i.

When displacement sensitivity is present in addition to the pressure sensitivity, it is convenient to define mean values of the displacement interaction indices by

$$\tilde{m}_r = \frac{\int_0^1 \int_0^{2\pi} \mu^\circ m_r \delta_{r0} p_0^* r dr d\theta}{\mu^\circ_m \int_0^1 \int_0^{2\pi} p_0 p_0^* r dr d\theta} \quad (4.2.2\text{–}31)$$

$$\tilde{m}_\theta = \frac{\int_0^1 \int_0^{2\pi} \mu^\circ m_\theta \delta_{\theta 0} p_0^* r dr d\theta}{\mu^\circ_m \int_0^1 \int_0^{2\pi} p_0 p_0^* r dr d\theta}$$

where the zeroth order displacement components are given by

$$\delta_{r0} = \frac{v_0}{s_0} = -\frac{P_{00}}{\gamma s_{\nu\eta}^2} \frac{d\Psi_{\nu\eta}}{dr} \Theta_\nu \quad (4.2.2\text{–}32)$$

$$\delta_{\theta 0} = \frac{w_0}{s_0} = -\frac{P_{00}}{\gamma s_{\nu\eta}^2} \frac{\Psi_{\nu\eta}}{r} \frac{d\Theta_\nu}{d\theta}$$

The stability boundary condition is expressed by

$$\mathcal{R}e[(nA_{\nu\eta} + \tilde{m}_r + \tilde{m}_\theta)(1 - \exp[-s_0\bar{\tau}])] = G_R \quad (4.2.2\text{–}33)$$

and G_R is given by Eq. (4.2.2–29). If the displacement response of the combustion process is assumed to be instantaneous, rather than with the same time lag as the pressure response, the stability boundary equation becomes

$$\mathcal{R}e[A_{\nu\eta}\mathcal{P} + \tilde{m}_r + \tilde{m}_\theta] = G_R \quad (4.2.2\text{–}33a)$$

If the displacement indices m_r and m_θ are the same for all injector sprays, the mean values $\tilde{m}_r$, $\tilde{m}_\theta$ can be written in the form

$$\tilde{m}_r = m_r B_{\nu\eta} \quad (4.2.2\text{–}31a)$$

$$\tilde{m}_\theta = m_\theta C_{\nu\eta}$$

where $B_{\nu\eta}$ and $C_{\nu\eta}$ are eigenfunction expansion coefficients (similar to $A_{\nu\eta}$) for the combustion response to radial and tangential gas displacements—Eq. (4.2.2–33) then becomes

$$\mathcal{R}e[(nA_{\nu\eta} + m_r B_{\nu\eta} + m_\theta C_{\nu\eta})(1 - \exp[-s_0\bar{\tau}])] = G_r \quad (4.2.2\text{–}33b)$$

Eq. (4.2.2–33b) can be also written in terms of the velocity indices l_r and l_θ,[582, 187] where

$$l_r = \frac{m_r}{i\omega_0}$$

$$l_\theta = \frac{m_\theta}{i\omega_0}$$

From Fig. 4.2.2i it can be seen that the tangential modes are especially sensitive to combustion at radii greater than about $\frac{2}{3}$ of the chamber radius, whereas radial modes are most sensitive to combustion near the center of the chamber.

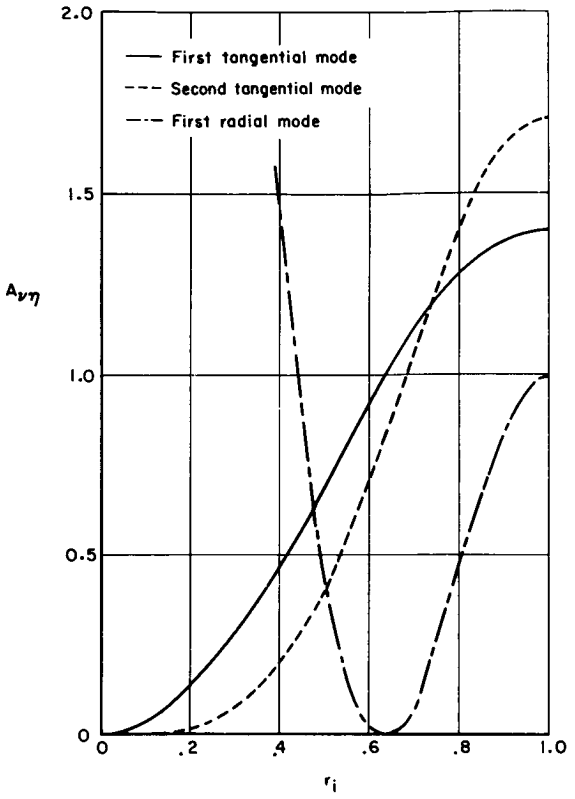

FIGURE 4.2.2i.—Injection distribution coefficient $A_{\nu\eta}$ for pressure sensitivity. Injection concentrated on a single circle of radius r_i.

Thus, if both radial and tangential modes are likely, the stability of an engine will be enhanced by varying the injection density across the injector face such that the largest value occurs at a radius about half that of the chamber. The practical application of this principle was successfully demonstrated on the GEMSIP program[11] and is the design basis for the injector of the LM descent engine (see Sect. 7.4.5).

The linear transverse-mode theory has been verified by several experiments. At Princeton University, a variable-angle sector chamber was used to measure stability limits of tangential modes.[582,187] The test results showed the expected close similarity to the longitudinal mode (variable length, Fig. 4.2.2b) results. A typical example of the transverse stability limits is given in Fig. 4.2.2j, for injection concentrated near the outer periphery of the chamber. Testing with the same injector pattern, but with the injection near the half-radius, resulted in complete stability over the entire range of mixture ratio and sector angle.[582] In addition, values of n and τ obtained from the experimental results of Fig. 4.2.2j were found to be in excellent agreement with corresponding values obtained from longitudinal mode testing.[187]

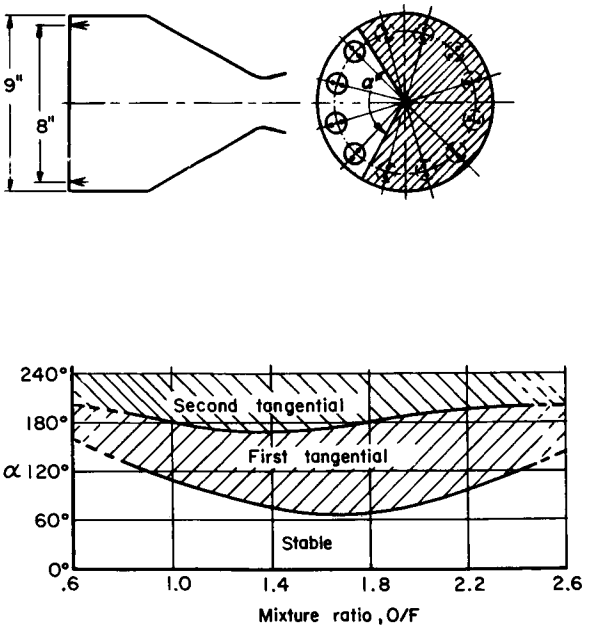

FIGURE 4.2.2j.—Experimental stability limits for tangential modes obtained with Princeton variable-angle sector chamber, unlike-doublet injector, 150-psia chamber pressure, and LOX/ethanol propellants.

Transverse testing in the same program also indicated the strong spin direction preference of certain injector patterns. This is illustrated in Fig. 4.2.2k, where a pulse gun directed opposite to the preferred spin direction causes only a momentary spinning wave before the wave reverses to the preferred direction. The mechanism for such preferences is the velocity/displacement effect and is described in Sect. 3.3.2.2.

An experimental program conducted at Aerojet-General encountered combined longitudinal-transverse modes.[7] The extension of the transverse-mode theory to cover the combined longitudinal-transverse modes is straightforward, although care must be taken in the order-of-magnitude analysis required by the series solution method (Sect. 4.2.2.2). The excellent agreement between theory and experiment obtained on this program is illustrated in Fig. 4.2.2l.* The theoretical stability limit curves for modes which were unstable, either spontaneously or as a result of a tangential pulse (Sect. 10.3) are shown by a solid line, whereas a dashed line is used to show the theoretical stability limits for modes that were not found to be unstable. Velocity or displacement effects were not considered in the calculation of these limit curves. In agreement with the results for purely transverse modes (Fig. 4.2.2h), increasing the chamber Mach number was destabilizing, especially for the higher-order modes. The incidence of higher-order modes at the larger Mach number indicates an interaction between the combustion dynamic response and the mean flow in the chamber. It should be noted that the linear theory is quite useful in guiding and interpreting the results of pulse tests as well as linear stability limits tests.

4.2.3 Nonlinear Theory

The theoretical treatment described in the preceding Section 4.2.2 is based on the assumption of infinitesimal perturbations. In that case it is meaningless to speak of the actual perturbation amplitude, since the amplitude is either undefined (for neutral oscillations) or grows to infinity (in the unstable case). Of course, this infinite growth

* A range of operating conditions was used to obtain these data and hence τ varied over a range of values.

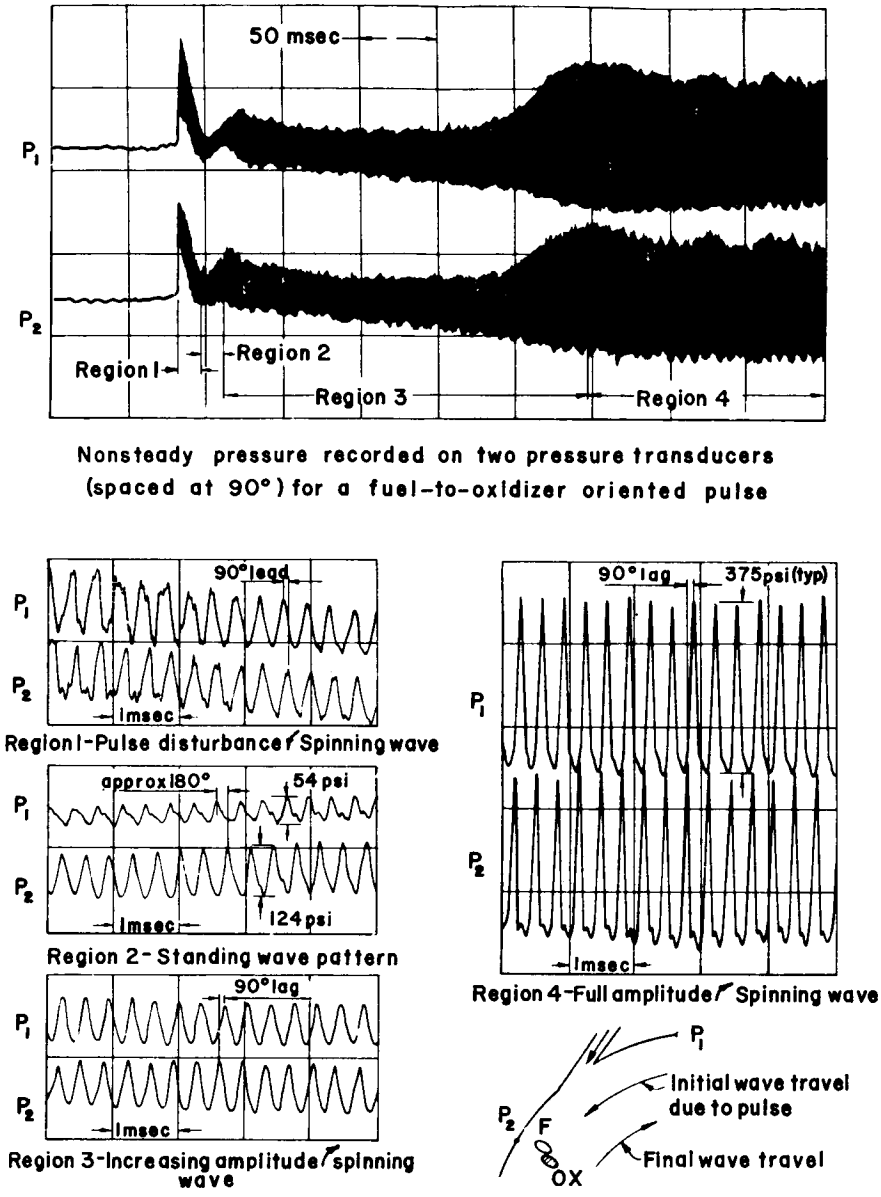

FIGURE 4.2.2k.—Preferred spin direction for one injector design.

is fictitious, since it violates the initial assumption that has allowed the equations to be linearized. In reality, as soon as the amplitude grows beyond a certain level nonlinear effects become important. Eventually they dominate the whole process. For example, for linear instability, that is, oscillations growing from infinitesimal perturbations, nonlinear effects prevent the indefinite growth and determine some kind of limiting cycle with finite amplitude, the magnitude of which is related to the nonlinear effects. Or, for linearly stable operation, there may be an inversion of the balance between energy feedback and damping when a certain amplitude level is reached, again as a result of nonlinearities. Perturbations below that level are damped, in agreement with the linear behavior, whereas perturbations above that level are amplified, eventually reaching a limiting

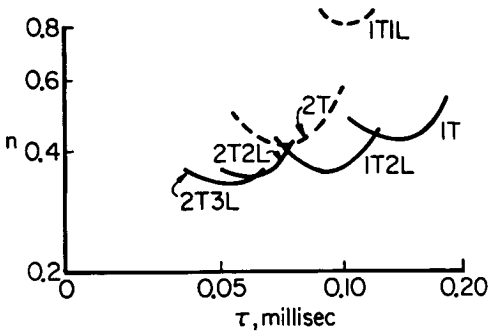

Mode	Incidence, % of tests	
	Spontaneous	Spont.+ pulsed
IT	20	40
1TIL	0	0
1T2L	20	60
2T	0	0
2T2L	20	60
2T3L	20	20

a) $A_c/A_t = 4.2$; $\bar{u}_e = 0.14$

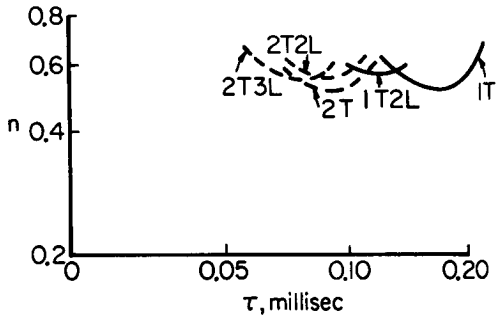

Mode	Incidence, % of tests	
	Spontaneous	Spont.+ pulsed
IT	0	27
1TIL	0	0
1T2L	0	13
2T	0	0
2T2L	0	0
2T3L	0	0

b) $A_c/A_t = 46.6$; $\bar{u}_e = 0.01$

FIGURE 4.2.21.—Experimental and theoretical results for tangential and tangential-longitudinal modes. Propellants, O_2/H_2; coaxial-element injection; chamber pressure, 1000 to 2500 psia; chamber diameter, 14 in.; chamber length, 24 in.

cycle of larger amplitude. The latter example is characteristic of nonlinear instability, also called triggered or pulsed instability.

Nonlinearities in the oscillatory operation of liquid propellant rockets derive from two sources. First, the combustion processes themselves may present important nonlinear effects. This is especially true of the displacement-sensitive processes, as mentioned in Sect. 4.2.1.1. Second, independently of the behavior of the combustion processes, the wave motion is characterized by the well known nonlinear effects of steepening and dispersion, culminating in the appearance of shock waves. These two sources of nonlinearity are discussed separately in the following sections.

The following nomenclature pertains to Sect. 4.2.3 (see also Sects. 4.1.2, 4.2.1, and 4.2.2):

F_p, F_r, F_θ	Nonlinear combustion response functions
f_p, f_r, f_θ	Describing functions used to linearize nonlinear combustion response functions
g_r, g_s	First order perturbation shape functions
$\tilde{g}$	Wave amplitude
Δg	Shock amplitude
K, K_0, K_1	Constants in periodic wave condition
y	Peripheral distance
$\alpha = t - y$	Independent variable in annular chamber analysis
δ	Displacement of nonlinear stability

limit from linear stability limit on n, τ plane

ϵ Dimensionless amplitude parameter

4.2.3.1 *Nonlinear combustion response.*—For this discussion, it will be supposed that the only nonlinearity is that associated with the combustion response. Aside from the obvious analytical simplification, this case has some practical significance, as shown by numerical calculations of combustion instability (see Sects. 4.3 and 6.4). To insert a nonlinear combustion response into the framework of the linear theory, some method of equivalent linearization must be used. The approach chosen by Reardon[11,650] makes use of the well-established describing function method of nonlinear mechanics.[138]

If the perturbation of the rate function appearing in Eq. (4.2.1–1) is taken as

$$\Re e\left[\frac{\tilde{f}-\bar{f}}{\bar{f}}\right]=nF_p+m_rF_r+m_\theta F_\theta \qquad (4.2.3\text{–}1)$$

where F_p, F_r, and F_θ are nonlinear functions of the perturbations of pressure, radial displacement, and tangential displacement, respectively, it is found that only those Fourier components of F_p, F_r, and F_θ that oscillate at the same frequency and in phase with the argument affect the stability. As a result, the following equation is obtained for the "effective" part of the burning rate perturbation M_1:

$$M_{1\text{eff}}=\bar{M}_1(\mathcal{P}f_pp_0+\mathcal{F}_r\delta_{r0}+\mathcal{F}_\theta\delta_\theta) \qquad (4.2.3\text{–}2)$$

where the describing functions f_p, f_r, and f_θ are defined by

$$f_p=\frac{\omega_0}{\pi p_0p_0^*}\int_0^{2\pi/\omega_0}F_p[\Re e(p_0e^{s_0t})]\cdot\Re e(p_0\exp[s_0t])dt$$

$$f_r=\frac{\omega_0}{\pi\delta_{r0}\delta_{r0}^*}\int_0^{2\pi/\omega_0}F_r[\Re e(\delta_{r0}e^{s_0t})]\cdot\Re e(\delta_{r0}\exp[s_0t])dt \qquad (4.2.3\text{–}3)$$

$$f_\theta=\frac{\omega_0}{\pi\delta_{\theta0}\delta_{\theta0}^*}\int_0^{2\pi/\omega}F_\theta[\Re e(\delta_{\theta0}e^{s_0t})]\cdot\Re e(\delta_{\theta0}\exp[s_0t])dt$$

It can be seen that the describing functions reduce to unity when F_p, F_r, and F_θ coincide with their arguments. The stability boundary is given by Eq. (4.2.2–33) or (–33a), as before, but with the describing functions introduced into the integrands of the numerators of Eq. (4.2.2–30) and (–31), e.g., for the nonlinear case, $A_{\nu\eta}$ is given by

$$A_{\nu\eta}=\frac{\int_0^1\int_0^{2\pi}\mu^\circ f_pp_0p_0^*rdrd\theta}{\mu^\circ_m\int_0^1\int_0^{2\pi}p_0p_0^*rdrd\theta} \qquad (4.2.2\text{–}30a)$$

rather than Eq. (4.2.2–30).

Because of the nonlinear functions F_p, F_r, and F_θ the coefficients $A_{\nu\eta}$, $\tilde{m}_r$, and $\tilde{m}_\theta$ depend on the actual amplitude of the perturbations. Therefore, the stability boundary will be obtained from Eq. (4.2.2–33) or Eq. (4.2.2–33a) as a function of perturbation amplitude. For example, stability limits are shown in Fig. 4.2.3a for a deadband type of nonlinear combustion response to a tangential displacement (the pressure sensitivity is assumed linear, and radial displacement effects are neglected). The unstable operating region above the stability boundary is seen to enlarge as the amplitude is increased, leading to the possibility of nonlinear triggering as a direct result of the combustion response nonlinearity.

It should be observed that any nonlinear function F(x) can be split into a symmetric part, for which $F_s(x)=F_s(-x)$, and an antisymmetric part, for which $F_a(x)=-F_a(-x)$. The symmetric part does not contribute to the value of the corresponding describing function. However, it does produce a variation of the mean burning rate with respect to the steady burning rate, and hence a shift of the mean chamber pressure. Therefore, this approach to nonlinear instability analysis should be used only for combustion response functions with a relatively small symmetric part. Such mechanisms as nonlinear vaporization (relative velocity effect), and liquid jet or droplet shattering cannot be treated by this method, whereas the temperature dependence of chemical reaction rates and the enhanced mixing due to vapor displacement are amenable to analysis by the describing function method. Finally, it should be observed that the formulation given here ignores the effects of interactions

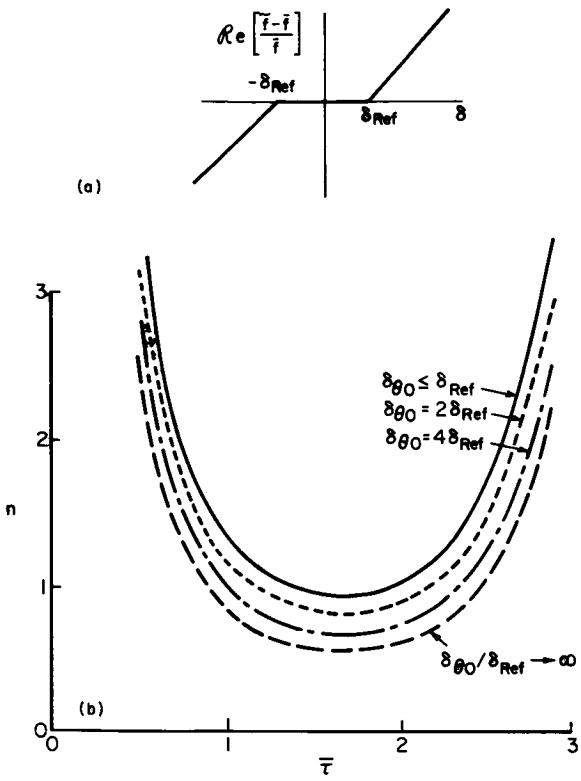

(a) Combustion response function.
(b) Stability limits on n,τ diagram.

FIGURE 4.2.3a.—Stability limits for deadband combustion response to tangential displacement. First tangential mode; $m_\theta = n$; $m_r = 0$.

between different sensitivities. Although in the linear case this procedure is always correct, in the nonlinear case such interactions are possible, and may be quite significant.

4.2.3.2 *Nonlinear wave motion.*—The treatment of the nonlinear effects originating from the wave process itself is by its very nature more complicated. In this case it is definitely wrong to start with the assumption of infinitesimal perturbations, and one must actually establish a scale to which the amplitudes can be referred. Also, it is wrong to prescribe the form of the time dependence of the perturbations, since their various Fourier components may interact.

Concerning the scale for the perturbations, it is evident that this scale should be related to the injection density such that the amplitudes increase with the amount of combustion energy available. With the sensitive time lag model, the proper scale is found to be proportional to the injection density, although with other models the choice may be different. Thus the perturbations can be expressed as

$$p' = \mu^\circ p_1 + \mu^{\circ 2} p_2 + \cdots$$

$$\mathbf{V}' = \mu^\circ \mathbf{V}_1 + \mu^{\circ 2} \mathbf{V}_2 + \cdots$$

where the primed quantities now represent the entire perturbations rather than just their amplitudes, and $\mu^\circ = \rho_{Li} u_{Li}$ is the injection density.

The steady-state quantities must also be expanded in powers of μ°. Making use of Eq. (4.2.1–11) through (–15), and taking ρ_{Li} to be of $\mathcal{O}(1)$, as before, this procedure gives

$$\bar{u} = \mu^\circ \bar{u}_1 + \mu^{\circ 2} \bar{u}_2 + \cdots$$

$$\bar{u}_L = \mu^\circ \bar{u}_{L1} + \mu^{\circ 2} \bar{u}_{L2} + \cdots$$

$$\bar{\rho} = 1 + \mu^{\circ 2} \bar{\rho}_2 + \cdots$$

$$\bar{p} = 1 + \mu^2 \bar{p}_2 + \cdots$$

$$\bar{\sigma} = \mu^2 \bar{\sigma}_2 + \cdots$$

In these expansions all the coefficients are of $\mathcal{O}(1)$ and do not depend on μ°. If the combustion is well spread along the length of the chamber, $d\bar{u}/dx$ is of $\mathcal{O}(\mu^\circ)$, hence,

$$\bar{M} = \mu^\circ \bar{M}_1 + \cdots$$

with $\bar{M}_1 = d\bar{u}_1/dx$.

The case of pure pressure sensitivity will be considered here, to show the method of solution and typical results. From Eq. (4.2.1–4), the burning rate perturbation is obtained in the form

$$M' = \mu^{\circ 2} M_2 + \cdots$$

with

$$M_2 = \bar{M}_1 n[p_1(t) - p_1(t - \bar{\tau})] \quad (4.2.3\text{–}4)$$

The derivation of the nozzle admittance equation discussed in Sect. 3.6 is subject to severe limitations that make it inapplicable to the case in which shock waves are present. This difficulty can be circumvented by choosing a special nozzle geometry, consisting of many orifices.[197] If a large number of very small, individual nozzles are distributed uniformly at the exhaust end of the chamber, the oscillatory behavior can be approximated in all cases by quasi-steady flow.[179] In this case, the nozzle condition gives

$$u_1=0; \qquad u_2=\frac{\gamma-1}{2\gamma}p_1+\tfrac{1}{2}\sigma_1$$

as the boundary conditions at $x=L$, both for longitudinal and for transverse oscillations.

To simplify the discussion, the effect of the droplet drag will be neglected in the present analysis. That is, the coefficient $k=0$ and $u_L=u_{Li}$ everywhere, so that $u_{L_1}=u_{Li}/\mu^\circ$ is constant.

The expansions in powers of μ° given above for the steady-state and perturbation quantities are substituted into the conservation equations. Then the equations corresponding to each power of μ° can be satisfied separately. The first-order equations show that $\sigma_1=0$, so that $p_1=\gamma\rho_1$, and that the first-order perturbations satisfy the partial differential wave equations

$$\frac{\partial}{\partial t}\left(\frac{p_1}{\gamma}\right)+\nabla\cdot\mathbf{V}_1=0 \qquad (4.2.3\text{–}5)$$

$$\frac{\partial}{\partial t}(\mathbf{V}_1)+\nabla\left(\frac{p_1}{\gamma}\right)=0$$

The general solution of Eq. (4.2.3–5) is known for the longitudinal modes, viz.,

$$u_1=g_r(t-x)-g_s(t+x)$$

$$v_1=w_1=0$$

$$\frac{p_1}{\gamma}=g_r(t-x)+g_s(t+x)$$

where g_r and g_s are arbitrary functions of their arguments. The solution is also known for the purely transverse case in a thin annular chamber:

$$u_1=v_1=0$$

$$w_1=g_r(t-y)-g_s(t+y)$$

$$\frac{p_1}{\gamma}=g_r(t-y)+g_s(t+y)$$

where y is the peripheral variable. In this case it is clear that g_r and g_s must be periodic, of period unity if the reference length is chosen to be the wave length. In the fundamental mode, this length would be the periphery of the annulus. In the longitudinal case the functions g_r and g_s must be periodic also if it is required that the oscillation be periodic. Considering separately the two transverse waves spinning in opposite directions, the first-order solution may be taken as

$$u_1=v_1=0$$

$$w_1=p_1/\gamma=\rho_1=g(\alpha) \qquad (4.2.3\text{–}6)$$

$$\alpha=t-y$$

Introducing Eq. (4.2.3–6), with $g(\alpha)$ arbitrary, into the second-order equations, which are of the same form as Eq. (4.2.3–5), but with terms on the R.H.S that involve the first-order solution, the result is obtained that p_2, $\mathbf{V}_2, \ldots$, are not periodic in general. Indeed, the second-order solution is periodic only when a certain balance of terms takes place, which can be expressed by the following equation:*

$$L(\gamma+1)(g-K)\frac{dg}{d\alpha}$$

$$=\left(\gamma+1+\frac{\gamma-1}{2}\right)g-\int_0^L M_2dx \qquad (4.2.3\text{–}7)$$

Substituting for M_2 from Eq. (4.2.3–4), and noting that

$$\int_0^L \bar{M}_1dx=\bar{u}_1(L)-\bar{u}_1(0)=1$$

Eq. (4.2.3–7) becomes

$$(\gamma+1)Lg\frac{dg}{d\alpha}-(\gamma+1)LK\frac{dg}{d\alpha}$$

$$=\left(\gamma+1+\frac{\gamma-1}{2}\right)g(\alpha)-\gamma n[g(\alpha)-g(\alpha-\bar{\tau})]$$

$$(4.2.3\text{–}8)$$

The constant K is related to the first-order perturbation of the frequency (the zeroth-order value is unity). In the case that a shock exists, K must coincide with the mean value of g at the shock, that is, taking the shock location as $\alpha=0, 1, 2, \ldots$,

$$K=g_m=\tfrac{1}{2}[g(0)+g(1)]$$

Hence, the balance condition, Eq. (4.2.3–8), contains only g as a dependent variable. Any solution of this equation represents the wave

* The details of the derivation are given in Ref. 177 and Appendix I of Ref. 650. The analysis makes use of the method of coordinate stretching, which is quite helpful in the solution of nonlinear partial differential equations[451,706].

shape of a possible periodic oscillation. Any other wave shape is subject to distortions. In the first-order solution, Eq. (4.2.3–6), the shock position is independent of x and so the shock is planar. However, to second order the shock is curved; its shape can also be obtained from the second-order solution.[177]

The physical interpretation of the various terms of Eq. (4.2.3–8) is instructive. On the L.H.S., the first term represents the effect of the nonlinear wave shape and the second term the effect of the frequency shift. On the R.H.S., the first term, γg, corresponds to the perturbation of the pumping work that the gases have to do against the prevailing pressure at the act of generation. The second term, g, represents the work required to produce the transverse momentum of the generated gases. The third term, $\frac{1}{2}(\gamma-1)g$, corresponds to the perturbation of the work spent in pushing the gases through the nozzle. These three terms are of the same sign; they are damping terms and cannot sustain instability. Therefore, instability must come from the remaining term, which must provide the combustion energy feedback necessary to balance the damping terms.

Shockless solutions of Eq. (4.2.3–8) can be obtained[650] by introducing the expansions

$$g=\epsilon g_1+\epsilon^2 g_2+\cdots$$

$$n=n_0+\epsilon n_1+\cdots$$

$$K=K_0+\epsilon K_1+\cdots$$

in terms of an amplitude parameter ϵ that is independent of $\dot{\mu}$. The resulting first-order equation is linear, and is satisfied by

$$g_1=\sin 2\pi\alpha$$

for the zeroth-order values of n and K given by

$$n_0=\frac{3\gamma+1}{2\gamma(1-\cos 2\pi\bar{\tau})}$$

$$K_0=\frac{3\gamma+1}{4\pi L(\gamma+1)\tan \pi\bar{\tau}}$$

For $\epsilon=0$, $n=n_0(\bar{\tau})$. This result represents the linear stability limit, and can be obtained directly from the equations of Sec. 4.2.2.4 for $k=0$, $\mu=\bar{u}_e$, $\mathcal{E}_r=-\frac{1}{2}(\gamma-1)\bar{u}_e$. For higher-order solutions, it is found that solutions with finite ϵ exist only for $n>n_0$ if $\frac{1}{3}<\tau<\frac{2}{3}$ and for $n<n_0$ outside of that τ-range. This ϵ-expansion method is used in References 645 and 143 to determine solutions of the longitudinal-wave problem, but without the assumption of small $\bar{u}_e$ and u_{Li}. The results are more complicated, but are in substantial agreement with the results obtained for transverse modes by the combined $\dot{\mu}^\circ$- and ϵ-expansion approach.[488,489,194]

If there is a shock, Eq. (4.2.3–8) must, in general, be solved numerically.[488] Typical results are shown in Fig. 4.2.3b and the shock amplitude Δg and wave amplitude $\tilde{g}$ are illustrated in Sketch (c) of Fig. 4.2.3b. The solid line representing $n_0(\bar{\tau})$ is symmetric with respect to $\bar{\tau}=0.5$, where n_0 is minimum. At this value of $\bar{\tau}$ any $n>n_0$ provides a shock-type solution. The behavior of the shock amplitude Δg and the wave amplitude $\tilde{g}$ with respect to the distance $\delta=n-n_0$ from the $n_0(\bar{\tau})$ curve is qualitatively shown in an expanded scale by Sketch (a) of Fig. 4.2.3b. In the range $\frac{1}{3}<\bar{\tau}<\frac{2}{3}$, the typical behavior of the solutions with the normal distance δ is expanded in Sketch (b) of Fig. 4.2.3b. In this region, the shock amplitude Δg goes to zero for some finite δ_s, at which $\tilde{g}$ is still finite. For $\delta<\delta_s$, the oscillations are shockless and coincide with the shockless waves discussed above. Finally, when $\bar{\tau}<\frac{1}{3}$ or $\bar{\tau}>\frac{2}{3}$, the solutions behave as shown in Sketch (c). As $\delta\to 0$ from above (i.e., within the linearly unstable region), the shock and wave amplitudes tend to finite values, so that solutions exist also for $\delta<0$, that is, in the linearly stable region, down to a certain negative δ_{min}. Between δ_{min} and a certain (negative) δ_s two shock-type solutions are obtained. For $\delta_s<\delta<0$, one shock-type and one shockless solution exist, the latter coinciding with the shockless solution discussed previously. This result can be interpreted, by extension of the studies of Ref. 645, or by direct investigation, or by topological considerations, as follows. Only the upper branches of the curves of Sketch (c) of Fig. 4.2.3b provide mathematically stable and physically possible periodic solutions, in the sense that any distortion from the corresponding wave shape tends to die out with time. The lower branches are mathematically unstable, and cannot correspond to a physically possible periodic solutions. However, the lower branches do provide

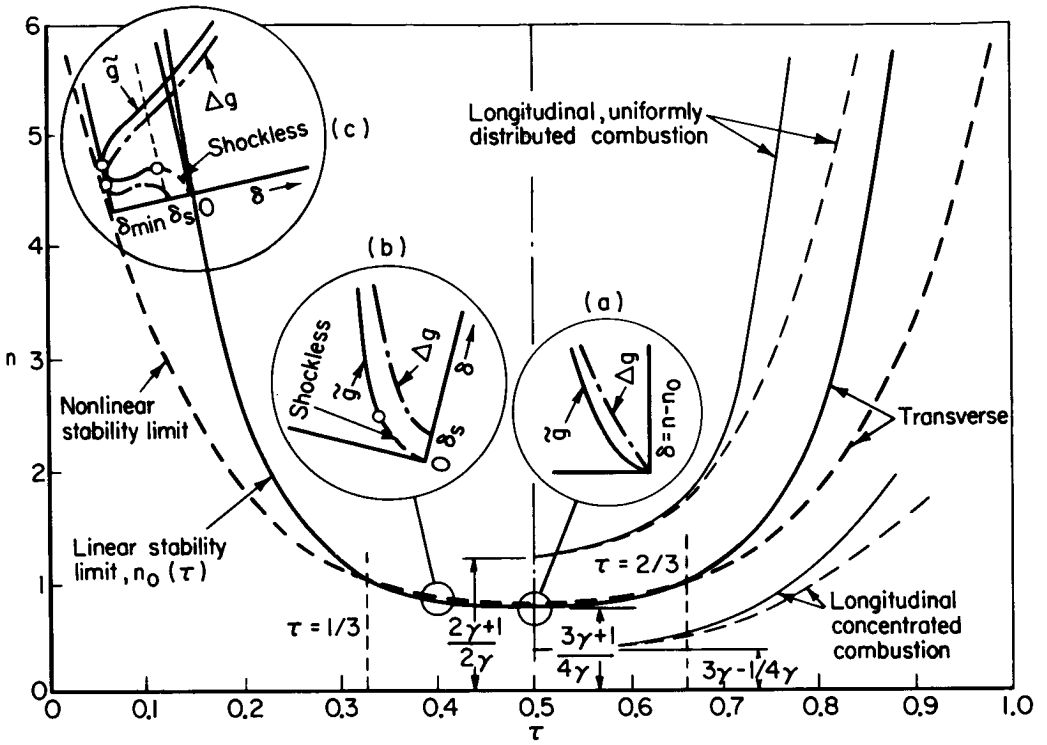

FIGURE 4.2.3b.—Stability limits and behavior of solutions for nonlinear wave motion.

a "triggering limit" for the perturbation amplitude. That is, below this limit the perturbation decays, whereas above the limit the perturbation is amplified, and tends with time to the solutions of the upper branch. This behavior is, of course, only possible for the region above the dashed line of Fig. 4.2.3b, which can appropriately be called the nonlinear stability limit.

The preceding discussion of the behavior of transverse oscillations applies also to longitudinal oscillations, for which an equation similar to Eq. (4.2.3–8) can be derived.[630,769] On the right side of Fig. 4.2.3b are plotted the linear and nonlinear stability limits for two limiting cases of longitudinal-mode oscillations: (1) the case of combustion concentrated within a very short distance of the injector, and (2) the case of combustion distributed uniformly along the length of the chamber. The similarity of the longitudinal and transverse cases is apparent from this illustration.

A final observation is useful. Since Eq. (4.2.3–4) is linear in p_1, the effects of the combustion response nonlinearity are excluded. This is the reason that although a nonlinear instability region exists within the linearly stable region of Fig. 4.2.3b, it does not extend over the whole range of $\bar{\tau}$, for example by decreasing the minimum value of n for which instability can be produced. If the nonlinear combustion response were included in the treatment along with the wave motion nonlinearity, the two effects would reinforce each other, resulting in a nonlinear stability limit $n_{NL} < n_0$ for all values of $\bar{\tau}$.

4.3 NUMERICAL INTEGRATION METHODS*

Other sections of this chapter show how stability limits and wave characteristics of pressure oscillations in combustion chambers can be determined analytically. Such approaches have to make some assumptions to obtain a solution, e.g., (1) small-amplitude oscillations (except for some of the nonlinear theories), (2) single-frequency sinusoidal oscillations, (3) burning rate linearly proportional to pressure and/or

* R. J. Priem, Author.

velocity. These assumptions are not always consistent with observed instability phenomena. That is, finite disturbances are often required to excite instability; waves are usually steep-fronted; and the burning rate is inherently nonlinear. This section describes a technique for determining stability characteristics without the assumptions stated above. It should not be inferred that the technique presented in this section gives the complete answer, since other non-realistic assumptions are made to obtain solutions. Rather, the numerical integration method should be considered to be complementary to the others, each providing information that cannot be obtained by another approach because of basic assumptions and limitations.

The following nomenclature pertains to Sect. 4.3:

$\mathfrak{B}$	Pre-exponential factor in Arrhenius rate expression
C	Instantaneous concentration of vaporized but unreacted propellants
E_{act}	Activation energy
F	Drag force per unit volume exerted on gas by liquid
$\mathfrak{J}$	Viscous dissipation parameter
$\mathfrak{L}$	Burning rate parameter
M_x	Fractional burning rate per unit length
$\mathfrak{M}$	Dimensionless mass accumulation parameter, $\frac{m_{acc}(t)}{\bar{m}_{acc}}$
m_a	Mass injected but not atomized
m_L	Mass of liquid drop
m_v	Mass atomized but not vaporized
m_{acc}	Mass accumulated prior to either atomization or vaporization
n	Order of chemical reaction
Δp	Instantaneous difference between maximum and minimum pressures in chamber
t_b	Breakup time of liquid jet or drop
θ_j	Angular calculation location for numerical integration
$\langle\ \rangle$	Average value (of quantity enclosed)

4.3.1 Basic Concepts*

The numerical integration approach to combustion instability originated from the attempt to describe the unsteady combustion process by the equations presented in Chapter 3, retaining the nonlinear relationships. These combustion process equations define the mass, momentum, and energy sources included in the conservation equations discussed in Sect. 4.1. The source terms are coupled to the conservation equations, since the combustion rates are dependent on gas velocities, pressure, density, etc., specified by the conservation equations. Therefore, simultaneous solution of all equations is required. Because of the complexity of the equations the only practical method of solution appears to be numerical integration.

A numerical solution begins with specified conditions at some starting time. These initial conditions are usually assumed to correspond to the steady-state solution. Having specified all properties at numerous positions in the combustor at this initial time, the governing equations, in difference form, are integrated at each position to determine time histories. The accuracy of the solution depends on the number of positions selected in the chamber at which histories are obtained. If the combustor is spontaneously unstable, any deviation from the exact steady-state solution of the equations will result in oscillations that grow to a finite amplitude. If the combustor is not spontaneously unstable, a finite-amplitude disturbance may excite instability. By introducing disturbances at the initial conditions it is possible to determine whether the combustor can be driven unstable by a finite disturbance.

4.3.1.1 *Approach and assumptions.*—In principle, it is possible to follow the complete time history of an engine firing, including starting, full-thrust operation, throttling, and shut-down, to determine conditions at all positions in the engine. At present this procedure is impossible because of the excessive computer size and time required to perform the calculations. Although it is possible to follow the complete buildup of an oscillation and to determine the equilibrium amplitude and wave shape, it is difficult and time consuming.[131] Therefore, it has generally been assumed that if a disturbance initially grows in amplitude, the system is unstable; whereas if a disturbance initially decays, the system is stable to

* R. J. Priem, Author, and D. T. Campbell, Contributor.

this disturbance. These assumptions save considerable computing time, since only a few periods of oscillation must be computed. However, this assumed rule of stability is not always valid. Engines have demonstrated oscillations that grow for a short time and then decay; others first decay and then become very large (see Chapter 10).

The magnitude of the problem of obtaining a numerical solution for instability can be illustrated by use of Tables 4.3.1a, b, and c.[276] The number of subdivisions in each space dimension determines the amount of detail in the solution. Using 10 subdivisions gives only a sketchy picture of the oscillations. An adequate solution can be obtained with 100 subdivisions, but 1000 are required to describe clearly a steep-fronted wave. Present-day computers have internal storage capacities of the order of 10^5. It can be seen from Table 4.3.1a that detailed two-dimensional solutions and other than rough three-dimensional solutions cannot be accomplished without auxiliary storage. The times required to compute 100 steps listed in Table 4.3.1b are based on an IBM 709 class computer. It is clear that the computing time increases rapidly as the number of dimensions or subdivisions is increased. Perhaps a more meaningful time for combustion instability studies is the time required to compute one period of oscillation. For numerical stability, the number of time steps for one period is related to the number of space subdivisions. Hence, the information in Table 4.3.1b can be used to generate Table 4.3.1c, which shows that a three-dimensional analysis with adequate detail would be extremely costly and time-consuming. Therefore, work performed

Table 4.3.1a.—Approximate Computer Storage Required for Numerical Solution

Number of space dimensions	Number of subdivisions in each space dimension	Required storage
1	10	10
	100	10^2
	1000	10^3
2	10	10^2
	100	10^4
	1000	10^6
3	10	10^3
	100	10^6
	1000	10^9

Table 4.3.1b.—Approximate Time to Compute 100 Time Steps

Number of space dimensions	Number of subdivisions in each space dimension	Computing time
1	10	1 min
	100	1 hr
	1000	1 wk
2	10	6 min
	100	1 wk
	1000	10 yr
3	10	1 hr
	100	1 yr
	1000	10^4 yr

Table 4.3.1c.—Approximate Time to Compute One Period of Oscillation

Number of space dimensions	Number of subdivisions in each space dimension	Computing time
1	10	0.1 min
	100	1 hr
	1000	10 wk
2	10	1 min
	100	1 wk
	1000	100 yr
3	10	10 min
	100	1 yr
	1000	10^5 yr

using numerical integration methods has been limited to one- and two-dimensional systems.

4.3.1.2 *Governing equations.*—The equations on which the numerical stability analysis is based can be derived from the conservation equations written for a parcel of gas through which liquid propellant droplets move as they are converted into combustion products. These conservation equations are essentially the same as Eqs. (4.1.2–1), (4.1.2–2), and (4.1.2–5), but are presented here in a somewhat different form and with viscous effects and heat conduction included:[359]

Mass:

$$\frac{\partial \rho}{\partial t} = -\nabla \cdot \rho \mathbf{V} + M_F + M_{OX} \qquad (4.3.1\text{–}1)$$

Momentum:

$$\rho \frac{\partial \mathbf{V}}{\partial t} = -\rho(\mathbf{V}\cdot\nabla)\mathbf{V} - \nabla p - \nabla \cdot \mathfrak{T} - (\mathbf{V}-\mathbf{V}_{LF})M_F - (\mathbf{V}-\mathbf{V}_{LOX})M_{OX} - \mathbf{F}_F - \mathbf{F}_{OX} \qquad (4.3.1\text{–}2)$$

Energy:

$$\rho c_v \frac{\partial T}{\partial t} = -\rho c_v(\mathbf{V}\cdot\nabla)T + \mathfrak{K}\nabla^2 T - p\nabla\cdot\mathbf{V} - \mathfrak{T}:\nabla\mathbf{V} + M_F(e_{LF}-c_vT) + M_{OX}(e_{LOX}-c_vT) + \mathbf{F}_F\cdot(\mathbf{V}-\mathbf{V}_{LF}) + \mathbf{F}_{OX}\cdot(\mathbf{V}-\mathbf{V}_{LOX}) + M_F(\mathbf{V}_{LF}-\mathbf{V})\cdot(\mathbf{V}_{LF}-\mathbf{V}) + M_{OX}(\mathbf{V}_{LOX}-\mathbf{V})(\mathbf{V}_{LOX}-\mathbf{V}) \qquad (4.3.1\text{–}3)$$

The gas is assumed to be perfect, so that

$$p = \rho \frac{\mathfrak{R}T}{\mathfrak{W}} \qquad (4.3.1\text{–}4)$$

and

$$e = c_vT$$

or

$$c_v = \frac{de}{dT} = \text{const.} \qquad (4.3.1\text{–}5)$$

It should be noted that the burning rate is written as the sum of the fuel and oxidizer burning rates, M_F and M_{OX}, respectively. This formulation allows the treatment of fuel and oxidizer sprays with quite different characteristics. The forces $\mathbf{F}_F$ and $\mathbf{F}_{OX}$ are the drag forces acting to accelerate the unburned propellants.

The stability analysis can be performed using the equations in either dimensional or nondimensional form. Nondimensionalization has the advantage that parameters that control stability appear in groups rather than as individual terms. Typical reference quantities are: combustor radius or length, speed of sound of the combustion gases, and appropriately selected steady-state values of pressure, temperature, density, and burning rate.

Solution of the governing equations requires the establishing of initial and boundary conditions. The usual approach is to specify the initial conditions as the steady-state values modified by an arbitrary disturbance. The boundary conditions (spatial) are largely dependent on the combustor geometry. For a full, three-dimensional chamber, the appropriate conditions are (a) no flow through the solid walls of the chamber and injector, (b) specified propellant flow through the injector orifices, and (c) sonic flow at the nozzle throat. Boundary conditions for other configurations are given in Sects. 4.3.2 and 4.3.3. In specifying the boundary conditions, one must be careful not to give too many or too few conditions or to use unrealistic conditions. A good understanding of the physical phenomena associated with combustion instability is the best guide to establishing the proper boundary conditions.

4.3.1.3 *Burning rate models.*—The driving energy for combustion instability comes from the combustion process, whereby chemical energy is expended to gasify the liquid propellants and heat the reaction products. In the numerical integration methods the local, instantaneous rate per unit volume at which these processes occur is described by a burning rate M, which may be different for oxidizer and fuel. It is important that the dependence of the burning rate on both the local reactant character (propellant spray drop size distribution, velocity, concentration, etc.) and the local gas dynamic environment be adequately represented. When time derivatives are suppressed, the burning rate equations must reduce to the same

equations used to define the steady-state characteristics of the combustor.

The steps that are normally considered to make up the combustion process for a liquid propellant rocket are atomization, vaporization, gas-phase mixing, and chemical reaction.* A single step is usually assumed to control the overall combustion process. For example, Priem[563] employed vaporization- and chemical-reaction-controlled burning rate expressions in the original development of the numerical integration technique, and subsequently added atomization as a possible controlling mechanism.[556] Based on his theoretical studies he concluded that chemical reaction is normally so fast that it would not be controlling, except possibly for gaseous propellant rockets. In most of the numerical stability analyses the burning rates have been treated as being vaporization-limited, although a gas-phase mixing limitation on the burning rate has recently been used.[135] In the following paragraphs the various burning rate equations are presented, with a brief description of their origin. The experimental data and analytical assumptions can be found in the references quoted.

ATOMIZATION-LIMITED BURNING RATE: The burning rate equation used by Priem[563] was obtained by use of the breakup time measured by Morrell[500] for a water jet in a transverse shock wave:

$$t_b = 1.91 \frac{d_L}{\Delta V}\left(\frac{\rho_L}{\rho}\right)^{2/3}\left(\frac{\mu}{\mu_L}\right)^{1/3}\frac{(Re/2)^{3/4}}{(We)^{1/2}} \qquad (4.3.1\text{–}6)$$

where

$$Re = \frac{d_j \rho \Delta V}{\mu}; \qquad We = \frac{d_j \rho (\Delta V)^2}{\mathcal{S}}$$

Morrell's data were obtained from high-speed photographs of the liquid deformation and breakup. Jet velocities were relatively low (20 to 46 ft/sec) unlike the gas velocities (up to 1000 ft/sec). An average atomization rate was then obtained by dividing the instantaneous mass concentration of unatomized propellant m_a by the breakup time. When normalized by the appropriate steady-state quantities, the result is

$$\frac{M}{\bar{M}} = \frac{m_a}{\bar{m}_a}\left(\frac{\rho}{\bar{\rho}}\right)^{5/12}\left(\frac{\Delta v}{\Delta \bar{v}}\right)^{5/4} \qquad (4.3.1\text{–}7)$$

Other atomization rate or breakup time equations can also be used. For example, the breakup time derived by Wolfe and Anderson[755] specifically for the secondary breakup of droplets in a gas stream would lead to an equation similar to Eq. (4.3.1–7) but with slightly larger exponents for both gas density and relative velocity factors. Campbell[135] introduced a droplet shattering rate into a vaporization-limited combustion model. The secondary droplets are considered small enough to burn as soon as they form. This model is based on a capillary-wave breakup mechanism. After local achievement of gas dynamic conditions suitable for breakup (viz, $We/(Re)^{1/2} > 10$), there is an induction period[134] followed by capillary-wave breakup.[500]

A major unanswered question in the use of any of the droplet breakup equations is the importance of the sheltering of a given drop by clouds of neighboring droplets. The available equations were obtained by observing the shattering of isolated droplets and may well predict breakup rates too high for dense propellant sprays.

VAPORIZATION-LIMITED BURNING RATE: The vaporization-limited burning rate equations all derive from the equation given by Priem and Heidmann[564] for the case of simultaneous energy and mass transport between a spherical droplet and the surrounding gas:

$$\frac{dm_L}{dt} = \frac{2\pi r_L \mathfrak{W}_L \mathfrak{D} p Nu_m}{\mathfrak{R} T_f} \ln\left(\frac{p}{p - p_v}\right) \qquad (4.3.1\text{–}8)$$

Although this equation is quasi-steady in nature, it does allow for droplet heating and thus differs from many well known combustion models, such as those of Godsave,[290] Penner,[536] and Williams.[740] The dimensionless forms of the burning rate actually introduced into the numerical integration differ rather widely. Using the Ranz-Marshall[577] expression for the Nusselt number, and using the approximation $\mathfrak{D}p \sim T_f^{1.7}$, the nondimensional form of the unsteady burning rate is

* Where liquid-liquid reaction occurs, as with hypergolic propellants, some of these steps may be bypassed. Such reaction may have a profound effect on spray formation through the phenomenon of stream separation (Sect. 2.3), but is generally considered to account for a very small fraction of the overall energy release.

$$\frac{M}{\bar{M}} = \left(\frac{r_L}{\bar{r}_L}\right)\left(\frac{T_f}{\bar{T}_f}\right)^{0.7}\left[\frac{2+0.6Sc^{1/3}Re^{1/2}}{2+0.6\bar{S}c^{1/3}\bar{R}e^{1/2}}\right]$$

$$\left[\frac{\ln\,(1-p_v/p)}{\ln\,(1-\bar{p}_v/\bar{p})}\right] \qquad (4.3.1\text{–}9)$$

where

$$Re = 2r_L\rho\Delta V/\mu$$

If it is assumed that the ratio of vapor pressure to static pressure always remains at the steady-state value and that variations in film temperature T_f are insignificant, Eq. (4.3.1–9) reduces to[135]

$$\frac{M}{\bar{M}} = \left(\frac{r_L}{\bar{r}_L}\right)\frac{2+0.6Sc^{1/3}Re^{1/2}}{2+0.6\bar{S}c^{1/3}\bar{R}e^{1/2}} \qquad (4.3.1\text{–}10)$$

Kosvic et al.,[410] neglected the droplet radius variation, and introduced a droplet "Reynolds number based on the speed of sound"* so that ΔV could be expressed in terms of velocities normalized by the sound velocity. The resulting burning rate equation is

$$\frac{M}{\bar{M}} = \frac{2+0.6Sc^{1/3}(\rho/\bar{\rho})^{1/2}(\Delta V/\bar{a})^{1/2}Re_d^{1/2}}{2+0.6\bar{S}c^{1/3}(\overline{\Delta V}/\bar{a})^{1/2}Re_d^{1/2}} \qquad (4.3.1\text{–}11)$$

where

$$Re_d = \frac{2r_L\bar{\rho}\bar{a}}{\bar{\mu}}$$

It is of some interest that the effect of p_v/p variations, which is neglected in most of the numerical studies, is of primary interest in the analytical model of Dykema (Sect. 4.4.1.3). Also, in the studies of Heidmann and Wieber,[346,347] both the p_v/p and T_f terms were considered important, and produced a burning rate that was frequency dependent. Thus, the vaporization models used in the numerical integration methods have ignored the frequency dependence of the burning rate, a dependence that is of primary importance in the theories discussed in Sections 4.2 and 4.4.

POLYDISPERSE SPRAYS: The actual injection spray in a liquid rocket engine consists of a wide range of drop sizes. To provide a valid description of a non-steady combustion process for such a spray, account must be made for contributions to the burning rate of drop sizes over the whole range. Because the burning of small droplets generates gas that accelerates the burning of larger drops, the spray cannot be simulated properly by a single mean size. Two approaches have been used to solve this problem. In the first, a moderate number (e.g., 10 to 20) of discrete drop size groups is used to simulate the actual spray.[135] The local drop size distribution must first be obtained from a steady-state combustion calculation. The burning rate equation is applied separately to each drop size group and the contributions of all of the groups are summed to obtain the overall rate of gas generation and energy release.

In the alternate approach, the burning rate is expressed as a function of drop radius, weighted by a distribution function, and numerically integrated over all drop radii.[358] This approach has the advantage of considering all sizes and of providing a convenient means of varying mean drop size and variance to determine their effects on stability. However, it is more restrictive in that the distribution may not vary from steady state, and it would not be convenient to use when variable factors that are implicitly dependent on drop size (e.g., droplet velocity, temperature, vapor pressure) are included in the burning rate. This approach also gives undue importance to the small drop sizes, since it is assumed that they are never burned but always exist as in steady state.

GAS-PHASE-MIXING-LIMITED BURNING RATE: When the vaporization rate becomes extremely high, it is possible that small pockets of unmixed propellant vapors may form. Such might be the case when a droplet is heated rapidly through its critical temperature, or with droplet shattering, in which clouds of the very fine secondary droplets are rapidly gasified. In such cases, the burning rate could be controlled by the rate of gas-phase turbulent mixing. Unfortunately, there does not appear to be a suitable model available to describe such mixing under highly convective conditions. Even if such a model were available, the required experimental turbulent diffusivity data does not exist at the present time. However, as a first step in describing local gas-phase mixing rates, a model developed by Spalding[662] has been modified and introduced into

* This Re_d is actually equivalent to 2/Kn, where Kn is the Knudsen Number.

a numerical integration burning rate model.[135]* Spalding's derivation assumed spherical symmetry, uniform gas density, and no convection. The modifications included approximate corrections for bipropellant combustion and a Nusselt number factor to account for convective effects.

CHEMICAL-REACTION-LIMITED BURNING RATE: As an alternative to the vaporization-limited burning rate, Priem and Guentert[563] examined a model in which the burning rate was equal to the chemical reaction rate, as given by

$$\frac{M}{\bar{M}} = \left(\frac{C}{\bar{C}}\right)^n \left(\frac{\rho}{\bar{\rho}}\right)^n \exp\left[\frac{E_{act}}{\mathfrak{R}\bar{T}}\left(1-\frac{T}{\bar{T}}\right)\right] \quad (4.3.1\text{-}12)$$

where the instantaneous concentration of vaporized but unreacted propellants was determined from

$$\frac{C}{\bar{C}} = 1 + \frac{\mathfrak{L}}{\bar{C}}\int_0^t \left(1 - \frac{M}{\bar{M}} \cdot \frac{\bar{\rho}}{\rho}\right) dt \quad (4.3.1\text{-}13)$$

The steady-state concentration of unreacted propellants, $\bar{C}$, related to the burning rate $\bar{M}$ by the Arrhenius expression

$$\bar{M} = (\bar{C}\bar{\rho})^n \mathfrak{B} \exp\left[-E_{act}/\mathfrak{R}\bar{T}\right] \quad (4.3.1\text{-}14)$$

is the primary controlling factor for this model.

4.3.2 One-Dimensional Analysis†

As discussed in Sect. 4.3.1.1, reducing the number of space dimensions to one drastically reduces the storage and time requirements for a numerical integration stability analysis. Therefore, one-dimensional models have been the most commonly used. Starting from a cylindrical coordinate system (Fig. 4.3.2a), the coordinate retained could be x, θ, or r, corresponding to axial, tangential, or radial oscillations, respectively. One-dimensionality implies that nothing is known about the variables in the other dimensions.

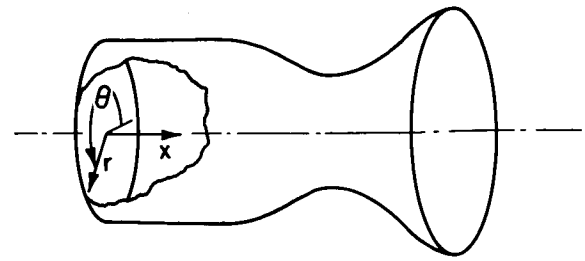

FIGURE 4.3.2a.—Cylindrical coordinate system for stability analysis.

Hence only the steady-state values of the parameters can be used in the other dimensions. However, in using the tangential or radial models with nonlinear burning mechanisms, if steady-state values and derivatives in the axial direction are used at all times, the average pressure of the system will continually increase. That is, the nonlinear burning rate increases the amount of propellant burned in the volume under consideration, whereas using the steady-state axial derivatives leads to constant mass flow out of the volume. To compensate for this result, the mass, momentum, and energy equations are integrated over the space dimension at each instant. By assuming no change with time of the mass, momentum, and energy in the control volume, average axial velocity, density, and temperature gradients are obtained. This approach is clearly not exact. Experimental engine tests and two-dimensional analyses show that at any axial position the volume averages do not remain constant with time. This is one of the shortcomings of a one-dimensional model; information is needed in other dimensions and is not available.

4.3.2.1 *Simplification of equations.*—To illustrate how the equations are simplified for a one-dimensional analysis the continuity equation will be derived for a tangential ("θ") model. The control volume for this analysis is an annular ring, as shown in Fig. 4.3.2b. In cylindrical coordinates the continuity equation is

$$\frac{\partial \rho}{\partial t} = \frac{-\partial(\rho u)}{\partial x} - \frac{\partial(\rho v)}{\partial r} - \frac{\rho v}{r} - \frac{1}{r}\frac{\partial(\rho w)}{\partial \theta} + M_F + M_{OX} \quad (4.3.2\text{-}1)$$

where u, v, and w are the velocity components in the x, r, and θ directions, respectively. With the

* The form of this relationship is

$$M = 2\pi N_d m_{d_0} \mathfrak{D}(2 + 0.6\, Re^{1/2} Sc^{1/3})\left(\frac{\rho(\mathfrak{r} - \mathfrak{r}_{st})}{m_{d_0}\mathfrak{r}(1+\mathfrak{r}_{st})}\right)^{2/3}$$

where N_d is the number density of droplets, m_{do} is the initial mass of a single droplet, $\mathfrak{D}$ is the diffusivity, $\mathfrak{r}$ is the instantaneous mixture ratio, $\mathfrak{r}_{st}$ is the stoichiometric mixture ratio, ρ is the gas density, Re is the Reynolds number and Sc the Schmidt number.

† R. J. Priem, Author, with T. C. Kosvic and R. Van Wyk, Contributors.

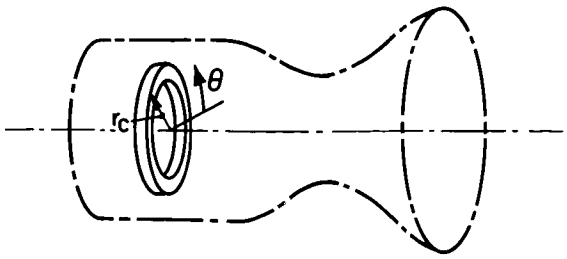

FIGURE 4.3.2b.—Annular-ring control volume for one-dimensional stability model.

one-dimensional θ model, nothing is known about the radial direction. Therefore, all radial velocity components and radial derivatives must be taken to be zero:

$$V = \frac{\partial \rho}{\partial r} = \frac{v}{r} = \frac{\partial v}{\partial r} = 0 \qquad (4.3.2\text{–}2)$$

In the axial direction there is additional information, from the steady-state equation

$$0 = -\frac{1}{r}\frac{\partial(\bar{\rho}\bar{w})}{\partial\theta} - \frac{\partial(\bar{\rho}\bar{u})}{\partial x} + \bar{M}_F + \bar{M}_{OX} \qquad (4.3.2\text{–}3)$$

and with no tangential flow in the steady state,

$$\frac{\partial(\bar{\rho}\bar{u})}{\partial x} = \bar{M}_F + \bar{M}_{OX} \qquad (4.3.2\text{–}4)$$

This is all the information known about the axial direction unless it is assumed that the total mass in the annular ring remains constant. Then

$$\int_0^{2\pi} \frac{\partial \rho}{\partial t} d\theta = 0 = -\frac{1}{r}\int_0^{2\pi} \frac{\partial(\rho w)}{\partial\theta} d\theta - \int_0^{2\pi} \frac{\partial(\rho u)}{\partial x} d\theta + \int_0^{2\pi} (M_F + M_{OX}) d\theta \qquad (4.3.2\text{–}5)$$

The first term on the RHS of Eq. (4.3.2–5) is zero, since it is a closed integral. Then from Eq. (4.3.2–5) the average axial mass flux $\langle \rho u \rangle$ is related to the burning rates by

$$\frac{\partial\langle \rho u\rangle}{\partial x} = \frac{1}{2\pi}\int_0^{2\pi} (M_F + M_{OX}) d\theta \qquad (4.3.2\text{–}6)$$

Thus, there are two possible continuity equations. If the local axial mass flux is taken to be equal to the steady-state value, or

$$\frac{\partial(\rho u)}{\partial x} = \frac{\partial(\bar{\rho}\bar{u})}{\partial x}$$

the continuity equation is

$$\frac{\partial \rho}{\partial t} = -\frac{1}{r}\frac{\partial(\rho w)}{\partial\theta} + (M_F - \bar{M}_F) + (M_{OX} - \bar{M}_{OX}) \qquad (4.3.2\text{–}7)$$

Alternatively, if the total mass flux in the control volume is assumed to be constant, the local mass flux can be equated to the average value from Eq. (4.3.2–6) to give

$$\frac{\partial \rho}{\partial t} = -\frac{1}{r}\frac{\partial(\rho w)}{\partial\theta} + M_F + M_{OX} - \frac{1}{2\pi}\int_0^{2\pi} (M_F + M_{OX}) d\theta \qquad (4.3.2\text{–}8)$$

Similar procedures are used to simplify the other governing equations.[563] Caution must be used in deriving the burning rate equation for a one-dimensional analysis. Many of the terms in the burning rate equation are functions of time; it is always desirable to retain these variables. However, since the burning material is moving axially, a knowledge of the oscillations in that dimension is required. Hence the only one-dimensional model that can truly include time dependent burning rates is an axial model.

4.3.2.2 *Method of solution.*—Several techniques are available for the numerical integration of differential equations.[276] Two basic types of solution have been used in stability analyses, the first-order explicit method[563] and the predictor-corrector method.[91, 131, 135]

In the first-order explicit scheme the spatial derivatives of all quantities are determined at time t from known values at adjacent calculation locations. Thus,

$$\frac{\partial p}{\partial\theta}(t, \theta_j) = \frac{p(t, \theta_j + \Delta\theta) - p(t, \theta_j - \Delta\theta)}{2\Delta\theta} \qquad (4.3.2\text{–}9a)$$

where the θ_j are the locations at which the calculations are performed. From the conservation equations, the values and spatial derivatives of the dependent variables are used to determine the time derivatives at time t:

$$\frac{\partial p}{\partial t}(t, \theta_j) = f\left[p(t, \theta_j), \frac{\partial p}{\partial \theta}(t, \theta_j), \cdots\right] \quad (4.3.2\text{–}9b)$$

Then the values of each variable at time $t+\Delta t$ are found by adding the product of the time derivative and the time increment to the value at time t,

$$p(t+\Delta t, \theta_j) = p(t, \theta_j) + \frac{\partial p}{\partial t}(t, \theta_j)\Delta t \quad (4.3.2\text{–}9c)$$

In the predictor-corrector method the value of each variable at time $t+\Delta t$ is first predicted or assumed. Then mean values of the variables (at a mean time t_m)

$$p(t_m, \theta_j) = g[p(t, \theta_j), p(t+\Delta t, \theta_j)] \quad (4.3.2\text{–}10a)$$

are used to obtain spatial derivatives at the mean time,

$$\frac{\partial p}{\partial \theta}(t_m, \theta_j) = \frac{p(t_m, \theta_j+\Delta\theta) - p(t_m, \theta_j-\Delta\theta)}{2\Delta\theta} \quad (4.3.2\text{–}10b)$$

The mean quantities are used in the conservation equations to determine mean time derivatives,

$$\frac{\partial p}{\partial t}(t_m, \theta_j) = f\left[p(t_m, \theta_j), \frac{\partial p}{\partial t}(t_m, \theta_j), \cdots\right] \quad (4.3.2\text{–}10c)$$

The value of each variable at time $t+\Delta t$ is then found using the mean time derivative. If the calculated value does not agree with the predicted value a new (corrected) prediction is made for the variable at time $t+\Delta t$ and the cycle is repeated. When agreement is reached within the desired accuracy for all θ_j, the calculation is advanced to the next time step.

The determination of the mean values is an important part of the predictor-corrector method. The simplest technique is to use an arithmetic mean.[136] In correcting the predicted values, several techniques have been used, including the complex Gauss-Seidell method[136] and the Crank-Nicholson method.[91, 410] The more complex methods minimize the iteration steps needed to obtain agreement between predicted and calculated values at $t+\Delta t$. A variation of the method described above is to convert the conservation equations to finite difference form right at the beginning.[131, 135, 136, 359, 410]

Numerical stability is of paramount importance in this approach. With numerical instability the calculated results oscillate with growing amplitude about the true solutions. Since the objective of the combustion stability analysis is to determine the level of disturbance (superimposed on the steady-state solution) required to produce oscillatory flow in the combustor, numerical instabilities cannot be distinguished from actual combustion system instabilities. Numerical stability is usually verified* by observing the behavior of the calculated results when the burning rate is held at a constant value. With a numerically stable method the disturbance will decay when the burning rate is constant.

4.3.2.3 *Typical results.*—The output of a numerical integration stability analysis computer program generally lists flow characteristics at each spatial location for selected times. One way to analyze the results is to plot the important flow variables as functions of time. For example, Figs. 4.3.2c and 4.3.2d show pressure-time plots for one location. In these plots, the variables are given in dimensionless form: the "reduced" pressure is the actual, instantaneous pressure divided by the steady-state pressure; the reduced time has been normalized by use of the mean radius of the annulus and the speed of sound. Overall stability determination usually requires an examination of the oscillations at all spatial locations. It is convenient to use the difference Δp between the maximum and minimum pressures in the annulus at each instant as the dependent variable. Figs. 4.3.2e and 4.3.2f show the pressure difference (reduced by the steady-state pressure) for the same two cases as Figs. 4.3.2c and 4.3.2d. It is clear from these plots that the disturbance with initial amplitude equal to 1% of the steady-state pressure was damped, whereas the disturbance with 5% initial amplitude resulted in oscillatory combustion. By performing such calculations for a series of initial disturbance amplitudes, the stability boundary for the given steady-state operating condition can be determined.

To give a more general understanding of the factors that control combustion instability it is

* However, in general, it is difficult to distinguish positively between numerical instability and physical instability.

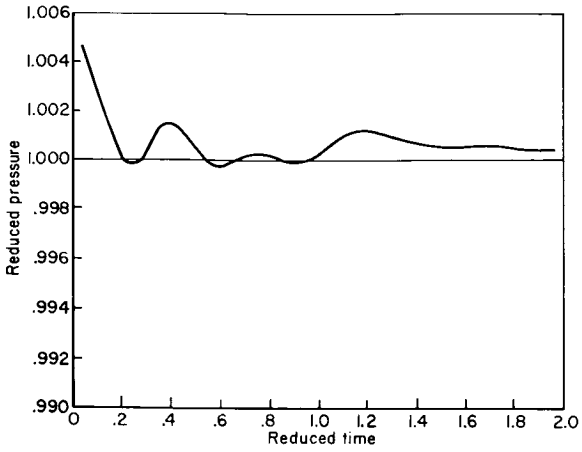

FIGURE 4.3.2c.—Typical pressure history with initial disturbance amplitude of 0.01. Annular-ring model.

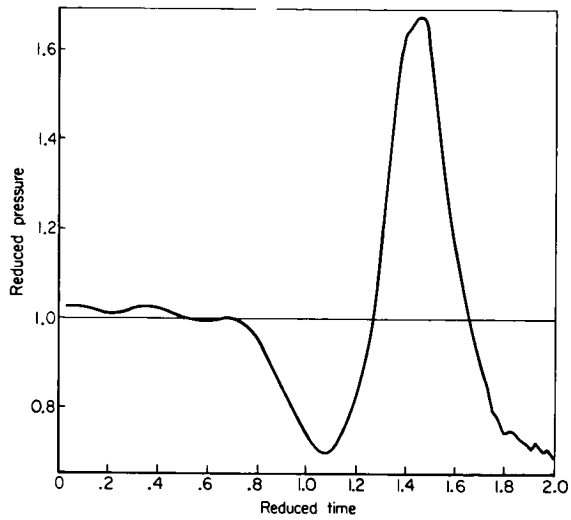

FIGURE 4.3.2d.—Typical pressure history with initial disturbance amplitude of 0.05. Annular-ring model.

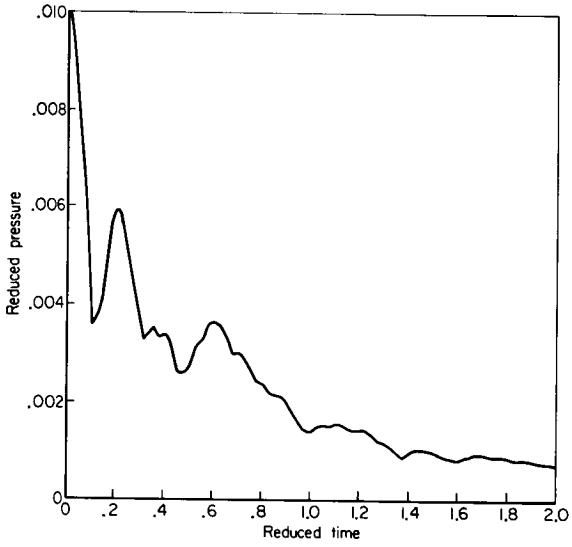

FIGURE 4.3.2e.—Pressure difference history. Initial disturbance amplitude, 0.01.

helpful to conduct parametric studies, using dimensionless quantities. Three such dimensionless parameters result directly from the nondimensionalization of the conservation equations for an annular-ring control volume: a burning rate parameter,

$$\mathfrak{L} = \frac{r_c M_x}{\epsilon_c} \qquad (4.3.2\text{–}11)$$

a viscous dissipation parameter,

$$\mathfrak{J} = \frac{\bar{\mu}\bar{c}^*}{r_c \bar{p}_c} \qquad (4.3.2\text{–}12)$$

and a velocity difference parameter,

$$\Delta V = \frac{\overline{V} - \overline{V}_L}{\bar{a}} \qquad (4.3.2\text{–}13)$$

However, analyses of both one-dimensional and two-dimensional models have shown that large changes in $\mathfrak{J}$ have negligible effect on the stability boundaries. Hence the viscous dissipation parameter is not usually considered. It should be noted that for a given engine the values of these dimensionless parameters depend on the location of the control volume, since M_x, the fraction of propellant burned per unit length, and ΔV, the relative velocity, vary along the length of the chamber.

The influence of $\mathfrak{L}$ and ΔV on the stability limits for a simple vaporization-limited combustion model in which only the Reynolds number variation was considered is shown in Fig. 4.3.2g.[563] Decreasing the velocity difference parameter decreases the disturbance amplitude required for instability, for any value of the burning rate parameter. However, it is expected that a minimum value of $\Delta V = 0.01$ (approximately) exists, corresponding to the level of turbulence in a typical rocket engine combustion chamber. The burning rate parameter for minimum stability is seen to be 0.8, for $\Delta V = 0.01$, and increases slightly as ΔV is increased. The curves shown in Fig.

4.3.2g were obtained with the explicit integration technique. Corresponding calculations using a predictor-corrector method yielded curves slightly higher in the low-$\mathfrak{L}$ region.

When other combustion mechanisms are considered, additional parameters must be specified. For example, when mass accumulation is added to the vaporization model, the additional parameter is

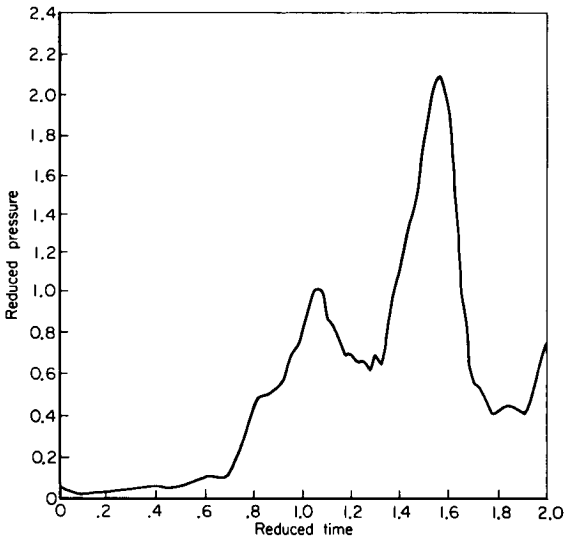

FIGURE 4.3.2f.—Pressure difference history. Initial disturbance amplitude, 0.05.

$$\mathfrak{M}_v = \frac{m_{acc}\bar{a}}{\bar{M}r_c} = \frac{2\pi m_{acc}}{\bar{M}t_w} \qquad (4.3.2\text{–}14)$$

where m_{acc} is the mass concentration of atomized, but unvaporized propellants in the control volume. From Eq. (4.3.2–14) it can be seen that the mass accumulation parameter can also be interpreted as the ratio of the time to burn the accumulated propellant at the steady-state rate, $m_{acc}/\overline{M}$, to the wave time. Fig. 4.3.2h illustrates the effect of mass accumulation on stability. The less mass is accumulated, or the shorter the burning time of the accumulated propellant, the greater is the disturbance required to trigger instability.

For the purely atomization-controlled combustion process, the mass accumulation parameter $\mathfrak{M}_a$ is defined also by Eq. (4.3.2–14), except that the quantity m_{acc} refers to the mass injected but not yet atomized. Typical stability limits are presented in Fig. 4.3.2i. The trends are similar to those obtained with the vaporization model. Comparison of Figs. 4.3.2h and 4.3.2i shows that the atomization process is more sensitive to disturbances than vaporization for large $\mathfrak{L}$ and small $\mathfrak{M}$.

Stability limits derived from the chemical-reaction-controlled combustion model are shown in Fig. 4.3.2j for limited concentrations of vaporized but unreacted propellants. When an unlimited supply of unburned propellant was assumed, all disturbances examined excited insta-

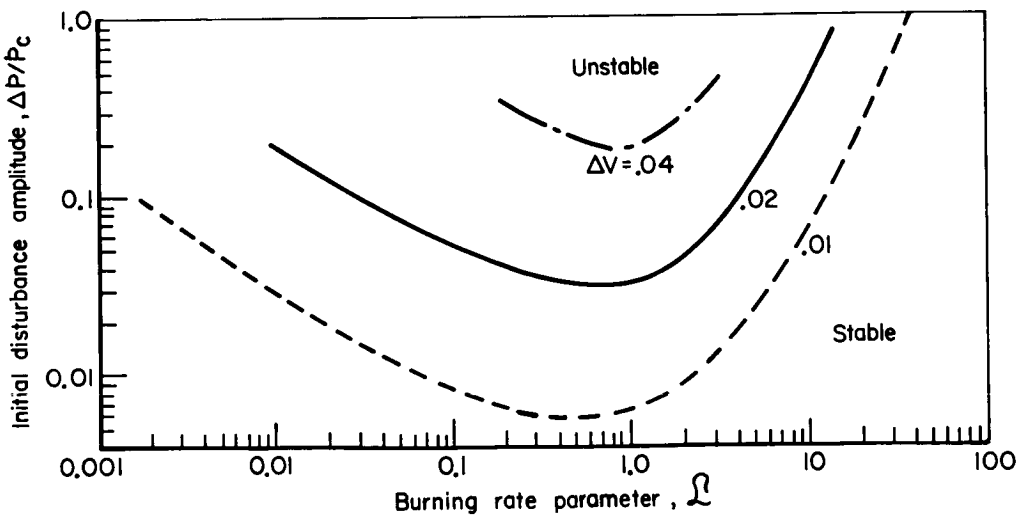

FIGURE 4.3.2g.—Stability limits for vaporization-controlled combustion. Annular-ring model.

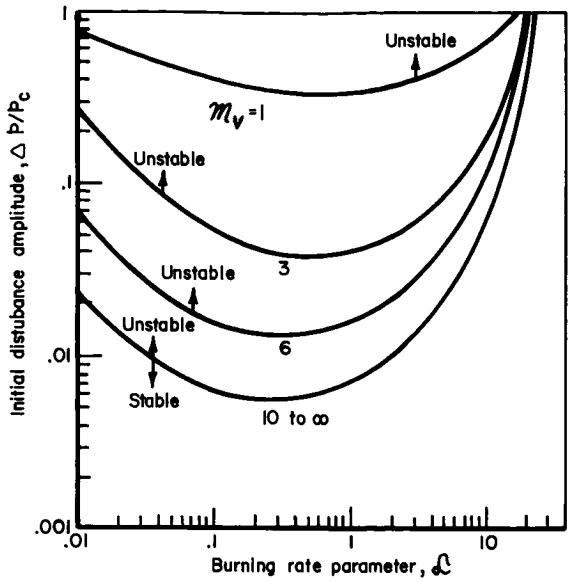

FIGURE 4.3.2h.—Stability limits for vaporization-mass accumulation model.

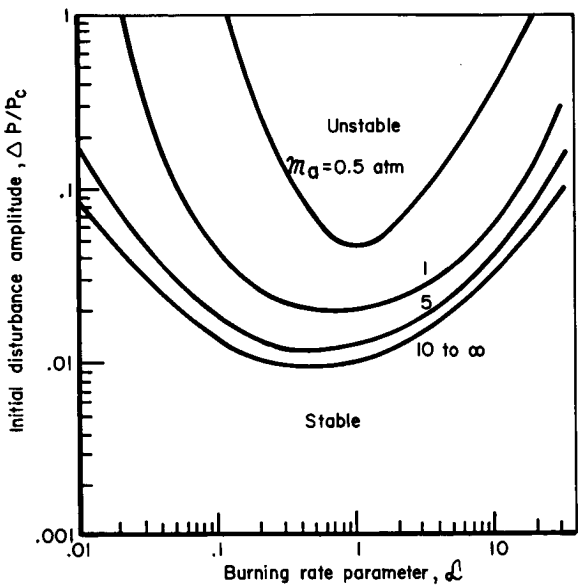

FIGURE 4.3.2i.—Stability limits for atomization model.

bility because of the extreme sensitivity of the exponential temperature dependence of the reaction rate. However, for realistic values of the average steady-state concentration of unreacted propellant C_0 (viz, 0.1 to 0.01) the stability limits occur at very low values of $\mathfrak{L}$. Such low

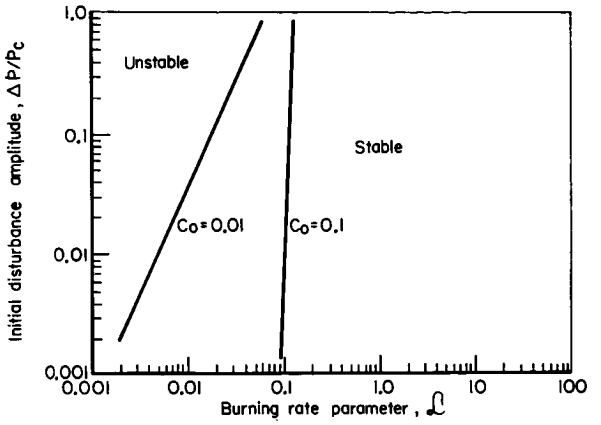

FIGURE 4.3.2j.—Stability limits for chemical reaction model.

burning rate parameter values usually are found only in small-scale research combustors.

4.3.3 Two-Dimensional Analysis*

Only limited attention has been given to two-dimensional stability analysis using numerical integration techniques. The primary reason, of course, is the very large computer size and time requirements, as discussed in Sect. 4.3.1. Two types of analysis have been carried out. The circumferential surface ($\theta-$x) model is based on a control volume extending the length of the combustion chamber but having very small thickness in the radial direction, as shown in Fig. 4.3.3a. The transverse plane (r$-\theta$) model considers a control volume that covers the entire cross-section of the chamber but has a small axial thickness (Fig. 4.3.3b). The third possible type of two-dimensional model, the meridional plane (r$-$x) model, has not received sufficient study to be included in this discussion.

4.3.3.1 *Circumferential surface ($\theta-x$) model.*—In the $\theta-$x model, the velocity components and radial derivatives are assumed to be zero, just as in the one-dimensional, annular-ring model. However, it is not necessary to make simplifying assumptions about the variations in the z-direction. Instead, new boundary conditions must be added at the injector and at the nozzle. One possibility for the nozzle condition is to extend the

* R. J. Priem, Author.

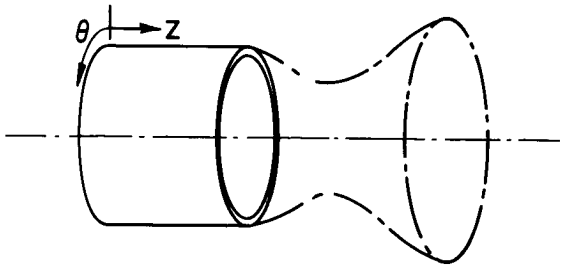

FIGURE 4.3.3a.—Control volume for two-dimensional, circumferential-surface model.

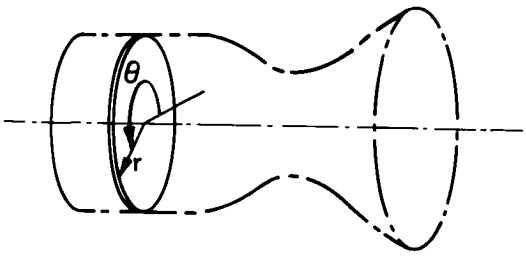

FIGURE 4.3.3b.—Control volume for two-dimensional, transverse-plane model.

control volume all the way to the throat, taking the boundary condition to be unity Mach number at the throat. A simpler approach is to end the control volume at the nozzle entrance and to use the approximate boundary condition of constant axial Mach number at the nozzle entrance. Boundary conditions at the injector include zero axial gas velocity and some means of defining the unburned propellants, e.g., injection velocity and/or flow rate. Other propellant injection boundary conditions depend on the burning rate model used in the analysis. That is, a vaporization-controlled burning rate requires the specification of the drop size distribution, atomization requires jet or drop size information, and chemical reaction requires temperatures and concentrations. Turbulent gas flow should also be accounted for by adding vectorially the rms level of turbulence.

The additional boundary conditions for the propellant and the added space dimension greatly complicate the task of obtaining general results concerning the effects of design parameters on stability. Calculations have been performed using a vaporization-controlled combustion mechanism with a turbulence level of 20 ft/sec.[561] A typical result is shown in Fig. 4.3.3c. One of the general conclusions drawn from these calculations was that the minimum disturbance that will excite instability in the circumferential model is about the same as that determined by the one-dimensional, annular-ring model.

The circumferential model allows many aspects of combustion instability to be examined that cannot be treated by other one- and two-dimensional models. An example is the combination of longitudinal and transverse modes. In the calculations cited above, longitudinal modes were observed primarily when the ratio of chamber length to radius exceeded 3 to 4. For shorter lengths the oscillation was primarily transverse. Also, with the $\theta-x$ model the time variation in the burning process, which is accompanied by axial movement, can also be included. Thus, the frequency dependence of the burning rate can be treated in a nonlinear analysis using numerical integration.

The $\theta-x$ model also allows the effects of radial baffles to be studied by adding the boundary condition that tangential velocities must be zero at specified tangential locations for specified lengths. A few calculations with such baffle simulation led to the observation that the baffles were very effective in increasing the minimum disturbance levels required to excite instability.

However, because the length and cost of the

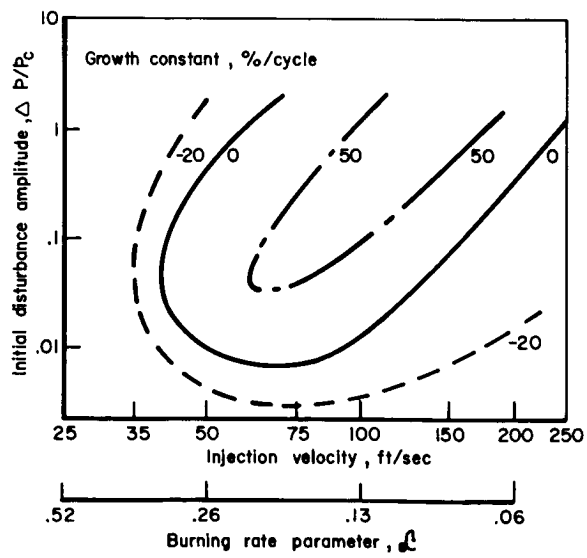

FIGURE 4.3.3c.—Stability limits for vaporization-controlled, circumferential-surface model.

calculations rapidly become prohibitive, the circumferential-surface model is recommended only when specific information is desired.

4.3.3.2 *Transverse plane* $(r-\theta)$ *model.*—With the transverse plane model (see Fig. 4.3.3b), radial velocity components and parameter changes in the radial direction are included. Axial gradients are treated in the same way as in the one-dimensional, annular-ring model. Hence many of the complexities added in the $\theta-x$ model are not present in the $r-\theta$ model. However, the addition of the radial dimension permits the study of chamber wall effects, such as viscous boundary layers and acoustic liners. Calculations of boundary layer influence have shown that the viscous forces have an insignificant effect on stability.[561] Acoustic liners have not yet been incorporated into a transverse-plane numerical stability analysis. The boundary condition imposed by a resonating liner is presented in Sect. 8.3.1, and so could readily be incorporated into such an analysis.

Stability limits calculated with a simple vaporization-controlled burning rate equation in the $r-\theta$ model are shown in Fig. 4.3.3d. The explicit integration scheme was inadequate in the low-$\mathfrak{L}$ range because of numerical instability. Problems were also encountered in attempting to calculate properties at the center of the chamber. More recent studies have eliminated these problems by using an implicit integration scheme and by avoiding the center of the combustor as a calculation point.[131] The latter studies also have shown that for some conditions a steep-fronted, shock-type wave is produced.

4.3.3.3 *Comparison with one-dimensional model.*—Comparisons between the one- and two-dimensional models are difficult because of the very small amount of work done with the latter. However, results of calculations based on a simple vaporization-controlled burning rate mechanism exhibited remarkable agreement, as shown in Fig. 4.3.3d. The minimum perturbation required to excite instability determined from the $\theta-x$ model (circumferential surface) agrees closely with that obtained from the θ model (annular ring). The stability limits for large $\mathfrak{L}$ obtained from the $r-\theta$ (transverse plane) and θ models are also in reasonable agreement. There are differences in the results, too, as Fig. 4.3.3d clearly indicates. It would be worthwhile to make additional comparative calculations to gain a better understanding of the differences between the stability limits determined by the different models. Additional comparisons based on more sophisticated combustion models would also be desirable.

Two-dimensional combustion stability models are valuable for investigating certain features of combustor design that cannot be included in a one-dimensional analysis. Examples of such

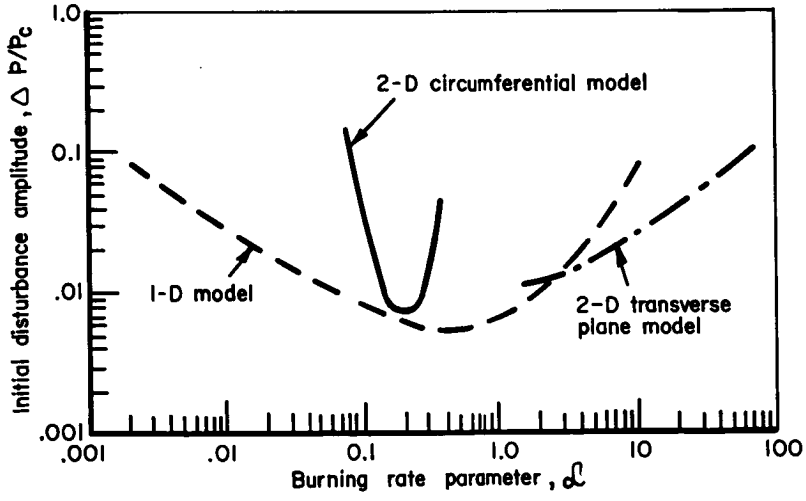

FIGURE 4.3.3d.—Stability limits for two- and three-dimensional, vaporization-controlled stability models.

features are injector-face baffles, axial combustion distribution, and nozzle admittance for the $\theta-x$ model, and acoustic liners, nonuniform injection distribution for the $r-\theta$ model. Otherwise, the information provided by a one-dimensional model is about as good as that provided by a two-dimensional model in the prediction of full, three-dimensional engine stability characteristics. Both models require experience and engineering judgment to extrapolate to actual, three-dimensional conditions.

4.4 SIMILITUDES AND OTHER MODELS

In the preceding sections of this chapter, comprehensive analytical models of high frequency combustion instability are developed. The advantages and disadvantages of each model are brought out there; further comparisons are made in Sect. 4.5. The sensitive time lag theory and the numerical integration methods share one deficiency, namely, the inherent conceptual or computational difficulties tend to prevent the design or development engineer from achieving a practical understanding of the relationships between the physical and chemical processes, hardware design parameters, and the phenomenon of combustion instability. The approaches described in this section are aimed at removing this deficiency.

The response factor approach, discussed first, is admittedly not comprehensive or completely rigorous. In general, the various combustion and gas dynamic processes are assumed to interact only weakly, so that in the first approximation coupling effects are absent. Primary attention is given to intentionally simplified models of the unsteady combustion process. However, allowance is made for the effects of acoustic resonance and certain damping processes.

The alternative approach of similitude is taken up next. Recognizing that stable engines have been developed, one naturally asks how the experience gained in developing such engines can be used effectively in the future. Analytical similarity studies are reviewed first. Unfortunately, these studies have not been completely successful. Therefore, a recent empirical study, involving the statistical analysis of experimental engine stability data, concludes this section.

The emphasis in this section is on the fundamental principles on which the response factor and similitude analyses are based. The considerations involved in applying the analyses to design and development problems are discussed in Chapter 6.

4.4.1 Response Factor Approach

4.4.1.1 Basic principles.—As stated by Rayleigh, the general criterion for wave growth or decay is, in the simplest terms, that a wave will grow if heat or mass is added in phase with the pressure. Conversely, the wave will damp if the addition is out of phase. When applied to a system in which several mechanisms are releasing heat or mass at once, the growth or decay of the wave is determined by the net in-phase or out-of-phase heat or mass addition. The response factor approach is basically an application of this principle. Variations of this approach have been used by several investigators to analyze unstable combustion systems and are presented in the following sections.

An advantage of the response factor approach is that it allows the designer to focus attention on the separate processes that influence the stability of a chamber. The effect on stability because of changes made to any part of the combustor, such as the injector, can be evaluated by examining their relative effect on the response factors of the various processes. The approach is general in nature since the response factor of any process or mechanism of importance can, in principle at least, be determined.

Three analyses of the response factor type are described in the sections following. The Heidmann-Feiler analysis is based on an unsteady mass balance for an axial column (stream tube) within the combustion chamber. Detailed consideration is given to three processes affecting the combustion rate: vaporization, injection of a gaseous propellant, and atomization. The Dykema analysis considers only a single process, that of unsteady vaporization of a droplet in a region of the chamber where the liquid and gas velocities are approximately equal. Finally, the modal energy analysis is expressed in terms of an energy balance for the "acoustic" modes of the combustion chamber. Since this is a more recent development than the two preceding analyses, it is formulated in

more general terms and has not been subjected to extensive experimental checking. Also, further analytical consideration needs to be given to some of the terms in the energy balance. Application techniques and comparisons with experiment for all three response factor analyses are discussed in Sect. 6.5.

*4.4.1.2 Heidmann-Feiler analysis.**—The following nomenclature pertains to Sect. 4.4.1.2:

b	Ratio of nondimensional vapor-pressure perturbation to nondimensional liquid temperature perturbation, p_v'/T_L'
C_D	Drag coefficient
$\mathcal{C}$	Capacitance of fuel manifold, $\bar{\rho}v/\gamma\underline{\dot{m}}$
$\mathcal{L}$	Inertance of fuel injection orifice, $\dot{m}L/A_1\bar{p}_2$
$\dot{m}_j$	Mass flow rate associated with j^{th} process
N	Response factor, $(\dot{m}^{o\prime}/p_c^{o\prime})\cos\phi$
N_j	Response factor of jth process
S	Critical distortion of jet diameter
t_{50}	Half-life of a droplet
u_f	Final gas velocity
z	Correction factor for heat transfer
β	Vapor-pressure parameter, defined in Table 4.4.1a
τ_a	Atomization time
τ_b	Combustion time
ϕ	Phase angle between mass flow rate and chamber pressure perturbations

Subscripts:

d	Fuel injection manifold
1, 2	Entrance, exit of cylindrical part of fuel injection orifice (see Fig. 4.4.1c)

Superscripts:

$()^o$ $\hat{()}$	Maximum value (amplitude) of an oscillating quantity

The response factor used in the Heidmann-Feiler analysis is based on the mass flow rate and is the real, or in-phase, part of the nondimensional mass flow rate perturbation with respect to the chamber pressure perturbations. Attention is focused on equilibrium conditions, that is, on the stability limit. A stability criterion based on such response factors may be derived in simple form by considering a purely transverse mode of oscillation within the chamber. For this mode there are no axial pressure variations and the pressure at any radial and angular position is time dependent only. A mass balance for the gas in an axial column can be expressed as

$$\frac{dm}{dt}=\Big[\sum_j \dot{m}_j\Big]_{in}-\Big[\sum_j \dot{m}_j\Big]_{out}$$

The summations in this balance are for a multiplicity of mass flow rates that may be entering or leaving the volumes of gas. For small perturbations, this mass balance is given by

$$\frac{\bar{m}}{\underline{\dot{m}}_T}\frac{dm'}{dt}=\left[\sum \frac{\underline{\dot{m}}_j}{\underline{\dot{m}}_T}\dot{m}_j'\right]_{in}-\left[\sum \frac{\underline{\dot{m}}_j}{\underline{\dot{m}}_T}\dot{m}_j'\right]_{out} \tag{4.4.1–1}$$

Assuming that gases in the volume are homogeneous and that they behave adiabatically, Eq. (4.4.1–1) becomes

$$\frac{1}{\gamma}\frac{\bar{m}}{\underline{\dot{m}}_T}\frac{dp_c'}{dt}=\left[\sum_i \frac{\underline{\dot{m}}_j}{\underline{\dot{m}}_T}\dot{m}_j'\right]_{in}-\left[\sum \frac{\underline{\dot{m}}_j}{\underline{\dot{m}}_T}\dot{m}_j'\right]_{out} \tag{4.4.1–2}$$

For the conditions prescribed above, the chamber pressure perturbation is assumed to be a complex function given by

$$p_c'=p_c^{o\prime}\exp\left[(\lambda+i\omega t)\right]=p_c^{o\prime}e^{st}$$

where λ is a growth constant. Any mass flow rate perturbation which results from a linear response to chamber pressure perturbations will, in general, be phase-shifted with respect to the pressure perturbations. Thus,

$$\dot{m}'=\dot{m}^{o\prime}\exp\left[(\lambda+i\omega t)\right]\exp\left[i\phi\right]$$

where ϕ is a phase angle.

With these expressions for pressure and flow rate, Eq. (4.4.1–2) becomes

$$\frac{1}{\gamma}\frac{\bar{m}}{\underline{\dot{m}}_T}(\lambda+i\omega)=\left[\sum_j \frac{\underline{\dot{m}}_j}{\underline{\dot{m}}_T}\frac{m}{p_c^{o\prime}}\exp(i\phi_j)\right]_{in}-\left[\sum_j \frac{\underline{\dot{m}}_j}{\underline{\dot{m}}_T}\frac{\dot{m}^{o\prime}_j}{p_c^{o\prime}}\exp(i\phi_j)\right]_{out} \tag{4.4.1–3}$$

Equating the real parts of Eq. (4.4.1–3) yields an expression for the growth constant λ. The stability limit is obtained when $\lambda=0$ and is given

* M. F. Heidmann and C. E. Feiler, Authors.

by the relation:

$$\left[\sum_j \frac{\dot{m}_j}{\dot{m}_T} N_j\right]_{in} = \left[\sum_j \frac{\dot{m}_j}{\dot{m}_T} N_j\right]_{out} \qquad (4.4.1\text{–}4)$$

where the response factor N is defined as

$$N = \mathcal{R}e\left(\frac{\dot{m}'}{p_c'}\right) = \frac{\dot{m}^{\circ\prime}}{p_c^{\circ\prime}} \cos\phi \qquad (4.4.1\text{–}5)$$

The stability limit as expressed by Eq. (4.4.1–4) shows the effects of the various processes to be additive with the response factor for each process weighted by the fraction of the total weight flow entering into the process.

This stability criterion for an axial column also applies to the entire chamber volume in most linear analyses because the response factors for such analyses do not depend on pressure amplitude. In the general case, when the response factor is not uniform across the cross-sectional area of the chamber, or the mass flow rate responds nonlinearly to pressure, the response factor, N can be determined by the relation

$$N = \frac{\int^V \int^t \dot{m}' p_c' \, dt \, dV}{\int^V \int^t (p_c')^2 dt \, dV}$$

This equation reduces to Eq. (4.4.1–5) for sinusoidal perturbations in weight flow rate and chamber pressure.

The response factor given in Eq. (4.4.1–5) can be positive or negative, depending on the phase angle ϕ between the pressure and flow rate perturbations. The ratio $\dot{m}^{\circ\prime}/p_c^{\circ\prime}$ is the gain, or magnitude, of the response and is independent of the phase angle.

The combustion of propellants has been considered to be rate-limited by several processes, including droplet vaporization, gaseous injection and jet atomization. The remainder of this section will be devoted to presenting the response factors for these processes and examining their behavior. The utility of the response factor model, however, is not restricted to these processes or by the specific forms of analysis performed.

DROPLET VAPORIZATION: The response factor for the vaporization process will depend on the particular model formulation used for a vaporizing spray (see Sect. 3.4.2). The analyses of Heidmann and Wieber[346,347] are reviewed here because these results have been specifically applied to the response factor approach. Other models can be applied in a similar manner.

In a three-dimensional, nonlinear, numerical study,[347] vaporization histories in the presence of a traveling transverse acoustic mode were computed for uniformly injected n-heptane drops in a cylindrical chamber. The local and volume averages of that portion of the vaporization rate in-phase with the pressure oscillation were evaluated as a function of frequency using the expressions given in Table 4.4.1a. Drop size, chamber pressure, final gas velocity, pressure amplitude, injection velocity, and initial injection temperature were parametrically varied. A correlation of the results is shown in Fig. 4.4.1a. The abscissa is essentially a frequency nondimensionalized by a vaporization time t_{50} where

$$t_{50} \simeq \frac{1}{1200}\left(\frac{r_L}{50}\right)^{3/2}\left(\frac{300}{p_c}\right)^{1/3}\left(\frac{800}{u_f}\right)^{1/3}$$

with the droplet radius r_L in microns, the chamber pressure p_c in psia, and the final gas velocity u_f in ft/sec.

From these results, it is possible to estimate the response factor for specific combustion variables. These results are applicable only to n-heptane; however, from a consideration of steady-state correlation factors the relative effect of combustion variables on vaporization time is expected to apply to other propellants.

A linearized analysis[346] of the same process, performed by combining the pertinent equations of Table 4.4.1a, provides a relation between vaporization rate and chamber pressure perturbations in the form of the following transfer function:

$$\frac{\dot{m}'}{p_c'} = \frac{1}{2}\left[\frac{2\tau_v s}{1+2\tau_v s}\right]\left[\frac{1+(1-2\beta)(c_p T_L/h_v\beta b)\tau_v s}{1+(c_p T_L/h_v\beta b)s}\right]$$

where

$$s = \lambda + i\omega$$

The gain and angle needed to evaluate the response factor,

$$N = \frac{\dot{m}^{\circ\prime}}{p_c^{\circ\prime}} \cos\phi$$

TABLE 4.4.1a.—EQUATIONS FOR VAPORIZATION PROCESS

	Nonlinear analysis	Linear analysis[a]
Mass balance	$\frac{dm_L}{dt}=\dot{m}-\dot{m}_v$	$\tau_v m_L's=-\dot{m}_v'$
Vaporization rate	$\dot{m}_v=\frac{2\pi\mathfrak{D}\mathfrak{W}r_L Nu_m p_c}{\mathfrak{R}\bar{T}}\ln\frac{p_v}{p_c-p_v}$	$\dot{m}_v'=\frac{1}{2}m_L'+\beta p_v'-(\beta-\frac{1}{2})p_c'$
Vapor pressure	$\ln p_v=c_1-\frac{c_2}{T_L-c_3}$	$p_v'=bT_L'$
Drop temperature	$\frac{dT_L}{dt}=\frac{1}{c_p m_L}(q_{in}-q_{out})$	$\frac{\bar{c}_p\bar{T}_L}{h_v}\tau_v T_L's=q_{in}'-q_{out}'$
Heat transfer	$q_{in}=2\pi\mathfrak{K}r_L(T_b-T_L)zNu_h$ $q_{out}=h_v\dot{m}_v$	$q_{in}'=\frac{1}{2}m_L'-\frac{1}{2}p_v'$ $q_{out}'=\dot{m}_v'$
Drop motion	$\frac{du_L}{dt}=-\frac{3}{8}C_D\frac{\rho}{\rho_L}\frac{(\Delta v)^2}{r_L}$	$u_L's=0$

[a] In the linearized equations, $Nu_m\sim(r_L\rho_L)^{1/2}$; $Nu_h\sim(r_L\rho_L)^{1/2}$; $\mathfrak{D}\sim p_c^{-1}$; $m_L\sim r_L^3$; c_p, (T_b-T_L), Z, h_v, u_L, $\dot{m}_{in}$, C_D, and ΔV are constant;

$$\beta=\left(\frac{p_v}{p_c-p_v}\right)\Big/\ln\left(\frac{p_c}{p_c-p_v}\right);\text{ and } b=\frac{C_2T_L}{(T_L-C_3)^2}.$$

are given by

$$\frac{\dot{m}^{o\prime}}{p_c^{o\prime}}=\frac{1}{2}\frac{2\tau_v\omega}{[1+(2\tau_v\omega)^2]^{1/2}}\times\left\{\frac{1+[(1-2\beta)(c_pT_L/h_v\beta b)\tau_v\omega]^2}{1+[(c_pT_L/h_v\beta b)\tau_v\omega]^2}\right\}^{1/2} \quad (4.4.1\text{–}6a)$$

and

$$\phi=\frac{\pi}{2}-\tan^{-1}2\tau_v\omega+\tan^{-1}(1-2\beta)\frac{c_pT_L}{h_v\beta b}\tau_v\omega-\tan\frac{c_pT_L}{h_v\beta b}\tau_v\omega \quad (4.4.1\text{–}6b)$$

The response factor is a function of certain propellant properties at equilibrium conditions of vaporization. Typical values of these properties, established from previous steady-state solutions for several propellants,[564] are given in Table 4.4.1b.

Frequency response curves based on these values are shown in Fig. 4.4.1b. The curves, although more approximate than the nonlinear results, allow an estimate to be made of the response factor of the various propellants. The mean vaporization time τ_v is related to the droplet half-lifetime t_{50} found in the nonlinear analysis, by $\tau_v\simeq(1/4.5)t_{50}$. The difference in these values exists because axial variation of the vaporization rates is not considered in the linear analysis.

GASEOUS INJECTION: It has been observed experimentally that decreasing the hydrogen injection temperature in a gaseous hydrogen-liquid oxygen rocket results in combustion instability. This observation led to the suspicion that the gaseous hydrogen flow could respond to high frequency combustion oscillations in the same way that a liquid flow responds to low frequency

oscillations. The particular injector element modeled is shown in Fig. 4.4.1c together with the perturbation equations applying to each element in the lumped parameter treatment.[260] Combination of these equations yields the following transfer function expressing the response of the hydrogen flow rate to a chamber pressure perturbation:

$$\frac{\dot{m}_b'}{p_c'} = -\frac{\left(\frac{\bar{p}_c}{\Delta p_2}-\frac{1}{\gamma}\right)\left(\frac{\bar{p}_2}{\Delta p_1}-\frac{1}{\gamma}\right)\left(\frac{\Delta p_2}{\bar{p}_2}\right)\left(\frac{\Delta p_1}{\bar{p}_d}\right)\mathcal{C}s\exp(-\tau_b s)}{1+2\frac{\Delta p_2}{\bar{p}_2}\left[1+\frac{\Delta p_2}{p_2}\left(\frac{\bar{p}_2}{\Delta p_1}-\frac{1}{\gamma}\right)\right]\mathcal{C}s+\frac{\Delta p_1}{\bar{p}_d}\left(\frac{\bar{p}_2}{\Delta p_1}-\frac{1}{\gamma}\right)\mathcal{C}\mathcal{L}s^2}$$

where τ_b is an effective time delay between injection and combustion. The gain and phase angle for the response factor,

$$N = (\dot{m}^{o\prime}/p_c^{o\prime})\cos\phi$$

are

$$\frac{\dot{m}^{o\prime}{}_b}{p_c^{o\prime}} = -\frac{\left(\frac{\bar{p}_c}{\Delta p_2}-\frac{1}{\gamma}\right)\left(\frac{\bar{p}_2}{\Delta p_1}-\frac{1}{\gamma}\right)\left(\frac{\Delta p_2}{\bar{p}_2}\right)\left(\frac{\Delta p_1}{\bar{p}_d}\right)\mathcal{C}\omega}{\left(\left[1-\frac{\Delta p_1}{p_d}\left(\frac{\bar{p}_2}{\Delta p_1}-\frac{1}{\gamma}\right)\mathcal{C}\mathcal{L}\omega^2\right]^2+\left\{2\frac{\Delta p_1}{\bar{p}_d}\left[1+\frac{\Delta p_2}{\bar{p}_2}\left(\frac{\bar{p}_2}{\Delta p_1}-\frac{1}{\gamma}\right)\mathcal{C}\omega\right\}^2\right)^{1/2}} \tag{4.4.1–7a}$$

and

$$\phi = \frac{\pi}{2}-\omega\tau_b-\tan^{-1}\frac{2\frac{\Delta p_1}{\bar{p}_d}\left[1+\frac{\Delta p_2}{\bar{p}_2}\left(\frac{\bar{p}_2}{\Delta p_1}-\frac{1}{\gamma}\right)\right]\mathcal{C}\omega}{1-\frac{\Delta p_1}{\bar{p}_d}\left(\frac{\bar{p}_2}{\Delta p_1}-\frac{1}{\gamma}\right)\mathcal{C}\mathcal{L}\omega^2} \tag{4.4.1–7b}$$

A general response curve for a gaseous injection process cannot be presented because of the interacting effects of changes in geometry, gas properties and flow conditions on the response factor. Specific evaluations must be made for each design. The frequency dependence of the hydrogen response factor for a typical injection design used in a 20,000 pound thrust rocket engine is shown in Fig. 4.4.1d. Since the hydrogen injection temperature or density has been a primary variable in the study of the hydrogen-oxygen propellant combination, curves are shown for several hydrogen densities.

As shown in the figure, there is a frequency range at each density for which the response factor is positive. Also, as density increases, the coupling of the flow and pressure perturbations increases as indicated by the magnitude of the response factor. The progression of the frequency of peak response with increasing density is a result of the effect of density on the reactance or tuning of the flow system (for details see Ref. 260).

The magnitude of the hydrogen flow response factor is large compared to that for other processes considered in this section. The hydrogen flow system would therefore be expected to have a significant role in determining the stability of a hydrogen-oxygen rocket engine.

JET ATOMIZATION: The atomization process is of particular dynamic importance when extremely small drops are formed in the vapor of the partner propellant and cause rapid burning. Atomization rate may then be the rate controlling process in the dynamic system and the response factor for the atomization process is required to establish stability criteria.

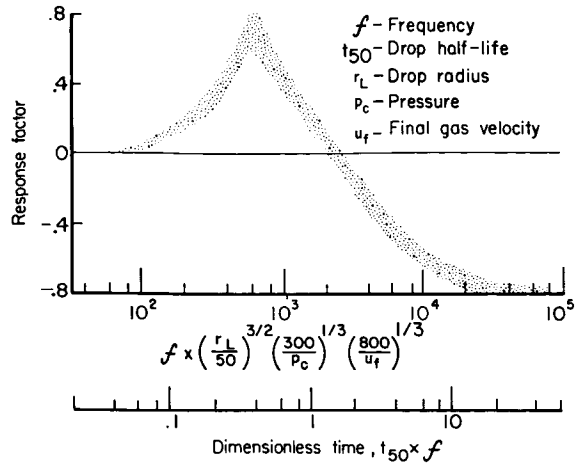

FIGURE 4.4.1a.—Nonlinear frequency response for n-heptane vaporization process.

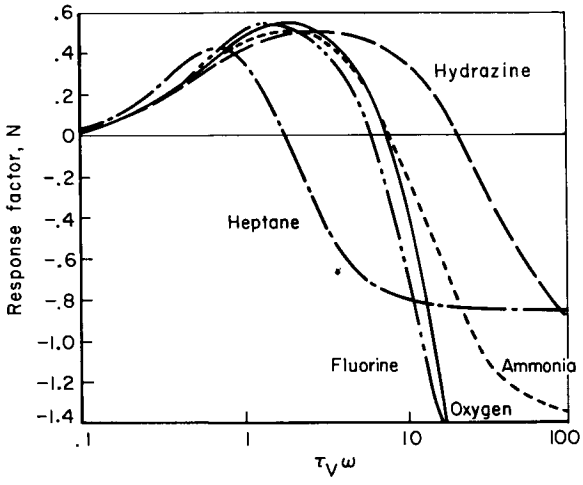

FIGURE 4.4.1b.—Linear frequency response for vaporization process of various propellants.

Analysis of liquid jet atomization,[340] has provided some insight into the magnitude and variations of the response factor for the atomization process. The results of the analysis have a degree of applicability to liquid sheets, drops, ligaments and possibly gaseous jets because a basic distortion or dispersion mechanism has been analyzed. The mechanism is that of liquid distortion caused by forces related to environmental conditions within the combustion chamber. Atomization or breakup of a liquid mass occurs when this distortion reaches a critical value. For an

TABLE 4.4.1b.—PROPERTIES AT EQUILIBRIUM DROP VAPORIZATION TEMPERATURE

[$p_c = 300$ psi]

Propellant	T_L, °R	p_v, psia	c_p, Btu/(lb−°R)	h_v, Btu/lb	β	b
Heptane	845	133	0.701	93.8	1.36	8.1
Oxygen	234	275	.421	63.8	4.43	6.5
Fluorine	220	255	.376	47.8	2.95	6.9
Ammonia	554	205	1.152	48.3	1.88	8.8
Hydrazine	859	165	.754	1318	1.53	10.0

element of liquid jet this time dependent atomization mechanism is given by

$$S = \frac{2}{\rho_L d_L^2} \int_{t-\tau_a}^{t} dt' \int_{t-\tau_a}^{t'} \rho(t'')[\Delta V(t'')]^2 \, dt''$$

The following atomization rate expression is obtained when a constant critical distortion, S, is assumed for all jet elements:

$$\dot{m}' = \frac{\int_{t-\tau_a}^{t} \rho(t')[\Delta V(t')]^2 \, dt'}{\tau_a\{\rho(t-\tau_a)[\Delta V(t-\tau_a)]^2\}} - 1$$

For atomization within a traveling transverse acoustic mode, the response factor obtained from considering only first harmonic content of the applied force is given by

$$N = \frac{1}{\gamma}\left[\frac{|u_L - u_x|^2 + \frac{3}{4}\hat{u}_\theta'^2 + \frac{1}{4}\hat{u}_r'^2}{|u_L - u_x|^2 + \frac{1}{2}\hat{u}_\theta'^2 + \frac{1}{2}\hat{u}_r'^2}\right] \times \left(\frac{\sin \omega\bar{\tau}_a}{\omega\bar{\tau}_a} - \cos \omega\bar{\tau}_a\right) \quad (4.4.1\text{–}8)$$

Properties of this function are shown in Fig. 4.4.1c. The periodic variation of the response factor with $\omega\bar{\tau}_a$ is characteristic of a time delay mechanism. The response factor attains extreme

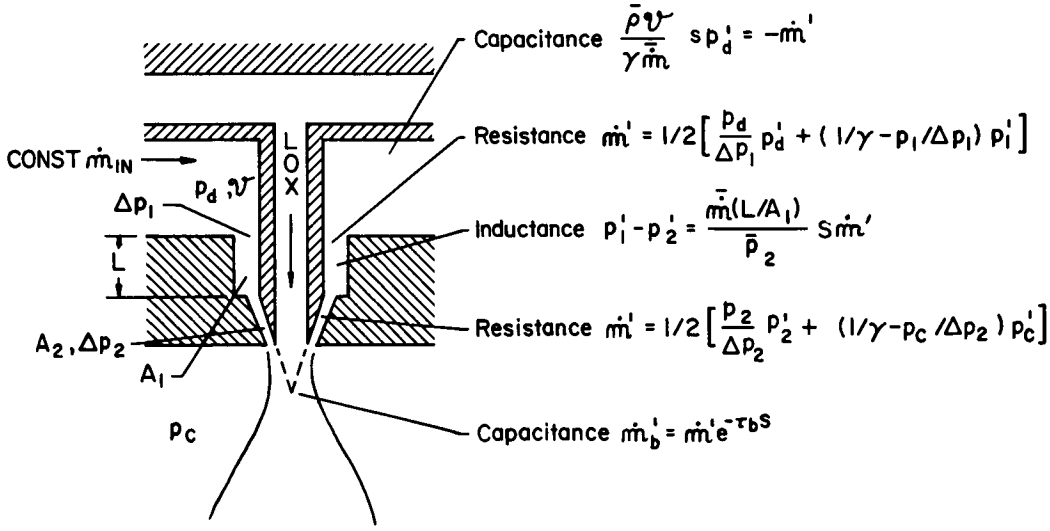

FIGURE 4.4.1c.—Model for gaseous hydrogen injection process.

values of about ± 1 for small amplitude perturbations ($\hat{u}_\theta'$ and $\hat{u}_r'$ approaching zero). These values are exceeded for finite amplitude oscillations. For a particular frequency of oscillation, the mean atomization time, $\bar{\tau}_a$, determines whether the process has a positive or negative contribution to stability. For a liquid jet this time can be estimated from the jet velocity and the mean breakup length.[146]

Although this analysis depends on a simplification of a very complex process, it shows the significance of the atomization process in the dynamic system, a probable magnitude of the response factor, and the relative effect of atomization parameters.

*4.4.1.3 Dykema analysis.**—The following nomenclature pertains to Sect. 4.4.1.3:

l	Radial distance from drop surface to flame
N_s	Stability correlating parameter, $\pi f(r_f - r_L)^2/\mathfrak{D}_F$
$\mathfrak{N}$	Number of drops of mean-size d_{30} per unit volume near the injector face
$\mathfrak{N}_i$	Number of injection orifices
Q'	Unsteady component of heat added per unit volume when the pressure is greater than the mean
$\dot{Q}_0'$	Unsteady component of heat release rate per unit volume near the injector face
Y_F	Mass fraction of fuel
$\bar{Y}_{FL}$	Mean mass fraction of species F at droplet surface
β	Frequency parameter, $\sqrt{\omega/2\mathfrak{D}_F}$
κ	Ratio of flame radius to droplet radius, r_f/r_L
ϕ_F	Phase angle between heat release and chamber pressure oscillations
ψ	Dimensionless parameter related to in-phase combustion gain, $\frac{\sqrt{N_s}\cos\phi}{(\cosh 2\sqrt{N_s} - \cos 2\sqrt{N_s})^{1/2}}$

High-frequency combustion instability has been observed in large engines at frequencies as low as 500 Hz, corresponding to an oscillation period as long as 2 millisec. Instabilities of this type appear to be wholly thrust-chamber-oriented, and appear to exhibit a time delay behavior, as evidenced by regions of stability and instability. Some process or series of processes in the spray combustion, therefore, must be sufficiently slow to affect appreciably the dynamics of spray combustion at frequencies as low as 500 Hz. The intent of this

* O. W. Dykema, Author.

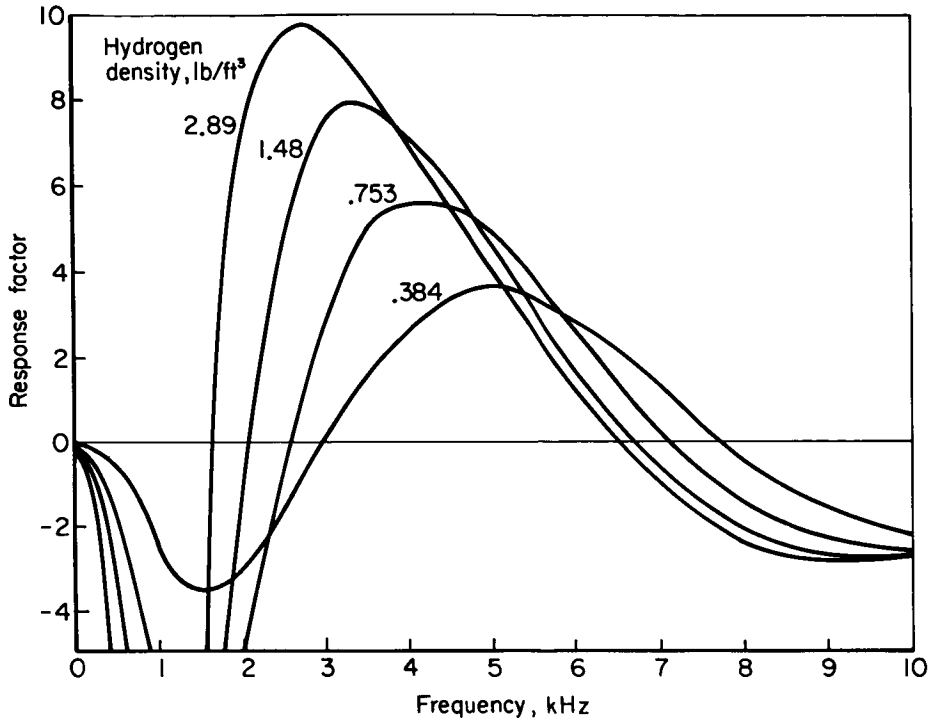

FIGURE 4.4.1d.—Typical frequency response for gaseous hydrogen injection process.

analysis was to develop an engineering model, of the response factor type, that can be used to correlate stability experience and serve as a guide for design and development efforts.[236]

It is assumed that the controlling process is that of mass transfer from the liquid surface to the flame by molecular diffusion due to concentration gradients. Mass transfer due to radial pressure gradients in the region of the burning droplet is considered to occur much more rapidly than that due to concentration gradients, and is therefore neglected. One result of this assumption is that the diffusion coefficient is a function of the mean pressure level, but not of the oscillatory component of pressure. Similarly, the scale of the burning droplet is considered small compared to the combustion chamber dimensions and, therefore, pressure gradients due to the oscillating pressure in the chamber are assumed to be negligibly small in the region of the droplet.

In considering the unsteady burning of a single droplet, the following assumptions are made in addition to those presented above:

1. The droplet is spherical and is surrounded by a concentric spherical flame.
2. Droplet and flame radii and droplet temperature are constant over the period of the oscillation.
3. Liquid-vapor phase equilibrium is maintained at the droplet surface.

The following simplifying assumptions are necessary to apply the single droplet results to a combustion chamber:

4. Mass transfer by molecular diffusion is very rapid if the boundary layer around the droplet is scrubbed thin by high relative gas velocities. The chamber axial location where this boundary layer is thickest is at the region where the relative velocity passes through zero. This region has been found to be close to the injector face and does appear to coincide with a region of greatest sensitivity to combustion instability. Therefore, this axial location, within the first few inches of chamber length, is assumed to be the important region.

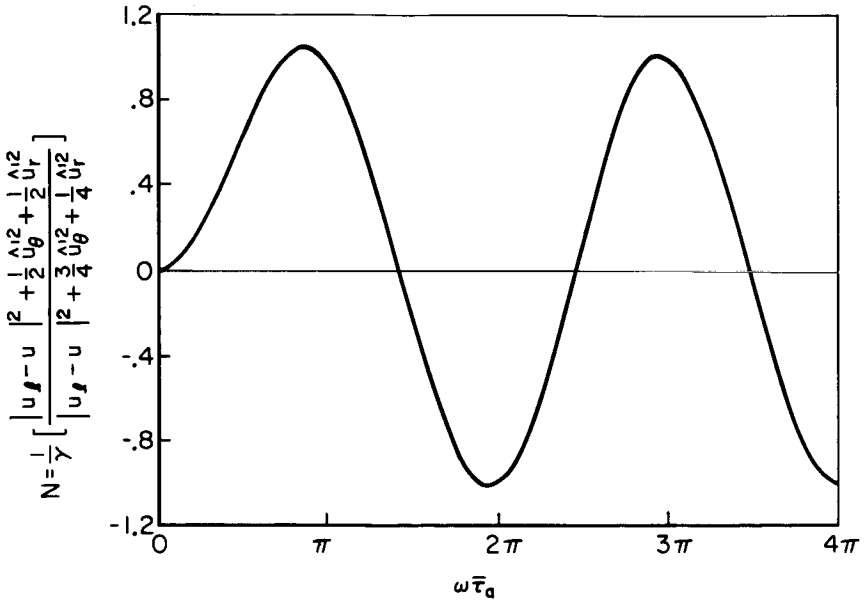

FIGURE 4.4.1e.—Frequency response of liquid jet atomization process.

5. As a result of assumption 4, only the initial spray size distribution is of interest. The decrease in spray mean size and/or the change in distribution as the burning spray proceeds down the chamber can be neglected.
6. Considering the accuracy with which a spray mean size and distribution can be predicted in a hot firing of a large rocket engine using standard production injectors, it is considered that only the variation of the mean drop size with orifice diameter and injection velocity can be assumed sufficiently general to be useful. Therefore, the spray is considered to be of a single mean size,[375] and the distribution of sizes is ignored.
7. Finally, for purposes of simplicity, the assumption is made that the axial velocity of the spray near the injector face is constant and equal to the orifice exit velocity.

From the basic assumption that molecular diffusion by concentration gradient is the important mass transfer process, the unsteady-state equation for fuel vapor mass fraction Y_F as a function of radial position and time is

$$\frac{\partial Y_F}{\partial t} = \mathfrak{D}_F \left[\frac{\partial^2 Y_F}{\partial r^2} + \frac{2}{r}\frac{\partial Y_F}{\partial r} \right] \qquad (4.4.1\text{–}9)$$

where the boundary conditions are

$$Y_F = 0 \qquad \text{at } r = r_f \quad \text{(flame)}$$

$$Y_F = Y_{FL} \qquad \text{at } r = r_L \quad \text{(liquid surface)}$$

Assuming oscillations of the form

$$p_c = \bar{p}_c + p_c' e^{i\omega t}$$

$$Y_F = \bar{Y}_F + Y_F' e^{i\omega t}$$

The solution of Eq. (4.4.1–9) can be expressed as

$$\bar{Y}_F = \bar{Y}_{FL}\left(1 - \frac{r}{r_f}\right)$$

$$Y_F' = Y_{FL}' \frac{r_L}{r} \frac{\sinh[\beta(r_f - r)(1+i)]}{\sinh[\beta(r_f - r_L)(1+i)]} \qquad (4.4.1\text{–}10)$$

where

$$\beta = \sqrt{\frac{\omega}{2\mathfrak{D}_F}}$$

Assuming that phase equilibrium is maintained at the droplet surface and that the chamber gases are perfect,

$$\frac{Y_{FL}'}{\bar{Y}_{FL}} = -\frac{p_c'}{\bar{\rho}_c \Re T_c} \qquad (4.4.1\text{–}11)$$

Then the perturbation of the mass flux into the flame is given by

$$\dot{m}_F' = -4\pi r_f^2 \bar{\rho}_c \mathfrak{D}_F \left.\frac{dY_F'}{dr}\right|_{r=r_f}$$

$$= \frac{4\pi r_f r_L l \omega \bar{Y}_{FL}}{\Re T_c} \left[\frac{-\exp(i\phi_F)}{\beta l(\cosh 2\beta l - \cos 2\beta l)^{1/2}}\right] \qquad (4.4.1\text{–}12)$$

where

$$l = r_f - r_L$$

and

$$\phi_F = \frac{\pi}{4} - \tan^{-1}(\coth \beta l \tan \beta l)$$

A solution can be obtained for the unsteady component of the heat release rate in a unit volume of the chamber by summing the contributions of all droplets in the unit volume. Since Eq. (4.4.1–12) includes a dependence on the drop radius, the drop size distribution of the spray at the particular location in the chamber should be included in the calculation. To simplify the analysis, the droplets are assumed to be of uniform size. Then the perturbation heat release per unit volume is

$$\dot{Q}_0' = \mathfrak{N} h_R \dot{m}_F'$$

where

$$\mathfrak{N} = \frac{3}{4\pi} \frac{A_i}{A_c r_L^3}$$

is the number of drops per unit volume.

According to the Rayleigh criterion, instability will result if an excess of heat is added during the time that the chamber pressure is greater than the mean. Therefore, since the pressure oscillation is given physically by

$$\Re e(p_c' e^{i\omega t}) = p_c' \cos \omega t$$

the stability criterion is obtained by integrating $(\dot{Q}_0'/p_c') \cos \omega t$ over the half-period

$$-\pi/2 \leq \omega t \leq \pi/2,$$

which yields

$$\frac{Q'}{p_c'} = 6 \frac{A_i}{A_c} \frac{\kappa(\kappa-1)}{\Re T_c} h_R \bar{Y}_{FL} \left[\frac{-\cos \phi_F}{\beta l(\cosh 2\beta l - \cos 2\beta l)^{1/2}}\right] \qquad (4.4.1\text{–}13)$$

where $\kappa = r_f/r_c$. Thus, neglecting damping, instability will occur when Q'/p_c' is positive. Since the term preceding the brackets is inherently positive, stability depends only on the value of the bracketed term, which can be written in the form

$$\left[\frac{\psi(N_s)}{N_s}\right]$$

where

$$N_s = (\beta l)^2 = \frac{\pi(\beta-1)^2 f r_L^2}{\mathfrak{D}_F} \qquad (4.4.1\text{–}14)$$

is a stability correlating parameter, and

$$\psi(N_s) = -\frac{\sqrt{N_s} \cos[\pi/4 - \tan^{-1}(\coth \sqrt{N_s} \tan \sqrt{N_s})]}{(\cosh 2\sqrt{N_s} - \cos 2\sqrt{N_s})^{1/2}} \qquad (4.4.1\text{–}15)$$

The dependence of the combustion gain on the parameter N_s is shown by the plot of Q'/Q'_{max} in Fig. 4.4.1f. The first four zeros occur at 5.6, 30, 75, and 140, with two ranges of positive gain, $5.6 < N_s < 30$ and $75 < N_s < 140$. These ranges correspond to potentially unstable operation. Damping can be considered semi-quantitatively by requiring the combustion gain to be sufficiently large, i.e., above some threshold value. The gain is so small in the range $75 < N_s < 140$ that most systems should have enough damping to remain stable under those conditions.

It can be seen from Fig. 4.4.1f and Eq. (4.4.1–14) that the frequency of greatest combustion gain increases with decreasing droplet size, which is in general agreement with other theoretical and experimental evidence. Detailed discussion of the application of this analysis in the design and development of stable rocket combustors is presented in Sect. 6.5.2.

*4.4.1.4 Modal energy analysis.**—The following nomenclature pertains to Sect. 4.4.1.4:

A_k	Cross-section of an equivalent one-dimensional mode
B_{kj}	Dimensionless shear coefficient
C_{ik}	Coupled work coefficient

* C. K. Leeper, Author.

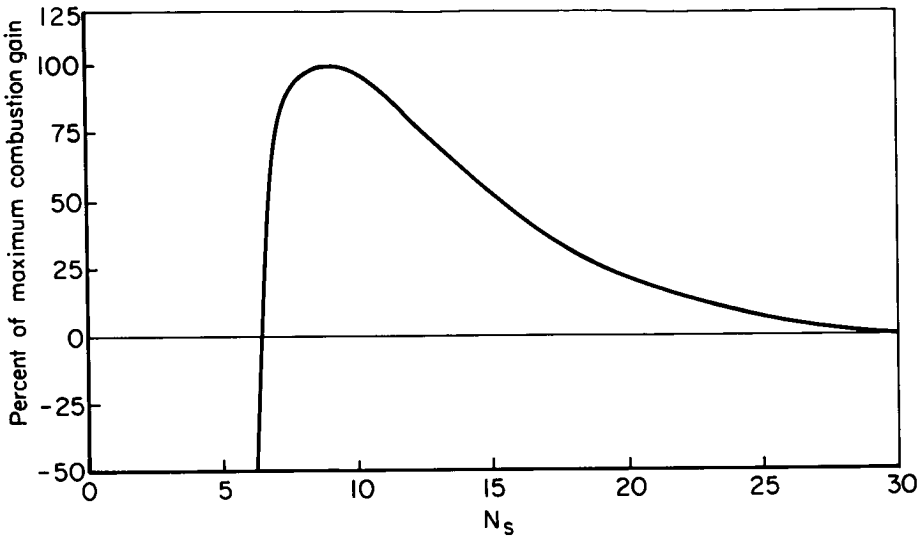

FIGURE 4.4.1f.—Theoretical variation of combustion gain with the stability parameter N_s.

e_{kj}	Energy density at position j on system boundary
E_k	Energy stored in k^{th} mode
G_{kj}	Coefficient relating energy outflow to pressure oscillation
H_{kj}	Coefficient relating energy outflow to velocity oscillation
$\overline{K}_k$	Ratio of k mode to one-dimensional-mode average energy density
$\overline{K}_p$	Volume-averaged correction for nonlinear compression
K_v	Correction for kinetic energy residuals
k_k	Number of wavelengths in k^{th} mode
l_{wk}	Wavelength of kth mode, at_{wk}
$\mathfrak{M}_{nj}$	Mach number normal to boundary at location j
N_{kj}	Nozzle energy density coefficient
p_k'	Instantaneous pressure oscillation amplitude, k^{th} mode
$\hat{p}_k'$	Largest value of p_k'
q	Radiant heat transfer coefficient
$\dot{Q}_k$	Rate of heat transfer to k^{th} mode
R_k	Logarithmic rate of divergence of kth mode, $R_k = \left(\frac{10}{2.303}\right)\frac{l_{wk}}{aE_k}\frac{dE_k}{dt}$
dS	Area element of boundary
$\frac{U_{kj}\cos\phi_k}{A_j}$	Outflow per unit area of boundary in phase with pressure oscillation
v_k'	Velocity oscillation amplitude (instantaneous), k^{th} mode
$\hat{v}_k'$	Largest value of v_k'
v_{kj}	Velocity oscillation at location j
$\dot{W}_k$	Rate at which work is done by k^{th} mode
$\dot{W}_{ik}$	Coupled work (of kth mode or i^{th} mode)
α	Specific admittance

Subscripts:

k	Mode under consideration
i	Mode interacting with k^{th} mode
j	Position on boundary

The degree of stability of both high and low frequency oscillations of combustion systems may be analyzed by examining the mechanical energy stored in each mode of oscillation of the system and the growth or decay of this stored energy as a function of time. When the net gain rate for a mode is positive, it stores the excess by increasing its amplitude, a regenerative process that can destroy the system.

The modal energy analysis describes the growth or decay rate of stored energy, E_k, of the kth mode in terms of system variables and loss and gain coefficients for the combustion process and the

several boundaries. Coefficients may be obtained from full- or subscale experiments or theory. This section derives general system equations from postulated boundary gain and loss laws, and describes the use of these equations to obtain coefficient data.

The energy stored in the kth mode is obtained by integrating the potential and kinetic energies for all compliances and masses in the system. The energy stored in the fluids, to which must be added the energy of vibration of walls and other boundaries, if significant, is given by

$$E_k = \int_v \left(\frac{p_k'^2 K_p}{2\rho a^2} + \frac{\rho v_k'^2}{2} \right) d\mho \quad (4.4.1\text{–}16)$$

where p_k' and v_k' are the pressure and velocity oscillation amplitudes. If one selects the time of maximum pressure in the mode to perform the integration, the kinetic energy will be small and, in the absence of significant stored energy in the boundaries, the system energy may be expressed as

$$E_k = \left[\frac{(\hat{p}_k')^2}{2\rho a^2} \right] \left(\frac{\bar{K}_k}{2} \right) (A_k l_{wk} k_k) \bar{K}_p K_v \quad (4.4.1\text{–}17)$$

The first factor in this equation is the potential energy density at the point of largest k-mode pressure oscillation in the system ($\hat{p}_k'$). The second term relates the peak energy density to the average for the mode, where $\bar{K}_k$ is the ratio of the average energy density for the k mode to that for a one-dimensional (sinusoidal) mode. The third term is the mode volume, where A_k is the cross section of an equivalent one-dimensional mode, and k_k is the number of wavelengths in the mode. The coefficients $\bar{K}_p$ and K_v are the volume-averaged correction for nonlinear compression and the correction for kinetic energy residuals, respectively. In a linear, one-dimensional system, with velocity oscillation 90° out of phase with pressure, the K's are all unity.

The rate of divergence of the kth mode stored energy can be expressed in terms of heat transfer, work, coupled work, and net outflow of material

$$\frac{dE_k}{dt} = \dot{Q}_k - \dot{W}_k - \dot{W}_{ik} - \int_S e_{kj} \mathbf{V} \cdot \overline{\mathbf{dS}} \quad (4.4.1\text{–}18)$$

Here, the subscript i refers to any other mode that interacts with the kth mode, and j is a position summation index identifying a specific portion of the boundary S and the conditions there.

The heat transfer $\dot{Q}_k$ (which is normally negligible) consists of the radiant transfer from the gas in the chamber to the chamber walls plus shear losses at the walls:

$$\dot{Q}_k = -q \left[\frac{(\hat{p}_k')^2}{2\rho a^2} \right] \left(\frac{K_k}{2} \right) (A_k l_{wk} k_k) - \int_S \frac{B_{kj} (v_{kj}')^2}{2\rho a} \left(\frac{\hat{p}_k'}{\hat{v}_k'} \right)^2 dS \quad (4.4.1\text{–}19)$$

where the radiant transfer is taken to be linearly proportional to the potential energy. The second term represents the shear losses, and is written in terms of a dimensionless shear coefficient B_{kj} and the local oscillating bulk velocity v_{kj}'. The constant 2 results from using peak values ($\hat{p}_k', \hat{v}_k'$) rather than rms values.

Work terms are provided by the combustion zone, wall damping, nozzle damping and feed system damping. Each is considered to be a frequency-dependent oscillating source which is pressure-and-velocity-sensitive, but insensitive to the rates of change of the amplitudes of these quantities. The general expression for work is given by

$$\dot{W}_k = \int_S \frac{p_k' U_{kj} \cos \phi_k}{2A_j} dS \quad (4.4.1\text{–}20)$$

where $(U_{kj} \cos \phi_k)/A_j$ is the in-phase outflow per unit area of wall, injector or nozzle flow cross section, which can be related to the pressure and velocity oscillations of the kth mode by

$$\frac{U_{kj} \cos \phi_k}{A_j} = \frac{G_{kj}}{\rho a} p_{kj}' + \frac{H_{kj}}{\rho a} \left(\frac{\hat{p}_k'}{\hat{v}_k'} \right) v_{kj}' \quad (4.4.1\text{–}21)$$

where G_{kj} and H_{kj} are dimensionless coefficients.

The combustion zone normally produces an in-phase inflow, and does work *on* the system, leading to a negative value of G. Similarly, a portion of the stored energy being swept out the nozzle by the steady flow re-radiates into the system, giving a negative G. Wall work quantities for ablative chambers are usually positive and small. Tuned resonator (linear) wall work quantities are positive and significant in selected frequency ranges.

The feed system contributes damping or work input by oscillating the propellant feed rates at

the points of injection. If the combustion process output, resulting from the feed oscillations, is 180° out of phase with the chamber pressure, p_{kj}', then the resulting work output and G are positive and damping is enhanced. The coupled work term

$$\dot{W}_{ik} = \frac{C_{ik}E_k}{\bar{K}_p K_v} \qquad (4.4.1\text{–}22)$$

expresses the outflow of k-mode energy to each of the other system modes.

The nozzle work terms result from the sweeping of material having energy density e_{kj} out of the chamber and the work done by this oscillating material on the chamber contents as the material flows out (see G_{kj} above). The energy density at the nozzle control surface can be expressed in terms of the pressure amplitude and the local pressure and kinetic energy coefficients as

$$e_{kj} = \frac{(p_{kj}')^2 K_p}{2\rho a^2} + \frac{\rho (v_{kj}')^2}{2}$$

$$= N_{kj}\left[\frac{(\hat{p}_k')^2 K_{pj} K_{vj}}{2\rho a^2}\right]\left(\frac{\bar{K}_k}{2}\right) \qquad (4.4.1\text{–}23)$$

Traveling waves, flowing in from the portion of the nozzle not included within the control volume, contribute energy influx. Crocco and Sirignano[196] and Culick[202] have derived theoretical expressions for these terms (also see Sect. 3.6).

The equivalent one-dimensional-mode cross section A_k is defined in terms of the system volume and the mode wavelength l_{wk}

$$A_k = \frac{\mathcal{V}}{l_{wk} k_k} = \frac{\mathcal{V}}{a t_{wk} k_k} \qquad (4.4.1\text{–}24)$$

where t_{wk} is the k-mode oscillation period.

The energy balance of the kth mode can be expanded by substituting Eq. (4.4.1–19) through (–24) into Eq. (–18) and defining a logarithmic rate of divergence

$$R_k = \frac{+10}{2.303}\frac{d \ln E_k}{dt a/l_{wk}} = \frac{+10}{2.303}\frac{dE_k}{dt}\frac{l_{wk}}{a}\frac{1}{E_k}$$

where R_k has the units db/cycle. Thus,

$$R_k = \frac{-10}{2.303}\frac{1}{\bar{K}_p K_v k_k}\left\{\frac{k_k l_{wk}}{a}\left(q + \sum_i C_{ik}\right)\right.$$
$$+ \sum_j \left(\frac{A_j}{A_k}\right)\mathfrak{M}_{aj} N_{kj} K_{pj} K_{vj} + \frac{2}{\bar{K}_k}\sum_j \left(\frac{A_j}{A_k}\right)$$
$$\times\left[\left(\frac{v_{kj}'}{\hat{v}_k'}\right)^2 B_{kj} + \left(\frac{p_{kj}'}{\hat{p}_k'}\right)^2 G_{kj}\right.$$
$$\left.\left. + \left(\frac{v_{kj}'}{\hat{v}_k'}\right)\left(\frac{p_{kj}'}{\hat{p}_k'}\right) H_{kj}\right]\right\} \qquad (4.4.1\text{–}25)$$

Note that the G_{kj} sum includes terms from the combustion elements, wall absorption, feed system damping and nozzle traveling-wave feedback. Terms q and C_{ik} are bulk terms, while B_{kj}, H_{kj} and N_{kj} express wall shear, combustion sensitivity to oscillating velocity, and nozzle outflow of energetic material, respectively.

To make use of Eq. (4.4.1–25) coefficients must be obtained by comparison tests in sub- or full-scale apparatus. The coefficient G for an absorbing wall material is obtained by measuring R_k (at the desired frequency) for a test chamber, injector and nozzle, using first a hard wall chamber as standard and then a chamber lined in whole or in part with the absorbing material. The G value for the hard wall is assumed negligible. The G for the absorber is calculated by eliminating common unknowns from Eq. (4.4.1–25) for the two systems. Relative G values for two types of injection elements can be determined similarly, using R_k values from comparison firings of one injector of each type in a common system, and solving, Eq. (4.4.1–25) for the change in G. Coefficients H_{kj} are determined by comparing the uncharacterized element with a symmetrical injection element, for which H_{kj} is zero, in successive firings in a common system.

Measuring of absolute values for combustion G's and nozzle G's and N's is more difficult. Combustion G's can, of course, be based on measured R_k values and calculated nozzle coefficients. For example, the theory yields a nozzle conductance, $\mathfrak{Re}(\alpha) = N'_{kj}$, where N'_{kj} combines both N_{kj} and nozzle G effects. Further, if one can determine one nozzle coefficient as a function of frequency, all other nozzle and combustion coefficients can then be obtained by comparison tests. Cold-flow nozzle tests corrected for gain or loss

characteristics for the cold flow into the chamber could prove useful here. Or, the external acoustic field of a nozzle could be integrated to determine the nozzle work output. Care is needed to assure negligible acoustic field radiation from the test chamber in field tests of a nozzle.

Combustion element G values are best determined by measuring R_k while firing the elements in chambers having simple geometry, known wall absorption, and a nozzle having calibrated losses. By using a series of chambers with one element type, a G vs. frequency plot can be obtained for the element. Simple geometries facilitate the calculation of K_k and minimize coupling (C_{ik}). Values for B_{kj} and q can usually be assumed to be negligible.

The modal energy analysis has three principal applications: (a) correlating measured gain and loss characteristics of system elements for comparison with theories, (b) assessment of stability improvements to be realized by substituting one (characterized) element or chamber material for another, and (c) combining measured characteristics from a variety of sources to predict the stability sign and magnitude for new designs. Data from subscale systems may be used in all three applications. Knowledge of mode pressure and velocity distributions in the full scale geometry is necessary for the last application. This may be approximated analytically, or measured in an acoustical model.

4.4.2 Similarity Approach*

4.4.2.1 Similarity techniques.—In the most general sense, all approaches to the development of models of rocket combustion can be regarded as similarity approaches. The universal objective is to establish combustor characteristics which are "similar" in all combustors exhibiting the same dynamic combustion behavior. The similarity characteristics may or may not involve geometric variables.

Weller, in his review of similarities in combustion,[730] defines five classes of similarity techniques:

1. Complete solution
2. Simplified solutions, such as boundary-layer theory
3. Similarities
4. Dimensional analysis and rational scaling or modeling
5. Empirical scaling or modeling

The discussion of analytical models in this chapter is organized, more or less, according to Weller's classification. There are no models existing today which can be regarded as complete solutions to combustor dynamics. However, most of the models described in the preceding sections of the chapter can be regarded as simplified solutions or similarity solutions since, to varying degrees, they are based upon a priori knowledge of equations governing certain aspects of combustor behavior. In this section, we will review accomplishments in the last two classes, dealing first with analytical similitudes or rational scaling, and second with empirical similitudes.

4.4.2.2 Analytical similitudes.—A classical work on similarities in chemical systems, and one universally cited in subsequent works, is that of Damköhler.[213] In his treatise, Damköhler specified a series of dimensionless groups of variables, or similarity parameters, as being important in scaling chemical reactors. The underlying principle of the approach is that equality of the parameters between a reactor model and prototype will assure similarity of performance of the two systems. Since the number of different processes occurring in a chemical reactor is large, the number of parameters required to relate these processes also is large. Consequently, it is rarely, if ever, possible to achieve equality of all similarity parameters between the model and prototype systems. Therefore, in dealing with a specific reactor type, such as a rocket combustor, one must identify those parameters which are most significant and attempt to achieve similarity among this limited selection.

Penner[538] was among the first to utilize similarity parameters in developing scaling rules for combustors with similar steady-state performance characteristics. Penner's set of parameters includes five groups associated with flow systems without chemical reaction, viz., Reynolds, Schmidt, Prandtl, Mach and Froude numbers, and two of Damköhler's chemical reaction parameters. To

* E. K. Bastress, I. Miller, and G. H. Harris, Authors.

achieve a workable set of scaling rules, Penner specified a constant chamber pressure and a fixed propellant combination, and ignored the Froude and Mach numbers on the basis that chamber velocities are small. To extend the resulting rules to cover dynamic behavior,[537] i.e., combustion stability, he added a parameter consisting of a ratio of chemical time to wave propagation time. However, this new parameter is incompatible with the others, and Penner essentially concluded that dynamic similarity could be achieved only by abandoning the steady-state performance scaling rules.

Crocco[175] also developed combustor scaling rules for preserving steady and dynamic performance. Instead of utilizing the Damköhler parameters, Crocco defined simple ratios of relevant dimensions, velocities, and times. He also assumed that all significant chemical times are proportional to p^{-n}. Thereupon, Crocco established two scaling rules for steady performance consisting of relationships between the dimension, velocity, and time ratios, and the pressure index, n. His first rule achieves fluid-mechanical similarity, but not combustion similarity. His second rule achieves similarity in combustion processes at the expense of Mach number similarity. The rules coincide for cases where $n = 1$. In extending the rules to include dynamic similarity, Crocco also encountered incompatibilities which become increasingly serious as the value of n departs from unity. Since the pressure dependencies of the complex reactions between rocket propellants are unknown, the validity of the Crocco rules is equally uncertain.

Ross[602] developed combustor scaling rules involving practical chamber design parameters. His treatment of dynamic similarity, however, is limited to the identification of a critical diameter beyond which unstable operation is anticipated.

More recently, Priem and Morrell[566] developed a pair of similarity parameters for correlating high-frequency instability behavior. The first is related to propellant burning rate and is regarded as a measure of energy available for support of a pressure wave. The second is related to viscous effects and is regarded as a measure of the rate of energy extraction from a wave. On this basis, the stability of a combustor would be expected to increase with an increase in the ratio of the second to the first parameter. Priem and Morrell were successful in correlating stability data from a series of oxygen-hydrocarbon combustors using this approach.

It would be difficult to comment on the validity of the approaches described as they remain largely untested, with the possible exception of the last (Priem & Morrell). Effort on the development of scaling rules in the manner of Penner and Crocco has declined in recent years. The following factors have contributed to this decline:

1. With increasing experience in combustor development, high combustion efficiency is achieved more readily than in past years. Consequently, performance scaling rules are no longer a significant goal of combustor research.
2. Combustion instability, on the other hand, continues to plague development efforts, and has become the object of extensive study more or less independent of performance considerations.
3. The availability of high-speed computers has caused effort to be directed toward more complete analytical solutions of combustion dynamics, i.e., upwards on the Weller classification of similarity techniques.

It appears that, because of factors such as these, analytical similitude development offers less promise than other approaches as a means of attaining stable combustor performance.

4.4.2.3 Empirical similitudes.—The following nomenclature pertains to Sect. 4.4.2.3:

BF	Baffle parameters: 1 if baffle present; 0 if no baffle
$b_0, b_1, \ldots b_m$	Coefficients in regression equation
EPA	Number of injection elements per unit injector area, in.$^{-2}$
FO2	Propellant parameter: 1 for LO_2/RP–1; 0 for other
FO3	Propellant parameter: 1 for N_2O_4/A–50; 0 for other
ID_F	Fuel injection distribution parameter (1 for uniform injection)
IDE_F	Fuel injection distribution eccentricity parameter (0 for uniform injection)

L_F	Fuel orifice length
LR	Liner parameter: 1 if acoustic liner present; 0 if none
MPE	Propellant mass flow per injection element, lbm/sec
PE1	Injector element parameter: 1 for coaxial; 0 otherwise
PE2	Injector element parameter: 1 for unlike-impinging; 0 for any other
R^2	Coefficient of determination
S_y^2	Variability of y values
S_e	Standard error of estimate
TPVM	Thrust per unit chamber volume, lb/in.^{3}
$x_1, \ldots x_m$	Independent variables in regression equation
y	Observed value of stability index: 0 for stable test; 1 for unstable test
y_p	Predicted value of stability index
$y^{(s)}$	Stability index for non-pulsed tests
$y^{(p)}$	Stability index for pulsed tests

A purely empirical approach to the development of models of combustion instability was undertaken in 1965.[82] At that time, a vast amount of data on combustor performance existed in various research laboratories and development centers. In preceding years, rocket engines had been developed over wide ranges of thrust level, propellant type, and combustor configuration, and these had exhibited an equally wide range of stability characteristics. The project which was initiated was an attempt to derive meaningful stability models from this backlog of data.

The objectives of the project were to collect experimental data from records of engine stability tests, to use these data to derive empirical relationships between engine design and stability characteristics, and to establish criteria, based on these relationships, for the design of stably operating engines. In this section a brief description of the statistical procedures is given, together with some of the resulting correlation equations. Comparisons with experiment and possible methods of applying the correlation equations in engine design are discussed in Sect. 6.6.

To facilitate the collection of data, a data collection system was developed consisting of a series of computer coding sheets and an instruction manual. This system was adopted later by the ICRPG Working Group on Liquid Propellant Combustion Instability as a standard data collection method.[10] Using this system, data from approximately 3900 engine tests were recorded by nine different organizations. These data then were filed on magnetic tape and analyzed by statistical methods to determine correlations between engine stability and design and operational parameters.

The principal method used in the analysis of data was regression analysis. This method is based on the assumption that a linear relationship exists between a dependent variable and a number of independent variables.

The dependent variable for the study was combustor instability. In order to be able to assign a numerical value to the level of stability of each engine test, several approaches were tried. The most satisfactory criterion of stability was a simple, two-valued parameter which was assigned a value of zero for a stable test and unity for an unstable test. The assessment of stability was different for pulsed and non-pulsed tests. In the non-pulsed case, if any high frequency pressure oscillations were reported, the test was deemed unstable. All other non-pulsed tests were considered to have been stable. In the pulsed case, a test was considered unstable if a high frequency oscillation developed subsequent to the pulse and did not decay prior to the end of the test. If the oscillation decayed, or if no oscillation was reported, the test was considered stable.

In defining independent variables, it was expected, on the basis of past experience, that relationships between stability and combustor design would be complex and nonlinear. In order to introduce nonlinearity into the analysis, functions of design variables were sought which could be used as independent variables in the regression analysis. Most of the functions used were taken from earlier studies of combustion instability. Additionally, a number of simple design variables and functions of these variables were utilized in the analysis.

To facilitate the analysis, the data were divided into groups based on major design features such as injector element type. Also, engines containing baffles or acoustic absorption liners, and those

which were pulsed, were segregated into separate groups. A correlation, or stability prediction equation, was developed for each data group, the equation incorporating variables appropriate to the engines in that group. The stability prediction equation can be used to calculate a value of an instability parameter for a new engine design. The lower the predicted value of the instability parameter, the higher is the probability that this engine, if built, will be stable.

In the development of a prediction equation, the problem is one of describing a complex multivariate relationship. The resulting relationship, expressed in the form of a "regression equation," is determined from the observations by the method of least squares, which minimizes the sum of the squared deviations between the observed values of the stability characteristic (y) and the predicted values (y_p).

The prediction equations developed are of the form

$$y_p = b_0 + b_1x_1 + b_2x_2 + \cdots + b_mx_m$$

In this equation, y_p is called the *dependent variable* (read "y-predicted"), and it is a measure of predicted stability (a value of a stability parameter); the variables, $x_1, x_2, \ldots, x_m$ are called the *independent variables*, and they are measures of operating conditions and design parameters. This equation is linear in the coefficients $b_0, b_1, b_2, \ldots, b_m$ but it may be nonlinear in one or more of the x-variables. Nonlinearities can be introduced by means of such terms as log x, x^2, etc.

The coefficients $b_0, b_1, \ldots, b_m$ are constants, estimated from the data, which purport to give the effects of the corresponding x-values on y as approximated by y_p. For example, b_1 gives the effect on stability of a unit change in the operating or design variable x_1. If b_1 has a value not statistically significantly different from zero, then we say that x_1 "has no influence" on stability.

Unfortunately, the interpretation of b_1 as the "effect of x_1" is seriously clouded if x_1 is highly correlated with, say, x_2. The effects of two or more highly correlated independent variables are divided in some difficult-to-determine way among the values of their coefficients. Thus, in a nonorthogonal relationship (one with correlated independent variables) such as one ordinarily encounters when working with historical data rather than with the results of a statistically designed experiment, it can be grossly misleading to isolate a given coefficient and argue that its value expresses the effect of varying the associated independent variable. This statement does not imply, however, that use of the *entire equation* for the purpose of predicting values of the dependent variable is invalid.

Associated with a prediction equation are a number of statistical measures which describe its efficacy. Let us denote the original variability of the values of y (the observed stability measure) over all the data points entering the analysis by S_y^2, and the remaining (residual) variability after fitting the regression equation by S_e^2. If the regression equation is to be useful for prediction, we would expect S_e^2 to be much smaller than S_y^2; the quantity $S_y^2 - S_e^2$ measures the *reduction* in variability achieved by the equation. The *relative* reduction in variability,

$$R^2 = \frac{S_y^2 - S_e^2}{S_y^2}$$

is called the *coefficient of determination* and its square root, R, is the *multiple correlation coefficient* associated with the regression equation.

The process of developing prediction equations for stability, was guided by the principle that each equation should contain the least number of meaningful terms consistent with as high a value of R^2 as possible while containing correlations among the independent variables (internal correlations) that are as small as possible. The criterion of "least number of meaningful terms" is a simple application of the philosophical principle of "Occam's Razor" which states in essence that of two competing descriptions of nature which are equally verifiable, the simpler one is preferable. The criterion of high R^2 was adopted to assure the maximum predictive power, and the criterion of low internal correlations was adopted to avoid the inclusion of grossly misleading coefficients in the equations.

These general criteria are in constant competition with one another. One can usually increase R^2 by the simple expedient of including more independent variables (though the increase may be illusory); even when the increase in R^2 is significant (though perhaps slight from a practical point

of view), the inclusion of extra terms may "confound" the relationship by introducing high internal correlations. Thus, in the development of prediction equations for rocket-engine stability, it was found necessary to pass through many iterations, and to apply both engineering and statistical judgment at each step.

The stability prediction equation derived for non-pulsed tests is given in Table 4.4.2a. The equation is based on 1105 observations; the coefficient of determination is

$$R^2 = 0.592$$

and the standard error of estimate is

$$S_e = 0.278$$

Thus, approximately 59 percent of the original variability in the values of the stability parameters was "explained" by the regression equation. The standard error of estimate, $S_e = 0.278$, gives the amount of variability (as measured by the standard deviation) remaining in the value of the stability parameter after the regression equation has been applied.

The prediction equation derived for pulsed tests, shown in Table 4.4.2b is similar in form to the equation for non-pulsed tests, but contains a different set of independent variables. This equation is based on 1284 observations of pulsed tests, and the coefficient of determination is

$$R^2 = 0.259$$

The standard error of estimate is

$$S_e = 0.434$$

Note that the predictive power of the non-pulsed equation ($R^2 = 0.592$) is considerably better than that obtained for the pulsed equation. The reasons for this difficulty in describing the results of pulsed tests are not clearly understood. However, lack of knowledge of the exact positioning of the pulse, difficulties in measuring the severity of the pulse, and the resulting behavior of the engine probably

TABLE 4.4.2a.—GENERAL EQUATION FOR NONPULSED TESTS

[All logarithms are taken to base 10.]

$$
\begin{aligned}
y_p^{(s)} = [&0.49583 - 0.0014639\ (LR - 0.25068) \\
&- \bar{p}_{ci} - 329.95023) \\
&+ 0.024960\ (L_c - 16.24385) \\
&- 0.45096\ (\log \epsilon_c - 0.33429) \\
&- 7.15205\ (BF - 0.36833)\ (\log ID_F + 0.01452) \\
&+ 0.11250\ (LR - 0.25068)\ (L_c/D_c - 2.13785) \\
&- 0.05177\ (FO3 - 0.28507)\ (IDE_F - 1.92209) \\
&- 0.27789\ (FO3 - 0.28507) \\
&- 0.0006173\ (IDE_F - 1.92209)\ (EPA - 3.76607) \\
&+ 1.43317\ (LR - 0.25068)\ (MPE - 1.93154) \\
&+ 2.09309\ (LR - 0.25068) \\
&- 0.30534\ (BF - 0.36833) \\
&- 0.80153\ (PE1 - 0.16561) \\
&+ 0.001229\ (L_c - 16.24385)^2 \\
&+ 0.002199\ (MPE - 1.93154)^2 \\
&- 0.26849\ (\log \epsilon_c - 0.33429)^2 \\
&+ 0.00035321\ (\bar{p}_{ci} - 329.95023)\ (L_c/D_c - 2.13785) \\
&- 0.087008\ (L_c - 16.24385)\ (\log \epsilon_c - 0.33429) \\
&- 0.17222\ (L_c - 16.24385)\ (\log ID_F + 0.01452) \\
&- 0.000131\ (L_c - 16.24385)\ (MPE - 1.93154) \\
&- 0.81565\ (\log ID_F + 0.01452)\ (IDE_F - 1.92209) \\
&- 0.030990\ (L_c/D_c - 2.13785)\ (MPE - 1.93154) \\
&- 0.033444\ (IDE_F - 1.92209)\ (MPE - 1.93154) \\
&+ 0.25448\ (PE1 - 0.16561)\ (L_c/D_c - 2.13785) \\
&- 0.90924\ (PE1 - 0.16561)\ (MPE - 1.93154) \\
&+ 0.17428\ (PE1 - 0.16561)\ (IDE_F - 1.92209) \\
&+ 0.0957\ (PE1 - 0.16561)\ (\log \epsilon_c - 0.33429) \\
&- 0.0003465\ (FO3 - 0.28507)\ (\bar{p}_{ci} - 329.95923) \\
&+ 0.03243\ (FO3 - 0.28507)\ (L_c - 16.24385) \\
&+ 0.00098624\ (BF - 0.36833)\ (\bar{p}_{ci} - 329.95023) \\
&- 1.20213\ (LR - 0.25068)\ (\log \epsilon_c - 0.33429)]
\end{aligned}
$$

TABLE 4.4.2b.—GENERAL EQUATION FOR PULSED TESTS

[All logarithms are taken to base 10]

$$
\begin{aligned}
y_p^{(k)} = [&-5.56684 - 0.16675\ (L_c/D_c - 1.45926) \\
&- 0.26577\ (L_F/d_{iF} - 8.20992) \\
&+ 0.03456\ (TPVM - 4.40439) \\
&+ 0.00009267\ (V_{iOX} - 1065.97697) \\
&- 13.67581\ (\log d_{iF} - 1.69583) \\
&+ 0.15923\ (FO2 - 0.12461) \\
&- 74.95672\ (LR - 0.08022) \\
&- 0.36162\ (BF - 0.11682) \\
&+ 12.57151\ (LR - 0.08022)\ (PE1 - 0.14330) \\
&+ 0.27624\ (BF - 0.11682)\ (PE2 - 0.42991) \\
&- 0.003242\ (TPVM - 4.40439)^2 \\
&- 0.42891\ (\log d_{iF} - 1.69583)^2 \\
&- 0.044068\ (L_c/D_c - 1.45926)\ (TPVM - 4.40439) \\
&+ 0.0003075\ (V_{iOX} - 1065.97697) \\
&(\log d_{iF} - 1.69583) \\
&- 3.09641\ (LR - 0.08022)\ (L_F/d_{iF} - 8.20992) \\
&+ 0.0003577\ (LR - 0.08022)\ (V_{iOX} - 1065.97697) \\
&- 163.91664\ (LR - 0.08022)\ (\log d_{iF} - 1.69583) \\
&- 0.12184\ (PE1 - 0.14330)\ (L_F/d_{iF} - 8.20992) \\
&- 0.15581\ (PE2 - 0.42991)\ (L_c/D_c - 1.45926) \\
&- 0.00002194\ (PE2 - 0.42991)\ (V_{iOX} - 1065.97697) \\
&+ 0.03835\ (PE2 - 0.42991)\ (TPVM - 4.40439) \\
&- 0.40008\ (PE2 - 0.42991)\ (\log d_{iF} - 1.69583)]
\end{aligned}
$$

contributed to the poorer predictive power of the pulsed equation.

For certain engine types it was possible to find special equations having better predictive power than the applicable general equation. Data groups were defined by considering all 32 combinations of the five variables: baffle, liner, pulsing, impinging jets, and annular jets. Based on the availability of data, fourteen principal groups were selected for individual study. A separate prediction equation was developed for each of these groups and compared with the applicable general equation. For certain engine types, these special equations are recommended over the general equations for design purposes. The special equations are similar in form to the general equations, but contain fewer terms. Details are given in Ref. 82.

4.5 COMPARISON OF ANALYTICAL MODELS*

Analysis of unsteady behavior in a rocket combustion chamber is, of course, a special problem within the general field of fluid mechanics. Thus, it encompasses not only the difficulties associated with the nonlinear equations of motion, compressibility, and viscous effects, but also the added complications of chemical reactions and phase changes. Moreover, the behavior actually found in a rocket engine, particularly in the case of a liquid propellant rocket, is likely to be closely related to certain peculiarities of the hardware involved (e.g., the geometry of the chamber and nozzle and the kind of injection system used), which cannot easily be incorporated into a formal analysis. The relatively idealized problems that can be treated must, therefore, be rather carefully interpreted.

It is perhaps not surprising that even with all the effort that has been expended on analysis, observations and measurements contain much information that must be handled quite apart from formal or numerical results. This situation merely emphasizes the obvious fact that the predictive value of available theories is very seriously limited. Even the similarity parameters provided by theory are insufficient for correlation of all data.

* F. E. C. Culick, Author.

Nevertheless, a great deal of understanding and intuition for the problem can be gained by studying even restricted models. In this section the general features of the various analysis methods already covered will be discussed; the differences and similarities will be exposed in some detail. Perhaps the most obvious simplification of the general problem is the use of linearized equations. For this reason, it is convenient to discuss linear and nonlinear models separately. However, many of the assumptions used in the linear models are carried over into the nonlinear case.

The following nomenclature pertains to Sect. 4.5 (see also Sect. 4.2.2):

$\tilde{A}$	Complex quantity measuring time-averaged energy loss at exhaust nozzle
$\tilde{C}$	Complex quantity proportional to time-averaged energy extraction by convection, momentum exchange, and viscous losses in chamber
E_N^2	Quantity proportional to time-averaged total energy in chamber
k	Complex wave number, $\omega - i\lambda$
$\tilde{\chi}$	Complex quantity proportional to time-averaged energy addition due to combustion

Subscript:

N	Denotes N^{th} natural mode

4.5.1 Linear Models

All of the linear calculations have been done for harmonic motions in time. Concern is really with the linear *stability* problem; no truly transient motions have been treated specifically. For example, the behavior subsequent to a small amplitude input pulse has not been analyzed, although this would be an interesting problem to solve, and no particular difficulties should be encountered.

It is true, of course, that for linear problems almost all general information one desires can be obtained from analysis of harmonic motions. The reason for this is that any function of time that is likely to arise in a physical problem can be decomposed into its harmonic components according to the principle of superposition. Thus, for the study of the stability of small disturbances, an arbitrary disturbance may be prescribed at an initial instant as a function of position throughout the chamber. Clearly, the disturbance is stable (i.e., dies out

in time) if and only if all of the component modes decay in time. Hence it is sufficient to examine only the harmonic natural modes.* This general approach to the problem of stability is exactly the kind discussed by Crocco in Sect. 4.2. The results of such an analysis can yield no information concerning the influence of the amplitude of a disturbance.

4.5.1.1 Characteristics of linear stability models.— The simplest oscillation in a rocket chamber is a purely longitudinal wave in which the vibrations are always parallel to the axis. The standing-wave mode shape is only slightly different from the standing wave in an organ pipe closed at both ends. At the injector face the fluctuating velocity vanishes, and at the nozzle it is not quite zero, corresponding to the fact that some energy is lost through the action of the exhaust nozzle. A nonzero time average of the product of velocity and pressure fluctuations means a flow of wave energy out of the chamber due to "p–v" work done by the material in the chamber on that downstream. Because the velocity fluctuation is nearly zero at the entrance to the nozzle, it is not only convenient but realistic to regard the nozzle as a boundary condition on the waves in the chamber and hence break off the calculation of its influence as a separate problem (Sect. 3.6). If a steady wave exists, then the rate at which energy is provided by the combustion-wave interaction is just sufficient to compensate the rate at which energy is lost through the nozzle and due to other possible influences distributed throughout the chamber. The latter include wave interaction with the mean flow, viscous damping at the walls, and drag forces between the gas and liquid phases.

Now, as far as the stability problem is concerned, one is not particularly interested in the mode shape, that is, the distribution of the amplitude of motion in the chamber. The truly important quantity is the rate at which a particular mode will grow or decay in time if it is excited. In such a stability analysis it is convenient to use exponential functions; the time dependence is assumed to have the form $\exp(st)$, where s is the complex frequency $s=\lambda+i\omega$. The decay or growth rate is given by the real part λ, and the principal purpose of the analysis is to determine λ.

Observation of waves in the chamber, as well as the organ pipe analogy, suggests that the linearized problem should not differ very much from the classical problem of acoustics in a closed chamber in the absence of mean flow, combustion, and all energy losses. Hence, one can find formulas for the frequency ω and the growth constant λ in the following form

$$\omega^2=k_N^2+\frac{\gamma\mathfrak{M}_e k_N}{E_N^2}(\tilde{\chi}_I-\tilde{A}_I-\tilde{C}_I) \qquad (4.5.1\text{–}1)$$

$$\lambda=\frac{\mathfrak{M}_e}{2E_N^2}(\tilde{\chi}_R-\tilde{A}_R-\tilde{C}_R) \qquad (4.5.1\text{–}2)$$

where k is a complex wave number such that $s=ik$, E_N is a normalizing quantity proportional to the time-averaged total energy in the chamber, the subscript N indicates the Nth normal mode of the chamber, $\tilde{\chi}$ represents the time-averaged energy addition from the oscillatory combustion process, $\tilde{A}$ corresponds to energy extracted at the chamber boundaries (including the exhaust nozzle), and $\tilde{C}$ includes all other energy losses, such as the drag force on liquid drops and transfer of momentum between the average and oscillatory motions in the gas phase.

The results of any linearized analysis can be put into this form, provided that the admittance function is small. Otherwise the frequency must be found as the solution of a transcendental equation (Sect. 4.2.2.3). For high contraction-ratio chambers the frequencies of the natural modes in a rocket chamber do not differ much from the classical values (i.e., $\omega\approx k_N$), since $\tilde{\chi}$, $\tilde{A}$, and $\tilde{C}$ all have the mean flow Mach number as a multiplying factor. In transverse modes the shift in frequency is normally too small to distinguish experimentally, owing to other uncertainties, and is in any case not of practical interest. On the other hand, for longitudinal modes the frequency shift, due primarily to nozzle effects, can amount to as much as 20%.

The general result for the growth constant,

* In contrast, if nonlinear effects are studied, a disturbance cannot be examined by studying only its harmonic components, although one may choose as a special case a finite-amplitude harmonic motion. The failure of superposition accounts for the qualitative differences and greatly increased complexities of nonlinear as compared to linear calculations.

Eq. (4.5.1–2), contains the stability criterion. Since all fluctuations have the time factor $\exp(st)=\exp(ikt)\sim\exp(\lambda t)$, the necessary and sufficient condition for stability of small disturbances is $\lambda<0$, or

$$\tilde{\chi}_R<\tilde{A}_R+\tilde{C}_R \qquad (4.5.1\text{–}3)$$

Thus, in order for a particular mode to die out, the contribution to the wave energy from the combustion processes should be less than the dissipative contributions due to the nozzle ($\tilde{A}_R$) and the volume contributions represented in $\tilde{C}$ (e.g., convection, momentum exchange, viscous losses).

It should be noted that the quantities $\tilde{\chi}$, $\tilde{A}$, and $\tilde{C}$ must account for all possible contributions throughout the chamber and on the boundaries, with the effects properly weighted according to the mode shape. The results, of course, are complex numbers having different values for each mode. Thus, as one expects, λ is the sum of fractional energy changes due to the processes accounted for in the particular model used.

By far the most uncertain contribution is that represented by $\tilde{\chi}$, which depends on the response of the combustion process to oscillatory motions. It is clear that the distribution of the combustion response relative to the mode shape is an important factor in the stability of a mode. The phase relationship between the pressure and combustion response is expressed by the fact that $\tilde{\chi}$ is a complex number. If, for example, the combustion fluctuation lags the pressure oscillation everywhere by 90°, then $\tilde{\chi}_R=0$ and combustion cannot drive the wave. Maximum driving by the combustion process occurs when the fluctuations are in phase with the pressure oscillations. This is true even if the response is sensitive to velocity fluctuations.

4.5.1.2 Comparison of linear calculations.— Equations (4.5.1–1) and (4.5.1–2) can be used to show how the linear analyses presented in this chapter are related. In the first place, it must be observed that only the sensitive time lag analysis (Sect. 4.2) is complete in the sense that all of the contributions discussed above are taken into account. Thus, only those results can be used to determine a stability boundary with reasonable confidence that significant contributions have not been ignored.

In Sect. 4.2 both longitudinal and transverse modes are treated. Although the time lag model of the combustion response is used, it is clear that other models of the response can equally well be used to compute $\tilde{\chi}$. However, it must be emphasized that numerical results and comparison with data have been obtained only for the time lag model. It is of interest to note that all of the results of Sect. 4.2 have been used essentially in an inverse way. That is, it has been supposed that all other quantities are known, and the two equations for the stability boundary have been used to compute values of the pressure index n and the time lag $\bar{\tau}$ necessary to satisfy the equations. The internal consistency of this procedure has been checked by comparison with experimental results. An important assumption, which seems to be justified by the favorable comparison, is that n and $\bar{\tau}$ are supposed to be independent of frequency. Thus it appears that the values of these two parameters are indeed dominated by the fluid mechanical and chemical processes in the chamber. This is by no means obvious a priori, for in spite of the heuristic argument leading to the response equation, Eq. (4.2.2–10), the latter is really a very special function of frequency.

An obvious feature of the experimental results that was predicted by the theory is the existence of both upper and lower critical lengths, as discussed in connection with Fig. 4.2.2b. The distribution of combustion in the chamber is an important influence on that prediction. In fact, the shape of the stability boundary depends mainly on the fact that combustion occurs in a region of fixed length (independent of total chamber length) and on the particular function of frequency produced in $\tilde{\chi}$ by the time lag model. The results are modified only in detail by the variation of the nozzle admittance function with length and hence with frequency.

It is quite possible that other response functions, when used in the general scheme for computing stability, might also lead to the prediction of upper and lower critical lengths. Since the necessary computations have not been carried out, however, it is not possible to assess quantitatively how the various models compare. Nevertheless, some qualitative observations can be made. In the first place, it is clear that the combustion response, and hence $\tilde{\chi}$, must be a complex number.

This simply expresses the fact that the conversion of liquid to gas and the associated, or subsequent, energy release during combustion cannot follow pressure changes instantaneously. There must be locally a lead or lag, which is expressed for the chamber as a whole by the integral $\tilde{\chi}$.

The response factors discussed in Sect. 4.4.1 are essentially pieces of Eq. (4.5.1–2), the formula for λ given above. They are all proportional to the ratio of a time-averaged energy input to the time-averaged total energy in the chamber. Thus, the response factor introduced by Heidmann and Feiler, Eq. (4.4.1–5a), is practically the same as $\tilde{\chi}/E_N^2$, except for possible numerical multipliers. Subsequently, they consider several specific contributions to this response factor and correctly emphasize the importance of the real part, i.e., the part that is in phase with the pressure fluctuations, and therefore the part that appears in Eq. (4.5.1–2) for the growth constant λ. The response function for the nozzle suggested in Sect. 4.4.1.1 corresponds to the factor $\tilde{A}$ in Eqs. (4.5.1–1) and (4.5.1–2).

Similarly, the analysis by Dykema (Sect. 4.4.1.3) is also a computation of the real part of $\tilde{\chi}$; the result is Eq. (4.4.1–12). However, the calculation is restricted in an essential respect by the assumption that the processes considered respond instantaneously to changes of the environment. As a result, the response is always in phase with the pressure oscillations (i.e., $\tilde{\chi}_I = 0$). Recent work[668] has shown some limitations of this assumption. In particular, it implies that a very important resonance effect of transient heat conduction in the liquid phase is eliminated, thus reducing the magnitude of the response in the frequency range of interest for oscillations in rocket chambers. This transient heat conduction resonance is a well-known effect in the response of a burning solid propellant to pressure oscillations, and has been found to be the dominant contribution to a peak in the response in the frequency range of a few hundred Hz to several thousand Hz.

Obviously, the results of the various computations of the response can be related directly. For example, any model properly handled and integrated will give numbers for $\tilde{\chi}_R$ and $\tilde{\chi}_I$, which in turn can, if desired, be interpreted as the predictions of the pressure index and time lag. In this way one could, in principle, compute stability boundaries directly and avoid the inverse procedure followed by Crocco. There appear to be no complete results of this kind, although some values of n and $\bar{\tau}$ were computed from the Heidmann-Feiler model.[347] This comparison is discussed further in Sect. 6.3.3.

Finally, the modal energy analysis of Sect. 4.4.1.4 is an approach leading to an expression for the logarithmic rate of divergence of the energy, Eq. (4.4.1–22), which is essentially equivalent to Eq. (4.5.1–2). This correspondence is easily seen, for as λ was originally defined, the pressure amplitude grows as $\exp(\lambda t)$ so that the energy E, proportional to the square of the pressure, varies as $\exp(2\lambda t)$. Hence $d\ln E/dt = 2\lambda$, which merely reproduces the interpretation of λ given above. Thus, the various terms of Eq. (4.4.1–22) can either be put in one-to-one correspondence with terms in Eq. (4.5.1–2) or else represent contributions that can be added to λ by arguments similar to those of Sect. 4.4.1.4. A difficulty with the analysis proposed by Leeper is that the correct form of the various convective and momentum exchange terms is far from obvious. It appears that the only way to handle these terms, appearing as $\tilde{C}$ in Eq. (4.5.1–2), is to begin with the full set of differential equations.

These brief remarks may serve to clarify the fact that the various linear analyses are more closely related than perhaps appears at first to be the case. However, some of the analyses are limited to pieces of the problem. A truly comprehensive analysis of the stability boundary must be based on the full equations of motion and consideration of all contributions to the acoustical energy gains and losses. An alleged stability criterion based, for example, on the combustion response alone must be quantitatively in error and qualitatively misleading.

4.5.2 Nonlinear Models

Linear analysis provides a rather general understanding, which is useful both for its own sake and as a guide to the study of nonlinear problems. Owing to vastly increased complications, the analyses of nonlinear problems amount to examination of quite special problems. The results are therefore useful mainly for particular cases and obviously provide some information that cannot be gained from linear calculations. Two approaches

to nonlinear aspects of the stability problem are presented in this chapter. Unlike the linear analyses, these do not fit into a common framework.

First, the nonlinear computations discussed in Sect. 4.2.3 constitute natural extensions of the comprehensive linear analysis discussed in Sect. 4.2.2. An attempt is made to retain all the features that distinguish the problem of motions in a rocket chamber from other nonlinear acoustics problems. It is clear from the discussion given that one is forced to back away from that ambitious goal. The effects on the stability boundaries of nonlinearities in the time lag model of combustion response are found without exceptional difficulty (Sect. 4.2.3.1). However, in treating the deeper nonlinearities associated with the wave motion (Sect. 4.2.3.2), numerous approximations are required. For example, although the presence of the mean flow and the nozzle are accounted for, they are very much simplified.

The calculations of Sect. 4.2.3 are for steady waves (i.e., the solution does not grow or decay with time) so that the results are valid only on the stability boundary. Although an unrealistic boundary condition is used at the exhaust end, and the exchange of momentum between the gaseous and liquid phases is ignored, the results do indicate the kinds of effects due to nonlinear behavior. Thus, both large amplitude continuous oscillations and solutions representing the presence of a finite discontinuity or shock wave appear in the n, τ stability diagram, Fig. 4.2.3b, and direct comparison with the linear results is made.

The second approach (Sect. 4.3) is entirely numerical. In contrast to the linear calculations and the nonlinear analysis of Sect. 4.2.3.2, an initial value problem is treated. That is, a disturbance is introduced and its subsequent growth or decay is calculated numerically. The only practical restriction on the information that can be obtained is the capacity of the computer. As the discussion of Sect. 4.3.1 emphasizes, this restriction is so severe as to prevent examination of the complete three-dimensional problem.

Initially, however, the same basic information must be included: proper specification of the mean flow, the nozzle, combustion, etc. In addition, the viscous terms in the equations of motion are retained in the general formulation. If the viscous terms are ignored, this formulation differs essentially from that of Sect. 4.2 only in the representation of the coupling between the burning rate and the oscillations. The difference in that respect is quite significant, for all of the computations discussed in Sect. 4.3 are based on quasi-steady models of the coupling processes. Thus, if these formulations were linearized, one would find that for purely pressure-sensitive coupling the quantity $\tilde{\chi}$, defined in Sect. 4.5.1, would be real; the fluctuations of energy release would always be in phase with the pressure fluctuations. Any lags in the response would arise only through dependence on velocity fluctuations which, for standing acoustic waves, are 90° out of phase with pressure fluctuations. As remarked above in connection with Dykema's calculations, such an assumption may exclude an important contribution to the coupling, and one that would be strongly dependent on frequency. This must be regarded as a serious drawback of the numerical integration approach as described in this Chapter. It is a restriction, however, that can presumably be corrected within the framework of the numerical approach.

A second limitation of the numerical results is the practical necessity of treating only one- or two-dimensional problems. A treatment of a complete problem accounting correctly for both the exhaust nozzle and three-dimensional features of the injection process and distribution of combustion has not been carried out. Although the favorable effects of both baffles and acoustic liners have been shown,* it is not clear how one can confidently assess the stability of a three-dimensional chamber on the basis of the restricted problems that have so far been handled. In view of the assumptions used, it appears that the numerical results are useful mainly as an indication of local nonlinear effects associated with the viscous processes and exchanges of momentum. Since the combustion processes have been assumed to respond quasi-steadily, any conclusions one draws should strictly be limited to frequencies that are low compared to the characteristic frequency of the controlling combustion process.

Unfortunately, the differences in detail between

* Certain aspects of baffles and liners can, of course, be examined within a linear analysis.

the two types of nonlinear analysis are such that the results cannot be meaningfully compared in a quantitative way.

4.5.3 Concluding Remarks

The ultimate value of an engineering analysis derives from its success in accurate prediction of results required for design and development. However, the problem of combustion instability is so complicated and involves so many variables and parameters that one must settle for much less. In fact, complete analytical solutions cannot now and probably never will be found. Nevertheless, even though short of this goal, modeling and approximate analyses can provide useful understanding and perhaps scaling laws. At the very least, these analytical models can suggest ways of correlating and interpreting experimental observations.

CHAPTER 5

Analytical Models of Low and Intermediate Frequency Instability

5.1 INTRODUCTION*

In this chapter, methods of analysis are presented for those types of combustion instability that depend on the interaction of feed system and combustion process dynamics. Since various aspects of the physical processes involved have been discussed in some detail in Chapter 3, the emphasis here is on constructing useful analytical models for stability prediction. Examples of calculated stability behavior and some experimental data are given, to enhance the reader's understanding of the feed system-combustion process interaction and to indicate the validity of the models. However, details of how the analyses are applied to engine development are saved for Chapter 6.

In addition to the fact that acoustic modes are not excited in the combustion chamber, two characteristics of low and intermediate frequency instability distinguish these types from high frequency combustion instability. First, the feed system is an integral part of the resonant system, whereas in the case of high frequency oscillations the feed system can usually be neglected. The second characteristic is related to the first; that is, because of the injection rate fluctuations, the combustion response is associated primarily with the total time delay between injection and combustion, and only secondarily on the sensitivity of this time delay to local chamber conditions. The distinction between low and intermediate frequency instability is made on the following basis. "Low frequency" implies that wave motion in the combustion chamber is not important. "Intermediate frequency" refers to the situation in which wave motion must be taken into account, but the acoustic modes of the chamber are not excited.

Analyses of feed-coupled combustion instability differ according to the theoretical treatment of the combustion process, and of the feeding process, as well as in the method of obtaining a solution to the governing equations. For example, one of the earliest theories of low frequency instability used a combustion response based on a single, constant time lag and assumed a nonresonant feed line.[673] Later analyses included wave effects in the feed lines,[622] a sensitive (variable) combustion time lag,[173] and separate time delays for fuel and oxidizer combustion.[731] For convenience in presentation, theoretical models of the combustion response are considered first, followed by a discussion of methods of including feed system effects in the stability analysis. Finally, solution methods are presented and compared.

For most low frequency applications, it is sufficient to regard the combustion response as dependent on a constant time delay between injection of the propellants and their conversion to products. Theoretical treatments based on this principle differ mainly in their assumption of either a single time lag to represent both propellants or two time lags, one for each propellant. For intermediate frequency instability, it is desirable to include the sensitivity of the time lag to local changes in the state of the combustion gases. In this case, it is also important to include wave effects, in which phase and amplitude differences between different locations in the chamber exert significant influence on the overall combustion gain.

Solutions of the equations governing the coupled feed system-combustion process behavior can be obtained either by analytical or analog methods. Analytical techniques include a modified Nyquist criterion, evaluation of the conditions at the boundary between stable and unstable

* F. H. Reardon, Author.

operation, and frequency response calculations. Alternative to these analytical methods, it is possible to set up analog models of the engine systems. The stability analysis then consists of introducing a disturbance and observing whether or not the disturbance grows or decays. By varying the system parameters, the limits of stable operation can be traced, and the importance of the various parameters can be determined. Either analog or digital computers can be used for obtaining such a solution.

5.2 CONSTANT COMBUSTION TIME LAG MODELS*

The analyses presented in this section have as their objective the determination of a realistic, tractable representation of the response of the chamber pressure to variations in the propellant injection rates, for use in predicting stability behavior. It must be remembered that the unsteady combustion process in a liquid propellant rocket is extremely complicated and not completely understood. For purposes of stability analysis, it is not necessary nor desirable to attempt to include all of the refinements currently available in steady-state models. It has been demonstrated that the combustion time lag approach is satisfactory for feed-coupled instability analysis. For most low frequency problems, the use of a constant time lag, or lags, gives sufficiently accurate predictions.

The following nomenclature pertains to Sect. 5.2:

G	Dimensionless injection admittance, $-\frac{\bar{p}}{\underline{\dot{m}}} \cdot \frac{\dot{m}_i'}{p'}$
r	Mixture ratio
θ_c	Gas residence time in combustion chamber
μ_b	Fractional burning rate perturbation, $(\dot{m}_b'/\underline{\dot{m}}_b)e^{-st}$
τ_F	Total fuel combustion time
τ_m	Mixing-combustion time
τ_{OX}	Total oxidizer combustion time
τ_T	Overall (total) combustion time lag
τ_v	Atomization-vaporization time
ϕ	Fractional pressure perturbation, $\frac{p'e^{-st}}{\bar{p}}$

* F. H. Reardon and J. Szuch, Authors.

5.2.1 General Approach

In developing a usable combustion equation for application to low frequency instability, the same general scheme of analysis is employed regardless of the model chosen to represent the actual combustion process. Equations are obtained for the variations in chamber pressure, mass flow rate, and density. These quantities are then related by a suitable burning rate equation. This set of equations is reduced to a single equation involving pressure and injection rates by the application of boundary conditions at the injector and nozzle ends of the chamber. The unsteady flow in the chamber is taken to be one-dimensional, consisting of small perturbations superimposed on the steady-state flow. Other general assumptions about the combustion chamber flow are the same as those presented in Sect. 4.1.2.

For low frequency oscillations, the basic governing equation is the mass conservation equation applied to the gas phase, i.e., the rate of increase of the mass of gas within the chamber is equal to the difference between the rate of production of hot gases and the rate of exhaust of these gases. Stated mathematically,

$$\mathcal{V}\frac{\partial \rho}{\partial t} = \dot{m}_b(t) - \dot{m}_e(t) \qquad (5.2.1\text{–}1)$$

where $\mathcal{V}$ is the chamber volume, ρ is the gas density, and $\dot{m}_b$, $\dot{m}_e$ are the mass rates of gas production and exhaust, respectively. Eq. (5.2.1–1) is based on the assumption that the volume occupied by the liquid is very small compared to the total chamber volume. Also, this equation is valid only at low frequencies, such that the period of oscillation is long compared to the time required for a pressure wave to travel the length of the chamber and return. Thus, any small change in pressure will be transmitted essentially instantaneously throughout the chamber; the flow is, therefore, taken to be quasi-steady.

Writing each quantity as the sum of a steady-state part ($^-$) and a perturbation ($'$), Eq. (5.2.1–1) can be rewritten as

$$\theta_c \frac{\partial}{\partial t}\left(\frac{\rho'}{\bar{\rho}}\right) = \frac{\dot{m}_b'}{\underline{\dot{m}}} - \frac{\dot{m}_e'}{\underline{\dot{m}}} \qquad (5.2.1\text{–}2)$$

where

$$\theta_c = \frac{\bar{\rho}\mathcal{V}}{\underline{\dot{m}}} \qquad (5.2.1\text{–}3)$$

is the chamber gas residence time, and $\underline{\dot{m}} = \underline{\dot{m}}_b = \underline{\dot{m}}_e$. Assuming that the combustion gases are perfect, the LHS of Eq. (5.2.1–2) is

$$\theta_c \frac{\partial}{\partial t}\left(\frac{p'}{\bar{p}}\right) - \theta_c \frac{\partial}{\partial t}\left(\frac{T'}{\bar{T}}\right)$$

Although the instantaneous pressure can be assumed to be uniform throughout the chamber, the same cannot be said about the temperature. Because of mixture ratio oscillations produced by the different dynamic response characteristics of the fuel and oxidizer feed systems, the temperature of the burned gases in the combustion zone also oscillates. After burning, each parcel of gas can be assumed to flow isentropically through the chamber. Therefore, the temperature oscillation at the nozzle entrance is not the same as that at the combustion front. The mean temperature perturbation should be obtained by integrating over the chamber volume.[179] However, the usual procedure is to assume that the average chamber temperature is approximately constant. Then the LHS of Eq. (5.2.1–2) becomes simply

$$\theta_c \frac{\partial}{\partial t}\left(\frac{p'}{\bar{p}}\right)$$

For the exhaust flow, the temperature variations can be taken into account, because of the isentropic flow of each gas parcel downstream of the combustion zone. For very low frequency oscillations, the exhaust flow can be assumed to be quasi-steady, so that

$$\dot{m}_e \sim p/\sqrt{T}$$

Hence, the exhaust mass flow perturbation is

$$\frac{\dot{m}_e'}{\underline{\dot{m}}_e} = \frac{p'}{\bar{p}} - \frac{1}{2}\frac{T'}{\bar{T}} \qquad (5.2.1\text{–}4)$$

Substituting this result into Eq. (5.2.1–2) gives

$$\theta_c \frac{\partial}{\partial t}\left(\frac{p'}{\bar{p}}\right) + \left(\frac{p'}{\bar{p}}\right) = \frac{\dot{m}_b'}{\underline{\dot{m}}} + \frac{1}{2}\frac{T'}{\bar{T}} \qquad (5.2.1\text{–}5)$$

for the chamber equation.

More commonly, the last term on the RHS of Eq. (5.2.1–5) is expressed in terms of the characteristic exhaust velocity, c*, i.e.,

$$\frac{1}{2}\frac{T'}{\bar{T}} = \frac{c^{*\prime}}{\bar{c}^*}$$

Since c* is a function of both chamber pressure and mixture ratio,

$$\frac{c^{*\prime}}{\bar{c}^*} = \frac{\bar{r}}{\bar{c}^*}\left(\frac{\partial c^*}{\partial r}\right)_p \frac{r'}{\bar{r}} + \frac{\bar{p}}{\bar{c}^*}\left(\frac{\partial c^*}{\partial p}\right)_r \frac{p'}{\bar{p}}$$

However, the pressure dependence of c* is normally much smaller than the mixture ratio dependence, so that the second term can be neglected. The burning rate $\dot{m}_b$ can be written as the sum of the oxidizer and fuel burning rates:

$$\dot{m}_b = \dot{m}_{OX_b} + \dot{m}_{F_b}$$

The perturbations in burning rate and mixture ratio can then be written in terms of the oxidizer and fuel mass flux perturbations in the combustion zone as

$$\dot{m}_b' = \dot{m}_{OX_b}' + \dot{m}_{F_b}' \qquad (5.2.1\text{–}6)$$

$$\frac{r'}{\bar{r}} \cong \frac{(1+\bar{r})}{\bar{r}\underline{\dot{m}}} \cdot \dot{m}_{OX_b}' - \frac{(1+\bar{r})}{\underline{\dot{m}}} \cdot \dot{m}_{F_b}' \qquad (5.2.1\text{–}7)$$

Inserting the above relations into Eq. (5.2.1–7) yields the governing equation for low frequency oscillations,

$$\theta_c \frac{\partial}{\partial t}\left(\frac{p'}{\bar{p}}\right) + \left(\frac{p'}{\bar{p}}\right) = \frac{1}{\underline{\dot{m}}}\left\{\left[1 + \frac{1+\bar{r}}{\bar{c}^*}\left(\frac{\partial c^*}{\partial r}\right)\right]\dot{m}_{OX_b}' + \left[1 - \frac{\bar{r}(1+\bar{r})}{\bar{c}^*}\left(\frac{\partial c^*}{\partial r}\right)\right]\dot{m}_{F_b}'\right\} \qquad (5.2.1\text{–}8)$$

It remains to determine explicit relations between the burning rates, the injection rates, and the chamber pressure. This is done in the following two sections, using two combustion models appropriate to low frequency instability. Both models are based on the concept of a combustion time lag, which is discussed in detail in Sect. 4.2.1. Here it will suffice to observe that for analytical convenience, the gradual evolution of gaseous combustion products from the initially liquid reactants is represented as a sudden conversion at a time τ_T after injection of the reactants. The time τ_T is variously known as the

combustion time delay, total time lag, or "dead" time. For most cases of low frequency instability, it is sufficiently accurate to regard the total time lag as a constant for a given engine operating point. The consequences of a non-constant combustion time lag coupled with oscillatory injection rates are explored in Sect. 5.3.

5.2.2 Single Time Lag Model

The simplest combustion model is that in which only a single time lag is considered. Since the time lag can be envisioned as the time required for the liquid propellants to travel from the injector to an effective combustion "front," the use of a single time lag implies either that the propellant injection velocities are equal or that only one of the propellants controls the combustion dynamics. For example, with LOX/RP-1 propellants, the liquid oxygen vaporizes so much faster than the RP-1 that the fuel exerts control over the combustion process rates. On the other hand, for a combination such as N_2O_4/A-50, there is no such large difference in vaporization rate to force one propellant to be controlling. Therefore, a single time delay model would be reasonable only when the injection velocities are approximately equal or when one of the feed systems is designed to produce negligible injection rate oscillations in response to chamber pressure fluctuations.

The combustion time lag concept is expressed mathematically as

$$\dot{m}_b(t) = \dot{m}_i(t-\tau_T) \qquad (5.2.2\text{–}1)$$

which introduces the dynamic responses of the feed systems into the combustion chamber analysis. The pressure dependence of the burning rate would enter through the variability of τ_T. However, in this section it is assumed that $\tau_T =$ constant. Therefore, the burning rate perturbations are given by

$$\dot{m}_{OX_b}'(t) = \dot{m}_{OX_i}'(t-\tau_T) \qquad (5.2.2\text{–}2a)$$

$$\dot{m}_{F_b}'(t) = \dot{m}_{F_i}'(t-\tau_T) \qquad (5.2.2\text{–}2b)$$

It is convenient to define injection admittances G_{OX} and G_F by

$$G_{OX} = -\frac{\bar{p}}{\dot{m}} \cdot \frac{\dot{m}_{OX_i}'}{p'}; \qquad G_F = -\frac{\bar{p}}{\dot{m}} \cdot \frac{\dot{m}_{F_i}'}{p'} \qquad (5.2.2\text{–}3)$$

Then

$$\frac{\dot{m}_{OX_b}'(t)}{\dot{m}G_{OX}} = \frac{\dot{m}_{F_b}'(t)}{\dot{m}G_F} = -\frac{p'(t-\tau_T)}{\bar{p}} \qquad (5.2.2\text{–}4)$$

For this linearized theory, the perturbations can be assumed to have exponential time dependence, exp (st), where s is the complex frequency, $s = \lambda + i\omega$. Letting

$$\frac{\dot{m}_b'(t)}{\dot{m}} = \mu_b e^{st}; \qquad \frac{p'(t)}{\bar{p}} = \phi e^{st}$$

Eq. (5.2.2–4) becomes

$$\frac{\mu_{OX_b}}{G_{OX}} = \frac{\mu_{F_b}}{G_F} = -\phi \exp[-s\tau_T] \qquad (5.2.2\text{–}5)$$

Substituting Eq. (5.2.2–5) into Eq. (5.2.1–8) yields

$$\frac{\exp[-s\tau_T]}{1+s\theta_c}\left\{\left[1+\frac{(1+\bar{r})}{\bar{c}^*}\left(\frac{\partial c^*}{\partial r}\right)\right]G_{OX} + \left[1-\frac{\bar{r}(1+\bar{r})}{\bar{c}^*}\left(\frac{\partial c^*}{\partial r}\right)\right]G_F\right\} = -1 \qquad (5.2.2\text{–}6)$$

which is the equation governing the stability of low frequency oscillations. That is, if a value of s that satisfies Eq. (5.2.2–6) has a positive real part (λ), the oscillation will grow. On the other hand, if λ is negative, the oscillation will decay and the engine system will be stable with respect to that oscillation.

5.2.3 Double Time Lag Model

For more general application the double time lag model should be used. In this model, each propellant is assumed to have its own time delay between injection and combustion. Thus,

$$\dot{m}_{OX_b}'(t) = \dot{m}_{OX_i}'(t-\tau_{OX}) \qquad (5.2.3\text{–}1a)$$

$$\dot{m}_{F_b}'(t) = \dot{m}_{F_i}'(t-\tau_F) \qquad (5.2.3\text{–}1b)$$

It is useful to separate the vaporization process from the mixing and reaction, and to assume that the total time lag is the sum of an atomization-vaporization time and a mixing-reaction time, the latter being common to both propellants. In this way the individual atomization and vaporization characteristics of the fuel and oxidizer can be included explicitly in the analysis. Then since

$$\tau_{OX} = \tau_{vOX} + \tau_m \qquad (5.2.3\text{–}2a)$$

$$\tau_F = \tau_{vF} + \tau_m \qquad (5.2.3\text{–}2b)$$

the stability condition expressed by Eq. (5.2.2–6) becomes, for the double time lag model,

$$\frac{\exp[-s\tau_m]}{1+s\theta_c} \left\{ \left[1 + \frac{(1+\bar{r})}{\bar{c}^*}\left(\frac{\partial c^*}{\partial r}\right)\right] G_{OX} \exp[-s\tau_{vOX}] + \left[1 - \frac{\bar{r}(1+\bar{r})}{\bar{c}^*}\left(\frac{\partial c^*}{\partial r}\right)\right] G_F \exp[-s\tau_{vF}] \right\} = -1 \qquad (5.2.3\text{–}3)$$

Both Eq. (5.2.2–6) and Eq. (5.2.3–3) show that low frequency stability depends on the product of a combustion chamber transfer function and a feed system transfer function. In the double time lag model, the vaporization time can be considered to be part of the feed system response. In the case of a gaseous propellant, for example hydrogen fuel, the vaporization time vanishes. Hence

$$\tau_{OX} = \tau_{vOX} + \tau_F$$

and the stability equation becomes

$$\frac{\exp[-s\tau_F]}{1+s\theta_c} \left\{ \left[1 + \frac{1+\bar{r}}{\bar{c}^*}\left(\frac{\partial c^*}{\partial r}\right)\right] G_{OX} \exp[-s\tau_{vOX}] + \left[1 - \frac{\bar{r}(1+\bar{r})}{\bar{c}^*}\left(\frac{\partial c^*}{\partial r}\right)\right] G_F \right\} = -1 \qquad (5.2.3\text{–}4)$$

5.3 VARIABLE COMBUSTION TIME LAG MODELS

The analytical treatment given in Sect. 5.2.2 is based on the interactions of the feed system with the combustion system when the dynamic behavior of the latter is simplified to the point that one parameter alone, the steady-state total time delay, is sufficient to represent it. Certainly this is not rigorously true, even within the schematization of the time delay model. Even the improvement offered by the double time delay concept (Sect. 5.2.3) falls well short of reality, since the time lags are assumed to be constant. Indeed, one explanation of the occurrence of the most important type of instability (high frequency) is based on the variability of the time delay under the effects of the oscillations of the chamber conditions (Sect. 4.2). It is important, therefore, to determine the effects on feed-coupled instability when the time delay is not a constant, but is dynamically affected by the chamber conditions. It has been found that the effect of the time lag sensitivity on low-frequency instability can be neglected if the portion of the total time delay that is sensitive is only a small fraction of the total delay. However, for intermediate-frequency instability, in which both feed system response and wave motion in the chamber are important, the variability of the time lag cannot be neglected. The treatment in this section considers first the low frequency problem in order to show the combustion response modifications introduced by the sensitivity of the time lag. Then the case of intermediate-frequency oscillations is examined to show the wave effects. For simplicity, the latter discussion is concerned with a single combustion time delay.

The following nomenclature pertains to Sect. 5.3 (see also Sects. 4.2.2 and 5.2):

$\mathcal{A}, \mathcal{G}$	Nozzle admittance coefficients
$\tilde{f}$	Overall combustion rate
$\mathcal{H}(s)$	Function representing effect of mixture ratio oscillations
$J(s)$	Ratio of fractional injection velocity perturbation to fractional chamber pressure perturbation
$\mathcal{K}(s)$	Function expressing effect of mass flux oscillations
k	Momentum interchange coefficient
M_1	Mass burning rate perturbation (first-order approximation)
n_r	Mixture ratio "interaction index"
$\mathcal{P}(s)$	Combustion response function for pressure oscillations
W_1, X_1, Y_1, Z_1	Functions defined in Eq. (5.3.2–4)
x_c	Location of concentrated combustion front
ν	Fractional injection velocity perturbation amplitude

τ Sensitive (variable) combustion time lag

τ_i Insensitive (constant) combustion time lag

5.3.1 Low-Frequency Instability*

When the total time lag varies, the injection and burning rates satisfy the equation

$$\dot{m}_b(t)dt = \dot{m}_i(t-\tau_T)\cdot d(t-\tau_T) \quad (5.3.1\text{–}1)$$

Assuming the perturbations from the mean flow to be small, one obtains

$$\frac{\dot{m}_b'(t)}{\underline{\dot{m}}} = \frac{\dot{m}_i'(t-\tau_T)}{\underline{\dot{m}}} - \frac{d\tau_T}{dt} \quad (5.3.1\text{–}2)$$

The first term on the RHS of Eq. (5.3.1–2) has already been discussed in connection with the constant, single time lag model; its influence on stability is included in Eq. (5.2.2–6). In this section, the additional effects introduced by the second term are outlined and added to the stability equation. For clarity, the effects of chamber pressure, mixture ratio, and injection velocity are examined separately, a procedure that is consistent with the linearized theory.

Following Crocco,[173] it is assumed that the total time lag τ_T can be expressed as the sum of a constant ("insensitive") time lag τ_i and a variable ("sensitive") time lag τ, so that $d\tau_T/dt = d\tau/dt$. It is further assumed that the time lag is related to the chamber conditions by

$$\int_{t-\tau}^{t} \tilde{f}[p(t'), T(t'), \cdots]dt' = \bar{f}\bar{\tau} \quad (5.3.1\text{–}3)$$

where $\tilde{f}$ is an overall combustion rate. The product $\bar{f}\bar{\tau}$ on the RHS of Eq. (5.3.1–3) represents a threshold, defining the instant of conversion from reactants to products in the time lag schematization of the combustion process. For small perturbations the combustion rate can be written as

$$\tilde{f} = \bar{f}\left(1 + n\frac{p'}{\bar{p}}\right) \quad (5.3.1\text{–}4)$$

where

$$n = \frac{\bar{p}}{\bar{f}}\left(\frac{\partial \tilde{f}}{\partial p} + \frac{\partial \tilde{f}}{\partial T}\frac{\partial T}{\partial p} + \cdots\right)$$

is generally called the "pressure interaction index." Inserting Eq. (5.3.1–4) into Eq. (5.3.1–3) gives an expression for the sensitive time lag perturbation

$$\tau - \bar{\tau} = -n\int_{t-\tau}^{t} p'/\bar{p}(t')dt' \quad (5.3.1\text{–}5)$$

from which

$$\frac{d\tau}{dt} = -n\left[\frac{p'}{\bar{p}}(t) - \frac{p'}{\bar{p}}(t-\bar{\tau})\right] \quad (5.3.1\text{–}6)$$

or, taking $p'/\bar{p} = \phi e^{st}$,

$$\frac{d\tau}{dt} = -n[1 - \exp(-s\bar{\tau})]\phi e^{st} \quad (5.3.1\text{–}6a)$$

The effect of mixture ratio oscillations on the combustion time lag is derived by noting that both the combustion rate $\tilde{f}$ and the threshold product $\bar{f}\bar{\tau}$ are actually functions of mixture ratio.[630] Hence, Eqs. (5.3.1–3) and (5.3.1–4) become (considering *only* mixture ratio effects)

$$\int_{t-\tau}^{t} \tilde{f}[r(t')]dt' = \int_{t-\tau}^{t} \tilde{f}\left[1 + \frac{n_2 r'(t-\bar{\tau}_T)}{\bar{r}}\right]dt'$$

$$= \bar{f}\bar{\tau}\left[1 + \frac{n_3 r'(t-\bar{\tau}_T)}{\bar{r}}\right] \quad (5.3.1\text{–}7)$$

It should be noted that the mixture ratio perturbation in Eq. (5.3.1–7) is evaluated at the instant of injection, since the integration is carried out following a particular propellant parcel, and the threshold is that appropriate to the same parcel. This model assumes equality of the fuel and oxidizer liquid velocities. The treatment of a more realistic case would involve substantial complication of the analysis and would still be based on quite arbitrary models of the actual physical processes.

Since the mixture ratio perturbation is constant with respect to the integration in Eq. (5.3.1–7), a relation for the time lag perturbation is obtained quite simply as

$$\tau - \bar{\tau} = \frac{(n_3 - n_2)r'(t-\bar{\tau}_T)}{\bar{r}} \quad (5.3.1\text{–}8)$$

Defining

$$n_r = n_3 - n_2$$

and using Eqs. (5.2.1–7) and (5.2.2–5), the time

* F. H. Reardon, Author.

lag perturbation is given by

$$\tau-\bar{\tau}=-\frac{n_r\bar{\tau}(1+\bar{r})}{\bar{r}}\exp\left[-s\bar{\tau}_T\right](G_{OX}-\bar{r}G_F)\phi e^{st} \tag{5.3.1-9}$$

from which the derivative is obtained as

$$\frac{d\tau}{dt}=-n_r s\bar{\tau}\exp\left[-s\bar{\tau}_T\right]\frac{(1+\bar{r})}{\bar{r}}(G_{OX}-\bar{r}G_F)\phi e^{st} \tag{5.3.1-10}$$

which is the contribution of mixture ratio oscillations to the unsteady burning rate.

Finally, the effect of the injection velocity on the total time lag will be evaluated. The analysis, consistent with the foregoing derivations, is simplified by neglecting spatial variations in comparison with temporal ones. Although the spatial effects can be of comparable magnitude locally, their influence on the overall stability is always of higher order.[630] Additional approximations introduced here are (a) the combustion is concentrated at a location $x=x_c$ (constant), and (b) the liquid velocity $(0<x<x_c)$ is equal to the injection velocity, which is the same for fuel and oxidizer.

The total time lag can be written as

$$\tau_T(t)=\frac{x_c}{\bar{V}_L(t-\tau_T)} \tag{5.3.1-11}$$

Letting

$$V_L=\bar{V}_L(1+\nu e^{st})$$

and neglecting higher-order terms,

$$\tau_T=\bar{\tau}_T(1-\nu\exp\left[s(t-\bar{\tau}_T)\right]) \tag{5.3.1-12}$$

For liquid propellants the fractional injection velocity perturbation is equal to the fractional injection mass flux perturbation. Therefore, Eq. (5.3.1-11) yields

$$\frac{d\tau_T}{dt}=s\bar{\tau}_T\exp\left[-s\bar{\tau}_T\right](G_{OX}+G_F)\phi e^{st} \tag{5.3.1-13}$$

for the linearized effect of injection velocity perturbations.

Combining the three effects just discussed, which are described by Eqs. (5.3.1-6a), (5.3.1-10), and (5.3.1-13), with Eq. (5.3.1-2) and the results of Sect. 5.2.2 gives the variable-time-lag stability condition corresponding to Eq. (5.2.2-6):

$$\frac{\exp-s\bar{\tau}_T[\mathcal{K}(s)+\mathcal{H}(s)]-\mathcal{P}(s)}{(1+s\theta_c)}=-1 \tag{5.3.1-14}$$

where

$$\mathcal{K}(s)=(1+s\bar{\tau}_T)(G_{OX}+G_F) \tag{5.3.1-15}$$

$$\mathcal{H}(s)=\frac{(1+\bar{r})}{\bar{r}}\left[\frac{\bar{r}}{\bar{c}^*}\left(\frac{\partial c^*}{\partial\bar{r}}\right)-n_r s\bar{\tau}\right](G_{OX}-\bar{r}G_F) \tag{5.3.1-16}$$

$$\mathcal{P}(s)=n[1-\exp(-s\bar{\tau})] \tag{5.3.1-17}$$

The function $\mathcal{K}(s)$ includes the effects of total mass flux oscillations into the combustion zone, which has been termed the "Klystron effect"[268] (see also Sect. 3.3.1). $\mathcal{H}(s)$ accounts for the effects of mixture ratio fluctuations on both exhaust flow and burning rate. The pressure-effect term $\mathcal{P}(s)$ is the same as that used in the analysis of high-frequency modes (Sect. 4.2).

Typically, for low-frequency instability $\omega\bar{\tau}_T=0(1)$. If the sensitive time lag is small compared to the total time lag, $\exp(-s\bar{\tau})$ will be about unity, so that the pressure effect will be negligible, as will the factor $n_r s\tau$ in $\mathcal{H}(s)$. The $s\bar{\tau}_T$ term in $\mathcal{K}(s)$ gives some increase in gain, but not a large amount, compared to the constant time lag case. Hence, for low-frequency oscillations, if $\tau\ll\tau_T$, the models described in Sect. 5.2 should be adequate. On the other hand, for intermediate frequency instability, where $1/\bar{\tau}_T<\omega<1/\bar{\tau}$, the effects of the time lag variation must be taken into account, with the Klystron effect probably dominating.

It can be seen from Eq. (5.3.1-14) that the pressure-sensitivity of the combustion time lag allows the possibility of low-frequency instability even if $G_{OX}=G_F=0$. This is the case of so-called "intrinsic" instability; the stability condition reduces to

$$n(1-\exp\left[-s\bar{\tau}\right])=1+s\theta_c \tag{5.3.1-18}$$

Using this equation, Crocco and Cheng[179] have shown that intrinsic instability can occur only if $n>\frac{1}{2}$, and that there is a critical time lag for each n,

$$\bar{\tau}_{cr}=\frac{\theta_c[\pi-\cos^{-1}(1-n/n)]}{\sqrt{2n-1}} \tag{5.3.1-19}$$

such that the combustor operation is unstable for $\tau>\tau_{cr}$.

5.3.2 Intermediate-Frequency Instability*

In the low-frequency analysis of the preceding section, the effects of wave motion in the combustion chamber were neglected. Such effects cannot be omitted from the analysis of intermediate-frequency instability. Thus, in the latter case considered in this section, the chamber dynamics are governed by the equations developed in Sect. 4.2.2 for high-frequency instability, although in the present case there is no coupling with the acoustic modes of the chamber. The combustion response must include the effects discussed in connection with low-frequency instability, viz., mass flux oscillations, mixture ratio oscillations, and the sensitivity of the combustion rates to local chamber conditions (Sect. 5.3.1).

Since the chamber dynamics equations are the same as those used in the high-frequency analysis, the series expansion method of solution is also applicable here. Thus, letting

$$p' = p_0 + p_1 + \cdots$$
$$\mathbf{V}' = \mathbf{V}_0 + \mathbf{V}_1 + \cdots$$

the zeroth-order equations are the acoustic equations

$$\frac{sp_0}{\gamma} + \nabla \cdot \mathbf{V}_0 = 0$$
$$s\mathbf{V}_0 + \frac{\nabla p_0}{\gamma} = 0 \qquad (5.3.2\text{–}1)$$

and the first-order equations are the corresponding inhomogeneous equations

$$\frac{sp_1}{\gamma} + \nabla \cdot \mathbf{V}_1 = -sX_1 + \nabla \cdot \mathbf{Y}_1 + M_1$$
$$s\mathbf{V}_1 + \frac{\nabla p_1}{\gamma} = -s\mathbf{Z}_1 - \nabla \cdot \mathbf{W}_1 \qquad (5.3.2\text{–}2)$$

Considering only longitudinal oscillations, the zeroth-order solutions are

$$p_0 = P_{00} \cosh sx$$
$$\mathbf{V}_0 = u_0 = -\frac{P_{00}}{\gamma} \sinh sx \qquad (5.3.2\text{–}3)$$

To simplify the presentation, only those terms will be retained that eventually provide first-order contributions. Accordingly, the functions on the RHS of Eq. (5.3.2–2) are

$$X_1 = (\gamma - 1)\bar{u}u_0 + (1 + \bar{r})\left(\overline{\frac{dh_L}{dr}}\right)$$
$$\frac{\overline{M} \exp[-s\bar{\tau}_T]}{s}(G_{OX} - \bar{r}G_F)P_{00} \qquad (5.3.2\text{–}4a)$$

$$Y_1 = -\bar{u}p_0 \qquad (5.3.2\text{–}4b)$$

$$Z_1 = \frac{\bar{u}p_0}{\gamma} + \rho_L{}^{\circ}u_{L0} \qquad (5.3.2\text{–}4c)$$

$$W_1 = 2\bar{u}u_0 \qquad (5.3.2\text{–}4d)$$

Except for X_1, these functions are the same as those given in Sect. 4.2.2.2. The new term in Eq. (5.4.2–4a) accounts for the fluctuating enthalpy h_L of the liquid propellants resulting from the mixture ratio oscillations. The combustion response M_1 is given (to first-order) by

$$M_1 = \overline{M}e^{-s\tau_T}[\mathcal{K}(s) + \mathcal{H}(s)]P_{00} - \overline{M}\mathcal{P}(s)p_0 \qquad (5.3.2\text{–}5)$$

where $\mathcal{K}$, $\mathcal{H}$, and $\mathcal{P}$ are defined in Eqs. (5.3.1–15) to (5.3.1–17). As a result of the oscillating flow in the feed system, the liquid velocity perturbation

$$u_{L0} = \frac{ku_0}{s} + \frac{\bar{u}_{Li}{}^2}{\bar{u}_L(x)} J(s) \exp[-(s+k)\tau_T]P_{00} \qquad (5.3.2\text{–}6)$$

includes an additional term, not required in the high-frequency analysis of Sect. 4.2.2. The function $J(s)$ is the ratio of the fractional injection velocity perturbation to the fractional chamber pressure perturbation, and is given by[630]

$$J(s) = -\frac{(G_{OX} - \bar{r}G_F)(\bar{u}_{LiOX} - \bar{u}_F) + \left(\frac{1+\bar{r}}{\bar{r}}\right)(\bar{r}\bar{u}_{LiOX}G_{OX} + \bar{u}_{LiF}G_F)}{\bar{r}\bar{u}_{LiOX} + \bar{u}_{LiF}} \qquad (5.3.2\text{–}7)$$

where u_{LiOX}, $\bar{u}_{LiF}$ are the axial components of the oxidizer and fuel injection velocities, respectively.

* L. Crocco, Author.

The first-order solution can be written as follows:

$$u_1 = -\bar{u}p_0 + \int_0^x \{[s(W_1 - X_1) + M_1] \cosh s(x-x') + s(Y_1 + Z_1) \sinh s(x-x')\} dx' \qquad (5.3.2\text{–}8)$$

$$p_1 = -2\bar{u}u_0 - \int_0^x \{[s(W_1 - X_1) + M_1] \sinh s(x-x') + s(Y_1 + Z_1) \cosh s(x-x')\} dx' \qquad (5.3.2\text{–}9)$$

This solution already satisfies the boundary condition at the injector face. At the chamber exit, $x = L_c$, the solution must satisfy the nozzle admittance relation

$$u'(L_c) + \mathcal{A}p'(L_c) + \mathcal{G}\sigma'(L_c) = 0 \qquad (5.3.2\text{–}10)$$

where $\mathcal{A}$ and $\mathcal{G}$ are the complex admittance coefficients discussed in Sect. 3.6. The entropy perturbation σ' is given, to first order, by the expression

$$\sigma' = \sigma_0 + \sigma_1 = -\frac{1}{\bar{u}} \int_0^x \left\{ \left(\frac{\gamma - 1}{\gamma}\right) p_0 + (1 + \bar{r}) \left(\frac{\overline{dh_L}}{d\bar{r}}\right) (G_{OX} - \bar{r}G_F) P_{00} \exp[-s\tau_T] \right\} \overline{M} \exp\left[-s \int_{x'}^x \frac{dx''}{\bar{u}}\right] dx' \qquad (5.3.2\text{–}11)$$

The first term in Eq. (5.3.2–11) coincides (to first order) with the result obtained in the high-frequency analysis, Eq. (4.2.1–18). The second term results from the mixture ratio variation introduced by the feed system response.

When the perturbation expressions are inserted into Eq. (5.3.2–10), the result is a complex equation for s, from which it is possible, although difficult, to determine the oscillation frequency ω and the amplification factor λ. A simpler procedure (used also in the high frequency analysis) is to set $\lambda = 0$, regard ω as an independent variable, and use Eq. (5.3.2–10) as a relation between two of the engine design or operating parameters, holding at a stability limit. This is the procedure followed by Scala,[630] who was able to demonstrate the possibility of intermediate frequency instability. However, a complete, systematic study of this type of instability has not been made.

5.4 FEED SYSTEM RESPONSE

In the preceding sections the equations governing oscillatory flow in the combustion chamber were presented. These equations included propellant feeding effects by means of the normalized injection admittances G_{OX} and G_F, defined by

$$G_{OX} = -\frac{\dot{m}_{oxi}'}{p'} \cdot \frac{\bar{p}_c}{\dot{m}}; \qquad G_F = -\frac{\dot{m}_{Fi}'}{p_c'} \cdot \frac{\bar{p}_c}{\dot{m}}$$

In this section the general approach for calculating injector admittances for rocket engine feed systems is outlined, making use of the material presented in Sect. 3.2. Because of the complexities and design variations of typical feed systems, it is not possible to give a single, generalized expression that will pertain to all feed systems. However, several examples of simplified systems are presented to illustrate the approach and to point out some of the important influences of feed system response on stability.

The following nomenclature pertains to Sect. 5.4:

E	Elastic modulus of pipe material
G	Dimensionless flow admittance, $-(\bar{p}/\dot{m})(\dot{m}'/p')$
t	Time constant (component indicated by subscript)
t_r	Residence time (component indicated by subscript)
Z	Characteristic impedance (component indicated by subscript)
δ_w	Feed line wall thickness
$\tilde{\zeta}$	Ratio of line impedance to injector impedance
$\tilde{\zeta}_p$	Ratio of pump impedance to injector impedance
$\tilde{\zeta}_v$	Ratio of valve impedance to injector impedance
$\tilde{\nu}$	Ratio of manifold volume to feed line volume

Subscripts:

A	Area change
c	Chamber
i	Injector, injection orifice
l	Feed line
m	Manifold

o Orifice
p Pump
t Tank
v Valve
∞ Unconfined medium

5.4.1 Calculation of Injection Admittance*

A propellant feed system usually consists of a series arrangement of various flow components, such as pipes, valves, manifolds, and possibly a pump. For each component, the admittance can be evaluated at one end if its value is known at the other. Thus, if the admittance is known at one point in the feed system, it can be extended through the system to the combustion chamber, thereby obtaining the injection admittance, by use of the component admittance ratios:

$$G_i = G_0\left(\frac{G_1}{G_0}\right)\left(\frac{G_2}{G_1}\right)\cdots\left(\frac{G_m}{G_{m-1}}\right)\left(\frac{G_i}{G_m}\right) \quad (5.4.1\text{–}1)$$

Some feed systems, particularly those on static test stands, have branch lines, which may be closed off at some distance from the main feed line. Such cases can be treated by summing the admittances of the main line and the branch line to obtain the admittance just downstream of the branch point. The admittance of the branch line is obtained in the same manner as that of the main line, requiring a starting value to be known at some point in the branch line. The analysis of a dead-ended line is straightforward, but if the branch line returns again to the main line, the analysis is considerably more complicated. Additional complications are introduced if the branch loop contains another combustor, as in the staged combustion cycle (Sect. 1.1.2).

In the following paragraphs admittance ratios are given for several common feed system components. The reader is referred to Sect. 3.2 for a general discussion of unsteady flow in feed systems, including techniques of analysis. Special stabilizing devices for feed system application are considered in Sect. 6.2.3.

5.4.1.1 *Constant-area feed line.*—A large portion of any feed system consists of tubing with constant cross-sectional area. The admittance ratio for low-speed flow in a lossless line is[479]

$$\frac{G_2}{G_1} = \frac{1+(1/G_1Z_l)\tanh st_l}{1+G_1Z_l\tanh st_l} \quad (5.4.1\text{–}2)$$

where

$$Z_l = \frac{a_L}{A_l}\frac{\dot{m}}{\bar{p}_c} \quad (5.4.1\text{–}3)$$

is the "characteristic impedance" of the line, and

$$t_l = \frac{l}{a_L} \quad (5.4.1\text{–}4)$$

is the time constant. In these equations the subscript 1 denotes the upstream end of the line, a_L is the effective speed of sound in the liquid, l is the length of the line, A_l is the cross-sectional area, and $\dot{m}$, $\bar{p}$, and s have the same meanings as given in Sect. 5.2.

The requirement of low flow velocity, i.e.,

$$\mathfrak{M}_L = \frac{\bar{V}_L}{a_L} \ll 1$$

is normally met in rocket engine feed lines. However, it should be observed that the effective speed of sound c_L may be considerably smaller than the sonic velocity in a liquid medium of infinite extent, $a_{L\infty}$, because of the structural compliance of the pipe walls. Thus,

$$a_L = \frac{a_{L\infty}}{\sqrt{1+\rho_L a_{L\infty}^2 D_l/E\delta_w}} \quad (5.4.1\text{–}5)$$

where ρ_L is the liquid density, D_l is the mean pipe diameter, δ_w is the wall thickness, and E is the elastic modulus of the pipe material. If the flow Mach number is appreciable, the admittance ratio becomes[586,721]

$$\frac{G_2}{G_1} = \frac{1+\dfrac{(1-\mathfrak{M}_L^2-G_1Z_l\mathfrak{M}_L)}{G_1Z_l}\tanh\left(\dfrac{st_l}{\sqrt{1-\mathfrak{M}_L^2}}\right)}{1+(G_1Z_l+\mathfrak{M}_L)\tanh\left(\dfrac{st_l}{\sqrt{1-\mathfrak{M}_L^2}}\right)} \quad (5.4.1\text{–}2a)$$

Eqs. (5.4.1–2) and (5.4.1–5) imply that the liquid temperature and density are constant over the length of the feed line. If these properties vary appreciably, it may be necessary to subdivide the line into several shorter ones, for each of which suitable average properties may be chosen to represent that line section.

* F. H. Reardon, Author.

5.4.1.2 Line with area change.—In general, the problem of oscillating flow in a line with variable cross-sectional area must be solved numerically. Hence the admittance ratio cannot be given in a form applicable to all systems. However, for incompressible flow in a rigid-wall pipe, the governing equations are greatly simplified, and yield the expression[13]

$$\frac{G_2}{G_1} = \frac{1}{1+Z_A G_1(1+st_A)} \qquad (5.4.1\text{–}6)$$

with

$$Z_A = \frac{\dot{m}}{\bar{p}_c} \cdot \frac{\bar{V}_{L1}}{A_1}\left(\frac{A_1^2}{A_2^2}-1\right) \qquad (5.4.1\text{–}7)$$

and

$$t_A = \frac{\dot{m}_L}{2\overline{\Delta p}} \int_1^2 \frac{dx}{A(x)} \qquad (5.4.1\text{–}8)$$

where $\dot{m}_L$ is the liquid flow rate through the line (not to be confused with $\dot{m}$, the total propellant flow to the engine) and $\overline{\Delta p}$ is the steady-state pressure change (p_1-p_2) from the upstream end to the downstream end of the area change.

5.4.1.3 Orifice or valve.—An orifice is essentially a special case of a line with area change, in which there is a reduction in area very close to the upstream end. For a long orifice,

$$\frac{G_2}{G_1} = \frac{1}{1+Z_o G_1(1+st_o)} \qquad (5.4.1\text{–}9)$$

with

$$Z_o = \frac{2\overline{\Delta p}}{\dot{m}_L} \cdot \frac{\dot{m}}{\bar{p}_c} \qquad (5.4.1\text{–}10)$$

and

$$t_o = \frac{l_o \dot{m}_L}{2\overline{\Delta p} A_o} \qquad (5.4.1\text{–}11)$$

where l_o is the effective orifice length* and A_o is the orifice cross-sectional area. Since the time constant t_o is directly proportional to the orifice length, for a short orifice, Eq. (5.4.1–9) reduces to

$$\frac{G_2}{G_1} = \frac{1}{1+Z_o G_1} \qquad (5.4.1\text{–}12)$$

A valve is most commonly treated as an orifice; hence the admittance ratio across a valve is given by Eq. (5.4.1–9) or (5.4.1–12). In some cases, however, there is a capacitance associated with the valve. Such a valve can be considered as a series combination of a manifold (Sect. 5.4.1.5) and an orifice.

5.4.1.4 Pump.—Based on the discussion of Sect. 3.2.2, the admittance ratio for a high speed propellant pump can be written as

$$\frac{G_2}{G_1} = \frac{1+s\mathcal{C}_p/G_1}{1-Z_p G_1(1+s\mathcal{C}_p/G_1)(1+st_p)} \qquad (5.4.1\text{–}13)$$

where

$$\mathcal{C}_p = \frac{\bar{\rho}_L \mathcal{V}_p}{K_L} \cdot \frac{\bar{p}_c}{\dot{m}} \qquad (5.4.1\text{–}14)$$

$$Z_p = \frac{\dot{m}}{\bar{p}_c}\left(\frac{\overline{dp}}{d\dot{m}}\right)_p \qquad (5.4.1\text{–}15)$$

$$t_p = \left(\frac{l}{A}\right)_p \Big/ \left(\frac{\overline{dp}}{d\dot{m}}\right)_p \qquad (5.4.1\text{–}15a)$$

The effective pump capacitance $\mathcal{C}_p$, the slope $(dp/d\dot{m})_p$ of the pressure-flow characteristic, and the inertance $(l/A)_p$ must be determined from experimental data.

5.4.1.5 Manifold.—For a low-frequency stability analysis, it is appropriate to assume that the fluid in a manifold undergoes a bulk oscillation. Hence the admittance ratio across a manifold takes the form

$$\frac{G_2}{G_1} = 1 + \frac{s\mathcal{C}_m}{G_1} \qquad (5.4.1\text{–}16)$$

where the normalized manifold capacitance is given by

$$\mathcal{C}_m = \frac{\bar{\rho}_L \mathcal{V}_m \bar{p}_c}{K_L \dot{m}} \qquad (5.4.1\text{–}17)$$

in which $\mathcal{V}_m$ is the manifold volume and K_L is the bulk modulus of the liquid propellant.

In the case of intermediate-frequency instability, it may be necessary to consider the effects of wave motion in the manifold. For such an analysis the manifold would be divided into a number of interconnecting flow paths, as outlined in Sect. 3.2.2. Since the mathematical model of the manifold flow is directly tied to the design features of the manifold under study, it is not possible to derive general admittance relationships.

* See Sect. 3.2.2.

5.4.2 Injection Admittance for Simple Feed Systems*

The procedure and equations discussed in the preceding section can be illustrated by applying them to simplified systems. Although systems actually used are considerably more complex than those discussed here, the admittance calculation method and some general characteristics of feed system dynamic response are more effectively shown by the simpler systems. Three examples are considered: pressurized-tank, constant-rate, and centrifugal pump. The influences of feed system components are shown by examination of certain limiting cases. Only a single propellant feed system is considered, since the equations presented in Sect. 5.2 and Sect. 5.3 indicate how the individual systems interact with the other parts of the engine.

5.4.2.1 Pressurized-tank feed system.—The system considered is made up of a propellant tank, a constant-area line, a manifold, and injection orifices, as shown schematically in Fig. 5.4.2a. The admittance ratios for these components are given in Eqs. (5.4.1–2), (5.4.1–12), and (5.4.1–16). The system dynamic parameters (normalized by the steady-state chamber pressure and total flow rate) are also defined in Fig. 5.4.2a in terms of the line length l and cross-sectional area A_l, the tank and manifold volumes $\mathcal{V}_t$, $\mathcal{V}_m$, and the propellant properties ρ_L, a_L, and K_L. It should be noted that in a bipropellant rocket engine the flow rate $\dot{m}_L$ of the propellant under consideration is less than the total flow rate $\dot{m}$ of both propellants.

The starting point for the admittance calculation is taken at the top of the propellant tank, where there is no propellant flow. Hence $G_o=0$. Working progressively through the feed system, the injection admittance is found to be

$$G_i=\frac{1}{Z_i}\left[\frac{sZ_i(\mathcal{C}_t+\mathcal{C}_m)+[(Z_i/Z_l)+s^2\mathcal{C}_m\mathcal{C}_tZ_lZ_i]\tanh st_l}{1+sZ_i(\mathcal{C}_t+\mathcal{C}_m)+[(Z_i/Z_l)+s\mathcal{C}_tZ_l+s^2\mathcal{C}_mZ_lZ_i]\tanh st_l}\right] \tag{5.4.2–1}$$

Since the propellant tank is usually very large compared to the other system components, the tank capacitance $\mathcal{C}_t$ is much larger than the other system parameters. For simplicity, assume $\mathcal{C}_t=\infty$, which corresponds to a constant tank pressure. Then

$$G_i=\frac{1}{Z_i}\left[\frac{1+s\mathcal{C}_mZ_l\tanh st_l}{1+[(Z_l/Z_i)+s\mathcal{C}_mZ_l]\tanh st_l}\right] \tag{5.4.2–2}$$

The frequency response of such a constant-pressure feed system is obtained by setting $s=i\omega$ $(\lambda=0)$ in Eq. (5.4.2–2):

$$G_i=\frac{1}{Z_i}\left[\frac{1-\omega\mathcal{C}_mZ_l\tan\omega t_l}{1-\omega\mathcal{C}_mZ_l\tan\omega t_l+i(Z_l/Z_i)\tan\omega t_l}\right] \tag{5.4.2–3}$$

Defining

$$\tilde{\zeta}\equiv\frac{Z_l}{Z_i}=\frac{\bar{a}_L\bar{V}_l}{\bar{V}_i^2}=\frac{(V_l/a_L)}{(V_i/a_L)^2} \tag{5.4.2–4}$$

and

$$\tilde{\nu}=\frac{\mathcal{C}_mZ_l}{t_l}=\frac{\mathcal{V}_m}{\mathcal{V}_l} \tag{5.4.2–5}$$

Eq. (5.4.2–3) can be written as

$$G_iZ_i=\frac{1-\tilde{\nu}\omega t_l\tan\omega t_l}{1-\tilde{\nu}\omega t_l\tan\omega t_l+i\tilde{\zeta}\tan\omega t_l} \tag{5.4.2–6}$$

The feed system response is thus governed by four parameters: the injector impedance Z_i, the feed-line time constant t_l, the velocity parameter $\tilde{\zeta}$, and the manifold-to-line volume ratio $\tilde{\nu}$. For a very large manifold, $\tilde{\nu}\rightarrow\infty$, and $G_iZ_i\rightarrow 1$, i.e., the feed system response is controlled entirely by the injector orifice design. The same result is obtained for very low line velocity or very high injection velocity, so that $\tilde{\zeta}\rightarrow 0$. For most systems, however, $\tilde{\nu}=0(1)$ and $\tilde{\zeta}=0(10)$. A typical injection admittance function is shown by the frequency response curves (magnitude and phase) of Fig. 5.4.2b. The injection admittance is appreciable only near the half-wave (open-open) resonances of the feed line. At the quarter-wave (open-closed) resonances, the admittance vanishes, since the

* F. H. Reardon, Author.

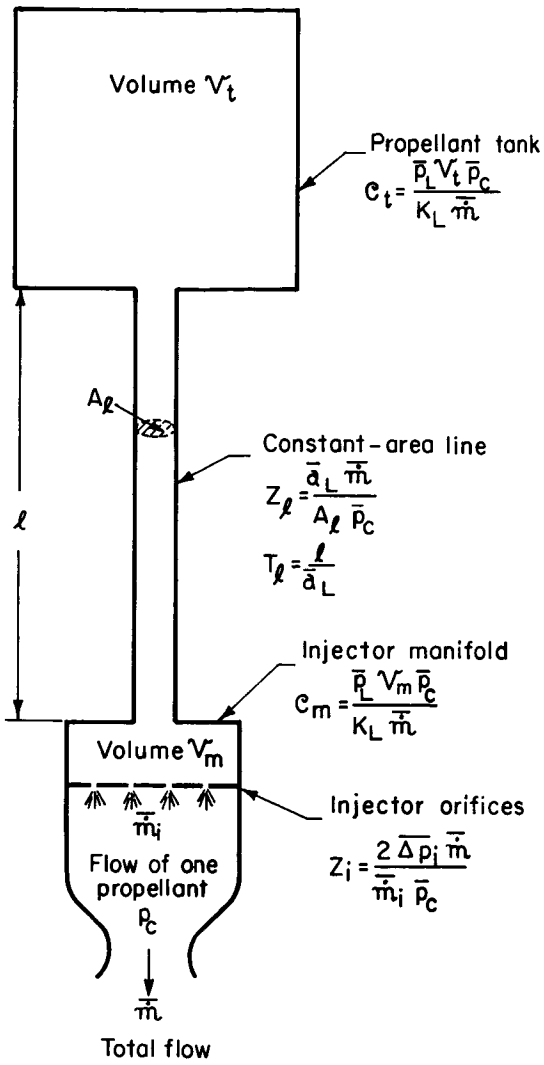

FIGURE 5.4.2a.—Schematic of pressurized-tank feed system.

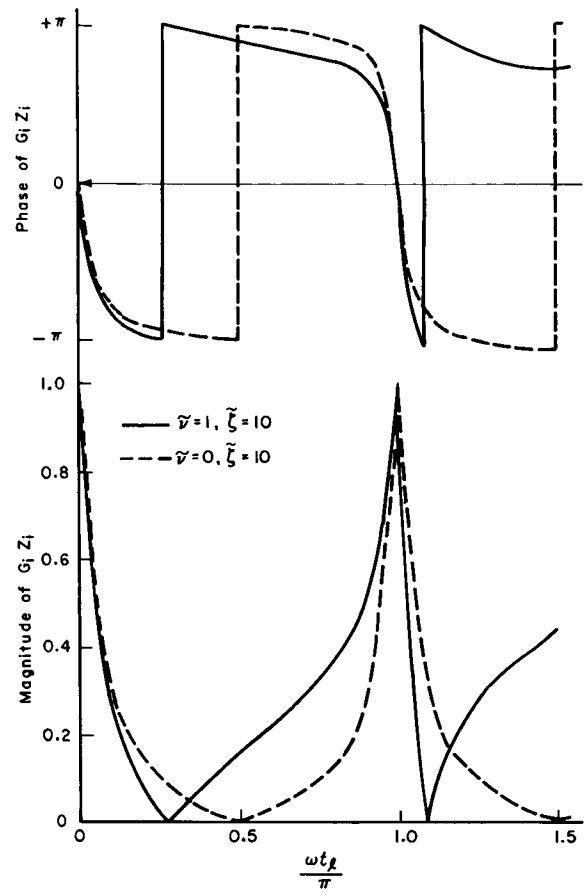

FIGURE 5.4.2b.—Injection admittance for constant-pressure feed system, showing effect of manifold volume.

injector is at a velocity node. The effect of the manifold can be seen by comparing the curves for $\tilde{\nu}=0$ (negligible manifold volume) with those for $\tilde{\nu}=1$, in Fig. 5.4.2b. The quarter-wave resonant frequencies are lowered, but the half-wave frequencies are not altered. The effect of the velocity parameter $\tilde{\zeta}$ is shown by Fig. 5.4.2c. Increasing $\tilde{\zeta}$ does not affect the resonant frequencies, but narrows the half-wave peak, decreasing the magnitude of G_iZ_i, except at the resonances. Thus, increasing $\tilde{\zeta}$ will have, in general, a stabilizing effect on feed-coupled oscillations, provided that Z_i is not decreased at the same time.

If a valve is added to this simple feed system, dividing the propellant line into two parts (Fig. 5.4.2d), the injection admittance for a constant tank pressure is found to be

$$G_i = \left(\frac{1}{Z_i}\right) \frac{1+\mathfrak{M}_v^2 \mathrm{st}_{rm}+\tilde{\nu}_1 \mathrm{st}_{l_1} \tanh \mathrm{st}_{l_1}+\tilde{\zeta}_1/\tilde{\zeta}_2 \tanh \mathrm{st}_{l_1} \tanh \mathrm{st}_{l_2}+(\tilde{\nu}_2 \mathrm{st}_{l_2}+\tilde{\zeta}_v/\tilde{\zeta}_2) \tanh \mathrm{st}_{l_2}}{1+\tilde{\zeta}_v+\mathfrak{M}^2 \mathrm{st}_{rm}+(\tilde{\zeta}+\tilde{\nu}_1 \mathrm{st}_{l_1}) \tanh \mathrm{st}_{l_1}+\tilde{\zeta}_1/\tilde{\zeta}_2 \tanh \mathrm{st}_{l_1} \tanh \mathrm{st}_{l_2}+(\tilde{\zeta}_2+\tilde{\nu}_2 \mathrm{st}_{l_2}+\tilde{\zeta}_v/\tilde{\zeta}_2) \tanh \mathrm{st}_{l_2}} \tag{5.4.2-7}$$

where

$$\tilde{\zeta}_1 = \frac{Z_{l_1}}{Z_i}; \quad \tilde{\zeta}_2 = \frac{Z_{l_2}}{Z_i}; \quad \tilde{\nu}_1 = \frac{\mathcal{C}_m Z_{l_1}}{t_{l_1}}; \quad \tilde{\nu}_2 = \frac{\mathcal{C}_m Z_{l_2}}{t_{l_2}}$$

are similar to the parameters involved in Eq. (5.4.2–6). Additional parameters are

$$\tilde{\zeta}_v = \frac{Z_v}{Z_i} = \frac{\overline{\Delta p_v}}{\overline{\Delta p_i}}; \qquad \mathfrak{M}_v = \frac{\bar{V}_v}{a_L} \qquad (5.4.2\text{–}8)$$

where $\bar{V}_v$ is the exit velocity from the valve (orifice), and

$$t_{r_m} = \frac{\bar{\rho}_L \mathcal{V}_m}{\dot{m}} \qquad (5.4.2\text{–}9)$$

which is the residence time of the propellant in the injector manifold.

The effect of the valve can be seen, at least qualitatively, by assuming that $Z_{l_1} = Z_{l_2} = Z_l$, so that

$$\tilde{\zeta}_1 = \tilde{\zeta}_2 = \tilde{\zeta}$$

$$\tilde{\nu}_1 s t_{l_1} = \tilde{\nu}_2 s t_{l_2} = s \frac{\mathcal{V}_m}{\mathcal{V}_l} \cdot t_l$$

then

$$G_i = \left(\frac{1}{Z_i}\right) \frac{1 + \dfrac{\mathcal{V}_m}{\mathcal{V}_l} s t_l \tanh s t_l + \dfrac{\mathfrak{M}_v^2 s t_{r_m} + (\tilde{\zeta}_v/\tilde{\zeta}_2) \tanh s t_{l_2}}{1 + \tanh s t_{l_1} \tanh s t_{l_2}}}{1 + \left(\tilde{\zeta} + \dfrac{\mathcal{V}_m}{\mathcal{V}_l} s t_l\right) \tanh s t_l + \dfrac{\tilde{\zeta}_v + \mathfrak{M}_v^2 s t_{r_m} + (\tilde{\zeta}_v/\tilde{\zeta}_2) \tanh s t_{l_2}}{1 + \tanh s t_{l_1} \tanh s t_{l_2}}} \qquad (5.4.2\text{–}10)$$

where $t_l = t_{l_1} + t_{l_2}$ and $\mathcal{V}_l = A_l(l_1 + l_2)$. Thus, if $\tilde{\zeta}_v = \mathfrak{M}_v = 0$, Eq. (5.4.2–8) reduces to Eq. (5.4.2–2), the admittance ratio for a single, constant-area line. As $\tilde{\zeta}_v$ and $\mathfrak{M}_v$ become large, corresponding to a large pressure drop across the valve, the influence on the injection admittance of the feed line downstream of the valve is increased, and the line upstream of the valve becomes of lesser importance.

5.4.2.2 Constant-rate feed system.—Returning now to Eq. (5.4.2–1), the case of $\mathcal{C}_t = 0$ corresponds to a feed line supplied from a constant-rate source, such as a constant-rate pump or cavitating venturi. In this case the injection admittance is

$$G_i = \left(\frac{1}{Z_i}\right) \frac{\tilde{\nu} s t_l + \tanh s t_l}{\tilde{\zeta} + \tilde{\nu} s t_l + \tanh s t_l} \qquad (5.4.2\text{–}11)$$

which can also be written in the form

$$G_i = \left(\frac{1}{Z_i}\right) \frac{\mathfrak{M}_i^2 s t_{r_m} + \dfrac{1}{\tilde{\zeta}} \tanh s t_l}{1 + \mathfrak{M}_i^2 s t_{r_m} + \dfrac{1}{\tilde{\zeta}} \tanh s t_l} \qquad (5.4.2\text{–}11a)$$

where $\mathfrak{M}_i = \bar{V}_i / a_L$ and t_{r_m} is the injector manifold residence time defined in Eq. (5.4.2–9).

For a short feed line or very low frequency oscillations, Eq. (5.4.2–11a) simplifies to

$$G_i = \left(\frac{1}{Z_i}\right) \mathfrak{M}_i^2 s (t_{r_m} + t_{r_l}) \qquad (5.4.2\text{–}12)$$

where $t_{r_l} = l/\bar{V}_l$ is the feed line residence time. Defining

$$\mathcal{C}_{eff} = \frac{\bar{\rho}_L}{K_L} (\mathcal{V}_m + \mathcal{V}_l) \cdot \frac{\bar{p}_c}{\dot{m}}$$

it can be seen that

$$G_i = s \mathcal{C}_{eff} \qquad (5.4.2\text{–}12a)$$

That is, if the acoustic resonances of the feed line are not excited, the whole feed system acts as a capacitance.

On the other hand, for a long feed line, the acoustic properties of the feed line lead to resonant peaks in the frequency response of the feed system. Typical magnitude and phase curves for $G_i Z_i$ are shown in Fig. 5.4.2e. Two cases are presented: a relatively large injector manifold (solid lines) and a vanishingly small manifold (dashed lines). These results are similar to those of Fig. 5.4.2b, except that in the present case, the venturi or pump acts acoustically as a closed end. Hence the quarter-wave (closed-open) resonances give the admittance peaks. As before, the effect of the injector manifold is to lower the resonant frequency of the zero admittance (closed-closed) resonance. In addition, increasing the velocity parameter $\tilde{\zeta}$ will reduce G_i for all non-resonant frequencies.

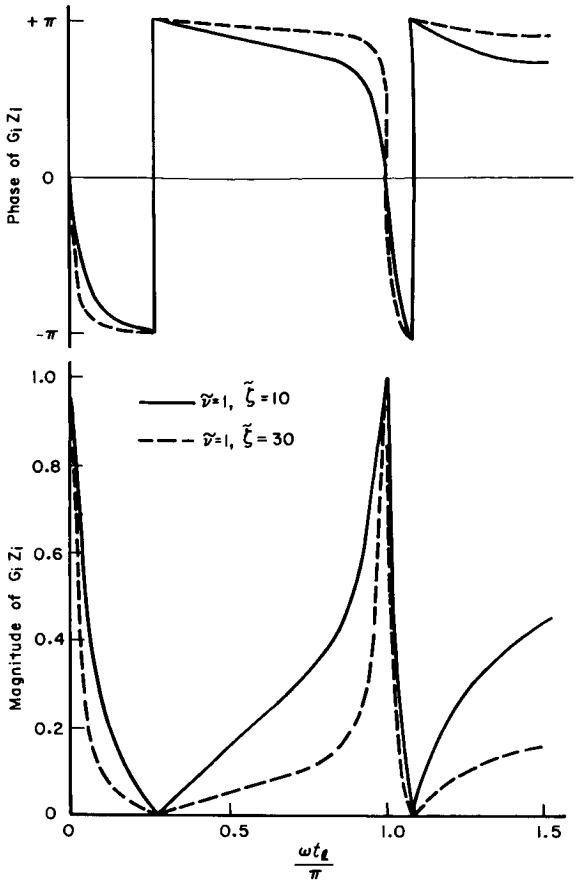

FIGURE 5.4.2c.—Injection admittance for constant-pressure feed system, showing effect of velocity parameter ζ.

5.4.2.3 Centrifugal-pump feed system.—The final example is that of a centrifugal-pump feed system in which, for simplicity, the manifold volume is zero (Fig. 5.4.2f). From the relations given in Sect. 5.4.1, the injection admittance is determined to be

$$G_i = \left(\frac{1}{Z_i}\right) \cdot \frac{N(s)}{D(s)} \qquad (5.4.2\text{–}13)$$

where

$$N(s) = 1 + \mathfrak{M}_i^2 s t_{rp} \tilde{\zeta}_1 \tanh s t_{l_1} - \frac{\tilde{\zeta}_p}{\tilde{\zeta}_2}(1+st_p)\tanh s t_{l_2} + \frac{\tilde{\zeta}_1}{\tilde{\zeta}_2}\left[1 - \mathfrak{M}_i^2 s t_{rp} \tilde{\zeta}_p (1+st_p)\right] \times \tanh s t_{l_1} \tanh s t_{l_2} \qquad (5.4.2\text{–}13a)$$

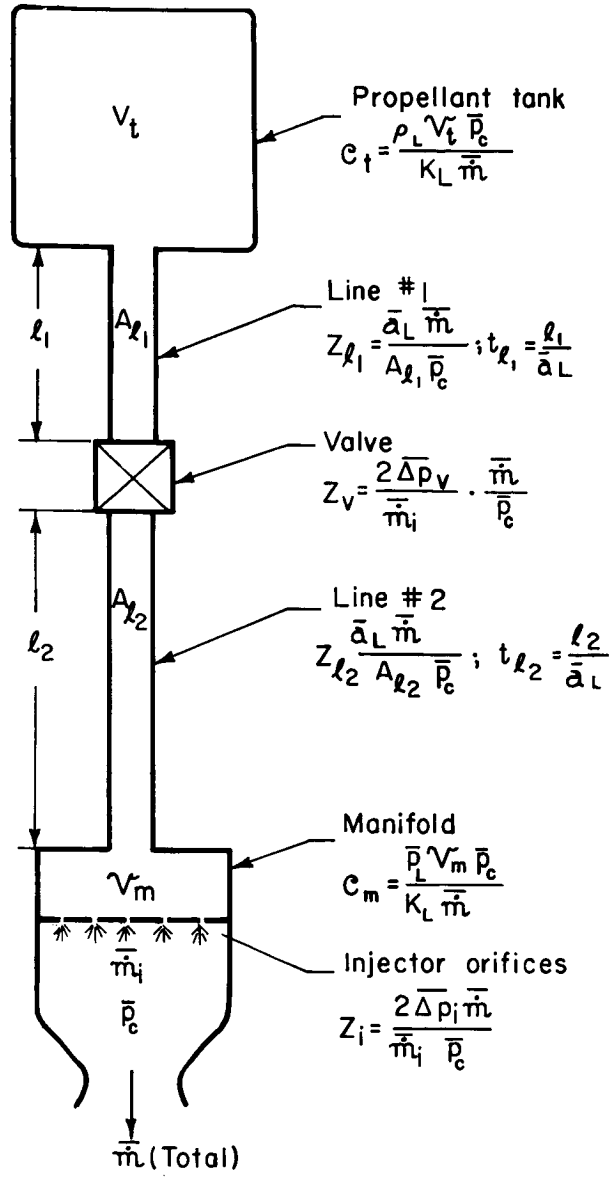

FIGURE 5.4.2d.—Schematic of pressurized-tank feed system with valve.

$$D(s) = 1 - \tilde{\zeta}_p(1+st_p) + \tilde{\zeta}_1\left[1 + \mathfrak{M}_i^2 s t_{rp}(1 - \tilde{\zeta}_p[1+st_{rp}])\right]\tanh s t_{l_1} + \left[\tilde{\zeta}_2 - \frac{\tilde{\zeta}_p(1+st_p)}{\zeta_2}\right]\tanh s t_{l_2} + \left[1 + \mathfrak{M}_i^2 s r_{tip}(\tilde{\zeta}_1\tilde{\zeta}_2 - \tilde{\zeta}_p[1+st_p])\right] \times \tanh s t_{l_1} \tanh s t_{l_2} \qquad (5.4.2\text{–}13b)$$

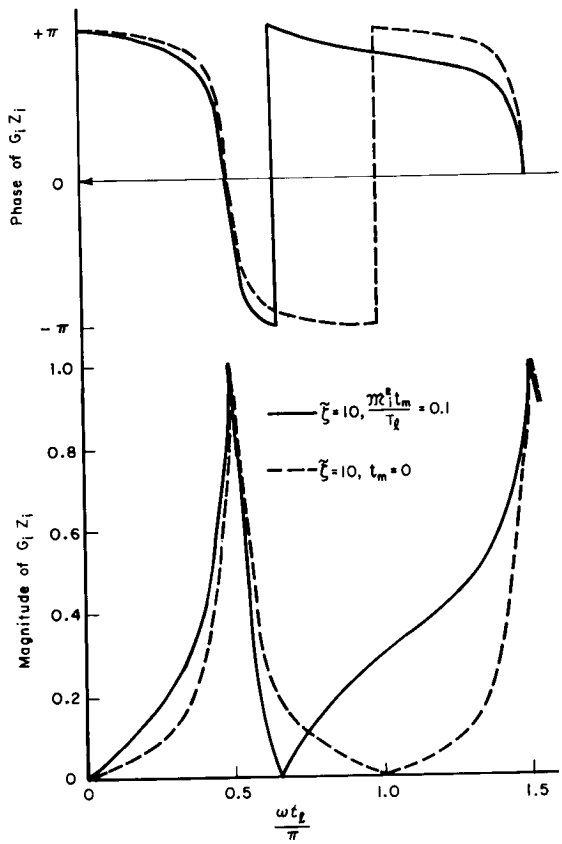

FIGURE 5.4.2e.—Injection admittance for constant-rate feed system.

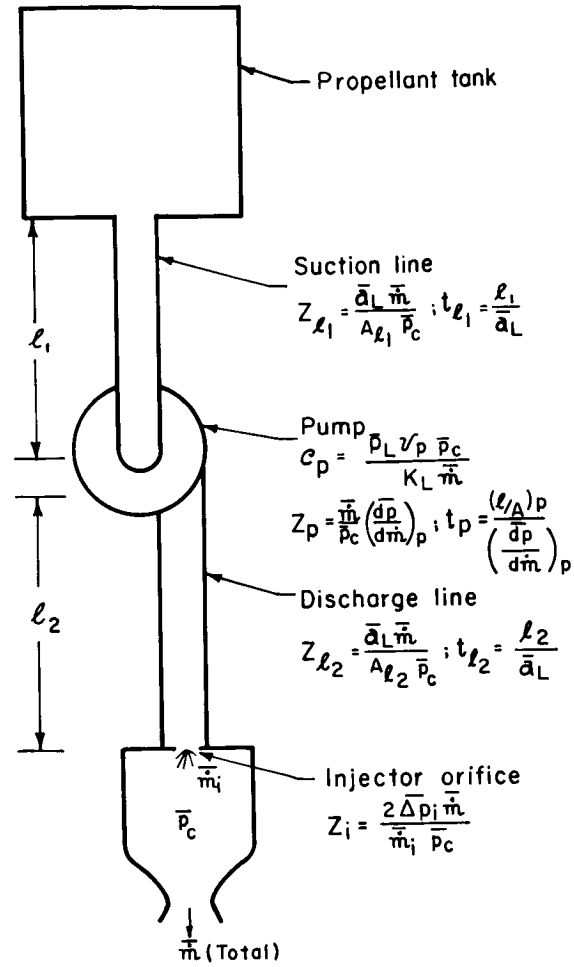

FIGURE 5.4.2f.—Schematic of centrifugal-pump feed system.

The parameters controlling the response of this system are Z_i, $\mathfrak{M}_i$, $\tilde{\zeta}_1$, $\tilde{\zeta}_2$, t_{ℓ_1}, t_{ℓ_2}, all defined previously, the pump/injector impedance ratio

$$\tilde{\zeta}_p = \frac{Z_p}{Z_i}$$

and the residence time of the propellant in the pump

$$t_{rp} = \frac{\bar{\rho}_L \mathcal{V}_p}{\dot{m}_i} = \mathcal{C}_p \frac{K_L}{p_c} \cdot \frac{\dot{m}}{\dot{m}_i}$$

The pump impedance Z_p and the time constant t_p are defined in Eqs. (5.4.1–15) and (5.4.1–15a).

Eq. (5.4.2–13) illustrates one of the major difficulties of feed system response analysis. That is, the complexity of the admittance function and the large number of controlling parameters makes it virtually impossible to obtain general results. Only by drastic simplification is a generalized analysis feasible. Accordingly, in the following discussion it is assumed that $\tilde{\zeta}_1 = \tilde{\zeta}_2 = \tilde{\zeta}$.

The effect of the pump capacitance is to reduce the influence of the suction line on the feed system response. In the limit $t_{rp} \to \infty$,

$$G_i Z_i = \frac{1 - \tilde{\zeta}_p/\tilde{\zeta}(1+st_p) \tanh st_{\ell_2}}{1 - \tilde{\zeta}_p(1+st_p) + [\tilde{\zeta} - (\tilde{\zeta}_p/\tilde{\zeta})(1+st_p)] \tanh st_{\ell_2}} \tag{5.4.2–14}$$

The admittance thus depends on the interaction of the pump pressure-flow characteristic and the discharge line acoustic resonance properties. It can be seen that $\tilde{\zeta}_p = 0$ corresponds to a simple constant-pressure feed system (Eq. (5.4.2–2) with $\mathcal{C}_m = 0$). At the other extreme, $\tilde{\zeta}_p = \infty$ for a

constant-rate pump, in which case Eq. (5.4.2–14) reduces to

$$G_iZ_i = \frac{(1/\zeta)\tanh st_{l_2}}{1+(1/\zeta)\tanh st_{l_2}}$$

which can also be obtained from Eq. (5.4.2–11a) for $t_{r_m}=0$. In both of the previous cases it was observed that increasing ζ was stabilizing. Thus, it can be expected that this result will hold also for values of ζ_p of the order of unity, such as correspond to centrifugal pumps.

For the case of negligible pump capacitance, the injection admittance can be written in the form

$$G_iZ_i = \frac{1-\zeta_p(1+st_p)\left(\dfrac{(1/\zeta)\tanh st_{l_2}}{1+\tanh st_{l_1}\tanh st_{l_2}}\right)}{1+\zeta\tanh s(t_{l_1}+t_{l_2})-\zeta_p(1+st_p)\left(\dfrac{1+(1/\zeta)\tanh st_{l_2}}{1+\tanh st_{l_1}\tanh st_{l_2}}\right)} \tag{5.4.2–15}$$

It is evident that $\zeta_p=0$ corresponds to the case of a constant-pressure feed system with line length $=l_1+l_2$, whereas $\zeta_p=\infty$ corresponds to a constant-rate feed system with line length $=l_2$. Fig. 5.4.2g illustrates the nature of the injection admittance frequency response for an intermediate value of ζ_p. For the particular case shown, $\zeta_p=-1$, $l_2=2l_1$, $t_p=0$, and $\zeta=10$. For comparison, the dashed lines in Fig. 5.4.2g give the admittance for a constant-area line without a pump (Fig. 5.4.2b).

5.4.3 Stabilizing Effect of the Feed System*

The feed system nearly always adds a stabilizing influence to the combustion chamber dynamics. In a pressurized feed system it is obvious that the dynamic elements (inertia and compressibility) can only provide transient storage for energy input to the system. The injector orifices remove energy at a rate of $(p_i-p_c)\dot{m}_i/\rho_L$. Hence the rate at which energy is supplied to the passive elements of the feed system is $p_i\dot{m}_i/\rho_L$.

When driving the feed system with chamber pressure at any frequency, sufficient energy must be supplied to the system across the injector orifices to account for the energy losses of the orifices themselves and to result in steady-amplitude forced oscillations. Assuming the only system loss to be the injector orifices, the feed system could be dynamically conservative at a given frequency only if the sinusoidal component of the injector flow rate had zero amplitude. Only if the injection pressure is exactly in phase and equal in amplitude to the chamber pressure will the injector flow oscillation have zero amplitude and the system be conservative. In this special case the injector is a flow node but correspondingly the flow input to chamber pressure is also zero.

Similarly, if the injection pressure amplitude is zero, the orifice flow oscillation can be large, but the rate of energy supply to the passive elements of the feed system is zero; all of the input energy is absorbed by the injector orifices. The feed system as a whole is therefore not conservative.

At frequencies other than those at which the injector pressure oscillations are zero the feed system inhibits flow variations. This inhibiting of flow oscillations adds stability to the combustion chamber since the combustion process cannot couple to the feed system unless a flow oscillation exists. Hence only certain discrete frequencies are left without benefit of external stabilization due to the feed system, and in general, at no time can the feed system destabilize an otherwise stable combustion process.

5.5 ANALYTICAL METHODS OF SOLUTION*

The stability of an engine system is examined analytically by solving a characteristic equation, e.g., Eq. (5.2.2–6), (5.2.3–4), or (5.3.1–14). That is, the unsteady operation of the engine is described by equations such as

* J. A. Nestlerode, J. R. Fenwick, L. E. Sack, Authors.

* F. Reardon and J. Szuch, Authors of Sects. 5.5.1 and 5.5.2.

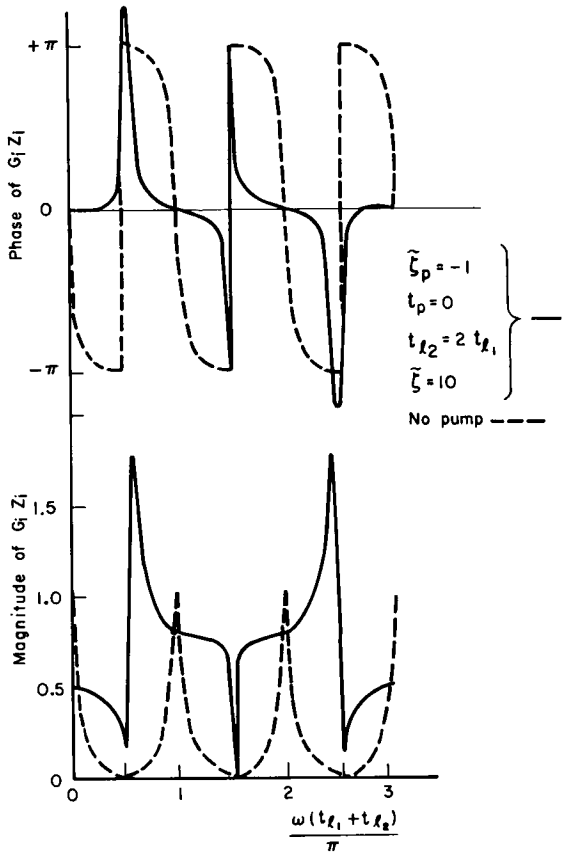

FIGURE 5.4.2g.—Injection admittance for centrifugal-pump feed system.

$$p_c = \bar{p}_c + \sum_j p_j' \exp s_j t$$

where $s_j = \lambda_j + i\omega_j$ are the roots of the characteristic equation. If all roots have $\lambda_j < 0$, the perturbations from steady state die out and the system is said to be stable. However, if any of the roots s_j has a positive real part, the corresponding perturbation term describes an oscillation that grows with time. Such a system is termed unstable. To ascertain whether a given system is stable or unstable, it is not necessary to obtain all roots of the characteristic equation. It is sufficient, for a stability analysis, to determine whether or not there are any roots of the characteristic equation in the right half-plane. Such information can be obtained graphically by use of the Nyquist method. Alternatively, by setting $\lambda = 0$ $(s = i\omega)$ in the characteristic equation, one can derive relationships between design and/or operating parameters at the boundary between stable and unstable operation. These two approaches, together with some open-loop and multi-loop techniques, are discussed in this section.

The following nomenclature pertains to Sect. 5.5 (see also Sect. 5.2):

$\mathfrak{C}$	Contour on s-plane used for Nyquist criterion
$\mathfrak{D}$	Domain of s-plane bounded by contour $\mathfrak{C}$
$D(s)$	Denominator of $g(s)$
$F(s), f(s)$	Functions defined by characteristic equation of engine system, $f(s) = F(s) - 1$
$G(s), g(s)$	Functions used in Satche technique, $g(s) = G(s) + \exp(-s\tau_T)$
K	Injection rate sensitivity factor

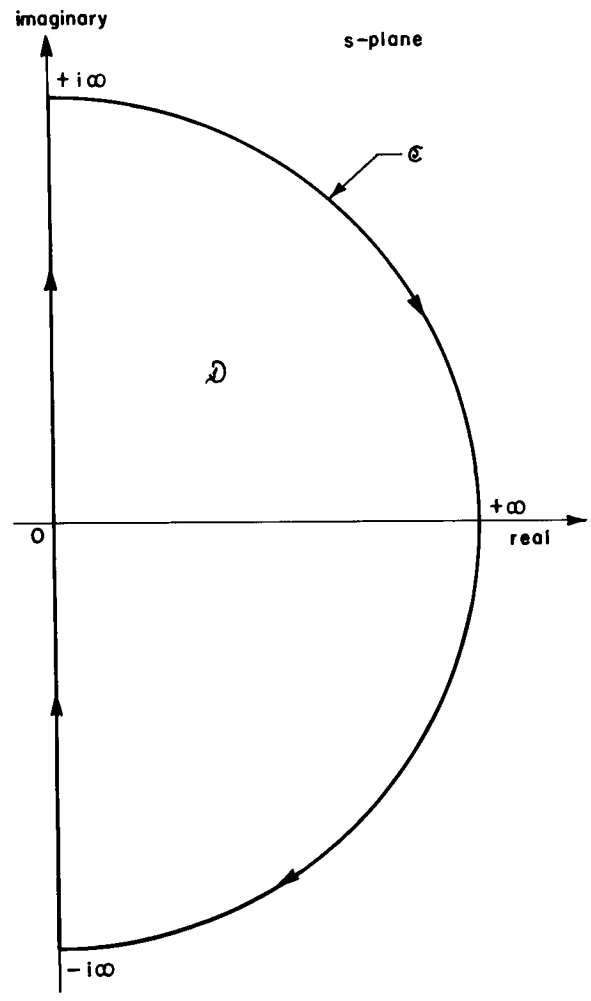

FIGURE 5.5.1a.—Nyquist contour $\mathfrak{C}$ in s-plane.

$\delta_1, \delta_2, \delta_3$ System parameters controlling stability

ϕ Phase margin

5.5.1 Nyquist and Satche Methods

The Nyquist stability method[699] is based on the theorem of Cauchy which states that if a function F(s) is analytic inside a given domain $\mathfrak{D}$ bounded by a contour $\mathfrak{C}$, except for a finite number of poles in $\mathfrak{D}$, then when s traces the contour $\mathfrak{C}$ in a clockwise direction, the vector representing F(s) in a complex plane will rotate about the origin, and the number of complete clockwise rotations that F(s) makes is equal to the difference between the number of zeros and the number of poles of F(s) in $\mathfrak{D}$. For a stability analysis, F(s) is obtained from the characteristic equation, written as

$$F(s)=0$$

The domain $\mathfrak{D}$ is taken to be the right half-plane, and the contour $\mathfrak{C}$ consists of the imaginary axis and an infinitely large semicircle in the right half-plane connecting $\pm\infty$, as shown in Fig. 5.5.1a. The plot of F(s) in the complex plane is known as the Nyquist diagram. If F(s) is analytic everywhere inside $\mathfrak{D}$, the stability criterion is that the Nyquist diagram of F(s) should not encircle the origin.

Since the characteristic equation is typically of the form

$$F(s)=f(s)+1=0$$

an alternative procedure is to plot f(s) on the complex plane and to observe the rotation of the vector drawn from the point $-1+i\cdot 0$ to f(s). This procedure is entirely equivalent to that described in the preceding paragraph (see Fig. 5.5.1b). If f(s) is analytic in $\mathfrak{D}$, the stability criterion is that f(s) must not encircle the point $-1+i\cdot 0$. In this case it is convenient to define the "phase margin" ϕ, which is the angle between the vector $f(i\omega)$ and the negative real axis, i.e.,

$$\phi=\arg f(i\omega)-180^\circ$$

The stability criterion can then be expressed in

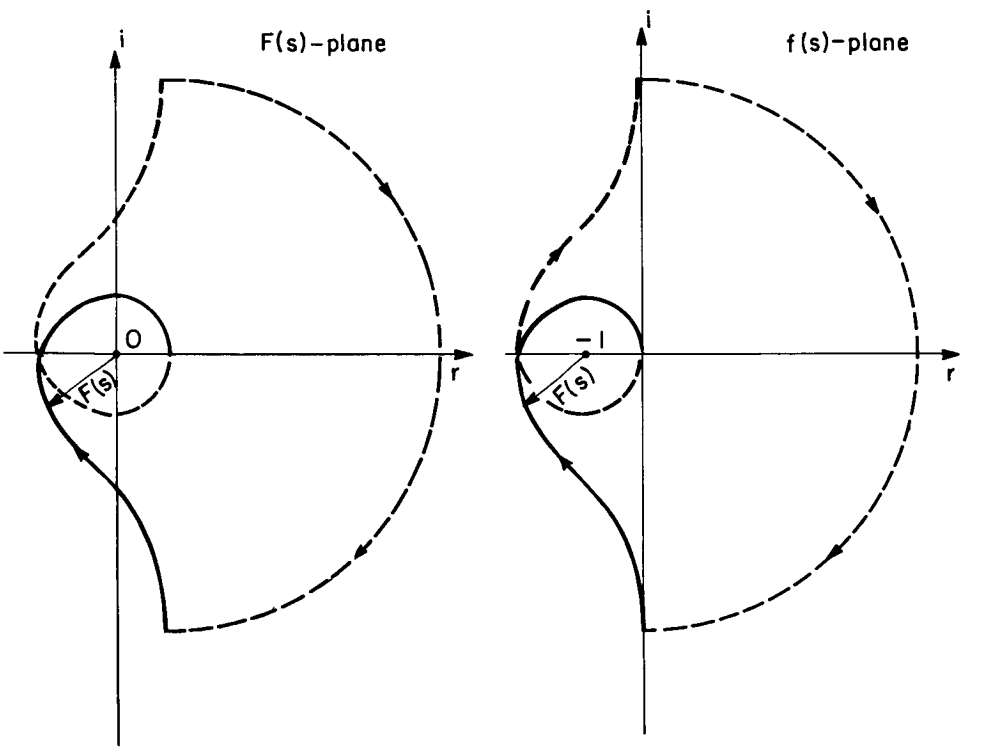

FIGURE 5.5.1b.—Nyquist diagrams in F(s) and f(s) planes.

terms of ϕ. At the frequency ω for which the magnitude $|f(i\omega)| = 1$ (called the "gain crossover"), the phase margin ϕ must be positive. This criterion is illustrated in Fig. 5.5.1c.

In rocket engine systems, the function f(s) includes the factor exp $(-s\tau_T)$, which complicates the Nyquist diagram by introducing a number of loops. Because of these loops it is necessary to use very small steps in the frequency ω when calculating f(s), in order to have a reasonably accurate plot.[179] In this situation, the modified Nyquist technique originated by Satche[626] is helpful. The characteristic equation is written in the form

$$G(s) = g(s) - \exp(-s\tau_T)$$

where

$$g(s) = -\frac{\exp(-s\tau_T)}{f(s)} = \frac{N(s)}{D(s)}$$

Since

$$G(s) = -\frac{\exp[-s\tau_T]F(s)}{F(s)-1}$$

the stability condition is still the same, that is, no zeros of G(s) may exist in the domain $\mathfrak{D}$ (right half-plane). However, a finite number of poles may have been introduced, corresponding to the zeros of D(s).

Rather than plotting F(s), the Satche method involves plotting g(s) and the unit circle, exp $(-i\omega\tau_T)$. The vector G(s) is the difference of the vectors g(s) and exp $(-s\tau_T)$. That is, the vertex of the vector G(s) is on the line g(s) and the origin is on or within the unit circle, as shown in Fig. 5.5.1d. The system is stable if the vector G(s) makes as many clockwise rotations (when s traces the contour $\mathfrak{C}$) as there are zeros of D(s) in $\mathfrak{D}$. The number of zeros of D(s) can be determined by making a separate Nyquist plot. Thus, the Satche method involves the examination of a "Satche diagram" (Fig. 5.5.1d) for G(s) and the associated Nyquist diagram for D(s). In general, it is necessary to investigate the rotations of the vectors G(s) and D(s). However, in the case that

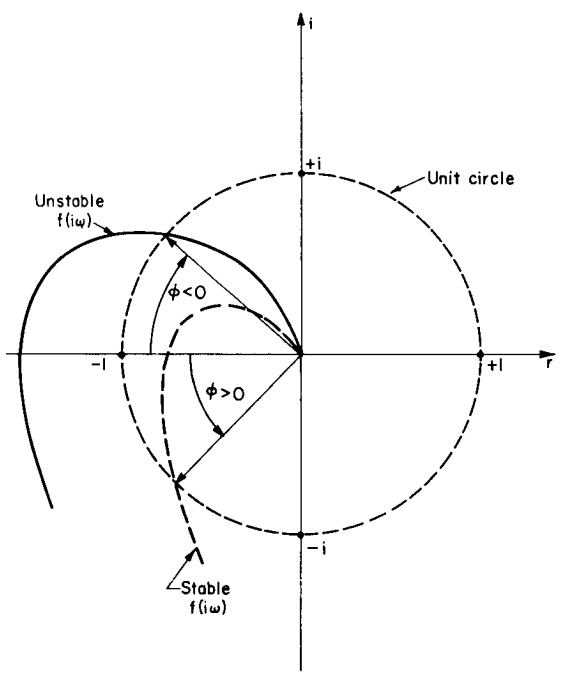

FIGURE 5.5.1c.—Phase margin and Nyquist stability criterion.

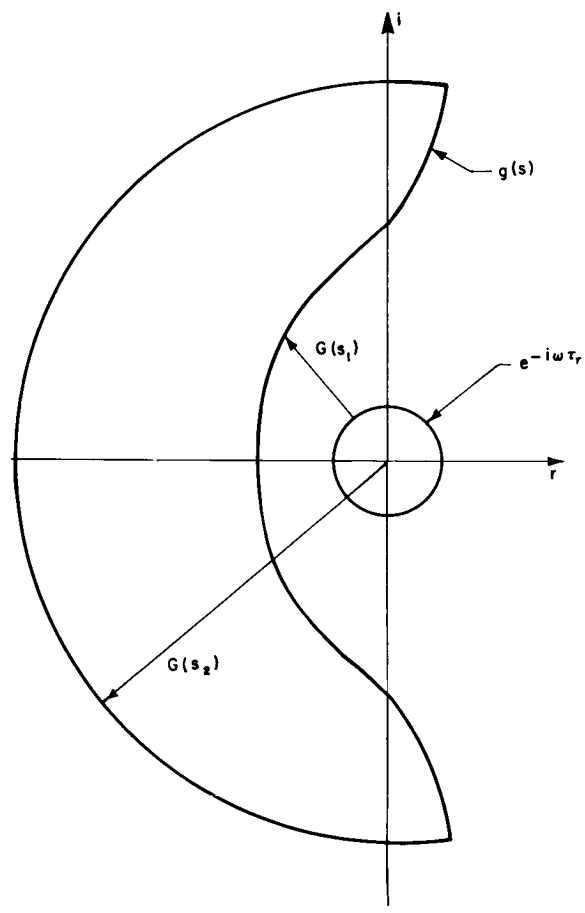

FIGURE 5.5.1d.—Satche diagram (schematic).

D(s), on the Nyquist diagram, does not encircle the origin, the system will be stable unconditionally if g(s), on the Satche diagram, does not encircle nor intersect the unit circle.

5.5.1.1 Example (single time lag model).—To illustrate the Nyquist and Satche methods, a simplified O_2/H_2 engine system is considered. For this engine, the manifold capacitances are very large, effectively decoupling the feed lines from the combustion chamber dynamics. The injector orifice impedances are purely resistive, with the fuel injector pressure drop equal to 80% of the mean chamber pressure and the oxidizer pressure drop equal to 50% of the chamber pressure. It is assumed that the combustion dynamics can be represented by a single, constant time lag of 2.75 millisec. At a mixture ratio of 5.2, $c^*=7920$ ft/sec, $(\partial c^*/\partial r)=-185$ ft/sec, and the chamber gas residence time $\theta_c=0.7$ millisec. Using Eq. (5.2.2–6), the functions f(s) and g(s) are given by

$$f(s)=\frac{K\exp(-s\tau_T)}{1+s\theta_c}\;;\qquad g(s)=-\frac{1+s\theta_c}{K}$$

where

$$K=\left[1+\frac{1+\bar{r}}{c^*}\left(\frac{\partial c^*}{\partial r}\right)\right]\frac{\bar{r}}{(1+\bar{r})}\;\frac{\bar{p}_c}{2\overline{\Delta p}_{OX}}$$

$$+\left[1-\frac{\bar{r}(1+\bar{r})}{c^*}\left(\frac{\partial c^*}{\partial r}\right)\right]\frac{1}{(1+\bar{r})}\;\frac{\bar{p}_c}{2\overline{\Delta p}_F}$$

$$=0.894$$

The complex-plane plot of $f(i\omega)$ is shown by the solid line labeled f_1 in Fig. 5.5.1e. The looping introduced by the exponential factor is apparent. It can also be seen that the phase margin ϕ at the gain crossover is approximately $+90°$, indicating a stable system. That is, since there are no poles and no rotations of the vector drawn from the point $-1+i\cdot 0$, there are no zeros of F(s) in the right half-plane. It is clear that this result holds in general when $K<1$. However, if the oxidizer pressure drop is reduced to 30% of the chamber pressure, K is increased to 1.372. For this latter case, illustrated by the dashed line in Fig. 5.5.1e, there are two rotations, hence two zeros (complex conjugates) of F(s) exist in the right half-plane.

The corresponding Satche diagram for this engine is shown in Fig. 5.5.1f. The simplicity of the g(s) curve (compared to f(s) in Fig. 5.5.1e) can be seen. It is clear that the system is unconditionally stable for $K<1$, as in the present example for $\Delta p_{OX}/p_c=0.5$ (the solid curve labeled g_1). For the case of $\Delta p_{OX}/p_c=0.3$ (dashed curve) the Satche curve intersects the unit circle, and unconditional stability is not possible. However, stable operation of this engine can be achieved for certain values of τ_T and θ_c. It can be shown[179] that the engine will be stable if

$$\frac{\tau_T}{\theta_c}<\frac{\pi-\tan^{-1}\sqrt{K^2-1}}{\sqrt{K^2-1}}\qquad(5.5.1\text{–}6)$$

For the example under consideration, with $K=1.372$, $\theta_c=0.7$ millisec, $\tau_T<1.78$ millisec corresponds to stability and $\tau_T>1.78$ millisec, to instability. Moreover, it can be seen that for such a simple engine system increasing either the combustion time lag τ_T or the injection rate sensitivity K is destabilizing, whereas increasing the residence time θ_c is stabilizing. These effects are shown much more clearly on the Satche diagram than on the Nyquist diagram.

5.5.1.2 Application to other engine systems.—The Satche method can also be applied to more complex engine systems, such as those with small injection manifolds that allow the feed line dynamics to be coupled with the combustion chamber oscillations.[179] However, looping of the Satche diagram may be introduced by the feed system resonances, requiring calculations at smaller frequency intervals and hence adding to the time and cost of the stability analysis. Similar looping effects are obtained with use of the double-time-lag combustion model (Sect. 5.2.3). For example, with a liquid oxygen/gaseous hydrogen engine in which feed line effects are not important, Eq. (5.2.3–4) gives

$$f(s)=\frac{\exp(-s\tau_F)}{1+s\theta_c}\left[K_{OX}\exp(-s\tau_{vOX})+K_F\right]$$

or (5.5.1–7)

$$g(s)=-\frac{1+s\theta_c}{K_{OX}\exp(-s\tau_{vOX})+K_F}\qquad(5.5.1\text{–}8)$$

where

$$K_X=\left[1+\frac{1+\bar{r}}{\bar{c}^*}\left(\frac{\partial c^*}{\partial r}\right)\right]\frac{\bar{r}}{(1+\bar{r})}\cdot\frac{\bar{p}_c}{2\overline{\Delta p}_{OX}}$$

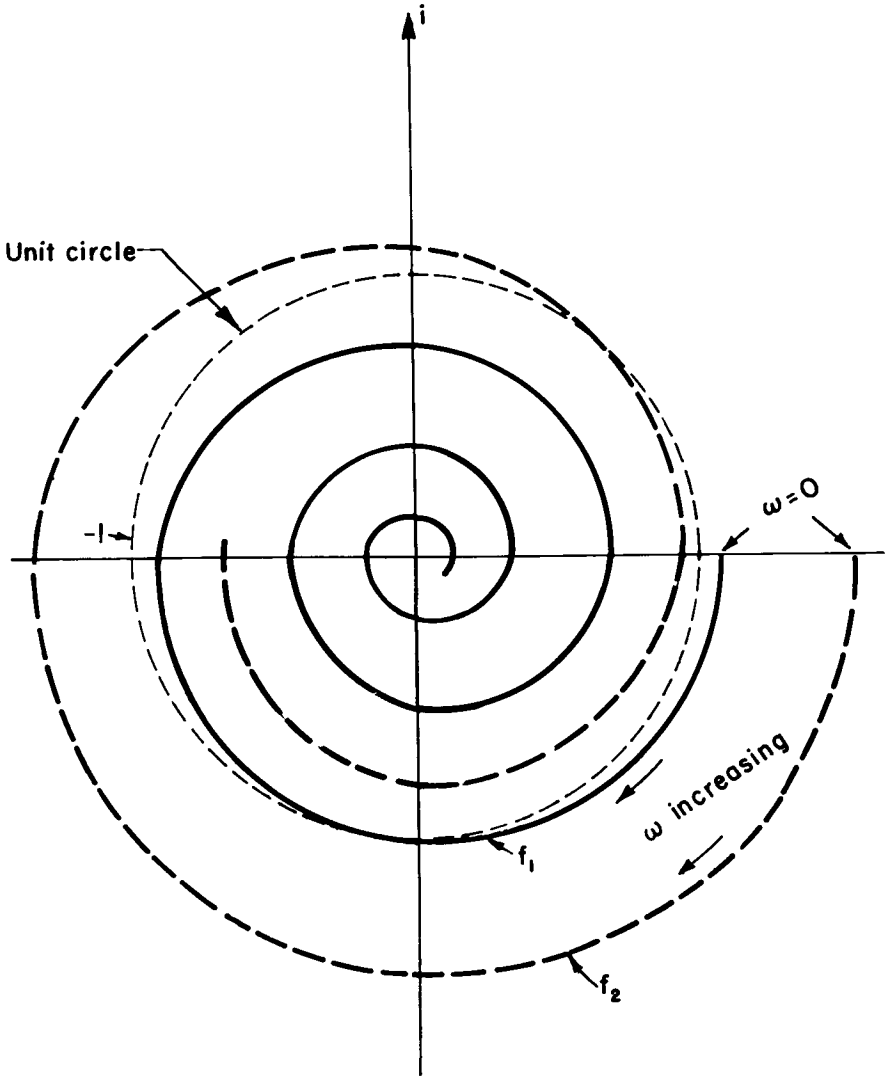

FIGURE 5.5.1e.—Nyquist diagram for rocket engine characterized by a single combustion time lag.

$$K_F = \left[1 - \frac{\bar{r}(1+\bar{r})}{\bar{c}^*}\left(\frac{\partial c^*}{\partial r}\right)\right]\frac{1}{(1+\bar{r})} \cdot \frac{\bar{p}_c}{2\overline{\Delta p_F}} \tag{5.5.1-9}$$

If K_{OX} is small compared to K_F, but not negligible, moderately-large loops are introduced into the Satche diagram, as shown in Fig. 5.5.1g. However, if $K_{OX} > K_F$, the Satche diagram spirals outward, as illustrated by Fig. 5.5.1h. In the latter case the associated Nyquist diagram for D(s) encircles the origin. Prediction of stability thus involves rather careful study of relatively complicated diagrams, drawn for particular cases, and much of the advantage of the graphical method is lost.

5.5.2 Stability Limit Approach

When it is desired to investigate the trends of stability behavior of an engine with various design or operating parameter changes, the stability limit approach is most useful. For a given type of oscillation, the stability limit is specified by a relation between the controlling parameters such that the oscillation is neither stable (decaying) nor unstable (growing). In

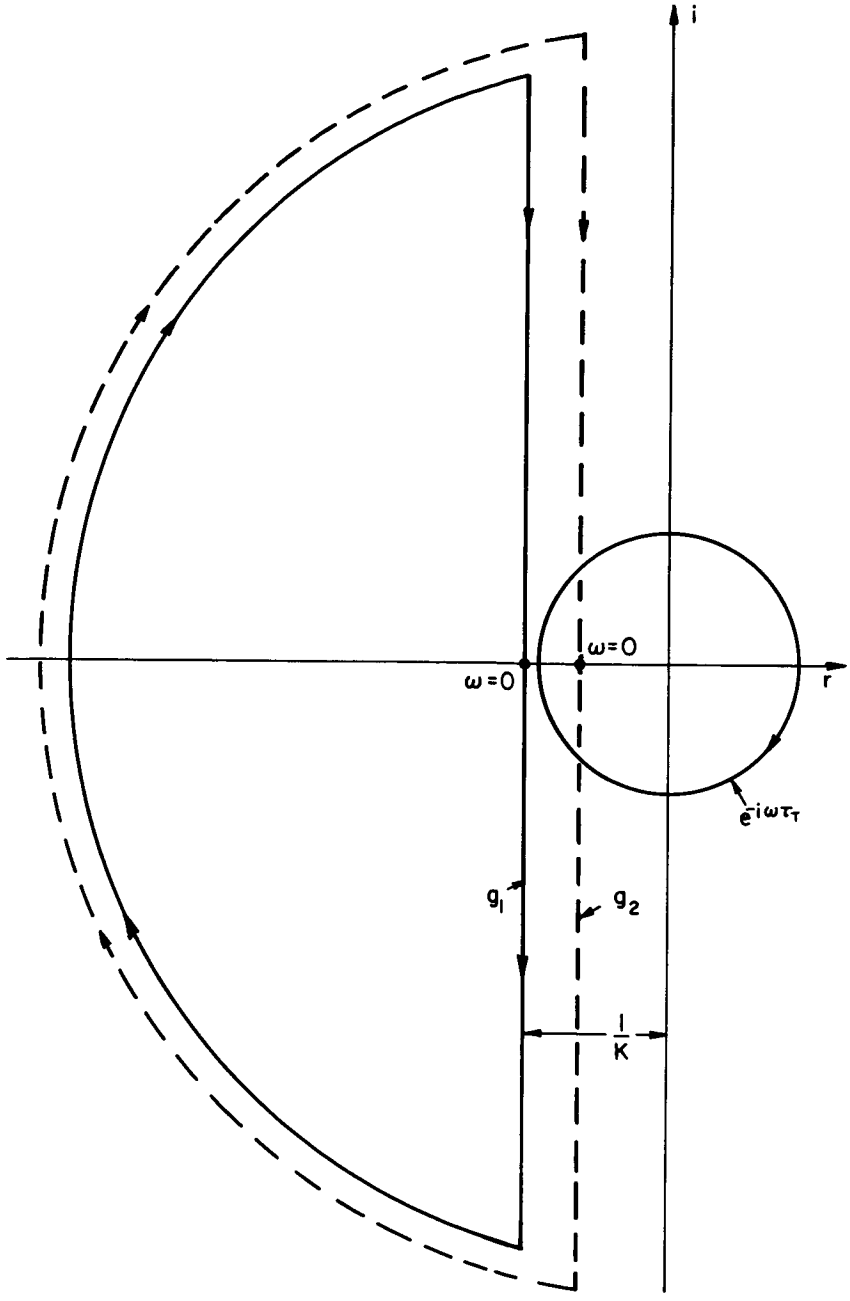

FIGURE 5.5.1f.—Satche diagram for same rocket as Fig. 5.5.1e.

other words, λ, the real part of s, vanishes. The stability limit is thus a hypersurface that divides the hyperspace formed by the engine parameters into two regions. In one region the operation of the engine is stable ($\lambda<0$); in the other region, on the opposite side of the stability limit, the engine operation is unstable ($\lambda>0$). If the variation of a certain parameter shifts the stability limit so as to decrease the size of the unstable region, that parameter variation is said to be stabilizing.

Inserting $s=i\omega$ into Eq. (5.5.1–1) yields a

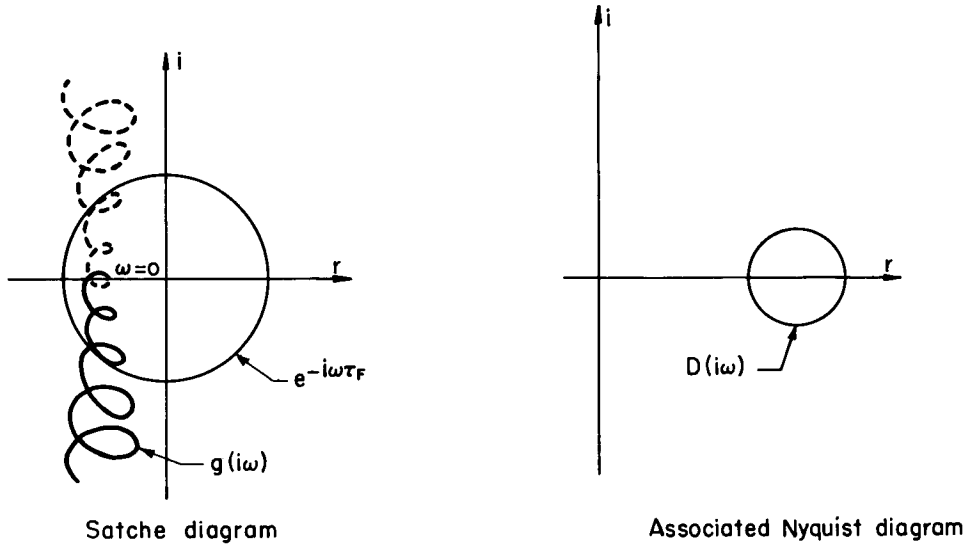

FIGURE 5.5.1g.—Satche diagram for hydrogen/oxygen engine (double time lag). $K_{OX} \ll K_F$.

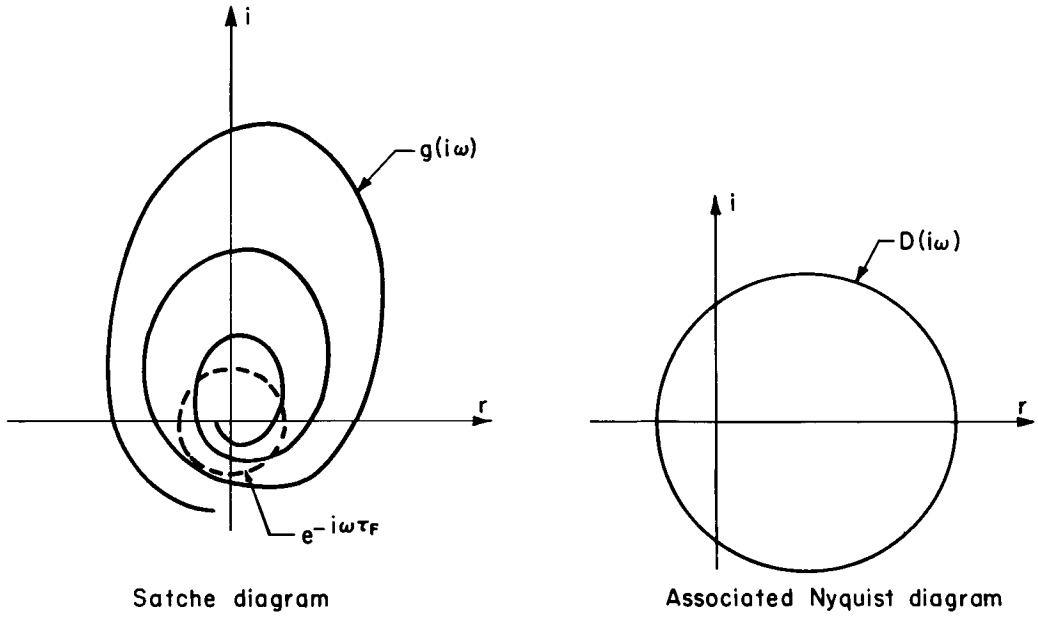

FIGURE 5.5.1h.—Satche diagram for hydrogen/oxygen engine. $K_{OX} > K_F$.

complex equation that defines the stability limit, which can thus be expressed as a relation between any two system parameters, δ_1 and δ_2, with all other parameters held constant. It is usually most convenient to divide Eq. (5.5.1–1) into its real and imaginary parts, and then to solve for δ_1 and δ_2 as functions of the frequency ω. After this the frequency can be eliminated, graphically or numerically, to give the stability limit in the form $\delta_1 = \delta_1(\delta_2)$. When the results are plotted on a δ_1, δ_2 diagram, the effect of a third parameter δ_3 can be shown by contours of $\delta_3 = \text{constant}$.

To illustrate the stability limit approach, consider the engine described in Sect. 5.5.1.1.

It is convenient to let

$$\delta_1 = \frac{\overline{\Delta p_F}}{\bar{p}_c}; \qquad \delta_2 = \frac{\overline{\Delta p_{OX}}}{\bar{p}_c}; \qquad \delta_3 = \bar{\tau}_T \qquad (5.5.2\text{–}1)$$

Stability limits are shown on the $\Delta p_F/p_c$, $\Delta p_{OX}/p_c$ diagram in Fig. 5.5.2a for three values of the total combustion time lag $\bar{\tau}_T$. For a given $\bar{\tau}_T$ value, the region of stable operation is above the limit curve. Thus increasing either $\Delta p_F/p_c$ or $\Delta p_{OX}/p_c$ is stabilizing. Since an increase in τ_T shifts the stability limit upward and to the right, thus decreasing the stable region, it is concluded that an increase in the total combustion time lag is destabilizing. Many other useful stability limit plots are possible, e.g., τ_T vs. θ_c, τ_T vs. $\Delta p_{OX}/p_c$. It should be observed that suitable experimental data can be combined with stability limit calculations to provide information about the combustion time lag $\bar{\tau}_T$ (Sect. 6.2.2), just as can be done in the high-frequency case (Sect. 6.3.3).

When the double-time-lag combustion model is used, the stability limit diagram in terms of the parameters of Eq. (5.5.2–1) is somewhat more complicated. Fig. 5.5.2b shows stability limits for the hydrogen/oxygen engine discussed in Sect. 5.5.1.2, for $\bar{r}=5.2$, $\bar{c}^*=7920$ ft/sec, $\partial c^*/\partial r=-185$ ft/sec, $\tau_{vOX}=2.0$ millisec, and $\theta_c=0.7$ millisec.

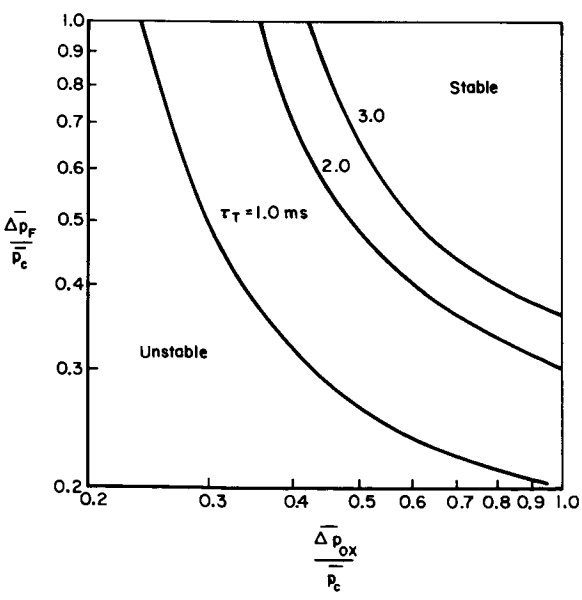

FIGURE 5.5.2a.—Stability limits for single combustion time lag model.

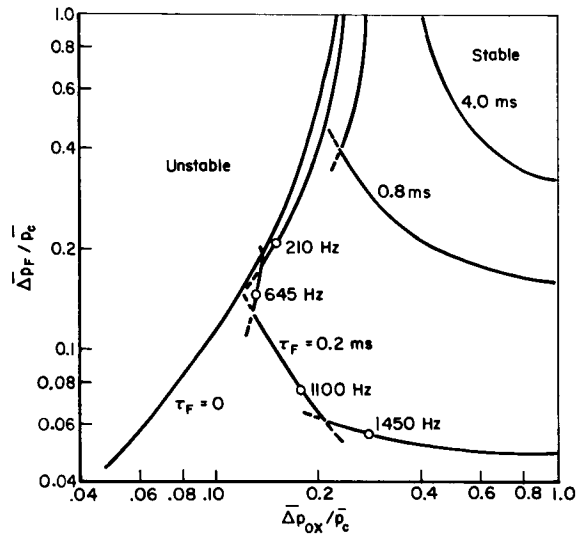

FIGURE 5.5.2b.—Stability limits for double combustion time lag model.

The looping behavior shown in Fig. 5.5.1h is reflected in the multiple, intersecting branches of the stability limits of Fig. 5.5.2b. It should be noted that each branch corresponds to a different frequency range, and that to define the entire stability limit the calculations must be extended to significantly higher frequencies than required for the single-time-lag model. It is clear from the stability limit diagram (Fig. 5.5.2b) that increasing the fuel injector pressure drop may in some cases be destabilizing, unless the oxidizer pressure drop is also increased sufficiently (see also Sect. 5.5.1.2).

5.5.3 Other Analysis Methods*

Most of the analytical techniques that have been developed for conventional control systems can also be applied to the low frequency liquid rocket combustion instability problem. The presence of the combustion time lag, or lags, will complicate the analysis in much the same way as discussed in the preceding sections.

The frequency response (Bode diagram) approach is often of great benefit in visualizing the influence of various stabilizing and destabilizing components of the engine system. The primary advantage of this approach is that the system

* L. Bickford, Author.

gain and phase are simultaneously presented as functions of oscillation frequency. Actually, the frequency response plot contains the same information as the Nyquist diagram, and the use of the frequency response to predict stability behavior follows from the properties of the Nyquist diagram.

In the frequency response method, the procedure is to plot the magnitude of $f(i\omega)$, defined by Eq. (5.5.1–1), in decibels (db), and the phase margin ϕ, defined by Eq. (5.5.1–2), in degrees, versus the log of the frequency. If $f(s)$ is analytic in the right half-plane, the simplified Nyquist criterion (no encirclements of the point $-1+i\cdot 0$) can be used, expressed in terms of the magnitude $|f(i\omega)|$, or "gain," and the phase margin. This stability criterion can be stated for the Bode diagram, in two, essentially equivalent ways:

1. If the phase margin is positive at the frequency at which the gain, in db, decreases through zero for increasing frequency, the system is stable (see also Sect. 5.5.1);
2. If the gain (in db) is negative at the frequency for which the phase margin is zero, the system is stable.

The equivalence of these criteria can be verified by reference to Fig. 5.5.1c. Criterion (2) may have a somewhat greater appeal to one's physical intuition.

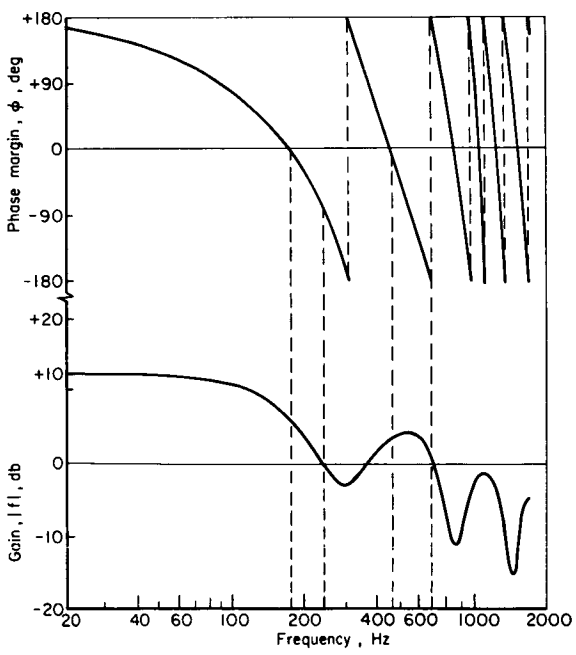

FIGURE 5.5.3.—Frequency response characteristics for same engine as Fig. 5.5.1h.

To illustrate the use of the frequency response approach, Fig. 5.5.3 shows the gain and phase margin as functions of frequency for the hydrogen/oxygen engine discussed in Sect. 5.5.1.2, the Satche diagram for which is presented in Fig. 5.5.1h. For convenience, the phase margin has been restricted to the range $-180° \leq \phi \leq 180°$. It can be seen that the system is unstable; the "dangerous" frequency range is that between 150 and 700 Hz, where the phase margin passes through zero twice while the gain is positive. Attention would thus be directed by the development engineer toward modifying the response in this frequency range.

In the analysis of very complex systems, the governing equations for the system components form a large set of simultaneous equations. For this situation, it is convenient to use matrix techniques. The frequency-dependent coefficients of the perturbation form of these equations constitute the elements of the system matrices. Using a high-speed digital computer, the solution of the equation set can be obtained for a given frequency by Gaussian elimination or by matrix inversion. A computer such as the IBM 360 is capable of solving 30 equations at 30 frequency points in about one minute. This time includes the printing of the input matrix and the values of the perturbations at each specified frequency. When resonant peaks with low damping are encountered, it is helpful to run the computer program twice. On the first run, the approximate locations of the resonances are determined. Then the second run supplies the detailed shape of the response curve in the regions of high resonance. A detailed description of matrix techniques is given in Ref. 98.

5.6 ANALOG METHODS OF SOLUTION*

There are severe limitations inherent in the analytical methods discussed in Sect. 5.5 for solving the equations governing unsteady operation of a rocket engine in the low and intermediate frequency range. To make the equations tractable,

* A. Lytle and J. Szuch, Authors.

it was necessary to linearize about a particular steady-state operating point. Investigation of a range of operating conditions or of transient operation requires many repetitions of the solution procedure.

An alternate approach is to set up an analog model of the engine system, including all of the nonlinearities and complications of the physical processes. When a disturbance is input, one can then observe directly whether or not the disturbance grows. By varying system parameters, the limits of stable operation can be traced, and the importance of the various parameters can be evaluated. Such an analog can be constructed using either a digital or analog computer. Most of the discussion in this section is applicable to either kind of computer, although some remarks are directed specifically toward the use of the analog computer. After a discussion of the general approach, the problem of representing the combustion time lag is taken up. The final portion of this section presents some typical solutions.

The following nomenclature pertains to Sect. 5.6:

G	Injector admittance
Z_c	Characteristic impedance of feed line segment
τ	Total combustion time lag

Subscripts:

t	tank
th	nozzle throat

5.6.1 Mechanization of the Engine Model

In the study of low frequency combustion instability, such phenomena as thermochemical reaction, nozzle exhaust, injector flow, and feed line dynamics are strongly coupled. The analog method simulates these engine processes by use of combinations of the following mathematical operations: inversion, algebraic summation, multiplication by a constant, integration with respect to time, multiplication and division of one variable by another, generation of trigonometric functions, generation of arbitrarily-specified functions, and representation of discontinuities and restraints.

The equations used in the analog analysis are essentially those discussed in Sects. 5.2–5.4. However, in this case the equations are not linearized and the perturbations are not assumed to have the exponential time dependence. Rather, the time derivative of the chamber pressure is evaluated in terms of the instantaneous injection, burning, and exhaust rates and then integrated to give the instantaneous pressure. Thus,

$$p_c = \frac{\mathfrak{R}(r)T_c(r)}{\mathcal{V}_c} \int \left(\frac{dm_c}{dt}\right) dt$$

where

$$\frac{dm_c}{dt} = \dot{m}_{OX_b} + \dot{m}_{F_b} - \frac{A_{th}p_c}{c^*(r)}$$

$$\dot{m}_{OX_b}(t) = \dot{m}_{OX_i}(t-\tau_{OX})$$

$$\dot{m}_{F_b}(t) = \dot{m}_{F_i}(t-\tau_F)$$

$$\dot{m}_{OX_i} = G_{OX}(p_{OX_t} - p_c)$$

$$\dot{m}_{F_i} = G_F(p_{F_t} - p_c)$$

$$r = \frac{\dot{m}_{OX_b}}{\dot{m}_{F_b}}$$

The pressure-dependence of the various rates is introduced by suitable feedback loops, as illustrated by the block diagram of Fig. 5.6.1a. Function generators are needed for the thermochemical data, e.g., $c^*(r)$, $T_c(r)$, and $\mathfrak{R}(r)$, which can be experimentally or theoretically obtained.

The dynamic characteristics of the propellant feed processes, denoted in Fig. 5.6.1a by the blocks G_{OX} and G_F, may require a considerable amount of equipment. Because of the dependence on the specific design of the feed system, it is not possible to give a general description of a feed system dynamics loop. Appropriate equations from Sect. 3.2 would form the basis of the simulation. As an example, Fig. 5.6.1b shows analog diagrams for a lossless feed line and two methods of incorporating damping. A composite feed line composed of a series of constant cross-section, pipes of various lengths may be simulated by cascading applicable sections such as shown in Fig. 5.6.1b.

Depending on the analyst using this approach, realistic system properties may be readily simulated. For example, the injector dynamics block may include injector fill time effects, by allowing the output to begin after the flow volume, integrated from $t=0$, equals the injector cavity volume. For certain injector configurations flow impedance varies inside the injector. If this variation is calculated or otherwise defined the

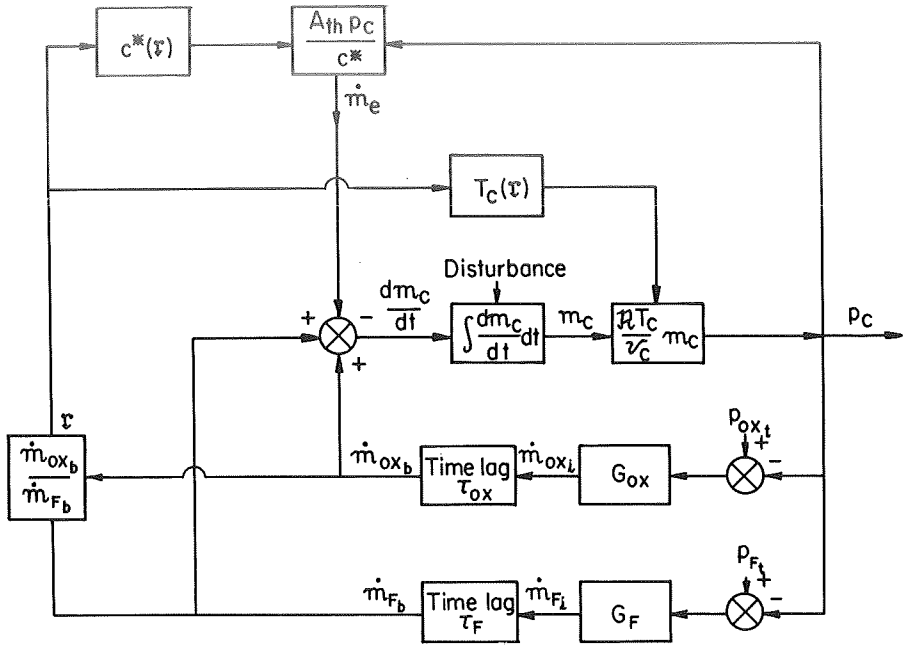

FIGURE 5.6.1a.—Block diagram of rocket engine analog.

coefficient $\mathcal{R}$ may be programmed to simulate this variation. In many systems valve opening time and dynamic properties are negligible. However, if they are not, a similar loop may be placed in series with the flow resistance loop to describe this phenomenon. The physical equations in each case may be linear or nonlinear. A similar simulation may be made for a gas system. The flow resistance section of Fig. 5.6.1c can be replaced for this case by equations or data for flow rate vs. pressure ratio (Ref. 641, pg. 175, Fig. 6.9a).

5.6.2 Representation of a Time Lag

A time delay, such as the combustion time lag, can be represented approximately by a ratio of polynomials in powers of $i\omega\tau$, known as a Padé expansion.[699,270] The order of the expansion is chosen to match the unity gain and linear phase characteristics of the pure time delay over the desired frequency range. Tables of coefficients for Padé expansions are available. An example of a pure time delay mechanization is given in Fig. 5.6.2. At some sacrifice of flexibility, it is possible to reduce the number of amplifiers needed by employing passive elements. Also, the Padé approximation method can be extended to represent variable time lags.

Time delay modules based on the Padé expansion or similar principles are available commercially. Also available are step-variable delay units consisting of cascaded, passive-element networks[411] and continuously-variable delay lines. The latter are essentially physically condensed (coiled) radio-frequency cables with one conductor spaced close to the other. A large amount of time delay, selected by positioning a slider, is possible with little attenuation at high frequencies.

5.6.3 Obtaining the Solution

The general procedure used to study stability behavior by the analog approach involves the following steps:

1. Set up the desired initial (steady-state) conditions for pressure, flow rates, etc.
2. Disturb the system by introducing a small voltage pulse at the input to the chamber pressure integrator (see Fig. 5.6.1a) to simulate the explosion of a bomb in the chamber.
3. Observe the resulting chamber pressure

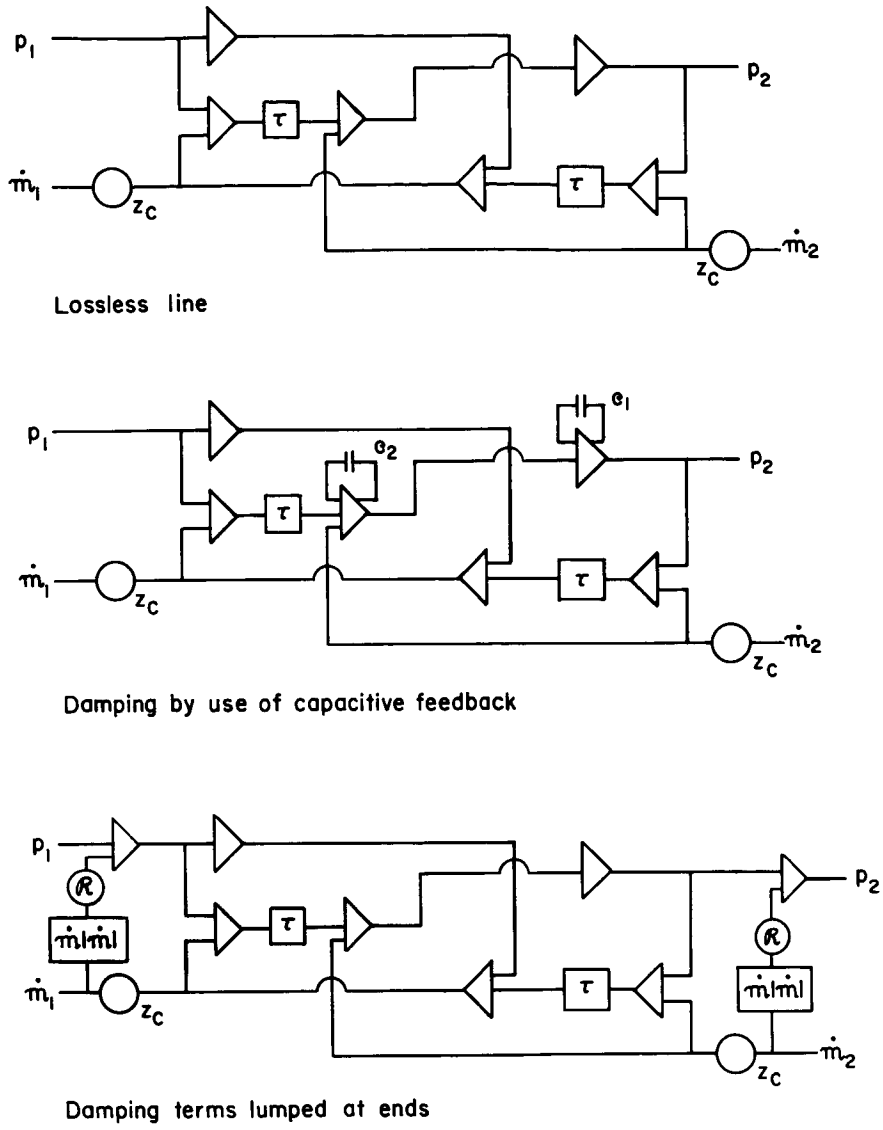

FIGURE 5.6.1b.—Analog diagrams for a feed line.

oscillations on a strip-chart recorder or a cathode-ray oscilloscope.

4. Repeat steps (1) to (3) for new initial conditions until the desired range of operating conditions has been covered.

To illustrate the method in a simple manner, an engine system is assumed to be composed of a single length of constant cross-section pipe fed from a constant pressure tank, an injector with prescribed dynamic properties, and a combustion chamber. An analog line dynamics simulation for such a system is shown in Fig. 5.6.1c. The time delay is twice the pressure-wave transport time from one end of the pipe to the other. Junctions 1, 2 are shown to indicate that if another line segment (as in a composite line) is required, an applicable configuration (see Fig. 5.6.1b) may be inserted. In fact, as many segments may be inserted as will be required to simulate the actual physical system. The frequency-dependent characteristics of the injector may readily be incorporated in the simulation.

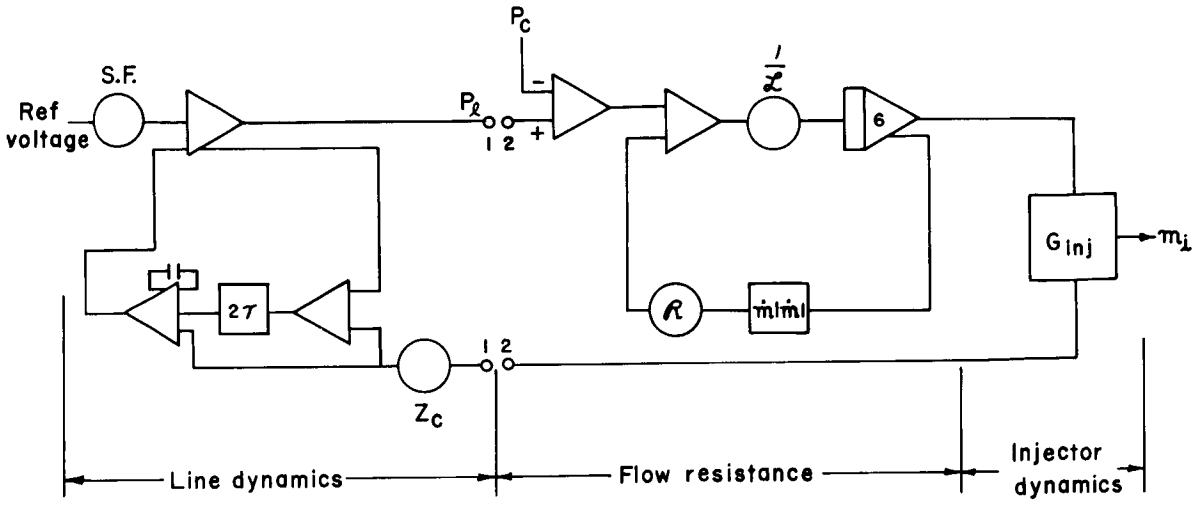

FIGURE 5.6.1c.—Analog diagram for a simple feed system.

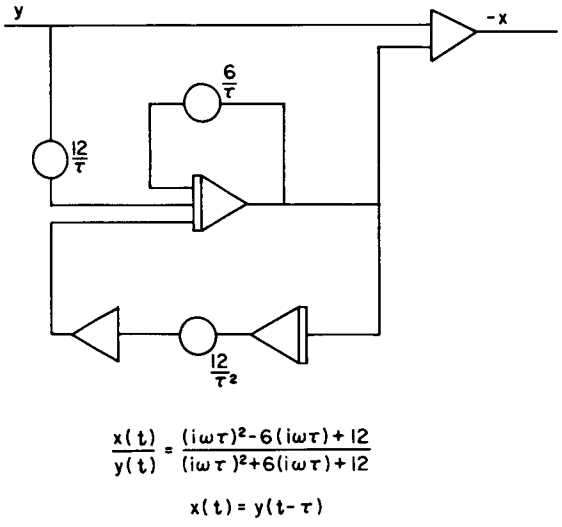

FIGURE 5.6.2.—Mechanization of pure time delay.

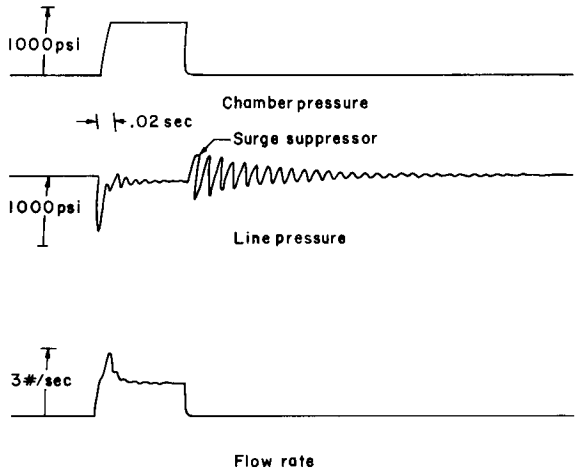

FIGURE 5.6.3.—Results of a typical analog run.

Figure 5.6.3 shows the results of an analog simulation of this engine system. The injector dynamics have been neglected; however, injector fill time is included, as can be seen by the delayed chamber pressure. Feed system pressure response, transient flow rates, and injector-fill time effects are of primary concern in this simulation.

The ultimate goal of a simulation is to approximate chamber pressure so as to detect and define the source of undesired pressure variation. Since the thermodynamic (chamber) loop couples with the feed system loop, chamber pressure coupling is important. A simplified thermodynamic loop is shown in Fig. 5.6.1a. It must be strongly emphasized that the thermochemical loop should include all applicable relationships. The diagram of Fig. 5.6.1a is only a base from which a more complete description of the actual processes may be made. Depending on the ingenuity of the analyst, various parameters, both primary and secondary, can be included. For example, thermal or thermochemical stability may be a function of $\partial c^*/\partial r$ and should be included in a more complete simulation.

Most large analog computers are 100 volt devices. That is, the voltage representing any physical quantity must not exceed 100 volts during any phase of the solution. Therefore, all variables must be amplitude-scaled. For example, if a certain pressure is known to vary between 100 and 200 psia, one might select a scale factor of 3 psia/volt for that variable. The computer voltage representing that pressure would then be expected to vary between 33.33 and 66.67 volts.

In addition to amplitude-scaling, time-scaling must be considered when mechanizing the engine model. Consideration must be given to the frequency response characteristics of the computer elements and of the data recording equipment and the ranges of the available time delay units. If, for example, a 4 millisec time delay is required in the simulation and the maximum delay available is 100 millisec, the problem can be slowed down by a factor of 25 or less.

Stability limits can be determined in terms of any significant design or operating parameter. The amplitude of the pulses needed to produce a sustained oscillation or the oscillation growth rate can be used to identify the stability limit. Disturbances may also be introduced at points other than the input to the chamber pressure integrator. For example, for a given application it may be desirable to perturb an injector or tank pressure. In fact, the flexibility allowed in the location and shape of the disturbance is one of the advantages of the analog approach.

CHAPTER 6

Use of Analytical Models in Design and Development

6.1 INTRODUCTION*

The preceding two chapters have described several theoretical approaches to the study of combustion instability. In this chapter the emphasis will be placed on the application of these theoretical models to practical problems.

The initial application of any theoretical analysis is that of interpreting and correlating experimental data. Closely related to this process is the use of theory to guide efforts to stabilize an engine that has demonstrated unacceptable stability behavior. A step beyond these applications is the prediction of stability before any actual test firings are made, so that design modifications can be made in time. Ultimately, it is hoped that some analytical considerations of combustion stability will be part of the initial design process of every new engine.

Since the basic principles and underlying assumptions of each theoretical approach were discussed in the previous chapters, they will not be repeated here. Following a brief review of the approach, the emphasis will be on the way the theory is applied to practical situations. That is, the information that must be obtained about the engine is listed, together with any preliminary operations that must be performed. Then, the calculations that must be made are outlined, with examples of the format in which the results are obtained. Finally, the use of these results to interpret data and guide development is described. Specific hardware aspects are introduced only as they illustrate and support the discussion of the method of applying the theory.

Low and intermediate frequency instability models are taken up first. Because the feed system is of primary importance, considerable attention is given to the alterations in stability that can be produced by modifications of the feed system, as predicted by the theoretical analysis. The effects of changing the combustion process and thrust chamber dynamic response are also described. Empirical correlations of the combustion time lag are used to make the connection between theoretical model and hardware design.

The three different types of high frequency combustion stability analysis are discussed in separate sections: the sensitive time lag theory in 6.3, the mechanistic combustion model in 6.4, and the response function approach in 6.5. In each case, the procedure for applying the theory is illustrated by considering the modifications of stability behavior that result from changes in design or operational factors. Experimental data are introduced to support the discussion.

The similitude approach is discussed in Sect. 6.6, with the major emphasis on empirical correlations of stability test results. In addition to a review of the similarity rules that have been obtained to date, suggestions for further development and application of this approach, along with a review of its limitations, are presented.

Finally, the use of more than one model in the development of an engine is considered. The complementary nature of the different models is outlined, and the use of one model to extrapolate, in an engineering sense, the results of another is illustrated.

6.2 LOW AND INTERMEDIATE FREQUENCY MODELS

In this section, the emphasis is placed on the application of analytical models and experimental data to low and intermediate frequency combustion instability problems in practical engine systems. The material presented here relies

* F. H. Reardon, Author.

heavily on the concepts and techniques introduced in Chapter 3, in which the dynamics of the various combustion and flow processes that occur in a liquid propellant rocket engine are discussed in detail. Frequent reference is also made to the overall engine stability models presented in Chapter 5. Although no universally successful stabilization method is recommended, several approaches to improved stability are presented and illustrated with practical examples.

The following nomenclature pertains to Sect. 6.2 (see also Sect. 5.2 and 5.4):

F_S	Feed system transfer function
F_V	Liquid transport and vaporization transfer function
F_B	Mixing and combustion transfer function
F_C	Combustion chamber flow transfer function
$f(s)$	Transfer function product, defined in Eq. (6.2.1–3)
L_n	Length of subsonic part of exhaust nozzle
$\tilde{L}_n$	Effective nozzle length for low-frequency oscillations
l	Length of feed line
l_{eff}	"Effective" chamber length for vaporization correlation
l_{50}	Effective length (l_{eff}) corresponding to 50% of propellant vaporized
$\mathfrak{S}$	Nozzle shape factor, $\mathcal{V}_n/A_cL_n$
$\mathcal{Y}_s$	Shunt admittance of lossy line
Z	Impedance ($p'/\dot{m}'$) of feed system component
Z_c	Characteristic impedance
Z_{co}	No-loss characteristic impedance
Γ	Propagation function

Subscripts:

$\grave{a}$	Shunt resonator (lossy line)
l	Main flow

6.2.1 Approach*

Low or intermediate frequency combustion instability generally involves the interaction of several components of an engine system. Any analysis of stability must consider not only the dynamics of these components, but the relationships between them. Such relationships are illustrated by the simplified block diagram of Fig. 6.2.1. In this diagram, perturbations of pressure (p') and mass flux ($\dot{m}'$) are shown at various points in the engine system. The equations governing the unsteady operation of the engine can be written schematically as follows:

$$\begin{aligned} p_c' &= F_C \dot{m}_b' \\ \dot{m}_b' &= F_{BOX}\dot{m}_{vOX}' + F_{BF}\dot{m}_{vF}' \\ \dot{m}_{vOX}' &= F_{VOX}\dot{m}_{iOX}' \\ \dot{m}_{vF}' &= F_{VF}\dot{m}_{iF}' \\ \dot{m}_{iOX}' &= F_{SOX}(p_{tOX}' - p_c') \\ \dot{m}_{iF}' &= F_{SF}(p_{tF}' - p_c') \end{aligned} \qquad (6.2.1\text{–}1)$$

where F_C, F_{BOX}, . . . are complex, frequency-dependent transfer functions of the engine components. These equations can be combined into a single equation in terms of p_c', p_{tOX}', and p_{tF}':

$$p_c' = \frac{F_C(F_{BOX}F_{VOX}F_{SOX}p_{tOX}' + F_{BF}F_{VF}F_{SF}p_{tF}')}{1 + F_C(F_{BOX}F_{VOX}F_{SOX} + F_{BF}F_{VF}F_{SF})} \qquad (6.2.1\text{–}2)$$

As discussed in Sect. 5.5, the stability of the engine is determined by the equation

$$F_C(F_{BOX}F_{VOX}F_{SOX} + F_{BF}F_{VF}F_{SF}) = f(s) = -1 \qquad (6.2.1\text{–}3)$$

where the real part of the complex frequency $s = \lambda + i\omega$ is the amplification coefficient and the imaginary part is the frequency. The engine operation will be unstable if any of the s-values that satisfy Eq. (6.2.1–3) has a positive real part. Usually, the stability condition can be expressed in terms of the magnitude or "gain" of the function $f(i\omega)$. That is, for stability $|f| < 1$ when the phase angle is $-(2k+1)\pi$, where $k = 0, 1, 2, \ldots$.

Eq. (6.2.1–3) shows clearly that the stability of an engine can be affected by making changes to any one of the components. Stabilization can be accomplished by reducing the component gain or by changing the time constant, i.e., "detuning" the system. However, it is to be expected that all changes will not be equally effective, nor equally feasible. The nature of the function $f(s)$ is such that the importance of a component change can only be determined by considering a specific engine system at a given operating point.

* J. Szuch, Author.

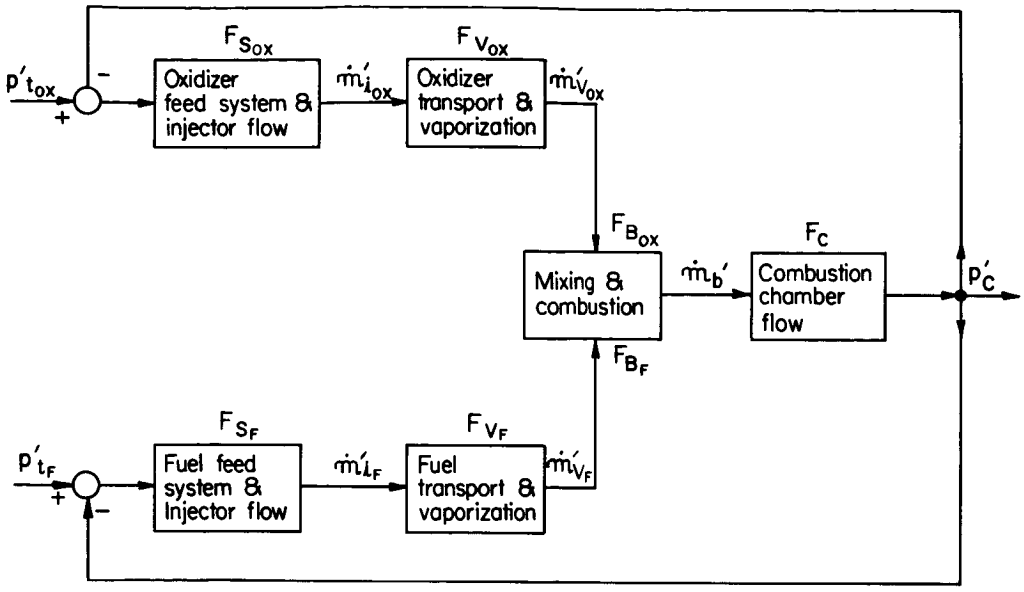

FIGURE 6.2.1.—Simplified block diagram of liquid rocket engine system.

In the remaining articles of this section, the transfer functions of the various engine system components are discussed. Primary attention is given to predicting the *stability trends* associated with possible design changes. As much as possible, general design principles are brought out. Such principles should be helpful both to the designer of a new engine system and to the development engineer seeking to improve the stability of an existing engine.

6.2.2 Combustion Time Lag Modification*

The controlling factors in the stability of a given engine system are the time delays associated with the atomization, vaporization, mixing, and chemical reaction of the propellants. Without these time lags, the basic injector-chamber system would be inherently stable, regardless of the available injector pressure drops. Unfortunately, the time delays of the combustion processes are the least known of the parameters that appear in the stability analysis. The importance of the total, or overall, combustion time lag is illustrated by Figs. 5.5.2a and 5.5.2b. These figures show theoretical stability limits, for various time lag values, as functions of the reduced injector pressure drops ($\Delta p/p_c$). Increasing the total time lag is destabilizing, since larger injector pressure drops (resistances) are required to ensure stable operation. This result is obtained for both the single and double combustion time lag theoretical models, although the shape of the stability limit depends on the model used.

Very little effort has been devoted to the experimental measurement of low frequency combustion response. Both Matthews[469] and Drain et al.[233] expressed their results in terms of a single, overall combustion delay (τ_T) such that the mass burning rate at any instant is equal to the mass injection rate τ_T seconds earlier. Matthews introduced sinusoidal perturbations into the injection rates of both oxidizer and fuel, measuring the resulting oscillations of chamber pressure. Using an unlike-impinging doublet injector (with orifice diameters about 0.040 in.) with the propellant combination LOX/ethanol, he inferred τ_T values between 0.1 and 0.3 msec for chamber pressures between 300 and 600 psia (Fig. 6.2.2a). The total time lag values of Drain et al., also shown in Fig. 6.2.2a, were obtained with a LOX/hydrogen combustor, using a showerhead injector pattern with about the same orifice size as that of Matthews. They varied both chamber pressure and mixture ratio, making use of a step-

* J. Szuch, Author.

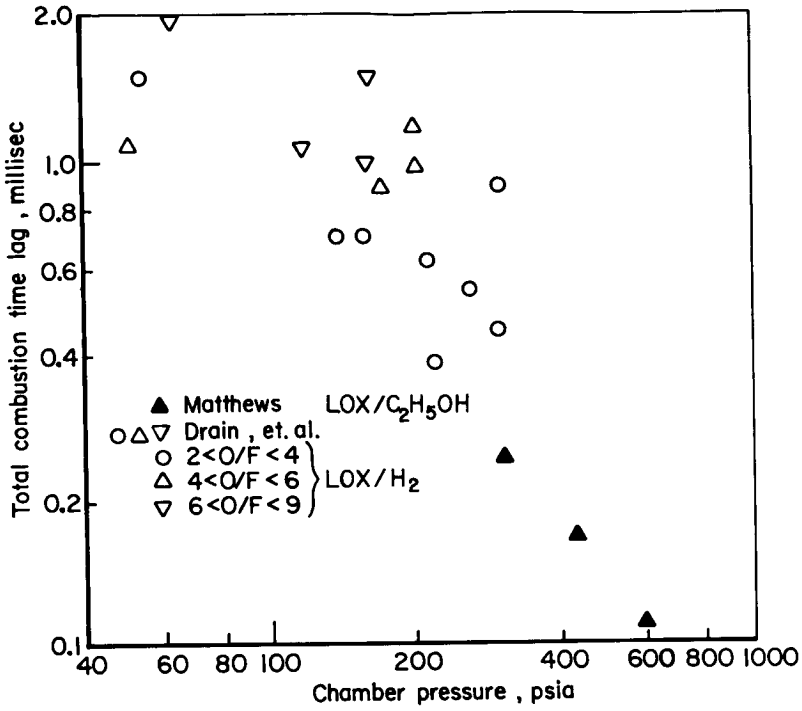

FIGURE 6.2.2a.—Experimental values of total combustion time lag for subcritical chamber pressure.

function change in the oxidizer injection rate. In addition to the pressure-dependence, similar to that found by Matthews, it was observed that increasing the mixture ratio tended to increase the total time lag.

At high chamber pressures, above the critical pressures of the propellants, there are indications that the trend shown in Fig. 6.2.2a no longer holds. Fig. 6.2.2b presents results for coaxial-tube injectors of varying sizes, covering chamber pressures from 1000 to 2500 psia.[7] It is interesting to note that the τ_T curve is roughly parallel to the curve representing the mean of the sensitive time lag (τ) data*. The ratio τ_T/τ varies between 5 and 10. Matthews also obtained τ values from his data, and found that τ_T/τ was about 3 for his test conditions.

Although the assumption of a single combustion time lag gives satisfactory results in many applications, it is shown in Chapter 5 that a better representation of the combustion response is obtained by dividing the total time lag for each

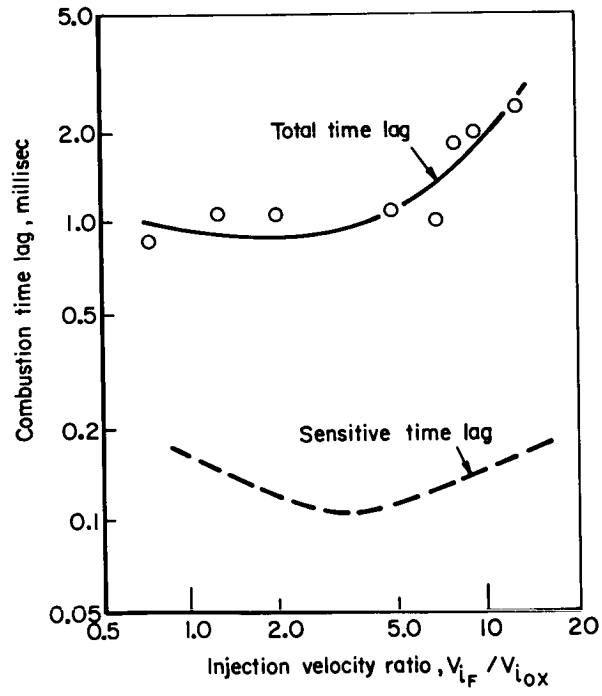

FIGURE 6.2.2b.—Experimental values of combustion time lag for supercritical chamber pressure.

* The sensitive time lag is defined in Sect. 4.3.

propellant into a vaporization time (different for the two propellants) and a mixing, burning time (same for both propellants). To date, no direct experimental measurements of these separate time delays have been published. However, good estimates of the vaporization time can be obtained from the analysis of Priem and Heidmann.[564] Assuming vaporization to be the rate-controlling process, calculations of fraction vaporized and droplet trajectory were made for a large number of initial spray and combustor conditions. The results were correlated by means of an effective chamber length, defined in terms of the various design parameters (viz, cylindrical length L_c, subsonic nozzle length L_n, contraction ratio $\epsilon_c = A_c/A_t$, nozzle shape factor $\mathfrak{S}$ = nozzle volume/A_cL_n, chamber pressure p_c, propellant temperature T_L, mean droplet diameter $\bar{d}_L$, and injection velocity V_i) by the equation

$$l_{eff} = \left[\frac{L_c}{\epsilon_c^{0.44}} + \frac{0.83L_n}{\epsilon_c^{0.22}\mathfrak{S}^{0.33}}\right] \times \left[\frac{(p_c/p_{ref})^{0.66}}{(1-T_L/T_{crit})^{0.40}(\bar{d}_L/\bar{d}_{ref})^{1.45}(V_i/V_{ref})^{0.75}}\right] \qquad (6.2.2\text{–}1)$$

where $p_{ref} = 300$ psia, $\bar{d}_{ref} = 0.006$ in., $V_{ref} = 100$ ft/sec. Fig. 6.2.2c shows the calculated fraction vaporized as a function of the effective length, for sprays of various propellants with drop-size distributions having geometric standard deviations of 2.3.

In a later study, Heidmann and Wieber[346] calculated the frequency response of unsteady droplet vaporization and showed that the time lag for vaporization was equal to the time to vaporize 50% of the mass of a mean-size droplet. The calculated droplet histories of Priem and Heidmann showed that the droplet velocity is very nearly equal to the injection velocity in this time interval. Thus, the vaporization time lag can be determined by using Fig. 6.2.2c to find the effective length corresponding to 50% vaporized, l_{50}, using Eq. (6.2.2–1) to find $L_{c_{50}} = L_c(l_{eff} = l_{50})$,* and finally using the relation

$$\tau_v = \frac{L_{c_{50}}}{V_i} \qquad (6.2.2\text{–}2)$$

The least known of the parameters in Eq. (6.2.2–1) is the mean droplet diameter $\bar{d}_L$. In the absence of systematic spray measurements, Priem and Heidmann[564] used experimental performance data, in a reverse application of Eq. (6.2.2–1), to determine $\bar{d}_L$ as a function of orifice diameter. Results for three injector types are shown in Fig. 6.2.2d. For coaxial-tube injector elements, Hersch and Rice[352] correlated cold-flow experimental data with the equation

$$\bar{d}_L = \text{constant} \cdot d_i \sqrt{\frac{\dot{m}_i V_i}{\dot{m}_o V_o}} \qquad (6.2.2\text{–}3)$$

* The notation indicates that L_c is determined from Eq. (6.2.2–1) for the condition $l_{eff} = l_{50}$.

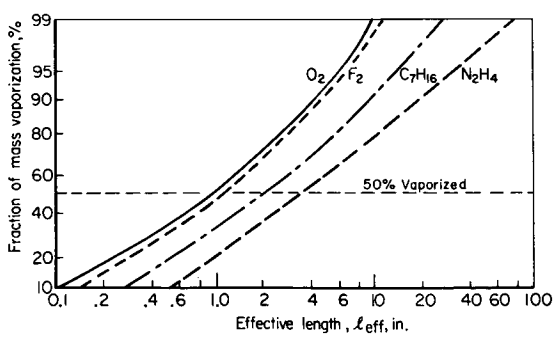

FIGURE 6.2.2c.—Priem-Heidmann correlation of mass vaporized with effective chamber length for several propellants. Geometric standard deviation of spray, 2.3.

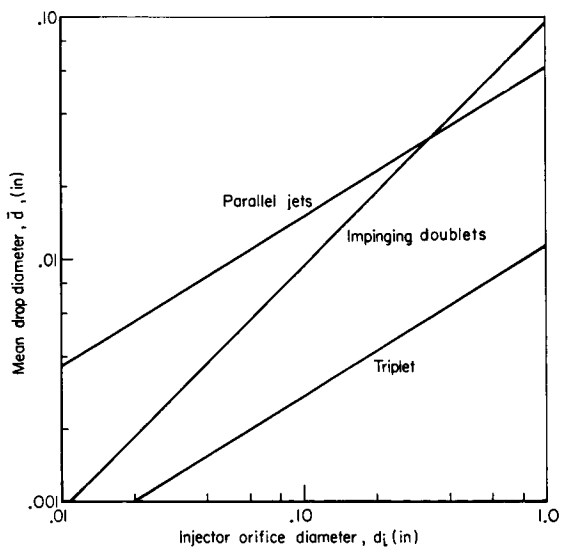

FIGURE 6.2.2d.—Mean drop sizes determined from experimental combustor performance and effective length correlation.

where the subscript i refers to the central tube and o denotes the annulus. For LOX/hydrogen, experimental stability-limit measurements yielded a value for the constant in Eq. (6.2.2–3) of 0.296.

Once the vaporization time delay has been found (and added to the impingement time for impinging-jet injectors), the problem still remains of determining the value of the mixing and reaction time τ_m. The most commonly used method is to adjust τ_m to match observed chugging frequencies, using the theory developed in Chapter 5. If no experimental data are available, stability limits can be calculated for a range of values of τ_m (e.g., Fig. 5.5.2b). As experimental instability data are accumulated for different engine configurations, it should be possible to develop correlations similar to those for the sensitive time lag (see Sect. 6.3). Another possibility is to make use of the results of Hersch,[351] who correlated the loss in performance due to incomplete mixing with such factors as chamber length, element spacing, and number of injection elements.

6.2.3 Feed System Changes

Although rocket engine feed systems have been represented in Fig. 6.2.1 very simply by the transfer functions $F_{S_{OX}}$ and F_{S_F}, these transfer functions are actually quite complicated. There are several places in a typical feed system where changes can be made to improve stability. These places include the injector orifices, manifolds, and feed lines. In addition, special stabilizing devices may be added; most commonly, resonators have been mounted on or close to the injection manifolds. However, techniques for increasing the dynamic losses in the feed lines have also been proposed, and are also considered in this section.

*6.2.3.1 Injector impedance.**—The simplest approach to low frequency stabilization would seem to be the incorporation of additional pressure drop (if available) into the injector elements. This change would decrease the feed system gain and, consequently, the overall engine system gain. However, in certain cases it is actually possible to destabilize an engine by increasing one of the injector pressure drops. Such a possibility has been shown theoretically by the double combustion time delay model (Sect. 5.2.3). An additional complication is the influence of the injector element design on the combustion time delays. Therefore, when a change in the injector impedance is considered, the associated changes in propellant injection velocity and combustion time lags must be included in the analysis.*

As an example, consider a LOX/hydrogen engine using concentric-tube injector elements. Assuming, for simplicity, that the feed lines are decoupled from the injector by large manifold capacitances, but including the effects of injection velocity on the oxidizer vaporization time, the low frequency stability boundary is shown in Fig. 6.2.3a. As the reduced injector pressure drop of the fuel is increased, the effect is destabilizing for low pressure drop but is stabilizing for reduced

* J. Szuch, Author.

* Other injection effects are discussed in Sects. 3.3 and 5.3.

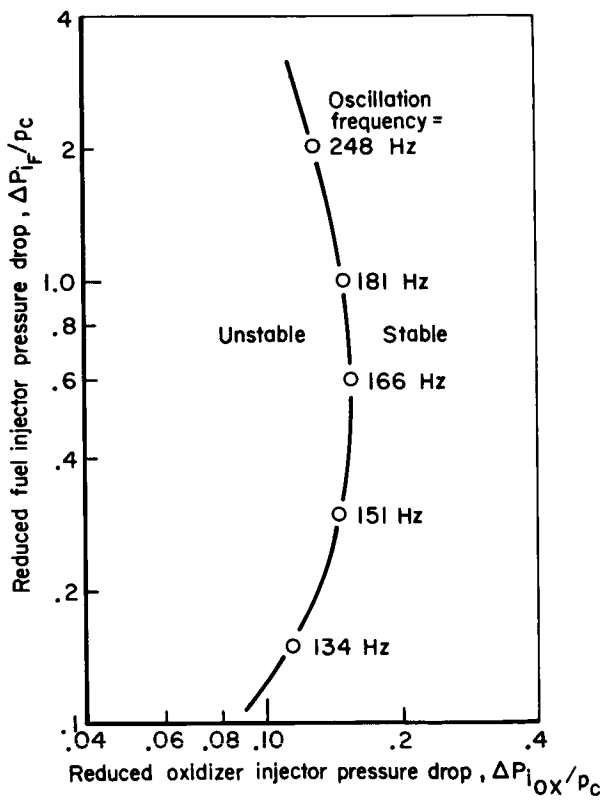

FIGURE 6.2.3a.—Theoretical low-frequency stability limit for gaseous-hydrogen/liquid-oxygen rocket engine. Infinite injector capacitances.

pressure drop greater than 1.0. The stabilizing effect results from the reduced oxidizer vaporization time caused by the higher fuel velocity. It should be noted that the chugging frequency increases with increasing fuel injector pressure drop because of the interaction of injector element design and combustion time lag. If a constant vaporization time were assumed, the frequency would decrease with increasing fuel injector pressure drop (see Fig. 5.5.2b).

6.2.3.2 Manifold capacitance.†—The capacitance of the injection manifold, which is a measure of the ability of the manifold to store mass, includes both the compressibility of the propellant and the flexibility of the hardware. The response of the feed system to chamber pressure oscillations depends on the interaction of the manifold capacitance with the resistance and inertance properties of the injector and feed lines.* At low frequencies, the impedance of a feed system, looking upstream from the injector, approaches that of a pure resistance, equal to the sum of the injector and line resistances. At very high frequencies, the impedance approaches that of a pure inertance. In the intermediate range of frequencies, the manifold capacitance can have a strong effect on the feed system impedance and, hence, on engine stability.

To show the effects of manifold capacitance, it is convenient to assume that the feed line upstream

† J. Szuch, Author.

* See Sect. 3.2 for definitions of these impedance quantities.

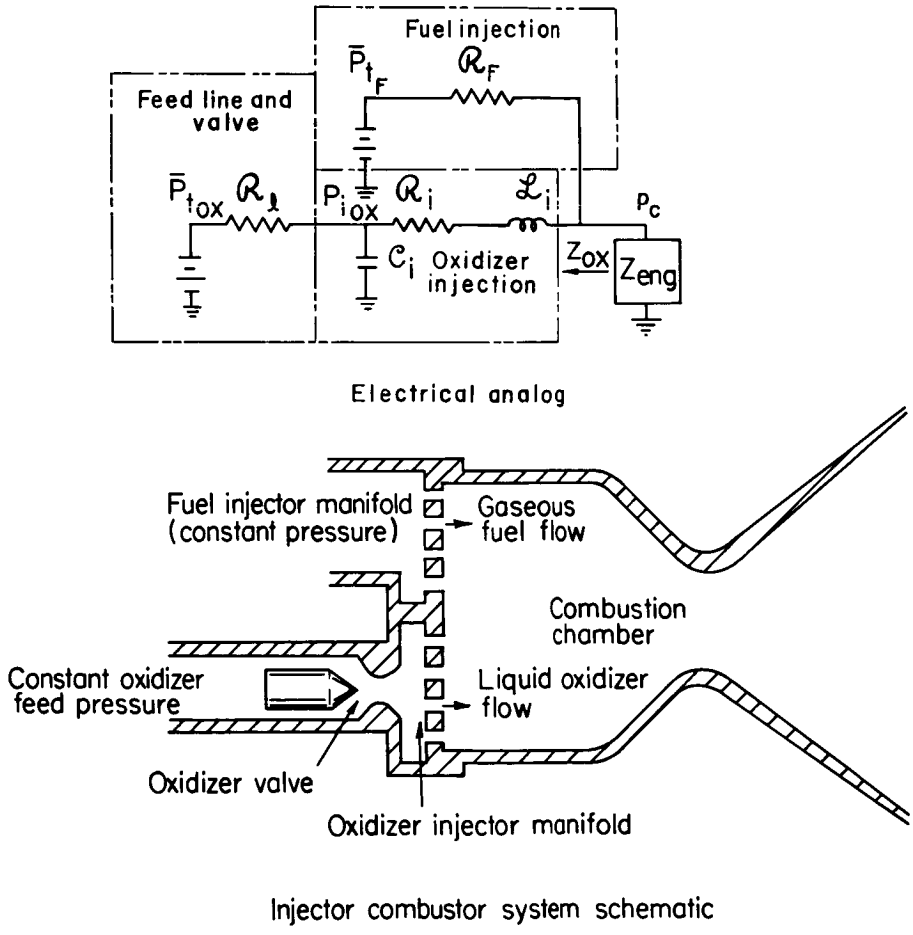

FIGURE 6.2.3b.—Electrical analog for injector-combustor system using gaseous fuel and liquid oxidizer.

of the manifold is purely resistive, such as the oxidizer system shown in Fig. 6.2.3b. The impedance of this feed system is given as a function of the angular frequency ω by

$$Z_0(\omega) = \frac{\mathcal{R}_i + \mathcal{R}_l + i\omega\mathcal{L}_i - \mathcal{C}_i\mathcal{R}_l\mathcal{L}_i\omega^2}{1 + i\omega\mathcal{R}_l\mathcal{C}_i} \qquad (6.2.3\text{–}1)$$

where the component properties are identified in Fig. 6.2.3b. If the feed line resistance is very high (at the frequency of interest), the chamber sees an impedance resulting from the series combination of the injector resistance and inertance and the manifold capacitance. Alternatively, if the manifold capacitance is sufficiently large, the manifold impedance will be so small as to isolate the injector from the feed line. On the other hand, for a small manifold capacitance, the impedance seen by the chamber will be the sum of the injector and line impedances and will be larger than the injector impedance alone.

These ideas can be clarified by means of an example. Fig. 6.2.3c shows the stability limits for the engine illustrated in Fig. 6.2.3b, which is essentially the same as that considered in Fig. 6.2.3a, except that the manifold capacitance is now a parameter (whereas in Fig. 6.2.3a, the capacitance was assumed to be infinite). It is seen that capacitance values below about 0.00025 in.^{2} have a great effect on engine stability. For a capacitance value of about 0.00010 in.^{2}, the engine can operate stably with little or no oxidizer injector pressure drop.

One of the serious problems in predicting the stability of a proposed engine is determining accurately what the capacitance is going to be during actual operation. Bubbles of propellant vapor or of gases dissolved in the propellant can

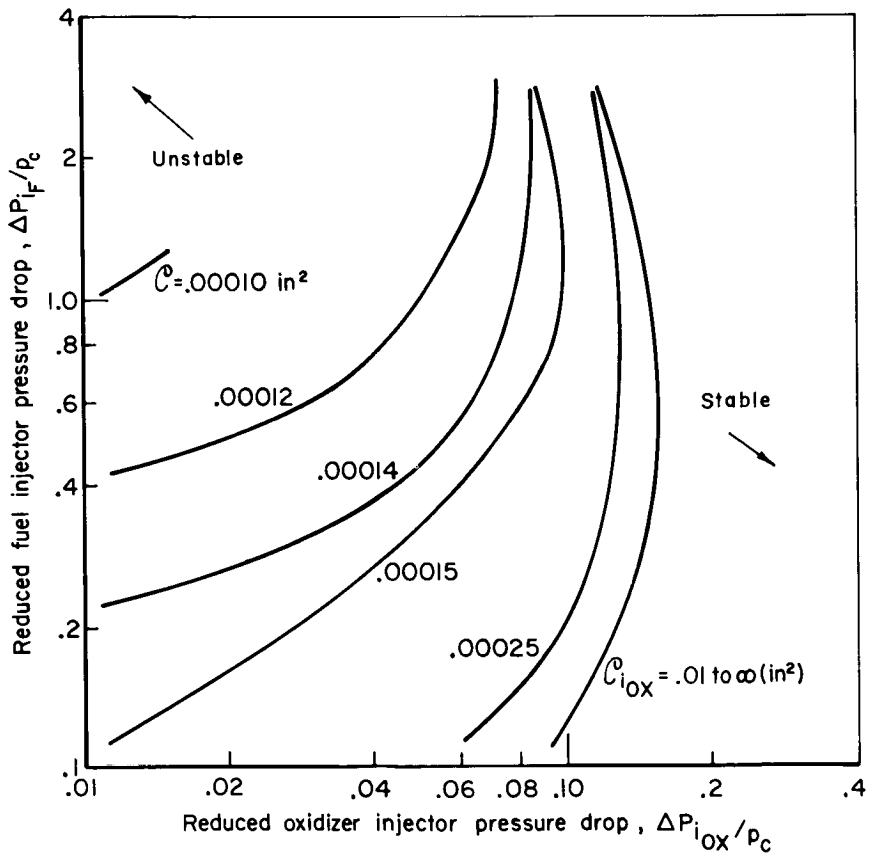

FIGURE 6.2.3c.—Effect of oxidizer injector capacitance on theoretical stability limit for gaseous-hydrogen/liquid-oxygen engine. Infinite fuel capacitance.

make drastic changes in the manifold capacitance. Pressure-fed engines are particularly susceptible to dissolved gas in the propellants. The release of this gas when the propellant undergoes a decrease in pressure (such as in passage through the valve in Fig. 6.2.3b) may decouple the injector from the rest of the feed system, and lead to oscillatory engine operation.[396] Sampling of propellants under typical operating conditions may be necessary to obtain valid capacitance information.

*6.2.3.3 Resonators.**—Generally, the feed system of a rocket engine is more complex than the simple resistive configuration discussed in the preceding section and may, itself, be the cause of undesirable oscillations. It is possible for the feed system to have a low impedance, looking downstream from the pressure source (tank or pump), at a certain frequency. This frequency is not necessarily at the characteristic chugging frequency (at which the impedance looking upstream from the chamber is low). In this case, a perturbation in pressure at the upstream end of the feed system could result in sizable oscillations in flow rate and chamber pressure.

For such cases of discrete-frequency sensitivity, some form of resonator may be used to dissipate energy in an oscillating feed system. The simplest form of resonant device is the quarter wave tube.

* J. Szuch, Author.

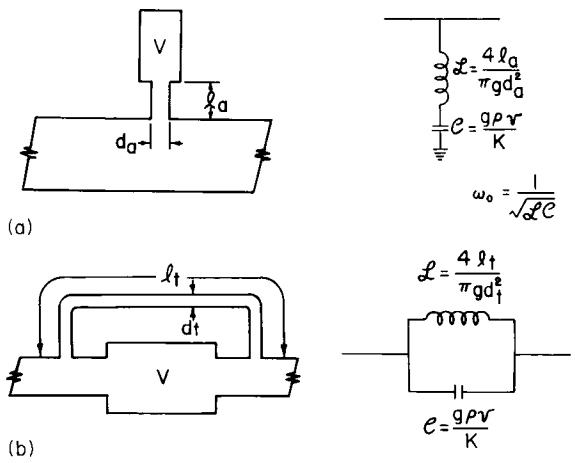

(a) Helmholtz resonator.
(b) Parallel (Quincke-tube) resonator.
FIGURE 6.2.3d.—Two types of resonators for feed system stabilization.

Another simple device is the Helmholtz resonator,[503] shown in Fig. 6.2.3d(a), consisting of a cavity and entrance aperture. By correctly sizing the cavity and aperture, the device can be made series resonant at any desired frequency. That is, the Helmholtz resonator will have a minimum, purely resistive flow impedance at that frequency and will prevent pressure waves from traveling downstream to the chamber.

Another form of resonator that can be used is the parallel-resonant configuration, known as the Quincke resonator, Fig. 6.2.3d(b). This device has the characteristic of a very high flow impedance at the resonant frequency. In addition to attenuating flow oscillations in the feed system, the added impedance could be helpful in preventing chamber driven instabilities.

*6.2.3.4 Feed line losses.**—Losses of oscillatory energy can be achieved in the propellant feed lines by means of the "lossy" line,[98] the hydraulic capacitor,[381] or gas injection.[760] The analysis of an absorptive or "lossy" fluid transmission line is based on one-dimensional wave propagation in a duct lined with distributed Helmholtz resonators. A network that represents one stage of the line is shown in Fig. 6.2.3e. The series impedance term Z_s consists of the inertance $\mathcal{L}_l$ and resistance $\mathcal{R}_l$ of the fluid in the main flow path. The shunt admittance term $\mathcal{Y}_s$ results from the parallel combination of the main flow fluid capacitance $\mathcal{C}_l$ and the resonator admittance, consisting of the inertance $\mathcal{L}_{\grave{a}}$, the resistance $\mathcal{R}_l$, and the capacitance $\mathcal{C}_{\grave{a}}$.†

The fundamental equations describing sinusoidal pressure and flow oscillations in a feed line with low mean-flow velocity are the Fourier-transformed, one-dimensional wave equations.[648] From these equations, the relation between the input impedance ($Z_1 = p_1'/\dot{m}_1'$) in terms of the output impedance ($Z_2 = p_2'/\dot{m}_2'$) for a line of length l is obtained:

$$Z_1 = \frac{Z_2 + Z_c \tanh \Gamma l}{1 + (Z_2/Z_c) \tanh \Gamma l} \qquad (6.2.3\text{–}2)$$

* L. L. Bickford, Author.

† See Sect. 3.2 for definitions of these impedance quantities.

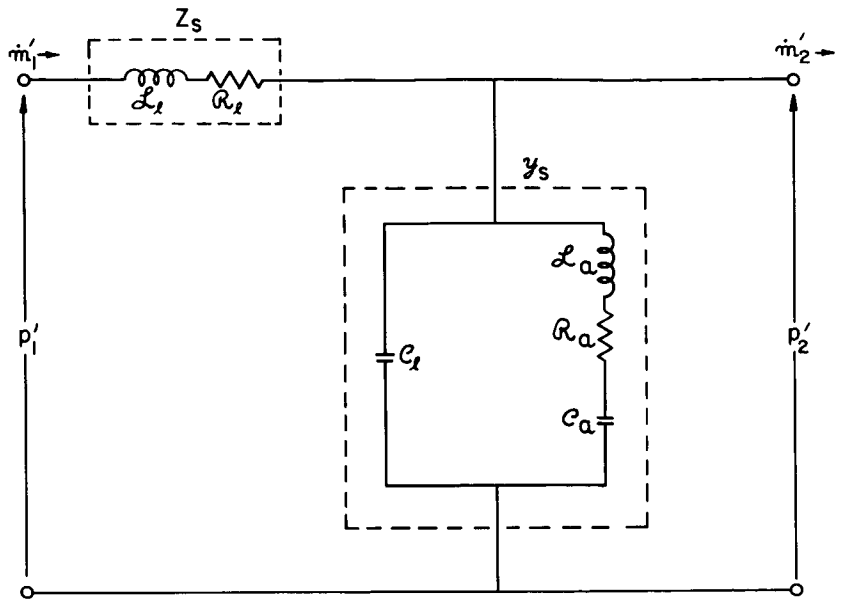

FIGURE 6.2.3e.—Electrical analog for one section of a "lossy" line.

where $Z_c = \sqrt{Z_s/\mathcal{Y}_s}$ is called the "characteristic impedance" and $\Gamma = \sqrt{Z_s\mathcal{Y}_s}$ is the "propagation function." Fig. 6.2.3f shows the dependence of Z_c on frequency and capacitance ratio $\mathcal{C}_a/\mathcal{C}_l$. Similar information is given for Γ in Fig. 6.2.3g. For generality, both figures make use of normalized variables, for which the reference quantities are the no-loss characteristic impedance $Z_{co} = \sqrt{\mathcal{L}_l/\mathcal{C}_l}$, the resonant frequency of the resonator $\omega_a = (\mathcal{L}_a\mathcal{C}_l)^{-1/2}$, and the nominal acoustic velocity in the line $a_L = \Delta x/\sqrt{\mathcal{L}_l\mathcal{C}_l}$*.

Eq. (6.2.3–2) and Figs. 6.2.3f, g are valid only when the mean flow velocity $\bar{V}_L$ is much smaller than the nominal acoustic velocity a_L. For a line with a very large distributed capacitance $\mathcal{C}_l$, this condition may be violated even at low flow velocities because the nominal acoustic velocity is greatly reduced.

The fluid dynamic behavior of a propellant feed line can be modified by injecting a non-condensable gas.[760] The gas bubbles affect the acoustic proper-

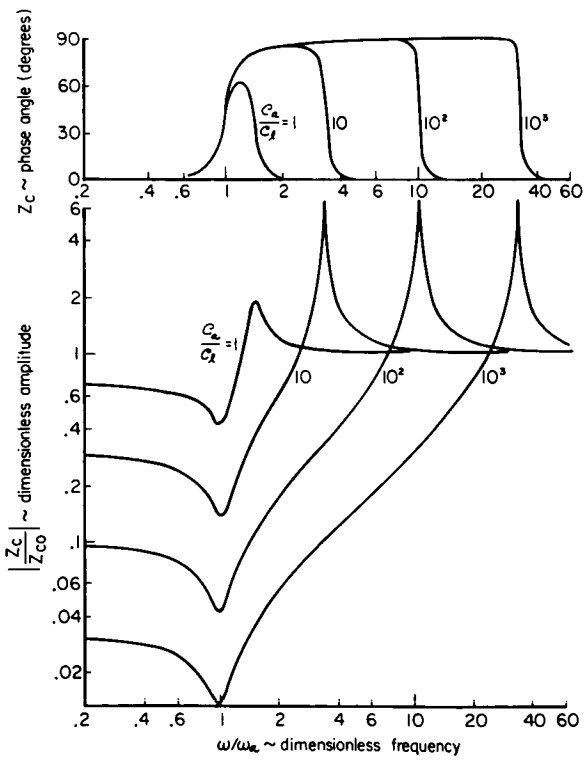

FIGURE 6.2.3f.—Characteristic impedance of a "lossy" line. $\mathcal{R}_a/2\omega_a\mathcal{L}_a = 0.1$.

* The nominal acoustic velocity is not necessarily equal to the velocity of sound in an infinite fluid medium. It may be considerably reduced by the structural compliance of the pipe walls (see Sect. 5.4.1).

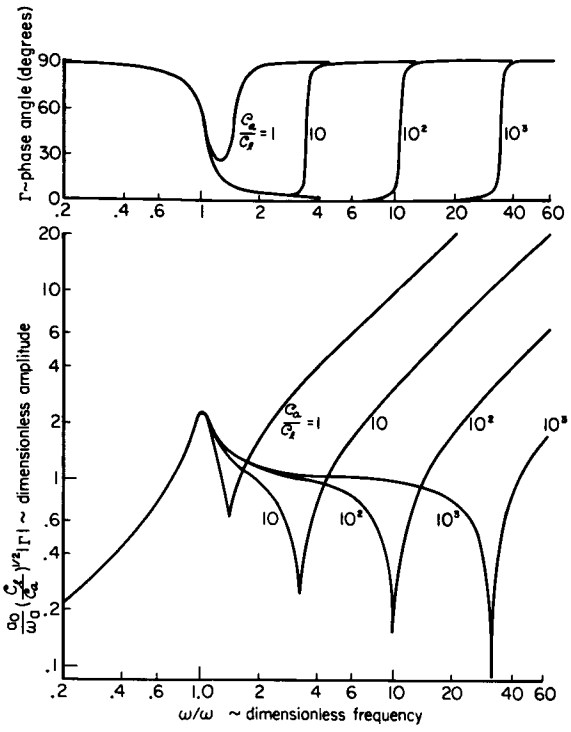

FIGURE 6.2.3g.—Propagation function for a "lossy" line. $\mathcal{R}_{\dot{a}}/2\omega_{\dot{a}}\mathcal{L}_{\dot{a}}=0.1$; low velocity flow.

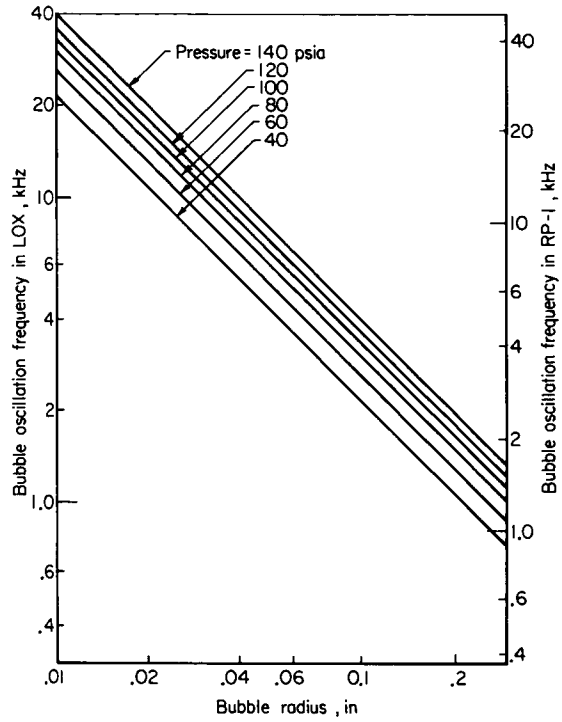

FIGURE 6.2.3h.—Bubble oscillation frequencies for helium bubble in LOX and RP-1.

ties of the line by energy dissipation as well as by added compliance. The dissipation is caused primarily by thermal effects, such as irreversible heat transfer across the bubble walls. The thermal damping is maximum for frequencies corresponding to pulsations that are somewhere between isothermal and adiabatic. The analytical model for the absorptive or "lossy" line can also be applied to a line in which the bubbles are well distributed. In the bubble-filled line, the shunt resonator action is associated with the lowest frequency mode of bubble oscillation. In this case, the inertance $\mathcal{L}_{\dot{a}}$ is due to the virtual mass of the liquid, the resistance $\mathcal{R}_{\dot{a}}$ includes acoustic radiation, viscous, and thermal losses, and the capacitance $\mathcal{C}_{\dot{a}}$ is due to the bubble compliance. Typical bubble oscillation frequencies are shown in Fig. 6.2.3h; it should be noted that these frequencies are very high as compared to typical feed line values. Normalized parameter graphs similar to those given in Figs. 6.2.3f, g are available for bubble-filled lines.[98]

6.2.4 Combustion Chamber Response†

For bulk oscillations (chugging) of the combustion chamber gases, the residence time $\theta_c = L^*c^*/\mathfrak{R}T_c$ is the controlling parameter. Since the combustion chamber response falls off at frequencies above $\omega = 1/\theta_c$, increasing θ_c is a stabilizing trend. The residence time can be expressed in terms of the chamber cylindrical length L_c and contraction ratio ϵ_c as

$$\theta_c = \frac{(L_c + \tilde{L}_n)\epsilon_c c^*}{\mathfrak{R}T_c} \qquad (6.2.4\text{–}1)$$

where $\tilde{L}_n$ is an end correction for the subsonic portion of the exhaust nozzle. From Eq. (6.2.4–1) it can be seen that increasing either the chamber length or contraction ratio is stabilizing. These trends are illustrated in Figs. 6.2.4a and 6.2.4b. Increasing chamber length also lowers the chugging frequency, whereas increasing contraction

† J. Szuch, Author.

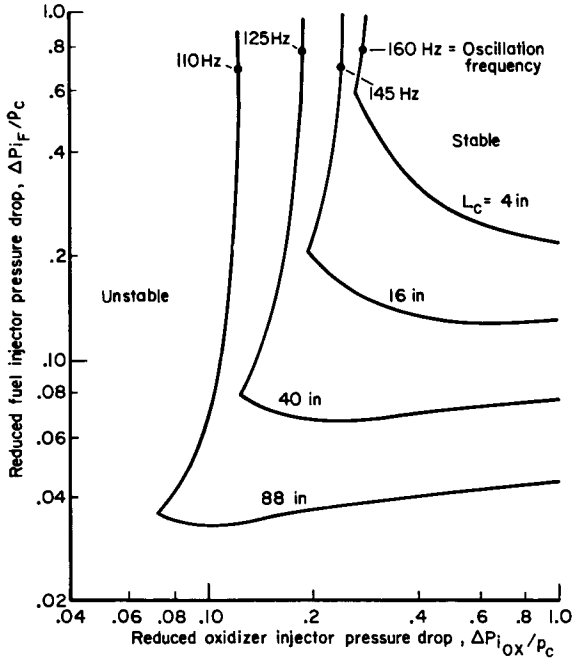

FIGURE 6.2.4a.—Effect of chamber length on theoretical stability limit for a gaseous-hydrogen/liquid-oxygen rocket engine. Infinite injector impedances; constant combustion time lags and contraction ratio.

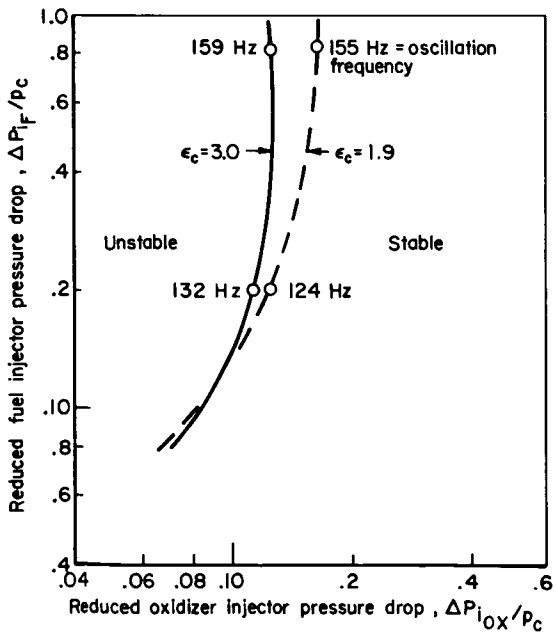

FIGURE 6.2.4b.—Effect of chamber contraction ratio on the theoretical stability limit for a gaseous-hydrogen/liquid-oxygen rocket engine. Infinite injector impedances; constant chamber length.

ratio leads to slightly higher frequencies. Unfortunately, these stabilizing design changes are usually not desirable for steady-state operation. Adding length to the chamber beyond that required for essentially complete combustion adds useless weight to the engine and may increase the wall cooling problems.[676] Increasing the contraction ratio has similar effects and, moreover, may alter the combustion efficiency and the total combustion time delays.

The gain factor for the combustion chamber response must be separated into two terms, corresponding to the oxidizer and fuel contributions, respectively:

$$\frac{p_c'}{\dot{m}_{OX}'} = \frac{\dot{m}_{OX}}{\bar{p}_c}\left[\frac{\bar{r}}{\bar{r}+1} + \frac{\bar{r}}{c^*}\left(\frac{\partial c^*}{\partial r}\right)\right]$$

$$\frac{p_c'}{\dot{m}_F'} = \frac{\dot{m}_F}{\bar{p}_c}\left[\frac{1}{\bar{r}+1} - \frac{\bar{r}}{c^*}\left(\frac{\partial c^*}{\partial r}\right)\right] \qquad (6.2.4\text{–}2)$$

It can be seen from Eq. (6.2.4–2) that the mixture ratio plays an important part in establishing these gain factors. Fig. 6.2.4c illustrates the changes in the gain factors as functions of mixture ratio for a LOX/hydrogen engine. In

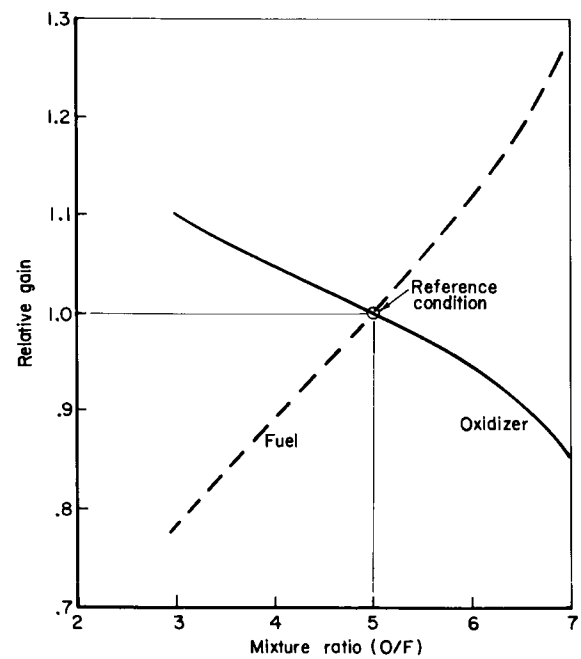

FIGURE 6.2.4c.—Effect of mixture ratio on feed system gain for a gaseous-hydrogen/liquid-oxygen rocket engine.

addition to the effect shown, the mixture ratio has an influence on the residence time, through $\mathfrak{R}_c$, T_c and c^*, and on the combustion time lags. Since the feed system response is also related to the mean propellant flow rates, the effects of a mixture ratio variation on the stability of an engine can only be determined by considering a specific system.

If the feed system is responsive to high frequencies, wave effects (Sect. 3.5) may be important in the combustion chamber, although acoustic modes may not be excited. The response of the chamber for this intermediate frequency range is quite complicated. In fact, it is not possible to make a neat separation between combustion response and chamber response, as it is for low frequency oscillations, since temporal and spatial effects are interrelated. Scala[630] developed a combustion chamber analysis for the intermediate frequency range as part of a study of entropy wave instability. However, little practical application has been made of this analysis.

6.3 HIGH FREQUENCY: SENSITIVE TIME LAG MODEL†

The following nomenclature pertains to Sect. 6.3 (see also Sects. 4.1.2, 4.2.1, and 4.2.2):

b	Exponent indicating dependence of time lag on orifice diameter, Eq. 6.3.3–4
p_r	Reduced chamber pressure (p_c divided by critical pressure of controlling propellant)
β_p	Time lag pressure-dependence factor
β_{VR}	Time lag velocity-ratio-dependence factor
ϕ	Impingement angle (included angle) of injection streams

6.3.1 General Approach

The basic approach used in the sensitive time lag theory, as detailed in Section 4.2, is that the effects of the combustor geometry and steady-state combustion and flow pattern are separated from the unsteady combustion effects. This separation allows the generalization of test results and the accumulation of meaningful stability data. With regard to the unsteady effects, the theory is based on the observation that there are two conditions for the occurrence of high frequency instability: (1) the acoustic resonance frequency of the combustion chamber must be matched with the preferred frequency of the combustion process, and (2) the sensitivity of the combustion process to variations in chamber conditions must be sufficient for the excitation to exceed the damping. In the sensitive time lag theory, the first of these conditions is expressed in terms of the sensitive time lag (τ), which is essentially the reciprocal of the preferred combustion frequency. The second condition involves the pressure and velocity interaction indices (n and l, respectively).

If the only unsteady combustion effects are those associated with small changes in thermodynamic state, often referred to as linear pressure-sensitivity, the conditions for the occurrence of instability can be represented in a simple graphical fashion of an n, τ-diagram, shown in Fig. 6.3.1. The combustor resonance properties are portrayed by instability zones, one zone for each acoustic mode. The coordinates of the minimum point show the characteristic time and the minimum damping. The unsteady aspects of the combustion process are represented by a point, located by the values of the sensitive time lag and the pressure interaction index for that particular combustion process. The larger the interaction index for the combustion process, the greater the excitation and, consequently, the greater is the tendency toward instability. Superposition of the instability zones for the combustor and the n, τ point for the combustion process shows the stability of the system. That is, if the n, τ point falls within an instability zone, the operation of the combustor will be unstable in that mode. Stabilization is thus achieved by shifting either the point or the zone to avoid intersection.

The dynamic aspects of the combustion process are determined primarily by the injection pattern, particularly the type and size of the injection element, the propellant combination, and the operating conditions, e.g., the chamber pressure and the mixture ratio. There may also be interactions with the chamber geometry. The location of the instability zones is dictated by the combustor geometry and the steady-state combustion characteristics.

† F. H. Reardon, Author.

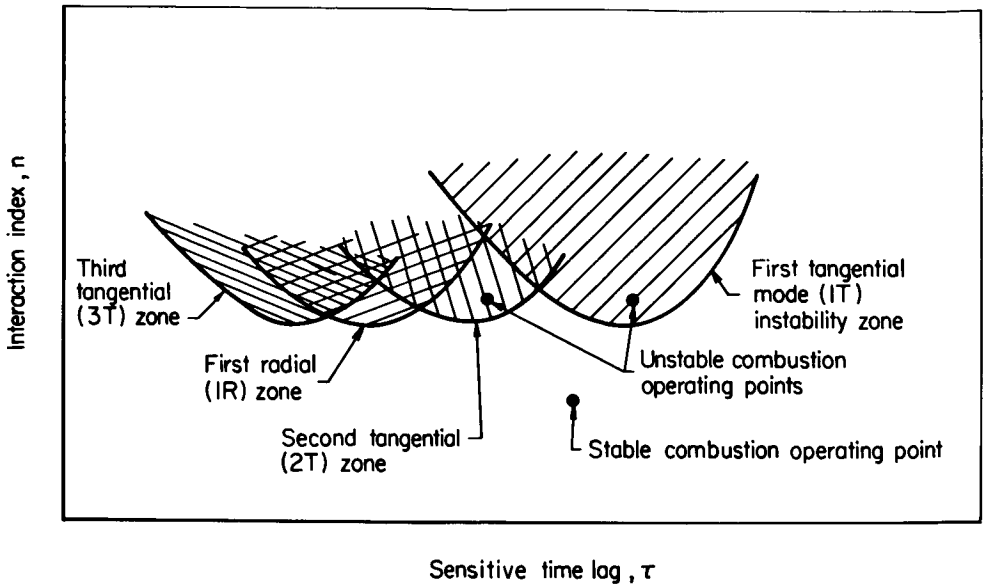

FIGURE 6.3.1.—An n,τ diagram, showing instability zones for several modes and operating points for stable and unstable combustion.

Velocity or displacement effects have been treated[583] by defining two more combustion parameters, the radial and tangential velocity indices, l_r and l_θ, which are really components of a single vectorial index (see Sect. 4.2.1). These indices are essentially empirical, just as the pressure index and sensitive time lag, and depend on the same design and operational factors. Although the combustion excitation for this more general case comes from more than one source, it is still convenient to represent stability graphically on the n, τ diagram. Now, however, the instability zones show only that part of the excitation to be supplied by the pressure-sensitive combustion processes. In effect, the velocity effects appear to modify the resonance characteristics of the chamber. The contribution of the velocity effects to the excitation can be seen by comparing the instability zones with those calculated for pressure effects only.

Nonlinear effects can be treated in the same way as the velocity effects. Clearly, as additional features are added to the theoretical model to make it more realistic, more detailed information is needed to make a stability analysis and the graphical representation becomes more difficult. Even so, the time lag concept and the n, τ diagram remain useful, practical engineering tools.

The following sections take up the various aspects of the application of the sensitive time lag theory to design and development of stable combustion chambers. Several items of importance in the calculation of instability zones are first presented, followed by a discussion of the currently available correlations of the combustion parameters (n, τ, l). Finally, considerations involved in design and development for dynamic stability are discussed.

6.3.2 Calculations Required

In currently available computer programs for calculating the boundaries of the instability zones (e.g., Ref. 650), the combustion chamber is assumed to be a right circular cylinder, either full or annular, with a planar injector at one end and a converging-diverging nozzle at the other. It is assumed also that combustion is completed prior to the entrance of the exhaust nozzle. For the present, other chamber shapes can only be treated by defining an "effective" cylindrical chamber. The exhaust nozzle is assumed to be conical, with circular arc sections at the throat and at the chamber exit (nozzle entrance). Other shapes can easily be handled, but this one is consistent with current practice and allows a wide variety of nozzle designs to be analyzed with a fairly simple

computer program. Analytical procedures for including the stabilizing effects of acoustic liners are available (Sect. 8.3.1), but a corresponding analysis of injector-face baffles has not yet been made. Baffles, therefore, must be treated qualitatively, usually with the assumption that only modes that are compatible with the baffle configuration can occur if the baffles are sufficiently long (Sect. 8.2).

Both the axial and transverse distributions of combustion are important in determining the location of the instability zones on the n, τ diagram. Unfortunately, this information is not widely available because it requires special instrumentation and test hardware. However, reasonable estimates can be made for most cases of interest. Analytical models for calculating the axial combustion distribution, for several propellant combinations, are described in Refs. 91, 165, 421, and 564. Experimental studies of the axial distribution for various types of injectors and propellants are given in Refs. 321, 401, and 649. Transverse distribution of combustion, of great significance in the analysis of transverse modes of instability, can be identified with the injection flux distribution.[584] Calculation of the effects of the transverse distribution can readily be incorporated into the instability zone computer program if the injector pattern is repetitive, with the orifices grouped into elements. The computer program described in Ref. 650 includes such calculations. Combustion distribution is further discussed in Sect. 7.2.4 and 7.2.5.

The effects of the unreacted liquid propellants, which contribute to the damping, are represented by the droplet momentum interchange coefficient k. This coefficient is defined as the constant of proportionality between the acceleration of a mean-effective droplet and the relative velocity between liquid and gas. That is,

$$\frac{D\mathbf{V}_L}{Dt} = k(\mathbf{V} - \mathbf{V}_L) \qquad (6.3.2\text{–}1)$$

Several studies of droplet acceleration have been made, comparing results of burning and nonburning drops with theoretical calculations.[199,240] In practice, it may be difficult to determine the mean droplet diameter, the Reynolds number, and the drag coefficient—Reynolds number relation appropriate to rocket combustor conditions. However, since the coefficient k is usually quite small, extreme accuracy is unnecessary.

It has been demonstrated that velocity effects, either linear or nonlinear, can be of great importance in determining the stability of transverse modes,[582,583] but systematic studies to obtain quantitative data have not been made. Some approximate expressions for the velocity interaction index for unlike doublets and like-on-like injector elements are discussed in Ref. 650.

Nonlinear effects can enter in two ways: (1) in the fluid mechanical behavior of the gases in the chamber, and (2) through the dynamics of the combustion response. The analyses of Zinn[771] and Mitchell[488] emphasize the fluid mechanical aspects and consider only pressure sensitivity. On the other hand, Reardon[13] used a describing-function approach to analyze certain types of nonlinear combustion response functions, with particular emphasis on velocity effects. Significant enlargement of the instability zones has been shown (see Sect. 4.2.4). However, because of the complexities and inherent limitations of the nonlinear analyses and the lack of quantitative data for determining combustion response functions, only the linearized theory is available for routine use at the present time.

In addition to the geometrical and combustion dynamic parameters noted above, calculation of the instability zones in terms of the dimensional time lag requires the value of the effective sound velocity in the chamber. This quantity is difficult to specify with precision, since it depends on the completeness of combustion and, in fact, may vary over a wide range between the injector and nozzle ends of the chamber. For design calculations, it is usually adequate to use the theoretical value for the appropriate mixture ratio, corrected by a typical combustion efficiency factor.

As discussed in Sect. 4.2.1, it is most convenient to perform the calculations using the frequency f as independent variable. The characteristic equation then yields values of the interaction index and sensitive time lag along the limiting curve that defines the instability zones. It has been found that the frequency range required for the calculation of instability zones is from about 10% below to 10% above the frequency of the corresponding acoustic mode, which is given by

$$f_{j\nu\eta} = \frac{a_{eff}}{\pi D_c}\sqrt{s_{\nu\eta}^2 + \left(j\frac{\pi}{4}\frac{D_c}{L_c}\right)^2} \qquad (6.3.2\text{–}2)$$

where a_{eff} is the effective sound velocity, D_c is the chamber diameter, L_c is the chamber length, j is the order of the longitudinal mode, and $s_{\nu\eta}$ is the dimensionless frequency of the transverse mode, the order of which is specified by the double subscript $\nu\eta$. If there is no longitudinal oscillation, $j=0$. The first longitudinal mode corresponds to $j=1$, and so on. Similarly, if no transverse oscillations are of interest, $\nu=0$, $\eta=1$, and $s_{\nu\eta}=0$. The tangential modes correspond to nonzero values of ν, and radial modes correspond to values of $\eta>1$. Reference 650 lists values of $s_{\nu\eta}$ for tangential modes up to the fifth, radial modes up to the third, and combined modes up to the third tangential–third radial.

Typical results of such a calculation are shown by the curves of $n(f)$ and $\tau(f)$ in Fig. 6.3.2. These curves apply at the stability limits, at which small oscillations with the given frequency neither grow nor decay. It can be seen that for any frequency there is only one value of τ and one value of n consistent with neutral oscillations. A larger n value corresponds to a growing oscillation. or instability, and a smaller n corresponds to a decaying oscillation, or stability. The value τ_M, corresponding to the minimum value of $n(f)$, is given approximately by

$$\tau_M = \frac{1}{2f_{j\nu\eta}} \qquad (6.3.2\text{–}3)$$

For practical applications, it is more convenient to plot $n(f)$ against $\tau(f)$, giving the stability limit curves on the n, τ diagram as shown in Fig. 6.3.1.

6.3.3 Empirical Correlations of Combustion Response

Empirical values of the combustion response parameters, especially the sensitive time lag and the pressure interaction index, have been obtained by comparing experimental stability data with calculated instability zones. The approach[650] is essentially to determine the answer to the question: on the basis of the instability zones calculated for the given combustor, what values of n and τ would produce the test results observed?

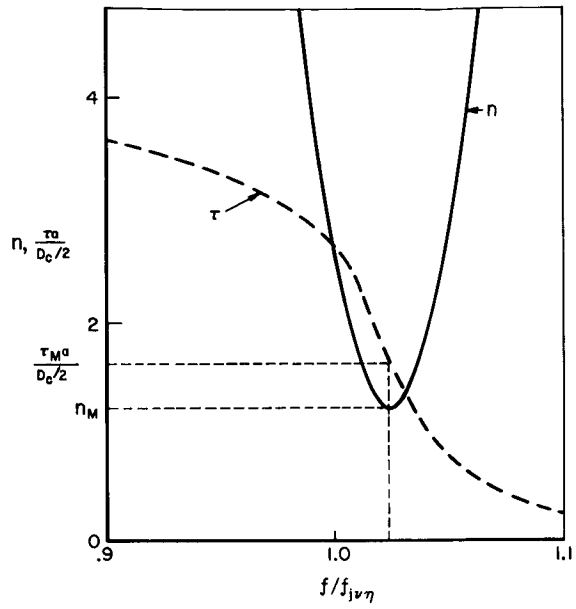

FIGURE 6.3.2.—Typical solution curves for $n(f)$ and $\tau(f)$.

For variable-geometry combustors, such as used by Crocco and Harrje,[184,187] the determination of n and τ can be quite precise. However, most test data have been obtained from combustors with fixed geometry. For these cases a certain amount of uncertainty is introduced into the n, τ values, since it can only be concluded that the values lie within certain ranges, which may be as large as $\pm 50\%$ of the mean value, but which more often do not exceed $\pm 25\%$. This uncertainty is reduced if the dimensions of the combustion chamber are large enough that the higher-order modes are excited, since the instability zones for these modes are more closely spaced on the n, τ diagram (Fig. 6.3.1).

Another source of uncertainty in the combustion parameter values derived from experiment is the use of the linearized theory to interpret test results where bombs or pulse guns have been used to trigger oscillations. Although such interpretation has only been semi-quantitative, it has been guided by theoretical studies of nonlinear instability. The pressure interaction index value is particularly influenced by nonlinear velocity effects.[13]

Other contributions to the uncertainty come from the lack of detailed information concerning

the steady-state combustion, which limits the accuracy of the stability limit curves, and test-to-test variations in the steady-state operating conditions.

Since the sensitive time lag and the interaction index describe the overall response of the combustion process, which consists of a multitude of interrelated, complex processes, it is not reasonable to expect that they can be correlated completely with parameters controlling just one or another of the intermediate processes. For this reason, n and τ have been correlated by use of design and operating parameters that are subject to the control of the engineer. However, the selection of correlating variables has been restricted somewhat by the nature of the data available. For example, very little systematic variation of mixture ratio is included in the data, and injection velocity data are too few to be helpful. Even for the correlating parameters selected, the data tends to be concentrated in a few areas of popularity among designers, which inhibits the development of general correlations.

The correlations presented here are based on the data collected and analyzed by Reardon over a period of about six years and published in Ref. 650. Ten propellant combinations are represented, about equally divided between hypergolic and nonhypergolic types. Seven types of injection are included: unlike-impinging doublets, triplets, quadlets (2-on-2), and pentads (4-on-1); nonimpinging (showerhead); self-impinging; and coaxial elements, both impinging and nonimpinging. The chamber pressure range covered is from 100 to 2500 psia. The chamber Mach numbers range from 0.01 to 0.44.

In forming the correlations, consideration of the basic physical processes, as well as the study of the data points themselves, suggested the separation of the data into three groups: (1) coaxial injectors with nonhypergolic propellants, (2) noncoaxial injectors with nonhypergolic propellants, and (3) all injector types with storable, hypergolic propellants. The correlations for each group are discussed separately in the following paragraphs.

Coaxial injectors with nonhypergolic propellants.—Most of the data in this group are for the cryogenic propellant combination LOX/LH_2, but there are two data points for the cryogenic-storable combination O_2/RP-1. In all cases, the central stream was the less volatile propellant (viz, O_2 for the O_2/H_2 combination and RP-1 for the O_2/RP-1 combination), which can be regarded as the rate-controlling propellant. The correlating variables used in developing the correlation were the diameter d_i of the central stream, the velocity ratio VR (the injection velocity of the outer, annular stream divided by the velocity of the central stream), the angle of impingement ϕ of the annular stream on the central stream (see Fig. 6.3.3a), the reduced pressure p_r (chamber pressure divided by the critical pressure of the controlling propellant), and the nozzle entrance Mach number $\mathfrak{M}_e$.*

The sensitive time lag values have been correlated by the equation

$$\frac{\tau \mathfrak{M}_e^{1/7} \beta_p}{\beta_{VR}} = 0.076 \text{ millisec} \qquad (6.3.3\text{–}1)$$

where the pressure dependence factor β_p is given by

$$\beta_p = \begin{cases} p_r^{1/3} & p_r < 1 \\ 1.0 & p_r \geq 1 \end{cases} \qquad (6.3.3\text{–}2)$$

and the velocity ratio factor β_{VR}, an empirical function of VR and ϕ, shown in Fig. 6.3.3a. The time lag correlation is illustrated in Fig. 6.3.3b.

These data indicate that the combustion response is essentially independent of element size and is only weakly influenced by the mean gas flow in the combustion chamber. Such a result is consistent with the model of Combs and Schuman,[165] according to which the coaxial injector spray pattern is controlled by the shearing between the high velocity annular stream of rapidly vaporizing or gaseous propellant and the central, low velocity liquid stream. However, as shown by Fig. 6.3.3a, the time lag is independent of velocity ratio for nonimpinging coaxial elements (i.e., β_{VR} is constant, at 0.9, for all VR). The combination VR $\sin \phi$ was derived on a purely empirical basis, and gives what amounts to a central stream breakup parameter.

The chamber pressure dependence for pressures less than the critical pressure of the controlling

* Conical chambers present a problem in the definition of this quantity, as discussed in Sect. 8.4.1.

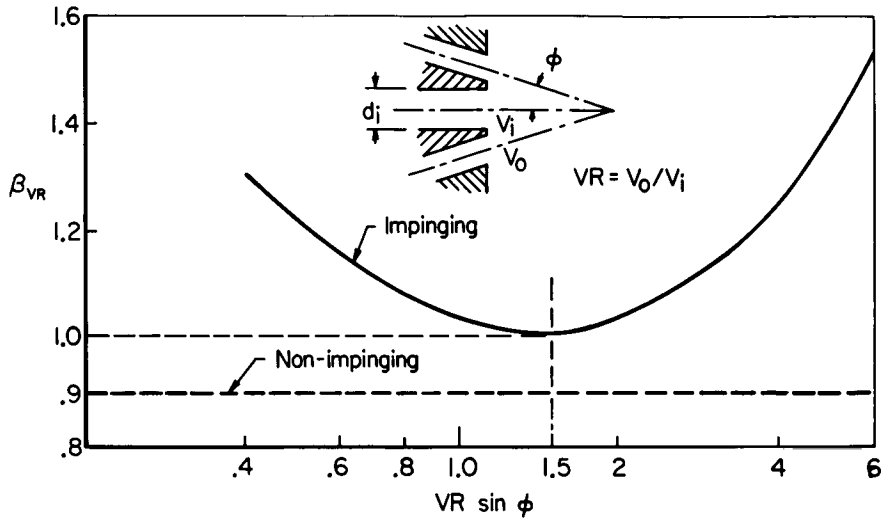

FIGURE 6.3.3a.—Empirical injection-velocity-ratio factor β_{VR} for coaxial injectors.

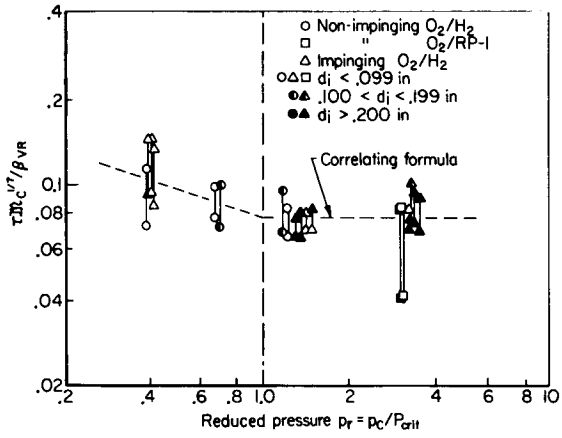

FIGURE 6.3.3b.—Sensitive time lag correlation for coaxial injectors with nonhypergolic propellants. Correlating variables defined in text.

(central) propellant is the same as that found analytically by Heidmann and Wieber[346] for vaporization-controlled combustion. Above the critical pressure the experimental time lag values appear to be independent of pressure. Unfortunately, corresponding theoretical studies have not yet been made. The sharp break in the mean line of Fig. 6.3.3b at the critical pressure is undoubtedly a gross simplification, but current knowledge of combustion dynamics hardly warrants greater sophistication.

The pressure interaction index for coaxial injectors appears to be essentially constant, independent of element size, velocity ratio, and chamber pressure, at about 0.5. No experimental data are available regarding transverse velocity oscillation effects; the symmetry of the coaxial element would be expected to minimize such effects.

Noncoaxial injectors with nonhypergolic propellants.—Unlike doublet and pentad, like-on-like, and showerhead types of injection are included in this group. The oxidizer in all cases is liquid oxygen; the fuels are hydrogen, ethanol (C_2H_5OH), iso-octane, RP-1, and hydrazine. The correlating variables are essentially the same as used for the preceding group; injection orifice diameter d_i of the controlling propellant, reduced pressure p_r, and chamber Mach number $\mathfrak{M}_c$. However, injection velocity and impingement angle have been omitted because of lack of data.

For the impinging injector types, the sensitive time lag is correlated by a formula with the same pressure dependence factor β_p as that for the coaxial injectors (see Eq. (6.3.3–2)):

$$\frac{\tau\mathfrak{M}_c^{1/3}\beta_p}{d_i^{1/2}} = 0.165 \text{ millisec-in.}^{-1/2} \qquad (6.3.3\text{–}3)$$

This correlation is shown in Fig. 6.3.3c. Also included in the plot are data points for the non-impinging injector types.

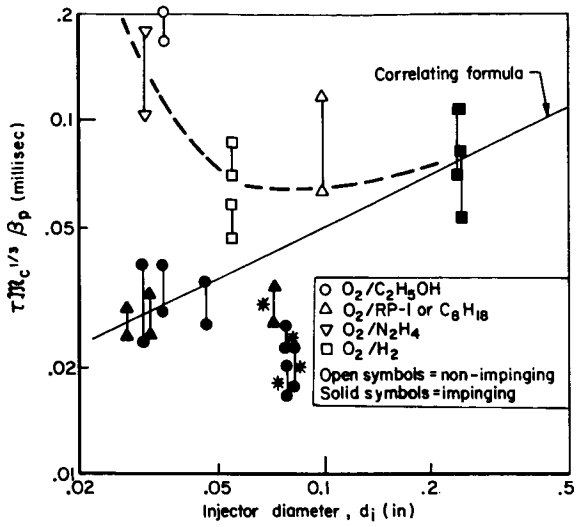

FIGURE 6.3.3c.—Sensitive time lag correlation for non-coaxial injectors with nonhypergolic propellants.

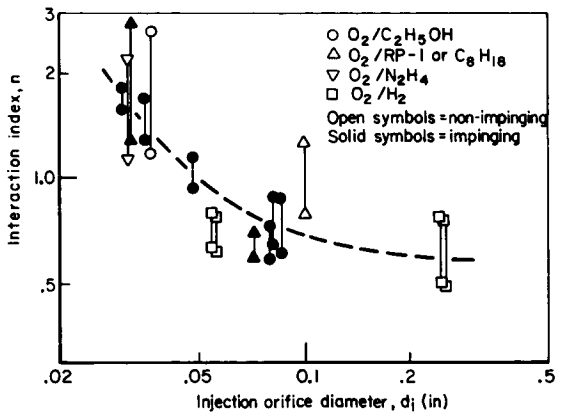

FIGURE 6.3.3d.—Pressure interaction index correlation for non-coaxial injectors with nonhypergolic propellants.

The simple correlating formula of Eq. (6.3.3–3) clearly does not include all of the factors that control the time lag for this data group. For example, it has been noted that mixture ratio has a strong influence and that large-scale recirculation eddies can reduce the time lag by a factor of 2 (points marked with * in Fig. 6.3.3c).[650] The time lag values for the showerhead and like-on-like injector patterns can be considerably larger than those for the unlike-impinging patterns, and the dependence on the injection orifice diameter is quite different. The result that the difference between the two injector types is greater for the smaller orifice sizes is in agreement with intuitive expectations.

The interaction index correlation for this data group is shown in Fig. 6.3.3d. No correlating formula has been determined; n decreases with increasing orifice diameter, but there is no consistent dependence on the other injection and operational variables. The large amount of scatter in the data limits the usefulness of this correlation.

All injector types, storable hypergolic propellants.—With the nonhypergolic propellants of the previous two groups, it was not hard to select one of the propellants as controlling because of the significant difference in vaporization rates. The injection orifice diameter and critical pressure served as useful correlating variables. For the hypergolic propellants in this group, viz, nitrogen tetroxide, chlorine trifluoride, chlorine pentafluoride as oxidizers, and hydrazine and mixtures of hydrazine with unsymmetrical dimethylhydrazine or monomethyl hydrazine as fuels, the selection of the controlling propellant is not so clear (see Chapters 2 and 3). Therefore, for this group an average injection orifice diameter is used, and, since none of the data pertain to supercritical operation, the critical pressure of the propellant has been omitted from the correlation.

The correlation for the time lag is presented in Fig. 6.3.3e. It should be noted that the dependence on pressure and chamber Mach number is the same as for the preceding nonhypergolic propellant data group. Writing the correlation formula for the time lag as

$$\tau\mathfrak{M}_c^{1/3}p_c^{1/3} = \text{constant}\cdot d_i^b \qquad (6.3.3\text{–}4)$$

it can be seen from Fig. 6.3.3e that the exponent b ranges from 1.0 for the smallest orifices, to 0.5 at midrange, and approaches 0.33 for the largest orifice size. This trend is heavily dependent on the one data point at the largest diameter, without which a constant exponent between 0.5 and 1.0 would fit the data. For unlike-impinging injectors, the constant of proportionality is about 10 millisec-psi$^{1/3}$-in.$^{-1/2}$, whereas for nonimpinging types it is about 50% larger.

Fig. 6.3.3f shows the interaction index correlation. The interaction index for hypergolic propellants appears to be little affected by design or

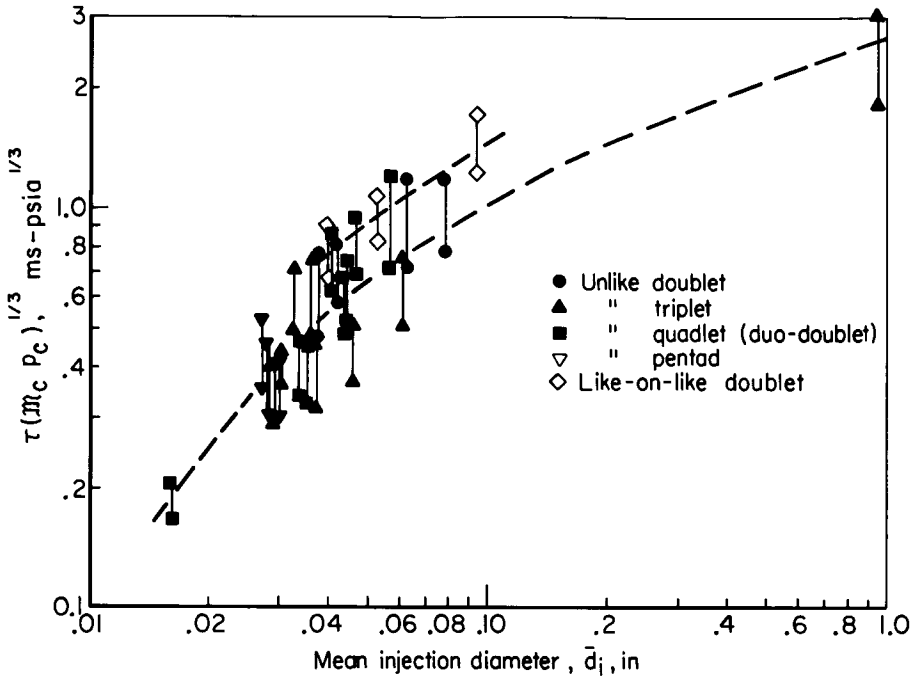

FIGURE 6.3.3e.—Sensitive time lag correlation for storable hypergolic propellants; all injector types.

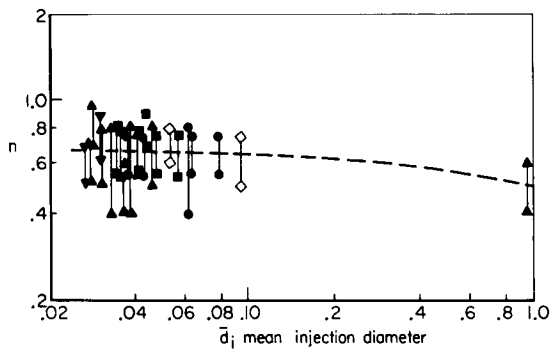

FIGURE 6.3.3f.—Pressure interaction index correlation for storable hypergolic propellants; all injector types. Symbol key same as Fig. 6.3.3e.

operating variables, although there may be a slight decrease of n with increasing element size.

6.3.4 Stability Prediction

The preceding sections have dealt with the various aspects of the sensitive time lag theory as it is applied to the prediction of the stability of existing or proposed thrust chambers. In this article, the method of prediction will be illustrated by considering an example. The characteristics of the combustor used in this example have been chosen to show the method rather than as being typical of current designs.

Consider a thrust chamber that consists of a circular cylinder of 16 inches diameter, 10 inches long, joined to an exhaust nozzle with a conical subsonic portion 6 inches long, with a cone half-angle of 30°. The nozzle contraction ratio is 2.5, so that the chamber Mach number is about 0.25. It is to operate at a chamber pressure of 500 psia using storable, hypergolic propellants. The injector designer has selected a triplet element, two oxidizer streams impinging on one fuel, with orifice diameters of 0.075 in. The question is now asked, what will be the stability of such a combustor?

From the given geometry and reasonable estimates of the combustion distribution and mean drop size, the instability zones for several modes can be calculated, on the basis of small perturbations and pressure-sensitive combustion. These instability zones are shown in Fig. 6.3.4a. It is clear that the first longitudinal mode will not be a cause for concern, since it requires a sub-

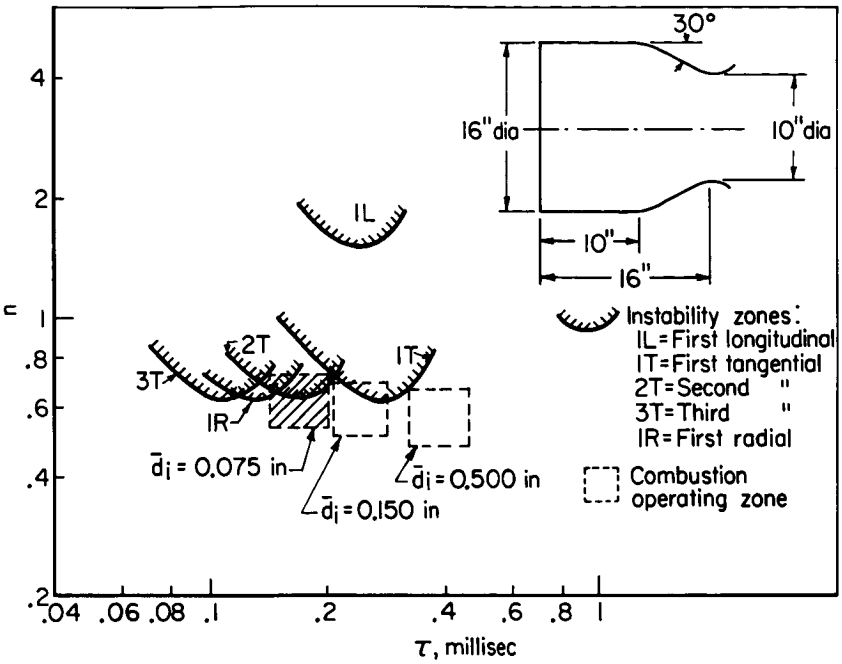

FIGURE 6.3.4a.—Example of stability analysis using n,τ diagram.

stantially more responsive combustion process than the other modes. Using the given injection diameter, design chamber pressure, and Mach number, one finds from the correlations of Fig. 6.3.3e and Fig. 6.3.3f that the sensitive time lag and pressure interaction index are expected to lie in the ranges:

$$0.14 \leq \tau \leq 0.20 \text{ millisec}$$

$$0.6 \leq n \leq 0.8$$

That is, the operating point for the given injector pattern is expected to lie somewhere within the shaded rectangle in Fig. 6.3.4a.

From this result it would be concluded that the combustor would only be marginally stable at best. The most likely mode of oscillation is the second tangential, which might develop spontaneously from the random combustion noise or be triggered by some kind of local disturbance. Although the symmetry of the triplet injector is such as to minimize linear velocity effects, nonlinear effects (both velocity and pressure) associated with such disturbances would be significant destabilizing factors. Depending on the nature of the triggering disturbance, the first radial, first tangential, or third tangential mode could also occur. This design would be highly undesirable from the viewpoint of stability.

At this point, one can examine possible ways to achieve a stable design. One way would be to increase the size of the injector orifice to produce a larger time lag. As shown in Fig. 6.3.4a, it would require an orifice diameter of 0.500 inch to move the operating point into the stable region to the right of the first tangential mode instability zone. It is likely that such a coarse injector pattern would not have sufficiently high steady-state performance, and so would be unacceptable. Mechanical damping devices are also available (Chapter 8), but in this case the design of an acoustic liner or baffle would be difficult because of the wide frequency range (1700 to 3900 Hz) and the variety of oscillation patterns to which the combustor is susceptible (using the 0.075 inch orifices). If, however, the injection diameter can be increased to 0.150 inch without degrading performance, the combustion response is altered so that only the first tangential mode can be initiated without a strong disturbance. The frequency range that must be protected by an

acoustic liner is reduced to 1700–2800 Hz, and dynamic stability is possible with a relatively simple baffle (e.g., one with five radial blades). Additional stabilizing effects can be obtained by appropriate radial variation of the injection density.[584]

All of the above design modifications could be investigated rapidly—without hardware fabrication or testing—by use of the sensitive time lag theory. Other parametric variations could also be studied. For example, the effects on stability of chamber diameter, length, nozzle convergence angle and contraction ratio can be checked independently of injector type, orifice diameter, propellant combination, and chamber pressure. It should be noted, however, that the chamber Mach number effect on the time lag does introduce a coupling between the injector and chamber design. This fact can be seen by comparing Fig. 6.3.4b with Fig. 6.3.4a. In Fig. 6.3.4b the instability zones are shown for a combustor similar to the one discussed except that the chamber diameter has been reduced to 12 inches. Because the throat diameter has not been changed, the contraction ratio is reduced to 1.4 and the Mach number increased to 0.49. Thus, although the instability zones have all been shifted to smaller time lags (by the ratio 12/16 or 0.75), the operating point for the combustion process has also been shifted toward smaller τ (by the ratio 0.25/0.49 raised to the $\frac{1}{3}$ power, or 0.8). The result is that the stability of the combustor is changed very little, except that the frequency range of interest is now from 2300 Hz to 5200 Hz.

6.4 HIGH FREQUENCY: NUMERICAL INTEGRATION METHODS

The numerical integration of the differential equations governing high frequency combustion instability, the details of which are presented in Sect. 4.4, offers several advantages over other methods. This approach permits the determination of stability boundaries in terms of disturbance amplitude and for very complicated, nonlinear combustion mechanisms, as well as for nonsinusoidal initial perturbations. Although a completely three-dimensional analysis for any shape of chamber is possible in principle, the computer size and time required are prohibitive at present.

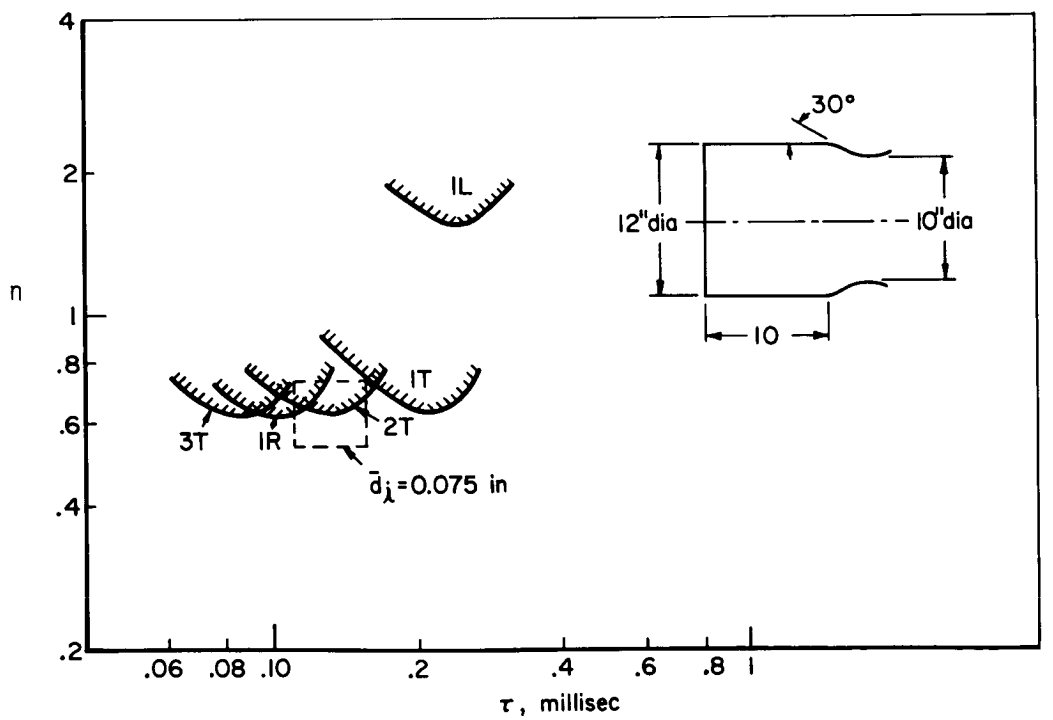

FIGURE 6.3.4b.—Effect of reducing chamber diameter on stability; other design variables unchanged from Fig. 6.3.4a.

Therefore, numerical analyses currently make use of one- or two-dimensional models and are conducted for selected zones within the combustion chamber. Most commonly, the zone analyzed is a thin annular ring. For conciseness, the discussion in this section is mainly concerned with numerical integration methods as applied to the annular ring geometry. The extension of this approach to other configurations is straightforward, since the general procedures are the same in all cases.

The following nomenclature pertains to Sect. 6.4 (see also Sect. 4.3):

C_D	Drag coefficient
D_d	Droplet drag parameter
$\mathfrak{L}$	Burning rate parameter
M_x	Fractional burning rate per unit length
$\mathfrak{M}$	Dimensionless mass accumulation parameter, $\frac{m_{acc}(t)}{\bar{m}_{acc}}, \frac{m_{acc}}{\dot{m}t_w}$
m_{acc}	Mass accumulated prior to either atomization or vaporization
Re_d	Modified droplet Reynolds number
t_w	Wave travel time, oscillation period

6.4.1 General Approach*

The numerical integration methods are basically analog solutions of the stability problem. That is, the steady-state combustion and flow parameters are perturbed analytically and numerical integration is used to find the time history of the perturbations. This technique may be used to determine the stability limits of a given combustor or to make parametric studies of the effects of design and operational factors. In either case, the analysis is carried out in two stages: (1) the characterization of the steady-state operation, and (2) the tracing of the development of the initial perturbation.

The quantities used to describe the steady-state conditions include gas and liquid velocities, burning rate, local concentration of unburned propellant, and liquid droplet sizes. Normally such data are obtained by calculation using a steady-state combustion model. Experimental data, obtained by means of streak photography with transparent-wall chambers, have also been employed.[170] The analytical combustion models now in use trace their origin to that developed by Priem and Heidmann.[564] Subsequent improvements have been contributed by several teams of workers.[91,135,224,421] Although multidimensional steady-state models have been developed for certain specific injectors,[166] one-dimensional models have been used almost exclusively in stability analyses. Such models cannot be applied in regions near the injector face where propellant injection, spray formation, gas recirculation, and interspray mixing predominate.

The first step in the unsteady analysis is to select the zone of interest within the combustion chamber. A single, representative zone may be chosen, or else the analysis may be carried out for a large number of zones to determine a spatial sensitivity map for the combustor. Of course, the type of zone selected must be consistent with the chamber geometry and the oscillation mode of interest. Most work has been done using an annular ring of small length and thickness (Fig. 6.4.1a). Such a zone is most appropriate for investigating tangential modes in an unbaffled, circular cylindrical chamber. Stability within a baffle compartment can be studied by using a rectangular zone.[170]

Next, the combustion response model must be chosen. Most available models emphasize vaporization as the controlling step. However, high-speed photographs of oscillations in transparent, two-dimensional chambers, in which the instability wave often obliterates the injection streams, suggest that atomization may be as important as vaporization. At high pressures, the combustion model should include droplet heating as well as phase change.

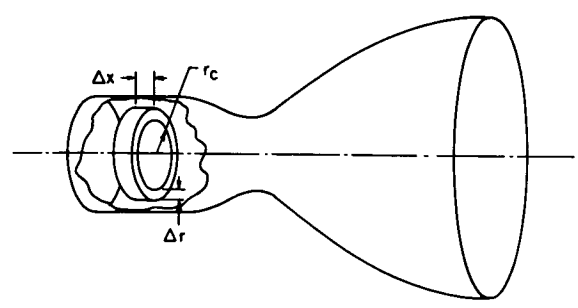

FIGURE 6.4.1a.—Annular-ring zone for stability analysis.

* R. J. Priem, Author, and D. T. Campbell, Contributor.

Finally, the form of the initial perturbation is specified. Usually this has been a single, sinusoidal pressure wave with the associated isentropic gas density and temperature waves, the liquid spray being initially undisturbed. However, steep-fronted disturbances, better able to simulate the perturbations introduced by bombs or pulse guns, are now used in many analyses.

Starting from the specified initial values, integration of the governing differential equations (Sect. 4.3) yields gas and liquid properties at selected locations within the zone of interest at successive time intervals. The calculated pressure profiles are then examined to determine whether the input disturbance has damped or whether a self-sustaining oscillation has developed. A convenient guide to the damping or amplification of a disturbance is the difference between the maximum and minimum values of the static pressure in the zone (normalized by the steady-state chamber pressure) at any given time. Typical plots of this parameter against a dimensionless time parameter are shown in Figs. 6.4.1b and 6.4.1c. If the initial perturbation damps, the numerical integration is repeated at successively larger initial amplitudes until a sustained oscillation is obtained. In this way the stability limit is determined for the given engine.

6.4.2 Calculations Required*

In discussing the input data and calculations required by the numerical integration approach, the steady and unsteady portions will be taken up separately. Of course, since the steady-state calculation serves to provide an input to the stability analysis, it is possible, at least in principle, to combine the two calculations into a single computer program. Steady-state data could also be obtained by hand calculation or from experimental measurements (e.g., drop size distribution,[222] mean gas velocity profile).[401]

6.4.2.1 Steady-state calculations.—The following description of a one-dimensional steady-state combustion model is generally valid, although there are some differences in detail between the methods used by different investigators.

* R. J. Priem, Author, and D. T. Campbell, Contributor.

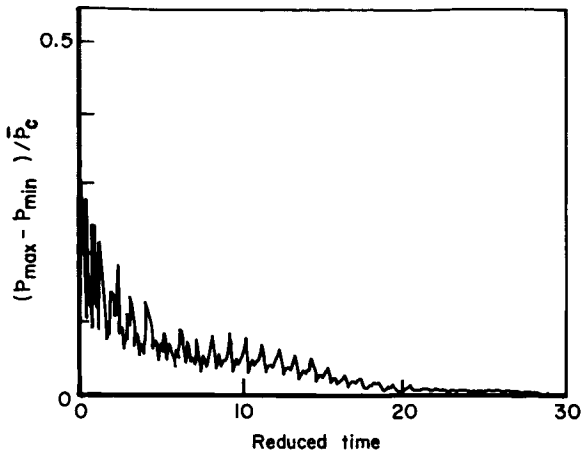

FIGURE 6.4.1b.—Computer plot of $(p_{max} - p_{min})/p_0$ versus reduced time. Stable operation.

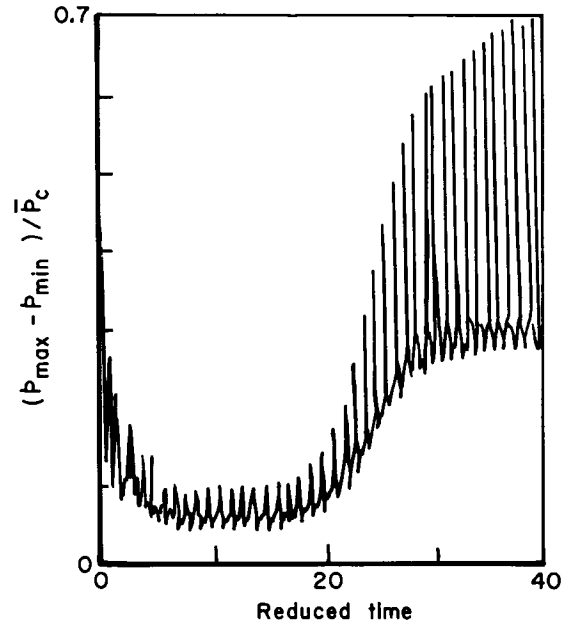

FIGURE 6.4.1c.—Computer plot of $(p_{max} - p_{min})/p_0$ versus reduced time. Unstable operation.

The input data must completely describe the chamber geometry and the characteristics of the liquid spray and the gas at the location where computation is started. With a one-dimensional model, the starting location cannot be the injector face; it is necessary to estimate the location where "uniform, one-dimensional" flow begins on the basis of available experimental data.

For the liquid sprays, it is necessary to specify the drop size distributions, the drop velocities, temperatures, and the fractions of fuel and oxidizer already burned at the point where calculations start. Gas phase data include composition, flow rate, and pressure at the starting point. In addition, propellant liquid and vapor properties such as specific heat, viscosity, thermal conductivity, and molecular diffusivity are needed, as well as corresponding gas mixture properties as functions of composition at the nominal chamber pressure. This information may be in equation or tabular form.

The steady-state calculation proceeds in a stepwise manner, moving downstream to the nozzle throat. At each step, interphase transfers of mass, momentum, and energy are evaluated. Solution of the gas-phase continuity, momentum, and energy equations then yields drop sizes, velocities, and temperatures, and gas composition, velocity, and pressure at the new location. Typically, the transport equations[99,564] use mean film transport properties, and rely on empirical correlations of Nusselt number and drag coefficient to account for convection, turbulence, and lack of sphericity of the burning droplets. The gas-phase energy equation is normally simplified by the assumption that the composition and stagnation temperature are the equilibrium values for the gas-phase oxidizer/fuel ratio and chamber pressure. Other gas properties (e.g., static temperature, density) are evaluated from the stagnation values by applying the local Mach number to the isentropic expansion equations.

The calculation of droplet heating may lead to (numerical) oscillations in droplet temperature as the wet bulb temperature is approached. Two methods have been used to overcome this problem: (1) the use of iteration or higher-order numerical integration, and (2) changing to a constant-droplet-temperature model for calculating the burning rate when the droplet temperature reaches a predetermined percentage of the wet bulb temperature.

In most steady-state combustion models the injection spray is assumed to consist of a number of drop-size groups rather than a continuous distribution. Each group is characterized by a mean diameter, the number of drops in the group, and the group velocity. Both the oxidizer and fuel sprays can be divided independently into many drop-size groups. To be realistic, the distributions of drop size must approximate those occurring in actual rocket engines. This condition introduces a major uncertainty into the analysis, since only a limited number of studies of atomization[224,375] have been made. The molten wax technique[224] might resolve this difficulty if it were applied to enough injector element types and combined with suitable physical property correlations and extended to variable gas velocity fields.

A more difficult problem is the quantitative description of the secondary breakup of the initial spray by high velocity combustion gas. Currently used vaporization-limited models become invalid for low-contraction-ratio or tapered chambers in which secondary atomization takes place. Although several experimental studies of single droplet breakup have been made,[211,569,755] incorporation of these results into the analytical models will almost always lead to unrealistically high combustion efficiencies. Two possible explanations for this disagreement are (1) the sheltering effect of clouds of closely-spaced droplets tends to reduce or retard secondary breakup processes, and (2) shattered and rapidly vaporized droplets produce pockets of unmixed propellant vapors, the burning rate of which is limited by turbulent gas-phase mixing.

For most propellants, the assumption of vaporization-limited, bipropellant combustion is quite good. However, for hydrazine-type fuels, exothermic decomposition reactions occurring very close to the droplet can be important in that they tend to increase the vaporization rate by increasing the rate of heat transfer to the droplet.[87,353,629] Such a "two-flame" combustion mechanism should be applied under conditions of weak convection, in which the decomposition flame is well embedded in the droplet boundary layer.

6.4.2.2 Stability analysis.—Once the steady-state flow in the combustion chamber has been determined, the zone of interest for the unsteady analysis can be selected. Because of the strong sensitivity of the stability results to the relative velocity between gas and liquid (see Sect. 4.3), the axial location where the average relative velocity passes through a minimum is normally

chosen as the location of the zone of interest. This choice will give the most unstable result. Actually, if this "least stable" region were narrow enough, more stable adjacent regions might act to damp its oscillations. Thus, one would expect that applying the analysis to an averaged zone of finite axial dimension would be more realistic. Unfortunately, clear-cut guidelines for selection of a suitable width for the analysis zone are yet to be developed.

The numerical integration approach can be used with any combustion mechanism that has been expressed in quantitative form. In practice, most stability analysis computer programs are based on a quasi-steady vaporization-limited model. However, atomization, gas-phase mixing, and chemical reaction models have also been developed, and corrections for these effects have also been added to vaporization-controlled analytical models (Sect. 4.3.1). The selection of the most appropriate model for a given analysis requires an understanding of the nature of the combustion process in the engine under consideration. For example, at high chamber pressure a large fraction of the energy received by the droplet goes into raising the droplet temperature. Therefore, a combustion model based on quasi-steady, isothermal vaporization would be unrealistic. For chamber pressures above the critical pressures of the propellants a combustion model describing the rate of turbulent mixing of vapor "pockets" with the surrounding combustion gases would be desirable.

The input parameters are conveniently expressed as dimensionless groups of variables. Typical parameters are the following:

The *burning rate parameter*,

$$\mathcal{Y} = \frac{r_c M_x}{\epsilon_c}$$

is a measure of the energy that can be added to a wave by combustion. For practical engines, stability is improved by decreasing $\mathcal{Y}$.

The *reduced velocity difference* between gas and liquid (at steady state) is defined as

$$\Delta V = \frac{V - V_L}{\bar{a}}$$

Large ΔV has a powerful stabilizing influence, since transient cross-winds caused by a disturbance represent relatively small changes in the gas dynamic environment.

The *modified droplet Reynolds number*,

$$Re_d = \frac{d_L \bar{\rho} \bar{a}}{\bar{\mu}}$$

is a measure of the sensitivity of the vaporization rate to changes in the relative velocity between gas and liquid. Large values of Re_d are destabilizing.

The *droplet drag parameter*,

$$D_d = \frac{3 C_D r_c m_{acc}}{8 \pi \bar{\rho}_L d_L}$$

is associated with the momentum exchange between the gas and the liquid spray. Larger values of D_d indicate increased ability of the spray to damp transient gas velocity components.

The *mass accumulation parameter* is defined as

$$\mathfrak{M} = \frac{m_{acc}}{\underline{\dot{m}}_i t_w}$$

It is the local mass concentration of unburned propellant normalized by the net influx during approximately one cycle of an acoustic oscillation. Low values are stabilizing.

The numerical integration is carried out in terms of a dimensionless, "reduced" time, which is the actual time divided by an acoustic wave travel time. For an annular zone, the appropriate wave travel time would be

$$t_w = \frac{2\pi r_c}{\bar{a}}$$

Another reference time, used by some investigators, is $r_c/\bar{a}$. Integration is terminated at a predetermined value of the reduced time. The selection of this termination time is an important factor in any stability analysis. Excessively long times are wasteful of computer operation and may introduce numerical instability. On the other hand, both theoretical and experimental results have shown that in many cases oscillations that initially damped have eventually grown into sustained instabilities. The stability of a given input perturbation may not become clear until a reduced time of about 20 is reached (Fig. 6.4.1c). If the determination of stability is questionable,

the integration must be repeated, and carried out for a longer reduced time.

6.4.3 Correlation With Test Data*

Several analytical and experimental investigations have been performed to establish a correlation between thrust chamber design parameters and stability. One study[556] used an eight-foot diameter toroidal combustor, burning liquid oxygen and gaseous hydrogen, with four different injectors. Experimental results and theoretical curves for atomization- and vaporization-controlled combustion models are compared in Fig. 6.4.3a. The two injectors that were predicted analytically to be less stable were spontaneously unstable, whereas the two injectors predicted to be stable to disturbances of about 0.5 amplitude (perturbation pressure amplitude divided by steady-state chamber pressure) each recovered from a pulse of 0.2 amplitude.

A more recent analytical-experimental stability program,[729,90] using nitrogen tetroxide/monomethyl hydrazine, investigated the influence of propellant mixture ratio, injection velocity, droplet size and distribution, and chamber pressure on the minimum pulse strength required to trigger instability. Two injector configurations were tested. One consisted of a quadlet pattern of two oxidizer jets impinging on two fuel jets. The mass median drop radius for this injector was estimated to be about 70 microns. The second injector consisted of a combination of quadlets and triplets with an estimated mass median drop radius of 30 microns. Experimental results are shown in Fig. 6.4.3b together with the theoretical calculations. The second injector (TRAX-21-11B) showed greater stability than the first (TRAX-21-1D), as predicted by the theory. However, the level of disturbance predicted theoretically to excite instability was significantly lower than that observed experimentally.

The same propellants were used in another study[46] of the effects on stability of injector design and operating conditions. The experimental apparatus consisted of a 15-inch-diameter pulse motor with a spud-type injector, allowing several self-impinging patterns to be tested. Actual test

* R. J. Priem, Author, and D. T. Campbell, C. J. Abbe, and B. P. Breen, Contributors.

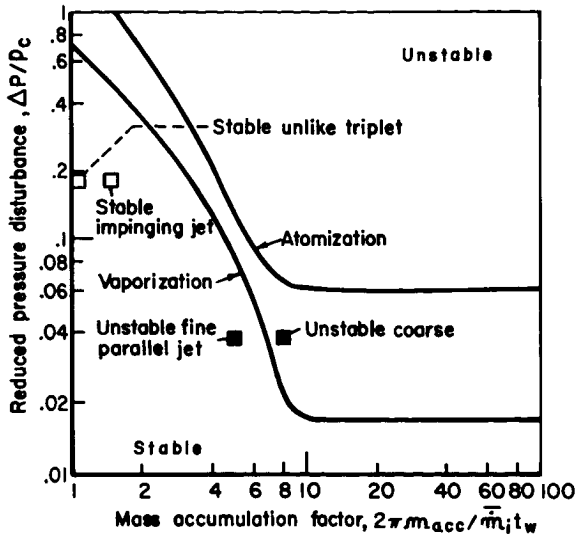

FIGURE 6.4.3a.—Experimental and theoretical stability limits for toroidal combustor. $\mathcal{L} = 0.015$.

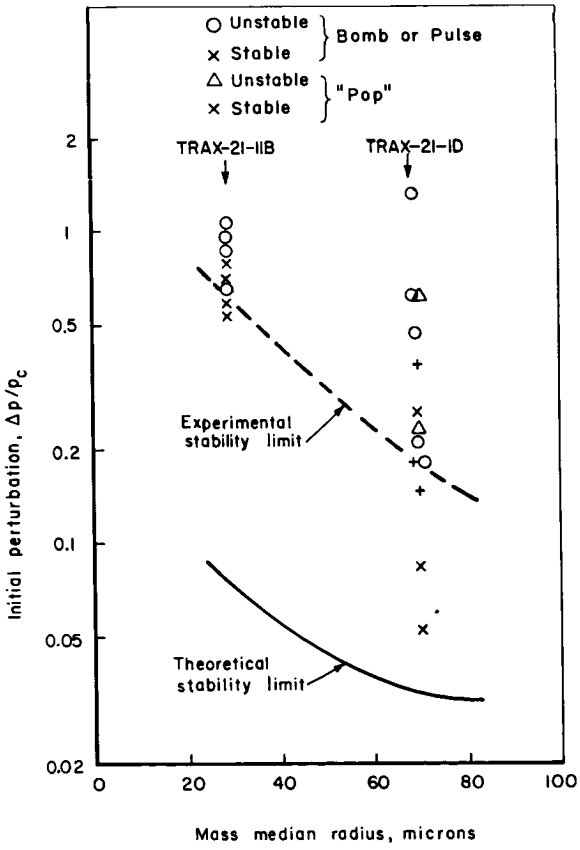

FIGURE 6.4.3b.—Influence of mass median drop radius on stability for a transtage combustor with NTO/MMH propellants.

conditions were used as inputs to the numerical stability analysis. For each test condition the theoretical pulse amplitude at the stability limit was calculated for comparison with the experimental stability results. An initial series of tests was made to relate the perturbation amplitude to the pulse gun charge size. It was found that a nearly linear increase in $\Delta p/p_c$ was obtained as the charge size was increased from 10 to 80 grains. Analytical and experimental results for chamber pressure variation are compared in Fig. 6.4.3c; the effects of total propellant flow rate are shown in Fig. 6.4.3d. Agreement between theory and experiment is good in the latter case, particularly in the relative magnitude of the changes in stability produced by the changes in operating conditions. As in the preceding example (Fig. 6.4.3b), the analytical model underestimated the perturbation amplitude at the stability limit.

A fundamental principle underlying most applications of the numerical integration approach to stability analysis is that stability can be measured in terms of the amplitude of the disturbance just strong enough to induce a sustained acoustic instability. Weaker disturbances are expected to be damped and stronger ones always lead to instability. However, studies of rating techniques have shown that it is not always possible to correlate ultimate stability with the measured perturbation amplitude.[167] In fact, it is well known that there are many instances in which engines have recovered from strong pulses whereas they were unstable to weaker ones. High speed photographs of transparent chamber tests have suggested a probable explanation: the large overpressure following the strong disturbance may virtually shut off propellant injection and by the time sufficient new propellant enters the chamber the disturbance has been damped, so that what ensues is substantially a re-start of the engine. One numerical integration stability program[135] has been extended to consider the effects of chamber overpressure on the supply of unburned propellant to the zone being analyzed. Sufficient experience with this model has not yet been obtained to determine its success or failure.

Most numerical stability analyses are limited to testing the stability of tangential or, for rectangular combustion chambers, transverse acoustic modes. Strictly speaking, those based on an annular zone of interest are applicable only to toroidal chambers, although they are commonly applied to cylindrical chambers. The representation of wave shape leaves much to be desired, and the predicted stability limits often differ appreciably in magnitude from those observed in hot firings.

On the positive side, the numerical integration

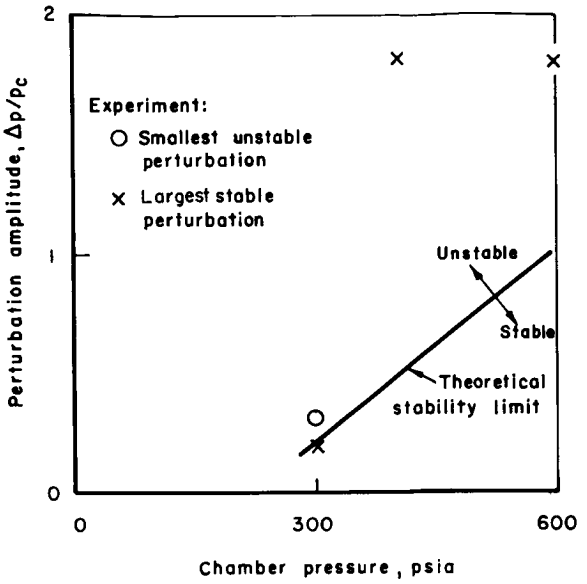

FIGURE 6.4.3c.—Effect of chamber pressure on pulse motor stability.

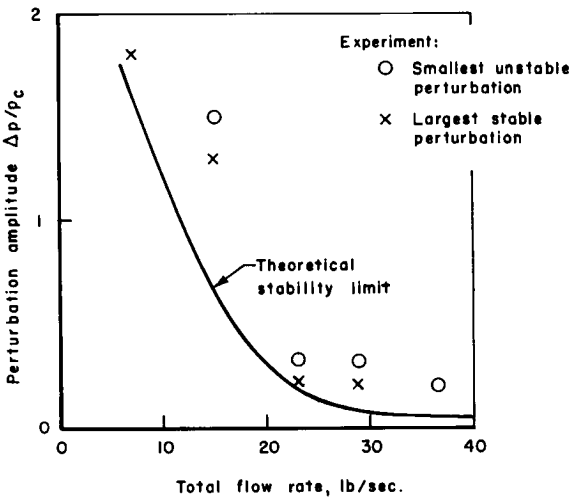

FIGURE 6.4.3d.—Effect of total flow rate on pulse motor stability.

models have been used rather successfully to predict trends of sensitivity to instability with changing design and operational conditions. Since it is not presently possible to rely with confidence on the absolute values of predicted stability limits, it is recommended that their application be limited to predicting stability relative to rocket engines that have been experimentally tested for stability. When employed in this manner and with careful interpretation these models offer useful design guidance.

6.5 HIGH FREQUENCY: RESPONSE FACTOR ANALYSIS

As discussed in Sect. 4.4.1 the response factor approach is intended to aid the engineer in evaluating the possible effects on stability of various design parameter or operating condition changes. Since the governing mathematical relations are discussed in some detail in Chapter 4, only the results of the analytical developments are repeated here. Instead, the emphasis is on the use of this approach in the solution of practical engine stability problems. Experimental data are used to illustrate the application techniques as well as to demonstrate the validity of the approach.

6.5.1 Heidmann-Feiler Approach*

The stability criterion obtained from the response factor model based on mass flow rates (Sect. 4.4.1) is†

$$\left[\sum_j \frac{\dot{m}_j}{\underline{\dot{m}}} N_j\right]_{in} \leq \left[\sum_j \frac{\dot{m}_j}{\underline{\dot{m}}} N_j\right]_{out} \qquad (6.5.1\text{–}1)$$

Basically, this states that a system will be stable when the sum of the contributions of the processes controlling the input of combustion gases is less than the sum of those controlling the outflow. The contribution of a process is measured by a weighted response factor, $(\underline{\dot{m}}_j/\underline{\dot{m}})N_j$, where the response factor, N_j, is the in-phase or real part of the fractional perturbation in mass flow rate with respect to the pressure perturbation.

* C. E. Feiler and M. F. Heidmann, Authors.

† See Sect. 4.4.1.2 for Nomenclature.

6.5.1.1 Process selection.—Certain simplifying assumptions were made in developing this criterion so as to allow the designer, developer or analyst to focus attention on the individual processes that influence the stability of an engine. In keeping with this objective, additional simplifying assumptions are made in applying the criterion to a specific rocket engine. The initial step in such applications is identification of the processes which control combustion gas flow rates.

The major contribution to the outflow term, $[(\underline{\dot{m}}_j/\underline{\dot{m}})N_j]_{out}$ is readily assessed for conventional engines. It is the response factor of the exhaust nozzle process with a weighting factor of unity. Ideally, the response factor obtained from a three-dimensional analysis of the nozzle flow process should be used (Sect. 3.6). In practice, the response factor of $1/\gamma$ derived for constant-temperature flow in a simple resistive nozzle (Sect. 4.4.1) is usually adequate for an initial assumption. This value is less than the optimum value of $(\gamma+1)/2\gamma$ derived from a one-dimensional analysis and, thereby, tends to compensate for reductions obtained from three-dimensional considerations. Experimental or analytical evidence, however, may dictate additional compensation to obtain quantitative agreement between theory and experiment.

Assessing the inflow term, $[(\underline{\dot{m}}_j/\underline{\dot{m}})N_j]_{in}$ is more difficult. The processes which control the production or generation of combustion gases and the fraction of the total mass flow rate associated with each process must be established. One of two generalizations is usually adequate to represent most bipropellant rocket combustors. The first is that all the mass release of combustion gases is controlled by a process associated with one of the propellants. The second is that the processes associated with both propellants act independently in the production of combustion gases. The decision as to which of these two extremes best represents a particular combustor is based on both intuition and analysis.

Control of the total mass release by one propellant characterizes many oxygen-hydrocarbon combustors where the oxygen atomizes and vaporizes rapidly and the hydrocarbon vaporizes and burns in a steady flow of the oxygen vapor. This behavior may also apply to other propellant combinations. The concept and method of

establishing its applicability are developed in the steady-state combustion theory (Chapter 2) and are also applicable to the dynamic system. The additional requirement, that the rapidly prepared propellants arrive at the combustion zone as a steady flow, however, is not established by steady-state theory. Process dynamics must be examined for this requirement. In general, rapid preparation is associated with a small time to atomize and vaporize and flow rate perturbations are negligible at normal resonant frequencies ($\omega\bar{\tau}$ is small). The exception usually involves the injection dynamics. Even though preparation is rapid, the injected flow rate may respond at normal resonant frequencies and cause flow rate perturbations of the prepared propellant. However, when steady flow can be justified the stability criterion for a combustion process controlled by one propellant is simply given by

$$N_{OX,F} \leq N_n \qquad (6.5.1\text{–}2)$$

Processes associated with both propellants affect mass release of combustion gases for many combustors. Dual propellant control occurs when the preparation of both propellants proceeds together and therefore have similar characteristic times. Again, steady-state theory can be used for the evaluation. Dual control also occurs when injection dynamics cause flow rate perturbations in the prepared propellant as previously discussed. This latter condition typifies gaseous hydrogen-liquid oxygen combustors under proper conditions. Gaseous injection systems can respond to acoustic mode frequencies and thus affect the mass release of combustion gases. Rigorous methods of establishing the fraction of total mass flow rate associated with each propellant in these dual control systems remain to be developed. It has been satisfactory in analyzing hydrogen-oxygen combustors to assume both propellants act independently and affect the mass release in proportion to their steady-state flow rates. This is an adequate initial assumption for any dual control combustion process but subject to modification on the basis of experimental evidence. For the case of independent action of both propellants the *stability criterion* becomes

$$\frac{\dot{m}_{OX}}{\dot{m}} N_{OX} + \frac{\dot{m}_F}{\dot{m}} N_F \leq N_n \qquad (6.5.1\text{–}3)$$

6.5.1.2 Hydrogen-oxygen combustors.—The most extensive application of the response factor model to an actual engine system has been with the gaseous hydrogen-liquid oxygen propellant combination. A systematic study of this combination for several injector and operating parameters has been performed in a 20K thrust engine.[716,719] The experimental technique consisted of decreasing the hydrogen injection temperature until instability was observed. The stability limit of the system was prescribed by the operating conditions including the hydrogen injection temperature at this transition point. A detailed account of the application of the response factor model to these experiments is found in Refs. 259 and 260. The stability criterion is expressed for gaseous hydrogen-liquid oxygen as

$$0.55 \frac{\dot{m}_{OX}}{\dot{m}} + \frac{\dot{m}_{H_2}}{\dot{m}} N_{H_2} \leq \frac{1}{\gamma} = 0.833 \qquad (6.5.1\text{–}4)$$

In this equation the nozzle response factor is taken

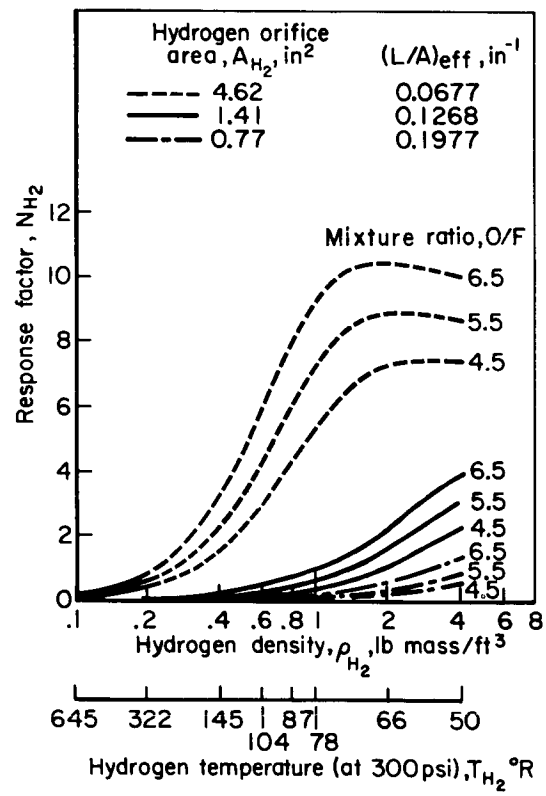

FIGURE 6.5.1a.—Variation of response factor with hydrogen density.

as $1/\gamma$, as discussed previously. The oxygen response factor is taken as 0.55, the maximum value found by linear analysis for oxygen vaporization (see Fig. 4.4.1b). This choice is an engineering estimate rather than an analytical evaluation. With these two response factors and the mixture ratio prescribed, Eq. (6.5.1–4) defines the stability of the engine in terms of the hydrogen response factor. For a mixture ratio of 5.5 the value of N_{H_2} at the stability limit is 2.39.

The hydrogen response function for the type of injector element used in the experiments of Ref. 719 can be calculated using Eq. (4.4.1–7a) and (4.4.1–7b) of Section 4.4.1.2. The calculation is straightforward, except that the combustion time lag τ_b must be estimated. For the comparison between theory and experiment under discussion here, an initial τ_b value was estimated from the injection velocity and the standoff distance of the flame. This value was then adjusted to produce the best fit with the experimental data, giving a final time lag value between 0.08 and 0.09 millisec.

Figure 6.5.1a shows the variation of the hydrogen response factor with hydrogen density or temperature for three values of hydrogen orifice area A_{H_2}, and three values of mixture ratio (O/F). The curves illustrate the increase of the response factor as temperature is decreased (density increased). This result is in accord with the experimental observations on the effect of temperature. The effect is one of increased coupling between the hydrogen flows and chamber pressure perturbations as the density is increased. At the stability limit, the density corresponding to the value of N_{H_2} can be read from each curve.

Figure 6.5.1b shows predicted stability limits in terms of the hydrogen density at the transition point* as a function of O/F and hydrogen orifice area A_{H_2}. Also shown are the corresponding experimental data. It can be seen that the trends, both with O/F and orifice area, are reasonably

* This transition point to resonant combustion is discussed in the hydrogen ramping techniques, Sect. 10.

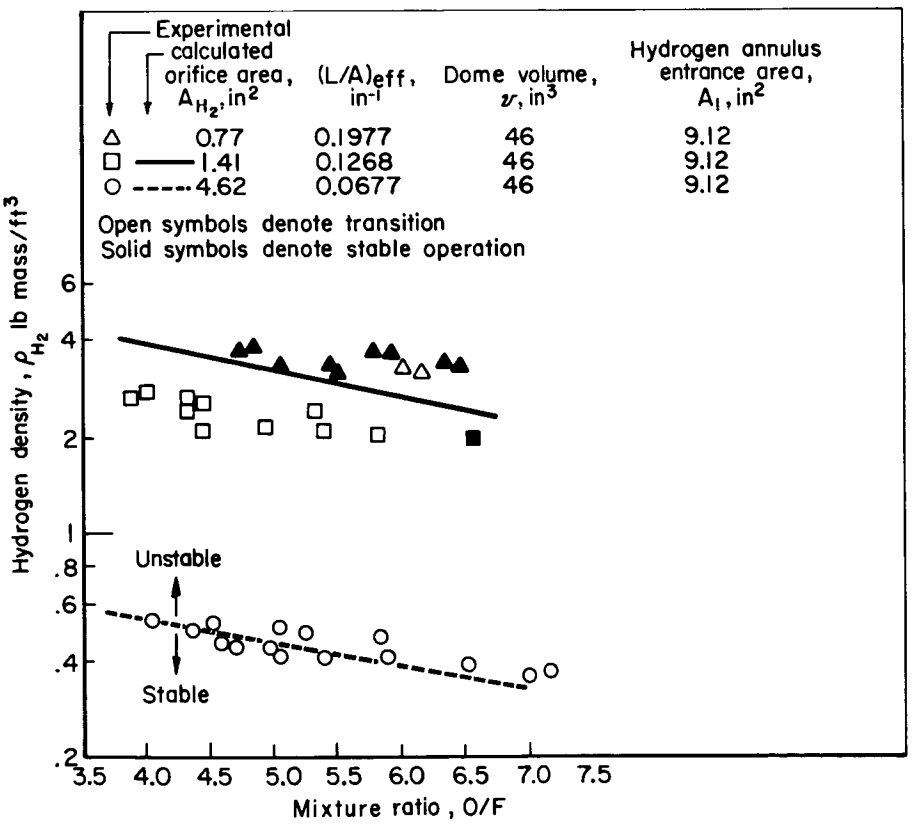

FIGURE 6.5.1b.—Comparison of experimental and calculated hydrogen-density stability boundaries.

well predicted by the analysis. The stability limit was not obtained for the smallest orifice since it occurred at a temperature below that available in the experimental facility. Similarly, the analysis indicated a temperature or density exceeding that which was possible.

In another set of experiments, nozzle area, weight flow rate, and chamber pressure were varied in pairs while holding the remaining parameters constant.[716] The injector parameters were those shown in Table 6.5.1. Figures 6.5.1c, d, and e compare the results of these experiments with the analytical results at an O/F of 5.5. The agreement found is quite good.

TABLE 6.5.1.—INJECTOR PARAMETERS

Chamber pressure, P_c, lbf/in.^{2}	300
Total flow rate, $\dot{m}$, lbm/sec	65
Frequency, ω, rad/sec	21 350
Oxidant-fuel ratio, O/F	5.5
Hydrogen orifice area, A_{H_2}, in.^{2}	*4.62
Dome volume, $\mathcal{V}$, in.^{3}	46.0
Hydrogen annulus length-to-area ratio, $(L/A)_{eff}$, in.$^{-1}$	*0.0677
Hydrogen annulus area, A_1, in.^{2}	*9.12
Time delay constant for burning, τ_b, sec	0.00009
Hydrogen density, ρ, lb/ft^3	0.1 to 4.04
Temperature, T, °R	645 to 50

* At 20 atm.

It has been found experimentally that the stability limit can be moved to lower hydrogen temperatures by increasing the oxygen injection diameter. It would be expected that the oxygen drop size and therefore the vaporization time τ_v increases with hole diameter. From Fig. 4.4.1b the value of the oxygen response factor should decrease, since the smallest diameter was associated with the peak value of the response factor. Correspondingly, according to Eq. (6.5.1–3), the hydrogen response factor at the limit will increase, leading to the prediction of a larger transition density (lower temperature). The predicted trend of the stability limit with increasing oxygen hole diameter is thus qualitatively correct.

This application of the response factor model to the gaseous hydrogen-liquid oxygen system illustrates how it is used and its utility as a diagnostic tool. Similar procedures are followed in its application to other combustion systems whether

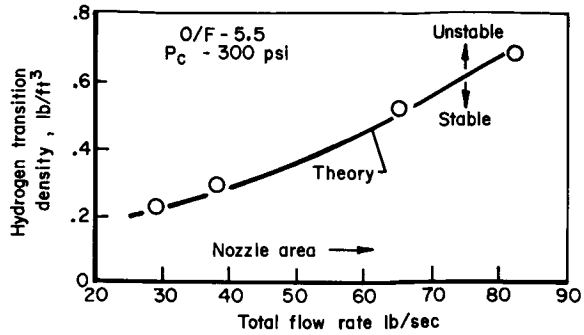

FIGURE 6.5.1c.—Effect of flow rate on hydrogen transition density at constant chamber pressure.

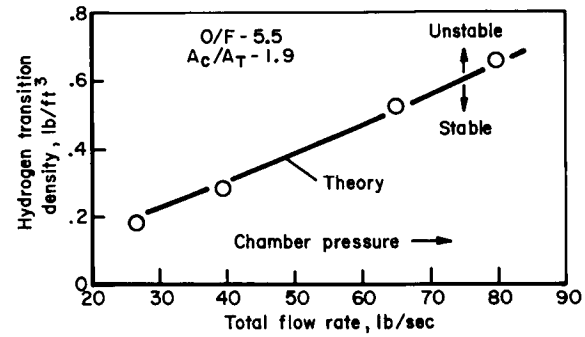

FIGURE 6.5.1d.—Effect of flow rate on hydrogen transition density at constant contraction ratio.

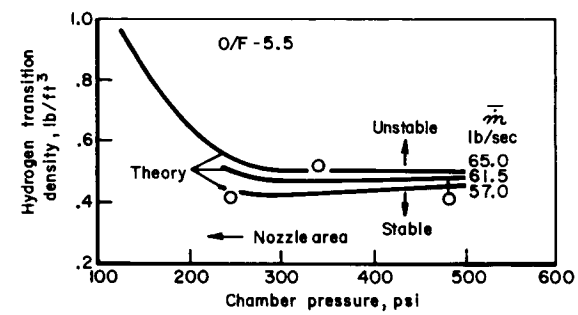

FIGURE 6.5.1e.—Effect of chamber pressure on hydrogen transition density.

for the purpose of designing a stable system or analyzing an existing system. In application, attention is focused on the response factors of the processes comprising the system and on those variables that affect the response factors. An important key to the success of any application of the model lies in the selection of the processes that enter into Eq. (6.5.1–1); of somewhat less

importance will be the exact dynamic modelling of the processes. As found for the hydrogen-oxygen system, certain approximations and assumptions will enter into the modelling of the processes. These, however, will not impair the usefulness of the result, which is the acquisition of physical insight into the mechanisms of instability and of the parameters of importance.

6.5.2 Dykema Analysis*

The following nomenclature pertains to Sect. 6.5.2 (see also Sect. 4.4.1.3):

A_s	Stability constant defined in Eq. (6.5.2–2)
d_{30}	Volume-number mean droplet diameter
K_d	Proportionality constant between d_{30} and $\sqrt{d_i/v_i}$

Subscript:

atm	Conditions at standard atmospheric pressure

In Sect. 4.4.1.3, an approximate response factor for unsteady droplet vaporization was given by

$$\frac{Q'}{p_c'} = \frac{6A_i}{A_c}\frac{\kappa(\kappa-1)}{\Re T_c} h_R \bar{Y}_{FL}\left[\frac{\psi}{N_s}\right]$$

Many of the quantities in this expression are very difficult to determine within factors of two or three in accuracy.† Generally, these quantities are established for a given engine by other important design considerations and are, therefore, considered constant. For these reasons it is usually sufficient, and advisable, to consider only the variation of the combustion response factor caused by the dimensionless term ψ/N_s. This term is a function only of the stability correlating parameter N_s (see Fig. 4.4.1f), which is defined as

$$N_s = 2\pi\frac{fl^2}{2\mathfrak{D}_F} \qquad (6.5.2\text{–}1)$$

It can be shown that $l^2/2\mathfrak{D}_F$ represents the time for diffusion over the distance l in the presence of a linear concentration gradient. The frequency f is the reciprocal of the acoustic mode period. Thus, N_s is the ratio of a characteristic molecular diffusion time to a characteristic acoustic time.

Eq. (6.5.2–1) can be reduced to readily measurable engineering terms with the help of two additional assumptions: (1) the ratio of flame radius to droplet radius is independent of droplet size; and (2) the initial spray drop size distribution can be approximated by the empirical relation established by Ingebo[375] with the relative velocity between liquid and gas set equal to zero. Then, using the following relations,

$$l^2 = (r_f - r_L)^2 = \frac{(\kappa-1)^2}{4} d_{30}^2$$

$$\mathfrak{D}_F = \mathfrak{D}_{F_{atm}} \cdot \frac{p_{atm}}{\bar{p}_c}$$

$$d_{30} = K_d\sqrt{d_i/V_i}$$

$$\dot{m}_i = \rho_L A_i \bar{V}_i$$

the expression for N_s can be written

$$N_s = A_s \mathfrak{N}_i d_i^3 \frac{f\bar{p}_c}{\dot{m}_i} \qquad (6.5.2\text{–}2)$$

where

$$A_s = \left(\frac{\pi}{4}\right)^2 \frac{\rho_L}{144} K_d^2 \frac{(\kappa-1)^2}{\mathfrak{D}_{F_{atm}} p_{atm}}$$

This engineering approach to high frequency combustion instability thus involves the use of Eq. (6.5.2–2), with an empirically-determined constant, A_s, in conjunction with the combustion gain curve of Fig. 4.4.1f.

The general objective in the use of N_s is to establish a combustor design such that the combustion gain is minimized in all acoustic modes. If it is not possible to obtain negative gain for all modes, then damping must be introduced for those specific modes having positive gain by means of baffles or resonators. Large thrust-per-element injectors are typical of the case where all transverse modes have negative gain. More conventional injectors, such as those used on the Titan IIIM Stages I and II engines represent cases where the first two transverse modes have positive gain (unstable without baffles) and are stabilized with baffles designed to introduce damping into these two modes.

To apply the N_s approach the propellant that controls the stability must be determined. This is generally the more poorly atomized, slower vaporizing propellant, but this should be determined empirically. The controlling propellant can

* O. W. Dykema, Author.

† These problems are also considered in Refs. 667, 669, and 670.

usually be readily ascertained by observing the variation of stability with mixture ratio when all other parameters are held constant. If, for example, an increase in mixture ratio causes the instability to shift to a higher mode, the oxidizer is the controlling propellant, and its flow rate is used in Eq. (6.5.2–2). For several propellant systems the controlling propellants appear to be as follows:

Propellant combination	Controlling propellant
O_2/RP-1	RP-1
N_2O_4/Various N_2H_4 blends	N_2O_4
B_5H_9/N_2H_4	N_2H_4
IRFNA/UDMH	IRFNA

Applying Eq. (6.5.2–2) to the controlling propellant, the readily measurable engineering parameters are obtained or calculated. It should be noted that the quantities $\mathfrak{N}_i$, d_i, and $\underline{\dot{m}}_i$ apply to the active matrix elements only; that is, film cooling, baffle tip injection, etc., are to be excluded. If the orifice sizes vary across the injector face, engineering judgment must be applied in selecting those orifices which inject propellant in the region of pressure anti-nodes of each particular mode.

The remaining problem in using Eq. (6.5.2–2) is the value of the empirical constant A_s. If instability data are available for the specific engine of interest, careful study of frequency analyses of one or more instabilities usually indicates one or both of the stability boundaries (at $N_s = 5.6$ or 30) and/or the maximum gain (at $N_s = 9$). An empirical value of A_s can then be determined and Eq. (6.5.2–2) used to determine a stable design. It is important to recognize that since little is known of the magnitude of the gain or the damping in the coupled combustion/acoustic system it is possible that a given mode could be stable even though the combustion gain is positive, but a mode should never be unstable if the combustion gain is negative. An example of this approach is given in Ref. 236.

If no instability data are available, a reasonably accurate initial estimate of the value of A_s can be obtained from the results of previous analyses. Applicable constants have been estimated for nearly all production engines in the industry, ranging from some of the small, 100 pound thrust attitude-control motors to the F-1 engine, a range of 10^4 in thrust. Although the reason is not entirely clear, the empirical values of A_s do not appear to vary a great deal despite the wide ranges of parameters in N_s. Thus, an initial estimate of A_s can be obtained from

$$A_s = (6.0 \times 10^{-3})\,(\text{S.G.}) \qquad (6.5.2\text{–}3)$$

where S.G. is the specific gravity of the controlling propellant. From the empirical data used, the standard deviation associated with Eq. (6.5.2–3) is 20%.

6.5.3 Design Applications of Modal Energy Analysis*

The modal energy analysis was developed to facilitate design of new combustion systems using data accumulated from tests of existing systems. This section will present procedures used for new designs, and will indicate ways in which the analysis is used in correcting designs found to be unstable during development. The section concludes with a discussion of special cases and comments on the validity of the method as applied.

The following nomenclature pertains to Sect. 6.5.3 (see also Sect. 4.4.1.4):

A_j	Boundary surface area at location j
$\mathfrak{A}$	Specific acoustic admittance
G_c	Combustion response (gain) function
K_{pj}	Correction for nonlinear compression at location j
K_{vj}	Correction for kinetic energy residuals at location j
R_{kG}	Combustion gain contribution to system divergence rate
R_{kL}	Contribution of losses to system divergence rate

6.5.3.1 Design procedure.—In Section 4.4.1.4, the following expression for the logarithmic growth rate, R_k, was derived:

* C. K. Leeper, Author.

$$R_k = \frac{-10}{2.303}\frac{1}{\bar{K}_p K_v k_k}\left\{\frac{k_k l_{wk}}{a}\left(q+\sum_i C_{ik}\right)\right.$$
$$+\sum_j\left(\frac{A_j}{A_k}\right)\mathfrak{M}_{nj}N_{kj}K_{pj}K_{vj}$$
$$+\frac{2}{\bar{K}_k}\sum_j\left(\frac{A_j}{A_k}\right)\left[\left(\frac{v_{kj}'}{\hat{v}_k'}\right)^2 B_{kj}\right.$$
$$\left.\left.+\left(\frac{p_{kj}'}{\hat{p}_k'}\right)^2 G_{kj}+\left(\frac{v_{kj}'}{\hat{v}_k'}\right)\left(\frac{p_{kj}'}{\hat{p}_k'}\right)H_{kj}\right]\right\} \tag{6.5.3–1}$$

where the coefficient q measures the radiative heat loss, C_{ik} indicates the energy scatter to other modes, N_{kj} expresses the nozzle outflow of energetic material, B_{kj} is the wall shear coefficient and H_{kj} represents the combustion sensitivity to velocity oscillations. The terms in G_{kj} include pressure-sensitive combustion response as well as wall absorption, feed-system damping, and nozzle traveling-wave feedback. Usually it is reasonable to assume

$$q = C_{ik} = B_{kj} = 0$$

and

$$\bar{K}_p = K_v = 1$$

Then Eq. (6.5.3–1) simplifies to

$$R_k = -\frac{10}{2.303}\frac{1}{k_k}\left\{\sum_j\left(\frac{A_j}{A_k}\right)\mathfrak{M}_{nj}N_{kj}K_{pj}K_{vj}\right.$$
$$+\frac{2}{\bar{K}_k}\sum_j\left(\frac{A_j}{A_k}\right)\left(\frac{p_{kj}'}{\hat{p}_k'}\right)^2 G_{kj}$$
$$+\frac{2}{\bar{K}_k}\sum_j\left(\frac{A_j}{A_k}\right)\left[\left(\frac{p_{kj}'}{\hat{p}_k'}\right)^2 G_c\right.$$
$$\left.\left.+\left(\frac{v_{kj}'}{\hat{v}_k'}\right)\left(\frac{p_{kj}'}{\hat{p}_k'}\right)H_{kj}\right]\right\} \tag{6.5.3–2}$$

where the combustion terms G_c have been separated from the loss terms (G_{kj}). Eq. (6.5.3–2) is of the form

$$R_k = R_{kG} - R_{kL}$$

where R_{kL} and R_{kG} are the contributions to the system divergence rate of the losses and combustion gain, respectively.

Performance and chamber cooling requirements usually establish the chamber cavity size and shape, nozzle, profile, propellants, injection density, sound velocity, and gas constant, and the feed system configuration. The designer then selects injection element and pattern designs to achieve the desired (negative) values of the rate of divergence, R_k, for all anticipated system modes. Auxiliary damping devices may be added to permit use of high performance injection elements.

The first step is to determine the frequencies and shapes ($p_{kj}'/\hat{p}_k'$ distributions) of the several chamber acoustic modes, using classical solutions[503] for simple geometries and lumped parameter relaxation techniques[713] or experimental microphone surveys of model chambers[473] for more complex cavities. The number, k_k, of wavelengths in each mode, the chamber volume, the wavelengths, l_{wk}, and equivalent mode cross sections, A_k, are then calculated (see Sect. 4.4.1.4). Basic orientation in wave processes is given in Ref. 495.

Loss coefficients, G_{kj}, are then tabulated for the wall materials and resonance absorbers, and N_{kj} for exhaust nozzles. Either Eq. (6.5.3–1) or (–2) is used to calculate the coefficients G_{kj} from changes in R_k measured in subscale comparison tests with and without the material. Data should be selected from tests at wavelengths and local conditions similar to those of the application. Nozzle coefficients for conventional geometries may be determined by theoretical analysis. More complex geometries may require cold-flow acoustic measurements. The contribution R_{kL} of losses to the system divergence rate, R_k, for each mode is computed by summing the weighted G_{kj} and N_{kj} over the boundaries of the system. The wall area is divided into incremental areas, A_j, associated with absorbing units having reasonably constant properties and p_{kj}' values. The mode shape coefficient $\bar{K}_k$ is computed as the volume average of $(p_{kj}'/\hat{p}_k')^2$ for each mode. Coefficients q, C_{ik}, and B_{kj} are assumed to be zero and $\bar{K}_p$ and K_v are considered to be unity. The results are plotted as $(-R_{kL})$ vs. frequency, i.e., one value for each mode.

Inspection of Eq. (6.5.3–2) shows that the contribution of a loss element to R_{kL} for a mode depends on the square of the local-to-maximum pressure amplitude ratio, $p_{kj}'/\hat{p}_k'$. It is thus important to locate absorbers in regions where the most suspect modes have maximum pressure

excursions. In systems having no preferred mode orientations, perturbations in cavity shape (e.g., a small baffle) or periodically-spaced absorber patches should be introduced to determine antinode positions. Shape perturbations can also damp potentially destructive traveling waves (e.g., spinning modes).

The basic injection element is now selected, using available gain (G_c) vs. frequency data. Since element and chamber frequency characteristics are virtually independent, it is possible to seek elements whose gain peaks do not coincide with the chamber resonant frequencies. Further, present data suggest that elements symmetrical about two axes (planar triplets, pentads, coaxial elements) have zero velocity coefficients, H_{kj}, and are, therefore, preferred.

A considerable body of data indicates that maximum values of G_c are essentially independent of element design features, but that the high frequency gain "cutoff" is inversely proportional to some power of the thrust-per-element. (A useful approximation for the maximum value of G_c for a uniformly distributed group of injection elements is $G_c = \gamma \dot{m}/A_j \rho a$, where G_c is dimensionless and γ is the ratio of specific heats for the combustion gases.) Then stability is assured if the element selected has a cutoff frequency lower than that of the fundamental resonance of the chamber. Unfortunately, such elements generally have low combustion efficiencies, thereby delivering low I_{sp} performance.

One approach which improves performance uses one element, the G_c peaks of which purposely overlap the lowest two or three mode frequencies, and a second element with no frequency overlap but with the same thrust-per-element as the first element. The first (high performance) element is distributed over all portions of the injector where $p_{kj}'/\hat{p}_k'$ is below some value (say, 0.8) for all modes k having frequency overlap. The remainder of the injector is populated with the second element. Mass distribution of propellant is held uniform over the injector.

The degree of stability predicted is now determined by calculating the gain contributions R_{kG} to the system divergence rate, R_k, using Eq. (6.5.3-2), the element G_c values, the $p_{kj}'/\hat{p}_k'$ distributions, driving-to-driven area ratios A_j/A_k, and mode shape coefficients, $\bar{K}_k$. The R_{kG} points are added to the $-R_{kL}$ vs. frequency plot and the net R_k values noted. Positive values indicate statically-unstable modes. Negative values of 1 db/cycle indicate mildly damped, statically stable modes. Negative values of 2 and 3 db/cycle indicate adequate and excellent static damping, respectively.

The following example illustrates the method. The chamber consists of a cylinder, capped at each end with flat plates, and vented by a side outlet nozzle running the length of the cylinder. (See Fig. 6.5.3a). Injection elements are distributed on the cylinder interior opposite the nozzle. The modal frequencies are approximately 1400, 2000, 2800, 3320, 4160 and 4560 for the 1L, 1T, 2L, 2T, 1R and 3T modes, respectively, for the cylinder radius of 0.88 feet, length 2.15 feet and a = 6000 fps. Damping rates $-R_{kL}$ are shown in Fig. 6.5.3a.

Two element types are chosen: type A, with frequency peaks at 1100, 2000 and 3600 Hz and type B, with peaks at 550 and 1000 Hz. Both have maximum G values of 0.1 (Fig. 6.5.3b). The high-frequency element (type A) is used in the zones L/8 to 3L/8 and 5L/8 to 7L/8 and the low frequency element (type B) in zones 0 to L/8, 3L/8 to 5L/8 and 7L/8 to L, as shown in Fig. 6.5.3b. (The use of type B in the zone at the cylinder midpoint is intended to decrease 2L mode gain, although this is theoretically unnecessary in this case.) The circumferential

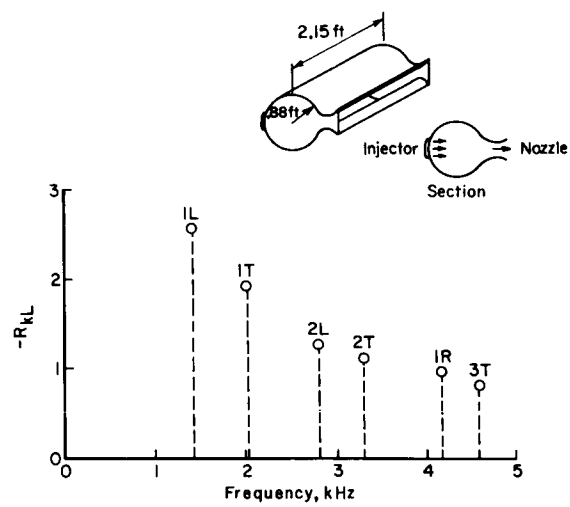

FIGURE 6.5.3a.—Damping rates for several modes; cylindrical chamber with full length side nozzle.

distribution can be similarly zoned to avoid high frequency elements in the 2T antinode zone. The combustion amplification R_G is shown in the lower graph of Fig. 6.5.3b.

The completed divergence rate vs. frequency plot (Fig. 6.5.3c) shows acceptable decay rates at all frequencies but 2000 Hz (1T). Addition of tuned resonator absorbers in the 1T antinode zones would correct this condition. Use of resonators throughout the chamber would probably permit use of higher cutoff frequency elements. This can be checked by using calculated values of the real part of admittance of the resonators to determine G values for use in Eq. (6.5.3–2) where $G = \rho a \mathcal{R}e(\mathcal{A})$ and $\mathcal{A}$ is the specific acoustic admittance.

Finally, dynamic stability of the design is checked by recomputing R_{kG} for the more sensitive modes, using G values measured under nonlinear oscillatory conditions for the subject elements as fired in subscale chambers. Limited data indicate that nonlinear G values are 2 to 4 times linear values. Using this ratio, it can be seen that the example would be dynamically stable in all modes except the 1T mode.

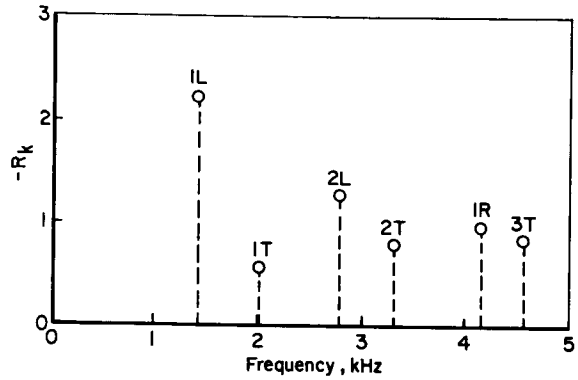

FIGURE 6.5.3c.—Net damping rate for simple combustion system of Fig. 6.5.3a.

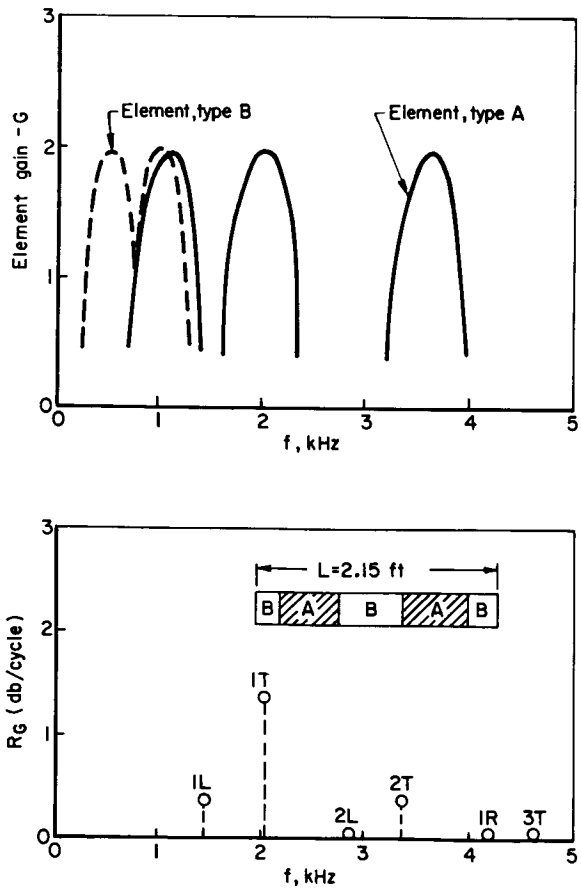

FIGURE 6.5.3b.—Element gain coefficient and combustion amplification.

Positive or small negative values for R_k as determined from developmental test records (preferably tape) signal the need for additional corrective measures. From the observed frequency, the mode pressure distribution $\bar{K}_k$, and A_k values can be approximated. Eq. (6.5.3–2) is then used to assess the ΔR_k to be realized by element substitutions, pattern changes, and added absorber materials or devices.

6.5.3.2 Special considerations.—Note that the R_{kG} for a combination of injection elements is the result of a weighted summation, and that an average value for G for the elements cannot be used. Mode shapes are distorted by the mean flow in high Mach number chambers.[642] Compliant walls and nozzles having net compliance or inertance in the admittance cause slight mode shape and frequency shifts. Mechanical capacitance (in walls parallel to the oscillation) reduces the speed of sound, and, therefore, the frequency. Combustion zones can also shift frequency by introducing an apparent length change in the system. The amount of this effect can be calculated by observing actual vs. theoretical wavelength in subscale chambers.

Coupling, (C_{ik}) and radiation (q) terms can be

omitted from design calculations and treated as additional margins of safety, since each adds damping. Nonlinear compression effects, $\bar{K}_p$, alter the magnitude but not the sign of R_k. In general, special terms in Eq. (6.5.3–1) are included to remind the experimentalist to eliminate their effect in apparatus used to measure coefficients. The design should consider all terms in unusual cases.

Typical data for actual hardware are given in Ref. 436. Values used in the example are for illustration only. Injector element data, G_{kj}, must generally be measured, as needed, in subscale apparatus (see Sect. 7.4). Nozzle data are readily calculated from admittance analyses. Acoustic linear data are similarly converted. Measurement of R_k values requires high frequency surface pressure instrumentation and Fourier transform or graphic reduction techniques. Although linear data are reasonably reliable, nonlinear data exhibit considerable variation. For a small data sample, agreement between frequencies of peak G values and those obtained from $n-\tau$ correlations for injection elements (Sect. 6.3.3) is excellent.

6.6 HIGH FREQUENCY: SIMILARITY RULES*

6.6.1 Stability Prediction Equations in Decision Making

This section contains a discussion of empirically-derived similarity rules or stability prediction equations obtained by means of a statistical analysis of engine test data. The background of this discussion is presented in Sect. 4.4.2, and Ref. 689.

The following nomenclature pertains to Sect. 6.6 (see also Sect. 4.4.2.3):

D_y	Generalized distance between stable and unstable statistical distributions
$\bar{y}_s$	Mean of y_p-distribution, stable tests
$\bar{y}_u$	Mean of y_p-distribution, unstable tests
z	Variable in statistical analysis indicating whether a test was pulsed ($z=1$ if pulsed; $z=0$ if not pulsed)

It must be emphasized that it can be grossly misleading to isolate a given coefficient from the prediction equations given in Sect. 4.4.2.3 and argue that its value expresses the effect of varying the associated independent variable. In addition, although the prediction equations are based on a wide range of engines, they are not applicable to engines with design innovations not represented in the data. Under these circumstances, how can an engine designer make use of the appropriate stability equation in designing an engine?

There are three legitimate uses of the prediction equations which do not violate the caveat implied by the above statements, and nonetheless should be helpful in saving both time and funds. The designer can use the equations as a checking device, to verify whether the application of his ideas is likely to produce a stable engine; he can use them as a standard against which proposed design changes can be evaluated; and the program manager can use the equations to assist in making the final decision on whether or not the engine should be built and tested. In no case should it be inferred that a prediction equation can substitute for the application of engineering and physical principles to rocket engine design, nor should decisions involving construction and testing be based *solely* on the predicted stability obtained from an instability regression equation.

In using the prediction equation as a checking device, the designer develops his ideas to the point where he can supply a value for each of the independent parameters or variables called for by the appropriate stability equation (given in Sect. 4.4.2). Substitution of these values into the equation yields a predicted value, the *index of instability*, y_p. If the analogy is not carried too far (values of y_p occasionally will be less than zero or greater than 1), it is possible to regard the index of instability as an estimate of the probability that the engine, if built and tested as represented by the values chosen for the independent variables, will be unstable. This index provides the designer with an early check on whether the direction of his thinking is inherently sound from a stability point of view. It should cause him to reevaluate his concepts if he gets an "early warning" of the likelihood of instability in the form of an unacceptably large value of y_p.

In using the prediction equation as a standard for evaluation of proposed design changes, the designer recalculates y_p to conform to each

* I. Miller, G. H. Harris, and E. K. Bastress, Authors.

change in design and reacts to the trend in the resulting values. A progression of design changes leading to reduced values of y_p (all other things–such as cost, efficiency, etc.–being equal) is the direction in which he should wish to proceed. Note that the use of the equation is not recommended for direct mathematical "optimization" of stability. It usually is not possible to change the value of one design parameter without also being required to alter other parameters in compensation. Some of these other parameters may not even appear in the equation. Thus, it is necessary for the designer continually to "use his best judgment," checking stability retrospectively by means of the equation each step of the way.

One of the frustrating consequences of the use of equations such as the stability prediction equations involves the interpretation of the resulting number, y_p. According to our heuristic interpretation, large values of y_p are less desirable than small values because they reflect a higher probability that the resulting engine will be unstable. But what interpretation should be placed on a result such as $y_p = 0.35$? Is it "good" or is it "bad"? The answer to this question comes best from experience. After repeated application of a prediction equation to a given class of engines, the line between "acceptable" and "unacceptable" values of y_p will begin to emerge. A discussion of how the past experience represented by this study can be brought to bear in determining the line between acceptable and unacceptable values of y_p is given in the following paragraphs. It should not be inferred from the ensuing discussion, however, that there really exists a sharp dividing line.

Ideally, a perfect stability-prediction equation should produce the predicted value $y_p = 0$ for each stable test and the value $y_p = 1$ for each unstable test. In this event, it is said that the equation produces "complete separation" of the stable and unstable tests. More realistically, a prediction equation will produce values of y_p that are somewhat scattered; hopefully, however, the y_p-values for stable tests will cluster about some small value, the y_p-values for unstable tests will cluster about some large value, and the distance between these two "cluster points" will be large relative to the scatter.

To put these ideas into more precise form,

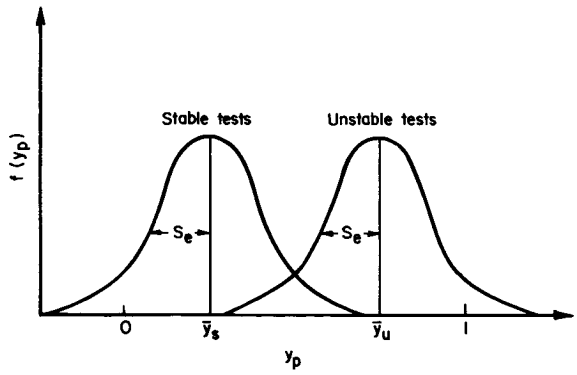

FIGURE 6.6.1a.—Distributions of predicted stability index.

consider the distributions of the y_p values for the stable and the unstable tests separately, as indicated in Fig. 6.6.1a. The mean of the distribution of stable tests will be denoted by $\bar{y}_s$, and the mean of the distribution of unstable tests will be denoted by $\bar{y}_u$. The symbol S_e denotes the standard error of estimate associated with the prediction equation. The "generalized distance" between these two distributions,

$$D_y = \frac{\bar{y}_u - \bar{y}_s}{S_e}$$

describes the degree of discrimination between stable and unstable tests achieved by the equation. It can be interpreted as the number of standard deviations separating the distributions of the stable and the unstable tests, and provides a figure-of-merit for evaluating the goodness of the prediction equation.

To examine these distributions in greater detail, they are plotted on a probability scale. On this scale, the cumulative distribution is a straight line for normally-distributed data, and the slope of the line provides a measure of the standard deviation. Such graphs are shown in Fig. 6.6.1b and 6.6.1c for the general non-pulsed equation and the general pulsed equation, respectively. Notice that the data points do not lie in a straight line, indicating departures from the normal distribution. However, the trends are nearly parallel, indicating approximately equal standard deviations. The parallel lines shown on the graphs represent the best-fitting normal distributions with equal standard deviations. The lines pass through the points ($\bar{y}$, 50%) and ($\bar{y}+S_e$, 84%)

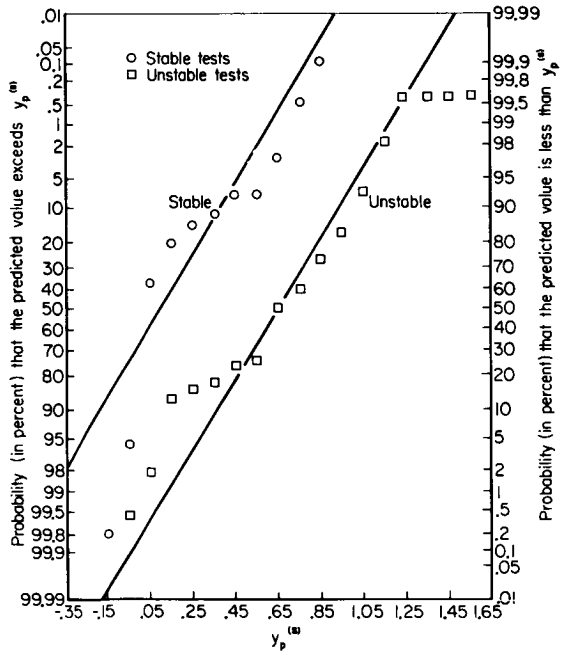

FIGURE 6.6.1b.—Cumulative distributions of predicted stability index $y_p^{(s)}$ for stable and unstable tests; general nonpulsed group.

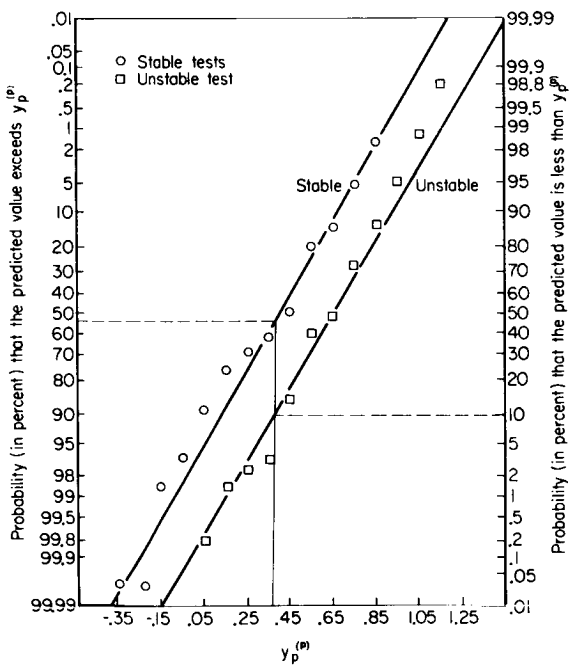

FIGURE 6.6.1c.—Cumulative distributions of predicted stability index $y_p^{(p)}$ for stable and unstable tests; general pulsed group.

where S_e is the appropriate pooled standard deviation.

Fig. 6.6.1d shows the two parallel lines from the non-pulsed data of Fig. 6.6.1b. Assuming that the underlying distributions of $y_p^{(s)}$ are as represented by these lines, we can state, for example that the probability is approximately 0.10 that an unstable test would have yielded an instability index value $y_p^{(s)}$ *less than* 0.36. Similarly, the probability that a stable test would have yielded a predicted value greater than 0.36 is approximately 0.12. In other words, if we had decided to set a value of 0.36 as the cutoff value of $y_p^{(s)}$, thereby rejecting as potentially unstable all designs having $y_p^{(s)} > 0.36$ and accepting as potentially stable all designs having $y_p^{(s)} < 0.36$, 90% of the engines that actually went unstable would not have been built. The cost of this decision is characterized by the statement that 12% of the engines that proved to be stable would also not have been built.

Similarly, one could establish a decision criterion based upon the pulsed data represented in Fig. 6.6.1c such that all but 10% of the unstable tests would be eliminated. In this case, the cutoff value of $y_p^{(p)}$ is 0.37. However, this criterion would also

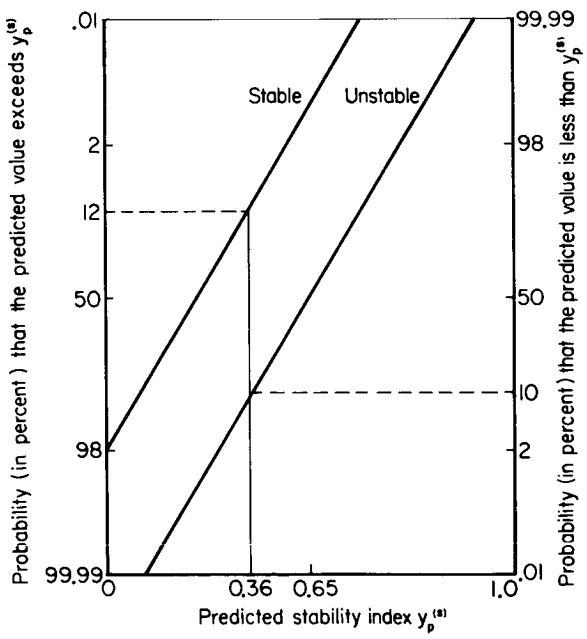

FIGURE 6.6.1d.—Interpretation of cumulative distributions of predicted stability index.

eliminate 54% of the stable tests because of the relatively poor separation of stable and unstable tests by the stability prediction equation.

These cutoff values are by no means recommended values. They have been chosen for illustrative purposes only. The selection of cutoff values could be based upon the relative costs of building engines that would later prove to be unstable and deciding not to build engines that would have been stable. The value of this kind of analysis lies not in that it provides a hard-and-fast rule for making the decision to build and test an engine (it should not), but that it gives otherwise unavailable insights into the consequences of any proposed decision criterion. Moreover, the empirical similarity approach has the potential for substantially reducing the number of unsatisfactory and costly engines constructed and tested, without at the same time causing an unacceptable number of potentially useful engines not to be constructed.

6.6.2 The Role of Pulsing in Stability Determination

In the preceding discussion, the pulsed and non-pulsed tests were treated separately, and the empirical instability prediction equations involved substantially different sets of independent variables. This result raises the question of the relation between the two sets of data. Two investigations were made in this regard:[82] (a) The stability of the pulsed tests was predicted on the basis of the non-pulsed equation and compared with the experimental results, and (b) the two sets of data were combined and an instability prediction equation was determined for the combined set.

Using the general instability prediction equation for non-pulsed tests (Table 4.4.2a), the value of the instability index $y^{(s)}$ was obtained for each of the 1234 pulsed tests. This was the index for spontaneous instability for the hardware and test conditions included in the pulsed-test set. To determine the relationship between the predicted *spontaneous* instability and the observed *pulsed* instability, the distributions of $y_p^{(s)}$ for the stable and unstable (pulsed) tests were examined separately. The generalized distance between the two distributions was calculated to be $D_y = 0.218$. Comparing this value with those obtained previously, viz, $D_y = 1.98$ for the non-pulsed tests and $D_y = 0.576$ for the pulsed tests, it can be seen that there is a very poor separation between the stable and unstable tests. Thus, knowledge of the likelihood of spontaneous instability contributes very little information about whether or not the combustor will recover from a pulse.

In a further effort to explore the relation between the pulsed and non-pulsed tests, a regression equation was computed for all available data (2133 points). The dependent variable was chosen to be appropriate to the nature of each test, that is, $y_p^{(s)}$ for non-pulsed tests and $y_p^{(p)}$ for pulsed tests. The independent variables that appeared to be significant for either of the two data sets were included in the model for the combined set. In addition, an independent variable z was included to denote whether or not the test belonged to the pulsed group. If a test was pulsed, $z = 1$; otherwise, $z = 0$.

The resulting model, including squares and cross products of the variables, contained 79 terms. After the first 32 terms were included in the model, $R^2 = 0.37$, and the standard error of estimate was $S_e = 0.39$. Because of the inhomogeneous nature of the dependent variable, the use of such an equation for instability prediction is not practical. The coefficient of z was found to be†

$$
\begin{aligned}
&1.232 - 0.078L_c - 0.740 \log \epsilon_c - 0.001FO3 \\
&\quad - 0.463PE1 + 0.159(L_c/D_c) + 0.029TPVM \\
&\quad + 0.039(MPE)^2 - 0.180(\log \epsilon_c)^2 \\
&\quad - 0.076(\log d_{iF})^2 - 0.003\bar{p}_{ci} \log d_{iF} \\
&\quad + 0.00001L_cV_{iox}
\end{aligned}
$$

indicating that the effect of pulsing depends in a very complicated way on the particular engine design, including variables that are not strongly related to spontaneous instability.

6.6.3 Stability and Efficiency

The designer of a rocket engine is concerned with the steady-state performance of the engine as well as its stability. In the statistical investigation of Ref. 82, c* efficiency was used as a measure of

† The quantities are defined in Sect. 4.4.2.3.

steady-state performance, and its relation to stability was studied in three ways: (a) regression equations for c* efficiency were developed using the same independent variables as the corresponding instability prediction equations, (b) the strength of the relationship between c* efficiency and the observed value of the instability parameter was examined, and (c) the extent to which the c* efficiency could be predicted from a knowledge of the predicted value of the instability index was examined.

The prediction equations for c* efficiency use essentially the same terms as those in the corresponding prediction equations for stability. The statistics associated with the pulsed and non-pulsed data sets are compared in the following table:

	c* efficiency		Stability	
	R^2	S_e	R^2	S_e
Non-pulsed tests	0.588	0.052	0.592	0.278
Pulsed tests	0.255	0.065	0.259	0.434

Thus, the predictive power of the c* regression equations is seen to be about as good as that of the equations representing stability.

The distributions of c* efficiency values were examined separately for stable and unstable, pulsed and non-pulsed tests. A comparison of the means and standard deviations of the four groups is shown in the following table:

	Non-pulsed Tests		Pulsed Tests	
	Stable	Unstable	Stable	Unstable
Mean	0.90	0.91	0.91	0.95
Standard deviation	0.08	0.07	0.10	0.06

It can be concluded from these results that the distribution of values of c* efficiency is essentially the same for both stable and unstable tests.

Another way to compare performance and stability is to develop a regression equation relating c* efficiency to the predicted value of the instability index. This procedure was followed separately for non-pulsed and pulsed tests. For the non-pulsed tests, a linear regression equation was found to relate c* efficiency (CSE) to the instability index $y_p^{(s)}$:

$$(CSE)_p = 0.879 + 0.050 y_p^{(s)}$$

The relationship is a very weak one, the coefficient of multiple correlation being only $R^2 = 0.043$. However, a test of the null hypothesis that the true coefficient of $y_p^{(s)}$ equals zero shows that it cannot be rejected at the 0.001 level of significance. In other words, the relationship, however weak, nonetheless is statistically significant.

For the pulsed tests, the resulting regression equation is

$$(CSE)_p = 0.903 + 0.057 y_p^{(p)}$$

Again, the relationship is very weak; $R^2 = 0.035$. It is interesting to note that the coefficient of the instability index in each equation is very nearly the same.

From the statistical studies of c* efficiency and stability, it can be concluded that in the process of selecting design parameter values to minimize the possibility of instability, the designer is not necessarily paying a serious price in terms of reduced steady-state performance.

6.7 USE OF COMBINATIONS OF MODELS†

From the discussion in the preceding sections it should be clear that there exists no comprehensive theoretical approach that is able to treat all aspects of the problem of liquid rocket combustion instability. Low frequency oscillations must be considered separately from high frequency acoustic modes. Each analytical approach to high frequency instability emphasizes certain features of the phenomenon and omits others. Thus, a general stability analysis must involve more than a single approach or analytical model. To see how the several models may be used in combination, it is helpful to review the advantages and limitations of each.

† R. J. Priem and F. H. Reardon, Authors.

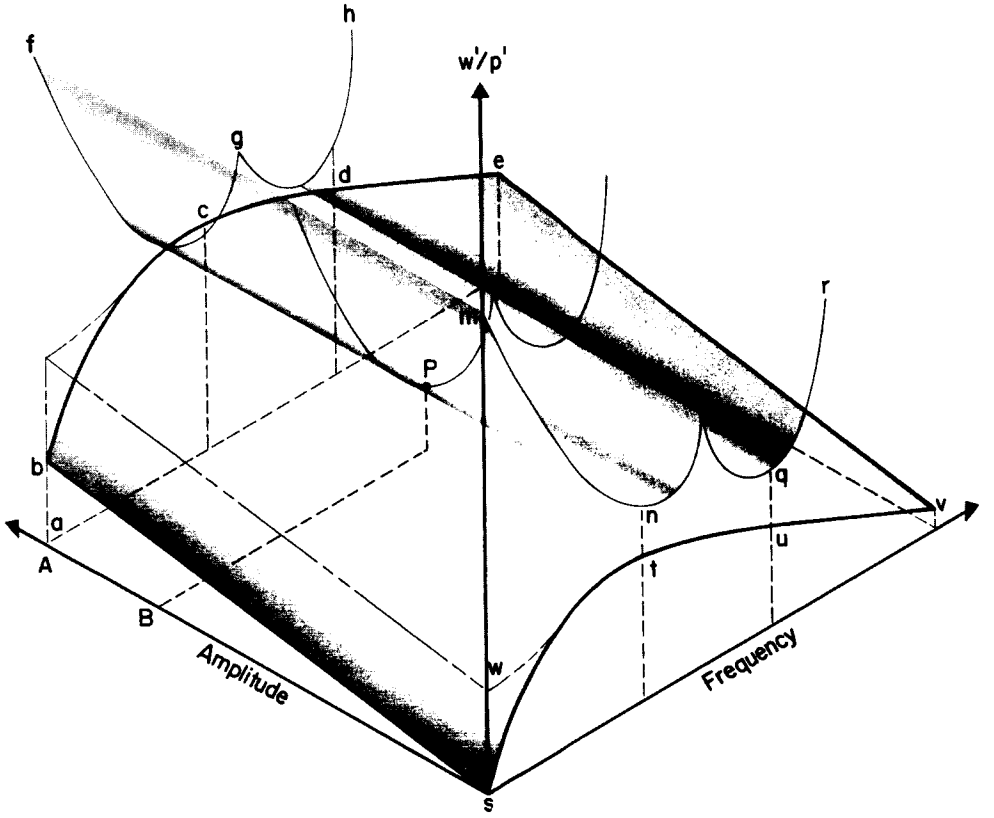

FIGURE 6.7.—Stability map for typical liquid propellant rocket engine.

The sensitive time lag theory circumvents the problems inherent in the description of unsteady combustion by use of a simplified two-parameter response function. However, the gas dynamic flow field is treated rigorously, so that the effects of the exhaust nozzle and of three-dimensional wave motion can be properly taken into account.

The response factor approach involves a much simplified treatment of the flow field, concentrating on the combustion mechanisms that contribute to the oscillations. The nozzle response factor is usually taken to have the constant value of $1/\gamma$. The various gain and loss mechanisms are assumed to act independently.

The numerical integration method makes it possible to extend the consideration of specific combustion mechanisms to include nonlinear combustion response functions, non-sinusoidal waves, and the effects of finite disturbances. However, the analysis is usually restricted to one space dimension with a simplified flow field having an effective energy loss factor of $1/\gamma$.

Empirical correlation equations are based directly on experimental results and employ engine design parameters. Because of their statistical nature and their inability to improve understanding of the phenomena involved in combustion instability, the best use of these equations is in checking the theoretical analyses using the other approaches.

The complementary nature of the several theoretical approaches can be illustrated with Fig. 6.7, which is a three-dimensional stability map for a typical liquid rocket engine. The vertical axis represents the combustion response, that is, the magnitude of the burning rate oscillation divided by the pressure oscillation amplitude. The other axes represent the frequency and amplitude level of the oscillation.

The curve s-t-u-v represents a typical response curve for small perturbations. Such a curve can be obtained by use of the linearized response factor approach. The curve m-n-p-q-r indicates the combustion response required for continuing

oscillations, for two acoustic modes, and may be obtained from the sensitive time lag theory. The most sensitive frequencies are those corresponding to the points n and q. The margins of stability for these two modes are indicated by the vertical distances n-t, q-u. If the response curve s-t-u-v (available oscillatory energy) crosses the stability limit curve m-n-p-q-r (required oscillatory energy) spontaneous instability is expected. That is, the stability margin of one or more modes becomes negative. It can be seen from Fig. 6.7 that the simple criterion that the combustion response factor equals $1/\gamma$ at the stability limit is only a rough approximation and can be improved considerably by use of the sensitive time lag theory. From another point of view, it is clear that ability to investigate specific combustion mechanisms, inherent with the response factor approach, permits a greater understanding of the instability phenomenon than is possible with the sensitive time lag formulation of the combustion response.

The influence of wave amplitude and the possibility of nonlinear triggering must also be taken into account in a comprehensive stability analysis. Extension of the sensitive time lag theory to include finite amplitude, non-sinusoidal waves (Sect. 4.2.4) has shown that, for pressure-sensitive combustion processes, the U-shaped stability limit curves become broader with increasing amplitude, but are not shifted in the vertical direction. Thus, a stability limit surface (f-g-h-r-q-p-n-m), representing the combustion response required for continuing oscillations, can be visualized in the response-amplitude-frequency space. Correspondingly, the available combustion response for a given mechanism can be extended into the finite amplitude domain by means of the numerical integration method. Fig. 6.7 illustrates the case in which the combustion response factor increases with amplitude, so that at a certain amplitude A the response curve b-c-d-e crosses the stability limit curve f-g-h, resulting in amplification of the oscillations. Hence, nonlinear triggering of instability is possible for this case. The point P, where the two surfaces intersect in a single point, indicates the threshold condition for triggering by a finite disturbance (amplitude B).

Actually, the several theoretical models have not been combined in the manner discussed above; each is formulated to determine the overall stability of the engine. However, it should be clear that a thorough analysis of stability cannot be restricted to a single approach. In lieu of combining the models, each can be used separately in the area where it is most appropriate. For example, the sensitive time lag theory can be used to investigate the effects of changes in the geometry of the combustion chamber and exhaust nozzle. The linear response factor approach can be used to evaluate the importance of particular combustion mechanisms. Then the numerical integration method can be used to determine the possibility of nonlinear triggering, and the influence of wave shape. The empirical correlation equations provide a general check on the theoretical stability analysis. Finally, the importance of low frequency oscillations or the interaction of feed system dynamics with wave motion in the combustion chamber should also be studied. Although a comprehensive theoretical stability model, covering all of these aspects of the problem, would certainly be advantageous, it is quite possible to perform a thoroughgoing stability analysis by combining the existing models.

CHAPTER 7

Design Factors Affecting Excitation

7.1 INTRODUCTION*

This chapter, together with Chapter 8, is primarily concerned with the phenomena of instability as observed in the rocket hardware rather than with analysis as in the previous chapters. Heavy reliance is placed on experimental evidence, when available, to show trends which are expressed as far as possible in quantitative terms. Current knowledge of the effects of mean flow conditions, propellant combinations, injector design and feed system coupling is outlined. The point of view is specifically one of "how oscillatory operation may be excited in liquid propellant rockets." This and the following chapter, more than any other chapters in this reference book, are oriented to the needs of the designer.

The first section of this chapter considers the overall combustion design conditions. A common problem with the individual parameters discussed (chamber pressure, contraction ratio, injection density, axial and transverse energy release and boundary effects) is the interrelationships that exist within the rocket combustion chamber. Several of the authors discuss this problem with relation to the parameter they are treating. That no clean separation is possible with regard to the effect of each parameter on stability, only adds to the complexity of finding solutions to the various types of instability problems. Even so, the history based upon a number of hardware designs and the influence of parametric variations does point the way to at least limited solutions. Although the reader may be left with the impression that there is an exception to every design rule, the attempt here, wherever possible, is to point out the "firm" versus the "spongy" ground.

In the next section the discussion turns to the effect of propellants on stability. The point is made that whereas effects are extremely significant in some instances, that in other cases propellant properties are not important. Viewing the problems connected with the choice of propellant, the relation of chemical properties to such characteristics as stream separation, popping and spiking incidences, preferred frequencies, etc., are considered. Possible chemical kinetic influences are also discussed and additives, including powdered metals and gelling agents, are covered in this section. It is pointed out that chemical characteristics appear to enter primarily in determining whether the fuel and oxidizer are hypergolic or if the fuel can act as a monopropellant.

Section 7.4 covers the favorite design approach to achieving a stable rocket engine, i.e., the appropriate choice of injector pattern. The similarities that exist between the various injector designs and the droplet sprays and associated combustion each injector type produces are pointed out in this section. The comparison yardstick is the droplet size and the distribution of the droplets within the chamber. The reader is encouraged to evaluate the similarities between injector designs that look, at first glance, quite dissimilar physically. However, as with the other sections, contradictions are also present. Thus, the designer, to be more completely prepared for the instability potential that exists in his application, should keep in mind this injector/stability history. Those references that best conform to his proposed design and operational environment should also be utilized and trends of other operating parameters should be taken into account (as much as possible) in making extrapolations.

Although the bulk of this chapter is concerned with events as they take place within the com-

* D. T. Harrje, Author.

bustion chamber, the coupling with the feed system has not been overlooked. In Sect. 7.5 aspects of the feed system coupling that may have been buried within the analytical treatments of previous chapters are resurrected for further discussion. Such practical considerations as the role of injector impedance, the effect of gases trapped in the injector manifold (or created by the presence of cavitating venturis), mechanical vibration, and the effect of imposed oscillations on the system are discussed in this section. Again the emphasis is on the design problems; however, the use of the related analytical background material, covered in Chapters 3 through 6, is encouraged.

7.2 OVERALL COMBUSTION DESIGN CONDITIONS

The following nomenclature pertains to Sect. 7.2:

$\mathcal{E}_R$	Real part of nozzle admittance coefficient
$f(\gamma)$	Function of specific heat ratio
k	Droplet drag parameter
$\mathfrak{L}$	Burning rate parameter
M_x	Fractional burning rate per unit length
p_{cr}	Critical pressure of propellant
Δp	Pressure drop across injector, $p_i - p_c$
V_w	Local wave velocity
V_{wm}	Average (mean) wave velocity
VR	Injection velocity ratio, V_F/V_{OX}
ΔV	Gas-liquid velocity difference
δ	Low frequency stability parameter, $\Delta\bar{p}L^*/\bar{p}_c$
ϕ	Injection stream impingement angle
$\hat{\mu}$	Injection density
τ	Sensitive combustion time lag (see Sect. 4.2)

7.2.1 Chamber Pressure*

7.2.1.1 General statement of the problem.—The investigation of the effects of various operating parameters, such as chamber pressure, on low frequency or high frequency instabilities (or on the incidence of popping) is beset with many difficulties. Analytical investigations are hampered by the complexity of the combustion process to the extent that simplifying assumptions must be introduced, which limit the analytical models. Empirical investigations are often hampered by the statistical nature of the data required and hence the associated cost to produce a representative result. It is the intent herein to indicate the problems associated with the accumulation of empirical data and explain why the effects of such parameters as chamber pressure have not been thoroughly established.

Perhaps the biggest problem with an empirical study to determine the effect of chamber pressure on instability is the high cost associated with changing *only* the chamber pressure. One approach consists of varying only the total flow thereby maintaining the same thrust chamber hardware. However, this results in revised injection characteristics (new injection velocities, different jet and droplet breakup, etc.) which can be expected to alter the combustion process. Therefore, a change in chamber pressure by varying the total propellant flow has introduced a "sympathetic" independent variable. The sympathetic parameter can be eliminated by modification of the injector; however, manufacturing costs then become very significant. Another approach to changing the chamber pressure consists of changing the exhaust nozzle throat area. However, changing the throat area is no better solution, since this modifies the contraction ratio and the chamber Mach number, which also alters the combustion response. It can be seen that this approach necessitates alterations in the geometry of the engine for each datum point. Inasmuch as statistical analyses require fairly large sample sizes, the cost of such a program becomes prohibitively high.

It is possible to reduce hardware cost by testing smaller-sized engines but here the uncertainties associated with scaling techniques are encountered. Furthermore, scaling techniques are applicable only when a suitable mathematical model is available, which is often not the case.

For these reasons, the experimental information concerning the role of chamber pressure in low frequency or high frequency instability is incomplete and scattered. Therefore, only the trends and how these trends agree with existing analytical models can be reported.

7.2.1.2 Low frequency instability.—One effect that the mean chamber pressure has on the low

* A. J. Smith, Jr., Author.

frequency (chugging) modes of instability is that an increase of chamber pressure, in general, stabilizes an engine. This effect was investigated by Ross and Datner.[603] Figure 7.2.1a indicates the observed stability at a given mixture ratio and percent of design chamber pressure. The particular tests show that, at any mixture ratio greater than 2.5, the unstable motor operation at low pressures can be stabilized by a suitable chamber pressure. These results are typically obtained by varying tank pressures to change mixture ratio and chamber pressure, while keeping the rocket motor and injector configuration constant. The stabilizing effect of chamber pressure on chugging was verified by Heidmann et al.[345] (see Fig. 7.2.1b). In that study (using a different feed system, rocket motor configuration, and propellants) whereas one again obtains an increase in stability by an increase in chamber pressure, the line of stability demarcation is clearly different.

It is of interest to study the behavior of the chugging mode as the chamber pressure is increased. Assuming that the mode is initially at a mixture ratio and chamber pressure point deep within the unstable region, it is generally observed that the mode wave shape is of a nonlinear nature. As the chamber pressure is increased and as the operating point approaches the stability boundary, the frequency of the chug increases, the amplitude of the chug decreases, and the nonlinear wave shape degenerates to a sinusoidal wave. As the operating point crosses over the stability boundary, the chug amplitude disappears into the noise generated by the combustion process and the system stabilizes.

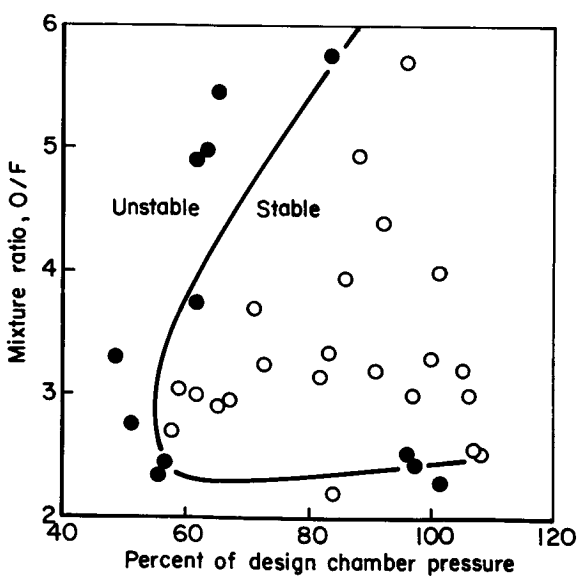

FIGURE 7.2.1a.—Low frequency stability limit map.

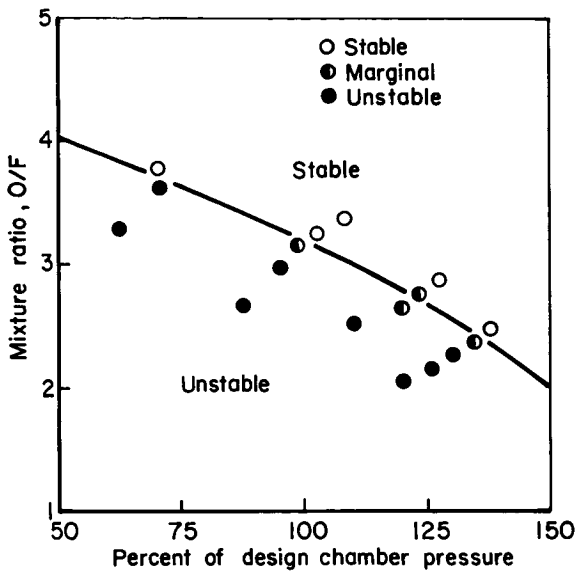

FIGURE 7.2.1b.—Comparative low frequency stability limit map.

The influence of the chamber pressure on the frequency of the chug is shown in Fig. 7.2.1c. It can be seen that, in all four cases shown, the frequency of the chug increases as the chamber pressure increases; however, the rate of increase is not necessarily the same. Curves (a) and (b) are of particular interest in that they illustrate the effect of the propellants, and therefore the combustion process, upon the chugging frequency. The only variation between the tests conducted to generate these two curves was a change in the fuel.[78] At a chamber pressure of 213 psia, the nitric acid/furfuryl alcohol propellant combination (hypergolic) chugged at approximately 100 Hz at an amplitude of 10 percent. At the same pressure, nitric acid/octane (nonhypergolic) chugged at approximately 35 Hz at an amplitude of approximately 25 to 30 percent. With an entirely different system operated at a chamber pressure of 270 psia, the nitric acid/heptane combination (nonhypergolic) chugged at 26 Hz at an amplitude of almost 100 percent.[688]

The final aspect to be discussed in this section is

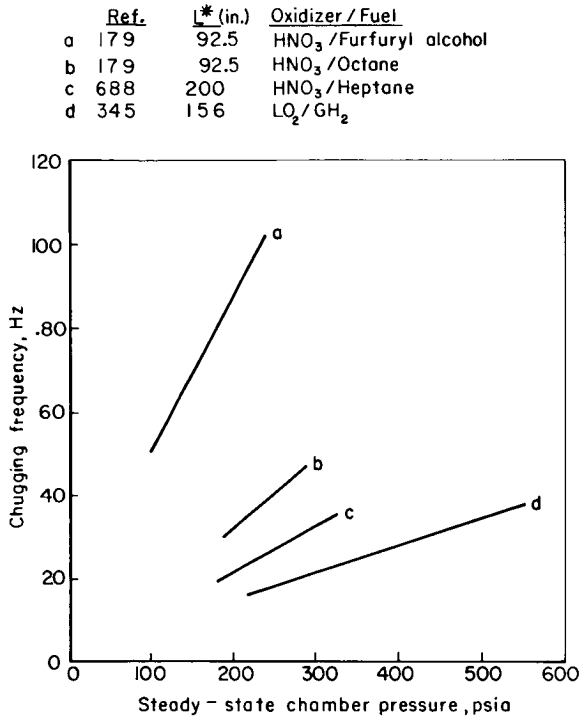

FIGURE 7.2.1c.—The variation of chugging frequency with respect to the mean chamber pressure.

the effect that the mean chamber pressure has on the chugging stability plane when viewed with respect to the correlating parameters that are generally incorporated in chugging studies. The two correlating parameters used for bipropellant motors are the ratio of pressure drop (i.e., from tank to chamber or from injector inlet to chamber) to the steady-state chamber pressure†, and this same parameter multiplied by the characteristic length of the chamber (see Ref. 7, Appendix C), i.e.,

$$\delta = \frac{\Delta p}{p_c} L^*$$

For the study conducted in Ref. 678, a high impedance source was installed in the injector to decouple the feed system from the chamber. The flow rate was held constant while the chamber pressure was changed from 300 psia to 650 psia by changing the nozzle throat diameter. This led to a small change in the characteristic length of the chamber, L*. If the reported data is multiplied by

† See Sect. 6.2 for a further explanation of this stability parameter.

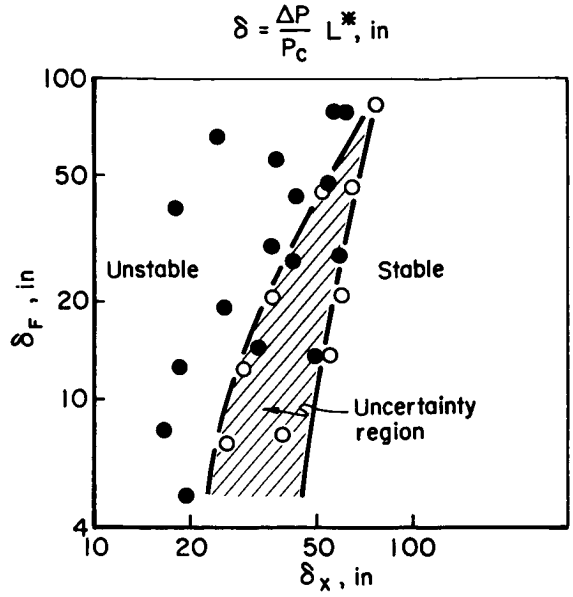

FIGURE 7.2.1d.—Low frequency stability limit map relative to the correlating parameters δ_X and δ_F.

the L* and plotted as a function of the correlating parameter δ, one obtains the result shown in Fig. 7.2.1d. It can be seen that the δ-correlation does not lead to a precise definition of the stability boundary. In support of their analytical chugging model, Szuch and Wenzel[678] were looking for two chugging frequencies simultaneously. These two frequencies were the result of a "real-life" situation that, if the bipropellant system was unstable, either one or both of the propellants could be involved, thereby producing two frequencies. These two frequencies are referred to as "lower" and "higher" chugging frequencies.

If the reported data is plotted at the two pressure levels and at the observed chug situation as shown in Fig. 7.2.1e, it is seen that the lower and higher frequencies individually generate stability boundaries and, therefore, the motor stability map divides itself into a more complicated relationship (compared to the data previously discussed). Also, it can be seen that the mean pressure has a definite effect on the nature of the stability zone.

7.2.1.3 High frequency instability.—High-frequency instability has been experimentally observed under a variety of rocket motor geometries,

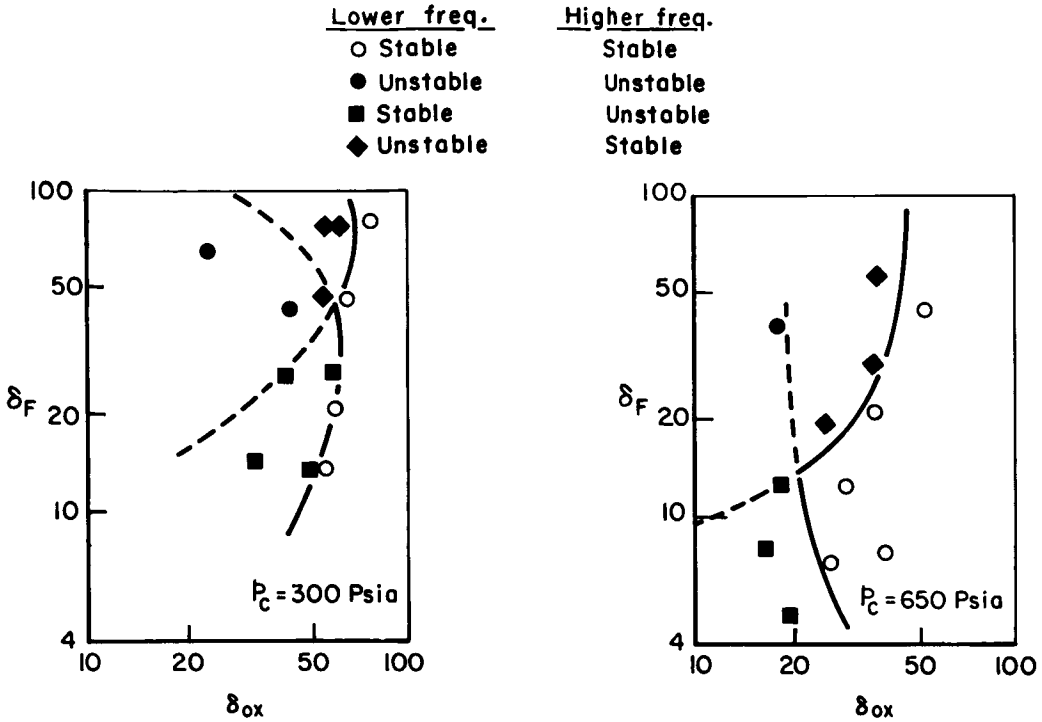

FIGURE 7.2.1e.—The effect of the mean chamber pressure on the chugging stability limits relative to the correlating parameters δ_X and δ_F.

propellant combinations, and operating conditions as evidenced in the earlier chapters. An unstable rocket motor is analogous to a driven acoustic system where the geometry of the motor determines the acoustic properties of the system and the combustion process, determined by the propellants, injector elements, and operating conditions, represents the driver. Because of the strong interrelationship of the driver and acoustic cavity, it is very difficult to change one parameter in the system, such as pressure, and not effect another parameter. Therefore, in acquiring empirical data, it is necessary to keep account of all variables considered to be meaningful and resort to statistically-oriented numerical correlation techniques to indicate parameter trends. Such is the case of the effect of chamber pressure on the combustion response to high frequency instability.

Recent accumulation of experimental stability results[650] indicate that the characteristic combustion time decreases as the chamber pressure is increased as shown in Figs. 7.2.1f and 7.2.1g.

In the case of hypergolic propellants (Fig. 7.2.1f), the dependent variable is the product of the chamber Mach number, $\mathfrak{M}_c$, diameter of the orifice related to the controlling propellant (usually selected as the least volatile), d_i, and the sensitive time lag (or period), τ, associated with the instability frequency, where approximately

$$\tau = \frac{1}{2f}$$

The independent variable is the ratio of the chamber pressure to the critical pressure of the controlling propellant. In this case,*

$$\tau \sim p_c^{-1/3}$$

There are no data in the supercritical pressure region for storable propellant combinations; consequently, the effect of supercritical pressures on the combustion response is not known.

* The relationship indicates shorter characteristic combustion times for higher pressures hence a tendency toward higher modes as shown in Fig. 7.4.3h.

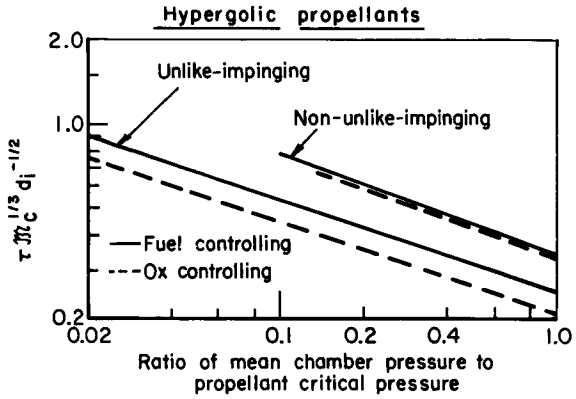

FIGURE 7.2.1f.—The effect of mean chamber pressure on the high frequency combustion response characteristics of hypergolic propellants.

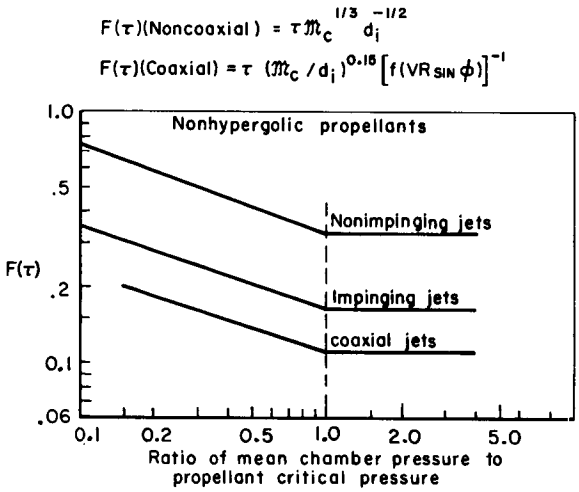

FIGURE 7.2.1g.—The effect of mean chamber pressure on the high frequency combustion response characteristics of nonhypergolic propellants.

In the case of nonhypergolic propellants (Fig. 7.2.1g), an additional parameter is added to the dependent variable for coaxial injectors. The parameter is a function involving the ratio of the fuel velocity to the oxidizer velocity, VR, and the impingement angle, ϕ, between these two streams. It is seen from this figure that for subcritical pressures,

$$\tau \sim p_c^{-1/3}; \qquad p_c < p_{cr}$$

and for supercritical pressures,

$$\tau \neq \tau(p_c); \qquad p_c > p_{cr}$$

An explanation of this subcritical/supercritical role of chamber pressure has been offered based on the fact that the heat of vaporization decreases as the chamber pressure approaches the critical pressure of the propellant.[333] At subcritical pressures, the time lag is postulated to be composed of a vaporization time, diffusion time, etc., whereas at supercritical operation, the vaporization time is absent in the determination of the time lag.

7.2.2 Contraction Ratio*

The behavior of most processes which occur inside the combustion chamber of a liquid-propellant rocket motor (e.g. atomization, mixing, vaporization, droplet drag) is affected by the magnitude of the Mach number $\mathfrak{M}_c$ of the chamber mean flow. The Mach number is controlled by the nozzle contraction ratio ϵ_c, and it is important to understand how a change in ϵ_c affects the stability characteristics of a particular engine. In order to answer this question it is necessary to know how the above-mentioned processes depend on $\mathfrak{M}_c$ during both steady and unsteady operation. Only when this and any other relevant information becomes available is it possible to perform an analysis that can predict the engine stability under various operating conditions.

Our present lack of understanding and inability to describe analytically the various processes taking place inside the combustion chamber of a liquid-propellant rocket engine limit the degree of confidence that can be placed in the theoretical predictions of various stability analyses, in the interpretations of available experimental data, and in design changes aimed at eliminating combustion instability. This situation becomes particularly clear when one is trying to determine the dependence of the stability limits of high-frequency combustion instability on $\mathfrak{M}_c$. A survey of available researches trying to answer this question indicates a serious lack of agreement between the predictions of various theories and a lack of appropriate experimental data capable of checking the theoretical predictions. Numerous development programs and experimental endeavors conducted in the past provide us with a considerable amount of data where proper

* B. T. Zinn, Author.

interpretation requires a careful statistical analysis. The results of such an analysis in which ϵ_c (and hence $\mathfrak{M}_c$) is a parameter, are presented in Ref. 82. In the remainder of this section the predictions and observations of those theoretical and experimental studies, which explicitly consider the $\mathfrak{M}_c$ dependence of the stability limits, will be discussed.

The majority of this discussion will concentrate on the more detrimental and less understood case of high-frequency combustion instability. In discussing this case it is important to classify the instability according to its amplitude (i.e. linear vs. nonlinear) and mode of oscillation. Available linear analyses are separated into those considering longitudinal oscillations[179] and those considering transverse[582] or three-dimensional[202,567,772] oscillations. The majority of these analyses is limited, however, to situations in which $\mathfrak{M}_c \ll 1$. It has been shown[178,202,582] that when $\mathfrak{M}_c \ll 1$ the chamber's oscillations are qualitatively similar to the acoustic modes that can be excited in a cavity whose geometry is similar to the chamber's geometry. Hence when $\mathfrak{M}_c \ll 1$, acoustic solutions can be used as a first approximation to describe the oscillations in the combustion chamber; this is not the case when neither $\mathfrak{M}_c$ nor the amplitude of the oscillations are small.

Crocco[178] provided an approximate analysis that can serve to illustrate the manner in which the rocket's stability limits for both longitudinal and transverse oscillations depend on $\mathfrak{M}_c$ (when $\mathfrak{M}_c \ll 1$). Since the stability criteria for both the longitudinal and transverse types of oscillations are qualitatively similar, only the one applicable to transverse oscillations will be discussed here. According to Crocco (Sect. 4.2) neutral transverse oscillations can occur in the chamber when the following relation is satisfied:

$$\mathcal{E}_R - (\gamma+1)\mathfrak{M}_c + \gamma \int_0^L \left(\frac{M'}{p_c'}\right)_R dz' - \int_0^L \bar{\rho}_L k \, dx = 0 \qquad (7.2.2\text{–}1)$$

Eq. (7.2.2–1) represents the energy balance that must exist between various energy sources and sinks in the combustion chamber when the oscillations are neutrally stable.

It is of interest to consider briefly the significance and Mach number dependence of the various terms in Eq. (7.2.2–1). The first term $\mathcal{E}_R$ represents the energy loss or gain at the nozzle entrance. It has been shown[179,190,196] that $\mathcal{E}_R$ depends on $\mathfrak{M}_c$ and that it can be positive (i.e. destabilizing) or negative (i.e. stabilizing); the same references show that in the case of longitudinal oscillations $\mathcal{E}_R$ is always stabilizing while in the case of transverse oscillations its effect depends, among other factors, on the magnitude of $\mathfrak{M}_c$. The negative term $-(\gamma+1)\mathfrak{M}_c$, which explicitly represents the effect of the mean flow, is always stabilizing. The third and fourth terms represent, respectively, energy gain due to combustion oscillations and energy loss due to droplet drag. The dependence of these terms on $\mathfrak{M}_c$ depends on the particular analytical models which are chosen to represent these processes; relevant discussions of these topics may be found in Refs. 346, 516, 582, 665 and 739.

Once the $\mathfrak{M}_c$ dependence of all the terms appearing in Eq. (7.2.2–1) has been established, this equation can be used to evaluate the $\mathfrak{M}_c$ dependence of the rocket's stability limits. Similar theoretical studies have been conducted by Crocco and Cheng[179] and Mitchell (pg. 116 of Ref. 188) for the case of longitudinal oscillations and by Culick,[202] Priem,[567] Reardon[582] and Zinn[772] for the case of three-dimensional oscillations. The conclusion in the case of longitudinal instability (for both low and high values of $\mathfrak{M}_c$) was that increasing $\mathfrak{M}_c$ has a destabilizing effect. The predictions of the various three-dimensional theories are contradicting. No general conclusions can be stated, but the indications are[202,567,772] that when $\mathfrak{M}_c$ increases a larger combustion response is necessary in order to drive instability which implies that, in the case of three-dimensional oscillations, increasing $\mathfrak{M}_c$ is stabilizing. An interesting result was obtained in the studies of Priem[567] and Zinn[772] which predicted, that as $\mathfrak{M}_c$ increases, the range of frequencies over which the operation of the system may become unstable also increases. These references predict that an increase in $\mathfrak{M}_c$ increases the chances of obtaining instabilities of the mixed acoustic modes which are associated with a given pure transverse mode. Priem has considered the effect of acoustic liners, and predicts that increasing $\mathfrak{M}_c$ reduces the effectiveness of the liners (also see Sect. 3.5.3.2).

Theoretical studies of nonlinear combustion

instability relevant to this discussion are scarce. Different studies conducted by Mitchell,[488] for longitudinal instability, and Zinn,[771] for three-dimensional instability, present results which indicate the Mach number dependence of the nonlinear pressure wave forms at various locations in the rocket combustor. While discussing nonlinear effects it is important to mention that Priem's[563] nonlinear model, which has been studied extensively by various investigators,[46,359] is not capable of predicting the $\mathfrak{M}_c$ dependence of the stability limits except through an injection density effect.[563]

There are few systematic experimental studies whose results are relevant to this discussion. Reardon and Smith[585] report that a decrease in the nozzle contraction ratio resulted in an increase in the frequency of occurrences of instabilities with respect to the mixed acoustic modes. This observation is in agreement with the predictions of Refs. 567 and 772. Using a temperature-ramping technique with a hydrogen-oxygen engine Bloomer et al.[107] conducted a set of experiments specifically designed at checking the effects of changing the nozzle contraction ratio. In one set of experiments (see Fig. 7.2.2a) the mixture ratio, chamber pressure and throat area were held constant and the contraction ratio was decreased as a result of introducing full-length spools in the combustion chamber. The experimental results indicate no change in the stability characteristics. A possible explanation is that the insertion of the spools also resulted in an increase in the chamber L/D. According to the results presented in Refs. 567 and 772 increasing L/D is destabilizing and decreasing the contraction ratio is stabilizing; it is quite possible that in these experiments these opposing tendencies exactly cancelled one another. In another set of experiments (see Fig. 7.2.2b) the combustion-chamber area was held constant while the nozzle throat area was decreased, thus decreasing the Mach number at the nozzle entrance. The results of this experiment indicate that such a decrease is destabilizing with respect to the first tangential mode. Based on these experimental results Bloomer suggests that increasing the throat area may be used as a means of improving the stability of marginally stable oxygen/hydrogen engines. A theoretical study,[259] which is relevant to Bloomer's

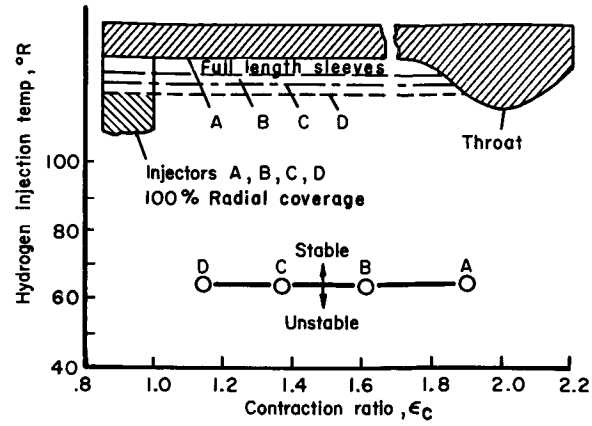

FIGURE 7.2.2a.—Effect of contraction ratio. Hydrogen-oxygen propellants; $p_c = 300$ psi; O/F = 5.0.

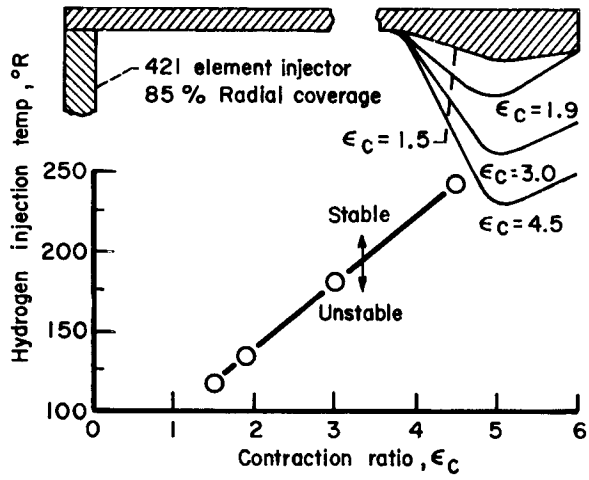

FIGURE 7.2.2b.—Effect of contraction ratio. Hydrogen-oxygen propellants; $p_c = 300$ psi; O/F = 5.0.

experiments, shows that $\mathfrak{M}_c$ effects are not needed to explain the results.

The above discussion concentrated on the more detrimental and complex case of high-frequency combustion instability. The case of low-frequency instability (i.e. "chugging") is better understood; and available analyses[179,673] and experiments[345] indicate that one method to suppress the low-frequency oscillations is simply to increase L*. Such a change can be accomplished by simply increasing the nozzle contraction ratio (i.e. decrease $\mathfrak{M}_c$). It may be of interest to note that the same "remedy" is recommended for the

elimination of low-frequency combustion instability in solid-propellant rocket motors.

In conclusion it can be said that more theoretical and experimental research must be conducted before the dependence of high-frequency instability on $\mathfrak{M}_c$ is properly understood. Until such information becomes available the designer, who for some reason contemplates changing the contraction ratio, must keep in mind that such a change may have adverse effect on the stability of some modes but a favorable effect on the stability of others.

7.2.3 Injection Density*

Injection density is an engine design parameter which is sometimes referred to in connection with combustion instability. It is defined as the mass flux of propellant (usually total of oxidizer and fuel) which is injected into the chamber per unit area. Injection density can be a quite ambiguous term since in no case is the propellant injected exactly uniformly across the injector face. In many cases the propellant may be injected in two or more axial locations in the chamber, or the chamber may not be of uniform cross sectional area. Generally, however, the injection density quoted for an engine will be determined from the total propellant flow rate, and a nominal cross sectional area. In other cases the local injection density for a specific location may be of interest. In the short discussion that follows some of the problems in precisely relating injection density to stability are presented.

Since injection density cannot be varied independently, it is difficult to show conclusively its effect on combustion stability. For instance, raising the injection density with a fixed chamber contraction ratio necessarily increases the chamber pressure and simultaneously increases injection velocities of both propellants. The contraction ratio may be lowered to retain the same chamber pressure at the higher injection density, and the number or size of the injection holes may be increased to retain the same injection velocity. Many other combinations exist, such as increasing the number of injection holes of only one propellant and changing the mixture ratio; changing the density of the injected propellant, etc. Unfortunately, each of these changes is known to influence combustion instability.

A little more quantitative insight into the effect of injection density upon combustion instability may be seen from the dimensionless parameters used in the Priem-type combustion instability analysis. In this theory two of the most important parameters are ΔV and $\mathfrak{L}$. The former is usually found to be the most important; greater relative velocity between the two phases (gas and liquid) being the more stable. These variables are discussed in greater detail in Sect. 4.3. The other stability factor $\mathfrak{L}$ was originally written as

$$\mathfrak{L} = \frac{r_c M_x}{\epsilon_c}$$

where M_x is the steady-state burning rate in fraction of total propellants per inch, r_c is the chamber radius, and ϵ_c is the contraction ratio.

The results of the Priem analysis showed that for a constant ΔV, there was minimum stability at some value of $\mathfrak{L}$ close to unity. This proved an unfortunate set of parameters. It led one to believe, for instance, that if the contraction ratio was low and the radius of the engine large, then stability would be possible by increasing the burning rate, M_x. In several cases this was tried, and indeed effective stabilization was achieved, for the lowest acoustic mode, but the engine became unstable at a higher mode.

Another way of writing $\mathfrak{L}$ is

$$\mathfrak{L} = \frac{M_x \hat{\mu} t_w}{2\pi f(\gamma) \bar{\rho}}$$

where

- $\hat{\mu}$ is the injection density in pounds of propellant per unit area, per unit time
- t_w is the wave time (defined by $2\pi r_c/a$) where a is the speed of sound
- $f(\gamma)$ is a function of the ratio of specific heats, and
- $\bar{\rho}$ is the steady-state gas density in the chamber at the location of interest.

From this representation of $\mathfrak{L}$, it is seen that the wave time is an important parameter. To achieve stability (see Sect. 6.4) it is always necessary to reduce the value of $\mathfrak{L}$. Conceivably, one may operate in a metastable region between modes,

* T. A. Coultas, Author.

but that appears to be risky since any perturbation of burning rate or other variable will make the engine more unstable in one mode or the other, depending upon the direction of the perturbation (Fig. 6.3.4a illustrates the multiple mode situation).

It should be kept firmly in mind that the values of M_x, ΔV, chamber pressure, injection density, and contraction ratio are not independent of each other. In a limited range, however, where M_x and ΔV may be considered constant, say at a high contraction ratio and at a position near the injector face where burning rates are primarily hydraulically controlled (as opposed to gas dynamically), maximum stability would come at minimum injection density. Thus, if chamber pressure and thrust are fixed, one would like to have a maximum contraction ratio (note that although t_w varies directly with the size of the chamber, $\hat{\mu}$ varies inversely with the square of the chamber size). Such an apparent anomaly was experimentally observed by Abbe et al.[46] Under these rather restrictive conditions, high injection densities would be expected to be more prone to instabilities than a lower injection density.

Injection density is, however, often used as a rule of thumb to estimate the difficulty of curing resonant combustion. For instance, the F-1 rocket engine had an extraordinarily high injection density of approximately 5 lb/in.^{2}-sec. Experience proved that it was very difficult to make this engine dynamically stable. On the other hand, the Atlas (injection density of approximately 1.5 lb/in.^{2}-sec) was easily stabilized. Space engines, such as the LM ascent or LM descent engine, have injection densities on the order of 0.5 lb/in.^{2}-sec and their stability problems have not been as severe.

One explanation of this *apparent* relationship between injection density and stability is that with the higher injection density, more unburned propellants are present when a chamber is perturbed (as with a rating device). Thus, a larger amount of propellant is available for combustion augmentation of the initial disturbance. The resultant overpressure caused by the perturbation may be much larger with the high injection density (pressures of several thousand psi have been recorded). However, the ratio of overpressure to steady-state chamber pressure is obviously not a direct function of injection density.

Another use of injection density as a stability parameter is in assessing, a priori, the probable damage which may result from an instability. Damage is often greater and occurs much more rapidly in an engine with a high injection density should resonant combustion be present. In fact, in large chambers without baffles, extensive damage to both injector and chamber will often result even if a Rough Combustion Monitor device begins to shut down the engine after 100 milliseconds of instability. On the other hand, with a low injection-density injector resonant combustion is less likely to cause significant damage. Thus, the hazard of combustion instability would appear to be less in engines with low injection density. Again, however, it is not obvious that the resultant damage is not simply caused by the already higher steady-state heat fluxes which result from the higher chamber pressure and low chamber contraction ratio associated with high injection density.

7.2.4 Axial Energy Release*

The importance of axial energy release to the designer results from the often direct relationship of this parameter and the ability of an engine to initiate or sustain combustion instability. The subject of axial energy release has been discussed in a number of other sections, e.g., in Sect. 3.5.2 in connection with nonlinear wave motion, in Chapter 4 as an input to the theories of resonant combustion, and later in this chapter with regard to variation with injection type (also discussed in Sect. 3.5.2). The emphasis here is on the role this parameter plays in controlling resonant combustion, and on a method which makes possible the exact determination of the axial energy release for a given test engine.

A knowledge of the axial combustion rates is of great significance since one approach to stable motor operation, short of resorting to damping devices, is to tailor the combustion axially to the chamber involved.[318] For example, consider the case of longitudinal mode instability. If combustion of the propellants is essentially completed

* F. V. Bracco and D. T. Harrje, Authors.

in the first few inches of the chamber, the ability of the first pressure antinode region (associated with the longitudinal oscillations) to couple with the combustion is enhanced since the maximum pressure oscillations occur close to the point of maximum combustion. This improves the chances for instability to occur.

On the other hand, if the combustion is spread over the available chamber length far less combustion is available at the favorable coupling locations, thus favoring stable operation. Although the axial variation of pressure amplitude is different for sinusoidal and shock-type longitudinal waves,[35] both have pressure antinodes at the injector end and hence would exhibit similar stability trends.

Perhaps even more important to the designer is the fact that transverse resonant combustion also produces the maximum unsteady pressure amplitudes at the injector end.[151,191] In general, this amplitude is found to decay rapidly (based upon pressure measurements taken further downstream). Therefore, as in the longitudinal case, the axial energy release pattern has been proven to be important.

To appreciate the unsteady environment existing in liquid propellant rocket chambers it is necessary that the steady state be well understood. Available steady-state models (see Chapter 2 and discussion in Sect. 2.1.8) have contributed toward the understanding of the complexities of the rocket environment and the axial combustion distribution, however, certain anomalies continue to exist. To attack the problem differently, in a way that did not require a prior knowledge of the dominant mechanism, the so-called "direct method" was used.[114] In this approach experimental observations are used to characterize the individual combustor environment and only then are the models of combustion (e.g., the droplet burning models) compared for agreement. This allows the steady-state parameters to be well-defined; thus more detail can be incorporated into the final model. Also important is the removal of the requirement for extensive assumptions. In the more common approach, a model is first postulated, the mathematical solution is obtained and comparisons are made with the experimental data.

The "direct method" was applied to the LOX/ethanol system and there it was found that all the engine parameters could be calculated if the axial distribution of static pressure was measured* and the assumptions of chemical equilibrium of the reaction products and of no recirculation were made.[114] Figures 7.2.4a through 7.2.4f show the axial profiles for a specific engine characterized by the following parameters: LOX/ethanol mixture ratio (O/F) = 2.33; chamber pressure (injector end) = 295 psia; a 4×4 grid-type injector design was used consisting of like-on-like doublets with orifice diameters of 0.059 in. and an impingement angle of 55°. The measured axial static pressure profile is given in Fig. 7.2.4a. The calculated gas velocity (u), gas density (ρ), and gas temperature (T) are given in Figs. 7.2.4b-d. Finally, the fraction of liquid fuel not yet burned at a given distance from the injector ($A_c\rho_L u_L/\dot{m}_{iF}$) is given in Fig. 7.2.4e.

Complete combustion values were used as reference values for u, ρ and T [namely, u_f = 17,080 cm/sec (560 ft/sec); $\rho_f = 1.83210^{-3}$ g/cm^3 (0.114 lb/ft^3); T_f = 3290° K (5922° R)]. The local liquid fuel flow rate ($\dot{m}_F$) is nondimensionalized by the injection fuel flow rate ($\dot{m}_{iF}$). Notice that the local derivative of ($\dot{m}_F/\dot{m}_{iF}$) gives the local rate at which the liquid fuel is burned. Actually Figs. 7.2.4b-e give ranges within which the values of the above parameters are found at any given distance from the injector. Further resolution would not be particularly rewarding due to the natural scattering of the measurements and the natural randomness of the processes occurring in the combustion chamber. To check the validity of this approach the particle velocity was measured at 5″ and 20″ using streak photography. The measured values, reported in Fig. 7.2.4b with their scattering ranges are seen to agree with those calculated.

It should be emphasized that even though no drop burning process was postulated, the axial distribution of the overall liquid burning rate was determined (Fig. 7.2.4e). The most important of the results is the finding of significant axial variations of the combustion parameters as

* Experimentally one can determine, for example, the velocity of the gaseous products (see Sect. 9.4.1 on Streak Photography) or the static pressure (this can be measured by high pressure manometers[190] or by sensitive pressure gauges[544]).

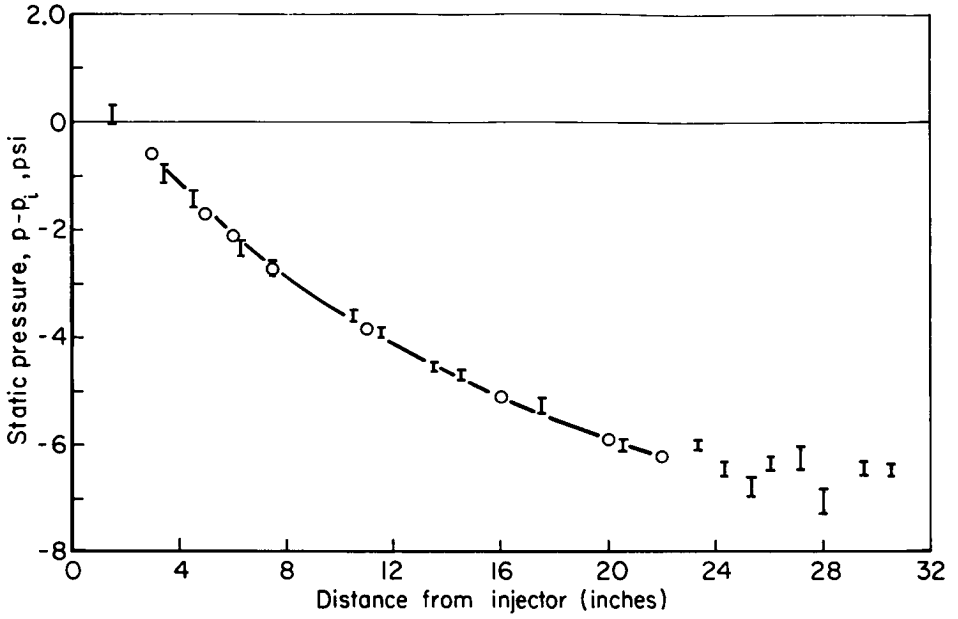

FIGURE 7.2.4a.—Measured static pressure loss versus distance from injector.

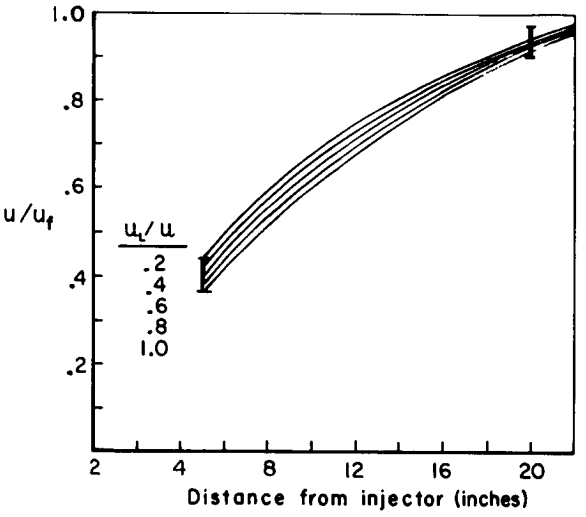

FIGURE 7.2.4b.—Dimensionless gas velocity versus distance from injector.

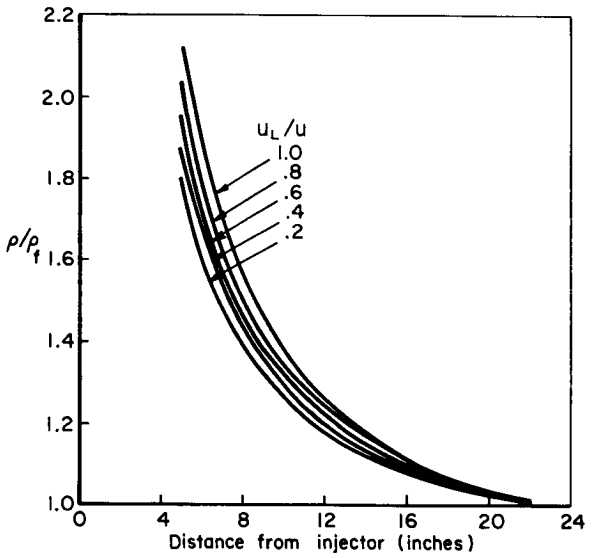

FIGURE 7.2.4c.—Dimensionless gas density versus distance from injector.

demonstrated by Figs. 7.2.4c and d, namely, density is *greatly increased* near the injector end and temperature at that location is *less than* $\frac{1}{2}$ of the downstream temperature.† Independent c* measurements indicate a temperature profile close to that given in Fig. 7.2.4d. The same temperature trend was also verified by measuring amplitudes and velocities of shock waves moving toward the injector. Thus the assumption of no recirculation, which has led to the calculation of

† The nonuniformities noted here were for oxidizer-rich combustion. More recent experiments at maximum c* mixture ratio showed somewhat reduced nonuniformities.

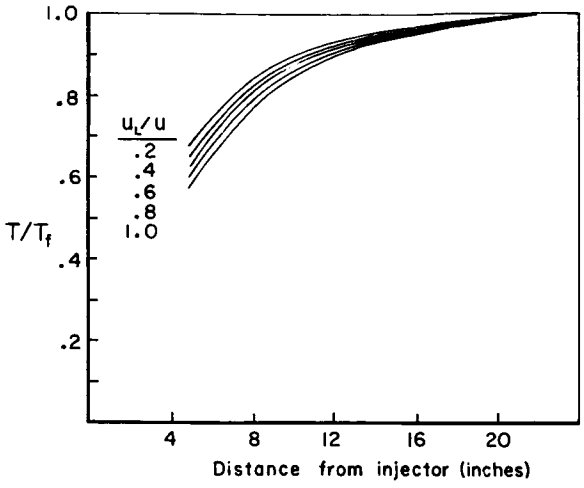

FIGURE 7.2.4d.—Dimensionless gas temperature versus distance from injector.

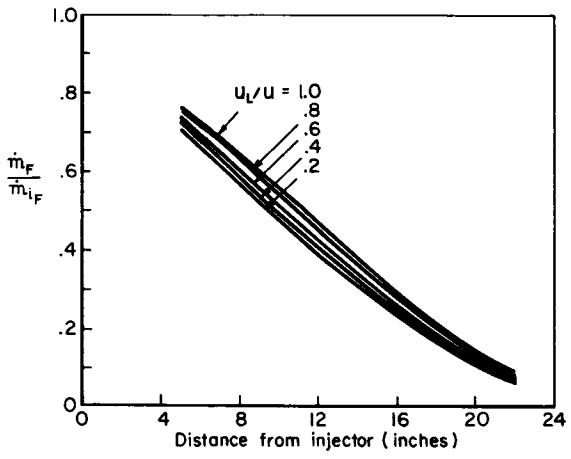

FIGURE 7.2.4e.—Percent of liquid fuel versus distance from injector.

axial nonuniformities, was a good one in the engine studied. It could be speculated that when the distance between the injector elements is small in comparison with the combustion length, recirculation effects are limited. This is indeed the case for the injector tested in this study and for most of the injectors of practical use (injectors with many elements, closely spaced).

Figs. 7.2.4b-e show no solutions within the region extending to 5″, where ethanol drops are formed and liquid oxygen is probably still present. The nonuniformities of the region tend to make

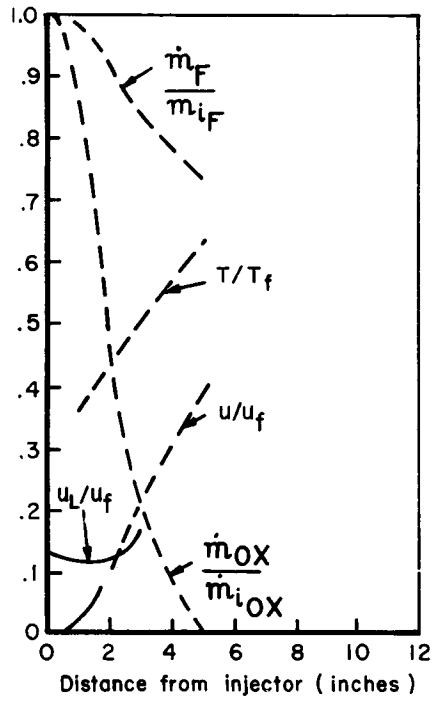

FIGURE 7.2.4f.—Estimates of the combustion parameters in the "near region."

one-dimensional calculations qualitative. Using the measurements of temperature and static pressure, an approximate description of this region was obtained and is given in Fig. 7.2.4f. From the standpoint of stability this near region is of great interest. When shock waves are sent from the nozzle-end toward the injector of the LOX/ethanol rocket[115,193] little amplitude growth is recorded until the near region is reached. However, in this zone the amplitude more than doubles.

Another interesting result is related to the frequency of shock-type longitudinal instability. Under the assumption of uniform chamber temperature, one would expect the frequency of the oscillating shock to be higher than the acoustic frequency since a shock wave moves faster than the speed of sound (e.g., for $p_2/p_1 = 1.5$ the shock velocity would be about 1.20 times the speed of sound) and gas velocity effects cancel out over a cycle. However, hot firings show that the frequency of the oscillating shock is close to the acoustic frequency. This contradiction disappears if the usual assumption of uniform chamber

properties is removed. The acoustic frequency calculated with the axially nonuniform temperature profile of Fig. 7.2.4d is indeed some 20% smaller than that calculated with the assumption that the temperature is axially uniform.[114a] In other words, the longitudinal shock instability frequency as calculated with the speed of sound based upon the temperature for completed combustion is generally accurate because of the cancelling of the errors from two inaccurate assumptions.

In the case of transverse instability, the maximum amplitude is found where the speed of sound would be depressed as indicated from T/T_f in Fig. 7.2.4f. Provided the amplitudes are not so great as to shatter the liquid streams and droplets near the injector end, thus intensifying the local combustion (increasing the speed of sound), frequency depression* should be anticipated and indeed has been repeatedly observed. As previously discussed, axial tailoring of the combustion can reduce the energy available near the injector face. Techniques that have been used to control resonant combustion include increasing the fuel orifice diameter and/or decreasing the impingement angle in like-impinging fuel doublets (to increase the fuel droplet sizes), increasing the oxidizer velocity (to reduce the oxidizer concentration near the injector, see Fig. 7.4.3i), and altering the relative velocities between adjacent propellant streams (see discussion in Sect. 1.2.2.2). Naturally as the combustion intensity is reduced at the injector end care must be taken so as not to lose performance because the combustion is too stretched out.

In summary, it has been found that the axial combustion distribution directly influences combustion stability for both longitudinal and transverse waves. Examination of the axial combustion profile reveals major variations in the parameters (e.g., temperature and density) which influence the frequency of the instability as well as the coupling between pressure, velocity and combustion. The combustion region close to the injector face, where the early reactions are taking place, are particularly sensitive to pressure and velocity disturbances. Axial tailoring of the combustion can reduce this sensitivity and the related coupling.

* Other factors, such as injector-end impedance caused by baffles, can also be responsible for transverse frequency depression (as discussed in Sect. 3.5.3.3).

7.2.5 Transverse Energy Release Distribution*

The control of the spatial distribution of the transverse energy release has been utilized in some cases[13,584] to provide a useful tool to designers so that they might achieve more stable operation of liquid rocket engines. In essence the technique involves moving the energy release location to a region considered to be less "sensitive" to the initiation and maintenance of resonant combustion. For the transverse modes, the most important variations in the oscillating quantities obviously occur across the face of the injector rather than perpendicular to it.[494] Therefore, the problem of improving the stability involves defining the injector areas of pressure and velocity "sensitivity" for the different transverse modes, and adjusting the energy release pattern in such a way that the rocket engine remains stable.

A number of theoretical† and experimental‡ studies are available for indicating the sensitive injector areas associated with a particular modal pattern. However, the variety of modes possible,[494] and the uncertainty as to the mechanism responsible for the sensitivity,[172,583,726,739] complicate the problem. Thus there may be some question with regard to the precise energy distribution to be employed in a given rocket engine.

Based upon the analytical work (as described in Chapter 4) it may be stated that two physical parameters are important in maintaining resonant combustion. They are pressure and particle velocity. The discussion that follows will center about these quantities.

The location of the energy release in the transverse plane can be tailored by altering the injection system of a liquid rocket engine.* This results in a change of the local injection density as compared to the average injection density for the entire injector. Some typical injection characteristics of six different radial profiles are

* J. R. Osborn, Author.

† References include 172, 579, 583, 726 and 739.

‡ Experimental references include 13, 216, 527, 573, and 584.

* References include 50, 147, 153, 225, 226, 611 and 620.

presented in Fig. 7.2.5a. In that figure the length of the arrow represents the quantity of locally injected reactants, e.g., Profile I is uniform, whereas Profile IV represents concentrated injection at the center of the injector. It is assumed that the energy release is directly related to the mass flux, hence, the energy release of Profile I will be uniform across the face of the injector, and Profile IV will be concentrated near the center of the combustion chamber.

According to Rayleigh,[579] the energy release should be located at a pressure nodal point for the combustion system to operate in the most stable manner. The results of the experimental work[216,527,573] conducted with a combustion system having the injection distribution as shown in Fig. 7.2.5a were found to agree with Rayleigh's criterion. An analysis of the regions of mass flux distribution with the unsteady pressure distributions associated with two transverse modes indicates the relative stability for each injection array. That is, Region A corresponds to the location of the pressure antinodes for oscillations of the first radial mode, and energy addition in Region A would tend to produce oscillations in that mode. Both the radial and the tangential modes have pressure antinodes in Region C and hence energy released at that location would be expected to sustain radial and/or tangential oscillations. In contrast, energy released in Region B would not be at the pressure antinodal location of either type of oscillation, and therefore would be predicted to be rather ineffectual in sustaining those modes, thus resulting in a stable system.

The results of an experimental study using the injection profiles just described are listed in Table 7.2.5a. The tests employed a 7-inch-diameter, 6-inch-long chamber into which premixed gaseous propellants, ethylene and air, were injected through showerhead orifices. Interpreting the results of Table 7.2.5a (also see Fig. 7.2.5a), Profile I has an equal amount of energy release per unit area in each of the three regions; A, B, and C, and will supply equal amounts of driving energy to the tangential and radial modes. The tangential mode is predominant although the amplitude is somewhat low.

Profile II yields stable operation even though energy is released in locations well suited for sustaining transverse mode oscillations. That is, Region A receives the largest amount of the total energy released, and this energy acts to drive the radial mode of oscillation. The considerably

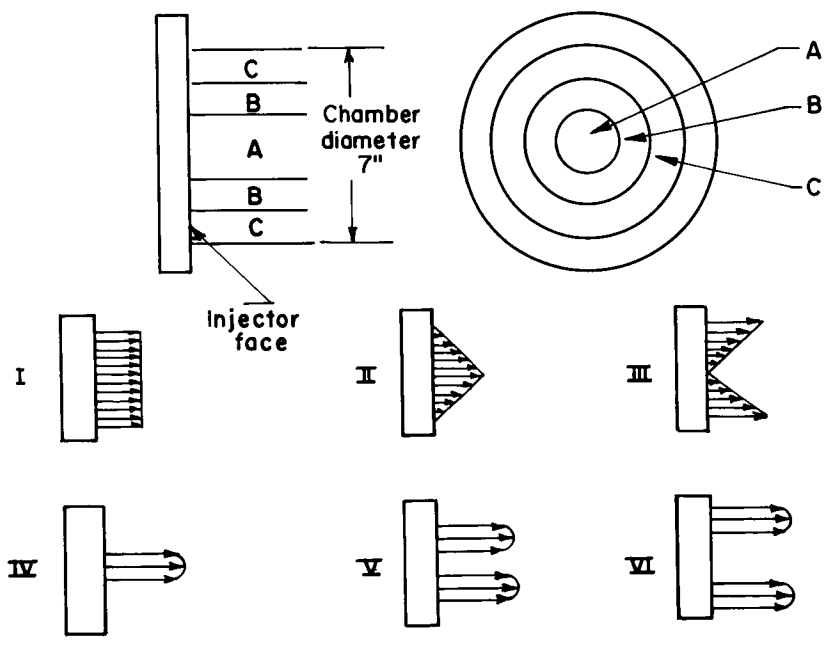

FIGURE 7.2.5a.—Injection radial profile comparison.

TABLE 7.2.5a.—GAS ROCKET TEST HISTORY WITH VARIOUS INJECTION PROFILES

[Instabilities initiated spontaneously and linearly; mean chamber pressure, 150 psia; combustion chamber diameter, 7 in.; combustion chamber length, 6 in.]

Profile	Amplitude, psi	Mode
I	7	1st tangential
II	0	Stable
III	11	1st tangential
IV	13	1st radial
V	0	Stable
VI	40	1st tangential

smaller amount of energy released in Region C tends to sustain the tangential mode. If the radial mode were predominant for this chamber one would have anticipated resonant combustion in that mode. When the energy distribution is reversed (i.e., large energy release in Region C, small amounts in Region A), as shown in Profile III, reasonably strong tangential mode oscillations result. Comparisons between the Profile II and III results indicate that the first tangential mode (the lowest transverse mode) is apparently preferred.

Profiles IV, V, and VI (again referring to Fig. 7.2.5a) have one ring of injection holes, located at diameters of 2, 4, and 6 inches, respectively, thereby corresponding to injection solely in Regions A, B, and C. Profile IV (injection near the center of the injector) produces instability in the radial mode, whereas Profile V (injection near the mid-radius) achieves stable operation, and Profile VI (injection near the chamber wall) results in *very strong* tangential oscillations.

In summary, Profiles IV and VI, which each contribute energy to only one mode, produce the strongest oscillations. Profiles I and III share available energy between two modes and hence the oscillations are weaker. However, Profile III exhibits stronger oscillations than Profile I because the energy release pattern in that case more heavily favors the preferred tangential mode. In contrast, Profiles II and V produce stable operation. The reasons for this behavior are not the same in both cases. Profile V is stable because its energy is released in a location that does not readily excite either tangential or radial modes. Profile II, however, does not provide sufficient energy release in the preferred location for the radial mode to initiate resonant combustion at that higher mode (frequency is 2.1 times the first tangential mode).

More recent experimental work[584,13] using a liquid rocket engine has further indicated the importance of pressure effects and mass flux. The injection density distribution variations

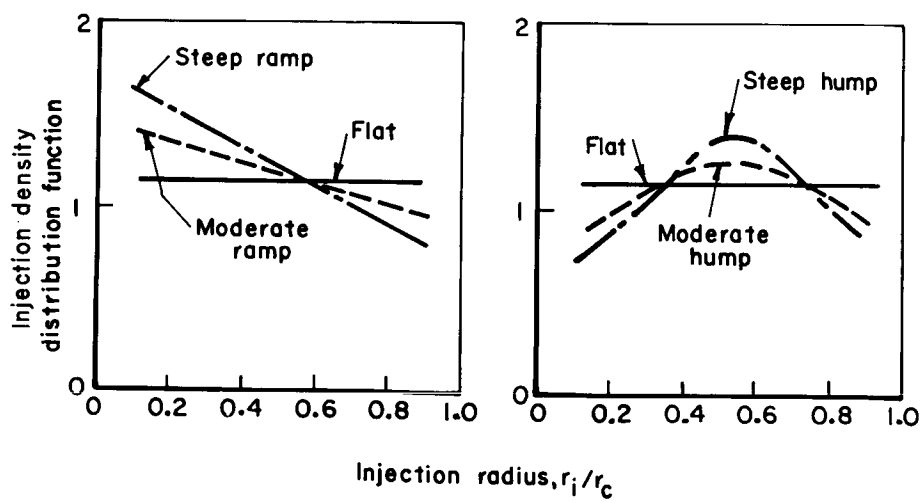

FIGURE 7.2.5b.—GEMSIP injection distributions.

utilized in that experimental program are shown in Fig. 7.2.5b. They were achieved by adjusting the number of elements in each row, while keeping the orifice sizes and the total number of elements very nearly constant. The flat distribution was designed for a constant injection density (flow rate per unit injector face area) across the injector face. The ramp distributions were designed to give a linear variation of injection density, with the maximum at the smallest injection radius. The hump patterns were designed to provide the maximum injection density at the mid-radius location. Two variations of each ramp and hump distribution were tested with the results shown in Table 7.2.5b. Agreement with Table 7.2.5a data is evident; the steep hump (Profile V is similar) was stable with respect to bomb-induced perturbations. Again, the injection distribution with the least energy at the pressure antinode was shown to be the most stable. Reardon[584] attempted to correlate stability with both pressure and velocity coefficients derived using the time lag concept. It was concluded that a pressure coefficient would correlate the results, but that the radial velocity coefficient would not.

It appears that the control of the transverse energy release distribution via local injection density variations can be utilized to obtain stable operation of liquid rocket engines. There are limitations, however, in that detrimental performance and heat transfer changes may take place (see Sects. 2.5 and 8.5.3) thereby restricting the selection of local injection density based on stability alone.

7.2.6 Boundary Effects*

7.2.6.1 The boundary region.—The boundary regions include all regions adjacent to the combustor inner surfaces—the chamber and nozzle walls, the injector face, and the baffle surfaces if the engine is so equipped. The concern for good engine durability leads to injector designs that control the propellant distribution near the boundaries in order to decrease heat flow to those

* R. M. Clayton, Author.

TABLE 7.2.5b.—RESULTS OF GEMSIP INJECTION DISTRIBUTION TESTING

Distribution	Pulse type[a]	Stability	Max amplitude, psi	Recovery time (if stable), msec	Predominant frequency (if unstable), cps	Predominant mode[b]
Steep hump	14 ND	Stable	82	4	...	...
	14 ND	Stable	222	5	...	...
	100 ND	Stable	504	10	...	...
	220 ND	Stable	769	10	...	...
Moderate hump	100 ND	Stable	598	...	...	...
	100 ND	Unstable	[c]518	...	3800	1R
	220 ND	Stable	1614	9	...	...
	None	Unstable	70	...	[d]1200	1T
Flat	100 ND	Stable	667	15	...	...
	220 ND	Unstable	562	...	3700	1R
Moderate ramp	100 ND	Unstable	595	...	3800	1R
Steel ramp	40 T	Stable	155	7	...	...
	80 T	Stable	352	7	...	...
	100 ND	Stable	661	10	...	...
	220	Unstable	795	...	3600	1R

[a] T, tangential pulse, fired during the starting transient; ND, nondirectional bomb, fired at steady state; number indicates charge size in grains of powder or explosive.

[b] R, 1st radial mode; 1T, 1st tangential.

[c] Low amplitude 1T oscillations were present at the time the bomb was fired.

[d] Normal frequency of the 1T mode (in an unbaffled chamber) is 1900 cps.

surfaces.[677] Regardless of how such control is achieved (by film, barrier, transpiration, or combined cooling techniques), the combustion properties near the boundary influence the engine's performance[147] and its high frequency combustion stability.

As discussed in Sect. 7.2.5, the effect of transversely nonuniform injection distribution on incipient tangential modes has been assessed for both linear and nonlinear perturbations, with the result that decreasing the unreacted mass flux in the outer radius of the chamber cross section has a stabilizing influence against those modes of nonsteady combustion. But just how significant is the very outer environment—the wall boundary region?

There are no published analyses emphasizing this aspect of the stability problem, although it is established practice for engine developers to vary the placement and flow of injection elements in the proximity of wall and baffle surfaces. Significant improvements in combustion stability have been observed by these trial and error methods, but "fixes" devised for one engine design rarely produce the same results for another. Thus, most of the results to date are from rating procedures (Chapter 10) performed on injection arrangements used in operational designs and thus fail to provide a well-defined insight into the actual importance of the near-wall environment on stability.

Recently, experiments were conducted investigating the influence of wall boundary effects on fully-developed, spinning tangential waves.[148,154] The resonance and its initiation was of a highly nonlinear nature involving either nondirectional bombs or the spontaneous "popping" phenomenon (Sect. 7.6). Two results will be discussed: (1) the effect of the boundary flow injection on the wave characteristics of an 18-inch engine,[148] and (2) some effects on the wave properties for an 11-inch engine having a nonuniform injection distribution in the circumferential direction.[154]

The injector design (Fig. 7.2.6a) used to obtain the first result was based on a concept that flow from each concentric row of elements would feed proportionately sized annular areas of the chamber. Therefore, deletion of boundary flow was considered to reduce the local flux for the boundary annulus ($\sim\frac{1}{2}$ in. wide) to zero while retaining a constant flux for the main flow; although it was realized that normal spray divergence from the main elements produces overlap into the boundary annulus and that separation effects in the main flow sprays[147] further modify the actual near-wall distribution.

Typical pressure records obtained for two measurement locations near the chamber corner (i.e., in the proximity of the chamber-wall-to-injector-face junction) are compared for three configurations of this injector in Fig. 7.2.6b. These two measurement locations are illustrated because the most severe transients for the rotating mode are found in this region.[152] The pressure measurements were made using ablatively-cooled, flush-mounted Kistler instrumentation and high response tape recording techniques described in Ref. 151.

For the full injector, the tangentially traveling wave exhibited a shock-like frontal structure, having over an 800 psi pressure rise above the base pressure of 70 psig and a period of 690 μsec for 360° of rotation. With the boundary flow deleted both the amplitude and the wave sharpness decreased markedly, and a somewhat greater period (decreased propagation velocity) was obtained. On the other hand, with main flow deleted (nozzle barely choked) the boundary flow itself sustained a sharp, higher velocity wave of nearly the same amplitude as for main flow only. It was also noted that no preferential spin direction was observed, apparently as a result of the axially symmetric propellant distribution.

This engine exhibited a popping phenomenon under certain conditions and was dynamically unstable to these self-generated pressure pulses as well as to bomb pulses when the injector was not equipped with baffles. Ultimately it was determined that the popping was associated with unsteady impingement processes in the system.[149,618]

The second set of experiments was conducted using an 11-inch diameter engine producing 20,000 lbf thrust for a nominal 300 psia chamber pressure with N_2O_4 and A-50 propellants. The injector had no provision for separately controlled boundary flow conditions, but comprised an arrangement of identical unlike-impinging doublet elements producing a nonuniform propellant distribution near the wall. The distribution

(a)

Parameter	Main		Boundary		Overall	
	F	O	F	O	F	O
Flow rate, lbm/s	22.98	48.48	3.48	4.44	26.46	52.92
Injector Δp, psi (manifold to chamber)	129	120	108	96	—	—
Injection velocity, ft/s	86	58	92	68	—	—
Mixture ratio	2.11 ✱		1.27 ✱		2.00	
Fraction of total flow	0.90		0.10		1.00	
Number of injector elements and dia., in.	84 0.101	0.142	24 0.073	0.073	108 —	—

Conditions: A_t = 127.7 in.^{2} p_c = 100 psia
ϵ_e = 2.95 $F_{exp} \cong$ 14,700 lbf
ϵ_c = 2.00

✱ Satisfies uniform mixing criterion (Ref. 613)
N_2O_4 / A-50 propellants

(b)

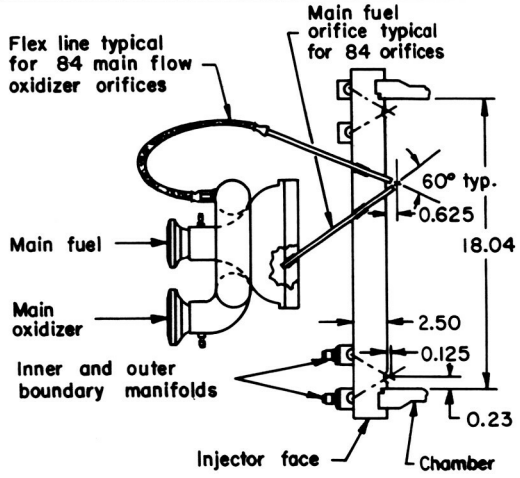

(c)

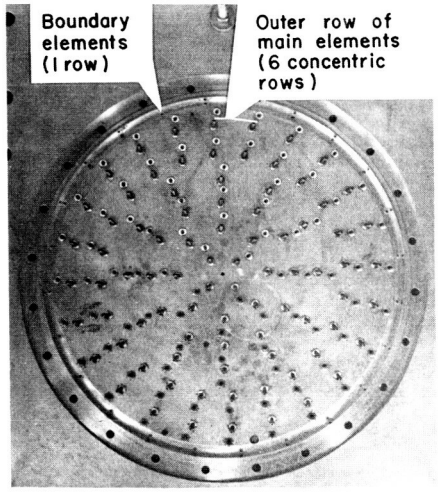

(a) Design conditions.
(b) Design geometry.
(c) Face photograph.

FIGURE 7.2.6a.—Basic design of JPL 18-inch-diameter research injector.

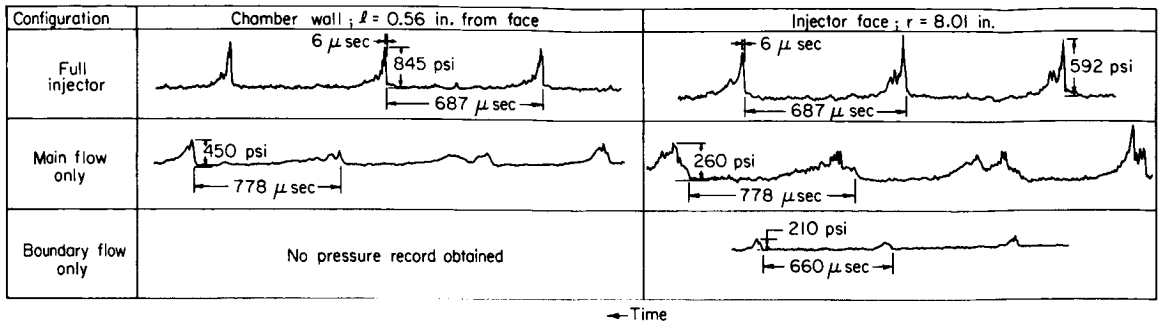

FIGURE 7.2.6b.—Typical pressure records for near the chamber corner for various near-wall propellant distributions. JPL 18-inch-diameter cylindrical engine with N_2O_4 and A-50.

at a plane 2.13 inches from the impingement plane is shown in Fig. 7.2.6c.

Two dominant characteristics were observed for this combustor when the wave was initiated by a nondirectional 13.5 grain bomb placed near the wall at various circumferential locations with respect to the injector. These characteristics are summarized in Fig. 7.2.6c where they are compared to the assumed injected mass distribution. This comparison shows that:

1. The regions exhibiting maximum local wave velocity (shown as the ratio of local to average wave velocity V_w/V_{wm}) appear where propellant impingement on the wall is most probable and where wave motion is nearly "broadside" to the element spray patterns.
2. The velocity profiles for the respective directions of motion are nearly mirror images of each other.
3. The direction of rotation coincides with the direction from the bomb to the nearest high-velocity region.

Reardon et al.[583] have investigated transverse gas displacement effects on linear transverse mode stability, but the connection between their results concerning spray displacement and the above is not clear. It is reasonable to expect that the size of the orifice elements used here (0.173 inch diameter) yields significant stream separation effects so that the circumferential spray distribution near the walls would be nominally oxidizer-rich from 0° to 180° (Fig. 7.2.6c) and vice versa from 180° to 360°, yet no clear dependence of the wave on these gradients is apparent—rather, a dependency on mass distribution at the wall seems to be dominant for the nonlinear wave observed.

Relatively little effort has been expended in this country to applying two-phase detonation theory to the combustion stability problem, particularly with regard to the early reaction region of the boundary environment (i.e., near the chamber corner). Based on linearized acoustical theory, the frequency of the spinning modes discussed has been within 15% of the expected values. But this theory does not explain the nearly instantaneous development of the high amplitude, shock-like nature of popping, bomb pulses, or the fully-developed wave, when propellant is in close proximity with the wall. It is well-known that detonation waves can be supported in fuel droplet fields. More recently the work of Dabora, et al.[209] has demonstrated that a fuel film on the walls of a detonation tube will also support a wave. Thus the application of theory for shock propagation along curved surfaces with the attendant wave interactions with a high energy combustion field is suggested as a supportive mechanism for the destructive spinning modes (also see Sect. 3.4.3.3).

In summary, an attempt has been made to show the trend of the impact of the boundary environment on the combustion stability problem. It was seen that for the traveling tangential wave, the conditions near the wall serve to shape the wave form, and to modify amplitude and period of rotation. The direction of the trend is, in general, contrary to the conditions desirable for minimizing the heat flux to the wall, in that the presence of barrier or film fuel-rich flow sharpens and amplifies

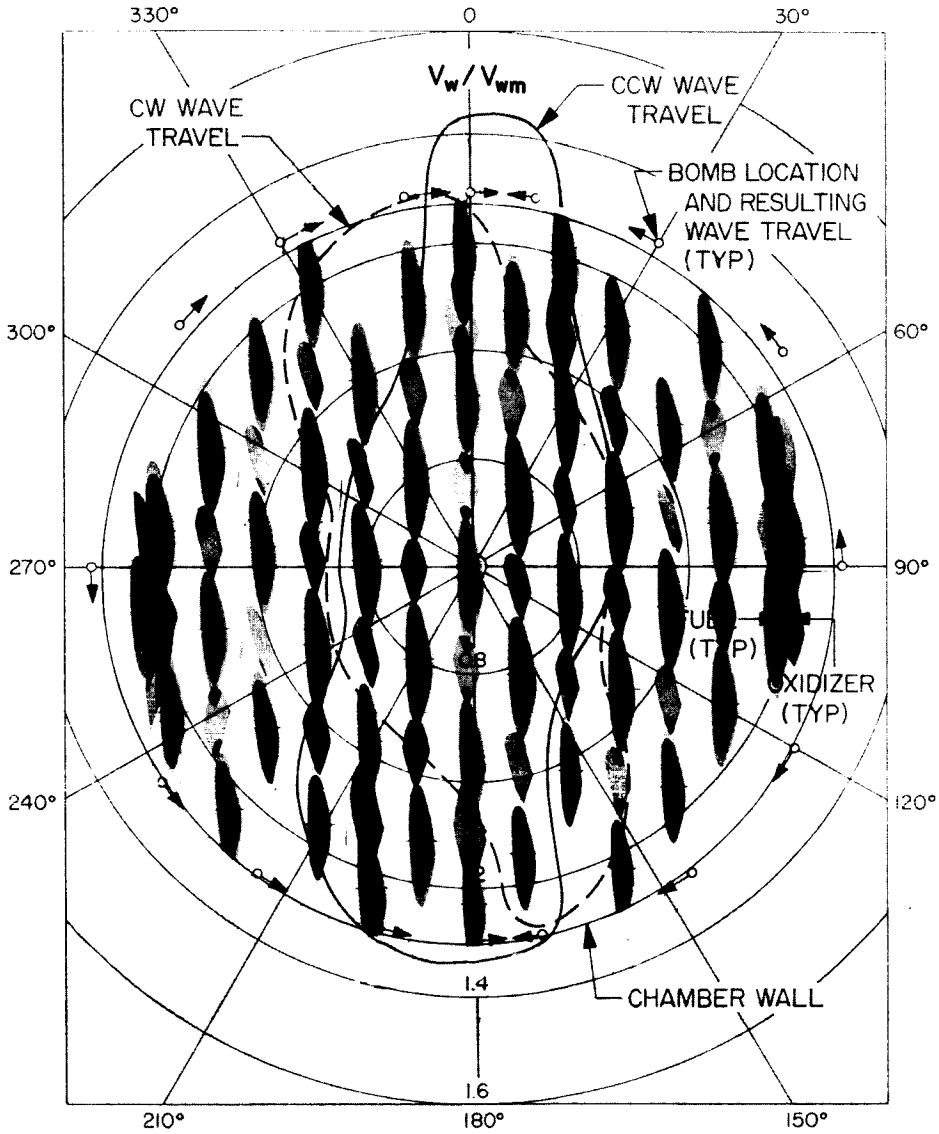

FIGURE 7.2.6c.—Comparison of tangential velocity variation with injection distribution, and of bomb position with sustained wave-travel direction. JPL 11-inch-diameter research engine with N_2O_4 and A-50.

the wave. Wave excitation effects have not been illuminated here, but it is difficult to believe that nonlinear precipitating disturbances would not be affected in the same manner as the fully-developed wave properties.

7.2.6.2 Boundary control factors.—As was shown in Sect. 7.2.6.1, the wall-boundary environment has a significant influence on tangential wave properties. Although the presence of fuel-rich boundary injection apparently degrades engine stability, it is generally necessary to enhance chamber wall endurance. What, then, are some of the major considerations for achieving control of this environment? Two categories of control considerations will be discussed: (1) degraded mass and mixture ratio distribution due to poorly controlled injection properties, and (2) combustion effects which can modify not only the intended primary mixing processes of the boundary

injection, but which may also cause unintentional interactions with the adjacent main flow environment.

For the first category, consider the boundary flow as an annular zone completely isolated from mixing with the main flow environment. In order to achieve the desired uniform mass and mixture ratio, it is geometrically convenient to arrange the boundary injection scheme so as to align the major axis of the resultant spray patterns chordally. For the unlike-impinging doublet element, the arrangement shown in Fig. 7.2.6a is typical. Besides the obvious requirement of proper element spacing and uniform flow rates, the distribution of mixture ratio and mass in the resultant sprays is crucial. For this orientation of the elements, there is little opportunity for secondary mixing of the boundary propellants; hence the initial composition distribution in the sprays will essentially fix the subsequent axial condition.

A design criterion for optimizing the mixture ratio distribution and methods of determining mass distributions for impinging jets (in the absence of stream separation effects) were discussed in Sect. 2.3, and it is evident that poorly-controlled impinging elements (either from fabrication errors or poor hydraulic design) will seriously degrade the attainment of the desired uniform boundary conditions. From a combustion stability viewpoint, the occurrence of the popping phenomenon has been related to leaks, hydraulically unstable orifice flow,[705] and unstable impingement processes.[149,618] Nonuniformly distributed heat transfer and wall compatibility also have been related to nonuniform boundary conditions.[168,620]

The second category of effects which can modify the intended boundary environment involves both stream separation effects and secondary mixing between the boundary and main zones. Analyses and experiments on the separation phenomena[364,416] have indicated that the dominant controlling factors are related to propellant reactivity, element size scale, and stagnation pressure in the interfacial region of impingement. The correlating parameter has been termed contact time and is defined as the ratio of stream diameter to stream velocity. In general, larger contact times increase the separation effect. For the nitrogen tetroxide/hydrazine system, initial propellant temperature is predicted to have a pronounced influence on the onset of separation. Thus, for example, it would be expected that changing propellant temperature could drastically alter the near-wall conditions for a typical barrier-controlled wall environment. Furthermore, engine operation near incipient separation conditions would be predicted to produce sporadic combustion variations. Therefore, a randomly occurring cause of pops is suggested which has effectively the same significance as a hydraulically unstable jet.

If the boundary zone is now allowed to interact with the adjacent main stream zone, it is apparent that the near-wall environment can be further modified. One obvious mechanism which increases such interactions is, again, separation effects which are even more likely to occur for the main elements since they are usually larger than the barrier flow elements. Thus regardless of the separated condition of the barrier, main spray divergence into the boundary zone is an important consideration. A complementary "crosswind" mechanism through which these zone interactions can be produced has been analyzed by Conn et al.[168] and is discussed in Sect. 8.5.3.2.

Both the separation and crosswind (radial wind) mechanisms, insofar as they can be applied to the near-wall environment, have the potential of providing insight to design factors which control the boundary region.

7.3 EFFECT OF PROPELLANT COMBINATION ON STABILITY*

Although the propellant combination for a given engine is normally selected on the basis of specific impulse, heat transfer, cost, and handling considerations, the effects of the physical and chemical properties of the propellants on combustion stability should not be neglected. Unfortunately, systematic investigations of propellant effects have seldom been attempted. There was considerable early emphasis on propellants, but recent efforts have concentrated on the injection pattern. For the most part, available data on propellant effects are difficult to interpret because of the strong influence of the injection pattern, and the interaction of these two effects

* F. H. Reardon, Author.

has not been systematically examined. It is well known that propellant properties are extremely significant in some instances. However, an equal number of cases show no discernible influence of propellant properties.

Propellant combinations are commonly grouped into three classes, according to the temperature range in which they exist in the liquid phase. These classes are

1. cryogenic propellants, which are liquid only at temperatures well below normal ambient temperatures,
2. earth-storable, or simply storable propellants, which are liquids at normal temperatures, and
3. cryogenic-storable combinations, in which one of the propellants is cryogenic, the other storable.

For convenience, the discussion of the effects of propellant combination on combustion stability will be organized around this classification scheme.

In general, physical properties are much more important than chemical properties in liquid propellant rocket combustion stability, consistent with the thin-flame character of droplet burning at the pressures encountered in rocket combustion chambers. Even for gaseous-propellant rockets, Zucrow, Osborn and Bonnell[775] have demonstrated that unless the propellants are premixed, chemical factors are not important. It is reasonable that this result should be generally applicable also to liquid-propellant rockets. However, where the fuel has monopropellant characteristics or where the propellants react strongly in the liquid phase (hypergolic propellants), chemical properties can have a substantial influence on the overall combustion response.

Physical properties that are important in combustion dynamics include the liquid density, viscosity, and surface tension, which, along with gas density and injection velocity, control the drop size distribution (Sect. 2.2). The vapor pressure and heat of vaporization have been shown to be significant properties in nonsteady droplet vaporization. With the recent trend to very high chamber pressure, the critical properties are of growing importance, since burning mechanisms, even in steady state, are different for near-critical and super-critical than those studied extensively at low pressure. It should also be mentioned that the compressibility of the liquid propellants, which influences the injection rate in nonsteady operation, is a property that must be considered not only in low frequency stability, but also in engine systems where the feed rate can couple with the acoustic modes of the combustion chamber.

The most important chemical properties of liquid propellants are those related to liquid-phase reactivity and monopropellant (exothermic) decomposition. It has been demonstrated that rapid reactions between liquid propellants can lead to inefficient mixing and hence to strong mixture ratio gradients in the combustion zone. Decomposition, which is often sensitive to catalytic effects, has also been shown to have a strong influence on the overall burning rate.

The following nomenclature pertains to Sect. 7.3:

$f_{\text{pref.}}$	"Preferred" frequency of unsteady combustion process
τ	Sensitive combustion time lag (Sect. 4.2)
τ_c	Contact time

7.3.1 Cryogenic Propellants

The only cryogenic propellant combination that has been tested extensively, and somewhat systematically, is oxygen hydrogen. Research and development studies have made use of several types of injection and rather wide ranges of operating conditions. Fluorine has been proposed for use with hydrogen for higher steady-state performance, but no useful stability data has been reported. A small amount of information has been obtained for propellant combinations involving a mixture of fluorine and oxygen (FLOX) as oxidizer with various light hydrocarbon fuels, such as methane, ethane, propane, butane, and butene.

In general, the physical properties of the cryogenics are of much greater importance than the chemical properties, since they all have relatively low critical pressures and temperatures, are not hypergolic, and do not act as monopropellants. Fluorine is an exception; its highly reactive nature may lead to some of the combustion characteristics observed with the storable

propellants (see below). However, this expectation remains to be verified experimentally.

7.3.1.1 Oxygen/hydrogen (LOX/LH_2).—Because of its very low critical pressure (188 psia) and temperature (60° R), hydrogen enters the combustion chamber in nearly all cases as a supercritical gas. Hence the combustion response is controlled by oxygen droplets burning in a hydrogen-rich atmosphere.[681] Since the critical pressure of oxygen is only 738 psia, supercritical combustion is common, particularly in launch vehicle applications.

For most liquid propellants, the combustion process exhibits a "preferred frequency" characteristic, that is, under oscillating conditions, the amplitude of the burning rate perturbation reaches a maximum at a characteristic frequency (Sect. 3.4). This frequency is related to the sensitive time lag τ defined by Crocco (Sect. 4.2) by

$$f_{\text{pref.}} = \frac{1}{2\tau}$$

Hefner, Reardon and Smith[333] correlated experimental stability data for chamber pressures from 300 to 2500 psia in terms of the sensitive time lag. They found that $\tau \sim p_c^{-1/3}$ for chamber pressures below the critical pressure of oxygen, whereas τ was independent of pressure for supercritical operation.* This result seems to be in general agreement with the theoretical and experimental determinations of droplet burning times at sub- and supercritical pressures (Sect. 2.4). That is, for quasi-steady combustion in a quiescent atmosphere, it has been found that the ratio of the burning time at supercritical pressure to the burning time at low pressure is proportional to $p_c^{1/3}$. However, studies of nonsteady burning at high pressure have not yet been made. The subcritical time lag behavior found by Hefner, Reardon and Smith is in agreement with the unsteady vaporization analysis of Heidmann and Wieber.[346] In fact, the pressure dependence of the time lag has been found to correlate with the pressure dependence of the heat of vaporization of oxygen. In general, the time lag data, correlated in terms of oxygen parameters, has been found to fit in well with data from other propellant combinations, correlated on the basis of the noncryogenic fuel parameters. One must conclude that oxygen/hydrogen, from the point of view of the combustion response, is not fundamentally different from other nonhypergolic propellant combinations.

Extensive testing at the NASA Lewis Research Center has shown that decreasing the hydrogen injection temperature tends to produce high frequency instability, spontaneously initiated.[719] The stability limit temperature has been found by these workers to be much more sensitive and reproducible than the threshold amplitude of a bomb-induced perturbation. The explanation for this temperature-sensitivity of the oxygen/hydrogen combustion process has recently been attributed to the effect of hydrogen compressibility on the injection dynamics. That is, decreasing the temperature increases the density, thus decreasing the injection velocity and reducing the injector impedance, allowing the hydrogen injection rate to oscillate in response to the chamber pressure. The oscillating injection rate leads to an oscillation in the burning rate, which tends to enhance the pressure oscillation. In agreement with this concept is the additional experimental result that increasing the mean hydrogen injection velocity increases the stability limit temperature.

However, the hydrogen temperature approach has not been universally accepted as the best stability rating technique for these propellants. Other workers have found bombs and pulse guns to be equally successful. Moreover, hysteresis behavior was observed in the testing of a large (42-inch diameter) combustor.[215] When the temperature was reduced, the stability limit was found to be 80° R, but then the temperature had to be increased to 105° R before the combustion again became stable. Records of the initiation of oscillations shown in Ref. 215 indicate that the instability started quite abruptly, as it would have if triggered by a bomb or pulse. Such behavior is common with the storable, hypergolic propellants, but has not been reported elsewhere for oxygen/hydrogen.

7.3.1.2 FLOX/light hydrocarbons.—Only very preliminary stability information is currently available for the FLOX/light hydrocarbon pro-

* See Sect. 6.3.3 for a discussion of these correlations.

pellants; the indications are that their stability behavior is essentially the same as that for other nonhypergolic propellants. Critical data are listed in Table 7.3.1. Thus it is to be expected that the fuel will be the controlling propellant in these combinations.

In one investigation, tests were made at 100 psia (6.8 atm.) with a constant fuel injection temperature of 180° R.[157] Using nine variations of three basic injection patterns, and relying completely on spontaneous initiation, it was observed that methane was most stable, butene most unstable, and propane was intermediate. Hence the stability trend could be correlated with the degree of subcooling, the more subcooling, the more unstable. However, the incidence of instability with butene was not significantly different when the injection temperature was maintained at 530° R. Such apparently contradictory data is not surprising in view of the randomness of the testing, the large number of injector patterns, and the fact that the chamber geometry was constant. More systematic studies will be required to define the stability characteristics of these propellants with greater certainty.

7.3.2 Storable Propellants

Currently, the most widely used storable propellant combination is nitrogen tetroxide with a mixture of 50% hydrazine and 50% unsymmetrical dimethylhydrazine (UDMH) referred to as A-50. Because of combustion instability and "popping" problems encountered, several other fuel mixtures, involving monomethylhydrazine (MMH) as well as hydrazine and UDMH, have been tried, but have not replaced the 50-50 mixture of hydrazine and UDMH in practical systems. Other oxidizers have also been tested with hydrazine-based fuels, including chlorine trifluoride and chlorine pentafluoride. Pentaborane has received some attention as a storable fuel, as have gelled mixtures of hydrazine and powdered metals, primarily aluminum. Stability data on these alternative propellants is, however, extremely limited.

In general, these storable propellants are also hypergolic, i.e., self-igniting. At ambient conditions, liquid-phase reactions are sufficiently energetic to produce substantial vaporization and initiate vapor-phase combustion. Hydrazine and hydrazine-derivative fuels are also monopropellants, a characteristic that must be taken into account even in a consideration of bipropellant combustion. It is clear that in a liquid propellant rocket combustor these chemical factors cannot be separated from the hydrodynamic factors associated with the injection processes. Therefore, propellant properties can be expected to have a significant effect on both the characteristic combustion time (or preferred oscillation frequency) and the response of the combustion process to disturbances. In fact, one of the outstanding features of most of the storable propellant combinations is the tendency to develop spontaneous, random pressure perturbations, which have the appearance of localized explosions, i.e., popping and spiking (see Sect. 7.2.1).

TABLE 7.3.1.—CRITICAL VALUES FOR FLOX/LIGHT HYDROCARBON PROPELLANTS

Propellant	Critical pressure, atm	Critical temperature, °R
Oxygen	50.1	280
Fluorine	55.0	259
Methane	45.8	343
Ethane	48.2	549
Propane	42.0	665
Butane	37.5	765
Ethylene	50.0	490
Butene	40.0	755

7.3.2.1 Nitrogen tetroxide/50% hydrazine-50% UDMH (N_2O_4/A-50).—Because of its wide use in space and weapon systems the N_2O_4/A-50 propellant combination has received the most study to determine the tendency toward popping and spiking. The mechanisms of these phenomena, as discussed in Sect. 7.2.1, depend in some way on the complex chemical behavior of this combination of propellants. For example, Sawyer[629] found that the vapor-phase reaction rate of nitrogen tetroxide with hydrazine varied by a factor of 1000, depending on whether or not the reactants were allowed to decompose prior to mixing. It is not surprising, therefore, that changes in the spray pattern can have dramatic effects on the burning rate, leading to random pressure waves.

Nitrogen tetroxide is particularly susceptible to "hydraulic flip" and other irregular injection stream behavior (see Sect. 2.2.2) because of its high vapor pressure, which is a sensitive function of temperature.

Another property of nitrogen tetroxide is its ability to dissolve substantial amounts of helium, a commonly-used pressurizing gas.[396] The solubility is a strong function of pressure and temperature. Hence bubbles may form in the liquid as it passes through the injector, leading to irregularities in the flow rate and spray formation. Also, with nitrogen tetroxide, it is important to design the injector passages to avoid eddy regions where trapped gases and vapors can accumulate, increasing the compliance of the injector. The result of this increased injector compliance (or capacitance) is to eliminate the stabilizing effect of the feed system pressure drop upstream of the injector, with the increased possibility of low frequency instability.

With hypergolic propellants, spray formation is closely linked with the chemical behavior. Evans, Stanford, and Riebling[252] found that separation of impinging streams of nitrogen tetroxide and A-50 because of liquid phase reactions was important for stream sizes greater than about 0.050 in. Analytical studies, backed by some laboratory data, have yielded a separation criterion in terms of a contact time

$$\tau_c = \frac{d_j}{V_j}$$

where d_j is the jet diameter, and V_j is the jet (injection) velocity. If the contact time is greater than a characteristic chemical reaction time, the streams will separate. Kushida and Houseman[415] found liquid phase reactions controlling at low pressures and short contact times, whereas gas phase reactions controlled separation at high pressures and long contact times, as shown in Fig. 7.3.2. Operation at a condition of marginal separation is undesirable, since the general unsteadiness associated with typical injection streams can produce irregularly alternating separation and mixing, with consequent fluctuations in the burning rate.

Stream separation can be an important factor in determining the preferred frequency of the combustion process. The sensitive time lag

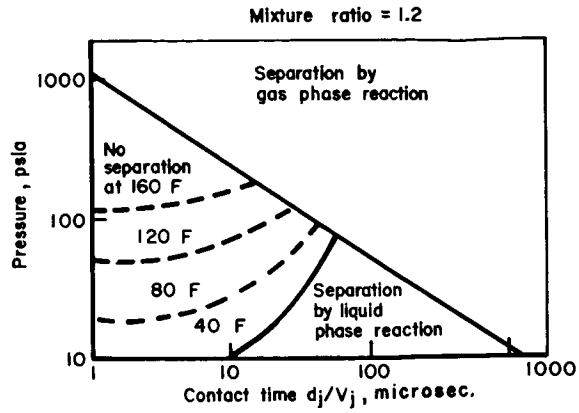

FIGURE 7.3.2.—Stream separation criteria for N_2O_4/N_2H_4.

correlations presented in Sect. 6.3 indicate that differences between the characteristic combustion time between unlike-impinging injector types (e.g., doublet, triplet, pentad) and even between impinging and nonimpinging types are of the same order of magnitude as the scatter in the data (Fig. 6.3.3c). In part, this results from the fact that the data was obtained largely from developmental testing. However, such behavior is to be expected also on the basis of stream separation. Non-hypergolic propellants (Fig. 6.3.3c) showed a substantial difference between the characteristic times for unlike-impinging and nonimpinging types for orifice diameters less than 0.100 in., reflecting the improved atomization and mixing produced by impingement. It is also interesting to note that for a given injection orifice size the hypergolic propellants show a somewhat larger characteristic time than the non-hypergolic ones. Other trends (e.g., with chamber pressure, orifice diameter, chamber Mach number) are similar for the two kinds of propellant combination, indicating their common dependence on the mechanism of droplet combustion (Sect. 3.4).

7.3.2.2 Other storable propellants.—In general, no large differences have been found between the stability characteristics of the different storable propellant combinations. Some attempts have been made to compare the popping incidence and response to perturbations for nitrogen tetroxide with amine fuels other than A-50. When tested with two typical injector patterns, both MMH and a 50-50 blend of hydrazine and MMH (M-50) were slightly less sensitive to perturba-

tions (natural and artificial) and MMH appeared to have a slightly smaller incidence of popping combined with smaller pop amplitudes.[729] Other recent data indicate that the resonant frequency associated with hydrazine combustion is somewhat higher, for a given injection orifice size, than either A-50 or MMH.[4b]

Laboratory efforts to influence the combustion characteristics of liquid hydrazine showed that small amounts (1% to 2%) of such additives as water, pyridine, MMH, and UDMH could produce approximately 10% burning rate decreases.[119] Water was the most effective additive; 10% water caused a 60% burning rate reduction. However, these tests were conducted at pressures well below those of interest in rocket combustion, and under stagnant (actually free convection) conditions. As Sawyer[629] has indicated, because of the pressure dependence of the complex set of chemical reactions involved in the nitrogen tetroxide/hydrazine combustion process, it is doubtful that studies carried out at pressures below 2 atmospheres can yield data of significance for rocket combustors operating at 6 atmospheres and above. In addition, it has been shown that convection effects are dominant, rather than chemical kinetics, when the ratio of the relative velocity to drop diameter is greater than about 1000 sec^{-1}. For a drop size of 200μ, the chemical effects should not be controlling for relative velocities above one foot-per-second. On the other hand, at least one investigation, involving a production-type engine, demonstrated that water was effective in eliminating hard start characteristics observed with nitrogen tetroxide/A-50 propellants.

Addition of small amounts of aluminum powder has been found to be an effective method of suppressing combustion instability in many solid propellant rocket motors. A few attempts have been made to apply the same technique to liquid propellant rockets. In one study, aluminum and aluminum oxide powders were added to hydrazine and fired with nitrogen tetroxide in a moderate-size combustor.[404] A gelling agent, Carbopol 940, was used to ensure that the solid particles remained well dispersed throughout the hydrazine. The stability of the combustor was rated by use of bombs of varying sizes (see Sect. 10.2). It was found that an increase in the stability of the combustor was obtained simply by gelling the hydrazine. Moreover, the damping times of the disturbances and the limiting amplitudes of sustained oscillations were nearly independent of the particle additive type, size, and concentration (which varied from 10% to 43% of the fuel). The stability improvement was attributed to the effect of the gelling agent in the inhibition of fuel atomization and droplet breakup. On the other hand, a laboratory investigation in which aluminum powder was added to the gas phase showed definite stabilizing effects of the aluminum when the concentration was greater than 0.02% (in all cases it was less than 1%) of the fuel.[342] The differing results of these two studies may be due to the size and spatial distribution of the particles, since Dobbins and Temkin[228] have shown that strong damping effects are possible because of solid particles in the chamber (Sect. 8.5.2).

7.3.3 Cryogenic-Storable Combinations

Historically, propellant combinations consisting of one cryogenic and one storable propellant were among the earliest used. Most commonly, the oxidizer in such combinations is liquid oxygen, although recent attention has been given to liquid fluorine. Fuels used with oxygen have included alcohol, pure hydrocarbons such as heptane and octane, hydrocarbon blends such as JP-4, RP-1, and hydrazine and its derivatives. The most popular combination for production engines has been liquid oxygen/RP-1.

Just as with the other two classes of propellants, it is difficult to separate the effects on stability of the propellant properties from those of the injection scheme. Moreover, most of the investigations were made using fixed-geometry combustion chambers. The results of such studies are difficult to generalize, since an improvement in stability may be caused either by an increase or decrease in the characteristic time of the combustion process, or by a decrease in the sensitivity to disturbances. Therefore, it is possible only to determine whether or not propellant properties have any significant influence. Beyond that, any conclusions must be regarded as speculative.

Pass and Tischler[534] used an injection pattern consisting of a hollow-cone fuel spray between two axial jets of liquid oxygen to study the effects of fuel type. The incidence of spontaneous, first

longitudinal mode instability was correlated with relative evaporation rate and with laminar flame speed, to the extent that such data were available. Their results showed that the physical properties that made for higher evaporation rate led also to higher incidence of instability. A moderate increase in the instability rate with increasing gaseous flame speed was also observed. Regarding the chemical type of the fuel, straight- and branched-chain paraffins and alicyclics had high evaporation rates, alcohol and amines had low evaporation rates, and aromatics were intermediate. For a given evaporation rate, straight-chain paraffins and aromatics were more unstable than branched-chain paraffins and alicyclics.

A similar investigation of the effect of fuel type on stability with the propellant combination liquid oxygen/hydrocarbon was reported by Greenfield.[297] The combustor was a large cylindrical chamber with a very high contraction ratio (to keep the thrust level low), with injection concentrated near a circle having a radius $\frac{3}{4}$ of the chamber radius. Tangential mode instability was initiated by means of a steady flow of nitrogen gas (Sect. 10.4). The higher the nitrogen flow required, the more stable was the propellant combination. It was found that the data could be correlated with the product of fuel density and surface tension. This product was taken to represent the degree of fuel atomization, with a larger product corresponding to a larger fuel droplet size. The test results showed that increasing droplet size was associated with better stability (for that chamber, first tangential mode). It was also observed that the data fell into three groups, according to fuel chemical type. Paraffinics were most stable, naphthenics intermediate, and unsaturates least stable. In addition, the paraffinics showed the strongest dependence on atomization, the unsaturates the weakest. The difficulty of generalizing purely empirical stability trends is illustrated by the fact that later tests in somewhat different combustion chambers failed to show any effect of propellant combination.[425] These later tests used (1) a high-thrust chamber of the same diameter as the low-thrust unit, and (2) a two-dimensional chamber of the same width as the cylindrical ones (see Sect. 9.2).

The lack of strong propellant effects on the characteristic time (or preferred frequency) of the combustion process is seen also in the sensitive time lag correlations assembled by Reardon.[581] The time lag was correlated with chamber pressure, Mach number, and injector orifice diameter. For the cryogenic-storable propellants, very little data variation can be attributed to propellant properties, even with such diverse fuels as hydrazine, ethyl alcohol, and RP-1. In fact, for non-coaxial injector elements, all-cryogenic data fit into the cryogenic-storable correlation, provided that oxygen parameters, rather than hydrogen, are used as independent variables.

The preceding remarks, of course, are intended to apply to large-scale trends. In certain, somewhat marginal cases, a change in propellant characteristics can cause a substantial alteration of stability. Such tendencies can best be investigated by use of dynamic stability rating techniques (Chapter 10). For example, Weiss[727] employed the tangential pulse method to study the effect of adding small amounts (up to 15%) of Hyballine A14 ($C_8H_{17}NH_2Al(BH_4)_3$) to the fuel in a liquid oxygen/RP-1 combustor. Increasing amounts of Hyballine produced increasing stability, as determined by shorter damping times of pulse-induced perturbations. The stabilizing effect was greater at low mixture ratios. Because of the limited scope of the test program, it is not possible to determine the nature of the stabilizing effect, although it is known that Hyballine is much more reactive than RP-1 and is hypergolic with most oxidizers.

For all three classes of propellant combination, the effects of propellant properties on stability have not been thoroughly or systematically explored. Chemical characteristics appear to enter only in determining whether the fuel and oxidizer are hypergolic or if the fuel can act as a monopropellant. Physical properties, particularly of the less volatile propellant, help to determine drop size and hence droplet burning rate. However, the injection pattern is at least as significant as the propellant combination in determining the nature of the combustion dynamics.

7.4 INJECTOR PATTERN*

The grouping of propellant orifices into injector elements and the arrangement of these elements over the injector face are termed the injector

pattern. The injector pattern determines the propellant spray characteristics and, therefore, the combustion response characteristics. Solutions to combustion instability problems almost always involve variation of the injector pattern to achieve spray characteristics which will yield stable combustion response in the particular engine. This section discusses the effects of variations in injector pattern on combustion instability.

The following nomenclature pertains to Sect. 7.4:

C_d	Orifice discharge coefficient
f_μ	Injection density distribution function, $\hat{\mu}/\hat{\mu}_m$
Δp	Injector-chamber pressure drop
$\hat{\mu}$	Injection density
ϕ	Impingement angle
$T_{H_{trans}}$	Hydrogen transition temperature for resonant combustion

7.4.1 General Considerations†

The definition of combustion instability includes both high frequency instability (for example, Chapter 4) and feed system coupled modes of instability (Chapter 5). There is some question whether this artificial separation into specific types of instability should be made. To date, largely to simplify analysis, such a separation nevertheless has been maintained.

Feed system coupled modes of instability are largely controlled by the response of the combustion to oscillatory flow from the injector. The injector pattern determines the spray characteristics which establish this response. In particular, the injector pattern determines the "flight time" of propellants from the injector to the impingement point and the subsequent atomization, mixing and combustion processes.

The dynamics of the feed system are also an integral part of feed system coupled modes. Because the feed system can be analyzed rather easily, the usual analysis of a feed system coupled mode of instability often involves a very detailed study of the feed system whereas the complex combustion processes are described only by one or two simple time delays. With this kind of analysis, the only useful conclusions likely to be reached must largely involve the feed system and not the injector pattern. The usual conclusion (re-established in practice at least once a year) is that the injector impedance should be sufficiently high (see Sect. 7.5.1).

Often the effect of chamber pressure phenomena on feed system coupled modes has been neglected in the design phase. As a result this form of instability has continued to plague engine development programs in recent years. Some important aspects of the injector design and the role played in the feed system coupled modes will be discussed in this chapter, however, Chapters 3 and 5 should be consulted for further details.

Injection effects on the excitation of resonant combustion have been studied for many years in rocket chambers and in related combustion devices. These effects are often very complex and hence are often only partially understood and therefore the governing mechanisms remain in question. One point of general agreement from the theories discussed in Chapter 4 is that droplet size and propellant distribution are important. However, the relationships between these spray parameters and the injector geometry are also very complex and much still is to be learned.

Most theories show that the spray droplet mean size (and distribution) controls both the frequency of maximum combustion response and the magnitude of that response. In general, both the frequency and the magnitude of the response decrease as the mean drop size increases. A decrease in magnitude should always be a stabilizing influence. A decrease in response frequency, however, may only shift the predominantly unstable mode to a mode of lower frequency. If the original unstable mode is the fundamental, however, there is no lower frequency mode and a decrease in response frequency would also be a stabilizing effect. No stability investigation is complete without consideration of the mode of instability.

The empirical correlations of mean spray drop size and distribution to injectory geometry are limited both in the range of injector variables and

* O. W. Dykema, Section Editor. Contributions from C. J. Abbe, H. L. Burge, J. Campbell, Jr., E. C. Clinger, D. T. Harrje, J. J. Lovingham, A. I. Masters, J. M. McBride, J. M. Senneff, A. J. Smith, Jr., and J. P. Wanhainen.

† For the reader interested in an overall view of the various injector characteristics, the summary of each section that follows is presented in italics.

the element types studied. Almost all correlations have been obtained in cold flow, with simulated propellants, in atmospheric environments. Thus, such major effects as hydraulic flip and flow separation of hypergolic propellants at the impingement point are not accounted for.

In general, there appears to be agreement that the mean spray drop size is proportional to the injector orifice diameter, and inversely proportional to the injection velocity, both to some fractional power. Thus, the effects of increasing drop size on stability, previously mentioned, could be generally ascribed to increasing orifice diameters and/or to decreasing injection velocity.* It is possible that much of the difficulty in understanding combustion instability arises directly from the lack of understanding of the relations between spray drop size and injector geometry as well as the associated unsteady combustion phenomena.

The problem of spray drop size is not involved directly in the effects of propellant mass and mixture ratio distributions on stability. In theory, there are two main effects. The first concerns the efficiency of coupling between the combustion and the pressure and/or velocity oscillations of the combustion chamber gases. This coupling can be minimized by reducing the quantity of propellant injected into those regions of the chamber where the pressure or velocity oscillations are maximum (Sect. 7.2.5). The second effect of mass and mixture ratio distributions concerns the magnitude of the combustion response to transverse gas displacements (Sect. 3.3.2). This response can be minimized if the propellant burning rates are approximately the same in the steady-state and the displaced conditions. This is often done, through the injector pattern, by minimizing transverse mixture ratio gradients.

Thus, a number of injector design factors are shown, in theory, to have significant effects on excitation of combustion instability. A wide variety of experimental programs have been conducted to evaluate and verify these effects. In general, each individual program can investigate only a limited range of injector design parameters, within the framework of limited hardware, operating conditions and propellant combinations. Often the changes made to the parameter under investigation necessarily cause small changes in other parameters which also affect stability.

Few studies set out to confirm a general theory of the combined effects of several injector design changes. Great care must be exercised, therefore, in interpreting the effects of variations in single design factors as observed in a single, limited experimental program. In the absence of a complete, accurate theory to account for all variations in such programs, only broad areas of general agreement between theory and experiment and between experimental programs should be considered established.

The results of some of these experimental programs are briefly summarized in this section. An attempt is made to show such general agreement (and disagreement) which exists between the experimental conclusions and the theoretical considerations just discussed, or covered in Chapter 4. The experimental studies are separated into unlike- and like-impinging jet, and coaxial jet element types. These element types represent widely different physical mechanisms for atomization, mixing and distribution of the propellants and might be expected to yield quite different stability results. Also, two unique injector types, representing departures from the conventional axial injection scheme, are also discussed.

Injector design is normally constrained by the necessity of achieving high performance, chamber compatibility and durability of the injector, reproducibility in manufacture, and providing stable operation.[318] These requirements have resulted in a similarity of the injector designs emanating from the various propulsion companies. (Further information on the overall injector design is found in Sect. 7.4.3 in the discussion of large injectors, see Fig. 7.4.3a.)

To achieve high performance the important parameters include the distribution of mass and mixture ratio, the sizing of the orifices to achieve the proper droplet sizes for efficient combustion and the basic choice of injector type.

Chamber compatibility and injector durability involve the control of the combustion environ-

* It should be noted that injection velocity affects stability in other ways as well, such as altering the axial combustion profile (Sect. 7.2.4).

ment. Off-mixture ratio or fuel cooled regions adjacent to chamber walls or baffle surfaces help to regulate the heat transfer. Injection type, element placement, and impingement distances are variables that influence the heat transfer to the injector face and hence influence injector durability. Vibration levels related to the stability of the combustion are also related to durability and may influence the heat transfer environment.

Reproducibility is typically a direct result of the choice of injector element type, complexity of the pattern, complications introduced by damping devices, etc.

When these requirements are all taken into account the resulting injector will often closely resemble that shown in Fig. 7.4.1. Three distinct zones of injection are shown. The core region for maximum performance, the barrier region (or film coolant region) for heat transfer control and the baffle tip region which is necessitated by the coolant requirements of the baffles (dump cooling). In the case of regenerative cooling of the baffles this latter region is eliminated.

With this general injector design in mind, the individual characteristics of the various element types are considered next. At times in this discussion cross comparisons will be made. The nature of the data often necessitates this approach.

7.4.2 Unlike-Impinging Jets

Unlike-impinging jet elements are characterized by one or more jets of oxidizer impinging directly on one or more jets of fuel. Although doublets and triplets have perhaps been the most popular unlike-impinging jet element designs, greater numbers of jets (e.g., two-on-two, represented by the quadlet; or four-on-one such as the pentad) have also been highly developed. The point of impingement for various designs has ranged anywhere from the injector face (or even behind the face) to distances normally approaching an inch (in some extreme designs even further downstream). Unlike-impinging

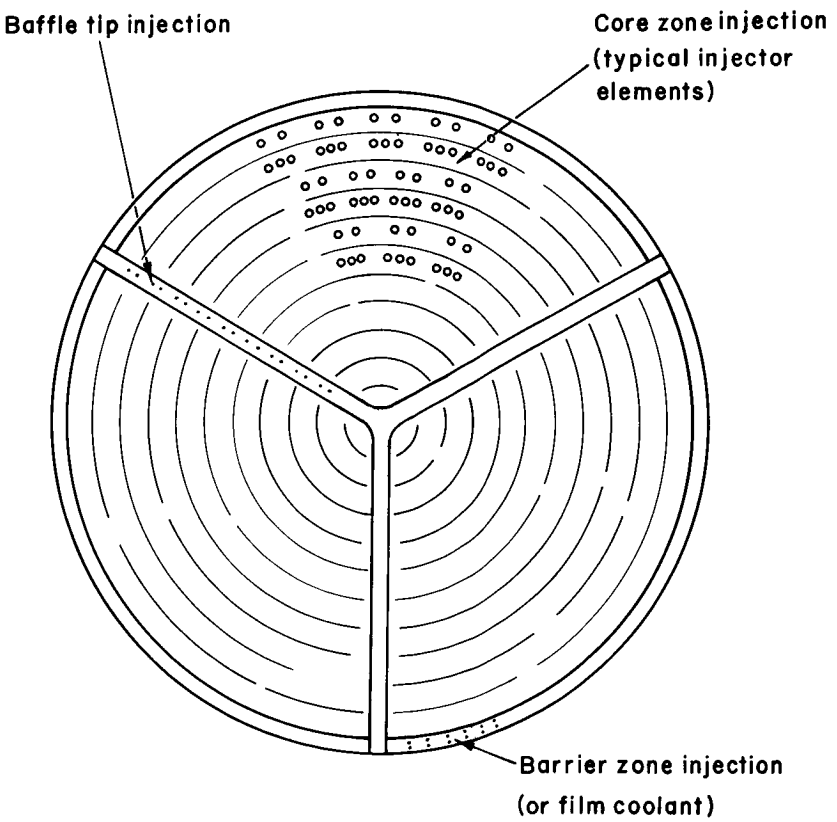

FIGURE 7.4.1.—Typical injector face showing various zones.

jets tend to provide rapid liquid mixing, generate mixed specie droplets, and therefore result in combustion that is characteristically concentrated near the injector face. This has prompted the use of these elements in the smaller engines where combustion must be completed quickly if reasonable performance is to be achieved.

Two examples of injectors developed by Bell Aerospace using unlike-impinging jets are described here by J. M. Senneff. Design of injector patterns must of course, consider performance, durability and compatibility with the combustion chamber walls, as well as combustion stability. Some of these specific injector design factors, as well as some observations on stability, are discussed here and are representative of typical problems to be faced by any injector designer.

To meet the stability specification on two engine programs, an extensive evaluation of the stability of unlike triplet and doublet injectors was conducted at Bell Aerospace. Most of this effort was related to achieving dynamic stability for an 8-inch diameter injector operating at 120 psia chamber pressure. Additional data were obtained from tests on a 3-inch diameter injector operating at approximately 125 psia. Storable propellants were used with N_2O_4 as the oxidizer. Fuel consisted of the 50/50 blend of hydrazine and UDMH for the 8-inch hardware,* while MMH was used on the other. Both injectors were designed to have equal mass distribution across the injector surface to reduce radial winds and recirculation.

The eight-inch injector originally provided two combustion zones, the inner primary zone used triplets of two-fuel-on-one oxidizer operating at a mixture ratio of 1.89. The region near the chamber wall consisted of unlike doublets (fuel on the outside) operating at a mixture ratio of 0.85. The sensitivity of this design to bombing (2 grains of PETN were generally used) necessitated the incorporation of a baffle. The final flow-through baffle design included both fuel and oxidizer passages where the issuing streams impinged to form unlike doublets, thus establishing a third propellant injection zone. The three zones were: primary, barrier, and baffle with mixture ratios of 1.80, 1.05 and 1.60 respectively. Additional injector design parameters are listed in Table 7.4.2a.

The same general type of injector was also used on the three-inch diameter engine. The design was basically a flat face, circumferentially distributed, 2-row injector, where the outer row of triplets was run at lower mixture ratio to control chamber wall temperatures. The inner rows were unlike doublets. The impingement distance was 0.250 inch for both rows. This unit was found to self-trigger at simulated altitudes because of a sharp pressure pulse (or spike) at the initiation of combustion.

During the stability evaluation phase for the larger injector, which involved several injector modifications, certain variations in injector pattern were identified that produced a greater degree of stability but not necessarily dynamic stability. For example, the reduction of the number of barrier doublets appeared to increase stability. This modification was accomplished by reducing to two thirds the number of doublets in the peripheral pattern. A proportional increase in flow rate was used while all other parameters such as impingement distance and angle were held constant. Increasing orifice diameters to maintain Δp resulted in a reduction of orifice L/D since L was constant. Another change was an injector modified to alter the radial mass flow distribution to that of the hump-type (see Sect. 7.2.5) which in this case showed no stability improvement. The alteration was accomplished by reducing the propellants in the outer triplet row and near the baffle to 87% of nominal value. The remaining first, second and third row triplets increased flow to 123%, 160% and 104% of the nominal value respectively.

The result of the study was that to achieve dynamic stability the final design in the larger unit required a three-bladed, $1\frac{1}{4}$-inch-long baffle supplemented by a $\frac{1}{2}$-inch circular ring located at approximately the injector mid-radius. The smaller

* When photographic techniques were used in conjunction with the 8-inch diameter study, the sprays of droplets under actual operating conditions could be studied (see Sect. 9.4.4). The fine droplets observed in both the ligament breakup and aerodynamic breakup extended down to the 20 micron size range. These small droplets tend to verify the high rates of combustion actually encountered with unlike impingement. Even more important is the fact that this photographic approach allows droplet size measurements under the identical environment encountered in the actual engine.

TABLE 7.4.2a.—TYPICAL ORIFICE DESIGN PARAMETERS FOR AN UNLIKE-TYPE INJECTOR DESIGN (SHARP ENTRY CONDITION)

Parameter	Zone					
	Primary (triplet)		Barrier (doublet)		Baffle (doublet)	
	Fuel	Oxidizer	Fuel	Oxidizer	Fuel	Oxidizer
L/D	4.2 3.3	3.5 3.5	3.0 3.0	5.6 5.6	2.6 2.6	3.3 3.3
Orifice flow angle with ℄, deg	28	0	30	5	15	15
Impingement distance, in.	0.403		0.106		0.403	

unit employed a toroidal acoustic damper cavity connected to the chamber by orifices located at the injector-chamber interface to provide dynamic stability.

The programs just described immediately introduced the reader to the complexities of injector design; the two or three separate zones, the choice of injector elements for each, the necessity in most cases for damping devices to be present, etc. The table provides the actual dimensions and entrance conditions that have been used to control the orifice flow on one engine design so that reproducibility between injectors can be maintained.

Senneff makes the observation that decreasing the number, and increasing the diameters, of the outer row of orifices improved the stability of one injector. It is probable that this change increased the droplet size in the region of highest chamber pressure oscillations, near the wall. The stabilizing effects of increasing drop size were already discussed and will be further documented in the remainder of this section.

Looking further into the detailed characteristics of injectors, the existence of a frequency dependent combustion response has been noted by numerous investigators. The experimental techniques used in such studies are described in Chapter 9. Some of the program results at Aerojet relating to combustion response are summarized here by J. M. McBride.

In order to place some quantitative measure on the stability characteristics of an injector element, experimental measurements of the energy input to a given system have been determined indirectly by the measured increase or decrease in pressure amplitude for three systems, a full scale engine and two subscale experimental engines. In the case of the full scale engine, data are presented giving a comparison of decay rates of two injectors in the same chamber. One of the injectors is comprised of elements where two oxidizer jets impinge on two fuel jets (quadlet), whereas the other is a like-on-like pattern (see Sect. 7.4.3). The propellants used are N_2O_4 and A-50.

From the data presented in Fig. 7.4.2a it can be seen that the like-on-like injector has a reduced response; the decay rate based on the unfiltered traces is approximately 1.5 times that of the quadlet injector. The filtered data shows the same trend. This result indicates that for injector patterns having nearly equal number of elements the like-impinging injector would be expected to be more stable. These results must be qualified by the theoretical consideration (discussed in Chapter 4) that the frequency at which the maximum response factor can occur may vary even though the absolute magnitude of the factor may be the same for two injectors. The conclusion is that, although the like-impinging injector shows increased stability over the impinging element in the particular example cited, this may not be true

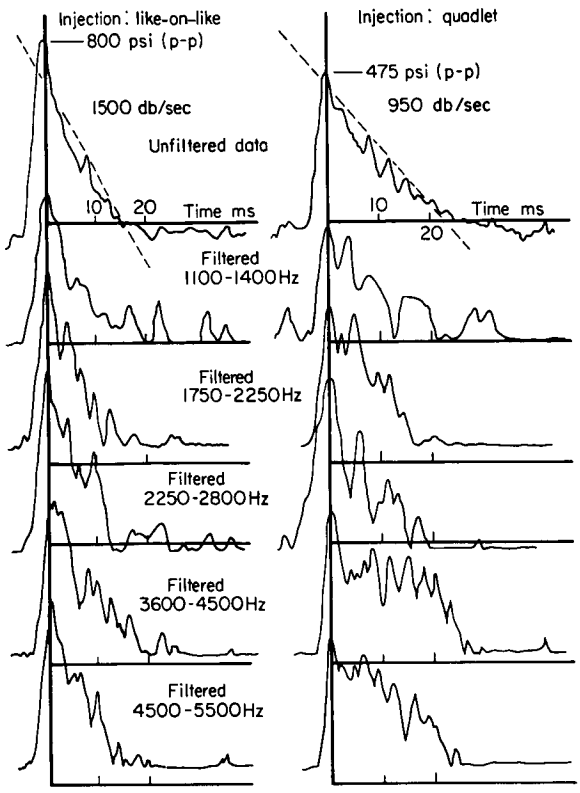

FIGURE 7.4.2a.—Pressure amplitude decay rates for like-on-like versus quadlet injector elements.

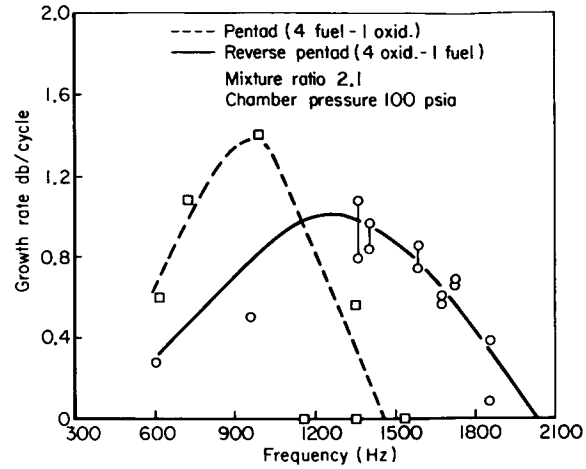

FIGURE 7.4.2b.—Effect of diameter on pressure amplitude growth rate versus frequency for N_2O_4/A-50 impinging elements.

for a larger engine which would have lower frequency acoustic modes.

Another study of interest to the designer was done by McBride and Veglia.[474] This is an experimental comparison of two impinging injector patterns, one being four-fuels-on-one-oxidizer and the other four-oxidizers-on-one fuel. The experimental results are given in terms of growth rate as a function of frequency (Fig. 7.4.2b) and indicate that the most sensitive frequency (frequency at which maximum growth occurs) was reduced by a decrease in fuel orifice diameter and a corresponding increase in oxidizer diameter. Based on the physical models of droplet burning discussed in Chapters 2–4 this would imply that the oxidizer was controlling the response characteristics of this propellant combination (N_2O_4 and A-50) and that reduction in oxidizer orifice size would increase the frequency at which an injector would be sensitive. It is also interesting to note that a detailed frequency survey with one of the injectors indicates the possibility of more than one sensitive frequency, as can be seen from Fig. 7.4.2c. A mixture ratio survey (see Fig. 7.4.2d) using the same experimental approach indicates that decreases in mixture ratio for the propellant combination decreases stability.

A second experimental motor has been developed to measure the response of an injector element to transverse modes of instability. The elements under evaluation consisted of two-oxidizer-on-one-fuel triplets using the cryogenics LOX/H_2. The limited data available[37] from the tests are presented in Fig. 7.4.2e. Perhaps the most significant conclusion which can be reached is that these injector elements do appear to have a preferred frequency and a similar response shape. This result lends credibility to the physical models based on droplets as well as the assumed response functions postulated by Crocco (Sect. 4.2).

This concept of a combustion response, and the effect of thrust-per-element (closely related to drop size) on this response, was used in a large engine program at Aerojet to develop a dynamically stable injector. Such studies are further described by A. J. Smith, Jr.

The Gemini Stability Improvement Program (GEMSIP) was a program directed at producing a dynamically stable injector configuration for the second stage engine of the Gemini flight series. Similar to its predecessor the Titan II, this engine used the storable, hypergolic propellant combination of N_2O_4/A-50 and operated

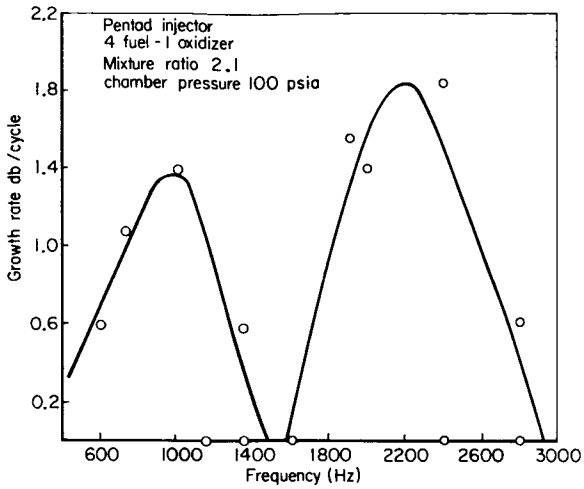

FIGURE 7.4.2c.—More than one frequency maximum as observed for N_2O_4/A-50 impinging elements.

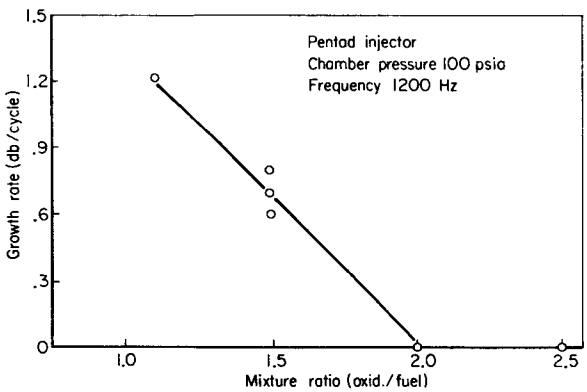

FIGURE 7.4.2d.—Mixture ratio and the effect on growth rate for N_2O_4/A-50 impinging elements.

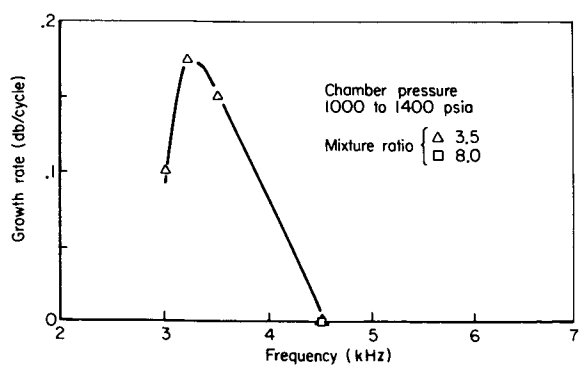

FIGURE 7.4.2e.—Growth rate vs frequency for LOX/H_2 impinging triplet elements.

at a nominal chamber pressure of 825 psi. The injector orifice configuration used during this program was a quadlet with two fuel streams and two oxidizer streams impinging about 0.1-in. from the injector face.[584]

The injector program was divided into two parts: (1) investigate the effect of various baffle configurations, and (2) investigate different injector propellant distribution schemes. For the purposes of the discussion herein, only the latter part is of interest. The results to be discussed were obtained with an injector that had seven radially aligned baffles, which were five inches long at the center of the injector and five inches long at the rim.

The propellant distribution portion of the program was also subdivided into (1) determining the effect of element number on the relative stability of the engine, and (2) determining the effect of varying the injection density across the injector face on the stability of the engine. In the former case, the number of elements tested was 400, 600, and 800 corresponding to a thrust per element of 200, 150, and 100, respectively. In the latter case, the 800 element injector was used and variations in the injection density were accomplished by changing the number of elements in respective, concentric rows.

Before proceeding, it is necessary to define the terminology associated with the ensuing discussion. The injection distributions will be referred to as flat, hump, and ramp (also see Sect. 7.2.5). Defining the local injection density, $\hat{\mu}$, as the ratio of the local, total propellant flow to the local injector surface area serviced by the flow and the mean injector density, $\hat{\mu}_m$, as the ratio of the total injector flow to the total injector surface area, then it is possible to define a distribution function, f_μ, as the ratio of $\hat{\mu}$ to $\hat{\mu}_m$. The flat distribution had an $f_\mu(r)$ that was constant from the center to the rim of the injector. The ramp distribution had an $f_\mu(r)$ that was highest at the center of the injector and lowest at the rim of the injector. The hump distribution had an $f_\mu(r)$ that was lowest at the center and rim of the injector and highest at approximately the mid-radius of the injector. These distributions were shown in Fig. 7.2.5b for two variations of hump and ramp distributions.

Decreasing the number of elements resulted in

a corresponding increase in the orifice sizes since the total orifice area was to be kept constant. For this study, the flat injection distribution was used throughout and resulted in the following.[11,329]

1. The 200 F/E (i.e., pounds thrust per element) injector was dynamically stable and could not be pulsed into instability with a 1300 psi over-pressurization.
2. The 150 F/E injector was also dynamically stable and could not be pulsed into instability with a 1100 psi over-pressurization.
3. The 100 F/E injector was pulsed into a 1st radial mode instability by a 550 psi pulse. The conclusion reached in this portion of the program was that large diameter orifices decrease the combustion response characteristics to the point of providing dynamic stability.

The results of the injection distribution tests (all conducted with 100 F/E injectors) were as follows:

1. The steep hump distribution was the most stable in that pulses up to 770 psi could not drive it unstable.
2. All the other distributions were driven unstable by pulses less than 770 psi. The resultant instability mode was the 1st radial mode as was anticipated for this baffled injector.

The conclusion reached in this portion of the program was that injection distribution did indeed contribute to the relative stability of an injector as predicted by the analysis in Ref. 583. This conclusion was also reached in the case of tangential modes.[150,584]

Although not specifically studying the concept of combustion response, a wide variety of studies with unlike-impinging jets have been conducted or monitored by the Air Force Rocket Propulsion Laboratory (AFRPL). Some general conclusions on the effects of injector design factors on drop size and the effects of drop size and injection velocity on stability are discussed here by C. J. Abbe.

It is useful to begin this discussion by referring to Table 7.4.2b which illustrates how increased injector orifice size decreases the likelihood of instability for a liquid fluorine/hydrazine blend engine in the 8000 pound thrust range.[631] The great majority of the injector elements were triplets with two fuel streams impinging on a central oxidizer jet. Note that as the hole size increases, the number of elements decreases, or thrust per injector element increases. Thrust/element, though not fundamental in nature, is often used to characterize the relative stability of an injector design. The combustion performance for all the test conditions included in Table 7.4.2b are within 2.4% of each other. Additional data for this engine system indicate that increasing the injection velocity by welding some injector holes shut and maintaining the same total flow rate also improved stability. In this case, the stabilizing influence of increased velocity and increased thrust per element more than offsets any destabilizing influence of smaller propellant drop sizes.

The influence of impingement angle and orifice size (drop size) is again clearly indicated in a combustion study of the Titan III Transtage Engine System.[729] Two different injectors were

TABLE 7.4.2b.—STABILITY CHARACTERISTICS FOR A LF_2/HYDRAZINE BLEND ENGINE

Number of elements	Injection velocity, ft/sec		Average orifice diameter, in.		Stable tests / Unstable tests
	Oxidizer	Fuel	Oxidizer	Fuel	
215	47	59	0.0315	0.0250	1/3
158	47	62	.0313	.0215	1/4
96	44	54	.0730	.031	1/4
68	49	60	.0827	.033	13/13

evaluated; they were designated TRAX 21-1D and TRAX 21-11B. The 1D injector elements consisted of two fuel and two oxidizer streams impinging at a common point at an impingement angle of 80°. The 11B injector was the same as the 1D injector except that the two oxidizer streams were converted to a single enlarged stream in approximately half the number of quadlet elements. The area of the single oxidizer orifice was made equal to the combined area of the two streams it replaced, so that injection velocity remained constant. This change also resulted in a decrease in impingement angle between the fuel and oxidizer streams. In addition, the 11B injector did not have the film coolant holes that the 1D injector had. Even though the thrust per element for each injector remained the same, the 11B injector was considerably more stable to high frequency instability with either N_2O_4/A-50 or N_2O_4/MMH propellants. The increased oxidizer orifice sizes and the decreased impingement angle both have the effect of increasing propellant drop size and so improving stability. The removal of the film cooling may have had some influence on the stability of the thrust chamber, but it is not considered to be a major factor in this instance (however, see Sect. 7.2.6).

The influence of injection pattern alone on combustion stability is often not clearly defined; however, there is some basis for concluding that unlike impinging designs are slightly more unstable than self-impinging elements. Experimental data obtained in a 35,000 pound thrust engine utilizing N_2O_4/A-50 earth storable propellants indicate this may be true.[94] Data were obtained over a range of chamber pressures and contraction ratios for both a 218 element triplet (654 holes) and a 304 element self-impinging doublet (608 holes) injector. All orifice sizes were exactly the same, and injection velocities and flow rates were nearly identical. The doublet did, however, have a slight mass distribution bias at the mid-radius of the injector while the triplet had a uniform distribution. The triplet injector tended to be spontaneously unstable in the tangential mode whereas the doublet normally required a 10, 15, or 20 grain pulse gun discharge to initiate instability. The total included impingement angle in each case was 50°. The fact that combustion starts rapidly at the impingement point for the unlike-impinging schemes, while being dependent on secondary fan interaction for the self-impinging doublets (distributed combustion), is one explanation for the stability difference; though the radial mass distribution can also affect injector stability characteristics as pointed out previously in this section (and Sect. 7.2.5).

The extensive and continuing studies at Princeton University have included a wide variety of experiments on stability with unlike-impinging jets. Most of the work discussed so far in this section has concerned the transverse modes of instability. This is largely because longitudinal modes are rarely, if ever, a problem in large rocket engines. This does not preclude the use of longitudinal modes, however, in research on combustion stability. In the following comments, D. T. Harrje shows characteristics of the combustion response similar to those observed in transverse modes. Effects of injection distribution are also discussed.

With propellant combinations such as LOX/RP-1 and LOX/ethanol, unlike doublet and triplet designs have been used in the instability research at Princeton for a number of years.[180,187,583] In general, these injector elements consisted of 90° angle impingement at the injector face, often in a conical recess, with orifice $L/D \approx 5$, square entrance conditions ($C_d \approx 0.7$), and jet velocities in the 100 ft/sec. range. This face impingement approach suppresses interactions between the jets and the local velocity environment as well as eliminating problems of misimpingement; however, it is recognized that effects of impingement are transmitted upstream[613] and that injector face heat transfer could be enhanced.

In longitudinal mode testing such unlike designs were used to confirm the predictions of the Crocco sensitive time lag theory (see Sect. 4.2). The stability limits were well-defined and included higher longitudinal modes as the hardware was lengthened. However, it is vital to note, as is shown in Fig. 7.4.2f, that such higher modes still possess the same band of characteristic frequency* thus relating injection, combustion, and propellant

* Another example would be if this same injector were used in a large diameter annular motor. Again the same frequency would be anticipated even if it represented a very high harmonic mode in the annular configuration.

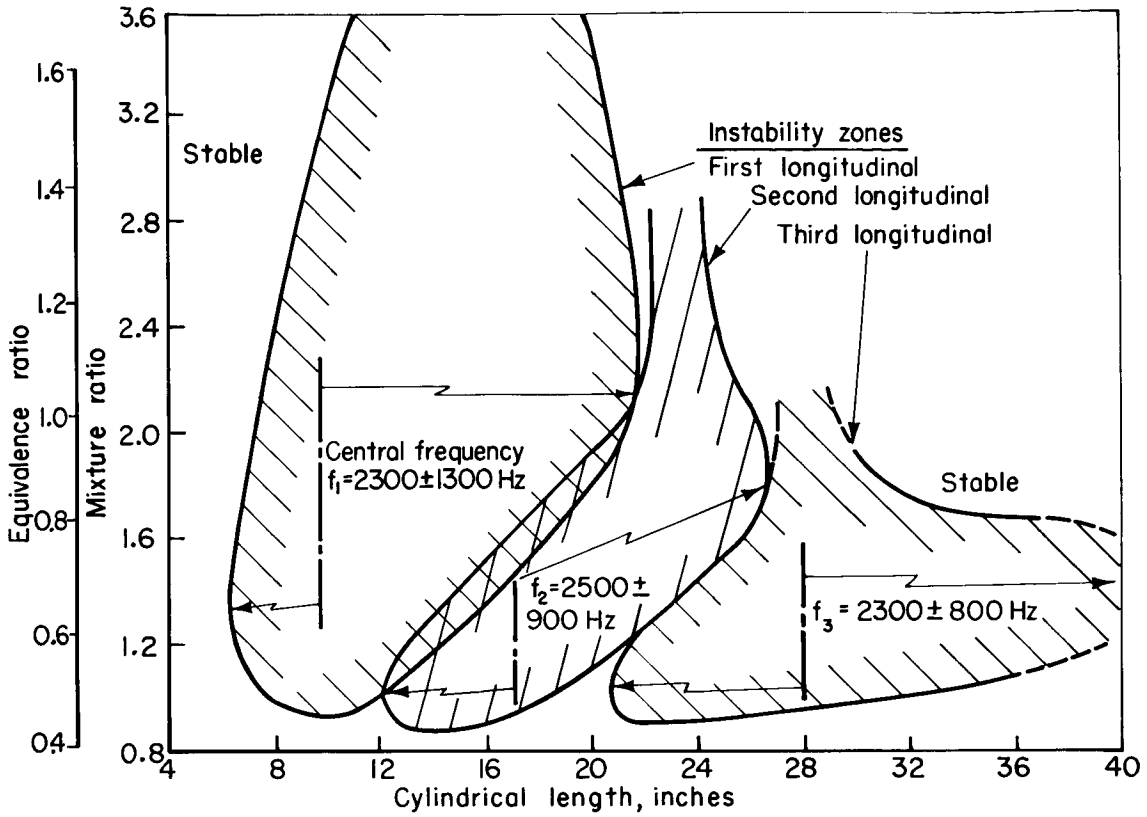

FIGURE 7.4.2f.—Characteristic frequency behavior for a given injector design and propellant combination (unlike doublet; LOX/ethanol).

factors to a definite frequency response range.[180] The character of the instability in such tests is spontaneous, sinusoidal near the boundaries, but shock-type within the unstable regime. Axial streak film surveys reveal that combustion is essentially completed a few inches downstream of the injector face in steady-state operation.[322]

Even in the early longitudinal testing it was evident that while stability limits were directly related to the combustion process (the more concentrated the combustion, the shorter the length at which instability could be attained), and combustion was dependent on the characteristics of the droplets generated, other factors, such as recirculation patterns, could also influence burning rates. For example, in one series of tests as injection diameters were enlarged (to increase droplet size and spread combustion), and the number of unlike injection elements reduced (to maintain constant thrust), a point was reached where recirculation became dominant and the instability boundaries expanded to those characteristic of the finer droplet sprays.[323]

These same unlike doublet and triplet injectors when used as spuds in transverse mode, pulse-motor hardware indicated the same spontaneous mode tendencies with LOX/RP-1 and LOX/ethanol. Although the unlike-doublet design represents one popular approach to achieve maximum performance,[613] within the spray fan there still exists a mixture ratio gradient[583] (e.g. see Fig. 2.3.2). When the gradient (which is in line with the orifices) was placed in the tangential direction, only unstable tests resulted for a variety of injection diameters (the pulse motor has only a single ring of injection spuds as shown in Fig. 9.2.2a, however, the ring diameter can be varied). When the mixture ratio gradient was oriented in the radial direction improved stability in the form of a mixed stable and unstable regime was found.[583] Through these and other tests velocity/displacement effects were thus shown to play an important

role in determining the combustor stability (see discussions in Sects. 3.3 and 7.2.5).

Testing these unlike elements (both tangentially and radially oriented) in a variable-angle sector motor (Fig. 10.6.2b) provided frequency dependent limits similar to those of the longitudinal testing.[187] These stability-limits data are directly related to baffle cavity mode instability and illustrate the differences in degree of instability when velocity/displacement fields are altered (even with mode constant) by physical barriers (sector plugs, baffle blades, etc.). Stabilization via mechanical damping devices of such *spontaneous instability* has given indications that the baffle is more effective than the acoustic liner in that case.[192]

In addition to investigations of high frequency instability, unlike doublet injector designs have been used in intermediate frequency research.[181] Variations in the impedance matching of the fuel and oxidizer orifices resulted in alterations of the mixture ratio response, and therefore changes in the incidence of intermediate frequency instability (in that case, instability of the entropy wave type). In the same study another version of the unlike doublet injection added cavitating venturis as an integral part of the injection orifices. This was done to eliminate pressure feedback from the chamber and thus stabilize mixture ratio variations. Problems arose, however, with that venturi placement since reattachment to the divergent walls must occur if the limiting vapor pressure conditions are to be provided at the throats of the venturis. It was concluded that the venturi-type of mass-limiting device was better placed in the feed lines or internal manifolding.[380,574]

All of the preceding discussion, and nearly all of the available theory, concern combustion response and stability where the combustion is occurring under pressures less than the critical pressure of the propellants. An intriguing question arises when chamber pressure is greater than critical. One could easily suspect that liquid droplet combustion, as such, no longer exists in this environment and the resulting stability characteristics should be quite different. Stability in this environment was explored experimentally by Aerojet in their High Chamber Pressure Programs. Results are briefly described here by A. J. Smith, Jr.

Inasmuch as there is a trend toward launch vehicles that are propelled by engines operating at high combustion chamber pressure, the Hi-Pc program was established in an effort to anticipate the combustion instability problems associated with elevated combustor pressures. One of the objectives of the program was to obtain data concerning the role of injector design on the relative stability of the system.[333]

The entire program was divided into four separate studies: (1) initial exploratory study with an injector element survey, (2) scaling effects study with an injector element survey, (3) coaxial injector element study with propellant mixture ratio and velocity ratio survey, and (4) annular combustion chamber study with mixture ratio and velocity ratio survey.[38] The operating parameters that are of interest are tabulated in Table 7.4.2c.

The first two studies tested pentad, coaxial, and conventional injector elements whereas the third study concerned itself strictly with the coaxial injector element. The pentad element, rated at 5000 F/E (i.e., pounds thrust per element) for both studies, consisted of four oxidizer streams impinging on one fuel stream. The coaxial element, rated at 1100 F/E for all three studies,* consisted of an annular fuel stream impinging on a central oxidizer stream. The conventional injector element, rated at 220 F/E for the first two studies, consisted of like-on-like impingement of fuel doublets and showerhead oxidizer. The impingment half-angle used in all cases was 30°.

The results of the first two studies were as follows:[6,18]

1. The conventional injector pattern was unstable at all combinations of chamber length, chamber diameter, and chamber pressures except for the 8-in. diameter, 6-in. length, and 1000 psi chamber pressure condition. One test was spontaneously unstable whereas instability was induced by relatively small pulses for the other unstable tests. The stable test could not be triggered into instability by a moderately large pulse.
2. The coaxial injector pattern was dynami-

* One injector in the third study was designed for 550 F/E.

TABLE 7.4.2c.—HI-PC PROGRAM OPERATING PARAMETERS

Study	Propellant combination	Chamber diameter, in.	Chamber lengths, in.	Nominal thrust, lb	Chamber pressures, psia	Nominal mixture ratio, O/F	Nominal velocity ratio, F/O
Exploratory	LO_2/LH_2	8.0	6.0 12.5 26.0	20 000	1000 1500 2500	5.5	2.93 3.93 4.0
Scaling effects	LO_2/LH_2	14.0	6.0 12.5 26.0	60 000	1000 1500 2500	5.5	3.33 4.16
Coaxial injector	LO_2/LH_2	14.0	6.0 24.0	60 000	1000 2500	[a]5.5	3.0 4.0
						[b]1.0	2.0 6.0

[a] Mixture ratio was varied from 1.4 to 9.6 while the velocity ratio was varied from 12.6 to 2.1.
[b] Mixture ratio was varied from 0.40 to 2.85 while the velocity ratio was varied from 10.0 to 0.70.

cally stable at all of the test conditions except for the long chamber lengths at the 2500 psi chamber pressure condition. A first longitudinal instability was promoted by a small pulse in the 8-in. diameter chamber in contrast to a first longitudinal-second tangential combined mode that was spontaneously induced in the 14-inch diameter chamber.

3. The pentad injector pattern was dynamically stable at all test conditions except for the 14-inch diameter, 24-inch long chamber operating at 1000 and 2500 psi chamber pressure. A first tangential mode was observed in both these cases and was triggered by a moderately large pulse. The 8-inch diameter chamber was stable to pulses of equal or greater size at the same conditions that were previously unstable in the 14-in. chamber.

The conclusions reached after these two studies were:

1. There is no qualitative difference in the general nature of the combustion instability associated with low and high chamber pressure.
2. The sensitive time lag theory could be used as a scaling tool (another objective of the Hi-Pc program) for high frequency instability as long as the injector pattern was repetitive. (Also see Sect. 7.2.1.3.)

No conclusions could be reached as to the effect of orifice hole size or propellant mixing schemes, because both of these parameters were varied between injectors. For example, the pentad injector had much larger orifices than the conventional injector but, at the same time, four oxidizer streams were impinging onto the fuel stream (in the case of the pentad) whereas the oxidizer streams of the conventional injectors were directed downstream without impinging on any other propellant stream.

For the third study,[7] the coaxial injector element was selected as the element to be used because of its popularity among various researchers using this propellant combination.* This study used five injectors with three injectors designed for a nominal mixture ratio of 5.5 (engine condition) and two injectors designed for a nominal mixture ratio of 1.0 (gas generator condition). Two of the engine injectors were designed for

* Further discussion of the coaxial injector element is found in Sect. 7.4.4.

velocity ratios (fuel to oxidizer) of 3.0 and 4.0 while the third engine injector was designed at the same mixture ratio and velocity ratio as another of the engine injectors except that it had twice as many elements as its predecessor. The two gas generator injectors were designed at velocity ratios of 2.0 and 6.0 (see Sect. 7.4.4 for background on coaxial jets).

The results of this program are presented in Fig. 7.4.2g.[333] These figures were made by plotting the observed stability at each given mixture ratio and velocity ratio point. It can be seen that there exists a region of dynamic stability, a region of pulse sensitivity, and a region of spontaneously occurring instability. Any discussion of the drop sizes or mixing effects must give way to other effects that were imposed by the experimental technique. A thorough discussion of this can be found in Ref. 7.

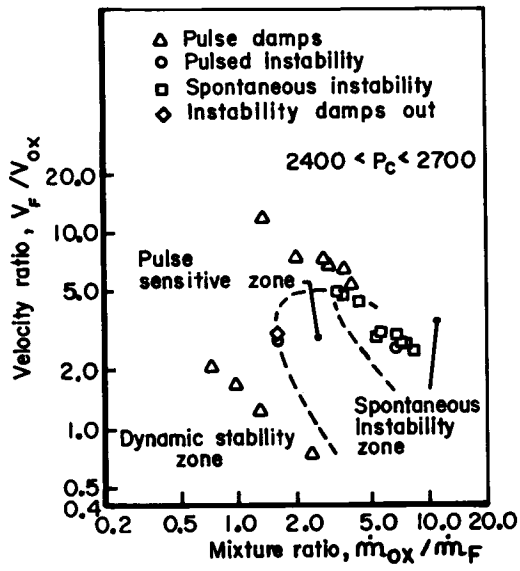

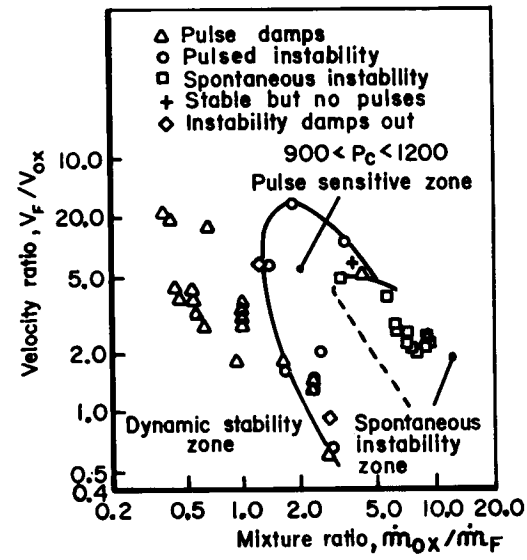

FIGURE 7.4.2g.—Coaxial injector study results.

7.4.3 Like-Impinging Jets

The previous section discussed briefly some of the experimental results of stability programs employing unlike-impinging jet injector elements. There is apparently general agreement in the experiments and in theory on the existence of a frequency-dependent combustion response and on the effects of drop size and injection distribution on stability. Like-impinging jets represent a considerable difference in the physical mechanisms of atomization, mixing and distribution from those with unlike-impinging jets. Here the elements are characterized by two or more jets of the same propellant impinging on one another. This self-impingement forms a droplet spray which is usually perpendicular to the injector face (i.e., heading in a path toward the nozzle). These droplet sprays must then mix and burn with the adjacent sprays of the opposite propellant. Depending on the relative spacing, droplet sizes, etc., the rate of the combustion process can be varied.

Some of the programs conducted with like-impinging jets are summarized in this section. It was indicated in the previous section that unlike-impinging jet injectors appear to be more unstable than like-impinging types. Note that most stability theories do not distinguish between like- and unlike-impinging jet elements other than by a description of the axial combustion distribution.

Among the largest users of like-impinging jet injectors are the Atlas, H-1 and F-1 engines of Rocketdyne. This experience is largely with the LOX/RP-1 propellants. All of the discussion in this section depends on reproducibly providing the injection characteristics which are considered to be related to stability. While this is reasonably simple in research devices and motors, the limitations inherent in development of large engine injectors

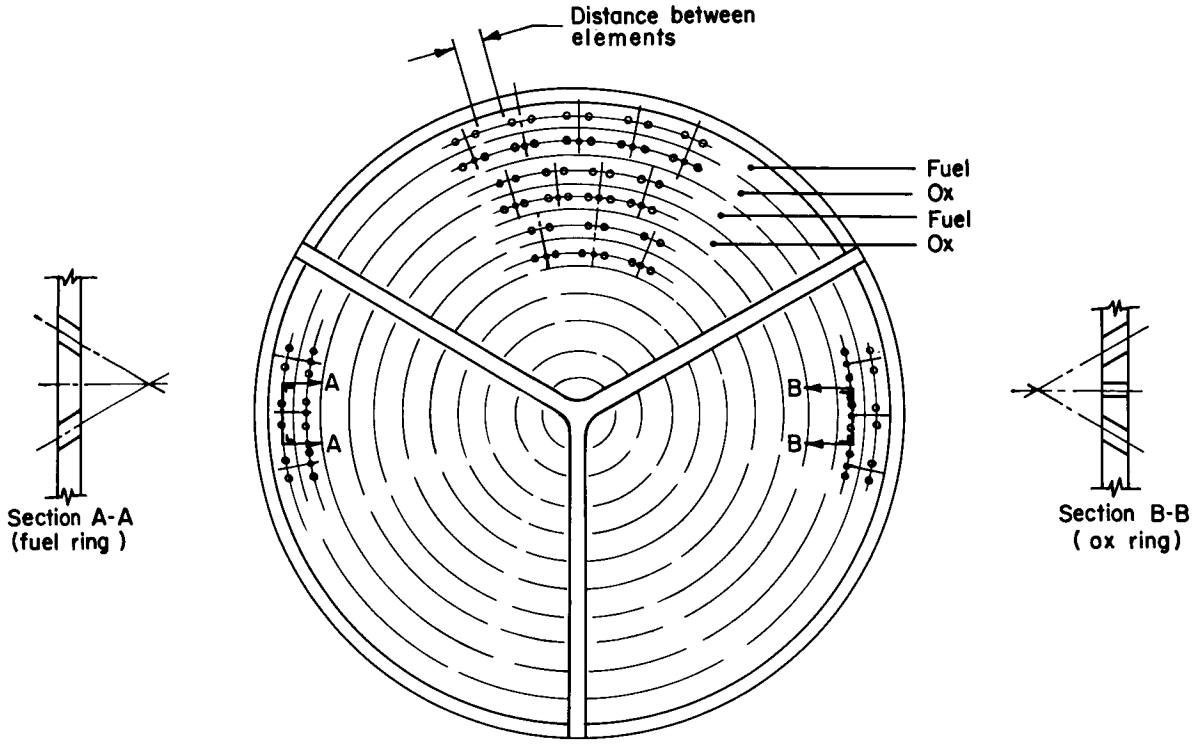

FIGURE 7.4.3a.—Typical injector face pattern using like-impinging doublets and triplets.

complicate the problem. Some general observations on like-impinging jet injector development problems and stability are summarized here by E. C. Clinger.

A majority of the injectors for large liquid rocket engines use like-impinging jets. A typical injector pattern formed of doublet and triplet like-impinging jets is depicted in Fig. 7.4.3a. There are many parameters to consider when such an injector is being designed. The size of the orifices, impingement angle, thickness of the ring, depth of the ring groove, entrance conditions, spacing of the orifices and groups of orifices, impingement point of two or more orifices, and the placement of the orifices with relation to the baffles and the thrust chamber wall. These factors alone or in combination, have an effect on stability, performance, and durability.[21]

The diameters of the orifices play an important part in determining the droplet spray fan characteristics (including the drop sizes generated). Large orifices (0.10-inch diameter and above) cause more concentration of the propellant in the center of the spray and therefore spread the combustion of the propellant longitudinally in the thrust chamber. Smaller orifices generate smaller droplets that provide a more concentrated area of energy release close to the injector face thereby raising the temperature of the injector face and increasing the heat transfer to the propellants being injected. This high energy release near the injector face is often directly associated with combustion instability.

The impingement angle (Fig. 7.4.3b) also affects the resulting droplet size to some degree. The smaller the included impingement angle of the propellant jets, the larger the droplets.[339] The minimum angle, and therefore the largest droplets, would be expected where the orifices are normal to the injector face and thus not impinging on each other (i.e., showerhead injection). The other extreme is where the angle of impingement is very large and the resultant fan or spray is close to the face of the injector. Impingement angles of 30° to 40° are common in large engine design. A buzz-type instability was characteristic of one large engine when the included impingement angle exceeded 55°.

The distance between orifice groups (Fig.

7.4.3a) is another parameter associated with stability. While a wide spacing is beneficial to stability, it can cause problems in heat transfer to the face of the injector and, in some cases, a loss of performance. Certainly, local recirculation is also dependent on spacing.

The point of impingement from the injector face of the two or more jets must also be considered (see Fig. 7.4.3b). This point may vary from a location inside the ring to a spatial distance of an inch or more from the injector face. The farther the impingement point is located from the face, the closer must be the orifice tolerances with regard to angle and size, to avoid misalignment of the propellant jets. Misalignment of the jets prevents full development of the fans because of the loss of the breakup energy. If a gross misalignment of the orifices exists, uncontrolled sprays may even cause instability.

As previously mentioned, spacing of the orifice groups with relationship to each other is important. However, perhaps even more important is the placement or position of the orifice groups with respect to the thrust chamber wall and baffles. This placement must allow for the normal expansion of the fans and the resulting gases (versus wall confinement) so that pressure waves cannot trigger energy release from these baffle or wall regions (see Sects. 7.2.6 and 8.5.3 for further discussion).

Consideration must also be given to the injection velocities of the propellants and particularly the velocity ratio of the two propellants. The injection velocities as well as the orifice sizes and impingement angles determine the nominal drop size distribution of the propellants. Higher injection velocities will form smaller droplets and cause more dispersion (as defined in Fig. 7.4.3c). An injection velocity ratio of 3 to 1 (or greater) of the more volatile propellant to the other propellant has been found to be a *stabilizing influence* in LOX/RP-1 large engine design.

Orifice entrance factors have also been shown to contribute to the stability of an injector design by

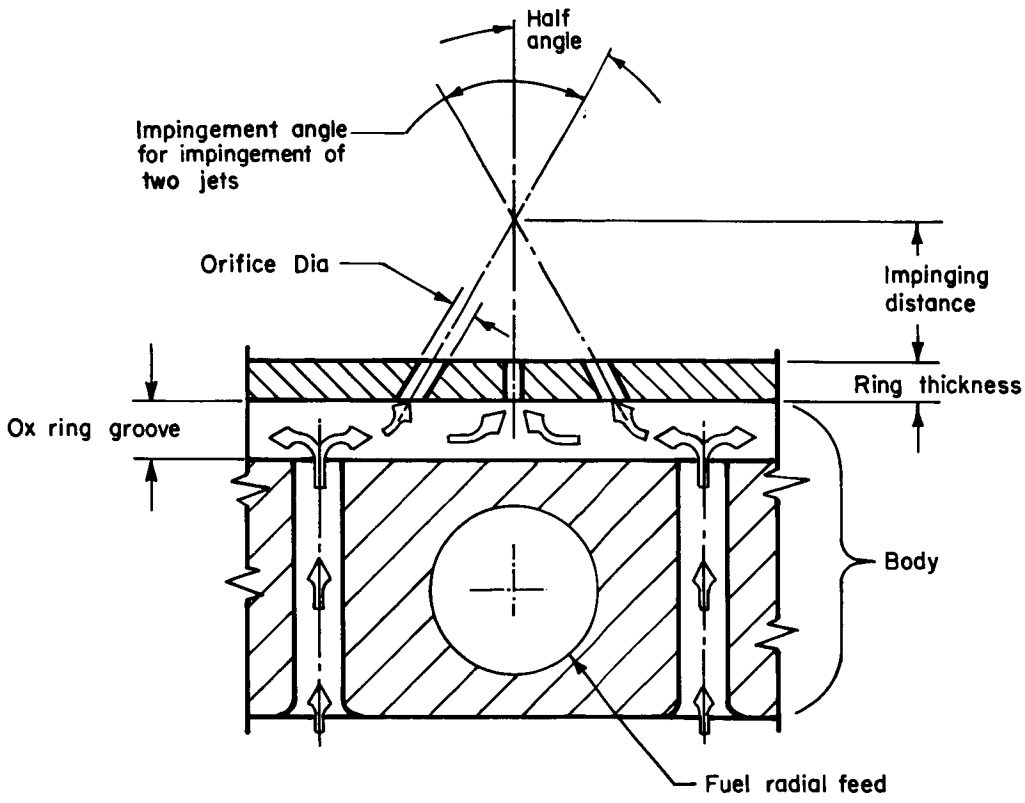

FIGURE 7.4.3b.—Impingement angle and manifold flow for a typical like-impinging design.

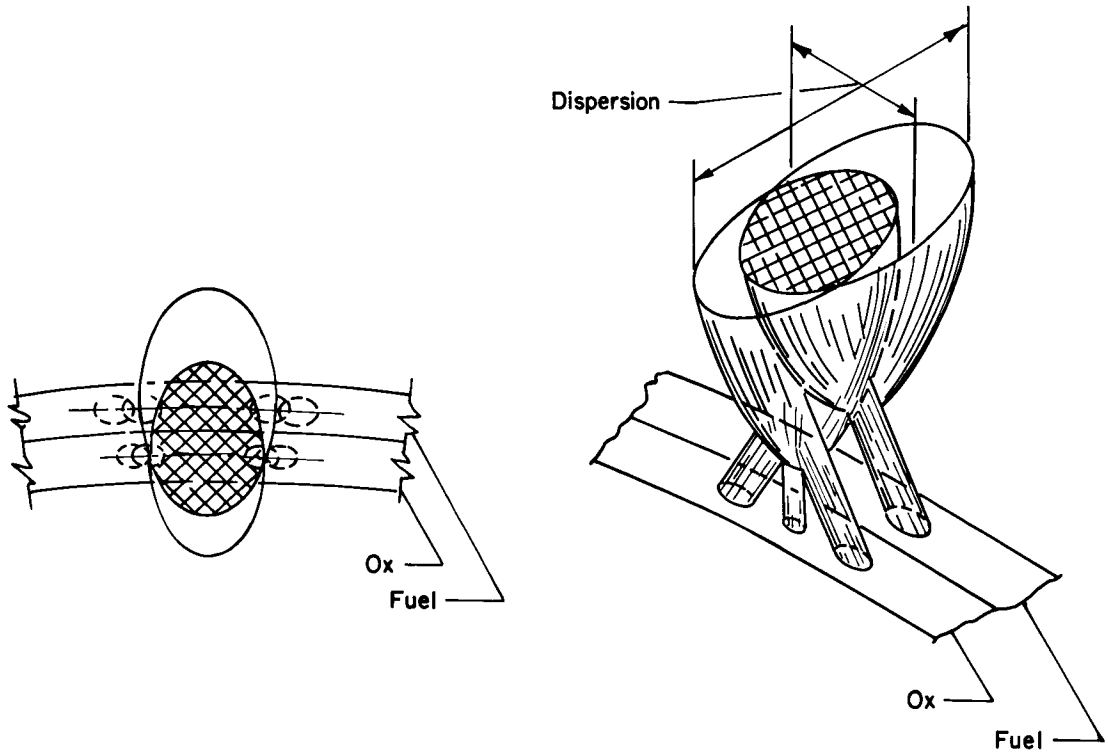

FIGURE 7.4.3c.—Dispersion and the zone of droplet interaction shown schematically for an element composed of a like-impinging doublet and triplet.

influencing the spray fans. Improvement of the orifice discharge coefficient (e.g., use of a ASME rounded entrance) may not result in stability improvement as illustrated in one test series. Another point to consider in orifice design is the thickness of the material containing the injection orifices. This often influences the length to diameter ratio (L/D) of the orifices and this ratio should be such that "hydraulic flip" will not occur over the range of injector operation.

Large engine experience has shown that the manifolding behind the injection ring should have sufficient volume so that the propellant velocities in those locations are low. This allows the developed fans to be perpendicular to the face (Fig. 7.4.3c) rather than being canted because of a higher propellant flow (caused by variations in cross flow) to one orifice as compared to the other. The associated minimum pressure drop also aids in providing the best possible propellant distribution (see Sect. 2.2.1).

The engine configuration normally determines the allowable pressure drop for the injector. An evaluation must be made to determine if this injector impedance is sufficient to inhibit feed system coupled modes of instability (discussed in Chapters 3 and 6). The injector should be designed such that the maximum portion of this impedance is provided as orifice pressure drop (i.e., just prior to injection across the rings in a ring-type injector).

These general comments by Clinger on high-thrust engine design indicate that while many similar stability characteristics are observed with like-impingement (compared to unlike-impingement) the stability improvement has made the like design the popular choice in the large diameter hardware. One difference between the two element types is the large mixture ratio gradients predominant in the like-impinging injectors. The gradients axially spread the combustion reaction while at the same time the transverse mixture ratio variations contribute to potential velocity/displacement coupling between local burning rate and the pressure field.

This effect has been extensively investigated at Princeton University and salient conclusions are discussed here by D. T. Harrje.

In Sect. 7.2.4 axial tailoring of the combustion to the chamber was discussed with reference to combustion instability. Like-impinging designs effectively stretch out the combustion as compared to the unlike types. Three examples of like-impinging injector designs that were used in the Princeton research are shown in Fig. 7.4.3d. Impingement of the streams was either at or behind the injector face, even though such close impingement can result in interaction with the orifice flow.[613] However, benefits result in such designs in that there are no streams of liquid to be displaced by the local velocity field (hence a minimized misimpingement problem), and no backflow can occur. The first design (Fig. 7.4.3d(i)) employs an impingement angle of 55° to produce the ellipitical spray pattern as shown. The orifices are drilled from milled recesses on the injector face. The second design (Fig. 7.4.3d(ii)) uses 90° impinging doublet streams which emanate from a 90° conical recess that restricts the cross section of the spray fan. The third design makes use of a small spray angle and a deep recess to provide further control of the spray fan. The result is a relatively restricted spray angle (Fig. 7.4.3d(iii)). The orifice length to orifice diameter ratio for all of these designs is approximately 5 to 1 with basically a square edge entry condition based on the method of fabrication. Thus, the discharge coefficients are approximately 0.7. Orifice diameters ranged from 0.020 to 0.170 inches in the studies.

In longitudinal instability testing, where unlike-injector designs were previously found to be spontaneously unstable at chamber lengths ranging from 6 to 9 inches[180]; in contrast, the like-impinging doublet designs required lengths of 30 inches or more before instability was encountered. Whereas the unlike-impinging injection pattern showed little effect from pulsing, the like-impinging design responded with expanded resonant combustion regimes in both the longitudinal and the transverse studies[190] (although these regimes were still not as extensive as those associated with the unlike designs). Hence if disturbances are taken into account the relative stability of like and unlike designs must be carefully reassessed.

In an evaluation of the effect of injector pattern interaction on stability, tests were made using a square-motor (representing a small area taken from the pattern of a full-scale injector). Four typical patterns are illustrated in Fig. 7.4.3e. The tests indicated that two of the four patterns were preferred. The Type II pattern, in which the

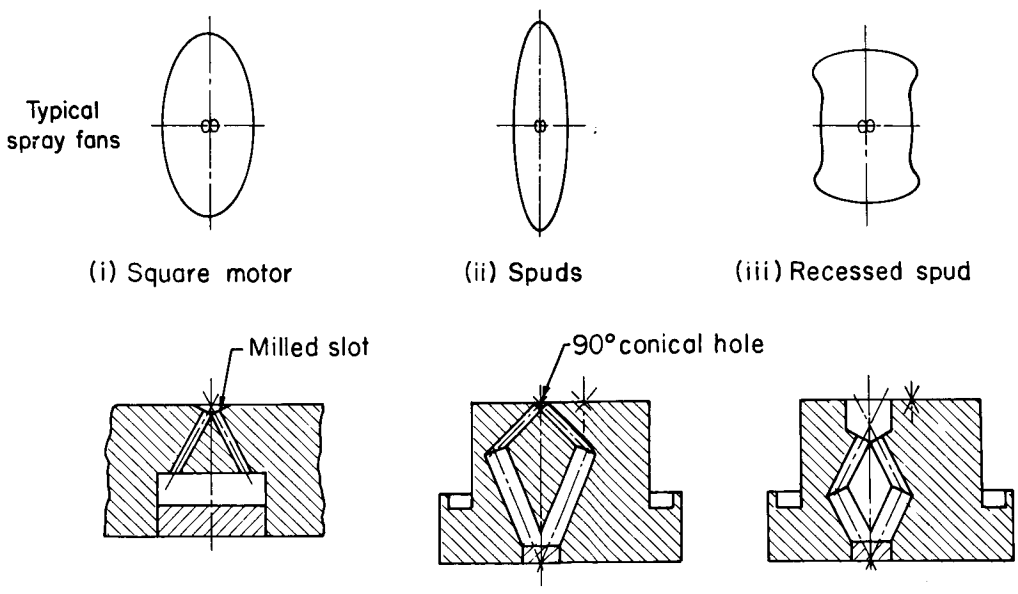

FIGURE 7.4.3d.—Three like-impinging doublet designs in which spray fan cross-section is altered.

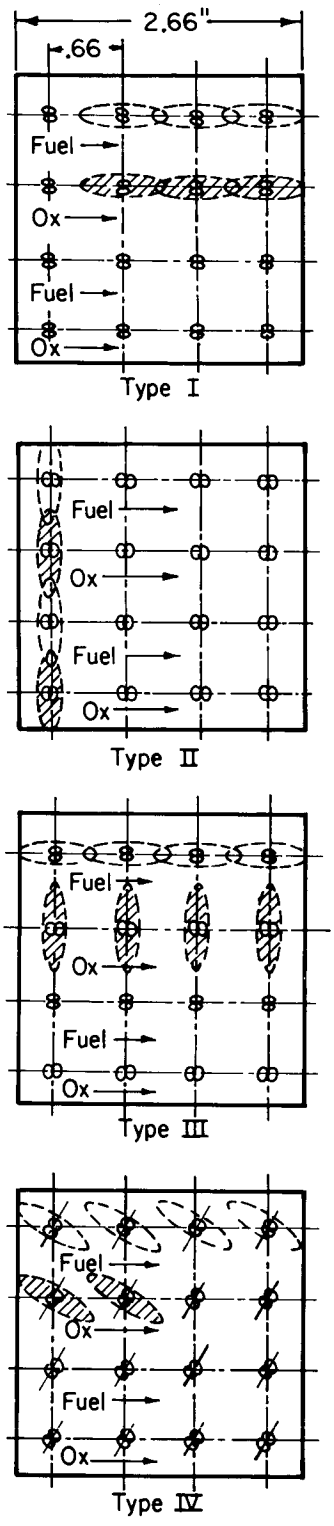

FIGURE 7.4.3e.—Typical spray fan interaction patterns for adjacent like-impinging doublets.

fuel and oxidizer droplet sprays were forcibly mixed with each other, and Type IV, where spray fans were isolated, were found to be superior from a stability standpoint when compared to Types I and III (where like spray fans interacted). One explanation may lie in coalescence of like sprays into large droplets (for Types I and III) resulting in rougher combustion which initiated the triggered type of instability. Certainly the pressure traces of the onset of instability support this explanation.[186] These interactions between adjacent elements illustrate the care which must be exercised when placing hundreds, or thousands, of such elements in close proximity across an injector face.

Evaluation of other like-injector designs, as incorporated in spuds in pulse-motor-type hardware, also revealed that stability was maximized in the case where the unlike spray fans interacted.[186] A prime example is the Type II design where both fuel and oxidizer spray fans are in line (the so-called "zero spacing" design). Because this pulse motor had only a single injection diameter (a single ring of spuds) performance suffered when the propellants on the extremes of the spray fans failed to interact with the other propellant. This would not be the case for the multi-ring injector designs used in the high-thrust

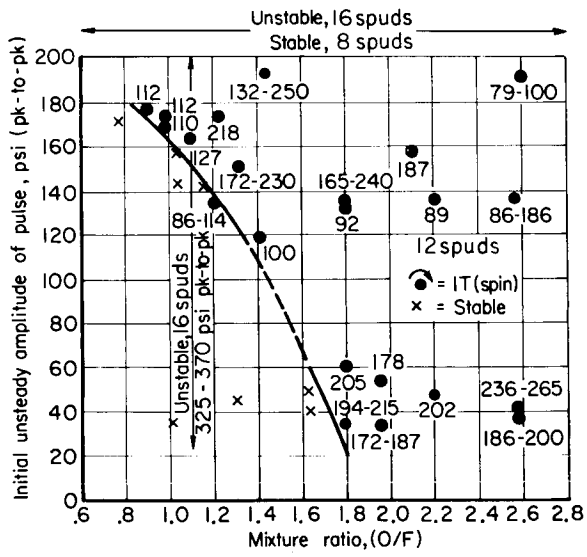

FIGURE 7.4.3f.—Stability boundary for 12 spuds on a 7-inch injection diameter (9-inch-diameter motor). Spacing effects of 8 and 16 spuds are noted.

hardware just described by Clinger. When fuel and oxidizer spray fans were oriented parallel to each other, stability was directly related to factors such as spud orientation, spacing of the spuds and the pressure level in the chamber.

From a spud orientation standpoint, directional sensitivity was to be expected based on the velocity/displacement mechanisms outlined in Sect. 3.3. Depending on the pulse gun orientation, as well as the spud orientation, disturbances were shown to amplify or decay.[190] In a number of cases the nonpreferred initial spinning mode (produced by the pulse gun) decayed only to build up again as an oscillation with the preferred spin direction (refer to Fig. 4.2.2k).

Control of the degree and intensity of instability could be achieved by varying the spud spacing. Spacing the spuds further apart stabilized an otherwise mixed stability region (Fig. 7.4.3f). When the spacing was decreased the test regime was completely unstable and the pressure oscillation doubled.[188] Such spacing is closely related to thrust per element (F/E) and the presence or absence of strong recirculation.

Pressure trends were shown to affect the type and mode of instability using the like doublets (Fig. 7.4.3g). Pressure increases altered the mode preferences to the higher tangential or radial modes* (first tangential modes shifting to second tangential or first radial). Also enhanced were the chances for spontaneous instability as contrasted with the higher amplitude, triggered instability characteristic of the lower chamber pressure operation. Special orientations (6×2, six groups of two spuds alternately oriented) improved stability characteristics.[188]

Spreading the combustion axially in this transverse mode hardware via smaller impingement angles and recessed injection (Fig. 7.4.3d(iii)) further reduced the ability to pulse the chamber unstable. These like-doublet spuds were designed specifically to avoid impinging on the walls of an annular version of the pulse motor.[192] The limited impingement angle has also resulted in reduced

* This follows the pressure sensitivity relationship, $\tau \sim p_c^{-1/3}$, discussed in Sect. 7.2.1.3.

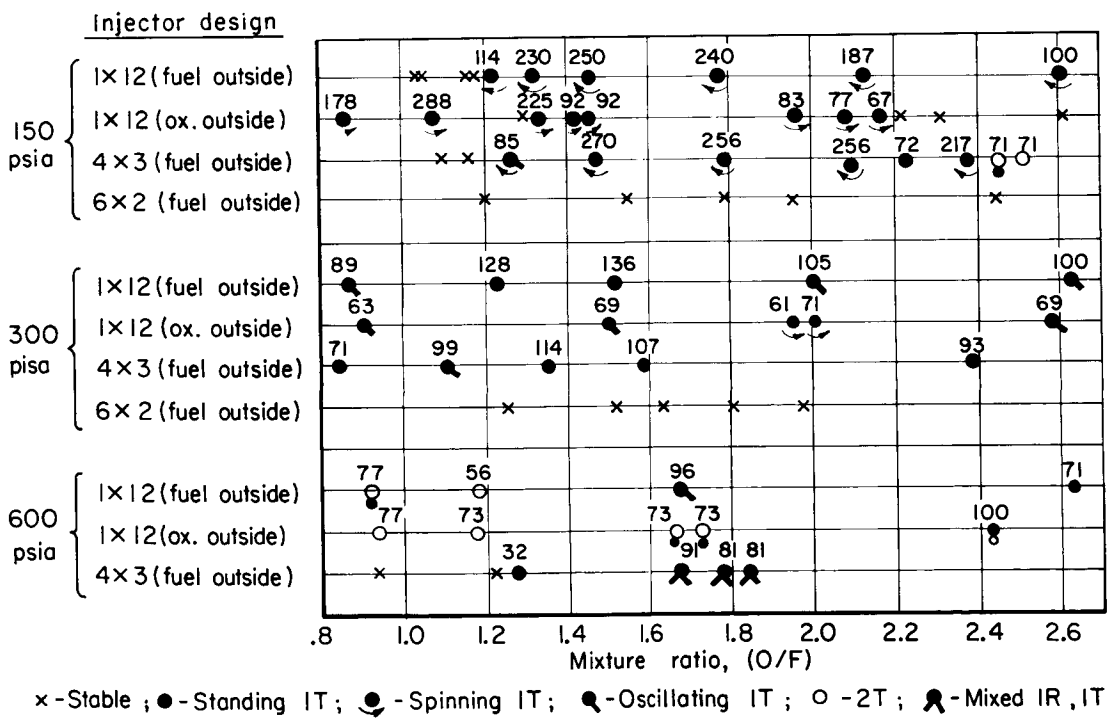

FIGURE 7.4.3g.—Effect of pressure and spud orientation on mode preference for like-impinging injector designs. (Numbers near points indicate peak-to-peak pressure amplitude.)

performance, necessitating a longer combustor length to compensate.

One point concerning like-doublet designs that demands considerable attention is the relative velocities existing between the streams. Control of the axial combustion distribution can be achieved through the sizing of the orifice diameters which, together with the pressure drop, control the velocity of injection. Fig. 7.4.3h provides performance data on variations in the oxidizer orifice size (normally the fuel orifice size, and the resulting fuel droplet size distribution, are considered to control the rate of LOX/hydrocarbon combustion[564]). This rather coarse injection pattern used in the square-motor hardware (fuel and oxidizer doublets were separated by 1.34 inches and hence high c* values could not be expected) illustrates how low fuel velocities (68 ft/sec) used in conjunction with higher oxidizer velocities (112 ft/sec for 2.45 mixture ratio) results in a more stable, slower burning combustion environment[188] (0.12-inch diameter data). In contrast, when the same fuel velocity is compared with lower oxidizer velocity (56 ft/sec as shown by the 0.17-inch diameter results), a less stable, more rapid burning design results from the increased oxygen near the injector. This later arrangement increases the axial burning rate such that the maximum c* values are reached at 25 inches rather than 38 inches (see Fig. 7.4.3h).

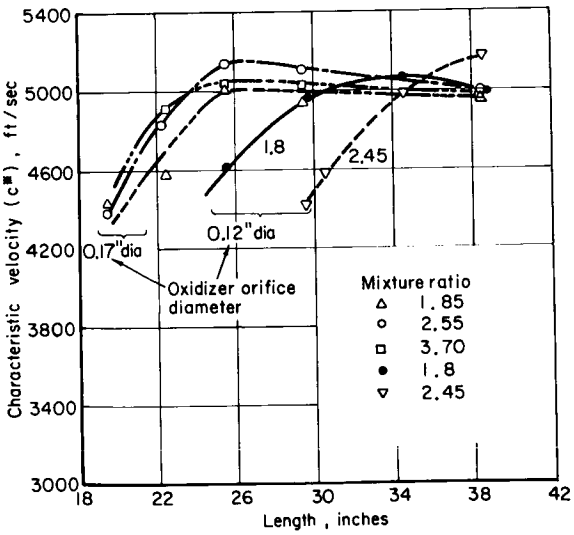

FIGURE 7.4.3h.—Performance versus chamber length for various liquid-oxygen orifice sizes.

Many of the factors that govern combustion and combustion instability on the large scale like-impinging injector designs (e.g., the axial spreading of the combustion) have been shown here to be capable of research and modeling. However, basic agreement as to like-impingement characteristics extends beyond size alone. Propellant combinations other than LOX/hydrocarbon also have been used with this type injection.

An extensive in-house combustion instability study was conducted at AFRPL using other propellants. This study was a careful attempt to use an existing theory of combustion stability to guide the testing so that all factors affecting stability were kept constant except a single variable parameter. General conclusions are summarized here by C. J. Abbe.

A recent experimental study[46] has extensively evaluated the relative stability characteristics of the like-impinging doublet type of injector element as a function of orifice diameter and injection velocity. Testing was conducted in pulse motor hardware (see Sect. 9.2) at 5000 lbs thrust utilizing the storable propellant combination N_2O_4/monomethyl hydrazine. Stability was determined for each test condition by the use of pulse guns (see Sect. 10.3). The relationship between injector orifice diameter and tangential high frequency instability is shown in Fig. 7.4.3i for changes in oxidizer and fuel hole size individually as well as together. All other parameters such as injection velocity, flow rates, impingement angle, and chamber pressure were held constant; therefore, the number of elements was reduced as hole size increased. For all three cases, *larger orifice sizes resulted in improved stability*, with the

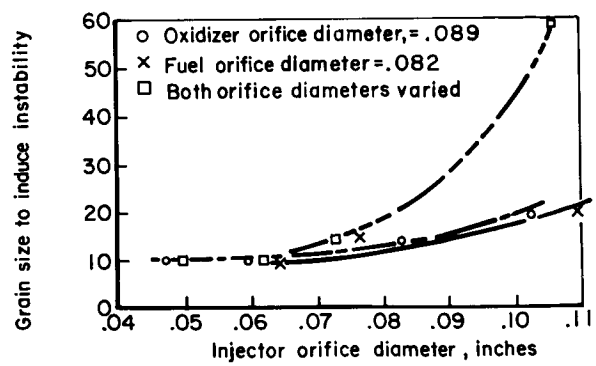

FIGURE 7.4.3i.—Effect of orifice size on high frequency instability.

combined influence of both fuel and oxidizer orifice diameter changes greater than either individually. The primary mechanism whereby larger orifice size improves stability is by increasing the initial average propellant drop size. Larger drops tend to reduce propellant vaporization rates somewhat, which is a stabilizing influence (see Sect. 6.4), and thus, by the same token, decrease combustion performance in volume- or length-limited chambers.[224] An additional stabilizing effect evident in the above data is that as orifice sizes increased and the number of orifices decreased, mass and mixture ratio distribution became slightly less uniform (see Ref. 78, pp. 694–695). However, this is not a major factor in this case.

The influence of injection velocity alone on stability is indicated in Table 7.4.3.[46] These data were obtained using like-impinging doublets and pulse motor hardware. Increased injection velocity improved stability by spreading out the combustion zone and reducing the amount of propellant vaporized at any particular location near the injector face. In these tests, in order to isolate the influence of velocity alone, the injector orifices were made larger as the velocity increased so as to keep propellant drop size constant. The data of Ingebo[375] were used to estimate the effect of injection velocity and orifice size on drop size. In addition, in order to maintain constant flow rate and chamber pressure, the number of elements had to be decreased.

When injection velocity is increased but orifice size remains constant, stability trends are often not clear. The higher velocity in itself tends to promote stability but also results in smaller propellant drop sizes which degrade stability. The data of Ref. 46, taken at constant total flow rate (thrust), show little stability change over a range of injection velocities and constant orifice diameters for self-impinging doublets in the pulse motor.

TABLE 7.4.3.—EFFECT OF INJECTION VELOCITY ON HIGH FREQUENCY INSTABILITY FOR CONSTANT PROPELLANT DROP SIZE

Average injection velocity, ft/sec	Pulse size inducting instability, grains
88	10
117	Stable to 80
125	Stable to 80

From this discussion it is seen that similar characteristics regarding stability are found for this earth-storable combination as compared to the LOX/hydrocarbon types previously discussed. Again the effects of drop size, or thrust-per-element are predominant. A rather clear effect of injection velocity, per se, is indicated although the difficulty of isolating the velocity effect on drop size from the velocity effect alone is also pointed out. Indeed an even broader comparison of injectors would indicate that like-impingement designs have a number of points in common with the unlike designs. Perhaps this is not too surprising if one considers that the like-impinging design is most often used in the relatively long, high-thrust chambers, whereas the unlike designs are most often placed in shorter length, lower thrust units. If combustion intensity is compared with fraction of chamber length, the combustion intensity patterns may be quite similar for the two design types.

7.4.4 Coaxial Jets

Coaxial injection, as the name implies, refers to elements in which a jet of one propellant is injected into the combustor surrounded by an annular jet of the other. Figure 7.4.4a illustrates some typical designs. Coaxial injection elements are in wide use today, but almost exclusively with the oxygen/hydrogen propellant combination. The coaxial element appears particularly adapted to mixing of gaseous propellants, such as hydrogen, with liquid propellants such as oxygen. Much of the obvious difference in the effects of injector design factors on stability between impinging jets and coaxial elements is undoubtedly due to the differences in propellant state rather than to the elements themselves.

One of the propellants commonly used with coaxial elements, however, is a liquid which still must be atomized and mixed with the other propellant, as in the impinging jet-type elements. Certain similarities in stability behavior then should still exist. The effects of liquid droplet size on combustion response magnitude and frequency should be the same with impinging jet and coaxial elements. The difficulty in comparing injector

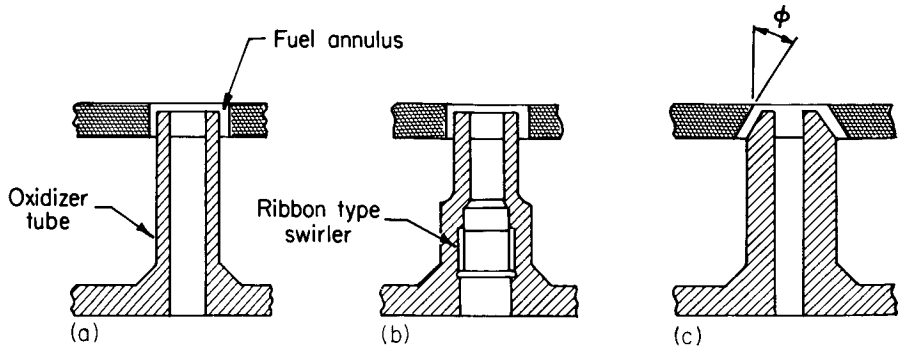

(a) Simple coaxial element. (b) With swirler. (c) With angular fuel annulus.
FIGURE 7.4.4a.—Typical coaxial element configurations.

effects on stability, however, is further complicated by the wide differences in atomization and mixing mechanisms between the element types. Analytical and/or empirical methods to relate coaxial element geometry and operating conditions to spray drop size and distribution are even less known than with impinging jet elements.

Mass and mixture ratio distribution effects should be quite similar and almost independent of the element type. As will be seen in one study in this section, however, the mass distribution effect was found to be exactly opposite to that generally found with impinging jet injectors. This discrepancy is not yet resolved.

Many of the early, engine-development-oriented studies with coaxial element injectors were conducted in support of the RL-10 and J-2 engine programs. Some of the conclusions on injector effects on stability derived at Pratt and Whitney are summarized here by A. I. Masters.

Coaxial or concentric element injectors consist of tubes or drilled posts that provide the flow area for one propellant, and concentric annuli that provide the flow area for the second propellant (Fig. 7.4.4a(a)). Properly designed coaxial injectors provide high efficiency and stable combustion; however, their application is limited by several geometric and fluid dynamic restraints. Propellant atomization is promoted by momentum exchange between the fuel and oxidizer, hence high differential velocities are a fundamental requirement for efficient combustion. With few exceptions,[349] fuel is injected through the annulus at a velocity several times that of the oxidizer. Even when oxidizer atomization is enhanced by a swirl device, such as the ribbon swirler shown in Fig. 7.4.4a(b), high fuel velocities are necessary. For a given oxidizer post diameter, the minimum fuel annulus width that can be maintained (without excessive variation in element-to-element annulus area) dictates a minimum fuel area. Generally, for practical values of thrust-per-element, the fuel flow area must be somewhat larger than the oxidizer flow area. The common requirements of a high fuel-to-oxidizer velocity ratio and a lower limit of fuel-to-oxidizer injector flow area ratio have limited the application of coaxial injectors almost entirely to gaseous fuel-liquid oxidizer applications.

Because most coaxial injector data are based on gas-liquid injection, it is difficult to separate the inherent stability of the element configuration from that of the propellant inlet state. Furthermore, all of the comprehensive studies of stability limits have been with oxygen-hydrogen propellants, thus imposing a further restriction on generalization.

Investigations by Jones[391] and Dahlberg[212] showed that oxygen-hydrogen coaxial injector stability was dependent primarily upon hydrogen inlet temperature, propellant momentum ratio, and chamber contraction ratio, as shown in Fig. 7.4.4b. Other investigations have also shown the importance of hydrogen inlet temperature on stability. Hydrogen temperature (or corresponding density) has such a major effect on acoustic stability that it has frequently been used to rate the stability of the coaxial element design and chamber geometry.[212,311,312,719] All of these investigations have shown complete stability for

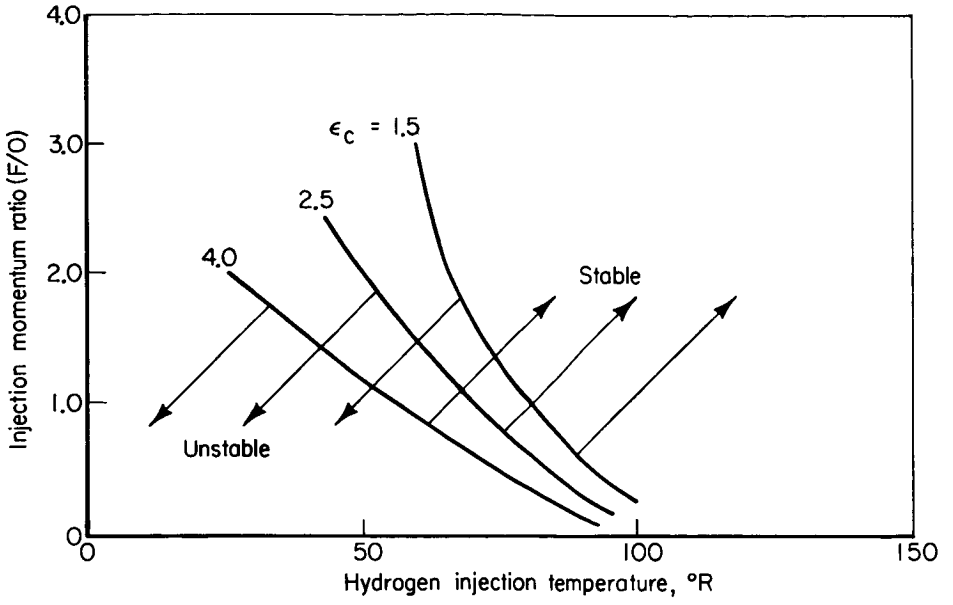

FIGURE 7.4.4b.—Effect of injection momentum ratio and hydrogen temperature on acoustic stability.

hydrogen injection temperatures above 140° R with one exception. Bloomer, et al.[106] found a 15-degree tapered chamber to be unstable at temperatures above 240° R and concluded that the high flow velocity in the chamber near the injector was destabilizing. For a practical injector with fuel-to-oxidizer velocity ratios high enough to produce efficient combustion at design conditions, it is unlikely that acoustic instability would be encountered above 100° R.

Investigations of element design have shown that several variables may be used for acoustic stabilization at low hydrogen inlet temperatures. Stabilization can be accomplished by (1) increasing the hydrogen injection angle (ϕ in Fig. 7.4.4a(c)), (2) optimizing the tube base thickness, (3) recessing the oxidizer tube, and (4) increasing the thrust-per-element. Optimizing one or more of these design variables has produced stable combustion with hydrogen inlet temperatures as low as 50° R.[311] Baffles and acoustic liners have also been used for stabilization at low inlet temperatures. A 20,000-lb thrust chamber, which was unstable at approximately 125° R, was found to be stable down to 55° R with 2-inch baffles.[312] Stable combustion at temperatures as low as 51° R has been achieved with acoustic liners.[285]

Rocket engines using oxygen-hydrogen coaxial injectors include the Pratt & Whitney RL-10, the Rocketdyne J-2, and Aerojet M-1. Due primarily to the relatively high hydrogen injector inlet temperature (300° to 350° R) no high frequency instability was encountered during development of the (~300 psi) 15,000-lb thrust RL-10 engine.[508] As engine "design point" thrust increases, the heat load per pound of propellant is diminished. Thus, with the larger (~800 psia) 230,000-lb thrust J-2 and (~1,000 psia) 1,500,000-lb thrust M-1 engines, instability was of greater concern. M-1 testing with baffled injectors and reduced hydrogen inlet temperatures produced acoustic instability when the hydrogen inlet temperature was reduced to 80° R. Stable combustion was restored as the hydrogen temperature rose to above 100° R. This low temperature limit on stability provided a substantial margin based on the engine design operating temperature of 142° R.[690] Later M-1 injector testing indicated that the baffles did not appear necessary for stable operation at the engine design point.[215]

Coaxial injectors have also been used with fluorine-hydrogen, and mixtures of fluorine and oxygen (FLOX) with methane, propane, 1-butene, and a eutectic blend of pentane and isopentane.

With fluorine-hydrogen, fuel inlet temperatures as low as 216° R, have produced no instability.[72] Additional completely stable results with ambient temperature hydrogen are reported in Ref. 530. With the FLOX/hydrocarbon combinations, all tests have been with fuel inlet temperatures above 500° R, and these tests also have been completely stable.[467]

Masters indicates the predominant effect of hydrogen temperature on stability. This is clearly a function of the gaseous propellant used with the coaxial element rather than the element itself. The same temperature effect exists with LOX/LH₂ propellants in impinging jets. Such injector element design factors as hydrogen injection angle, tube base thickness, recessed oxidizer tube, thrust-per-element and propellant momentum ratio suggest liquid atomization effects similar to those observed with impinging jets. Similar experience with coaxial element injectors, such as those used in the Rocketdyne J-2 engine, are summarized here by J. Campbell Jr.

An injector assembly of coaxial tube injection elements typical of that used in the J-2 engine is illustrated in Fig. 7.4.4c. As shown, the oxygen tubes are recessed and there is an outward flare on the hydrogen tubes (i.e., another variation of Fig. 7.4.4a(iii)). This figure indicates typical flow paths for the oxygen and hydrogen regenerative coolant prior to reaching the injection element. Again, as discussed previously, the injection design relies on a large differential velocity between fuel and oxidizer to accomplish the desired mixing and breakup of the propellants. Hence the design favors propellant combinations in which one of the injectants is a gas. Most oxygen-hydrogen engines have injected the hydrogen as a gas, at the 150° to 400° R temperatures provided by a regenerative chamber. These injectors typically furnish c* efficiencies on the order of 98 percent of theoretical equilibrium value, have a peak-to-peak chamber pressure variation on the order of 1 percent of "mainstage" chamber pressure during stable operation, and are extremely durable.

Engine experience agrees with the previous discussion in that the operating condition having the greatest influence on the excitation of combustion instability (with a given regenerative chamber and LOX/LH₂ concentric orifice injector) is the temperature of the injected hydrogen.

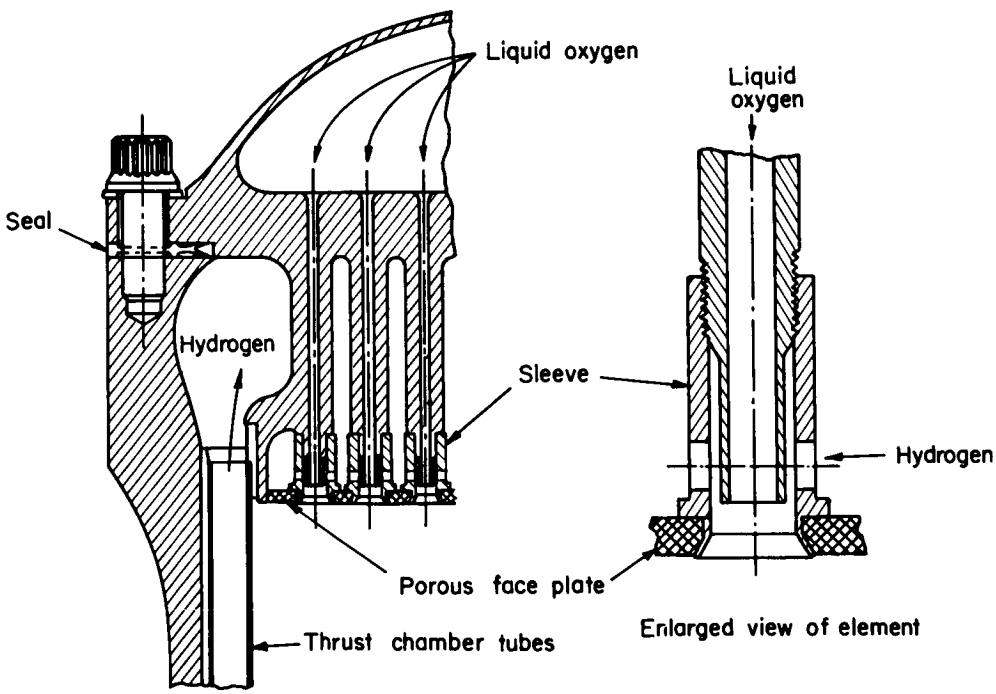

FIGURE 7.4.4c.—Typical O_2/H_2 concentric orifice injector.

The injection elements are sized for operation under normal steady-state temperature conditions but may be required to accept much lower hydrogen temperatures during the engine start transient. Such a coaxial injector usually has a lower limit of safe operating hydrogen temperature, which is a function also of chamber pressure and mixture ratio. If operated for more than a fraction of a second below this limit a combustion instability will be excited. Conversely, operation at normal temperature levels is very stable and combustion pops are not present. The problem in LOX/LH_2 engine development is usually that of developing an adequate low temperature stability margin. There is some thought that orifice configurations providing improved resistance to resonant combustion associated with low temperature hydrogen also provide improved resistance to triggering by artificially imposed disturbances. Such a relationship is presently unproven.

The instabilities encountered with oxygen-hydrogen coaxial injection are typically much less damaging to the injector and thrust chamber than are instabilities with other injector types and other propellant combinations. This characteristic sometimes makes it feasible to experiment with coaxial injection systems by progressively reducing hydrogen temperature until resonant combustion is induced (see Sect. 10.6.1). If desired, it is also possible to then raise the temperature to determine if the instability will cease. Adjustment of the physical parameters of the injection system can be made and their effects on the resonant combustion zone determined. In this manner the injector can be developed to meet the requirements of the engine system, or the stable region of the injector defined.

The operating parameters that appear to affect excitation are chamber pressure, mixture ratio, and hydrogen temperature. Oxygen temperature is assumed constant at about 165° R. The hydrogen temperature at instability threshold is also affected by the intimate physical details of the injection element design. The effects of variations in these details can be conveniently observed by plotting experimental data in the format of Fig. 7.4.4d. At a given oxidizer flow the element pattern least sensitive to resonant combustion, and therefore described by a low hydrogen temperature, will permit stable operation with the lowest ratio of fuel flow to the square root of fuel density.

The plot format of Fig. 7.4.4d is based on the assumption that the initiation of an instability with a given injector pattern, and with a given oxidizer flow, is dependent on reaching some lower limiting ratio of hydrogen to oxygen momentum. For a given injector this assumption appears to hold over a wide range of chamber pressures, mixture ratios, and hydrogen temperatures, but

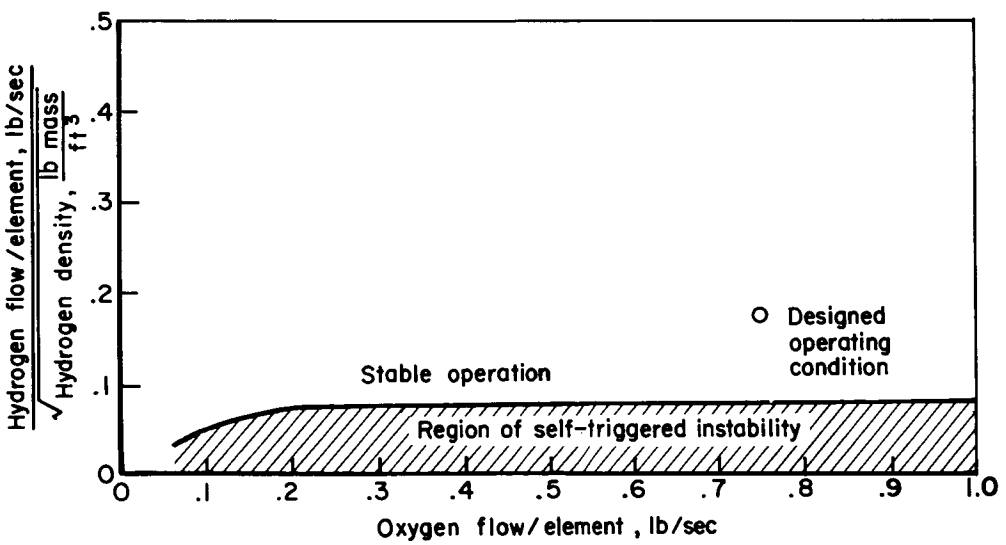

FIGURE 7.4.4d.—Typical self-triggering experimental results for one injector design.

prudence would advise gathering experimental data in the region of operating interest. Caution is also indicated with regard to data collected below the 188 psia critical pressure of hydrogen, where pressure and temperature do not completely determine the density of hydrogen.

The physical parameters which appear to influence instability threshold temperatures are as follows:

1. High relative fuel and oxygen velocities are desirable. Typical design values under mainstage operation are about 50 feet per second oxygen velocity and about 700 feet per second hydrogen velocity. The experimental work at constant 300 psia chamber pressure reported in Ref. 719 was found to be well correlated by the observation that instability would result if the ratio of hydrogen to oxygen injection velocity was permitted to drop below 6.5 during low temperature operation. This applied to nonrecessed elements.
2. A slight recess of the oxidizer orifice below the exit of the fuel annulus has a marked beneficial affect. Typically a recess of 0.2 inch, or a length to diameter ratio of the recess on the order of 0.6, is appropriate. A 0.1 inch recess of the element of Ref. 719 improved the stability margin by about 50° R. A 0.2 inch recess of the J-2 element improved the stability margin by about 25° R. Recessments to 0.5 inch were evaluated in Ref. 311. Recessment also increases both fuel and oxidizer pressure drops.
3. Experience in J-2 and M-1 engine development indicates that the addition of conventionally spaced baffles to the injector face does not prevent resonant combustion caused by low hydrogen temperature, nor greatly affect the temperature at which the instability occurs. Such baffles do appear to moderate the intensity of the chamber pressure excursions during the instability, and they probably aid in re-establishing stable operation if engine operation is moved into a "normally stable" region.[215] The previously mentioned research on a 20,000 pound thrust 300 psi motor indicates that the addition of *finely* spaced baffles can *lower* the triggering temperature (see Sect. 8.2.2.1).
4. Since control of the entrance flow conditions are extremely important, icing of the orifices must be avoided (by appropriate drying conditions prior to firing). Also, thin oxidizer post tips should be used (with a typical thickness 0.030 inch or less). Injection other than through the elements themselves must be avoided (e.g., flow from cracks in the regenerative coolant tubes). Low frequency feed system instability should also be avoided since it may act as a triggering mechanism.

Both Masters and Campbell have indicated the strong effect of hydrogen temperature on stability as well as observed effects of some injector design factors and operating conditions. Campbell points out that the critical low hydrogen temperature region may often be reached during the engine start transient. There appears to be general agreement that excellent stability can be maintained in LOX/LH$_2$ engines if the hydrogen is used as a coolant and never allowed, even in the start transient, to reach the transition temperature.

Much of the stability research with coaxial injector elements and the LOX/LH$_2$ propellant combination has been done at the NASA Lewis Research Center. This work is often done in direct support on stability problems in NASA LOX/LH$_2$ engines, as is evidenced by the cross references among the three writers on this topic. Some of the conclusions on the effects of coaxial injector design factors on stability, derived at NASA Lewis, are summarized by J. P. Wanhainen.

The desirability of providing a high hydrogen injection velocity and a low oxygen injection velocity has been previously discussed. More recent tests at NASA Lewis Research Center[719] determined that the minimum stable hydrogen injection temperature, which was used as a stability rating technique (Sect. 10.6.1), varied almost linearly with the ratio of hydrogen to oxygen injection area as shown in Fig. 7.4.4c. The experiments were conducted with 421 element, 10.78-inch diameter injectors in 20,000-pound thrust engines operating at a chamber pressure of 300 psia. Stability improved as the injection area ratio was decreased until the transition temperature was below the minimum value obtainable

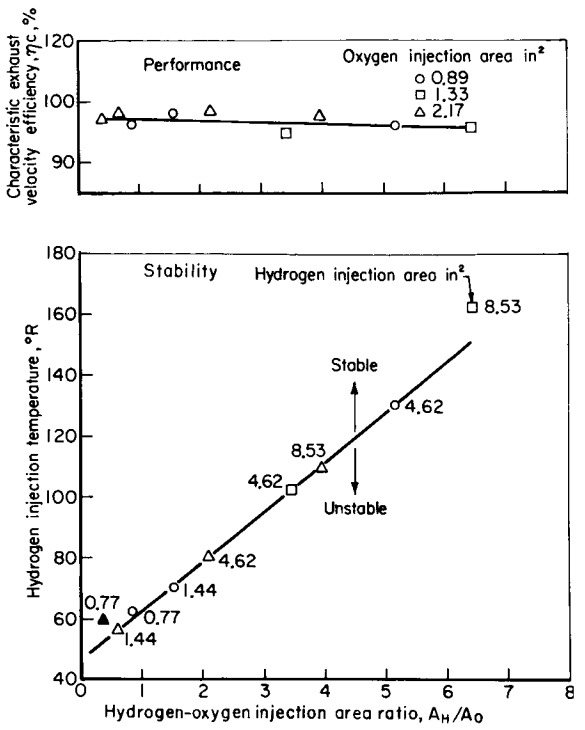

FIGURE 7.4.4e.—Correlation of instability limits with injection area ratio at O/F = 5.

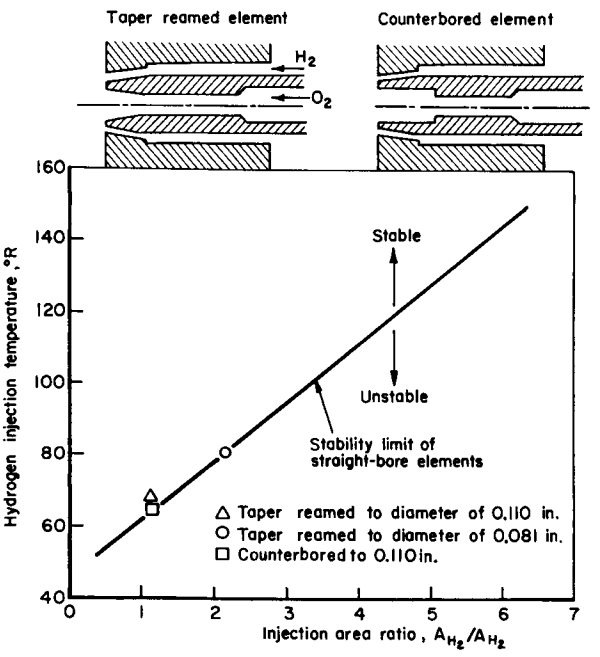

FIGURE 7.4.4f.—Correlations of instability limits for tapered and counterbored oxidizer tube configurations with area ratio at O/F = 5.

with the facility (55° to 60° R) at area ratios below about 0.5. It is important to note in Fig. 7.4.4e that, for these relatively fine pattern injectors, the improved stability was achieved with no decrease in performance. Values of characteristic exhaust velocity efficiency above 0.97 prevailed to values of hydrogen temperature as low as 60° R.

The relation between the minimum hydrogen temperature for stable operation and the injection configuration (taper-reamed, counterbored and straight bore oxidizer tubes) is illustrated in Fig. 7.4.4f in terms of the previous established correlation parameter of injection area ratio. The temperature limits for both tapered and counterbored configurations show good agreement with straight bore configuration data when based on exit area ratio. The use of taper or counterbore techniques, therefore, will allow the large oxidizer tube exit area needed for suppression of resonant combustion as well as maintaining adequate injector pressure drop to avoid chugging instability.

Another injector design parameter that influences stability of LOX/LH_2 combustion (using coaxial tube injectors) is injector element radial distribution. Typical stability limit points are presented in Fig. 7.4.4g for several 397 element injectors in 20,000-pound thrust engines operating at a chamber pressure of 300 psia.[718] Note that the nozzle throat diameter was constant (7.82 inches), thus, in the cases where chamber diameter was varied to change face coverage, contraction ratio was also a variable. At any given element spacing, the minimum stable operating hydrogen injection temperature varied linearly with face coverage without any apparent independent effect of chamber diameter or contraction ratio. At all chamber diameters the results show, that for maximum stability, the injectors should be designed for 100 percent face coverage without voids at the chamber wall.*

* The anomaly between the destabilizing effect with reduced face coverage cited here and the stabilizing effect previously described (Sect. 7.2.5) could be associated with the differences in atomization and mixing characteristics between element types with various propellants. These differences could depend on such factors as flow rate per element (thrust per element), contraction ratio and cross velocities (radial winds). Some of these parameters must vary in an experimental study of injector face coverage.

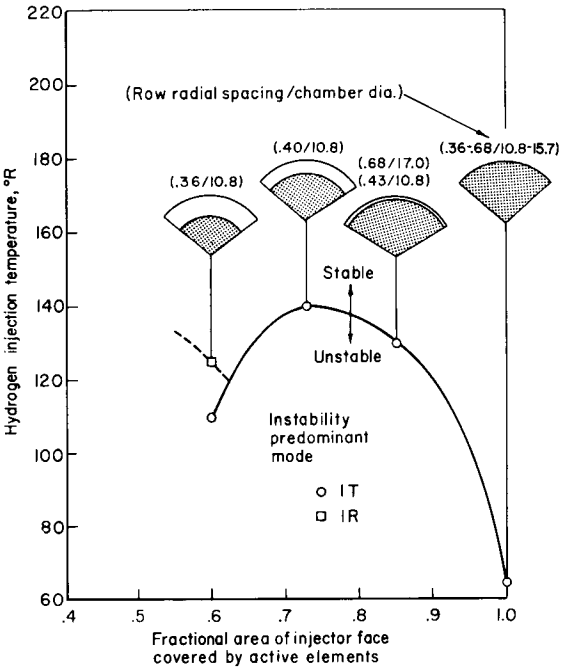

FIGURE 7.4.4g.—Effect of element radial face coverage and element spacing on stability limits. O/F = 5; throat diameter, 7.82 inches.

A parameter of interest not only from the viewpoint of stability but also from economic considerations is element size. Summarized in Fig. 7.4.4h are results of experiments in a 20,000-pound thrust size engine[624] using injectors with varying number of coaxial tube elements from 8 to 992. In 10.78-inch diameter thrust chambers, injectors with 100 elements or less operated stably to a hydrogen temperature of 60° R (minimum obtainable with the facility). The stability characteristics of the 35 and 20 element injectors were further evaluated near this temperature limit by bombing with four successive 45 grain charges of RDX (MIL-R-398) explosive. In each case, the resulting perturbations were damped within 20 milliseconds. The utility of this technique as a solution to the acoustic mode stability problem depends also on the effect of element size on combustion performance. Referring to Fig. 7.4.4h, the loss in performance to provide stable combustion down to a hydrogen temperature of 60° R was small. The characteristic exhaust velocity efficiency of the 100 element injector was 95½ percent which represents a loss

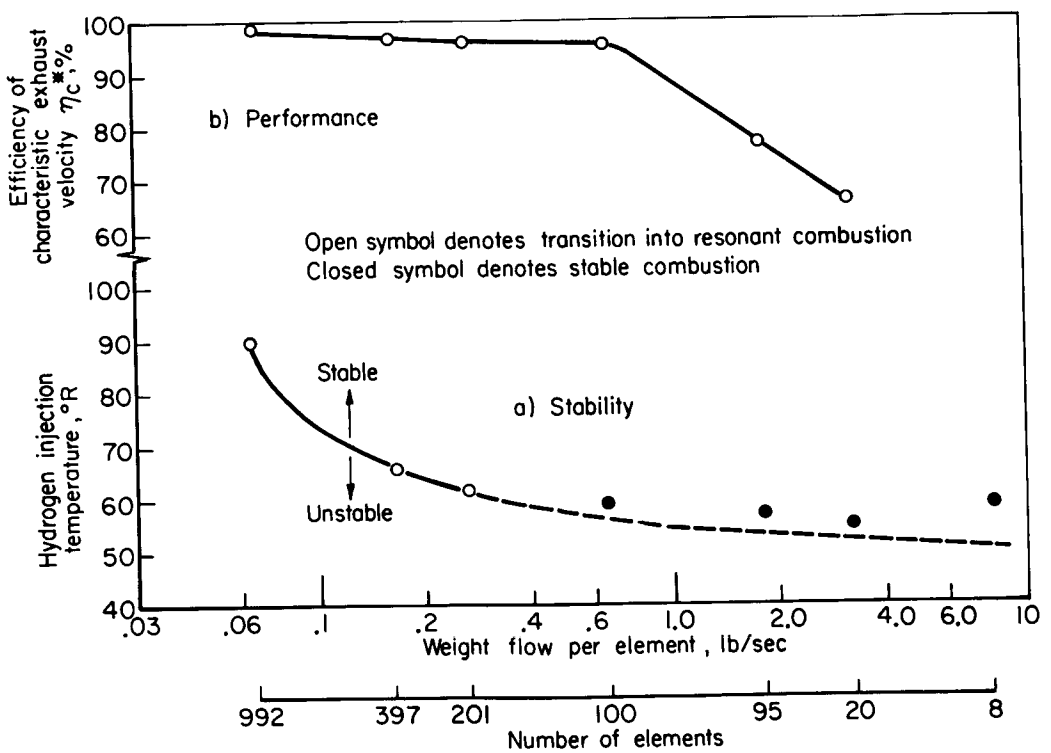

FIGURE 7.4.4h.—Effect of weight flow-per-element on hydrogen temperature stable operating limits. O/F = 5.

of only $3\frac{1}{2}$ percentage points. At higher weight flows per element, the loss in performance was more serious, however, it should be noted that the injectors were not an end product of development and improvements in performance could be made by proper design.[310]

Two other coaxial tube element variables which are likely to affect drop size and, therefore, combustion stability are stream impingement angle and oxygen tube recess depth. The effect of variations in these parameters on stability are shown in Fig. 7.4.4i and Fig. 7.4.4j. The tests[311] were conducted in 20,000-pound thrust engines using 157 element concentric tube injectors operating at a chamber pressure of 300 psia. Stability varied linearly with impingement angle and improved as the angle was increased from 0° to 45°. Recessing the oxidizer tube improved stability continuously with depth until complete stabilization was achieved at a depth of 0.35 inch. In regard to performance, the element modifications had no major effect on engine performance over the range of variables investigated.

Oxidizer tube eccentricity and oxidizer tube base thickness do not appear to have a strong effect on stability. Summarized in Fig. 7.4.4k are results of experiments in a 20,000-pound thrust size engine[311] using injectors with 157 elements. The use of washers to insure concentricity of the oxidizer tubes within the fuel annuli produced no measurable change in stability limits compared to an injector without washers and, therefore, a random concentricity due to normal manufacturing tolerances.

In summary, significant improvements in stability on the hydrogen temperature stable operating limits can be accomplished by proper selection of several injector design parameters. The variation in hydrogen transition temperature for resonant combustion is also predictable for several design and operating variables with the correlating parameter.[716]

$$T_{H_{trans}} \approx \left(\frac{p_c}{\Delta p_H}\right)^{1/2} \frac{1}{\rho_{ox} d_{iox}^{1.25}} r^{1/2}$$

where $T_{H_{trans}}$ is the hydrogen transition temperature for resonant combustion, p_c is the chamber pressure, Δp_H is the hydrogen injector differential pressure, ρ_{ox} is the oxygen density at injection, d_{iox} is the oxygen injection orifice diameter, and

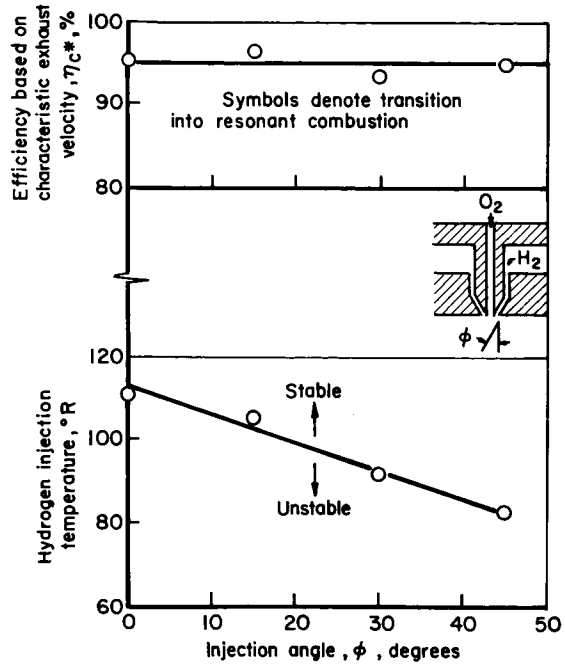

FIGURE 7.4.4i.—Effect of injection angle on stability. O/F = 5; 157-element injector.

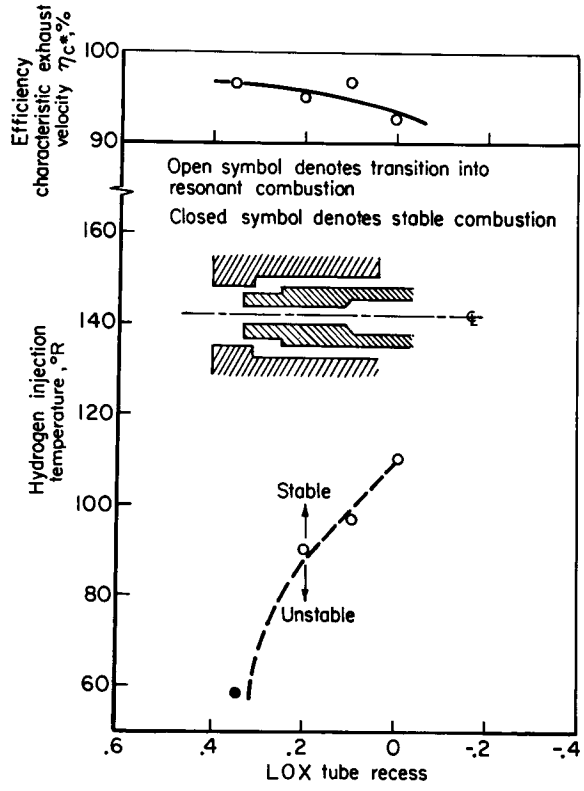

FIGURE 7.4.4j.—Effect of LOX tube recess on stability. O/F = 5; 157-element injector; parallel streams.

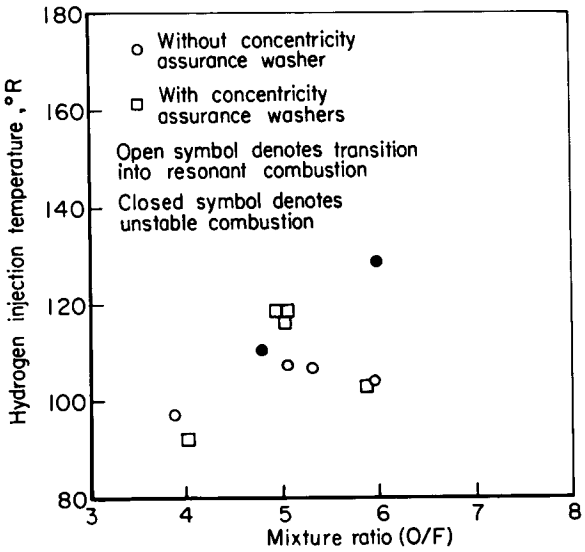

FIGURE 7.4.4k.—Effect of oxidizer tube eccentricity on stability. 157-element injector.

r is the mixture ratio. This equation also provides some insight to the combustion instability phenomenon in oxygen-hydrogen rocket engines. Considering parameters of the equation related only to the hydrogen system and neglecting the minor contribution of the oxidant-fuel ratio term, hydrogen injector pressure drop is seen to be the real determinant of the resonant combustion boundary at any given chamber pressure operating condition. It must be noted that increasing pressure drop to promote stability is not limited to changes in injection flow area and may be achieved through changes in orifice hydraulic characteristics with the same effect on stability. Parameters related to the oxygen system influencing stability are the oxygen density and the oxygen jet diameter. The oxygen droplet size will vary with orifice diameter and since the oxygen response factor depends strongly on drop size, a strong influence on stability might be expected. The effect of oxygen temperature is less obvious, however, it may be associated with the physical properties of the fluid.

Wanhainen shows, in Figure 7.4.4g, the result that concentrating the propellants near the center of a LOX/LH$_2$ coaxial injector tends to make the combustion more unstable. This is contrary to the theory and experiments cited earlier for impinging jet injectors with different propellants. This result should be kept in mind in the discussion, in the following section, on the TRW injector. Wanhainen notes that chamber diameter and element spacing were varied in order to vary the face coverage. This could change the combustion characteristics and thereby offset the expected stabilizing effect of face coverage. Harrje, earlier in this section, has shown that element spacing and orientation influence stability with impinging jet injectors. Also, when element geometry and spacing are held constant, stability has also been shown to depend on chamber diameter which changes the transverse mode frequencies. In order to draw a firm conclusion on the sole effect of face coverage, from experimental data, a much larger test program is necessary in which all possible effects are in some way accounted for.

Wanhainen shows several element design factors that could be expected to affect oxidizer drop size which also strongly influence stability. Certainly the ratio of hydrogen/oxygen injection area, weight flow rate per element, stream impingement angle and oxygen tube recess depth should have some effects on drop size. The effect of these factors on drop size, however, is not well known, in direction or in magnitude. One might expect the increase in weight flow per element to result in larger drop sizes and, therefore, in greater stability. This result is shown by Wanhainen, in agreement with other data with impinging jet injectors.

7.4.5 Other Injector Element Types

The results reported thus far in this section have concerned injectors using impinging jet or coaxial elements. These are by far the most widely used types of injector elements. There are two other unique injector types in use today that deserve some comment. One is the centrally located injection system used by TRW in the LM descent engine, and the other is the vortex injector concept used by RMD in the Surveyor Vernier ACS engine system.

The TRW concept depends largely on radially non-uniform injection distribution for stability. This is similar to the radially non-uniform, axial injection schemes discussed earlier with more conventional impinging jet or coaxial element injectors. These data support the conclusion that injectors which concentrate propellant nearer to the center of the chamber tend to be more stable (there is, of course, the completely opposite result with coaxial tube injectors reported by Wanhainen). Also, an

injection distribution which minimizes the energy release in the region of the pressure anti-node for one transverse mode must, necessarily, maximize the energy release in the pressure anti-node of some other transverse modes but due to frequency considerations the latter may not be important. The stability results obtained with this injector concept are considered further evidence of the greater stability of a properly designed radially non-uniform injection scheme and are discussed by H. L. Burge.

When acoustic instability modes and coupled energy release profiles are examined in conventional rocket engine combustion chambers, it is possible to postulate various means of injection to minimize susceptibility to coupling between the chamber natural acoustic modes and the combustion energy release (see Sect. 7.2.5). This approach has been taken with the TRW injector concept.[243,245] This concept employs a centrally located injection element as shown in Fig. 7.4.5a. This injector utilizes an annular sheet of fuel which impinges into a radial fan of oxidizer, created by selected sizing of slot-type orifices. Part of the fuel is allowed to flow in between the orifices and with hypergolic propellants the elements are sized such that the resulting gas phase reactions are interlocked within the radial oxidizer fan to promote further local mixing and atomization. Through control of the oxidizer/fuel pressure drops and oxidizer sizing geometry the combustion profile can be controlled to provide mixture ratio temperature control near the combustion chamber wall as well as overall energy release proximity to the injector. The injection impingement point can be located axially within the chamber to provide space for heat transfer control as well as recirculation mixing for performance. It is recognized that the possible locations for abnormally high energy release in a combustion chamber can have a dominant effect on whether the engine will be dynamically stable or not (without aid of mechanical damping).

If a large local pressure pulse is generated in a region corresponding to a pressure antinode for a given acoustical mode, the probability of that mode being initiated will be high. If unburned propellants exist in a mixed or near mixed condition in the pressure antinode region, the pressure disturbance can result in accelerated burning rates and consequent energy release by enhancing pressure sensitive reactions and mixing to drive the mode. If the propellant feed into the zone is

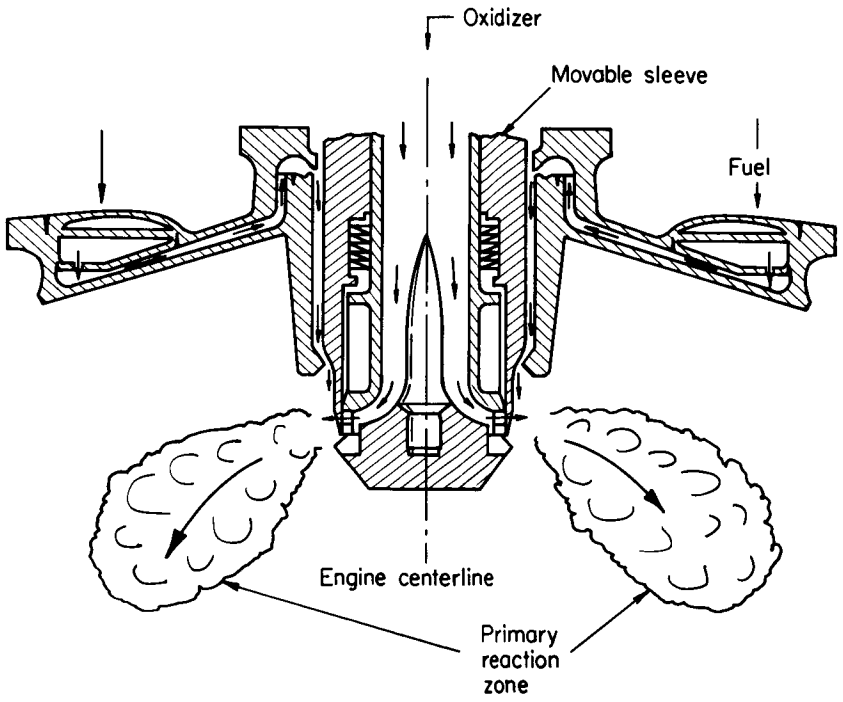

FIGURE 7.4.5a.—Central coaxial flow injector with throttling sleeve.

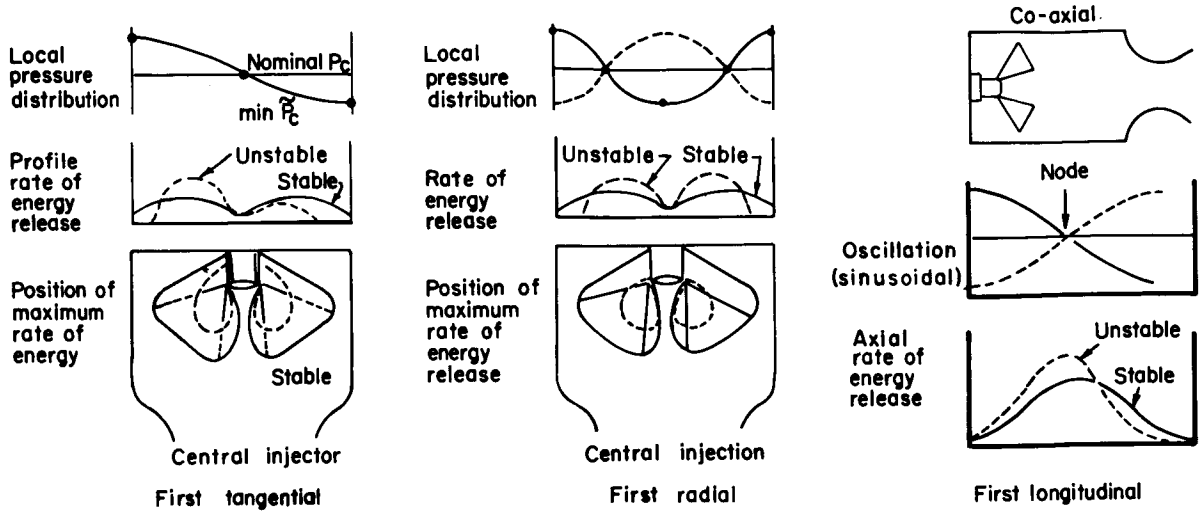

FIGURE 7.4.5b.—Schematic comparison of resonant combustion and steady-state energy release patterns for central injection.

sufficient and time phase matched to the passing wave the mode will be sustained.

For comparison purposes the pressure nodes and indications of energy release profiles are shown in Figure 7.4.5b for the tangential, longitudinal, and radial fundamental modes. Since the tangential modes are usually most damaging in development programs, attention is first given to these modes. The local pressure distribution for a fundamental tangential wave is seen to be most susceptible to continuous excitation through energy release at the circumferential boundary of the chamber. The stabilizing nature of the centralized injection to this mode is brought about in the following manner; increased combustion rates force the combustion zone toward the source of the propellant, which in this case is at a pressure node. Therefore, a pressure pulse induced combustion wave which moves toward the nodal point of the system becomes less effective to sustain the tangential mode of instability, thus providing some measure of damping.

With respect to the longitudinal mode the injection and combustion regions are removed from the antinode region, and the injection densities are high in the center of the combustor. Thus, for a given chamber length the stable maximum energy release occurs nearer the pressure node. A pressure disturbance cannot drive the energy release profile uniformly to the antinode region to result in a sustained longitudinal wave.

The use of high injection density near the mid-radius of the combustion chamber also tends to prevent the establishment of the radial mode of instability. As illustrated the normal maximum energy release zone is near the pressure node of the radial mode. A continued displacement of energy release from this region is difficult to sustain.

The concept has been employed in engines ranging in size from 25 lbf to several hundred thousand lbf, with dynamic stability demonstration at each thrust level. Propellant combinations have included: N_2O_4/UDMH, N_2O_4/50% N_2H_4-50% UDMH,[325] F_2/N_2H_4,[532] FLOX/LPG,[458,750] CTF/Gelled Fuel,[83] N_2O_4/N_2H_4.[85] A typical chamber pressure recovery for the LMDE engine from a bomb detonation is given in Figure 7.4.5c at varying degrees of throttling.

The other injection design to be considered here was not conceived to insure stability. Rather, the RMD vortex-type injector seeks to improve performance and control heat transfer for size-limited rocket designs. The design and stability history is discussed by J. J. Lovingham.

Vortex injection provides a form of swirl or cyclone combustion for a rocket engine similar to systems often employed in industrial furnaces. The latter promote efficient combustion of pulverized coal, liquid and gaseous fuels. When

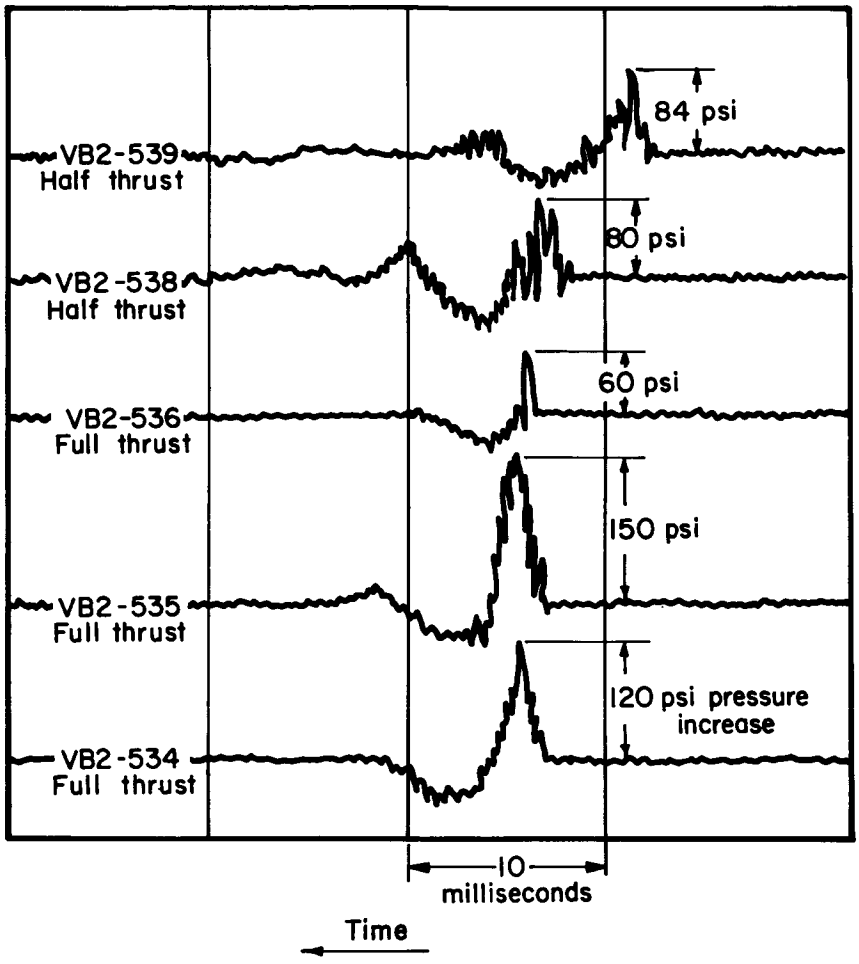

FIGURE 7.4.5c.—Typical pressure recovery for central injection design in LMDE engine.

compared to other combustor systems, vortex furnace systems operate at high efficiency over wider ranges of fuel to air ratios. It has been experimentally demonstrated[59,317,362,633] that the vortex furnace system is highly stable, requires a minimum of combustor volume, and imposes reduced thermal loads on the combustor walls. In rocket engines, vortex injectors have been used with a number of propellant combinations and at combustion pressures from subatmospheric to several thousand pounds per square inch. A notable application of this injector is in the Surveyor Vernier ACS engine system (Fig. 7.4.5d) which has been used in the soft landing of five vehicles on the lunar surface.

The generation of a rotational flow pattern within a combustor by the tangential injection of one or more of the propellants is necessary for vortex combustion. (Swirling flow generated merely by the introduction of vanes or baffles into a normally non-tangential injected combustor does not constitute a vortex injector system as defined and discussed in this section.) The rotational flow field tends to increase the chamber stay time of the reactants which encourages the promotion of high combustion efficiencies.[327]

Although gaseous, liquid, or slurry propellants may be used in various combinations the subsequent discussion will be limited to liquid bipropellants. Further, the introduction of the fuel at the outer periphery, although not a restricting condition, will be used as the base of

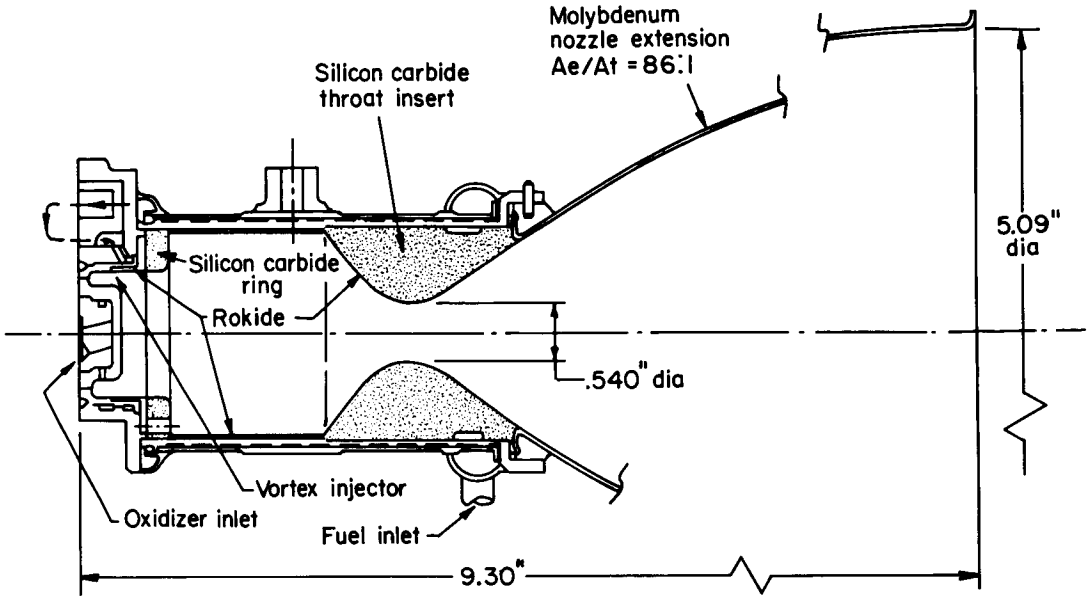

FIGURE 7.4.5d.—Surveyor vernier engine thrust chamber and injector assembly.

this discussion since it provides a preferred case of fuel barrier cooling in a rocket engine.

The vortex injector concept is shown schematically in Fig. 7.4.5e. As shown in the figure, fuel, injected tangentially from the outer periphery of the injector into the combustion zone, forms a cool boundary layer which swirls along the chamber walls; oxidizer is injected in essentially a radial direction to provide intimate mixing with the swirling fuel. The resultant momentum of the injected propellants follows a helical pattern. The tangential momentum provides longer mixing times than conventional axial injectors (i.e., impinging stream). Based on flow studies and experimental work with uncooled vortex injectors, it is evident that oxidizer stream impingement does not completely disrupt the swirling fuel layer and that a cool fuel film is maintained around the injector-chamber periphery. Since this fuel-rich boundary layer extends to some degree throughout the chamber, thermal margins are enhanced and combustion chamber durability is thereby improved.

Vortex injection gives rise to a steady-state flow which is highly three-dimensional with complex recirculatory patterns in the combustion chamber. While the results of the sensitive time lag theory and the numerical integration analysis (see Chapter 4) may be qualitatively used in analyzing combustion instability for a vortex injector, additional work is required to extend the theory to this special case.

An extensive investigation of combustion instability with vortex injection was undertaken in the course of the development of the 100-lb thrust C-1 ACS engine (see Fig. 7.4.5f). During the development program the engine, when operating in pulse mode under certain conditions of pulse width and fire fraction (ratio of on-time to elapsed-time) occasionally entered an unstable combustion mode on start.[86] (Qualification testing of the C-1 engine under steady-state duty cycles of 2 seconds to 200 seconds duration revealed no combustion instability over accumulated firing times of 64,960 seconds.) The engine generally would not recover from this condition and, if operation was continued, severe erosion to the injector and/or combustion chamber liner resulted. The engine was most susceptible to this mode of operation under the condition of maximum injected fuel temperature resulting from prolonged pulse mode operation and heat soak. The instability, the first tangential mode which occurred at 17.5 kHz with an incident level of 0.36%, was attributed to the injection of two-phase fuel during start which resulted from

fuel boiling, entrained helium bubbles, or cavitation in the coolant jacket, valve, or injector, aggravated by a significant drop in fuel pressure on start. Although the investigation of a number of design modifications showed promising approaches it was found that the most effective and direct approach to damping was the use of chamber baffles positioned adjacent to the injector. However, durability of the baffles in the steady-state mode was limited.

Further work, recently completed, in which the periphery of the fuel injector was modified to function as an acoustic liner has shown that this approach can suppress the instability.[70] From a heat transfer standpoint, the vortex injector has definite merits for this method of suppression.

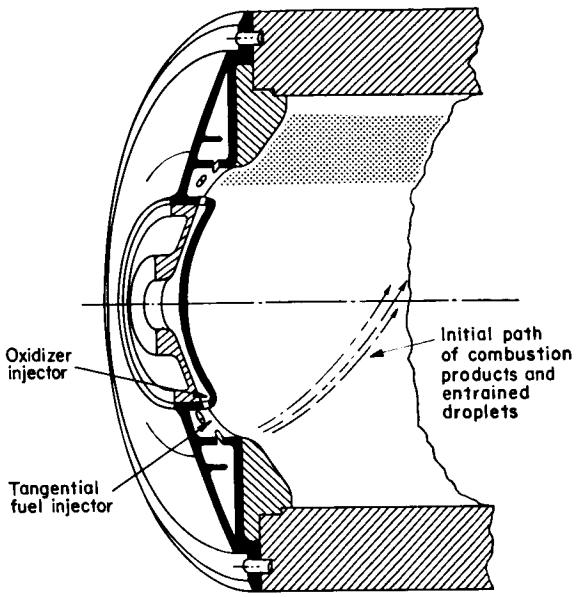

FIGURE 7.4.5e.—Typical vortex injector.

7.4.6 Summary of Conclusions

As discussed in Section 7.4.1, theories of high frequency combustion stability tend to agree on several major effects of injector design on stability. In general, the combustion response of a burning spray is a function of frequency and there is a frequency of maximum combustion response for that spray. The magnitude and frequency of maximum response are both functions of drop size and, therefore, vary inversely with orifice diameter and directly with injection velocity. Thus, when the drop size is increased, both the magnitude and the frequency of maximum combustion response decrease. One experimental result of this variation of response magnitude and frequency, then, should be an improvement in stability with large drop sizes.

There appears to be sufficient general agreement in the experimental data and conclusions to verify these theoretically predicted effects of injector

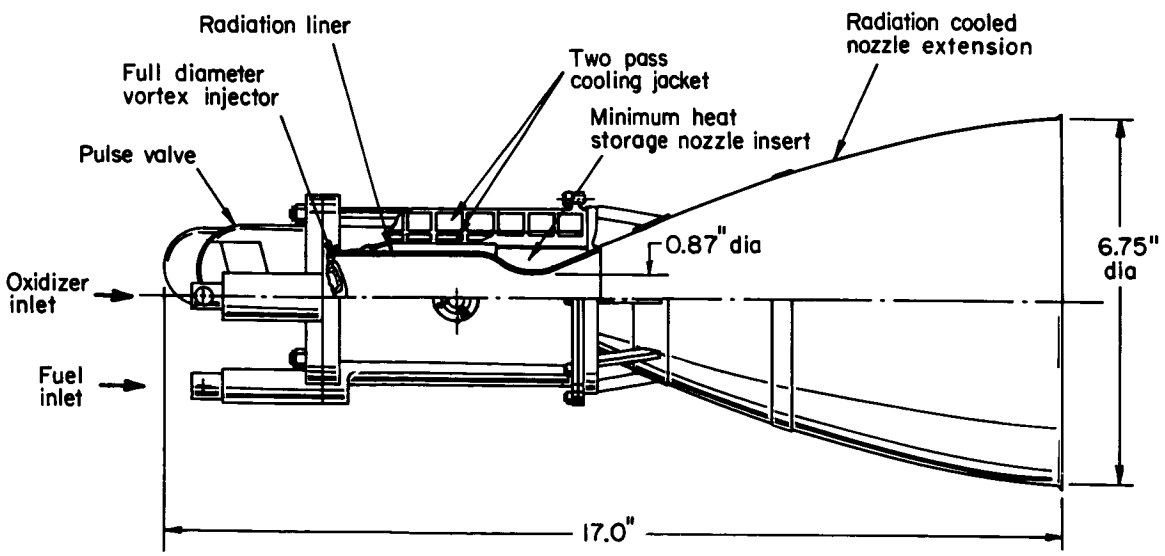

FIGURE 7.4.5f.—C-1 thrust chamber assembly.

design. McBride shows the variations of oscillation growth rate (as a measure of combustion response) with frequency for a given injector. Harrje also confirms the existence of a single band of frequencies that a given injector can support. This band of frequencies appears to be constant if the spray is constant, regardless of changes in chamber geometry or mode frequencies. Smith shows the same type of combustion response even with very high chamber pressures and oxygen/hydrogen propellants.

Many studies show that stability is strongly controlled by injector design factors which affect spray drop size, with earth storable propellants or with propellant combinations which include one cryogenic. McBride shows the inverse relation between orifice diameter and the frequency of maximum combustion response. McBride, Abbe, Masters and Wanhainen all indicate the stabilizing effect of increased thrust-per-element. These investigators, plus Harrje and Smith, all ascribe this thrust-per-element effect to increasing drop size.

There is not general agreement, however, on how this change in drop size affects stability. Many theories and experimental data tend to indicate a strong effect of drop size on the frequency of the combustion response. Other theories and data indicate the major effect is to spread out the combustion axially, minimizing the coupling between the region of sensitive combustion and the oscillations in chamber gases. As a result, the effects of other major injector design factors on stability are not generally clear.

In particular, the effect of injection velocity, or orifice pressure drop, is not clear. Empirical correlations of drop size show that increased velocity reduces drop size, which should be destabilizing. The Priem theory, however, indicates that increased injection velocity spreads out the combustion and has a stabilizing effect. These opposite effects are discussed by Abbe and Harrje.

Several other injector design details which could have significant effects on drop size have also been shown to have significant effects on stability. Unfortunately, empirical correlations between these factors and drop size are not available. Some of these design factors, in coaxial tube injectors, are (1) hydrogen injection angle, (2) oxidizer tube base thickness, (3) oxidizer tube recess, and (4) hydrogen/oxygen momentum ratio. Since these factors represent individual, empirical observations, their interdependence is difficult to assess. Generalizations, applicable to all combinations of these factors in all combinations of hardware and environments, are difficult to make.

Besides the effects of injector design factors on the spray itself, the postulated effects of injection mass and mixture ratio distributions, as discussed in 7.4.1, appear reasonably confirmed. McBride indicates the stabilizing effect of a "hump" mass distribution. The stability of the TRW injector concept is ascribed by Burge largely to the injected mass distribution concentrated near the center of the chamber. Clinger indicates the need to keep injected propellants away from walls to optimize stability. Many experiments (not reported here) with "wall gap," a zone near the wall where no propellants are injected, indicate improved stability. The data shown by Wanhainen, however, indicate exactly the opposite effect; i.e., uniform face coverage was the most stable. Although other effects in the single experimental program discussed by Wanhainen could explain this disagreement, it cannot be concluded, at this time, that there is universal agreement on the effect of mass distribution.

The effects of mixture ratio distribution are discussed largely by Harrje. Based on these data, it appears the uniform mixture ratio profiles, even across the individual injector elements, promote stability with regard to velocity/displacement effects. The data discussed appear to be clear on this point. One might expect, therefore, that like-impinging jet elements, which should create larger mixture ratio gradients than unlike impinging elements, should be more unstable than the unlike elements. Harrje indicates the greater sensitivity of like impinging jet injectors to velocity coupling. The more rapid combustion of the unlike elements, however, is thought to concentrate the combustion closer to the injector face than with the like impinging elements. This is considered a de-stabilizing effect. As a result, the relative inherent stability of these two element types is not clear and may not always be the same in all configurations. McBride, Abbe and Harrje all indicate data showing that the like-impinging

elements appear to be more stable than the unlike type (and lower performing, as well).

Aside from this difference between the like- and the unlike-impinging jet injector elements discussed above, the general stability characteristics of these two element types appear to be quite similar. The differences between impinging and coaxial types also do not appear too great, where comparisons can be made. Obviously, such injector design factors as base thickness, tube recess and concentricity, in the coaxial types, do not exist in the impinging types. Also, there has not been the concentrated study of the oxygen/hydrogen propellant combination with impinging element injectors. Where drop size effects can be related, all element types appear to be much the same.

In the two special injector element types discussed, comparisons with the more standard, axial injection types are even more difficult. Available theory is generally less applicable to these injector types. Drop size correlations are unknown. The effects of injector design factors on stability can only be discussed generally, as Burge and Lovingham have done. There is generally an insufficient range of instability data on either type to determine whether the stability varies as with other element types. The specific discussions of these injector types are included here because these are injectors used in developed, operating engines.

More recently other injection designs have been tested experimentally. For example, Riebling[590] has concentrated on sheet-type impingement designs. Other groups[52,476] have been developing micro-orifice injectors to achieve high combustion efficiency in small chambers. Stability of such designs will naturally influence the incorporation into production engines.

7.5 FEED SYSTEM COUPLING

The preceding sections of this chapter have concentrated on the combustion-related factors which are responsible for excitation of various types of combustion instability. Another source of excitation is the feed system and the coupling of that system with the combustion processes. This important aspect has been discussed in several of the previous chapters, however, the present emphasis is on certain hardware oriented problems. The injector impedance and the role of fluid inertance is discussed. Stability problems associated with bubbles trapped in the injector manifold are presented. The relationship of structural vibration and instability is also brought into focus together with the role of blade wake frequencies.

The following nomenclature pertains to Sect. 7.5:

A_o	Orifice cross-sectional area
g	Gravitational acceleration
K	Steady-state gain factor
K_d	Dynamic gain
l_{eff}	Effective orifice length
p_d	Pump discharge pressure
p_s	Pump suction pressure
Δp	Injection pressure drop
$\mathcal{R}_p$	Pump dynamic resistance
t_o	Orifice time constant
ω_t	"Break" frequency, $1/t_o$

Subscript:

d	Discharge

7.5.1 Injector Impedance*

The injector is often the most favorable system component for controlling feed-system-coupled instability.[272] The designer's goal is to maintain constant injector flowrate. Instantaneous flowrate is a function of chamber pressure, injector pressure, and injector impedance (for a detailed discussion see Chapter 3). In general, stability is improved as orifice impedance (resistance+inertance) is increased and injector volume is decreased. Thus, the stability benefits of injector orifice design can be cancelled by an overly large manifold volume. For simplicity, only the injector impedance is discussed here; the more complex effects of injector volume (capacitance) are discussed in Chapters 3, 5 and 6.

It is necessary that the designer have a physical understanding of the concept of inertance. Simply stated, the inertance of an injector orifice is the tendency of the flow rate through the orifice to remain constant despite instantaneous changes in the pressure drop across the orifice. The relation

* J. A. Nestlerode, J. R. Fenwick, and L. E. Sack, Authors.

between injector pressure, chamber pressure, and flow rate can be expressed by the equation

$$p_i(t) - p_c(t) = \mathcal{R}\dot{w}^2(t) + \mathcal{L}\frac{d\dot{w}(t)}{dt} \qquad (7.5.1\text{–}1)$$

$$\begin{bmatrix}\text{Injector}\\ \text{pressure}\\ \text{drop}\end{bmatrix} \quad \begin{bmatrix}\text{Steady-}\\ \text{state}\\ \text{flow}\\ \text{loss}\end{bmatrix} \quad \begin{bmatrix}\text{Orifice}\\ \text{inertance}\end{bmatrix}$$

where $\mathcal{R}$ and $\mathcal{L}$ are the orifice resistance and inertance, respectively, and are related to steady-state flow and injector configuration by

$$\mathcal{R} = \frac{\overline{(p_i - p_c)}}{\underline{\dot{w}}^2} = \frac{\overline{\Delta p}}{\underline{\dot{w}}^2} \qquad (7.5.1\text{–}2)$$

$$\mathcal{L} = \frac{l_{eff}}{A_o g}$$

in which A_o is the cross-sectional area of the orifice and l_{eff} is its effective length (Sect. 3.2.2.1).

The role of the injector impedance on stability can be shown by a simplified analysis. Assuming the injector manifold pressure to be constant, but allowing small perturbations in chamber pressure and flow rate, with

$$p_c(t) = \bar{p}_c + p_c' e^{st}$$

$$\dot{w}(t) = \underline{\dot{w}} + \dot{w}' e^{st}$$

Equation (7.5.1–1) yields the impedance relation

$$\frac{\dot{w}'}{p_c'} = \frac{(\underline{\dot{w}}/2\overline{\Delta p})}{1 + (\underline{\dot{w}}/2\overline{\Delta p})(l_{eff}/A_o g)s} = \frac{K}{1 + t_o s} \qquad (7.5.1\text{–}3)$$

usually referred to as "first-order lag." The parameter K is the steady-state gain, i.e., the ratio of flow rate variation to chamber pressure variation for very low oscillation frequencies. The time constant t_o is the determining factor for non-steady behavior, in which the acceleration forces are important.

The frequency response of the flow rate, assuming first-order lag and constant injector manifold pressure, is determined by substituting $s = i\omega$ into Eq. (7.5.1–3). A typical response curve is shown in Figs. 7.5.1a and b. Quasi-steady behavior is obtained for low frequencies, where inertial effects are insignificant, so that $\dot{w}'$ is proportional to p_c', and lags only slightly behind it. As the frequency is increased the phase lag increases, but the magnitude of $\dot{w}'/p_c'$ remains nearly constant up to the so-called "break frequency"

$$\omega_t = \frac{1}{t_o} = \frac{2\overline{\Delta p} A_o g}{\underline{\dot{w}} l_{eff}}$$

For $\omega > \omega_t$ the magnitude of $\dot{w}'/p_c'$ decreases continuously ("roll-off") with increasing frequency as the inertial forces overpower the imposed acceleration forces. The phase lag passes through 45° at $\omega = \omega_t$ and approaches 90° for very high frequency oscillations.

The dashed line in Fig. 7.5.1a shows the effect of increasing Δp. The quasi-steady flow rate perturbation (for a given chamber pressure perturbation) is decreased and the break frequency is increased. Increasing the orifice inertance ($l_{eff}/A_o g$) decreases the break frequency but has no effect on the gain K. Both of these changes have stabilizing effects since $\dot{w}'$ is reduced for part of the frequency range. For typical injector designs, the break frequencies lie between 100 and 2500 Hz.

Although the orifice break frequency is an important system characteristic, there has been little direct reporting of the effect of ω_t on feed system coupling. A review (by the author) of data from a number of different engines has indicated that there have been no clear-cut evidences of coupling of the feed system through the injection orifices when the oscillation frequency is greater than twice the orifice break frequency ($\omega \geq 2\omega_t$).

The phase lag introduced by the orifice inertance is an effect that must be considered by the designer. It is conceivable that this phase lag, together with the transport and combustion time delays, could tend to destabilize an otherwise stable system. This possibility can be investigated by the methods described in Chapters 5 and 6, and must be considered separately for each engine system. However, as seen in Figs. 7.5.1a and b, the maximum phase lag is 90°, whereas the attenuation benefits are limitless (i.e., the response goes to zero as $\omega \to \infty$).

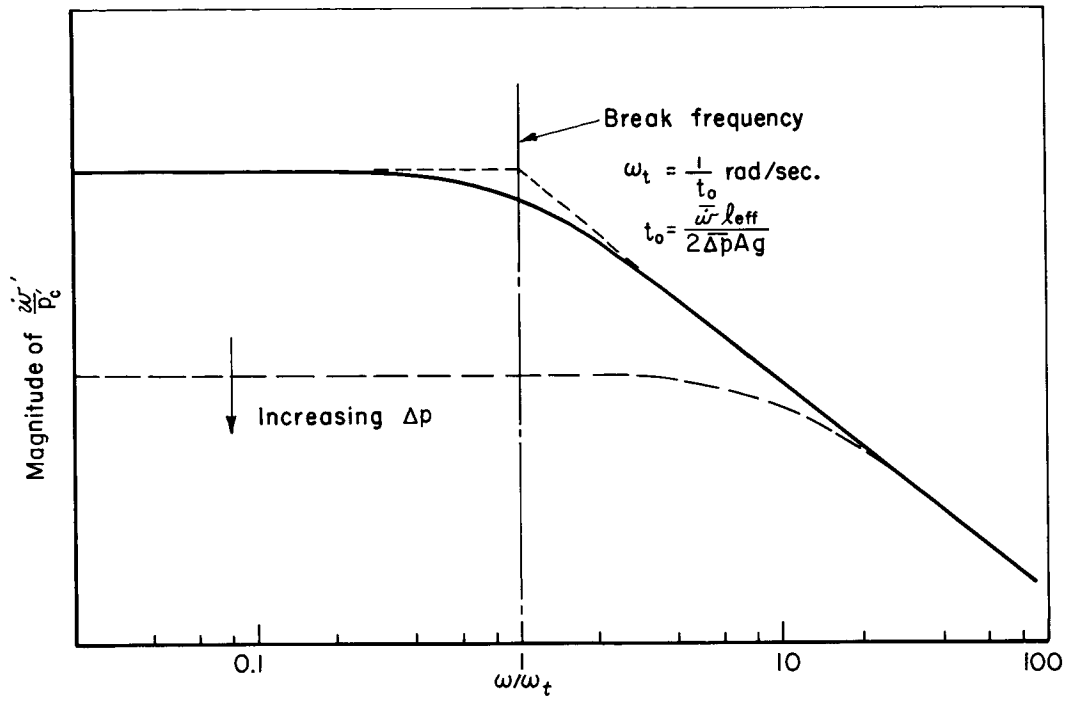

FIGURE 7.5.1a.—Response magnitude versus frequency, where the magnitude is defined as

$$\frac{\tilde{w}}{\tilde{p}_c} = \frac{\dot{w}/2\Delta p}{1 + i(w/2\Delta p)(\ell/Ag)\omega}.$$

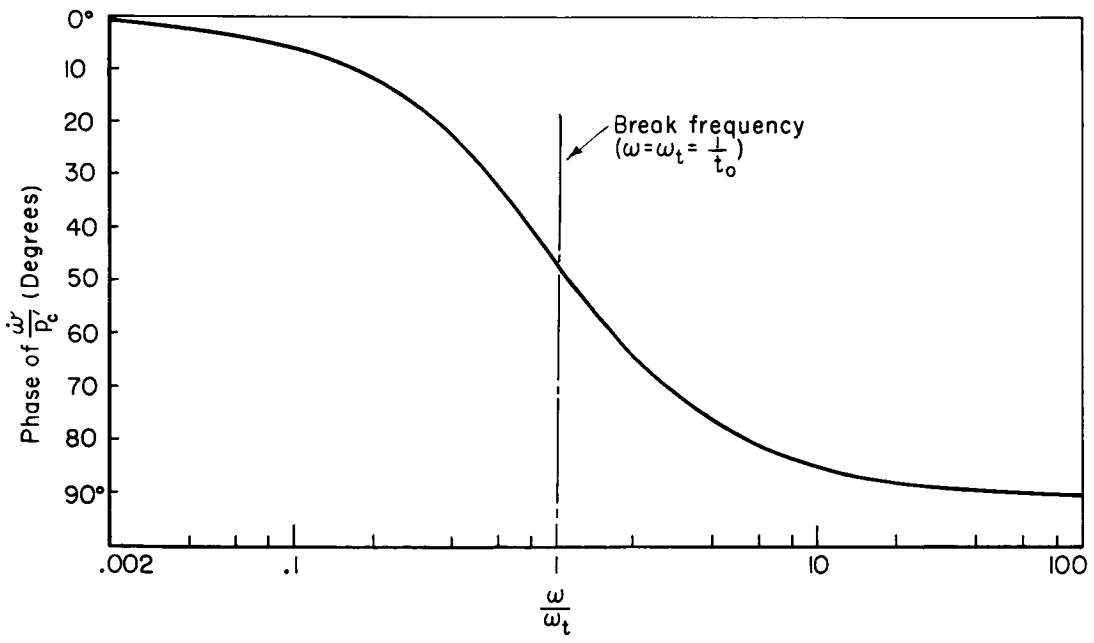

FIGURE 7.5.1b.—Phase angle versus frequency (same parameters as in Fig. 7.5.1a, but expressed in degrees of phase angle).

7.5.2 Coupled Resonances*

7.5.2.1 *Lumped parameters.*—Lumped parameter resonances in the propellant system are frequently encountered. They result from the coupling of injector fluid inertance (or mass effects) with an inlet torus or dome fluid capacitance.

One example of lumped parameter resonances involved tests on a pressure-fed bipropellant engine system operating at 1400 psia chamber pressure.[227] Pressure instrumentation revealed the presence of a 650 Hz intermediate frequency combustion instability that was due to this instability mechanism. The test data indicated that the peak-to-peak oscillatory amplitude of the chamber pressure was just less than half of the steady-state value. The inclusion of an orifice at the oxidizer torus inlet, to provide additional energy dissipation, was ineffective and only served to further isolate the resonant phenomenon from the upstream fluid dynamics. The dynamic coupling for this system can be represented by the circuit shown in Fig. 7.5.2a. The stabilization of this type of system coupling requires either a change in torus or dome volume, in order to shift the resonant frequency sufficiently to provide phase stabilization, or an increase in the pressure drop in the injector circuit to "gain stabilize"† the system.

Any additional capacitance encountered due to inlet dome mechanical capacitance makes the resonant circuit more difficult to define. Engine tests and analytical studies have revealed that stability is sensitive to oxidizer dome mechanical capacitance. In that case, dome compliancy tests are valuable for defining the changes due to various structural stiffening schemes and to provide data for the combined model of dome fluid and mechanical capacitance which can be used to analytically verify the resonant system behavior.

Another example of lumped parameter resonance is the coupling between the injector inertance and the vapor capacitance associated with a cavitating venturi located directly upstream of the injector. For example, in the same pressure-fed, bipropellant engine operated at 425 psia chamber pressure, with the propellant flow rates maintained constant by cavitating venturis directly upstream of the injector, instability at 70 Hz was noted.[227] The test data shown in Fig. 7.5.2b indicate that the peak-to-peak chamber pressure oscillations were 43% of the steady-state value. Likewise, large oxidizer feed system pressure oscillations were measured downstream of the venturi where the peak-to-peak oscillations in $p_{i_{ox}}$ were 22% of the steady-state value. Note that the uniformity of the test data waveforms indicate the presence of a single dominant resonance frequency.[232]

In order to understand this behavior, consider the model of the dynamically coupled system shown in Fig. 7.5.2c. The cavitating venturi has a

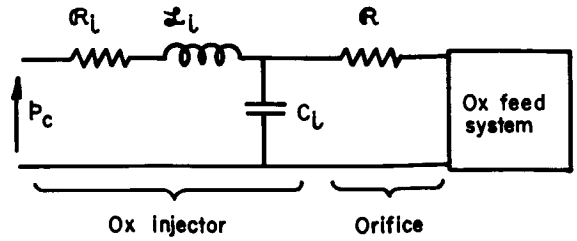

FIGURE 7.5.2a.—Dynamically coupled injector circuit.

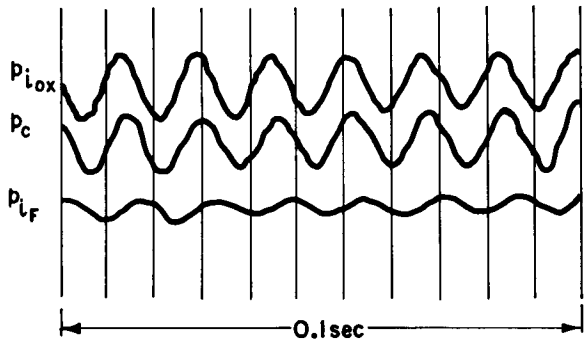

FIGURE 7.5.2b.—Unstable engine test data.

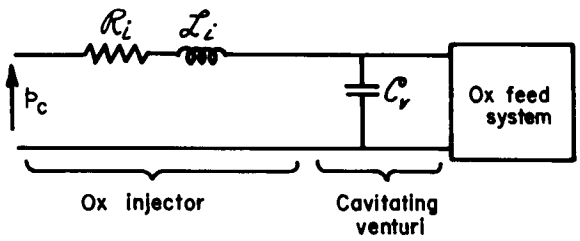

FIGURE 7.5.2c.—Dynamically coupled system.

* L. L. Bickford, Author.

† Gain stabilization is the reduction of the gain (amplifying factors) to a level which can no longer support oscillatory behavior.

cavitation vapor region downstream of the venturi throat which can be treated as a vapor spring or capacitance.[735] This analytical model was used to predict the 70 Hz resonance for the oxidizer circuit. Initial attempts to provide gain stabilization by increasing the venturi pressure drop were not successful since the resonance occurs downstream of such changes. However, system stabilization was achieved by inserting a pressure dropping orifice between the venturi and the injector.

A similar dynamic resonance has been observed on tests of a bipropellant throttlable engine. This pressure-fed engine uses movable pintles in the throat of cavitating venturis to obtain variable thrust control. The venturis are located immediately upstream of the injector and contribute to combustion instability. The frequency of instability was found to vary between 130 to 450 Hz while operating throughout the variable thrust range.

An additional resonance can occur for a pump-fed engine involving the turbopump inlet cavitation compliance and the combined discharge line and injector inertance. Since the actual value of the cavitation compliance is difficult to define, this compliance is inferred analytically from the suction line resonances obtained from the power spectral density data taken from the pressure instrumentation records. The analytical model for such a system is shown in Fig. 7.5.2d where, for lower frequencies, the turbopump is an active circuit device[98] which can be represented by a pressure-controlled source due to a dynamic gain, K_d, and a pump dynamic resistance, $\mathcal{R}_p$. Determining the effective capacitance for this active network requires the application of the Reduction Theorem[66] that yields an equivalent passive circuit model. Stabilization can be obtained by increasing $\mathcal{R}_p$, which is achieved by changing the pump operating point.

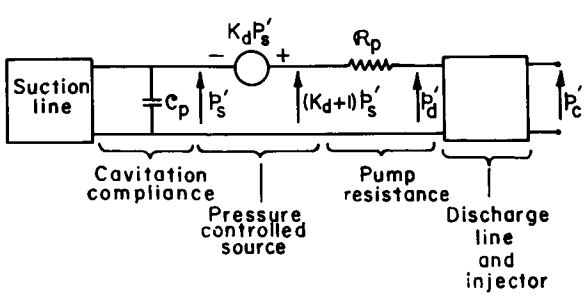

FIGURE 7.5.2d.—Dynamically coupled pump-fed system.

7.5.2.2 Distributed parameters.—The presence of fluid transmission lines in propellant feed systems results in multiple distributed parameter resonances. In pressure-fed engine systems these resonances can result in low or intermediate frequency instability. As a typical example, engine tests on a pressure-fed bipropellant engine resulted in a combustion instability with characteristics as summarized in Figs. 7.5.2e and 7.5.2f. At the operating chamber pressure of 100 psia, the frequency of instability was near 600

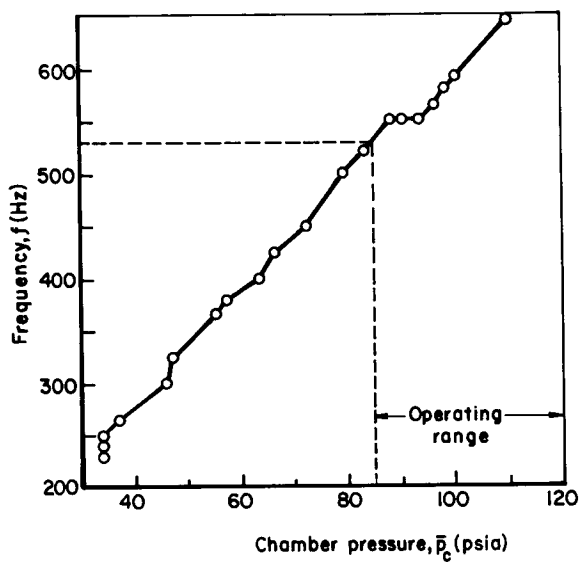

FIGURE 7.5.2e.—Frequency of combustion instability.

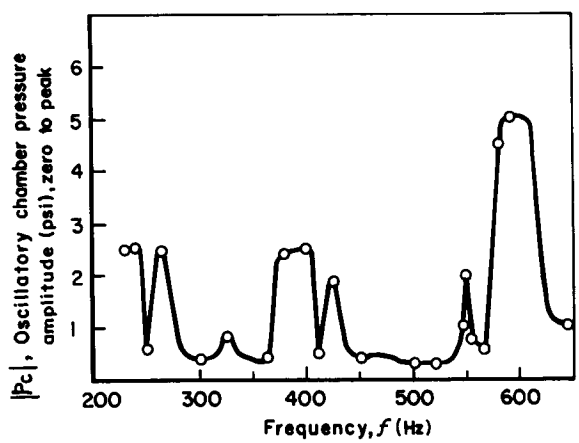

FIGURE 7.5.2f.—Oscillatory chamber pressure.

Hz. An analytical investigation of the complex feed system admittance was conducted for the test stand configuration shown in Fig. 7.5.2g which included many branched appendages terminated with closed propellant valves. This analysis revealed the resonant admittances for the fuel and oxidizer systems shown in Figs. 7.5.2h and 7.5.2i, respectively. Note from Fig. 7.5.2h that the fuel circuit admittance peaks occur in the region of 600 Hz. Since no additional pressure drops were allowed for engine stabilization, a Helmholtz resonator was attached to the fuel feed system as shown in Fig. 7.5.2j. This provided the necessary stability modification of the fuel feed line and resonances were eliminated on subsequent engine tests.

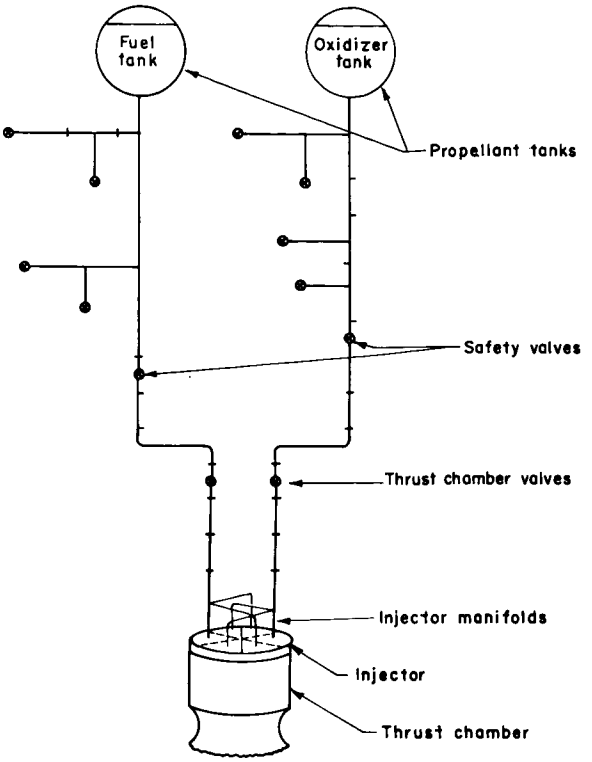

FIGURE 7.5.2g.—Propellant feed system schematic.

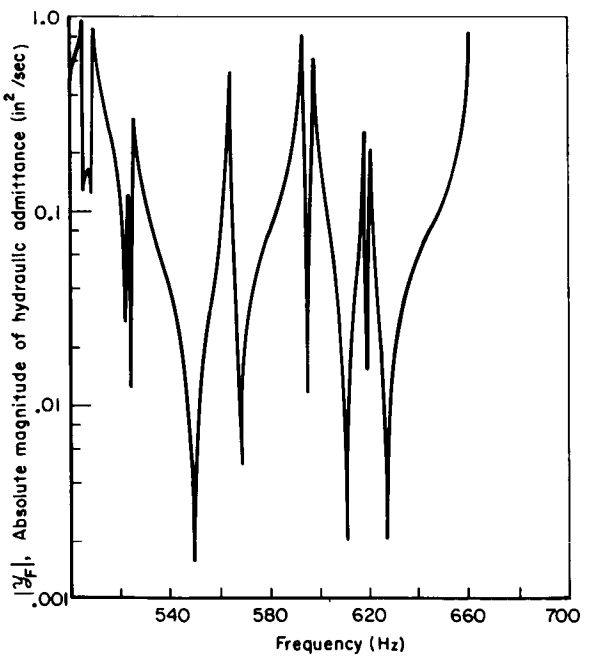

FIGURE 7.5.2h.—Fuel feed system admittance.

7.5.3 Imposed Oscillations

7.5.3.1 Structural vibrations.—In a liquid rocket engine the propellant injection flow rate is affected by the physical displacement or structural vibration of the injector plate and feed system ducting. When the structural vibrations are in turn excited by engine operation, a closed loop relationship exists.[736] There are two major types of structurally coupled modes of vibration that have been encountered in engine programs. One type involves the flexing of regenerative cooling tubes which cause fuel flow pulsation. The second type of vibration is the diaphragm motion of the injector plate where this motion can have a substantial effect on the liquid stream formed by the orifice. A sketch of the vibrating injector is shown in Fig. 7.5.3a where the injector face is presumed to be vibrating as a diaphragm which is driven at its mechanical natural frequency by the chamber pressure fluctuations. For example, oscillatory engine test data are shown in Fig. 7.5.3b where an accelerometer was mounted at the center of the injector.[272] Vibration shake table testing of this injector revealed a 1330 Hz mechanical resonance which correlates well with the engine test data. The elimination of structural couplings can be achieved by mechanically stiffening the flexible members.

7.5.3.2 Pump blade wakes.—Another cause of imposed oscillations is the turbopump. Rotating pump blades impart pressure oscillations and thereby flow fluctuations to the fuel and oxidizer

propellant feed systems. The "pump blade wake frequencies" are simply a function of the pump rotational speed and the geometry of the components. These blade frequencies become important candidates for a stability investigation when they approximate the frequencies that are characteristic of other system components, primarily the combustion chamber.

A typical example of possible blade wake frequency influence was found in a pump-fed engine system experiencing 1000 Hz chamber pressure oscillations. Tracing through the system this frequency could be attributed directly to the fuel pumps.

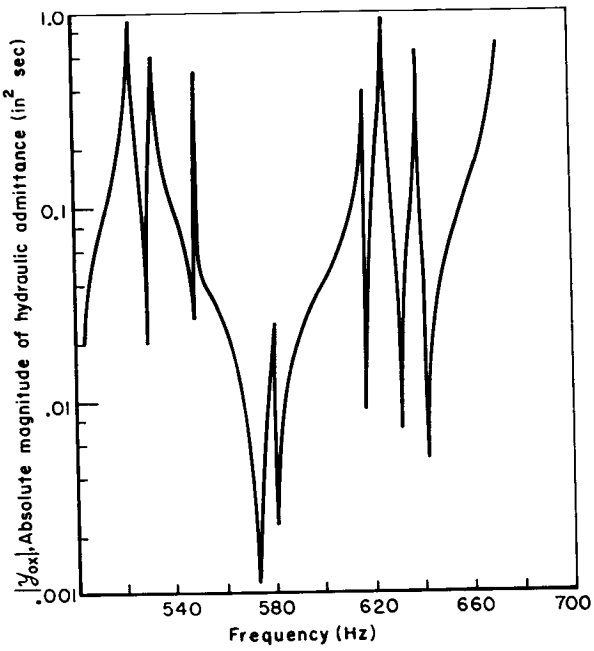

FIGURE 7.5.2i.—Oxidizer feed system admittance.

In order to evaluate the effectiveness of these pump-produced signals in modulating chamber pressure, a transfer function can be analytically defined using the techniques described in Chapter 3 which relate the engine chamber pressure to the pump discharge pressure. For the pump-fed engine system, this transfer function is evaluated where the fuel pump discharge pressure, p_{dF}, is the input signal. The resulting frequency response plot for the magnitude of this transfer function is shown in Fig. 7.5.3c. The magnitude variation indicates that any fuel pump-produced pressure oscillations in the region of 1000 Hz are greatly attentuated by the time they reach the chamber and are ineffective in modulating the chamber pressure. If the blade wake oscillations are found to be a problem, they can be removed from the system by using one of the acoustical filters described in Sect. 6.2.3.

7.6 POPPING AND SPIKING*

The tendency of certain rocket designs and propellant combinations† to develop spontaneous, random pressure perturbations, which have the

* Contributions from A. J. Smith, Jr., and R. M. Clayton.

† See Sect. 7.3.2 for further discussion of propellant combustion effects.

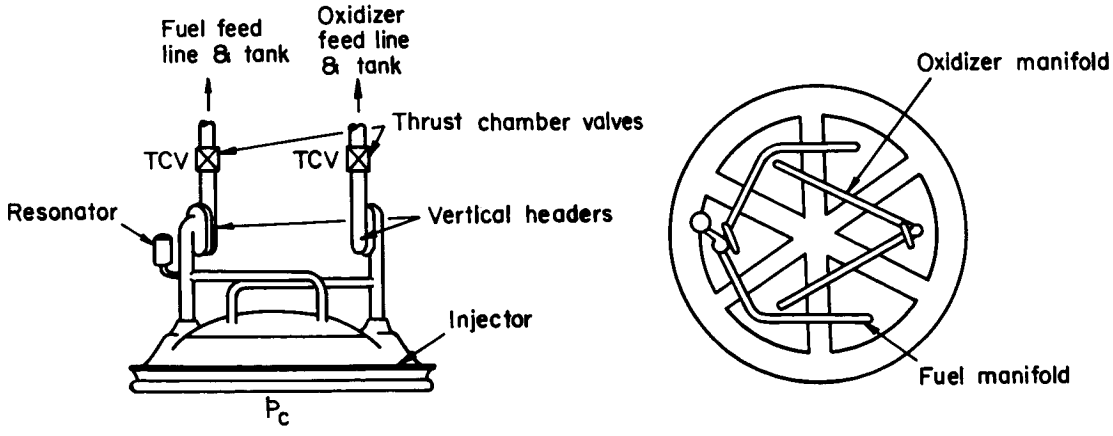

FIGURE 7.5.2j.—Engine header-injection system including a Helmholtz resonator.

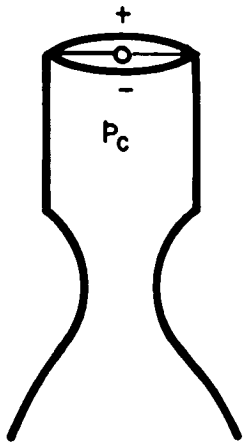

FIGURE 7.5.3a.—Injector vibration.

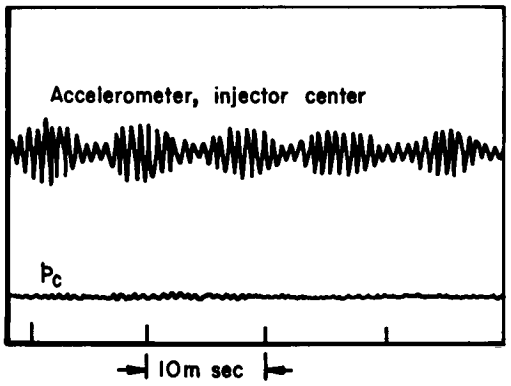

FIGURE 7.5.3b.—Engine test data.

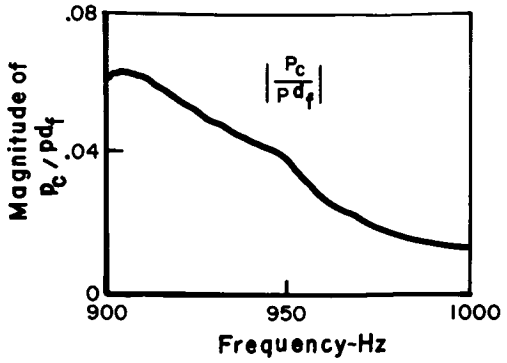

FIGURE 7.5.3c.—Frequency response.

appearance of local explosions, has become a concern of the combustion instability community in recent years.[331] Such perturbations have been observed to occur during steady-state operation as well as during the starting transient. Although there is no generally accepted terminology, the former are usually called "pops" and the latter, "spikes." Further complicating the popping/spiking picture are similar disturbances that originate in the injector manifold because of condensation of one propellant in the manifold of the other following certain space start sequences.[487] Often, popping and spiking have been known to trigger resonant combustion unless care has been taken to design the combustor for dynamic stability.

The amplitude of the popping/spiking disturbances often exceeds 100 percent of the chamber pressure. Investigations with sensitive instru-

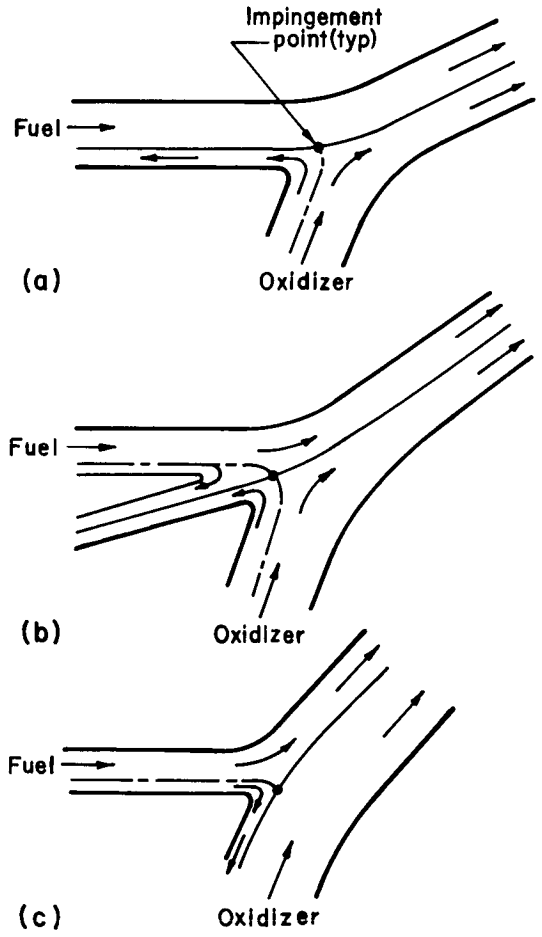

(a) $q_F > q_{ox}$.
(b) $q_F = q_{ox}$.
(c) $q_F < q_{ox}$.

FIGURE 7.6a.—Three configurations of stream impingement.

TABLE 7.6.—A COMPENDIUM OF POPPING/SPIKING DATA

Reference	Propellants		Injector element type	Chamber pressure, psia	Mixture ratio, OX/F	Remarks
	Oxidizer	Fuel				
32	N_2O_4	N_2H_4	Showerhead	150	1.0	$\Delta p_{OX} = 118$ psia; $\Delta p_F = 80$ psia
715	N_2O_4	N_2H_4	Triplet	10	0.875	$\Delta p_{OX} = \Delta p_F = 16$ psia (pops); $\Delta p_{OX} = \Delta p_F = 25$ psia (no pops)
705	N_2O_4	[a](A–50)	Unlike doublet	100	2.0	One or two pops per 100 sec; as high as one pop per sec; Δp's not reported; pops reduced by orifice rework
329	N_2O_4	[a](A–50)	Quadlet	90	—	One pop per 100 sec for trax 21–1D; one pop per 530 sec for trax 21–11B; Δp's not reported
639	N_2O_4	[a](A–50)	Unlike doublet	120	1.6	$\Delta p_{OX} = \Delta p_F = 30$ psia; pops eliminated by extending sides of baffle to chamber wall

[a] Denotes a 50%/50% blend of N_2H_4 and UDMH.

mentation have indicated that the gross disturbance is actually a series of sharp spikes closely spaced in time.[431] This is apparently the result of multiple reflections of an initial wave from the chamber boundaries.

Those investigators who have encountered popping are in general agreement that the disturbances derive their energy from unburnt propellants (or intermediate products) that exist within the combustion chamber, near the injector face. Collection of propellants on wall surfaces, corners, under the baffle blades, in the pressure tap ports, etc., has been shown to be responsible for popping in a number of instances.[728] Another explanation of the energy source for spiking and popping involves local collection of a pre-ignition reaction product (adduct), with monomethylhydrazine nitrate the prime candidate.[627] This clear, yellow, viscous liquid with very low vapor pressure can provide considerable energy and has the characteristics of a monopropellant.

Along with the potential energy source for pops there must exist a mechanism to trigger this reaction. For spiking, this mechanism may be supplied by the start transient itself. Proposed mechanisms to initiate popping include (1) impinging stream flow-field phenomenon,[149,618] (2) injection stream hydraulic instability,[705] and (3) discontinuous flow through the injector because of dissolved gases.

The search for a common denominator associated with engine development programs that have experienced popping and spiking phenomena has resulted in the tabulated data shown in Table 7.6. Examination of this table indicates the following:

1. The propellant combination generally associated with popping and spiking is N_2O_4/N_2H_4. (However, similar occurrences have been experienced with propellants such as UDMH and MMH.[431])
2. Popping appears to be independent of the injector element type.
3. The chamber pressure is generally low. Tests with N_2O_4/A-50 at 500 psia,[649] 750 psia, and 830 psia[329] have not resulted in popping.
4. Popping occurs when the ratio of injector

pressure drop to the chamber pressure exists in the range from 0.25 to 1.60. In one instance,[715] the popping was eliminated by extending this pressure ratio from 1.6 to 2.5.

Although these general observations are of interest to the designer, more specific information is required in the form of a design criterion. Such information is available from a recent study at JPL where Clayton et al.[149,618] have investigated the reactive impingement process as a source of popping.

The model proposed is that three distinct flow conditions can exist with impinging streams, one of which is unconditionally unstable. These configurations are shown in Fig. 7.6a for the case of two-dimensional, inviscid, impinging sheets. Stream dynamic pressures are the basis for comparison (where the dynamic pressure is $q=\frac{1}{2}\rho V^2$), and the three stream configurations are (1) $q_F > q_{OX}$ (Fig. 7.6a(a)), (2) $q_F = q_{OX}$ (Fig. 7.6a(b)), and (3) $q_F < q_{OX}$ (Fig. 7.6a(c)). The flow field for cylindrical jets is more complex; however, at least for inviscid fluids, physics requires that it exhibit the same behavior, i.e., only for equal q do both streams stagnate simultaneously. Moreover, it can be shown[618] that the equal-q configuration is transitory, since small fluctuations in velocity head for either stream will discontinuously shift the flow field to that associated with unequal q.

Central to coupling this flow-field model to hypergolic impingement and popping triggers is that a small quantity of reactant(s) may be stagnant at the impingement point. When operating near the equal-q condition, depending on the instantaneous relative q's, either one or both reactants may be stagnant. For example, in (1) the oxidizer is stagnant with the fuel stream

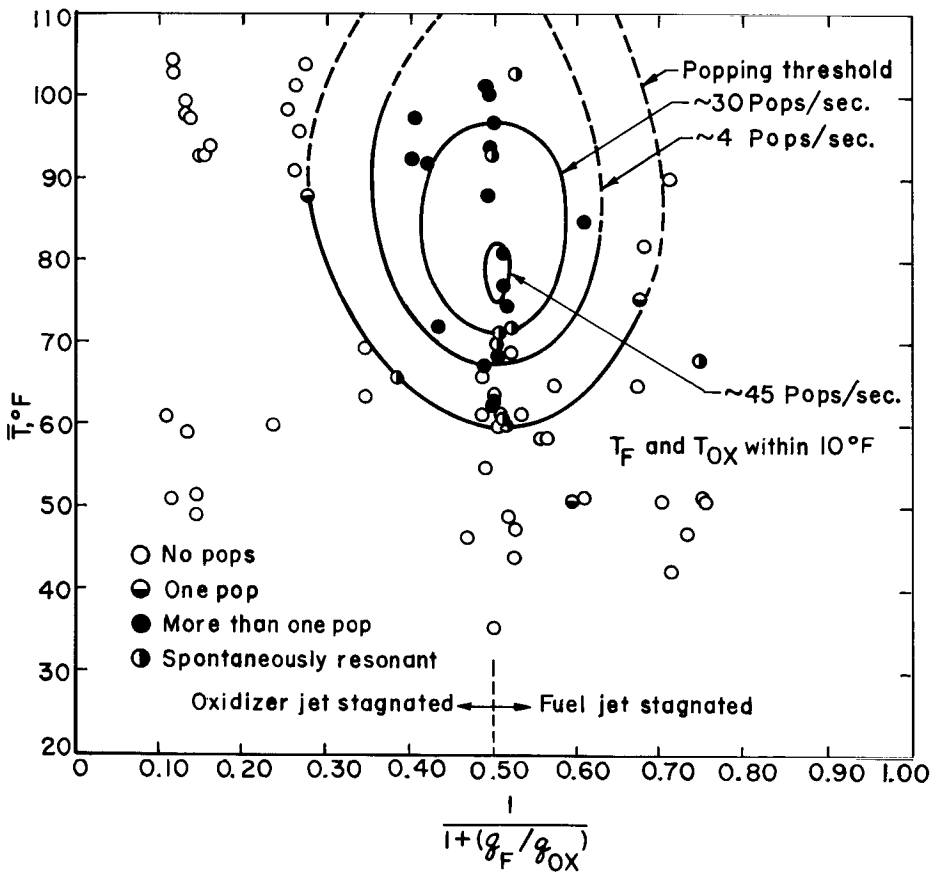

FIGURE 7.6b.—Correlation of popping occurrence.

sweeping past, whereas in (3) the reverse situation exists. Contact time[415] may be relatively short in these cases as compared to case (2) where both reactants are temporarily stagnant, $q_F = q_{OX}$. This longer period to react could result in a small explosion and therefore supply the initial disturbance for a pop.[484] Most of the single element stream separation and popping experiments are in this regime. Randomness of popping could also be explained by this model since a time to recover would follow each disturbance. Higher reactant temperatures would also be expected to enhance the reaction rates and hence could be an important popping parameter.

The test results using N_2O_4/A-50 propellants, which tend to confirm the applicability of these concepts,[149] are presented in Fig. 7.6b. Each data point represents a single firing. No distinction is made between baffled and unbaffled firings since this parameter is not pertinent to popping occurrence.[147] As predicted by the flow-field model, the occurrence of popping is centered on the $q_F = q_{OX}$ line. The data indicate that propellant temperatures greater than 60° F are necessary to initiate popping.

From considerations of the temperature and contact times there appears to be a close relationship between the data of Clayton[149] (Fig. 7.6b) and the stream-separation-temperature data given in Ref. 430 for N_2O_4/N_2H_4 propellants at ambient pressures. Hence, impingement-related popping sources and stream separation may be regimes of the same phenomena.[149] This may explain why the popping tendency *appears* to be reduced as the temperature is raised to higher levels (>110° F in Fig. 7.6b) where increased separation effects may modify the reactive conditions at the impingement interface.

CHAPTER 8

Design Factors Affecting Damping

8.1 INTRODUCTION*

In the previous chapter, design factors affecting excitation of combustion oscillations were discussed. Various design procedures were presented which lead to a decrease in the amount of energy provided to the oscillatory system by the combustion process. The most effective procedures in stabilizing liquid rocket motors, however, have been to either remove energy from the oscillation or prevent certain modes of oscillation by geometrical design (such as by means of injector-face baffles).

The most significant results in the stabilization of transverse modes of oscillation have been produced by baffles and acoustic liners. An extensive discussion of injector blade arrangement and design is given in Sects. 8.2.2 and 8.2.3, respectively. A discussion of the theory of the effect of small-cavity baffles on the frequency of oscillation is given in Sect. 8.2.1. No theory exists which predicts the other important effects of the baffles. These effects are the protection of the combustion process from the oscillating flow and the dissipation of energy due to the vortex-shedding and separation of the flow over the baffles. The protection of the combustion zone is believed to be the most important effect of the two. Of course, prevention of the excitation of the combustion process occurs here while damping occurs with the vortex shedding and separation of the flow. So the baffle is unique in that it affects both excitation and damping.

Due to these effects, the baffles (if sufficiently long) allow only certain modes to exist in the chamber. Spinning modes are not allowed; only those standing modes are allowed which have velocity nodal points at the baffle blades. For this reason, baffles tend to prevent the lower transverse modes. It follows that injector-face baffles are not as effective in the stabilization of longitudinal modes[497] where the oscillations are parallel to the baffle blades. Any orientation of the baffle blades, other than one parallel to the flow, would cause blockage and therefore would not be used.

Acoustic liners are equally important as damping devices. They are effective for both transverse and longitudinal modes. Energy is dissipated by the liner on account of the jet formation in the flow through the liner orifices. The fluid mechanical operation of acoustic liners is fairly well understood and is discussed in Sect. 8.3.1. This energy dissipation has been shown theoretically in Sect. 3.5.3 to have a very large stabilizing effect.

Various factors which must be considered in liner design are discussed in Sects. 8.3.2 through 8.3.5. These factors include environmental factors, sizing of the resonators, and the number and placement of these resonators. The information contained in those sections is a result of both theoretical considerations and design experience which are available to date.

Another factor affecting the combustion oscillation is the thrust chamber shape which is discussed in Sect. 8.4. Here, the nozzle convergent section is considered as a portion of the thrust chamber. Changes in the shape of the chamber can produce changes in damping in that the amount of energy removed from the chamber oscillations depends upon the shape. The chamber shape also determines the waveform and the frequency of the oscillation, thereby having a secondary effect on the stability of the oscillation.

Other damping effects which may be employed by the designer are discussed in Section 8.5. These effects are due to chamber wall materials, condensed phases, and corner effects.

As a result of the overall knowledge of damping devices, based on both theoretical considerations

* W. A. Sirignano, Author.

and practical experience, a certain design procedure is suggested. Injector-face baffles should be employed to stabilize the lower transverse modes. In addition, acoustic liners should be employed, when necessary, and "tuned" to stabilize the higher transverse modes and any longitudinal modes which might persist. The other factors such as chamber shape should be examined, finally, to seek further improvements.

8.2 INJECTOR FACE BAFFLES

The following nomenclature pertains to Sect. 8.2 (see also Sect. 4.2.2):

A_b	Baffle surface area
D_{eq}	Equivalent diameter
f_s	Sensitive frequency of combustion process
$h_g^{(e)}$	Gas-side film coefficient determined from experimental heat transfer tests
$h_g^{(p)}$	Gas-side film coefficient predicted from modified Bartz equation
L_c	Chamber length from injector to nozzle entrance
L_u	Length of unbaffled portion of chamber
l_b	Baffle length
l_w	Wavelength
Q	Quality factor of resonant system (resonance frequency divided by half-power bandwidth)
T_f	Theoretical flame temperature
T_g	Gas-side wall temperature
T_m	Mean film temperature, $\frac{1}{2}(T_g+T_s)$
T_s	Free stream static temperature
ΔT_L	Temperature rise of cooling liquid
W	Characteristic baffle dimension; circumferential blade spacing
$\dot{w}_L$	Flow rate of cooling liquid
$\mathcal{Y}_n$	Nozzle admittance
$\mathcal{Y}_t$	Axial admittance at baffle tip
η_{c^*}	Ratio of actual to theoretical c*
Ω	Frequency parameter, $(s^2+s_{\nu\eta}^2)^{1/2}$

Subscripts:

b	Solution in baffled region
u	Solution in unbaffled region

8.2.1 Available Theory*

Three stabilizing effects have been identified with regard to the transverse mode instability by injector-face baffles (Sect. 3.5.3.3). These are (1) the modification of the acoustic properties of the combustion chamber, (2) restriction of the oscillatory flow patterns between baffle blades, thus protecting the sensitive pre-combustion processes, and (3) damping of the oscillations by vortex generation, separation, or frictional effects (the friction must be considered a secondary effect).

With certain injector patterns, namely, those with strong velocity or displacement sensitivity, the protective effect of the baffle on transverse, oscillating flow is predominant. The influence of vortex generation and separation associated with baffles has received little theoretical attention in connection with rocket applications,[177] and hence the relative importance of this mechanism cannot be accurately evaluated at this time. However, the change of the chamber acoustic properties has received theoretical study and has been successfully correlated with experimental tests of baffle stabilization and hence will constitute the main subject matter of this section.

Because a comprehensive theoretical treatment of baffle damping has not yet been developed, baffle design has had to proceed on the basis of largely qualitative principles, although these principles have relied on analytical studies of oscillating combustion and flow. To explain certain results obtained on the Gemini Stability Improvement Program, particularly the change in transverse mode frequency, Reardon successfully used a simple acoustical model of the baffle in combination with the sensitive time lag theory.[179] The same acoustical model can be used, without invoking a particular combustion model, to show the effects of baffle and chamber design on the resonant frequency and damping rate.

In this model,[456] the flow in the "pockets" between baffle blades is assumed to be one-dimensional. That is, only longitudinal oscillations can exist in the baffle pockets, although three-dimensional oscillations are allowed in the combustion chamber downstream of the baffle. To show the effects of the baffle on chamber acoustics more clearly, the effects of combustion, condensed phases, and mean flow are neglected in the analysis given here.* However, the significant

* F. H. Reardon, Author.

* The effects of combustion and mean flow are considered in Ref. 456.

coupling between the exhaust nozzle and the baffle is included, in the form of the nozzle admittance boundary condition at the chamber exit (see Sect. 3.6).

The combustion chamber is assumed to be cylindrical, with a planar injector face, as shown in Fig. 8.2.1a. The baffle blades are of length l_b, and the length of the chamber from the injector to the nozzle entrance is $L_c = L_u + l_b$. Since only longitudinal oscillations are considered in the baffle pockets, it is not necessary to specify the blade arrangement, although it is apparent that a relatively large number of blades (small pocket cross section) is implied by this assumption.

Small perturbations around the mean conditions are assumed, the perturbations are taken to have an exponential time dependence, e.g.,

$$p(x, r, \theta, t) = 1 + p'(x, r, \theta)e^{st}$$

where $s = \lambda + i\omega$, and all quantities are dimensionless, with the mean pressure, sound velocity, and chamber radius as reference quantities. The perturbations must satisfy the wave equation, which, in terms of the space-dependent amplitude p', is

$$\frac{\partial^2 p'}{\partial x^2} + \frac{\partial^2 p'}{\partial r^2} + \frac{1}{r}\frac{\partial p'}{\partial r} + \frac{1}{r^2}\frac{\partial^2 p'}{\partial \theta^2} = s^2 p' \qquad (8.2.1\text{–}1)$$

Assuming a solution of the form

$$p' = P(x)\Psi(r)\Theta(\theta)$$

it is found that, for the unbaffled part of the chamber, $x > l_b$,

$$\Psi(r) = J_\nu(s_{\nu\eta} r)$$

$$\Theta(\theta) = \begin{cases} e^{-i\nu\theta} & \text{spinning mode} \\ \cos \nu\theta & \text{standing mode} \end{cases}$$

However, in the baffled part of the chamber, $x < l_b$, because of the assumption of one-dimensionality, $\Psi = \Theta = 1$.

The approach taken is to obtain the solutions separately for the baffled and unbaffled parts of the chamber and then to match the two solutions by use of the axial admittance at the baffle tip,

$$\mathcal{Y}_t = \left.\frac{u'}{p'}\right|_{x=l_b}$$

where u' is the axial component of the velocity oscillation. The transition from the one-dimensional oscillations in the baffle pockets to the three-dimensional oscillations downstream occurs in a region of complex flow near the tip of the baffle. In this simplified analysis the effects of this transition region are neglected and the region itself is assumed to be very narrow.

Using the subscripts b and u to denote the solutions in the baffled and unbaffled regions, respectively, the equations to be solved are

$$\frac{d^2 P_b}{dx^2} - s^2 P_b = 0 \qquad (8.2.1\text{–}2)$$

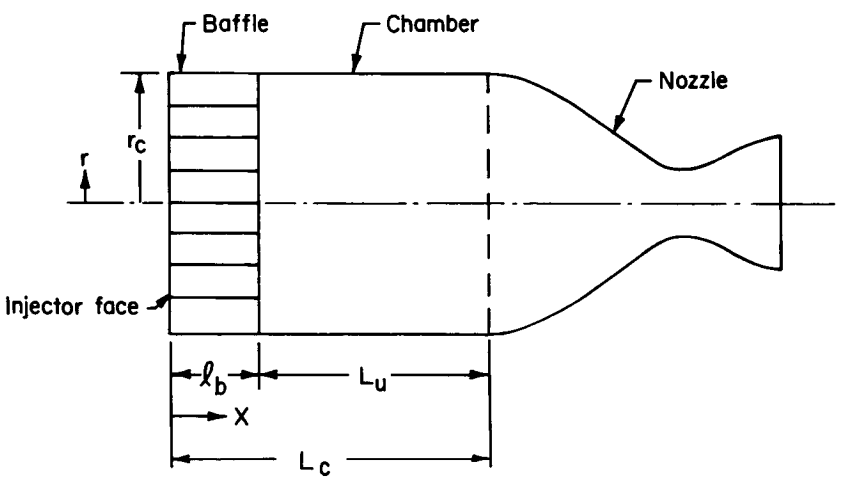

FIGURE 8.2.1a.—Schematic illustration of baffled combustion chamber.

$$\frac{d^2P_u}{dx^2} - (s^2+s_{\nu\eta}^2)P_u = 0 \qquad (8.2.1\text{–}3)$$

The injector face can be assumed to behave acoustically as a solid wall, so that

$$P_b = P_o \cosh sx$$

and since

$$u' = -\frac{1}{\gamma s}\frac{dp'}{dx}$$

for small perturbations, the admittance at the baffle tip is

$$\mathcal{Y}_b(l_b) = -\frac{1}{\gamma}\tanh sl_b \qquad (8.2.1\text{–}4)$$

The solution for P_u can be written as

$$P_u(x) = A \sinh \Omega(x-l_b) + B \cosh \Omega(x-l_b)$$

where $\Omega^2 = s^2+s_{\nu\eta}^2$. The constants A and B must be determined by use of the boundary conditions. At the nozzle entrance, $x-l_b = L_c - l_b = L_u$,

$$\mathcal{Y}_u(L_c) = \mathcal{Y}_n = -\frac{\Omega}{\gamma s}\frac{(A \cosh \Omega L_u + B \sinh \Omega L_u)}{(A \sinh \Omega L_u + B \cosh \Omega L_u)} \qquad (8.2.1\text{–}5)$$

and at the baffle tip, $x-l_b = 0$,

$$\mathcal{Y}_u(l_b) = -\frac{\Omega}{\gamma s}\frac{A}{B} \qquad (8.2.1\text{–}6)$$

Combining Eq. (8.2.1–5) and (–6) gives the relation between the baffle and nozzle admittances:

$$\gamma\mathcal{Y}_u(l_b) = \frac{\gamma\mathcal{Y}_n + \frac{\Omega}{s}\tanh \Omega L_u}{1+\frac{s}{\Omega}\gamma\mathcal{Y}_n \tanh \Omega L_u} \qquad (8.2.1\text{–}7)$$

The nozzle admittance has been calculated in the form

$$\mathcal{E}(\omega, s_{\nu\eta}) = \mathcal{E}_r + i\mathcal{E}_i = -\gamma\mathcal{Y}_n \qquad (8.2.1\text{–}8)$$

Making use of Eq. (8.2.1–8), and setting $\mathcal{Y}_b(l_b) = \mathcal{Y}_u(l_b)$ gives

$$\tanh sl_b\left(\mathcal{E}\tanh \Omega L_u - \frac{\Omega}{s}\right) = -\left(\frac{\Omega}{s}\right)\mathcal{E} + \left(\frac{\Omega}{s}\right)^2 \tanh \Omega L_u \qquad (8.2.1\text{–}9)$$

Since Eq. (8.2.1–9) is complex, it is equivalent to two real equations. Therefore, for given values of the parameters $\mathcal{E}$, L_u, l_b, and $s_{\nu\eta}$, the appropriate values of the oscillation frequency ω and the amplification factor λ can be determined. However, since the nozzle admittance has only been calculated for neutral oscillations ($\lambda=0$), Eq. (8.2.1–9) can only be solved for small values of λ, such that it can be assumed that $\mathcal{E}(s) \approx \mathcal{E}(\omega)$.

The case of an unbaffled chamber is obtained by setting $l_b = 0$, so that Eq. (8.2.1–9) becomes

$$\left(\frac{\Omega}{s}\right)\tanh \Omega L_c = \mathcal{E} \qquad (8.2.1\text{–}10)$$

and if the nozzle is replaced by a closed end, Eq. (8.2.1–10) reduces to

$$\tanh \Omega L_c = 0$$

Thus, for a closed-end cylinder with no baffles,

$$\lambda = 0$$

$$\omega = \sqrt{s_{\nu\eta}^2 + \frac{j^2\pi^2}{L_c^2}} \qquad j = 0, 1, 2, \ldots \qquad (8.2.1\text{–}11)$$

It is clear that when either baffles or a nozzle are added both λ and ω take on values somewhat different than those of Eq. (8.2.1–11).

For acoustic oscillations in a closed-end cylinder with baffles at one end, Eq. (8.2.1–9) becomes

$$s \tanh sl_b = -\Omega \tanh \Omega L_u \qquad (8.2.1\text{–}12)$$

Assuming that λ is small, Eq. (8.2.1–12) can be split into two real equations:

$$\omega \tan \omega l_b = \Omega_R \tanh \Omega_R L_u \qquad (8.2.1\text{–}13a)$$

$$\lambda\left(\tan \omega l_b + \frac{\omega l_b}{\cos^2 \omega l_b}\right) = -\Omega_I\left(\tanh \Omega_R L_u + \frac{\Omega_R L_u}{\cosh^2 \Omega_R L_u}\right) \qquad (8.2.1\text{–}13b)$$

Since $\Omega^2 = s_{\nu\eta}^2 - \omega^2 + 2\lambda\omega i$, for small λ, Ω_I is directly proportional to λ so that Eq. (8.2.1–13b) is satisfied only by $\lambda = 0$. That is, the mechanism considered here will produce no baffle damping unless there is another loss-producing device in the system. However, the frequency is modified by the presence of the baffle, as shown by Eq. (8.2.1–13a). For very short baffles, this equation simplifies to

$$\omega^2 l_b \approx \Omega_R^2 L_u$$

so that

$$\omega \approx s_{\nu\eta}\sqrt{\frac{1}{1+l_b/L_u}} \approx s_{\nu\eta}\left(1-\frac{1}{2}\frac{l_b}{L_u}\right)$$

As the baffle length is increased, the frequency is further depressed and Ω_R becomes an appreciable fraction of $s_{\nu\eta}$. Then $\tanh \Omega_R L_u \rightarrow 1$ and the frequency is given by the following equation, which is independent of chamber length,

$$\omega^2 = \frac{s_{\nu\eta}^2}{1+\tan^2 \omega l_b}$$

provided that L_u is unity or greater.

8.2.2 Blade Arrangement*

This section is devoted primarily to the effect of blade arrangement on the stabilizing efficiency of a baffle system. However, before going into this characteristic of a baffle, it is necessary to further discuss the nature of the problem that baffles are intended to solve. There are an infinite number of baffle configurations possible, all of which cannot be covered in this text. Therefore, it is important that the reader understand the underlying principles of baffle design in order to be able to extend these basic concepts to new and original designs. (See Sects. 8.2.1 and 3.5.3.3.)

Injector-face baffles are intended as a damping device for the high frequency modes of instability referred to in Chapter 4 as the transverse modes. These modes of instability are characterized by oscillations parallel to the injector face. In a cylindrical chamber, the pressure and velocity vary in both the radial and circumferential directions for the tangential modes, and only in the radial direction for the radial modes.

The tangential modes of instability can be further divided into two classes: spinning modes, which are the result of a single pressure wave traveling tangentially in either a clockwise or counterclockwise direction; and a corresponding velocity perturbation in phase with the pressure or a standing tangential mode which consists of two counter-rotating waves with the velocity perturbation $90°/\nu$ out of phase with the pressure in space dimensions (where ν is the order of the mode).

Particle motion close to the injector face is restricted to the baffle cavities. By means of such an incompatible boundary condition one can reduce the tendency toward spinning tangential modes by the use of radial blades as shown in Fig. 8.2.2a. Hub or ring-type baffles are used to control the radial modes. The number of baffle cavities is important in controlling the standing modes. These standing tangential and the radial modes of instability are depicted in Fig. 8.2.2b, which shows the particle paths and the pressure antinodes for the first two tangential and radial modes. Also shown are the three common combined modes: the first tangential–first radial; first tangential–second radial; and second tangential–first radial modes.

A number of references[169,582] can be found which discuss the pure transverse modes, as well as the combined tangential and radial modes. In general, baffle design principles that apply to damping of the pure transverse modes apply equally well for the combined modes.

Of major concern in the design of an effective baffle is the location of the blades and hubs relative to particle paths, since the baffle constitutes an obstruction to particle motion. There are a few general comments concerning the tangential modes that can be helpful in understanding baffle design. For example, with the exception of the first tangential mode or combinations thereof, the velocity at the center of the injector is zero (see Fig. 8.2.2c). Also, the radial unsteady velocity is greater than the tangential unsteady velocities. In general, as the tangential modes become of higher order, the major gas particle motion and pressure variations are limited to the outer circumference of the chamber. This characteristic becomes important in considering placement of baffles to suppress the higher order modes. The number of radial blades is most important in this region. Also the radial blades must extend close to the chamber wall (small baffle tip gap) or the anticipated damping will not be achieved (e.g., see Sect. 8.3.6).

In the case of pure radial modes, the velocity perturbations are limited to the radial direction, with the axis of symmetry being the chamber axis at the center of the injector and again, as in the case of the tangential modes of higher than the

* J. M. McBride, Author.

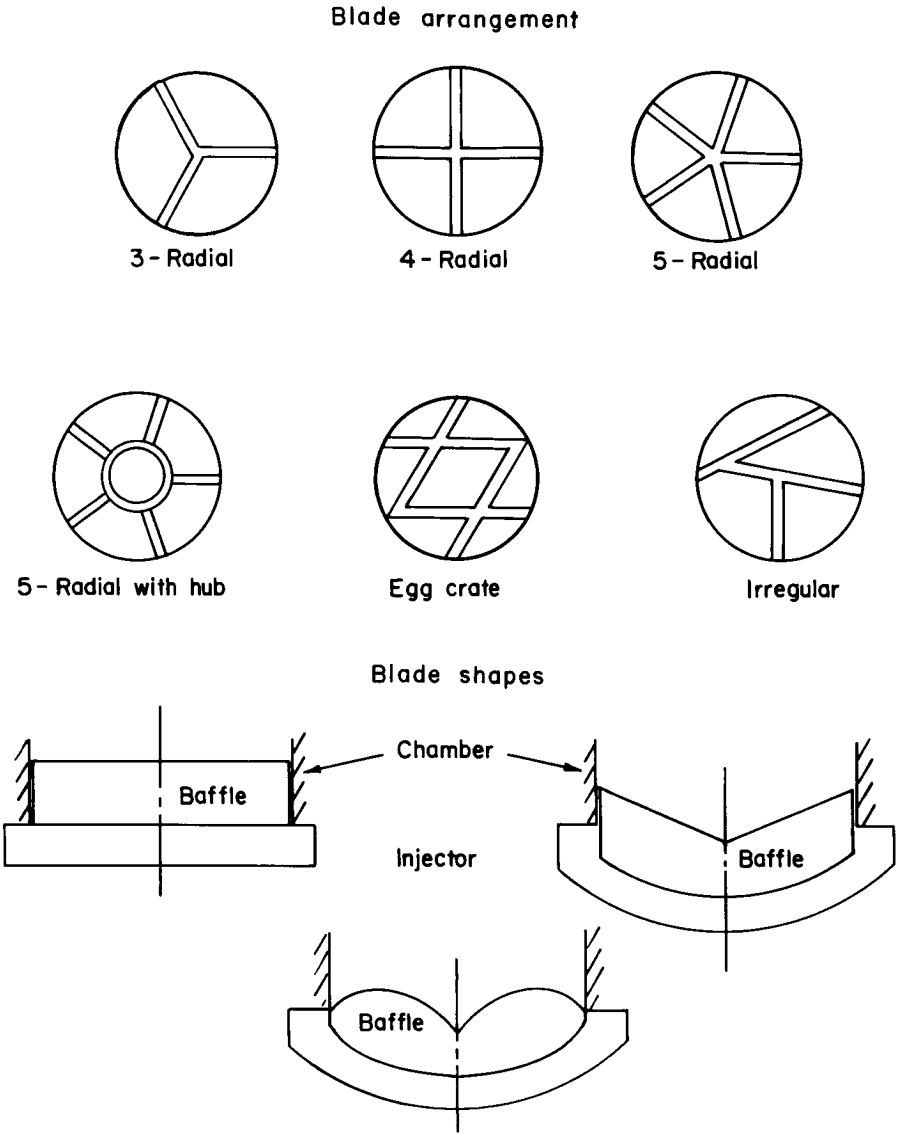

FIGURE 8.2.2a.—Types of baffles.

first order, no velocity perturbations occur at the center of the injector. The order of a radial mode is determined by the number of velocity antinodes, as shown in Fig. 8.2.2b.

The physical characteristics of the baffle are involved directly with the several mechanisms considered to be responsible for suppression of resonant combustion (Sect. 3.5.3.3). Unfortunately, the state-of-the-art of baffle design is such that no argument can be presented to prove conclusively that only one dominant mechanism exists. Hence in the design of an effective blade arrangement the selection of compartment size, blade length, number, position and degree of symmetry may follow different paths of logic. The following discussions cover these baffle design parameters in some detail.

8.2.2.1 Number of blades.—The optimum number of blades for any baffle configuration depends primarily on the mode of instability to which the system is most susceptible. The char-

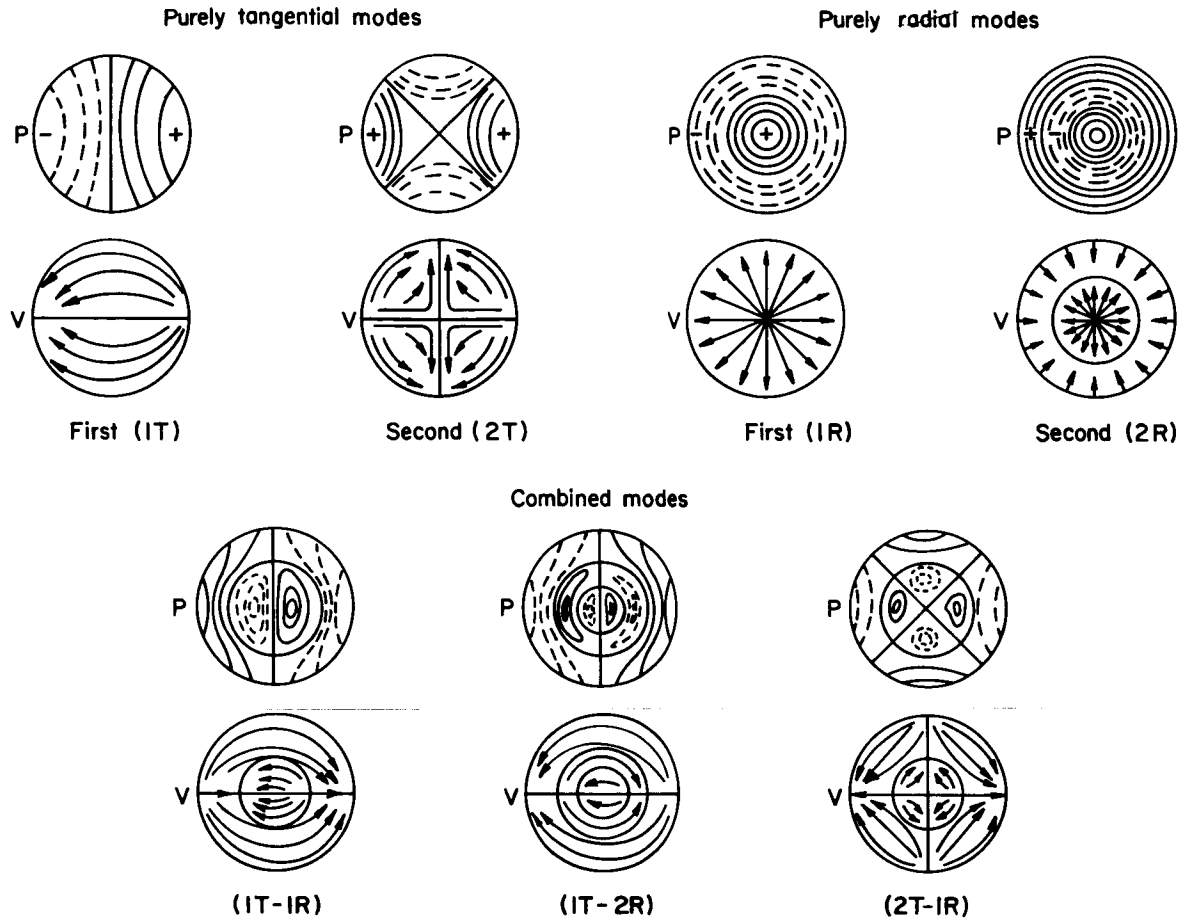

FIGURE 8.2.2b.—Transverse mode characteristics.

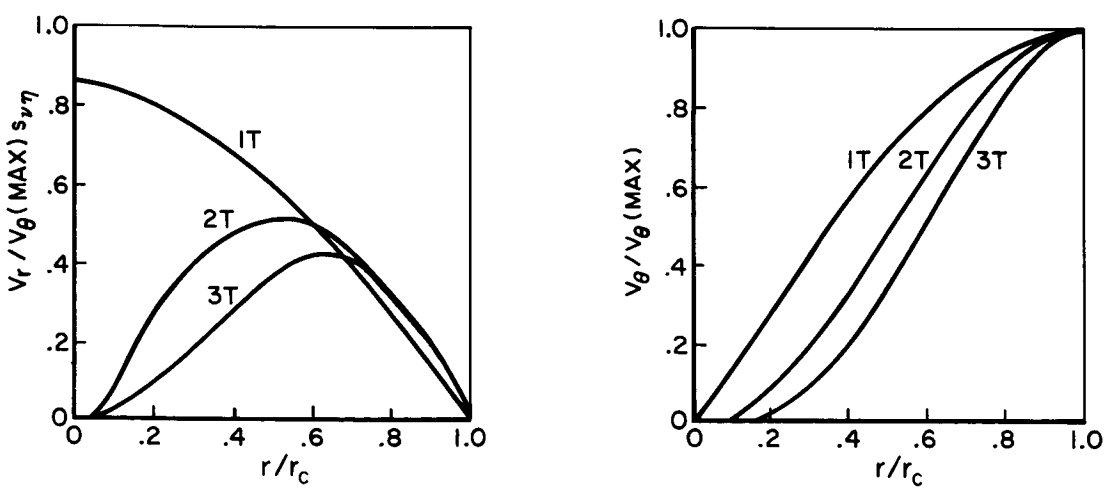

FIGURE 8.2.2c.—Tangential mode velocity profiles.

acteristics of a baffle, as related to the blade and hub arrangement, depend strongly upon the ability of the baffle to alter the acoustics of the combustion chamber. This can be accomplished by introducing radial baffle blades or ring-shaped hubs such as shown in Fig. 8.2.2d, that interfere or alter the transverse mode particle paths. For example, the selection of the minimum symmetrical baffle configuration to damp a first tangential mode would be a three-bladed design. It is also apparent that a one or two-bladed baffle could, at the most, only cause the mode to stand in the baffle cavity with pressure antinodes at the baffle blade and the velocity antinodes displaced 90°. The same type of logic applied to a second tangential mode as depicted in Fig. 8.2.2d would indicate that a symmetrical three-bladed baffle also would be effective for this mode, and that

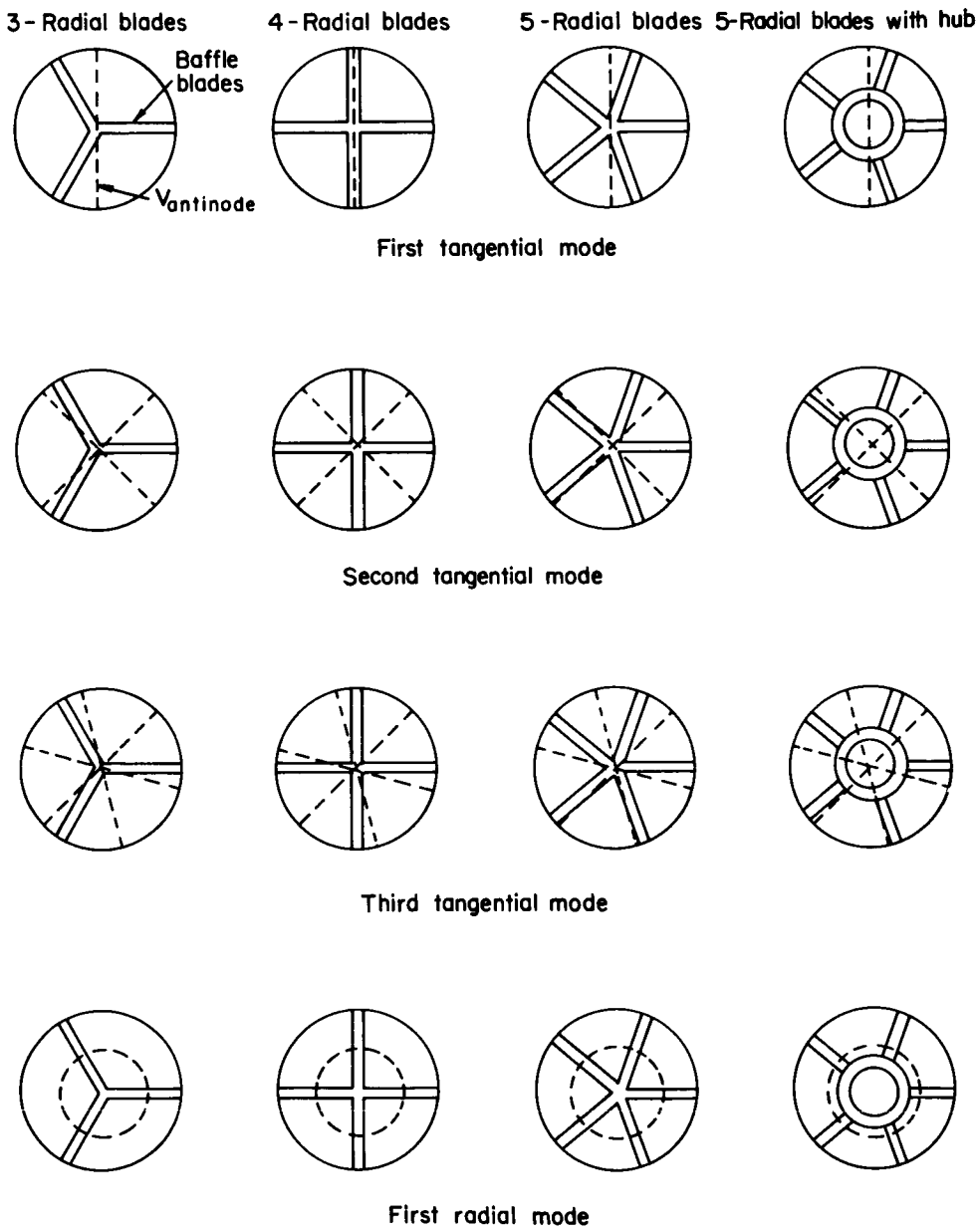

FIGURE 8.2.2d.—Possible mode orientations for various baffles.

the symmetrical four-bladed baffle would have little or no effect because the second tangential mode can exist within the baffle cavities.

Extension of these considerations to the higher order tangential modes leads to the generalization that a baffle configuration having an *odd* number of radial blades (with the exception of a single blade) would offer protection from modes which are of the order less than the number of blades and, to some degree, protection from modes of an order higher than the number of blades (provided the order of the mode divided by the number of blades is not equal to an integer). This then gives the designer a criterion for the minimum number of blades required in the case of a symmetrical baffle arrangement. However, this generalization only indicates the minimum number of blades required, and does not provide information on the optimum number of blades required to maximize damping and alter chamber resonant frequencies. For this information, certain experimental data are useful which are discussed in detail in Refs. 309, 473, 711, and 737.

Of interest to the injector designer is the trade-off between baffle length and compartment size because of system considerations such as heat transfer, performance, system pressure drop and compatibility. There is little quantitative data available; however, what is available indicates that–as might be expected–when the order of the tangential mode approaches the number of blades, the trade-off becomes quite significant in terms of damping rate, as can be seen from Fig. 8.2.2e. Two modes and two ratios of blade length to chamber diameter (l_b/D) are shown; all trends are toward higher decay rates for greater blade number. The trend of increasing blade number allowing reduction in the blade length required for stability is shown in Fig. 8.2.2f, based on Ref. 711 data. The plot is for the first tangential mode. The dashed extension is drawn to indicate that the boundary between the stable and unstable regions should approach asymptotically a value of circumferential blade spacing at the chamber wall, W, over wavelength l_w $W/l_w = 0.92$ at $l_b/D_c = \infty$. This asymptote represents a baffle configuration having two blades ($W = \pi r_c$), therefore $W/l_w = S_{\nu\eta}/2 = 0.92$, where it is assumed damping of the mode will take place at long baffle lengths.

This trend of stability improvement for smaller baffle cavities (smaller W/l_w) was investigated experimentally and the test firing data are presented in Fig. 8.2.2g. The indication is that there is nothing to be gained if $W/l_w < 0.2$. Decreasing the cavity characteristic dimension any further may, in fact, prove detrimental for very low W/l_w as shown by the destabilizing behavior in these LOX/LH_2 tests (higher transition temperatures). Additional support for this conclusion can be found in Figs. 8.2.2h and i where the decay rate and frequency shift, as indicated from

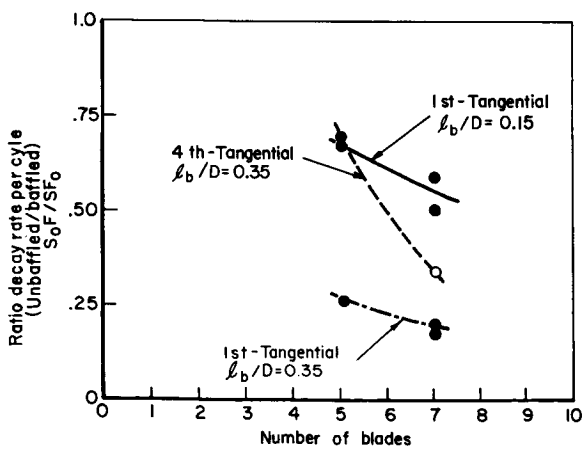

FIGURE 8.2.2e.—Effect of number of blades.

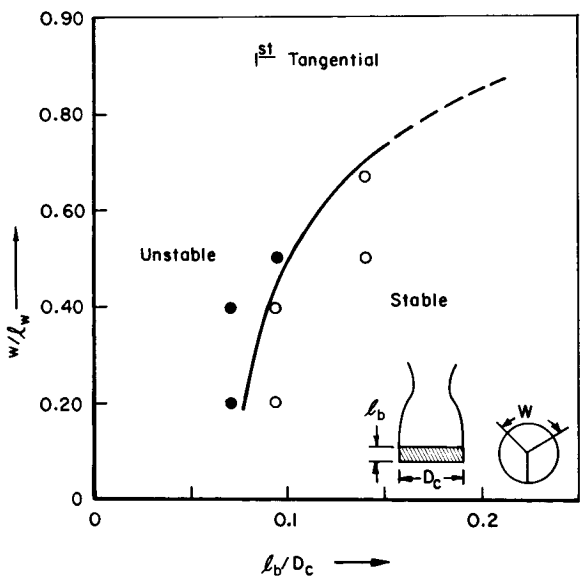

FIGURE 8.2.2f.—Effect of baffle spacing versus baffle length.

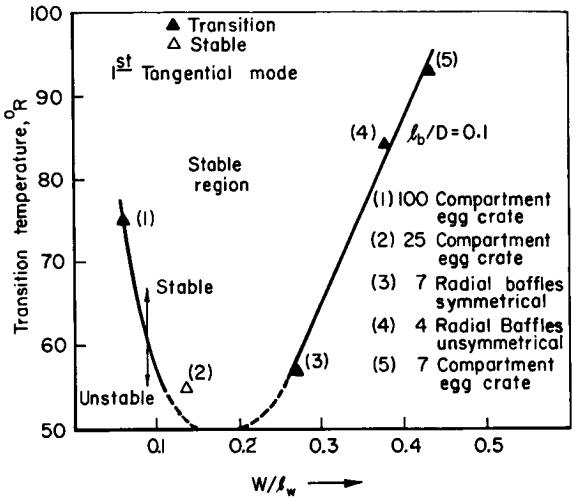

FIGURE 8.2.2g.—Effect of baffle spacing.

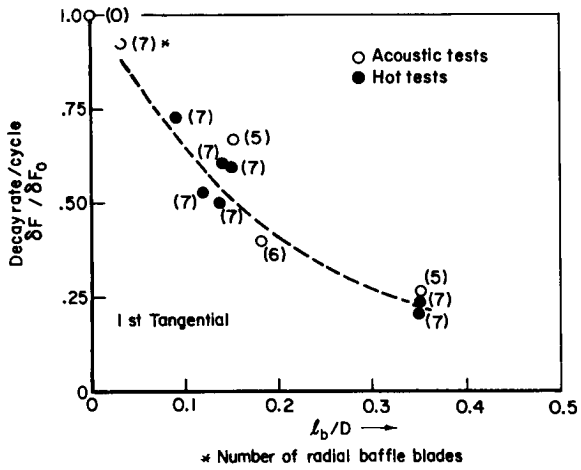

FIGURE 8.2.2h.—Damping versus baffle length and number of blades.

acoustic tests, was not significantly altered (for the first tangential mode) by changing the number of blades. Figure 8.2.2h illustrates changes from a five-bladed symmetrical baffle ($W/l_w = 0.37$) to a seven-bladed baffle ($W/l_w = 0.26$) whereas Fig. 8.2.2i supplies data covering 3 to 20 blades.

This discussion thus far has been limited to the tangential modes, principally the first tangential mode. However, there are data available which indicate that similar trends are present for the higher order tangential modes and the radial modes. For the radial modes, W is the average cavity dimension along the chamber radius.[473]

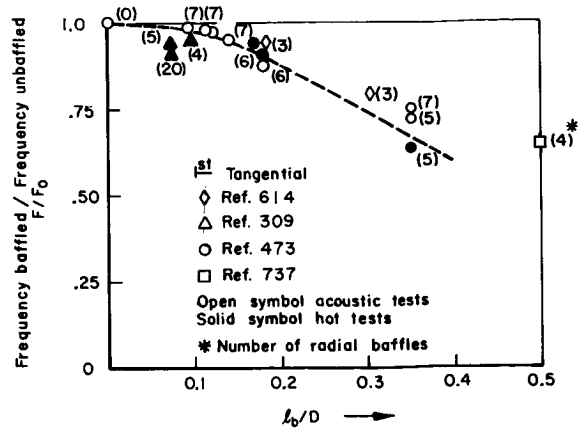

FIGURE 8.2.2i.—Frequency depression versus baffle length and number of baffles.

A possible explanation of the trend which indicates that excessively small baffle compartments can be detrimental is that the baffle surfaces interfere with the combustion processes (surface impingement and stream confinement slow the attainment of mixing so that steady-state combustion is delayed). This makes the baffle less effective. Another point to consider is that at extremely small W dimensions the baffle could behave as a series of closed-open tubes which have cross-sectional dimensions in the order of 1/16 wavelength.* For this case the baffles would exhibit the characteristics of a quarter wavelength tube, such as shown in Fig. 8.2.2j, which illustrates only narrow band effectiveness (high Q) and makes the baffle length a critical parameter.

8.2.2.2 Symmetry.—There is at present a tendency to use symmetrical baffles in rocket engines. This is primarily because of the difficulties associated with feeding coolants to an asymmetric baffle system from a feed system that is generally symmetric. However, some experimental work has been done with asymmetric baffles of the type shown in Fig. 8.2.2a. Several reasons have been stated as to why an asymmetric baffle system would be superior to a symmetric system, all of which basically revolve about the idea that asymmetrically placed baffles will "scatter" the

* When the cross-sectional dimensions are in this range uniform pressure is approximated for the closed-open tubes.

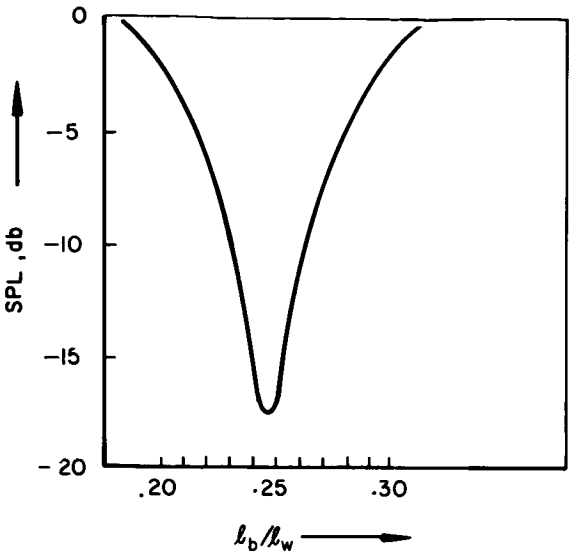

FIGURE 8.2.2j.—Attenuation of closed-open tube.

energy generated in a broader frequency band.* Limited data has been accumulated on what could be considered a truly asymmetric baffle.[614] Some data is available on configurations[332] in which the radial blades of the baffle have unequal sector angles or in which the baffle legs are directed in other than a radial direction. The results from tests with units of this type[473,309,711] indicate no obvious superiority of this type of baffle over a symmetrical baffle having the same number of baffle blades. Comparing the limited results between the unequal sector angle baffles and the asymmetric baffles of Ref. 614 indicate no obvious superiority in the gross stability characteristics of the various injectors tested. It is apparent that additional work in this area is required before any more specific comparisons could be made.

8.2.3 Blade Design†

One aspect of baffle design, the size of the baffle cavity or pocket, is discussed in Sect. 8.2.2.1. The data accumulated indicate that characteristic cavity dimension to combustion instability wavelength ratios of the order of 0.20 are desirable. What remains to be determined is the optimum baffle length and shape viewed from the side of the baffle (examples are shown in Fig. 8.2.2a) and, finally, design considerations related to cooling of the baffles.

8.2.3.1 Baffle length.—The mean baffle length is defined in Ref. 473 as

$$l_{bm} = \frac{1}{r_c}\int_0^{r_c} l_b(r)\,dr \qquad (8.2.3\text{–}1)$$

for the tangential modes. This definition is used here in defining baffle length since it applies to the various configurations discussed. However, a significant deviation from a baffle arrangement in which the blades do not extend to the center of the chamber will require some judgement in specifying the baffle height since, in the case of the tangential modes, baffle height at the wall of the chamber is more effective in increasing phase and gain stabilization. This is because the major portion of the gas motion in tangential modes occurs near the chamber walls. The gas motion becomes more concentrated at the chamber wall as the order of the mode increases, which would indicate that the effective height may change, depending on the mode being considered.

From the standpoint of acoustics, Fig. 8.2.2h indicates that baffle length has maximum effect on gain changes when the baffle height to chamber diameter ratio is between zero and 0.10. At $l_{bm}/D_c = 0.1$ the damping rate is twice that for $l_{bm}/D_c = 0$. Increasing this ratio to 0.30 again doubles the damping using the $l_{bm}/D_c = 0.1$ point as a reference. Similar trends have been noted in test firing data[473] which are also presented in Fig. 8.2.2h. However, a word of caution is warranted. Consider the feedback mechanism such as those proposed by Dykema and Heidmann (discussed in Chapter 4). Response curves from these mechanisms are typically of the shape depicted in Fig. 8.2.3a. Also consider the frequency shift illustrated in Fig. 8.2.2i. It can be deduced that, if the unbaffled resonance of the chamber is to the left of peak response, increasing the baffle length will indeed increase the stability of the system in both a phase and gain stabilizing manner. However, if the unbaffled resonance is to the right of the peak response of the controlling feedback

* The energy will be distributed between a number of discrete and mixed frequencies based on the individual baffle cavity geometries and interactions rather than being concentrated in a narrow frequency band.

† J. M. McBride, Author.

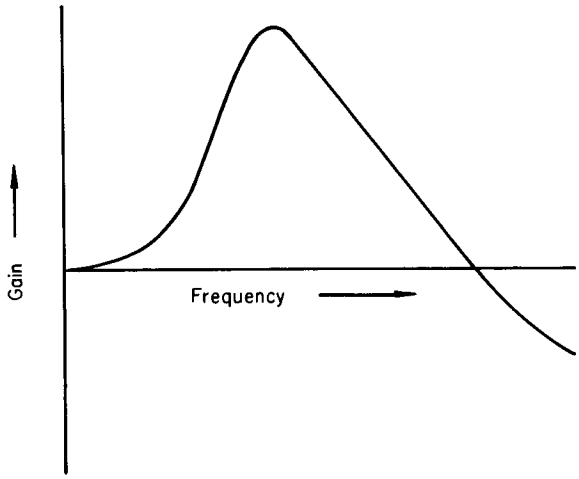

FIGURE 8.2.3a.—Typical response curve.

mechanism, and if the rate of increase in gain for this mechanism as a function of frequency is greater than the damping increase due to increasing the baffle length, the system will become less stable.

The adverse effect of injector element design on the effectiveness of a given baffle can be found in the data presented in Ref. 14, where both a seven- and a five-bladed baffle configuration, having the acoustic characteristics indicated in Figs. 8.2.2h and i exhibited dynamically stable combustion characteristics when tested with a coarse injector pattern. This same configuration, when tested with a fine injector pattern, failed to stabilize combustion. This does not make the design of an optimum baffle an impossible task, but rather one which requires consideration of both the injector pattern and the baffle. The designer must in his selection of an injector-baffle system use an analytical technique such as discussed in Chapter 4 to determine, as a minimum, the sensitive frequency range of his candidate patterns. This can be rather easily done using Crocco's sensitive time lag (τ). Reardon[580] (see Sect. 6.3.3) has developed correlations for τ as a function of injector parameters. The values can be used to estimate the sensitive frequency (f_s), where

$$f_s = \frac{1}{2\tau} \qquad (8.2.3\text{–}2)$$

or by determining the point of peak response for Dykema's response function (see Sects. 4.4.1.3 and 6.5.2) and evaluating how the baffles will alter the chamber resonances relative to the estimated sensitive frequency. Although neither of these techniques will insure design of a stable system, it will minimize the amount of development work required.

Turning now to the stabilizing aspect of a baffle attributed to protection of the sensitive combustion zone, this mechanism was postulated based on observation of the combustion process in a transparent thrust chamber (see Sect. 9.2.2.5). In the experiments it was observed that a certain length of baffle was required to minimize the interaction between adjacent streams of propellants when perturbed by a bomb. From various studies (e.g. pg. 93 Ref. 190) it has been shown that baffles must be present in the early combustion region to be effective in reducing stream interaction. Additional support can be found for this mechanism in the data presented by Hefner[332] where he postulated that the initial high decay rate with baffle length measured from test firing data[473] (Fig. 8.2.3b) was significantly greater than that measured in acoustic tests and therefore could be attributed to the combustion zone protection concept. From the data available it is apparent that selection of a baffle length on the basis of its optimum frequency and amplitude stabilizing effects should be sufficient to satisfy the baffle length criterion for the combustion zone protection concept, since the most intense combustion occurs within two to three inches of the face. Baffle l_d/D values of 0.2 to 0.3 have also

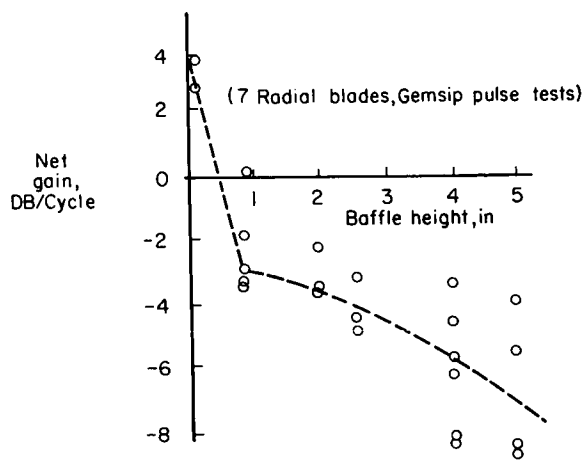

FIGURE 8.2.3b.—Effect of baffles on first tangential mode.

proved to be successful when applied to high performance, small diameter engines where the baffles were only $\frac{1}{4}$ inch long and the injector patterns were very fine.[476]

8.2.3.2 Blade shape.—Data on the acoustic effects of baffle shape are limited to that reported by Weiber[737] and others.[14] In the case of the Wieber data, the baffle shape change was a result of a change in the contour of the injector face, which resulted in the baffle being longer at the chamber wall than at the center. The test results are not conclusive because the variation in the injector face contour in itself has a significant effect on the decay rates measured, making the effect of baffle shape difficult to interpret.* However, the results do indicate that based on the average height (as determined using Eq. 8.2.3–1) the baffle shape described above is more effective than an equivalent constant height baffle in damping oscillations.

In the case of the data from Ref. 14, the same trend is indicated. However, the variation in baffle shapes is not significant, making correlations between baffle shape and damping characteristics impossible. Additional work in this area is required. The trends indicated are consistent with the observation made earlier that the major gas motion for the tangential modes occurs near the chamber wall. This effect becomes more noticeable for the higher order modes.

The effectiveness of radial baffles extending approximately $\frac{1}{3}$ the chamber radius from the chamber wall has been demonstrated by Moberg with a 1750-lb-thrust engine.[492] In this demonstration, dynamic stability was not evaluated. From the discussion and data presented the following general rules can be used in designing a baffle.

1. An odd number of baffle blades is best for the tangential modes providing the order of the mode divided by the number of blades is not an integer.
2. For the radial modes, hubs located at the velocity antinodes indicated in Fig. 8.2.2a are best. The minimum number of hubs required are equal to the order of the mode (i.e., first radial requires one hub).
3. Making the baffle compartments too small may be detrimental. A baffle characteristic cavity dimension (W) in the range $0.4 > W/l_w \geq 0.2$ where $l_w = a/f$ appears to be most desirable.
4. Baffle length to chamber diameter ratios in the range of 0.2 to 0.3 appear to be optimum.

8.2.3.3 Blade cooling.—In addition to the stabilizing effects of baffles, consideration must be given to such factors as methods of baffle cooling, the effect the baffle will have on performance and the magnitude of system pressure losses that can be attributed to the addition of baffles. Detailed considerations of each of these factors is beyond the scope of this section and are, in general, influenced by the injector systems in which the baffles are to be installed. However, some discussion is warranted.

The effect of baffles on performance of a rocket engine has never been documented in the open literature; however, limited data is available for a few engine systems and is summarized below:

System	Change in specific impulse, sec
Atlas	−0.3
Thor	+1.1
F-1	+5.3
H-1	−0.5
Titan	−0.9 (Stage I)
Titan	−0.4 (Stage II)

Though this data would seem to indicate that there is no significant performance loss attendant to the addition of baffles to the injector, this conclusion must be tempered by the probability that the injector pattern was altered during the process. Since with the addition of baffles, the system would be considerably less susceptible to instability, the injector pattern could be modified to produce more efficient combustion. The net result would be very little loss (or perhaps, even a small gain) in performance for the baffled system.

A survey of several engine systems indicates

* The interrelationship of injector face contour and baffle shape is largely a result of alterations in the baffle height at the critical location near the chamber wall. Often with a face contour the baffle length at the wall is minimized.

that a properly designed regeneratively-cooled baffle system will require an increase in propellant feed pressure on the order of 7% of chamber pressure in order to operate reliably. However, this is strongly dependent on the cooling techniques used. For example, with tip-injecting baffles, the pressure drop in some cases has to be maintained at the unbaffled injector pressure drop.

At least one set of experimental measurements of the thermal environment in which a baffle must operate,[14,477] as well as several related articles on similar design problems with cooled chambers, are available. The most complete set of baffle design cooling data is a result of work discussed in Ref. 14. This experimental study of blade cooling utilized a highly instrumented water-cooled baffle. The significant results of this work are presented in Figs. 8.2.3c and d. The first figure gives what is referred to as the calorimetric heat fluxes from three separate tests. The calorimetric heat flux, defined by

$$q/A = \frac{\dot{w}_L c_L \Delta T_L}{A_b} \qquad (8.2.3\text{–}3)$$

represents an average heat flux for a series of coolant channels located at various distances from the injector face. The fluxes are determined from the bulk temperature rise of the coolant in the individual channels. The variation in heat flux as a function of baffle length is apparently the result of combustion intensity as a function of distance from the injector face. (i.e., steadily increasing combustion intensity in the first few inches). Perhaps the most significant data from the standpoint of the designer is a comparison of the predicted and experimental gas side film coefficients. The predicted value is based on a modification* of the Bartz correlation.[81]

$$h_g^{(p)} = \frac{0.026}{D_{eq}^{0.2}} \left(\frac{\mu^{0.2} C_p}{Pr^{0.6}}\right)_m \left(\frac{\dot{w}}{A_d}\right)^{0.8} \left(\frac{T_s}{T_m}\right)^{0.8} \qquad (8.2.3\text{–}4)$$

where

$$T_m = \frac{T_g + T_s}{2}$$

* The $(T_s/T_m)^{0.8}$ term replaces the boundary layer correction in the Bartz relation.

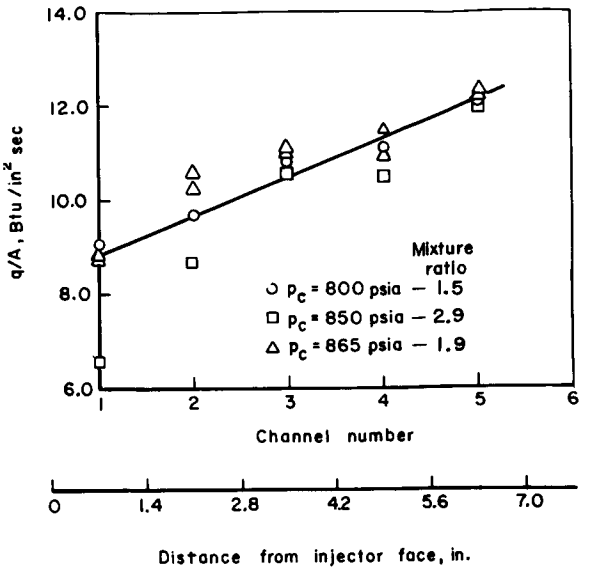

FIGURE 8.2.3c.—Calorimetric heat flux.

and T_s is the static temperature defined by

$$T_s = \eta_c^{*2} T_f$$

The experimental film coefficient $h_g^{(e)}$ is calculated from

$$h_g^{(e)} = \frac{q/A}{T_s - T_g(\text{expt.})} \qquad (8.2.3\text{–}5)$$

The quantity plotted in Fig. 8.2.3d is the ratio of film coefficients (H) defined by

$$H = h_g^{(e)}/h_g^{(p)}$$

The results indicate that the gas-side film as estimated by the modified Bartz equation can be in error by as much as 50% on the low side.† It should be noted that no film cooling was used on the experimental baffle.

A great number of baffle cooling schemes have been proposed and many of them subsequently tested. Tomazic et al.[690] have evaluated five designs for the M-1, LOX/LH_2 combustor (baffle configurations (a) through (e) in Fig. 8.2.3e). Considering a number of engine development programs, the most widely used method has been

† This is not unexpected when one considers the Bartz correlation was derived for heat transfer in the nozzle where convection plays the major role rather than near the baffles where recirculation, injection pattern, etc., are dominant.

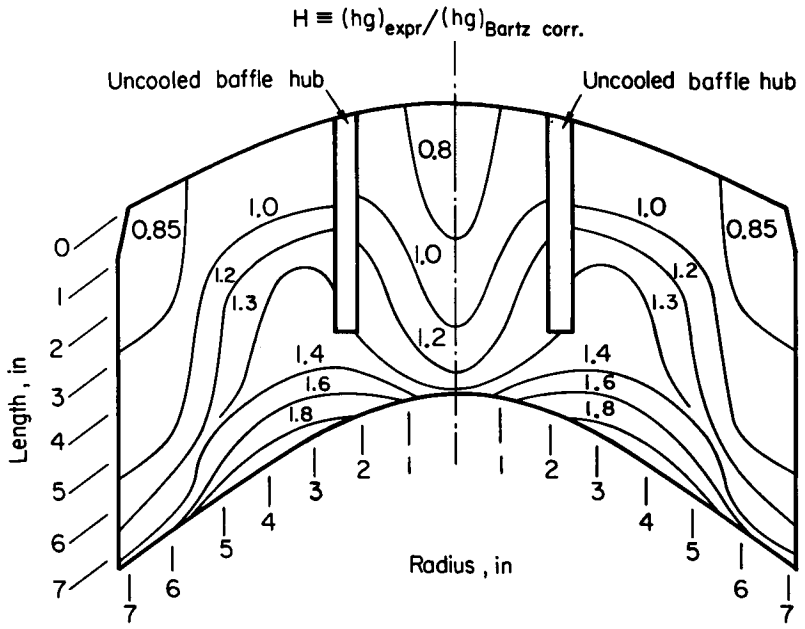

FIGURE 8.2.3d.—Gas side film coefficient profile.

the single-pass coolant system. Here the propellant (or propellants) are injected into the chamber at the baffle tips, i.e., the "dump" cooling approach shown as configuration (a), Fig. 8.2.3e. This method of baffle cooling has been the subject of much discussion because it could introduce a secondary combustion zone downstream of the baffle and therefore be detrimental to stability. To date, however, no conclusive evidence to confirm this secondary zone has been obtained from injector development programs. Lately, another baffle cooling concept, which is designed to eliminate secondary injection, has received increased attention. A schematic version of this double-pass design, or "regenerative-cooled" baffle, is illustrated as configuration (f) in Fig. 8.2.3e (note that configuration (c) also approaches this design goal by moving the coolant injection close to the injector face).

8.3 ACOUSTIC LINERS

The following nomenclature pertains to Sect. 8.3:

a	Ratio of aperture area to resonator cross-sectional area; percent open area
$\grave{a}$	Ratio of the jet-velocity amplitude on the cavity side of the orifice to the jet-velocity amplitude on the chamber side (see Eq. 8.3.1–25)
A_o	Cross-sectional area of orifice (aperture)
b	Amplitude of chamber velocity in phase with the pressure divided by $\epsilon^{1/2}\bar{a}_1$
B	Constant related to orifice entrance conditions
C_c	Contraction coefficient
C_d	Discharge coefficient
C_f	Orifice flow coefficient
$\bar{C}_p$	Average pressure coefficient representing the interaction between the orifice-jet flow and the chamber-cross flow. The average is taken both time-wise and circumferentially around the jet.
C_v	Velocity coefficient
$\mathcal{C}_{cav}$	Cavity capacitance
d_o	Orifice diameter
F_d	Dissipation force per unit liner-surface area (see Eq. 8.3.1–24)
g	Amplitude of chamber velocity out of phase with the pressure divided by $\epsilon^{1/2}\bar{a}_1$
K	Constant defined by Eq. (8.3.1–14)
l_o	Orifice length
l_{eff}	Effective orifice length
l_w	wavelength

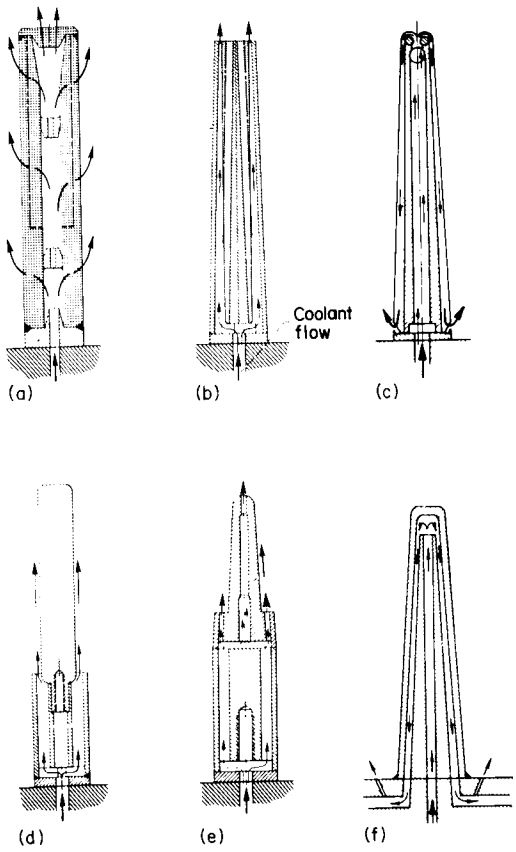

(a) Transpiration. (b) Convection ("dump"). (c) Reverse flow convection. (d) Film. (e) Film and convection. (f) Regeneratively cooled.

FIGURE 8.2.3e.—Baffle cooling concepts investigated.

L_{cav}	Backing cavity depth
$\mathcal{L}_o$	Orifice inductance (inertance)
M	That part of the orifice-velocity amplitude which is in phase with the chamber pressure divided by $\epsilon^{1/2}\bar{a}_1$
$p_3^{(2)}$	Second-order approximation to fundamental cavity pressure oscillation
$\mathcal{R}$	Resistance
$\mathcal{R}_o$	Resistance per unit orifice-cross-sectional area
$\mathcal{R}_s$	Resistance per unit liner-surface area
S	Surface
U	Velocity oscillation amplitude
u	Velocity in orifice
V_1	Combustion gas velocity in thrust chamber
$\mathcal{V}_{cav}$	Cavity volume
x	Displacement of fluid particle in orifice
$\mathcal{Y}$	Resonator admittance
Z	Impedance
α	Absorption coefficient
α_d	Damping coefficient
δ	Orifice length correction
ϵ	Amplitude of pressure oscillation divided by $\bar{p}_1$
$\bar{\theta}$	Nondimensional resistance (see Eq. 8.3.1–27)
ϕ	Phase shift
$\bar{\chi}$	Nondimensional imaginary part of the impedance (see Eq. 8.3.1–27)
ω_r	Resonant frequency
$\bar{\omega}$	Nondimensional angular frequency ($\bar{\omega} = l_o\omega/a = 2\pi l_o/l_w$)

Subscripts:

1	Chamber side of orifice
2	Within orifice
3	Cavity side of orifice
nf	No-flow case

Superscripts:

(2)	Second-order approximation to oscillating quantity
^	Maximum value, or near-maximum value

8.3.1 Liner Damping Theory*

The theory of Helmholtz resonators was treated mathematically for the first time by Helmholtz in 1860 and was afterwards greatly simplified by Lord Rayleigh (1871). Since then these resonators have been used extensively as sound filters and noise suppressors.[105,407,778] In the 1950's arrays of resonators were successfully used in the suppression of combustion oscillations in air-breathing engines,[104,278] and they are presently being used as damping devices for unstable liquid-propellant rocket engines.[523]

A Helmholtz resonator is made of a small cavity of volume $\mathcal{V}_{cav}$ that is connected through an orifice of length l_o and diameter d_o to the main chamber where undesirable pressure oscillations are expected to occur (see Fig. 8.3.1a). When the dimensions of the various elements of the resonator are small in comparison with the wavelength of the oscillation, the motion of the gas in the

* B. T. Zinn, Author.

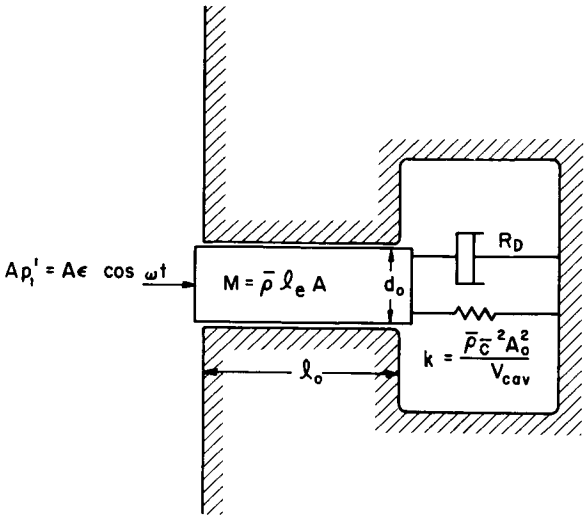

FIGURE 8.3.1a.—Mechanical analog of a Helmholtz resonator.

resonator can be shown to be analogous to that of a mass-spring-dashpot system.[407,579] Under these conditions the gas in the orifice and its immediate vicinity is considered to move as a unit and provide the mass element of the system. The gas in the resonator cavity, which is alternately compressed and expanded due to periodic influx and efflux of gas through the cavity opening, provides the stiffness element; the energy losses which are associated with viscous dissipation provide the resistive element. An illustration of this mechanical analog is presented in Fig. 8.3.1a. Elementary analysis[407,579] shows that the displacement x of this mechanical analog is controlled by the following ordinary differential equation:

$$A_o\bar{\rho}l_{eff}\frac{d^2\hat{x}}{dt^2}+\mathcal{R}_D\frac{d\hat{x}}{dt}+\frac{\bar{\rho}\bar{a}^2A_o^2}{\mathcal{V}_{cav}}\hat{x}=A_o\epsilon\cos\omega t \qquad (8.3.1\text{–}1a)$$

where $l_{eff}=l_o+\delta$ is the effective length in which δ is a length correction* that accounts for the flow effects in the vicinity of the orifice ends, A_o represents the orifice area, $\mathcal{R}_D$ is the resistance which results from the presence of viscous forces, $\bar{\rho}$ is the unperturbed gas density, $\bar{a}$ is the mean speed of the sound of the gas in the resonator,† and ω and ϵ represent the angular frequency and amplitude of the pressure oscillations at the chamber end of the orifice.

The Helmholtz resonator can also be considered from an electrical analogy viewpoint. Given a cavity whose largest dimension is less than one-quarter of the wavelength of the imposed oscillation, the properties of the cavity and associated orifice can be lumped into an orifice resistance $\mathcal{R}_o$, and an orifice inductance $\mathcal{L}_o(\mathcal{L}_o=\rho A_o l_{eff})$ and a cavity capacitance $\mathcal{C}_{cav}(\mathcal{C}_{cav}=\bar{a}\rho A_o^2/\mathcal{V}_{cav})$. The response of the cavity to oscillating pressure can then be described as

$$u'=p'\Big/\left[\mathcal{R}_o+i\left(\omega\mathcal{L}_o-\frac{\mathcal{C}_{cav}}{\omega}\right)\right] \qquad (8.3.1\text{–}1b)$$

where u′ is the oscillatory velocity and p′ is the oscillatory wave pressure. The quantity $\mathcal{R}_o+i(\omega\mathcal{L}_o-\mathcal{C}_{cav}/\omega)$ is the impedance and $(\omega\mathcal{L}_o-\mathcal{C}_{cav}/\omega)$ is the reactance. The role of these parameters in damping, as well as admittance and absorption coefficient, are discussed in Sect. 8.3.1.2.

When conditions in the chamber are oscillatory, the gas in the orifice oscillates back and forth. The amplitude of these oscillations reaches a maximum value when the frequency of the chamber's oscillations approaches the natural frequency of the resonator. The latter can be easily determined by considering the behavior of the mechanical analog of the resonator.

Since maximum damping occurs when the product of the amplitude of the velocity oscillations and the orifice area is maximized, it is desirable to design resonators with a natural frequency close to that of the most detrimental acoustic mode. The basic Helmholtz equation for the resonant frequency, ω_r is simply

$$\omega_r=\bar{a}\sqrt{\frac{A_o}{l_{eff}\mathcal{V}_{cav}}} \qquad (8.3.1\text{–}2)$$

Based upon the maximized damping mentioned above, resonator designs with a frequency slightly above the chamber frequency are often desirable.[692]

* δ is further defined in Eq. (8.3.2.1).

† Here it is assumed one gas temperature exists, as pointed out in Sect. 8.3.2 temperature can vary in the resonator cavity and orifice.

This is evident in the situation where volume is limited and orifice length is fixed. Enlarging the orifice diameter (increased A_o) provides improved damping by involving additional gas mass. However, this gain is soon erased by the loss in unsteady velocity in the orifice as the resonator is operated further from the design condition.

8.3.1.1 Nonlinear analyses.—While designs based on the solution of Eq. (8.3.1–1) are adequate for various applications involving small amplitude sound, this is no longer the case when the amplitudes become finite and the frequency increases beyond a certain limit.[105] To analyze the behavior of resonators when exposed to various external conditions it becomes necessary to reexamine the derivation of Eq. (8.3.1–1a) by considering the same problem from a fundamental fluid mechanical point of view.

When subjected to external pressure oscillations the flow in the orifice reverses direction during each cycle, flowing from chamber to cavity during one half of the cycle and in the opposite direction during the other half. Flow visualization studies[372] and hot wire measurements[371] conducted by Ingard and coworkers indicate that the flow field in the vicinity of the orifice ends is very complex; it depends on the frequency and amplitude of the oscillation as well as the geometry of the orifice (i.e., length to diameter ratio l_o/d_o). It is shown in Ref. 372 that for a given orifice geometry and frequency of oscillation, external secondary flow patterns that resemble vortex rings and are stationary relative to the orifice are established in close vicinity to the orifice ends at relatively low pressure amplitudes. An increase in the amplitude of the oscillation* results in a change in the direction of rotation of the secondary flow patterns; a further increase in amplitude results in the appearance of jets, that coexist with the secondary vortex motion, at the orifice exit; a still further increase in amplitude results in the "strengthening" of the jets and the disappearance of the secondary flow patterns. The viscous interaction of the jets with the quiescent surroundings results in the formation of vortex rings at a distance of the order of several orifice diameters away from the orifice. Once formed, the vortex rings move away from the orifice and in the process they disintegrate into turbulence. The formation and disintegration of the vortex ring and other jet breakup phenomena appear to be a major energy dissipation mechanism and result in other energy losses in addition to the viscous losses.

Recent theoretical investigations of the nonlinear aspects of resonator behavior have been performed by Sirignano[644] and Zinn.[770] The following simplifying assumptions were introduced in each: (1) the gas is calorically perfect; (2) there is no mean flow through the orifice; (3) the flow in the orifice and in the vicinity of its exit is one-dimensional; (4) the flow in the orifice is not choked at any time; (5) the flow conditions on both sides of the orifice are symmetrical (i.e., conditions exactly reverse during the cycle); (6) the amplitude of the oscillation is sufficiently high so that the flow at the orifice exit may be considered to be always separated; (7) typical orifice and cavity dimensions are considerably smaller than the wavelength of the oscillations; (8) at each instant the amplitude of the velocity perturbation is constant along the orifice and the jet;* (9) Viscous forces are of second order and can be described by boundary layer shear averaged over the orifice cross-sectional area. While all of the above assumptions were used in the analyses of Refs. 644 and 770 the difference between them lies in the treatment of the flow in the entrance region. Sirignano[644] assumed this flow to be quasi-steady and irrotational, Zinn[770] assumed instead that the axial momentum of the flow entering the control volume in front of the orifice may be neglected.

The flow region for the Zinn assumption[770] is illustrated in Fig. 8.3.1b. In the entrance region of this model (as well as in the Sirignano model[644]) the unsteady pressure is written as $p_1 = \bar{p} + \epsilon \cos \omega t$, where the amplitude of the oscillating pressure is represented by ϵ. This disturbance is located a distance δ from the orifice entrance.

Using the principle of equivalent linearization[486]

* The experimental measurements also indicate that an increase in the amplitude of the oscillation results in a decrease in the orifice reactance.[371] These measurements show that at high amplitudes orifice resistance varies as $\bar{\rho}U$.

* At low frequencies the gas oscillations behave as if they were incompressible.[417,644] Velocity oscillations are referred to here since pressure and density do not behave in this manner but vary through the orifice.

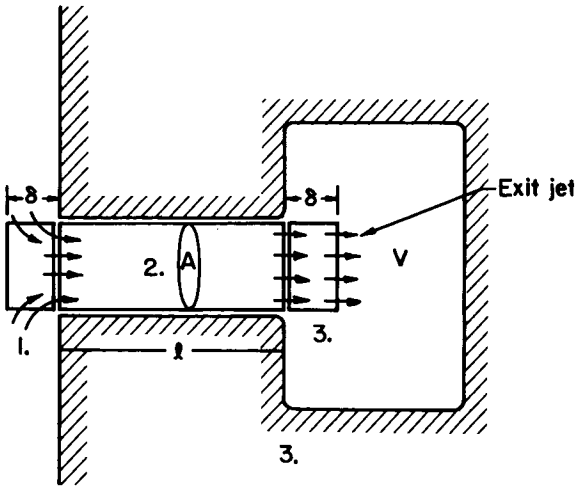

FIGURE 8.3.1b.—Resonator flow field during finite amplitude oscillations.

a solution was obtained. It can be shown that the second-order approximation for the fundamental pressure oscillation in the cavity (to be denoted by $p_3^{(2)}$) is controlled by the following ordinary differential equation:

$$\frac{l_{eff}\mathcal{V}_{cav}}{A_o\bar{a}^2}\frac{d^2p_3^{(2)}}{dt^2}+\frac{\mathcal{V}_{cav}}{A_o\bar{p}}\left\{\left(1+\frac{l_o}{d_o}\right)\sqrt{8\bar{\rho}\mu\omega}+\frac{B}{3\pi}\bar{\rho}U^{(2)}\right\}\frac{dp_3^{(2)}}{dt}+p_3^{(2)}=p_1'=\epsilon\cos\omega t \tag{8.3.1–3}$$

where $U^{(2)}$ is the second-order approximation for the velocity, amplitude, γ is the ratio of specific heats, $\bar{p}$ and $\bar{\rho}$ are the mean pressure and density of the gas, μ is the viscosity and B is a constant related to the orifice entrance assumptions. B is 8 for the moderate amplitude case ($\leq$120db) treated by Zinn,[770] and 4 for the higher amplitude case studied by Sirignano.[644] The second order solutions are given by the following expressions:

$$p_3^{(2)}=\frac{-\omega_r^2\bar{\rho}l_{eff}\epsilon\cos(\omega t+\phi)}{\omega\left\{\left[\omega l_{eff}\bar{\rho}\left(1-\frac{\omega_r}{\omega}\right)^2\right]^2+\left[\left(1+\frac{l_o}{d_o}\right)\sqrt{8\mu\bar{\rho}\omega}+\frac{B}{3\pi}\bar{\rho}U^{(2)}\right]^2\right\}^{1/2}}=-\frac{A_o\gamma\bar{p}}{\mathcal{V}_{cav}\omega}U^{(2)}\cos(\omega t+\phi) \tag{8.3.1–4}$$

Eq. (8.3.1–4) is used to define $U^{(2)}$. Furthermore,

$$u^{(2)}=U^{(2)}\sin(\omega t+\phi) \tag{8.3.1–5}$$

where $u^{(2)}$ is the second-order approximation for the velocity, and the phase shift, ϕ, is

$$\phi=\tan^{-1}\frac{\sqrt{8\mu\bar{\rho}\omega}(1+l_o/d_o)+B/3\pi\bar{\rho}U^{(2)}}{l_{eff}\bar{\rho}\omega(1-(\omega_r/\omega)^2)} \tag{8.3.1–6}$$

Using the relation* $u=d\hat{x}/dt$ (where $\hat{x}$ is the displacement of the fluid particle in the orifice) together with an energy equation and assumption (8) it can be shown that Eq. (8.3.1–3) indeed describes the oscillations of an analogous mechanical system made up of a mass-dashpot-spring combination. The resistance of this analogous mechanical system is amplitude-dependent and according to Eq. (8.3.1–3) it varies as $0.86\bar{\rho}u$. This theoretical prediction is in close agreement with available experimental data[371] that shows that the resistance varies as $\bar{\rho}u$.

The analysis presented in Refs. 19, and 644 is particularly relevant to large amplitude oscillations of interest to the rocket designer. Under these conditions the orifice inflow may be assumed to be irrotational and the flow in the orifice and the jet to be quasi-steady. Quasi-steady flow assumptions have also been employed in the studies of Oberg[521] and Garrison.[286] Considering a steady flow between the orifice entrance and the vena contracta, it can be shown[365] that the orifice velocity and the real jet velocity are related as follows:

$$u_j=u_o/C_vC_c=u_o/C_d \tag{8.3.1–7}$$

where u_j and u_o respectively denote the velocity perturbation in the vena contracta and in the

* It should be noted that $d\hat{x}/dt$ is a Lagrangian quantity while u is an Eulerian quantity. It can be shown[366] that the difference between these quantities is of second-order and will produce particular solutions that are proportional to higher harmonics. The latter are not considered in this analysis.

orifice; C_c is the contraction coefficient, C_v is the velocity coefficient that accounts for frictional losses in the orifice, and C_d is commonly referred to as the discharge coefficient. The discharge coefficient is an experimentally determined quantity which remains fairly constant in the range of interest considered here (although the C_d is known to be quite sensitive to orifice shape and surface conditions as well as the jet Reynolds number). For high Reynolds number flows in sharp-edged orifices C_d approximately equals 0.61.

The above relation together with the Euler equation for the perturbations yields the following differential equation that controls the behavior of the cavity pressure oscillations

$$\frac{\bar{\rho} l_{eff}}{A_o \bar{a}^2} \frac{d^2 p_3^{(2)}}{dt^2} + \frac{\mathcal{V}_{cav}}{\gamma A_o \bar{\rho}} \frac{4}{3\pi} \frac{U^{(2)}}{C_d^2} \frac{dp_3^{(2)}}{dt} + p_3^{(2)} = p_1' = \epsilon \cos \omega t \qquad (8.3.1\text{–}8)$$

The solution of Eq. (8.3.1–8) has the same form as the expressions given by Eqs. (8.3.1–4) through (–6) when B = 4, the only difference being that in the present case the resonator resistance is given by

$$\mathcal{R}_o = \frac{4}{3\pi} \frac{\bar{\rho}}{C_d^2} u = \frac{0.425}{C_d^2} \bar{\rho} u \qquad (8.3.1\text{–}9)$$

where u is the velocity amplitude of the fundamental component. Based on extensive resonator impedance measurements, Garrison[286] shows that the following empirical expression for the resistance

$$\mathcal{R}_o = \frac{0.37}{C_f^2} \bar{\rho} u \qquad (8.3.1\text{–}10)$$

where C_f is the orifice flow coefficient (that approximately equals the discharge coefficient), provides the best correlation with the available experimental data. It is quite possible that a better agreement between the theoretical predictions and the available experimental resistance data would have been obtained if the theory that resulted in the derivation of Eq. (8.3.1–9) was extended to third or higher orders.

To evaluate the liner effect on engine stability it is necessary to know its admittance (see Sect. 3.5.3.2). Using complex notation and Eqs. (8.3.1–4) and (–5) it can be shown that the real part of the admittance $\mathcal{Y}$, of a single Helmholtz resonator, can be expressed in the following form

$$\mathcal{Y}_R = \frac{u/\bar{a}}{p_1/\bar{p}} = \frac{\bar{p}}{\bar{a}} \frac{U^{(2)}}{\epsilon} \cos\left(\phi - \frac{\pi}{2}\right) \qquad (8.3.1\text{–}11)$$

Of special interest is the frequency dependence of $\mathcal{Y}_R$ which is a measure of the energy dissipation in the liner. Calculations of $\mathcal{Y}_R$ show that at low amplitudes the liner dissipation is very effective over a narrow band of frequencies centered around the resonant frequency.[644,770] An increase in the amplitude of the oscillation results in a decrease in the maximum value of $\mathcal{Y}_R$ and in an increase in the range of frequencies over which the liner is effective. At large amplitudes the resonator has a flat frequency response and at the same time it is considerably less effective than at lower amplitudes. The difference in the calculated low- and high-amplitude responses is caused by the fact that at low amplitudes the magnitudes of the resonator resistance and reactance are of the same order of magnitude while at high amplitudes the resonator resistance is considerably larger than its reactance. The calculated flat frequency-dependence of $\mathcal{Y}_R$ during high-amplitude oscillations suggests that there is no need to carefully "tune" liners that are designed to attenuate large amplitude pressure oscillations.

While the above discussion is concentrated on the unsteady behavior of a single Helmholtz resonator, analyses and experimental data on the unsteady behavior of lined chambers may be found in Refs. 286, 521 and 552. In this connection it is important to emphasize that in addition to the ability to dissipate energy the use of a liner will change the natural frequencies of the chamber under consideration. Such a change could conceivably result in the destabilization of an otherwise stable rocket motor.

There are several interesting aspects of the resonator problem that became clearer through the use of the fluid-mechanical approach. It has been shown that energy losses in the resonator are due to viscous dissipation at the walls as well as due to the "conversion" of the momentum of the jets into vortex rings that dissipate into turbulence. The frictional wall losses are constant while the jet losses are amplitude-dependent and they dominate both the constant resistance term and the resonator reactance during high amplitude oscillations. While it appears that the nature of the observed losses is qualitatively understood,

their quantitative determination is still dependent on the use of experimentally measured discharge or flow coefficients. Due to the extremely complex nature of the flow field near and inside the orifice available theories cannot determine the exact magnitude of the effective orifice length. In the absence of appropriate theories liner designers must resort to the use of empirical expressions (e.g., see Refs. 286 and 552) in their attempts to evaluate the effective orifice length. Fortunately for rocket designers the resonator reactance has little effect upon the resonator's response during high-amplitude oscillations; hence the precise knowledge of the effective length is of secondary importance in rocket liner design.

It should be kept in mind that the theory described in this section was limited to considerations of the behavior of a single Helmholtz resonator when it is subjected to pressure oscillation wavelengths that are long compared to the resonator dimensions. Considerations of the conditions inside unstable rocket motors point out the need for improved theories that will analyze the low- and high-amplitude behavior of arrays of Helmholtz resonators over a wide frequency range. The dependence of liner behavior upon the presence of mean flow past and/or through the resonator should also be considered and will be discussed in the following sections.

*8.3.1.2 Flow effects.**—In addition to the occurrence of oscillatory pressure, the environment within a rocket chamber undergoing combustion instability contains velocities of both mean and oscillatory character. The direction between the mean and oscillatory velocities, and the phase between the oscillatory velocity and pressure, depends upon the particular instability mode. The mean gas velocity is small near the injector and increases downstream. Mean flows through the orifices (apertures) of the liner may also be present. Such flows occur when there are appreciable pressure gradients within the chamber, and the backing volume of the lined surface is not properly partitioned. At times, a mean orifice flow is introduced purposely for cooling.

Depending upon the pertinent magnitudes, any of the above flow effects can have considerable influence upon the liner design. An analysis has been performed that utilizes the jet model of Helmholtz resonator flow and accounts for these additional flow effects.[691–693] The analysis contains two parts: an off-resonance solution, and a near-resonance solution. The off-resonance solution considers the effects of chamber flows, whereas the near-resonance study considers, in addition, the effects of mean flows through the orifices. In both studies, it is not necessary that the wavelength associated with the oscillations be much larger than the orifice length. The assumptions are discussed in Refs. 691 and 693.

The analysis shows that both the chamber velocity and pressure must be considered as forcing functions for the orifice motion. The chamber velocity can change the phase of the orifice velocity independently from the chamber pressure. Therefore, the force required to accelerate the orifice fluid to the jet velocity is not precisely that force due to the part of the chamber pressure in phase with the orifice velocity. In other words, the resistance (defined for no orifice mean flow, as the force leading to dissipation divided by the orifice oscillatory velocity) is not, in general, equal to the real part of the impedance. This means that the chamber velocity can force the motion such that the orifice velocity does work against the chamber pressure, and indeed, regions are found where the real part of the impedance (or real part of the admittance, see Sect. 8.2.1.3) is negative. In particular, near the resonant point, the real part of the admittance is always positive, and is always increased by a chamber flow (when the average pressure coefficient on the chamber side is negative), but in regions not too far from resonance, negative values of this quantity do occur. These negative regions should be avoided in practice, since the liner can then provide a mechanism by which energy is extracted from the chamber velocity field and fed into the chamber pressure field, causing instability to be augmented.

In Sect. 8.3.1.3, it is noted that, for maximum damping, a surface integral should be maximized under near-resonance conditions. In most cases of practical interest, this maximization is equivalent to the maximization of the real part of the admittance coefficient ($\mathcal{Y}_R$). Here, the concern is primarily with these cases. Now, under near-resonant conditions,

* T. Tonon, Author.

$$\mathcal{Y}_R = \bar{a}aM/\epsilon^{1/2}\bar{p}_1 \qquad (8.3.1\text{–}12)$$

where $\bar{a}$ is the mean speed of sound, a is the percent open area ratio, ϵ is the amplitude of the non-dimensional chamber oscillatory pressure, $\bar{p}$ is the mean chamber pressure, and M is that part of the orifice-velocity amplitude which is in phase with the chamber pressure. The conclusion is that both a and M should be maximized.

When there are no mean flows through the orifices, the resonator geometry which gives the maximum value of M is given at least approximately by

$$A_o l_o/\mathcal{V}_{cav} = \tilde{\omega} \tan \tilde{\omega} + \epsilon^{1/2}\tilde{\omega}K/\pi\hat{M} \cos^2 \tilde{\omega} \qquad (8.3.1\text{–}13)$$

where

$$K \equiv 2bg(1-\bar{C}_p)/3 + \pi\bar{V}g \cos \psi(\bar{C}_p+1)/2 \qquad (8.3.1\text{–}14)$$

$$\hat{M}^2 = 3C_D^2[\pi/\gamma + (V^2+2b^2/3+g^2/3)(1-\bar{C}_p) + \pi\bar{V}b \cos \psi(\bar{C}_p+1)/2]/2(1+|\cos^3 \tilde{\omega}|) \qquad (8.3.1\text{–}15)$$

where A_o is the orifice cross-sectional area, l_o the orifice length, $\mathcal{V}_{cav}$ the cavity volume, $\tilde{\omega} = 2\pi l_o/l_w$, l_w the wavelength, $\hat{M}$ a maximum or near-maximum value of M, C_D the coefficient of discharge of the orifice when quasi-steady orifice flow occurs (when the orifice motion is not quasi-steady, $C_D = 1$), γ is the ratio of specific heats, and $\bar{C}_p$ is the average pressure coefficient for the jet interaction with the chamber cross-flow. The chamber pressure and velocity are assumed known in the following forms:

$$p_1/\bar{p} = 1 + \epsilon \cos \omega t \qquad (8.3.1\text{–}16)$$

$$\mathbf{V}/\bar{a} = \epsilon^{1/2}[\bar{\mathbf{V}} + \mathbf{V}'] \qquad (8.3.1\text{–}17)$$

with the magnitudes

$$|\bar{\mathbf{V}}| = \bar{V} \qquad (8.3.1\text{–}18)$$

$$|\mathbf{V}'| = \bar{V}' = e \cos \omega t + g \sin \omega t \qquad (8.3.1\text{–}19)$$

The angle ψ is the angle between the direction of $\bar{\mathbf{V}}$ and $\mathbf{V}'$ when both vectors are considered positive. That M will be a near maximum with this geometry has not been proven rigorously; however, calculations tend to confirm this result. This geometry should provide at least an approximately maximum value of M since it requires that the chamber oscillatory pressure be in phase with the orifice velocity, and since M represents that part of the orifice velocity in phase with the chamber pressure. This condition can be called resonance.

As mentioned earlier in this section, it can be proven that the chamber flow terms in Eq. (8.3.1–15) only increase the value of $\hat{M}$ above the no-flow value. It may be concluded that a chamber flow can be used to aid performance. Note that when the chamber flow terms are zero, the geometry given by Eq. (8.3.1–13) is the Helmholtz resonant geometry, with no end-correction applied to the orifice length. No end-correction appears here since the flow fields exterior to the orifice are assumed to be quasi-steady. When fluid motion is quasi-steady, the fluid particles experience no acceleration in time, and thus no inertia is present.* Note also the $(1+|\cos^3 \tilde{\omega}|)$ term in the denominator of the expression for $\hat{M}$. This term suggests that unsteady effects in the orifice aid liner performance.

When there are mean flows through the orifices, the geometry which gives the maximum value of M must be found by numerical solution of simultaneous algebraic equations. This more general form of the solution is not presented here because of its complexity, and the references should be consulted.

In certain situations, the chamber conditions are not known precisely enough to attain the necessary confidence in a design geometry calculated as described. In other cases, it is desirable to restrict the orifice length to a value which is much less than the wavelength associated with the oscillating chamber gases. In both cases, the designer should seek to provide a quasi-steady flow condition in the liner. The quasi-steady regime provides a safer design in that damping is effective over a broad frequency range about resonance. The resonator response is essentially insensitive to the orifice length (i.e., the curve of M versus orifice length near resonance is quite flat). The acoustic effective length of the orifice in this case approaches zero.

For the case of no orifice mean flow, when the K-factor in Eq. (8.3.1–13) is zero, the quasi-

* An end-correction is not the result of the contraction of streamlines exterior to the orifice. When the entrance region is quasi-steady, the contracted streamlines are present, but the end-correction is zero.

steady-resonant point is achieved by making the orifice length as small as possible, and the cavity volume as large as possible. The approach is asymptotic so that some sloppiness in the design can be tolerated. If this K-factor is not zero, then, there exists a certain finite, optimum, cavity volume and/or a non-zero, optimum, orifice length. Thus, more care must then be taken in selecting the liner geometry, which still can be found from Eq. (8.3.1–13). It is important to always keep the orifice length to diameter ratio large enough so that the flow has reattached to the orifice wall. It was found in the analysis that a vena contracta without reattachment further limits the mass flow through the orifice, and thus hinders operation in the cases where $\mathcal{Y}_R$ should be maximized.

In certain volume-limited situations, it is not possible to vary the liner geometry such that both M and a are maximized independently. In these situations, where the cavity volume is fixed, the maximum value of $\mathcal{Y}_R$ will appear at a frequency above which M is a maximum. This result is discussed in Refs. 691, 692. The optimum condition should then be found by direct calculation. The proper equations to be solved are more general than those appearing in this section, and can be found in Refs. 691 and 693. These references should also be consulted when maximization of $\mathcal{Y}_R$ does not produce the optimum design. See Sect. 8.3.1.3 for these situations in which the optimization is more complicated.

8.3.1.3 Parameters to evaluate liner designs.— The mathematical treatment of the flow field associated with a rocket combustion chamber involves, like most physical problems, the solution of governing equations together with boundary conditions. Thus, the events that take place at (or near) the chamber walls have a significant effect upon the behavior of the internal flow field. Viewing the problem from a stability standpoint, in certain cases, conclusions of practical interest may be drawn from a study of the boundary effects alone (without a detailed consideration of the governing equations).

COMPLEX RATIOS: Complex ratios serve as a convenient means of treating boundary effects. From these complex parameter ratios, conclusions may be drawn as to the effectiveness of liner operation.

Since the flow at the liner surface is spatially irregular because of the perforations (orifices), a surface is considered that is displaced from the liner surface. On this surface of interest, a spatially-averaged-normal velocity is defined. In order that this average be at least approximately equal to the actual values, this station of interest must be sufficiently far from the liner surface. When the orifice flow is characterized by jets, this distance should be at least the jet-break-up length or the characteristic spacing between orifices, whichever is larger. The flow field between the lined surface and this imaginary surface is then assumed to be quasi-steady. It is also assumed here that the orifice axes are at least approximately perpendicular to both surfaces, and that the lined surface is uniform at least locally. The definitions and assumptions in this paragraph also apply to the resistance and absorption coefficients, when these concepts are applied to a lined surface. The definition of these latter two concepts will be made shortly.

IMPEDANCE: The impedance Z is defined as the ratio of pressure oscillation to velocity oscillation at a given point in space, for a given frequency. For a lined surface, this definition is applied along the displaced surface discussed above. The velocity of interest is the velocity normal to this surface. Thus,

$$Z \equiv Z_R + iZ_I \equiv p_1'/au' \qquad (8.3.1\text{–}20)$$

where p' is the oscillatory pressure, u' the oscillatory orifice velocity on the chamber side of the liner, and a the percent open area ratio of the lined surface. Since, in general, u' is not in phase with p_1', the impedance contains both a real part Z_R and an imaginary part iZ_I.

ADMITTANCE: The admittance $\mathcal{Y}$ is defined as the reciprocal of the impedance. Thus,

$$\mathcal{Y} \equiv \mathcal{Y}_R + i\mathcal{Y}_I \equiv au'/p_1' \qquad (8.3.1\text{–}21)$$

From the above definitions,

$$\mathcal{Y}_R = Z_R/(Z_R^2 - Z_I^2); \qquad \mathcal{Y}_I = -Z_I/(Z_R^2 - Z_I^2) \qquad (8.3.1\text{–}22)$$

$$Z_R = \mathcal{Y}_R/(\mathcal{Y}_R^2 - \mathcal{Y}_I^2); \qquad Z_I = -\mathcal{Y}_I/(\mathcal{Y}_R^2 - \mathcal{Y}_I^2) \qquad (8.3.1\text{–}23)$$

RESISTANCE: The resistance is a real quantity, and is useful in describing the energy dissipation. For the case of simple harmonic orifice motion (no mean flows through the orifices), the surface resistance $\mathcal{R}_s$ can be defined as the force which leads to the dissipated energy per unit area, divided by the velocity au'. The force per unit area used in the definition will be equal to the part of the pressure p_1' in phase with the velocity u' only when the pressure is the sole forcing function for the orifice motion; i.e., the chamber flow must be zero. Thus, as mentioned in Sect. 8.1.3.2, $Z_R = \mathcal{R}_s$ only in this special case. A mistake often made in the literature is to define the resistance as the real part of the impedance, even in the presence of a chamber flow. This definition does not reflect the physical mechanisms taking place. Thus,

$$\mathcal{R}_s \equiv F_d/au' \qquad (8.3.1\text{–}24)$$

where F_d is the force leading to dissipation per unit surface area. For the jet regime, F_d contains the force necessary to accelerate fluid particles to the jet velocity at which dissipation occurs, starting from *rest* (even though these particles may have been moving in a chamber velocity field prior to entrance into the orifice).

For the jet regime, the resistance is a time-dependent quantity, reflecting the nonlinear aspect of the motion. However, in Refs. 691 and 693, it is shown that an equivalent* linear resistance can be found which is a constant of the periodic motion. The expression derived is

$$\mathcal{R}_o = a\mathcal{R}_s = \frac{2}{3\pi}\rho\hat{u}(1+\hat{a}^3) \qquad (8.3.1\text{–}25)$$

where $\mathcal{R}_o$ is the resistance per unit area A_o, ρ is the orifice density, $\hat{u}$ the amplitude of the orifice motion on the chamber side, and $\hat{a}$ is the ratio of the jet-velocity amplitude on the cavity side of the orifice to the jet-velocity amplitude on the chamber side. Equation (8.3.1–25) is valid when the jet flow area equals the orifice area. If the orifice motion is quasi-steady, the vena contracta can be accounted for (as well as friction). The result then is

$$\mathcal{R}_o = a\mathcal{R}_s = \frac{4}{3\pi}\frac{1}{C_d^2}\rho\hat{u} \qquad (8.3.1\text{–}26)$$

where C_d is the coefficient of discharge for the orifice. As mentioned in Refs. 691 and 693,

$$Z_R = \mathcal{R}_s + F(\omega, \omega_o, \epsilon, \mathbf{V}_1)$$

where the function F is zero when the chamber flow $\mathbf{V}_1$ is zero.

ABSORPTION COEFFICIENT: Since the absorption coefficient is a parameter often used by the designer, it is important that it be considered in relation to the parameters previously discussed.

The absorption coefficient α can be defined, in general terms, as the power absorbed by a surface (i.e., the power removed from the enclosed volume), divided by the power which arrives at the surface in the form of travelling waves. This definition is usually applied only for periodic occurrences; i.e., the transient times are small compared to the period of oscillation. The absorption coefficient is then (approximately) a constant. It is also usually applied to plane waves incident on a plane surface. When the transmitting medium contains no appreciable velocity effects, and there are no mean flows through the orifices, the application of this definition is straightforward.[778] The absorbed power (per unit area) is the product of the velocity at the surface, squared, and the real part of the impedance (resistance). The incident intensity is that associated with the travelling pressure waves moving toward the surface. When the incident waves are normal to the surface, the result is

$$\alpha = 4\bar{\theta}/[(\bar{\theta}+1)^2+\bar{\chi}^2] \qquad (8.3.1\text{–}27)$$

where $\bar{\theta} = \mathcal{R}_s/\bar{\rho}_1\bar{a}_1 = Z_R/\bar{\rho}_1\bar{a}_1$, and $\bar{\chi} = Z_I/\bar{\rho}_1\bar{a}_1$, when there is no chamber velocity. In terms of the admittance, this can be written as

$$\alpha = \frac{4\mathcal{Y}_R(\mathcal{Y}_R^2-\mathcal{Y}_I^2)\bar{\rho}_1\bar{a}_1}{[\mathcal{Y}_R+\bar{\rho}_1\bar{a}_1(\mathcal{Y}_R^2-\mathcal{Y}_I^2)]^2+\mathcal{Y}_I^2} \qquad (8.3.1\text{–}28)$$

When there are appreciable velocity effects in the medium, or mean flows through the orifices, the above methods used in the calculation of the absorbed power and incident intensity do not account for these effects. As indicated earlier, the resistance, and not the real part of the impedance

* The accuracy of the linear representation improves as the amplitudes approach zero.

should be used in finding the absorbed power. Likewise, there is energy contained in the velocity field as well as the pressure field, thus the proper normalization for α becomes more complicated. It may be possible to incorporate these velocity effects into the concept of an absorption coefficient, but there appears no need to do so. An analysis of the fluid mechanical problem yields results in which such a concept does not enter. Such an analysis is described below.

OPTIMUM DESIGN: Based upon the results of a derivation by Cantrell and Hart,[137] it can be shown that, for the cases of most practical interest, the optimum design can be achieved by making $\mathcal{Y}_R$ as large as possible.

The result of interest from that reference is

$$2\alpha_d = -\frac{\left\langle \int_s d\mathbf{S}\cdot\left\{\epsilon\bar{p}_1\mathbf{V}_1' + \frac{\epsilon^2\bar{p}_1^2\bar{\mathbf{V}}_1}{\bar{\rho}_1\bar{a}_1^2} + (\bar{\mathbf{V}}_1\cdot\mathbf{V}_1')\left(\bar{\rho}_1\mathbf{V}_1' + \frac{\epsilon\bar{p}_1}{\bar{a}_1^2}\bar{\mathbf{V}}_1\right)\right\}\right\rangle}{\left\langle \int_{\mathcal{V}} d\mathcal{V}\left\{\frac{1}{2}\bar{\rho}_1\mathbf{V}_1'^2 + \frac{\epsilon^2\bar{p}_1^2}{2\bar{\rho}_1\bar{a}_1^2} + \frac{(\bar{\mathbf{V}}_1\cdot\mathbf{V}_1')\epsilon\bar{p}_1}{\bar{a}_1^2}\right\}\right\rangle} \qquad (8.3.1\text{–}29)$$

This relationship expresses the stability of a volume $\mathcal{V}$ enclosed by a surface S within which there are no volume-loss mechanisms, and all fluid motion is isentropic and irrotational. In applying this result to the problem at hand, the surface S is identified with the imaginary surface defined earlier in this section, and it is assumed that any volume-loss (or gain) mechanisms present in an actual combustor do not alter the results. In Equation (8.3.1–29), $\langle\ \rangle$ denotes a time average much larger than a period of oscillation, but still much less than a damping time. Thus, all flow quantities must have a slow exponential growth with time; p_1', ρ_1', etc., $\sim\alpha_d t$, which serves to define α_d, the damping coefficient.

From this result, it is evident that the optimum condition comes about when α_d is made as largely negative as possible. Since the transient motion is considered slow, the conditions within the volume can be considered fixed. Thus, we need only maximize the time average of the surface integral in the numerator. Proceeding in this way, and making use of the relative magnitudes of the terms involved, it can be shown that the optimum condition will be obtained in moving towards resonance of the liner system. It can be shown further that, under near-resonance conditions, in certain cases, α_d becomes largely negative when the real part of the admittance is maximized to a positive value over the liner surface. These special cases, which include most cases of practical concern, are listed as follows:*

1. Transverse modes with either no mean flows through the liner or $a^2 \ll 1$.
2. Longitudinal modes in which the chamber oscillatory velocity is 90° out of phase with the chamber pressure (standing mode), with the orifice oscillatory velocity in phase with the chamber pressure, and in addition, if either there are no mean flows through the orifices or if $a^2 \ll 1$.
3. All modes, if the mean flow in the chamber is very small (e.g., near the injector), and in addition, either no mean flows through the liner or $a^2 \ll 1$.

In the above cases, only the first term of the surface integral is important, and this term leads a quantity which is proportional to $\mathcal{Y}_R$. The arguments leading to the above conclusions, starting from the result of Eq. (8.3.1–29), are presented in Ref. 691.

It is thus concluded that, for most cases of practical concern, the optimum condition for stability will be obtained by maximizing the real part of the admittance coefficient $\mathcal{Y}_R$ over the liner surface. It is noted here that $\mathcal{Y}_R$ does depend significantly upon the chamber flow terms and orifice mean flows. Indeed, it is possible for chamber flow effects to produce negative values for $\mathcal{Y}_R$. In these special cases, α_d will then become positive, indicating that instability is enhanced.

Now, from Eq. (8.3.1–28), for conditions near resonance ($\mathcal{Y}_I \approx 0$), there results

$$\alpha = 4\bar{\rho}_1\bar{a}_1\mathcal{Y}_R/(1+\bar{\rho}_1\bar{a}_1\mathcal{Y}_R)^2 \qquad (8.3.1\text{–}30)$$

In addition, under near-resonance conditions,

* It is assumed that the chamber geometry is cylindrical, with the lined surface on the outer-curved wall.

$\mathcal{Y}_R = \mathcal{O}(a/\delta)$, where δ is a small amplitude parameter ($u' \approx \delta \bar{a}_1$, $p' \approx \delta^2 \bar{p}_1$). Thus, when $a/\delta \ll 1$, $\alpha \approx 4\bar{\rho}_1 \bar{a}_1 \mathcal{Y}_R$, and when $a/\delta \gg 1$, $\alpha \approx \frac{1}{4}\bar{\rho}_1 \bar{a}_1 \mathcal{Y}_R$. It is thus concluded that, only in special cases, will maximization of the commonly-used absorption coefficient, at resonance, correspond to maximization of $\mathcal{Y}_R$. In other situations, such a maximization may result in a design which is far from the optimum.

8.3.2 The Effects of the Environment on Resonator Behavior*

Conditions in and about a typical rocket engine liner are normally quite different from many of those discussed in the previous section. The differences often require substantial modification of the design equations.[552] These new conditions include

1. The presence of mean flows
2. Variations in cavity gas composition and temperature as a function of propellants, injector type, O/F, position, etc.
3. High-amplitude nonsinusoidal waves (i.e. beyond the acoustic regime)
4. Nonperpendicular wave incidence angles due to the presence of rotating pressure fronts in cylindrical cavity modes.

A cross-section of a typical rocket liner is shown in Fig. 8.3.2a. The figure introduces the nomenclature used in this section as well as indicating the complexities of liners employing circumferential and axial partitions.

In terms of the effects of the environment on liner behavior, one of the most significant factors is the presence of mean flows or turbulence. The source of these mean flows can be the gaseous combustion products flowing by the liner, purge gases flowing through the aperture,† or streaming flows due to violent oscillations in the aperture. The presence of any one of these has a large effect on both the aperture effective length, l_{eff}, and the resistance, $\mathcal{R}_o$.

The aperture effective length consists of the aperture thickness plus some correction, δ, due to streamline contraction. Although briefly discussed in Sect. 8.3.1 the more detailed equation for l_{eff} is

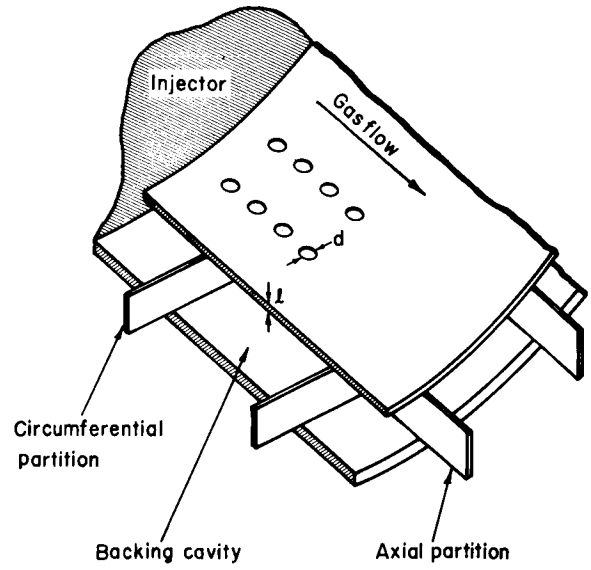

FIGURE 8.3.2a.—Typical liner configuration.

$$l_{eff} = l_o + \delta = l_o + .85 d_o (1 - 0.7\sqrt{a}) \quad (8.3.2\text{–}1)$$

where a is the ratio of aperture area to resonator cross section area (a expressed in percent is referred to as "percent open area"). Figure 8.3.2b represents the results of an analysis of the streamline contraction for an orifice plate.[733] The parameter actually shown is the distribution of the kinetic energy near the aperture where $\frac{5}{8}$ths of the energy is in the hemispherical caps and the other $\frac{3}{8}$ths of the energy is external. The entire process is associated with the transition from planar to spherical waves. Dealing with an orifice plate, the l_{eff} is equal to the δ alone. The results of Westervelt's analysis[733] show that when turbulence is present, the position of the streamline contraction is altered such that the $(\frac{5}{8})\delta$ associated with the hemispherical caps is eliminated. This corresponds to a reduction in the δ by a factor of 0.625; the δ with turbulence then would be equal to 0.375 times the δ without turbulence. The required turbulence was found to occur when the magnitude of the oscillatory displacement became appreciably greater than the orifice diameter.

Experimental evaluation of this reduction in l_{eff} for a range of values of the ratio of particle

* B. Phillips, Author.

† "Aperture" is an alternate terminology for "orifice" referred to in the previous section.

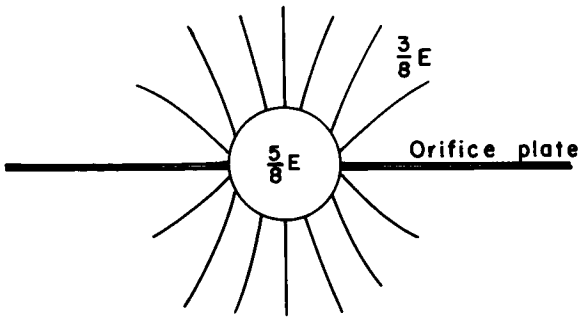

FIGURE 8.3.2b.—Distribution of kinetic energy for oscillatory flow through an orifice according to Westervelt.[733]

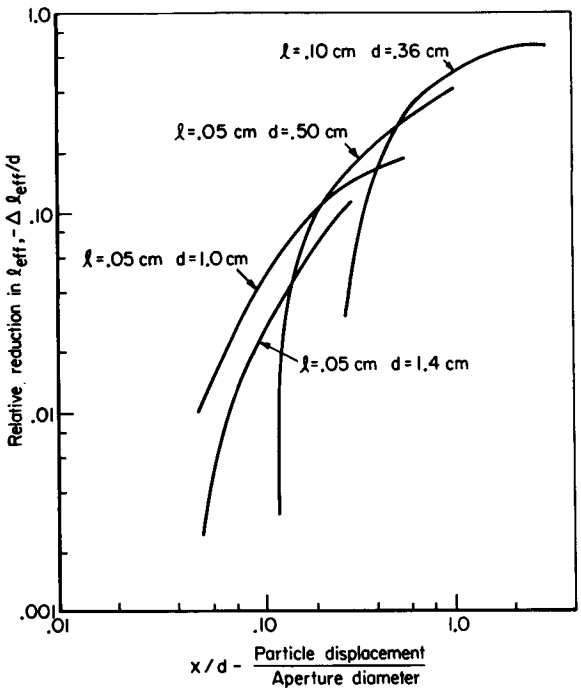

FIGURE 8.3.2c.—Relative reduction in effective length as a function of x/d.

displacement to diameter, $\hat{x}/d_o$ is shown in Fig. 8.3.2c. The plot was obtained from figures 29–32 of Ingard.[370] There, the reduction in l_{eff} was shown as a function of $\hat{x}/l_o$. The results of plotting the average values on the new scale indicate that, for $\hat{x}/d_o > 3$, the ratio of l_{eff}/d_o is reduced by 0.65 to 0.70. Two comments can be made on the results. The first is that the aperture lengths were small (0.05 to 0.10 cm) compared to the diameters (0.36 to 1.4 cm) so that the l_{eff} was almost completely defined by δ. The second is that the results are presented as $-\Delta l_{eff}/d_o$. If l_{eff} without turbulence is $\mathcal{O}(d_o)$, then it appears that δl_{eff} has been reduced by ~0.6 to 0.70 which corresponds to Westervelt's prediction.

The effects of mean flow on l_{eff} are shown in Fig. 8.3.2d. The results are taken from Refs. 472, 478, and 549 and plotted on the same vertical scale. The effects of flow past and flow through could be nearly superimposed if a 20:1 ratio of velocities was assumed. Although there is some variation, the results indicate that at values of flow past corresponding to 120 m/sec the aperture mass was reduced to 0.375 times its nonflow value. The aperture lengths for Refs. 472 and 478 were substantially less than the aperture diameters indicating that, to a good approximation, the reduction in l_{eff} was equivalent to a reduction in δ. The relationship of "velocity past" to "velocity through," and a fundamental reason for the 20:1 difference remain open questions at this time. In terms of design, however, the results indicate that, to a good approximation, the effective length in the presence of *high mean flow or high wave amplitudes** is

$$l_{eff} = l_o + 0.375\delta_{nf} \qquad (8.3.2\text{–}2)$$

The results of an experiment to study the effect of mean flow past the aperture on the resistance is shown in Fig. 8.3.2e, taken from Ref. 478. The parameter used to correlate the data is frequency dependent; however, recent experimental results indicate that the effect should not be considered as a function of frequency.[39,549] Note should be made of the apparent leveling off of the flow effect for the circular symbols. Comparison of the results shown in Fig. 8.3.2e with those reported in Refs. 39 and 549 is shown in Fig. 8.3.2f. In order to compare the results it was necessary to replot the data as shown in the symbol list. The results from Refs. 478 and 549 indicate a threshold value of the flow (below which no significant effect is noted) that corresponds to a velocity

* High amplitude quasi-steady flow was discussed in Sect. 8.3.1. In that regime a change in the effective length is also predicted. When the amplitude is sufficiently high the end correction can be entirely eliminated and indeed l_{eff} can be less than l_0[766] approaching zero as the flow becomes entirely quasi-steady. Amplitudes in the 190 db range, where jet-type flow is well established (figure 5 of Ref. 694), indicate that $l_{eff} = l_0 + \delta/2$ and represents a single-end correction (one hemispherical cap).

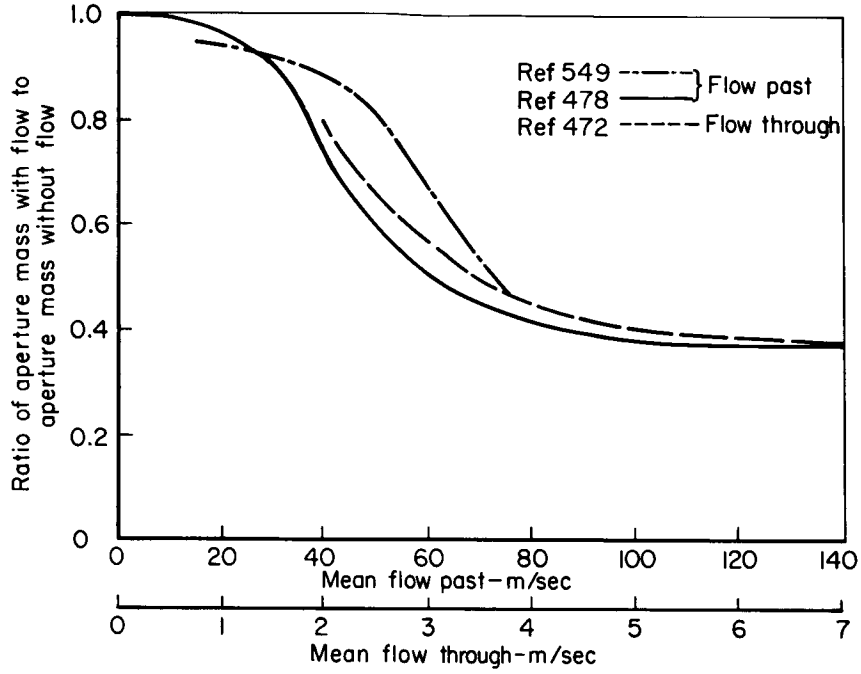

FIGURE 8.3.2d.—Effects of mean flow past and mean flow through the apertures on the ratio of aperture mass with and without flow.

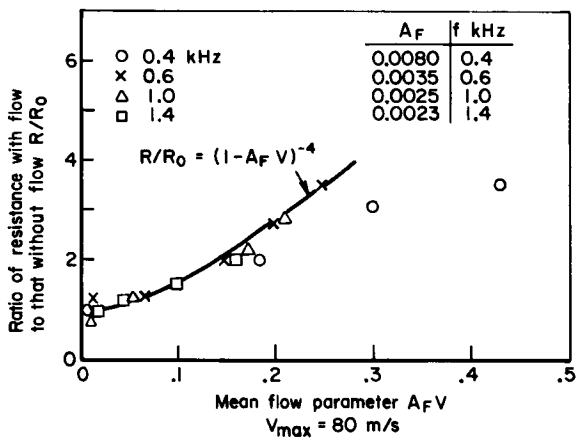

FIGURE 8.3.2e.—The effect of mean flow past on acoustic resistance (where A_F is an empirical frequency dependent parameter).

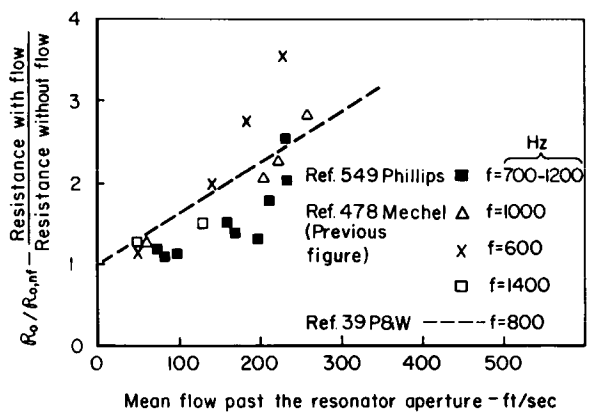

FIGURE 8.3.2f.—Effect of mean flow past on the ratio of resistance with flow to resistance without flow.

past of ~100 ft/sec. Increasing the flow velocity corresponds to a linear increase in the ratio of resistance with flow to the nonflow resistance (the dashed curve represents the linear increase based on Ref. 39, which differs somewhat from the other data cited.) The maximum value of the resistance ratio measured is 3.5.

The effects of mean flow through the aperture have been studied and reported in Refs. 39, 371 and 472. The results are compared in Fig. 8.3.2g. The results from Refs. 371 and 472 indicate that a threshold value of flow through corresponding to ~3 ft/sec must be exceeded before the effect is seen. Increasing the flow caused a linear increase in the resistance ratio. It is not clear at this time why the results of Ref. 39 differ so greatly from

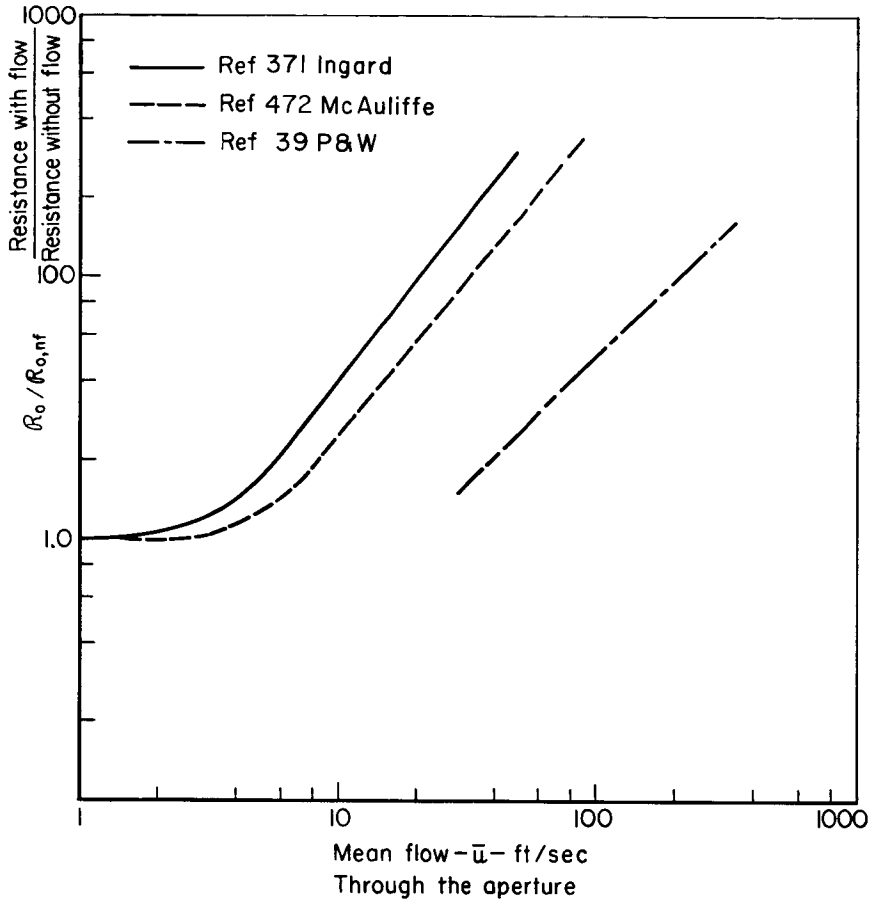

FIGURE 8.3.2g.—Effect of mean flow through the aperture on the resistance.

Refs. 371 and 472. The similarity in slope, however, is of interest. Recent analyses indicate that the slope of the line should correspond to the gas density, i.e.,

$$\mathcal{R}_o = \rho_2 \bar{u} \qquad (8.3.2\text{–}3)$$

This result is obtained when it is assumed that the resistance changes from a friction-controlled to a jet-controlled value. If this is the case, then the threshold velocity corresponds to such a transition.

The results of the comparison between the effects of flow past and through on l_{eff} prompt a similar comparison for resistance ratio. The results of such a comparison are shown in Fig. 8.3.2h.

The lines plotted represent average values of the data from Figs. 8.3.2g and 8.3.2h. A comparison of the two sets of data show surprising agreement considering the possible sources of error. Also worthy of note is the comparison of the threshold velocity of ~100/ft sec past with the threshold velocity from Fig. 8.3.2d corresponding to ~100 ft/sec. Agreement between the two prompts speculation that the effect of ~100 ft/sec of flow past or ~5 ft/sec of flow through induces a turbulent transition which reduces δ while simultaneously changing the character of the resistance from a frictional to a jet loss effect. In addition, comparison of the effects of mean and oscillatory flow on δ indicate that violent oscillations play a similar role in the turbulent transition.

The effects of variations in cavity gas composition and temperature on the behavior of a liner are determined by noting which of the equations presented earlier are strong functions of the gas properties. The obvious equations are (8.3.1–2 and 8.3.2–3) for the resonant frequency

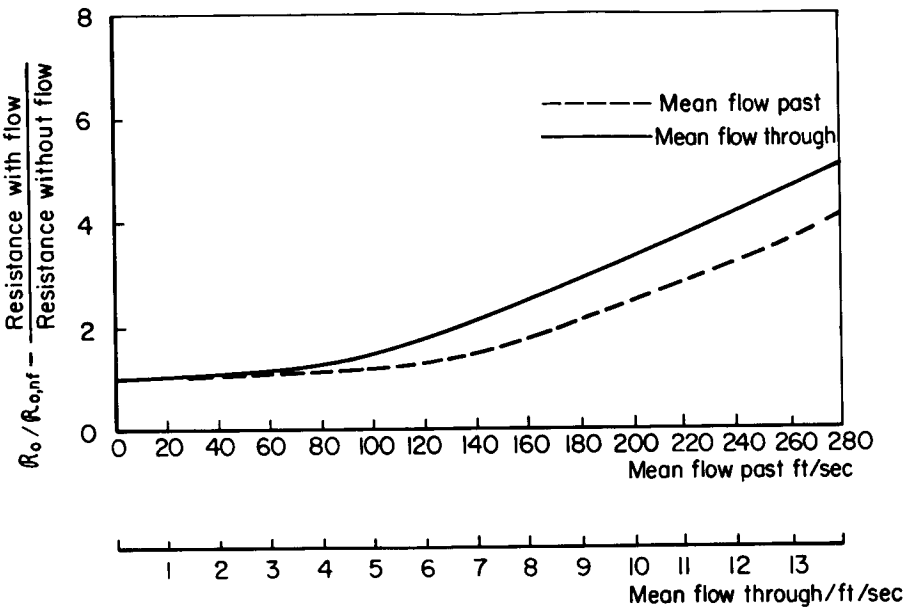

FIGURE 8.3.2h.—Comparison of the effects of mean flow past and mean flow through on the ratio of resistance with and without flow.

and the aperture resistance. The gas properties are the cavity gas sonic velocity a_3, and the aperture gas density ρ_2. These properties, in turn, are dependent on the gas temperature, pressure, and composition or molecular weight. While pressure can generally be specified, it is necessary to measure the gas composition and temperature. Typical results obtained from thermocouples mounted in a liner cavity are shown on Fig. 8.3.2i.[710,714] The results shown indicate the strong effect of propellant combination on backing cavity gas temperature as well as the effect of transition to instability. The cavity temperature for the H-O system is 900° R corresponding to a combustion temperature of about 6000° R whereas the result with earth storables corresponds to a combustion temperature of about 5000° R. Thus, the ratio of cavity to combustion temperatures varies from 0.15 for the H-O system to 0.36 for the storables.

Factors other than the propellants can also affect the cavity temperature as shown by Fig. 8.3.2j. A strong effect of liner open area ratio a on the gas temperature is indicated. The temperature in the cavity also increases with axial position (500° to 900° F higher temperatures are attained at the nozzle end, see Ref. 550, Fig. 25). The spread in cavity temperatures that can result from a typical test is shown in Fig. 8.3.2k.[551] The spread represents variations due to axial and circumferential position, as well as slight variations in O/F ratio from one run to the next.* For this particular configuration, it was necessary to resort to partitioning of the liner cavity and eventually to purging of the cavity with 1 lb/sec of hydrogen or helium in order to define the cavity gas properties.

In order to determine the composition of the gases, gas samples from either the liner cavity or the rocket engine boundary layer were obtained, refs. 552, 523, and 286. Factors such as element spacing, mixture ratio variations, etc. influence the gas composition and temperature, and wide variations may necessitate the purging of the liner cavity with a known gas.

The effects of nonperpendicular incidence angles, due to pressure fronts rotating in cylindrical cavities, are difficult to calculate. For cavities with no axial partitions (see Fig. 8.3.2a), the rotating pressure will tend to set up standing wave patterns in the cavity. Consequently, the

* Similar data have also been reported by other investigators, e.g., Ref. 324.

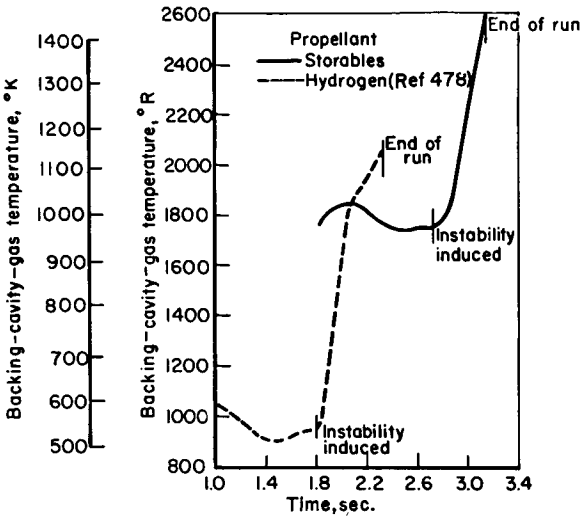

FIGURE 8.3.2i.—Comparison of backing-cavity-gas temperature of storable and hydrogen-oxygen propellant combinations during tests when instabilities were encountered.

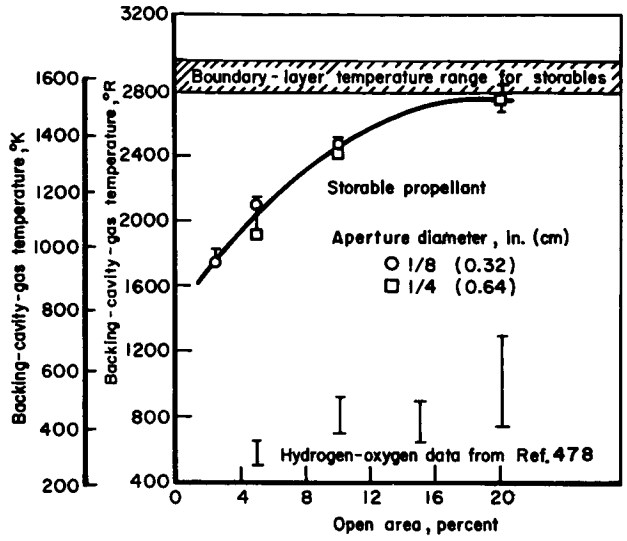

FIGURE 8.3.2j.—Effect of percent open area on liner backing-cavity-gas temperature during steady-state stable operation. Chamber characteristic length, 42 inches (106.7 cm); nominal mixture ratio, 2.0. (Average temperatures, denoted by symbols, were used for theoretical calculations.)

Helmholtz criterion for small cavity size will not have been met and the liner may suffer serious loss in performance. Although there is insufficient data from actual liner tests to support this, some acoustic bench tests have been run. The effects of partitioning the liner cavity on the liner damping are shown in Fig. 8.3.2l.[553] The circumferential or ring partitions had little or no effect whereas the axial partition had a marked effect on the damping of the first tangential mode. As expected, the radial mode damping was unaffected by the partitions.

8.3.3 The Sizing of Resonators*

The design of acoustic liners is based on matching the calculated resonant frequency of the liner to the frequency of the wave that is to be damped. The equation for the resonant frequency was stated in Sect. 8.3.1 and can be modified as follows:

$$\omega_r = a_3 \sqrt{\frac{A_o}{l_{eff}\mathcal{V}_{cav}}} = a_3 \sqrt{\frac{a}{L_{cav} l_{eff}}} \qquad (8.3.3\text{–}1)$$

where ω_r is now written in terms of the aperture open area ratio a, the backing cavity depth L_{cav},

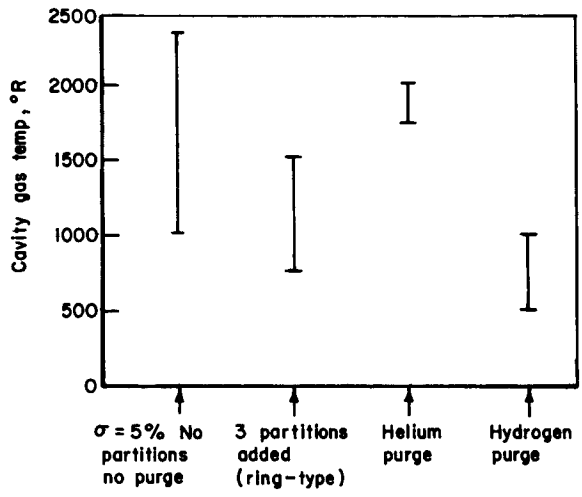

FIGURE 8.3.2k.—Effects of partitioning and purging the liner cavity on cavity gas temperature.

and the cavity gas sonic velocity a_3. The alternative form presented is based on the assumption that the resonators are grouped in a large array on a flat wall so that $A_o/\mathcal{V}_{cav} = a/L_{cav}$. The significant independent parameters for affecting tuning are the wave frequency ω, l_{eff}, and a/L_{cav} or $A_o/\mathcal{V}_{cav}$. Based on previous measurements and

* B. Phillips, Author.

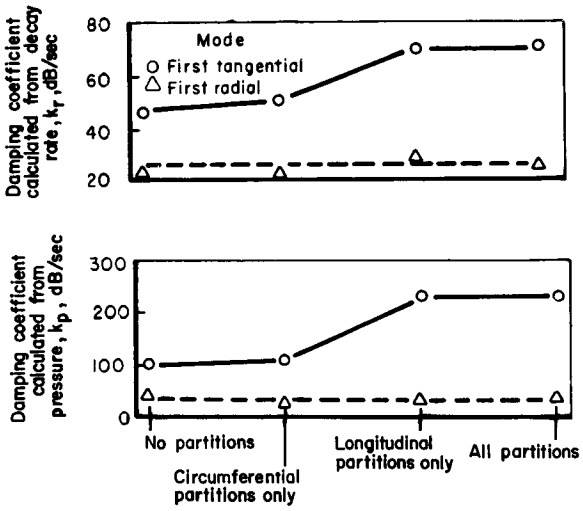

FIGURE 8.3.21.—Comparison of damping coefficients based on both pressure and decay rate for first tangential and first radial modes of oscillation with various conditions of backing cavity isolation. Electrical drivers; liner thickness, 0.45 inch; hole diameter, 5/16 inch; flow velocity, 0; hole spacing, 1 inch; backing distance, 0.55 inch.

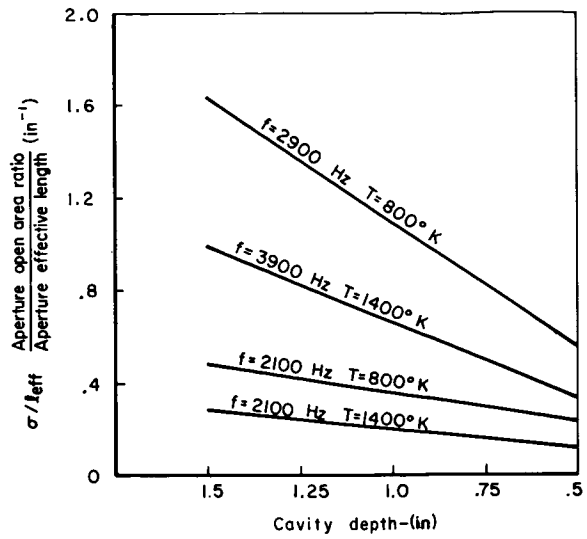

FIGURE 8.3.3a.—Lines corresponding to tuned operation for a system with temperature variation from 800° to 1400° K for frequencies of 2100 and 3900 Hz.

on engineering judgment, a range of expected cavity gas sonic velocity can be determined as well as estimates of the mean flows or turbulence near the apertures. The objective of the designer should be to minimize the sensitivity of the resonant frequency to variations in a_3, and turbulence or flow. Figure 8.3.3a is a plot of the ratio of a/l_{eff} as a function of cavity depth L_{cav} for given f with an expected variation in cavity gas temperature.† Each line represents tuned operation for a different temperature, and convergence of the lines (for decreasing L_{cav}) indicates a method of reducing the sensitivity to temperature variations.

In order to see how to reduce the sensitivity of tuning to variations in mean flow or turbulence, it is necessary to refer to that part of the tuning equation which depends on the presence of flows. The aperture effective length l_{eff} (from Sect. 8.3.2) is

$$l_{eff}=l_o+\delta=l_o+0.85d_o(1-0.7\sqrt{a}) \quad (8.3.2\text{–}1)$$

where it was determined that δ is a strong function of flow or turbulence. An obvious method of reducing the sensitivity of l_{eff} is to increase l_o, decrease d_o, or change both so as to reduce the contribution of δ to l_{eff}.

Under certain circumstances, it may not be possible to define a single frequency or range of frequencies of waves that are to be damped. This is the case where a rocket engine is prone to resonate at a number of distinct modes with large differences in frequency. One group has done a substantial amount of research related to this problem.[42] They have obtained significant improvements in absorption bandwidth by the use of resonators with more than one aperture size as discussed in Sect. 8.3.5 and shown in Figs. 8.3.5e and f (also see Ref. 42, Fig. v–31).

Another method of broadening the frequency bandwidth, which is relatively simple to accomplish, is to pack the cavity with a porous material such as steel wool. The effect of the steel wool is to substantially increase the resistance, and thus the bandwidth. An example of the successful use of this technique is shown on Fig. 8.3.3b.[714]

It may be necessary for certain applications to use aperture shapes which differ from circular holes. This is particularly true for full-length, cooled liners where the circular apertures tend to

† Data on these parameter trends are also provided in Ref. 324.

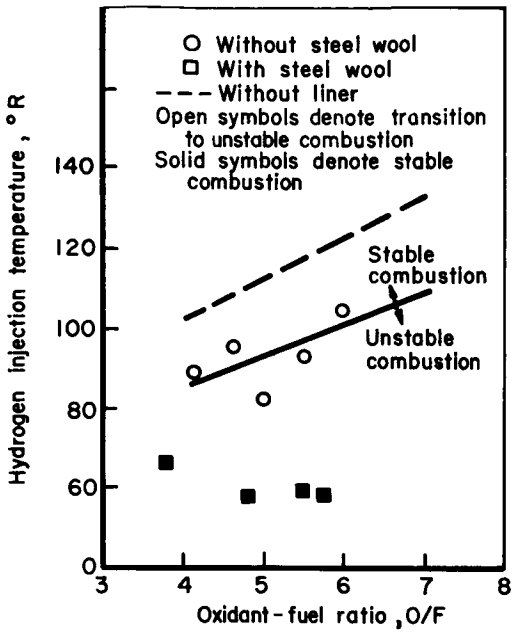

FIGURE 8.3.3b.—The effect of packing the resonator volume of an 0.2 open area, 3/16-inch-thick wall liner with steel wool.

burn out on the downstream edge (see Sect. 8.3.5). The use of axial slots is, therefore, preferred for such an application. Design equations for such systems are presented in Ref. 710 and involve modification of the l_{eff} and the resistance equations for circular apertures. Other experience with various aperture shapes is presented in Ref. 707. In general, the aperture shape is of secondary importance in determining the damping.

8.3.4 Number and Placement of Resonators*

If the location and the number of the resonators required to eliminate instability in the combustion chamber could be predicted from theoretical considerations alone, the design of absorbing liners would be relatively simple. Unfortunately, this is not the case; accordingly, considerable experimental research has been devoted to the problem.

Experiments to determine the number of resonators or the amount of absorption required in an array to stabilize combustion have been conducted by several researchers.† A summary of the results from two experiments[283,285] is shown in Fig. 8.3.4a. In these experiments full chamber length liners with absorption coefficients of up to 85 percent were used in tests with LO_2/LH_2 propellants at a chamber pressure of 300 psia and with N_2O_4/A-50 propellants at chamber pressures of 100 and 200 psia. All of the liners with absorption coefficients of 17 percent or greater suppressed the inherent, spontaneous instability of the test motors so that the resulting peak-to-peak pressure oscillations were less than 10 percent of the mean chamber pressure.‡ The absorption coefficients were computed using the array theory of Blackman[104] modified with an empirical theory to account for the effects of chamber gas flows. An incident pressure level of 190 db (re 0.0002 microbar) and a velocity equal to that of the free stream average in the chamber was assumed. A design curve depicting the theoretical relationship between the absorption coefficient and the open area ratio for the liners used in the storable propellant tests is shown in Fig. 8.3.4b.

Further evidence that the absorption coefficient is at least some measure of the suppression effectiveness of a resonator array is found in Ref. 710. By using common-cavity resonator arrays the effect of liner variables, i.e., open area ratio, aperture diameter and shape, and liner length, were experimentally evaluated in terms of the size of an explosive charge that would damp in a marginally stable thrust chamber and in terms of the reduction of oscillating pressure amplitudes in a spontaneously unstable motor. Absorption coefficients for the liners were computed. In no instance did a liner with a higher coefficient fail to provide at least as stable operation as one with a lower coefficient. The minimum coefficient required for stable combustion calculated using the average free stream Mach number at the liner was found to be 65 percent in that study.

The results from acoustic liner research including firings conducted with various numbers of individual resonators[324,647] reveal that to achieve stabilization different combustors require liners with significantly different numbers of resonators, open area or absorption coefficients. Furthermore,

* G. D. Garrison, Author.

† References include 283, 285, 324, 647, 710, and 714.

‡ Lacking a more definitive measure, the 10% oscillation level has often been used as the boundary separating stable and unstable operation.

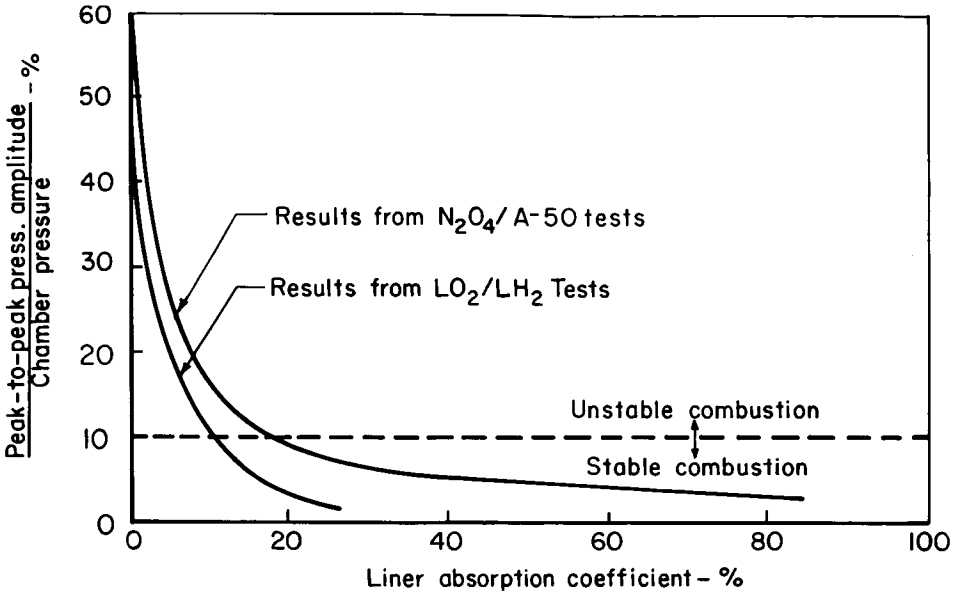

FIGURE 8.3.4a.—Summary of data from firings of motors with acoustic liners showing the effect of liner absorption on stability.

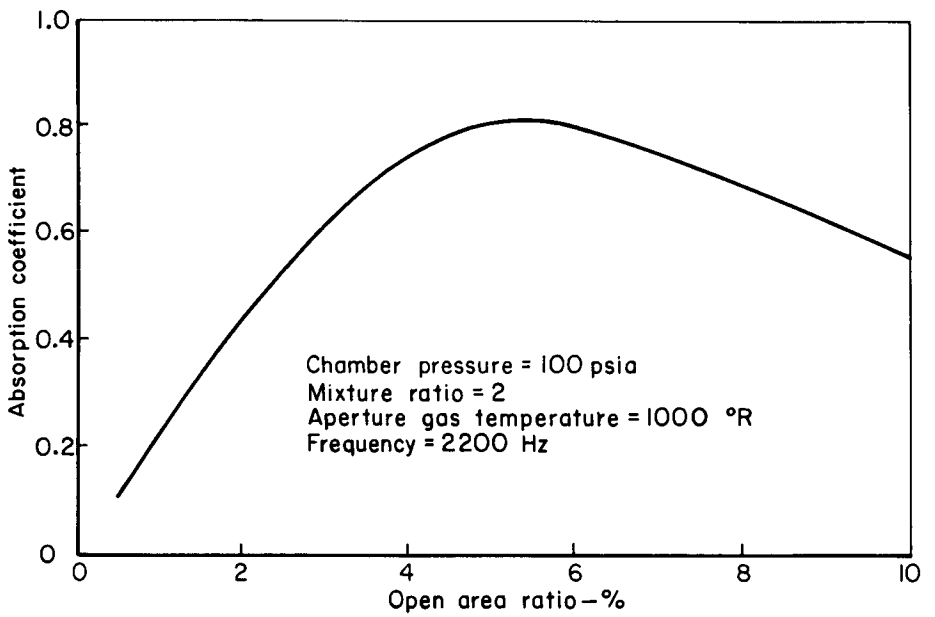

FIGURE 8.3.4b.—Theoretical dependency of liner absorption coefficient upon open area for a particular rocket motor.

no liner stability factor not based on assumptions similar to those required in the computation of absorption coefficients has yet been found. Although the history indicates that only a small amount of damping is required to stabilize most motors, the designer of the liner for a new application cannot be assured his requirements will be similar. For this reason, it is suggested that in addition to tuning the resonators so that the natural frequency corresponds to that of the instability, an analysis of the liner absorption characteristics should be conducted. The assumptions, procedures and digital computer program necessary to perform one type of absorbing liner

design analysis have been published.[282] This type of analysis would be more useful for design purposes if the effects of hot gas flows on absorbing characteristics were better understood and the necessity of arbitrarily assuming the amplitude of the incident pressure wave were eliminated or at least verified.

The amplitude of the incident pressure wave is important for the following reason: the principle of "absorbing" liner operation is based on the observation that combustion instability is a regular, cyclic oscillation, usually correlatable with one of the acoustic modes of the combustion chamber. This indicates a feedback mechanism in which each new cycle is triggered by the reflected pressure wave from the chamber wall that results from the incident pressure wave from the previous cycle. Thus, it is apparent that elimination of the reflection will eliminate the combustion instability. Unfortunately, as discussed in detail in Refs. 71 and 285, the incident pressure wave is not directly related to the fixed amplitude pressure oscillations of unstable motors and cannot be otherwise computed or directly measured at present. Therefore, an absorption coefficient based on an arbitrarily selected energy level, expressed as a pressure amplitude, is substituted for the design criterion. The relationship between the assumed energy and the actual value for a particular combustion process is unknown. However, the effectiveness of liners designed using this type of analysis in eliminating instability problems indicates that the arbitrarily selected value of 190 dB (13 psi) is greater than the actual incident energy of the motors tested, even though the unsteady pressure amplitudes in similar unlined motors are many times larger. Perhaps a more reasonable assumption than the arbitrary 190 db would be the maximum pressure oscillations allowable for the combustion process in a given motor to be considered stable (e.g., 10 percent of the mean chamber pressure).

In most practical liner designs the backing distance and the liner thickness will generally be fixed by strength and cooling requirements. Limitations on the values of aperture diameter that can be tolerated are set by the diameter of holes that can be conveniently machined, and by cooling requirements. For these reasons, it is usually better to use the open area ratio as the liner design variable. An optimum open area can be determined by computing the absorption coefficient versus selected values of frequency with the open area ratio as a parameter. The optimum open area is the value that gives the highest value of the absorption coefficient over the widest frequency bandwidth. The same procedure can be followed to optimize aperture diameter, liner thickness, and cavity volume if there are sufficient allowable variations to warrant the added difficulty.

Liner design to be successful requires good bandwidth* performance which is important for two reasons. First, typical acoustic liners of the Helmholtz-array type tend to possess resonant absorbing characteristics; i.e., high absorption coefficients are obtained near the resonant frequency of the assembly. However, at frequencies slightly different from resonance, the coefficients decrease to less than 50 percent of the peak value. The resonant frequency of the assembly can be determined with an accuracy no better than that of the assumed sonic velocity of the gas in the liner apertures and cavity. If the assumption is in error, peak absorption cannot be obtained since the liner must operate with incident pressures at a frequency different from that of the resonant frequency for which it was designed. Second, in some instances the use of a resonant-type liner with narrow bandwidth characteristics does not suppress the combustion instability, but rather causes it to shift to a different frequency with more or less the same pressure amplitudes. The additional wall impedance due to the presence of the liner apparently can cause the frequency to change only a few hundred Hz (a usual occurrence), or it can cause a complete shift in the mode and type of pressure wave; e.g., from first tangential to third longitudinal. The obvious solution to both of the above problems is to design the liner so that high absorption is obtained over a range of frequencies corresponding to the most destructive modes; i.e., the first through the third transverse modes. Unfortunately, it is difficult to design a liner for both high absorption and wide bandwidth performance, especially for operation

* Bandwidth refers to frequency bandwidth, the range of frequency over which the liner is effective in damping oscillations.

at low frequencies; therefore, some compromise is usually necessary. One approach to broadening bandwidth is the use of different aperture sizes as discussed in Sect. 8.3.5 and illustrated in Figs. 8.3.5e and f.

A resonator installed on the chamber wall near the injector face should be more effective than an identical one installed further downstream. The upstream resonator is in a position closest to the most critical zone* and, hence, can damp or absorb the pressure waves that would otherwise be reflected directly back to the source of the instability. The first test of this concept[274] used a liner consisting of an array of resonators with a common cavity volume (open area ratio of 5 percent) that had provided stable combustion in full-length liner tests. The liner was cut into quarter-length sections; each section was individually tested in its respective axial position to determine the most effective absorber location for preventing unstable combustion. The remainder of the chamber was made up of solid sections. Combustion was stable with the liner installed in the first two positions. Intermittent instability was encountered with the liner in the third position, and continuous instability was encountered with the liner in the fourth position (closest to the nozzle).

A second series of tests were conducted[283] with storable propellants to determine the effects of the liner length on suppression characteristics. Successive tests were conducted with liners of $\frac{1}{2}$, $\frac{1}{4}$, and $\frac{1}{8}$ of chamber length extending from the injector face; each liner section was a common-cavity array type with an open area ratio of 5.7 percent (absorption coefficient of 23 percent). Again, the remainder of the chamber was made up of solid sections. The tests were conducted at mixture ratios of 1.2 and 2.0 and at a nominal chamber pressure of 100 psia. Data in the form of the ratio of pressure amplitude to chamber pressure are shown in Fig. 8.3.4c as a function of liner length. A decrease in the liner length from $\frac{1}{2}$ to $\frac{1}{4}$ chamber length did not change the stability characteristics of the motor; however, a decrease in length from $\frac{1}{4}$ to $\frac{1}{8}$ chamber length resulted in pressure amplitudes greater than 10 percent of chamber pressure, an unstable condition.

Also, liner position tests[283] were conducted to determine if a $\frac{1}{4}$ chamber length liner, positioned three inches downstream of the injector face, is as effective in stabilizing combustion as an identical liner installed next to the injector face. These tests were conducted with the same $\frac{1}{4}$ length liner described above. It was found that moving the liner to the downstream position caused the pressure oscillation amplitudes to more than double.

Other tests were conducted to determine the most effective axial location for resonators.[548,710] It was shown[710] that a full chamber length liner (10 percent open area) could be shortened from the nozzle end to $\frac{1}{4}$ of the original length without affecting the stability of the combustor; however, the minimum liner length was found to be a function of the absorbing characteristics. A liner consisting of eight rows of 34 individual resonators per row was also evaluated.[548] It was concluded that it was only the row positioned closest to the injector that contributed to the damping characteristics of the array. Other experiments carried the "limited liner" concept still further, and have indicated that stability can be achieved with as few as three resonators.[324] The concept of combining liners with frequency-limiting baffles is also desirable in certain applications as discussed in Sect. 8.3.6.

The results of the above experiments do not imply that a partial length liner or only a few resonators positioned next to the injector are always adequate for suppressing instability. However, the results give further evidence that a sensitive zone exists near the injector face and for maximum effectiveness the resonators must be located on the combustion chamber wall surrounding this zone. For applications requiring only a few resonators the units may be located within the injector assembly itself, when space permits, thereby simplifying cooling requirements.

8.3.5 Thermal Design Considerations*

For extended duration firings the acoustic liner installed in a rocket thrust chamber must be

* This is the zone of highest unsteady pressure amplitude for both transverse and longitudinal mode resonant combustion.

* G. D. Garrison, Author.

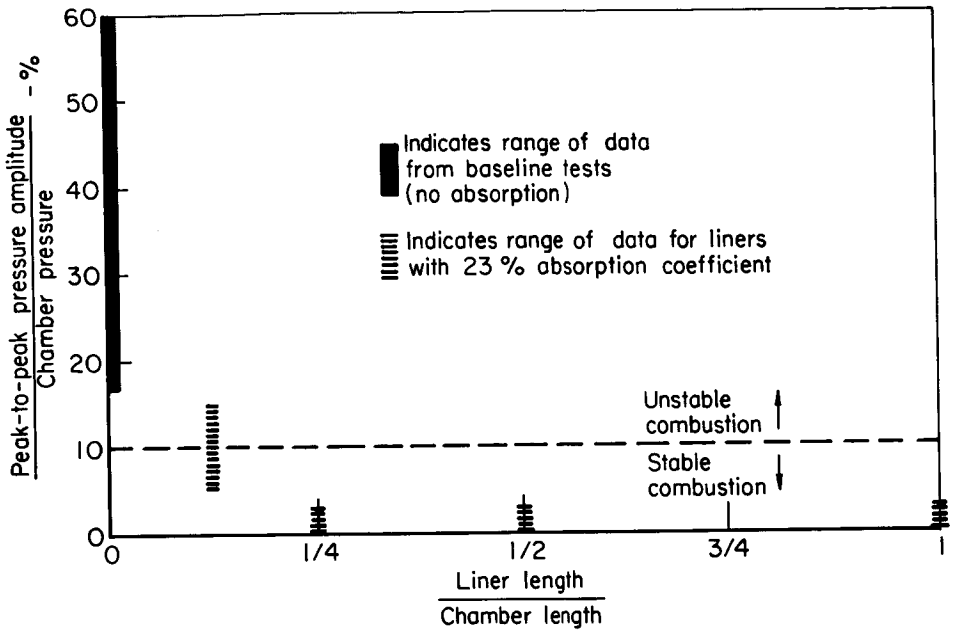

FIGURE 8.3.4c.—Effect of liner length on motor stability.

protected from its thermal environment. It has been experimentally shown that both convectively cooled and ablative acoustic liners are entirely feasible.† Furthermore, even though the presence of a liner may cause additional complexity in thrust chamber design analysis from a heat transfer standpoint (e.g., apertures of certain sizes can cause boundary layer disruption with a resultant increase in local heat fluxes), the type of analysis is basically the same as that required for any other cooled rocket motor. Film-cooled and transpiration-cooled liners have been tested;[284] however, certain problems, to be discussed later, may preclude these schemes from consideration as a primary thermal protection device for acoustic liners.

The primary problem in the design of a convectively cooled chamber with an absorbing device is to provide a large number of apertures in the chamber wall without retarding the cooling effectiveness of the assembly or allowing leakage of coolant into the resonator cavities. Many solutions to the problems exist.[274,285] Typical are the following three different techniques which have been successfully demonstrated in hot tests of cooled thrust chambers.

† See Refs. 71, 284, 285, 444 and 490.

The first tests of a flightweight, acoustically-lined, cooled thrust chamber[444] were conducted using a liner made from conventional coolant tubes that were crimped (dimpled) at many axial locations. The stainless steel tubes were brazed together so that the dimples coincided to form liner apertures as shown in Fig. 8.3.5a. A total of 9000 apertures, each with a nominal diameter of 0.060 inch, were formed producing an open area of 8 percent. After brazing, the liner was fitted with an uncooled outer pressure shell spaced one inch from the liner. Six uncooled circumferential (ring) partitions were installed between the liner and shell to support the assembly and to minimize the possibility of axial gas flows through the resonator cavity. Several long-duration firings were made using an injector known to produce spontaneous instability; propellants were LOX/LH_2 (hydrogen inlet temperatures of 45° R) and the coolant was water. Every test was extremely stable with peak-to-peak pressure oscillations of less than 2 percent of the mean 300 psia chamber pressure. Gas temperatures were measured in each resonator cavity; a maximum of 1580° R was recorded.

Another water-cooled acoustic liner[71] was fabricated by welding together fifty 0.25-inch OD stainless tubes with 0.040-inch walls to form a

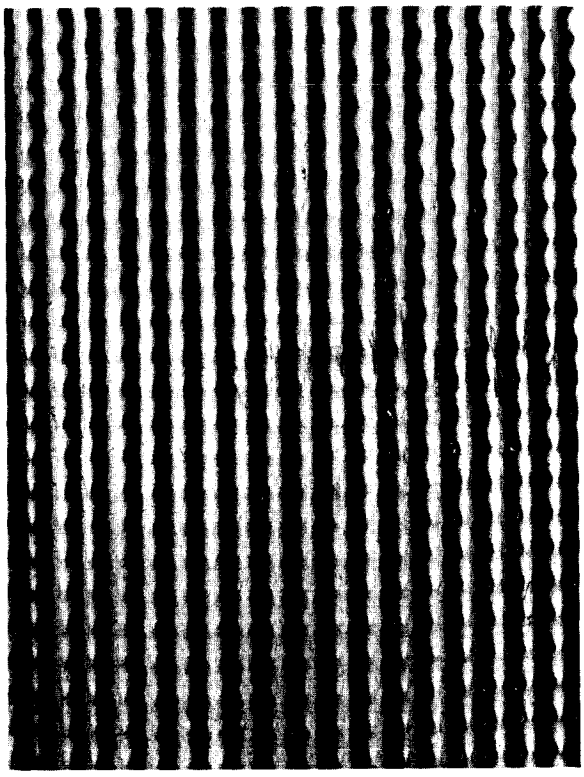

FIGURE 8.3.5a.—Close-up view of apertures formed in convectively cooled chamber by crimping coolant tubes.

3.73-inch diameter combustor. Thirteen hundred and fifty apertures (0.040-inch diameter) were drilled between the tubes producing a full chamber length liner with an open area of 2.5 percent. The resonator cavity was formed with an uncooled pressure shell. After several successful firings at a chamber pressure of 1000 psia (LOX/RP-1 propellants), the liner was shortened to half the original length by welding the apertures closed in the downstream half of the chamber. The shortened liner configuration proved to be equally effective in stabilizing the test motor which without an absorbing liner was shown to be spontaneously unstable. With either liner, pulse gun charges producing overpressures as high as 2600 psi were damped. A maximum temperature of 1903° R was recorded from thermocouples installed in the resonator cavity.

A third type of water-cooled acoustic liner was fabricated for use with a 15,000-pound thrust throttlable motor burning N_2O_4/50% UDMH–50% N_2H_4 propellants.[490] The chamber consisted of a composite cylindrical brazed shell with integral coolant passages. The liner apertures were drilled in spaces between the rectangular passages as shown in Fig. 8.3.5b. The outer pressure shell was uncooled. The motor was operated over wide ranges of chamber pressure and mixture ratio. No combustion instability occurred in any of the 72 firings while high performance and good hardware durability were demonstrated.

Another approach to achieve liner thermal protection utilizes ablative materials; however, this introduces several unique problems. The most significant of these are

1. The plugging of apertures by molten ablative products may cause a loss in suppression effectiveness.
2. Excessive wall recession rates or aperture erosion may change the liner performance.
3. Apertures may disturb the boundary layers on the chamber walls, thereby causing an increase in heat transfer rates and, as a result, reduced chamber life.
4. Outgassing of phenolic resin compounds may cause the combustion gas products in the apertures and cavity to be replaced by gases of a significantly different molecular weight, thereby deteriorating the damping effectiveness of the liner assembly.
5. Structural requirements may necessitate the use of more partitions in the cavity than is common with the typical array, thereby restricting the number of resonators that can be installed at the most sensitive combustion zone, i.e., near the injector face.

With absorbing liners made of some ablative materials, the effect of aperture size on liner erosion rate is important because a molten layer could form during operation and flow along the surface of the liner. Thus, small-diameter apertures could easily become plugged and lose their effectiveness. Larger apertures are not as likely to become plugged, but excessive erosion rates could be caused by the increased surface irregularities. Furthermore, as an ablator is fired, the absorbing characteristics might even improve since the resulting char layer is extremely porous. To answer the above questions and evaluate the effectiveness of ablative absorbing liners in general, the following series of rocket tests were conducted using a

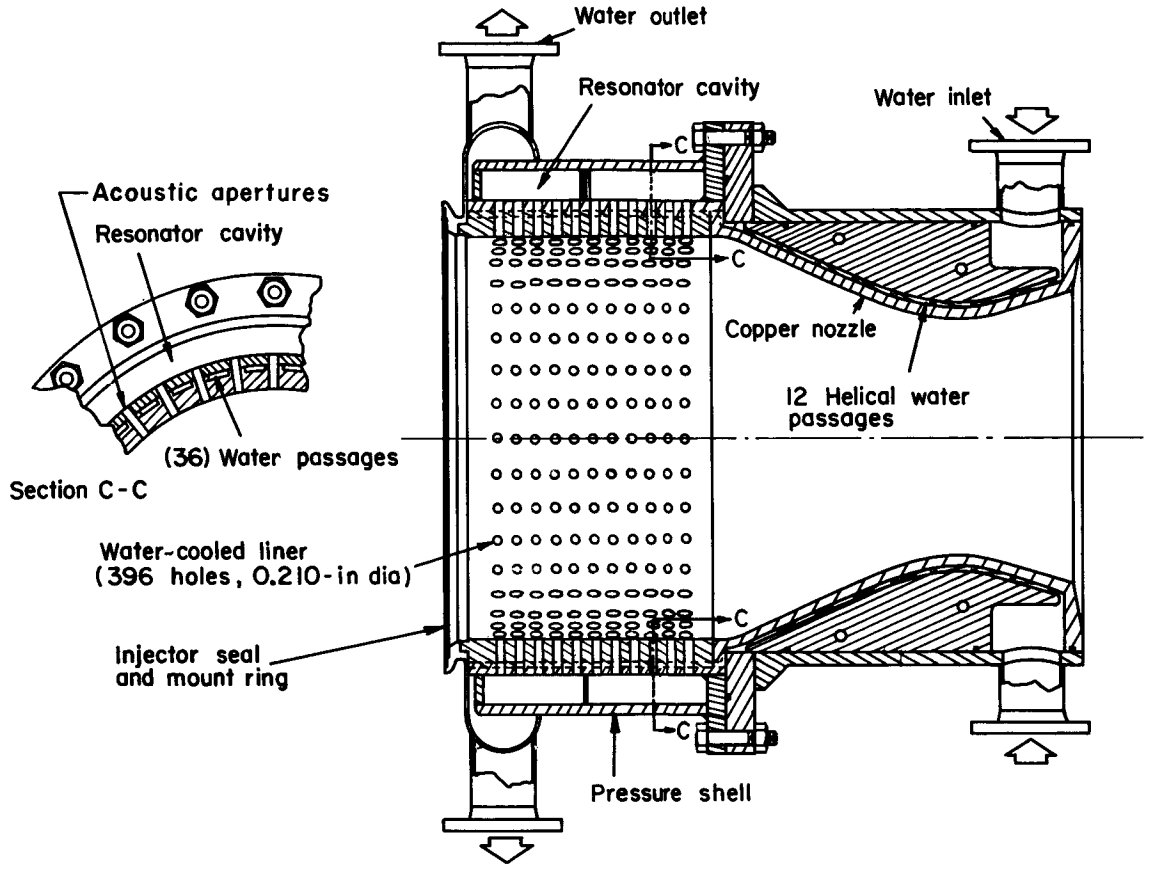

FIGURE 8.3.5b.—Convectively cooled thrust chamber with acoustic liner.

motor of known spontaneous instability characteristics.[285]

The liner, made of reinforced silica phenolic resin, was fabricated with circular apertures ranging in diameter from 0.10 to 0.35 inches, and a common cavity. Tests were conducted using LOX/LH_2 propellants at a chamber pressure of 300 psi; Fig. 8.3.5c is a photograph of the liner taken after several seconds of firing. Note that the larger apertures (diameters greater than 0.25 inch) experienced a significant amount of erosion, whereas the apertures of smaller diameters (0.10 and 0.15 inch) experienced little or no erosion. Also, it was found that a reduction in the pressure amplitude occurred as the char layer formed on the liner wall, e.g., the amplitude of pressure oscillations decreased from 60 psi to 3.5 psi in approximately seven seconds of testing. Based on these results a similar ablative liner for the same motor was designed for an open area of 5 percent with 0.160-inch diameter apertures, (absorption coefficient of 43 percent). A total of 336 seconds of firing time was accumulated in eleven tests; stable combustion was experienced throughout. After each test the liner was inspected for integrity and to estimate the effects of ablation on the apertures. The liner remained in excellent condition; both aperture erosion and liner ablation were found to be negligible.

One plausible explanation for the localized regions of high heat flux on the downstream edge of large apertures is that the downstream edge of the aperture presents itself to the compressible turbulent boundary layer flow of combustion gases adjacent to the heated surface as the leading edge of a flat plate. Local flow conditions necessary for this flat plate regime to occur would involve the aperture flow and the aperture size. The small flow oscillations present with the combustion noise (and the local absence of a solid boundary) must

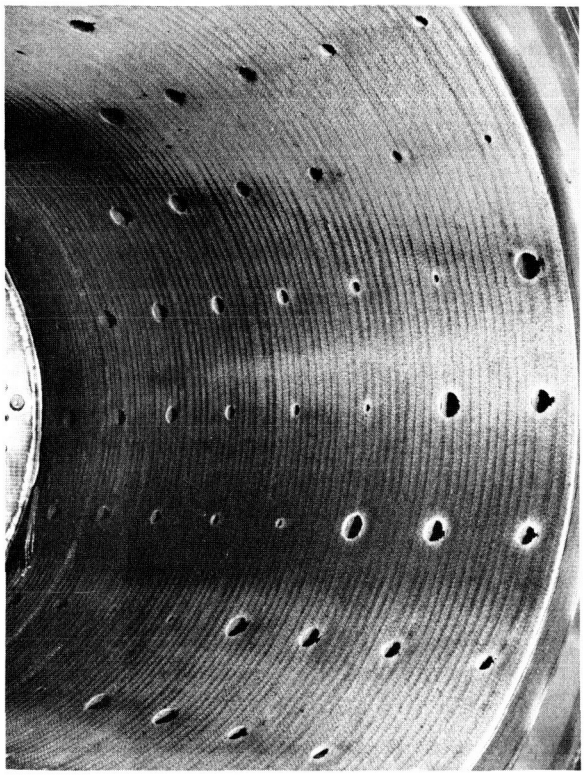

FIGURE 8.3.5c.—Ablative absorbing liner after firing showing effect of aperture diameter on erosion rates.

bring the core flow, with its associated high temperature, over to the wall. Under these conditions a new turbulent boundary layer could be initiated downstream of the larger apertures, and the heat flux profile would then correspond to that associated with the leading edge of a flat plate as shown in Fig. 8.3.5d. Using this model and the classical methods for determining the heat flux profile along a flat plate exposed to turbulent boundary-layer flow with heat transfer, estimates (for liner design purposes) may be made of the heat flux levels in this region. If it is determined that the presence of the apertures causes a significant increase in the local heat flux, appropriate steps may be taken to reduce the effects of the apertures to a tolerable level.

The approach taken in the above experiments[285] was to use a greater number of smaller apertures thereby reducing the "relative roughness" produced by the presence of the apertures. Another approach would be to alter the shape of the apertures to reduce the leading edge effect. Apertures having an elliptical, tear-drop or slotted cross section would achieve this result. The effects of noncircular apertures on the acoustic characteristics of liners have been extensively investigated.[283,710] An additional advantage of long slotted apertures is that for convectively cooled liners they may be more easily installed between coolant passages than circular apertures.[710]

Outgassing of resin compounds and structural limitations were of prime consideration in other ablative liner research.[284] The heat transfer and instability characteristics of the storable propellant injector were known to be especially severe; therefore, an ablative liner with maximum structural integrity was desired. The first design, a one-half chamber length liner fabricated with individual resonators, failed to suppress the combustion instability. The molecular weight of gas samples obtained from resonator cavities during several firings was found to be significantly different from that of the combustion products; but it was found that the properties of the cavity gases could be accurately predicted from theoretical thermochemical analysis. Although the outgassing had caused the liner damping characteristics to be different than expected, fabrication and testing of an identical uncooled steel liner showed that the poor liner performance was due to an insufficient number of resonators near the injector face. The steel liner was reworked to provide more resonators in the critical zone and tested. The instability that had plagued the ablative liner (first and second tangential, second longitudinal and first radial modes) was suppressed, but high pressure amplitudes appeared at much higher frequencies corresponding to the second radial and the fourth tangential modes where the liner absorption was negligible. Complete stabilization was achieved by fabricating a full chamber length ablative liner with two different types of common cavity arrays as shown in Fig. 8.3.5e. The absorption characteristics of the liner, Fig. 8.3.5f, were computed[282] based on the sample gas properties; the resonant frequencies of the two arrays were 3516 and 5770 Hz.

Tests with film-cooled liners and transpiration-cooled liners[284] have shown that the presence of external coolant flows can adversely affect both combustion characteristics and liner damping ability. The film-cooled liner data were obtained

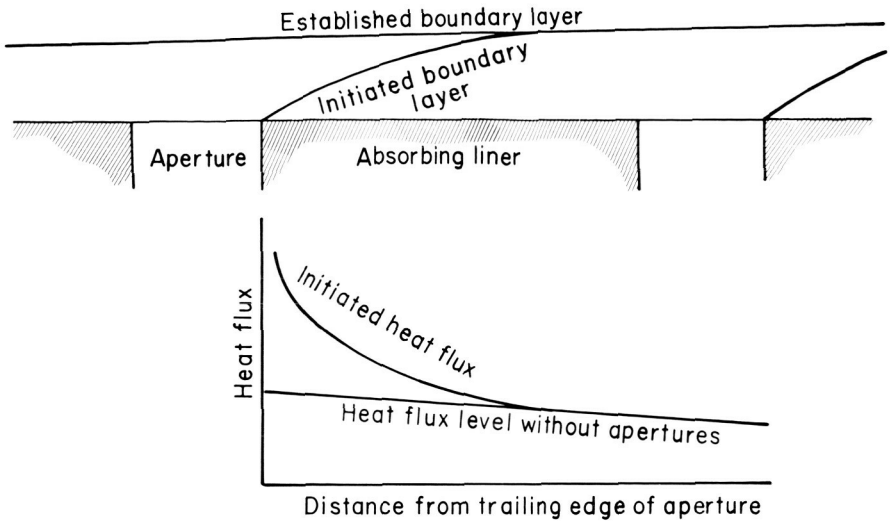

FIGURE 8.3.5d.—Effects of apertures on boundary layer development and associated heat flux profiles.

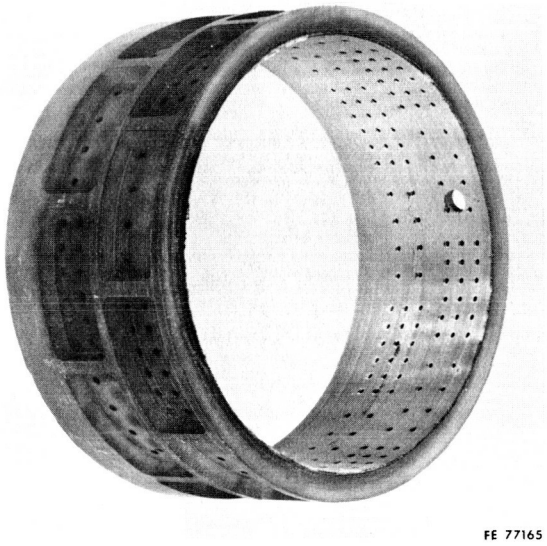

FIGURE 8.3.5e.—Ablative liner with dual arrays of common-cavity resonators.

from two one-half chamber length liners; one was fabricated for operation at a combustion pressure of 1000 and the other for 200 psia. The 50% N_2H_4–50% UDMH coolant was injected over the liner face from 0.021-inch diameter holes in a manifold on the upstream edge of the liner assembly; a sketch of the test configuration is shown in Fig. 8.3.5g.

Short duration firings with no coolant at a chamber pressure of 200 psia were stable; however, with coolant the motor was less stable and with the exception of two tests the amplitude of the pressure oscillations was found to be inversely proportional to the coolant flowrate. At the higher chamber pressure all tests were stable, i.e., no instability with pressure amplitudes greater than 10 percent of chamber pressure was measured; however, as in the 200 psia tests, the amplitude of the oscillations was inversely proportional to the coolant flowrate.

The successful application of film-cooled acoustic liners is difficult because of three factors:

1. The tendency of the coolant film to burn at the surface of the liner which causes the cavity gas temperature to rise, thereby changing the acoustic characteristics of the assembly
2. The inability to accurately estimate, for acoustic design purposes, the liner aperture gas properties
3. The uncertainty in absorbing characteristics caused by the presence of coolant flow over the apertures

Similar results were obtained from hot firings of a gaseous hydrogen, transpiration-cooled liner.[284] Analysis of combustion data showed that the hydrogen coolant caused the test motor to be more unstable than when no liner was used or with no coolant flowing through the apertures. In addition, the data indicated that instability increased with coolant flowrate. The mechanisms

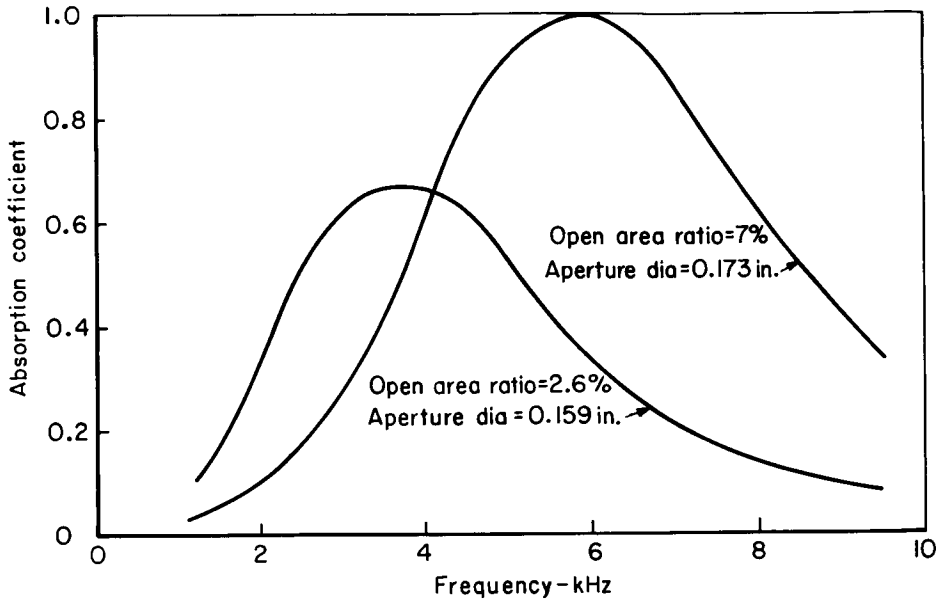

FIGURE 8.3.5f.—Theoretical absorption coefficients for ablative liner with dual arrays of resonators.

that cause the presence of coolant to degrade the stability characteristics of the motor and acoustic liner are not yet known. Additional basic research will be necessary before this type of liner can be considered for further application.

8.3.6 Further Acoustic Absorber Applications*

The characteristics of acoustic absorbers and baffles are such that it is desirable, at times, to use these devices in combination. A baffle arrangement can be employed to eliminate the lower modes (e.g., a three-bladed baffle would eliminate tangential modes below the third) and the acoustic absorbers are then tuned to the remaining higher modes. Since the acoustic absorbers (either resonant or nonresonant) tend to be more effective at higher frequencies, this division of damping is usually advantageous. In other examples cited in this section the acoustic absorbers, in limited numbers, performed the damping function alone. One form of acoustic absorber, acoustic cavities or slots, have been used both with and without baffles.[510,520]

Acoustic absorbers have proved to be most effective when located along the injector periphery at or near a pressure antinode (unsteady pressure maximum). These antinodes usually occur at the chamber wall or other confining surface (baffle surface or injector face). The first use of the corner location for an absorber was by Lawhead and Levine in the early fifties.[442] They investigated various types of acoustic absorbers, both resonant (Helmholtz) and non-resonant cavities, for control of combustion instability. Two-dimensional and annular horns were evaluated in both acoustic bench tests and rocket firing tests. In one case, a 3000 pound thrust engine, which had been spontaneously unstable at 3600 Hz, was completely stabilized (five tests) with an annular horn, nonresonant absorber.

Another type of absorber is the "acoustic slot." The usual acoustic slot consists of an annular cavity around the injector face with a thickness often less than $\frac{1}{8}$ inch and length on the order of an inch[520] (see Fig. 8.3.6a). This slot appears to act in a manner similar to an acoustic liner, i.e., it dissipates oscillatory energy. Because of its location, cooling problems associated with the slot are minor. Further, it is easily fabricated and incorporated into existing designs. Thus, the slot provides a very attractive stability aid. Acoustic slots are not likely to have as large a damping capability as full length acoustic liners. However, since damping due to the slot is introduced in the

* T. A. Coultas, C. L. Oberg, and J. M. Senneff, Authors.

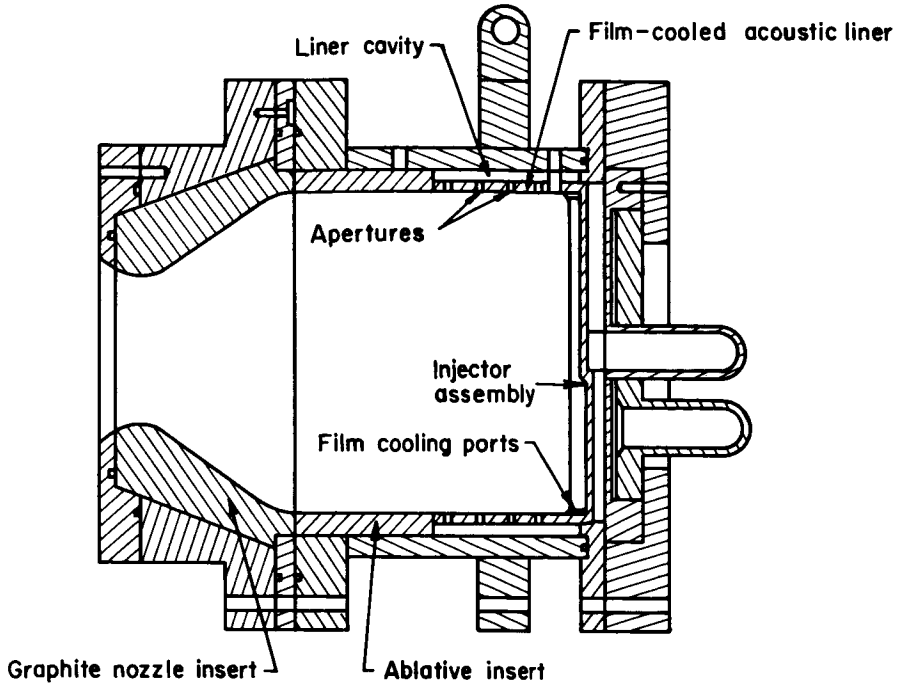

FIGURE 8.3.5g.—Test motor with film-cooled acoustic liner.

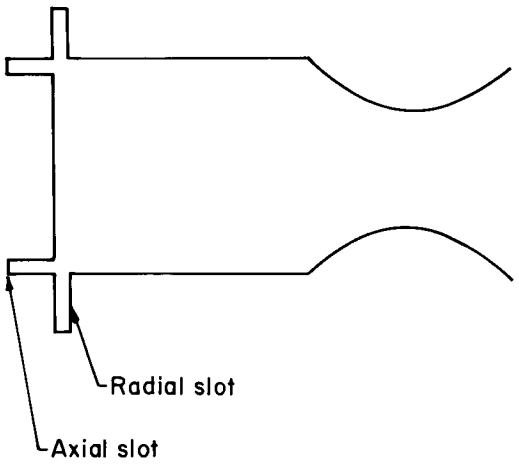

FIGURE 8.3.6a.—Slot configurations.

most effective region, its damping is likely to be comparable to a short ($\sim\frac{1}{8}$ length) liner.

Acoustic slots have been successfully applied to two different engine systems.* The first of these engines produced 300 lbf-thrust at a chamber pressure of 120 psia with N_2O_4/MMH propellants. Without the acoustic slot this engine exhibited marginal stability, being triggered unstable by hard starts approximately 6 times out of 200. The instability was identified as the first tangential mode with a frequency of 9000 Hz. The introduction of three baffle-like tabs in the engine reduced the frequency of occurrence of instability to approximately 1 percent, but did not eliminate it. After an acoustic slot was introduced, no instances of instability were encountered in over 5000 starts with the engine.

A detailed bench-type acoustic modeling study was carried out in conjunction with the slot design effort for this engine. The models comprised an actual thrust chamber, a plastic plug to close the nozzle, and several plastic injector simulants. The models were excited with an acoustic driver to amplitudes on the order of 155 dB (referred to 0.0002 dyne/cm^2). Tests were made both with air and with helium contained in the model. Data were obtained for five different slot configurations and with no slot.

Several interesting features were evident in the results from this testing. For example, it was found that the slot caused shifts in resonant

* Significant advances have been made since the original preparation of this material. The reader is encouraged to consult more recent literature, e.g., Ref. 520.

frequencies of the chamber. At times, the normal modes were split with two modes being evident in the frequency range where only one appeared without the slot. Further, the damping due to the slot was found to be reasonably large and surprisingly insensitive to slot dimensions. As might be expected, the damping was different with the two test gases, greater damping being found with helium. In an effort to develop rational means for extrapolating these modeling data to motor conditions for design purposes, an approximate, linear analytical model was developed based upon a viscous mechanism.

The analytical predictions agreed surprisingly well with the acoustic modeling data (both modal frequencies and decay rates were predicted). The analytical model was, however, much less successful when applied to the hot firing case. In the latter case, the predicted damping was negligibly small for the same slot design which had so completely stabilized the engine. Although the gas properties in the slot were uncertain, the uncertainty did not seem sufficient to explain the disparity.

The second engine in which an acoustic slot has been successfully applied is the LM ascent engine. This engine produces 3500 lbf thrust at a chamber pressure of 120 psia with N_2O_4/N_2H_4-UDMH (50–50) propellants. The injector design uses three equally-spaced radial baffles and an acoustic slot along the periphery as shown in Fig. 8.3.6b. The baffles are designed to eliminate first and second tangential modes. The slot is designed to eliminate the third tangential and first radial modes.

From these test results, it is evident that acoustic slots do provide sufficient damping to be of practical importance for prevention of combustion instability. However, proper design of slots requires an adequate analytical model. Such a model is currently under development, which includes the nonlinear effects in the slot. In addition, data are needed to describe the performance of the slot at high amplitudes.

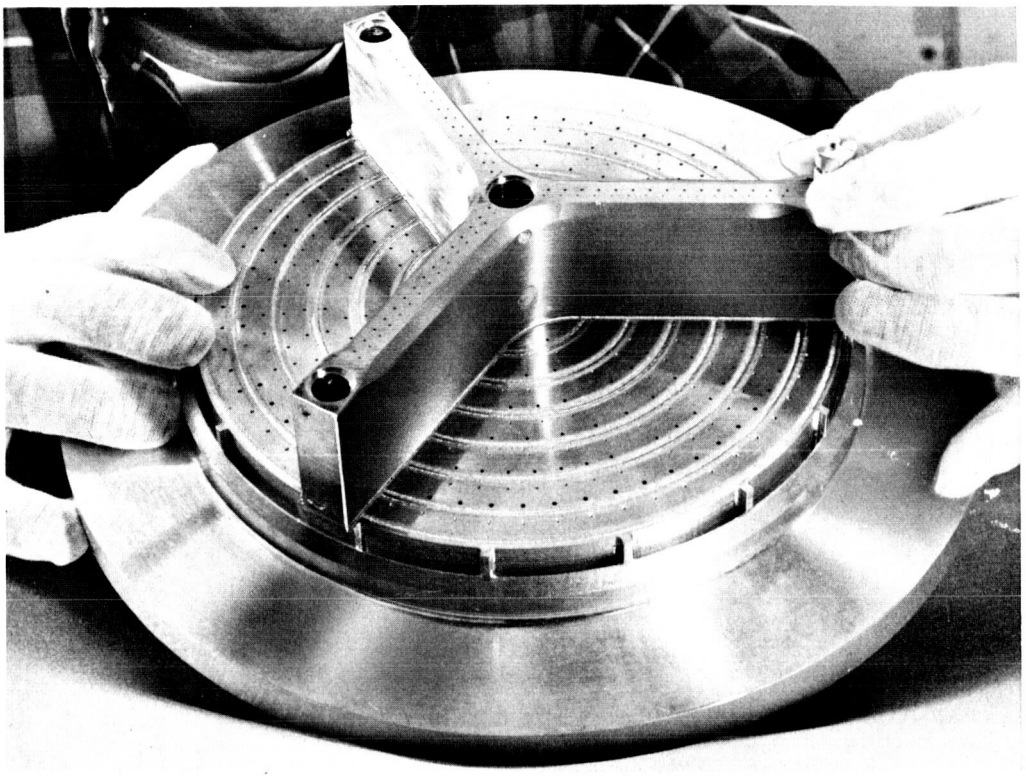

FIGURE 8.3.6b.—Baffled injector with acoustic slots in the corner.

Next are some examples of liner-baffle combinations as well as limited use of resonators. These examples were supplied by J. M. Senneff.

A single row of apertures connected to appropriately tuned backing volumes achieved a substantial reduction in instances of instability when located near the face of the 8-inch diameter unlike triplet/doublet injector having a three-bladed, 1.25-inch long baffle. The backing volume for the resonators required circumferential compartmentalization to be effective, otherwise communication beneath the baffle blades occurred and stability was not achieved (this is similar to the history with baffle tip gap on the same engine where gaps of 0.01 inch were successful for damping, whereas 0.1 inch gaps were not). The single-ring resonator approach was found to achieve stability at a discrete time following ignition with aperture open areas only 0.4% of the total wall area of the chamber. The time dependence involved the backing volume temperature which varied significantly so as to question the effectiveness of a single tuned design. Multiple-sized apertures appeared to be beneficial but these experiments were not pursued sufficiently to provide a final design solution.

Some experiments were also conducted with this same injector using a Helmholtz resonator array in the ablative chamber wall. The experiments indicated that significant damping resulted in the array tested. This array was in the form of twelve units each consisting of six apertures. The total open area of all elements was slightly less than $\frac{1}{2}$% of the wall surface area. The placement was related to the baffle blades and the associated third tangential cavity mode. Four resonators were in each sector with two units in the center of the sector (at one pressure antinode) and a unit at either end of each sector (the second antinode). The ablative chamber tests achieved damping but resulted in erosion and damage to the ablative resonator elements from bombing. The design was thus eliminated from further consideration based upon the success of other stability solutions. However, evidence from the testing indicated that significant damping was achieved with a very small open area when resonators were properly placed.

Another design used a single ring of resonators at the injector-chamber interface with the 3-inch hardware (the unlike injector design as described in Sect. 7.4.2). The aperture open area in the final version was slightly less than 1% of the total wall area of the chamber. Other experiments leading to this design included units having twice the open area and twice the number of orifices. The reduced area design was found to be acceptable in both start spike and bomb tests. Some aperture erosion was noted when the apertures were placed both between and in line with the triplet orifices. This indicated gas flow in and out of the toroidal cavity resonator. By placing the apertures only between the injection elements this flow was eliminated and erosion was absent. The resonator design with apertures between injection orifices was incorporated in the final design and tested under a variety of conditions for both stability and duration with complete success.

8.4 THRUST CHAMBER SHAPE

8.4.1 General Considerations*

In typical combustion chambers, acoustic liners and baffles may be considered as the primary damping devices and, as such, should be given first consideration by the designer. There exist, however, other practical approaches to an optimum-damping design which cannot be overlooked. These include the injector shape, the combustion chamber wall shape, and the nozzle convergent section shape.

In Sect. 8.4.2, a discussion is made of some experimental observations of the effect of divergent chambers on the transverse mode stability of the engine. The interest centers on the velocity difference between gas and liquid droplets which is influenced by the divergence of the chamber. Little is known, however, of the more interesting effect of converging chambers (such as conical chambers) on the stability.

No well-controlled experiments have been performed which would compare conical chambers to cylindrical chambers. Also, no mathematical analyses which predict the effect of tapering the chamber have been completed. Some discussion of this point is contained in Sect. 3.5.1.

The linear analyses of various cylindrical chambers where no tapering occurs but cross-sectional geometries differ is also discussed in

* W. A. Sirignano, Author.

that section. No explicit differences in the stability relation are found among the various shapes. Implicit differences which depend upon the cross-sectional shape occur in the acoustic liner and nozzle effects. Also, the shape influences the frequency, which in turn influences the effect of the acoustic liner, nozzle, and combustion response upon the stability. It should be noted that in a nonlinear situation, some other primary differences may depend upon the cross-sectional shape; e.g., transverse shock waves may form in an annular chamber but are less likely in a standard chamber.

The nozzle admittance has been shown to influence the stability of the engine (Sections 3.5 and 3.6) especially for longitudinal modes of oscillation. The important information for the designer is exact knowledge of the dependence of the nozzle admittance upon the nozzle shape or, more directly, the influence of the nozzle shape upon the stability. Since disturbances cannot propagate back from the supersonic portion, only the nozzle convergent section shape is of interest from a stability point-of-view. A summary of the effect of the nozzle convergent section is given in Sect. 8.4.3.

The injector shape can also have a significant influence on the stability of the rocket engine. One damping effect would be that the wave reflection process is altered by curvature of the injector face and another is that the combustion profile is affected by this curvature. Our understanding here is still empirical but some useful design information is contained in Sect. 8.4.4. Injector design factors affecting excitation are discussed in Sect. 7.3.

8.4.2 Combustion Chamber*

In this section and the one that follows it is immediately apparent that a close interrelationship exists between the chamber components. When does the combustion chamber end and the nozzle entrance begin? Certainly for the tapered chamber the nozzle entrance would appear to begin at the injector face, unless we specify a boundary between the two at some arbitrary point in the combustion process, say 90% complete.

Equally difficult to evaluate is the stability role played by the fully tapered chamber as compared to a partially tapered chamber design. This point will be discussed from a theoretical viewpoint in Sect. 8.4.3, however, experimental data using one injector, one contraction ratio, equivalent propellant flow and pressure, etc., while varying the taper, seem to be lacking. Systematic tests, however, have been performed on a number of diverging chambers and these will be discussed next. One problem in the evaluation of diverging chamber designs is also associated with the combustion rates, where high rates can produce sonic flow in the diverging section itself. However the diverging chamber with no physical throat is a design that could be of future interest.

In Section 7.4 it was shown that variations in coaxial injector element details in a cylindrical thrust chamber can significantly affect the stability of the LOX/LH_2 combustion process. By altering the shape of the thrust chamber, additional control can be maintained over parameters affecting the combustion process and thus, presumably, acoustic mode combustion stability. The velocity differential between the

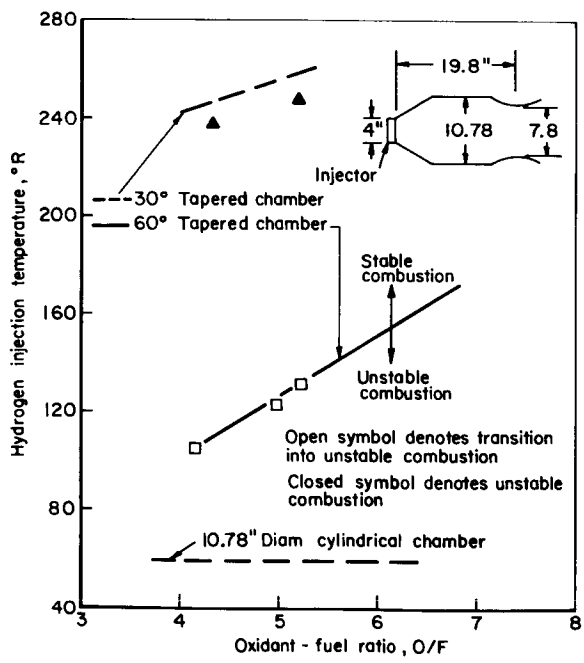

FIGURE 8.4.2a.—Effect of chamber shape on stability. Oxygen/hydrogen propellants; chamber pressure, 300 psia.

* J. P. Wanhainen, Author.

combustion gas and droplets is an important parameter in controlling the transverse-mode stability characteristics of a rocket combustor (see Sects. 4.3 and 6.4). Since the gas velocity is related to the chamber geometry, increasing the velocity differential parameter to produce stable combustion can be accomplished by simply altering the shape of the thrust chamber.

Typical stability results for chambers employing a divergence section to increase the combustion gas velocity axial profile are shown in Fig. 8.4.2a for the LOX/LH_2 propellants[717] and in Fig. 8.4.2b for the N_2O_4/A-50 propellants.[711] The combustors were the same size in both experiments; chamber diameter was 10.78 inches, contraction ratio was 1.9 and characteristic length was nominally 42 inches. Stability rating was accomplished with directional explosive charges for the storable propellants and ramping of the hydrogen injection temperature for the LOX/LH_2 combination (the lower the temperature the more stable the combustor, see Sect. 10.6.1). The comparison of the effects obtained in these experiments with theory[563] are only valid with the earth storable propellants because the predominant mode of instability changed from tangential to longitudinal as the combustor shape was varied for the LOX/LH_2 case. Increasing the chamber gas-droplet velocity differential increased the tendency for the longitudinal mode instability. For the N_2O_4/A-50 propellants, stability generally improved with increasing combustion gas velocity as predicted by the model. The combustor incorporating the 15 degree half angle divergence was dynamically stable to at least 41 grains of RDX explosive over the entire range of oxidant-fuel ratios investigated. (Note low mixture ratio instability for the 30° taper.)

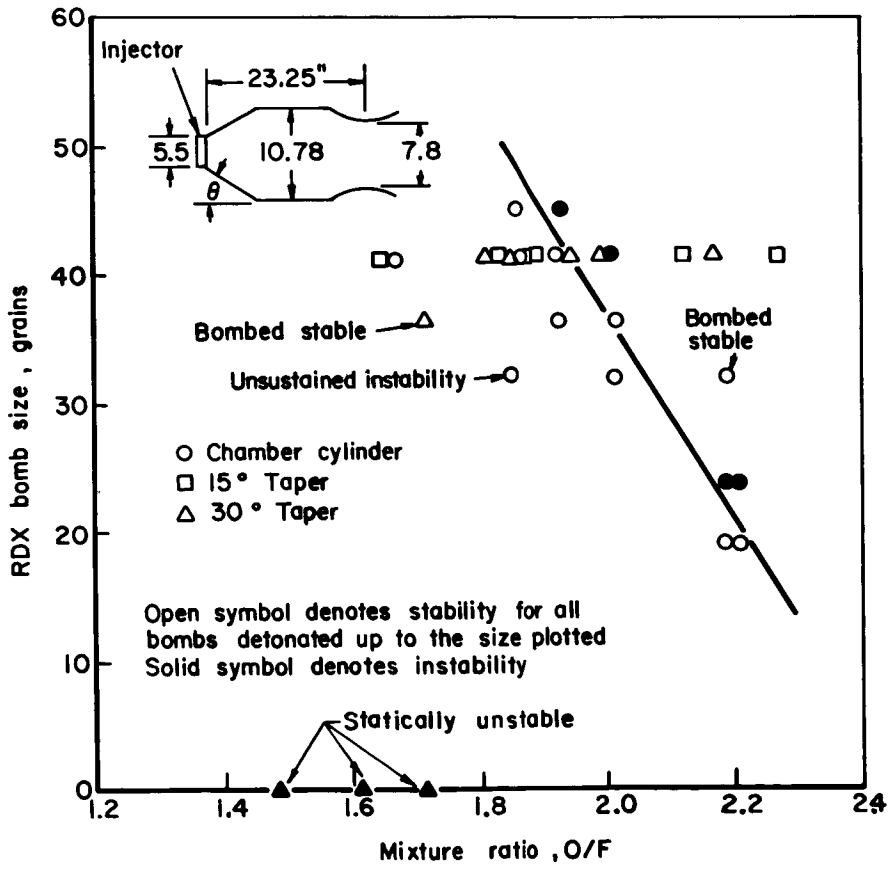

FIGURE 8.4.2b.—Effect of chamber shape on stability. Earth storable propellants; chamber pressure, 100 psia; thrust, 6.7 K.

The effect of step variations in cross-sectional area on stability in cylindrical thrust chambers is shown in Fig. 8.4.2c. The results were obtained in 20,000-pound thrust size engine using a 397 element concentric tube injector operating at a chamber pressure of 300 psig.[106,716] As shown, the effect on stability is associated with the early combustion zone. Once a length of 4 inches downstream of the injector is reached, the stability associated with the higher gas velocity (smaller diameter chamber) is attained (H_2 temperature at transition was 67° R which is equivalent to the full length 8.35-inch diameter cylindrical chamber). Moving the step change in chamber diameter to distances less than 4 inches from the injector face results in a continuous deterioration of the transition temperature finally reaching that associated with the 60 percent radial face coverage injector pattern (see Sect. 7.4.4).

In Fig. 8.4.2d is shown the effect of non-symmetrical variation in chamber cross-sectional area on stability of a LOX/LH_2 rocket combustor. The experiment was conducted with a 3-inch long spiral sleeve whose internal radius varied from 4.18 to 5.39 inches. The purpose of the sleeve was to interfere with spinning modes. In comparison to the stability limit of the 10.78-inch diameter combustor without sleeves, the temperature margin was improved by 24° R at an oxidant-fuel ratio of 5. However, the improvement was less than the improvement with the axisymmetric sleeve, Fig. 8.4.2c. The pressure oscillation frequency at the onset of instability varied generally between 3000 and 3500 Hz which corresponds to the frequency of a first tangential mode for a 10.78-inch diameter chamber.

In summary, the chamber shape and the resulting combustion gas velocity gradients in the region near the injector are important factors in determining the stability of a rocket motor.

8.4.3 Nozzle Convergent Section*

In studying the stability characteristics of a rocket combustor it is important to understand the effect of the nozzle shape upon the pressure oscillations inside the combustor. Pressure waves generated in the combustion chamber during combustion instability are known to enter the nozzle, where they are partially reflected from the nozzle walls and partially transmitted through the nozzle throat. From a practical point of view it is desirable to maximize the amount of wave energy that is transmitted through the nozzle throat; and in order to maximize this quantity,

* B. T. Zinn, Author.

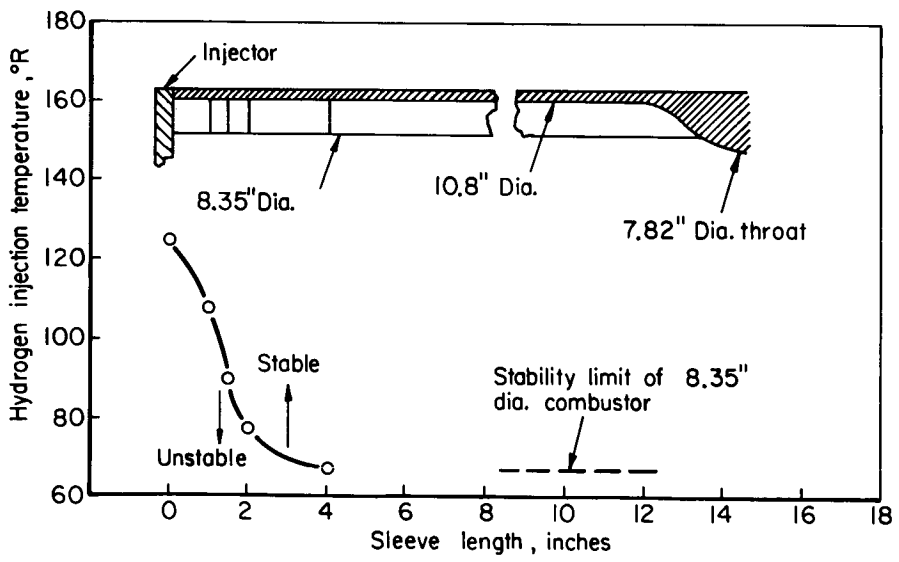

FIGURE 8.4.2c.—Effect of variation in chamber cross-sectional area on stability. Oxygen/hydrogen propellants; $p_c = 300$ psia; O/F = 5.0.

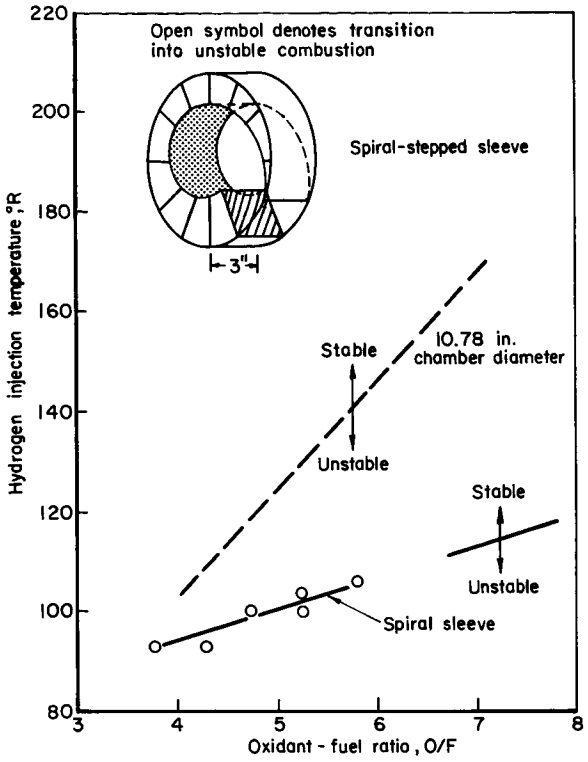

FIGURE 8.4.2d.—Effect of variable area thrust chamber geometry on stability of a 397-element injector. Spiral-stepped sleeve, 3 inches long.

it is important to understand how the shape of the nozzle convergent section affects the flow inside the nozzle during nonsteady operation.

Analytical studies of linear combustion instability usually yield a stability map (in an appropriate coordinate system) that is divided by a neutral stability line into a stable and an unstable region. Each point along this line represents a physical condition during which there is no net energy addition to the rocket combustor. This energy balance is determined by the various energy sources (e.g. the combustion process) and sinks (e.g. droplet drag) that are present in the system; when one of these processes is disturbed the others will have to adjust themselves if the energy balance is to be maintained. Such a change is reflected on the stability map as a change in the shape of the neutral curve, a change that will either increase or decrease the range of conditions for which the operation of the rocket motor may become unstable. Since the nozzle contributes to this energy balance it is important to determine how changes in nozzle shape affect the nozzle contribution; that is, what changes are stabilizing and which are destabilizing.

The following nomenclature pertains to Sect. 8.4.3:

n	Interaction index (see Sect. 4.2.1)
r_{ce}	Radius of curvature at nozzle entrance
r_{ct}	Radius of curvature at nozzle throat
r_t	Radius of throat cross-section
θ_n	Nozzle convergence angle
τ	Sensitive time lag (see Sect. 4.2.1)

An analytical study aimed at answering these questions for the case of three-dimensional combustion instability is presented in Ref. 772. To simplify the analysis and reduce the necessary amount of numerical computations it is assumed in this study that the combustion process is concentrated at the injector face and that the flow in the combustor and the nozzle is irrotational. Using this simple model, the combustion process, the mean flow, and the nozzle represent the only mechanisms capable of adding or deleting energy from the system. In one phase of this study the shape of the nozzle was changed systematically, and the resulting change in the combustion response that is necessary for maintaining neutral oscillations in the chamber was evaluated. Crocco's time-lag hypothesis was used to describe the combustion process, and the stability maps were described on an (n, τ) coordinate system. The nozzle under investigation is described in Fig. 8.4.3a. Its shape was changed by changing the radii of curvature of the circular arcs at the throat and nozzle entrance and by varying the angle of convergence of the conical section. The details of theory used to evaluate the nozzle admittance relation and the nozzle shape can be found in Ref. 196 or Sect. 3.6. The results indicated that increasing the convergence angle of the conical section and/or decreasing the radius of curvature of the wall at the throat region and/or decreasing the radius of curvature of the wall at the nozzle entrance have a stabilizing effect with regard to the first tangential mode. Typical results are presented in Fig. 8.4.3b. The three U-shaped curves which appear in this figure respectively enclose regions in which the 1T, 1T-1L and 1T-2L acoustic modes may become

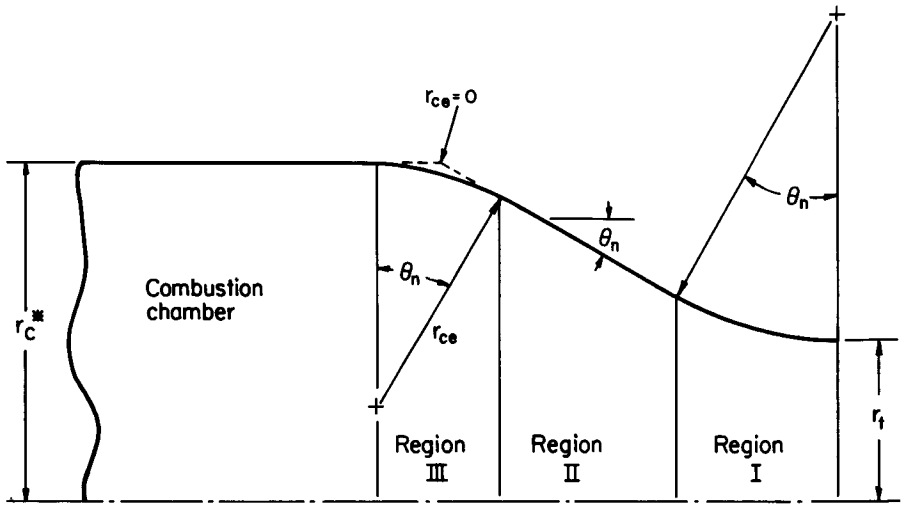

FIGURE 8.4.3a.—Nozzle entrance profile.

unstable. The results[772] indicate that changing the angle of convergence has the greatest effect upon the stability limits. This study also indicated that the addition of a circular section, which smoothes the transition between the combustion chamber and the conical section, has a negligible effect upon the calculated stability limits;* hence the presence of such a section in actual systems may be neglected in future analytical stability studies.

Based on the above results the conclusion is that "slowing" the convergence of a nozzle with a given contraction ratio has a destabilizing effect upon the stability of the first pure tangential mode.[172] The nozzle theory[196] used in this study to evaluate the nozzle admittance relation is only applicable to slowly-converging nozzles, a fact that should be borne in mind whenever the above conclusions are being utilized. In the case of longitudinal instability the indications are[179] that lengthening the convergent section of the nozzle has a stabilizing effect. Additional results showing the dependence of the admittance relation upon the nozzle shape are presented in the appendices of Ref. 196.

At present no experimental data exists that is capable of checking the above-mentioned results. Only the behavior of nozzles subjected to longitudinal pressure oscillation in a cold-flow setup has been studied experimentally.[127,195] While in Ref. 195 the applicability of Crocco's one-dimensional theory (see Appendix B, Ref. 179) was partially verified, the more important three-dimensional theory still awaits an experimental verification. In a different set of experiments[107] in which actual rockets were used, a conventional smoothly-converging nozzle was replaced by a sharp orifice nozzle. The results of the study indicated that changing the nozzles had essentially no effect upon the stability of the combustor in question. In another publication by the same authors[106] a wagon wheel nozzle was described. That short contraction section design also reinforced the argument that drastic changes in the nozzle shape had little effect on the stability of LOX/LH_2 chambers experiencing transverse resonant combustion.

In summary, available theories indicate that smoothing the convergence of the nozzle is destabilizing with respect to pure transverse modes and stabilizing with respect to longitudinal modes. Experimental results confirm the predictions in the longitudinal case. In the transverse case, however, the effects are not so evident as has been shown using various test nozzles.

8.4.4 Injector Shape*

The shape of the injector face influences the

* Earlier calculations produced similar results regarding stability.[11]

* A. J. Smith, Jr., Author.

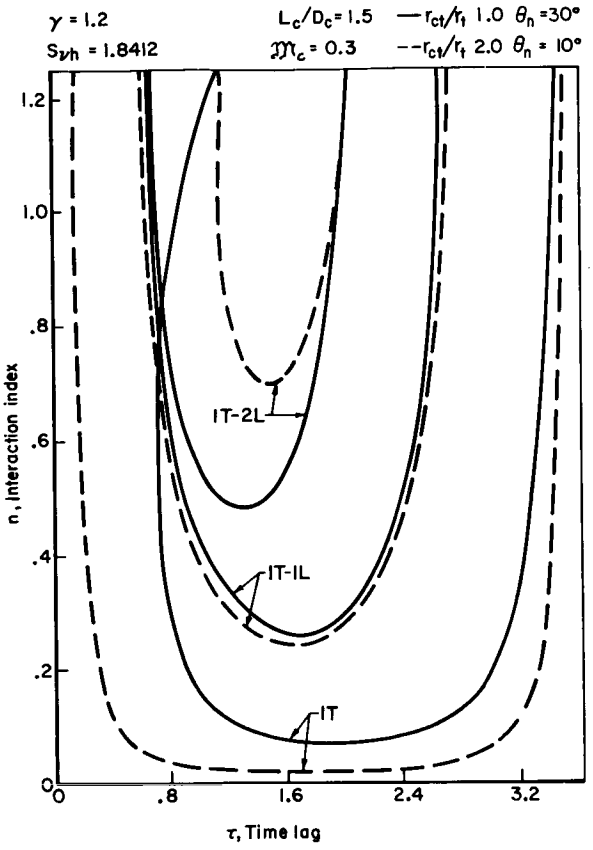

FIGURE 8.4.3b.—Stability map of the first tangential mode for various nozzle entrance configurations.

stability of a rocket motor in several ways:

1. By affecting the reflection of incident pressure waves subsequent wave amplitudes are altered.
2. The initial axial location of the injected spray is associated with the axial energy release profile.
3. The generation of any winds transverse to the injector face may be influenced by the face contour.

The two most common injector shapes are flat-faced and concave-faced, where the former is predominantly used. There are many variations to these two basic designs (such as, for example, concentric face depressions that are used in certain impinging designs). However, most injectors will generally be related quite closely to these two families of face shapes.

It is generally recognized that the concave injector shape is more stabilizing than a flat-faced injector in the event of longitudinal high-frequency instability. Whereas a flat-faced injector will permit the incident and reflected waves to simply add, a concave-faced injector will introduce a phase lag, when the waves at various radial locations are compared, thereby helping to attenuate the reflected wave. The degree of attenuation will depend on the amount of curvature associated with the concave face. This attenuation mechanism is similar to the attenuation exerted by the convergent section of a typical exhaust nozzle as discussed in the previous section.

Various investigators have measured the axial combustion distributions associated with a number of injector and propellant combinations, but the three-dimensional aspect of combustion has never been determined because of measurement difficulties. For this reason there is no conclusive experimental evidence that a flat-faced injector produces a flat, three-dimensional combustion profile or that a concave-faced injector produces a concave combustion profile. However, it is not unreasonable to assume that a given quantity of propellant requires a finite chamber distance to be converted into combustion products. If similar orifice elements are used over the entire face of the injector, then this same chamber distance may be assumed to hold approximately for all locations.

Unfortunately the experimental evidence available is such that no positive statement can be made as to the relative stability of the two injector shapes described. Tests have certainly been made with various propellants, baffle configurations and element designs with both injector shapes but never for the specific purpose of comparing the relative stability. Since from such tests no major differences were evident it would be safe to conclude that flat-faced and concaved injector designs were actually quite similar from a stability standpoint.

8.4.5 Annular Combustion Chamber*

The annular combustion chamber is receiving increased attention since it is the most logical combustion chamber geometry to be used with

* A. K. Varma, Author.

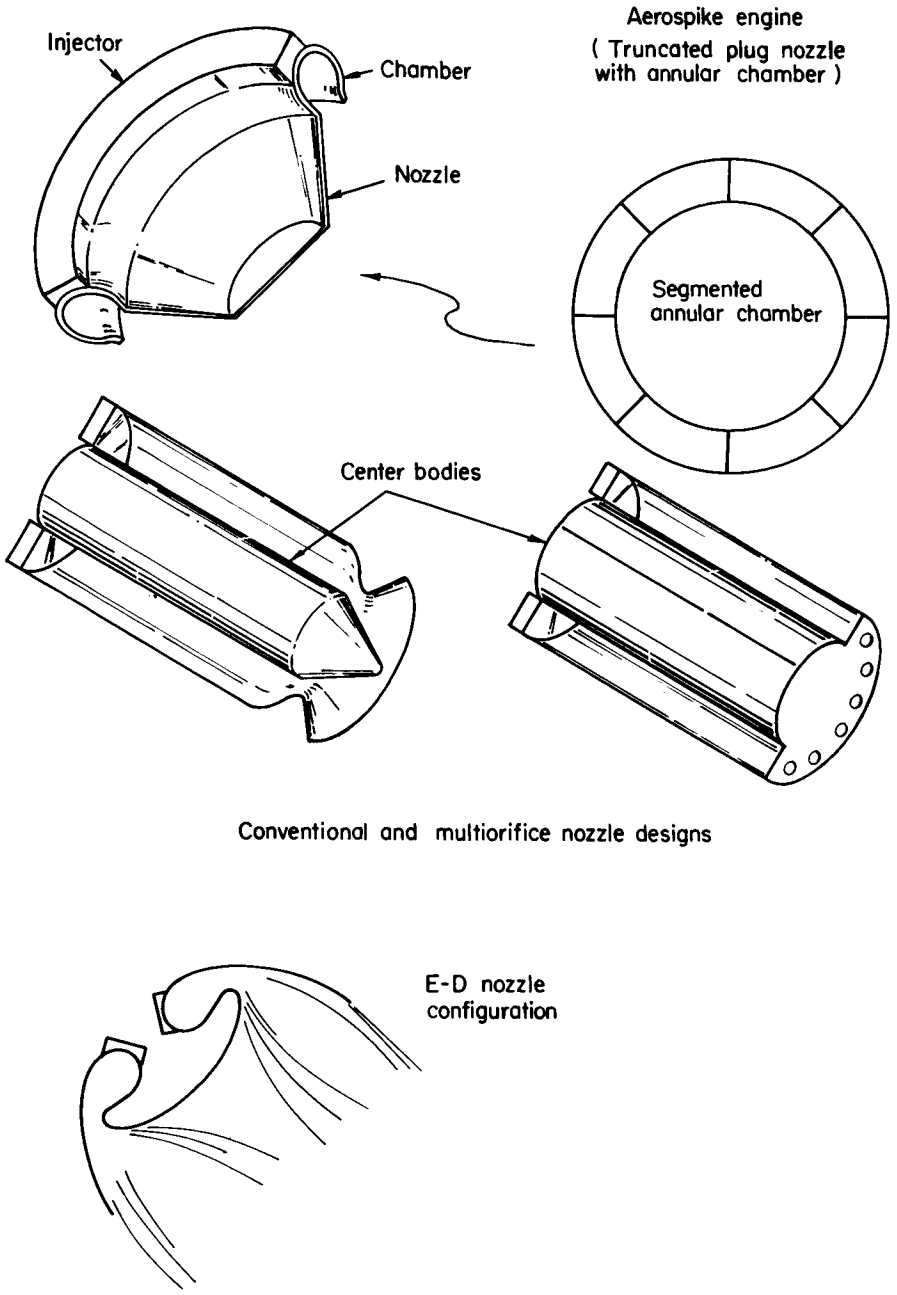

FIGURE 8.4.5a.—Representative annular chamber and nozzle combinations for rocket engines.

some of the advanced nozzle concepts. These nozzles include the plug or aerospike, and the expansion-deflection types.[1,3] Fig. 8.4.5a shows some possible thrust chamber designs. These newer nozzle concepts present definite advantages over the conventional conical or contour nozzles[368] for certain applications and are expected to be more widely used in the near future. The annular and the closely related toroidal geometry combustion chambers have been proposed as one method of applying high pressure thermodynamic cycles to rocket boosters.[528] One approach is the use of a combustion chamber formed by a series of wedge-shaped segments which, when tested

individually, provides the advantage of a less expensive test program. The suitably segmented annular combustion chamber is also less susceptible to combustion instability—an advantage which incidentally also applies to engine clusters using a common plug nozzle. In contrast, a non-segmented annular chamber is more susceptible to combustion instability than conventional designs. The improved combustion instability performance results from the reduced characteristic dimensions due to segmenting which raises the frequencies to higher, less sensitive, levels.

The frequency-motor size relationship for the first tangential mode of a cylindrical motor is $f_{1T(cyl)} = 0.586\bar{a}/D_c$ whereas for an annular geometry the frequency of the first tangential mode is given by $f_{1T(ann)} = 2\bar{a}/\pi(D_o + D_i)$. Here $\bar{a}$ is the speed of sound, D_c is the diameter of the cylindrical motor, D_o is the outer diameter of the annulus and D_i is the inner diameter of the annulus. If D_o is held constant, the frequency of the annular design is approximately 0.6 that of the cylindrical chamber. Thus in experimental research, to achieve the tangential mode frequency range characteristic of larger cylindrical chambers, an annular motor can be used that is considerably smaller and hence can operate at a lower thrust level.

Looking at a numerical example of cylindrical and annular motors retaining the same injection density and a nominal sound speed (3600 ft/sec), a cylindrical combustion chamber of 12-inch diameter exhibits first tangential mode instability at 2100 Hz. A thin annular motor with the same cross-sectional area will typically have a 16-inch outer diameter and a $10\frac{1}{2}$ inch inner diameter. The full annulus has a first tangential mode frequency of only 1030 Hz, i.e., half the frequency of the cylindrical motor. Therefore, based upon frequency considerations, the full annular motor would be expected to be more susceptible to combustion instability. This trend has been shown experimentally,[192] where tests have indicated that injector elements, which were dynamically stable in a conventional cylindrical chamber, tend to produce self-triggered instability in the annular motor. Also elements that were nonlinearly unstable in the cylindrical motor were self-triggered into instability in the nonsegmented annular motor. Returning to the numerical example, if the annulus were divided into only three equal segments the sensitive frequency of each segment is raised to 3090 Hz, thus improving the segmented motor significantly from a sensitive time lag standpoint (see Sect. 6.3). Also in a segmented motor the velocity/displacement effects[583] are reduced thus leading to greater stability.

An interesting annular motor concept has been suggested by Nicholls et al.[512] Known as a rotating detonation wave rocket motor, it is an attempt to use the characteristics of combustion instability to produce a more efficient motor with lower engine weight per unit thrust. The proposed motor consists of an annular combustion chamber wherein a controlled tangential mode instability is encouraged to exist. A feasibility study of this concept raises the following important questions: (1) Whether the performance potential would be competitive with conventional motors? (2) Whether the heat transfer to the walls will become excessive? (3) What are the characteristics of detonations at low temperature and high pressures and in a two-phase system as would exist in the chamber if cryogenic or storable liquid propellants are used? Unfortunately, the desired spinning tangential waves were not achieved in the test motor. With the limited data available it appears that the average heat transfer is not intolerably large and is of the order of the heat transfer at the throat of a conventional motor. The other questions regarding feasibility remain unanswered at this time.

Application of the annular concept in current propulsion systems has not been without instability occurrences. Combinations of baffles and acoustic cavities have been used to achieve stability but careful design has been necessary.[510]

Besides the practical application of the annular combustion chamber geometry, the annular motor continues to be a valuable tool for combustion research. Considerable simplifications in the governing gas dynamic equations are possible for a thin annular geometry. The simplifications in the analytical procedure allows one to obtain a much clearer understanding of the conditions that influence the growth or decay of pressure waves in combustion zones. In a narrow annulus it is possible to use a one-dimensional treatment of

tangential wave propagation. By providing a continuous circumferential path for the wave propagation, an annular geometry avoids one criticism of the normal two-dimensional chamber, namely, that the reflection of the wave at each sidewall could change the character of the wave and its effect in sustaining instability.

Because of these attributes the annular motor has been used in combustion instability research by almost every active group in this field. Priem and Guentert[563] developed a nonlinear theory for a one-dimensional model considering an annular section of very small thickness and length. A vaporization-controlled burning rate model was used. A portion of the experimental research was carried out in a large toroidal combustor. Bonnell[109] has studied the problem of combustion stability in an annular gas combustor burning premixed gases. His results are useful for estimating the stability trends due to changes in the parameters that characterize the gas phase of the combustion process. Annular combustors have also been used by researchers at JPL, Rocketdyne, Purdue University and Princeton University.

Typically, during unstable operation in an annular combustion chamber, the wave shape of the oscillations is different from those commonly observed in full cylindrical motors. If a sinusoidal disturbance is present in an annulus it is found that the inner boundary tends to make the waveform steeper while the outer wall tends to make the wave shape smoother. In the case of an annular rocket chamber the two competing effects would usually result in a shock-type wave. A typical waveform observed during unstable combustion in the annular motor is shown in Fig. 8.4.5b. In the case of a cylindrical motor, due to the absence of the inner wall, shock type solutions are less likely. However, experimenters have reported observing shock type waves in cylindrical motors[152] (see Sect. 3.5.2.2).

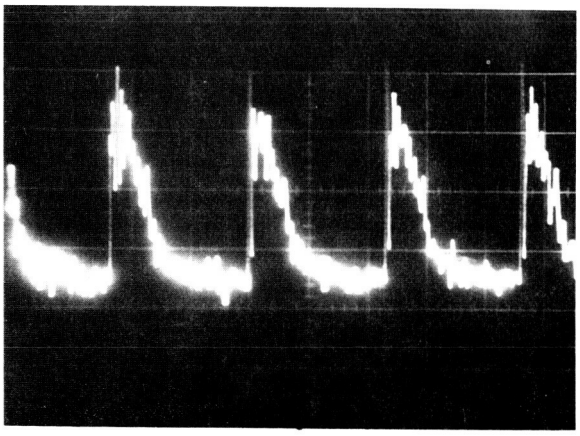

FIGURE 8.4.5b.—Typical wave form in annular combustors ($p_c = 126$ psia; $p' = 175$ psia, peak to peak; $f_{1T} = 1650$ Hz for a 9-inch-diameter chamber).

In summary, the annular motor concept is expected to be of increasing importance in the future with regard to both practical application and research. Even retaining the same injection densities, suitably segmented annular motors can compete with cylindrical chambers in areas of performance and stability.

8.5 OTHER DAMPING EFFECTS

8.5.1 Chamber Wall Materials*

The choice of chamber wall materials in the construction of a chemical rocket combustion chamber normally depends upon factors such as strength, heat transfer, cost and ease of manufacture. However, the effect of the material choice on the combustion stability characteristics of the chamber must also be considered. Several investigations have been made to determine the differences in stability for metal chambers versus ablative designs in liquid rockets.

Briefly reviewing the results of chamber material testing, one finds that two tentative conclusions can be drawn. First, with marginally unstable units, the choice of ablative rather than metal walls can significantly reduce the instances of resonant combustion. Second, in a high-amplitude or spontaneously unstable unit, the effect of the material choice does not appear to be sufficient to bring about stability. The reasons for this behavior have not been completely clarified but the following discussion of the data should prove helpful in outlining possible mechanisms.

First it should be stated that two distinctly different methods for evaluating the stabilizing characteristics of ablative versus metal chamber walls have been used. One involves testing the

* D. T. Harrje, Author, with contributions from R. R. Goelz, R. J. Hefner, and J. M. Senneff.

actual hardware; observing instances of instability, margin of stability, and measuring relative amplitudes. The other approach relies upon acoustic behavior, such as decay rate measurements, for comparison. The latter tests are conducted in a laboratory environment with sound generators and detectors as discussed in some detail in Sect. 9.6.6.

The firing data from a series of chamber material tests conducted at one company are summarized in Table 8.5.1. The ablative material was charred from approximately 460 seconds of firings.* The A's and B's in the table refer to injectors of similar design (i.e., A-1 is similar to A-2). Bombs were used to induce instability in these chambers. From the data it would appear that the choice of chamber wall material plays an important stabilizing role, since a 73% incidence of instability was observed when bombing in metal wall chambers, while only a 2.2% incidence was found when the same tests were performed in ablative chambers.

The first series of acoustic modeling tests of wall materials were performed by another organization in connection with an earlier engine development program. The tests were instigated because of a higher incidence of bomb induced resonant combustion with metal versus ablative chambers (less than 10% instability incidence reduced to zero with ablative). Tests were conducted in a chamber-injector assembly with the nozzle plugged. The acoustic driver was located near the chamber wall and a microphone was positioned at various locations. The frequency bandwidth and filter settings monitoring the microphone signal were used to check frequencies from approximately 0.2 to 45 kHz. Measurements followed the instantaneous cutoff of the random noise signal imposed by the driver. The results are plotted in Fig. 8.5.1a where it can be seen that the ablative damping rates were higher, for all frequencies and locations, by a factor which varied from 1.3 to 5.6 with a 2.6 mean. These tests were performed in air-filled chambers (frequency was therefore approximately 0.3 that of the hot environment). To better model the sound speed and molecular weight found in rocket chambers, helium and CO_2 tests were planned but never conducted.

In a third investigation[291] three candidate chamber wall materials were evaluated; virgin ablative, charred ablative and coated steel (0.030 inch protective coating of 0.012 inch nichrome plus 0.018 zirconium oxide). The ablative was made of high purity silica cloth reinforcement and phenolic resin (33% by weight). The reinforcement fibers were directed downstream at 60° to the engine centerline. The charred ablative chamber sample was obtained by exposing the previously tested ablative chamber to a 17-second firing. This resulted in an average char depth of 0.22 inch (surface roughness was 0.06 inch peak to valley).

The hot firings were conducted with LOX/LH_2 propellants where the liquid hydrogen temperature ramping technique (described in Sect. 10.6.1) was utilized to check the characteristic stability limits of each candidate material. Each chamber

* Average char depth was 0.90 inch with a surface roughness of 0.06 inch peak to valley.

TABLE 8.5.1.—BOMB TESTS OF METAL- AND ABLATIVE-WALL CHAMBERS

Chamber material	Injector design					Total instances of instability per total number of tests	Incidence of instability, percent
	A-1	A-2	B-1	B-2	C		
	Instances of instability per number of tests						
Metal	—	6/9	5/5	16/20	3/7	30/41	73
Ablative	0/12	—	0/4	1/60	1/14	2/90	2.2

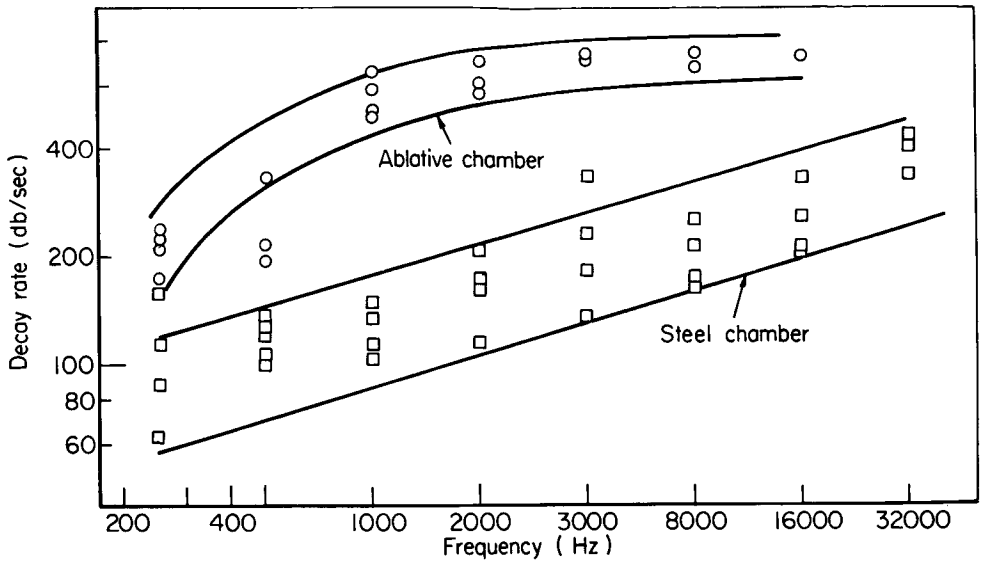

FIGURE 8.5.1a.—Decay rates for ablative and steel combustion chambers.

was stability rated over a range of mixture ratio. Hydrogen temperature was continuously decreased during each rocket test until resonant combustion was obtained. The results shown in Fig. 8.5.1b indicate that the choice of material causes no significant change in the engine stability thresholds (i.e. same hydrogen temperatures).

Measurements of the chamber pressure oscillation amplitudes also failed to indicate any significant changes with material (although an amplitude difference of 60 psi peak-to-peak was observed between two different injectors). The instability amplitude was reduced by only 5% with the ablatives (amplitudes were of the order of 200 psi pk-pk).

One factor that has not been discussed up to this point is the way in which a porous material, such as the charred ablative, might function as an energy absorber. Specifically there has been no differentiation between the behavior with regard to the initial disturbance and the subsequent functioning of the wall material in damping a specific frequency of resonant combustion or of impressed acoustic noise. The ablative might be expected to exhibit a certain degree of broad frequency damping, possibly improving at higher frequencies (because of the pore size). The ablative wall would be expected to behave as a damping device operating in the quasi-steady

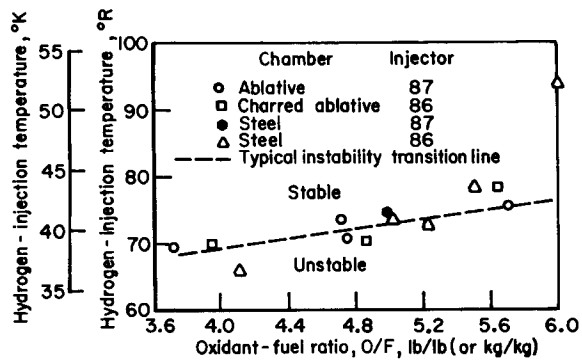

FIGURE 8.5.1b.—Variation in instability transition temperature with chamber material.

regime* with regard to the first waves produced by a bomb.

An example of initial wave damping is found in the testing of Helmholtz resonators with an incident shock wave.[766] Regardless of whether or not the resonator is designed for the impressed frequency, the initial shock wave is significantly attenuated at the pressure antinode location (30% pressure loss was shown). In contrast, the same untuned resonator provided a very low damping rate for the single frequency pressure

* With high unsteady pressure amplitudes tuning of a resonator becomes less important and damping can be achieved with off-resonant designs (see Sect. 7.2.2).

oscillation that remained (comparisons were made with a control experiment in which the resonator is removed from the chamber and with resonators that were properly tuned). Similar tests have recently been initiated to observe the effect of ablative chamber sections substituted for the resonator.

In the tentative conclusions as to the applicability of ablatives to damp instability, the point of spontaneous versus triggered resonant combustion was stressed. As discussed in Sect. 1.2.3, the spontaneous initiation of resonant combustion requires no threshold value of disturbance. Rather it is a case of a balance between energy sources and available damping. This is offered as an explanation as to why the ablative chambers used in the LOX/LH_2 materials test program described in this section only were capable of lowering the unsteady pressure amplitude 5% (although differences in the measurement distances from the face may also partially account for the low percentage loss, see Fig. 3, Ref. 291). The dissipation of a high amplitude, short duration pulse no longer is a factor in this case.

In bombing tests, such as those reported and those which justified the acoustic program, little doubt can exist that ablative wall material can make a significant difference in stability for the triggered type of resonant combustion. However, because of the present lack of any theoretical or experimental guidance as to the required characteristics of the ablative material (char thickness, degree of porosity, etc.) necessary to cure such a marginally stable engine, and because a low incidence of bomb induced instability can still be present even when ablatives are used, complete dependence on the ablative chamber approach to dynamic stability cannot be recommended at this time.

8.5.2 Acoustic Damping by Condensed Phases*

Condensed phases in a liquid or solid state that consist either of a fuel or oxidizer component, or that consist of a product of reaction between these species, are always present in liquid-propellant rocket motors. These materials are spatially distributed throughout the combustion chamber and contribute to volumetric damping along with two other mechanisms, viz, viscosity and heat transfer in the gas phase, and vibrational relaxation of polyatomic molecular products of combustion. The latter losses are small except at the highest frequencies, and are totally beyond the control of the designer. Damping by condensed phases, or particulate damping, is the only volumetric loss mechanism whose magnitude is significant. Interest in this damping mechanism is increased by the possibility that control of its magnitude may enable the designer to use more effectively a loss mechanism that is present to some extent.

From the historical viewpoint, the first interest in particulate damping arose in connection with instability in solid propellant rockets. The incidence of either acoustic instability or the associated catastrophic burning rate was reduced by the metallic aluminum added to the solid fuel for the purpose of increasing thrust. Early suggestions that the improved burning resulted from particulate damping by the Al_2O_3 formed by the burning of the metallic aluminum were discounted. A subsequent series of investigations provide strong evidence that particulate damping probably is a dominant factor in controlling instability in solid fuel rockets. Recent studies suggest particulate damping may be a factor in combustion instability of liquid propellants.

The following nomenclature pertains to Sect. 8.5.2:

c_s	Specific heat of particle material
C_m	Mass of particles per unit mass of gas
E	Acoustic energy
$f(r_s)$	Particle size distribution function
k	Complex wave propagation constant
P	Probability
R_{pq}	Generalized mean radius, defined in Eq. (8.5.2–9)
α	Spatial coefficient of acoustic attenuation
τ_d	Dynamic relaxation time
τ_t	Thermal relaxation time

Subscripts:

opt	Optimum value
s	Solid particles
0	Smallest-size particle
∞	Largest-size particle

8.5.2.1 Theory of particulate acoustic damping.— The theoretical basis for particulate damping is

* R. A. Dobbins, Author.

obtained from the equations of motion for a gas-particle mixture (see, for example, Ref. 463, pp. 175–215) for an unsteady, one-dimensional flow. The equations are linearized in the usual fashion to obtain a set of acoustic equations applicable for the gas-particle mixture. The interaction terms in the momentum and energy equations are given by Stokes' drag law and the corresponding expression for heat transfer rate. The details of this calculation are given elsewhere,[684] and here it is noted that the linearized momentum and energy equations for the particulate phase* reduce to

$$\frac{\partial u_s}{\partial t} = -\frac{u_s - u}{\tau_d} \qquad (8.5.2\text{–}1)$$

$$\frac{\partial T_s}{\partial t} = -\frac{T_s - T}{\tau_t} \qquad (8.5.2\text{–}2)$$

where u and T refer to the gas-phase velocity and temperature, u_s and T_s refer to the corresponding particulate properties, and t is time. The quantities τ_d and τ_t are the dynamic and thermal relaxation times, defined as

$$\tau_d = \frac{2}{9}\frac{r_s^2}{\mu}\rho_s \qquad (8.5.2\text{–}3)$$

and

$$\tau_t = \frac{3}{2}\frac{c_s}{c_p}\,\mathrm{Pr}\,\tau_d \qquad (8.5.2\text{–}4)$$

where c_s is the specific heat of the particles, c_p is the specific heat at constant pressure of the gas, Pr is the Prandtl number of the gas, r_s is the particle radius, μ is the dynamic viscosity of the gas, and ρ_s is the density of the particulate material.

Equations (8.5.2–1) and (–2) represent relaxation equations of the classical type proposed originally[354] to represent the transfer of translational energy into an internal degree of freedom. For this reason, we anticipate that the results of the study of acoustic propagation in gases with an internal degree of freedom will carry over directly to the case of acoustic propagation in a gas with particles in suspension. In particular, it is found that the maximum attenuation per unit wavelength for each of the above loss mechanisms occurs when $\omega\tau_d = 1$ and $\omega\tau_t = 1$ where ω is the circular frequency. (Particulate relaxation effects give rise to dispersion, i.e., a dependence of the velocity of propagation on frequency, just as in the case of vibrational relaxation. A discussion of particulate dispersion, which is significant at high particle mass fractions, is not within the scope of this article, but is available elsewhere.[228])

Equations (8.5.2–1) and (–2), together with the remaining linearized conservation equations for both gaseous and particulate species and the gas phase equation of state, represent a system of six partial differential and one algebraic equation in seven unknowns. By assuming a monochromatic disturbance in the form $\exp i(kx - \omega t)$, the equations are reduced to a system of linear algebraic equations specifying the complex wave propagation constant, k.[684] When the mass of particles per unit mass of gas, C_m, is small compared with unity, the particulate damping is expressed as

$$\bar{\alpha} = \frac{\alpha a}{\omega C_m} = \frac{\omega\tau_d}{1+\omega^2\tau_d^2} + (\gamma - 1)\frac{c_s}{c_p}\frac{\omega\tau_t}{1+\omega^2\tau_t^2}, \qquad (8.5.2\text{–}5)$$

where a = speed of sound in the gas surrounding the particles, γ = ratio of the specific heat at constant pressure to the specific heat at constant volume of the gas, and α = the spatial coefficient of attenuation of acoustic energy or twice the spatial coefficient for attenuation of acoustic pressure ($E/E_0 = e^{-a\alpha x} = e^{-a\alpha t}$ or $p/p_0 = e^{-\alpha x/2} = e^{-a\alpha t/2}$).

The classical theory for the attenuation of sound by a single droplet suspended in a gas due to Epstein and Carhart[251] can be expressed, by taking the appropriate limits, in the same form as Eq. (–5). Attenuation due to a finite particle mass fraction and particulate dispersion of sound are not given by the Epstein-Carhart theory.

From Eq. (–5) it is apparent that if the two relaxation times are nearly equal, the attenuation per unit wavelength is a maximum when $\omega\tau_d = 1$. A specified frequency of excitation is therefore most efficiently attenuated by particles of a size such that

$$r_{s_{opt}} = \left(\frac{9\mu}{2\rho_s\omega}\right)^{1/2} \qquad (8.5.2\text{–}6)$$

* This assumes inert particles, i.e., no particle gasification.

The noteworthy aspect of this result is the dependence of the optimum particle size solely on the square root of the dynamic viscosity of the gas and its independence of all other gas properties.

In many instances, the small mass fraction requirement is not fulfilled, and then it is not possible to express the attenuation in a simple algebraic form. Exact results for attenuation are then found by solving Eqs. 33 and 34 of Ref. 684 simultaneously. Two cases have been investigated that give an indication of trends. For particles of aluminum oxide in propellant gases ($c_s/c_p \approx 0.74$, $\gamma \approx 1.20$, and $Pr \approx 0.90$), τ_d and τ_t are numerically equal, and the second term in Eq. (–5) contributes only about 13 per cent of the total attenuation. The influence of finite mass fraction is depicted in Figure 8.5.2a, where it is seen that a change in C_m from 0.01 to 0.4 has a small effect on $\bar{\alpha}$. On the other hand, when the specific heat of the particle is higher, the two terms on the right hand side of Eq. (–5) become more nearly equal and the relaxation times more disparate. The magnitude of the maximum in $\bar{\alpha}$ is then reduced when C_m increases and its position in dimensionless frequency shifts (see Fig. 5, Ref. 684).

The value of $\omega\tau_d$ of interest in combustion instability in the case that the Al_2O_3 particles are formed by combustion reactions will range from very small up to a magnitude of order unity. For example, for particles of 1 micron diameter,* for a value of dynamic viscosity representative of propellant gases of 9.0×10^{-4} poise, and a frequency of 50 kHz, we find $\omega\tau_d = 0.8$. Particles of one micron diameter are most efficient in attenuating frequencies on the order of 65 kHz, and the value of $\bar{\alpha}$ will then be about 0.55. The high-frequency disturbances in rocket motors usually correspond to high order harmonics where the acoustic path length spans many wavelengths. The attenuation by optimum size particles of the high order harmonics over the distance corresponding to a half cycle of the fundamental mode would be substantial. Lower frequencies are attenuated far less effectively by the same

* This is a typical value where size estimates range from ½ micron to several microns.

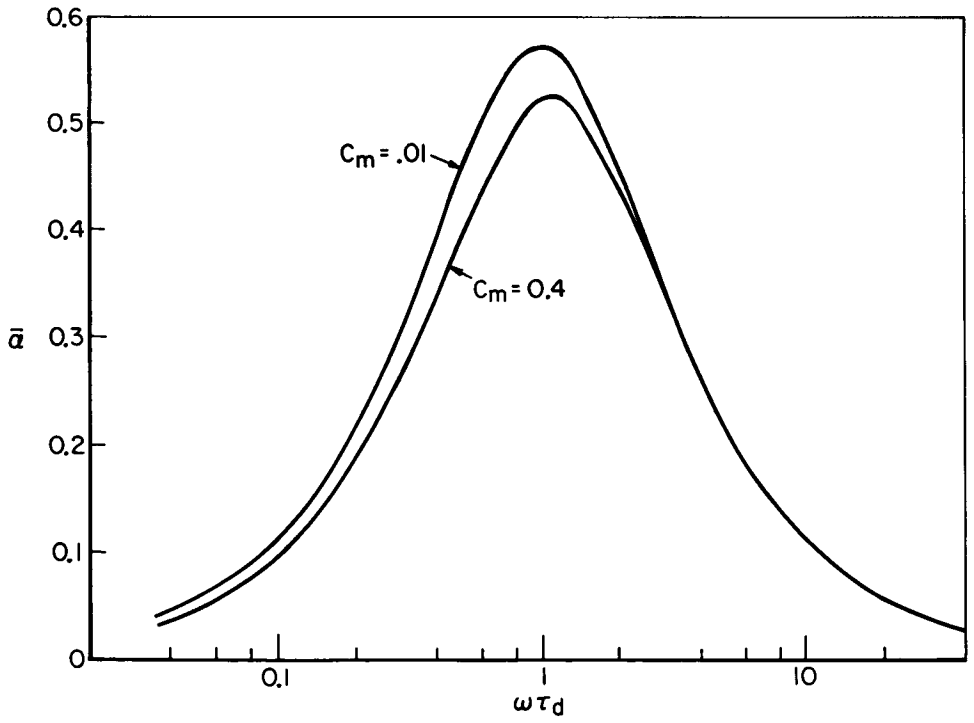

FIGURE 8.5.2a.—Specific attenuation ($\alpha_a/\omega C_m$) versus dimensionless frequency for small and finite mass fraction. Property values correspond to aluminum oxide particles in propellant gases: $c_s/c_p = 0.74$; $Pr = 0.90$; $\gamma = 1.20$. (From Ref. 228.)

particles because the attenuation per wavelength is smaller and also because the acoustic path length is a smaller number of wavelength intervals. A more detailed discussion of the role of damping by particles of aluminum oxide is given elsewhere.[228]

When the particulate phase is present in the form of fuel or oxidizer particles, then the average size of the particle will be substantially larger than the typical size of the particles formed by combustion reactions. The frequency for which attenuation per unit wavelength is greatest is then shifted to lower ranges, e.g., for a non-evaporating particle of 50 μ diameter whose specific gravity is unity, the value of $\bar{\alpha}$ is greatest for a frequency of 100 Hz. However, fuel and oxidizer particles are evaporating, and therefore the theoretical model is incomplete and the numerical results must be considered tentative. Other methods, discussed below, are available to treat the evaporating particle.

The theory for the attenuation and dispersion of sound by inert particles has been subjected to two experimental tests. Zink and Delsasso[768] measured the attenuation and dispersion by aluminum oxide particles in various gases and their results show good agreement with the Epstein-Carhart theory, but their experiments did not test the existence of a maximum in the curve of $\bar{\alpha}$ versus $\omega\tau_d$. Temkin and Dobbins[685] have more recently reported the results of their measurements over a wider range of $\omega\tau_d$ which show satisfactory agreement with the theory predicting a maximum attenuation per unit wavelength when $\omega\tau_d = 1$, see Fig. 8.5.2b.

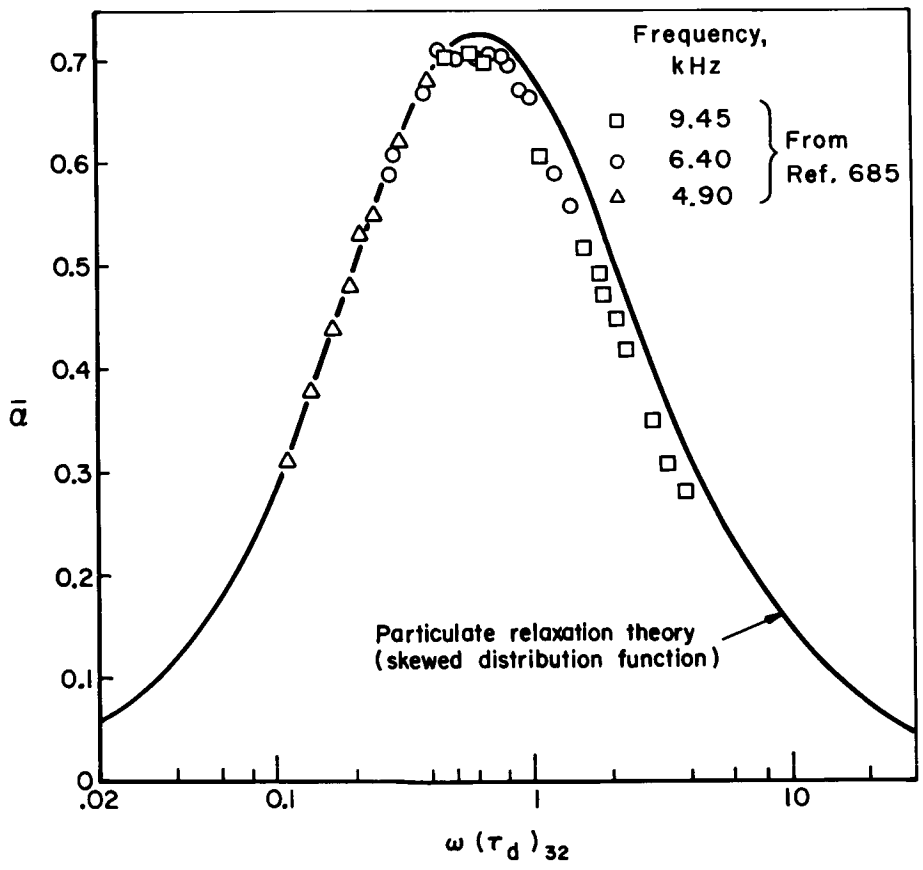

FIGURE 8.5.2b.—Comparison of measured acoustic attenuation and theory based on Eq. (8.5.2–5). Oleic acid particles in nitrogen; $\gamma = 1.4$; $Pr = 0.71$; $c_s/cp = 0.55$.

8.5.2.2 Role of particle size distribution.—The role of the particle size distribution in damping by condensed phases is obtained from the results given above by summing over all sizes in proportion to the number of particles of each size present.[684] We define the size distribution function such that its integral from size r_1 to r_2 is the probability of occurrence of sizes within this interval,

$$\int_{r_1}^{r_2} f(r_s)\,dr_s = P[r_1 < r_s < r_2] \qquad (8.5.2\text{–}7)$$

The attenuation is then expressed as

$$\frac{\alpha a}{\omega C_m} = \frac{1}{R_{30}} \int_{r_0}^{r_\infty} f(r_s) r_s^3 \times \left[\frac{\omega\tau_d}{1+\omega^2\tau_d^2} + (\gamma-1)\frac{c_s}{c_p}\frac{\omega\tau_t}{1+\omega^2\tau_t^2}\right] dr_s \qquad (8.5.2\text{–}8)$$

where R_{30} is a special case of the generalized mean radius defined by

$$R_{pq} = \left[\frac{\int_{r_0}^{r_\infty} f(r_s) r_s^p dr_s}{\int_{r_0}^{r_\infty} f(r_s) r_s^q dr_s}\right]^{1/(p-q)} \qquad (8.5.2\text{–}9)$$

In general, it is necessary to know the particle size distribution function, $f(r_s)$, in order to calculate the attenuation of sound by a polydispersion of particles. In two special instances the results can be expressed in a simpler form.

1. If, for the largest size present,

$$\omega\tfrac{2}{9}(r_\infty^2/\mu)\rho_s \ll 1,$$

then the attenuation can be expressed as

$$\frac{\alpha a}{\omega C_m} = \omega(\tau_d)_{53} + (\gamma-1)\frac{c_s}{c_p}\omega(\tau_t)_{53} \qquad (8.5.2\text{–}10)$$

where $(\tau_d)_{53}$ and $(\tau_t)_{53}$ are the relaxation times based on R_{53}^2, e.g.,

$$(\tau_d)_{53} = \frac{2}{9}\frac{R_{53}^2\rho_s}{\mu} \qquad (8.5.2\text{–}11)$$

Thus, the R_{53} mean radius is to be used in the theory for the attenuation of sound by monodispersed particles to correctly account for the effects due to polydispersions in the low frequency limit when the above inequality is satisfied. This limit will often be of applicable for the small size particles formed by combustion reactions when the frequencies correspond to fundamental longitudinal or transverse modes.

2. When, for the smallest particle present, $\omega\frac{2}{9}(r_0^2/\mu)\rho_s \gg 1$, then the attenuation can be expressed as

$$\frac{\alpha a}{\omega C_m} = \frac{1}{\omega(\tau_d)_{31}} + (\gamma-1)\frac{c_s}{c_p}\frac{1}{\omega(\tau_t)_{31}} \qquad (8.5.2\text{–}12)$$

where $(\tau_d)_{31}$ and $(\tau_t)_{31}$ are the relaxation times based on R_{31}^2, e.g.,

$$(\tau_d)_{31} = \frac{2}{9}\frac{R_{31}^2\rho_s}{\mu} \qquad (8.5.2\text{–}13)$$

Thus, the R_{31} mean radius is to be used in the high frequency limit in the theory for attenuation by monodispersed particles to account for size distribution. The high frequency limit will often be applicable for fuel or oxidizer particles when the frequencies correspond to high order transverse modes. The significance of these mean diameters was first noted by Kesselring and Oberg.[403]

Finally, it is noted that for arbitrary values of $\omega\tau_d$, the specific acoustic attenuation can be expressed as a function of *any* arbitrarily defined mean size when the form of the distribution function is prescribed. An example of this procedure is given in Ref. 685 where the R_{32} was chosen as the relevant mean size because it could be conveniently measured.

8.5.2.3 Particulate damping in rocket stability analyses.—The role of particulate damping of acoustic waves has been investigated in analytical models of combustion instability. Kesselring and Oberg[403] have used a vaporization-rate-limited version of the Priem theoretical model of combustion instability (see Sects. 4.3.1.3, 6.4.1.1, and 6.4.1.2) modified to include the influence of inert particle drag. They were able to calculate

the influence of particle size in this nonlinear analysis and to calculate the stabilizing influence of various concentrations of particles of selected sizes. They report that the optimum size from this nonlinear analysis agrees with the linear acoustic theory, viz, Eq. (8.5.2–6). Thus, the simpler linear theory can be used to guide the detailed complex calculations intended to describe combustion instability.

Hoffman, Wright, and Breen[359] have modified the Priem-type analysis for an annular combustion chamber to include the influence of drag by fuel and oxidizer droplets. Their results indicate the stability is sensitive to the value of the droplet drag parameter when the dimensionless burning rate parameter is small. The heat addition was found to be more stabilizing than droplet drag at higher values of the burning rate parameter. They point out the difficulty in obtaining general results because of the many parameters which cannot always be independently varied. It appears that an investigation of the role of evaporation on particulate acoustic attenuation in both linear and nonlinear regimes is a potentially important application of their analysis.

8.5.2.4 Experimental studies of particulate damping in liquid rocket motors.—An experimental study of damping by chemically reactive and inert particles in a rocket motor of 10^4 lbs. thrust was conducted by Kesselring and Oberg.[403] The oxidizer was N_2O_4 and the fuel was gelled hydrazine mixed with various concentrations of aluminum or aluminum oxide particles. Some general results of their study are as follows:

1. The observed increase in damping when particulate materials were added to the fuels was in general agreement with particulate damping theory. The particle concentration required to produce stability was strongly dependent on particle size distribution.
2. It was found that an aluminum content of about 11 per cent of total propellants was required to produce stability. The need for this relatively large fraction of particulate material was attributed to strong driving mechanisms present in liquid rockets.
3. Both aluminum and aluminum oxide were effective in stabilizing the rocket motor, but more particulate damping was required with metallic aluminum. (This difference appears to be due to the destabilizing influence of heat released by burning metallic particles.)
4. Control of particle size of Al_2O_3 formed by burning metallic aluminum, in order to control particulate damping, was not achieved. They report that the Al_2O_3 particle size was independent of all controllable variables. (This observation is in agreement with the latest results of studies of the size of Al_2O_3 produced in metallized solid propellant.)

The reader is encouraged to refer to the report of Kesselring and Oberg for further details on this valuable experimental study.

In summary, it appears that the attenuation of sound by condensed phases plays at least a minor role in the acoustic stability of liquid propellant rocket motors. It is doubtful if damping by fuel and oxidizer particles, even presuming the unrealistic possibility that droplet size and/or spatial distribution could be arbitrarily controlled, can be effective against the strong driving mechanism present in liquid propellant motors. Progress in the direction of using damping by condensed phases more effectively may result from the studies of the improved analytical models of combustion instability now being developed.

8.5.3 Corner Effects*

The details of the region near the corner or edge of an injector, i.e., the region which adjoins the chamber wall or baffle surface, is highly important. From a stability standpoint the corner location is unique in that it represents a pressure antinode for all tangential, radial and longitudinal modes. Thus this location is ideal for locating energy absorption devices. The injection in this region substantially defines the injector-chamber compatibility, as well as affecting the injector's performance and stability. Generally, every practical injector design employs a modified injection configuration along the periphery from that in the center. In one extreme, the outer injector orifices are used exclusively for injection

* T. A. Coultas and C. L. Oberg, Authors.

of film or boundary layer coolant. In other cases, the departure from the normal injector pattern along the periphery is modest. Injectors are generally designed to assure that only the more compatible reactive propellant (usually the fuel) is allowed to contact the wall. The methods used to assure high performance and chamber compatibility are beyond the scope of this section but they are discussed in some detail in Refs. 356, and 224, and Sects. 1.1.3 and 2.5.

8.5.3.1 Stability considerations.—Aside from the affecting chamber compatibility and performance, the combustion environment in the corner region can profoundly alter stability. One well-known effect is that due to nonuniform injection flux. The coupling between the combustion and acoustic fields is altered by varying the mass distribution. This approach is discussed in detail in Sect. 7.2.5.

Another mechanism responsible for changes in relative stability involves the generation of radial gas flow because of variations in the mass flux across the injector. These "radial winds" directly affect the combustion by influencing the environments of the individual elements and thereby effectively changing the stability environment.

A third, and closely related, factor involves the local mixture ratio in the vicinity of chamber and baffle surfaces. Local effects have been found important in large thrust engines as well as in research-size hardware. One important location was shown to be the corner formed by the baffle blade and chamber. There small changes in local mixture ratio were noticeable and altered the damping times (pg. 76 of Ref. 190).

8.5.3.2 Radial winds.—One means of promoting stability, in a circular engine, is to induce a radial wind, i.e., a velocity component directed toward the chamber wall. Other terms which have been used to describe this or similar effects are curved divergence, wall gap, humped distribution, etc. Radial winds are generally induced by employing a reduced injection density along the periphery of the engine. They may be obtained in other ways as well, such as canting spray fans away from the confining surfaces. Virtually no analytical description of the radial wind or its effect on stability is currently available. Calculation of the radial wind velocity in a rocket combustion chamber is very complex because of its multidimensional nature. A very simple approximate method is described below for a two-dimensional case. This method, coupled with the output from a steady-state combustion computer program (see Sect. 6.4.1.1) allows the quantitative determination of the transverse gas velocity.

The two-dimensional continuity equation may

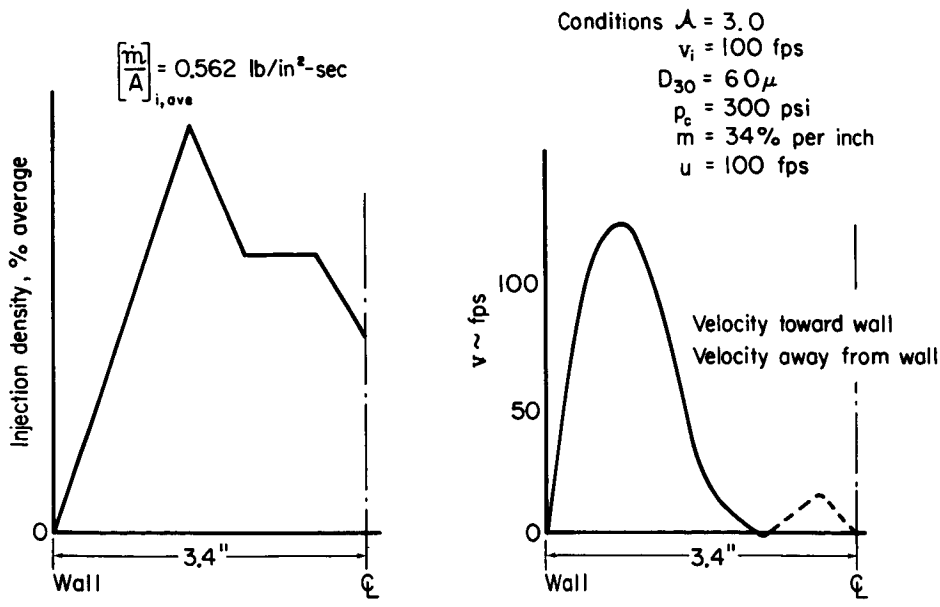

FIGURE 8.5.3a.—Calculated radial wind velocity for nonuniform injector density.

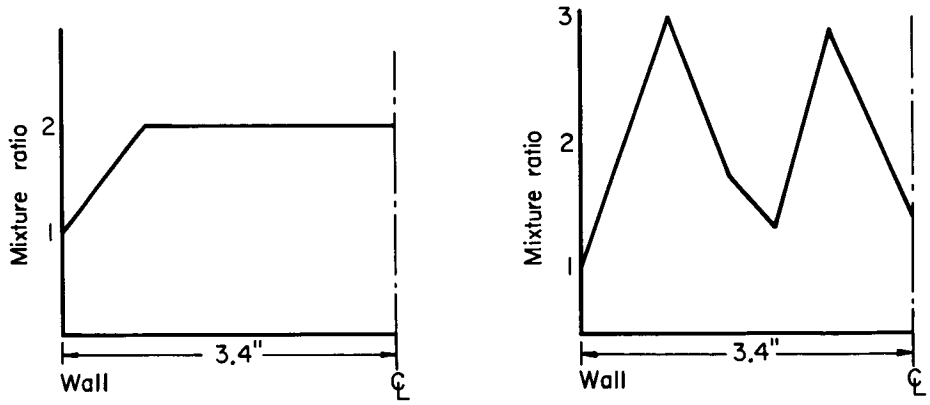

FIGURE 8.5.3b.—Mixture ratio distribution for N_2O_4/A-50 propellants.

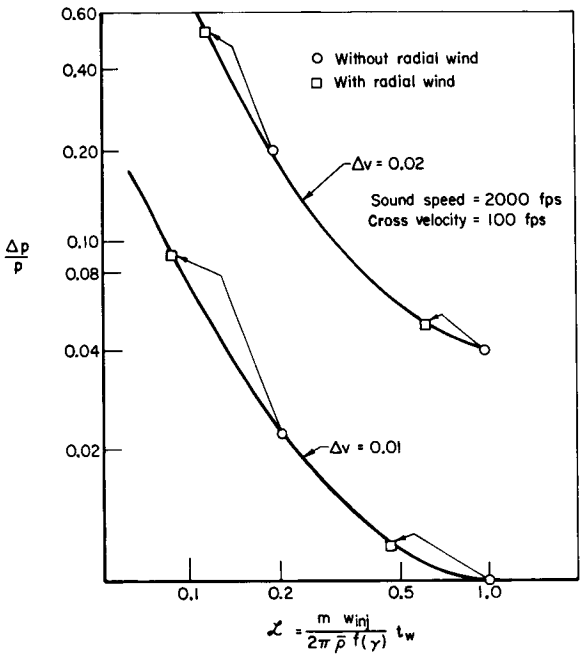

FIGURE 8.5.3c.—The effect of radial wind on the onset of instability.

be written as*

$$\rho \frac{\partial v}{\partial y} + v \frac{\partial \rho}{\partial y} + u \frac{\partial \rho}{\partial x} + \rho \frac{\partial u}{\partial x} = M$$

The spatially-averaged, steady-state burning rate, $\bar{M}$, is

$$\bar{M} = \rho \frac{\partial u}{\partial x} + u \frac{\partial \rho}{\partial x}$$

* The general nomenclature and that of Sect. 4.3 is used here.

since there is no mass flux through the wall. Assuming that u is not a function of y,

and $$v \frac{\partial \rho}{\partial y} \cong 0$$

then $$\rho \frac{\partial u}{\partial x} + u \frac{\partial \rho}{\partial x} \cong \bar{M}$$

thus $$\rho \frac{\partial v}{\partial y} \cong M - \bar{M}$$

which can be integrated at constant z to give the transverse velocity at any axial location, i.e.,

$$v(y) = \int_0^y \frac{M - \bar{M}}{\rho} dy$$

This expression has been used to calculate radial winds in several 2D chambers, with the aid of a steady-state, one-dimensional combustion model.

The assumptions made above appear reasonable in cases where the injection density is not extremely nonuniform, the contraction ratio is small, and the burning rate is high. A somewhat extreme example is shown in Fig. 8.5.3a. In this example the local burning rate M was calculated from

$$M = M_x \left(\frac{\dot{m}}{A}\right)_i$$

where M_x is the fraction of total propellant burned per unit length, and $\dot{m}/A$ is the local injection density.

The mixture ratio distribution has little effect

on the transverse velocity for these propellants. This velocity was calculated for the vastly different mixture ratio distributions shown in Fig. 8.5.3b, but with the same injection density distribution. No perceptible difference in the transverse velocity was found.

The effect of a radial wind on stability can be illustrated with the Priem instability map (Fig. 8.5.3c). It can be shown (although several assumptions and approximations are required) that the maximum effect of a 100 fps radial wind is equivalent to reducing the value of $\mathfrak{L}$ by approximately 50%. This has little effect if $\mathfrak{L}$ is large. However, if $\mathfrak{L}$ is smaller than about 0.3, radial winds of this magnitude can significantly raise the Δp required to drive the engine unstable. Figure 8.5.3c shows this effect for two values of $\mathfrak{L}$ and two values of Δv. The increased stability is shown by the shift from the points designated by the circles to the points designated by the squares for the radial wind. As shown, the change brought about by the radial wind is through a modification of the burning rate (Δv remains constant for each example).

CHAPTER 9

Experimental Evaluation of Stability Behavior

9.1 INTRODUCTION*

Previous chapters have described the analytical tools available to combustion dynamicists and development engineers. They have also discussed some of the design factors commonly used to modify the stability characteristics of engines when analysis or operating experience demonstrates the need for improvement. The objective of the next two chapters is to describe the tools and techniques used to evaluate combustion characteristics experimentally.

Chapter 9 describes some of the instrumentation and hardware commonly used to collect data pertinent to the problem of combustion instability data. It also discusses the display and interpretation of these data. Chapter 10 discusses the experimental tools and techniques used to evaluate the stability characteristics of liquid rocket engines.

This chapter considers the three interrelated topics of experimental hardware, instrumentation and data reduction, and evaluation of experimental data. In addition to the description of various classifications of experimental hardware, the characteristics and use of various types of instrumentation are given. More emphasis is placed on the pressure transducer than any other type of instrumentation both because of the wide variety of pressure transducers available and the general acceptance of dynamic pressure data as being the most widely used method for the detection and evaluation of unstable combustion in liquid rocket engines. Most of the data acquisition, display, and evaluation techniques are discussed with reference to the pressure transducer but the same equipment and techniques are generally applicable to any type of dynamic instrumentation.

It is not the intention of this chapter to provide the reader with complete criteria and procedures for the design, installation and operation of experimental hardware and instrumentation for investigating combustion and combustion instability. Rather the intent is to describe the characteristics and limitations of various types of hardware, instrumentation, and data evaluation techniques that have been utilized, which may aid the reader with the selection and development of techniques for his own requirements.

To evaluate the data from any test it is necessary to provide an accurate time base, simultaneously recorded on all test records. One technique that has been used for this purpose is that of a sequenced blanking signal that blanks the timing on all records for a few milliseconds. An alternate method involves the use of the "IRIG Standard Time Code Format A,"[25] which permits determination of the absolute time to 1/1000 of a second. The latter method is preferred, especially for large engine testing.

9.2 SPECIALIZED RESEARCH COMBUSTORS

A wide variety of devices have been used to investigate and study combustion instability phenomena in liquid rocket engines. Hardware size alone has ranged from a wire holding a single liquid drop to engines which produce well over one million pounds of thrust. It is beyond the scope of this text to discuss all of the various experimental tools and techniques used to investigate these complex phenomena. The following paragraphs will be restricted to brief discussions of representative types of apparatus that fall into one of the following categories: (a) full-scale simulators, which are geometrically similar to an actual rocket engine but which are instrumented to permit investigation and evaluation of details

* R. J. Hefner, Author.

within the combustor cavity, (b) subscale simulators, designed to investigate the combustion characteristics of a full-scale engine but which are more economical to operate and amenable to specialized instrumentation, and (c) basic combustion process apparatus, designed to investigate the basic mechanisms or processes of combustion.

9.2.1 Full-Scale Simulators*

In the investigation of combustion instability, the justification for full-scale simulation is that often the actual engine design conditions can only be achieved by this approach.[11,215,639] Special instrumentation is required which is generally not employed on flight hardware. Since nearly every engine at some point in development has been plagued with the problem of combustion instability, it is most desirable to fabricate specially instrumented hardware to simulate the actual engine. These simulators range from actual prototype hardware, modified as necessary to provide dynamic instrumentation, to heat-sink combustion chambers highly instrumented with pressure and vibration transducers, viewing windows, and pulsing devices.

The most commonly used full-scale simulator is a thrust chamber assembly comprised of all prototype components except for a heat-sink combustion chamber. Typically a heat-sink chamber has the same internal geometry as the prototype chamber, at least through the sonic throat. It is constructed of heavy metal (usually steel or copper) to permit operating durations of from one to five seconds depending upon the operating conditions of the engine. Heat-sink chambers have the advantages of being amenable to a wide variety of dynamic instrumentation and of being able to withstand the adverse effects of violent combustion instability for short durations.

The dynamic instrument most commonly used on heat-sink chambers is the high response pressure transducer although nearly all of the instrumentation techniques discussed in succeeding sections have been employed. The number of pressure transducers has varied from only one in some small chambers to as many as twenty on some tests of the F-1 Engine simulator. A discussion of optimum location and mounting techniques is given in Sect. 9.3.3. The heat-sink chamber is also commonly used for stability rating when pulsing devices are to be employed, not only because of the advantages listed above, but also because of its ability to withstand the shock and shrapnel effects of the explosive device.

It should be noted that although the heat-sink combustion chamber has many advantages for the investigation of instability, it may not provide an accurate duplication of the stability characteristics of the actual engine. For example, if the combustion chamber being replaced by the heat-sink chamber is regeneratively cooled, the feed system dynamics of the engine will probably be altered. Under these conditions, if either the actual engine or the simulator is susceptible to feed system coupled instabilities, the simulator may provide misleading data as to the stability characteristics of the engine. Also, the nonabsorbent metal wall of a heat-sink chamber may provide less damping (less stability margin) than the actual chamber. This latter may be true if the actual chamber is made of an ablative material (see Sect. 8.5.1).

Because of the inability of the heat-sink chamber to simulate all aspects of the actual engine and because of the limited test durations they impose, is is often desirable to provide special dynamic instrumentation on prototype hardware. This special instrumentation may vary from small passage transducers inserted between tubes of a regeneratively-cooled chamber to long probe transducers extended through the body or flanges of the injector (such instrumentation is discussed in Sect. 9.3.2). Because of the limited number and location of this type of instrumentation, as normally used, it is useful for detection of instability but is not generally sufficient for complete diagnostic evaluation.

9.2.2 Subscale Simulators*

The objectives of subscale simulations are (1) to develop design criteria that will substantially reduce the necessity for cut-and-try testing in new engine development programs, and (2) to attempt to understand the processes of instability well enough to eliminate any instability occurring in developed engine systems. Subscale research combustors must necessarily be of low thrust level

* R. J. Hefner, Author.

* T. A. Coultas and R. C. Kesselring, Authors.

in order that research test facilities may accommodate them. Hardware failures occurring with these low-thrust models are, of course, much less costly than hardware failures involving the full-scale engines.

In order to model properly a full-scale combustor, the characteristics of the combustor must be reproduced as closely as possible.[425] The propellant injection density, the contraction ratio and the chamber pressure should be closely simulated to ensure that the liquid droplets are subjected to the same combustion environment (see Sect. 7.2). This simulation is necessary since such quantities as combustion gas velocity, temperature, and pressure affect the droplet vaporization and burning processes and thus the stability of the combustion device. By maintaining the same injection hole sizes, impingement angles, element spacings, and injection velocities, it is possible to duplicate drop sizes and atomization and mixing characteristics of the injected liquid streams.

A hypothesis regarding the physical processes that sustain acoustic instability modes has been formulated in which the displacement of droplets and vapor by an acoustic wave plays an important role.[427,511] The acoustic displacement is inversely proportional to the frequency of the oscillations. Thus, it is necessary to have the instabilities exhibited by the model lie in the same frequency range as those occurring in the full-scale combustor if significant results are to be obtained. To meet this requirement a characteristic dimension of the model should be close to that of the full scale chamber. Various methods of meeting the dimensional requirement have been utilized. These methods are discussed below and are illustrated in Fig. 9.2.2a.

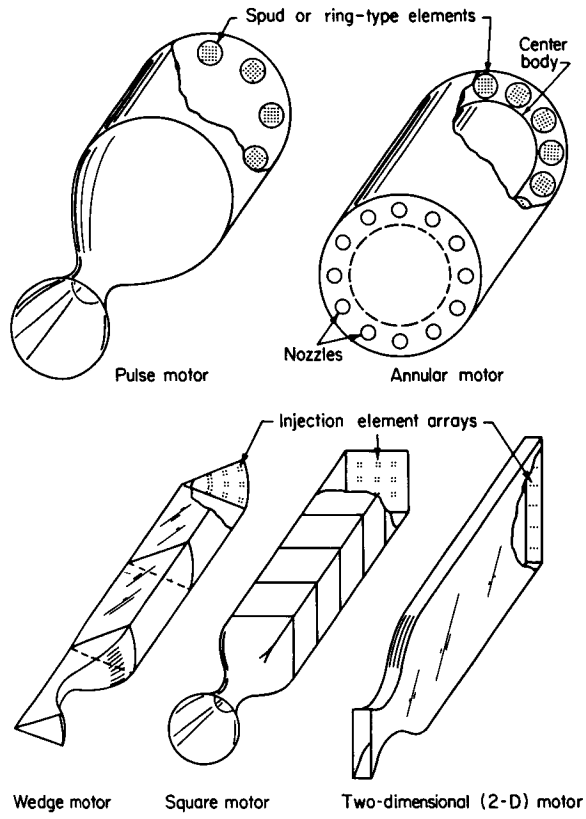

FIGURE 9.2.2a.—Sub-scale simulators.

9.2.2.1 Pulse motor.—The pulse motor was developed for the purpose of evaluating the effects of chamber pressure, chamber geometry, and injector pattern on the tangential mode of combustion instability.[94,190,242,540] The thrust chamber design favors the tangential mode by confining the propellant injection to an outer annular zone of the injector with the chamber diameter equivalent to that of the full-scale engine (hence exhibiting the same tangential frequencies). This permits stability tests in pulse motors to be conducted at reduced thrust levels while using full-scale combustion chamber cavities. To facilitate changes in injector patterns, the injector design has been based upon eight (or more) replaceable sections (spuds), which has resulted in a discontinuous injection pattern around the periphery of the combustion chamber as shown in Fig. 9.2.2a. Approximately 10 to 20 percent of the orifices of a full-faced injector pattern have been incorporated into the spuds.

Although tests using the pulse motor approach have provided one means for predicting stability trends in full-scale large-thrust hardware,[242] certain design deficiencies also have been evident.[541,94] Since the propellants are confined to the outer annular zone of the injector, the reduced overall propellant flow requires a much higher contraction ratio to achieve design chamber pressures. This in turn results in combustion gas velocities that are lower than those normally experienced in large-thrust units. Additionally, recirculation is also enhanced, making the overall effect on local

velocities difficult to ascertain. It is difficult or impossible to determine quantitatively the effects of other factors, e.g., the discontinuous injection pattern and how it affects the tangential displacement, or the relative role of the injection hydraulics on spray atomization with an altered steady-state velocity environment.

The problem of discontinuous propellant injection around the chamber periphery, experienced in the pulse motor, was avoided in the barrel thrust chamber.[427] Retaining the basic design features of the pulse motor, this model motor used a limited number of ring-type injection elements in the outer annular area of the injector. Naturally, with this fixed injector design the advantages of spud interchangeability as well as spud orientation possibilities had to be sacrificed. As in the other pulse motor designs, the barrel chamber faithfully modeled the chamber pressure, particle velocity and particle displacement distributions of the acoustic field as well as the identical radial and tangential mode frequencies (including combined transverse modes) of the parent combustor.

9.2.2.2 Annular combustion chamber.—Another modeling approach which provides both an equivalent propellant injection density and a reduced thrust level (compared to the full-scale, large-thrust hardware) is an annular combustion chamber.[164,192] This chamber employs a centerbody which effectively restricts propellant injection to a limited number of circular rings in the annulus. If the annular chamber, like the pulse and barrel chambers, has the same outer diameter as the full-scale engine, the nature of the instability is no longer that of standard chamber resonant modes. For example, the first tangential mode frequency is depressed (for a thin annulus the frequency is only 55% of that found in a conventional chamber with the higher tangential modes integral multiples of the fundamental), and the wave shape is altered[192] (a shock-type wave is characteristic). To properly model the frequency of the first tangential mode in a full-scale cylindrical chamber the outer diameter of the annular chamber must be decreased.[164] The radial mode frequencies in the full-scale chamber cannot be modeled in the annular chamber.

One possible disadvantage of the annular combustion chamber is that wall effects are accentuated. Tests in which a pulse motor was converted to an annular motor (with the same spud orientation and nozzle size) have indicated a greater tendency toward high frequency instability.[192] This may be explained by the shift in frequency of the tangential modes. Another point to remember is that the nozzle conditions associated with conventional hardware are difficult to model in the annular motor, although this design should better represent aerospike engine combustors (also see Sect. 8.4.5).

9.2.2.3 Wedge motor.—The wedge motor[408,560] also provides equivalent propellant injection density and contraction ratio but only a fraction of the total flow rate. The cross-section of this model chamber is typically a 60° sector of a circle. Since heat transfer conditions on the outer surface area are representative of the full thrust unit, heat transfer data are directly available from water cooling of this model. The use of a transparent wall and pressure instrumentation in the wedge motor provides a means for observing combustion phenomena. Simulation is limited to longitudinal, radial and high order tangential standing modes (the latter associated with the wedge angle).

9.2.2.4 Square motor.—One modeling approach to observe injector element interactions has been to take a small square section (4 to 25 elements) from a high density injection pattern.[184,189] The motor has been varied in length to observe c* variations and thereby measure axial combustion distribution for pressures to 1200 psia. Sensitive mercury manometer pressure measurements and streak film records have also aided in the interpretation of axial combustion rates. Small scale circular cross-section chambers have also provided data on combustion distribution.[55,180] Both square and circular sub-scale motors have also been used to study longitudinal wave interactions with the combustion processes–a subject more appropriate to other sections of this book (Sects. 3.5.2.1 and 7.2.4).

9.2.2.5 Two-dimensional motor.—Another means of obtaining an equivalent propellant injection density with a reduced thrust level is the two-

dimensional combustion chamber. In this section the two-dimensional (2-D) motor will be used as the detailed example of subscale simulation. This chamber consists of a thin radial (or diametrical) slice of a large thrust cylindrical chamber[425] without the diverging nozzle section.†

The 2-D motor, through the use of transparent chamber walls, offers the distinct advantage of being able to utilize high-speed motion picture photographic techniques to study the processes occurring *throughout* the combustion chamber‡ under both steady and unstable conditions (see Sect. 9.4). Closeups of particular regions of interest as well as streak pictures can be obtained. (A further discussion of the photographic methods possible with the two-dimensional motor is found in Section 9.4 and Ref. 424.) These photographic data help determine velocities of liquid droplets, combustion gases, and pressure waves throughout the chamber. This ability to view combustion is the most important capability of the 2-D motor, since it permits correlation of the visualized combustion processes with extensive pressure data taken simultaneously. This correlation provides insight into the nature of stable combustion, propellant droplet dynamics, triggering mechanisms resulting in combustion instability, and instability oscillations, all of which are important in formulating process mechanisms and mathematical combustion models. In addition, the 2-D motor can be used to study the effect of varying injector pattern, propellant combination, baffle geometry, etc., upon the efficiency and dynamic stability of the combustion process.

Two examples of 2-D modeling are (1) a 1-inch-thick diametrical slice of a 20-inch diameter, 150,000-pound-thrust (full scale) chamber,[427] and (2) a $1\frac{1}{2}$-inch slice of a 1,500,000-pound-thrust combustor.[67] The latter model shown in Fig. 9.2.2b has been operated up to 1100 psia with identical injector orifice characteristics, propellant injection densities and velocities, contraction ratio and chamber length as in the parent engine.

As with all of the subscale simulation, the 2-D approach also has certain disadvantages. The transverse* acoustic mode of instability in this chamber only simulates the acoustic field distributions of certain regions of the tangential or radial modes of a cylindrical chamber. The choice of an appropriate chamber width will result in a frequency of the transverse mode in the 2-D chamber close to the frequency of the mode of interest in the chamber being modeled. If the original injection pattern and spacing are retained intact, and the 2-D slice width is limited to the full-scale chamber diameter, then the frequency of the first transverse mode in the 2-D will be 15% less than the 1T (spinning or standing) mode in the cylindrical chamber, whereas the second transverse mode in 2-D is 3% greater than the 2T mode in the cylindrical chamber. Velocity oscillations and particle motions are restricted to the major dimension of 2-D chamber cross section. Minimum pressure and displacement amplitudes occur near the spacer bar walls and at other nodal locations, whereas maximum values are found at the antinodes (midway between the walls for the first transverse mode). In contrast, the spinning and standing tangential mode velocities and displacements occurring in full-scale hardware are generally perpendicular to those occurring in the 2-D case and are far more complex

FIGURE 9.2.2b.—High-pressure two-dimensional research combustion chamber with transparent walls.

† None of the various model motors require a diverging section for stability simulation.

‡ Of course, observation ports and slits at locations of interest have been used in other model chambers as well as in full-size combustors.

* Transverse, in the case of the 2-D hardware, is used to describe modes or displacements parallel to the major dimension of the injector face.

(e.g., elliptical, circular and curvilinear displacements, see Sects. 3.5, 7.2.5 and 8.2.2).

Another source of error in stability simulation is the choice of the narrow dimension (thickness) of the 2-D chamber. Through the choice of this dimension, the propellant injection density can be maintained at the same level as the full-scale chamber. However, if the narrow dimension of the 2-D chamber is too small and allows wall impingement of the propellant streams, the stability modeling will be affected to an unknown degree.

Returning to the components from which the 2-D motor is constructed, the walls of 2-D chambers may be either transparent or opaque. The surface of the opaque (solid) wall provides locations for various types of instrumentation. The transparent walls typically consist of $2\frac{1}{2}$-inch-thick Plexiglas to which are bonded $\frac{1}{4}$-inch-thick sheets of Pyrex. The Plexiglas is used to furnish the necessary mechanical strength and the Pyrex is utilized to protect the Plexiglas from the hot combustion gases during the firing. This prevents burning of the Plexiglas which might obscure the combustion process as well as destroy dimensional stability (throat area, etc.) of the motor. The chamber nozzle is formed by copper inserts which are welded to (or machined integral with) the spacer bars. The 1- to $1\frac{1}{2}$-inch-thick combustion space is maintained by spacer bars which provide longitudinal seals and a convenient location for pressure taps along the chamber. Bomb holders are also accommodated in these bars.

Flexibility of injector configuration is achieved by use of a stainless steel combination body and propellant manifold (Fig. 9.2.2c) incorporating replaceable, low cost, copper orifice element inserts. Thus, the injector element type (i.e., like-on-like doublet, unlike doublet, triplet, showerhead, etc.) may be easily changed. Thin baffles may also be welded in a variety of positions on the injector face in order to observe stability trends of such variables as baffle spacing, baffle length, and baffle gap.

The two-dimensional thrust chamber, like the majority of the subscale model motors, is uncooled. Thus the test durations are limited to approximately 1 second of full-thrust operation. Tests in opaque heat-sink hardware, free from window erosion problems, can be of somewhat longer duration. The test duration is usually limited by heat transfer to the nozzle which leads to nozzle erosion. Thus, the permissible test duration is calculated using a nozzle heat transfer analysis.[81]

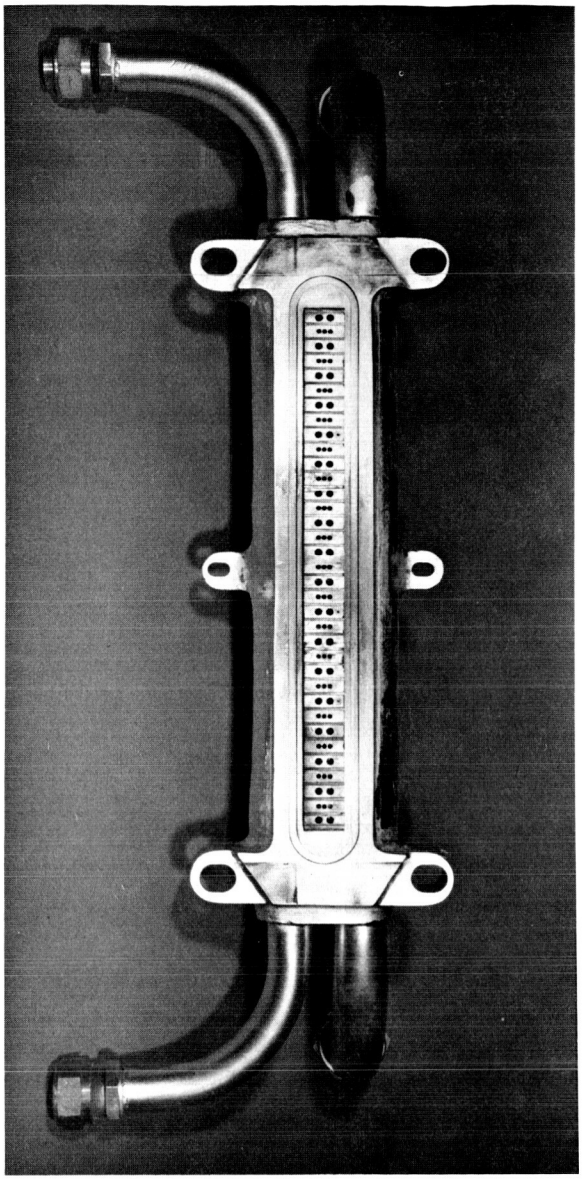

FIGURE 9.2.2c.—A typical high-pressure 2-D injector.

In summary, two-dimensional research motors have been operated for many years to simulate full-scale engines. Variables have included: size, pressures ranging from 75 to 1300 psia, a wide variety of propellant combinations, and variations in other operating conditions. Such motors have been found to be quite successful in duplicating many of the stability characteristics of the parent

engines, although, because of inherent design limitations of two-dimensional hardware, not all characteristics of the full-scale engines can be simulated. The application of the two-dimensional motor to the study of resonant combustion is reported in Ref. 440.

9.2.3 Basic Combustion Process Apparatus*

The apparatus used to investigate basic combustion processes in liquid rocket engines can be divided into two classifications: those that are used to study the characteristics and mechanisms of combustion during stable conditions and those used to investigate the combustion process during unstable or perturbed conditions. The apparatus used within either of these classifications have varied from the combustion of a single liquid drop suspended in a gaseous environment to rather large combustors with multiple orifice injection schemes.

Probably the simplest apparatus used in basic combustion process investigations consists of a single liquid drop suspended from the tip of a thermocouple and a high-speed motion-picture camera. The drop is combusted with air in an unenclosed environment with the thermocouple and camera providing the data for investigation of the basic mechanisms of the combustion process. One variation of this technique has been to enclose the droplet in a transparent enclosure which permits variation of the gas species with which the droplet burns and the temperature and pressure environment in which the combustion takes place.[429] Other simple experiments utilized candles in various environments.[696,695]

A more sophisticated apparatus for studying the normal combustion process of a single liquid drop was used by Faeth, Dominicis and Olson.[255,231] Their experiments covered a pressure range of 14.2 to 2000 psia and were conducted in a zero gravity environment to eliminate the effects of natural convection and to prevent the droplet from falling from its support. The primary instrumentation was a motion picture camera although a thermocouple was used to measure the liquid drop temperature on some tests. The combustion chamber and all associated instrumentation and controls were mounted in a free fall chamber to permit conducting the experiments in a zero gravity field (Fig. 9.2.3a).

A type of apparatus used to investigate the propellant mixing, atomization, vaporization, and chemical reaction processes of a bipropellant liquid injector is a combustor with a single element.[252] The combustion chamber may be constructed of a transparent material such as plastic or glass or it may be a conventional type of heat-sink chamber, with or without observation windows. The most common type of instrumentation used is the high response pressure transducer, photographic equipment and performance measuring instrumentation such as static pressure transducers and propellant flow meters.

Two types of apparatus will be described as being typical of those used to investigate combustion under unstable or perturbed conditions. Several groups have investigated the effect of shock waves and detonation waves on liquid propellant combustion. Nicholls et al.,[514] used a long vertical tube in which liquid drops were allowed to fall through a gaseous environment. A

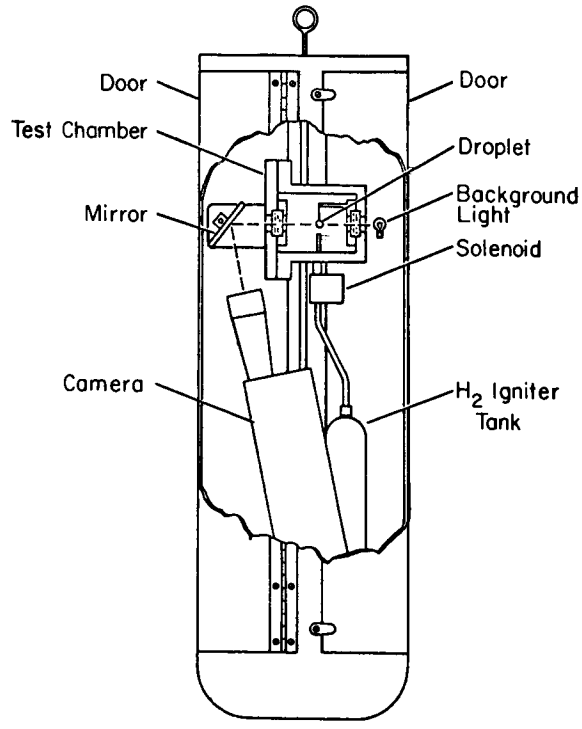

FIGURE 9.2.3a.—Sketch of free fall liquid drop combustion chamber.

* R. J. Hefner, Author.

shock wave was then introduced into the tube to investigate the droplet shattering and two phase detonation characteristics resulting from the shock. In these experiments both very high response pressure transducers and various photographic instrumentation techniques were used.

A second type of apparatus used to investigate unstable combustion is the excitation chamber.[708] In its original version the excitation chamber is an "organ pipe" with an injector on each end and a centrally located nozzle, Fig. 9.2.3b. The length of the combustion chamber is varied to permit studying oscillatory combustion at various frequencies. The particular configuration shown in Fig. 9.2.3b with the nozzle at the center provides minimum system damping for the fundamental and all other odd numbered longitudinal modes and maximum damping for the even numbered modes. By placing a baffle through the nozzle at the center of the tubular chamber damping is provided for the odd numbered modes. Once combustion is initiated and allowed to reach steady-state, stable operation, the baffle is removed which permits the initiation and growth of one of the odd numbered instability modes. From the growth rate of any resonant instability initiated, a direct measure of the combustion response can be obtained as a function of frequency.

In the version illustrated, if the combustion takes place near the injectors at the ends of the chamber, the combustion will be near a pressure antinode which then provides data on the responsiveness of the combustion process to pressure oscillations without any fluctuating velocity influences. A variation of the longitudinal excitation chamber utilizes a thin combustor cavity shaped like a sector of a circle with a curved injector at the periphery of the circular sector pointing toward a slit nozzle at the center of the circle.[436] This configuration permits transverse oscillations with pressure antinodes at the edges of the combustor. The injection elements and thus the combustion processes are distributed across the oscillating field where they are subjected to both the pressure and transverse velocity effects. By varying either the sector angle or radial length to the injector the fundamental resonant frequency is varied. Again, by measuring the growth rate of any spontaneous resonant instability, or the decay rate of an induced instability

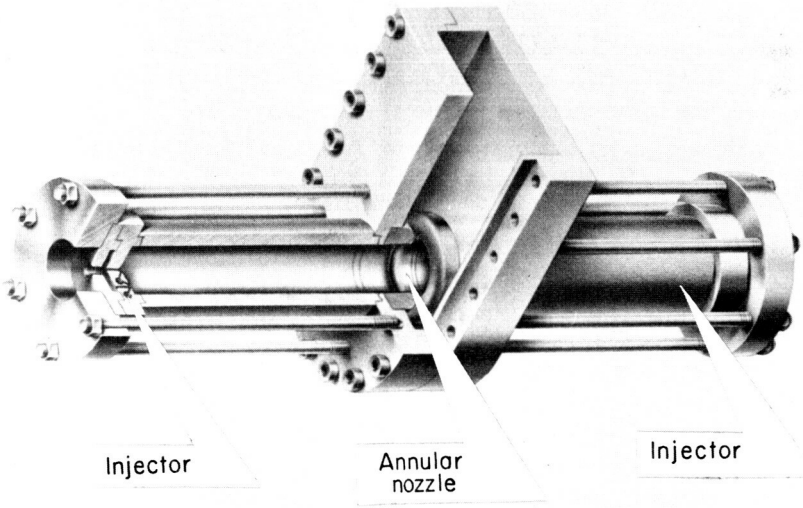

FIGURE 9.2.3b.—Excitation chamber for measuring combustion response to longitudinal mode instability.

as the resonant frequency is varied, the responsiveness of the combustion process to transverse oscillations can be directly measured with high response pressure transducers.

Only typical specialized research combustors have been described to give the reader an introduction to the types of apparatus available to the combustion dynamicist.

9.3 PRESSURE MEASUREMENTS

There are many ways of detecting combustion instability. The most widely used diagnostic methods are through the measurement of dynamic pressures in the combustor cavity. Through judicious selection of transducers and measurement locations within the combustion chamber, it is normally possible to make a sophisticated diagnosis of the dynamic characteristics of the combustion process, including instability mode identification on unstable tests and the stability index determination on pulsed tests.[330]

The liquid systems dynamics are also important. Many times an instability may be induced through the feed system, including the propellant lines, pump and injector cavities. It is important that these components be monitored as judiciously as the combustion zone, as a feed system coupled combustion instability can often be eliminated by modifying the propellant feed system.

The following nomenclature pertains to Sect. 9.3:

A_D	Transducer diaphragm area
A_L	Connecting passage cross-sectional area
$\mathcal{C}_c$	Cable capacitance
$\mathcal{C}_t$	Transducer capacitance
E	Output voltage
f_c	Filter cut-off frequency
f_n	Normalized frequency, f/f_c
L	Connecting passage length
Q	Charge sensitivity
$\mathcal{V}_o$	Transducer cavity volume

9.3.1 Transducer Requirements*

It would be most desirable to have one pressure transducer for performance measurements as well as stability characteristics. The environment in which the dynamic transducer must operate and the accuracy requirement for the performance measurement have made this impractical.[732]

For the analysis of combustion instability the requirements imposed on a pressure transducer are often very stringent. In the measurement of dynamic pressures a pressure transducer is exposed to high heat fluxes and high acceleration forces. It is also required to have a high frequency response.[151]

In general, in specifying a dynamic pressure transducer for hot gas measurements, one would desire it to be small in size with a small diaphragm area. The small diaphragm area ($\frac{1}{4}$ inch or less in diameter) allows the required high frequency response (resonant frequency to 100 kHz or better). It should be capable of withstanding sustained high heat flux (35 Btu/in.^{2} sec.) without sensitivity or zero shifts. Acceleration sensitivity must be low or correctable. High transducer output sensitivity is very desirable, since it allows low magnitude signals to be recorded above the system noise level. Transducers should be of sufficient stability to allow calibration in-place by electrical simulation. The design must be rugged enough to withstand the environmental conditions and the required handling without failure. Although not a technical requirement, transducer cost is a very real consideration.

9.3.1.1 Hardware considerations.—Consider some of the factors affecting a transducer selection for a hot gas measurement in a combustion chamber.[35] Each of these factors has a definite effect on the transducer requirement.

A. Type of combustion chamber
   1. Heat sink
   2. Ablative or ablative liner
   3. Regeneratively cooled (tube-wall chamber)
B. Size of combustion chamber
   1. Chamber diameter
   2. Chamber length
   3. Wall thickness
   4. Access area for transducer and transducer mounting boss
C. Test conditions
   1. Propellants
   2. Static chamber pressure level
   3. Test duration
D. Induced perturbations

* R. D. Wesley, Author.

1. Nondirectional bomb
2. Tangential or radial pulse gun
3. Gas injection

A variation in combinations of any of these factors can alter the specific transducer requirement and hence the selection from among commercially available transducers. Some of the specific transducer requirements will be examined to evaluate how they relate to the above factors.

9.3.1.2 Response characteristics.—Dynamic pressure transducers must be capable of high frequency response. This is dictated for the most part by the combustion chamber dimensions, because the frequencies of the instability modes are dependent on the acoustical path length. As the diameter of a combustion chamber is decreased, the tangential and radial mode frequencies for an equal order mode will increase in inverse proportion to the chamber diameter. Likewise as chamber length is decreased, the frequency of equal order longitudinal modes will increase. Since the size of current liquid combustion chambers ranges from the very large (over 40 inches in diameter) to the very small (less than 2 inches in diameter) the range of combustion instability frequencies can be quite wide (e.g., 500 to 17,000 Hz for the 1T mode).

It is evident that transducers are needed with a flat frequency response of greater than 20 kHz to monitor higher frequency instabilities. However, 10 kHz response is generally sufficient when chamber diameters are greater than 8 inches.

9.3.1.3 Environmental exposures.—In order to obtain the maximum frequency and amplitude response from a transducer, it is essential that it be flush mounted with the inner wall of the chamber. Under this condition the transducer will normally experience the most severe environmental conditions. Heat flux, vibration and shrapnel from gun or bomb pulse devices must also be considered.

Typical heat flux levels to be expected may vary from 6 to 8 Btu/in.^{2} sec. under normal burning conditions to perhaps 35 Btu/in.^{2} sec. during resonant combustion instability (see Sect. 9.6.5). The length of required exposure to the severe thermal conditions may vary from a few milliseconds to several seconds. Many schemes are used to protect the transducer from the heat, including dual diaphragms with water circulation between the diaphragms, fluid dump (that is, dumping a cooling fluid into the chamber after passing over the diaphragm), ablative coatings and diaphragm isolation by means of the small passage or helium bleed technique. All are effective to varying degrees and all have special applications.

Vibrations in a combustion chamber can become quite severe. Normal operating levels are 50 to 150 g's peak but may increase rapidly to 2000 g's peak (and above) under unstable operating conditions. When analyzing the data this can become a very important consideration, especially if a transducer is unusually sensitive to vibration. Most transducers used for dynamic measurements have a sensitivity of 0.001 to 0.002 percent full range per g (fs/g). A 2000 psi transducer with a 0.002% fs/g vibration sensitivity in a 1000 g environment will produce a 40 psi indicated pressure from the vibration environment alone.

In chambers where perturbations are artificially induced by pulse guns or bombs, there are usually high velocity shrapnel particles associated with the detonation of the perturbing device. These particles are especially destructive to unprotected diaphragms (Sect. 10.2.3). If a diaphragm is penetrated, the transducer will burn out. A logical conclusion is that diaphragm protection must be provided or, at the very least, small diaphragm devices must be used to reduce diaphragm damage.

9.3.1.4 Range selection.—When selecting a range, one should always keep in mind the job the transducer is expected to perform. This usually depends on the type of testing and the normal steady-state pressure level. Experience from previous test conditions is the best guide to use in choosing a range. However, in the absence of prior experience on specific hardware it is usually sufficient to select a dynamic transducer whose range is twice the expected steady-state pressure level, providing the chamber is not going to be pulsed. On pulse chambers it may be necessary to use a transducer which is rated at 3 to 5 times the steady-state chamber pressure level. This is, for the most part, dependent on the type of charge used, orientation of pulsing device, and the location of the transducers in relation to

the pulsing device. A charge directed toward a transducer can create a very high pressure initial shock wave at the transducer.

9.3.2 Available Instruments*

Many transducers are commercially available for the measurement of dynamic pressures in liquid propellant rocket engines.[16] Great strides have been made in the development of new transducers in recent years which have greatly alleviated the pressure measurement problems in large liquid rocket engines.[433] The relatively recent development of small rocket engines, including pulse motors, presents new measurement challenges. For these small engines, the emphasis must now be placed on higher frequencies in conjunction with a small transducer size.

The characteristics of general types and the applicability of available instruments will be discussed rather than attempting to describe each available transducer.

9.3.2.1 Transducers for combustion zone pressure measurements.—In order that the maximum response of the transducer may be met, it must be flush mounted with the internal chamber surface. Although desirable, flush mounting is not always possible. A flush-mounted transducer in an ablative chamber may result in transducer erosion along with the ablation of the chamber wall. Regeneratively cooled chambers have space problems for transducer mounting. It can be seen that each type of chamber has its own unique mounting problems.

PRESSURE TRANSDUCERS FOR HEAT-SINK CHAMBERS: Heat-sink chambers are generally the work horses of rocket engine development. This heavy-walled hardware imposes only minor restrictions on the number of transducers used and the type of mounting configuration employed. The heat-sink chamber, especially in the larger sizes, can adapt to a wide selection of available transducers. Transducers must successfully withstand the environmental exposure and yet produce valid data for subsequent analysis. Most commonly used are the double diaphragm water-cooled types, although other protection methods are also used. Such transducers are readily available in sizes which range from a 1 inch diameter down to $\frac{1}{4}$ inch diameter.[16]

The methods most often used in dynamic transducers to convert pressure input to electrical output are the bonded wire resistance strain gage bridge, variable capacitance, piezoelectric crystals, and the piezoresistive (semiconductor) strain gage bridge.[394,433]

Representative of the bonded wire strain gage types are the Dynisco PT-49A and the Norwood 14943 transducers, Fig. 9.3.2a. They are water-cooled with a thin diaphragm stitch welded to a coolant maze ribbon. The diaphragm is easily ruptured by pulse gun or bomb particles. A later Dynisco model, the PT-134, shows improvement over the PT-49A.[433] Transducer output is low, 3 mv/v with resonant frequencies in the 25 to 30 kHz range.

Two widely used capacitance types are the Photocon models 307 and 352A. The Photocon 352A, Fig. 9.3.2b, has been very popular in larger chambers (diameters > 8 inches) which are compatible with the relatively large transducer diameter (1 inch). The unique feature of this transducer is the flame shield that protects against diaphragm punctures from high velocity bomb particles without seriously affecting the frequency response. This flame shield presents two cooling surfaces to the hot gas, as both the flame shield and diaphragm are water-cooled, and allows operation under high heat flux environments (25 to 30 Btu/in.^{2} sec.). The resonant frequency of the transducer (25 to 45 kHz) is compatible with the required frequency measurement range of the larger chambers. As is true for most transducers, the higher range units have stiffer diaphragms and hence higher natural frequencies.

For smaller chambers, where space is at a premium the Photocon model 307 is useful, Fig. 9.3.2c. Its resonant frequency is approximately the same as the previously discussed Photocon 352A (25 to 45 kHz). Cooling is accomplished by recirculating water through a dual diaphragm. Since it has an exposed outer diaphragm (no heat shield), it is susceptible to puncture by high velocity bomb particles; however, the occurrence is reduced by the smaller diaphragm size.

* R. D. Wesley, Author.

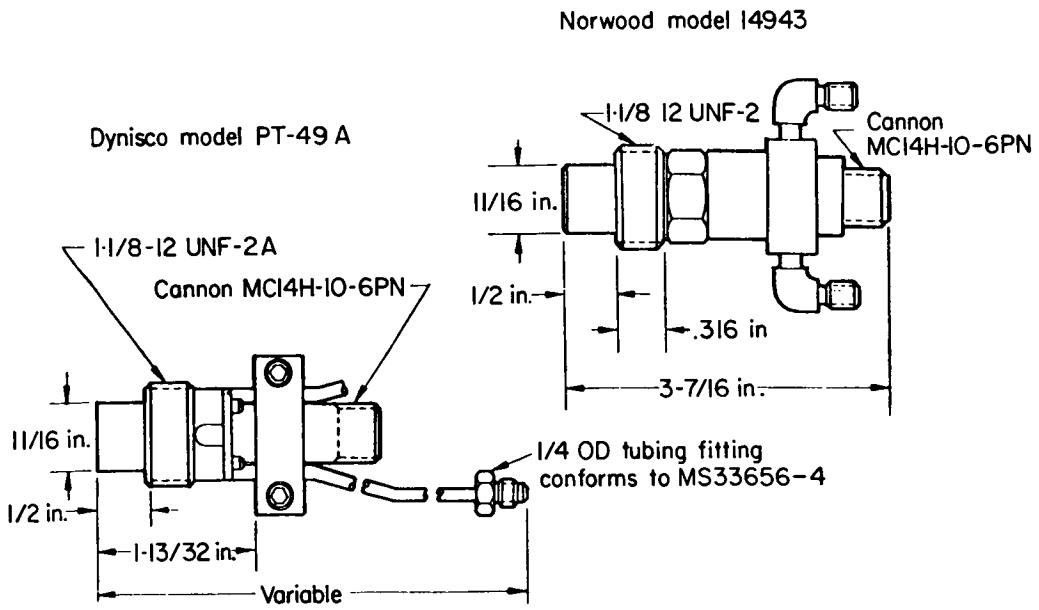

FIGURE 9.3.2a.—Dynisco and Norwood pressure transducers.

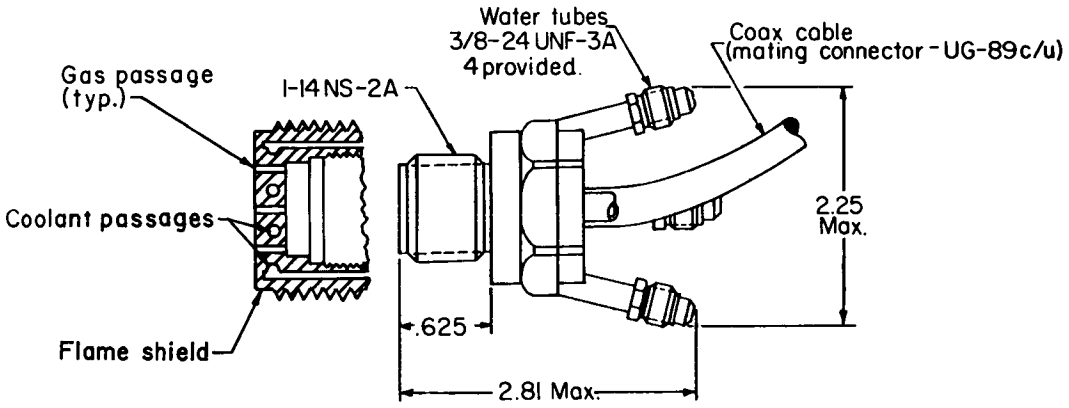

FIGURE 9.3.2b.—Photocon model 352A transducer.

A double diaphragm transducer of the solid-state, strain gage type is the model PT-150-5, Fig. 9.3.2d, manufactured by Electro Optical Systems, Inc. (EOS). It is a piezoresistive transducer utilizing a diffused four arm bridge on a silicon chip, which gives it a relatively high output, 300 mv full scale, prior to amplification. Because the diaphragm area is small, with a very short pin construction, it has been possible to realize a resonant frequency of 100 kHz.

One of the piezoelectric types in use is the Kistler 616, Fig. 9.3.2e. It is representative of an

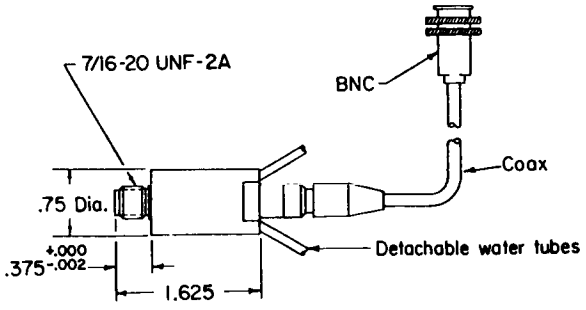

FIGURE 9.3.2c.—Photocon model 307 transducer.

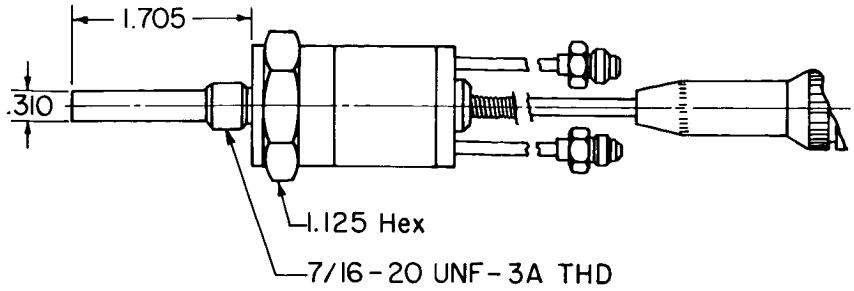

FIGURE 9.3.2d.—Water-cooled transducer (EOS model PT-150-5).

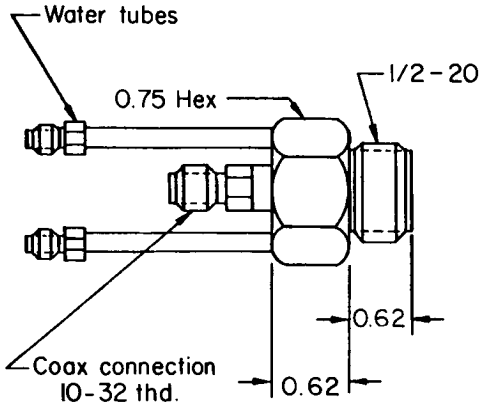

FIGURE 9.3.2e.—Kistler model 616 transducer.

uncooled transducer connected by a short passage in a water-cooled adapter. Although the transducer itself has a very high resonant frequency, the adapter limits its resonant frequency to the 40 kHz region. It has found applications in low heat transfer environments and short duration tests.[433]

The preceding paragraphs have presented the transducer types which are most commonly used in development testing, where instability mode identifications are of prime importance. Most of these are somewhat limited, however, in measuring wave shapes of very steep-fronted waves. One very useful transducer for this type of measurement is the small quartz crystal which utilizes the piezoelectric characteristics of the quartz. Kistler has been the principal supplier of the quartz pressure transducers although other companies are now marketing similar products. The Kistler 603A has been used extensively for determining wave shapes and identifying modes of instability. Since it has a very high resonant frequency (in excess of 400 kHz) it will respond faithfully to steep-fronted waves. Its main drawback, however, is the fact that it is an uncooled transducer and will withstand only a few milliseconds of heat exposure without damage; therefore further protection is needed. One popular method, the use of ablative coatings, is discussed in Sect. 9.3.3.2.

Only a small number of the available pressure transducer models have been discussed, but they are representative of the wide selection available. Other models, complete with their evaluations, can be reviewed in Refs. 16, 393, 433, 596 and 732.

PRESSURE TRANSDUCERS FOR ABLATIVE CHAMBERS: The selection of dynamic transducers which are usable in an ablative chamber is very limited. As the name implies, the chamber walls are cooled by ablation of the wall surface and any instrument which is flush mounted may protrude into the chamber as the walls char and ablate, thus subjecting the transducer to erosion and eventual destruction. The problem then becomes one of using a transducer which can survive some erosion and yet maintain data quality.

This has been made possible by utilizing the small passage technique.[432] A typical transducer of this type is shown in Fig. 9.3.2f. In this concept an uncooled miniature transducer is located at the end of a small diameter passage which usually is less than $\frac{3}{4}$ inch in length. Helium is bled under high pressure (at least 2.08 times the expected peak pressures[432]) through a choked orifice, across the transducer diaphragm and out the tube, filling tube and associated cavity with helium gas. The helium gas serves (1) as a signal path with known acoustic characteristics, (2) to cool the transducer diaphragm, and (3) to prevent tube

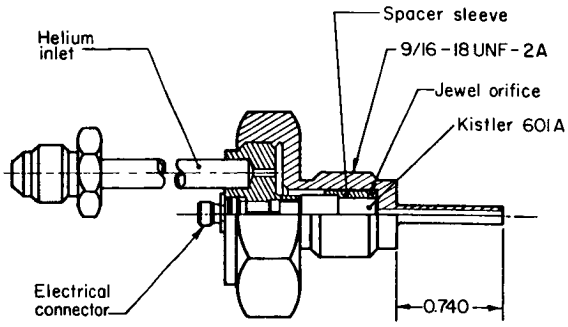

FIGURE 9.3.2f.—Helium-bleed transducer (Aerojet-General Corp. model HB3X).

clogging by combustion or ablative particles. Resonant frequencies will vary with the tube length and cavity configuration as shown in Fig. 9.3.2g. For the transducer model shown in Fig. 9.3.2f, which has a tube length of $\frac{3}{4}$ inch, the resonant frequencies range from 10 to 12 kHz with a usable flat response ($\pm 10\%$) to 3.5 kHz.[16] This can be extended with electrical compensation to approximately 80% of the resonant frequency.[433]

Utilizing the concept described, it is now possible to insert the small tube (0.080 in. O.D.) through the ablative material flush with the inner surface. As the chamber material ablates, the tube will burn back remaining flush with the wall. Although the resonant frequency will change slightly with operating time, it will be in the direction of an increased resonant frequency. Prior to use it is best to determine each transducer's individual frequency response characteristic via the shock tube or sinusoidal pressure generator.[394,433]

PRESSURE TRANSDUCERS FOR REGENERATIVELY-COOLED CHAMBERS: The helium-bleed transducer just discussed was first developed for use in regeneratively cooled chambers. This application is shown in Fig. 9.3.2h. Prior to its development it was impossible to make a dynamic pressure measurement through the side wall of a regenerative chamber, although measurements in the combustion zone were possible through the injector face. This, however, involved special modification to the injector face for insertion of the transducer.

Stability tests are not generally conducted in tube-wall chambers because of the difficulty of obtaining dynamic pressure measurements. Then too, some chambers will not withstand the severe instability environment. It is desirable, however, to make some measurement of stability on the final hardware design. As can be seen in the figure, it is necessary to provide an external boss for transducer mounting. The transducer tube is inserted between adjacent combustor coolant tubes which have been dimpled for this purpose.

Another approach to make dynamic pressure measurements possible in a regeneratively cooled chamber is the fluid dump transducer of which two models are shown in Fig. 9.3.2i. This type transducer is adapted to the injector or chamber flange (rather than the chamber itself) and mounted flush with the internal surface. The frontal size is 0.150-inch diameter with a diaphragm of 0.090-inch diameter. This particular transducer utilizes water as a coolant which sprays across the diaphragm and dumps into the chamber, hence the water pressure must be maintained sufficiently high to overcome the peak chamber pressure oscillations. Therefore, a high pressure filtered water system is required for its use.

9.3.2.2 Pressure transducers for propellant systems.—Requirements for dynamic pressure data in the propellant systems, as with the combustion chamber, dictate a transducer with a high frequency response capable of being flush mounted. Any recess or tube connection can degrade the data to a point where it is unusable for dynamic analysis.

It is therefore highly desirable to flush mount all propellant system transducers. In selecting a transducer consideration must be given to the frequency required, signal levels to be recorded, mounting configuration, measurement system compatibility, vibration environment and the propellant characteristics and temperature. The wide variance in propellant temperatures from ambient to cryogenic must be given prime consideration.

AMBIENT TEMPERATURE REGION: Since pressure fluctuations in the propellant system are often of low magnitude, the first preference would be to use a transducer with a relatively high output so that a better signal-to-noise-ratio might be realized. To this end several good semiconductor transducers are available. Representative of these is the PT 3f-C2 manu-

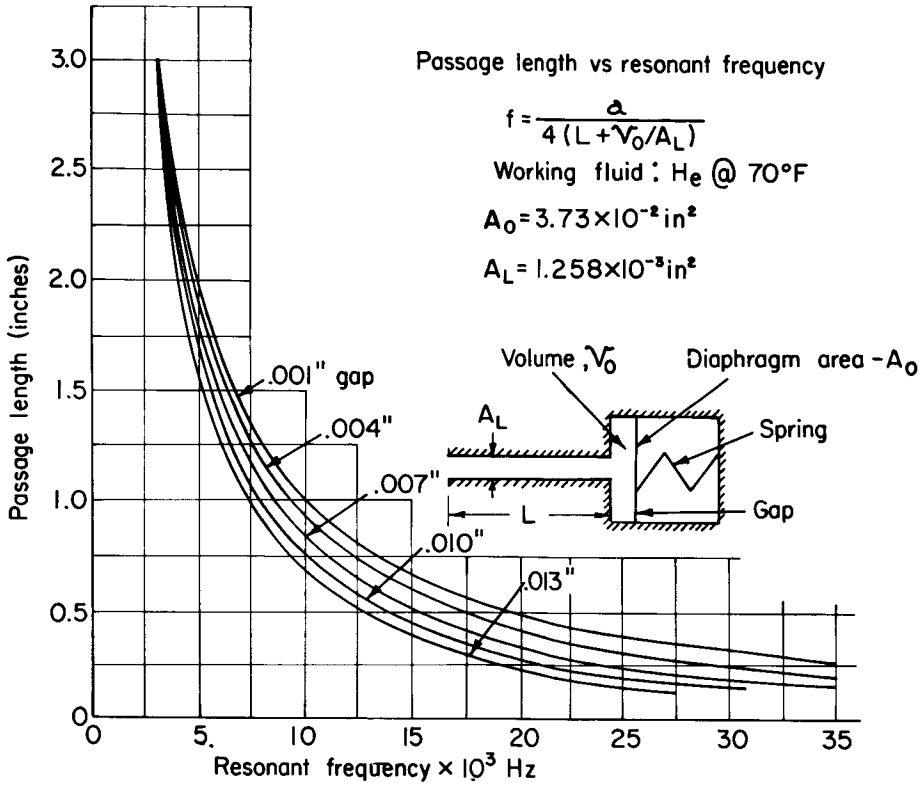

FIGURE 9.3.2g.—Passage length vs frequency for helium-bleed transducers.

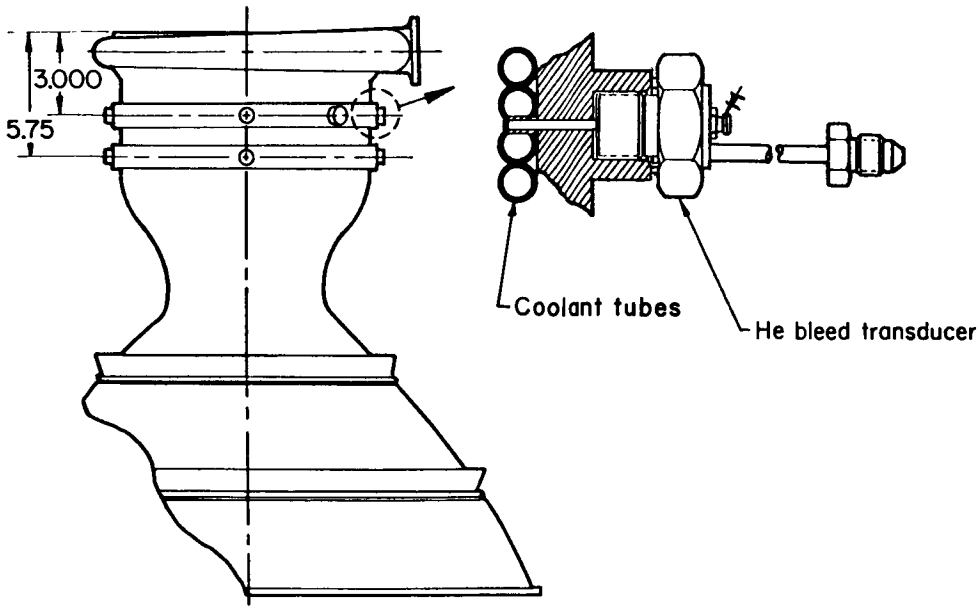

FIGURE 9.3.2h.—Instlalation of helium-bleed transducer in a regeneratively-cooled combustion chamber.

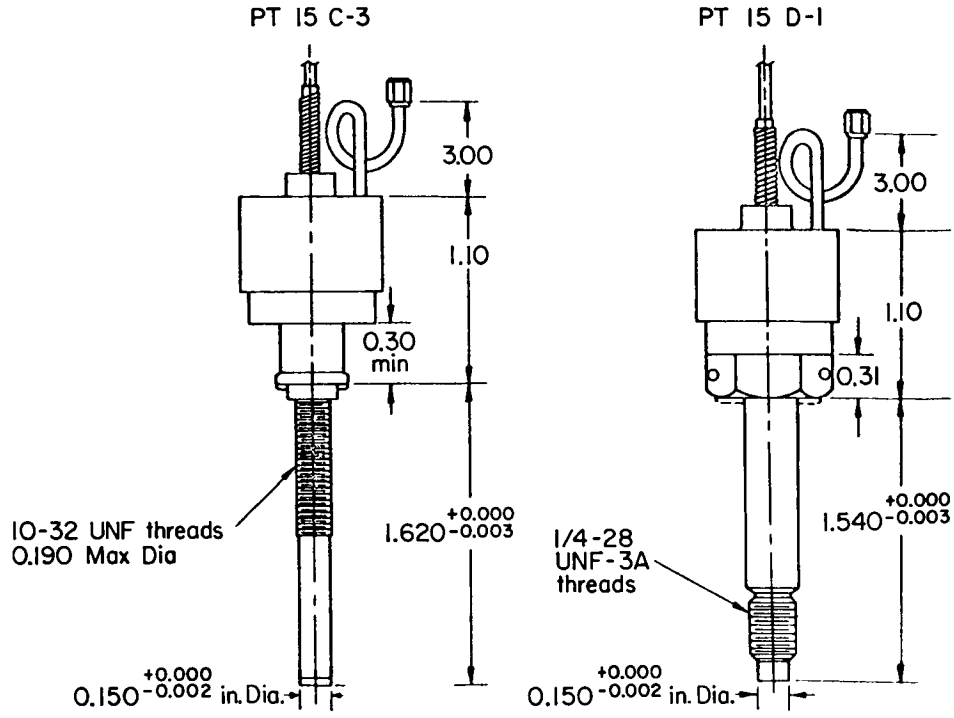

FIGURE 9.3.2i.—Fluid-dump piezoresistive transducers.

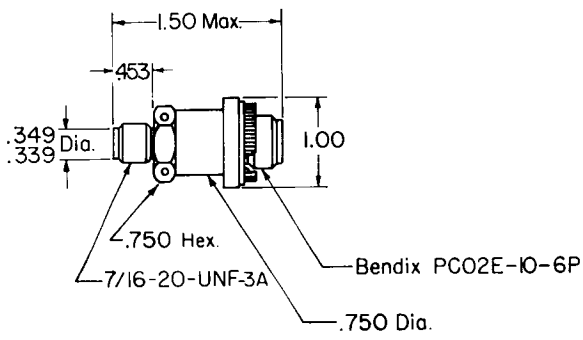

FIGURE 9.3.2j.—Piezoresistive pressure transducer for propellant feed system.

factured by Microsystems, Inc., Fig. 9.3.2j. This is a standardized piezoresistive, strain gage type transducer with a 500 mv full scale output prior to amplification and utilizes a standardized constant-current bridge supply and signal conditioning system. The transducer is small (adapts to a modified $\frac{1}{4}$ inch AN fitting) and is rugged enough to be easily handled without damage. It is a single diaphragm device with silicon gages bonded on the back of the diaphragm. Because of its diaphragm size and stiffness it has a very high resonant frequency, in excess of 100 kHz. High pressure units have been manufactured with a diaphragm as small as 0.090-inch diameter.

Wire strain gage transducers applicable to the ambient propellant environment are numerous. A representative model would be the Dynisco PT-76. It has a 3 mv/volt sensitivity or nominally a 30 mv full-scale output, is temperature compensated and standardized for shunt calibration. This transducer is capable of being flush mounted in a $\frac{3}{4}$-inch thread size boss. Its resonant frequency is 25 to 40 kHz.

Quartz crystals, utilizing the piezoelectric effect, can be adapted to a flush-mounted configuration and ranged for any desired signal level. The main drawback to using these transducers is the requirement for maintaining a high output impedance to ground. Connector contamination is the main reason for the lowered output impedance which affects the transducer sensitivity, low-frequency response and in many cases causes the transducer to saturate with the ultimate loss of data. Care must be taken to keep all connections dry and free from contaminants.

CRYOGENIC TEMPERATURE REGION:

Measurement of feed system dynamic pressures in the cryogenic region impose a new set of problems. Bonded wire strain gages exhibit radical shifts in both sensitivity and zero in the extreme low temperature liquid hydrogen region and are of questionable use for this application. Early attempts were made to adapt semiconductor-type strain gages to this region of measurement with similar results. Some of the shifts were as great as 100% in sensitivity and/or zero at liquid hydrogen temperatures. Recent attempts utilizing heavily doped* semiconductors have resulted in the development of a transducer whose sensitivity and zero shifts are less than 1% per 100° F from ambient to the liquid hydrogen region. It is designed to adapt to a $\frac{1}{4}$ inch AN fitting and has a resonant frequency in excess of 100 kHz, see Fig. 9.3.2k.

The Kistler transducer discussed previously is also useful in the cryogenic region. Although there are some zero shifts associated with the transducer in this regime, sensitivity shifts are less than 2% per 100° F. The major problem in its use, as was discussed previously, is a low output impedance to ground. This low output impedance is mainly due to the extremely cold temperatures causing the connector to absorb moisture. This can be successfully controlled by taking proper care to protect the cable connection to the transducer at the time of installation.

A third type of transducer for use in the cryogenic region is the water-conditioned Photocon. This is different from those used in the hot gas measurement in that the area in between the two diaphragms has a dead air space. Water is circulated through the transducer body, but not the diaphragm area, to condition the electronics which are susceptible to severe drifts with temperature changes. By maintaining the electronics at a constant temperature through water conditioning, this drift and resultant sensitivity shift is minimized. Also by eliminating water from the diaphragm area the earlier problem of freezing such water and splitting the diaphragm is eliminated.

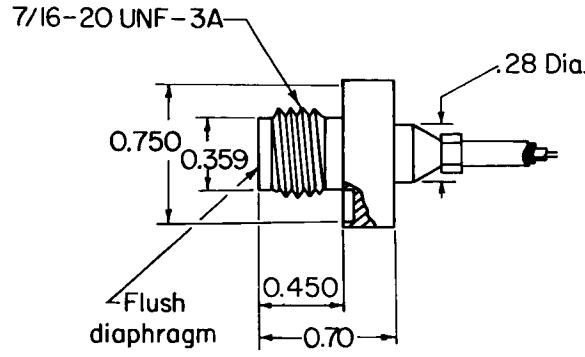

FIGURE 9.3.2k.—Miniature dynamic cryogenic pressure transducer (EOS model 101003-0134).

As can be seen, there is a wide variety of transducers for use in propellant systems, both in the ambient and cryogenic temperature regimes. The selection is often an individual choice which may consist of matching the signal conditioning available to the test stand, or of matching specific test objectives.

9.3.3 Location and Mounting*

The location of pressure transducers within a combustor is an important consideration in diagnosing resonant combustion instability modes. A single transducer is generally sufficient to detect the presence of resonant combustion instability but, as will be discussed in Sect. 9.7, the positive identification of resonant modes requires multiple transducers which are properly located to provide the phase and amplitude characteristics of the instability mode. Along with the location, mounting techniques play an important part in the quality of data acquisition. The proper analysis of combustion instability requires that frequency, phase and amplitude information must all be accurately detected and transmitted by the transducer.

9.3.3.1 Transducer locations.—The location of transducers should be chosen so that any acoustic resonance of the combustor cavity can be positively identified by the instantaneous phase and amplitude data. This can generally be accom-

* Doped as used here is the impurity which is diffused into the semiconductor. The heavily refers to the concentration of the impurity. With very heavy concentrations of the impurity, in many cases Boron, the gage factor of the resulting strain gage remains relatively flat with temperature allowing their use in the cryogenic regions.[625]

* S. Rogero, R. D. Wesley, and R. J. Hefner, Authors.

plished in the larger heat-sink combustion chambers, where typically only the cost and the possibility of structurally weakening the chamber limit the number and location of transducers. With nearly all prototype combustion chambers, however, the type and locations of transducer mounts is severely limited. For the optimum location of transducers within a heat-sink combustion chamber, consideration should be given to the types of instability likely to be encountered.

The longitudinal mode is characterized by a maximum pressure amplitude at the injector end of the chamber and also in the subsonic portion of the nozzle. For maximum utility the optimum transducer locations to identify this type of instability would be three transducers located in an axial alignment; one near the injector face, one near the sonic throat and one approximately halfway between the injector and throat. The transducer at the mid-acoustic length will record a pressure node or antinode depending upon which longitudinal mode is present (1L, 2L, 3L, etc.). Odd numbered modes (1L, 3L, . . .) will record 180° phase differences on the end transducers, and a nodal point at the center transducer. Even numbered modes (2L, 4L, . . .) will exhibit no phase difference on the end transducers but will have an antinodal point near the center transducer 180° out of phase. It is possible to identify all longitudinal modes with these three transducers by the consideration of phase, relative amplitude and frequency.[35]

For transverse mode identification multiple transducers spaced at various circumferential locations are required. These transducers should be located in a single plane parallel to and near the injector face since there is often significant distortion and/or attenuation of the characteristic waveform with axial position. There is generally no physical restriction, corresponding to the injector face for longitudinal modes, which guarantees the spatial orientation of the transverse waveform, however, the presence of baffles can often result in such positioning. Therefore, no single circumferential pattern of transducers has been found to be optimum for all transverse mode identification. Fig. 9.3.3a illustrates circumferential locations for varying numbers of transducers that have been found to be well suited for transverse mode identification.

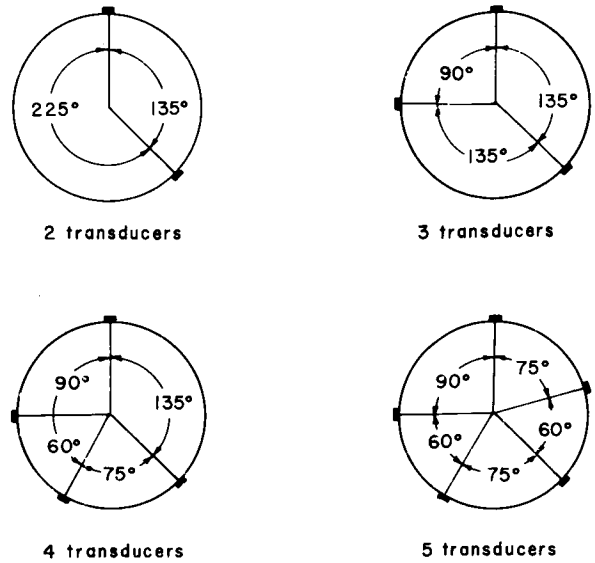

FIGURE 9.3.3a.—Circumferential transducer locations for transverse instability mode identification.

The phase and amplitude of a radial mode are the same at all points on the chamber wall at a single instant of time. Typically the transducer locations selected for transverse and longitudinal mode identification are adequate to detect this characteristic. The frequency is the only characteristic that is available to distinguish among the various radial modes.

As indicated, the number and location of pressure transducers to be used with a heat-sink chamber is flexible and should be selected based on considerations outlined above. For other types of chambers, however, both the number and permissible locations are quite limited and are typically restricted by structural limitations.

9.3.3.2 Mounting considerations.—The severe environmental conditions associated with high frequency combustion instability place stringent requirements on transducer location and mounting considerations. High heat transfer rates and vibration levels make difficult the task of designing environmental protection that will not seriously compromise the quality of high frequency pressure measurements. As often as not the design of environmental protection and analysis of its effects on transducer characteristics may be the major concern in the selection of a high response

pressure measuring system for use in instability studies.

A prime objective in mounting a transducer in a combustor is to have the sensing diaphragm flush with the chamber wall. Any recess between the combustor cavity and the diaphragm will have resonant characteristics of its own which may significantly affect the data recorded by the transducer. This is particularly true for higher frequency data or where accurate wave shape or phase angle determinations are required.

Recessing of pressure transducers can also affect the heat-transfer characteristics at the transducer and may even alter the stability characteristics of the combustor. The effect of recessing on the thermal characteristics may be either to increase or decrease the flux to the transducer as will be discussed later. The resonant characteristics of the recess may act as an acoustic absorber which could alter absorptive characteristics of the combustor and, thus, the stability characteristics of the engine.

ACCELERATION EFFECTS: Additional complications may be encountered in mounting because of the high vibrational environment imposed upon the transducer by a combustion instability.[151] The vibrational levels associated with high frequency instability in some rocket engines may be in excess of 1000 g.[433,597] Such extreme conditions may produce varying degrees of damage to the transducer or erroneous data due to acceleration sensitivity. In recent years transducer design has improved to the extent that the effects of acceleration on pressure transducers have been greatly reduced. Considering the severity of the conditions, however, the magnitude of these effects should always be determined in new or unknown test situations.

One of the best methods for measuring the effect of vibrational acceleration on the output of a pressure transducer is to monitor the output of a transducer whose sensing diaphragm is isolated from pressure during a firing. The transducer is otherwise installed in a normal manner. Such testing is illustrated in Figs. 9.3.3b through 9.3.3d. In the first figure the blanked transducer is seen to exhibit a higher amplitude output, following the pulse, than the normal transducer. Subsequent analysis of the blanked transducer revealed a loose coil. In such a situation the transducer tested obviously exceeded the manufacturer's specification of 0.002% fs/g. Fig. 9.3.3c illustrates measurements taken with both transducers operating properly. Even this amount of vibration sensitivity can prove objectionable with extremely high vibrational environments

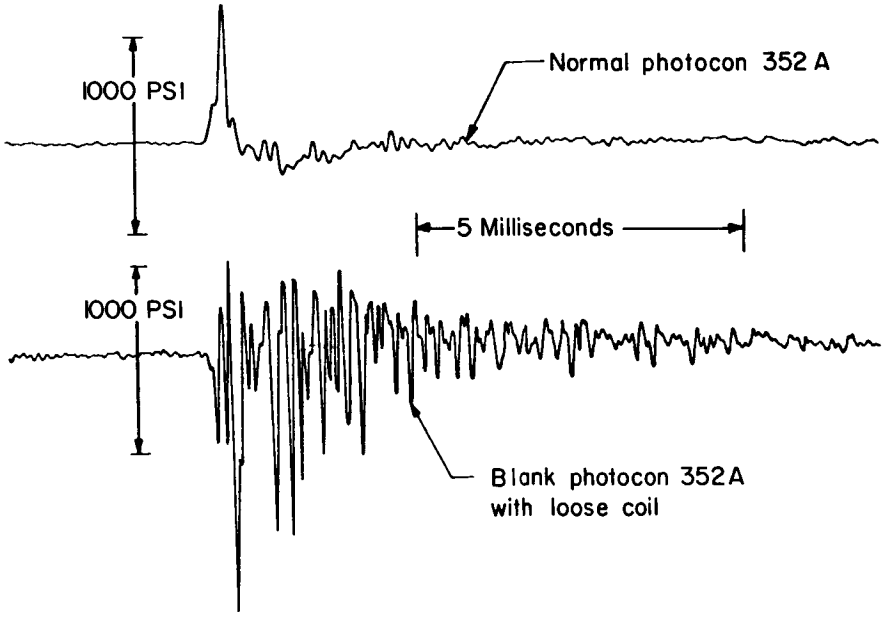

FIGURE 9.3.3b.—Vibration output of defective photocon 352A.

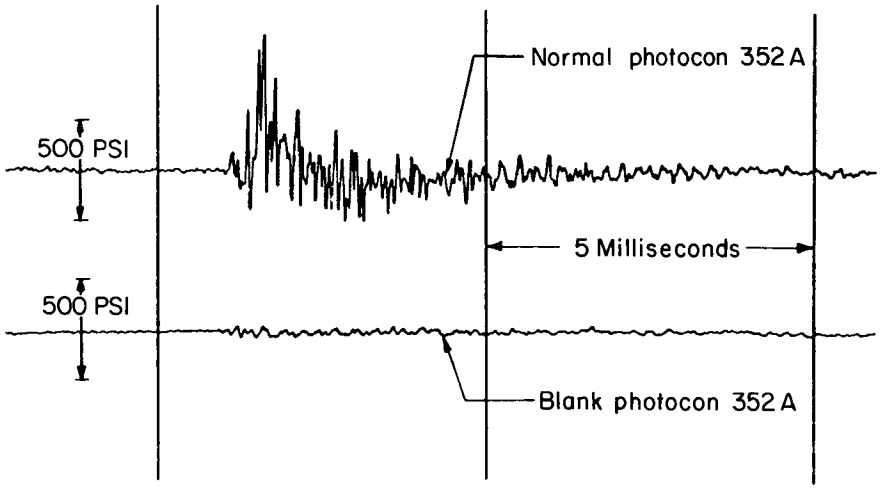

FIGURE 9.3.3c.—Vibrational output of properly operating photocon 352A.

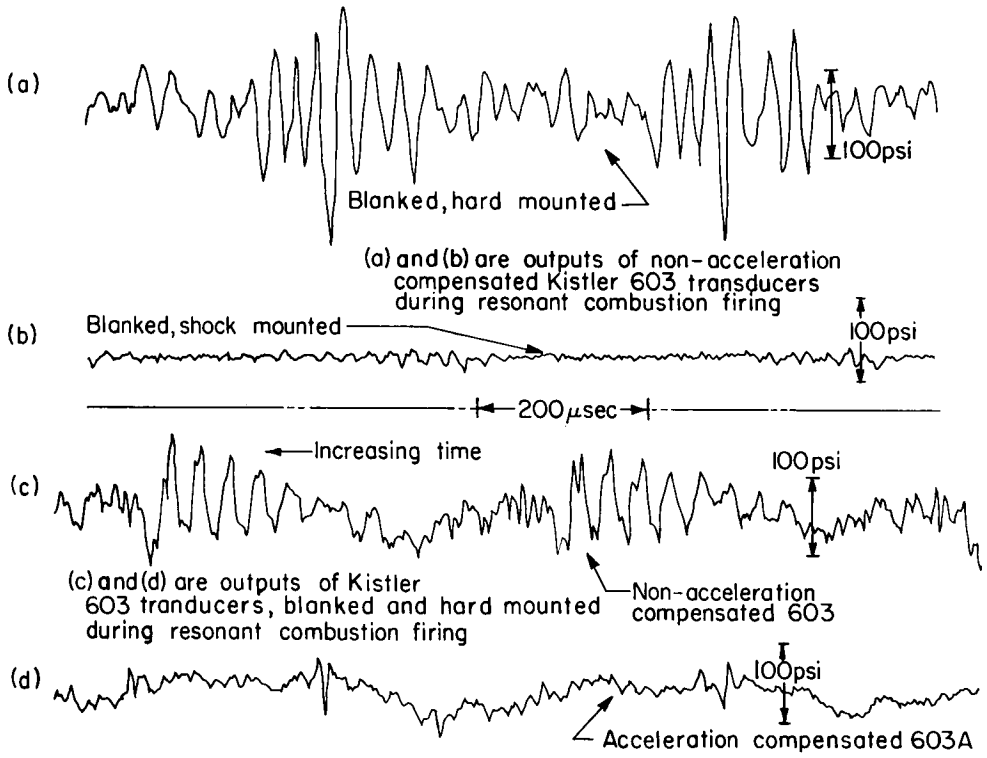

FIGURE 9.3.3d.—Acceleration effects in the output of Kistler 603 transducers.

when amplitude ratios and phasing are critical. In such instances it may be desirable to use acceleration compensated transducers or to shock mount the transducer.

An example of an evaluation of various techniques for reducing the acceleration effects in the output of pressure transducers is shown in Fig. 9.3.3d. The top two traces are the outputs of two Kistler Model 603 transducers recorded during instability. Neither transducer had any internal

acceleration compensation features, both had their diaphragms blanked and saw no pressure. The transducer whose output is shown in trace (a) was hard mounted whereas that shown in trace (b) was shock mounted.[151,596] In this instance shock mounting reduced the output due to acceleration by a factor of ten over the hard-mounted transducer. Traces (c) and (d) illustrate the benefits of built-in acceleration compensation. In this case both transducers were rigidly mounted to the chamber wall with their diaphragms blanked from pressure. Internal acceleration compensation reduced the output due to acceleration by a factor of three over the noncompensated transducer.

Although acceleration effects are usually minimized by the use of properly designed shock mounts, the particular application often dictates which technique should be employed. The complications associated with shock mounting transducers as shown in Fig. 9.3.3e may not be warranted if the acceleration levels are low or the effects not objectionable. Another consideration may be the occasional loss of frequency response attendant with some non-flush, shock-mount configurations.[596] Whatever configuration is finally decided upon it should be evaluated under test conditions. If the vibration effects are to be eliminated they must be prevented from becoming mixed with the pressure data. Once the two have been combined they are almost impossible to separate.

HEAT TRANSFER EFFECTS: In addition to the influence on frequency response, if the transducer is slightly recessed, the swirling action at the edge of the transducer hole will cause the chamber to erode around the transducer. This erosion, if allowed to continue, will soon cause the transducer to fail. Any protrusion of the transducer into the hot gas stream will have a similar erosion effect starting on the edge of the transducer. Once metal has started to flow, severe erosion and subsequent transducer failure is imminent.

In a flush installation the transducer will be subjected to heat-transfer rates which produce effects ranging from slight thermal drift to complete diaphragm burn through. Many of the available transducers utilize cooling or insulating techniques which affect the transducer response; some to the extent that they render the transducer worthless for making high response measurements. Uncooled transducers, such as the Kistler, can withstand added heat for only very short durations prior to burnout unless protected, although a carefully designed thermal barrier can provide maximum protection with minimum loss of frequency response. For these reasons the effects of thermal protection on the transducer's ability to measure pressure must be determined.

A considerable amount of work has been done by various investigators in the use of ablative material over the diaphragm of the transducer. This is accomplished by recessing the transducer diaphragm (recesses of a few thousandths to an $\frac{1}{8}$ inch have been used successfully[36]), and filling the cavity with a material such as silicone rubber (e.g., G.E. RTV 580). Care must be taken to first prime the surface, and to apply the RTV to the diaphragm so that no voids or irregularities are present in the application of this ablative material. Ablative protection can extend considerably the exposure time of the transducer diaphragm before damage occurs.

There is some effect on the resonant frequency of the transducer because of the RTV coating. The effect is minimal with very thin coats and does not alter the data appreciably. A 0.020-inch-thick coat of RTV on a Kistler diaphragm reduced the resonant frequency approximately 25%[36] (400 down to 300 kHz).

Figure 9.3.3f illustrates how various types of diaphragm protection affect thermal drift rates during bomb initiated instability firings. For purposes of comparison the entire chamber pressure run record has been compressed to better illustrate the thermal drift. Instantaneous heat-transfer measurements were not made, but were probably on the order of 50 Btu/in.^{2}/sec, sufficient to burn through a $\frac{3}{4}$-inch-thick steel chamber wall in less than 1 second. These records were played back from analog tape through a 1 kHz filter to eliminate unimportant (in this instance) high frequencies. Trace (a) is the output of a Kistler 603A transducer that lost its 0.060 inch coating of RTV 580 during instability. The change in drift rate just before firing termination is quite apparent. Trace (b) shows a drift rate on the order of 0.2 psi/msec throughout the entire period of instability. This rate, typical of those measured when the ablative coating remained intact, is

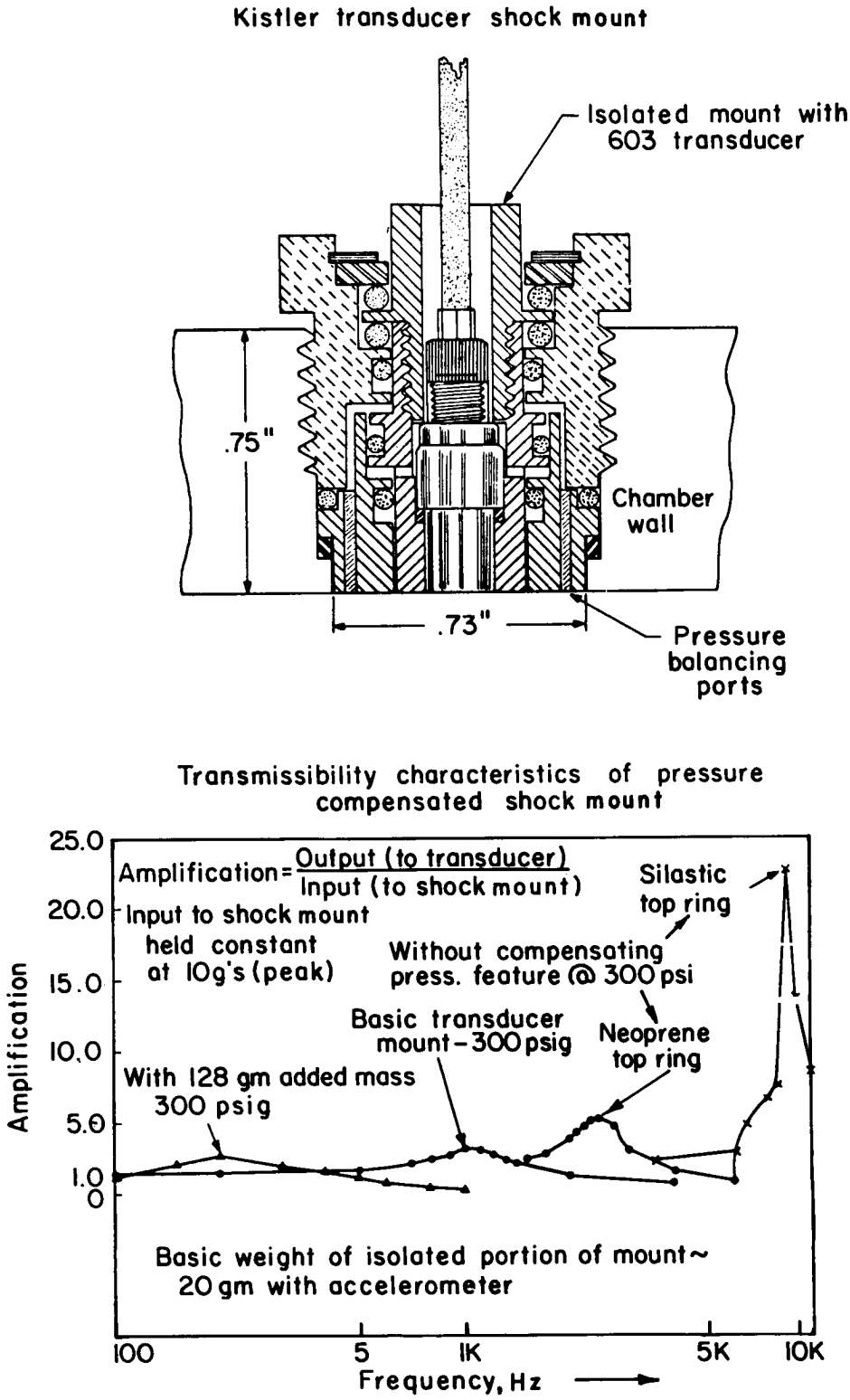

FIGURE 9.3.3c.—Design and performance of shock mount and transducer.

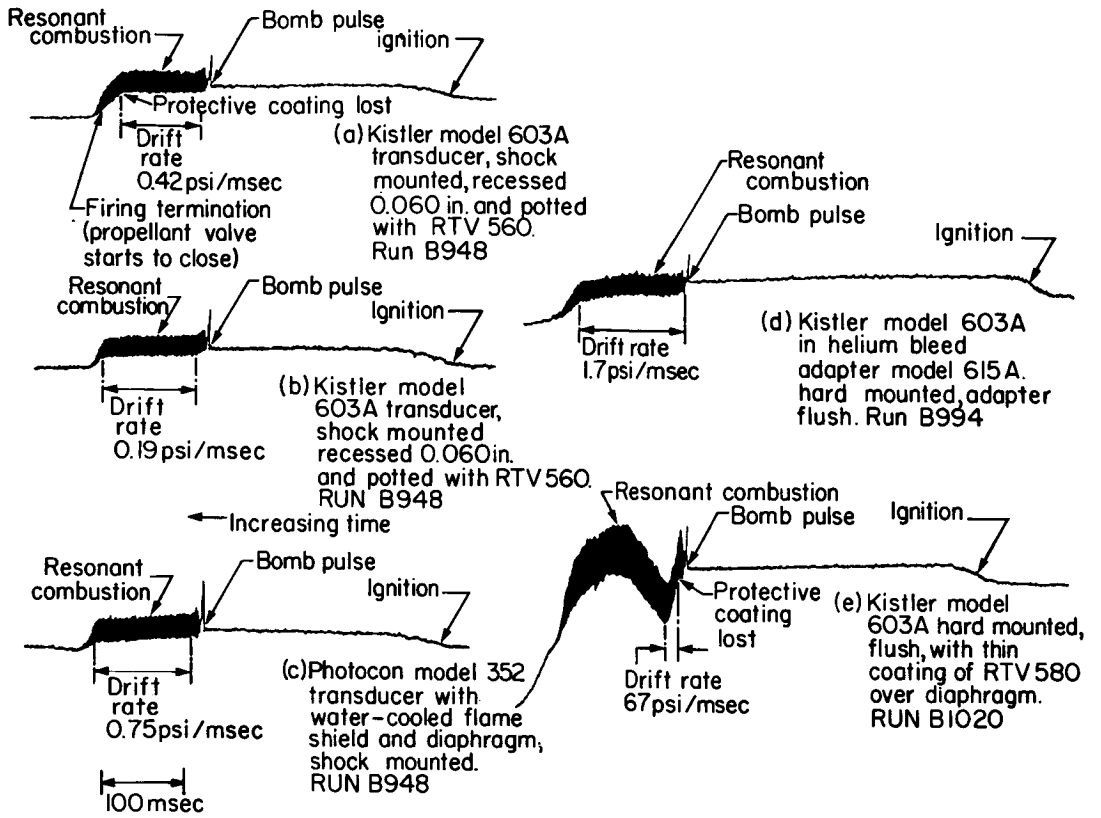

FIGURE 9.3.3f.—Comparison of transducer thermal drift rates during combustion instability.

quite good when one considers the severity of the environment. Trace (c) shows the output of a Photocon 352A transducer with water-cooled flame shield and diaphragm. Its drift rate prior to the start of instability is lower than that of the ablative coated transducer, but during instability is higher than the uncooled transducer. Trace (d) shows the output of a Kistler 603A transducer mounted in a helium bleed adapter (Model 615). The drift rate here, while not objectionable, is considerably higher than that of previous conditions. The reason is probably that the transducer diaphragm, although cooled, still sees a great deal of heat due to radiation. In even a short duration firing the radiation effects are significant and the thermal sensitivity can be greatly improved by the application of a thin coating of ablative or ceramic material. Helium-cooled transducers have the advantage of being able to withstand significantly longer duration firings than the ablative protected type. Trace (e) is the output of a 603A transducer mounted flush with the inside chamber wall. A thin coating of RTV 580 (less than 0.010 inch average thickness) was spread over the transducer diaphragm. Needless to say, the drift rate was high, but even here it is evident when the coating left the diaphragm. Prior to that point the drift rate appears to be acceptable. In an application where maximum frequency response is required, this type of installation could be used to obtain data in the early portion of a firing.

A few basic guidelines to the improvement of heat transfer characteristics can be summarized as follows:

1. If the transducer has a double diaphragm with internal water cooling, the outer or exposed portion of the diaphragm should be smooth—to minimize erosion by high velocity, hot gases. The use of such techniques as nickel-gold brazing or electron beam welding of diaphragm to internal passages[220] is often desirable.
2. Cooling water pressure should be kept high,

the only practical limit being the strength of the cooling passages or the point at which flow rates begin to produce noise.

3. The diaphragm should be protected from heating effects caused by radiation as well as conduction. A thin coating of ablative or ceramic material will usually accomplish the desired effect without significantly affecting frequency response.
4. If one of the RTV compounds is used, the cavity surfaces should be carefully primed and the RTV material applied in such a manner as to prevent voids. Poorly applied ablative material is of little value. As an additional safeguard against dislodging relatively thick ablative coatings during instability, the cavity can be slightly undercut at the diaphragm end.[36]
5. The technique of compressing firings into periods of substantially less than one second with useful combustion information available within 100 msec after ignition will greatly reduce the time the instrumentation is exposed to the severe combustion environment and its damaging effects. When these firing procedures can be employed, significant simplification of the environmental protection will result.

The importance of temperature sensitivity on data is influenced largely by the use to which the data will be put as well as the type of sensitivity the transducer exhibits. For instance, if dc or steady-state values are not required, thermal drift rates may be of no concern at all. If they are of interest and the drift rate is known they can be corrected. Certainly of greater concern is whether or not there is a change in the output sensitivity due to temperature. A significant change of this type can render high frequency data worthless. Fortunately, many of the high response transducers available show negligible output sensitivity change with temperature, although they may exhibit considerable zero drift under certain conditions. It may be true, therefore, that thermal effects are either unimportant or in some cases easily eliminated, but in all instances they must be considered.

9.3.3.3 Special mounting techniques.—It is often necessary to measure dynamic pressures when normal transducer mounting cannot be employed. Several specialized transducers and mounting techniques have been developed for such cases. For example, the small passage, helium bleed transducer described in Sect. 9.3.2.1 was developed to fit between adjacent tubes of a regeneratively cooled combustion chamber.

Mounting through the injector flange is another technique that can be used if space is available. Again it is usually a specially designed transducer for a particular application. This type of application is illustrated in Fig. 9.3.3g. In this case a boss was adapted to the injector flange through the outer fuel channel of the injector. The transducer shown in the boss is a helium bleed type with a 25 kHz resonant frequency. Measurement response is flat $\pm 10\%$ to approximately 10 kHz without any electrical compensation. With electrical compensation it is possible to maintain a flat response to 20 kHz. A measurement of this type can be made with any type of combustion chamber since the measurement location is made in the injector flange.

Recent advances in the heat transfer capabilities of water-cooled pressure probes now permit the measurement of high frequency pressure variations throughout the combustion volume (rather than only at the wall). Figure 9.3.3h illustrates two internal rocket motor probes designed and built by Greyrad Corporation[19] for a JPL combustion instability program. The probes can be adjusted within their adapters to measure high frequency pressure variations at locations $\frac{1}{2}$ inch to $5\frac{1}{2}$ inches from the inside of the chamber wall. Thermal protection is provided by high water flow rates through inner and outer tube bundles. Approxi-

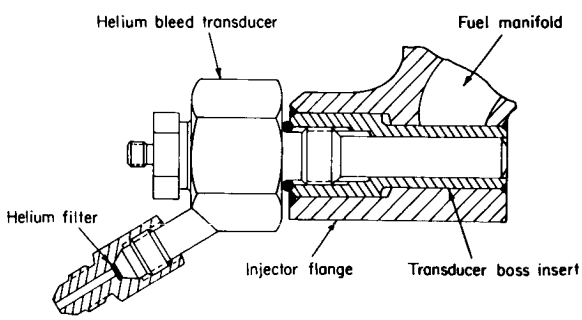

FIGURE 9.3.3g.—Typical transducer mounting through injector flange.

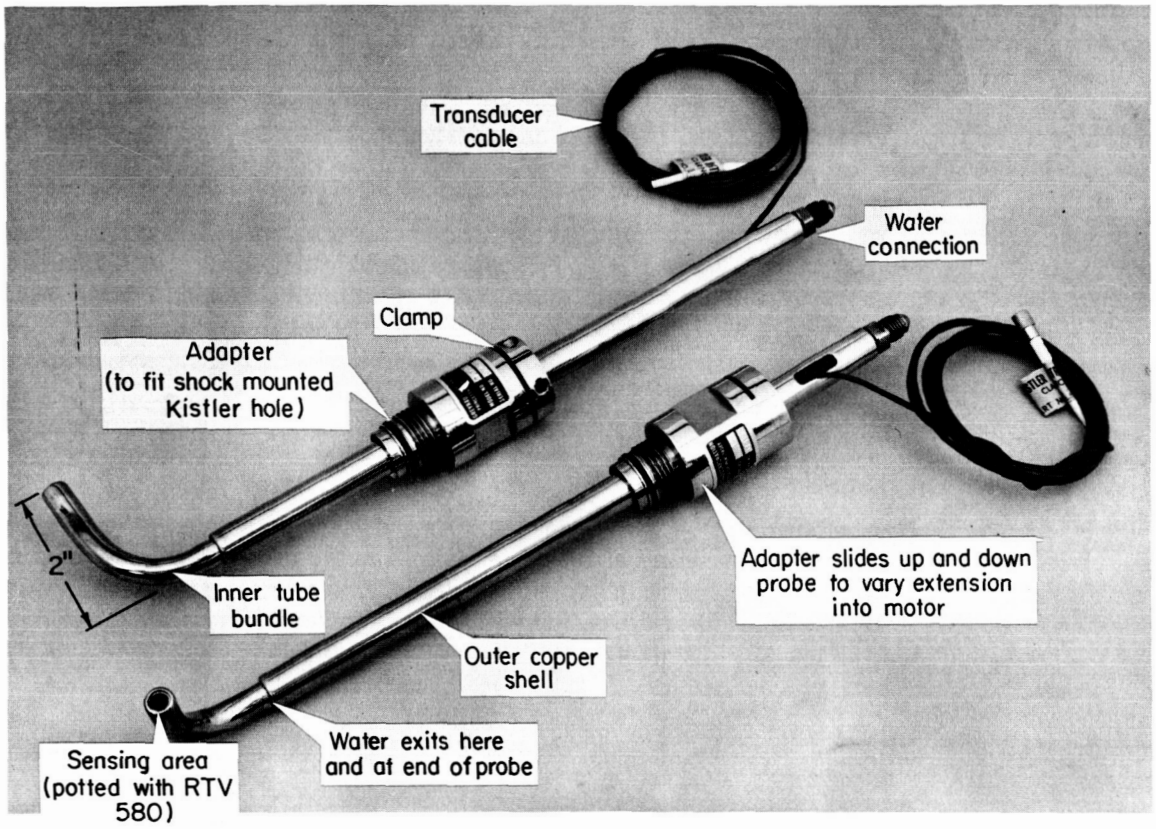

FIGURE 9.3.3h.—Internal rocket motor probe.

mately half the water is used to cool the outer tube bundle and exits above the 90° bend in the probe. The remainder is forced across the sensing area of the transducer (Kistler Model 603A) and out into the motor chamber. In addition to the water cooling there is a 0.020 inch coating of RTV 580 on the transducer diaphragm to provide previously discussed protection against thermal radiation.

9.3.4 Signal Conditioning and Recording*

The instrumentation system is only as good as its weakest link and in many instances of dynamic instrumentation this is the signal conditioning equipment or the recorder. In the discussion of dynamic pressure instrumentation the emphasis is usually placed on the transducer. For instance, the transducer will be quoted as having a resonant frequency of 100 kHz with a flat frequency response of 20 kHz and the assumption is that this is the quality of the measurement. Although the quality may very well be as quoted, often the signal conditioning system or the recorder is incapable of meeting the response required.

9.3.4.1 Signal conditioning.—To accommodate the transducers previously discussed any one of four types of signal conditioning systems is required. These are (1) the strain gage system (constant voltage), (2) the strain gage system (constant current), (3) the dynagage capacitance system, and (4) the charge system. Each has its own peculiarities but there are some general considerations which must be taken into account in all of the systems if acceptable data are to be obtained. For purposes of this discussion the signal conditioning is that portion of the system from the transducer to the recorder, including the transmission cable and all intermediate elements.

Frequency response has been discussed for the

* R. D. Wesley, Author.

transducer. Response is also important in the signal conditioning.[36] In the strain gage system the length of transmission cable from the transducer to the amplifier and/or recorder will have a pronounced effect on the frequency response. Multiconductor cables are the accepted transmission methods for strain gage systems and are quite satisfactory as long as certain precautions are taken in utilizing the data from the system. The frequency response is quite poor with long transmission lines. This is due primarily to the cable capacitance but it is also affected by the transducer output impedance. Frequency response of a given system can be calculated if the cable capacitance is known; however; a measurement of the responses will verify the system as installed.[596]

The normal strain gage system which has a cable length of 500 feet and more is totally unsatisfactory since at 10 kHz the output will be only 50% or less than the cable input. This can be overcome by installing wide band differential amplifiers as a buffer near to the transducer.[16] With the proper selection of cable type (low capacitance) and location of the amplifier, a usable system can be installed for the acquisition of dynamic data.

With the Photocon dynagage system, coaxial cable (RG-8U or a similar type) is required. If installed as specified by the manufacturer, maximum frequency response and linearity will be realized from the system. Since neither the Photocon transducer or the associated electronics are standardized, each transducer must be calibrated with the dynagage and channel used to record data to obtain correct sensitivity factors.[732] This generally requires that the calibration be made on the test stand with an accurate external pressure source over the full scale transducer range. Unless this is done, measurement errors of system sensitivity could be 25% and greater.

It is possible to make measurements from crystal transducers with either a high impedance voltage amplifier or a charge amplifier. With the voltage amplifier the voltage sensitivity of the transducer is inversely proportional to the total capacitance.

$$E = 1000 \frac{Q}{\mathcal{C}_t + \mathcal{C}_c}$$

where

E output voltage (mv/psi)

Q charge sensitivity (picocoulomb/psi)

$\mathcal{C}_t$ transducer capacitance (picofarads)

$\mathcal{C}_c$ cable capacitance (picofarads)

As cable length is added the capacitance increases and the sensitivity decreases. It is therefore recommended that the high impedance voltage amplifier be mounted as close as possible to the test item, so that the transducer sensitivity may be kept at a high level.

In using the charge amplifier the charge sensitivity of the pressure transducer can be used directly. Cable lengths have little or no effect on the transducer sensitivity, although there is some effect on response.[151] If possible, cable lengths between the transducer and the charge amplifier should be kept to a minimum, especially if extremely high response is required. Longer cables will also have a higher system noise level making it difficult to read low level signals. The use of low noise cable is recommended for all installations especially those with long cable runs (greater than 100 feet).

Advantages of charge amplifiers over high impedance voltage amplifiers include the following factors:

1. Cable capacitance effects on sensitivity minimized
2. Less susceptible to noise
3. Possibility for low frequency response

System noise is prevalent in all installations and every precaution should be taken to subdue it. Having central recording facilities remote from the test stand can add untold problems. Some of these noise sources are listed here:

1. Ground loops due to improper grounding
2. Transmission noise due primarily to improper shielding
3. Power or high voltage line interference
4. Cable generated noise because of cable vibration

Ground loops are due to circulating currents through measurement circuits. The cause is usually that of more than one ground in the system. To eliminate this situation the measurement system should be grounded in only one place. This is usually at or near the recorder. System designers should consider the best ground point for each installation.

All cables should be shielded and grounded to

eliminate interference (noise) from stray fields.[36] This is especially true in low level input systems. Electrostatic shielding is provided on commercially available cables by using braided copper, spiral wrapped copper, wrapped aluminum foil and wrapped aluminized mylar. The better materials for high frequency shielding are aluminum foil and aluminized mylar which achieve an effectiveness of nearly 100% against electrostatic noise when properly installed.

Magnetic fields can be effectively eliminated by providing an additional high permeability outer shield over the electrostatically shielded cable. Another way is to run the electrostatically shielded cables in heavy-wall steel conduits. All shields should be terminated but only at the system ground point.

Power line or power components are a prime source of system noise. The power lines can act as transmitter of externally generated noise or they may introduce the power line frequency into other circuits through power line ground loops. Power components such as motors, fluorescent lights, heating equipment and welding equipment are all common noise generators. To eliminate the effects of noise transmission via the power lines it may be necessary to add shielded line isolation transformers at the power input. Most present day instrumentation components contain shielded power transformers which may make the isolation transformer unnecessary.

Cable noise by vibration during a test is common, especially in the piezoelectric and capacitance transducers. Localized electrostatic charges can be generated by the relative movement of shield, dielectric, and inner conductor during flexing. Specially constructed "low noise" cable has been effective in reducing this noise by an order of magnitude.

9.3.4.2 Recording of dynamic data.—Considering the type of data that is required for combustion instability, the methods of recording are very limited. If any detailed analysis is to be performed on the data it must be recorded such that it is readily available in its raw form to various types of analysis equipment. FM analog magnetic tape recorders are ideal for this type of data handling.

Since the interest involves frequencies which extend to 20 kHz and above, the recorder must possess this capability. The industry has progressed rather rapidly in the improvement of FM tape records, so that 80 kHz is now easily obtained, and many manufacturers are, indeed, furnishing this capability in their FM tape recorders.[35]

This higher frequency response is most desirable when recording steep-fronted waves. Use of the tape recorder in the direct (AM) mode, although the response is 500 kHz, is not recommended. The channels are neither as stable nor as easy to use as the FM channels and the noise level is significantly higher.

Recordings can adequately be made with either 14 or 32 tracks on a 1 inch tape. All recording heads should conform to the IRIG format which has become an industry standard.[25] When recording the higher frequencies, 20 kHz and above, it may be desirable to make dynamic checks on the heads of the recorders being used to account for phase shifts due to head stack variations. This is especially important when different tape machines are used for recording and reproducing.

FM tape recorders generally have a ± 1.4 volt input capability. It is always a good practice to utilize the full dynamic range. If it is desired to look at the entire profile of a test, the signal should be recorded without high pass filtering so that the start transient, shut-down and steady-state are available in an absolute pressure sense. In this type of recording it is well to offset or bias the signal to a negative 1.4 volt, and range such that the full scale pressure is near a positive 1.4 volt.

Usually when making stability measurements the prime interest is in the AC portion of the data. In many instances this can be as little as 5% of the static level. To improve the dynamic signal on tape, a common technique is to filter out the DC portion of the data. This can be accomplished with an RC filter, taking care to keep the corner frequency well below the data frequency of interest. Any insertion losses in the filter may be accounted for by calibrating with the filter in place, using an AC calibration voltage at a frequency lower than that of the expected data, yet higher than the region which is affected by the filter roll-off. This has two basic advantages: (1) the AC data can be ranged for optimum scaling on the tape, and (2) zero shifts due to transducer heating or other causes do not affect the dynamic recording. Zero shifts can be very large and in many instances have driven channels

out of tape band limits when the recording is being made in the DC mode. Since the high frequency transducer is not basically an absolute measuring device, little information is lost by high pass filtering the data prior to recording on tape.

9.3.5 Display Techniques*

A wide variety of data presentations is available, with varying degrees of sophistication. These extend from the presentation of raw data, which leaves the engineer to interpret and make hand calculations, to completely machine-analyzed data which is presented in reduced form.

There are four logical methods of handling data. Each presents the basic information in a unique way to aid in the analysis of combustion instability data. The methods are, of course, not limited to only the analysis of combustion instability, but rather apply to the general category of all dynamic data analysis. It is the intent to acquaint the reader with the many tools available to him so that he might select the most meaningful presentations in the solution of any given problem. The four methods or types of data processing operations are (1) analog playback, (2) analog spectrum analysis, (3) hybrid spectrum analysis, and (4) digital analysis. Each operation utilizes given types of equipment and leads to a variety of data presentations as shown in Fig. 9.3.5a. It is the intent here to show the different processing operations available with a brief description of the resultant presentation method. In each case it is assumed that the data is available on FM tape, which has been properly recorded, utilizing signal conditioning systems and transducers capable of defining the frequencies to be analyzed.

9.3.5.1 Analog playback.—Analog playbacks of dynamic data, due to their oscillatory nature, require a maximum parameter-limitation of 6 to 8 individual functions for a 12-inch oscillograph paper width. It is therefore important to group functions for ease in instability mode identification. All parameters on a single axial plane should be grouped on the same record. With this record it is possible to identify a tangential mode. For longitudinal mode identification, transducers spaced longitudinally along the combustion chamber must be used. Again, if placed on the same record, identification is accomplished more easily. It is possible to work between records as long as an identifier channel is carried as a common function on all playback records.

It is desirable to look at all recorded data in its raw form–that is, as it has been recorded–in order to ensure that further analysis is performed only on valid data. This is normally referred to as a "quick look" record which is accomplished by using tape speed reduction and playing the data back to an analog recorder that has sufficient response to accurately present the recorded data. As an example, 10 kHz data could be accurately reproduced on an oscillograph which has 2500 Hz galvanometers with a 4:1 tape speed reduction. All that remains is running the oscillograph at sufficient speed to adequately review the data. The type of testing being performed will help to establish this; generally, an effective speed which allows one to count predominant frequencies is sufficient for a first look. For 10 kHz, under the above ground rule, an effective speed of 400 inches/second would be sufficient. This could be accomplished on an oscillograph run at 100 inches/second with a tape speed playback reduction of 4:1.

In many instances where the run is longer, a much slower effective speed may be sufficient as a quick look to determine the general quality of the data and areas of interest for further types of analysis. A direct-write device is recommended since time is often a factor in development testing. Several good direct-write oscillographs are on the market, with speeds up to 160 inches/second and high frequency response (recording light beam) galvanometers. A direct-write stylus recorder can be used, however, the galvanometer response is low (under 100 Hz) and a very high ratio of tape speed reduction would be necessary to obtain a 10 kHz frequency response. It should be noted that large tape speed reductions degrade the signal-to-noise ratio of the data (because of wow and flutter problems encountered in some tape equipment) but are satisfactory unless the data level is near the system noise level.

After a review of the originally recorded data, many options can be exercised for further data presentation on the oscillograph. Some of these

* R. D. Wesley and R. F. Hefner, Authors.

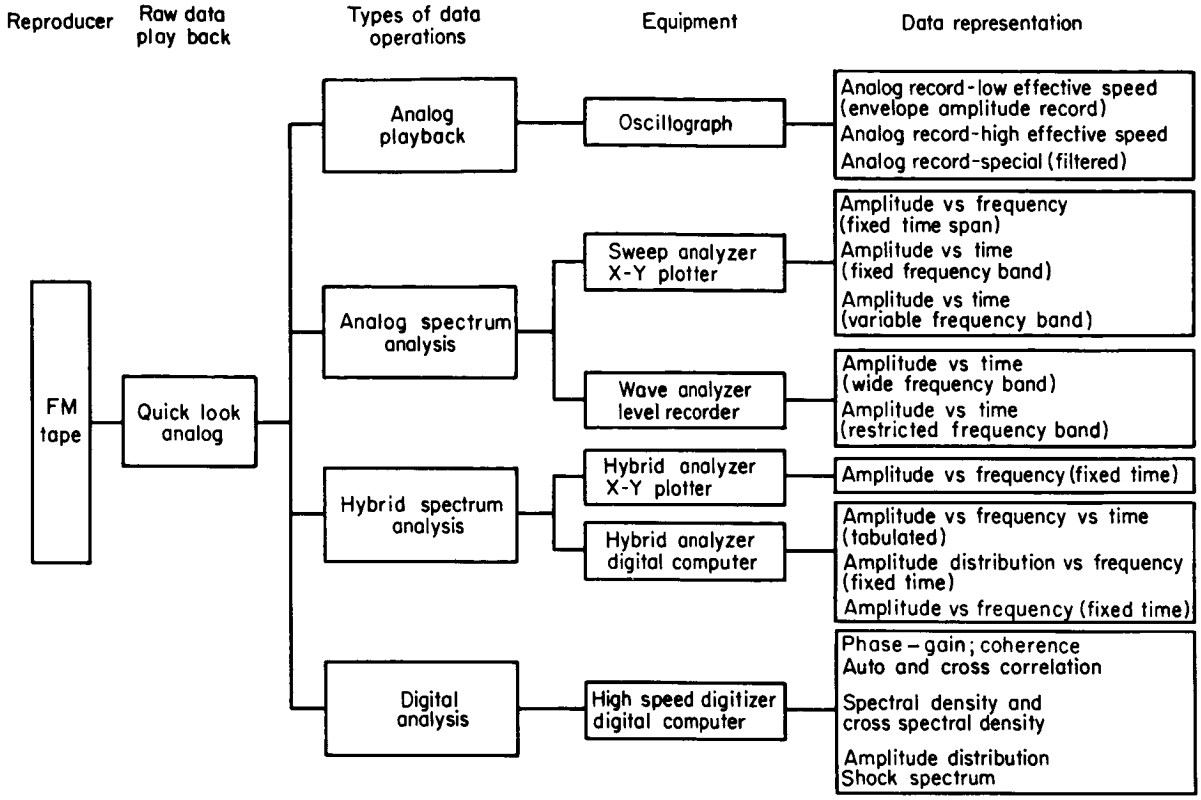

FIGURE 9.3.5a.—Typical data reproduction presentation methods.

are:

LOW EFFECTIVE RECORD SPEED (ENVELOPE AMPLITUDE RECORD): With this type of presentation, the pressure envelope can be determined over an entire run with a short record, usually 4 to 10 inches/second. This is especially useful on a single frequency and is accomplished by either bandpass, high pass, or low pass filtering, whichever is most appropriately and easily applied to the data being displayed.

HIGH EFFECTIVE RECORD SPEED: Many different speed combinations are possible with the wide variety of tape and oscillograph speeds which are available. The important point to remember is to keep the playback system frequency response compatible with the data being reproduced. As an example, if one is interested in determining the phasing characteristics of 5 kHz data between variously oriented transducers in a combustion chamber, an effective galvanometer response of 10 kHz and effective record speed of at least 2000 inches/second is desirable. This allows 0.4 inch/cycle, which is sufficient to determine phase angles for mode identification. If one is considering a single frequency mode, the playback can be accomplished without filtering and eliminates the associated filter considerations. If phase-amplitude analysis is to be accomplished on a complex mode, it may be necessary to isolate an individual frequency by filtering to make identification of the combustion instability mode possible. Extreme care must be taken when filtering data so that the original data integrity is not destroyed.

Since the high effective speed records use a considerable amount of paper, and a continuous record would present more data than it is possible to analyze effectively, it is a standard practice to reproduce, at high speed, only selected portions of the test as established from the quick look record. The recording of a time code channel is recommended for positive position location on the tape with a minimal effort, especially on longer tests.

ANALOG FILTERING: Special records are

often made through analog filters in order to separate the frequency components in a complex mode or to eliminate noise. Problems can be encountered with the analog filtering due to filter roll-off and ringing. Filters range from the simple passive RC type to the more complex multi-order active filters. It is not intended that a complete discussion of filters be included here, other than to indicate types available and special usage.

It was previously mentioned that it is desirable to high pass filter when recording on FM tape. In data reproduction it is best to use a multiorder active filter. Since the order of the filter determines the roll-off characteristics, a high order (generally 6) is desirable. A higher order filter produces a greater attenuation above the cut-off frequency.

Phase shift is another serious consideration when filtering data, especially if the phase shift through a number of filters is different for the same input conditions. This however, can usually be specified when purchasing a filter for delivery to acceptable limits. The optimum type of filter to use–such as Butterworth, Chebyshev, Bessel, or Linear Phase–will depend on the type of analysis to be performed after the data is filtered.[313,438,502,699] The Chebyshev filter of a given order is a closer approximation to the ideal filter than an equal order Butterworth filter; however the Butterworth filter has flat frequency response without peaking prior to roll-off, whereas the Chebyshev filter has some amplitude ripple and extreme phase distortion. Linear phase filters of which the Bessel type is representative are generally specified when time distortion is a consideration. Fig. 9.3.5b depicts the amplitude and phase characteristics of the filters mentioned.

9.3.5.2 Analog spectrum analysis.—Sweep analysis is performed on equipment in which a relatively narrow, fixed bandwidth filter is swept or incremented slowly through the frequency range of interest. Since the rate of this sweep must be quite slow in order to allow the filter time to respond to changes in the data amplitude, it is the usual practice to select a time period representative of the data and make this sample repetitive by means of a tape loop. The output of the filter is applied to a suitable detector, either true rms for power density analysis of random data, or average-responding for Fourier analysis of deterministic data. The resulting data are plotted on an X-Y plotter.

Several options are possible for displaying this spectral data depending on its end use. Some of the most common are[36]

1. Amplitude vs. frequency (fixed time span)
2. Amplitude vs. time (fixed frequency band)
3. Amplitude vs. time (variable frequency band)

Another approach uses fixed band wave analyzer equipment, represented by the Bruel & Kjaer 2111 Spectrometer and the General Radio 1564 Analyzer. On both of these instruments the data may be passed through either $\frac{1}{3}$-octave or 1-octave continuous filters, or may be unfiltered. The output is usually recorded on a high speed level recorder using a logarithmic (db) amplitude scale.

The principal differences between this class of instrument and the sweep analyzer are in the use of fixed filters whose width is a constant percentage of the analysis frequency rather than a fixed bandwidth, and the use of an associated recorder with much faster capability than the usual X-Y plotter. The relatively wide band filters and high recorder speed permit following much more rapid changes in amplitude than with the sweep analyzer.

As in the case of analog playbacks, a single frequency mode can easily be displayed by a fixed-band wave analyzer to show the rate of decay or increase. It is also relatively simple to calculate the decay rate with only one frequency present. Generally when an instability is induced, multi-frequency components are present. One of the indicators of the combustion stability index is the ability of an engine to sustain and recover from an induced perturbation. If the engine recovers, there will be some damping rate associated with the pulse in that particular engine. Further, each frequency associated with the pulse may have a different damping rate. If a low damping rate is indicated at a particular frequency, further refinements on the hardware may be made concentrating on further damping the given frequency.

Types of presentations include[36]

1. Amplitude vs. time (wide frequency band)
2. Amplitude vs. time (restricted frequency band)

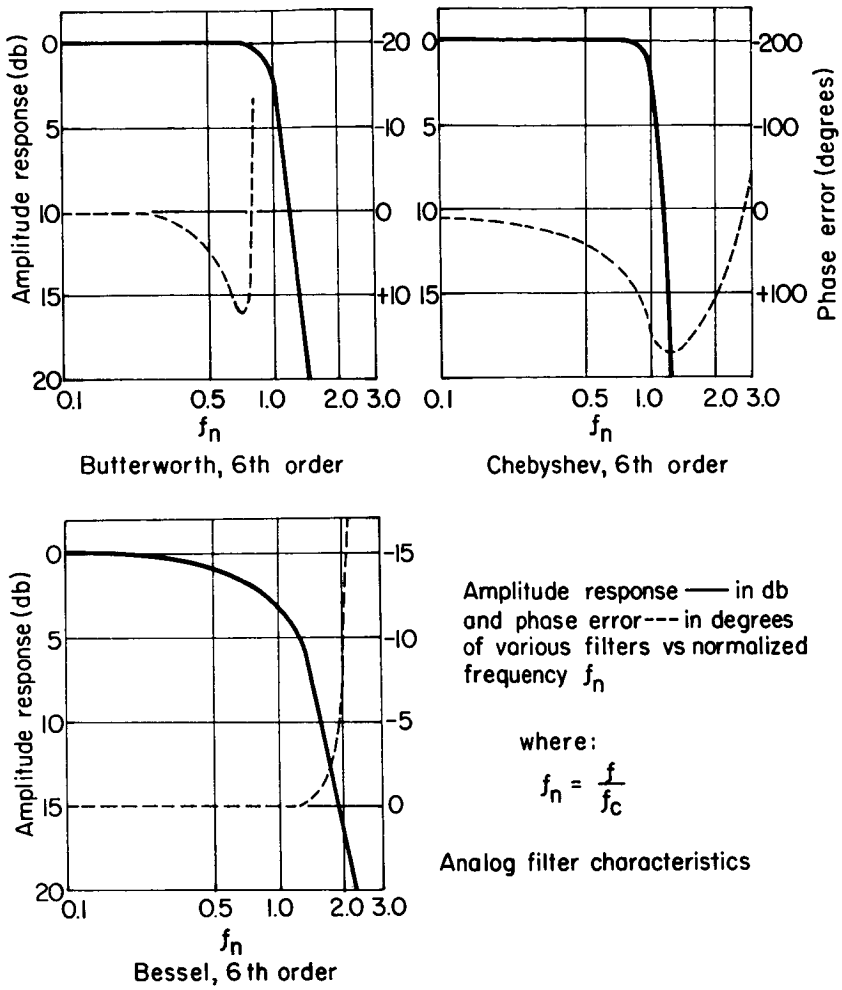

FIGURE 9.3.5b.—Analog filter characteristics.

9.3.5.3 Hybrid spectrum analysis.—A unique method of presenting a frequency-amplitude-time profile is by means of the Hybrid Spectral Analyzer. It is termed hybrid because both digital and analog techniques are used in one analysis system to produce the data.[16] With this equipment, data can be analyzed on a single channel basis in real time. It is unique in that the analysis can be made in real time over an entire test, or selected small sections of a test, with various data presentations. A detailed analysis can be readily performed on as little as 25 milliseconds of run data.

When used in conjunction with an X-Y plotter, the hybrid spectrum analyzer is used in the so-called "locked-up storage mode." The analyzer uses delay lines with fixed bit storage capacity. Record time length (effective data storage) in the fixed mode of operation is directly related to the analysis spectrum to be analyzed as shown in Table 9.3.5. It can be seen that very short sections of data can be locked up and analyzed. Fig. 9.3.5c is an example of a pressure trace and its spectrum analysis in a combustion chamber which has been subjected to a gun pulse and recovered. The same type of analysis can be made of unstable data over selected time spans.

The most used mode of operation of the hybrid analyzer is with a digital data processor. Here the same delay lines that were mentioned above are used. However, instead of locking the data up in the delay lines, new data bits are continually added and old data bits are dropped out such

TABLE 9.3.5.—HYBRID SPECTRUM-ANALYZER SPECTRAL SPECTRAL WIDTHS, FILTER BANDWIDTHS, AND EFFECTIVE DATA STORAGE TIME

Tape speed	Analysis spectrum (frequency range), Hz	Narrow-filter bandwidth (1/500 of freq. range), Hz	Wide-filter bandwidth (1/50 of freq. range), Hz	Effective data storage time, sec
1/1	0.01 to 5	0.01	0.1	100
1/2	10	.02	.2	50
1/4	20	.04	.4	25
1/8	40	.08	.8	12
1/16	80	.16	1.6	6
1/1	0.125 to 62.5	0.125	1.25	8
1/2	125	.25	2.5	4
1/4	250	.5	5.0	2
1/8	500	1.0	10.0	1
1/16	1 000	2.0	20.0	.5
1/1	0.5 to 250	0.5	5.0	2.0
1/2	500	1.0	10.5	1.0
1/4	1 000	2.0	20	.5
1/8	2 000	4.0	40	.25
1/16	4 000	8.0	80	.125
1/1	2.0 to 1000	2.0	20.0	0.5
1/2	2 000	4.0	40	.25
1/4	4 000	8.0	80	.125
1/8	8 000	16.0	160	.062
1/16	16 000	32.0	320	.031
1/1	10.0 to 5000	10.0	100.0	0.1
1/2	10 000	20.0	200	.05
1/4	20 000	40.0	400	.025
1/8	40 000	80.0	800	.012

that the analysis is continually made on a fixed length of data storage in essentially real time. After analysis, the data is recorded in digital form on a digital tape recorder for digesting and formating for useful presentations by a digital data processor. Again, as with the X-Y plotter output, the analysis spectrum is pre-selected, with filter bandwidth and effective data storage time as specified by Table 9.3.5. The selectability in the filter bandwidth is either narrow or wide as indicated with a 10:1 difference between the two filters. The frequency resolution is correspondingly different between the two modes in that with the narrow filter the analysis is made with 500 lines of data (that is, 500 equally spaced increments over the analysis spectrum) whereas with the wide band filter only 50 lines of data are presented.

An excellent method to survey an entire run, where complex or varying frequencies are present, is to tabulate *amplitude as a function of frequency and time.* Data are presented in a complete manner in that frequency spectrum analysis is made incrementally with time. As an example, if the analysis spectrum is 0 to 10 kHz, each frequency band is sampled every 0.050 second.

Once the data has been analyzed and recorded on the digital tape, one of the options available with the computer is to present the amplitude versus frequency over any number of periods of test time, or the entire test. This is useful when looking for energy levels over a discrete segment of a test such as that done under the analog method with a tape loop. The advantage here is that the length is extremely flexible. Output can be in the form of a tabulation or a plot. Other variations are also possible.

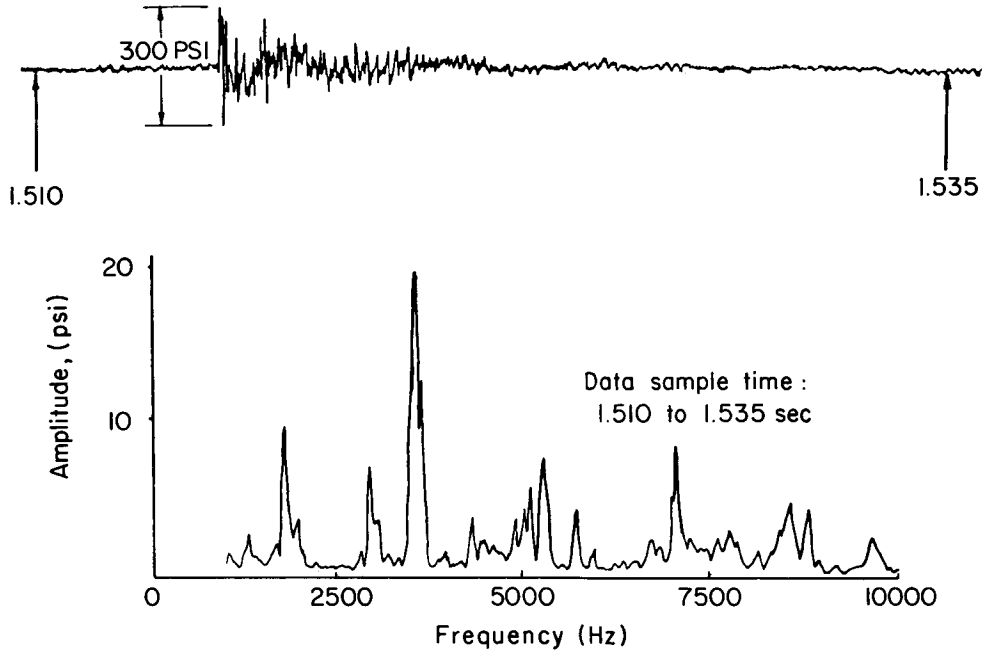

FIGURE 9.3.5c.—Pulse spectral analysis.

9.3.5.4 Digital analysis.—Advances in the state-of-the-art in analog-to-digital conversion equipment, digital processing equipment, and in program mathematics have made practical the processing of dynamic data by completely digital techniques. A few years ago the prohibitive cost of the large amounts of equipment time required for these types of processing made digital processing impractical except for data of relatively low or restricted frequency range.

The advent of analog-to-digital converters with basic conversion rates of up to 10^5 samples per second, higher speed computers, and the availability of computer routines such as the Cooltey-Tukey fast Fourier transform,[533] has made the application of completely digital techniques practical for dynamic data processing of a general nature. Some of the processes currently in use are described in the following paragraphs as representative of this type of dynamic data analysis.

One of the principal methods for the analysis of the dynamic behavior of a physical device or system is by comparing the system output with the input.[36] The transfer function of a physical device or system can usually be determined from these data, or the effect of it can at least be plotted as a function of frequency. This type of processing is known as phase-gain analysis since the phase and amplitude of the output data is developed and referenced to the phase and amplitude of the input to determine the gain and phase shift characteristics of the system over the desired frequency range. Programs have been written and are in use for this type of data.

Digital analysis of stability data is often carried out in the time domain rather than the frequency domain because of the simpler programming this method offers. The technique briefly consists of multiplying the data at time "t" by itself (auto correlation) or by another channel (cross correlation) at time "t+dt." A large number of products are generated, averaged, and normalized at each delay time dt as the delay time is varied from a low to a high value. A plot of the resulting normalized averages versus dt is the auto or cross correlation function.

If a definite periodicity is present in the data, the correlation function will show a repetitive shape with this period. The method has a powerful practical use in extracting low level data at a known frequency from very high accompanying noise. Spectral analysis using either hybrid analyzers or digital filters has largely supplanted correlation techniques due to the reduced machine

time or easier interpretation of the data they offer.

Spectral density and cross spectral density analyses may be thought of as special cases of auto and cross correlation. Here, the delayed function is also multiplied by the Fourier transform into the time domain of the frequency response of a specified filter. Since the entire process is digital, the frequency response of the simulated filter may be anything desired, even rectangular. The output is transformed to the frequency domain and plotted in mean square units per hertz.

If the input data is digitized from the raw analog, the output is equivalent to the amplitude probability distribution versus time. Detecting and smoothing of the raw data, before digitizing it, produces a probability distribution of the data envelope versus time.

The peak response of a number of single degree of freedom resonators to a transient waveform makes up a shock spectrum. A plot of the shock spectrum consists of the maximum acceleration experienced by these single degree of freedom systems (with specified damping characteristics) as a function of their own natural frequency in response to an applied shock. Although used primarily in environmental work, it has value in stability work in investigating the effect on the hardware of charges used in liquid engines. This method of analysis is also used to analyze shock tube data.

9.4 OPTICAL MEASUREMENTS

Optical measurements rank close to pressure measurements in both wide usage and in supplying pertinent data on combustion phenomena. A wide variety of optical techniques have been used which range from direct photography to analog recordings from optical sensors. This section describes some of the techniques that have been employed, outlining advantages and limitations, and how the techniques are dependent upon the combustion environment under investigation.

The following nomenclature pertains to Sect. 9.4.

B	Maximum bellows extension
C	X_c/f_c
D	Optical beam diameter at chamber window
D_c	Optical beam diameter at condenser lens
D_o	Optical beam diameter at camera lens
D_s	Spark gap size
D_s'	Optical beam diameter at flame light stop
d	Distance between field of view in chamber and center of condenser lens
F	Size of image on film plate
f_c	Focal length of condenser lens
f_o	Focal length of camera lens
h	Size of field of view
m	Magnification
W	Diameter of chamber window
X_c	Spark object distance
X_c'	Distance from condenser lens to spark image formed by condenser alone
X_o	Distance from camera lens to field of view
X_o'	Distance from camera lens to film plate
X_s	Distance from camera lens to spark image formed by condenser
X_s'	Distance from camera lens to flame light stop

9.4.1 Cinematography*

Motion picture photography is a long established, well-proven tool for studying combustion and combustion instabilities. The more sophisticated uses have been associated with transparent chambers or windows; however, excellent results have also been observed through the nozzle. Where it is impractical to view inside of the combustion chamber, useful data may be obtained from plume photography. In terms of potential failure analysis, overall test stand views are used. For instance, rocket engine production testing is recorded with several high speed motion cameras. Because the testing is so routine, the film is not developed. However, should a combustion instability or malfunction cause a premature cutoff, the film is processed and used to aid investigation. Thus, careful selection of test cinematography offers detailed data of the expected and, often, the only record of the unusual or unexpected.

9.4.1.1 Combustion zone photography.—Several techniques have been employed to obtain direct light emission photographs of rocket engine combustion processes. The two most common usages of motion picture photographic recording

* R. J. Hefner, T. A. Coultas, and W. M. Ford, Authors.

of combustion processes are those associated with combustion taking place in an unconfined environment and within special research combustors employing at least one flat transparent surface.[514,608,88] There have been several techniques developed, however, to permit direct photographic coverage of events occurring in full-scale rocket simulators and in prototype rocket engines.

Many of the subscale rocket simulators such as those described in Sect. 9.2.2 employ transparent windows or combustor walls to permit direct photographic recording of events taking place within the combustor. Generally these viewing windows are constructed of heat resistant glass or transparent plastic, although quartz is frequently used if the dimensions of the window are relatively small. The primary disadvantage of all of these window materials is that they generally limit the test duration to less than two seconds due to their relatively low heat capacity and melting points. Quartz and heat resistant glass have higher melting points than the plastics and thus are capable of withstanding longer exposure to the combustion environment but they have the added disadvantage of being brittle.

In steady-state combustion, high speed photography of transparent rocket chambers allows the qualitative visualization of propellant and combustion gas flow patterns, spray interactions, and jet breakup, and stripping* (Refs. 424, 421, and 74). Approximate distances required for consumption of gross liquid streams, recirculation patterns, cross winds (and mixing patterns) may be determined. Special effects such as ignition and tap-off (gases taken from the main combustion chamber to operate turbo-machinery) may also be effectively studied with transparent chambers and high speed cinematography.[275,440]

In the study of combustion instability, transparent chamber photography enables the investigator to observe the reaction of the injected streams to a combustion wave, the mode of the instability, the flow behind the combustion wave, the response of the feed system and other effects upon the combustion instability. In the case of resonant instability, most of the quantitative data is taken with streak photography rather than framing because of the very rapid processes involved. Framing photography is of most value to observe the onset or triggering of instability such as may be caused by a combustion "pop," an ignition "spike" or the buildup of a linear instability.

Relatively small general observation windows have been employed in the walls of the full-scale uncooled combustion chamber simulators of the second stage Gemini engine.[11] For this application it was found that either quartz or transparent plastic was adequate to permit surveillance of the overall combustion characteristics within the combustor. Although dramatic differences in luminosity between stable and unstable combustion were recorded, the speed and depth of focus of the cameras used did not permit recording data which could be used in diagnostic evaluation of instabilities.

Another use of high speed framing cameras for recording combustion instability within an engine involves the use of a window located in the center of the injector face of a full-scale combustor. For this application a small hemispherical quartz dome is mounted in the center of the injector. Behind this dome is a complex system of lenses to permit wide angle (160°) exposure of the complete cross section of the combustion chamber (Fig. 9.4.1a). High speed motion picture cameras mounted behind this "periscope" record the combustion process within the combustor. It has been found that wave patterns of the transverse mode instabilities can be clearly observed by the gradation of illumination.[525]

Both standing and spinning forms of transverse mode instabilities have been recorded using the apparatus shown in Fig. 9.4.1a. It was found that with the spinning mode of instability highly luminous waves, corresponding to the peak pressure of the unstable wave front, could be observed rotating within the combustor cavity. With the standing transverse mode the luminosity periodically increased and decreased in specific regions of the cavity corresponding to the pressure antinodal planes of the instability. The camera speed used with this type of apparatus is not critical so long as the shutter speed is sufficient to stop the wave motion within the cavity, and the frame speed is not an integral multiple of the frequency of instability.

All of the transparent window materials men-

* Removal of the surface fluid from a jet or droplet.

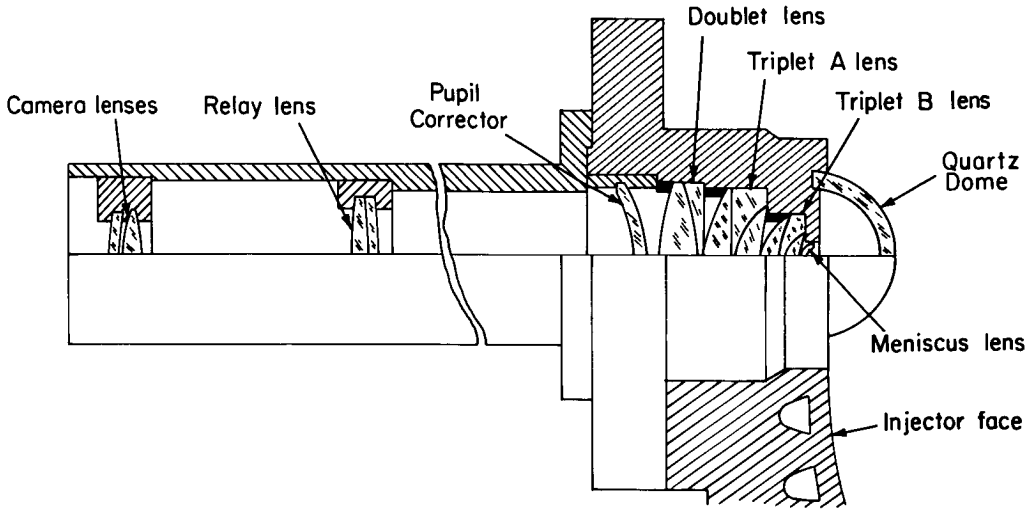

FIGURE 9.4.1a.—Injector periscope assembly.

tioned above are subject to surface deformation due to erosion which can result in distortion of the photographic images. In addition it has been observed that, under low chamber gas velocities, plastic materials will produce a combustion front at the inner surface of the window. The flame resulting from this phenomenon radiates strongly in the wavelength range of standard color and black and white films and is quite sensitive to velocity. This characteristic can be used to advantage to record wave motion at the chamber wall by focusing the camera on the flame front at the internal surface of the window. Under conditions of instability the fluctuating velocity patterns result in periodic ignition and extinguishment of the flame at the surface of the window. For observing phenomena *within the combustion zone* caution must be used to avoid obscuring the desired image. This can be accomplished either by locating the window in a relatively high velocity region of the combustor to prevent the surface combustion or by using appropriate filters on the camera.

Another technique that has been employed to provide data similar to that described for the periscope camera is to place a high speed motion picture camera beyond the chamber nozzle aimed into the combustor cavity.[655,163,150] The major difficulty of this technique is locating the camera in such a position as to observe most of the interior of the cavity and at the same time protecting it from the exhaust gases. This technique is limited to propellants whose exhaust products are transparent in part of the visible spectrum and are not clouded with particles. Depending upon the optical path length through the hot gases, some of the combustion process detail is lost. Although little may be seen of the detail, events such as "pops," "spikes," bomb or pulse guns are easily filmed through the nozzle. Combs has used streak cameras with curved slits to obtain quantitative data through the throat.[167] Clayton's movies[150] indicate the zones of intensified combustion as well as showing what appears to be considerable amounts of propellants thrown out of the chamber unburned.

9.4.1.2 Exhaust plume photography.—The exhaust gas plume from a rocket engine can provide significant information about the combustion phenomena within the combustor.[405] This is of particular advantage when it is impractical to use high response instrumentation or high speed photographic techniques to monitor the combustion process. In Sect. 9.4.3 the use of radiometry to record the temporal emissions from exhaust gases is discussed, while here the technique of photographing the exhaust gases is covered.

When resonant combustion is initiated and sustained within an engine, motion pictures of the exhaust typically record a dramatic change in

color or luminosity. The change in exhaust plume characteristics is not well understood and may reflect different mechanisms with different engines. It may be the result of a change in the composition of the exhaust gases or may be the result of increased ablation or erosion of the chamber walls. Regardless of the cause, the change of color or luminosity of the exhaust plume provides a simple means of monitoring production engine tests for instabilities by photographic techniques.

More quantitative monitoring of the combustion process by photographing exhaust gases can be accomplished by taking high speed motion pictures of the first shock diamond in the exhaust plume (see Sect. 9.4.3.3). The forward surface of this shock front is nearly flat and its relative distance from the sonic throat of the engine is directly proportional to the pressure within the combustor. If a high speed camera is located so that the plane of the shock front is normal to the film, changes in the location and the frequency of the motion can be accurately recorded.

It has been found that this shock surface responds very rapidly to pressure variations within the combustor. Feed system coupled instabilities and combustion disturbances can be easily detected by changes in the location of the shock surface. If the speed of the camera is sufficiently great, resonant instabilities can be detected and identified by monitoring the motion of the shock surface. It has been suggested that if simultaneous high speed photographs are made from different angles, the actual wave shapes of transverse and radial mode resonant instabilities could be reconstructed from the motion of the shock surface, but there are no published data indicating that this has ever been attempted.

9.4.1.3 Photographic techniques.—The key to maximizing information from high speed movie film includes an understanding of spectral characteristics of the camera equipment, film lenses, transparent hardware, filters and the reacting species. The spectral characteristics of several representative propellant combinations are shown in Fig. 9.4.1b. The visible spectrum is indicated for comparison purposes. The hydrogen-oxygen reactions are characterized by species which in part emit light with wavelengths between 0.2 micron and 1.2 microns. The principal emitting

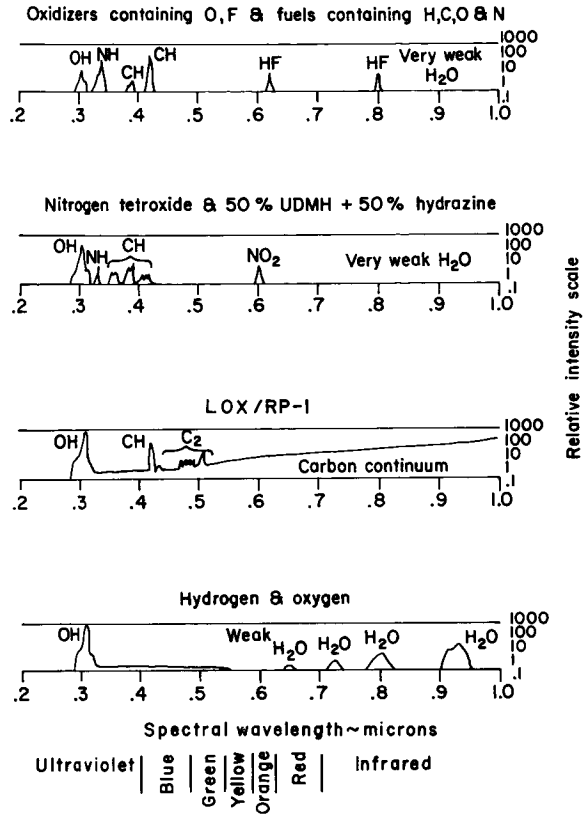

FIGURE 9.4.1b.—Typical propellant combinations–optical spectrum.

species are OH at 0.31 micron and water at 0.65, 0.73, 0.80, 0.93 and 1.1 microns. The characteristic light blue associated with the hydrogen-oxygen combustion is generally considered to be due to an OH recombination reaction.[529] From about 0.27 to 0.5 micron, emission from the OH species is an indication of combustion occurring since OH is primarily a transient reaction species. Water, on the other hand, is a product of the principal reaction and identifies regions where the reaction is at least partially complete.

When transparent chambers are used, the ideal window would pass light wavelengths from 0.2 to 1.5 microns,* be easily machinable, be equally strong in tension and compression, be insensitive to thermal shock, have a high melting point and

* Special hypersensitized film techniques are required to achieve 1.5 micron sensitivity, whereas optical techniques could supply useful data to 4 micron wavelengths or greater.

be inexpensive. Since such a material is not available, compromise materials are often used. Those which have been most successful are Plexiglas (or Lucite), Pyrex, and fused quartz. The composite of a Pyrex sheet (for dimensional stability) bonded to Plexiglas (for mechanical strength) with such adhesives as PS-18, RTV 602, or Uralane 5716 have been successfully used. Quartz windows, if they are kept small and installed very carefully to avoid being loaded in tension, even temporarily, are also very good. Fig. 9.4.1c shows the transmission characteristics of various chamber and bonding materials.

Many kinds and makes of camera have been used in combustion instability research, one of the most popular has been the Fastax camera,[8] although recently the Hycam camera is also receiving considerable attention.[367] The key features of the Fastax camera include a variable-speed film drive, rotating prism, neon timing light, drive cut-off switch and supply and take-up reels. The variable speed drive is controlled by the supply voltage to the drive motor. Motors operating at voltages between 30 and 220 volts result in framing rates between 1500 and 8000 frames per second for the 16 mm frame size. The exposure time for each frame is $\frac{1}{3}$ or $\frac{1}{5}$th the reciprocal of the framing rate, depending upon the camera model. A special eight sided prism offers twice the framing rate at the same film velocity by exposing only one half of each 16 mm frame. This is called a split-frame camera.

Lenses and rotating prisms are made from high quality optical glass and coated to protect their exposed surfaces. This equipment cannot pass wavelengths below about 0.4 micron. To photograph into the ultraviolet region requires special lenses and prisms. The transmission properties of some typical lens and prism materials as well as some typical filters are shown in Fig. 9.4.1d.

Although there are many types of photographic film available, only a few types need be considered for combustion photography. The film records the apparent brightness of the subject. Black and white film records brightness over the entire spectrum to which it responds, while color

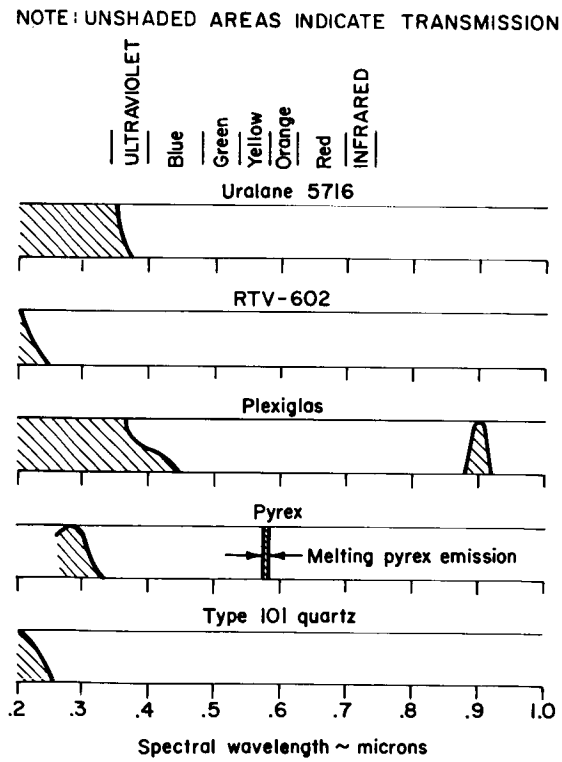

FIGURE 9.4.1c.—Transparent chamber materials–optical transmission.

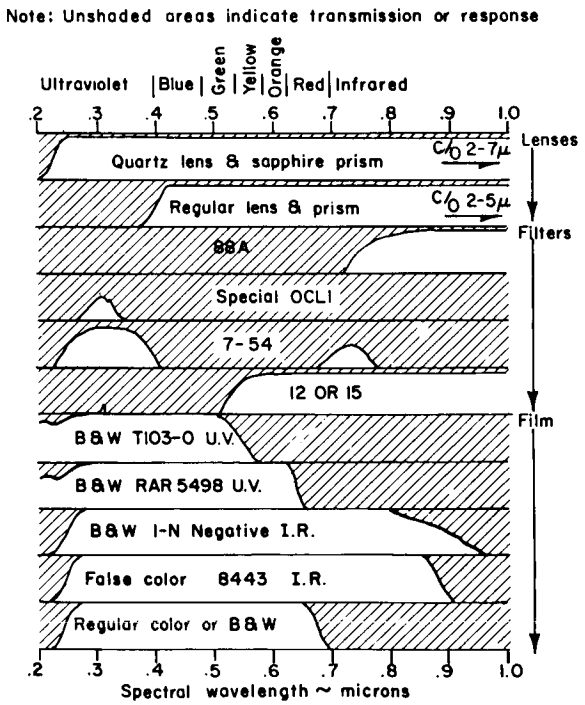

FIGURE 9.4.1d.—Film spectral response and camera equipment transmission.

film records brightness at a characteristic color wavelength. In general, for photography of combustion processes, color film shows more detail with better contrast. A summary of film spectral response is also shown in Fig. 9.4.1d. For observation in the infrared region there are false color films and black and white negative reversal films. The false color IR film is unique in that the color projected on the screen actually represents information received at another wavelength. For instance, infrared records as red, red light as yellow, and green light as blue, thus the entire spectrum is shifted toward the infrared.

9.4.2 Streak Photography*

9.4.2.1 General principles.—The use of streak pictures provides a valuable adjunct to the usual high-speed motion pictures. Streak pictures may be obtained by modification of high-speed cameras. For example, the framing prism of the Fastax camera can be replaced with a narrow slit (0.002 inch width typical) positioned at the film plane and perpendicular to the film edges. The film is then drawn past the slit at high speed with a direction of travel perpendicular to the slit. The optimum film transport speed depends on the velocity expected to be measured as well as the magnification of the optical system, and is selected so that the streaks will be at approximately 45° to the film edge. Figure 9.4.2a shows streak camera coverage of a transparent two-dimensional combustion chamber in which the film is continually exposed to luminous emission from a narrow field of view along the entire chamber length. A typical enlargement of such an axial streak is shown in Fig. 9.4.2b. Each trace on the film is of approximately parabolic shape and describes the trajectory of a particle (or cloud of particles) whose luminosity formed the image. The slope of such a trace represents the local axial velocity of the particle as it traveled through the chamber.

A 90° rotation of the camera from the position shown in Fig. 9.4.2a permits transverse streak photographs to be obtained. Fig. 9.4.2c shows simultaneous pressure and transverse streak measurements during the occurrence of instability. The streak photo was again obtained from a two-dimensional motor[403] and shows the sharply defined change in luminosity which occurs when the instability wave moves from one wall of the chamber to the other. Pressure was measured with a Photocon transducer located in the spacer

* R. C. Kesselring and T. A. Coultas, Authors.

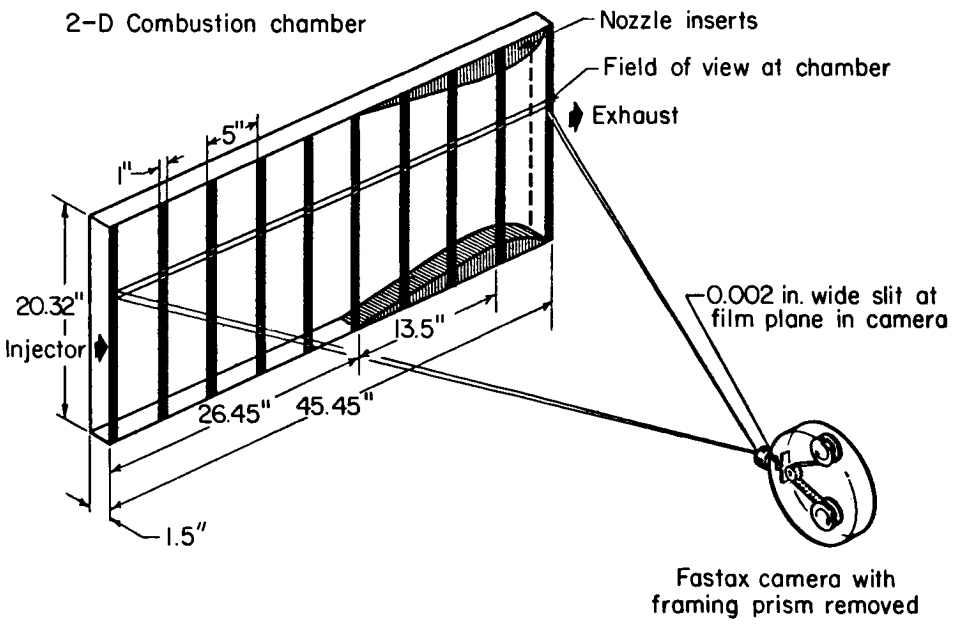

FIGURE 9.4.2a.—Typical axial streak-camera arrangement.

FIGURE 9.4.2b.—Typical axial streak photo.

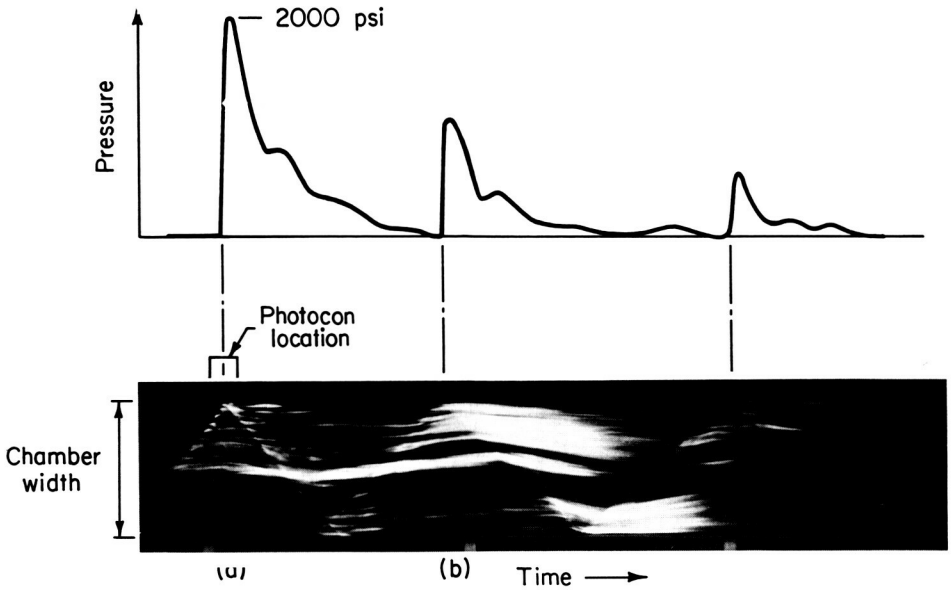

FIGURE 9.4.2c.—Typical transverse streak photo with simultaneous pressure measurement.

bar at the same axial location at which the vertical slit was positioned. The arrival of the instability wave at the spacer bar coincided with a sharp increase in the pressure recorded by the transducer. Further examination of the streak photo provides evidence of the spontaneous growth of a transverse wave from negligible amplitude to a 2000-psi disturbance in one pass across the 20-inch chamber, with damping observed after five passes. The total period, i.e., point a to b, can be easily measured and the velocity of the disturbance calculated.

By using several streak cameras having different fields of view, it is possible to examine (in a two-dimensional motor) specific combustion zones, i.e., near the injector, in the convergent section of the nozzle, close to the walls, etc. Successful streak pictures have been obtained by direct photography of the emitted light[424] as well as by the use of silhouette photography in which a high-intensity backlight is employed with a transparent chamber (see Sect. 9.4.4).

9.4.2.2 Steady-state combustion distribution.—The application of steady-state, streak photography to combustion instability is that of determining the axial distribution of combustion, which is needed for all theoretical models. The combustion distribution is related to the mean axial velocity of the combustion gases.[402] Although analytical models are available for calculating the steady-state combustion distribution,[421] many of the input quantities for these models (e.g., drop size distributions, evaporation coefficients, etc.)

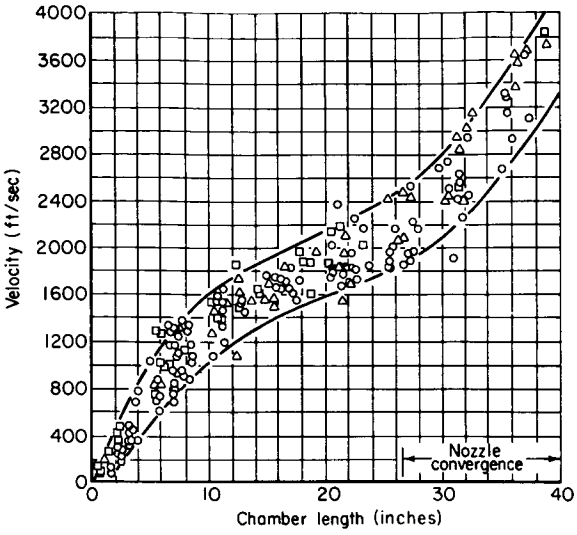

FIGURE 9.4.2d.—Typical axial streak velocity profile.

are not known with any certainty. Thus, streak photography data are necessary for accurate analysis of combustion instability.[419,158]

Steady-state streak film data are usually presented in the form of plots of streak velocity versus axial position in the chamber. Normally there is a range of velocities recorded at any location, as shown in Fig. 9.4.2d.

Lambiris and Combs[419] advanced the hypothesis that luminous traces caused by evaporating, reacting propellant particles (gases or very small droplets) traveling at or near the local combustion gas velocity account for the presence of the upper boundary of the velocity envelope. Possible explanations for the existence and meaning of the lower boundary of the velocity envelope have been advanced and are discussed in detail in Ref. 162. Physical phenomena that may explain the lower boundary include: the existence of large liquid propellant droplets,[419,421,158] combustion gas turbulence, concentration striations in the combustion gas stream,[402] boundary layer effects,[402] and condensation of water vapor near the injector.[162] Of these, the effects of unmixedness probably dominate in most cases, although the other phenomena may contribute to a certain extent, depending on the combustion system studied.

Although the true explanation for the lower boundary of the streak velocity envelope remains in doubt, useful comparisons and conclusions can still be obtained, using the upper boundary of the envelope, as identified with the combustion gas velocity profile.

9.4.2.3 Application to combustion instability.—Streak photography is one of the best methods by which the processes occurring during unstable combustion can be delineated and the various modes of instability identified.

In the study of unstable combustion involving wave motion in the chamber, the alignment of the desired field of view is dependent upon the mode of instability to be photographed. For example, axially aligned slits give best results for longitudinal wave motion. Tangential or circumferential (transverse in the case of a 2-D engine) slits are most informative when used to photograph tangential (or transverse) wave motion. This applies whether the tangential mode is standing or spinning. Streak photography shows that standing tangential waves have an appearance equivalent to a pair of co-existing, counter-rotating spinning tangential waves. Transverse waves in a 2-D engine have the appearance (see Fig. 9.4.2c) of traveling, steep-fronted waves. Radial wave motion is best photographed with a radially aligned slit. This, of course, entails viewing through the nozzle or through a window in the injector face.

Consider the cylindrical chamber and the slit location pictured in Fig. 9.4.2e. Because the slit is very narrow and its length corresponds to the film width (film running perpendicular to the long axis of the slit) the wave motion creates a luminous trace on the streak film such as shown in Fig. 9.4.2e. The shape of the luminous trace depends on the type of wave motion (or instability mode) encountered. Because the luminosity is intensified by the wave front, a distinct discontinuity is recorded on the viewing film as the wave moves along the slit. It appears sharp because the intersection of the wave with the field of view from the narrow slit produces a point source. (The luminous discontinuity of the wave moving through the combustion zone is almost always associated with the very front of the wave, the region of rapid pressure rise.) The slope of the luminous trace on the film is determined by the film and wave speeds. Knowledge of the film speed allows

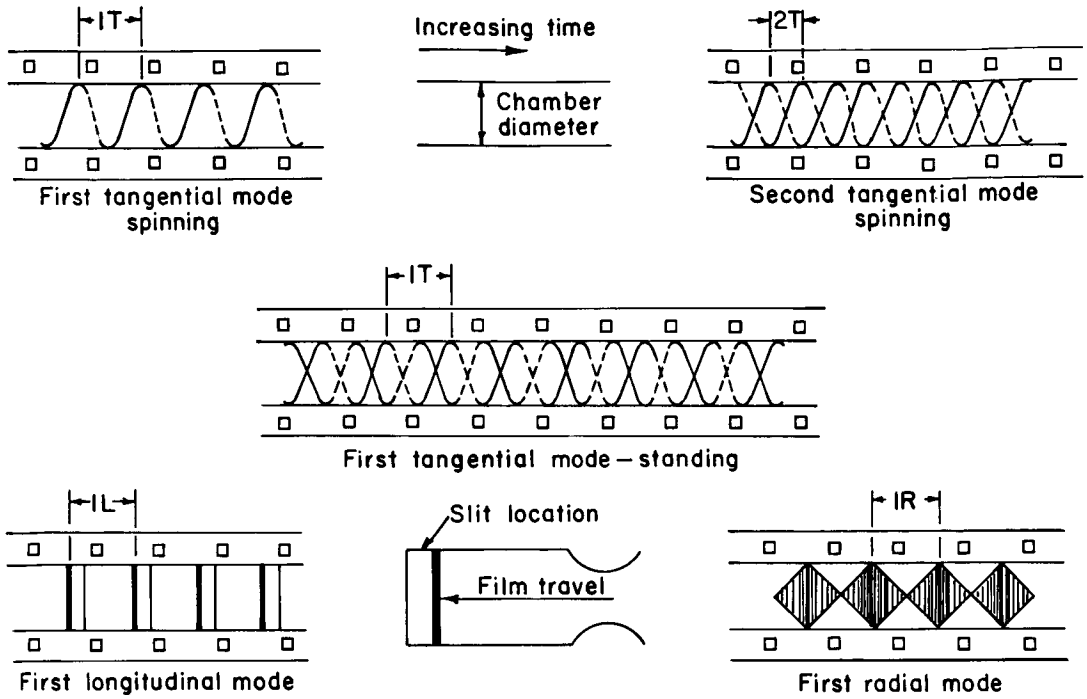

FIGURE 9.4.2e.—Typical streak film traces of various modes using circumferential slits.

determination of the wave velocity at any point and the number of waves passing the observation plane in a given time. Thus, direction of wave travel, wave speed, frequency and mode identification are all possible from streak data.

Luminous traces representing various modes of instability are illustrated in Fig. 9.4.2e for a circumferential slit location. The time corresponding to the inverse frequency of the various modes is also indicated in Fig. 9.4.2e. To best study longitudinal or radial wave motion slit configurations other than circumferential must be used. Fig. 9.4.2f illustrates luminous traces representing various instability modes for axial and radial slit alignment. In addition, the luminous trace representing a baffle compartment mode of instability is presented for a semi-circumferential slit positioned on the injector face.

Streak photographs obtained using circumferential slits have been used extensively in the identification of high-frequency instability modes in baffled, cylindrical chambers[12] and in pulse motor chambers.[242] Views through the nozzle have been used to verify the coexistence of the first radial and third tangential instability modes in test firings using a baffled, cylindrical chamber.[163] More recently, similar streak photography with narrow fields of view along and perpendicular to the axes of explosive bombs mounted inside a cylindrical chamber were used to determine shock wave velocities at various distances from the bombs.[167]

9.4.3 Electro-Optical Techniques

Several techniques have been developed to record optical data directly on magnetic tape. These techniques involve monitoring the combustion zone or exhaust plume with photodiodes or radiometers and recording the electrical output on a standard FM tape recorder. A display record of the taped data, produced in the same manner as pressure data records, provides an analog record of the optical emissions from the engine.

Electro-optical measuring devices can be used with transparent chambers in the same way as cameras. When transparent walls or windows are available, however, cameras and/or pressure transducers are normally used. The electro-optical techniques are typically used when the direct

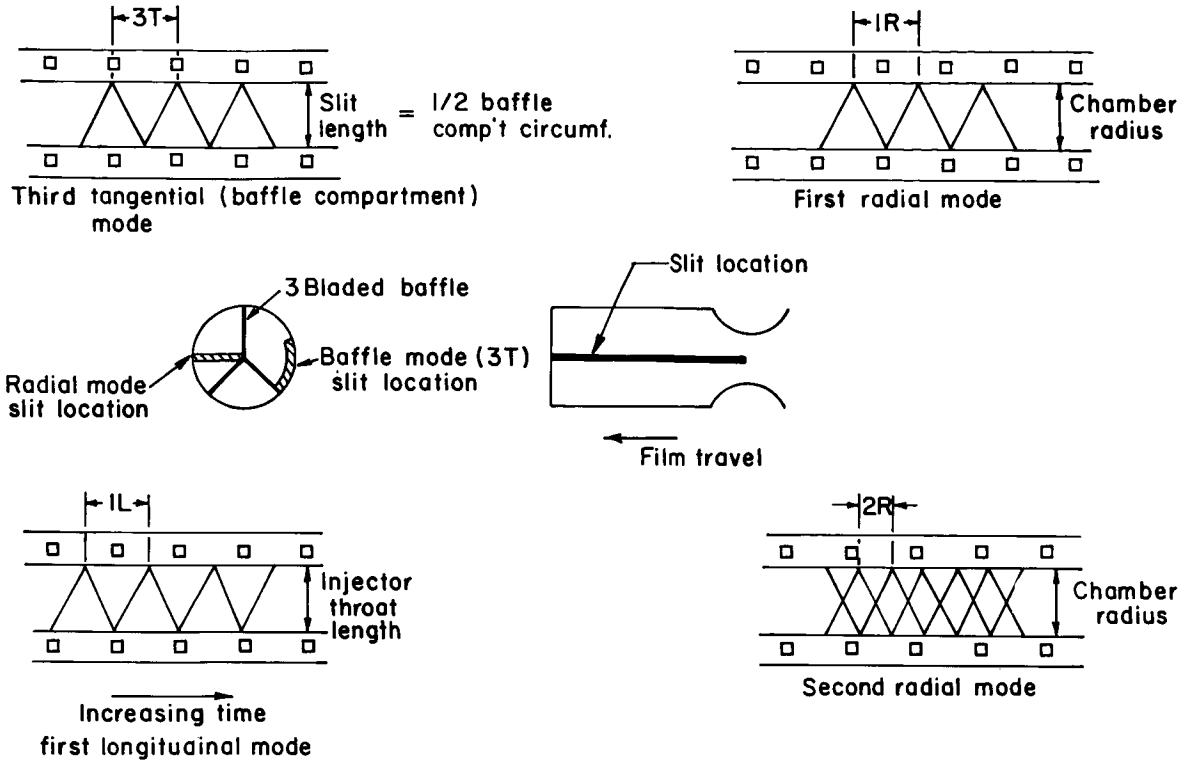

FIGURE 9.4.2f.—Typical streak film traces of various modes using axial and radial slits.

methods are impractical. Three such techniques are described.

*9.4.3.1 Fiber optics.**—A unique method of optically measuring an instability frequency through an extremely small access area in a combustion chamber has been developed with the aid of optical fibers in conjunction with photodiodes.[16] The optical fibers transmit the radiant energy given off by the combustion process in the chamber to the photodiode, which provides an electrical output that varies with the quantity of light incident upon the diode. Recording of the data is handled routinely on FM magnetic tape.

Instability frequencies have been well-defined by streak photography[12] and photomultiplier tubes,[776,361] indicating the presence of a high intensity light phenomenon at the same frequency as the pressure wave. Small light sensitive photodiodes are available which will measure changes in light intensities with rise times as short as 4×10^{-9} sec. Through their application to the measurement of the variation in light intensities in the combustion chamber, it is possible to handle the resultant data the same as that recorded from a flush-mounted pressure transducer (see Sects. 9.3.4 and 9.3.5).

In order to measure light intensities within a combustion chamber some means of access into the combustion chamber at the point of interest must be provided.

For cameras this requires a relatively large window in the wall of the chamber. Such a window is difficult to install and still maintain the structural integrity of the chamber. With optical fibers it is possible to provide this access through a very small opening, (typically 0.080 inch diameter) into the chamber at any location where a boss can be placed. This method differs from the photographic process in that the data can be recorded on FM tape instead of film. The recorded signal can then be processed the same as any other dynamic data which is recorded on tape. Multipoint recording can be used to identify instability

* R. D. Wesley, Author.

modes by the same techniques utilized in analyzing data from flush-mounted pressure transducers.

The two main components comprising such a transducer are the fiber optics and the photodiodes. Optical fibers can be drawn from various materials, the most common of these being optical glass with a transmission spectrum of 0.4 to 2.0 microns. This covers the visible spectra (0.4 to 0.76 micron) and into the infrared region. Fibers drawn from arsenic trisulfide will extend the transmission spectra farther into the infrared region; however these fibers have a much lower melting point. For use in the visible and near infrared region, glass fibers provide an excellent transmission medium.

Photodiodes have a wide variance in spectral response range depending on the type of material used to manufacture the diode. Silicon has a spectral response range of 0.4 to 1.1 microns which fits very well for measurements of light intensities in the visible and near infrared regions. For response in the infrared region Indium Arsenide would come under consideration because of its spectral response range of 1.0 to 3.5 microns.

A typical transducer, used to measure variations of light intensity in the visible and near infrared spectral region, was designed and fabricated from readily available components possessing the desired spectral characteristics. For this transducer optical glass fibers and a silicon photodiode were utilized. Since the optical glass fibers have a spectral range response of 0.4 to 2.0 microns they do not limit the light transmission in the spectral response region of the silicon photodiode. They serve three basic purposes: (1) to transmit the light to the photodiode, (2) to isolate the photodiode from the hot gas source, and (3) to filter out much of the infrared radiation which tends to heat the photodiode. Intense infrared radiation will damage the photodiode.

The actual transducer design is shown in Fig. 9.4.3a, and consists of multiple fibers within a small tube. Solid potting is used around the fibers at the diode end of the tube as a pressure seal, and a porous potting material is used to position the fibers at the exposed end. The fibers are subsequently trimmed and polished flat at both ends of the tube. If a small acceptance angle is desired into the chamber, the fibers can be recessed in the tube at the combustion chamber end. The most

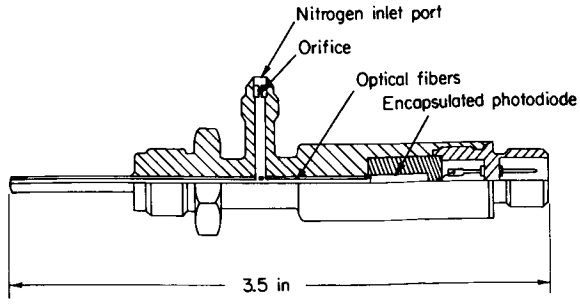

FIGURE 9.4.3a.—Typical fiber optic transducer.

successful acceptance (solid view) angle into the chamber is 10° to 20°. A photoconductive silicon photodiode is used because of its high output capability and high frequency response characteristics. To help maintain a clear optical path into the chamber and preserve the fiber integrity in the high temperature environment, high pressure nitrogen gas is orifice-controlled and bled around the fibers, exiting into the chamber through the porous potting material. With the fiber optics and the photodiode integral in a transducer, it is a simple matter to install the unit at any point in the chamber.

Data from large rocket engines using the optical transducer and compared with pressure data indicate the same instability frequencies from both types of transducers. The oscillatory data in the spectral range observed (0.4 to 1.1 microns) tends to be in phase with the pressure data at the same location. Total emission in this spectral range follows the pressure profile throughout a test.

Major problems encountered with the use of these transducers are (1) protection of the photodiode from saturation, (2) slight erosion of the fiber ends during violent instabilities and (3) standardization and calibration of the units.

*9.4.3.2 AC radiometry.**—The use of an optical technique termed temporal or "AC" radiometry allows the determination of chamber pressure oscillations without physical attachment of measurement equipment to the engine itself.[348] Typical installations may place the radiometer four hundred feet from the test stand. The hot exhaust

* R. Proffit and T. A. Coultas, Authors.

species (gases and/or particles) at the nozzle exit of a rocket engine exhibit not only steady-state radiation, but also possess a temporal variation. It has been experimentally shown that the detection of the various chamber pressure oscillations is possible by monitoring the time-varying component of the radiation from the engine exhaust. Frequency analysis of the time-varying radiation from rocket plumes has shown that this radiation is of two types. The first is a continuous frequency distribution, possessing an $1/f^n$ dependence caused by random processes. The second type involves coherent tones discontinuously distributed in the frequency spectrum which are caused by chamber pressure oscillations. Measurements made on engines using a variety of fuels have shown excellent agreement of AC radiometry with flush-mounted high-frequency pressure transducers, both in frequency and in spatial phasing.

An AC radiometer is a simple instrument consisting of an optical system to focus electromagnetic radiation from the engine plume onto a detector, a field stop to limit the field of view of the radiometer to a particular spatial region of the exhaust, and filters which allow only selected wavelengths to reach the detector. Such a radiometer is shown schematically in Fig. 9.4.3b. Some typical data obtained with an AC radiometer and compared to pressure transducer records are shown in Fig. 9.4.3c. This is a record taken during a low frequency, feed system induced, oscillation.

The output of the radiometer is usually recorded at several levels of amplification on separate channels on an FM tape recorder to provide accuracy over a wide intensity range. Typical frequency response is as high as 20 kHz. Other channels of the tape may be used for timing information and other dynamic measurements which may be made simultaneously.

Consideration must be given to the field of view of the radiometer. Since the variation in radiation intensity is caused by varying chamber pressure, if the field of view of the radiometer is such that both high and low regions of radiation intensity are viewed simultaneously, the integrated AC intensity may be zero. For instance, if the radiometer views the entire plume, as in Fig. 9.4.3d(a) only the radial and longitudinal acoustic modes may be detected, since the tangential modes will be effectively integrated at any instant of time. To observe tangential modes, only a small portion of the nozzle exit (along the edge of the plume) is viewed as in Fig. 9.4.3d(b). To rigorously identify all possible acoustic modes, it may be necessary to utilize as many as seven radiometers simultaneously viewing different portions of the plume. Usually, however, two or three are found adequate for either monitoring or mode identification purposes.

If the plume is optically thin, that is, very transparent, it may be possible for a radiometer to "see" completely through the plume. Thus a symmetrical view through the center of the plume would not be likely to detect a radial mode since the integration includes the entire plume. Thus the factors of opacity (at a particular wavelength) must be considered in data interpretation.

The proper wavelength regions of the spectrum to be used for the AC radiometry studies are primarily determined by the exhaust species. The wavelength should be selected so that a major combustion species is monitored. A typical system used for AC radiometry of hydrogen-oxygen plumes uses a lead selenide photoresistive

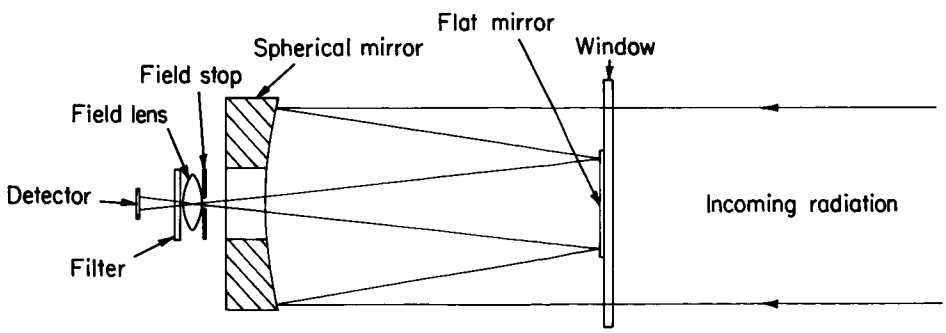

FIGURE 9.4.3b.—Schematic of radiometer optical system.

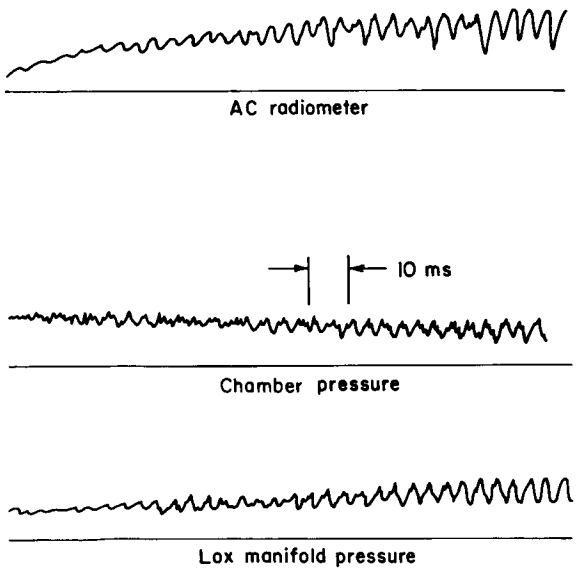

FIGURE 9.4.3c.—Comparison of typical AC radiometer trace with pressure measurement.

detector and a germanium filter to monitor infrared radiation from the H_2O molecule. The filter transmits radiation of wavelengths greater than 1.8 microns, and the detector responds to wavelengths up to 6.0 microns. Another system consists of a photomultiplier detector and a filter transmitting from 0.305 to 0.315 micron to monitor emission from the OH radical in the ultraviolet.

The mechanism whereby the oscillations in the chamber are exhibited in the radiation of the exhaust is not precisely known. There are, however, phenomenological explanations possible. The radiation or radiance of a gas is dependent upon the temperature and the number density of the radiating species. During combustion instability, the combustion gases in the chamber experience a pressure variation in time and space. This pressure variation causes a corresponding change in temperature and density of the gas. The temperature variation causes a change in the population of the excited states of a molecule, and thus increases or decreases the amount of radiation given off by that species. Similarly, the density change will change the number of excited species present at a point in space and time. As these combustion gases move out of the chamber, effects of chamber pressure oscillations are carried to the exhaust. This explanation is weakened by calculations which indicate that species excited in the chamber should have had ample time to decay before reaching the nozzle exhaust in some cases where AC radiometry had been successfully used.

Another explanation is similarly based on pressure variations causing gross effects on the chemical kinetics and equilibrium of the combustion gases. Reaction rates and local mixture ratio may be sufficiently disturbed so as to persist into the engine exhaust. Insufficient measurements have been made to date to further elucidate the basic mechanisms whereby chamber pressure oscillations are manifested by radiation oscillations in the exhaust plume.

STREAK RADIOMETER: A conceptual radiometric device for measurement of instability phenomena might be termed a "streak radiometer." This radiometer could be used in essentially the same way as a streak camera. Spectral response not limited to the normal (visible) photographic regions could prove advantageous.

The streak radiometer could consist of a lens or mirror system to focus radiation onto a detector array (usually 5 detectors in line), a filter to isolate the wavelength band (thus isolating species) of interest, and preamplifying electronics. In use, the object of interest (e.g., a portion of an exhaust plume) could be focused onto the detector array, and as a wave passes across the field of view the output from the detectors in the array should vary in proportion to the intensity of the traveling wave. The electrical signals of the detectors when recorded on a multi-channel recorder should produce data similar to a streak photo.

*9.4.3.3 Shock cone radiation.**—A unique method of determining the stability of the combustion processes, within a combustion chamber, is through the detection of emitted radiation from the first shock cone. Since the shock cone is formed downstream of the combustion chamber nozzle exit, it can be viewed or monitored without exposing measurement instrumentation to the severe combustion environment.

Associated with each firing rocket engine is a series of shock patterns in the exhaust stream. The first of these downstream of the chamber exit

* R. D. Wesley, Author.

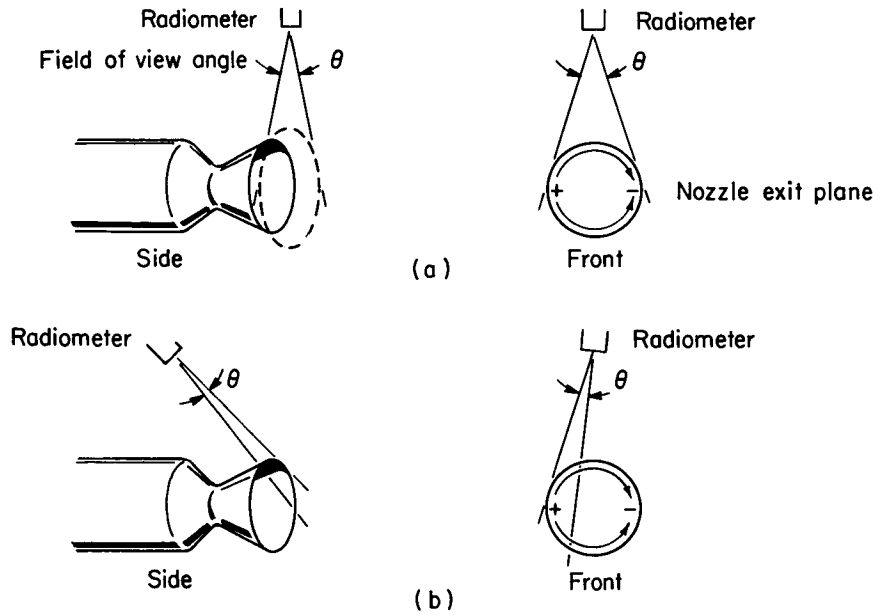

FIGURE 9.4.3d.—Effect of field of view.

may have a flattened top and appear to be essentially a cone shape. In observing the shock cone in both stable and unstable operating conditions, it is evident that the surface disturbance and coloration has a definite change from one state to the other. To the trained observer the distinction between stability and instability is quite evident from the shock cone. The determination of the type of instability or the absolute magnitude is another matter.

However, there are methods of obtaining additional information. One such method is with photodiode devices oriented to measure the radiation from the shock cone. More conventional photographic methods are discussed at the end of Sect. 9.4.1.1.

Measurements of light intensity of the shock cone with photodiodes are capable of identifying combustion oscillation frequencies even though they are not well-developed. This can be accomplished by the use of photodiodes which have the desired spectral range capability discussed in Sect. 9.4.3.1. The best data is obtained by limiting the acceptance angle to the photodiode to include only the shock cone flattened surface. The photodiode can be mounted remote from the engine, but at engine level, with the line of sight at an angle past the nozzle exit toward the shock cone.

Analysis of the data from the FM tape can be handled in the conventional manner as discussed in Sect. 9.3.5.

9.4.4 Shadow and Schlieren Methods

The function of both schlieren and shadow methods is to determine small variations in the index of refraction of transparent materials. It can be shown that, to a rough approximation, the schlieren method measures the first derivative of the refractive index, whereas the shadow method measures the second derivative. The direct experimental application of these methods in the evaluation of stability behavior is somewhat limited. However, both schlieren and shadow techniques have proven useful in the study of propellant injection and combustion processes under both steady and unsteady conditions.

*9.4.4.1 Schlieren applications.**—The general principle of the schlieren system is illustrated in Fig. 9.4.4a. Light from a point source A is focused on the knife edge D by the long focus, large

* R. C. Kesselring, Author.

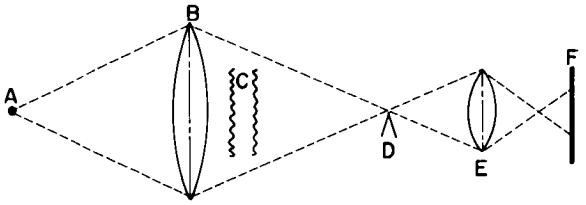

FIGURE 9.4.4a.—A simple schlieren system.

diameter (schlieren) lens B. If knife edge D is moved upward into the beam until it blocks out the image of A, no light will reach film F provided that lens B is of good optical quality and that there are no index of refraction gradients in the medium traversed by the light beam. If, however, the gaseous medium is disturbed in region C by a shock wave, such that some of the light rays are diffracted so that they pass above the knife edge D, these rays are focused by the lens E and an image is formed on the film F. A detailed discussion of schlieren principles and techniques is given in Ref. 30.

Schlieren examination of a shock wave in an operating liquid propellant combustor near the injector face presents a serious problem. The index of refraction gradients (caused by density gradients) in the gaseous medium (C) are probably sufficient to diffract a large percentage of the light rays significantly in one direction or another. If this diffraction were downward, only a weak image would be projected on F and the film would appear underexposed. Thus, any shock wave appearing at a later time would be difficult to observe. If the diffraction were upward, the film would appear over-exposed, creating similar difficulties. Optical distortions resulting from the high thermal gradients and high rate of mass transfer in the neighborhood of each liquid droplet are unavoidable. Similarly, thermal gradients exist throughout the combustion gas and in the injection/spray mixing region. These gradients may become severe enough to limit apparent depth of field and droplet resolution. For these reasons schlieren photography is best confined to situations where very few (if any) index of refraction gradients normally exist in the gaseous medium through which the light rays pass. However, it should be noted that some excellent schlieren pictures of gas-gas detonations have been obtained by Urtiew and Oppenheim.[701] A significant schlieren application in combustion stability research is the characterization of a shock wave generated by an instability rating device under "cold-flow" conditions, as discussed in Chapter 10, and illustrated in Figs. 10.2.1b and 10.3.2e.

*9.4.4.2 Shadowgraph techniques.**—In this section brief but sufficient instruction is given in the art of recording on film the shadow images of the liquid content of a firing combustion chamber. A simple two lens system is described and equations are derived whereby a reasonably accurate prediction can be made of the field of view and its magnification obtainable with a particular optical system composed of elements selected from inexpensive commercial supplies.

The shadowgraph system to be described is primarily intended to provide the investigator with a qualitative insight into what occurs in a firing combustion chamber. For example, Figs. 9.4.4b and 9.4.4c show sharp, high contrast, shadow images of the propellant spray produced by impingement of nitrogen tetroxide and a fuel blend composed of equal weights of hydrazine and unsymmetrical-dimethyl-hydrazine. Although 50 micron diameter liquid particles appear to be easily resolved, the optical system is not intended to provide precise quantitative information because the optical system has a deep depth of field and the images of small drops are surrounded by diffraction rings.

The optical phenomenon which produces the shadow images is refraction of spark light at the liquid-gas interface and not the absorption of spark light in the liquid. Thus the shadow images of optically transparent liquid spheres are dark circles. Conversely, a shadow image cannot be formed of a transparent plane liquid sheet.

Figure 9.4.4d shows the optical system in simple schematic form. The optical elements are (from left to right) a high intensity spark, a condenser lens, two diametrically opposed windows in the walls of the combustion chamber, a flame light filter, the camera lens, a flame light stop and the photographic film. These elements must have the following principal characteristics.

For the best results, the flame light filter must

* L. M. Wood, Author.

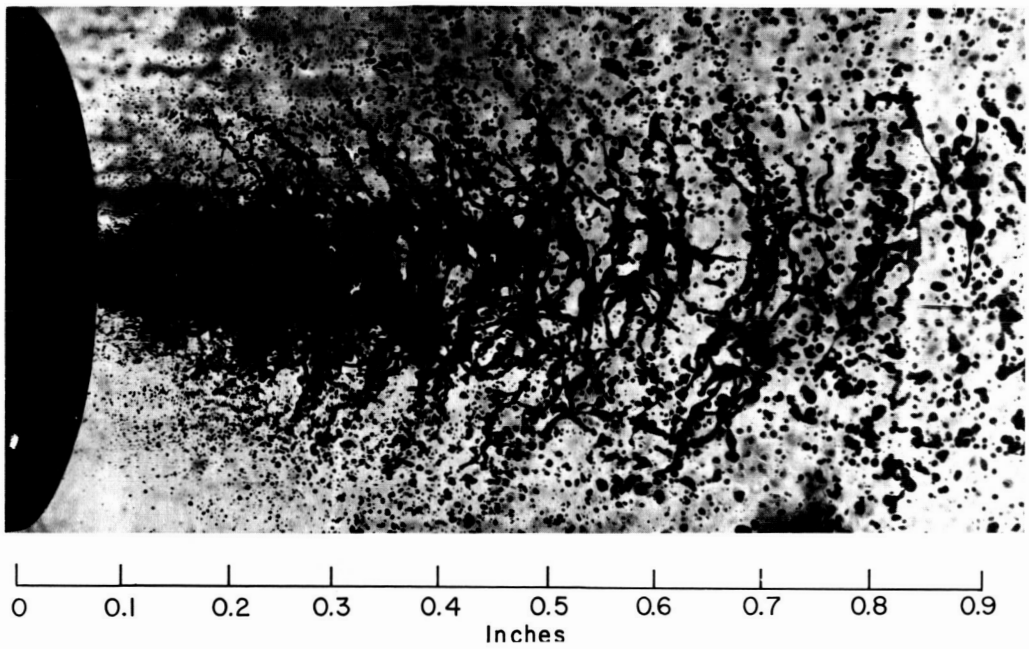

FIGURE 9.4.4b.—Shadowphotograph of spray fan produced by impinging one N_2O_4 jet on one 50% N_2H_4-50% UDMH jet at 120 psia in a 2.5-inch-diameter windowed chamber. Spark, EG&G point light source, $D_s = \frac{1}{16}''$; condenser, Aero-Ektar, $f_c = 178$ mm, $(f/D)_c = 2.5$; camera lens, Wollensak Raptar, $f_o = 135$ mm, $(f/D)_o = 4.7$; 22 inch maximum bellows extension; film plate, $4'' \times 5''$; d = 3.5 inch; W = 1.4 inches; m = 3.4.

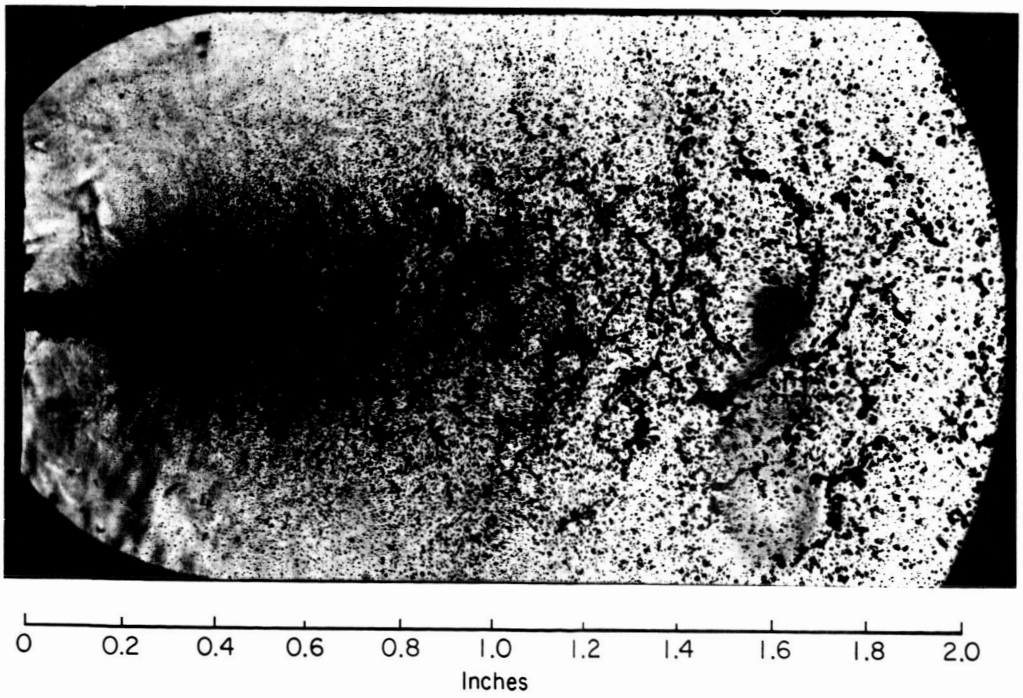

FIGURE 9.4.4c.—Shadowphotograph of spray fan produced by two fuel jets impinging on one oxidizer jet at 120 psia. Same apparatus as Figure 9.4.4b except condenser lens is Taylor-Hobson, with $f_c = 9.25$ inches, $(f/D)_c = 2.5$, and m = 1.6.

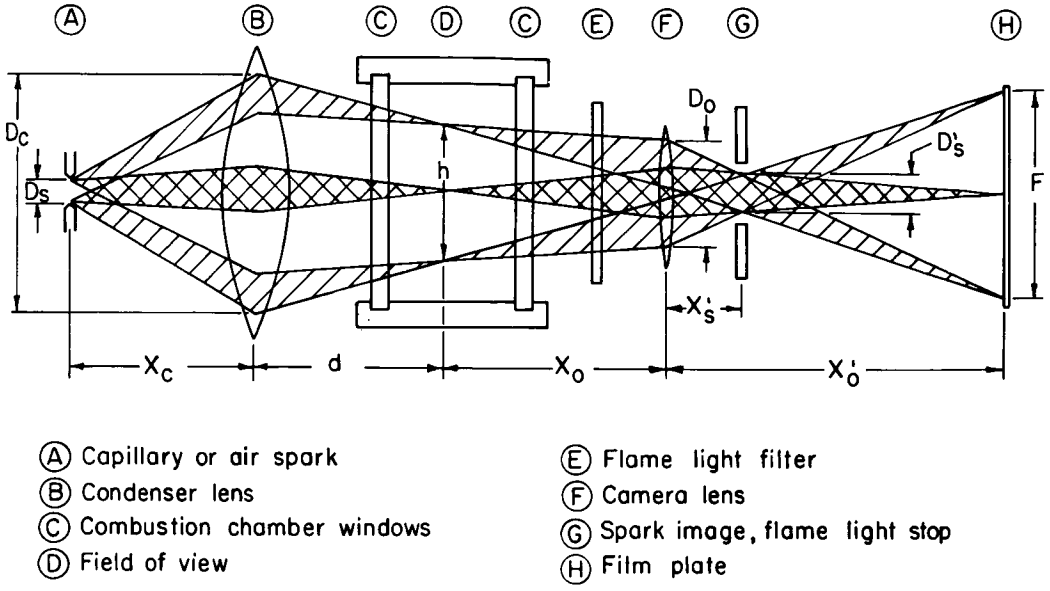

FIGURE 9.4.4d.—Schematic of optical system for taking shadow photographs.

have a transmission no smaller than that required to attentuate the combustion flame light to a level insufficient to expose the photographic film during the open time of the camera lens shutter (not shown in the schematic). A practical method of selecting the filter will be given below.

The spark must have an intensity many times greater than the combustion flame light so that after the inevitable reflection and absorption losses, especially in the transit of the windows, the combustion chamber contents and the flame light filter, sufficient intensity remains to form high contrast shadow images of the liquid content of the chamber. The spark duration must be a few microseconds or less to provide "stop action" images of the rapidly moving liquid particles. Many capillary and open air sparks satisfy these requirements. Note that the exposure time of the film is determined by the spark light duration and not the open time of the mechanical shutter of the camera.

The size of the condenser lens determines the illuminated field of view. This lens is located as close as possible to the chamber window. For a given field of view, the farther this lens is located from the window, the larger is its required diameter. The ideal condenser lens has a large diameter and a short focal length, that is, a low f-number (the ratio of focal length to lens diameter). Also, this ideal lens is optically corrected for that range of object distances of the spark which will be used. In practice, multi-element lenses are available with diameters between three and four inches and at f-numbers as low as 2.5. Although these lenses are most free of distortions at the designed object distances, the primary criterion for selection is large diameter and low f-number.

A suitable camera for combustion photography is the Speed Graflex Camera. Its main limitation is a short bellows extension which limits high magnification. This can be remedied by using the 22-inch bellows of a Calumet View Camera which has its own 4×5 inch film holder and which will accept the lens board of the Graflex camera. The use of this lens outside the design range of magnification produces image distortion, especially at the border of the imaged field of view. These distortions were not found objectionable at 3.5 magnification, bearing in mind that qualitative information is the primary purpose of this optical system.

An image of the spark is formed inside the camera between the lens and the lens focal plane. The limiting spark rays of the bundle of rays which pass through three points of the field of view in the chamber are shown in the schematic. It is seen that each image point receives spark light from the whole spark. This results in a nearly

uniformly illuminated background for the shadow images provided the spark intensity is independent of direction. The spark image location is also the location of the flame light stop, a thin metal plate with an aperture whose dimensions are slightly larger than the spark image. Without the stop and the flame light filter, each image point on the film receives flame light from the whole camera lens and only spark light from a small portion of the lens. Use of a stop with an aperture the size of the spark image ensures the same solid angle of illumination at the film plane for both flame and spark light. Thus the effect of flame light on the film is diminished without a reduction in spark light. This permits the use of a flame light filter with a much higher transmission than would be possible without the stop.

The refraction of spark light by the density gradients in the combustion gas of the firing chamber causes the spark image dimensions to be larger than is the case if the chamber is filled with ambient air. A flame light stop with an aperture the size of the spark image under non-firing conditions will act as a knife edge under firing conditions and will produce schlieren images of the density gradients and a loss of definition in the images of the liquid particles. A stop with dimensions several millimeters larger than the spark image under non-firing conditions will prevent unwanted schlieren effects. A suitable knife edge can be placed in the flame light stop when schlieren photographs showing the location of strong gas density gradients in the chamber are desired.

The film selection is a compromise between the opposing film properties of high contrast and high resolution and is dictated by the degree of suppression of flame light relative to spark light. Kodak Tri-X Panchromatic was used in Figs. 9.4.4b and 9.4.4c.

The spark to condenser lens distance controls the size of the illuminated field of view. The largest illuminated field of view is obtained with the spark at the focal plane of the condenser (parallel light). Moving the spark farther away from the condenser produces a converging light beam and thus a smaller illuminated field of view.

The illuminated field of view is not necessarily the observable field of view. The camera lens may not be large enough to intercept all of the spark light, or the film plate may be too small to receive the image of the illuminated field of view at the desired magnification.

The location and size of the spark image and thus the location and size of the flame light stop is dependent on the location of the spark and camera lens, except in the case of parallel light. Then the image occurs at the focal plane of the camera lens irrespective of the camera lens location. With nonparallel light, the spark image occurs any place between the camera lens focal plane and the camera lens and even on the lens itself. The size of the spark image is greatest at the camera lens focal plane and smallest at the camera lens. Thus for a particular optical system, there is a range of observable fields of view. The following mathematical analysis permits calculation of the observable fields of view and their magnification for a given spark, a lens chosen to serve as the condenser lens, a windowed chamber, a selected camera lens and a given film size.

The following equations describe the optical system.[498] Most of the symbols are defined in the schematic. Of the symbols not defined X_c' is the distance from the condenser lens to the spark image formed by the condenser lens alone. This image is a virtual image for the camera lens and lies on the optical axis at a distance X_s from the right side of the camera lens. Its image size is $X_c'D_s/X_c$.

$$X_c' = \frac{X_c f_c}{X_c - f_c} \tag{9.4.4-1}$$

$$X_s = X_c' - (d + X_o) \tag{9.4.4-2}$$

$$X_s' = \frac{X_s f_o}{X_s + f_o} \tag{9.4.4-3}$$

$$X_o = \frac{(1+m)}{m} \cdot f_o \tag{9.4.4-4}$$

$$X_o' = (1+m) \cdot f_o \tag{9.4.4-5}$$

$$D_c = \frac{X_c'}{X_c' - d}\left[h + \frac{d}{X_c} D_s\right] \tag{9.4.4-6}$$

$$h = \frac{F}{m} \tag{9.4.4-7}$$

$$D_o = \frac{X_o' D_s' + F X_s'}{X_o' - X_s'} \tag{9.4.4-8}$$

$$D_s' = \frac{X_c'}{X_c} \cdot \frac{X_s'}{X_s} D_s \qquad (9.4.4\text{–}9)$$

In the derivation of these equations, the lenses are assumed to be thin. This does not seriously affect the results. The sign convention of optics is not used, that is, all object and image distances are positive.

It is assumed that the chamber windows are sufficiently large so as not to be limiting apertures. For the sake of simplicity, the spark is assumed to be a thin circular radiating disk. Thus the illuminated field of view and its image are circles. The dimensions of the imaged field of view is taken to be the same as the fixed film size. Thus the magnification, m, of the field of view is given by the ratio of film diameter to the field of view diameter, Eq. (9.4.4–7).

Eqs. (9.4.4–1) through (–5) are simple lens equations specifying the locations of the centers of the objects, images and lenses on the optical axis. Eqs. (9.4.4–6) through (–9) specify the diameters of the lenses, the observable field of view and the spark image. The diameters specified by Eqs. (9.4.4–6) and (–8) may be less than the full diameters of the respective lenses.

In these equations, f_c, f_o, D_s, F and d are constants of the apparatus. The constant d is given by the distance between the field of view in the chamber and the center of the condenser lens. An inspection of the schematic shows that the system is completely specified, within limits imposed by the maximum diameters of the given lenses, by choosing the spark object distance X_c, and the magnification, m. The limitation imposed by the camera lens is

$$D_o \leq \left(\frac{D}{f}\right)_o \cdot f_o \qquad (9.4.4\text{–}10)$$

where $(D/f)_o$ is the relative aperture of the camera lens, that is, the reciprocal of the f-number. The limitation imposed by the condenser lens is

$$D_c \leq \left(\frac{D}{f}\right)_c \cdot f_c \qquad (9.4.4\text{–}11)$$

Eqs. (9.4.4–1) through (–9) are valid providing the spark image lies between or at the camera lens and the focal plane of the camera lens. This limitation is expressed by the following inequality:

$$X_c' \geq d + X_o \qquad (9.4.4\text{–}12)$$

The solution of Eqs. (9.4.4–10) through (–12) is $m \geq A + (A^2 - B)^{1/2}$

$$2A = \frac{(f_c/f_o)[C-(C-1)(d/f_c)] + D_s/F - (C-1)}{(D/f)_o(f_c/F)[C-(C-1)(d/f_c)] - D_s/F}$$

$$B = \frac{(C-1)}{(D/f)_o(f_c/F)[C-(C-1)(d/f_c)] - D_s/F} \qquad (9.4.4\text{–}13)$$

$$m \geq \frac{(F/f_c)C}{(D/f)_c[C-(C-1)(d/f_c)] - (d/f_c)(D_s/f_c)} \qquad (9.4.4\text{–}14)$$

$$m \geq \frac{(f_o/f_c)(C-1)}{C-(C-1)(d/f_c) - (f_o/f_c)(C-1)} \qquad (9.4.4\text{–}15)$$

where

$$C = X_c/f_c$$

For a chosen value of C greater or equal to one, the smallest magnification which satisfies Eqs. (9.4.4–13) through (–15) determines the largest field of view observable with the chosen spark location. Solving Eqs. (9.4.4–13) through (–15) for a range of spark locations determines the range of observable fields of view and their magnifications which can be obtained with the given optical system.

The limitations imposed by the chamber windows are determined by solving the inequality $D \leq W$ where D is the optical beam diameter at the chamber window of diameter W. The limitations imposed by the maximum bellows extension, B, is determined from the inequality $X_o' \leq B$.

The constants of the optical system used to produce Fig. 9.4.4b (parallel light) and Fig. 9.4.4c (converging light) are given in the figures. Fig. 9.4.4b was taken at the maximum magnification and Fig. 9.4.4c was taken at approximately the maximum observable field of view.

A rational selection of the flame light filter and the photographic film requires knowledge of the relative magnitude and the spectral distribution of the flame and spark light. Complete information is never available a priori, at least for flame light because the flame light intensity depends on the composition, pressure and radiating path length

(chamber diameter). This information can be obtained from densitometer readings of spectrograms of spark and flame light taken through the windowed chamber at the same spectrometer settings. With this information, a suitable film and filter can be selected.

In lieu of this approach, past experience can be utilized to make it certain that the first firing test will produce a good shadowgraph. Figures 9.4.4b and 9.4.4c were taken with a Kodak Wratten 47-B filter and Kodak Tri-X Panchromatic film with 0.007 Estar stable base. The exposed film was 175% overdeveloped in a Kodak Versamat Processor. The services of a professional photographer are indispensable in selecting the proper film and filter combination and in the processing and printing of the negatives.

The predicted performance of the optical system provided by the analysis is approximate but reasonably accurate. The analysis should be checked by mounting the apparatus on an optical bench, including the chamber windows, and taking shadowgraphs of the spray produced by an aerosol can. This test also provides information on the optical resolution, the depth of field and the shadow image sharpness and contrast.

The optical analysis and the experimental techniques just described are an extension of the works of Rossmann[608,607,606] which provide detailed information on the experimental aspects of combustion photography.

Shadowgraph methods have also been used to investigate the breakup and vaporization of liquid jets in the absence of combustion. Details on liquid droplets, ligaments and vapor patterns (including displacement with pulsing) have been obtained using Freon-21 as the pseudo-propellant.[638] A subsequent study investigated the effects of shockwaves and baffles on the spray and vapor boundaries.[190]

*9.4.4.3 Silhouette photography.**—In photographic studies of the combustion process in liquid propellant rockets it is often of interest to observe the individual fuel and oxidizer spray fans during both stable and unstable operation. From such observations it is sometimes possible to determine the existence of combined modes of instability (such as high frequency wave motion and low frequency chug) that would not otherwise be detected.[440] In this type of application shadow (silhouette) photography is employed. This type of photography should not be confused with the shadow method which measures the second derivative of the refractive index. The silhouette photographs are obtained simply by using a high-intensity monochromatic backlight (e.g., a mercury vapor lamp). A narrow-band optical filter which passes only the green line of the mercury (5470 Å) is used to eliminate the combustion light within the chamber. A typical shadow picture of propellant fans is shown in Fig. 9.4.4e. As in the case of schlieren photography, however, the presence of high thermal gradients may limit depth of field and droplet resolution.

Time-sequence silhouette photographs have also been found useful in studying the phenomenon of droplet shattering upon arrival of a shock wave under noncombustion conditions.[598] Figure 9.4.4f shows the various stages of shear-type droplet breakup upon arrival of a shock.

FIGURE 9.4.4e.—Typical shadow picture of propellant spray fans.

9.4.5 Holography of Liquid Rocket Engine Combustion*

A new technique of scene recording has evolved which yields a permanent three-dimensional record of a high velocity event. It is called holography and is based upon the recording of a light interference pattern rather than an intensity distribution as in photography. Although known for 20 years by optics specialists,[281,27,28] the technique did not become practical for transient events until the invention of the solid-state laser in 1960.[460,459] Pulsed laser holography has been

* R. C. Kesselring, Author.

* R. F. Wuerker and B. J. Matthews, Authors.

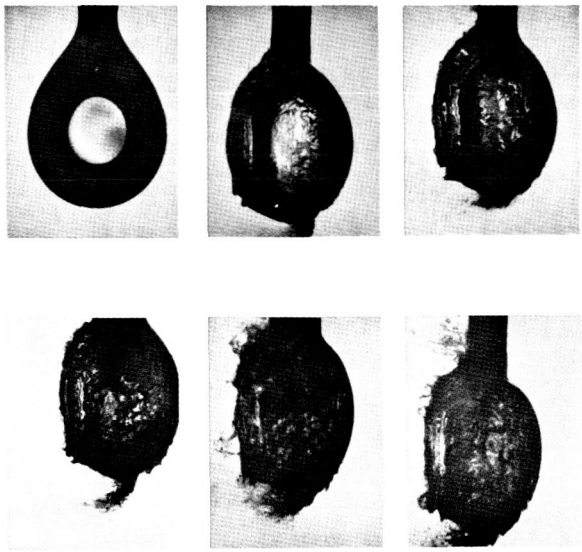

No. 4 t = 70 μsec No. 5 t = 90 μsec No. 6 100 μsec

← Shock direction

Various stages of shear-type droplet breakup

Liquid ▪ RP-1
Drop diameter = 1780 microns
Gas velocity = 320 ft/sec
Drop magnification = 23 diameters
Test section pressure = 1 atmosphere

FIGURE 9.4.4f.—Various stages of shear-type droplet breakup. Liquid, RP-1; drop diameter, 1780 microns; gas velocity, 320 ft/sec; drop magnification, 23 diameters; test section pressure, 1 atmosphere.

successfully used to record combustion of the fuels and oxidizers used in liquid rocket engines.[765] Holography of atmospheric (open flame) firings as well as combustion phenomena in windowed thrust chambers of 3-inch and 18-inch diameter have been recorded to date. This section summarizes the present state of the art in the development of this new diagnostic tool which, in addition to other applications, is uniquely suited to the study of the chemical combustion process.

9.4.5.1 Holography reviewed.—From a scientific or data recording point of view, holography is important because it (1) records volumes rather than the planes recorded by conventional photography; and (2) makes possible interferometric comparisons between either two holographically recorded volumes or between a holographically recorded volume and a real volume at a later time. In addition, it is a coherent process and can distinguish information in the presence of a strong background of incoherent radiation. All of these unique holographic features stem from the fact that it is based upon the recording of a portion of the stationary optical interference pattern which occurs when two beams of coherent light pass through one another. The recorded interference pattern (called a hologram) can then be used to recall the complete scene whenever it is illuminated by a beam which closely approximates one of the original beams. As a result, the recording and examining steps are separated; a hologram recorded with a pulsed laser can be leisurely examined in detail and under magnification at a later time with any of the classical optical instruments (eyes, microscopes, telescopes, cameras, interferometers, schlieren systems, etc.).

Since lenses are not required in holography, there is no focusing problem; as a result, small objects of unpredictable location or of large spatial distribution can be recorded completely. The recorded scene can be examined, measured, and objects located whenever the hologram is reconstructed. In essence, holography is free of the depth-of-field limitation of the conventional lens which, under high magnifications, can be particularly restrictive, making it almost impossible to study anything but near static events with the classical microscope.

Holography is a coherent process. It therefore requires the use of coherent illuminators which, in essence, are point monochromatic radiators equal in size to their wavelength. The technique or process of generating light via the amplification by stimulated emission of radiation (i.e., by a laser) approximates, in most cases, the coherent sources required in holography. For this reason holography did not come of age until after the reduction to practice of the first operating laser in 1960.

On the deficit side is the inherent slow speed (typically $1/5 \gtrsim \text{ASA} \gtrsim 1/300$) of the photographic plates required to store a part of the optical interference pattern. Motion restrictions are therefore a problem. The reconstructed scene can be greatly degraded by motion throughout the space of the interference pattern by as much as one-fourth of the wavelength.

For scenes illuminated by the transmission of radiation through them, the motion restrictions

are no different from those of conventional photography. Therefore, resolution of the reconstructed scene according to theory will be determined either by the geometrical aperture of the system, or by the smearing of the event by an amount equal to the product of the velocity of the original subject and the exposure time. Thus, a hologram made with a laser having a 0.1 microsecond pulse duration requires a velocity of the original event of less than 10 meters per second to have a 1-micron resolution. For 10-micron resolution, the velocity must be less than 100 meters per second, etc. For this reason, it is desirable to have short exposure times for high velocity events of interest; however, the extreme insensitivity of the films necessitates (in high resolution situations) illuminators of multi-megawatt irradiance. At present, only the solid-state ruby laser is adapted to the holography of high-speed events. This is due to the fact that the chromium ions in the sapphire host are optical energy storage means ($\sim$0.2 joule per cubic centimeter) which can be made to emit in times measured in terms of the light transit time between the mirrors of the optical resonator. Pumped ruby rods can also be used as simple optical power amplifiers to step up the oscillator radiation level to that needed to expose the presently insensitive high-resolution photographic plates.

Of all the solid-state lasers, the ruby laser emits at a wavelength which is within the sensitivity of high-resolution photographic plates and has a bandwidth narrow enough so that the optical interference pattern is not smeared appreciably during the exposure of the plate. Ruby laser systems have been built which emit as much as a billion watts; however, in many cases the coherence can be quite low. Gas lasers, in contrast, have intensities which are at best six to seven orders of magnitude less intense. As a result, a gas laser can be used only in the holography of quasi-static scenes or scenes spanning such a narrow angle that the resolution is quite low. This is true in spite of the fact that many gas lasers emit in regions of the spectrum where films are more sensitive. Compared to solid-state lasers, the gas lasers are more coherent in terms of both the monochromaticity (temporal coherence) and phase uniformity across a cross section of the emitted beam (spatial coherence). Pulsed lasers, as a result, require special precautions in the recombining of their radiations. When these precautions are followed, quality holograms of high velocity events are achieved to high resolutions.

Holography's main value is the fact that it separates the recording and examining steps in the permanent capturing of an event. As a result, with a pulsed laser, dynamic phenomena of an uncertain and unpredictable location can be recorded. After the hologram has been recorded, it can then be leisurely examined with any of the classical optical instruments, or can be used to make interferometric comparative measurements.[328c] For these reasons, the techniques should be of significant value in studying rocket engine ignition characteristics, combustion phenomena, and exhaust products.

9.4.5.2 Application of holography to rocket combustion.—Through the years, studies of liquid rocket combustion have been accompanied by a continuing evolution of optical systems designed to further the investigator's understanding of events occurring within the combustor. The application of pulsed laser holography is a natural extension in the development of such instrumentation systems. However, utilization of this technique to investigate high temperature combustion phenomena is a comparatively recent accomplishment.

An early pulsed laser holographic experiment with combustion involved making holograms of acetylene-air mixtures ignited by a spark plug.[763] Another important holographic experiment with combustion was the recording of a white-hot zirconium particle in free fall.[31] These experiments, while of considerable interest and importance, were not specifically directed toward liquid rocket combustion.

In 1967–68, two research programs using holography were initiated in the liquid rocket combustion area. The first involves the study of small droplets in a cold environment[468] with emphasis on (1) size resolution, (2) maximum droplet flux levels, (3) possibility of measuring mixture ratio, and (4) position flexibility. The second program is directed toward the feasibility of using pulsed laser holography to record the

droplet dispersion of reacting sprays in liquid propellant rocket engines.[764]

The two-beam holocamera arrangements used in the two studies were improved versions of a basic design developed by Brooks, Heflinger and Wuerker.[123] Representative of recent thinking in the design of two-beam transmission holocameras[764] is that which is presented in Fig. 9.4.5a.

As may be seen from the schematic of Fig. 9.4.5a the holocamera has two spatially and temporally matched scene and reference beams. Spatial matching is achieved by proper use of reflectors, a roof prism, and a large pair of condensing lenses. The latter pair of elements takes the light scattered by a ground glass screen and focuses it back onto the hologram. The mirrors and the roof prism insure that each scene ray combines once again with the equivalent reference ray at the plane of the hologram. Temporal matching is achieved by arranging the distances of the mirrors so that after division by the beam splitter, both scene and reference beams travel over the same optical path lengths; the accuracy of the path match is within the temporal coherence limits of the laser illuminator. The scene which is recorded is located between the focusing lenses and the hologram.

The hologram itself is a 4×5 inch glass photographic plate oriented at $67\frac{1}{2}°$. This angle was chosen so that the normal to the photographic plate bisects the angle between the direction of the reference beam and the axis of the condensing lens system. As a result, the interference pattern between scene and reference beam is perpendicular to the emulsion. Holograms made in this manner are thought to be freer of distortion than if the "blazing" is not perpendicular to the plate.

Holograms to be made of rocket combustion phenomena require adequate shuttering systems to prevent pre-exposure of the film plate. A simple focal plane or "window shade" shutter from an antique Graflex-type camera has been used successfully for this purpose; however, a better arrangement includes a secondary leaf-type (capping) shutter to augment the focal plane shutter and eliminate light leakage onto the film.[764]

The two rocket propulsion oriented studies involved the recording of holograms of impinging stream injector droplet spray patterns.[468,764] Both

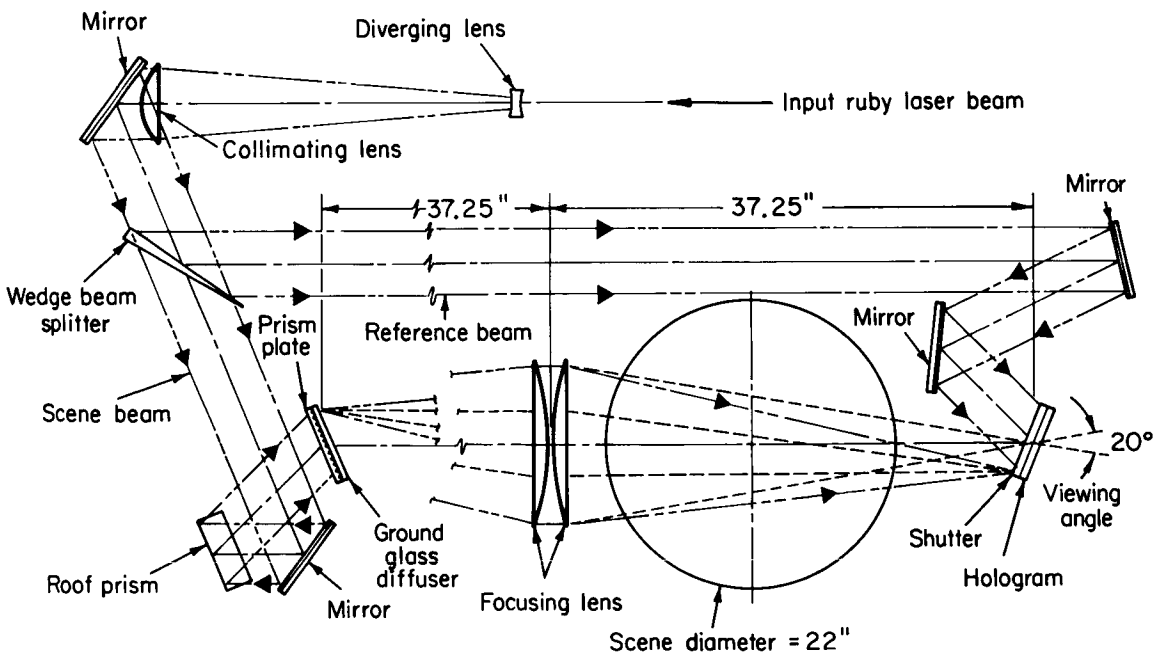

FIGURE 9.4.5a.—Schematic diagram of TRW focused ground glass transmission holocamera design for producing reacting spray holograms.

reacting liquid propellants (open flame and confined combustion) and non-reacting sprays (cold flow simulations) have been recorded.

These recordings have been made with Kodak 649F and Agfa 10E75 and 8E75 plates. The Kodak emulsion is panatomic* and has a resolution of ~4,000 lines/millimeter with an ASA rating of 1/40. It is even an order of magnitude less sensitive at the ruby laser wavelength (0.69 micron). In contrast, the Agfa emulsion is more sensitive at 0.69 micron, being sensitized primarily for the red and green regions of the visible spectra. The Agfa emulsion is a new film which was not available at the inception of the present programs and is preferred since it required a smaller laser illuminator, thereby making the whole holographic system more portable.

Fig. 9.4.5b is a photograph of the reconstruction of a ruby laser water flow hologram recorded on an Agfa 10E75 plate and developed for 5 minutes in Eastman HRP. The scene was reconstructed by properly orienting the hologram before a collimated beam from a 0.63 micron helium-neon continuous wave gas laser. The copy camera was focused on a plane passing through the impingement point and central portion of the spray fan. This hologram is typical of various recordings made during a series of holographic studies of injector water flow spray patterns.[764]

* Extremely fine grain panchromatic (sensitive to all visible colors and ultraviolet) film.

FIGURE 9.4.5b.—A reconstruction photograph of a laser hologram illustrating the water flow spray pattern from the single element impinging stream injector operating at a pressure drop of approximately 300 lb/in.^{2} and a flow rate of 2.35 lb/sec; orifice diameters are 0.173 inch.

In addition to recording holograms, the holocamera may be used to produce laser-illuminated photographs. This is accomplished by mounting a bellows-type copy camera positioned so that it views through the mechanical shutters and is focused on the spray fan produced by the injector element. For laser photography, the reference beam of the holocamera is blocked and only the scene beam is utilized. In this manner the copy camera uses the laser and beam-forming optics as a high grade transmission type illuminator. Such a laser-illuminated photograph of water flowing from the same type of injector element is shown in Fig. 9.4.5c.

The feasibility of applying laser holographic and photographic techniques to rocket combustion studies has been verified through a series of open flame and combustion chamber experiments.[765] Tests were conducted with N_2O_4 and A-50 and with FNA-UDMH propellants flowing through single element impinging stream injectors. In the initial series, the propellants ignited and burned in the atmosphere. Subsequent tests utilized windowed (acrylic) thrust chambers.

Holograms recorded of open flame reacting sprays are typified by the reconstruction photographs illustrated in Fig. 9.4.5d. This is a fan plane view of the N_2O_4 and A-50 reacting spray. Note the definite droplet wave formations present in the first few inches of this reaction. The two photographs in this illustration were made of the same focal plane within the reconstructed scene but from slightly differing viewing angles (by the copy camera). With the aid of a viewer, this pair

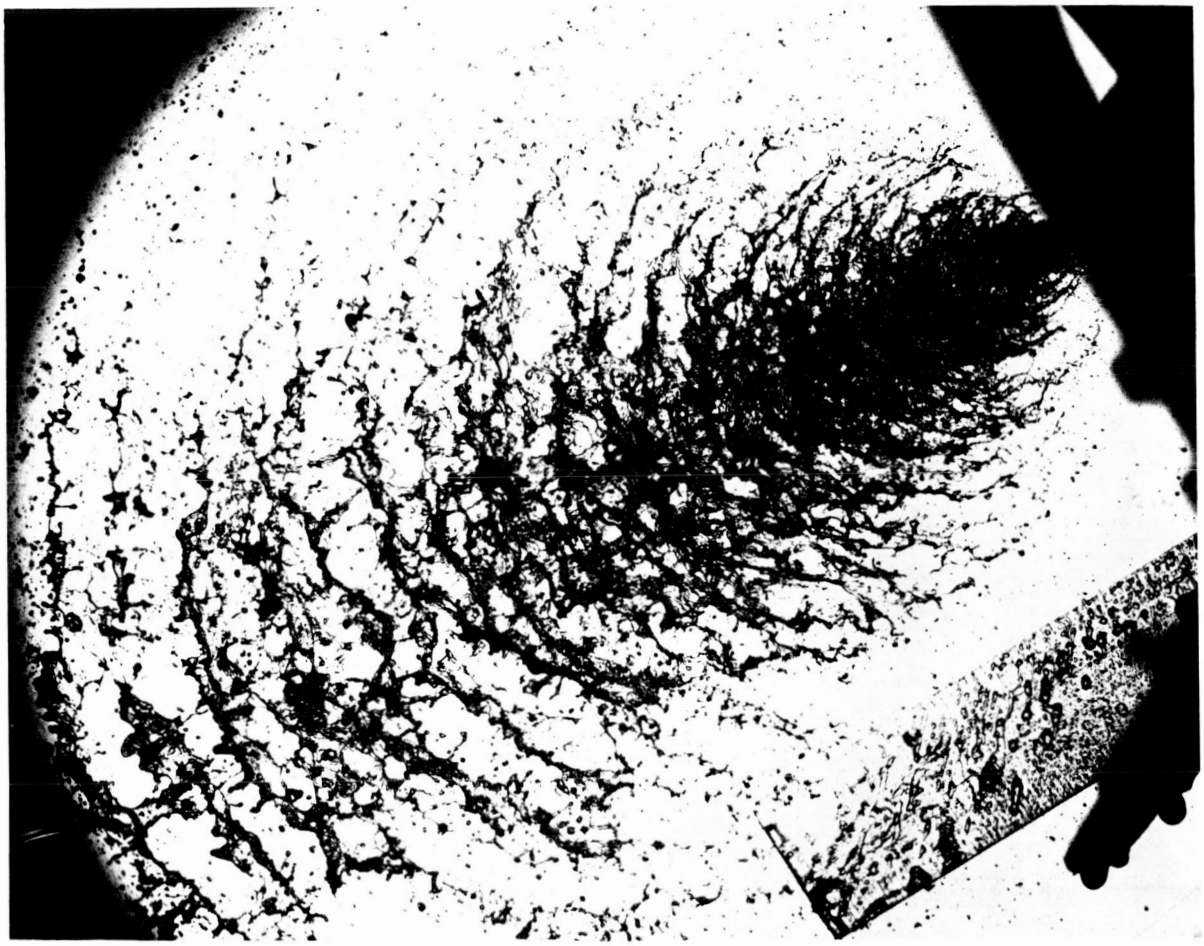

FIGURE 9.4.5c.—A direct laser-illuminated photograph of the water spray fan from a single element doublet injector with a flow rate of 1.22 lb/sec.

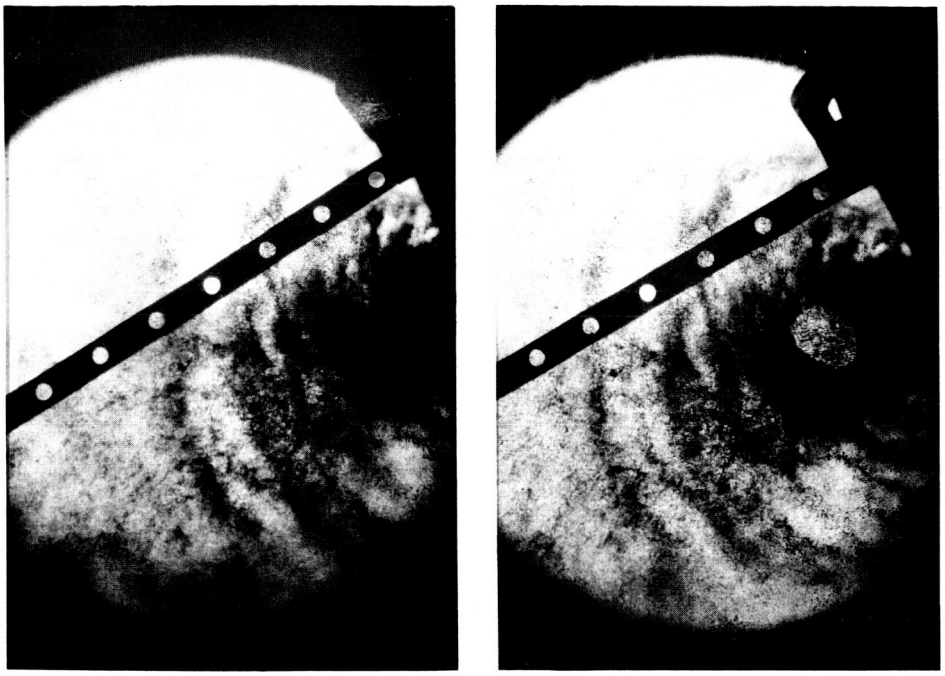

FIGURE 9.4.5d.—Two reconstruction photographs from a hologram of N_2O_4 and A-50 open flame combustion. The photographs differ by the reviewing angle of the copy camera; the photos are mounted as a stereo pair and may be so viewed with the aid of an appropriate viewer.

of reconstruction photographs can be viewed stereoptically. (Also shown is a $\frac{1}{2}$-inch wide steel bar with a series of $\frac{1}{4}$-inch diameter holes on 1-inch centers to permit the viewer to estimate the magnification of the reconstruction photograph.)

Figure 9.4.5e is a series of four reconstruction photographs of a hologram of FNA-UDMH combustion in a 3-inch diameter acrylic thrust chamber. The four photographs correspond to different focal positions within the reconstructed scene volume. For the lower photograph the copy camera was focused on the near side acrylic chamber wall. The upper photograph was made by focusing on the opposite or far side inner chamber wall. The remaining two photographs were made by focusing on intermediate planes within the combustion zone.

The photographs of Fig. 9.4.5e serve to illustrate the depth-of-field feature of holography. Definition of the reacting spray phenomena was somewhat degraded by the eroding acrylic chamber walls (note the longitudinal streaking).

Work conducted to date has demonstrated the feasibility of pulsed laser holography of reacting liquid propellant sprays under "field" conditions at a rocket test site. This type of work is continuing. Areas which warrant additional attention and refinement include (1) greater control of the scene/reference beam intensity ratios in order to compensate for absorption of the ruby light by unburned oxidizer; (2) lasers of shorter duration to eliminate image smear due to small droplets traveling at very high velocity in the combustion environment; and (3) lasers of greater spatial coherence.

Improved means of hologram reconstruction are needed in order to gain maximum resolution from the hologram recording. One problem at the present is the 10% difference in wavelength between the 0.6943 ruby light used to record the hologram and the 0.6328 helium neon light used for reconstruction. Use of helium neon lasers for reconstruction instead of ruby is an economic choice due to problems of operating a ruby laser continuously.[764] Theory predicts that holograms should have resolutions equivalent to that of the aperture subtended by the virtual image at the hologram. At large working distances, the resolution of holograms should compete with and exceed the resolution of lenses.

9.5 ACCELEROMETERS AND ACCELERATION DATA*

When a rocket thrust chamber is subjected to an internal pressure perturbation such as that experienced during unstable combustion, the loads applied to the hardware must of necessity cause mechanical strains. The magnitude of the strain is usually so small that measurement of the actual displacement is extremely difficult. This is especially true when pressure perturbations at the rate of several kHz are experienced. However, as displacement of any mass must involve acceleration, a convenient method of monitoring the response of the hardware to perturbations in the combustion chamber pressure is the judicious use of accelerometers. The data thus obtained can sometimes provide useful information which complements that derived from pressure transducers located in the combustion chamber.

9.5.1 Selection of Appropriate Instrument

There exist at present many types of accelerometers, all designed for specific purposes, and care must be exercised in the selection of the most suitable type.

Three basic types of instruments are available, namely:

1. Strain gage
2. Capacitance
3. Piezoelectric

There are many variations of these three basic types, so that the following discussion of their relative merits should be regarded only as a generalized summary of that type of instrument and not as a description of any one instrument produced by any manufacturer.

Strain gage type.—As its name implies, this instrument relies on the deformation of a strain gage foil (by the inertia loads associated with acceleration) to produce a change of resistance proportional to the acceleration forces exerted upon it. It is able to provide very accurate information as to the amplitude of the acceleration involved, providing that only low frequencies are experienced. A typical application would be the acceleration measurements associated with a centrifuge, where low rates of change of acceleration are experienced and accurate acceleration amplitude data are required.

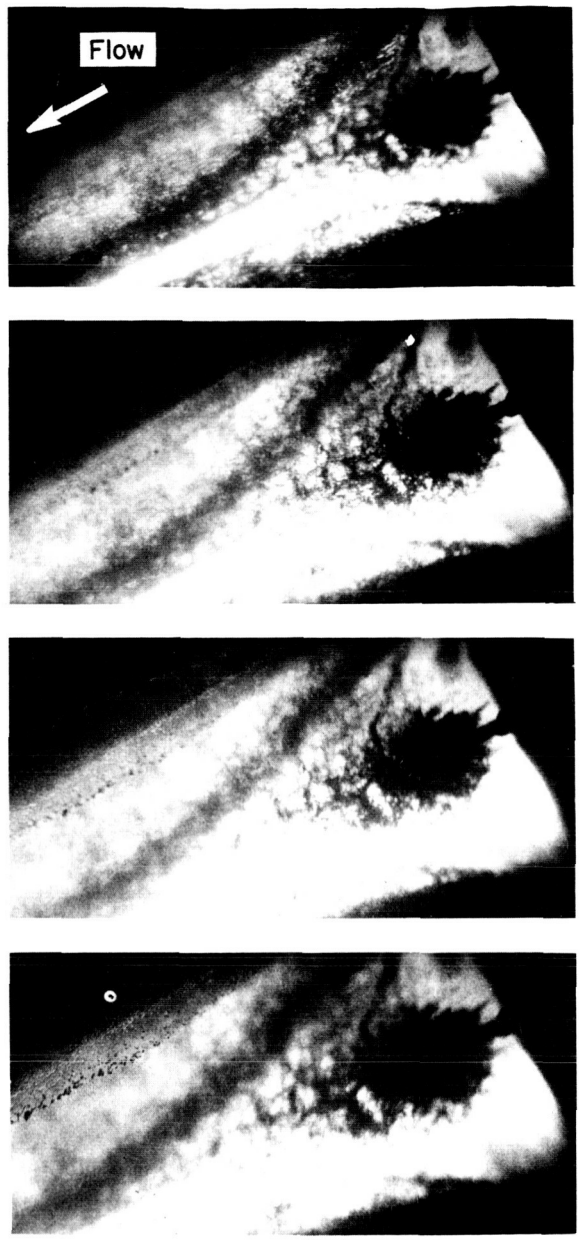

FIGURE 9.4.5e.—Four reconstruction photographs of a single hologram of FNA-UDMH combustion in an acrylic thrust chamber. The photographs correspond to different focal planes within the scene volume.

Capacitance type.—The charge on a capacitor is proportional to the thickness of the dielectric between the plates. Therefore, if these plates are distorted by inertia forces due to acceleration, a

* E. Howells, Author.

change in capacitance will be noted which can be correlated with the acceleration concerned. Such a transducer has good high frequency response coupled with accurate amplitude measurement. However, mechanical design considerations usually dictate that this instrument be somewhat larger in size than the other types. A typical application of this instrument could be the monitoring of a mechanical shaker used for vibration work. Here, the accelerometer mass would still be small as compared to the shaker.

Piezoelectric (crystal) type.—In a crystal accelerometer a measurement is made from the charge variation obtained by the deformation of a piezoelectric crystal. Although this instrument does not usually provide amplitude measurement accuracies as good as those associated with the capacitor type, the crystal accelerometer does have a broad frequency response, extending into the higher frequency ranges (e.g., 10 kHz)[406] and is usually smaller in size than the previously described instruments.

All types of transducers can suffer from cross-axis sensitivity, that is, acceleration in one plane induces an output in some other plane. However, some form of compensation is included in most instruments.

During the investigation of combustion instability the prime requirements of any accelerometer are

1. Suitable high frequency response
2. Miniaturized design, so that its mass does not substantially affect the structure to which it is attached
3. Sufficiently rugged to withstand overload and shock conditions.

The crystal (piezoelectric) transducer meets most of these requirements and is therefore the type generally preferred for combustion instability monitoring. A sketch of a typical crystal transducer is shown in Fig. 9.5.1.

9.5.2 Instrument Mounting

Care must be exercised in the selection of the instrument mounting, so that the mount itself does not compromise the quality of the data output from the transducer. Typical examples of mounting techniques are

1. The bonding of the transducer directly to the structure itself
2. Attachment of a mounting block, into which the transducer may be screwed.

The advantage of the bonding system is that the accelerometer may be placed at any convenient location on the structure where space permits. However, problems can arise regarding the bonding agent itself. It must possess sufficient elasticity to withstand shock loads without cracking. Yet it must not allow movement of the accelerometer relative to the face onto which it is bonded. A further complication arises when temperature changes are experienced, in that bonding agents are invariably degraded by high temperatures (say in the area of 300° F and above).

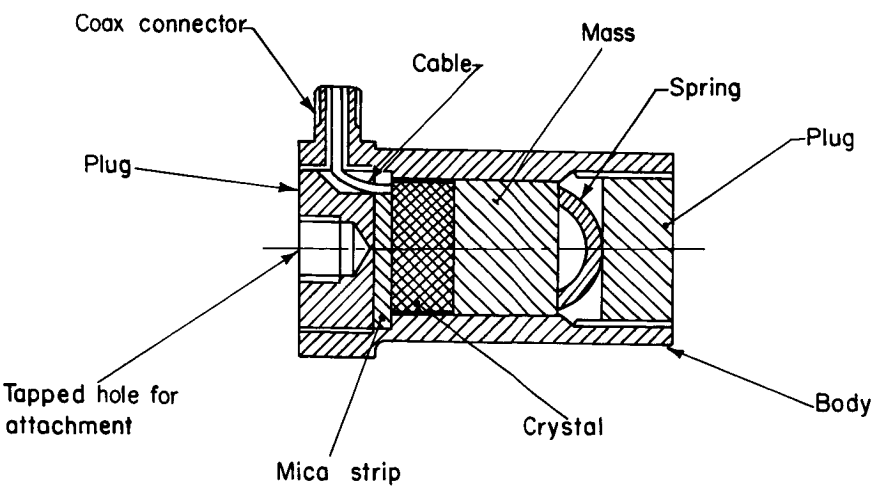

FIGURE 9.5.1.—Typical piezoelectric (crystal) accelerometer.

The mounting block system does circumvent the problems inherent in the bonding process. However, this approach does possess its own peculiar complications. Welding-on a block can, for instance, involve a stiffening effect on the structure being tested and this stiffening will obviously change the response characteristics of the structure. Therefore, to minimize this effect the block should be as small in size as is reasonably possible. It is also true that not all structures are either accessible for or amenable to welding. However, if a mounting block is used, it is usually possible to arrange for the installation of more than one instrument into that block. This is especially useful when it is required to monitor acceleration in various planes. As an example, accelerometers mounted on adjacent faces of a rectangular block (as shown in Fig. 9.5.2) will monitor acceleration in three mutually perpendicular planes.

9.5.3 Acquisition of Data

The output signal from a crystal accelerometer is similar to that obtained from a crystal pressure transducer and is handled in a like manner (see Sect. 9.3.4). Once acquired on magnetic tape the information is readily available for subsequent analytical manipulation such as

1. Time expanded playback for examination of pulse "shape," etc.
2. Frequency (harmonic) analysis and power spectral density determinations.

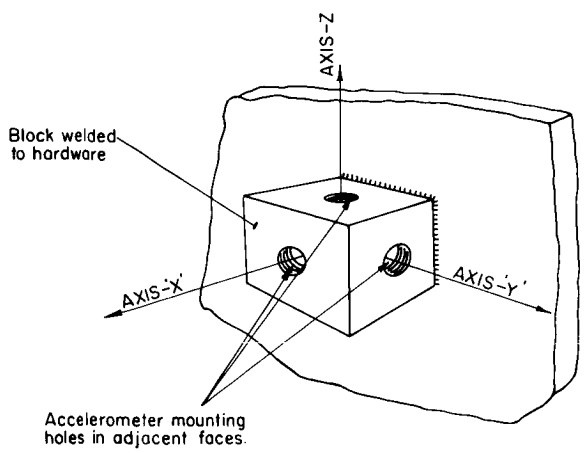

FIGURE 9.5.2.—Mounting block for monitoring acceleration in three perpendicular planes.

3. Filtered time history for the examination of the setting up of a particular frequency
4. Correlation of acceleration with the internal pressure field perturbations.

These techniques are of course identical to those which can be applied to high frequency pressure information (Sect. 9.3.5).

9.5.4 Typical Applications

9.5.4.1 Detection and characterization of combustion instability.—Initial stability testing of an injector is usually carried out in a chamber designed with adequate instrumentation, particularly for chamber pressure measurements. In the early development phase, tests may be run for comparatively short periods of time so that temperature effects on pressure transducers are kept to an acceptable level, whereas the duration of the actual mission duty cycle of the flight engine may far exceed this.

Accelerometers can usually be placed in locations where heat flux is at a minimum (such as the back face of the injector) and also are easily installed on most hardware whether it be R and D or flight-type. If both accelerometers and pressure transducers are provided at the development stage, the acceleration "patterns" can be correlated with the chamber pressure perturbations which are responsible for these acceleration patterns. The accelerometer records obtained from flight-type hardware can then be correlated with those previously obtained pressure perturbation versus acceleration patterns, and reasonable deductions made regarding the behavior of the pressure field even though adequate pressure monitoring was not possible.

The term "acceleration pattern" has been deliberately used because it is important to note the envelope shape of the signal as well as frequency content and amplitude. This is necessary, for example, when the chamber pressure perturbation frequency is lower than the hardware resonant frequency. A pressure pulse will then excite the hardware, which will oscillate at its resonant frequency. The hardware vibration will decay according to the inherent mechanical damping of the system. A subsequent pulse in the pressure field will re-excite the hardware causing the process to repeat itself. This type of signal (shown in Fig. 9.5.4a) therefore contains both

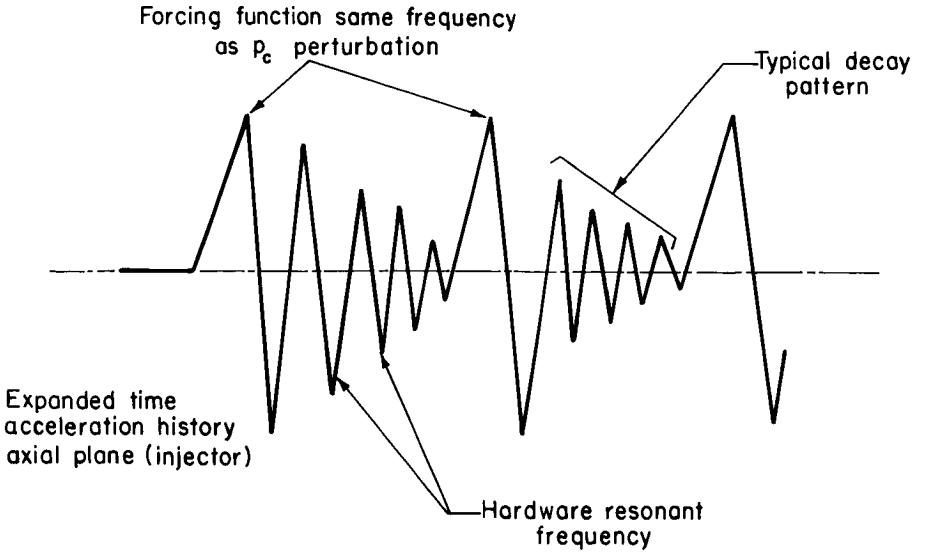

FIGURE 9.5.4a.—Typical acceleration pattern generated by a chamber pressure perturbation of lower frequency than the resonant frequency of the hardware.

mechanical resonance and "forcing function" information. The forcing function, of course, is the chamber pressure fluctuation and is the information of most interest. This rather simple example shows the importance of the overall envelope shape in the interpretation of acceleration data.

9.5.4.2 Determination of hardware resonance effects.—Unstable combustion occurs at certain well-defined frequencies. Care must be taken to ensure that the frequencies of the acoustic modes of the combustion chamber and the mechanical resonant frequencies of the hardware do not coincide. With such precautions, and the proper positioning of the accelerometers, data can be obtained on the combustion phenomena occurring in the chamber. A typical arrangement to check for hardware resonance effects is shown in Fig. 9.5.4b where chamber "ringing" frequencies will be displayed by accelerometers Y_1 and Y_2, while Y_3, X and Z will display the mechanical response of the injector to acceleration originating in the chamber and transmitted upstream through the structure. The excitation in a cold test is provided by a sharp blow delivered to the chamber at Point A. When interpreting data from such a test one should remember that the accelerations recorded are of an absolute nature and include acceleration of the injector relative to the chamber, and acceleration of the engine relative to the stand, as well as any movement of the stand. Therefore, it is expedient to instrument some portions of the test stand itself. This would enable these rigid body modes to be discerned and hence discounted from the rocket engine hardware frequency analysis.

The information to be gleaned from such a test can only be of an approximate nature due to the lack of pressurization effects on the hardware. These effects would obviously be present during engine firing; however, they are normally of second order importance and do not seriously compromise the data acquired.

9.5.4.3 Estimation of hardware distortion during instability.—During unstable combustion the hardware usually oscillates at a high frequency and experiences high acceleration forces. Some reasonable estimate of the displacement of the hardware may be obtained by assuming that the hardware moves with simple harmonic motion. The displacement from its "at rest" position is then given by the expression

$$x = \frac{a}{4(\pi f)^2}$$

where x is the displacement from the "at rest"

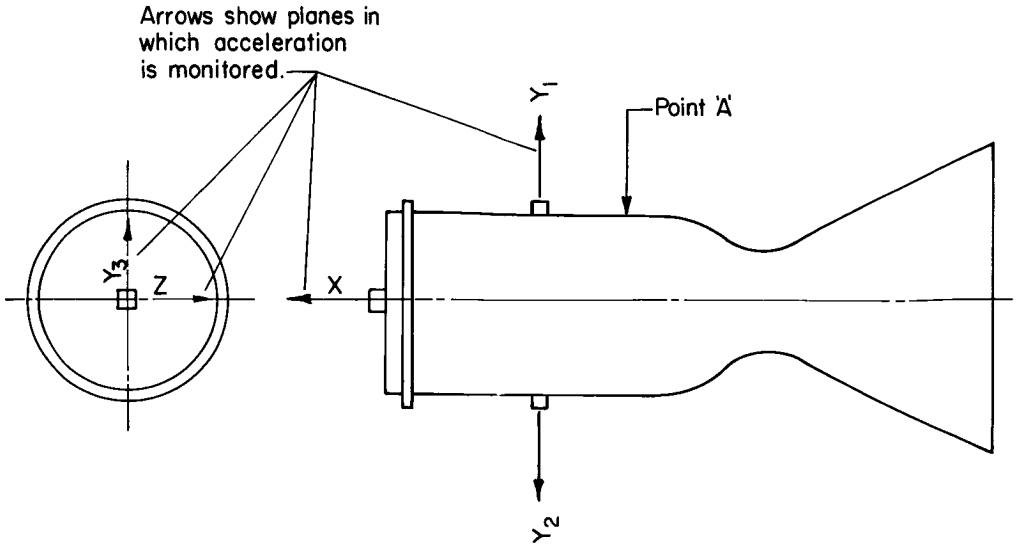

FIGURE 9.5.4b.—Positioning of instruments for hardware resonance investigation.

position, a is the acceleration, and f is the oscillation frequency. If the acceleration is measured in g's, as is typical, this expression becomes $x(\text{inches}) = 9.788a/f^2$. It can readily be seen that if the frequency (f) is several kHz, the displacement (x) is very small indeed, probably less than one thousandth of an inch. It is for this reason that actual measurement of this displacement is seldom attempted and that accelerometer measurements are taken instead.

The assumption that the acceleration is simple-harmonic is certainly an over-simplification (the signal is usually more peaked than sinusoidal). However, the estimated displacement usually provides a close approximation to that measurement which could only be provided by quite exotic instrumentation techniques.

9.5.4.4 Detection of short-duration combustion perturbations.—It is possible for localized explosions to take place in the combustion chamber and be either so positioned or be of such a short duration that they are not detected by chamber pressure transducers especially those transducers that are either frequency limited or nonflush-mounted, such as the helium-bleed type. However, if such an occurrence takes place close to the chamber wall (especially in an all metal chamber), the shock wave would result in an acceleration output. Typically, this output is similar to that obtained when the chamber is struck during resonant hardware frequency testing. That is, it consists of a single excitation pulse followed by a decaying mechanical resonant frequency. Of course, this type of signal is usually of quite low amplitude, but is nevertheless important during the study of combustion phenomena and injector design. An example of such an occurrence is shown in Fig. 9.5.4c. Here, an acceleration output of 730 g's was experienced in the thrust axis of the engine with no corresponding perturbation in the chamber pressure field. The monitoring accelerometer was located on the back of the injector (i.e., accelerometer "X" in Fig. 9.5.4c). This perturbation occurred well into the steady-state period of the run and clear of all start transients, etc.

The foregoing applications are typical of those current in the industry at present. However, advances in transducer design which increase their frequency range and amplitude reliability (while reducing their physical size) will undoubtedly lead to still more sophisticated applications.

9.6 OTHER MEASUREMENTS

The following nomenclature pertains to Sect. 9.6:

C_F	Thrust coefficient
F	Thrust
f_0	Resonant frequency

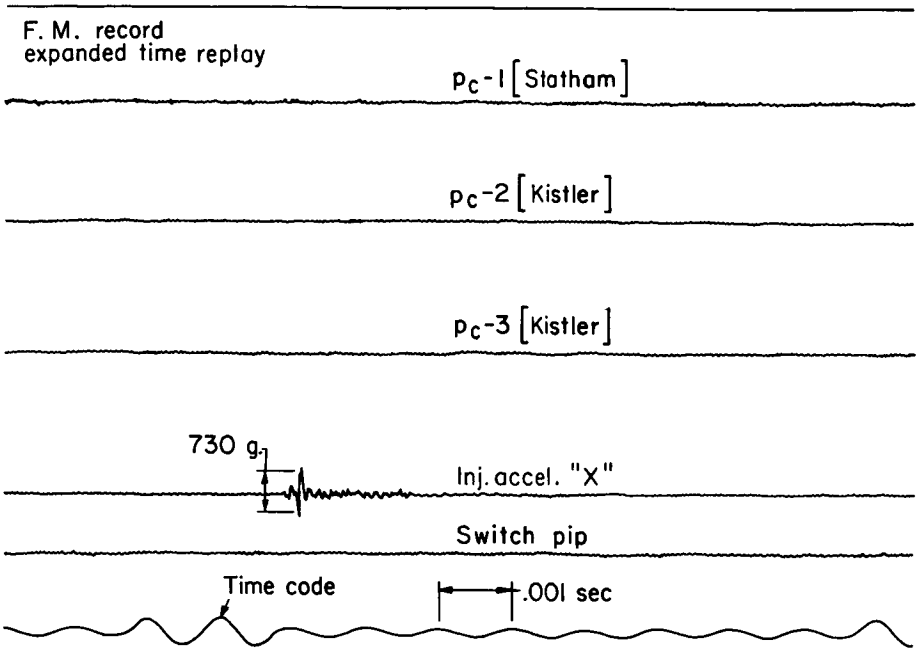

FIGURE 9.5.4c.—Portion of test record showing accelerometer response and no apparent "p_c" perturbation.

f_1, f_2	Half-power frequencies
g_c	Gravitational constant, 32.17 lbm-ft/lb-sec^2
$\hat{p}_t$	Acoustic pressure amplitude at any time
$\hat{p}_{max}$	Maximum acoustic pressure amplitude
$\hat{p}_o$	Amplitude before driving signal cut-off
Q	Quality factor of resonant system
α	Decay rate

Subscripts:

a	Ambient
c	Chamber
e	Nozzle exit
o	Chamber stagnation

9.6.1 Propellant Flow Rate*

The use of an instantaneous flow measurement device as an aid to the analysis of combustion instability is highly desirable. There are scores of companies which manufacture flow measurement devices, including both steady-state and dynamic types of flowmeters. The usual consideration is for highly accurate steady-state flow measurements for performance calculations. Dynamic considerations are important when it becomes necessary to determine transfer functions in the propellant system. Although there is much work yet to be done for dynamic flow measurements, several transducers are available with limited capability. Some of the most common flow measurement transduction methods and their limitations follow.[35]

Turbine flowmeters.—This type of flowmeter is the most commonly used for the measurement of static propellant flow rates in rocket engines. As its name indicates, a turbine is employed which is rotated by the fluid at a rate proportional to the stream velocity. A sensitive coil measures the speed of rotation as the blades pass the coil. The device is extremely linear over an operating range of about ten to one. Static accuracy of the flowmeter is excellent with an uncertainty of 0.1%. Since the flowmeter provides a direct measurement of velocity, mass flow rate is easily obtained when the fluid density is known. The inlet velocity profile, however, has been shown to dominate the flowmeter performance.[687]

The dynamic capability of the turbine flowmeter is rather limited.[298] The main cause of the frequency limitation in turbine meters is the inertia of the rotor. Measurements on different

* R. D. Wesley and R. J. Hefner, Authors.

models of $\frac{1}{2}$ inch flowmeters yielded typical time constants of 2 to 5 milliseconds.[640]

For additional information on turbine meters the reader may wish to consult the 42 references in the recent report by Thompson and Grey.[687] That report also includes a turbine meter users' survey.

Electromagnetic flowmeter.—The electromagnetic flowmeter is used to measure non-steady flow.[305] It is based on the principle of an electrically conducting fluid through a magnetic field, which produces an e.m.f. proportional to the fluid velocity. By locating electrodes on opposite sides of the pipe and 90° to the magnetic field, the resulting voltage can be measured. Types of fluid which can be measured with this principle are those which have free ions, such as the acids, White Fuming Nitric Acid (NNO_3), Red Fuming Nitric Acid ($NNO_3+NO_2+H_2O$), Nitrogen Tetroxide (N_2O_4) and certain of the hydrazine fuels. Measurements have been made experimentally with conductivities as low as 2.8×10^{-6} mhos/cm.[75]

With the use of a constant magnetic field the flow measuring device experiences electrode polarization. This is detrimental to measurement of steady-state flow due to signal drift. To combat this electrode polarization, the use of an alternating magnetic field is employed. This does away with the electrode polarization, but due to the behavior of rapidly changing currents in circuits containing inductance, it is difficult to alternate the field at the frequency necessary to provide the response desired without introducing transient voltages beyond tolerance. Furthermore, frequency response is only a fraction of field frequency, e.g., 60 Hz allows 10 Hz measurements.

Electromagnetic flowmeters with an alternating magnetic field have gained wide application in industry for measuring non-steady liquid flow. They are structurally simple and reliable to operate, although their use must be confined to conducting fluids. Some devices have been manufactured with a 500 Hz frequency response.[400]

Flowmeters which use a constant magnetic field have a theoretically unlimited frequency response. However, this has not been found to be the case in practice. One such device has been manufactured for pulse flow measurement with a 1 millisecond rise time from 10% to 90% of full scale output.[26]

Hot-wire anemometer.—By providing a constant electrical current through a wire suspended in the propellant stream,[2] it is possible to obtain a measure of flow velocity by measuring resistance changes in the wire as its temperature varies due to changes in heat transfer to the fluid (King's law). This is a simple description of a "constant current" hot-wire anemometer, however, where high frequency measurements (order of kHz) are required, electronically compensated anemometers that maintain "constant temperatures" on the wire are also available. Both types are relatively easy to use but the probes are subject to breakage or corrosion damage. Since the probe is sensitive to flow in more than one direction data analysis can become quite complicated.

Drag body flowmeters.—The drag body flowmeter works on the principle of impacting the flow stream on a target connected to a beam on which strain gages are installed.[289b] As the target deflects due to velocity of the flow stream the beam will bend causing an output from the strain gages. The force on the target is proportional to the fluid density and the square of the fluid velocity. The resonant frequency of the device is somewhat dependent on size, generally in the range of 500 to 600 Hz, although some have been higher. The frequency response for pulsating flow measurements will be limited by the resonant frequency.

9.6.2 Injection Characteristics*

Many attempts have been made to quantitatively determine the mixing, atomization, vaporization, drop size distribution, and mixture ratio distribution in bipropellant liquid rocket combustors with combustion taking place. The most successful of these investigations conducted to date, however, have resulted in providing only qualitative information.

A more common method of investigating injection characteristics is to measure the characteristic injection parameters in a simulated nonreactive environment and then to observe the effects of varying these parameters on the performance and stability characteristics of the

* R. J. Hefner, Author.

engine. The following will describe some of the typical techniques used in this approach.

There have been many methods employed to measure the mixing and atomization characteristics of nonreactive liquids. These generally involve using either high speed photographic or sampling techniques. By gathering samples of the liquid spray with a small diameter collecting probe at various points, a three-dimensional pattern of the mass and mixture ratio distribution can be reconstructed. High-speed motion pictures of the spray provide data on the drop size and mass distribution. If differently colored liquids are used to simulate the fuel and oxidizer, the mixture ratio distribution can also be determined from the photographs.

Typical of the type of investigation where the nonreactive injection characteristics are related to the combustion characteristics of a single element injector is the work of Evans, Stanford and Riebling.[252] They investigated the effect of injector element coarseness on the mixing and combustion characteristics of hypergolic propellants. To accomplish this they measured the mass and mixture ratio distributions generated by various sizes of unlike doublet injector elements using simulated nonreactive propellants. Then by investigating the characteristics of the same elements with the actual propellants they were able to determine in a gross sense the effect of the hypergolic reaction on the mixing characteristics of the propellants. The mixing characteristics of the actual propellants were determined by using a combustor that was segmented into two halves just below the impingement point of the injected liquid streams. This permitted the droplet breakup and mixing resulting from the impingement of the two streams but prevented any secondary mixing from turbulence and diffusion. By injecting additional fuel into one side of the segmented chamber and oxidizer into the other side well below the original combustion zone, they were able to establish that the hypergolic reaction at the initial impingement point resulted in forcing the unlike propellants apart, this resulted in fuel-rich and oxidizer-rich zones beyond the impingement point that had not been observed with the nonreactive simulators.

Water flow tests are commonly used to check the nonreactive flow and impingement characteristics on most full scale injectors. This type of testing is primarily intended to detect plugged or misaligned orifices, but it also provides data on the gross impingement and droplet breakup characteristics. More quantitative measurement of the mass and mixture ratio distributions generated by full scale injectors have been made using nonreactive sampling techniques.[12,485] Figure 9.6.2a illustrates a sampling probe used for measuring the mass distribution of simulated propellants as they emerge from the injector. The probe is sized to cover a single orifice or single

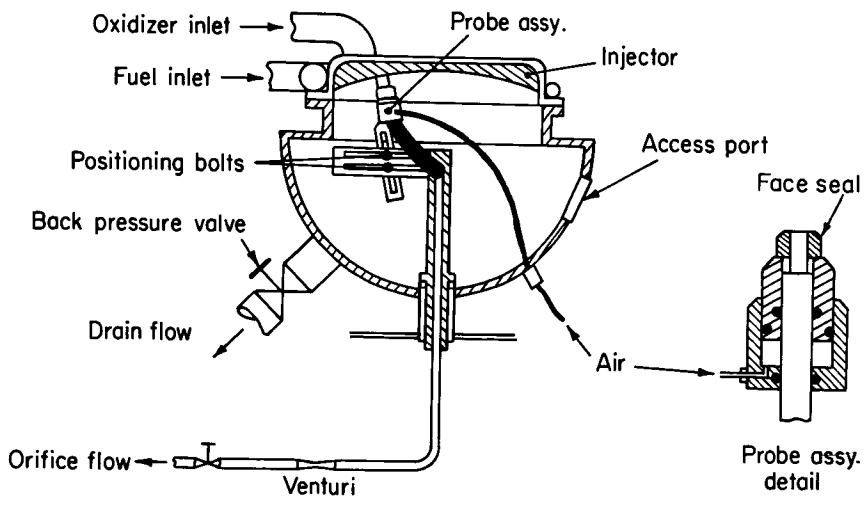

FIGURE 9.6.2a.—Injector orifice flow sampler.

injection element and is sealed against the injector face by air pressure. The injector and probe are sealed in a chamber to permit flowing the injector with a combustion simulated back pressure. By moving the probe from orifice to orifice or element to element the mass flow distribution through the injector under simulated steady-state operating conditions can be determined.[12]

Another type of nonreactive flow sampling device that has been successfully employed on full scale injectors[485] is illustrated on Fig. 9.6.2b. The entire simulated propellant flow is collected simultaneously in an array of tubes. The tubes are sufficiently long to collect all of the flow generated during the start and shutdown transients plus up to several seconds of steady-state flow rate. By measuring the quantity and composition (if immiscible nonreactive liquids are used) of liquid collected in each tube, the mass and mixture ratio distribution can be determined.[615] If the experiment is repeated with the inlet end of the collecting tubes located at different distances from the injector face, the nonreactive mixing characteristics can be established as a function of distance from the injector. For this type of sampler, where flow is collected from the time the flow starts until it ends, it is necessary to run repetitive tests with different durations to separate the steady-state and transient injection characteristics. The use of a flow shutter device has been used to eliminate multiple testing.[224]

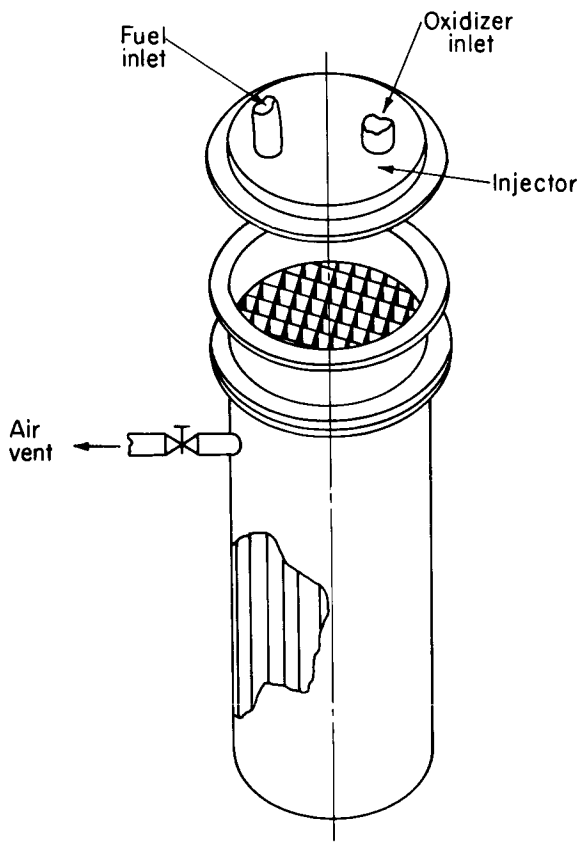

FIGURE 9.6.2b.—Injector total flow sampler.

Only a few of the many techniques employed in attempting to determine the injection characteristics of liquid propellant engines have been mentioned. As stated previously, most of these techniques involve investigating the characteristics of simulated nonreactive liquids which may or may not bear a direct resemblance to the actual combustion case. The general inability to determine the characteristics of drop size, mixing, atomization, vaporization and mass distribution in an engine with combustion has been a major factor in limiting the advancement of the state of knowledge and control of liquid rocket combustion processes.

9.6.3 Thrust and Other Performance Data*

9.6.3.1 Measurable quantities related to performance and stability.—Measurable parameters which are useful for determining rocket engine performance include: thrust, F; area ratio, A_e/A_t; propellant temperatures, T_{OX}, T_F; mass flow rates, $\dot{m}_{OX}$, $\dot{m}_F$; ambient pressure, p_a; nozzle exit pressure, p_e; and chamber pressure, p_c. The absolute performance in terms of specific impulse (I_{sp}) is determined by thrust per unit of mass flow, $F/(\dot{m}_{OX}+\dot{m}_F)$. The parameters are useful for relating performance to the theoretical value, extrapolating to other operating conditions, comparison of multiple tests on the same or similar units and for engine balancing of the flow rates via line orifices to achieve design mixture ratio.

THRUST: Thrust measurement is a necessity for experimental evaluation of rocket engine performance. This measurement can be avoided only if sufficient tests on a particular unit have been completed to allow correlation of thrust with some other parameter (such as p_c) within

* R. Valentine, Author.

desired statistical accuracy. If any changes are subsequently made to the injector, chamber or operating conditions, then recalibration is necessary to insure accuracy of measured performance. It is advisable to measure thrust on all tests, as no other parameter will permit accurate performance evaluation under all operating circumstances.

AREA RATIO: The ratio of nozzle exit area, A_e to throat area, A_t determines the degree to which pressure may be converted to kinetic energy with corresponding enhancement of thrust. These parameters are generally measured pre- and post-test, as no satisfactory method is available for direct measurement during firing.

PROPELLANT TEMPERATURE: Fuel and oxidizer temperature have a secondary effect on performance. Enthalpy effects alone account for 0.01 to 0.03 sec I_{sp} per degree Fahrenheit. An effect of similar magnitude may be noted as a result of temperature on surface tension and droplet vaporization characteristics.[564]

MASS FLOW: Knowledge of the rate of all primary and secondary propellant flow to the thrust chamber is necessary for any meaningful performance evaluation. Mass flows are best measured by use of redundant flow meters, calibrated with propellants. The total flow rate, $\dot{m}_{OX}+\dot{m}_F$ is used to evaluate I_{sp}, while the mixture ratio, $\dot{m}_{OX}/\dot{m}_F$, is required to relate the I_{sp} to theoretical expectations.

PRESSURE MEASUREMENTS: Ambient pressure (p_a) is measured during most rocket engine firings so that the measured performance may be related to vacuum performance by addition of the quantity p_aA_e to the measured thrust. If p_a is not constant on all external surfaces of the engine, the axial component of the actual gradient must be evaluated to determine thrust loss at ambient pressure versus the vacuum value.

Nozzle exit pressure, p_e can be related directly to chamber stagnation pressure, p_o if the exit velocity is known. This parameter is rarely measured, however, due to the extreme difficulty of measuring a representative value considering the normal pressure gradient at the exit plane.

Chamber pressure is commonly used as a performance parameter by evaluating characteristic velocity, $c^*=p_cA_tg_c/(\dot{m}_{OX}+\dot{m}_F)$. Specific impulse is then determined by the expression $I_{sp}=c^*C_F/g_c$. This method is not recommended, however, as the p_c measurement is rarely representative of true stagnation pressure for the nozzle entrance even when velocity corrections are made. Measured pressure at any given point in a thrust chamber is a function of injector and chamber design, and varies both axially and circumferentially. A method for evaluation of performance independent of p_c and c^* measurements is given in Ref. 703.

9.6.3.2 Effects of instability on measured quantities.—The incidence of combustion instability can cause changes in measured thrust, mass flow, and chamber pressure. Various combinations of effects have been noted. Performance can vary upward or downward when an instability occurs. Very high performance units generally suffer a loss in I_{sp} while low performance units often gain in performance.

These observations may be explained as follows: High performance units generally exhibit relatively uniform $\dot{m}_{OX}/\dot{m}_F$ distribution across the injector face and an injector which is highly efficient for atomizing the propellant stream into small droplets. This leads to rapid droplet vaporization, a relatively sharp energy release gradient and consequent high performance if combustion length is sufficient. These same characteristics are generally considered adverse to achieving combustion stability. If instability occurs, the motion of gases in the chamber can result in misimpingement of the liquid streams and sprays, thus producing a less satisfactory distribution of the mixture ratio. Designed mixing is also upset, which together with the off-mixture ratio, results in lower I_{sp}.

Conversely, lower performing units are often characterized by uneven $\dot{m}_{OX}/\dot{m}_F$ distribution, large orifices or poorly designed elements which do not yield a small droplet size distribution. Instability in this system may result in mixing of zones of varying $\dot{m}_{OX}/\dot{m}_F$ and more rapid droplet vaporization as a consequence of higher gas velocity past the drops. These phenomena may lead to higher I_{sp}.

The design and operating factors which tend to improve I_{sp} performance of rocket engines are generally in the direction of reducing stability. For example, performance is enhanced by even $\dot{m}_{OX}/\dot{m}_F$ distribution, small orifice size and even

mass distribution. These same parameters work against the achievement of stable operation. A satisfactory rocket engine must exhibit a balance between the factors influencing performance, compatibility and stability. It will not be ideal from any standpoint, but must meet minimum requirements of each.

9.6.3.3 Post shutdown observations.—The thermal, chemical and gas dynamic environment in a rocket combustion chamber is determined primarily by injector design characteristics. Analysis of local $\dot{m}_{OX}/\dot{m}_F$ zones and the mass distribution at the injector face permits prediction of approximate char and erosion patterns on ablative chambers, or thermal zones on instrumented metal chambers. Observation of fired chambers generally shows evidence of heat marks or char and erosion patterns which are characteristic of the injector design.[704] For example, on ablative chambers the protected zone near a film coolant orifice may generally be clearly seen. If an instability occurs however, the characteristic pattern will be obliterated. Chambers subjected to unstable operation exhibit rough textured surfaces, often with streaks indicating tangential flow of erosive gas streams. Observation of the post-fire condition of a chamber cannot be considered a satisfactory means of characterizing instability, however, due to the qualitative and variable nature of the results.

9.6.4 Sampling of Combustion Gases*

Experimental combustion gas sampling is valuable where theoretical predictions are suspected or difficult. Gas sampling provides a direct measure of mixture ratio, species distributions and average molecular weight.[316] This information is particularly useful for gas properties of tap-off gases for turbo-machinery operation, acoustic absorber entrance conditions, engine start conditions, mixture ratio distribution, and chamber boundary layer cooling. If concurrent static pressure and temperature measurements are taken, the combined data allows nearly all of the sampled gas properties to be calculated.

Gases may be extracted from either the combustor core flow or the boundary layer. Considerable gas sampling has been done downstream of the nozzle exhaust.[155,316] To assure a representative sample, considerable care is required in positioning the probe. In addition to the radial boundary layer effects, it has been found that variations in compositions may be nearly as great in the tangential direction.[620] Gas samples are normally taken during stable combustion, but it is possible to sample during combustion instability or during the start transient.

Sampling has been done in two ways. Usually a gas sample is removed from the engine, stored in a container and analyzed at a later time. This method is always used when liquid and/or solid phases are expected to be found. (Sampling of solid particles is discussed in Reference 34.) The other method uses an on-line mass-spectrometer and the gas is continuously sampled and analyzed.[674] In the latter case particular attention must be paid to the fluid system which leads from the chamber to the ionizer of the mass-spectrometer. Stratification must be avoided and the skimmers* are designed to deliver a representative sample of the original gas to the ionizer. In the former method of sampling, stratification is perhaps not so severe since a larger sample is actually used and, if necessary, the lead lines of the system may be cleaned out and used as part of the sample. To assure getting a representative sample in the bottle system it is usually necessary to purge the system prior to and after taking the sample. A typical arrangement for purging, valving and gaging is shown in Fig. 9.6.4.

In either sampling system it is essential that the probe have several attributes. If the flow is subsonic, the flow through the probe during sampling should be isokinetic, that is, the flow into the probe should be at the same velocity as the surrounding free-stream gases. Recently a subsonic type of probe has become commercially available.[19] If the flow is supersonic, the shock wave should be swallowed by the probe such that the bow shock standing off the probe tip does not deflect particles or striate the gas flow. One of the most stringent design aspects of the probe involves its structural integrity. It must be thoroughly

* W. M. Ford, Author.

* Skimmers are entrance orifices for the on-line mass spectrometer required to reduce the sample pressure to the order of 10^{-8} torr.

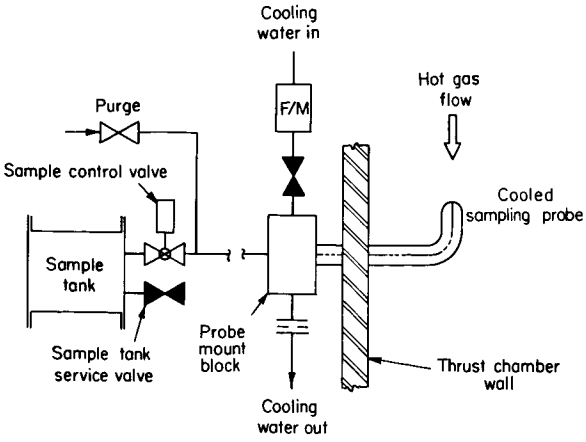

FIGURE 9.6.4.—Cooled sampling probe.

cooled and designed to withstand the corrosive environment and the aerodynamic loads imposed by the rocket engine hot gas flow.

The probe must also be designed to prevent further reaction of the sample. Reaction quenching may be accomplished by immediate expansion of the sample, quickly reducing the sample temperature by heat transfer, or by dilution with an inert fluid.

9.6.5 Thermal Measurements*

The main purpose of thermal measurements in a thrust chamber is the identification of heating rates that must be accommodated by some cooling method within the thrust chamber walls. The work of Bartz[382] indicates the types of studies that have been conducted to obtain experimental data and to develop correlating expressions for predicting thermal conditions during stable operation. This particular work represents only one important segment of a multitude of similar studies that have been carried out. From these, a fairly significant amount of thermal information exists for stable combustion and the methods of predicting heating rates in rockets. While admittedly not perfect, these methods are acceptable. The same cannot be said for unstable operation. Here, the amount of experimental information is quite limited and often rather qualitative in nature, sometimes taking the form of an observation that "heating rates were very high and severe hardware damage occurred." Actually, this helps explain why the amount of information is limited—first, these increased heating rates during unstable operation often jeopardize hardware integrity, thus increasing testing risk; and second, since unstable combustion is not a normal operational mode, thermal measurements have been considered to be of academic interest and therefore neglected.

On some occasions thermal measurements have been used to identify the existence and nature of combustion instability. Burrows[130] describes a method for using thermal radiation as a tool in analyzing unstable combustion. He shows that differences can exist between the thermal radiation emitted from the combustion gases during stable and unstable firings. Other investigators have identified the existence of combustion instabilities from the rapid response of thermocouples welded to the chamber walls. When an exceptional temperature rate is evident the firings can be stopped before physical damage begins. This simple method of detecting an instability could be particularly valuable when heating rates are normally low and pressure instrumentation is not readily available.

Within the framework of the available data one is forced to direct the discussion towards two simple goals: (1) identification of the experimental work, and (2) a qualitative reflection on the important parameters. In 1959, the most detailed study dealing with thermal measurements during resonant combustion in model-size rocket motors was reported.[320] Thrust chamber heat flux distributions were measured for intentionally induced longitudinal instabilities using LOX/Hydrazine propellants (the first longitudinal mode) and for transverse instabilities using LOX/Ethanol (the first tangential mode). The measuring instruments were water-cooled, plug calorimeters flush-mounted along uncooled chambers. These calorimeters were capable of accepting heat fluxes near 15 Btu/in.^{2} sec. Figure 9.6.5a, taken from Ref. 320, displays heat flux and pressure measurements from a longitudinal instability case with a 32 in. long combustion chamber. The steady combustion heat flux value of just under 2 Btu/in.^{2} sec was observed to increase by factors of nearly 3 with the instability. A direct and expected correspondence existed between the

* N. E. Van Huff, Author.

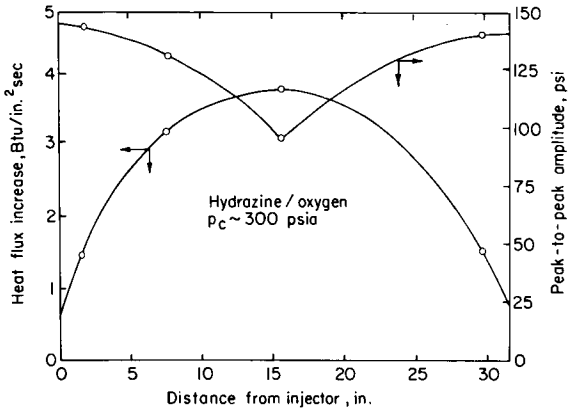

FIGURE 9.6.5a.—Heat flux increase with longitudinal instability.

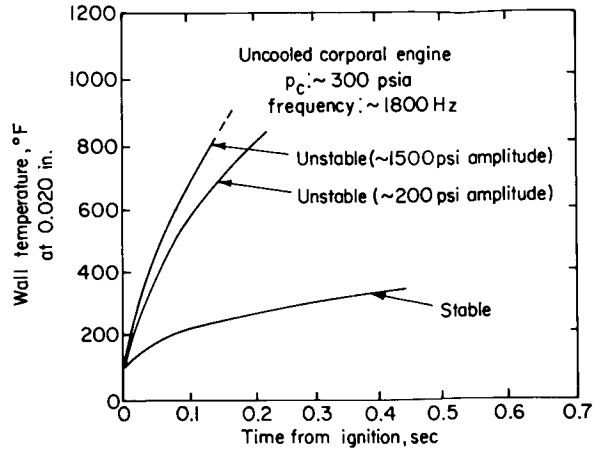

FIGURE 9.6.5b.—Wall temperature/time curves with transverse instability.

axial heat flux profile and the velocity variations that would be induced by the local pressure changes. Furthermore, the factor decreased linearly with increasing chamber length varying from about 3.5 for a 15 in. long chamber to 2.2 for a 48 in. chamber. For the 15 in. long chamber, oscillations were observed with peak-to-peak amplitudes of 129 psi and frequencies of 980 Hz. For the transverse instability case, heat flux values increased by factors of about 4 for a nominal chamber pressure of 150 psia and 2.5 for the 550 psia case. The oscillations during some of the transverse instabilities were noted to have peak-to-peak pressure amplitudes of 200 psi and frequencies of 4300 Hz.

Information from Rupe and Jaivin,[620] on the other hand, was obtained "accidentally" when an unintentional transverse instability occurred in their experiments (most likely, the first tangential mode). This "accidental" aspect is often the manner in which thermal measurements are made under unstable conditions. Their primary intention was the study of injector mass distribution on local heat transfer rates during stable operation with Stabilized Fuming Nitric Acid/Corporal Fuel propellants. Temperature/time responses from uncooled thermocouple plugs were used to infer heat fluxes; three typical curves are shown in Fig. 9.6.5b indicating the extreme wall temperature variations that can occur. These curves, when converted to heat flux, indicated (1) increases in heating rates by factors greater than 10 had occurred, and (2) the 200 psi to 1500 psi amplitude change had only a small effect on heat flux.

Another source,[477] involving an "accidental" instability, indicates an increase in heat flux to a water-cooled baffle by a factor of 1.7 for a transverse instability in a high pressure engine. This relatively low factor is actually consistent with the other information at higher pressures stated above. The implication is that local disturbances from instabilities have a far greater effect on lower heat transfer coefficients than they do on the already high coefficients which would exist at higher pressures.

Still another aspect which can influence the factors quoted above is the amount of local cooling expected from either intentional or unintentional film cooling near the injector. The onset of an instability tends to eliminate this cooling and under certain conditions, chamber heat fluxes have actually increased from near zero values with stable combustion and film cooling to near 3 Btu/in.^{2} sec for an equivalent unstable firing.[635]

The information above reflects, in general, the scarcity of thermal measurements during combustion instabilities. No bona fide method is presently available to predict the severity of the thermal conditions which may arise, although the work of Harrje[319] on heat transfer in oscillating flow is worthy of mention because he did explore this problem in reasonable depth. Thus, the topic can best be summarized by a series of qualitative observations that are based on the experimental

data. These are: (1) increased heat transfer rates have been measured with transverse and longitudinal instabilities of significant amplitudes; (2) transverse modes tend to create greater heat flux levels than longitudinal modes; (3) combustion instabilities at lower pressure indicate greater thermal variations on a percentage basis than at higher pressures; and (4) disturbance of a film-cooled boundary during an unstable firing can be particularly damaging.

9.6.6 Acoustic Modeling*

9.6.6.1 Introduction and scope.—Pressure and velocity oscillations during high-frequency combustion instability (resonant combustion) may be closely identified with the normal acoustic modes of cylindrical cavities. Even extreme distortion of the chamber shape from the cylindrical, by baffles, long conical nozzles, and curved injector faces, does not destroy this acoustic identity. It is, therefore, worthwhile to study separately the acoustic aspects of combustion instability. The objective of such a study is to determine the effects on the acoustic field of variations of the physical characteristics of the combustor. These variations may be caused by the presence of liquid particles, gas flows, injector-face baffles, or non-rigid walls. The effects of oscillations on combustion and liquid flow processes are not included in these acoustic modeling studies.

In this section, methods of characterizing and measuring the damping of acoustic modes in simulated combustion chambers are considered. Although the results of specific experiments will be presented, the investigations will not be discussed in detail. Acoustic and hot-firing test results are compared, and the usefulness of acoustic modeling in rocket engine development is appraised.

9.6.6.2 Acoustic damping coefficient.—The most useful measure of the response of an acoustic field to a specific system is the acoustic damping coefficient. If acoustical energy is put into a cavity over a broad frequency range, the energy will be distributed into a number of modes of resonance. The "response," i.e., the amplitude of sound pressure within the cavity, will show maxima at frequencies that correspond to each mode. The chamber may be excited either by a broad band, "white noise," signal or by a single frequency varied slowly over a wide frequency range. Either method gives the same cavity response.[553]

If the chamber damping of a particular mode is low, the response curve will have a high maximum, but will decrease rapidly for frequencies above and below the resonant frequency. If the mode damping is high, the response peak will be lower and the curve broader. This behavior suggests the use of the bandwidth or quality factor "Q" as a measure of damping. The quality factor is defined by

$$\frac{Q}{2\pi} = \frac{\text{time-average energy stored}}{\text{energy loss per cycle}}$$

The Q factor may be written in terms of the half-power bandwidth:

$$Q = \frac{f_0}{f_2 - f_1}$$

where f_0 is the resonant frequency, and f_1 and f_2 are the frequencies below and above f_0 for which the response power is half of the peak power. The half-power point corresponds to a pressure amplitude 0.707 times the maximum (or 3 decibels down from the maximum). A typical response curve, showing the measurements required to compute Q, is given in Fig. 9.6.6a.

The Q measurement is especially suitable for high damping rates (low Q), where the response

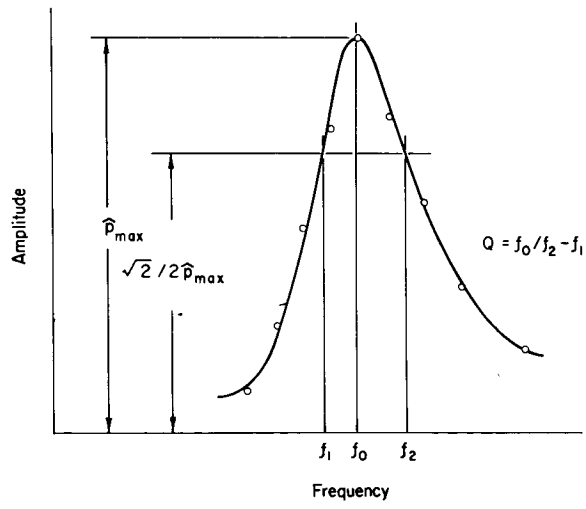

FIGURE 9.6.6a.—A chamber response curve (the ratio of the chamber to driver oscillation amplitude versus frequency).

* P. R. Wieber, Author.

curve is broad and insensitive to errors in frequency measurement. Determination of high Q values requires very accurate frequency measurements. For example, for a typical Q value of 55 at a longitudinal mode frequency of 550 Hz, an error of 1 Hz in the measurement of either of the half-power frequencies f_1, f_2 will produce a 10% error in Q. If two modal frequencies are very close together, their response peaks overlap and the Q factor cannot be determined. Often the power of the driver varies with frequency. In such a case, the response curve must be normalized to a constant driving power.

Although the Q factor is derived from a lumped parameter model and is strictly applicable to linear systems, it is also usable as a measure of the damping in systems that are nonlinear and have distributed elements. A thorough discussion of the assumptions which apply to the use of the Q factor is presented by Culick and Dehority.[204]

The acoustic models of combustion chambers are distributed parameter systems, but their behavior can be characterized successfully by the Q bandwidth measurements. The feasibility of this approach has been shown by Buffum et al.[127] from tests on solid propellant rocket motors. Lawhead[423] obtained Q values for elliptical chambers, and Lawhead and Levine[428] used Q values to evaluate the effectiveness of various absorbing devices for use in liquid propellant combustors.

Another damping measurement has been used by Phillips and Morgan.[553] At the resonant frequency, the damping rate is inversely proportional to the amplitude of the acoustic pressure measured at a pressure antinode. This method allows a quick comparison to be made between the damping abilities of two chambers that have roughly the same resonant frequencies. The use of a single measurement is also an attractive feature. However, the input power must be held constant for all comparisons. Furthermore, the measurement is sensitive to location. It has been observed that the pressure antinode can shift when devices such as baffles are inserted into a chamber. Thus, it must be verified that the pressure transducer is truly at the antinode if the measurement is to be meaningful.

The dynamic measurement of damping is given by the damping rate α, which is the rate at which the amplitude damps after the driving source abruptly stops exciting the chamber. If the cavity oscillates as a lumped parameter system with linear losses, the cavity pressure will damp according to the law

$$\hat{p}_t = \hat{p}_{max} e^{-\alpha t} \sin 2\pi f_0 t$$

where $\hat{p}_t$ is the acoustic pressure amplitude at any time t and $\hat{p}_{max}$ is the amplitude before the driving source is cut off at $t=0$. A typical exponential damping curve (from Reference 737) is shown in Fig. 9.6.6b. The damping rate α can be found graphically by plotting $\ln(\hat{p}_t/\hat{p}_{max})$ against time, where the $\hat{p}_t$ value is measured at the oscillation peaks. Such a plot will give a straight line with a slope of $-\alpha$. The damping rate per cycle is simply α divided by f_0. For isolated modes, it has been shown that the Q and α measurements are related.[127]

The damping measurement works well if damping is low. It fails at very high damping rates because several oscillation peaks are needed to establish the damping curve. The presence of nearby modes can complicate the measurement of a damping rate because the waves may interfere, giving rise to beat frequencies or a succession of different damping rates.

The measurement of damping rates has been used in research studies of the effects of chamber shape and baffle configuration[737] and of acoustic liner design.[553] This approach has also been used to

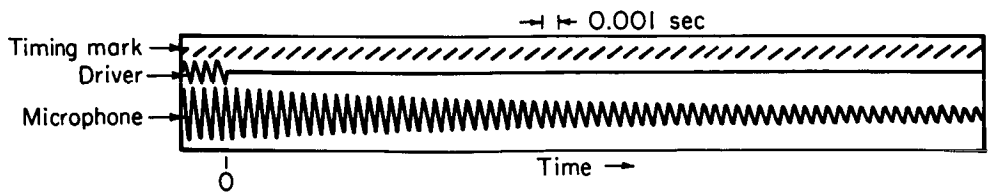

FIGURE 9.6.6b.—Typical damping trace for first standing transverse mode in a simulated rocket chamber.

guide the development of baffles for full-scale engines.[15,599]

9.6.6.3 Driving techniques.—The basic equipment needed for acoustic modeling consists of a driver, with its associated power supply and controls, to supply acoustic energy, and a pressure transducer or microphone to detect the cavity response. The instrumentation and analysis methods are essentially the same as those used on hot firings (Sect. 9.3). However, the different driving techniques deserve attention.

If no flow is needed, an electrodynamic loudspeaker driver can be mounted in the chamber wall, injector, or nozzle. The acoustic output of these drivers is low—less than 100 watts. One driver can produce any standing mode that has a pressure antinode near the driver location.[737] Two drivers separated by 90° around the chamber circumference, with inputs out of phase by 90°, are needed to drive traveling transverse modes.[509,553]

When bulk gas flow is included in the experiment, a siren or modulated-valve electropneumatic driver can be used to deliver both air flow and acoustic energy. These devices can deliver from 100 to above 10,000 watts of acoustic power. The electropneumatic driver can reproduce acoustically an electrical input over its working frequency response range. Gordon and Smith[295] used a reciprocating, porous piston to provide a combination of steady air flow with acoustic oscillations.

Transient driving may be produced by pulsing the cavity with a directed or non-directed explosive or by introducing a pulse of gas or a shock wave from a cold gas shock tube. However, such techniques have seldom been used in acoustic modeling studies.

The various methods of driving were compared by Buffum and his co-workers.[127] Q-factor data were obtained using a siren-type rotary valve. These data, transformed into values, agreed very closely with damping rates measured directly by shutting off the power to an electropneumatic driver. However, damping rates of a shock from a cold gas, burst-diaphragm shock tube were noticeably higher, and damping rates of a shock from a powder cartridge were even higher. The investigators concluded that the gases from the burnt powder altered the acoustic properties of the cavity and that better agreement would have been obtained from the shock tube tests if extraneous frequencies had been filtered out.

The pulsing techniques are not desirable for acoustic model tests because they bring into the measurement the ability of the pulser to excite the acoustic field. Moreover, the spectrum of the pulse produced by the shock tube or explosive charge must be examined to verify that acoustic energy is being produced in the frequency range of interest. For these reasons, electrodynamic or electropneumatic drivers used with the technique of abruptly switching off the driver are more desirable in measuring acoustic damping rates.

9.6.6.4 Applications.—Acoustic modeling has been used with success in rocket engine development programs for preliminary evaluation of proposed design changes aimed at stabilizing oscillatory combustion. Lawhead and Levine[428] studied several kinds of absorbing devices in acoustic model tests. Horn absorbers, which showed good damping, reduced or completely eliminated spontaneous instability in the hot firings.

An extensive acoustic model study of injector-face baffles was carried out as a part of the Gemini Stability Improvement Program.[15,331] It was shown that the variation of both frequency and damping with baffle height gave generally the same correlation for both hot and cold tests, even though the excitation on the hot tests was supplied by explosive charges. These results are illustrated by Fig. 9.6.6c.

In applying the results of acoustic model tests to full scale combustion chambers, the differences in geometrical scale and speed of sound between the model and the prototype must be taken into account. It must also be remembered that the effects of vaporizing propellant sprays, inhomogeneities in the chamber gases, and detonation-like waves are not modeled by the acoustic tests. Nevertheless, the good correlation between cold and hot damping rates gives credence to the use of acoustic models as valid approximations of combustion acoustics.

In addition to measurement of the damping of the various modes of the combustion chamber, acoustic modeling has proven useful in other types of tests related to combustion instability.

Nestlerode, Chadwick, and Gleason[509] modeled the feed system of the F-1 engine in an attempt to find damping devices that would decouple the feed system from the combustion chamber. Insertion of the most promising devices in the prototype engine eliminated feed system oscillations in engine testing. Rosen and Oberg[599] measured high acoustic gas velocities over the tips of baffles in a model combustion chamber and predicted a potential trouble area in another booster engine development program. Nozzle impedance measurements (see Sect. 3.6) have been made, using acoustic modeling techniques, to supplement theoretical studies of the effect of the nozzle on combustion instability.[126,195,295]

Water table modeling has had limited use in the study of acoustic liners.[40,41] Although there is little experience in quantitative applications, the pictures of wave patterns can give interesting qualitative understanding of the interactions between incident waves and acoustic resonators.

9.7 INTERPRETATION OF TEST DATA*

9.7.1 Resonant Combustion

The most destructive type of combustion instability experienced in liquid rocket engines involves a coupling of the combustion process with one or more of the acoustic resonances of the combustor cavity. This type of instability is variously referred to as resonant combustion, acoustic instability, or high frequency combustion instability. A discussion of the combustion mechanisms and physical manifestations resulting from resonant combustion are presented in Chapter 1. This section outlines the physical characteristics of resonant combustion and describes methods for the detection and identification of the various modes of resonant instability. For background see Refs. 495, 503, and 93.

Resonant combustion can generally be detected in a liquid rocket engine by the oscillatory signal recorded by a single high response pressure transducer. For diagnostic purposes, however, multiple high response pressure transducers are most commonly used. Streak photography, high speed motion pictures, and multiple light sensors have also been employed for this purpose. Regardless of the type of instrumentation employed, the positive identification of the specific mode of instability experienced (and whether it is spinning, standing or precessing) requires a reconstruction of the wave formation within the combustor.

The following is a description of techniques commonly used to translate data from analog pressure records of high response transducers into a form amenable to the identification of the specific mode of resonant instability encountered during the test. This will be followed by a discussion of the evaluation of these reduced data in determining the mode or modes of instability experienced. Although the discussion describes the reduction and interpretation of analog pressure data, the same techniques are applicable to other types of analog data.

9.7.1.1 Analog data reduction techniques.—In order to positively identify the specific mode or modes of resonant combustion instability experienced during a rocket engine firing, it is necessary to reconstruct the identifying characteristics of the waveforms that existed within the combustor. There are several ways of doing this from the analog data recorded by multiple high response pressure transducers. Three commonly used techniques will be described. Basically, all of the techniques involve the reconstruction of the pressure within the combustor as a function of position and the change of this pressure profile as a function of time. The analog recording of a single transducer provides the pressure versus time history at one point in the combustor, whereas the instantaneous pressures (recorded by several strategically located transducers) provide the data for reconstruction of the instantaneous pressure profiles within the cavity.

Transducers located circumferentially on the chamber wall provide data for identifying pure transverse pressure wave formations. Similarly axially located transducers provide data for identifying pure longitudinal pressure wave formations. The combined data from both of these planes permit reconstruction of the identifying characteristics of the three-dimensional waveform, although the radial wave characteristics can generally be deduced only indirectly. For purposes of illustration only circumferentially located transducers will be used to describe the data

* R. J. Hefner, Author.

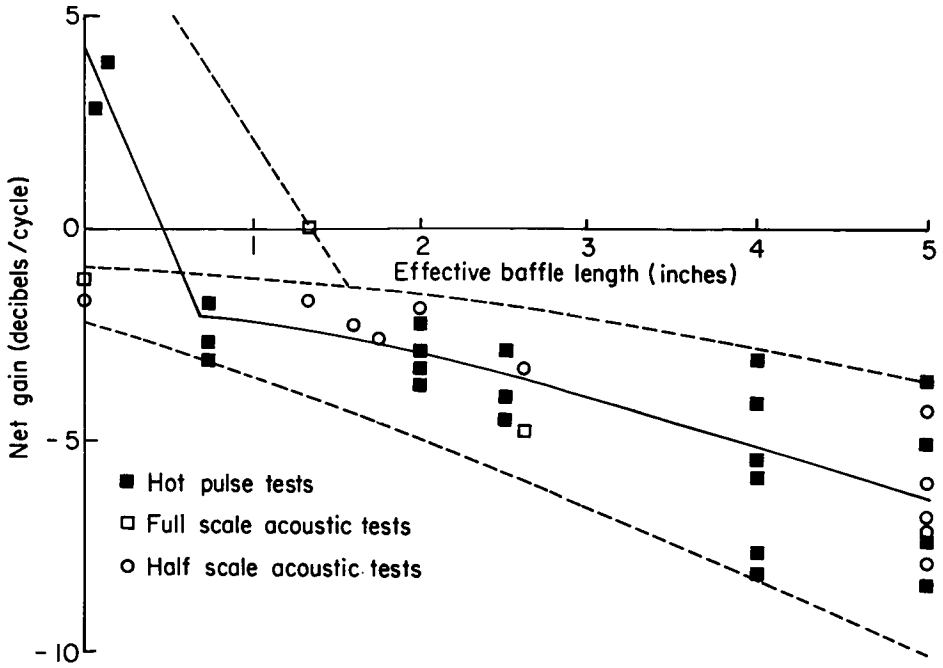

FIGURE 9.6.6c.—Comparison of acoustic model and hot pulse test data on the effect of baffle length on chamber damping.

reduction techniques. In practice, however, the same techniques should be applied to transducers in all planes for which data are available.

One method of reconstructing the tangential wave patterns within a combustor is to produce a pressure vs angular position vs time plot of the analog data. This is accomplished by measuring the magnitude of the oscillatory pressure from each transducer at one instant of time and plotting these values on an amplitude vs angular position diagram. By repeating this process at several time instances during a single wave period, the time history of the pressure profile can be observed. Fig. 9.7.1a illustrates this method of reducing the analog pressure data where, for clarity of illustration, instantaneous times have been taken during successive wave periods rather than during a single wave period. Fig. 9.7.1b shows the physical location of the various transducers and the amplitude-angular position-time diagram constructed from the data. This particular waveform uniquely describes a standing first transverse mode of instability, as will be discussed later.

The technique described above requires numerous instantaneous pressure measurements but does not require measuring the relative phase

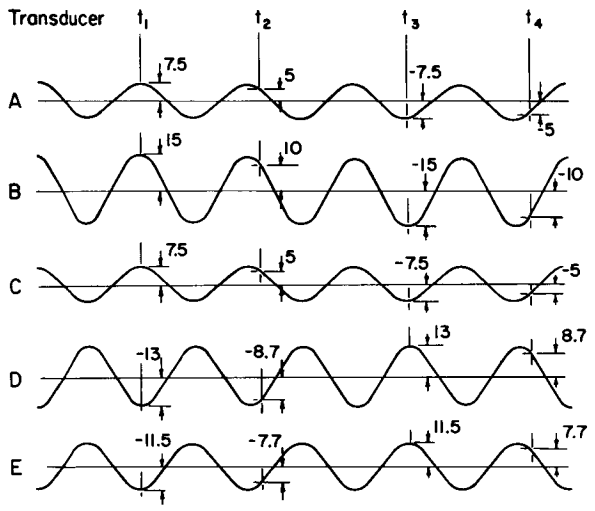

FIGURE 9.7.1a.—Analog pressure record of idealized standing transverse mode of instability.

angle between transducer recordings. An alternate technique requires measuring the phase relationship between the various pressure traces and only the maximum peak-to-peak amplitude encountered for each trace during the wave period. The phase angle is determined by measuring the fractional wave period that the peak positive

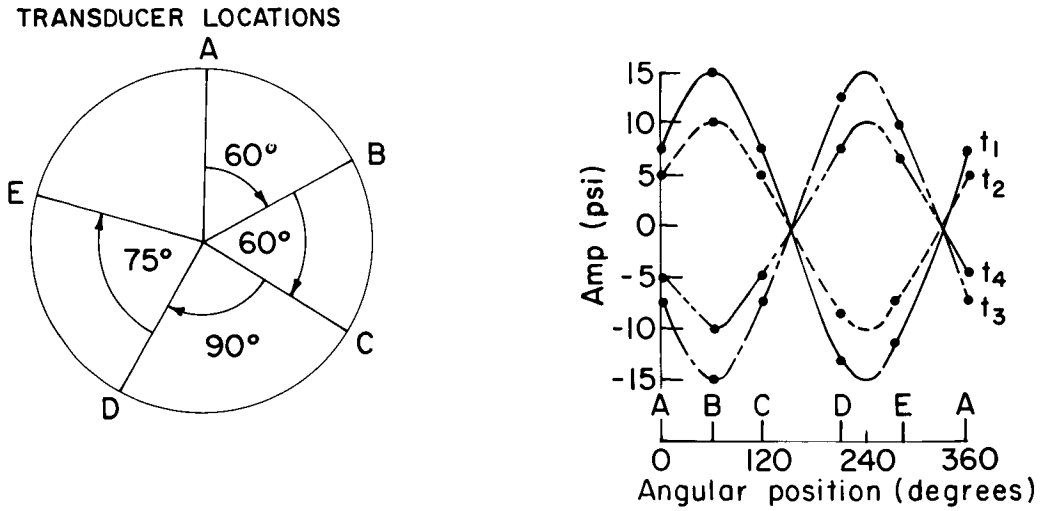

FIGURE 9.7.1b.—Transducer locations and amplitude-angular position-time diagram for an idealized standing first transverse mode instability.

pressure on one trace leads or lags that of a reference trace. (One wave period corresponds to a 360° phase angle.) Fig. 9.7.1c illustrates the method of constructing maximum amplitude and phase diagrams as functions of angular position by this technique. In this case the physical locations of the transducers are the same as that shown in Fig. 9.7.1b and, as will be discussed, the particular phase and amplitude diagrams uniquely describe a spinning second transverse mode of instability.

Either of the above techniques works well when the raw analog data indicate relatively sinusoidal waveforms with high signal-to-noise ratio. If the waves are steep-fronted, irregular, or have secondary perturbations superimposed on them, it is generally desirable to make time-to-peak pressure vs angular position and maximum peak-to-peak amplitude vs angular position diagrams. This is accomplished by constructing a reference time line on the analog record and measuring from this reference the times that the first five to ten positive pressure peaks are recorded on each trace. By plotting these times vs the angular position of the various transducers, the path of the positive pressure peaks can be reconstructed as a function of angular position and time. This in effect is a reconstruction of the phase angle vs angular position except that it covers several wave periods rather than a single cycle.

Consider the analog pressure record illustrated on Fig. 9.7.1d. The boldface points on the phase diagram represent the times to successive maximum pressure peaks measured from the analog record. The smaller points on the diagram represent the times to the smaller positive pressure peaks appearing on traces A, B and D. From these data points the path of the major and minor pressure waves can be reconstructed as shown. This phase diagram together with the maximum amplitude vs angular position diagram characterize a standing first tangential mode with steep-fronted waves.

9.7.1.2 Resonant combustion mode identification.—In order to identify the mode or modes of resonant combustion from analog pressure data it is necessary to understand the identifying characteristics of resonant combustion in rocket engines. To aid in illustrating some of these characteristics, consider a small diameter pipe open at both ends with a continuous sine wave generator at the left end of the pipe. The pressure within the pipe as a function of time and position, as the waves travel through the pipe, can be expressed by

$$p = p_+ \cos\left(2\pi \frac{x}{l_w} - 2\pi \frac{at}{l_w}\right)$$

where

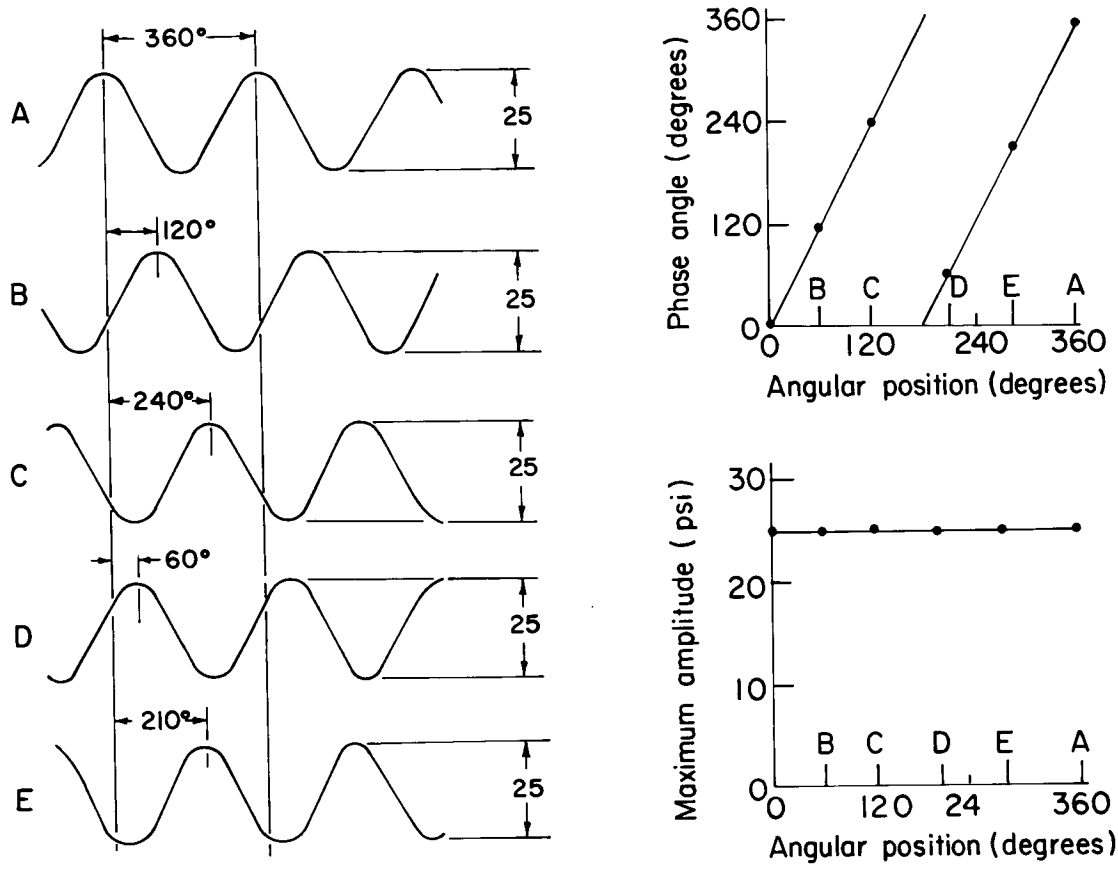

FIGURE 9.7.1c.—Analog pressure record, phase and amplitude diagrams of a spinning second transverse instability mode.

p_+ maximum positive pressure of generated wave (psia)
l_w wave length (ft), a/f
a speed of sound (ft/sec)
f frequency (Hz)
t time (sec)
x distance from left end of pipe (ft)

If the length of the pipe (L) is exactly one wavelength ($L=l_w$), it can be shown from the above equation that a positive pressure peak passes any point x in the pipe at time $t=t_0+x/a$, where t_0 is the time that a positive pressure peak passes the left end of the pipe ($x=0$). The magnitude of this pressure peak is $\pm p_+$ at every point as it passes through the pipe. If the pipe were two wavelengths long ($L=2l_w$) there would be two positive pressure peaks in the pipe at any instant given by $t=t_0+2x/a$ for $0\leq x/L\leq 0.5$ and $t=t_0+1-2x/a$ for $0.5\leq x/L\leq 1.0$. The maximum amplitude and phase diagrams in the pipe are constructed from individual records of maximum amplitude and wave arrival times at the various transducer locations. Figure 9.7.1e illustrates these characteristic diagrams for pipes of one and two wavelengths, where t_0 is taken to be zero.

Although the above equation is for a one-dimensional traveling wave in a pipe it is analogous to the circumferential pressure profile at the wall for a spinning tangential mode in a cylindrical chamber. Thus, a spinning tangential mode is characterized by a constant peak-to-peak pressure as a function of angular position and a linear phase angle as a function of position. The order of the tangential mode corresponds to the number of positive pressure peaks occurring simultaneously within the cavity.

If a continuous sine wave generator with peak pressure output p_- were placed at the right end of the pipe, instead of the left, the instantaneous pressure would be given by

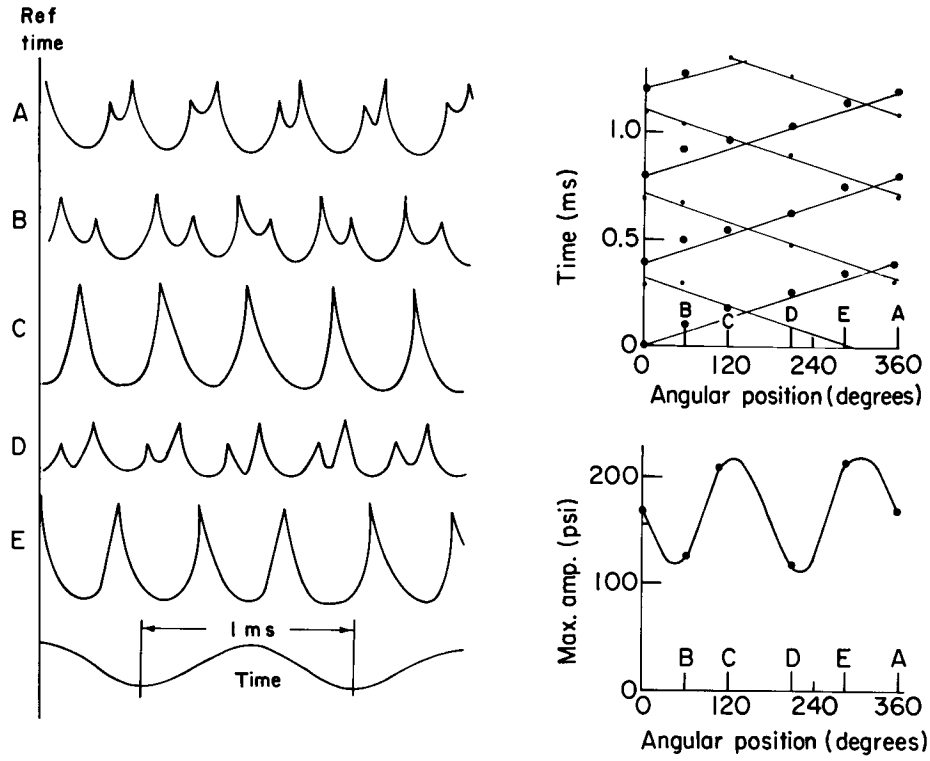

FIGURE 9.7.1d.—Pressure analog (phase and amplitude diagrams for standing first transverse mode with steep waves).

$$p = p_- \cos\left(2\pi \frac{x}{l_w} + 2\pi \frac{at}{l_w}\right)$$

The phase and maximum amplitude diagrams would be identical to those for the generator at the left except that the slope of the phase angle would be negative. Thus, not only does the constant maximum pressure profile and linear phase angle diagram uniquely characterize the spinning tangential modes, but the slope of the phase angle plot also characterizes the direction of motion of the wave.

The more general case of one-dimensional pressure waves in a pipe occurs when both generators are operating simultaneously. If they are both activated such that a positive pressure peak enters both ends of the pipe simultaneously, the pressure within the pipe as a function of time and position is given by

$$p = p_+ \cos\left(2\pi \frac{x}{l_w} - 2\pi \frac{at}{l_w}\right) + p_- \cos\left(2\pi \frac{x}{l_w} + 2\pi \frac{at}{l_w}\right)$$

If x is the linear distance from the injector face of a combustor, this is the general equation for the pressure profile of a longitudinal mode instability. Again, if x is expressed in terms of angular position, rather than linear distance, the above equation describes the pressure at the wall for transverse mode instabilities in a cylindrical chamber. If either p_+ or p_- is zero the equation describes a classical spinning tangential mode. If $p_+ = p_-$ the equation reduces to

$$p = 2p_+ \cos\left(2\pi \frac{x}{l_w}\right) \cos\left(2\pi \frac{at}{l_w}\right)$$

which is a classical standing mode. Solving for the time when the peak positive pressure is reached and the magnitude of that maximum pressure as functions of position yields the phase and amplitude diagrams illustrated in Fig. 9.7.1f for pipes one and two wavelengths long. In this case the maximum pressure profile as a function of position varies continuously with length going from a value of $\pm 2p_+$ at the ends of the pipe (pressure antinodes), to zero a quarter wavelength away from the ends as illustrated. The phase angle is a dis-

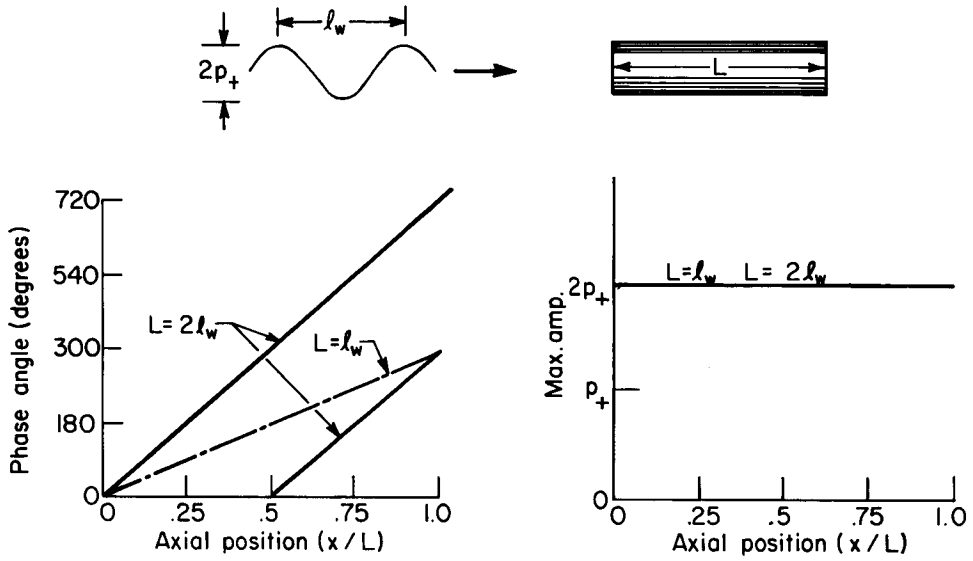

FIGURE 9.7.1e.—Phase and maximum amplitude diagrams for a traveling wave in a pipe.

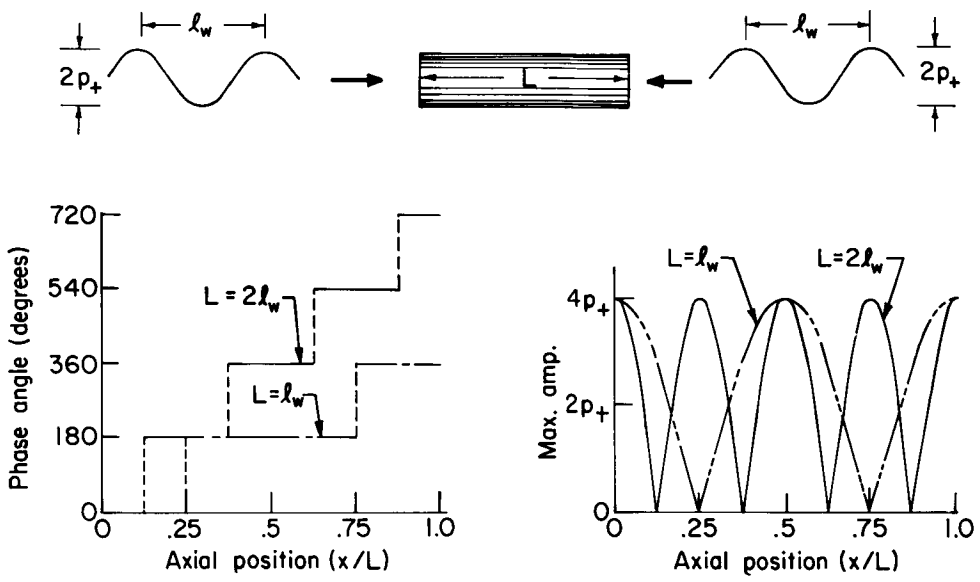

FIGURE 9.7.1f.—Phase and maximum amplitude diagrams for a standing wave in a pipe.

continuous function having a constant phase angle with a 180° phase shift at every point where the maximum pressure is always zero (pressure node).

If the amplitude of the waves are not equal in both directions ($p_+ \neq p_-$,) the resultant wave formation has characteristics different from either the spinning or classical standing modes of instability. Figure 9.7.1g illustrates the phase and maximum amplitude diagrams for such a case. It can be seen that as p_- increases and approaches p_+ the peak-to-peak pressure increases at the antinodes and decreases a quarter wavelength from the antinodes. At the same time the phase angle diagram shifts from the characteristic linear curve of the spinning mode toward the discontinuous step-function of the classical standing mode. The magnitude of the peak-to-peak pressure

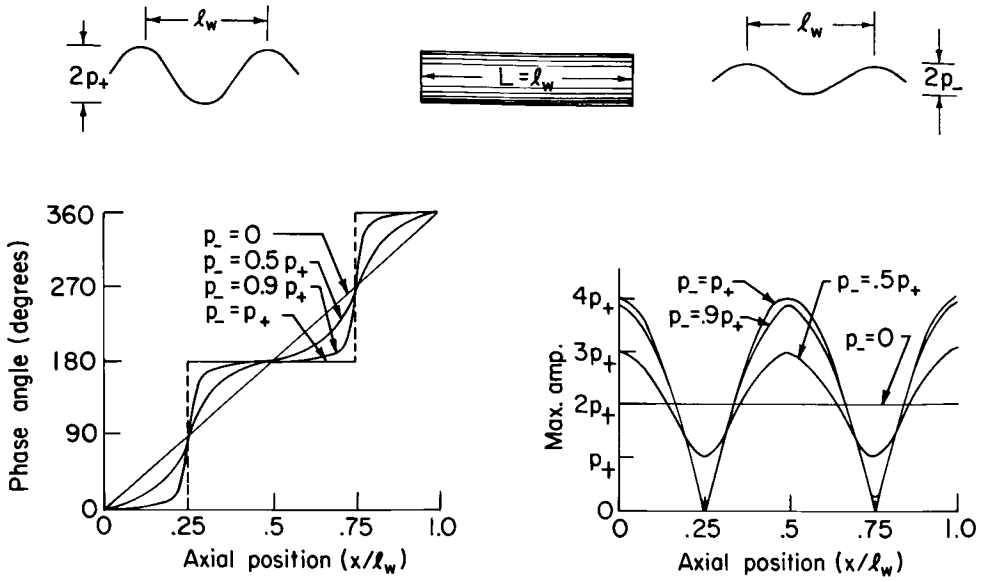

FIGURE 9.7.1g.—Phase and amplitude diagrams for opposed traveling waves in a pipe.

at the antinodes is equal to $p_+ + p_-$ and at a point a quarter wavelength away (corresponding to the nodes of a classical standing mode) is equal to $p_+ - p_-$. This type of instability is generally referred to as a quasi-standing mode.

The preceding paragraphs described the characteristics of resonant combustion modes when the waveform is sinusoidal. More often in actual rocket engine instabilities the waveform is steep-fronted. For a spinning tangential mode with steepened waves the characteristics are the same as those described for a sine waveform, but for all other modes the characteristics can be different. For example, consider the small diameter pipe one wavelength long but with generators introducing equal amplitude, steepened waves at each end of the pipe such that a maximum peak pressure enters both ends simultaneously (i.e., the second longitudinal mode). The waves moving in each direction are mirror images of each other as illustrated in Fig. 9.7.1h. The peak positive pressures of both waves in this case pass the two ends and the center of the pipe simultaneously resulting in pressure antinodes. The maximum amplitude at these antinodes is the sum of the maximum amplitude of the component waves, as in the case of sine waves. The resultant pressure halfway between the antinode points is never zero as it is with sine waves. Figure 9.7.1h illustrates the resultant pressure vs time history at several points along the pipe.

At a point one quarter of a wavelength from either end of the pipe, opposing sine waves would exactly cancel at all times resulting in a pressure node. For the steepened waves illustrated, however, the resultant is a periodic wave pattern with a wave period one half that of the component waves and peak amplitude somewhat less than that of either component wave. At any intermediate point between this point and the end of the pipe the waveform appears as a double peaked wave. One peak is larger than the other and the time period between peaks of equal amplitude is the same as that of the component waves. The time period between the larger and smaller peaks decreases as the position approaches the end of the pipe. This is, of course, the result of the superposition of the two component waves resulting in the peak pressures being in phase at the pipe ends. The phase angle between adjacent peaks increases linearly to 180° a quarter wavelength from the pipe end. The shapes of the component waves determine how close to the end of the pipe (pressure antinode) the two peaks can be distinguished.

The phase and maximum amplitude diagram of a typical standing first tangential mode instability with steepened waves is illustrated in Fig. 9.7.1d. As can be seen in that figure the component waves

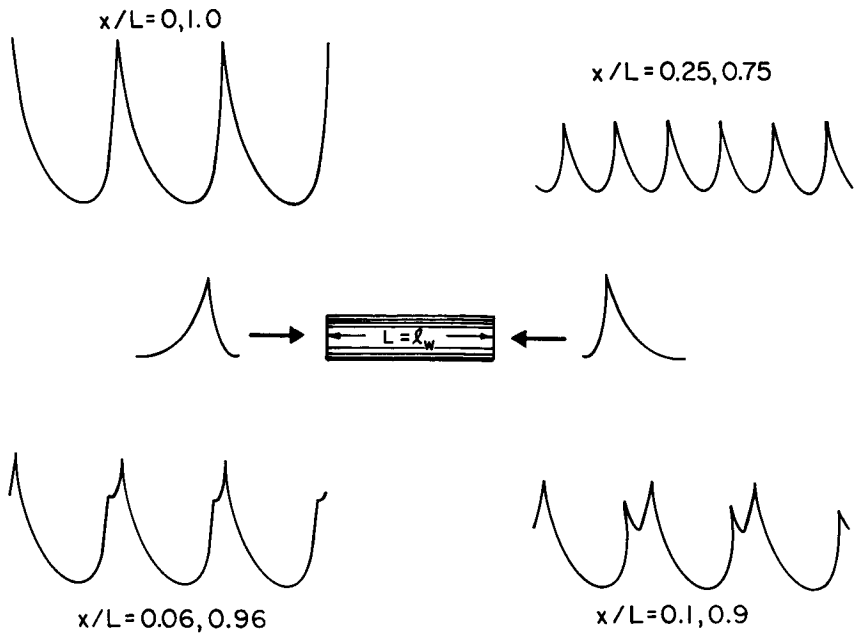

FIGURE 9.7.1h.—Pressure versus time for steepened waves in a pipe.

forming the standing mode can be distinguished by the individual positive pressure peaks. Each one produces a phase diagram characteristic of a traveling transverse wave but the maximum peak-to-peak amplitude varies as a function of position, characteristic of a standing mode. This diamond-shaped phase diagram and varying amplitude, maximum pressure diagram characterize the standing transverse modes with steepened waveforms. The location of pressure antinodes within the cavity correspond to the positions where the peak pressure vs position curves intersect on the phase diagram. The order of the tangential mode is equal to one half the number of antinodes existing around the chamber.

Another variation of standing tangential mode resonant combustion commonly experienced with liquid rocket engines is the precessing tangential mode. This type of instability has the characteristics of either the sinusoidal or steepened wave tangential modes previously described, except that the pressure antinodal points do not remain at a constant position with time. That is, the entire wave formation shifts circumferentially within the chamber. This motion of the standing tangential wave formation may be either a continuous rotation about the chamber or an alternate clockwise and counter-clockwise shift over a sector of the chamber. The rate of precession of the standing tangential wave formation can vary over a broad range. Typically the entire oscillating pressure profile may rotate completely around the combustor cavity in from five to one hundred cycles of the resonant instability frequency.

Figure 9.7.1i illustrates a precessing, standing first tangential mode of resonant combustion with steep-fronted waves. The peak-to-peak pressure oscillations recorded by each transducer vary significantly in a cyclic fashion with the amplitude changing from a maximum to a minimum in approximately four cycles of the resonant combustion frequency (8 cycles/period). The intersection of the times of peak pressure vs angular position on the phase diagram correspond to pressure antinodes in the cavity. From this diagram it can be seen that the pressure antinodes are moving clockwise at a rate of approximately thirty degrees per cycle.

Thus far the identifying characteristics of the pure tangential modes of resonant combustion instability have been described. The characteristics described for the standing and quasi-standing tangential modes with either sinusoidal or

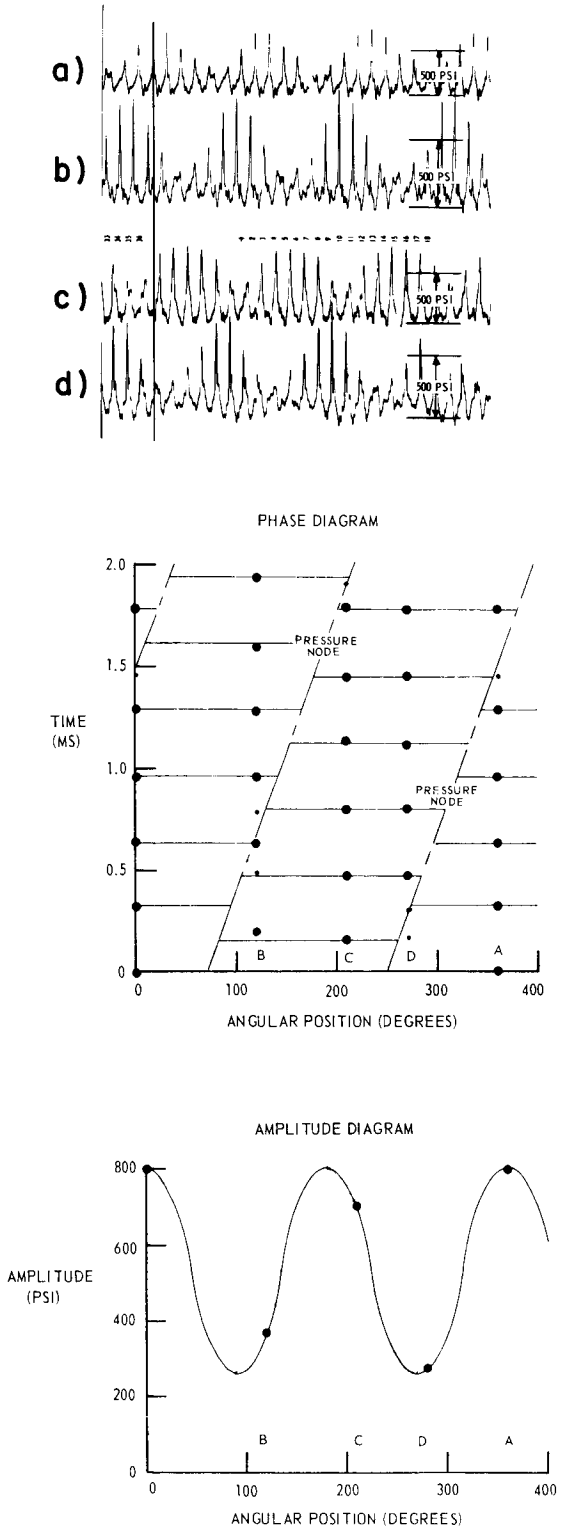

FIGURE 9.7.1i.—Precessing first transverse mode instability.

steepened waves are the same as those for the corresponding longitudinal modes when angular position is replaced by axial distance in the cavity. If there were radially oriented pressure transducers located in the chamber or on the injector face, the characteristics of the phase and amplitude diagrams with radial position would also be the same as those described for the tangential and longitudinal modes. Normally this orientation of instrumentation is not available. Thus the radial modes can typically be identified only indirectly. This is accomplished by determining that the instantaneous pressure is everywhere the same at the chamber wall and the frequency of the oscillating pressure corresponds to one of the radial modes analytically computed for the cavity (Sect. 3.5.1).

In addition to the pure tangential, longitudinal or radial modes, it is not uncommon to have combined modes of instability. A combined mode (or complex mode) is a unique resonance of the combustor which can be thought of as a combination of two orthogonal modes. The frequency of this type of resonance is equal to the square root of the sum of the squared frequencies of the pure component resonances. For example, a so-called first tangential-first longitudinal mode (1T = 1L) is not merely a combination of the two pure modes coexisting in the cavity but is a unique resonance of the cavity with a frequency $f = (f_{1T}^2 + f_{1T}^2)^{1/2}$. The phase and amplitude diagrams for this mode have characteristics of the first tangential mode in the circumferential plane and characteristics of the first longitudinal mode in the axial plane.

Multiple modes of instability can also coexist within the cavity at one time. The coexistence of instability modes may persist for long periods of time or may exist only briefly during the transition from one mode of instability to another. Figure 9.7.1j illustrates coexisting first and third longitudinal modes. The broken lines on the phase diagram characterize the first longitudinal mode while the solid lines characterize the third longitudinal mode.

There are so many variations of wave shapes and resonant modes that can, and have, been encountered in liquid rocket engine tests that it is impossible to describe them all. Only typical examples have been considered here. Experience has shown that instabilities involving only the

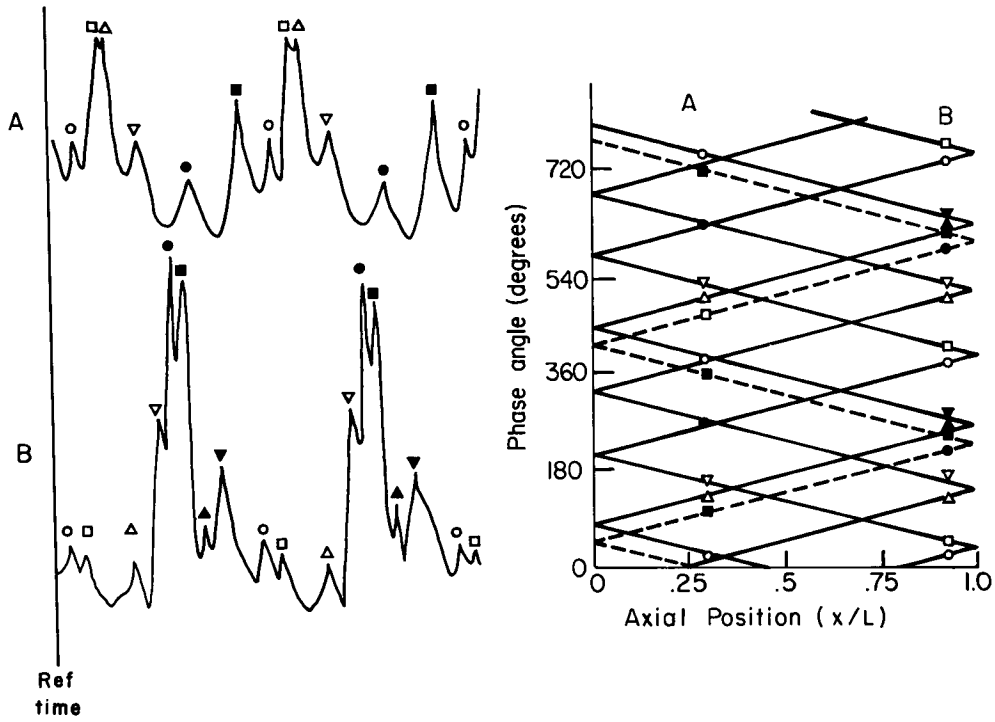

FIGURE 9.7.1j.—Coexisting first and third longitudinal instabilities.

lower order modes are readily identified by the methods described. However, when higher order modes or multiple modes are encountered the identification by these techniques is generally quite difficult. This is due both to the high frequency associated with the higher order modes and the problem of separating the resonant pressure fluctuations from random noise on the analog record.

9.7.2 Low Frequency Instability

Low frequency, or feed-system coupled, combustion instabilities are characterized by oscillations in one of the propellant feed circuits coupled with the combustion process in the chamber. This type of instability is generally less damaging to engine hardware components than resonant combustion instabilities. Low frequency instabilities have been known to cause ruptured feed lines or joints as a result of vibration or accelerated ablative chamber erosion resulting from the propellant flow fluctuations, but typically the adverse effects of low frequency instability appear as a loss of combustor performance.

High response pressure transducers are by far the most common form of instrumentation used to detect and identify low frequency instabilities. At least one transducer is required in each of the propellant feed circuits and in the combustor to identify this type of instability. For diagnostic purposes multiple transducers are desirable in the feed system as well as in the combustor.

Feed system coupled combustion instabilities typically generate relatively low amplitude quasi-sinusoidal pressure oscillations. It is generally easier to identify this type of instability than modes of resonant combustion instability both because of the normal absence of steepened waves and the lower frequencies.

The analog pressure records from both propellant feed circuits typically reflect the pressure oscillations characteristic of low frequency instabilities. Typically, only one of the circuits actively contributes to the instability while the other is merely driven by the oscillating chamber pressure. In this case the most difficult feature of identifying feed-system coupled instabilities is the determination of the role of each feed circuit.

If there is more than one pressure transducer located axially along the feed circuit, feed system resonances can be identified by techniques described in the previous section. If not, the active circuit must be identified indirectly. This can be done either by comparing the observed frequency with computed resonances of the two circuits or by careful examination of the oscillations in each circuit. Often the passive circuit does not respond to the instability until the amplitude reaches a relatively high value. In this case the active circuit can be identified by observing where the oscillations first appear.

Sometimes the passive circuit can be identified by the relative amplitude of the oscillations in the two circuits. The amplitude in the passive circuit may be significantly lower than that of the active circuit, but relying on this may lead to erroneous conclusions. For example, if the transducer in the active circuit is located near a pressure nodal point of the resonant oscillation, the recorded amplitude may be significantly lower than that observed in the passive circuit.

Thus far only the characteristics of the propellant feed circuits have been considered. For classical "chugging" modes of low frequency instability the wavelength of the instability frequency is typically very large compared to any characteristic dimension of the combustor cavity. This results in bulk fluctuations of pressure within the combustor. Therefore, this type of instability can be identified by resonant oscillations in one of the feed circuits, as previously discussed, coupled with a bulk oscillation in the chamber as identified by uniform instantaneous pressures throughout the combustor.

A second type of feed-system coupled combustion instability observed with larger engines involves a resonant oscillation in one of the feed circuits coupled with a distributed oscillation in the combustor cavity. This can occur if the frequency of the feed-system oscillation closely approximates a resonance of the combustor or if the resonant oscillation in the feed system is not uniform across the injector. For example, if an annular distribution manifold is used to feed one of the propellants to the injector, a resonant oscillation in the annulus will have a circumferentially distributed pressure amplitude and phase profile. This would result in a correspondingly distributed circumferential pressure distribution in the combustor cavity (also see Sect. 5.4).

Because low frequency instabilities are typically less damaging than resonant combustion instabilities, they have not received the same degree of concern or investigation by either the researcher or the development engineer. Experience has shown, however, that feed-system instabilities have often been as prevalent as resonant instabilities. Problems with this type instability are often late in appearing and can result in a serious setback to a development program. This late appearance results from the dependence of low frequency instability on the propellant feed system and the normal development practice of performing early thrust chamber testing in facilities that do not duplicate the flight-type circuits. For example, the degree of dissolved pressurizing gas in the propellant can dramatically affect low frequency oscillations.

9.7.3 Combustion Disturbances

The combustion process in a rocket engine, by its very nature, exhibits random pressure fluctuations. Normally this combustion noise, although random in frequency, exhibits a fairly constant amplitude of approximately one to two percent of the steady-state chamber pressure. Occasionally, however, a disturbance may appear in the combustor which is significantly greater than the random noise level. These functional disturbances cause a pressure perturbation whose amplitude may reach levels twice that of the steady-state chamber pressure. Typically these functional disturbances excite resonant oscillations in the combustor which may either be damped or sustained as a resonant instability. It is beyond the scope of this article to discuss the various causes of these "spikes" or "pops." The objective here is to discuss the measurement and interpretation of the physical characteristics of these disturbances.

In addition to functional or accidental disturbances which occur spontaneously in rocket engines, artificial disturbances are often intentionally introduced to excite instability or rate the stability characteristics of engines. These artificial disturbances are discussed in considerable detail in Chapter 10, but many of the measurement and

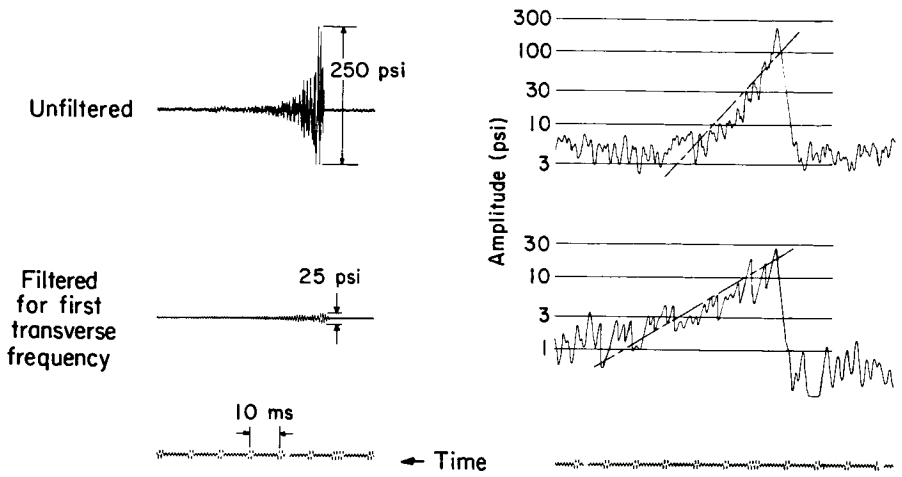

FIGURE 9.7.3.—Analog and integrated logarithmic pressure decay from a combustion disturbance.

data reduction techniques used are the same as those used for spontaneous disturbances.

The high response pressure transducer is most commonly used to detect combustion disturbances and the resultant effect on the combustion process, although accelerometers and photographic techniques are also used. Many pressure measurements taken directly from the analog records are used to characterize combustion disturbances and the resultant combustion response. Among these are the amplitude of the initial perturbation, the peak overpressure of the maximum resultant oscillation, the peak-to-peak amplitude of the maximum resultant oscillation, the time required for the resultant fluctuations to be attenuated, etc. These characteristics are obtained by direct measurement from the unfiltered analog pressure records and are used to compare the stability characteristics of various injector designs.

A second type of information used to characterize the result of combustion disturbances both to compare injectors and as a direct quantitative measure of the damping characteristics of the engine is the damping rate of oscillations generated by the disturbance. There are several techniques used to determine damping rates or growth rates from analog pressure data. One method is to measure the peak-to-peak amplitude of a single pressure cycle and the time interval between the initial pressure perturbation and this pressure cycle. By repeating this process at several times a plot of amplitude vs time can be constructed. The slope of the resulting curve is the damping rate of the unfiltered combustion response to the disturbance (also see Sect. 9.6.6).

Another technique is to play the tape recording of the analog data through a logarithmic amplifier and record the output on a level recorder. This produces an envelope of the amplitude of the oscillating pressure from which the logarithmic decay rate can be directly measured as the slope of the amplitude vs time.

When either of the above techniques is applied to the unfiltered pressure data, the decay rate of the overall pressure oscillations generated by the disturbance can be determined. Often, to measure the damping characteristics of specific resonant modes of the combustor it is desirable to filter the data prior to applying either of the above recording and data reduction techniques. When filters are used it is desirable to play the analog tape recording through the filter and display equipment in reverse. This is necessary because it normally takes three to five cycles for the filter to become sufficiently charged to output the full amplitude of the filtered signal. By playing the tape in reverse only the low amplitude cycles near the final stages of decaying oscillation will be distorted. Figure 9.7.3 illustrates the linear analog and integrated logarithmic data for the unfiltered

and filtered pressure oscillations resulting from a combustion disturbance. In this figure positive time is from right to left indicative of the reverse direction in which the tape playback was made. The slope of broken lines on the level recorder output is a direct measure of the decay rates as discussed above.

The utilization of the reduced data from both artificially or spontaneously induced disturbances provides the primary means of rating the stability characteristics of liquid rocket engines. Some of the instrumentation and data reduction techniques used to interpret the effects of disturbances have already been described. The following chapter discusses methods of utilizing combustion disturbances for rating the stability of liquid rocket engines.

CHAPTER 10

Stability Rating

10.1 INTRODUCTION*

10.1.1 Purposes of Stability Rating Tests

It is often necessary to obtain some measure of the susceptibility of a liquid rocket combustor to the occurrence of unstable combustion. Several techniques have been used for accomplishing this goal; their application is usually referred to as combustion stability rating.[426]

The primary purpose of combustion stability rating tests is to determine, in as few experiments as possible, the relative resistances of candidate engine systems or engine components to objectional combustion instabilities. The underlying philosophy and justification for stability rating tests is covered in Sect. 1.2.4. It is important to recognize that all stability ratings are relative. Current understanding of unsteady combustion and flow processes precludes an absolute determination of stability. Knowledge is needed in the areas of instability initiation mechanisms, the degree to which a rating technique simulates natural initiation mechanisms, and instability driving and damping processes.

A second purpose of stability rating tests has evolved from the development of effective stabilization devices, such as baffles and acoustic absorbers. That purpose is the demonstration that dynamic stability has been achieved, i.e., that recovery to steady operation will follow any arbitrary disturbance. This viewpoint arose from the expectation that properly designed devices could virtually eliminate the occurrence of unstable combustion and has been given increased impetus by the inclusion of quite specific stability requirements in engine development contracts. Accumulated experience with stabilization devices suggest, however, that none is a panacea and that it is still a practical necessity to obtain relative ratings in order to determine the most effective means of stabilization for a particular combustor and its specific operating conditions.

A third objective of stability rating testing may be the determination of the mode of instability most likely to be encountered during normal engine operation, so that effective preventive measures may be tailored to that mode.

Finally, rating techniques can be used for investigating the effect of various engine design parameters and operating conditions on combustion stability. This is particularly true for applied research studies.

The following nomenclature pertains to Chapter 10:

$B(\gamma)$	Energy parameter in blast-wave theory
D_{OX}	Oxidizer injection orifice diameter
E	Energy of explosion, ft-lb
g	Parameter defined by Eq. (10.3.2–3)
g_c	Gravitational constant, 32.17 lbm-ft/lbf-sec^2
$p_{ms}(x)$	Mean wave front pressure at distance x from origin, psi
$\mathfrak{R}^\circ$	Universal gas constant, 1545.3 ft-lbm/mole-°R
r_s	Shock front radius, ft
r_{bc}	Outer radius of bomb case, ft
T_w	Surface temperature, °R
T_y	Temperature of solid material a distance y below the surface, °R
U_0	Initial velocity of bomb case particles, ft/sec
$v_{a\infty}$	Ablation velocity of semi-infinite slab, ft/sec
$\mathcal{W}_{cr}$	Correlation factor, see Eq. (10.6–1)
W_c	Total weight of explosive charge, lb
x	Distance from entry point to expanding shock front in combustion chamber, ft

* L. P. Combs, Author.

x_0	Distance to shock front measured along $\theta = 0$ axis, ft
y	Distance normal to (and into) ablating surface, ft
α	Thermal diffusivity, ft^2/sec
δ_c	Bomb case thickness, ft
θ	Angle from shock entry coordinate, degrees

Subscripts:

bc	Bomb case
ct	Gas-flow connecting tube
e	Explosive charge
H	Hydrogen
r	Radial orientation of pulse gun
s	Shock front
1	Undisturbed ambient medium
2	Immediately behind shock front
3	Behind contact surface in shock tube
3A, 3B	Behind contact surface, upstream and downstream, respectively, in shock tube with area change at burst diaphragm
4	Driver section of shock tube

10.1.2 Experimental Approaches

Stability rating techniques may be divided into two broad categories: (1) those which rely upon spontaneous occurrence of unstable combustion, and (2) those in which finite disturbances are introduced to initiate instabilities artificially. The second category embraces the most used methods, which will occupy our attention throughout much of this chapter. Definite advantages and shortcomings may be ascribed to each category; these are summarized before proceeding to a discussion of the individual techniques. It is noted that the degree of stability of the combustion processes is usually presumed to be related to the magnitude of some characteristic disturbance from which recovery to steady operation may be experienced.

10.1.2.1 Spontaneous instability methods.—Disturbances large enough to trigger an instability may occur naturally during normal rocket engine operation; if they occur quite often, every test may be unstable, if infrequently, only an occasional test may be unstable. One method that may be used for stability rating, particularly during the early development stages of an engine, is observation of the percentage of tests in which instability arises spontaneously during normal operation. For systems which have been developed to the point that they are moderately to very stable, this method ordinarily becomes prohibitively expensive. Evaluation, for example, of the effects on system stability, when seemingly minor component variations or improvements are made, would require a large number[92] of engine tests.* Recognition of this fact gave considerable impetus to the development of artificial disturbance rating techniques.

An alternative rating method based on spontaneous instabilities employs a systematic variation of operating conditions until a region of spontaneous instability is found and its boundaries mapped out, at least partially (Sect. 10.6). The proximity of the normal (presumably stable) operating conditions to the stability boundary is presumed to be a direct indication of the combustor's resistance to the occurrence of spontaneous instability. The stability rating then consists of determining how boundaries of unstable regions shift when engine components or operating conditions are changed. Parameters that have been varied in this kind of stability rating are the injection mixture ratio, the chamber pressure (by variation of either propellant flowrates or chamber contraction ratio), instability frequency, and propellant temperature. Typical components varied are propellant injection pattern, injection hole sizes, chamber length, chamber contraction ratio and propellant feed system details.

Most stability boundary mapping has been conducted with research-scale rocket motors designed for relatively inexpensive and frequent testing. Its greatest use in large engine development has been in rating oxygen/hydrogen engines by varying the hydrogen injection temperature

* With restartable or pulse engines, large numbers of tests may not be very expensive, so that this method may be a preferred stability rating technique. In a recent development program, for example, the stability of a small pulse engine was evaluated by observing the number of unstable pulses among 600 pulse firings in a single test sequence. A characteristic sharp pressure transient (spike or hard-start) at the beginning of each pulse would occasionally initiate the first tangential spinning instability. Use of this rating method resulted in very rapid development of effective stabilization devices.

(Sect. 10.6.1). It should be noted that the mapping of stable and unstable operating regions is not only done with spontaneous instabilities; use is sometimes made of artificial disturbance methods (Sect. 10.6 and Ref. 7).

Some advantages of using rating techniques which rely on spontaneous occurrence of instability are that the ratings are associated with naturally-occurring disturbances, the normal propellant and combustion gas flow patterns are not disrupted by foreign bodies or substances, and when stability boundaries are mapped, they are usually quite reproducible. In addition to the relatively large number of tests that may be required to obtain a single rating, there are two major disadvantages to the stability mapping method. First, the mode of instability experienced at a boundary may be different than the mode most likely to be initiated by an occasional large disturbance at the normal operating conditions. Second, stability region boundaries may be associated with different instability driving mechanisms than those which are operative at normal operating conditions, e.g., regions may be encountered where combustion instability is coupled to feed system resonances. Finally, these techniques do not provide an indication of the initial disturbance magnitudes responsible for triggering the instabilities experienced.

10.1.2.2 Artificial initiation methods.—The second category of stability rating methods provides a means for obtaining ratings at the normal operating conditions. Although uncertainties as to the validity of the ratings are comparable to those of the spontaneous methods, the introduction of finite artificial disturbances into a rocket system offers such distinct advantages that several techniques have been widely used. Advantages are that (1) disturbances can be sequenced in graduated sizes so that quantitative relative ratings can be obtained, (2) the time of instability initiation can be controlled so that limited exposure of the system to a potentially destructive instability may be scheduled, (3) the number of tests required may be reduced by introducing more than one disturbance in each test, and (4) the mode of instability initiated sometimes may be selected by a proper choice of disturbance device and its placement.

Two fundamentally different approaches have been taken in perturbing steady-state combustion for stability rating: (1) introduction of disturbances in one of the propellant feed systems to disturb the combustion processes, and (2) direct disturbance of the combustion processes. While propellant feed system perturbations have occasionally been found to initiate high-frequency combustion chamber acoustic instabilities[524,712] and they are of interest for production engine rating, their effects seem to be critically dependent upon point of application, feed system capacitance, entrapped gas pockets, etc. Their applicability is usually restricted, therefore, to studies of low and intermediate frequency instabilities. Design and application of feed system perturbation devices are discussed in Sect. 10.5.

Three methods have been used for most ratings that have been obtained or sought by disturbing the combustion processes directly. They are (1) explosive bombs placed at selected locations within the combustion chamber, (2) explosive pulse guns connected to the combustion chamber by a connecting tube (barrel) through the chamber sidewall, and (3) flows of inert or reactive gases similarly directed through the chamber sidewall. The succeeding three sections in this chapter are devoted to descriptions of the methods and discussions of their application. The remainder of this section is essentially introductory, providing a brief overview of the general features of the methods. A discussion of their relative merits and limitations appears in the final section of this chapter.

The degree to which a rating technique simulates natural triggering mechanisms is pertinent to the technique's validity. Although a large number of phenomena have been identified or postulated as being probable instability triggers, it has usually not been possible to isolate any as being solely responsible for particular modes, etc. As a result, it is not possible to define the degree of simulation for a rating device. It would appear, therefore, not to be possible to obtain an unequivocal quantitative stability rating for a combustor. A corollary to this qualification is that a correspondence is not known to exist between an artificial disturbance stability rating and the actual combustion stability. (Indeed, in the statistical correlations of Ref. 82, such a correspondence was

found to be absent.) Nonetheless, these reservations have not been considered to invalidate stability ratings by artificial disturbance techniques. Rather, it is usually recommended that more than one of the methods be used in a test matrix which includes different disturbance positions and directions to improve confidence in the validity of a rating.[540,161,163]

The phenomena that might act as natural instability initiators have sometimes been considered to provide varying degrees of combustion field pressure disturbance and/or velocity disturbance.[540] Suppose, for example, that the propellant combustion processes are quite sensitive to pressure disturbances and relatively insensitive to perturbation of the combustion zone velocity field. Then a rating device that provides primarily a pressure disturbance would be expected to better simulate natural triggers than would a method which provides primarily a flow disturbance. Bombs and pulse guns provide strong pressure disturbances. The associated velocity disturbances which may be strong initially, are so short-lived that only a transient effect may be felt. In contrast, directed gas flows provide only velocity disturbances. Even these interpretations are subject to question since the weak velocity disturbances behind a bomb blast wave are strong enough to cause immediate, appreciable secondary droplet atomization and greatly increased propellant vaporization rates. Also, the effective directionality of the pulse gun is well known. Similarly, it is conceivable that gas flows perhaps distort the combustion field enough that it becomes susceptible to moderately low amplitude pressure disturbances, such as are naturally present in the combustion noise.

Detonation of a bomb within a combustion chamber is usually considered to produce an essentially omnidirectional pressure disturbance. The pulse gun produces a general pressure disturbance at its muzzle which propagates in all directions but is strongest along the direction of the gun barrel's axis. Some degree of selectivity as to mode of instability initiated results from this directionality, e.g., tangential pulse entry into cylindrical chambers is frequently employed for preferential triggering of the first tangential mode. In other situations, the nondirectionality of the bomb is attractive. Examples are initiation of the first radial mode and testing where it is desired not to favor any one mode but find which is most likely to occur. From this standpoint, small bombs probably come closest to simulating natural trigger phenomena.

It is usually found that the disturbances are most effective when placed (or directed) in a region immediately downstream of the propellant injector.[161] This presumably reflects a greater degree of sensitivity of the injection, atomization, mixing and combustion processes in this region than further downstream in the chamber. When comparing stability ratings among injectors which may have different spatial distributions of these processes, it is advisable to attempt to establish regions of maximum sensitivity to pulses, and then make the comparisons for those regions. Gas flow ratings have indicated that long narrow rectangular entry tube slots could give more reliable ratings than did circular cylindrical tubes,[386] but this approach has not been pursued for pulse guns.

The bomb and pulse gun rating devices are essentially single-shot tools which discern the instantaneous sensitivity at the particular instant that they are fired. There is some evidence that the combustion processes may possess a random distribution (in time) of sensitivity.[161] If that is so, the gas flow method would tend to delineate the minimum sensitivity during its period of application and thus might be expected to provide more reproducible ratings than could bombs or pulse guns.

10.2 EXPLOSIVE BOMBS*

In rating rocket combustion instability with bombs, small explosive charges are detonated at strategic locations within an operating combustion chamber, and the responses of the rocket engine are measured and analyzed. The bombs employed generally have three basic components: (1) a charge of high explosive, (2) a device for initiating charge detonations, and (3) an insulating casing structure. The explosive charges used may range in weight from only one or two grains to a sizable fraction of a pound depending upon the bomb design and placement, the extent of the combustor's response and the kind of response desired. As discussed earlier, the pressure amplitude

* L. P. Combs, R. J. Hefner, and J. M. Senneff, Authors.

of the bomb's shock wave is its output characteristic which is considered to evoke that response. The initial shock pressure amplitude may be predetermined in designing the bomb.

Design techniques and compromises required for sufficiently long bomb life and for avoiding bomb shrapnel damage are discussed extensively in the following articles. Also discussed briefly are methods for predicting the pressure amplitude of the shock as it expands away from the bomb. This is ultimately determined by the response of the combustion field, so that prediction must rely upon the analytical methods of Chapters 3 and 4. However, the steady-state combustion calculations are not very well developed for the case of the initial response to a finite shock.

10.2.1 Typical Designs

Bomb disturbances are usually intended to be nondirectional, i.e., to provide spherical shocks.[110] An ideal bomb configuration, then, might be a spherical explosive charge tightly confined in a spherical insulating shell. A spherical shell, however, introduces so many design and fabrication difficulties that most stability rating bombs are of a simple cylindrical design. Departures from the ideal spherical shock structure are particularly pronounced in the immediate neighborhood of the bomb, but tend to be averaged out in the shock expansion processes.[167] This is illustrated in Figs. 10.2.1a and 10.2.1b. Whether such shock asphericity is important to the stability rating depends upon how rapidly the combustion processes respond to the wave's passage.

In many applications, stability rating bombs simply are commercial high-explosive detonators housed in a protective case (Fig. 10.2.1a). Typically, such a design might be used for charge

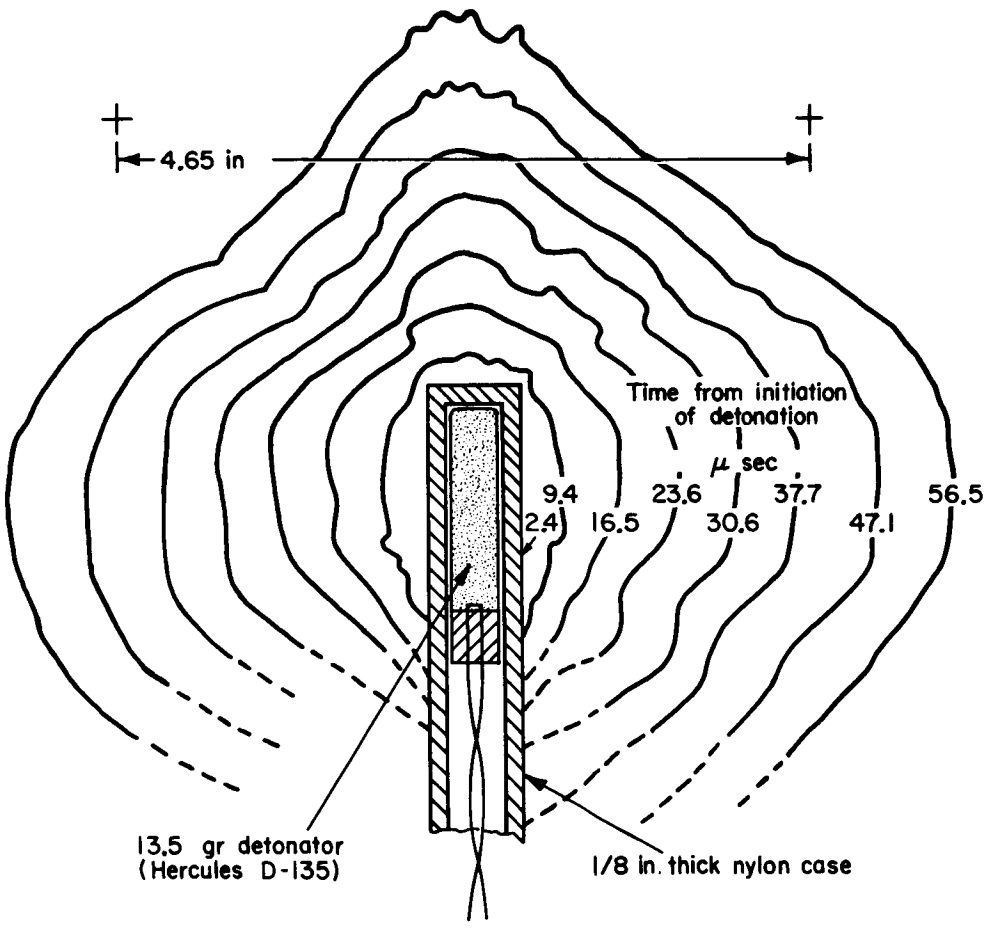

FIGURE 10.2.1a.—Shock front propagation from a cylindrical bomb.

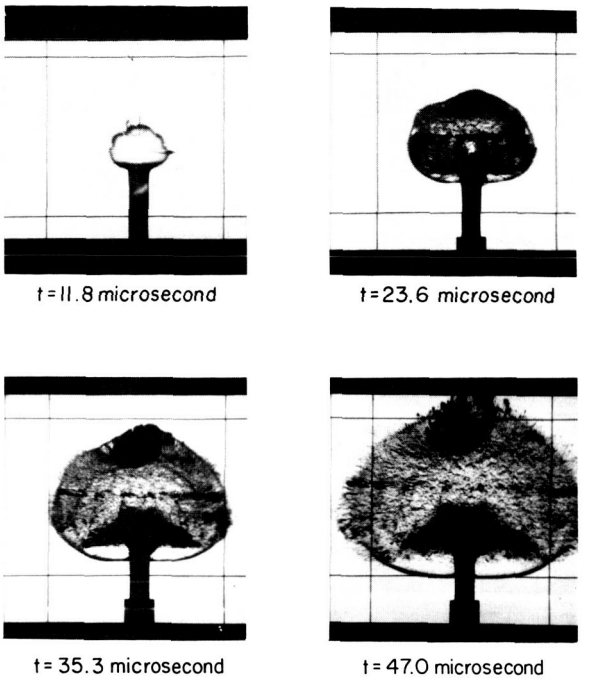

FIGURE 10.2.1b.—Schlieren photographs of shock wave propagation during a bomb cold flow test.

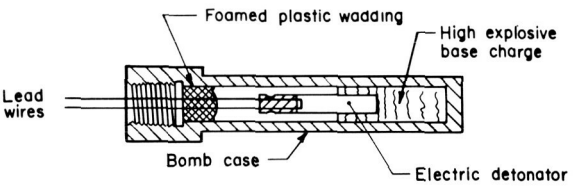

FIGURE 10.2.1c.—Bomb assembly with base charge and detonator.

weights up to about 15 grains. For larger charges, the addition of a base charge of secondary explosive to the commercial detonator is illustrated in Fig. 10.2.1c. These are examples of a fairly simple design which has been used for electrical initiation of a single bomb early in a test.

More complex designs have been used in applications requiring thermal protection or mechanical strength for longer periods of time. An example, shown in Fig. 10.2.1d, is the bomb developed for stability testing a 1,500,000-pound thrust booster engine. The explosive charge is a commercial detonator containing 13.5 gr. (equiv.) of PETN; it is initiated thermally. The moderately heavy-walled case is machined from a single piece of nylon. Its internal diameter is oversized for the detonator which is precisely and firmly positioned in the bore of a teflon adapter and held by the blasting cap wires. With large external threads, this assembly is threaded into a steel mounting member which is, in turn, attached to the injector face. An external ablative shroud was added for additional protection. The design was evolved over a long period of developmental thrust-chamber testing. It normally withstands 5- to 7-second-long ignition and starting transients and on the order of 0.8 second of mainstage operation before thermal detonation occurs.

Another design feature sometimes used for promoting controlled thermal detonation is shown in Fig. 10.2.1e. The hole in the tip of the case is to permit heat to leak in to ensure thermal actuation of the detonator prior to any thermal decomposition of the explosive charge. Although the moment of thermal actuation of the detonator is primarily controlled by the temperature and pressure characteristics within the combustor following ignition, some control can be achieved through the shape of the tip end of the bomb and the length and diameter of the hole in the tip. The more streamlined the tip, the greater the tendency to delay actuation. A long, small diameter hole also tends to delay actuation times. Thermal detonations have been achieved as long as five seconds after ignition in full-scale rocket engines by careful bomb case design. The overhanging thread design of the case is to prevent the drag forces of the combustion gases from shearing the bomb from its base mount.

Stability rating bombs utilize high explosives exclusively. Their detonation is important for achieving reproducible shock pressure amplitudes and pressure-time profiles. Low explosive (gun powder) charges burn so slowly that the confining case is ruptured before charge combustion is completed; erratic initial shock amplitudes and, occasionally, multiple shocks were observed in cold-flow characterization experiments.[163] Typical high explosives used are PETN (pentaerythritetra nitrate), RDX (cyclotrimethylene-trinitramine) and plastic explosives such as Composition C-4 (which is principally RDX). Among these, there are only minor variations in detonation velocities.

Thermal initiation of detonation is sometimes relied upon, as has been indicated. However, for

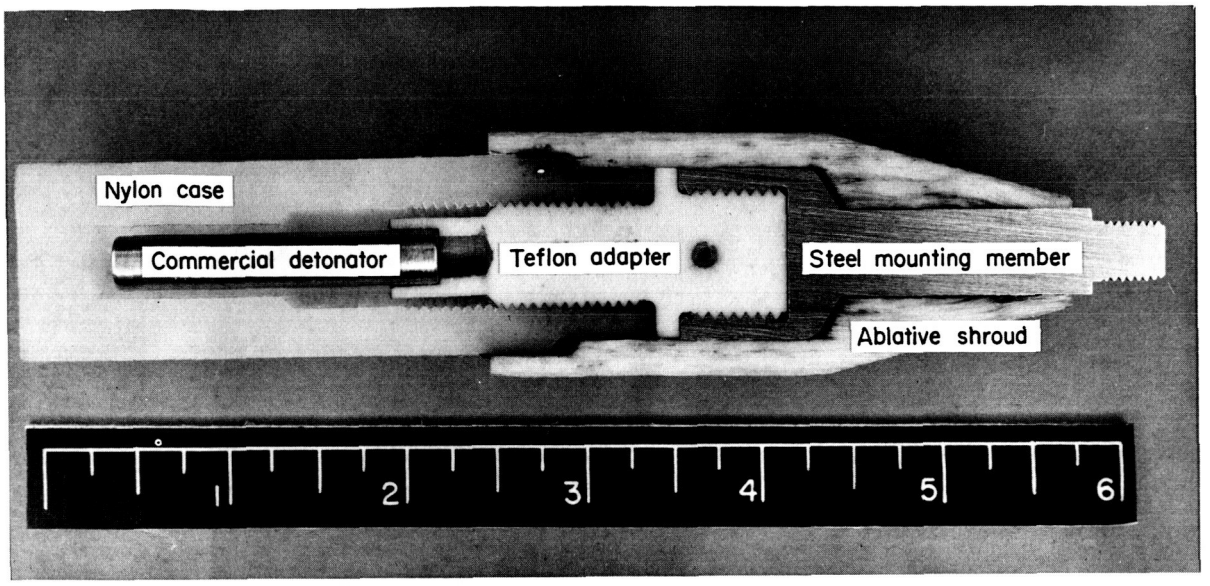

FIGURE 10.2.1d.—Thermally initiated bomb for high thrust booster engine rating.

precise control of the moment of detonation, electrically-actuated bombs are preferred. In most applications the lead wires are fed through the bomb mounting structure from the outside of the engine. This requires access through the engine wall or through a propellant manifold (together with tortuous insertion through injection passages) and a leadwire seal design.

A variation of the use of electrically actuated dentonators, particularily when access through the engine structure is impractical, is to use time-delay electrical detonators. A bomb design similar to that shown in Fig. 10.2.1e has been used except that an electrically-actuated time-delay detonator is used with the lead wires extended through the throat of the engine. The detonator is actuated by the signal to ignite the engine and then the time-delay detonator controls the moment of explosion. Time-delay detonators are commercially available which can be used to control the moment of detonation quite accurately for up to two seconds following ignition of the engine.

The preceding detonation initiation methods are all based on use of commercial detonators. These devices contain small primer charges of primary explosives, such as lead azide and tetryl. Primary explosives are considerably more sensitive to thermal (as well as shock or impact) initiation than are secondary explosives. For applications

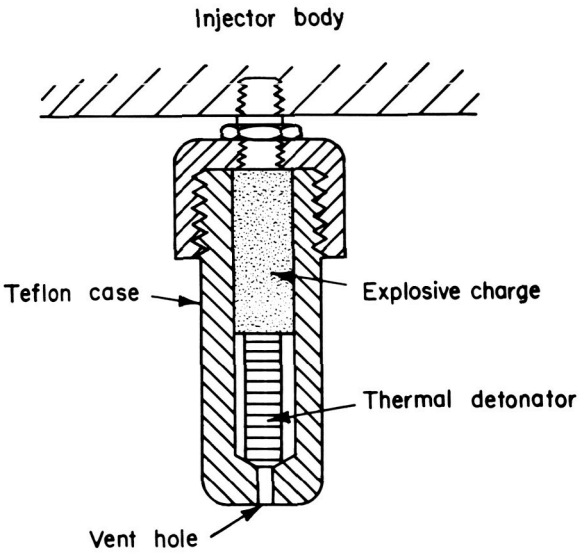

FIGURE 10.2.1e.—Thermally initiated bomb.

in which thermal sensitivity is undesirable, direct initiation of a secondary explosive charge may be obtained with an exploding bridge wire.[167] In addition to eliminating thermal sensitivity, handling hazards are reduced and the explosive charge is contained within a simple configuration whose shape, wall thickness, etc., are fully controlled (Fig. 10.2.1f). This latter feature will be

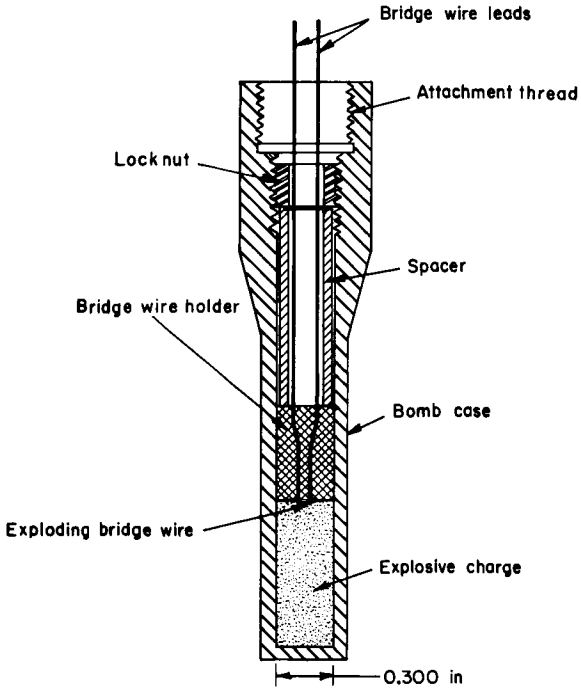

FIGURE 10.2.1f.—Exploding bridge wire initiated bomb.

seen in the next section to be desirable when predicting the shock characteristics and when trying to eliminate shrapnel damage.

Another recent innovation that may prove to be useful is direct initiation of a secondary explosive charge by focusing a laser beam, conducted through an optical fiber bundle, on the surface of the explosive. This technique, developed for reduced hazard of radio-frequency initiation,[443] has apparently not been used for stability rating device initiation.

The bomb case design is most important to adequate performance. The most influential design variables are the case material, its thickness and the mounting or attachment method. Some commonly used materials are teflon, nylon, phenolic-cloth (Micarta) and phenolic-refrasil. Others less frequently used are rubber, balsa wood, monofilament-wound quartz and both solid and pressed cork. Material selection is based on consideration of structural strength under high temperature conditions, thermal degradation and ablation and potential for inflicting shrapnel damage to engine components. Case thickness is similarly determined by the material strength, ablation rate, and the desired period of protection from thermal initiation of detonation or burning of the charge. These design variables are discussed quantitatively in the next two sections. Mounting methods are commented upon briefly in Section 10.2.4.

10.2.2 Effects of Design on Blast Amplitude

The information presented in this section is a summarization of results reported in Refs. 163 and 167, on the characterization and improvement of stability rating devices.

10.2.2.1 Effect of explosive.—The blast wave pressure amplitude is, to first order, directly proportional to the energy of the explosion. For a given explosive, then, shock amplitude increases linearly with charge weight. This may be seen from the results of blast-wave theory, the name given to a simplified similarity solution of the conservation equations for an explosion.[623,392] Shock velocity for spherical expansion is given by

$$V_s = \frac{dr_s}{dt} = \left(\frac{Eg_c}{B(\gamma)\rho_1}\right)^{1/2} r_s^{-3/2} \quad (10.2.2\text{–}1)$$

Substitution in the Rankine-Hugoniot relation for a perfect gas

$$\frac{p_s}{p_1} = \frac{2\gamma}{\gamma+1}\mathfrak{M}_s^2 - \frac{\gamma-1}{\gamma+1} \quad (10.2.2\text{–}2)$$

upon taking $\mathfrak{M}_s = V_s/a_1$ and $a_1 = (\gamma\mathfrak{R}^\circ T_1/\mathfrak{W})^{1/2}$ results in

$$\frac{p_s}{p_1} = \frac{2E}{144(\gamma+1)B(\gamma)p_1 r_s^3} - \frac{\gamma-1}{\gamma+1} \quad (10.2.2\text{–}3)$$

Although useful for illustrating the effects of explosive energy (or weight) on shock pressure, blast-wave theory is not generally applicable to bomb configurations used for stability rating. Principal reasons are that blast-wave theory assumes (1) the region of interest is far enough from the source that the finite mass of the explosive is negligible[121] (for typical rating bombs, such a distance is of the order of typical rocket combustion chamber diameters); (2) all of the energy is transmitted to the shock front (absorption of energy in accelerating case particles is not treated); (3) the ambient pressure is negligible compared with the shock pressure (pressure ratios in typical rating applications rarely exceed

values of 3 or 4 which are too low to satisfy this assumption).

To a limited extent, it is conceivable that the type and shape of the explosive charge can be used to control the shape and peak amplitude of the shock wave for a given quantity of explosive by taking advantage of the approximately constant detonation rate characteristic of the explosives. That is, the same total energy release from an explosive can be controlled to produce relatively slow pressure rise rate, long dwell and slow decay or a more rapid rise and fall with correspondingly higher peak amplitude. The former would result from a long, thin cylinder of explosive while the latter would result from a short fat cylinder of explosive. The blast-wave theory prediction for a cylindrical charge is similar to that of Eq. (10.2.2–3) except that the amplitude decays as r_s^{-2} rather than r_s^{-3}. As will be seen, it is found experimentally that cylindrical charges with length-to-diameter ratios (L/D) as high as 6:1 behave essentially as spherical charges. Perhaps L/D values in excess of 20 would be needed to approximate the infinitely long cylinder solution. The degree of control over pressure rise rate may be inferred by considering that if a given charge weight were elongated by one foot, the total detonation time would be increased by about 40 microseconds.

10.2.2.2 Case design effects.—The influences of bomb case thickness and explosive length-to-diameter ratio on air blast shock amplitude were studied experimentally using nylon and Micarta cases similar to those of Figs. 10.2.1a and c.[163] Initial overpressures* at the outer surface of the bombs were calculated by substituting initial shock velocities (obtained by streak photography) in Eq. (10.2.2–2). The results from 5.5, 13.5 and 50-grain bombs, shown in Fig. 10.2.2a, were found to be independent of charge L/D ratios between 1 and 4.[4]

It was observed in these experiments that the bomb case fragments usually had the same initial velocities as the shock waves; the shocks became distinct only about one bomb radius or more away from the surface. Therefore, by assuming the inverse, that the initial shock velocity is the same

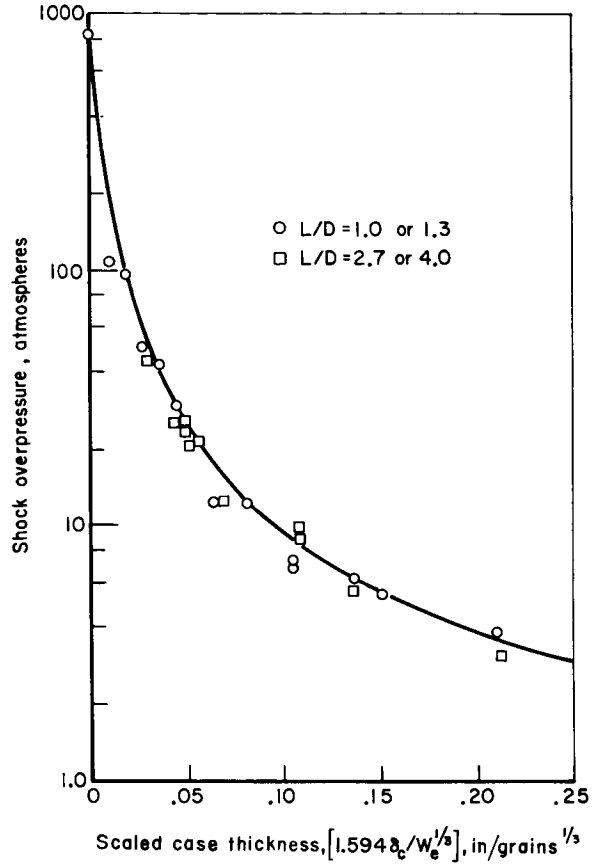

FIGURE 10.2.2a.—Initial air-shock overpressures with high-explosive, nylon bombs.

as the initial case particle velocity, analytical expressions for the particle velocity may be used to calculate overpressures. Correlation of the preceding air blast data to one expression for cylindrical bombs[686] and another for spherical bombs[301] again revealed that the stability rating bombs behave more nearly as spherical charges. The latter correlation, shown in Fig. 10.2.2b, supports the use of Gurney's expression for predicting initial bomb shock velocities.

$$U_0 = \left[\frac{2Eg_c}{W_e}\left(\frac{m_e/m_{bc}}{0.6(m_e/m_{bc})+1}\right)\right]^{1/2} \qquad (10.2.2\text{–}4)$$

In using this formula the energy output per unit mass of explosive (E/W_e) is needed and the explosive and case masses for an equivalent spherical charge are calculated using the actual bomb's charge diameter and case thickness.

* Peak pressure minus steady pressure.

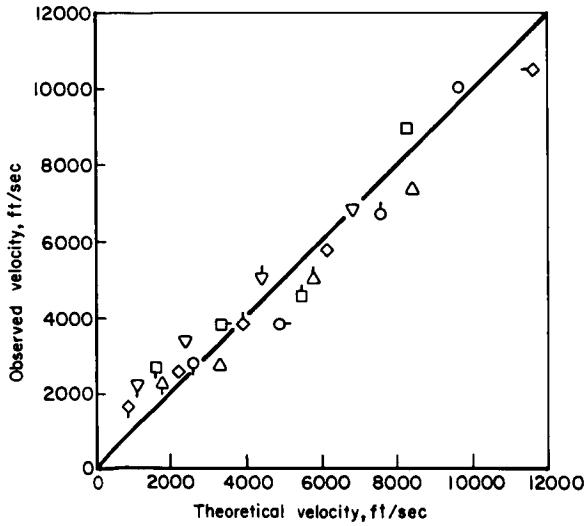

Explosive		Case thickness, in				
Weight grains	L/D ratio	0.063	0.125	0.250	0.500	0.016
50	1.0	○	○	○	○	
50	4.0	□	□	□	□	
13.5	1.0	△	△	△	△	
13.5	2.7	▽	▽	▽	▽	
5.5	1.3	◇	◇	◇	◇	◇

FIGURE 10.2.2b—Bomb case particle velocity (experiment versus theory for spherical bombs).

10.2.2.3 Ambient medium effects.—Substitution of the foregoing calculated case particle velocity (or its assumed equivalent shock velocity) into the Rankine-Hugoniot pressure relationship, Eq. (10.2.2–2) provides a prediction of the initial shock overpressure in any medium. The agreement between theory and experiments in ambient air was quite good* for bombs initiated with blasting caps.

Additional experiments were made with bombs detonated in a chamber pressurized with various inert gases (He, Ar, CO_2, N_2).[167] In this apparatus, the initial velocities could not be measured; shock pressure amplitudes were measured with a number of Kistler pressure transducers located 4.5 to 7.2-inches from the center of the bomb. The shock overpressure amplitude data, analyzed by multiple regression techniques, exhibited a functional dependence on ambient medium properties as follows:

$$\Delta p_s = p_s - p_1 \sim \frac{\gamma^{1.85} \rho_1^{0.35}}{\mathfrak{M}^{0.25}} \qquad (10.2.2\text{–}5)$$

For hot-firing conditions reported in Ref. 167 (N_2O_4/A-50 at 150 psia), this expression predicted shock overpressures only on the order of 37 per cent of the air shock values for fixed bomb parameters. It is seen in the next subsection that this value is in good agreement with actual hot-firing results. Eq. (10.2.2–5) is recommended for use with the empirical correlation discussed there in predicting shock overpressures some distance away from the bomb.

10.2.2.4 An empirical scaled blast correlation.—As discussed in Sect. 10.2.2.1, the similarity solution of blast wave theory is based on assumptions to which stability rating bombs do not conform. These bombs' blasts do, however, exhibit some correspondence[163] to existing empirical scaled correlations of blast waves from large explosions. An example is shown in Fig. 10.2.2c where the shock overpressure from a bare 13.5 grain commercial detonator is compared favorably with a correlation of Reutenik and Lewis.[588] The deviation of the detonator's overpressures from the Reutenik and Lewis curve at scaled distances less than about 1.5 presumably results both from approaching too close to the explosion source and from the detonator's finite case thickness (0.016-inch polyethylene). Reutenik and Lewis' experiments were with charges weighing 217 and 12,000 pounds; it is remarkable that a correlation should be found with charges weighing only 2×10^{-3} pound.

Additional data are compared with this correlation in Fig. 10.2.2d where, it will be noticed, the coordinates have been modified by inclusion of the ambient pressure. This change was made so that rocket motor firing data could be compared with cold flow data. The open circles labeled "cased bombs" are the same data which appeared

* Subsequent cold characterization of the *exploding bridge wire* initiated bomb of Fig. 10.2.1f gave less satisfactory correlation with the theory, particularly with small charges in moderately thick cases. While most of the data were within a factor of two of the predicted values, a limited number gave experimental shock overpressures nearly an order of magnitude higher than the predicted values. The measurements in this case were made with high speed motion photography rather than streak technique.

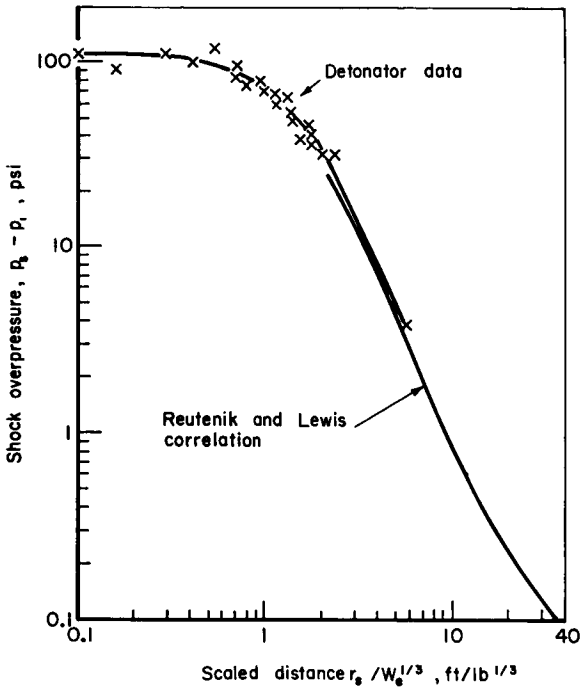

FIGURE 10.2.2c.—Comparison of 13.5 grain detonator blast with empirical scaled blast correlation.

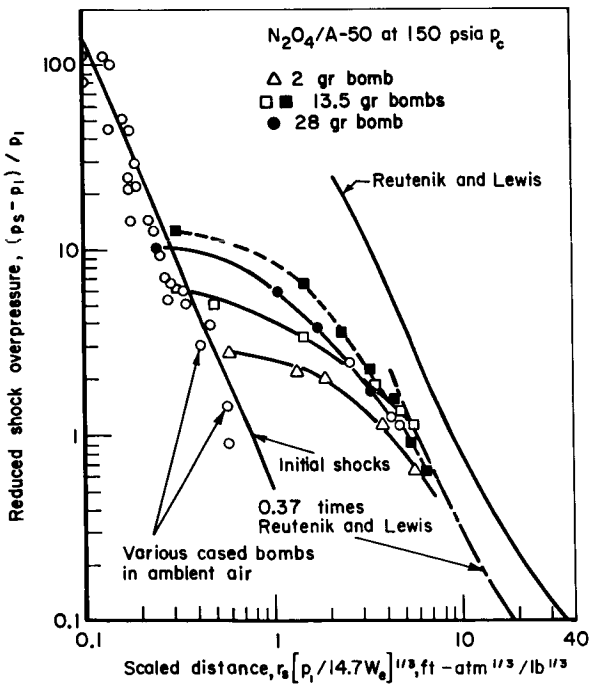

FIGURE 10.2.2d.—Comparison of cold-flow and hot-firing bomb shock overpressure with empirical scaled blast correlation.

in Figs. 10.2.2a and b; their values of scaled distance are based upon the outer radius of the bomb case. These points then represent the initial shock wave amplitudes. Within a factor of about 2, they are reasonably well represented by a straight line. Charge weights and case thicknesses were both varied by factors of about eight. This correlation then represents a reasonably accurate method for predicting a bomb's initial shock amplitude.

The value of that correlation of initial shock amplitudes is greatly enhanced by the hot-firing data in Fig. 10.2.2d. These data were obtained by direct streak photography of bomb detonations within an operating rocket motor by means of a streak camera viewing through the exhaust nozzle. Shock-front velocities were reduced from the streak films and, with the assumption of equilibrium combustion product properties, were used in Eq. (10.2.2–2) to calculate shock pressure amplitudes. Each set of connected points in Fig. 10.2.2d is from a single bomb firing, with the point at the smallest scaled distance representing the initial shock wave. These initial shock points fall among their one-atmosphere cold-flow counterparts, a result that is strongly suggestive that the indicated correlating line is perhaps valid for other combustor-operating conditions.* The equation of the initial shock line is

$$\log_{10}\left(\frac{p_s - p_1}{p_s}\right) = 0.536 - 1.61 \log_{10}\left[r_{bc}\left(\frac{p_1}{14.7W_e}\right)^{1/3}\right] \quad (10.2.2\text{–}6)$$

from which the shock overpressure is

$$\Delta p_s = p_s - p_1 = 0.815 r_{bc}^{-1.61} W_e^{0.536} p_1^{0.464} \quad (10.2.2\text{–}7)$$

In designing a bomb to give a particular overpressure, it is recommended that values be calculated both by Gurney's theory, Eq. (10.2.2–4) with Eq. (10.2.2–2), and by the foregoing Eq. (10.2.2–7) and that the higher of the two resultant initial pressure amplitudes be used.

It is noted that two 13.5 gr bombs in the hot-firing conditions gave initial shock amplitudes that differ by a factor of about two, which is

* Only nylon and Micarta case materials are represented here.

comparable to the deviations noted among the cold-flow data. This degree of irreproducibility is apparently what one must expect to experience with cased cylindrical bombs. Inconsistencies in explosive packing density and in the initiation of detonation, eccentric case machining and irregularities in case material density and (in the hot firings) nonuniform ablation probably all contribute to this degree of uncertainty.

As the shocks expand away from the bombs their amplitudes decay and, at scaled distances on the order of 5 to 8, appear to reach limiting values somewhat less than the Reutenik and Lewis correlation (see Fig. 10.2.2d and Sect. 10.2.2.3). Supporting data were obtained from pressure transducers in the combustion chamber wall. At distances from the bomb up to about 5 or 6 inches, the direct transducer data (without correction for wave incidence angle) fell along that asymptotic curve. Except for the 2 gr charge, transducers further from the bombs than 6 inches registered increased overpressures, indicating shock-wave augmentation by the propellant combustion processes.

This correlation clearly reveals the manner in which a bomb's shock would behave in an operating rocket if there were no interaction with the combustion processes. The several techniques summarized in this section are recommended as quantitative design bases. Interaction with the combustion processes may result in either more rapid attenuation or amplification depending upon the propellants, the spray field established by the injector and the position of the bomb. A design based on no interaction may need to be scaled up or down to account for an experienced combustion effect, but still represents a reasonable starting point in the absence of combustion response information.

10.2.2.5 Bomb case erosion and explosive heating.—Adequate performance of stability rating bombs is critically dependent upon protection of the explosive charge from premature detonation (or burning) as a result of explosive heating. As described earlier, this protection usually is provided by encasing the explosive in an insulating shell made of some heat-resistant material. Most explosives have thermal explosion temperatures lower than 500° F and typical rocket combustion gas temperatures are on the order of 5000° F. With such high temperature gradients, acceptable heating rates are achieved through judicious material selection and provision of an adequate thickness.

Selection of bomb case materials has usually been based on qualitative considerations of conductivity, strength, shrapnel damage potential and probable mode of erosion or ablation. Many of the materials used have also been used for other applications, such as ablative chamber walls, heat shields, etc. Analytical methods, together with a large body of experimental data, are available for effecting quantitative evaluation and selection. Recently, their applicability has been demonstrated by correlating dummy bomb case erosion rates with analytically predicted rates for three materials[167] in an N_2O_4/A-50 rocket motor operating at 150 psia chamber pressure. The analytical work* is summarized briefly in this section.

Erosion or ablation analysis was based on axisymmetric flow of rocket combustion products parallel to the axis of a cylindrical bomb.† A further analytical simplification, valid if the thermal penetration depth is small with respect to the bomb case radius, is the treatment of the cylindrical bomb case as a semi-infinite plane solid.

Based on a chamber pressure of 150 psia, a chamber contraction ratio of 2.54 and N_2O_4/A-50 propellants, several methods were considered in arriving at 2 Btu/in.^{2}-sec. as an expected cold wall convective heat flux to a bomb case for use in the following calculations.

Erosion or ablation mass loss may take place by one or a combination of mechanisms. It is important to know which mechanisms dominate for each material and to account for them in the analyses. Basic mechanisms include

Physical phenomena:	melting, vaporization, sublimation

* Performed by Dr. J. D. Seader, Jr., of the University of Utah.

† A flow direction normal to the bomb's axis is undesirable, both from an analytical standpoint and from the asymmetric erosion that results. Neither prediction nor control of the shock pressure amplitude are normally adequate with this latter orientation.

Chemical phenomena:	pyrolysis, oxidation, depolymerization
Mechanical phenomena:	surface shear, spalling and stress failure, particle impingement

Three types of material having mass loss mechanisms typical of most other available materials were studied: teflon (amorphous melt depolymerizes to monomer vapor at about 680° F), nylon (viscous melt formed at about 507° F may flow, pyrolyzes with little char at about 750° F), phenolic-silica (pyrolysis gases leave a dimensionally stable, silica-reinforced, porous char which may melt if surface temperature exceeds 3,115° F).

For teflon and nylon, the surface recession analyses of Landau[422] and Sunderland and Grosh[675] were applied. For phenolic-silica, a one-dimensional computer program[595] was used which solves the differential energy balance equation by an implicit finite difference method.

Calculated results are shown in Fig. 10.2.2e. Single predicted curves are shown for teflon and phenolic-silica, whereas two curves are shown for nylon, one for the extreme condition of instantaneous melt removal and the other for substantial melt retention and surface pyrolysis. Observed ablated depths for dummy teflon and nylon bomb cases in 0.5 to 2.0 sec. rocket engine tests are also shown in Fig. 10.2.2e. Good agreement is seen for teflon. The results with nylon suggest that substantially no melt removal by surface shear forces occurred.

Downstream of step decreases in bomb case diameter, there was a distinct necking of the bomb case as shown in Fig. 10.2.2f. The maximum surface regression rates in this necking were approximately 50 per cent greater than those near the downstream end. A tapered shoulder, as shown in Fig. 10.2.1f, eliminated this undesirable behavior. For teflon and nylon, thermal penetration was computed from the quasi-steady-state solution of the moving-boundary conduction problem for a semi-infinite slab

$$\frac{T_y - T_1}{T_w - T_1} = \exp\left(\frac{-v_{a\infty} y}{\alpha}\right) \qquad (10.2.2\text{–}8)$$

where y is measured from (and into) the receding surface. For the charring phenolic-silica, the transient temperature profile was part of the computer program output. To illustrate the approach, it was assumed that an RDX base charge was to be electrically detonated at 0.5 sec. into mainstage of a rocket test in which negligible heating occurred in ignition and pre-stage periods. The thermal explosion temperature for RDX was taken as 500° F. The results are given in Table 10.2.2. A study of that table will reveal that the thermal penetration is very shallow (or, for phenolic-silica, very slow) and that quite thin-walled bomb cases should suffice for this application.

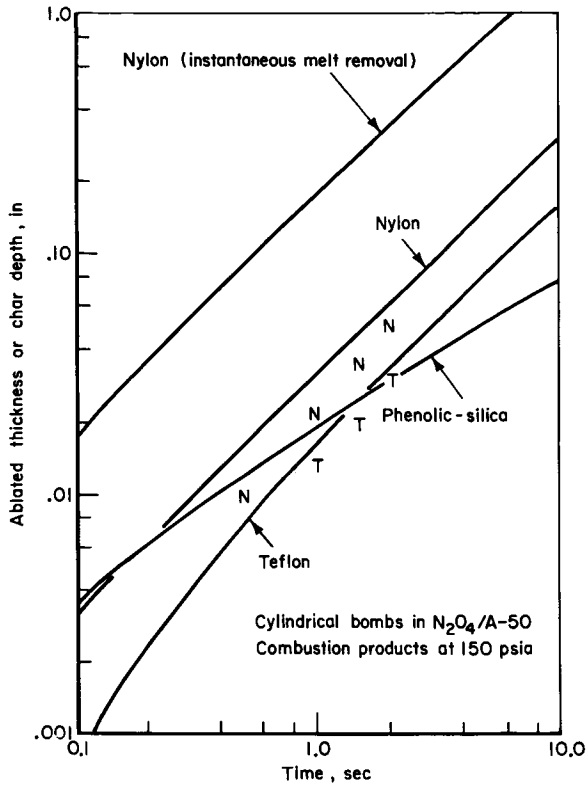

FIGURE 10.2.2e.—Predicted ablation rates for selected bomb case materials.

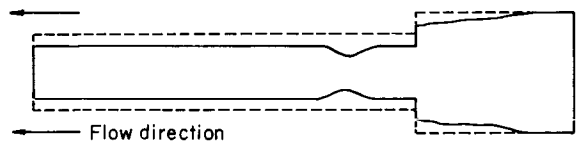

FIGURE 10.2.2f.—Flow effects on erosion.

TABLE 10.2.2.—PREDICTED THERMAL PENETRATION

Case material	Ablated or char (*) thickness at 0.5 sec, in.	Residual case thickness for 500° F inner wall, in.	Minimum initial wall thickness, in.	Minimum case wall mass remaining for 500° F inner wall, lbm/in.^{2}	Maximum wall mass loss, percent
Teflon	0.0073	0.0117	0.019	0.00153	38.5
Nylon (without melt removal)	.016	.004	.020	.000822	80.0
Phenolic-silica	.012*	.005	.017	.00102	9.8

10.2.3 Control of Shrapnel Damage

The use of explosive devices always presents the threat of causing damage to the engine. The size of the explosive charge can be made large enough to critically damage the engine simply by overpressurization. This is not the type of damage normally experienced in rating liquid rocket engines, however, since the quantity of explosive charge used is usually selected to produce a prescribed maximum overpressure which is well within the structural limitation of the combustor. The type of damage usually encountered as a result of using explosive bombs (aside from damage resulting from an induced instability) is damage inflicted by shrapnel. Shrapnel from an explosive bomb may penetrate the coolant passages of regeneratively cooled chambers or damage and distort the injector face and baffles. It may also rupture the cooling or sensing diaphragms of pressure transducers.

The types of damage observed with thin metal structures, such as regeneratively cooled chamber walls, may be divided into three broad categories: area deformation, dents and holes. It is difficult to establish absolute criteria for assessing the degree of damage. However, heat transfer, material stress and repair cost considerations indicate that area deformation and dents will normally cause very little, if any, degradation of engine performance or reliability. One exception to this might be very sharp dents with small radii of curvature at the apexes; there may be a possibility of the metal eventually cracking from repeated thermal stressing of such tips in engines fired many times. Holes are obviously undesirable, although many times they may have no deleterious effects on engine operation. Holes are customarily repaired before reuse of the damaged component. With tube-wall chambers, repair is considerably simpler with small holes than with large holes. Increasing severity of damage might then progress as no deformation, area deformation, rounded dents, sharp dents, few small holes, many small holes, few large holes, many large holes.

The simplest approach to reducing shrapnel damage is to locate the bomb as far as possible from sensitive engine components. For all but the largest chambers, this approach alone is inadequate because large fragments maintain enough momentum to inflict significant damage at distances in excess of one foot. Additionally, this restriction on bomb placement is undesirable with respect to versatility and preferred mode initiation.

Several design techniques are available for reducing the potential for shrapnel damage. One method would be to simply reduce the weight of the explosive charge which, in turn, can directly reduce the velocity imparted to the case fragments (Eq. 10.2.2–4). For a fixed case design, however, this implies a reduced shock pressure amplitude, which may be undesirable. Perhaps a more useful approach is simultaneous reduction of charge weight and case thickness. Even though case particle velocity may not be reduced with this approach, less shrapnel damage usually results from reducing the case thickness, probably as a result of reduced case mass as well as of fragmentation to smaller pieces.

Some degree of control can be exercised over the fragmentation characteristics. Two major design factors in this regard are the materials used in the bomb and the shape of the charge and bomb case. All metals should be avoided as far as possible in

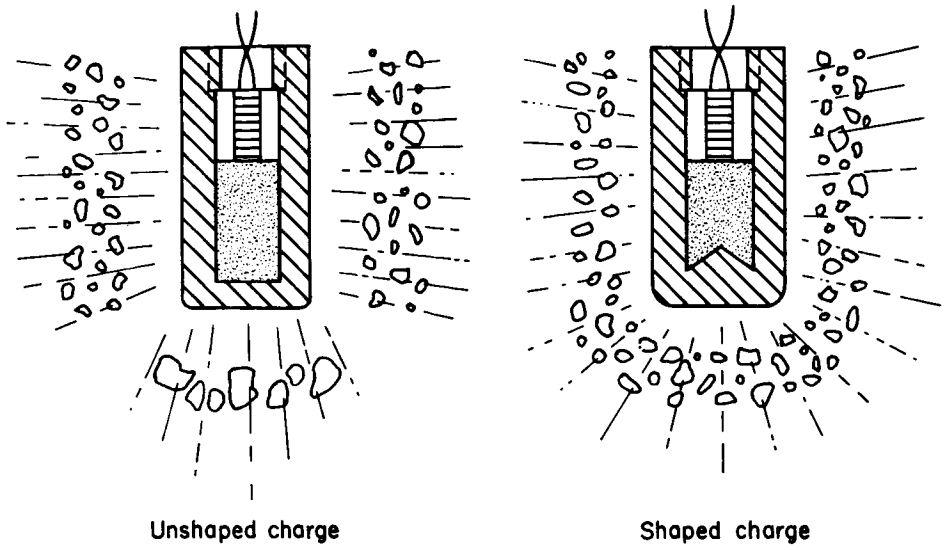

FIGURE 10.2.3a.—Effect of charge shape on case fragmentation.

the bomb design (this includes the detonator casing). Fiberglass, teflon and other plastic bomb cases can be designed to fragment into very small pieces which are either consumed within the combustion zone or are sufficiently softened by the time they reach a wall that little or no damage occurs.

It has been found that a cylindrically shaped explosive charge encased in a relatively thin case like that shown in Fig. 10.2.3a will produce a band of small fragments which move radially away from the cylindrical sides of the explosive and large fragments which cover about a thirty degree cone as they move away from the end of the cylindrical charge. If these large fragments from the end of the case can be directed out through the throat of the engine, the probability of shrapnel damage can be greatly reduced. The relatively narrow pattern of large fragments resulting from a cylindrical charge in a cylindrical case can be altered to form a broader pattern of much smaller fragments by changing the shapes of the charge and case, e.g., as illustrated in Fig. 10.2.3a.

Other material properties of importance are density, impact strength and the ability of fragments, already mentioned, to be softened quickly by convective heating. Lightweight materials are preferred because, for a given case thickness, less mass is involved, lower particle velocities are achieved, viscous drag brings about more rapid deceleration and less impact momentum is exchanged. Impact strengths, as determined by notch testing at ambient temperatures, vary by more than an order of magnitude among candidate plastic materials, Table 10.2.3. Bomb cases made of Lucite, polystyrene or cellulose acetate are attractive from this standpoint. Both Lucite and cellulose acetate were used in the uncooled motor tests of Ref. 167 and observed to have comparable ablation rates (about 20 to 40 percent higher than nylon). Cellulose acetate bomb cases, used in rating a high thrust hydrogen oxygen engine,

TABLE 10.2.3.—IMPACT STRENGTHS OF SELECTED MATERIALS

Material	Impact strength,[a] ft-lb/in.
Polymethylmethacrylate (Lucite, Plexiglas)	0.4
Cellulose acetate	0.4 to 1.9
Polytetrafluoroethylene (Teflon)	2.5 to 4.0
Nylon 66	0.9 to 2.0
Polystyrene	0.25 to 0.33
Methylpolystyrene	0.33
Polyethylene (high density)	0.4 to 6.0

[a] ASTM D 256, Izod notched.

produced considerably less shrapnel damage than nylon when bombs were discharged during full mainstage operation. However, they gave comparable damage when detonated during prestage at approximately 40 to 70 percent of mainstage chamber pressure. It was not determined how much of this difference was due to (1) hardening of the cellulose acetate because of its exposure to cryogenics early in the start transient, (2) altered fragmentation characteristics from the same cause, or (3) increased fragment softening before impact under mainstage conditions.

Another material having excellent characteristics for reduced shrapnel damage is Insulcork, a moderately high density reconstituted cork product with particles smaller than 0.03-in. diameter. Both its low ablation rate and good structural integrity make it more attractive than other low density materials such as natural cork, pressed cork (large particles), balsa wood, foamed teflon, styrofoam and foamed polyurethane.[167] Increased thicknesses of Insulcork, over those required for thermal protection, are needed for structural strength.

Cold-flow experiments for evaluation of shrapnel damage usually involve detonation of bombs at various distances from (and with various orientations with respect to) metal structures. The witness structures in some tests have been sections cut from discarded regeneratively-cooled chambers. A recent approach[167] utilizes a cylindrical structural cage with replaceable witness sheets. An eccentric positioning of the bomb, illustrated in Fig. 10.2.3b, provides simultaneous variation

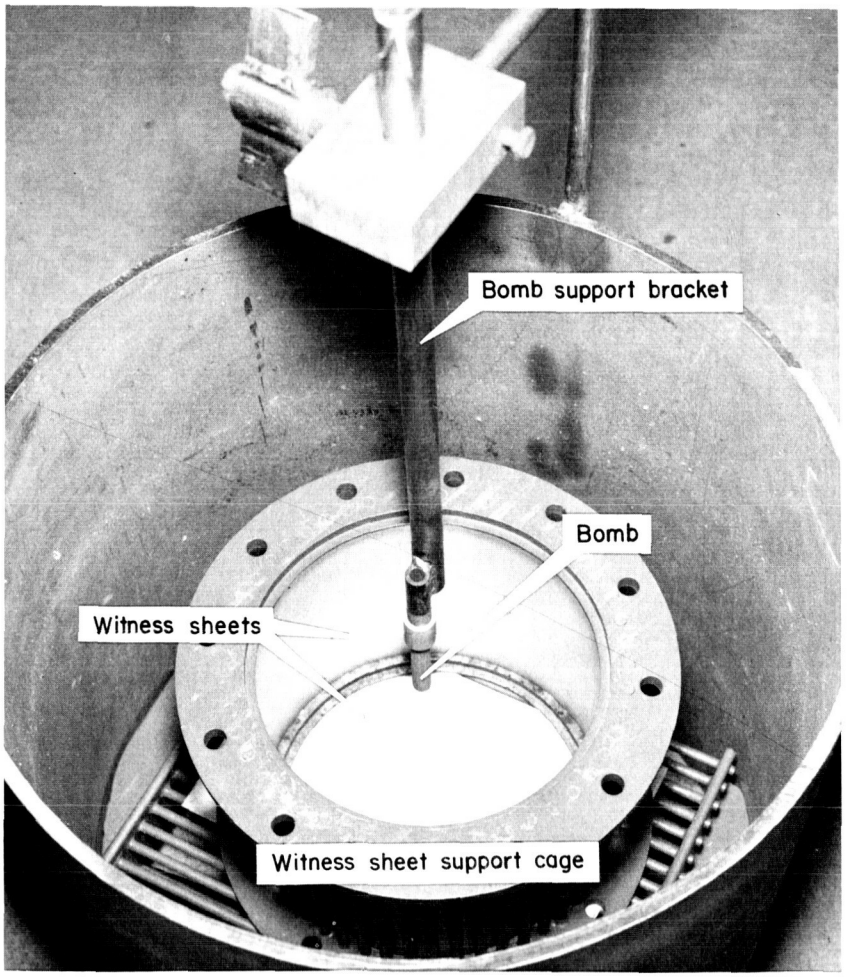

FIGURE 10.2.3b.—Apparatus for evaluating relative shrapnel damage potential for bombs.

of distance and fragment impact angle. Results of such evaluations, while qualitative, are valuable for performing an initial screening and reducing the number of hot firing tests required.

10.2.4 Application to Combustors

There are several factors to be considered in the application of explosive bombs as stability rating devices in liquid rocket engines. Among these are the bomb location, physical access to that location, mounting method and the physical size of the bomb assembly. Each of these factors is influenced to some degree by the bomb design parameters and characteristics already discussed, such as the charge weight, case thickness, method of initiating detonation, shrapnel damage potential, etc. Some different influences are examined in this article.

In using a bomb to evaluate the ability of a combustor to damp a specific mode of resonant instability, it is desirable to locate the bomb near a pressure antinode for that instability mode. This gives the highest probability that the energy generated by the bomb will go into exciting the desired acoustic resonance. The most commonly used locations are near the chamber wall at axial stations near the injector, in a central chamber location and at the entrance of the nozzle.

There are no well established criteria for obtaining the desired excitation characteristics within a combustor by use of explosive bombs. For this reason many different procedures have been used for establishing stability characteristics through explosive bombing techniques. One procedure sometimes used during engine development programs is to use one standard bomb size and location to rate various candidate injector designs. After this initial screening, one or two injectors are subjected to a series of bomb tests during which the bomb size and location are varied. Generally for the initial screening tests, an intermediate bomb size (one producing an overpressure between 50% and 100% of the steady-state chamber pressure) is used. A location near the combustion chamber wall and close to the injector is normally selected since this location is near a pressure antinodal point for all resonant modes of instability. Once the candidate prototype injectors are selected, bombs with larger and smaller explosive force are used at several locations within the combustor to obtain a broader knowledge of the stability of the injector design.

Explosive bombs may be mounted in the desired location by any convenient method. Frequently, a threaded attachment to the injector face or the downstream edge of a stabilizing baffle has been used. Provision of electrical leads to such an installation may become complicated, with conduits through propellant supply systems. Particularly with uncooled workhouse chamber assemblies, more ready access may be found by inserting the bombs through the chamber wall. In any event, the preferred orientation of a cylindrical bomb is with its axis parallel to the local flow direction. A chamber-mounted bomb installation might then appear as sketched in Fig. 10.2.4a. Rotation of such a mounting device about the elbow has sometimes been used for varying bomb position and orientation.[15]

Reduction of shrapnel damage to a bomb by detonation of another one and modest case thickness increases to offset increased erosion rates during instability appear to make regular use of multiple bombs feasible. The design of the bomb mount appears to be the key to being able to retain a bomb intact through a brief period of instability initiated by an earlier-detonated bomb. Development of strengthened bomb mount designs is needed.

The physical size of the bomb may disrupt and distort the gas flow pattern within the combustor, which may also alter the excitation effects of the

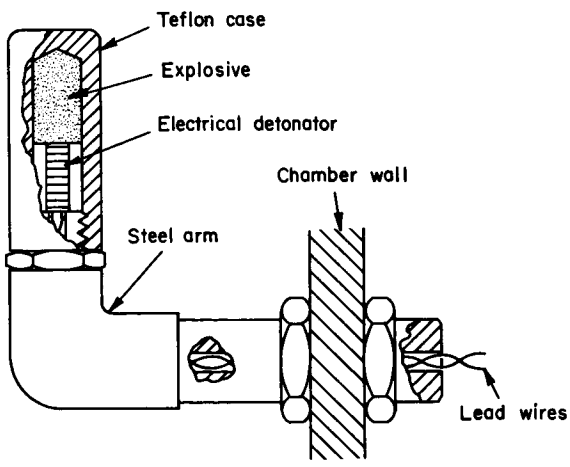

FIGURE 10.2.4a.—Chamber wall mounted bomb.

detonation. In small combustor applications, this possibility places limitations on bomb placement locations and on the number of bombs which can be accommodated.

10.2.4.1 Possibility of overbombing.—The type and amount of explosive charge may also affect the energy input to specific resonant modes through the shape and amplitude of the shock wave generated. The size of the bomb to be used has been the subject of many investigations. Some investigators have indicated that an increase in the size of the bomb increases the probability of instability. However, a number of instances have been reported in which larger disturbances proved less effective in producing instability than smaller ones.[188,11] Two examples may be cited. In the evaluation of a 3500 pound thrust engine, two grain PETN bombs were used. In several instances during a bomb location survey, unstable operation was initiated by these bombs. The occurrence rate was less than 100%; more like 1 out of 5. It was hoped that larger bombs would produce a more severe rate of incidence to reduce the testing required. When 5 grain, 15 grain and 25 grain bombs were used (at the same location and operating conditions) no instances of instability were noted.

This sensitivity to bomb size can be illuminated further by the observations made during the stability evaluation of a smaller engine in the 300 pound thrust class. It was first determined that instability could be self-induced during the altitude start sequence, primarily if a high pressure spike occurred at ignition. Normal operating chamber pressure on this unit was 125 psia but the starting pressure spike varied from a negligible overpressure to nearly 500 psi. Bomb tests were then instituted to develop a stable configuration. A test series was conducted to find whether a relationship could be established between the starting spikes and bomb shock pressures.

Fig. 10.2.4b shows the stability data obtained during tests of an undamped injector configuration, including tests with and without bomb detonations. The stability results are indicated as a function of measured overpressures. These data verified that variations in the rate of unstable occurrences could be correlated with overpressure whether self-induced or produced by a bomb.

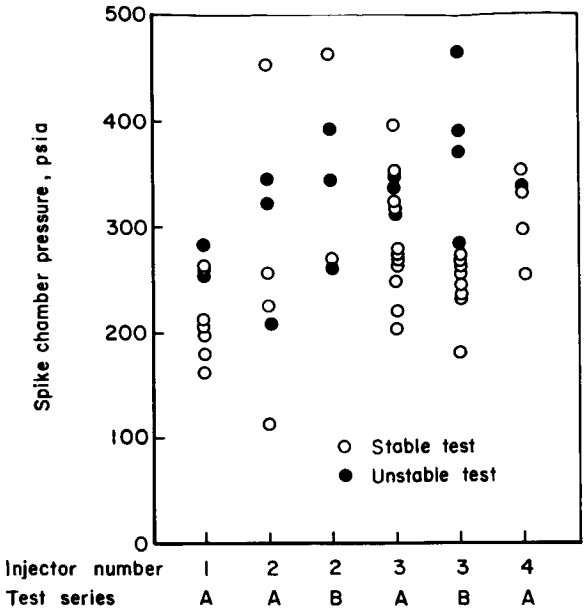

FIGURE 10.2.4b.—Peak chamber pressure recorded on transient spikes and bomb detonations in a 300-pound engine.

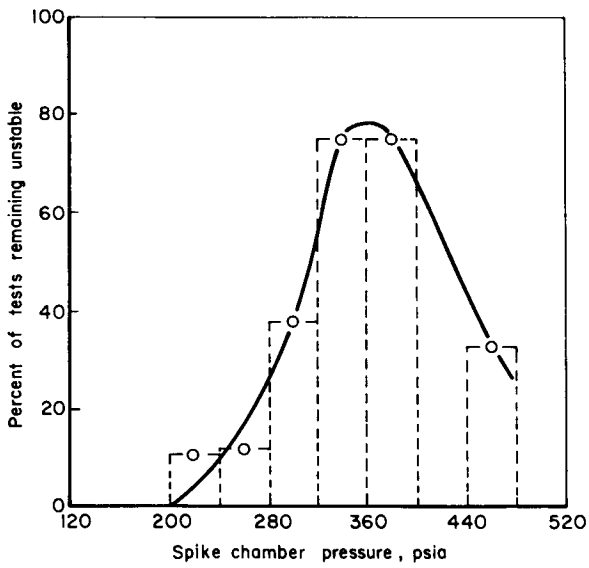

FIGURE 10.2.4c.—Percentage of tests in 40-psi chamber pressure intervals which remained unstable.

The data were then correlated in 40 psi pressure increments with the ratio of the number of unstable tests to the total number of tests in that pressure increment. The result of this correlation is shown graphically in Fig. 10.2.4c. The left-hand-side of the curve would leave little doubt

that the ratio of unstable to stable tests increases with overpressure up to a given size. In this case, a range of overpressures between 300 and 400 psi produced nearly 100% incidence of unstable operation and hence bombs were subsequently sized to provide mean-disturbance amplitudes in that range. (The shock pressures obtained with varied charge weight are shown in Fig. 10.2.4d.) Beyond this range there were indications of too large an overpressure (400 to 500 psi) which resulted in a lower incidence of triggered instability. The results of these tests were interpreted as indicating the existence of an optimum bomb size to evaluate a given combustor design.

In considering reasons for the apparent ability to overbomb a combustor, it has been suggested that a link may exist between the disturbance and the response of the feed system. According to this hypothesis the bomb overpressure (or the overpressure resulting from massive acceleration of the combustion processes) essentially stops the propellant flow, resulting in a stable restart after the induced chamber wave motion has decayed for lack of sustaining propellant sprays in the chamber.[440,759]

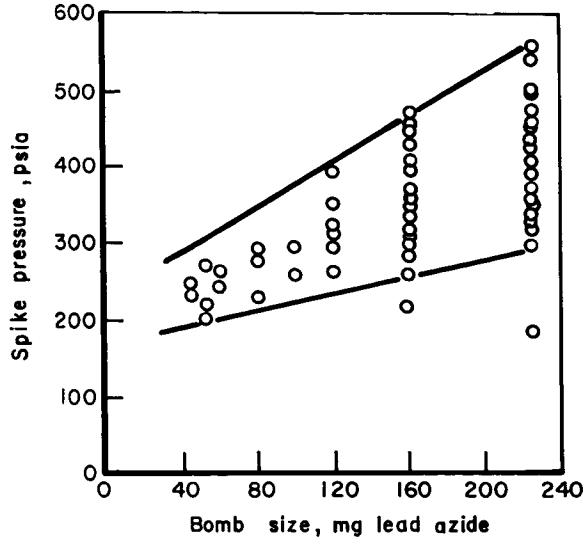

FIGURE 10.2.4d.—Peak chamber pressure amplitude observed in bombing a 300-pound-thrust engine at a p_c of 125 psia.

10.3 PULSE GUNS*

Pulse guns were originally used as an applied research tool to aid in investigating the basic mechanisms of initiating and sustaining instabilities. The pulse gun has now become one of the two most used engine stability rating devices. Many pulse gun characteristics and application techniques are different from those of explosive bombs, although their stability rating objectives are the same. Thus, the two rating devices are about as much complementary as they are competitive.

Pulse guns usually embody an explosive charge which is mounted outside of the rocket combustion chamber. Explosion products are directed into the chamber through a connecting gun barrel. Several different designs are in current use. These are described in Section 10.3.1 which is divided into discussions of those guns which use small arms cartridges loaded with a gun powder and those which use high explosives. Influences of pulse gun design variables on the blast admitted to the chamber are discussed in Section 10.3.2 using a natural subdivision into breech pressurization processes, barrel wave propagation phenomena, and expansion of the blast wave into the combustion chamber.[110] Considered in Sect. 10.3.3 is its interaction with the combustion process as affected by the operating conditions.

10.3.1 Typical Designs

As implied by its name, a pulse gun is normally comprised of a breech, an explosive charge, a firing mechanism and a barrel. The original designs, as well as most of those in current use, are modifications of small firearms' components and, therefore, utilize gun powder charges encased in standard caliber cartridges. Only recently have designs been modified so that high explosive charges might be used. In either case, a burst diaphragm is normally placed at the discharge end of the breech to protect the explosive charge from the adverse thermal environment of the combustor. For gun powder charges, the burst diaphragm acts, as well, to confine the explosion and intensify the initial blast before it enters the combustor.

Some pulse guns have been designed to operate

* L. P. Combs, R. J. Hefner, D. T. Harrje, and H. Bloomer, Authors.

with premixed gas charges rather than explosives. One design was very similar to the gun described in the following article, having a gas charge admitted through a valved port in the side of the breech, contained in the breech by a burst diaphragm and detonated by an electrical spark plug which replaced the firing pin. Another interesting design[391] had a continuous supply of detonable gases supplied to a pulse tube which had no burst diaphragm; alternating accumulation and detonation produced a series of repetitive pulses.

10.3.1.1 Pulse guns with gun powder charges.—Figure 10.3.1a illustrates a typical pulse gun design. The breech assembly is comprised of an electrically-actuated primer charge, a firing pin, a cartridge housing and a burst diaphragm housing. It should be noted that a spring-actuated firing mechanism typical of firearms breech designs is not generally used for pulse guns because of the requirement of gas-tight seal at high static pressures. (The breech of a typical small arm is not leak tight prior to firing but is sealed by the expansion of the cartridge case upon discharge of the gun.) The breech housing and barrel of the pulse gun are typically thicker than those of small arms to accommodate the higher peak pressures attained when a burst diaphragm is employed.

The cartridge housing of the pulse gun is typically designed to accommodate one of the standard, small-arm cartridges such as the .22-caliber long rifle, .38-caliber pistol, the .300-caliber magnum rifle cartridges or shotgun shells. The cartridge itself is preloaded with a prescribed weight of smokeless powder* held in place by a paper wad. The quantity of powder used has varied from as little as three grains to as much as 400 grains.

Burst diaphragms used to close the discharge end of the breech normally are matched to the gun powder charge weight. Burst diaphragm burst pressures ranging from 1,000 to 20,000 psi normally are used, although in some instances even weaker and stronger discs have been used. In most designs, plain precision burst diaphragms are specified. It has been shown recently[167] that reduced shrapnel damage results from using thicker scored diaphragms which rupture in a controlled pattern with little or no fragmentation.

For introducing multiple pulses at a single point in a combustor, a modified machine gun may also be used as a pulse gun.[652] A .30-caliber machine gun was mounted on a single-port bomb ring (Sect. 10.3.1.2) in either a tangentially or radially-oriented manner. Slight modifications to the gas-operated bolt were necessary. The machine gun was also altered by inserting a low mass check valve in the barrel. This was needed to prevent jamming at chamber pressures above 100 psi. The valve distorted and attenuated the pulse greatly, but it was possible to pulse the combustors unstable with the valve. Standard .30-caliber blanks were charged with a single base, tubular nitrocellulose propellant. During a normal run, eight increasingly larger gunpowder charge sizes,

* A fast-burning pistol powder (Hercules Bullseye No. 2) is commonly used. Slower burning, less energetic powders have been tried but not found to offer any particular advantages in improved repeatability or reliability.

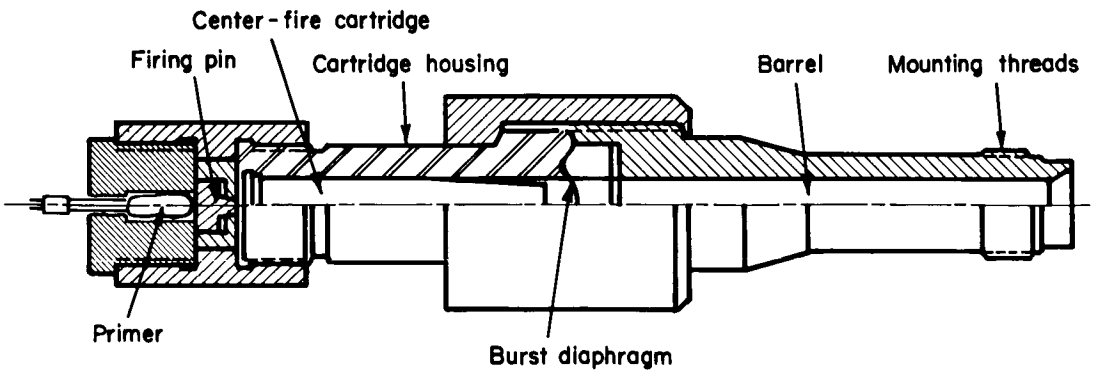

FIGURE 10.3.1a.—Typical pulse gun design.

which ranged from 18.5 to 39.0 grains, were fed to the gun via a standard link belt. The number of charges detonated consecutively was limited by run length, but generally eight charges were fired within a two-second time.

10.3.1.2 Pulse guns with high explosive charges.—Design modifications have been made to the basic pulse gun illustrated in Fig. 10.3.1a. The burst diaphragm seal has been improved to prevent leakage prior to rupture,[167] direct electrical initiation is used to eliminate misfires related to the firing pin and high explosive has been substituted for the gunpowder. The change from gunpowder was made in anticipation that the pulse wave shape (Sect. 10.3.2) would be simpler and more reproducible and thus more easily correlated to the combustor's response. A cross-sectional view of the modified gun is shown in Fig. 10.3.1b. This device has been used with charges of both PETN and RDX (as well as Bullseye pistol powder) ranging from 5 to 80 grains. Somewhat improved reliability was obtained, but the wave shape was essentially unaltered. Greater brissance of the high explosives increased the shrapnel damage potential: leaves of petal-leaf-scored burst diaphragms were consistently broken off by high explosive charges larger than 20 grains as compared to no leaf fragmentation with 40-grain and some break out with 80-grain gunpowder charges.

A more compact high-explosive pulse gun design has been incorporated into a so-called bomb ring,[652] which is designed to replace a standard combustion chamber section. A schematic of a typical bomb ring is presented in Fig. 10.3.1c. It has four tangentially-oriented ports located around the circumference. Each port is loaded with a specific size charge of explosive. The explosive can be a relatively low-energy gunpowder or a high brissance RDX with the explosive charge controlled by the number of pellets of explosive. Normally, increasingly larger size bombs are electrically detonated in a consecutive manner during a run. A 1.63-grain PETN charge is used as an initiator, while each RDX pellet weighs 4.36 grains. Ten bomb sizes, ranging from 1.63 to 40.9 grains of explosive, can be made by varying the number of RDX tablets in each bomb. A typical bomb assembly is also shown schematically in Fig. 10.3.1c.

10.3.2 Effects of Design on Pulse Amplitude

The pressure amplitude of the blast wave from a pulse gun may be considered in discrete stages: (1) breech pressurization and formation of a shock front, (2) propagation of the shock (and subsequent flow) through the gun barrel, and (3) expansion of the shock and explosion products into the combustion chamber.

10.3.2.1 Breech pressurization.—The pressure amplitude of the shock wave produced by a low explosive pulse gun is dependent upon charge weight, breech volume and burst diaphragm strength. Excessive void volume may grossly offset a substantial increase in charge weight. For example, it was found that the peak pressure

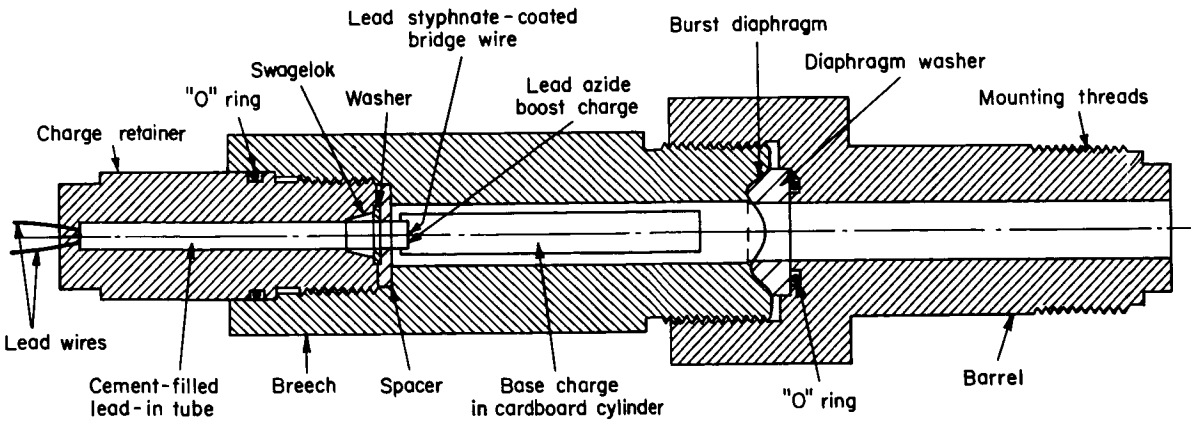

FIGURE 10.3.1b.—Pulse gun designed to fire either high explosive or gun powder charges.

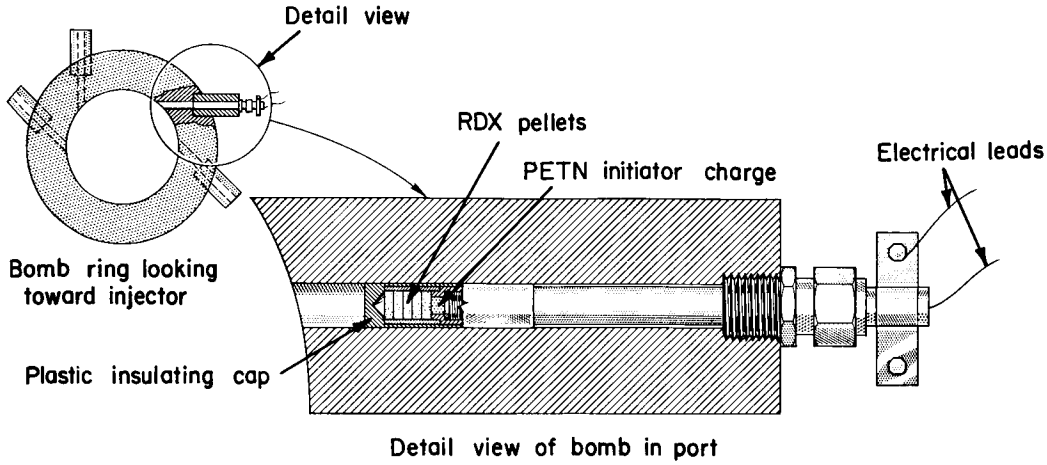

FIGURE 10.3.1c.—Bomb ring and explosive bomb details.

amplitude observed from the use of a 160-grain charge in a gun designed for a maximum charge load of 400 grains was equivalent to that observed from a 60-grain charge in a gun designed for a maximum charge of 80 grains.[7] The only difference in the internal breech design of these two guns was the volume provided behind the diaphragm. This volume was approximately seven times greater in the case of the 160-grain charge in the large breech than that of the 60-grain charge in the smaller breech.

With a pulse gun in which the cartridge essentially fills the entire breech volume, improved reproducibility may be gained by controlling the ratio of charge weight to cartridge or shell volume. Since one shell size is normally chosen for a given pulse unit, a wide range of charge weights may vary conditions from a lightly-loaded shell and a relatively large void volume, at one extreme, to a heavily-loaded shell with a minimum volume at the other. To achieve a more reproducible breech pressurization by making the filled volume fraction nearly constant, filler blocks can be used. Fig. 10.3.2a shows this design arrangement for a small charge. Uniform grain compaction is provided by filling the remaining volume with a metal spacer containing a central passage to guide the primer flash to the charge. The grains of powder are constrained (by a sheet of tissue paper) from filling this passage. An oaktag disk cemented in place with Pliobond cement completes the configuration. When used with precision burst diaphragms, this approach has resulted in a high degree of uniformity in the disturbances produced.[183]

Charge-volume effects have been examined analytically and are explicable in terms of constant-volume combustion and diaphragm rupture pressure.[167] A good design practice for gunpowder charges is to coordinate charge weight and diaphragm strength so that the calculated pressure for constant-volume combustion exceeds the diaphragm rating by 20 to 30 per cent. Then the maximum breech pressure is approximately equal to the diaphragm burst pressure. However, if the burst pressure is 20,000 psi or greater, the combustion reactions accelerate so much as the pressure increases that pressures substantially higher than burst pressure may be reached before the diaphragm ruptures. In this case the maximum breech pressure is approximately equal to the pressure that would be attained by constant-volume combustion in a cavity that is 10% larger than the actual breech. This result holds also when the constant-volume combustion pressure is more than twice the diaphragm burst pressure.

With high explosive charges, the burst diaphragm exerts little, if any, effect on pulse amplitude because the breach is pressurized by a detonation, essentially at constant volume, before much gas can escape. Again a pseudovolume of 1.10 times the actual volume is recommended for calculating predicted constant-volume breech pressures.

Some typical values of measured maximum breech pressures (using a Kistler Model 607A

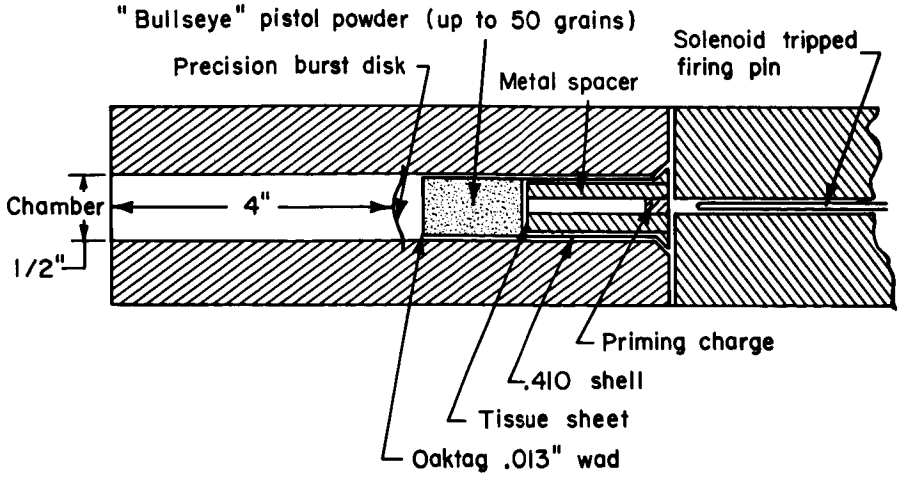

FIGURE 10.3.2a.—Use of a metal spacer to control ratio of pulse gun breech volume to charge weight.

transducer) are shown in Fig. 10.3.2b for a pulse gun like that of Fig. 10.3.1b with 10.7 cm^3 breech volume. A linear relationship between charge weight and breech pressure is seen to hold for Bullseye charges while a moderate curvature is observed with high explosive charges.

10.3.2.2 Shock propagation in the gun barrel.—Following the rupture of the burst diaphragm, a strong pressure wave is propagated down the gun barrel. It is followed by a flow of explosion products which may still be reacting and may contain burning grains of gunpowder. In general, these processes result in the discharge of a shock wave into the combustion chamber. How much of the barrel length is needed to effect steepening and coalescence of the pressure wave into a shock wave depends primarily upon the type of explosive, charge weight and combustion chamber back-pressure. High explosive detonations apparently result in immediate shock-front formation under all practical conditions. The blasts from gunpowder guns fired into ambient atmospheric pressure are not steep-fronted, and are observed to broaden as they propagate along the barrel. Under back pressures of 65 psia and higher, shock formation within 6 inches from the diaphragm has been observed.[167]

Pressure-time profiles in the barrel produced by different explosives are nearly identical at elevated pressures, differing primarily in the effect of explosive energy on amplitude. A single, well-defined shock wave is normally obtained with charges smaller than about 15 grains, while larger charges characteristically produce double-peaked profiles, Fig. 10.3.2c. The source of the second pressure peak has not been determined. Wave analyses of the breech and cartridge do not support any reflected wave hypothesis. The second peak has been attributed[163] to continued burning of powder in the breech after diaphragm rupture, but a similar occurrence with high explosive charges appears to refute that interpretation. Perhaps it is a secondary wave of the sort analyzed numerically by Brode[121] for spherical explosions, in which inward propagation of a rarefaction wave is reflected from the center of a finite mass of explosion products as a shock wave. Transducer measurements of pulse gun shocks in inert gas-filled chambers have revealed that the double fronts coalesce to a single front soon after expansion from the gun muzzle and so they may be unimportant to the pulse gun's use as a rating device.

The maximum pressure in the barrel is usually associated with the second pressure peak. Transducers placed at various positions in a gun barrel have shown that there is little attenuation of *initial shock amplitude* from charges of 40 grains and smaller. In contrast, significant losses in *maximum pressure* were observed with charges larger than 20 grains.[167]

The amplitude of the initial shock in the barrel may be calculated by ideal shock tube theory if

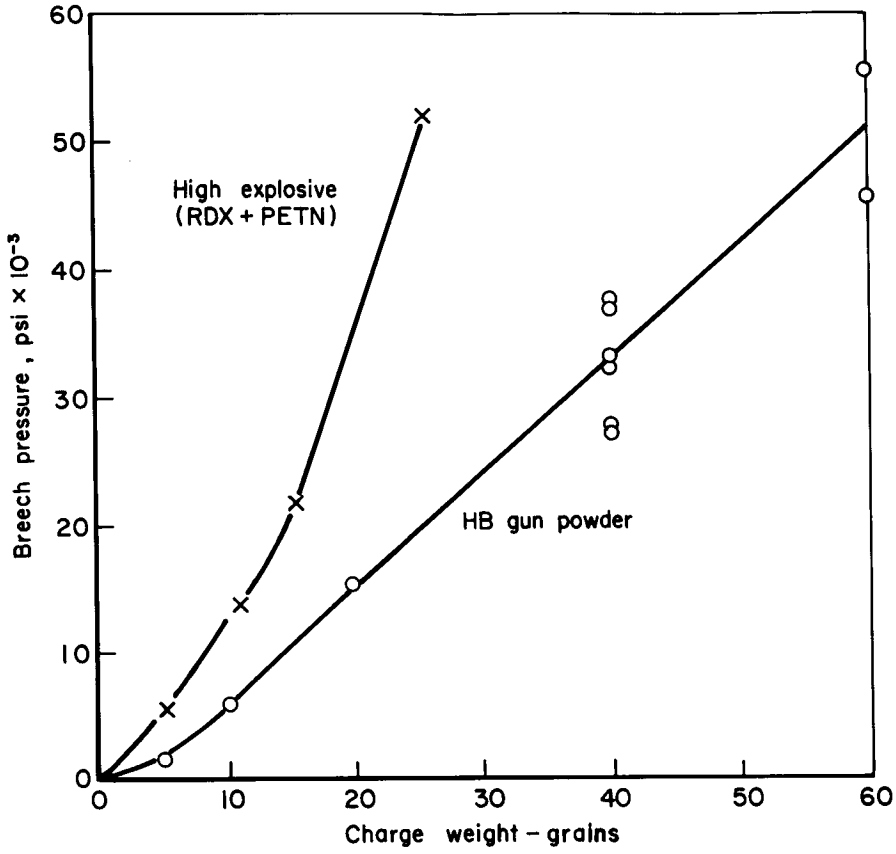

FIGURE 10.3.2b.—Maximum pulse gun breech pressure from gunpowder and high explosives in a 10.7 cm³ breech.

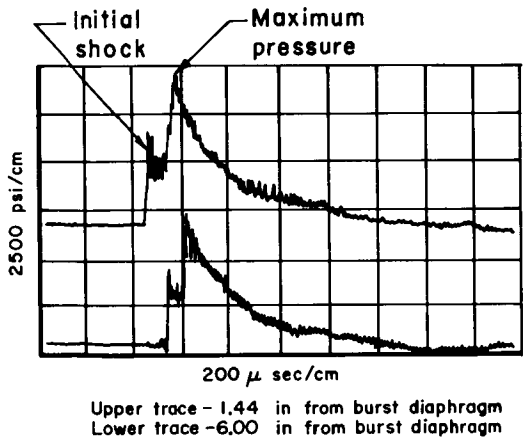

FIGURE 10.3.2c.—Pressures in a pulse gun barrel showing double pressure spikes from a 30-grain HB charge.

the breech pressure is known or predictable. Then, if the barrel is of moderate length–so that the initial shock amplitude is not degraded much by frictional and thermal losses to the barrel walls–that calculated initial shock amplitude may be a valid measure of the disturbance introduced into the combustion chamber. It is shown in Ref. 167, by analysis and experiment, that this is indeed the case. The analysis method given there is based on the formulation of Alpher and White[62] for a shock tube with variable cross-sectional area. The governing equations are

$$\frac{p_4}{p_1} = \frac{p_2}{p_1}\frac{1}{g}\left[1+\frac{\gamma_4-1}{2}\mathfrak{M}_3\right]^{2\gamma_4/(\gamma_4-1)} \tag{10.3.2–1}$$

$$\mathfrak{M}_3 = \left[\frac{a_1}{V_2}\frac{a_4}{a_1}g^{(\gamma_4-1)/2\gamma_4} - \frac{\gamma_4-1}{2}\right]^{-1} \tag{10.3.2–2}$$

$$g = \left[\left\{\frac{2+(\gamma_4-1)\mathfrak{M}_{3B}^2}{2+(\gamma_4-1)\mathfrak{M}_{3A}^2}\right\}^{1/2} \times \left\{\frac{2+(\gamma_4-1)\mathfrak{M}_{3B}}{2+(\gamma_4-1)\mathfrak{M}_{3A}}\right\}\right]^{2\gamma_4/(\gamma_4-1)} \tag{10.3.2–3}$$

$$\frac{A_4}{A_2} = \frac{\mathfrak{M}_{3B}}{\mathfrak{M}_{3A}}\left[\frac{2+(\gamma_4-1)\mathfrak{M}_{3A}^2}{2+(\gamma_4-1)\mathfrak{M}_{3B}^2}\right] \qquad (10.3.2\text{–}4)$$

$$\frac{V_2}{a_1} = \left(\frac{p_2}{p_1}-1\right)\left[\frac{\dfrac{2}{\gamma_1}}{(\gamma_1+1)\dfrac{p_2}{p_1}+(\gamma_1-1)}\right]^{1/2} \qquad (10.3.2\text{–}5)$$

Solutions are for barrel-pressure ratio, p_2/p_1, as a function of breech pressure ratio, p_4/p_1, specific heat ratios, γ_4 and γ_1, sound speeds, a_4 and a_1 and area ratio, A_4/A_2. For the case in which $A_4 = A_2$, then $g = 1$ and the equations then yield the standard shock tube equation relating the breech pressure ratio to the shock pressure ratio:

$$\frac{p_4}{p_1} = \frac{p_2}{p_1} \times \left[1-\frac{(\gamma_4-1)\left(\dfrac{a_1}{a_4}\right)\left(\dfrac{p_2}{p_1}-1\right)}{\sqrt{2\gamma_1}\sqrt{2\gamma_1+(\gamma_1+1)\left(\dfrac{p_2}{p_1}-1\right)}}\right]^{-2\gamma_4/(\gamma_4-1)} \qquad (10.3.2\text{–}6)$$

Typical calculated results are compared with experimental data from firing gunpowder and high explosive charges into pressurized nitrogen in Fig. 10.3.2d. Also shown are calculated values for the hot firing cases when the barrel is initially filled with combustion chamber gases; shock amplitudes in this case are only about one-third to one-fifth those observed in cold flow experiments.

10.3.2.3 Shock expansion into the combustion chamber.—There are two distinct effects imparted in the combustion chamber by a pulse gun firing. The first is a shock wave which propagates through the chamber cavity similar to that produced by an explosive bomb and the second is a momentum imparted to the gases in the combustion chamber.

The initial shock wave emerges from the barrel as a plane wave but then propagates approximately as an expanding hemisphere radially across the combustor cavity. The directional orientation of the gun barrel has been found to have only a moderate effect on the propagation of this initial shock wave. In order to study the history of the expanding wave, a double-pass schlieren system was used with an optically-ground injector plate, a low L/D chamber to preference tangential modes, and a full chamber diameter, thick glass, nozzle-end viewing window.[61,185] With that hardware, plus suitable optical and timing arrangements, it was possible to follow the path of the generated spherical shock wave. Time histories were constructed from a number of replicate tests using identical burst disks and charge weight combinations, but with a variation in the time at which photographs were taken (as lighted by a one-microsecond spark).

Figure 10.3.2e shows a typical schlieren photograph of the strong spherical shock produced by a 4-inch-long, ½-inch diameter pulse gun using the hardware just described. The tangential orientation of the pulse gun is seen to be of secondary importance with regard to the early history of the wave. Indications of the initial shock wave profiles at several times and for various chamber pressures are illustrated in Fig. 10.3.2f. It is clear that the initial wave expansion is basically hemispherical with only small variations due to changing pressure levels.

A similar schlieren photographic technique, which used a Beckman-Whitley Model 189 high-speed framing camera,[167] provided data on shock-front profiles similar to those in Fig. 10.3.2f but with more precisely known time intervals (since a series of as many as 25 photographs were obtained during each shock's expansion). An example of initial shock expansion from a radial pulse gun illustrated in Fig. 9.4.4b, is shown in shock-front sequence form in Fig. 10.3.2g. Both radial and tangential pulse gun orientations were used. In view of the lack of a strong effect of chamber pressure on the wave profile, Fig. 10.3.2f, the cylindrical chamber section was left open to the atmosphere at both ends.

The minor distortions from a truly hemispherical shape preclude quantitative comparison of the experimental shock-front profiles with ideal shock expansion theory. To promote such a comparison, Kuluva[167] derived empirical expressions for the

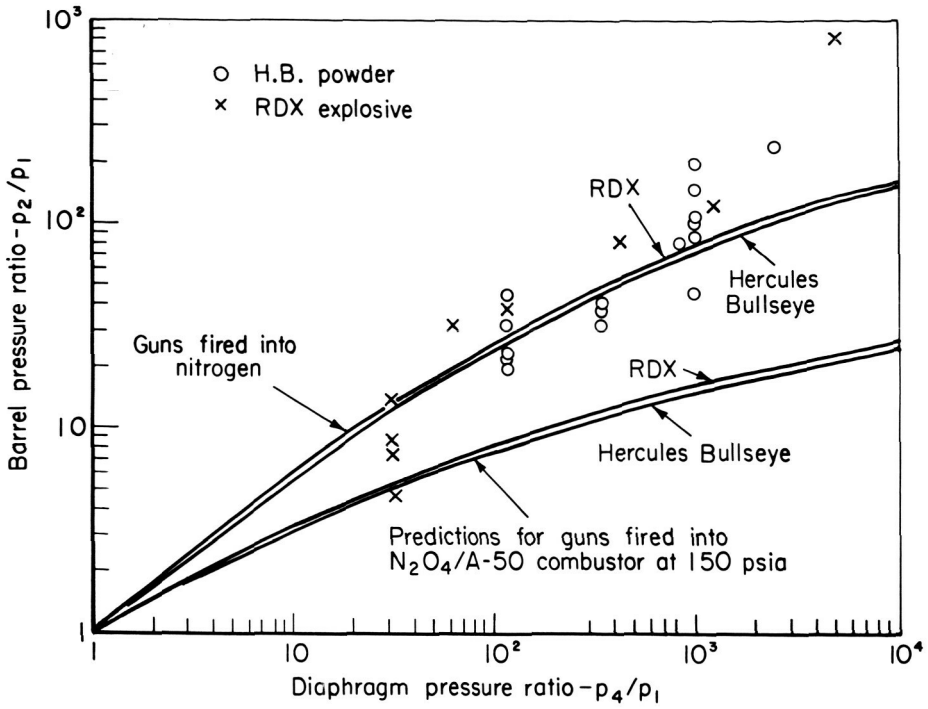

FIGURE 10.3.2d.—Comparison of measured barrel pressure ratios with ideal shock tube performance for RDX and Hercules Bullseye explosives.

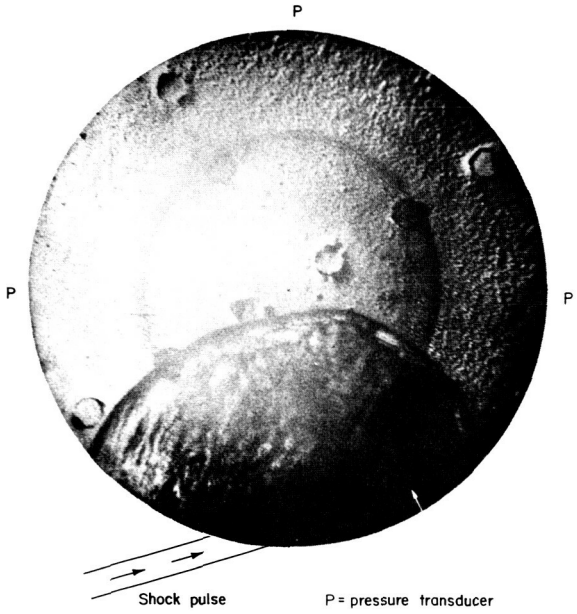

FIGURE 10.3.2e.—Schlieren photograph of shock pulse.

shock-front pressure ratio, p_s/p_1, at any radial distance x and angle θ (from reference pulse entry points and axes) to the mean integrated value over the entire wave front, p_{ms}/p_1. This latter value is related to that which ideal hemispherical shock-expansion theory yields. For details of the method and a discussion of the experimental evaluation of its validity, the reader is referred to Appendices D and E of Ref. 167.

The pulse gun's gaseous explosion products, as they emerge from the barrel, impart a momentum to the gases in the chamber. The gas flow characteristics in the combustor are thus altered for some period after the passage of the initial shock. The primary design parameter affecting the gas flow momentum exchange is the directional orientation of the gun. If the gun is mounted so that the barrel is tangentially oriented with the combustion chamber wall, the gaseous reactants from the explosive charge will tend to impart a vortex motion to the gases in the combustor. If it is oriented radially the tendency will be for a sloshing gas motion in the chamber. The quantity of powder used and the internal diameter of the gun barrel also influence this effect since these factors influence the quantity of explosive reactants and the duration they are emitted into the chamber.

When the initial motion is placed in proper perspective with the subsequent tangentially-oriented gas stream, which is believed to be responsible for the rapid generation of tangential modes (as contrasted to the initially-nondirected motion of gases associated with the bomb techniques), one is better equipped to analyze typical pulse gun stability-limits data. Such pressure records (as shown for both hot and cold testing in Fig. 10.3.2h) normally indicate the decay history of the shock wave phenomena in the first few cycles of the tangential mode oscillations. Although the tangential mode often requires a cycle or so to reach maximum amplitude, it is quite apparent that the tangentially-oriented pulse gun arrangement is highly efficient in generating both the spinning and standing tangential modes. A radial orientation alters the gas stream, whereas the shock phenomena are unaffected, with a resulting general preference exhibited for radial and standing tangential mode generation.

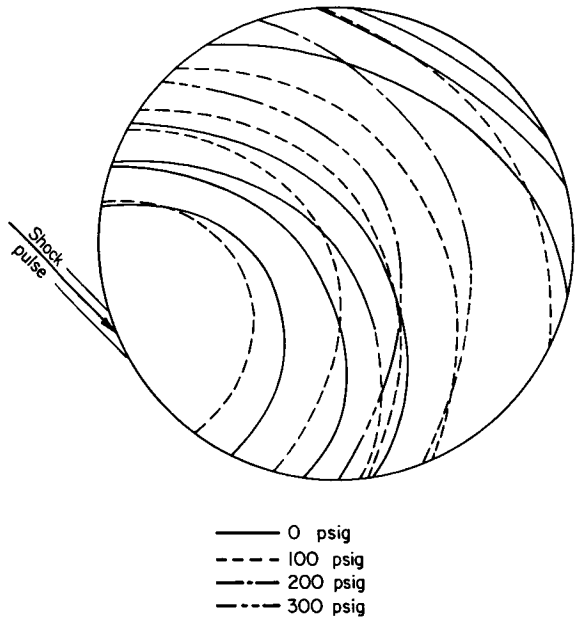

FIGURE 10.3.2f.—Profiles of the initial shock wave as it travels across the chamber for various initial chamber pressures. The shock precedes the spinning first tangential mode oscillations.

10.3.3 Effects of Combustor Operating Conditions

The discussion in Section 10.3.2 of shock expansion into a chamber was concerned with the behavior of ideal nonreacting gases. It has been found that the propellant injection and combustion characteristics can result in alteration of the shock wave as it propagates through the chamber.[514] That is, the initial wave may be either amplified or attenuated as it traverses the combustor. This effect can be so great as to overshadow the shock expansion processes described previously, and makes the correlation of the effects of combustor design and operating parameters difficult.

Some examples illustrate the complexity of observation and interpretation of a combustor's response to and interaction with the pulse gun perturbation. The same lack of well-established techniques and criteria exists for pulse guns as was noted in Sect. 10.2.4 for bombs. Perhaps the most fruitful approach would be application of an analytical model, such as that described in Section 4.3, to calculation of the initial shock wave's perturbation of steady-state. (Presumably, continued operation of the analysis would also give a prediction of the ultimate stability behavior, as well.) An attempt at such an analysis was made under the restriction of complete spray combustion immediately behind the advancing shock wave.[167] Execution was stopped after one complete wave passage across the chamber. The results were inconclusive because numerical difficulties were encountered when initial amplitudes were high enough to be realistic.

In stability evaluations, using both machine gun and bomb ring techniques[652] with two different propellant combinations, conflicting results were obtained regarding pulse growth. A storable propellant combination (N_2O_4/A-50) was burned at 100 psia chamber pressure yielding 6700 pounds thrust. The second propellant combination was hydrogen and oxygen burned at 300 psia chamber pressure and yielding 20,000 pounds thrust. The pressure history of each explosive pulse was unique for each propellant combination. With the storable combination, amplitude growth was noted as a wave traveled across the chamber. This was probably due to chemical augmentation. Conversely, amplitude decay with distance traveled was noted with the O_2-H_2 combination. In both cases, higher chamber pressures resulted in larger amplitude pulses. The effect of varying the

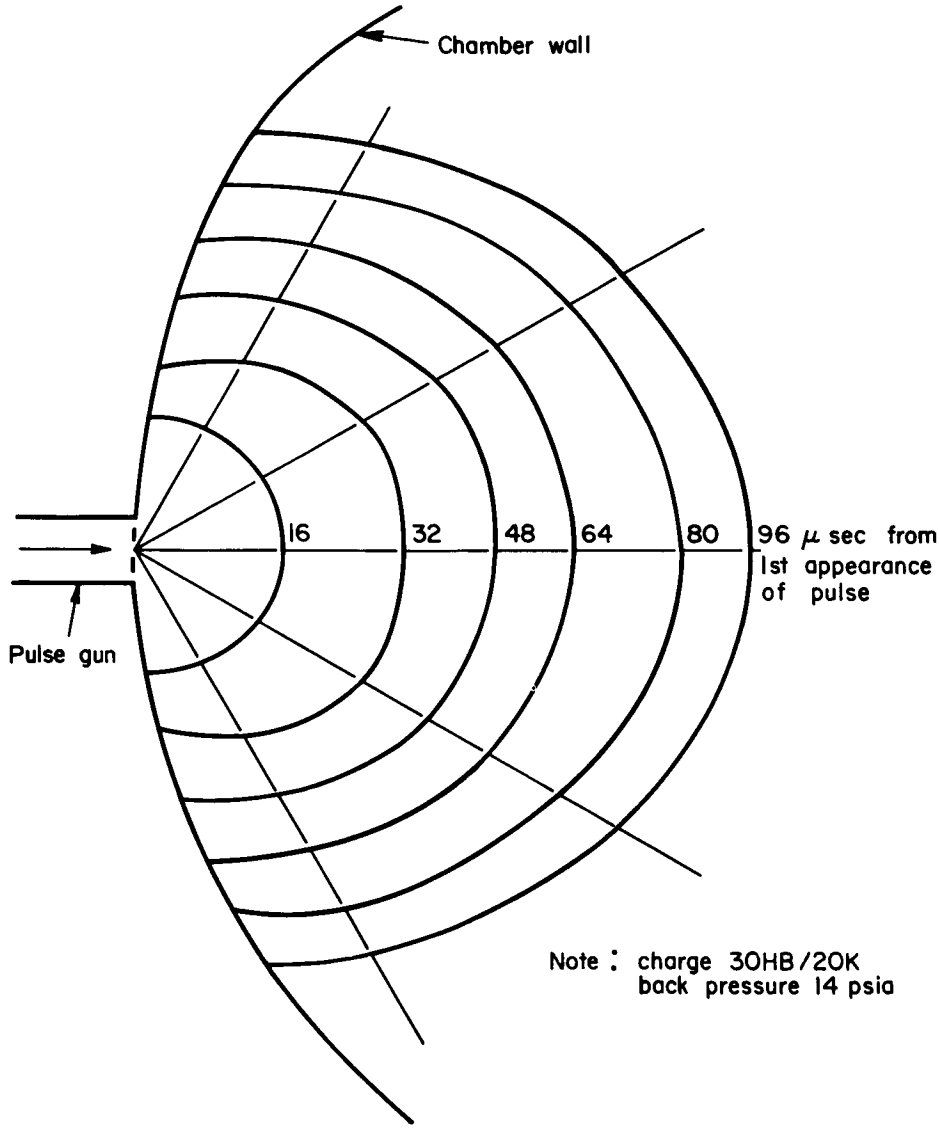

FIGURE 10.3.2g.—Shock front shape at successive times for a radially fired pulse gun.

oxidant-to-fuel ratio on pulse amplitudes was marginal with each combination. Finally, for the O_2-H_2 combination, decreasing the hydrogen injection temperature resulted in larger amplitude pulses.

Amplitude is affected by the distance the wave travels through the combustion gases. Thus, if distance variations exist between instruments and/or port locations, amplitudes will be in doubt as a stability parameter. Since the bomb ring incorporates four individual ports, a problem arises in that each bomb is detonated at a different point in the chamber. Not only does instrumentation location become critical but also each pulse is directed at a different location with respect to the injector pattern. Hence, large variations in stability rating can occur. The machine gun eliminates both problems by keeping the location of the injection port (barrel) constant while pulsing.[652]

The explosive used also affects the pulse amplitude. The RDX explosive used with the bomb ring produces a high energy detonation with high brissance. A plot of typical results

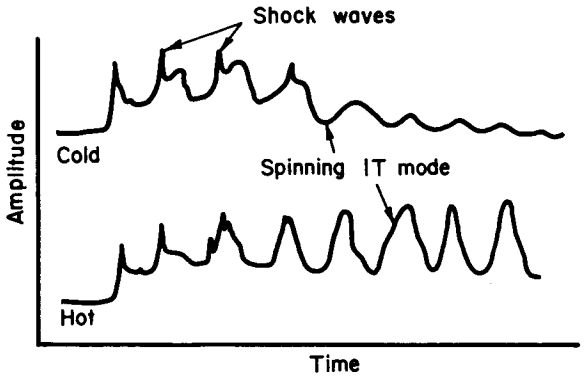

FIGURE 10.3.2h.—Comparison of pressure versus time records from cold-flow and hot-firing experiments.

appears in Fig. 10.3.3a where pressure spike amplitude is plotted as a function of RDX bomb size in grain. The nitrocellulose powder used in the machine gun tests burns rapidly (rather than exploding) and produces a lower brissance pulse. It was found, generally, that larger amounts of nitrocellulose, compared with RDX, were required to pulse combustors unstable.

Under conditions such that the chamber pressure oscillations induced by a pulse gun disturbance gradually decay, a useful indication of the influences of operating conditions may be obtained by measuring the decay rate. While tests in a closed cylindrical chamber with a well-known inert gaseous environment have exhibited reproducibility to within a few per cent,[183] the same cannot be said for actual rocket applications. Fig. 10.3.3b illustrates such controlled inert environment testing where the charge weight, burst disk combination has been varied in one test series and the chamber pressure has been varied in the other.

The increase in scatter and in the initial peak values of similar pulse guns fired into a liquid rocket chamber (9-inch diameter, LOX/ethanol, 150 psia, F = 1000 lb) is quite evident in Fig. 10.3.3c. Different initial amplitudes and damping rates were shown to be associated with the mixture ratio environment that was present. This is even more clearly shown in another series of tests as shown in Fig. 10.3.3d where it would appear that the enhanced combustion results from a rapid utilization of the available excess fuel in the chamber under low mixture ratio operation. Tangential pulse guns are generally placed close

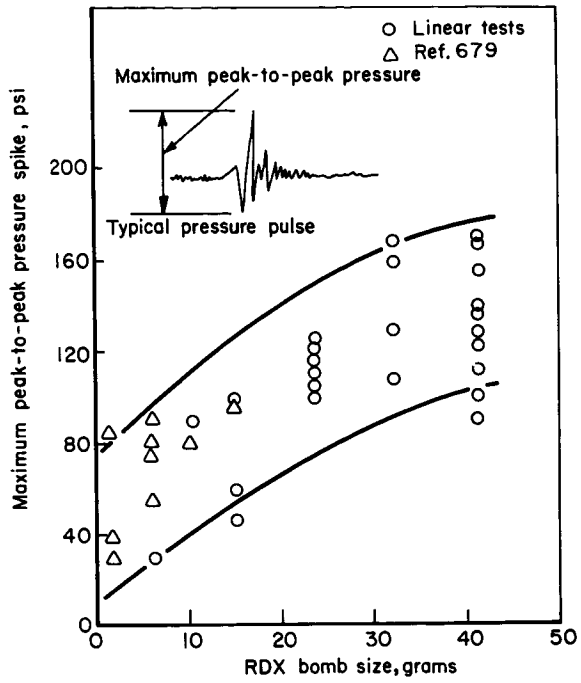

FIGURE 10.3.3a.—Pressure spike amplitudes produced by bomb ring blasts in storable engine firings.

to the injector face where axial and circumferential variations in local fuel and oxidizer concentrations are prevalent (especially in like-on-like designs). Under these conditions wave enhancement effects may prove quite complex.* In general enhancement effects are extremely significant and must be taken into account for all stability rating techniques.

In high chamber pressure rating experiments[7] it has been observed that with combustion taking place in the engine the initial shock wave propagates hemispherically from the exit of the gun barrel, but the amplitude of the wave is not constant over the hemispherical surface. That is, it has been found that the observed peak pressure of the initial shock wave is greatest at a point directly in line with the center line of the gun barrel and decreases proportionally in all directions. Some general observations that have been made are

* In Refs. 149, 618 and 704 such enhancement coupled with disturbances initiated by stream fluctuations is postulated as the responsible mechanism for popping.

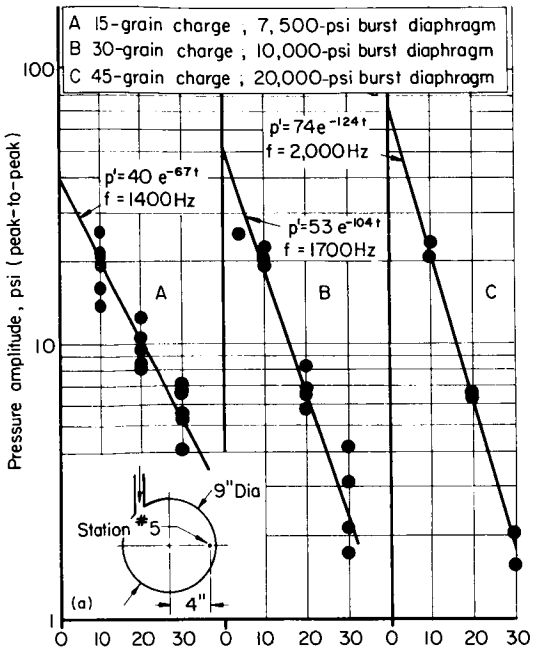

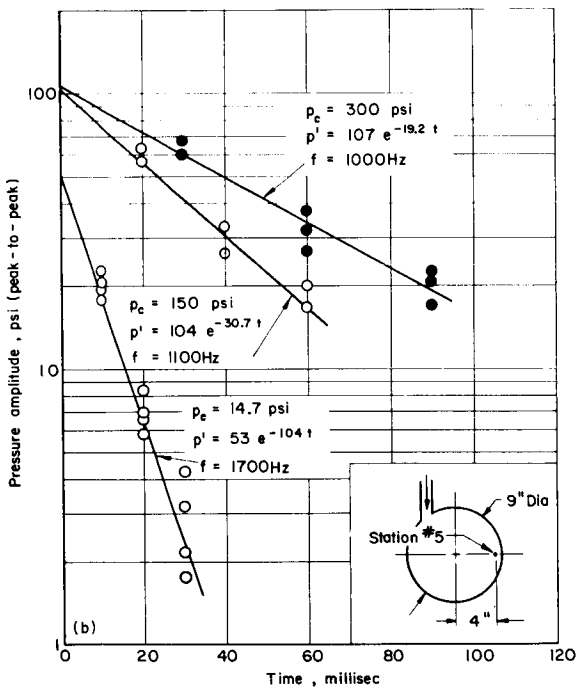

(a) Effect of variation in charge weight and burst diaphragm combinations.

(b) Effect of variation in initial chamber pressure (with 30-grain powder charges and 10,000-psi burst diaphragms).

FIGURE 10.3.3b.—Pressure amplitude time history of first tangential spinning wave produced by pulses introduced into a nitrogen-filled, 9-inch-diameter, cylindrical chamber at 1 atmosphere.

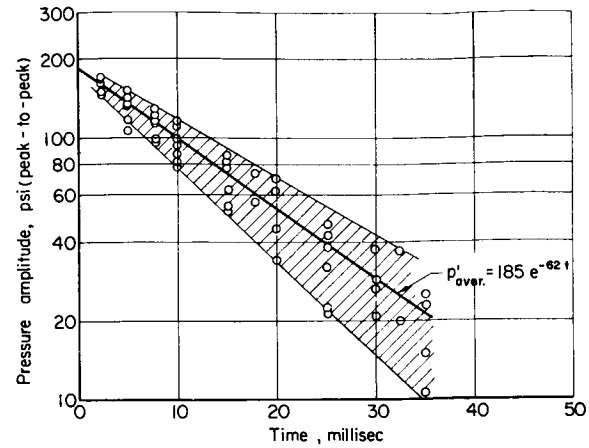

FIGURE 10.3.3c.—Pressure amplitude versus time for a number of 30-grain charges using the 10,000-lb burst disks in the stable, high mixture ratio range ($r \sim 2.0$).

(a) The perturbation amplitude decreases with increasing combustor size.

(b) The dimensionless perturbation amplitude (peak amplitude divided by steady-state chamber pressure) is approximately constant for a given charge size for chamber pressures below about 1000 psia.

(c) The perturbation amplitude is independent of the steady-state chamber pressure for pressures above approximately 1000 psia.

(d) The observed perturbation amplitude decreases with increasing coarseness of the injector pattern.

Tests have been conducted for direct comparison of transducer-measured pressure amplitude data with predictions of the shock expansion theory described in Sect. 10.3.2.[163,167] A liquid rocket combustor (11.4-inch diameter, N_2O_4/A-50, 150 psia, F = 10,500 lbf) was pulsed with a radially-oriented pulse gun (Fig. 10.3.1b) during firings with two injectors. One injector had an unlike triplet pattern while the other had a relatively slow-burning fuel showerhead, oxidizer doublet pattern designed for gelled fuel application (gel injector). Three flush-mounted Photocon pressure transducers were located near the pulse gun muzzle; their centers were 15, 30, and 45 degrees, respectively, from the gun's axis.

Values of the average pressure along the wave front divided by the initial steady-state pressure

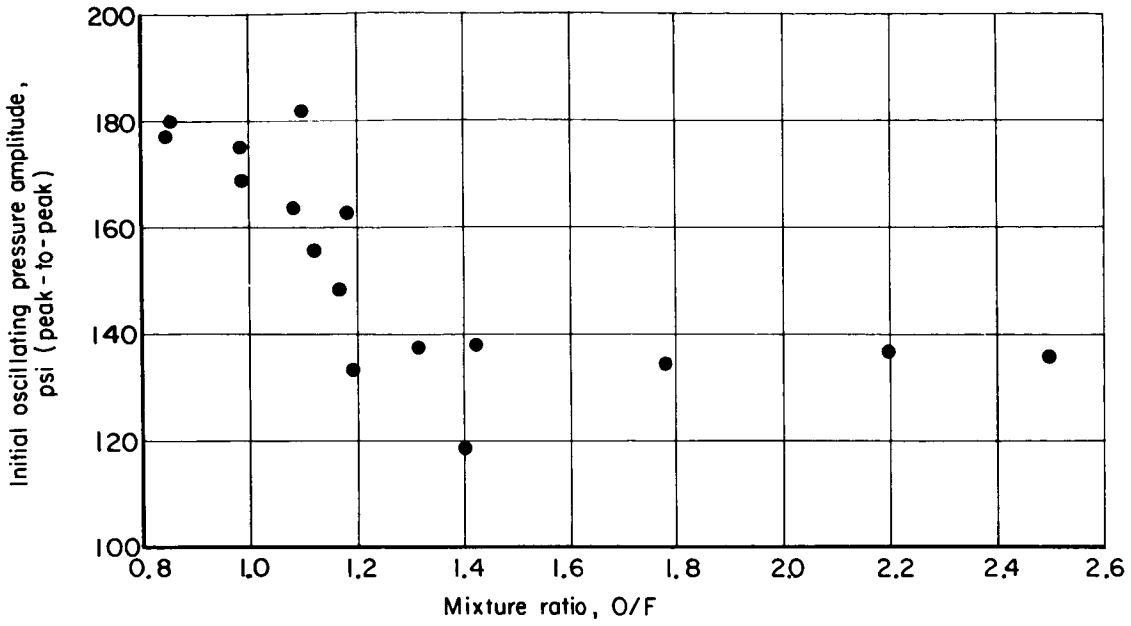

FIGURE 10.3.3d.—Variation of initial pressure amplitude of the spinning first tangential mode with mixture ratio when pulses are fired into an oxygen-alcohol rocket motor (45-grain powder charges and 20,000-psi burst diaphragms).

(p_{ms}/p_1) were calculated directly from the hot-firing data by use of the Kuluva method.[167] The effective distances, x_0, from the points of measurement on the wave front to the pulse gun exit along the axis $\theta=0$ were obtained from geometrical considerations. Comparisons between the semi-analytical predictions and the hot-firing data are shown in Fig. 10.3.3e for the radial pulse guns with both injectors using RDX high-explosive charges (little difference was seen between the HB and RDX explosives). It is evident that there is almost no comparison between the cold-flow results and the experimental hot firings. The presence of rapidly occurring combustion reinforcement of the shock wave in the chamber is most pronounced, especially in the case of the gel injector. In general, it appears that the initial shock wave, as it enters the chamber, is attenuated much more rapidly than is predicted by the semianalytical correlation. A suggested mechanism for this effect is rapid conversion of shock overpressure momentum to propellant spray momentum. A curious observation is that, with the triplet injector, shocks from charges of 10 to 80 grains were attenuated to about the same amplitudes before combustion augmentation became effective. This may be an indication that droplet disintegration is a tremendous momentum sink. Before the waves have propagated more than about 2 inches (effective) into the chamber, combustion reinforcement controls the response.

The combustor, propellants and operating conditions for the triplet tests were the same as those bomb test results that were discussed in Sect. 10.2.2.4. There the scaled-blast correlation appeared to be valid for about 4 to 5 inches from bombs before combustion-augmented amplification was experienced. The apparent disparity of an ideal gas correlation being valid for bombs, but not for pulse guns, is related to the disturbance locations. The centers of the bomb charges were 4 to 5 inches from the injector, whereas the pulse guns were only 2 inches from the injector. Although comparable tests were not made, it is expected that pulse gun disturbances introduced further downstream would behave as predicted. Rigorous, detailed analyses of the pressure wave interaction with the sprays and combustion processes could give improved predictions but fully developed models are not now available.

The ordering of the data points in Fig. 10.3.3e suggests that the wave penetration distance,

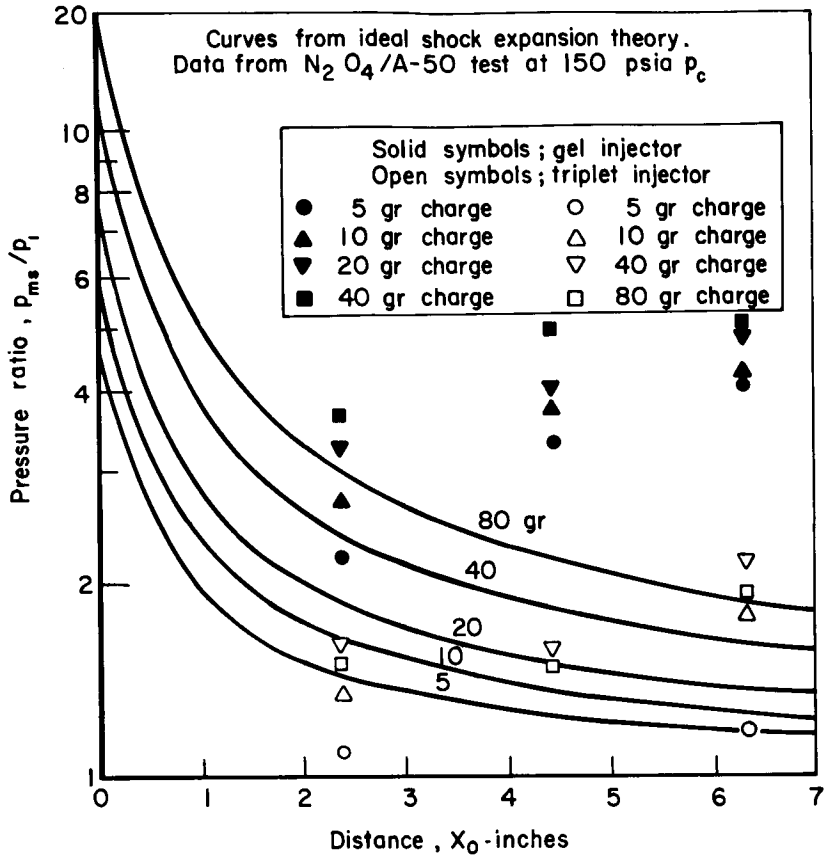

FIGURE 10.3.3e.—Pressure ratio versus distance for spherical expansion of a pulse gun shock–comparison between theoretical predictions and hot firings with RDX explosive.

before reinforcement became effective, was appreciably shorter for the gel injector than for the triplet. Furthermore, with the gel injector, the attenuation apparently did not persist long enough to accomplish as much degradation of the higher amplitude shocks as occurred with the triplet.

10.3.4 Application to Combustors

There are several design and operational features of pulse guns which have made their application popular as a stability rating device. Among these are the ability to utilize more than one pulse on a single test firing, easy access for reloading between firings, no obstruction to the gas flow characteristics within the engine, and reduced hazard of shrapnel damage. Since the pulse gun is mounted on the outside of the combustion chamber with only an access hole for the barrel, more than one gun can generally be mounted on the chamber. As many as five pulse guns have been successfully employed on an eight-inch-diameter chamber to produce multiple perturbations in graduated charge sizes during a single firing.

Along with the operational advantages of pulse guns listed above is the disadvantage that they normally cannot be used with prototype combustion chambers. As discussed in Sect. 9.2.1 it is often necessary to perform final stability evaluation tests in an actual prototype engine. This can often be done by mounting an explosive bomb from the injector but it cannot be done with a pulse gun.

The barrel of a pulse gun is threaded near the exit end and equipped with an O-ring or crush seal

to permit mounting in an adapter on the combustion chamber wall. Only sufficient barrel length is provided to permit access to the breech while the gun is mounted on the chamber. The chamber adapter is normally designed such that the gun barrel, when mounted, is directed either tangentially or radially into the combustion chamber.

The radially-oriented pulse gun has been used as a stability rating device during some development programs but it has been found to offer no advantages over the tangentially-oriented pulse gun. Because of the similarity between the results obtained by either orientation and the greater quantity of experience gathered with the tangentially-oriented gun, the radial gun appears to be losing popularity. For this reason the following discussion of the application of pulse guns will be directed toward the tangential pulse gun but much of the discussion is applicable to either.

The tangentially-oriented pulse gun has a tendency to excite the first tangential spinning mode of resonant instability. However, all of the basic types of resonant and feed system coupled instabilities have been excited in this manner. The predisposition for the first transverse spinning mode can be explained by the characteristics of the pulse gun as discussed in Sect. 10.3.2.3.

The initial shock wave is reflected from the chamber walls and injector at varying times and angles, resulting in multiple, reflected waves being propagated through the cavity. As the propellant sprays stored in the chamber are then burned at a higher rate, a rise in the mean chamber pressure occurs. This pressure rise is sufficiently prolonged to affect the flow through the injector orifices and thus may initiate a low frequency oscillation. It has been observed that this complex mixture of high and low frequency oscillations can excite any mode of instability to which the engine is susceptible.

If the engine has a high stability margin for the first tangential mode but a low margin for the first longitudinal mode, for example, the pressure traces from the test will typically record a few cycles of a clearly-defined first transverse spinning mode superimposed on a complex mixture of low and high frequency oscillations. This tangential mode will be spinning in the direction the gun was aimed and will be rapidly attenuated. At the same time, a first longitudinal oscillation will begin to emerge from the remainder of the decaying oscillations. With time, this longitudinal mode instability will grow to some limit cycle amplitude which will persist throughout the duration of the test.

The use of multiple pulse guns permits perturbing the combustion process at different locations or with different charge sizes during the same test. The normal procedure is to time the actuation of the various pulses to permit at least a 100-millisecond interval for the combustion process to return to normal or for an instability to develop fully prior to a subsequent perturbation.

Although both the bomb ring and machine-gun rating techniques have been easily adapted to research-type combustors, some doubt exists in adapting such devices to flight-type engines. Due to the inherent design of such engines, i.e., chamber geometry, strength of materials, regenerative cooling, etc., the placement of a heavy, multiport ring around the thrust chamber may be impossible. In this respect, the single-port injection used with the machine gun would be more easily adopted. Besides the previously mentioned advantages of the machine gun in regard to the measurement of quantitative data (Sect. 10.3.3), this technique is more economical to operate while providing finer charge graduations. Down time between runs would also be shortened, since the link belt contains enough cartridges for several runs.

The pulse gun is commonly used on rocket engine development programs as a stability rating device. It is also widely used on applied research and technology programs to initiate instabilities and to obtain a measure of instability damping characteristics. Recently, when it has been used on engine development programs it has been used in conjunction with the explosive bomb. On a typical development program two or more tangential pulse guns would be used in conjunction with a single explosive bomb on all heat sink chamber pulse tests to screen various injector design variations. The pulse gun perturbations may be actuated either before or after the explosive bomb. This technique provides a wider variety and greater quantity of perturbation data on the candidate injectors than with the bomb alone in the same number of tests. This procedure provides

a higher probability of success when the one or two best injectors are selected for testing with prototype chambers where only the explosive bomb can be used.

For either development or applied research testing the tangential pulse guns are typically mounted on a heat-sink combustion chamber in a single axial plane approximately two inches downstream from the injector face. Although referred to as a tangential pulse gun, the barrel is not typically directed tangent to the inside surface of the combustor wall.* Rather it is normally directed tangent to an imaginary circle typically two inches inside the chamber wall. If the chamber is sufficiently large to accommodate the desired number of pulse guns and high frequency pressure transducers in the same axial plane, it is desirable to do so. This will provide the most accurate measure of the perturbation characteristics introduced by the pulse. If this is not practical, several transducers are placed circumferentially in a plane as close to the pulse gun plane as possible. Also, additional transducers are desirable at various longitudinal locations to permit resonant instability mode identification. A more detailed discussion of the mounting of transducers and interpretation of test data is found in Chapter 9.

It should be noted that although the pulse gun charge is located external to the combustor, the time of actuation must be reasonably early in a test. Depending upon the operating pressures and temperatures of the engine the actuation may be as late as five to seven seconds after ignition. If actuation is delayed too long radiant and conductive heat effects may deteriorate the explosive charge.

A word of caution should be given when using pulse guns, particularly multi-gun arrangements. Since there is a definite cavity volume involved even prior to firing, and an even greater volume after firing, these volumes may aid damping. This is important to keep in mind for marginal systems (see Sect. 10.7.2.6).

10.4 DIRECTED GAS FLOWS†

The injection of directed flows of gases into the propellant spray combustion region has sometimes been found to be an effective means of initiating acoustic instabilities in rocket combustion chambers. Stability rating with this method consists of measuring some characteristic parameter associated with the flow, such as the gas stream weight flowrate or momentum flux at the instant of onset of the instability. Directed gas flows are not as widely used as bombs and pulse guns, principally because not all combustion systems are susceptible to instability triggering by them, they are less directly associable with natural instability triggers, and a moderately extensive gas supply facility is required. In situations to which it is applicable, however, this technique has some very strong advantages in minimization of test requirements and in reproducibility.

Inert gases (nitrogen and helium) have been used most often, in which case the directed gas flow apparently provides primarily a displacement and velocity disturbance. The technique must then affect the velocity-sensitive combustion mechanisms of atomization, spray mixing and spray evaporation. In general, the mechanisms whereby a finite amplitude pressure wave results from displacement disturbance of steady-state combustion are not understood at present. High-speed motion photography of inert gas flows disturbing LOX/ethanol combustion[424] sometimes showed very appreciable displacement of the propellant sprays for relatively long times before any pressure wave growth was evident (if it ever occurred) and, at other times, showed no apparent effects prior to an abrupt onset of instability. Some limited investigations using both oxidizer and fuel gases[161] have shown that reactive gases may give different ratings than inert gases.

10.4.1 Typical Designs

Several types of gas flow control systems have been used. Each contains elements for limiting the magnitude of the maximum flowrate (e.g. source pressure regulation) and for controlling the rate of variation of flowrate (e.g. a flow control valve). The simplest method of control provides for rapid activation of a simple shutoff valve to effect a more or less impulsive establishment of a constant flowrate. In an extreme application, the valve may be opened rapidly enough that a weak shock wave attends the onset of gas injection into

* This is the chordal orientation of Fig. 10.4.2b.

† L. P. Combs and M. F. Heidmann, Authors.

the combustor. This constant flow approach provides a single data point for each rocket engine firing so that multiple firings and staircase testing techniques are required.

A more productive flow control approach uses slow actuation of a linear or proportioning flow control valve, so that the gas flowrate increases gradually in a well-controlled and reproducible manner. Most often, linear variation of flowrate with time has been sought but the controls may be tailored to give a desired variation of some other parameter, e.g., linear variation of momentum flux with time has been used.[540] In this way, a wide range of an appropriate flow parameter may be covered in a single engine test. If the variations are slow enough, the magnitude of the flow parameter at the instant of instability initiation provides a direct quantitative indication of relative stability. Potentially, a stability rating may be obtained from each test firing in which an instability is initiated.

A schematic diagram of a gas flow supply system reported in Ref. 163 is shown in Figure 10.4.1. The flow valve is instrumented with a linear motion transducer for sensing valve stem position which is the primary control variable. Preprogrammed control of the gas flowrate is accomplished by scheduling the desired valve position as a function of time. Here, a servosystem is used to compare the actual valve position with the desired position and drive the valve stem in the proper direction to reduce the difference between them. This method of control requires a prior calibration of gas flowrate versus valve position. Full servo control, based on measured gas flowrate, has also been used.[163]

Other typical gas supply systems for stability rating have differed from this one in respect to (1) scale (the size of lines used, surge volumes and magnitude of flowrate) (2) metering system (some have used venturi meters), (3) valve design and actuation (butterfly valves, plug valves with various opening versus travel characteristics, quick opening and linear travel rates), and (4) connecting tube design, as discussed in the next section.

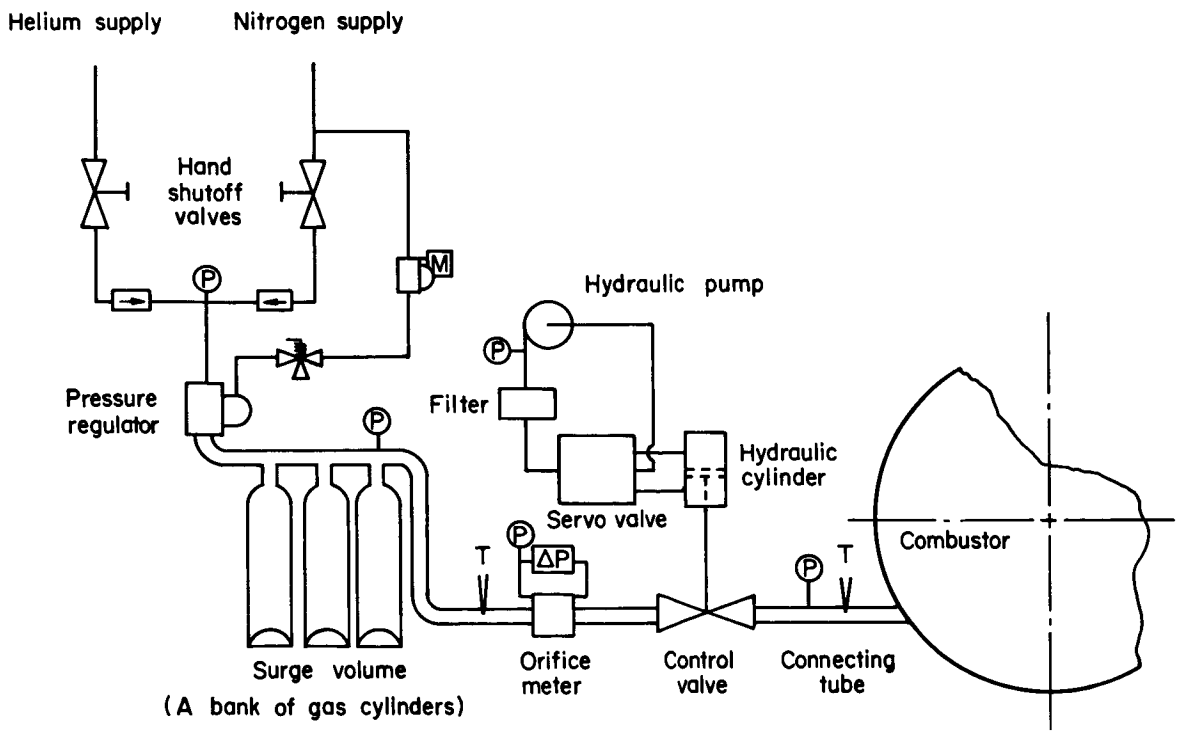

FIGURE 10.4.1.—Supply system for directed gas flows.

10.4.2 Effects of Design Variables

Many gas flow system design variables, e.g., supply pressure, supply volume, line sizes, system pressure drop and surge volume, do not ordinarily affect the stability ratings directly, but only indirectly as reflected by their effects on the maximum attainable gas flowrates and the permissible rates of change of flowrates.

A major effective design variable is the choice of an impulsively initiated constant flowrate or a slowly and continuously varying flowrate. It has been noted that the former approach requires multiple tests to attain a single rating and so is at a relative disadvantage. With that approach, however, variations of connecting tube diameter and pulse gas resulted in ratings which indicated that the effective rating flow parameter is the pulse gas momentum flux ($\dot{w}V/g_c$) entering the combustor.[161] The continuously varying flows have sometimes failed to corroborate this indication or to delineate any other fundamental correlating parameter.[540,161]

Another effect observed with constant flowrate rating tests is that a highly variable time delay from initiation of the gas flow to actual onset of instability almost invariably occurs* even though the gas flow magnitudes required to initiate instability are quite reproducible. It has been suggested that this may be the result of a distribution in time of the combustion processes' sensitivity to disturbances, with the most sensitive conditions occurring relatively infrequently. Then the constant gas flow rating might correspond with the highest value of sensitivity which occurred as frequently as the time duration of the pulse; the next occurrence of a sensitivity of that magnitude or higher might take place soon after the flow is started or much later.[161]

It is conceivable, then, that the appearance of instability with a constant varying gas flow disturbance is really the result of an earlier flow than that metered at the time of initiation.[540] If the rate of change of flowrate is small, the metered flow at the instant of initiation will be only slightly greater than the earlier, effective flowrate. A determination of how rapidly the flowrate may be varied without influencing the rating should probably be included in each engine application of this rating method.*

The connecting tube design can also affect the rating results greatly. Increasing the diameter of a cylindrical tube requires higher gas flowrates. For impulsively started, constant flowrate gas flows, the effect may be approximated, as noted earlier, by assuming constant momentum flux. For continuously varying flows, it has been found that tube diameter and shape effects may be approximated roughly by[9]

$$\left(\frac{\dot{w}_{gas}}{A_{ct}}\right)_1 = \left(\frac{\dot{w}_{gas}}{A_{ct}}\right)_2 \qquad (10.4\text{–}1)$$

Connecting tubes with rectangular cross-sections may provide more valid ratings than circular cylindrical tubes with comparable cross-sectional area, particularly if the combustion field contains a discrete position of maximum sensitivity. It has been found that a connecting tube having a long rectangular slot spanning the zone of maximum sensitivity produces ratings which compare well with those from small (less than 0.5-inch diameter) circular cylindrical connecting tubes located at the point of greatest sensitivity.[386] An example is shown schematically in Fig. 10.4.2a for a number of ratings obtained with a particular injector and fixed operating conditions (the throat of the exhaust nozzle was 28 inches from the injector). When rating different injectors, whose zones of maximum sensitivity may lie at different distances from their faces, a rectangular slot connecting tube should be much preferred to any which affect only a small local region.

The connecting tubes are customarily oriented with their axes contained in a plane normal to the combustor's axis. For cylindrical or annular combustion chambers, a tangential or chordal entry direction is usually preferred (Fig. 10.4.2b); enhanced sensitivity to initiation of spinning or

* An exception was noted in gas flow ratings of the Redstone engine. In those tests which experienced instability, it was initiated within 10 milliseconds of the pulse entry into the combustor. This apparently was caused by the control valve opening so fast that the flow initiation coalesced into a shock wave within the connecting tube.[160]

* In an extensive series of rating tests,[9] a linear ramp flowrate of nitrogen was injected into a 150,000 lb thrust combustor through a 0.50-inch diameter connecting tube with ramp slopes of 6 ± 1 lb/sec^2. For one set of conditions, doubling the slope did not alter the rating obtained.

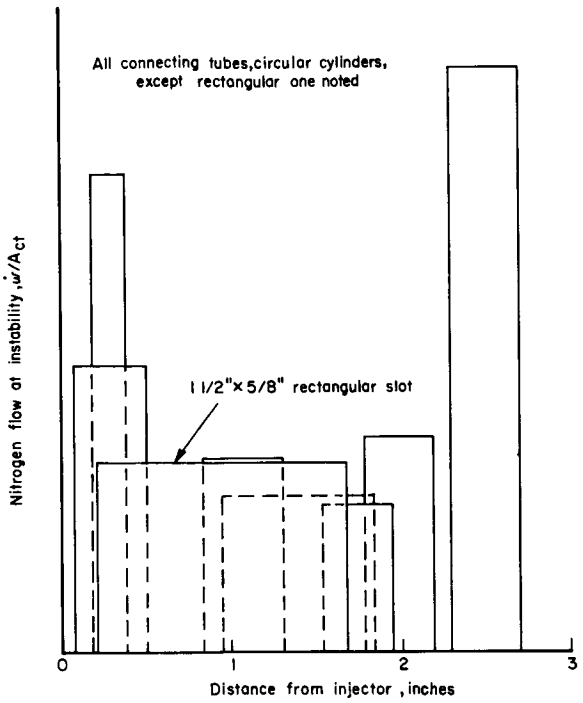

FIGURE 10.4.2a.—Comparison of stability rating for various connecting tube cross-sections.

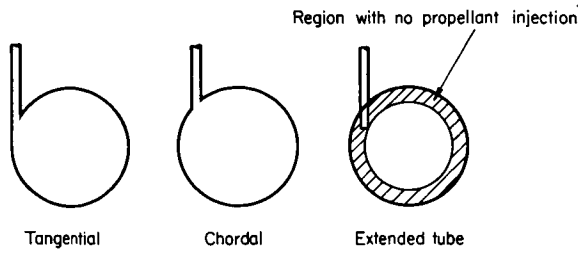

FIGURE 10.4.2b.—Typical gas flow connecting tube orientations.

traveling tangential modes is expected. In some cases, tangential orientation has been found to give more reproducible ratings than radial orientation. In some applications where there has been an appreciable injection-free space between the chamber wall and the nearest propellant injection, the connecting tube has been extended into the combustion chamber (Fig. 10.4.2b). Greater sensitivity (or lower required flowrates) resulted, but the ratings were extremely sensitive to erosion or distortion of the extension; unless damage can be completely prevented, this approach should not be used.

10.4.3 Applications

A majority of applications for directed gas flow stability rating that can be cited were conducted several years ago and primarily with liquid oxygen/hydrocarbon propellant combinations. In addition to research-scale barrel and two-dimensional combustors, full-scale engine evaluations have been obtained or attempted on Redstone,[160] Atlas-type 150K,[9] X-15[457] and Transtage[729] engines. Comparative ratings have been obtained with varied components (injectors and chamber contraction ratios), operating conditions (mixture ratio and chamber pressure), and propellant combinations. Gas species used have included nitrogen, helium, oxygen and methane.

Directed gas flowrating was used to evaluate the stability of seventeen different hydrocarbon fuels in a barrel combustion chamber–a large diameter, low thrust combustor having propellant injection concentrated along a circle of about $\frac{3}{4}$ the chamber radius. Individual propellant stability ratings varied over a range of about 6:1 in flowrate. However, when some of these propellants were rated by the same technique in a two-dimensional research combustor and in a 150,000 lb thrust engine, no differences among them were found in either engine.[425]

When gas flows of nitrogen, methane and oxygen were used to rate the stability of LOX/ethanol propellants, considerably lower flowrates of oxygen were required to initiate instability than of either nitrogen or methane. That observation was interpreted as supporting a displacement mechanism of sustaining instability,[76] wherein displacement of mostly vaporized oxygen spray into fuel sprays results in considerably greater transient energy release than does displacement of fuel spray into an oxygen rich region (see Sect. 3.3).

Experimental rating data on 150,000 lb thrust combustors led, in 1961, to a hypothesis that the steady-state combustion rate in the neighborhood of the injector is limited by interspray propellant mixing rates. Gas flowratings were taken as indications of how relatively easy or difficult it is to accomplish additional forced transient mixing. A geometric representation of the interspray mixing was formulated, and all parameters thought to influence that mixing were tabulated.

An empirical evaluation of influence coefficients was conducted, and a single stability factor was defined that proved to be capable of correlating gas flowrating data (Fig. 10.4.3a).[386] Stability ratings having a range of about four to one are seen to be quite well correlated. While this correlation approach was considered to be successful, it was developed at the same time that combustion chamber baffles were found to offer the possibility of achieving dynamic stability. As a result, this approach has not been carried to the point of predicting the stability of other unbaffled injector designs and extending the range of correlation.

Directed gas flows have recently been found to be ineffective for initiation of instability with N_2O_4/A-50 propellants in full-scale engines.[163,729] Photographic evidence of strong transverse flow displacements and formation of a large circulating eddy near the injector with no attendant chamber pressure disturbances indicate that combustion of this propellant combination is insensitive to "steady" transverse flow velocity effects.

A tangentially directed gas flow has been successful in two-dimensional circular combustor experiments.* The configuration is shown in Fig. 10.4.3b. The gas, usually nitrogen, was injected from a tangentially aligned orifice at the circumference of the combustor. Both steady and ramping flowrates were injected in amounts up to about 20 percent of the total propellant flow rate. For each design or operating condition, a threshold flowrate could be established above which the combustor exhibited traveling transverse mode instability. Pressure amplitude varied with flowrate above this threshold value in the region of linear instability. Above a certain amplitude and flowrate the instability for some propellant combinations became independent of the tangential gas injection indicating a nonlinear stability limit. The flowrates establishing these linear and nonlinear limits were used as indices of the degree of stability.

With tangential gas flowrating of research combustors, the parameters affecting the tangential momentum of the gas jet appeared important.[334] Jet area, total pressure, gas density and alignment angle affected the stability limit flowrates inversely to the effect of such variables on the tangential momentum of the gas jet.

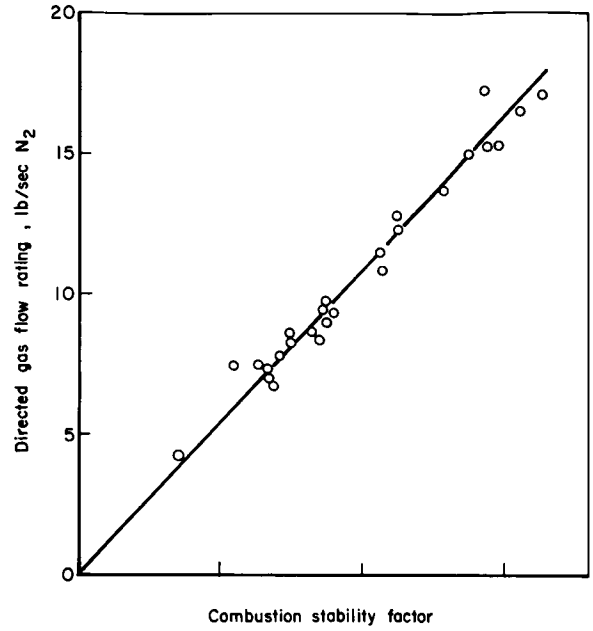

FIGURE 10.4.3a.—Gas flow stability rating correlated to stability factor calculated from mixing considerations.

A stability rating with tangential gas flows for a range in total propellant flowrates[338] is shown in Fig. 10.4.3c. This rating was obtained using gaseous hydrogen and liquid oxygen as propellants in the research combustor shown in Fig. 10.4.3b. The rating can be interpreted in various ways. For constant total propellant flowrates, stability is shown to improve at both very high and very low mixture ratios. A mixture ratio for minimum stability exists for any value of total flowrate.

Tangential flowrating was also used to evaluate the effectiveness of particulate damping on the stability of this combustor at a fixed value of propellant flowrates.[342] In these tests the tangentially injected gas, containing a constant mass fraction of aluminum particles, was ramped to relatively large values. Such increases in gas flow increased the fraction of aluminum particles in the combustion gases and affected the amplitude of pressure oscillations as shown by the solid line in Fig. 10.4.3d. The dashed lines represent an interpretation of this effect. The slope of the dashed lines was predetermined in tests without

* A pancake-shaped combustor see Refs. 337, 335, 334, 338, 342.

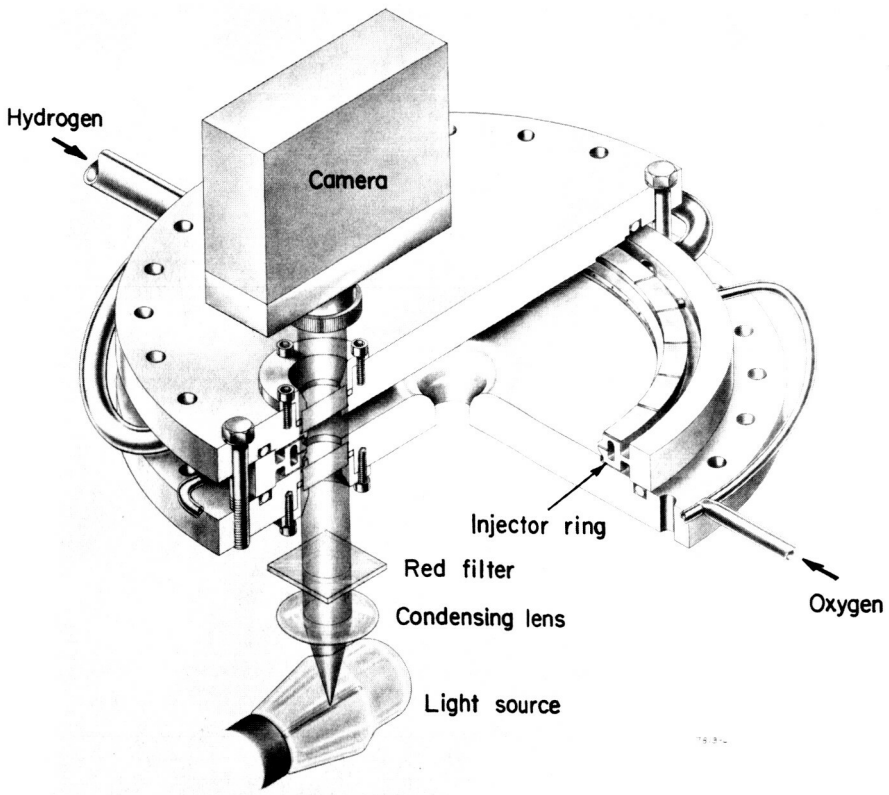

FIGURE 10.4.3b.—Two dimensional circular combustor and photographic arrangement.

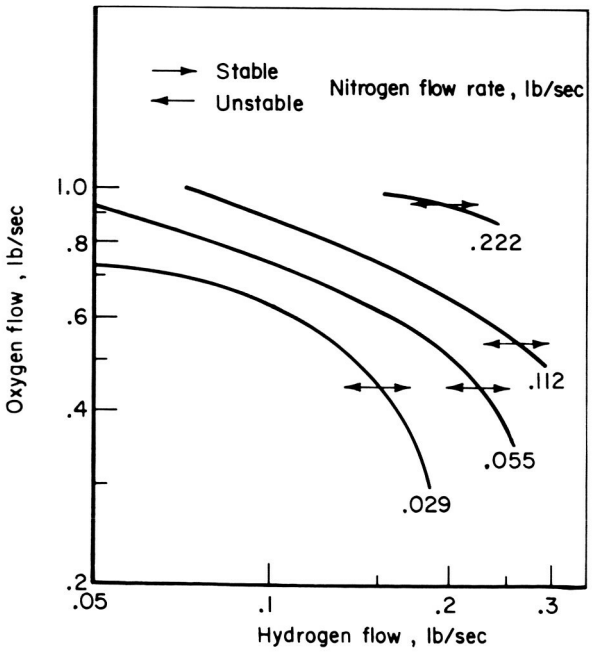

FIGURE 10.4.3c.—Stability boundaries in two-dimensional circular combustor.

aluminum addition. Assuming this slope is maintained for constant fractions of aluminum addition, as was done in constructing Fig. 10.4.3d, particulate damping is shown to be effective in improving linear stability limits.

10.5 FEED SYSTEM PERTURBATION*

Stability rating by introduction of disturbances directly into the combustion chamber has been discussed in the preceding three sections. A different stability rating technique, indirect disruption of the propellant combustion processes by perturbing one of the propellant feed systems, is the subject of this section.

As noted in Sect. 10.1.2.2, feed system perturbations are sometimes capable of initiating the combustion chamber acoustic modes of instability but are primarily of interest for evaluating stability to the low and intermediate frequency,

* D. Fairchild and J. Vincent, Authors.

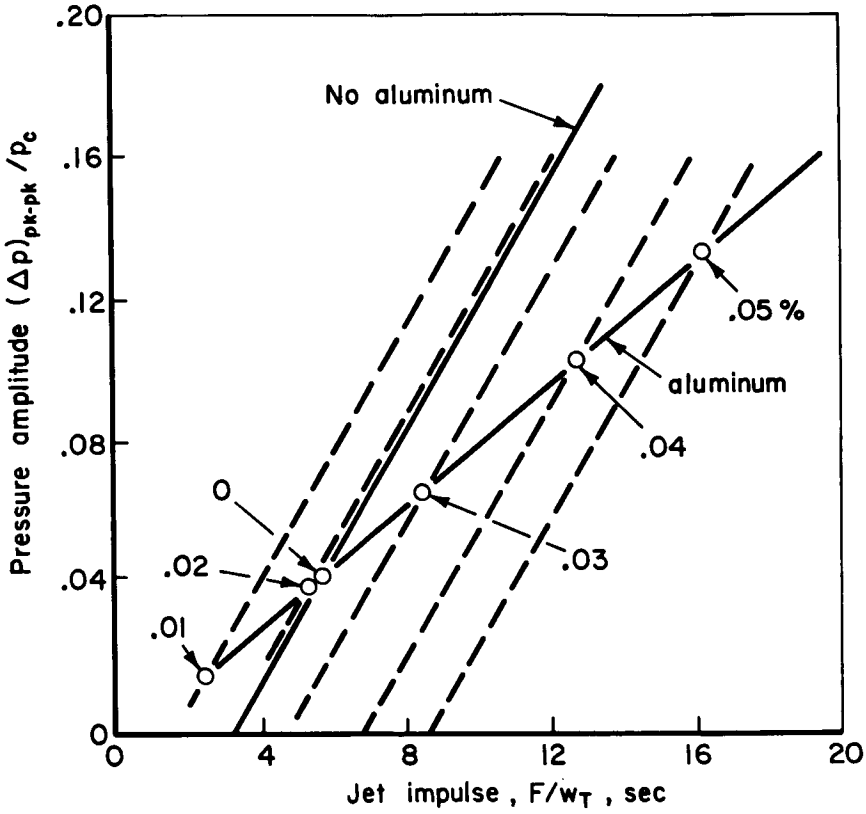

FIGURE 10.4.3d.—Indicated stability rating for aluminum addition.

feed-system coupled modes. Two distinctly different approaches have been used: pulsers, to provide single, short duration pressure pulses of moderate to very high amplitude; and sirens, to provide continuous feed system pressure oscillations of only moderate amplitudes. Ideally, the output of the pulser approaches a unit impulse or Dirac delta function, which is capable of exciting all frequencies, so that any inherent instability can conceivably be initiated by a single pulse. The output of the siren, on the other hand, is often nearly sinusoidal so that excitation is limited to a fairly narrow frequency band near the siren's operating frequency (and, of course, to harmonic multiples). Thus, in principle, the siren is best suited for evaluating stability of a particular known mode while the pulser may more readily reveal whether any mode of instability is likely to be encountered.

Whether or not meaningful results are obtained with either device depends critically upon its being positioned properly to achieve sufficiently large injection rate (and, as a result, burning rate) fluctuations. Design and installation must be engineered carefully to avoid gross attenuation of pressure disturbances before they reach the injection orifices. Such attenuation can result from locating the device far from the injector (or upstream of propellant valves, filter, etc.), from having high feed system capacitance (e.g., flexible manifolds, expansion joints or trapped gas pockets) or from tortuous injector passages.

10.5.1 Siren (Continuous Oscillations)

Several siren designs have been used.[605,182,469,15] One design approach is the sinusoidal displacement of a piston in the wall of a propellant line. This has been used in model motor firing experiments[182] for measuring the combustion time delay and interaction index as functions of frequency. With bi-propellant combustion, both the fuel and oxidizer systems were perturbed simultaneously with mechanically-coupled piston displacements.

Another design approach is the intermittent release of a quantity of propellant from a feed-system by installing a siren in a bleedoff line. Extensive stability rating experiments[605] employed a siren integrally designed around a section of feed line with a rotating cylindrical sleeve alternately opening and closing perforations in the feed line wall. Experimental results from tests with the siren in either the fuel or oxidizer system gave quantitative pressure oscillation amplitude and phase relationships throughout a research-scale combustor system. A more recent series of tests[15] using a siren for bleedoff oscillations is the subject of the remaining discussion of sirens.

The siren was designed to vary the bleedoff flows from 0 to 20 lb/sec by opening and closing two diametrically opposed inlet slots. A rotor with 20 slot openings matching the inlet slots is supported on two sets of matched radial ball bearings and is rotated inside the siren housing by a motor-driven protruding shaft, Fig. 10.5.1. Variances in average bleedoff flows are accomplished by adjusting the gate position to vary the slot area.

The siren was developed to explore the sensitivity of the combustion process to continuous feed-system disturbances, and to determine the dynamic response characteristics of the feed systems. Designed for use with nitrogen tetroxide, the siren was evaluated in the laboratory with water. For example, while 169 lb/sec of water was flowed through a pressure-instrumented, calibrated line, the rotor was driven at 600 RPM to achieve an oscillation frequency of 200 Hz. Amplitudes in excess of 200 psi peak-to-peak were experienced with a fairly sinusoidal wave shape. The physical vibration of the siren was excessive, however, and structural failure resulted in a weld on one of the inlet elbows. No further testing has been attempted.

The chosen bleedoff siren concept is completely feasible as a feed system continuous pulse method.

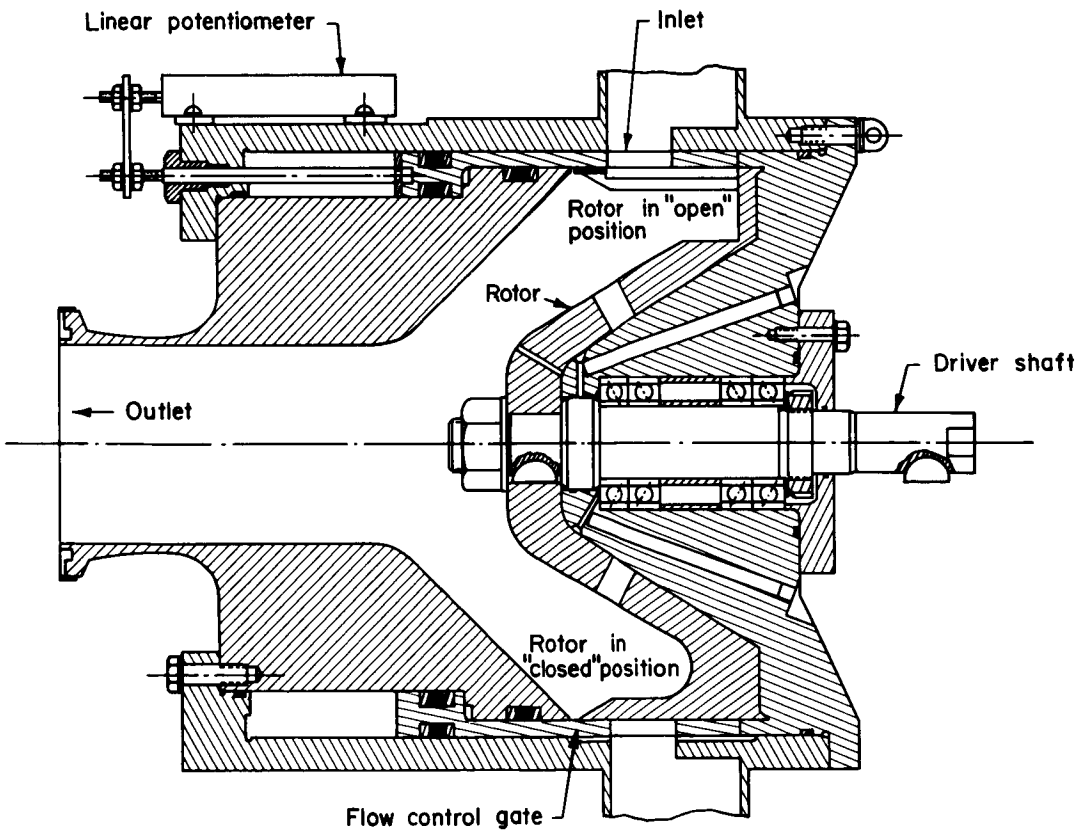

FIGURE 10.5.1.—Cross-section of siren for continuous perturbation of propellant feed system.

The cyclic pressure amplitude can be adjusted to meet a typical test requirement (e.g. exceed 25 psi) yet avoid excessive vibration loads at high amplitudes. The adjustment can be made by removing part of the obstruction that prevents a tangential flow direction between the rotor and the housing to the adjacent slots in the rotor when the rotor is in a "closed" position. With this alteration, flow is never fully obstructed, only the direction of the flow is varied.

10.5.2 Pulser (Single Pulse Generator)

A classical method of determining the dynamic characteristics of a linear system is to measure its response to an impulse which, in principle, excites equally all frequencies of the system under test.

In practice, of course, unit impulse functions cannot be obtained. If, however, a pulse function (finite amplitude and rise time) can be generated which has the same amplitude and phase characteristics as the impulse function in a limited frequency band, then the two functions are identical in that band.

To produce a steep-fronted, high-energy pressure wave in the propellant feed system of a rocket engine, the impact of a high-velocity "hammer" upon an "anvil" piston (in contact with the propellant) is used. By proper adjustment of the mass ratio between hammer and piston, a velocity amplification can be transmitted to the piston which results in greater pulse amplitudes than would be achieved from using only the hammer portion of the device. Pulse characteristics can be adjusted with appropriate design of the apparatus. Two designs are described below, one using explosive actuation[712] and another using gas pressure actuation.[15] The explosive pulser is illustrated in Fig. 10.5.2a. In the explosive design, shear pins of different materials, employed to retain the hammer until predetermined driving pressures are reached, provide a means of altering pulse amplitudes. Piston travel is varied by using spacers of selected sizes which control the duration of the generated pulse. Its method of operation is (1) an explosive charge mounted in the hammer housing cover plate (and contained within the hammer cavity) is ignited by an electrical signal; (2) when the burning charge generates sufficient pressure, the hammer-holding pins fail, permitting the hammer to be driven along the cylinder; (3) before contacting the stop, the hammer strikes the piston which has been positioned for the collision by system back pressure; (4) following the momentum exchange, the piston travels through a stroke adjustable from 0.100 to 0.200 inch before wedging into the piston housing; (5) the resulting compression of the liquid generates a high-energy, short-duration pressure pulse.

The explosive pulse generator was designed with the intent of rating the stability of a 165,000-pound thrust engine with a nominal chamber pressure of 600 psi.[712] The engine, at that time, utilized an injector configuration which was not dynamically stable (conclusively demonstrated during an extensive bomb test program). Chamber baffles were successful in suppressing the acoustic modes of the engine when bombed; however, a mode in the 200 cps region was consistently triggered. The propellants for that engine were liquid oxygen and RP-1. Program objectives were to demonstrate that a pressure pulse in the feed system would induce the same instability observed in the bomb test series, and to determine the optimum pulse input location. During the course of the test program, three pulser locations were evaluated: (1) tangential entry into the fuel injection manifold, (2) radial entry into the fuel injection manifold, and (3) on the oxidizer dome (manifold). The 200 Hz mode of instability was successfully triggered repeatedly by pressure pulses in the fuel injection manifold. Peak amplitudes of the pulses were varied between 10,000 and 15,000 psi when measured at the interface between the pulser and the fuel injection manifold. Pulses of less than 10,000 psi did not result in sustained instability. Rise times for these pulses averaged approximately 70 microseconds and total durations were 150 to 200 microseconds. Some differences were observed between the tangential and radial pulser locations. Both positions were used to induce instability; however, the tangential location often resulted in a stronger chamber pressure disturbance than did the radial position. The radial position failed on one occasion to generate a measurable disturbance when the injector was inadvertently rotated during assembly such that a chamber baffle was aligned with the pulser. The absence of a direct path to

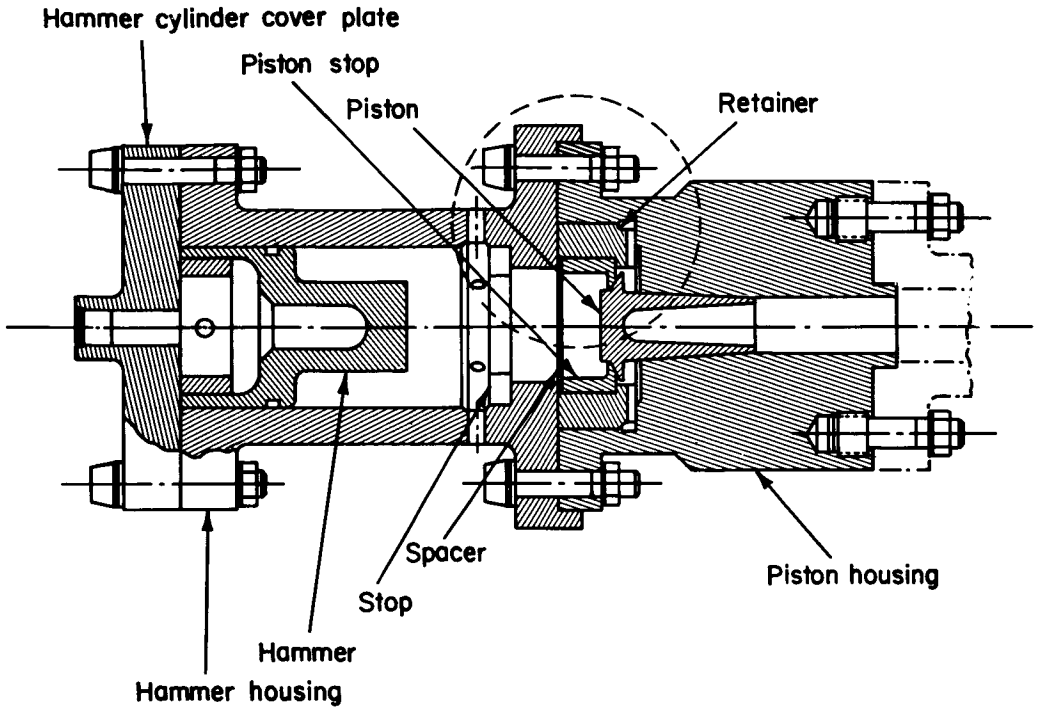

FIGURE 10.5.2a.—Linear system block diagram.

the combustion chamber in this instance was enough to critically attenuate the pulse.

The LOX dome mounted pulser did not produce any detectable disturbance either in oxidizer injection pressure or chamber pressure during the tests. It is undetermined whether the compressibility of the propellant or improper bleeding procedures was to blame. Since the engine was tested in a vertical attitude, the pulser could not be oriented to completely eliminate the possibility of a gas bubble at the piston face.

Subsequent tests with this device were conducted on the same engine but with an injector type which had been demonstrated to be dynamically stable. No instabilities were triggered during the remainder of the program and pulse induced disturbances were of such low magnitudes as to be virtually undetectable in chamber pressure data.

The second design, the pneumatic single pulse generator (shown in Fig. 10.5.2b), was developed to induce a pressure pulse with an overpressure 20 per cent greater than the static pressure in the propellant at the point of pulse generation. The design locks the hammer in position with a pressure-actuated, retractable trigger. Gas pressure (up to 1000 psig) is stored in the dome to control the amplitude, and the cavity between the two pistons is evacuated. When the trigger is disengaged, the hammer is driven against the anvil, thus transferring energy to the anvil through impact. The anvil then transfers the impact energy to the fluid, producing the required pulse. The Belleville washers act as shock absorbers to limit the travel of the anvil.

The pneumatic, single-pulse generator was developed to evaluate the dynamic response and coupling characteristics of the feed, injector, and combustion systems. For the fuel system, the pulser was installed on the feed line between the pump and the thrust chamber valve; some cases were run with the pulser mounted on a fuel injection pressure tap. On the oxidizer circuit, the pulser was mounted directly on the oxidizer injector dome.

Calibration tests of the pneumatic pulser were conducted with a simulated engine and water flowing at rated flows. For the fuel system, the pulse pressure was measured at the chamber inlet, nearly two feet down-stream of the pulser. For

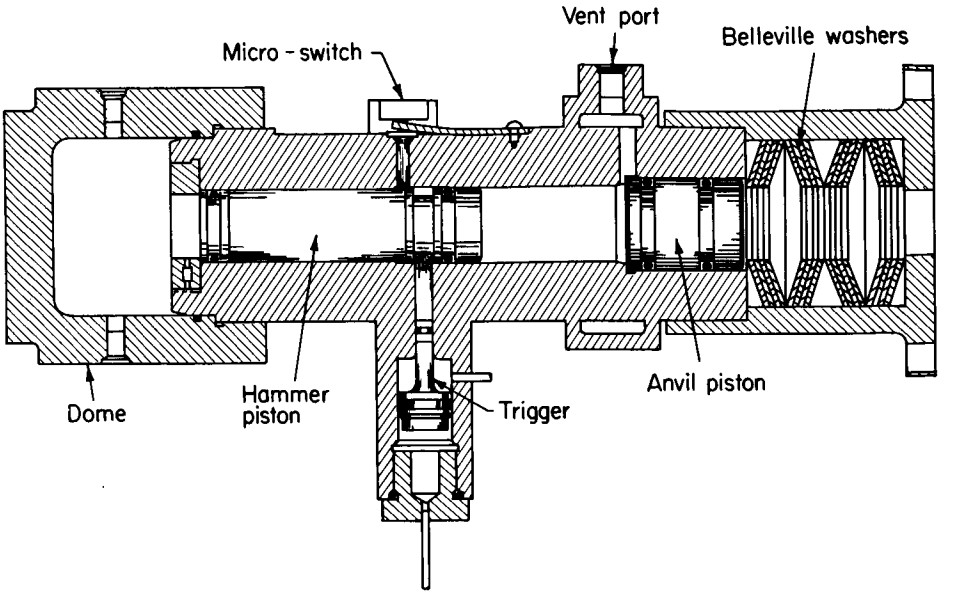

FIGURE 10.5.2b.—Pulse function.

the oxidizer system, the pulse pressure was measured adjacent to the mount on the injector dome. Fig. 10.5.2c depicts the measured pressure for pulser dome pressures up to 1000 psig. When the fuel pulser was mounted on a $\frac{1}{4}$-inch pressure tap at the injector inlet, pulse amplitudes less than 10 psi were measured in the manifold adjacent to the pulser.

The calibration tests showed that pulser dome pressure of 500 psi would meet the pulse amplitude requirements for both propellant circuits. In subsequent engine tests the pulser perturbed the fuel system with a 326 psi pulse and associated 820,000 psi/sec pressure rise rate. The oxidizer unit produced a 360 psi pulse with a 3,500,000 psi/sec pressure rise rate. The measured disturbances in each feed system are pictured in Fig. 10.5.2d. As in the calibration tests, the fuel system pressure disturbance was measured both at the chamber inlet (regeneratively cooled, two-pass system) and at the injector inlet. The pulse amplitude and rise rate criteria were met at the chamber inlet. The oxidizer system disturbance that is illustrated was also measured at the injector inlet. The oscillations created in the feed system due to the single pulses were attenuated within 12 milliseconds. The fuel pulse caused no perturbation in the combustion pressure, but a 30

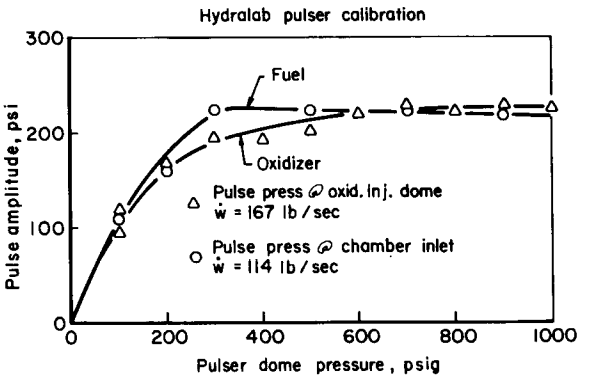

FIGURE 10.5.2c.—Amplitude and phase characteristics of unit impulse function.

psi disturbance was transmitted to the combustion as a result of the oxidizer pulse. No instabilities were generated; however, the pulsers were used only on systems with demonstrated, dynamically stable injectors. (Dynamic stability had previously been demonstrated with 220 grain, non-directed pulse charges mounted in the combustion chamber.)

In summary, it would appear that the principal role of the feed system pulse generators is in the evaluation of the feed system itself. Since the present trend in engine development is to use

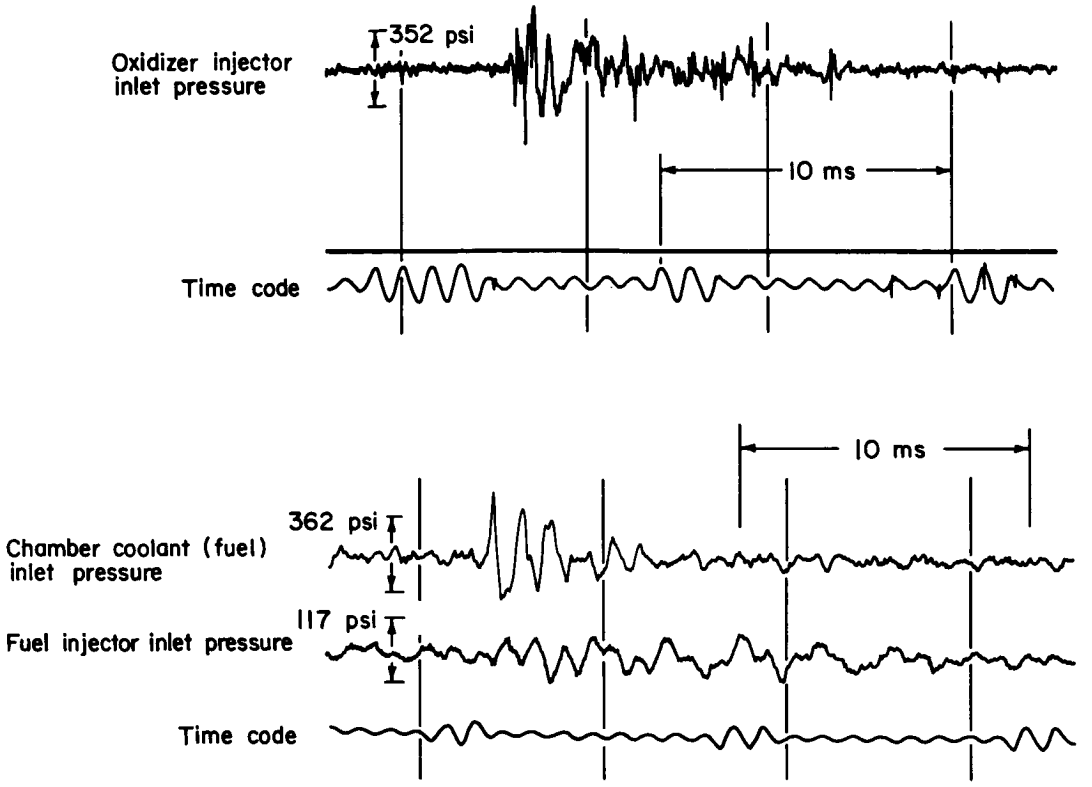

FIGURE 10.5.2d.—Theoretical pressure time characteristics of pulse generator output.

dynamically stable injectors, which have yet to be driven unstable via feed system pulsing, only the exceptional situation where other rating methods cannot be employed would encourage further feed system pulsing as a means of injector stability evaluation.

Within the feed system the pulse data can be interpreted to define feed system transfer functions for frequencies below the fundamental transverse mode of the combustion chamber. Data reduction techniques such as cross-correlation, auto-correlation, and Fourier spectrum can be used to describe the transfer functions. Further, the feed system resonance characteristics can be described by performing spectral analyses of the pulse data, and the pulse attenuation can be determined at discrete resonant frequencies using filtered playbacks of the pulse data.

10.6 OTHER RATING TECHNIQUES

In the previous sections of this chapter attention has been concentrated on rating techniques which either simulate natural disturbances or produce oscillations within a combustor. Factors such as damping rate, disturbance duration, amplitude, etc., serve as measures for determining the margin of stability. In this section another stability-limit concept is discussed, namely, alteration of combustor environment. Techniques include propellant change-of-state variations through temperature control, frequency variations through alterations in the combustor dimensions, and combustion changes through variations in mixture ratio, chamber pressure, etc. Such approaches have often been used in conjunction with the rating techniques previously discussed.

10.6.1 Liquid Hydrogen Temperature Ramping*

For rocket engines burning the liquid oxygen/liquid hydrogen (LOX/LH_2) propellant combination, the relative combustion stability normally is rated by a somewhat unique tech-

* D. E. Sokolowski, Author.

nique. The technique is to decrease the temperature of the liquid hydrogen prior to being injected into the combustion chamber until acoustic mode combustion instability is initiated. Consequently, this technique is commonly called liquid hydrogen temperature ramping.[5,719] The quantitative rating parameter is the hydrogen injection temperature when the transition from stable to unstable combustion takes place. A stability boundary for a specific combustor configuration may be established by varying the operating conditions (such as, oxidant-fuel ratio or chamber pressure) of the combustor between tests. By making a relative comparison of stability boundaries, different combustor configurations then can be evaluated. In general, the most stable configuration would have a stability boundary at low hydrogen injection temperatures.

Changing the temperature of the injected hydrogen is accomplished by mixing warm gaseous hydrogen with liquid hydrogen. Normally, a test begins with specific flow rates of liquid hydrogen at 60° R (33.3° K) and gaseous hydrogen at ambient temperature. By reducing the gas flow rate at a predetermined rate while simultaneously increasing the liquid flow rate in order to maintain a constant total flow rate, a rate of temperature reduction of as much as 25° R per second (12.9° K/sec) can be realized.

Liquid and gaseous hydrogen are mixed by swirling the liquid into a gaseous stream of flow. The mixing section is in a manifold just upstream of the injector. This section is four feet (1.312 m) long and has a volume of 1140 cubic inches (0.0187 cu m). In Fig. 10.6.1a is shown a schematic of the mixing section. Flow rates of gaseous hydrogen and liquid hydrogen to the mixer are controlled by valves which are operated by several electrohydraulic servosystems.

Operational parameters necessary for the servosystem include chamber pressure, flow temperatures, and flow rates. In Fig. 10.6.1b is shown a diagram of the propellant flow system and necessary test instrumentation types and locations to record the operational parameters. An oscillograph record of these parameters for a typical test is shown in Fig. 10.6.1c. In this example, combustion instability was initiated at a hydrogen injection temperature of 70° R.

Hydrogen injection temperature ramping is a

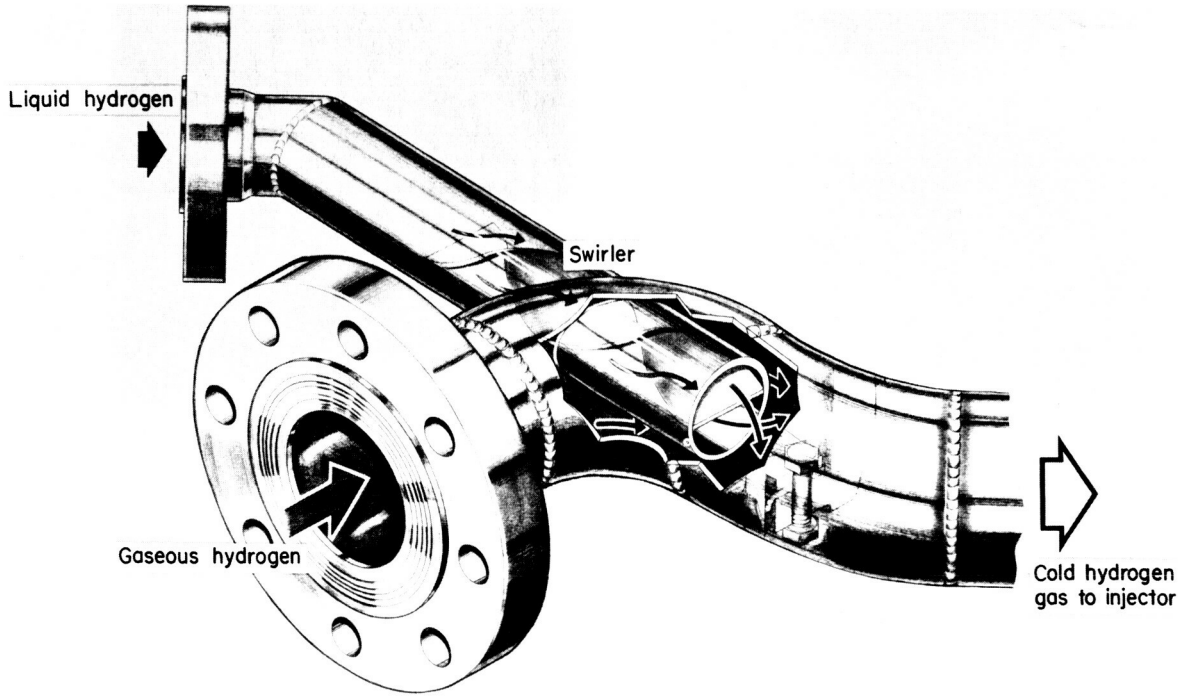

FIGURE 10.6.1a.—Hydrogen temperature ramp mixing station.

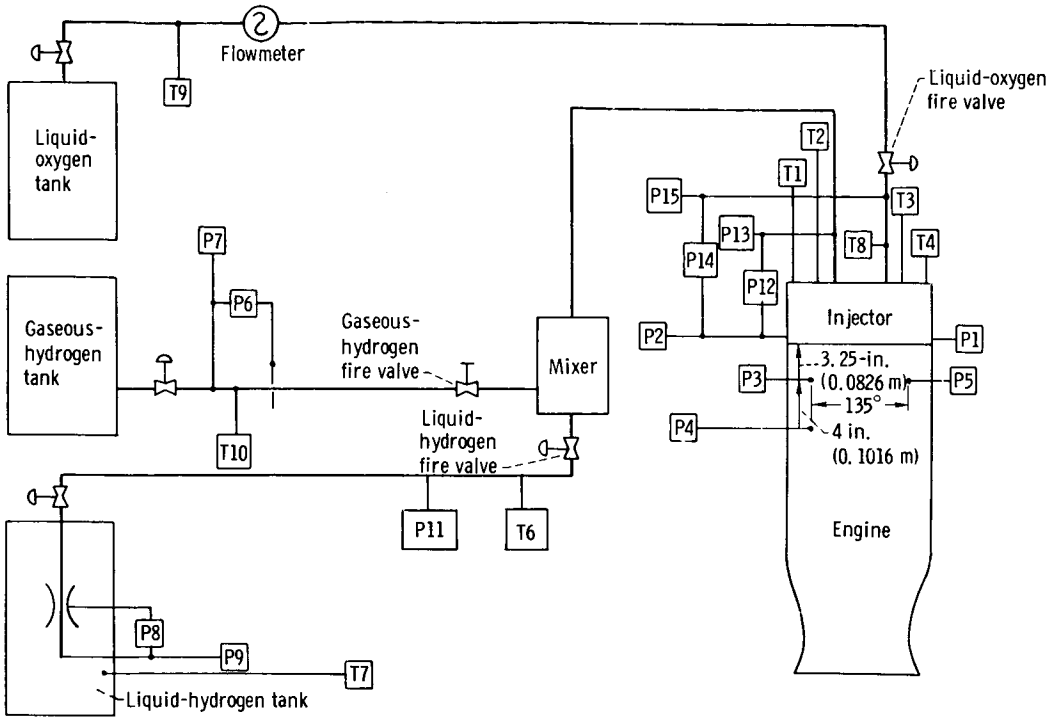

P1 Static chamber pressure (injector face), four-arm strain-gage transducer 1
P2 Static chamber pressure (injector face), four-arm strain-gage transducer 2
P3 Dynamic chamber pressure, water-cooled quartz pressure transducer 3
P4 Dynamic chamber pressure, water-cooled quartz pressure transducer 4
P5 Dynamic chamber pressure, water-cooled quartz pressure transducer 5
P6 Gaseous-hydrogen orifice differential pressure, four-arm strain-gage transducer
P7 Gaseous-hydrogen orifice pressure, four-arm strain-gage transducer
P8 Liquid-hydrogen venturi differential pressure, four-arm strain-gage transducer
P9 Liquid-hydrogen venturi pressure, four-arm strain-gage transducer
P10 Hydrogen-mixer pressure, four-arm strain-gage transducer
P11 Liquid-hydrogen line pressure, four-arm strain gage transducer
P12 Hydrogen-injection differential pressure, four-arm strain-gage transducer
P13 Hydrogen-injection pressure, four-arm strain-gage transducer
P14 Oxygen-injection differential pressure, four-arm strain-gage transducer
P15 Oxygen-injection pressure, four-arm strain-gage transducer
T1 Hydrogen-injector temperature, carbon resistor sensor probe 1
T2 Hydrogen-injector temperature, carbon resistor sensor probe 2
T3 Hydrogen-injector temperature, carbon resistor sensor probe 3
T4 Hydrogen-injector temperature, carbon resistor sensor probe 4
T5 Hydrogen-mixer temperature, carbon resistor sensor probe
T6 Liquid-hydrogen line temperature, carbon resistor sensor probe
T7 Liquid-hydrogen venturi temperature, platinum resistance thermometer
T8 Oxygen-injection temperature, copper-constantan thermocouple
T9 Oxygen flowmeter temperature, platinum resistance thermometer
T10 Gaseous-hydrogen orifice temperature, iron-constantan thermocouple

FIGURE 10.6.1b.—Instrumentation diagram for hydrogen temperature ramping.

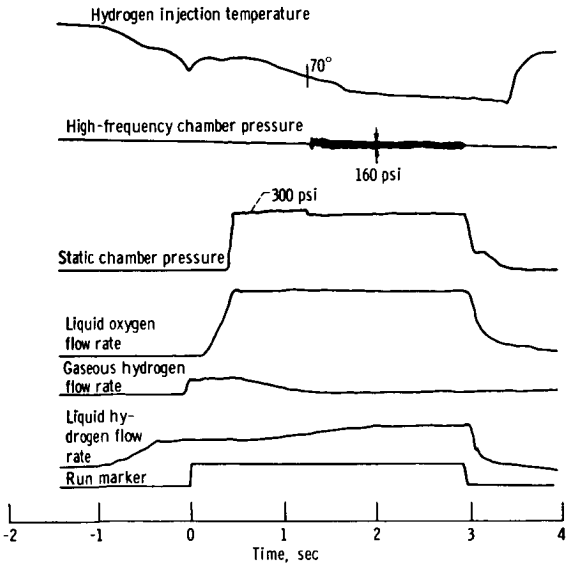

FIGURE 10.6.1c.—Oscillograph traces of typical resonant combustion test illustrating the hydrogen temperature ramping technique.

valid and reliable technique for rating the relative combustion stability of an engine. Although this technique has been used extensively at the NASA Lewis Research Center for evaluating research-type engines, it also has use in development programs for flight-type engines. For example, in the J-2 development program,[5] this technique was useful for selecting high performance and stable injector configurations. The J-2 engine injector utilizes a coaxial injection pattern with a transpiration-cooled face plate. The development program for this injector configuration included an extensive test program in which the stability characteristics of several coaxial injector element designs were determined over a range of propellant flow rates and hydrogen injection temperatures. Injector variables evaluated included injection areas, hydrogen injection method and location, oxygen injection with and without "swirlers," and premix cup shape and length. Analysis of data from these tests resulted in stability maps for each injector configuration which then permitted reasonably accurate prediction of the stability limits over wide ranges of operating conditions. Repeatability of approximately one degree Rankine was commonly observed over a wide range of operating conditions with the J-2 production-type injector assembly. This program demonstrated that liquid hydrogen temperature ramping of a large hydrogen-oxygen combustor is an accurate technique for the determination of stability boundaries.

At present, no mechanism has been hypothesized to fully explain how this rating technique causes instability. However, from the evaluation of data from research-type engines which were run over a wide range of geometric variables and operating conditions, a correlation was obtained which represents the stability boundary.[716] The correlation is represented by the expression

$$\mathcal{W}_{cr} = \left(\frac{2g_c\Delta p_H}{\rho_H}\right)^{1/2} \rho_{OX}(D_{OX})^{1.25}\left(\frac{1}{r}\right)^{1/2} \qquad (10.6\text{–}1)$$

where

Δp_H	hydrogen injection pressure drop
ρ_H	hydrogen density at injection
ρ_{OX}	oxygen density at injection
D_{OX}	oxygen injection orifice diameter
r	oxidant-fuel ratio

For the range of variables investigated, $\mathcal{W}_{cr}$ had a constant value of 4.4. At values ≥ 4.4, combustion was stable, whereas combustion was unstable at values below 4.4.

For purposes of comparing the hydrogen temperature ramping technique with the explosive rating technique,[652] several tests have been conducted using both techniques at the same time. Results show that exploding a large explosive charge at a hydrogen injection temperature far from the stability boundary produces only a small amplitude perturbation in chamber pressure. Repeating this at a temperature closer to the boundary results in a much larger amplitude and, quite possibly, initiates combustion instability. This seems to imply that a powerful damping process exists at temperatures far from the boundary.

10.6.2 Variable Frequency Testing*

Another stability-limits testing technique has involved changing the resonant frequencies of combustion chambers through changes in the physical dimensions, while retaining the same injectors and combustion patterns, and thus

* D. T. Harrje, Author of Sects. 10.6.2 to 10.6.4.

preserving the associated characteristic combustion response. Two examples of this approach are the variable length hardware used to alter the longitudinal mode frequencies,[180,184,634,773] shown in Fig. 10.6.2a, and the variable sector hardware designed to change the characteristic standing tangential mode frequencies[184,187] (see Fig. 10.6.2b). Examples of the stability-limits data provided by such tests were given in Sects. 4.2.2.2 and 4.2.3.1.

Another alternative might even include the use of chambers of several diameters which would alter the frequencies associated with both radial and tangential modes. However, a major disadvantage of such a test program would be the necessary changes in injection pattern and spacing. In the two approaches previously mentioned no changes were made in these parameters which are so critical to the combustion behavior. The sector motor did require portions of the injector face to be blocked off but injection density and element spacing were maintained.[187]

10.6.3 Mixture Ratio Alterations

Since the operating conditions of a given engine are customarily specified within narrow limits, major variations in the combustion require changes in the injector design itself. Much of Chapter 7 was devoted to that subject. However, in the testing phase, variations in the mixture ratio are sometimes employed as a means of providing additional insight to the margin of combustion instability safety of an individual injector design.

In the stability-limits testing described in 10.6.2, mixture ratio was the other variable which provided data on the combustion effects. In general, it was found in those tests that improved linear combustion stability could be achieved through such off-design mixture ratio operation.[180] However, the variation of mixture ratio to alter the triggering level in nonlinear stability-limit testing has also been found useful when testing the effect on stability of other parameters.

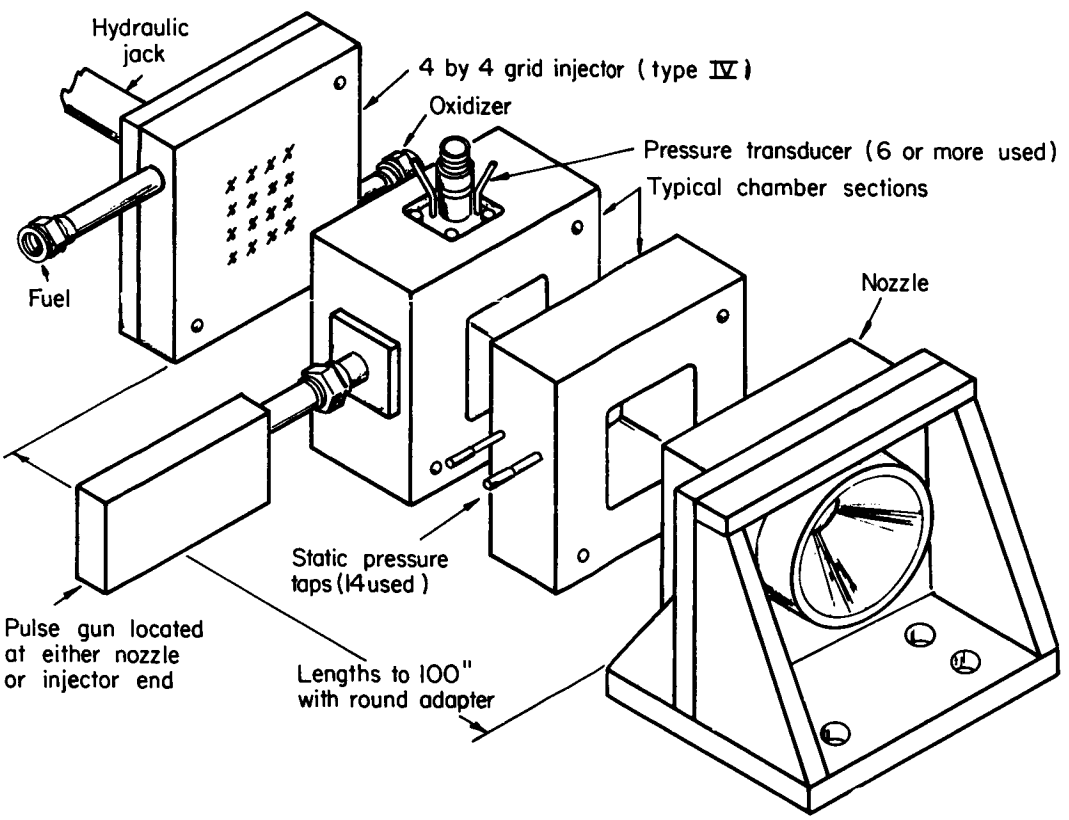

FIGURE 10.6.2a.—Square motor assembly.

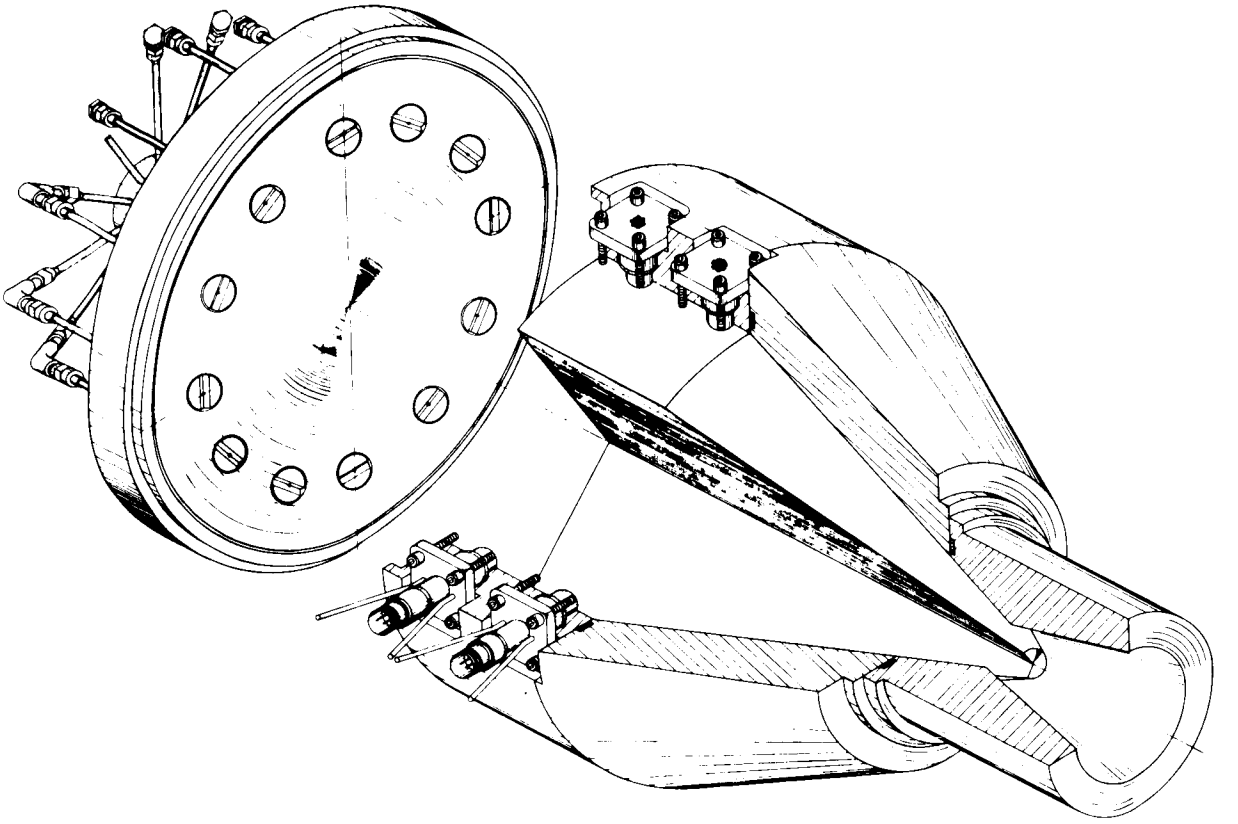

FIGURE 10.6.2b.—Sectionalized view of the variable-angle sector motor.

10.6.4 Pressure Level Changes

Still another variable that lends itself to stability-limits testing is chamber pressure. In N_2O_4/A-50 testing, for example, stability was found to be more critical in the start transient where only partial chamber pressure had been attained.[11] However, it must be stressed that only partial flow rates were present in those tests and such marked injection differences plus the associated alteration of feed system coupling were no doubt more important than the chamber pressure itself.

Retaining the identical flowrates while altering the throat diameter was the basis for a series of pressure level stability evaluations.[186] Such results are shown in Fig. 7.4.3g and the general subject of chamber pressure effects is discussed in Sect. 7.2.1.

Upgrading the thrust level of existing hardware via higher propellant flowrates is one situation in which development programs face stability-limit changes because of increased chamber pressure. In such instances, changes in the injector have been necessary to maintain dynamic stability.

10.7 COMPARISON OF RATING TECHNIQUES*

10.7.1 Correlations Between Techniques

The several stability rating techniques described in the preceding sections of this chapter disturb the steady-state operation of a combustor in a number of different ways, as previously discussed. The interaction or response of the combustion processes to these influences is very complex and has not been fully delineated. It is not possible, therefore, to draw direct, definitive comparisons among the rating methods on the basis of the effects of their input disturbance characteristics.

* L. P. Combs and R. J. Hefner, Authors.

Direct comparisons between two techniques have often been obtained experimentally, but usually for rather limited ranges of variation in engine design, operating conditions, etc. Some typical observations may be summarized, but exceptions have been found to nearly every generality.

Ratings obtained with artificial initiation methods are sometimes parallel to those obtained by spontaneous initiation methods. For example, an engine that has exhibited a higher incidence of spontaneous instability than has another engine would usually require a lower amplitude artificial disturbance to initiate a sustained instability. Similarly, smaller artificial disturbances have been needed to trigger instabilities as an instability boundary has been approached. This latter phenomenon has been observed in all types of boundary mapping, including variations of mixture ratio, chamber pressure, chamber length and hydrogen injection temperature. Unfortunately, the converse of this observation (i.e., that the requirement of a larger disturbance is associated with improved inherent stability) has too often been found invalid. Some specific instances are discussed in Ref. 161.

Disturbances from bombs and pulse guns frequently cause a combustor to experience identical sustained instabilities, even though the intermediate period before the establishment of the ultimate instability may be quite different for the two devices. Frequently, there are often unexplained differences in either the magnitudes of disturbances required to effect sustained instability or in the fraction of tests which are unstable with the two types of disturbances.

10.7.2 Limitations of Available Techniques

The primary objective in stability rating is assurance that the rocket engine will perform all of its mission requirements without sustaining an uncontrolled instability. To accomplish this, stability rating devices are intended to simulate any and all disturbing forces that might be encountered naturally by the engine. There are two major limitations which make the achievement of this goal a very difficult task. First, the types of disturbances to which an engine might be subjected are never completely known. Second, instrumentation limitations make it difficult to determine accurately the nature of the disturbances the rating devices produce in an engine and to discern effects of interaction with the combustion processes.

Each of the rating techniques has some specific limitations upon its application to rocket combustors. These are summarized, along with the techniques' advantages, in Table 10.7.2. The more important items listed there are discussed briefly in the following section.

10.7.2.1 Disturbance profile effects.—Both bombs and pulse guns appear to provide, primarily, transient pressure disturbances. Stability ratings obtained with them are, therefore, indications of the relative sensitivity of the combustion processes to pressure perturbations. A combustor's sensitivity may be directional, e.g., a bipropellant spray combustion field may be so structured that it is greatly influenced and responds massively to a transverse disturbance yet is only slightly affected by a longitudinal pressure wave. The rating devices provide pressure disturbances that are nondirectional (or, more precisely, omnidirectional) in the case of the bomb and somewhat directional in the case of the pulse gun. This difference may be a limitation or an advantage, depending upon the particular application. The pulse gun's directionality offers some degree of selectivity as to the predominant mode of instability initiated. For example, when it is desired to rate the tangential modes of instability, tangential pulse entry is frequently employed for preferential initiation of those modes. In other instances, the bomb's omni-directionality is appropriate; an example is general rating tests in which it is better not to favor one mode but to find which mode is most likely to occur.

10.7.2.2 Access ports through chamber walls.—A major advantage of bombs is their positional versatility. They are not restricted to insertion through the combustion chamber wall but can be mounted in almost any convenient location in the combustor. Pulse guns and gas flows are almost exclusively directed through the chamber wall;*

* There are isolated instances in which pulse gun ports have been machined in injectors.

TABLE 10.7.2.—ADVANTAGES AND LIMITATIONS OF RATING TECHNIQUES

Rating technique		
Bombs	Pulse Guns	Gas Flows
Advantages		
1. Affect pressure sensitive processes, primarily. 2. Disturbances are omni-directional. 3. Have positional versatility; not restricted to neighborhood of chamber walls. 4. Use of wands permit several positions from a single attachment point. 5. Several bombs per test sometimes possible. 6. Adaptable to regeneratively cooled combustion chambers. 7. Only modest external engine access required for most designs if internal access is available. 8. Small size. 9. Handling hazards reduced for exploding bridge wire bombs.	1. Affect pressure and velocity sensitive processes, depending on orientation. 2. Disturbances are predominately directional. Permits forcing particular modes. 3. No disruption of chamber flow processes prior to use. 4. Minimal shrapnel damage now possible. 5. Multiple guns per test sequenced routinely. 6. Electrical firing precisely timed. 7. Charges protected from heat, thermal initiation avoided. 8. Handling hazards minimized (for gun powder charges). 9. Charges not fired in a test are not discarded.	1. Affect displacement sensitive processes, primarily. 2. Directional disturbance permits forcing particular modes. 3. No disruption of chamber flow processes prior to use. 4. No shrapnel damage potential. 5. May provide ratings in very few tests. 6. Precise control of timing. 7. Good reproducibility of ratings. 8. Limited handling hazards.
Limitations		
1. Bomb orientation may influence combustion sensitivity. 2. May disrupt normal chamber flow prior to use. 3. Non-uniform heating or ablation of the case may introduce directional effects. 4. Subject to structural failure; often limited to one per test. 5. Most designs liable to thermal initiation of detonation. 6. Some shrapnel damage to engine parts possible. 7. Electrical initiation requires external access. 8. May be more hazardous to handle than pulse gun charges. 9. Must dispose of live bombs not exploded during a test. 10. Possibility of ejecting live bombs from the chamber.	1. Limited to chamber wall applications. Difficult to apply to regeneratively-cooled engines. 2. Ports may interact acoustically with chamber and influence stability. 3. Multiple bosses required for multiple pulses or for varying location. 4. Requires reasonable access to positions external to engine.	1. Pressure sensitive processes are little influenced. 2. Natural triggers are not known to be simulated. 3. Extensive supply and control system may be required. 4. Large quantities of gas may be needed for triggering. 5. Ports may interact acoustically with chamber and influence stability. 6. Multiple bosses required for varying location. 7. Limited to chamber wall applications.

this practice becomes a particularly severe limitation when a regeneratively-cooled engine is to be rated and is usually not attempted for obvious reasons. Adapting bombs for use in these engines needs only the simpler provision of injector or baffle mounting and of electrical lead-ins through the injector or thermal initiation of detonation.

10.7.2.3 Shrapnel damage.—Little use has been made of the preceding bomb advantage because of the high potential for shrapnel damage from most bomb designs. The design of bombs having reduced charge weights contained in thin-walled cases and made of low impact strength materials now appears to offer minimized shrapnel damage potential. A further reduction of shrapnel damage may be gained by using the exploding bridge wire initiation method, thus eliminating the extraneous components associated with commercial detonators. A less severe shrapnel problem associated with ejection of the pulse gun burst diaphragm has been virtually eliminated for all but the largest gun-powder charges, but remains partially unsolved for high-explosive pulse gun charges.

10.7.2.4 Multiple pulses.—A long-term advantage of pulse guns has been the possibility of scheduling more than one pulse per test. Typically three or four pulses are introduced at intervals of 100 milliseconds or more. Bombs, on the other hand, are subjected to the full force of any transient pressure disturbances or periods of instability which might precede their scheduled detonation. They have usually proven not to be structurally strong enough to survive the blast of another bomb or pulse gun or more than a few cycles of high amplitude acoustic instability. Normal practice, therefore, has been to provide only one bomb per test, or if multiple pulses are used, to make the first one a bomb and subsequent ones pulse guns. Recently, multiple bombs have been used successfully in development tests; design for good structural integrity is essential.

10.7.2.5 Thermal initiation of detonation.—Whereas most previous bomb designs have contained a booster charge of thermally-sensitive primary explosive (such as lead azide or tetryl) to ensure detonation of the base charge, the exploding bridge wire bombs contain no such booster and, as a result, are not sensitive to thermal initiation. This certainly can be considered to be an advantage in some cases, e.g., thermal initiation of detonation during pre-stage (before the bomb case is partially ablated and before the additional fragment drag due to higher gas density has become established) may entail greater shrapnel damage potential. This might be particularly true with cryogenic propellants, where both the bomb case is very hard and the chamber walls are very brittle during the start transient. Fracturing or dislodging the improved bomb would result in its loss but in a non-damaging manner. In some engine applications, where electrical lead-in access is not available, bomb detonation by thermal initiation has been counted upon; one of the earlier designs would then be appropriate.

10.7.2.6 Acoustic interaction.—Information was presented in Ref. 167 demonstrating that both pulse gun ports and bomb lead-wire passages may form acoustic cavities which influence a combustor's stability, and thus invalidate the stability rating. Gas flow inlet ports may behave similarly. The pulse gun and gas flow ports may be viewed simply as quarter-wave resonators while bomb passages are more complicated.[167] Care must be taken in designing and matching the devices to a combustor so that they do not provide damping for the instability. Because of gas temperature gradients which vary both in time and position within the devices, prediction of whether a cavity added to the system is active or passive is difficult and subject to inaccuracies. Bombs should be designed so that no uncontrolled cavities are left after detonation.

10.7.2.7 External engine access.—A rating device's physical size is important in relation to the external and internal engine access required. The bomb and pulse gun rating devices must be removed from the chamber and rebuilt after each test. This requires that each entry port be readily accessible from the outside of the engine, a requirement which may severely limit selection of application points and the number of pulse guns which may be used. The access problem is considerably reduced for installation of bombs if

there is good access to the inside of the chamber. The gas flow apparatus is certainly the largest of the techniques but it usually can be mounted in some unobtrusive location within a few feet of the combustor. Its only required connection to the engine is usually a simple flow line which, unless the flow entry point is varied from test to test, does not require continuous accessibility.

10.7.2.8 Handling characteristics.—Some discussion pertinent to the handling characteristics of each rating device has been given earlier. The relative effort required to effect changes or replacement between tests and the hazards associated with each technique are discussed briefly here.

Once the basic flow system has been installed for the gas pulse apparatus, very little additional handling is required. The only test hardware preparation consists of relocating the connecting line between the control valve and the appropriate chamber boss. The operation of the device, however, requires additional preparation. This includes the manipulation of numerous valves and the pressurization of the source tank to the desired value. Other than personnel association with high-pressure gas systems, no particular hazard is associated with gas pulsing equipment.

The bomb and pulse gun devices both contain small amounts of high explosives. Safety with explosives requires knowledge of the hazards involved and rigid adherence to the proper methods of performing each function. The greatest hazards to be guarded against are stray currents, static electricity, frictional heat, impact and carelessness. Pulse guns are less hazardous than bombs because the cartridge-loaded charges and the unidirectional blast make it easier to avoid direct personnel exposure.

Following a hot-firing test, any bombs that have not been detonated must be disposed of immediately. Extra precautions are called for because of the potentially higher sensitivity of explosives that have been heated; this work should be performed by personnel specifically trained in explosives-disposal techniques. Residual pulse gun charges, on the other hand, may simply be returned to storage and used in a subsequent test (unless there is external evidence of excessive heating of the pulse gun assembly).

Another hazard associated with bombs is the possibility that one may be dislodged and ejected from the combustion chamber as a live bomb. This is even more hazardous than having a residual bomb in the combustor; personnel may be completely unaware of its presence and so may unwittingly detonate it without benefit of protective equipment. Periodically, the test area should be searched thoroughly, and a specific search should be conducted whenever there is not positive evidence that a bomb actually detonated in the combustor.

10.7.3 Criteria for Selection of a Rating Technique

Several stability-rating techniques have been described in the preceding sections for evaluating both resonant and feed system coupled stability characteristics of rocket engines. Since each of these techniques evaluate the stability in somewhat different manners, it would be desirable to use all of them on an engine before it would be considered fully developed. This is not feasible economically and has been found to be unnecessary.

For evaluating the stability characteristics of engines using any propellant combination except hydrogen, the explosive bomb and/or pulse gun have been widely used with success. For engines using hydrogen, the temperature ramp technique has been most popular. The technique of varying both mixture ratio and chamber pressure for stability rating is commonly used in conjunction with both the hydrogen ramp and explosive techniques.

It has been found that both the hydrogen ramp and explosive device techniques provide stability information on feed system instabilities but for quantitative evaluation of feed system effects, the feed system pulsing devices have proved to be valuable and should be considered in selecting rating techniques for these modes.

Aside from these general guidelines, the selection of a rating technique for application to a particular combustion system is dependent upon a number of interrelated factors, most of which are associated with the nature of the program and of the engine system design and operating parameters. Discussion of these factors and their influences on the choice of a rating device is

approached in this subsection* from a parametric combustion chamber design viewpoint after attempting to eliminate major program variables. For simplicity, the discussion centers on the explosive devices. Included in this discussion are recommendations or guidelines regarding placement of the rating devices in the test hardware.

10.7.3.1 Program considerations.—Whether or not stability rating is a major program goal will influence the device selection. Questions which must be considered are concerned with whether or not there are contractual commitments to be fulfilled regarding stability demonstration, whether a general "as is" evaluation of stability traits is to be sought or whether some design changes are expected to be made for stability improvement, the number of tests projected for stability evaluation, how many engine design or operational variations are planned for those same tests, and how much calendar time is available for preparation and performance of experiments. The answers to these and similar questions define the scope of the stability evaluation problem. An experimental program can then be structured to provide the required characterization. A universal goal should be the accomplishment of the characterization in as few engine-firing tests as possible. If the program is limited to fewer tests than the definition of the scope of the problem appears to require, then it must be recognized that less than complete characterization may result and the program structured accordingly to seek definitive knowledge of the most crucial portions of the problem (see discussion in Sect. 1.2.4).

For the purposes of the ensuing discussion, the vicissitudes of program requirements can be averted, largely by assuming that

1. a new rocket engine system is to be developed;
2. a requirement exists to determine its stability characteristics;
3. detrimental instabilities are defined and, if they are experienced, system changes are to be made to eliminate them.

Less stringent actual program requirements generally will be satisfied by simplifications or deletions from the approaches suggested in the following discussions. More stringent program requirements, in the form of definitive contractual requirements for perturbation source, pressure disturbance amplitude, rate of pressure rise, recovery time, etc., may actually ease the selection task by restricting the range of choices.

A number of programs have contractual requirements for dynamic stability (several are listed and discussed in Ref. 726). Generally, these specify that recovery to stable operation must be effected within a stated time period following introduction of a disturbance of a specified amplitude (or from a given charge weight). Frequently, they also include a definition of what constitutes recovery. The demand for achieving dynamic stability followed the development of effective stabilization devices, particularly combustion chamber baffles. Initially, it was believed that demonstration of adequate recovery from very large blast waves was all that was needed. This is reflected in the requirement for 220-grain bombs and 400-grain tangential pulse guns for the Titan Stage III engine in the Gemini Stability Improvement Program.[726] It has been found (Sect. 10.2.4), however, that a combustor can be "over bombed," i.e., a disturbance may be so large that its disruption of propellant injection is very severe and, before combustion of freshly-injected propellant is resumed, pressure wave motion in the chamber has nearly subsided. The engine can, therefore, "come back on" stable. The current trend is for more modest disturbance amplitude requirements, e.g., the LM Ascent engine specification requires a pressure spike with a minimum peak overpressure that is 175 percent of the mean steady-state chamber pressure (120 psia). The disturbance is achieved with quite small (2 gr PETN) bombs as discussed in Sect. 10.2.4. For general stability evaluations, it is recommended that a wide range of disturbance amplitudes be provided so that engine response to quite small ($\sim$10 percent of p_c) and very large (several times p_c) pressure perturbations may be observed.

10.7.3.2 Engine design and operational considerations.—Shock waves from bombs and pulse guns disturb the steady-state combustion processes and evoke dynamic responses which may cause growth or decay of the initial waves. The resultant

* This subsection parallels closely a similar discussion in Ref. 167.

waves may be strong enough to excite acoustic resonances of the combustion chamber which may, in turn, be driven as sustained combustion instability. A proper coupling between the oscillatory wave motion and the combustion processes is required for driving the wave. Either longitudinal (axial) or transverse (radial or tangential) wave motion may be initiated and sustained; however, most frequently the latter are experienced. That observation can be attributed to a number of factors, but probably the most important ones are the different sensitivities of the combustion processes to motion in the different directions of wave propagation and greater acoustic energy losses from the nozzle for longitudinal wave motion.

Combustion chamber design parameters have direct influence upon the initiation and driving of combustion instabilities and, therefore, upon the selection and placement of rating devices for artificial initiation. The items of most interest are the size and shape, wall material construction of the combustion chamber, the injector spray pattern, and the presence of stabilization devices.

Sometimes an acoustic instability is augmented (or complicated) by induced oscillations in the propellant injection rates. For example, the longitudinal acoustic mode is occasionally driven by injection rate fluctuations. Another form of instability, known as "repeated pressure surging," has characteristics of a transverse mode superimposed on chugging.[440] Also, intermediate frequency "buzz" instabilities are sometimes excited[272] which have characteristics of feed system acoustic resonances. These and other examples clearly demonstrate that engine design parameters other than those listed in the preceding paragraph also affect the chamber instabilities.

COMBUSTION CHAMBER SHAPE: Three commonly used rocket combustion chamber shapes are (1) circular cylinder with a flat or "dished" injection-end closure and a deLaval exhaust nozzle, (2) annular combustion spaces, ranging from a cylindrical chamber with a centerbody to the very large diameter, very narrow combustion space of the aerospike engines, and (3) for research scale photographic and stability rating work, specialized rectangular two-dimensional configurations. Both bombs and pulse guns have been used in tests with each of these shapes. The shapes, per se, really have little influence on the rating device selection but do enter into consideration of device placement. With cylindrical chambers, bombs located near the chamber wall and tangentially (or chordally) oriented pulse guns are most often used. To avoid overlooking the possibility of initiating the first radial mode, bombs at the center of the chamber and/or radially disposed pulse guns should be kept in mind. The radially-oriented pulse gun is also recommended for potential initiation of the modes other than the first tangential. With annular chambers, the shape accentuates the likelihood of experiencing tangential instabilities so a reasonable practice is to orient pulse guns tangentially. Unless the annulus is narrower than about 2-$\frac{1}{2}$ inches, some effort should be made to initiate the radial mode. Either bombs or a radial pulse gun could serve this purpose. Pressure instrumentation capable of discerning oscillations to about 20 kHz might be needed to observe such a mode. In two-dimensional chambers, both bombs and pulse guns are normally mounted so that their blast waves propagate along the length of the injector (Ref. 403).

COMBUSTION CHAMBER SIZE: Large and small combustion chambers have been stability rated with bombs, while intermediate size chambers have been disturbed with both bombs and pulse guns. With small chambers, the volume of a 6-inch-long (unfired) to 9-inch-long (fired) pulse gun cavity would be large compared to the volume of the chamber and appreciable acoustic interaction between the volumes should be expected to alter the combustor's stability. No lower limit on chamber size has been established. Guide lines for estimating a gun's acoustic influence on the stability of a small chamber could perhaps be developed by correspondence to the effectiveness of acoustic liners and cavities.

Another approach which might be taken with small chambers is to reduce the size of the pulse gun. Correlations in Ref. 167 show that the amplitude of the shock discharged from a gun's muzzle is lower than predicted by the simplified theory if the gun barrel's L/D is less than about 16. Reducing the pulse gun size, particularly its length, may be considered as exchanging a measure of predictability for decreased acoustic interaction.

COMBUSTION CHAMBER CONTRACTION RATIO: The chamber contraction ratio has a direct influence on the predicted ablation rate of bomb cases.[167] Other influences on rating device selection are indirect, resulting from the interrelated effects of chamber pressure, contraction ratio and propellant injection density on the propellant combustion rate, discussed later.

COMBUSTION CHAMBER WALL DESIGN: Chamber wall design and materials are sometimes the largest controlling factors in the selection of a rating technique. As discussed under advantages and limitations, pulse guns are not commonly used with regeneratively-cooled chambers. Subject to restrictions concerning ability to initiate desired modes of instability, bombs should be positioned as far as practical away from the regenerative chamber's walls. They normally should be oriented with their axes parallel to the walls in order to minimize shrapnel damage potential. If the chamber shape is such that orientation places the end of the bomb close to a nozzle wall surface, reorientation closer to the center of the chamber or to a skew or radial mounting might be preferred in order to avoid damage from bomb-end fragments.

For reasons somewhat analogous to those for not using pulse guns with regeneratively-cooled chambers, they are infrequently used, as well, with ablative-walled chambers. The design and machining difficulties of providing pulse gun ports in ablative materials are not nearly so severe as with regeneratively-cooled walls, but the added possibilities of delamination of the ablative when the gun is fired and of irregular erosion around a tangential pulse gun muzzle usually result in selection of bombs. Ideally, bombs in ablative chambers should be mounted from the injector face or baffle assembly, but in several applications they have been inserted radially through the chamber wall.

INJECTOR INFLUENCES: The details of the propellant injector design set the course which the combustion processes will follow. Ultimately, to reduce stability ratings to meaningful, practical terms, they must be related to the injector design details. Basic injector type, element orientation, element spacing, thrust per element, injection velocities are all variables which affect the stability of the combustor. Their combined effects may be thought of heuristically in terms of three resultant subjects: degree of propellant atomization, transverse gradients in propellant mixing, and mean axial propellant combustion rate. The degree of propellant atomization and the transverse mixing, together with contraction-ratio-controlled axial combustion gas velocities, determine the axial propellant combustion rate. In general, the finer the atomization and the better the interdispersion of the propellants, the higher will be their burning rate. For some particular injectors, either the spray atomization or the propellant mixing may predominate in controlling the combustion rate, but they are usually both important, particularly in the region immediately downstream of the injector where the atomization and mixing are being accomplished. That region of early combustion has frequently been found to be the most sensitive portion of the combustion field in responding to a pressure perturbation and initiating combustion instability. The rating device selection, and more specifically, its placement and orientation must take cognizance of that sensitivity.

It is possible, by making a detailed examination of the injector pattern, to estimate the relative distributions of the propellant sprays[225] and the axial combustion rate[224] reasonably accurately. Consideration of the effects that pressure perturbations are likely to have on such predicted distributions usually gives little basis for the preferential selection of either bombs or pulse guns. Good bases for rating device placement and orientation can be found in this way, however. Examination of the transverse spray distributions can suggest regions that are most likely to exhibit strong sensitivity through increased mixing and whether there's a preferred radial or tangential direction for eliciting that sensitivity. Examination of the axial combustion rate profile can indicate, approximately, how important it is for the rating device to be located near the injector in order to be effective. No quantitative guideline can be stated for this latter point, except that if the propellants are more than about 40 to 50 percent burned by the point of disturbance introduction, it is likely not to be very effective. Placing the device further downstream than the point of maximum effectiveness, however, can be compensated for by using increasing charge sizes.

Within limits, then, compromises can be made between axial disturbance location and design variables, such as access through the chamber wall being impeded by propellant manifolds or injector attachment flanges, and such as moving a bomb with a thin wall case downstream to achieve more predictable and uniform ablation rates.

PROPELLANT INFLUENCES: The effects of the propellant combination on rating device selection are mainly felt through a heightening or reduction of the injector influences just described. Other considerations might be (1) whether there is a likelihood of potentially explosive or detonable propellants or propellant residues becoming trapped in rating device cavities and producing unwanted and uncontrolled pressure disturbances, (2) chemical compatibility of bomb case and diaphragm materials with the propellants and their combustion products. Unusual results may sometimes be encountered. An example is the apparent distillation of UDMH out of trapped 50% N_2H_4-50% UDMH fuel mixture, leaving an explosive pocket of hydrazine. Another example was the adsorption of prestage liquid oxygen onto a Micarta bomb case, which had been machined using cutting oil, to form an explosive gel within the case, resulting in detonation immediately upon propellant ignition.

STABILIZATION DEVICES: The use of baffles or acoustic liners to improve the stability of the combustor may influence the rating device selection by changing the modes of instability most likely to occur, altering preferred directions for greatest sensitivity, restricting access to the chamber for installing pulse guns, changing the range of positions available for bombs, and, if such devices are successful, increasing the probability that recovery to stable combustion will occur following a given disturbance.

As with cooled chamber walls, the complexity of the acoustic liner makes installation of pulse guns less attractive than bombs. A necessary caution, however, is that bombs be positioned to minimize the possibility of shrapnel damaging the liner. Otherwise, stability rating chambers with liners appears to be subject to the same considerations as for unlined chambers.

Baffles introduce the possibility of baffle compartment modes of instability being driven. Pressure perturbations should be introduced to evaluate the stability to both those baffle compartment resonances and the (perhaps altered) full chamber resonances. This can be accomplished by locating rating devices both upstream and downstream of the end of the baffles.

GENERAL NOMENCLATURE

The following symbols are used throughout the book. Additional symbols are given in Sections in which they are used.

A	Area
a	Acoustic velocity
$\mathcal{C}$	Capacitance
C_F	Thrust coefficient
c_P	Specific heat of gas at constant pressure
c_v	Specific heat of gas at constant volume
c_L	Specific heat of liquid
c^*	Characteristic velocity
D, d	Diameter
$\mathfrak{D}$	Diffusion coefficient
e	Specific internal energy (gas)
f	Frequency
h	Specific enthalpy
h_v	Heat of vaporization
h_R	Heat of reaction
$\mathcal{I}m(\ )$	Imaginary part of complex quantity in parentheses
i	Imaginary unit, $\sqrt{-1}$
I_{sp}	Specific impulse
J_ν	Bessel function of first kind, order ν
K_L	Bulk modulus of liquid
Kn	Knudsen number
$\mathfrak{K}$	Thermal conductivity
L, l	Length
L^*	Characteristic length of combustion chamber
$\mathcal{L}$	Flow inertia (inertance)
M	Mass burning rate per unit volume
$\mathfrak{M}$	Mach number
m	Mass or mass concentration
$\dot{m}$	Mass flow rate, mass flux
Nu	Nusselt number
$\mathcal{O}(\ )$	Of the order of magnitude of the quantity in parentheses
Pr	Prandtl number
p	Pressure (static)
p_v	Vapor pressure
q	Heat transfer rate
q	Dynamic pressure, $\frac{1}{2}\rho V^2$
Re	Reynolds number
$\mathcal{R}$	Flow resistance
$\mathcal{R}e(\ )$	Real part of complex quantity in parentheses
$\mathfrak{R}$	Gas constant
r	Radial coordinate (circular cross-section)
r_L	Radius of liquid droplet
$\mathfrak{r}$	Mixture ratio (OX/F)
Sc	Schmidt number
$\mathcal{S}$	Surface tension
s	Laplacian variable, complex amplification factor, $\lambda+i\omega$
T	Thermodynamic (absolute) temperature
$\mathfrak{T}$	Shear stress tensor
t	Time
$t_1, t_2, \ldots t_A$	Time constants
t_w	Oscillation period, wave travel time
u	Axial component of velocity
$\mathbf{V}$	Velocity vector
V	Velocity (magnitude)
$\mathbf{\Delta V}$	Relative velocity (gas-liquid)
ΔV	Magnitude of relative velocity
$\mathcal{V}$	Volume
v	Radial or lateral (y-direction) velocity component
We	Weber number
$\mathfrak{W}$	Molecular weight
w	Tangential or lateral (z-direction) velocity component
$\dot{w}$	Weight flow rate
x	Longitudinal coordinate
Y	Mass fraction
Y_ν	Bessel function of second kind, order ν
$\mathcal{Y}$	Admittance
γ	Ratio of specific heats (gas)
ϵ_c	Nozzle contraction (area) ratio
ϵ_e	Nozzle expansion (area) ratio

ζ	Vorticity (vector)
θ	Azimuthal angle coordinate (circular cross-section)
λ	Oscillation amplification factor
μ	Viscosity
ξ	Ratio of inner to outer radius (annular chamber)
π	3.14159 . . .
ρ	Density
σ	Specific entropy
τ	Time delay or characteristic time
ω	Angular frequency of oscillation

Subscripts (gas-phase quantities are not subscripted):

a	Atomization
b	Burning, burned gas
c	Chamber
e	Exhaust
F	Fuel
f	Flame; final (complete combustion)
I	Imaginary part
i	Injector, injection
j	Jet
L	Liquid, liquid drop
M	Minimum value
m	Mean value
OX	Oxidizer
R	Real part
t	Throat
v	Vaporization
w	Wave
0	Initial value
–	Steady state

Superscripts:

–	Steady state
′	Perturbation
*	Complex conjugate

REFERENCES

1. ANON: "Advanced Design Analysis on Annular Nozzles. Rocketdyne Rept. R-2354-3p, 1961.
2. ANON: Applications of the Heat Flux System in Low Temperature Gases and Liquids. Technical Bulletin No. 4, Thermo-Systems Inc., Minneapolis, Minn.
3. ANON: Combustion Instability Experience–Final Report. General Electric Company, July 1963.
4. ANON: Combustion Stability Rating Devices. Rocketdyne Rept. R-6807-P, Nov. 1966.

4b. ANON: Design Guide, Acoustic Liner Feasibility Program. Aerojet-General Rept. 8852-DG, April 1970.

5. ANON: Development History of the 200,000–225,000-lb-Thrust J-2 Rocket Engines–Final Report. Rocketdyne Rept. No. R-6700, Dec. 1966.
6. ANON: An Experimental Investigation of Combustion Stability Characteristics at High Chamber Pressures. Aerojet-General Interim Rept. 11741-I, Sept. 1965.
7. ANON: An Experimental Investigation of Combustion Stability Characteristics at High Chamber Pressure–Final Report, Phase II. Aerojet-General Rept. 11741/SA6-F, Vol. 1, Aug. 1966.
8. ANON: Fastax, High-Speed Motion Picture Instructions. Wollensak Optical Company, Rochester, New York.
9. ANON: Final Technical Report for WS-107A-1 Contributory Engineering. Rocketdyne Rept. R-2325-4P, Feb. 1961.
10. ANON: Format for the Collection of Liquid Propellant Rocket Combustion Instability Test Data. CPIA Publication No. 149, The Johns Hopkins University, Applied Physics Laboratory, Sept. 1967.
11. ANON: Gemini Stability Improvement Program (GEMSIP)—Final Report. Aerojet-General Rept. GEMSIP FR-1, SSD-TR-66-2, Aug. 1965.
12. Ibid., Vol. 2, Development Test Program.
13. Ibid., Vol. 3, Analytical Model.
14. Ibid., Vol. 4, Baffle Design Studies.
15. Ibid., Vol. 5, Development Tools.
16. Ibid., Vol. 6, Instrumentation.
17. ANON: Handbook of Recommended Practices for Measurement of Liquid-Propellant Rocket Engine Parameters. CPIA Pub. 179, Jan. 1969.
18. ANON: High Chamber Pressure Operation for Launch Vehicle Engines Program–Final Report. Aerojet-General Rept. No. 4008-SA4-F, April 1964.
19. ANON: High-Temperature Probes and Auxiliary Equipment. Greyrad Corporation Bulletin, GB-1, Jan. 1968.
20. ANON: History: Project First, F-1 Combustion Stability Program. Rocketdyne Rept. No. R-5615, 1964–1967.
21. Ibid., Column e, Book 4, Feb. 1967.
22. ANON: ICRPG Handbook for Estimating the Uncertainties in Measurements Made with Liquid-Propellant Rocket Engine Systems. CPIA Pub. No. 180, April 1969.
23. ANON: ICRPG Liquid-Propellant Thrust Chamber Performance Evaluation Manual. Working Group on Performance Standardization ICRPG, CPIA Pub. No. 178, Sept. 1968.
24. ANON: Injection and Combustion of Liquid Fuels. WADC Technical Report 56-344, ASTIA Document No. AD 118142 Battelle Memorial Institute, Wright Air Development Center, 1957.
25. ANON: IRIG Document 104-60 prepared by Tele-Communications Working Group, Inter-Range Instrumentation Group, Range Commanders Council; published by the Secretariat, Range Commanders Council, White Sands Missile Range, New Mexico 88002; April 1964, reprinted May 1966. (The above listed document covers IRIG Format A, Format B, Format C, Format D, and Format E. Other documents will cover reference time codes, as an example NASA 36-bit time code is covered by IRIG Document 104-59.)
26. ANON: Low-Flow, High-Response Flowmeter. Aerojet-General Technical Documentary Rept. AFRPL-TR-65-85, 1965.
27. ANON: Microscopy by Reconstructed Wave-Fronts. Proc. Roy. Soc., Vol. A197, 454–486, July 1949.
28. ANON: Microscopy by Reconstructed Wave-Fronts II. Proc. Phy. Soc. (London) B64, June 1951, pp. 449–469.
29. ANON: Performance and Properties of Liquid Propellants. Aerojet-General Rept. No. 8160–65, Apr. 1966.
30. ANON: Physical Measurements in Gas Dynamics and Combustion. Princeton University Press, Princeton, New Jersey, 1954.
31. ANON: Pulsed Laser Holography Techniques Applied to Chemical Rocket Propulsion. TRW Systems Rept. No. 4712.6.67-21, June 1968.
32. ANON: Research Summary No. 36-1, Volume 1 for the period 1 December 1959 to 1 February 1960. JPL, Feb. 1960.
33. ANON: Results of the Jupiter Engine Stability

Limits Evaluation Test Program. Rocketdyne Rept. R-2406, May 1960.

34. ANON: Review of Gas Sampling Techniques. Proceedings AFRPL, The Phase Flow Conference, AFRPL-TR-67-223, Vol. 1, March 1967.

35. ANON: Selection of Instrumentation for Analyzing Combustion Instability in Liquid Propellant Rocket Engines. CPIA Pub. No. 148, July 1967.

36. ANON: Special Consideration for Combustion Instability Instrumentation and Data Representation. CPIA Pub. No. 170, June 1968.

37. ANON: Stability Characterization of Advance Injectors–Final Report. Aerojet-General Rept. No. 20672-Fi, June 1968.

38. ANON: Stability Characterization of Advanced Injectors–Summary Final Report on Phase 1 of Contract NAS 8-20672. Aerojet-General Rept. 20672-PISF, Oct. 1968.

39. ANON: A Study of the Suppression of Combustion Oscillation with Mechanical Damping Devices. Pratt and Whitney Aircraft Quarterly Progress Rept. PWA FR-2491, June 1962.

40. ANON: A Study of the Suppression of Combustion Oscillations with Mechanical Damping Devices. Quarterly Progress Rept. No. 3, Pratt and Whitney Aircraft, PWA FR-960, April 1964.

41. ANON: A Study of the Suppression of Combustion Oscillations with Mechanical Damping Devices. Summary of Results for Tasks III through VI, Pratt and Whitney Aircraft, PWA FR-1330, Nov. 1964.

42. ANON: A Study of the Suppression of Combustion Oscillation with Mechanical Damping Devices–Final Report. Pratt and Whitney Aircraft, PWA FR 2596, Nov. 1967.

43. ANON: Symposium on Water Hammer. American Society of Mechanical Engineers, New York, 1933.

44. ANON: Turbulent Boundary Layer Nozzle Analysis Computer Program. Working Group on Performance Standardization, ICRPG. Available through CPIA, Aug. 1968.

45. ANON: Two-dimensional Kinetic Nozzle Analysis Computer Program. Working Group on Performance Standardization, ICRPG. Available through CPIA, Aug. 1968.

46. ABBE, C. J.; MCLAUGHLIN, C. W.; AND WEISS, R. R.: Influence of Storable Propellant Liquid Rocket Design Parameters on Combustion Instability. J. of Spacecraft and Rockets, Vol. 5, No. 5, May 1968, pp. 584–590.

47. ACRIVOS, A.; AND TAYLOR, T. D.: Heat and Mass Transfer from Single Spheres in Stokes Flow. Physics of Fluids, Vol. 5, No. 4, 1962, p. 387.

ABDOU, M. I.: See Ref. 247.

ADAMS, H. S.: See Ref. 315.

48. ADAMSON, T. C., JR.; AND SHEN, P. I. W.: Analysis of Transverse Combustion Instability in Liquid Propellant Rocket Motors Using a Two-Phase Detonation Wave Model. Sixth ICRPG Combustion Conference, CPIA Pub. No. 192, Vol. 1, Dec. 1969, pp. 135–140.

ADDOMS, J. F.: See Refs. 408 and 476.

49. ADELBERG, M.: Breakup Rate and Penetration of a Liquid Jet in a Gas Stream. AIAA Journal, Vol. 5, No. 8, Aug. 1967, p. 1408.

50. ADELBERG, M.: A Critical Velocity for Liquid Spray Fans. TN178-R-1-4-68. Published by Author, 4043 Cody Rd., Sherman Oaks, Calif., April 1968.

51. ADELBERG, M.: Mean Drop Size Resulting from the Injection of a Liquid Jet into a High-Speed Gas Stream. AIAA J., Vol. 6, No. 6, June 1968, p. 1143.

52. ADELBERG, M.: Three Advanced Micro-Orifice Injector Rocket Motors. J. Spacecraft and Rockets, Vol. 5, No. 3, Mar. 1968, pp. 353–355.

53. ADLER, J.: A One-Dimensional Theory of Liquid Fuel Rocket Combustion. Part II. The Influence of Chemical Reaction. A.R.C. Tech. Rept. No. 20-189, Current Paper No. 446, 1959.

54. AGOSTA, V. D.: Shock Wave Interaction With a Burning Solid Propellant. AIAA J., Vol. 4, 1966, p. 934.

55. AGOSTA, V.; HAMMER, S.; AND PESCHKE, W. T.: High Frequency Combustion Instability and Scaling of Liquid Propellant Rocket Motors. First ICRPG Combustion Instability Conference, Vol. 1, CPIA Pub. No. 68, Jan. 1965, pp. 153–164.

56. AGOSTA, V. D.; AND MAZZITELLI, D. A.: A Theoretical Study of the Forcing Functions in Axial Flow Turbojet Engines Due to Flow Pulsations. Wright Air Development Center, Tech. Rept. 56-74, 1956.

AGOSTA, V. D.: Also see Refs. 132, 306, 307, 308, and 481.

57. AGOSTON, G. A.; WISE, H.; AND ROSSER, W.: Dynamic Factors Affecting the Combustion of Liquid Spheres. Sixth Symposium (International) on Combustion, Reinhold, New York, 1957, pp. 708–717.

58. AGOSTON, G. A.; WOOD, B. J.; AND WISE, H.: Influence of Pressure on the Combustion of Liquid Spheres. Jet Propulsion, Vol. 28, 1958, p. 181.

AGOSTON, G. A.: Also see Ref. 752.

59. ALBRIGHT, L. F.; AND ALEXANDER, L. G.: Stable Cyclonic Flames of Natural Gas and Air. Jet Propulsion, Vol. 26, No. 10, Oct. 1956, pp. 867–873.

60. ALBER, I. E.: Comparison and Evaluation of Computer Programs for Rocket Engine Performance Prediction. Contract NAS 7-443, SN-82, Dynamic Science, Irvine, Calif., April 1968.

ALEXANDER, L. G.: See Ref. 59.

61. ALLEN, W. D.: Experimental Studies of Transverse Waves in a Cylindrical Chamber. Princeton University Aeronautical Engineering Rept. No. 607, June 1962.

62. ALPHER, R. A.; AND WHITE, D. R.: Flow in Shock Tubes with Area Change at Diaphragm Section. J. of Fluid Mech., Vol. 3, Feb. 1968, p. 457.

63. ALTMAN, D.; CARTER, J. M.; PENNER, S. S.; AND SUMMERFIELD, M.: Liquid Propellant Rockets. Princeton Aeronautical Paperbacks, Princeton University Press, New Jersey, 1960.

64. ALTMAN, D.; AND PENNER, S. S.: Combustion of Liquid Propellants. Section L (pp. 470–513), Vol. II, High Speed Aerodynamics and Jet Propulsion-Combustion Processes, (B. Lewis, R. Pease, H. S. Taylor, eds.), Princeton Univ. Press, Princeton, N. J., 1956.

65. ALTSEIMER, J. H.: Photographic Techniques Applied to Combustion Studies. JARS, Vol. 22, No. 2, March–April 1952, pp. 86–91.

66. ANGELO, E. J.: Electronic Circuits. McGraw Hill, New York, 1958.

ANDERSON, G. Y.: See Ref. 696.

ANDERSON, W. H.: See Ref. 755.

ANTL, R. J.: See Ref. 679.

67. ARBIT, H. A.: Design, Assembly, and Operation of a High-Pressure Two-Dimensional Research Motor. Rocketdyne Research Rept. No. 64-16, May 1964.

ARBIT, H. A.: Also see Ref. 221.

ARMITAGE, A. L.: See Ref. 408.

ARNDT, F. E.: See Ref. 750.

ARUNACHALAM, S. A.: See Ref. 240.

68. ATHERTON, R. R.: Applications Study for a High Performance Cryogenic Staged Combustion Rocket Engine. Pratt & Whitney Tech. Rept. AFRPL-RE-67-270, Nov. 1967.

69. ATHERTON, R. R.: Advanced Cryogenic Rocket Engine Program Staged-Combustion Concept, Final Report. Volumes I through III, Pratt & Whitney Tech. Rept. AFRPL-TR-67-298, Dec. 1967.

70. BAILEY, C. R.: Acoustic Liner for the C-1 Engine. Fifth ICRPG Combustion Conference, CPIA Publication No. 183, Dec. 1968, pp. 335–341.

71. BAILEY, C. R.: An Investigation of the Use of Acoustic Energy Absorbers to Damp LOX/RP-1 Combustion Oscillations. NASA TN D-4210, Nov. 1967.

72. BAILEY, T. E.: Research on a Hydrogen-Fluorine Propulsion System—Final Report. Pratt & Whitney Aircraft, NASA CR-70274, Oct. 1966.

73. BAKER, D. I.: Mixture Ratio and Temperature Surveys of Ammonia-Oxygen Rocket-Motor Combustion Chambers. JPL Rept. No. 25-2, Jan. 1954.

74. BAKER, P. D.; PEOPLES, R. G.; AND MILLS, T. R.: Two-Dimensional Motor Program. Aerojet General Rept. No. 2185, Jan. 1962.

BAKER, P. D.: Also see Refs. 172, 540, and 541.

BALDWIN, C. D.: See Ref. 286.

75. BALLING, N. R.; AND CONNER, B. U.: An Electromagnetic Flow meter for Low Conductivity Fluids. JPL Rept. No. 32-329, Aug. 1962.

76. BAMBANEK, R. A.; AND LEVINE, R. S.: A Sustaining Mechanism for the Transverse Acoustical Mode of Combustion Instability. A paper appended to Rocketdyne Research Rept. No. 8, Feb. 1956.

BAMBANEK, R.: Also see Ref. 441.

77. BARCHILON, M.; AND CURTET, R.: Some Details of the Structure of an Axisymmetric Confined Jet with Backflow. Trans. A.S.M.E, J. Basic Eng., Vol. 86, 1964, pp. 777–787.

78. BARRERE, M., ET AL.: Rocket Propulsion. Elsevier Publishing Co., New York, 1960.

79. BARRERE, M.; AND NADAUD, L.: Combustion of Ammonium Perchlorate Spheres in a Flowing Gaseous Fuel. Tenth Symposium (International) Combustion, The Combustion Institute, Pittsburgh, 1965, pp. 1381–1394.

BARSIC, N.: See Ref. 224.

80. BARTLETT, R. C.; AND NAGAI, C. K.: Design Criteria for Space Storable Propellants. Ninth Liquid Propulsion Symposium, CPIA Pub. No. 162, Vol. 1, 1967.

81. BARTZ, D. R.: A Simple Equation for Rapid Estimation of Rocket Nozzle Convective Heat Transfer Coefficients. Jet Propulsion, Vol. 27, No. 1, Jan. 1957, p. 49.

BARTZ, D. R.: Also see Ref. 241.

BASTIANON, R.: See Ref. 496.

82. BASTRESS, E. K.; HARRIS, G. H.; AND MILLER, I.: Statistical Derivation of Design Criteria for Liquid Rocket Combustion Instability. Arthur D. Little, NASA CR-72370, Dec. 1967.

BASTRESS, E. K.: Also see Ref. 247.

83. BAUER, J. M.; and REEVES, D. F.: Radial Flow Injector Development for Metallized Gelled Fuels at Temperature Extremes. NWC TP 4616, Nov. 1968.

84. BECKER, H. A.; HOTTEL, H. C.; AND WILLIAMS, G. C.: Mixing and Flow in Ducted Turbulent Jets. Ninth Symposium (International) on Combustion, Academic Press, New York, 1963, pp. 7–18.

85. BELL, G. S.: Second Monthly Status Report–Development and Demonstration of an N_2O_4/N_2H_4 Injector. Document 10287-MSR-2, AFRPL, June 1968.

86. BELL, H. S., ET AL.: C-1 Engine Final Report, C-1 Engine Instability Investigation. Reaction Motors (Thiokol) Rept. RMD 6203-S 6, July 1967.

BELLMAN, D. R.: See Ref. 688.

87. BELTRAN, M. R., ET AL.: Analysis of Liquid Rocket Engine Combustion Stability. Dynamic Science, AFRPL-TR-65-254, 1965.

88. BELTRAN, M. R.; BREEN, B. P.; AND GERSTEIN, M.: Liquid Rocket Engine Combustion Instability Studies. Dynamic Science Semi-Annual Rept. No. SN-68-SL, June 1965.

89. BELTRAN, M. R.; BREEN, B. P.; HOFFMAN, R. J.; KOSVIC, T. C.; AND SANDERS, C. F.: Analysis of Liquid Rocket Engine Combustion Instability. Special Report, Dynamic Science Rept. No. SN-68-52, Jan. 1966, (AD 482 021).

90. Beltran, M. R.; and Kosvic, T. C.: Parametric Study of Combustion Instability in MMH-NTO Liquid Rocket Engine. AIAA Paper No. 66-603, June 1966.

91. Beltran, M. R.; Wright, R. O.; Breen, B. P.; et al.: Combustion Stability Limits Calculated Utilizing a Nonlinear Model. Final Report on Contract NAS 7-366, Dynamic Science Rept. No. SN-70-F, Aug. 1966.

Beltran, M. R.: Also see Refs. 118 and 358.

92. Benedict, A. G.: Reliability-Confidence Combinations for Small-Sample Tests of Aerospace Ordnance Items. JPL Tech. Rept. 32–1165, July 1968.

93. Beranek, L. L.: Acoustics. McGraw Hill, New York, 1954.

94. Berls, G. O.; and Ensminger, J. F.: Stability Correlation Between the Pulse Motor Combustion Tool and a Full-scale Engine. AFRPL Tech. Rept. No. AFRPL-TR-69-184, Aug. 1969.

95. Berman, K.; and Cheney, S. H., Jr.: Rocket Motor Instability Studies. Jet Propulsion, Vol. 25, No. 10, Oct. 1955.

96. Berman, K.; and Logan, S. E.: Combustion Studies with a Rocket Motor Having a Full-Length Observation Window. JARS, Vol. 22, No. 2, March–April 1952.

97. Bevans, R. S.: Mathematical Expressions for Drop Size Distributions in Sprays. Conference on Fuel Sprays, University of Michigan, March 1949.

98. Bickford, L. L.; and Meisenholder, S. G.: "POGO" Analysis of the Saturn Propulsion System. Aerojet-General AMDR 9635-037, April 1967.

Biot, M. A.: See Ref. 713.

99. Bird, R. B.; Stewart, W. E.; and Lightfoot, E. N.: Transport Phenomena. J. Wiley and Sons, New York, 1960.

100. Bittker, D. A.: An Analytical Study of Turbulent and Molecular Mixing in Rocket Combustion. NACA TN 4321, Sept. 1958.

101. Bittker, D. A.: Effect of Ambient Air Velocity on Atomization of Two Impinging Water Jets. NASA TN D-2087, 1964.

102. Black, G. R.; and Harrje, D. T.: Mixture Ratio Survey Technique Based on Propellant Temperature Differences. Fourth ICRPG Combustion Conference, CPIA Publication No. 162, Vol. 1, Dec. 1967, pp. 281–285.

103. Blackburn, J. R.; Reethof, G.; and Shearer, J. L.: Fluid Power Control. Technology Press of M.I.T., 1960.

104. Blackman, A. W.: Effect of Nonlinear Losses on the Design of Absorbers for Combustion Instabilities. J. Amer. Rocket Soc., Vol. 30, No. 11, Nov. 1960, pp. 1022–1028.

105. Blackman, A. W.: An Investigation of Afterburner Screech on Small Scale Combustor. UAC Research Laboratory Report R-26597-2, March 1954.

Blackman, A. W.: Also see Ref. 702.

Blankenship, V. D.: See Ref. 144.

106. Bloomer, H. E.; Wanhainen, J. P.; and Vincent, D. W.: Chamber Shape Effects on Combustion Instability. Fourth ICRPG Combustion Conference, CPIA Pub. No. 162, Vol. 1, Dec. 1967, pp. 39–55.

107. Bloomer, H. E.; Wanhainen, J. P.; and Vincent, D. W.: Chamber Shape Effects on Combustion Instability. NASA TM X-52361, 1967.

Bloomer, H. E.: Also see Refs. 309, 711, 714, and 775.

108. Bolt, R. H.; Labate, S.; and Ingard, U.: The Acoustic Reactance of Small Circular Orifices. Journal of the Acoustical Society of America, Vol. 21, No. 2, 1949.

109. Bonnell, J. M.: Combustion Stability in an Annular Gas Combustor. AIAA J., Vol. 6, Oct. 1968, p. 1941.

110. Bonnell, J. M.: An Investigation of Spherical Blast Waves and Detonation Waves in a Rocket Combustion Chamber. JPL Tech. Rept. 32-1286, Aug. 1968.

Bonnell, J. M.: Also see Ref. 775.

111. Bonner, B. H.; and Jackman, P.: Studies of Propellant Injection Processes. Rocket Propulsion Establishment, Westcott, Gr. Britain.

112. Borman, G. L.; El Wakil, M. J.; Uyehara, O. A.; and Myers, P. S.: Graphs of Reduced Variables for Computing Histories of Vaporizing Fuel Drops and Drop Histories Under Pressure. NACA TN 4338, Sept. 1958.

Borman, G. L.: Also see Ref. 562.

113. Bowman, C. T.; and Glassman, I.: Longitudinal Combustion Instability Studies Using a Gaseous Propellant Rocket Motor. First ICRPG Combustion Instability Conference, CPIA Pub. No. 68, Jan. 1965, pp. 125–138.

114a. Bracco, F. V.: The "Direct" Method as Applied to Liquid Rocket Engine Combustion and Explosion Problems. Ph. D. Thesis, Princeton University Dept. of Aerospace and Mechanical Sciences Rept. No. 902, pp. 65–91, June 1970.

114b. Bracco, F. V.; and Harrje, D. T.: The Direct Method Applied to Steady Liquid Propellant Combustion: Investigation of Several Droplet Burning Models for a LOX/Ethanol Engine. Sixth ICRPG Combustion Conference, CPIA Pub. No. 192, Vol. 1, Dec. 1969, pp. 85–91.

115. Bracco, F. V.; Harrje, D. T.; and Crocco, L.: Use of Shock Waves to Study Combustion Parameters. Fifth ICRPG Combustion Conference, CPIA Pub. No. 183, Dec. 1958, pp. 313–320.

116. Bragg, S. L.; and Smith, I. E.: Heat Transfer to Rocket Engine Injectors. Paper presented at joint meeting A.S.M.E. and I. Mech. E. International Developments in Heat Transfer, 1961.

117. Breen, B. P., et al.: Injection and Combustion of Hypergolic Propellants, Part II, Extension

of Steady-state Combustion Model. Dynamic Science Final Tech. Rept. AFRPL-TR-69-48, April 1969.

118. BREEN, B. P.; AND BELTRAN, M. R.: Steady State Droplet Combustion with Decomposition; Hydrazine/Nitrogen Tetroxide. Paper presented at the AIChE 61st National Meeting, Feb. 1967.

119. BREEN, B. P.; AND LAWVER, B. R.: Effect of Additives on Hydrazine Droplet Combustion. Fourth ICRPG Combustion Conference, CPIA Pub. No. 162. Vol. I, Dec. 1967, p. 287.

BREEN, B. P.: Also see Refs, 88, 89, 91, 140, 353, 358, 359, 410, 430, and 484.

120. BRIDGE, J. F.; AND ANGRIST, S. W.: An Extended Table of Roots of $J'_n(x)Y'_n(\beta x) - J'_n(\beta x)Y'_n(x) = 0$. Mathematics of Computation, Vol. 16, No. 78, 1962, pp. 198–204.

BRIKOWSKI, H. J.: See Ref. 249.

BRIONES, R. A.: See Ref. 765.

121. BRODE, H. L.: Blast Wave from a Spherical Charge. Physics of Fluids, Vol. 2, Pt. 2, Mar.–Apr. 1959, p. 217.

122. BROKAW, R. S.: Analytical Solution to the Ignition Kinetics of the Hydrogen Oxygen Reaction. Tenth Symposium (International) on Combustion, The Combustion Institute, 1965, pp. 269–278.

123. BROOKS, R. E.; HEFLINGER, L. O.; AND WUERKER, R. F.: Pulsed Laser Holograms. IEEE J. of Quantum Electronics, QE-2, No. 8, Aug. 1966, pp. 275–279.

124. BRZUSTOWSKI, T. A.: Chemical and Physical Limits on Vapor-Phase Diffusion Flames of Droplets. Can. J. Chem. Eng., 43, 1965, p. 30.

125. BRYAN, R.: The Sampling of Rocket Combustion Gases. J. of the Aero. Soc., Vol. 68, Nov. 1964, pp. 759–763.

BUDNIK, C.: See Ref. 361.

126. BUFFUM, F. G.; DEHORITY, G. L.; AND SLATES, R. O.: Acoustic Attenuation in Resonant Model-Rocket Motors. AIAA/ICRPG Second Solid Propulsion Conference, 1967, pp. 173–180.

127. BUFFUM, F. G., JR.; DEHORITY, G. L.; SLATES, R. O.; AND PRICE, E. W.: Acoustic Attenuation Experiments on Subscale, Cold-Flow Rocket Motors. AIAA J., Vol. 5, No. 2, Feb. 1967, pp. 272–280.

BUGLER, G. J.: See Ref. 268.

128. BURKE, S. P.; AND SCHUMANN, T. E. W.: Diffusion Flames. Ind. Eng. Chemistry, Vol. 20, No. 10, Oct. 1928, p. 998.

129. BURROWS, M. C.: Radiation Processes Related to Oxygen/Hydrogen Combustion at High Pressures. Tenth Symposium (International) on Combustion, The Combustion Institute, 1965, pp. 207–215.

130. BURROWS, M. C.: Thermal Radiation as a Tool in Analyzing Unstable Combustion. First ICRPG Combustion Instability Conference, CPIA Pub. No. 68, Vol. 1, 1964, pp. 301–309.

131. BURSTEIN, S. Z.; AND CHINITZ, W.: Nonlinear Combustion Instability in Liquid-Propellant Rocket Motors. First, Second, Third and Fourth Quarterly Reports to JPL, Contract NAS7-100, Mathematical Applications Group, White Plains, New York, 1967–1968.

132. BURSTEIN, S. Z.; HAMMER, S. S.; AND AGOSTA, V. D.: Spray Combustion Model with Droplet Breakup: Analytical and Experimental Results, in Detonation and Two-Phase Flow, Vol. 6 of Progress in Astronautics and Rocketry (eds., S. S. Penner and F. A. Williams). Academic Press, New York, 1962, pp. 243–267.

BURSTEIN, S. Z.: Also see Ref. 697.

133. BUZUKOV, A. A.: The Breakup of Drops and a Fluid Stream by an Air Shock Wave. J. App. Mech. and Tech. Phys., FTD-TT- 63-839 (AD 435996), Foreign Technology Division, Jan. 1964.

134. BUZUKOV, A. A.: J. App. Mech. and Tech. Phys. (Collection of Articles), FTD-MT-64-87, Machine Translation by Foreign Technical Division, Wright-Patterson AFB, Ohio, 1966.

135. CAMPBELL, D. T.: Combustion Instability Analysis at High Chamber Pressures. Rocketdyne, AFRPL-TR-67-222, Aug. 1967.

135b. CAMPBELL, D. T., ET AL.: Reaction Stream Separation Photography–Interim Report. Rocketdyne Rept. R 81-10, Jan. 1970.

136. CAMPBELL, D. T.; AND CHADWICK, W. D.: Combustion Instability Analysis at High Chamber Pressure–Final Report. Rocketdyne AFRPL-TR-68-179, 1968.

137. CANTRELL, R. H.; AND HART, R. W.: Interaction Between Sound and Flow in Acoustic Cavities: Mass, Momentum, and Energy Considerations. J. Acoustical Soc. Amer., Vol. 36, No. 4, 1964, p. 697.

CARHART, R. R.: See Ref. 251.

CARTER, J. M.: See Ref. 63.

CAWOOD, G. W.: See Ref. 145.

CHADWICK, W. D.: See Refs. 136 and 509.

CHENEY, S. H., JR.: See Ref. 95.

CHENG, S. I.: See Ref. 179.

137b. CHERVINSKY, A.: Supercritical Burning of Liquid Droplets in Stagnant Environment. AIAA J., Vol. 7, July 1969, pp. 1815–1817.

138. CHESTNUT, H.; AND MAYER, R. W.: Servomechanisms and Regulating System Design. Wiley, 1955, Chapter 8.

CHEW, T. J. C.: See Ref. 728.

139. CHILDS, D. W.: Modal Simulation of Unidirectional Fluid Dynamics (Water Hammer). Simulation, Sept. 1965.

CHINITZ, W.: See Ref. 131.

140. CHOUDHURY, P. R.; KOSVIC, T. C.; NICKERSON, G. R.; AND BREEN, B. P.: Monopropellant Droplet Burning. Final Report on Contract NAS 7-467, Dynamic Science, 1968.

141. CHU, B. T.: Mechanism of Generation of Pressure

Waves at Flame Fronts. Johns Hopkins University, NACA TN 3683, 1956.

142. CHU, B. T.: Stability of Systems Containing a Heat Source by the Rayleigh Criterion. NACA RM 56D27, 1956.

143. CHU, B. T.; AND YING, S. J.: Thermally Driven Nonlinear Oscillations in a Pipe with Travelling Shock Waves. AFOSR-TN-686, (AD267069), Apr. 1961.

144. CHUNG, P. M.; AND BLANKENSHIP, V. D.: Equilibrium Structure of Thin Diffusion Flame Zone. Aerospace Corp. Rept. No. TR-669, (S6240-10)-1, Dec. 1965.

145. CLAPP, S. D.; AND CAWOOD, G. W.: Development of Injector Design Criteria Applicable to the Booster and Sustainer Engines of the Lance Missile. Rocketdyne Research Rept. No. 63-40, Dec. 1963.

CLAPP, S. D.: Also see Refs. 221 and 258.

146. CLARK, B. J.: Breakup of a Liquid Jet in a Transverse Flow of Gas. NASA TN D-2424, 1964.

147. CLAYTON, R. M.: The Influence of Several Near-Wall Injection Conditions on the Combustion Performance of a Liquid Rocket Engine. JPL Tech. Rept. No. 32-1283, Sept. 1968.

148. CLAYTON, R. M.: Resonant Combustion. JPL Space Programs Summary 37-49, Vol. III, Feb. 1968, pp. 223–236.

149. CLAYTON, R. M.: Resonant Combustion. JPL Space Programs Summary 37–56, Vol. III, April 1969, pp. 204–212. (Expanded form to be published as JPL Tech. Rpt. 32-1479, late 1970.)

150. CLAYTON, R. M.: Some Effects of Near-Wall Injection on Steady and Nonsteady Liquid Rocket Combustion Behavior. Fourth ICRPG Combustion Conference, CPIA Pub. No. 162, Vol. 1, Dec. 1967.

151. CLAYTON, R. M.; AND ROGERO, R. S.: Experimental Measurements on a Rotating Detonation-Like Combustion. JPL Tech. Rept. No. 32-788, Aug. 1965.

152. CLAYTON R. M.; ROGERO, R. S.; and SOTTER, J. G.: An Experimental Description of Destructive Liquid Rocket Resonant Combustion. AIAA Journal, Vol. 6, No. 7., July 1968, p. 1252.

153. CLAYTON, R. M.; RUPE, J. H.; AND GERBRACHT, F. G.: An Experimental Correlation of the Nonreactive Properties of Injection Schemes and Combustion Effects in a Liquid-Propellant Rocket Engine, Part II. JPL Tech. Rept. No. 32-255, May 1967.

154. CLAYTON, R. M.; SOTTER, J. G.; AND WOODWARD, J. W.: Resonant Combustion. JPL Space Programs Summary 37–41, Vol. IV, Oct. 1966, pp. 134–151.

CLAYTON, R. M.: Also see Refs. 618 and 655.

155. CLINE, G. L.; FORD, W. M.; HERGET, W. F.; AND SCHUMACHER, P. E.: Radiative and Structural Characteristics of Rocket Exhaust Plumes. Rocketdyne Rept. R-6742, Sept. 1966.

CLINE, G. L.: Also see Ref. 275.

156. CLINGER, E. C.: A Report on the F-1 Combustion Stability Development. Third ICRPG Combustion Conference, CPIA Pub. No. 138, Vol. 1, Feb. 1967, p. 359.

COATS, D. C.: See Refs. 266 and 410.

157. COLBERT, J. E.: Use of an Acoustic Liner to Attenuate FLOX-Light Hydrocarbon Instability. Fourth ICRPG Combustion Conference, CPIA Pub. No. 162, Vol. I, Dec. 1967, p. 271.

COLBERT, J. E.: Also see Ref. 467.

COLEMAN, B.: See Ref. 587.

158. COMBS, L. P.: Calculated Propellant Droplet Heating under F-1 Combustion Chamber Conditions. Rocketdyne Research Rept. No. 64-25, June 1964.

159. COMBS, L. P.: Mixing processes in Liquid Propellant Rocket Combustion Chambers–A Review. Paper presented at joint meeting of the American Institute of Chemical Engineers and the Institution of Chemical Engineers, London, 1965.

160. COMBS, L. P.: Rating of the A7 and A6 Redstone Engines by Gas Pulse Initiated Combustion Instability, Summary Report. Rocketdyne Research Memorandum RM 528/91, July 1959.

161. COMBS, L. P.: A Summary of Experience with Combustion Stability Rating Techniques. Second ICRPG Combustion Conference, CPIA Pub. No. 105, Vol. 2, May 1966.

162. COMBS, L. P.; AND HOEHN, F. W.: Steady-State Rocket Combustion of Gaseous Hydrogen and Liquid Oxygen, Part I: Experimental Investigation. Rocketdyne, Research Rept. No. 64-24, June 1964.

163. COMBS, L. P.; HOEHN, F. W.; WEBB, S. R.; ET AL.: Combustion Stability Rating Techniques–Final Report. Rocketdyne, AFRPL-TR-66-229, Sept. 1966.

164. COMBS, L. P.; AND LAMBIRIS, S.: Stabilization of Liquid Propellant Rocket Combustion by Combustion Chamber Baffles. Bulletin of the Second Meeting of the JANAF Liquid Propellant Group, LPIA. Applied Physics Lab., Johns Hopkins University, Nov. 1960, pp. 565–568.

165–166. COMBS, L. P.; AND SCHUMAN, M. D.: Steady-State Rocket Combustion of Liquid Oxygen and Gaseous Hydrogen, Part II: Analysis for Coaxial Jet Injection. Rocketdyne Research Rept. RR 64–29, 1965, and RR 64–25, 1964.

167. COMBS, L. P.; SCHUMACHER, P. E.; KESSELRING, R. C.; AND KULUVA, N. M.: Improvement of Bombs and Pulse Guns as Stability Rating Devices—Final Report. Rocketdyne, AFRPL-TR-68-18, March 1968.

COMBS, L. P.: Also see Refs. 272, 419, 420, 421, 425, 426, and 427.

168. CONN, T. E.; HESTER, J. N.; AND VALENTINE, R. S.: Experimental Effects Upon Rocket Injector/Chamber Compatibility. Journal of Spacecraft

and Rockets, Vol. 4, No. 12, Dec. 1967, pp. 1581–1585.

CONNER, B. U.: See Ref. 75.

CONRAD, E. W.: See Refs. 310, 311, 652, 690, and 719.

169. CONVERSE, J. W.; AND HOFFMAN, J. D.: Acoustic Standing Waves in a Rocket Combustion Chamber with Ring and Spoke Baffles. Purdue University, TM-67-5, Aug. 1967.

170. COULTAS, T. A.; AND KESSELRING, R. C.: Extension of the Priem Theory and Its Use in Simulation of Instability on the Computer. Second ICRPG Combustion Conference, CPIA Pub. No. 105, May 1966.

COULTAS, T. A.: Also see Ref. 222.

COURTNEY, W.: See Ref. 361.

171. CRAMER, F. B.: The Onset of Detonation in a Droplet Combustion Field. Ninth Symposium (International) on Combustion, Academic Press, New York, 1963, p. 482.

172. CRAMER, F. B.; AND BAKER, P. D.: Combustion Processes in a Bipropellant Liquid Rocket Engine. JPL Rept. No. 900-2, Jan. 1967.

173. CROCCO, L.: Aspects of Combustion Instability in Liquid Propellant Rockets. JARS Part I, Vol. 21, Nov. 1951, Part II, Vol. 22, Jan. 1952.

174. CROCCO, L.: Comments on the Zucrow-Osborn Paper on Combustion Oscillations. Jet Propulsion, Vol. 28, No. 12, Dec. 1958, p. 843.

175. CROCCO, L.: Considerations on the Problem of Scaling Rocket Motors. AGARD Selected Combustion Problems, Vol. 2, Butterworths Scientific Publications, London, 1956, pp. 457–468.

176. CROCCO, L.: The Relevance of a Characteristic Time in Combustion Instability. Second ICRPG Combustion Conference, CPIA Pub. No. 105, Vol. 1, May 1966, p. 115.

177. CROCCO, L.: Research on Combustion Instability in Liquid Propellant Rockets. Twelfth Symposium (International) on Combustion, The Combustion Institute, 1969.

178. CROCCO, L.: Theoretical Studies on Liquid Propellant Rocket Instability. Tenth Symposium (International) on Combustion, The Combustion Institute, 1965, p. 1101.

179. CROCCO, L.; AND CHENG, S. I.: Theory of Combustion Instability in Liquid Propellant Rocket Motors. AGARDograph No. 8, Butterworths Sci. Pub. Ltd., London, 1956.

180. CROCCO, L.; GREY, J.; AND HARRJE, D. T.: Theory of Liquid Propellant Rocket Combustion Instability and Its Experimental Verification. ARS J., Vol. 30, No. 2, Feb. 1960, pp. 159–168.

181. CROCCO, L.; GREY, J.; AND HILLIARD, F.: Combustion Instability in Liquid Rocket Motors—Fourteenth Quarterly Progress Report. Princeton University Aero Eng. Rept. No. 216-n, Dec. 1955.

182. CROCCO, L.; GREY, J.; AND MATTHEWS, G. B.: Preliminary Measurement of the Combustion Time Lag in a Monopropellant Rocket Motor. Fifth Symposium (International) on Combustion, Reinhold, 1965.

183. CROCCO, L.; AND HARRJE, D. T.: Combustion Instability in Liquid Propellant Rocket Motors. Experimental Methods in Combustion Research, J. Surugue, ed., Pergamon Press, London, 1961.

184. CROCCO, L.; AND HARRJE, D. T.: Nonlinear Aspects of Combustion Instability in Liquid Propellant Rocket Motors. First ICRPG Combustion Instability Conference, CPIA Pub. No. 68, Jan. 1965, pp. 47–72.

185. CROCCO, L.; HARRJE, D. T., ET AL.: Nonlinear Aspects of Combustion Instability in Liquid Propellant Rocket Motors. Princeton University Aero. Eng. Rept. No. 553, June 1961.

186. CROCCO, L.; HARRJE, D. T., ET AL.: Nonlinear Aspects of Combustion Instability in Liquid Propellant Rocket Motors–Third Yearly Progress Report. Princeton University, Aero. Eng. Rept. 553c, June 1963.

187. CROCCO, L.; HARRJE, D. T.; AND REARDON, F. H.: Transverse Combustion Instability in Liquid Propellant Rocket Motors. ARS J., Vol. 32, No. 3, March 1962, pp. 366–373.

188. CROCCO, L.; HARRJE, D. T.; SIRIGNANO, W. A.; ET AL.: Nonlinear Aspects of Combustion Instability in Liquid Propellant Rocket Motors–Fourth Yearly Progress Report. Princeton University Dept. of Aerospace and Mechanical Sciences Rept. 553d, June 1964.

189. CROCCO, L.; HARRJE, D. T.; AND SIRIGNANO, W. A.: Nonlinear Aspects of Combustion Instability in Liquid Propellant Rocket Motors. Second ICRPG Combustion Conference, CPIA Pub. No. 105, May 1966, pp. 63–105.

190. CROCCO, L.; HARRJE, D. T.; SIRIGNANO, W. A.; ET AL.: Nonlinear Aspects of Combustion Instability in Liquid Propellant Rocket Motors–Fifth Yearly Progress Report. Princeton University Dept. of Aerospace and Mechanical Sciences Rept. 553e, June 1965.

191. CROCCO, L.; HARRJE, D. T.; SIRIGNANO, W. A.; ET AL.: Nonlinear Aspects of Combustion Instability in Liquid Propellant Rocket Motors–Sixth Yearly Progress Report. Princeton University Dept. of Aerospace and Mechanical Sciences Rept. 553f, June 1966.

192. CROCCO, L.; HARRJE, D. T.; SIRIGNANO, W. A.; ET AL.: Nonlinear Aspects of Combustion Instability in Liquid Propellant Rocket Motors. Princeton University, NASA CR 72270, June 1967.

193. CROCCO, L.; HARRJE, D. T.; SIRIGNANO, W. A.; ET AL.: Nonlinear Aspects of Combustion Instability in Liquid Propellant Rocket Motors. Princeton University, NASA CR 72426, June 1968.

194. CROCCO, L.; AND MITCHELL, C. E.: Nonlinear Periodic Oscillations in Rocket Motors with Dis-

tributed Combustion. Combustion Science and Technology, Vol. 1, No. 2, 1969.

195. Crocco, L.; Monti, R.; and Grey, J.: Verification of Nozzle Admittance Theory by Exact Measurement of the Admittance Parameter. ARS J., Vol. 31, No. 6, June 1961, pp. 771–775.

196. Crocco, L.; and Sirignano, W. A.: Behavior of Supercritical Nozzles under Three-Dimensional Oscillatory Conditions. AGARDograph No. 117, 1967.

197. Crocco, L.; and Sirignano, W. A.: Effect of the Transverse Velocity Component on the Nonlinear Behavior of Short Nozzles. AIAA J, Vol. 4, No. 8, Aug. 1966, pp. 1428–1430.

198. Crocco, L.; Tang, P.; and Varma, A. K.: Theoretical Analysis of Nonlinear Transverse Combustion Instability in Liquid Propellant Rocket Motors Using a Droplet Evaporation Model. Fifth ICRPG Combustion Conference, CPIA Pub. No. 183, Dec. 1968.

Crocco, L.: Also see Refs. 115, 321, 322, 323, 489, 583, 646, 647, and 671.

199. Crowe, C. T.; Nicholls, J. A.; and Morrison, R. B.: Drag Coefficients of Inert and Burning Particles Accelerating in a Gas. Ninth Symposium (International) on Combustion, Academic Press, 1963.

200. Cruttenden, A. J.: Estimation of Reaction Ratio Fluctuations in Rocket Combustion Gases from Gas-sampling Measurements. R. P. E. Westcott, Great Britain, Tech. Rpt. No. 68/9, Oct. 1968.

201. Cruttenden, A. J.; and Jackman, P.: Unpublished work at R. P. E., Westcott, Gr. Britain.

202. Culick, F.E.C.: Stability of High Frequency Pressure Oscillations in Gas and Liquid Rocket Combustion Chambers. M.I.T. Aerophysics Laboratory Rept. 480, June 1961.

203. Culick, F. E. C.: Stability of High-Frequency Pressure Oscillations in Rocket Combustion Chambers. AIAA J, Vol. 1, No. 5, 1963, pp. 1097–1104.

204. Culick, F. E. C.; and Dehority, G. L.: An Analysis of Axial Acoustic Waves in a Cold-Flow Rocket. NWC TP 4544, Naval Weapons Center, China Lake, California, May 1968.

Cullen, R. E.: See Ref. 512.

Curley, J. K.: See Ref. 714.

205. Curtet, R.: Confined Jets and Recirculation Phenomena with Cold Air. Combustion and Flame, Vol. 2, 1958, pp. 383–411.

Curtet, R.: Also see Ref. 77.

206. Dabora, E. K.: Production of Monodisperse Sprays. Rev. Sci. Instr., Vol. 38, No. 4, Apr 1967, p. 502.

207. Dabora, E. K.; Ragland, K. W.; and Nicholls, J. A.: Drop Size Effects in Spray Detonations. Twelfth Symposium (International) on Combustion, The Combustion Institute, Pittsburgh, 1969.

208. Dabora, E. K.; Ragland, K. W.; and Nicholls, J. A.: A Study of Heterogeneous Detonations. Astronautica Acta, Vol. 12, 1966, p. 9.

209. Dabora, E. K.; Ragland, K. W.; and Ranger, A. A.: Two Phase Detonation and Drop Shattering Studies. University of Michigan, NASA CR-72225, April 1967.

210. Dabora, E. K.; Ragland, K. W.; Ranger, A. A.; and Nicholls, J. A.: Detonation in Two Phase Media and Drop Shattering Studies. University of Michigan, NASA CR-72421, 1968.

211. Dabora, E. K.; Ragland, K. W.; Ranger, A. A.; and Nicholls, J. A.: Two-Phase Detonations and Drop Shattering Studies—Second Annual Progress Report. University of Michigan, Rept. No. 06324-2-T, 1966.

Dabora, E. K.: Also see Refs. 513 and 572.

212. Dahlberg, D. E.: Combustion Instability for Liquid Oxygen and Liquid and Cold Gas Hydrogen Propellants—Phase II, Final Report. Pratt & Whitney Aircraft FR-1374, May 1965.

213. Damköhler, G.: Einflüsse der Strömung, Diffusion und des Wärmeuberganges auf die Leistung von Reaktionsofen. Z. Electrochem, Vol. 42, 1936, pp. 846–862.

214. Dankwerts, P. V.: Effect of Incomplete Mixing on Homogeneous Reactions. Chem. Eng. Sci., Vol. 7, 1958, pp. 93–102.

Datner, P. P.: See Refs. 539 and 603.

215. Datsko, S. C.; and Tomazic, W. A.: Stability and Performance Comparison of the M-1 Injector With and Without Baffles. Fourth ICRPG Combustion Conference, CPIA Pub. No. 162, Vol. 1, Dec. 1967, p. 1.

216. Davis, L. R.: Effects of Injection Location on Combustion Instability in Premixed Gaseous Bipropellant Rocket Motors. MSME Thesis, Purdue University, Jan. 1961.

Davis, L. R.: Also see Ref. 527.

217. D'Azzo, J. J.; and Houpis, C. H.: Feedback Control System Analysis and Synthesis. McGraw-Hill, 1960, p. 442.

Dean, L. E.: See Refs. 554 and 703.

218. DeCorso, S. M.: Effect of Ambient and Fuel Pressure on Spray Drop Size. Trans. ASME, Vol. 82, Series A, 1962, p. 10.

219. DeCorso, S. M.: Spray Distribution and Drop Size from a Swirl Atomizer. ASME Paper No. 61-WA-300, 1962.

Dehority, G. L.: See Refs. 126, 127, and 204.

220. Del Monte, J.: A Flush Mounted High Heat Flux Resistant Semiconductor Combustion Transducer for Rocket Motor Stability Studies. ISA, Vol. No. 10, Oct. 1964.

Del Notario, P. P.: See Refs. 681 and 682.

Delsasso, L. P.: See Ref. 768.

Derksen, W.: See Ref. 384.

DeWitt, R. L.: See Ref. 715.

221. Dickerson, R. A.; Arbit, H. A.; Clapp, S. D.; and Nagai, C. K.: Lithium-Fluorine-Hydrogen

Propellant Study. Rocketdyne, NASA CR-72325, Feb. 1968.

222. DICKERSON, R. A.; AND COULTAS, T. A.: Breakup of Droplets in an Accelerating Gas Flow. AIAA Paper No. 66-611, Second Propulsion Joint Specialist Conference, 1966.

223. DICKERSON, R. A.; AND SCHUMAN, M. D.: Atomization Rates of Droplets and Jets. Preprint No. 63-498, AIAA Heterogeneous Combustion Conference, 1963.

224. DICKERSON, R. A.; TATE, K. W.; AND BARSIC, N.: Correlation of Spray Injector Parameters with Rocket Performance. Rocketdyne Final Tech. Rept. AFRPL-TR-68-147, June 1968.

225. DICKERSON, R.; TATE, K.; AND NURICK, W.: Correlation of Spray Injector Parameters with Rocket Engine Performance. Rocketdyne Tech. Rept. AFRPL-TR-68-11, Jan. 1968.

DIEHL, L.: See Ref. 345.

226. DIPPREY, D. F.; RUPE, J. H.; PORTER, R. N.; AND EVANS, D. D.: On the Evolution of Advanced Propulsion Systems for Spacecraft. JPL Tech. Rept. No. 32-735, July 1965.

DIPPREY, D. F.: Also see Ref. 618.

227. DITORE, M. J.; HARTSELL, J. O.; AND THOMAS, R. M.: Investigation of Heterogeneous Propellant Two-Phase Flow Criteria. Aerojet-General, AFRPL-TR-67-62, April 1967.

228. DOBBINS, R. A.; AND TEMKIN, S.: Propagation of Sound in a Gas-Particle Mixture and Acoustic Combustion Instability. AIAA J, Vol. 5, No. 12, Dec. 1967, pp. 2182–2186.

DOBBINS, R. A.: Also see Ref. 684.

DODSON, D. S.: See Ref. 267.

229. DOMBROWSKI, N.; AND HOOPER, P. C.: The Effect of Ambient Density on Drop Formation in Sprays. Chem. Eng. Sci., Vol. 17, 1962, p. 291.

230. DOMBROWSKI, N.; AND JOHNS, W. R.: The Aerodynamic Instability and Disintegration of Viscous Liquid Sheets. Chem. Eng. Sci., Vol. 18, 1963, pp. 203–214.

DOMICH, E. G.: See Refs. 314 and 315.

231. DOMINICIS, D. P.: An Experimental Investigation of Near Critical and Supercritical Burning of Bipropellant Droplets. Mechanical Eng. Dept. Pennsylvania State University, NASA CR-72399, April 1967.

DOMINICIS, D. P.: Also see Refs. 255 and 256.

232. DORSCH, R. G.; AND WOOD, D. J.: Effect of Propellant-Feed System Coupling and Hydraulic Parameters on Analysis of Chugging. NASA TN D-3796, May 1967.

233. DRAIN, D. I.; SCHUM, H. J.; AND WASSERBAUER, C. A.: Relations of Combustion Dead Time to Engine Variables for a 20,000 Pound Thrust Gaseous Hydrogen—Liquid Oxygen Rocket Engine. NASA TN D-851, 1961.

234. DUNCAN, W. J.; THOM, A. S.; AND YOUNG, A. D.: Elementary Treatise on Mechanics of Fluids. Edward Arnold, Ltd., Publishers, London, 1960.

235. DYKEMA, O. W.: An Engineering Approach to Combustion Instability. Aerospace Corp. Rept. No. TDR-669(6126-22)-1, 1965.

236. DYKEMA, O. W.: An Engineering Approach to Combustion Instability. Second ICRPG Combustion Conference, CPIA Pub. No. 105, May 1966, p. 205.

237. DYKEMA, O. W.: Liquid Mixing of an Impinging Jet Using Immiscible Liquids. Rocketdyne Research Rept. RR 60-28, Nov. 1960.

238. DYKEMA, O. W.: A Proposed Mechanism of High Frequency Combustion Instability. Rocketdyne Research Rept. No. RR 60-25, Jan. 1961.

239. DYKEMA, O. W.; AND GREEN, S. A.: An Experimental Study of RP-1, UDMH and N_2H_4 Single Droplet Burning in Air and in Oxygen. Progress in Astronautics and Rocketry: Liquid Rockets and Propellants, Vol. 2, Academic Press, 1960, pp. 299–349.

DYKEMA, O. W.: Also see Ref. 380.

ECKEL, E. F.: See Refs. 289 and 748.

ECKERT, E. R.: See Ref. 317.

240. EISENKLAM, P.; ARUNACHALAM, S. A.; AND WESTON, J. A.: Evaporation Rates and Drag Resistance of Burning Drops. Eleventh Symposium (International) on Combustion, The Combustion Institute, 1967, pp. 715–728.

241. ELLIOTT, D. G.; BARTZ, D. R.; AND SILVER, S.: Calculation of Turbulent Boundary Layer Growth and Heat Transfer in Axi-Symmetric Nozzles, JPL Tech. Rept. 32-87, Feb. 1963.

242. ELLIS, H. B.; AND PICKFORD, R. S.: High Frequency Combustion Instability. Aerojet-General, AFOSR-TN-56-547, Sept. 1956.

243. ELVERUM, G. W., Jr.: Variable Thrust Bipropellant Rocket Engine. Patent No. 3205656 dated August 1962, assigned to TRW Inc.

244. ELVERUM, G. W.; AND MOREY, T. F.: Criteria for Optimum Mixture-ratio Distributions Using Several Types of Impinging-Stream Injector Elements. JPL Memorandum No. 30-5, Feb. 1959.

245. ELVERUM, G. W., JR.; STAUDHAMMER, P.; MILLER, J.; HOFFMAN, A.; AND ROCKOW, R.: The Descent Engine for the Lunar Module. AIAA Paper No. 67-521, AIAA 3rd Propulsion Joint Specialist Conference, July 1967.

246. ELVERUM, G. W.; AND STAUDHAMMER, P.: The Effect of Rapid Liquid Phase Reactions on Injector Design and Combustion in Rocket Motors. JPL Rept. 30-4, Aug. 1959.

247. EL WAKIL, M. M.; AND ABDOU, M. I.: The Self-Ignition of Fuel Drops in Heated Air Streams. Part I Experimental Data, Fuel, Vol. 45, No. 3, 1966, pp. 177–188; Part II Physical Ignition Delay, ibid., 1966, pp. 189–197; Part III Chemical Ignition Delay, ibid., 1966, pp. 199–205.

248. EL WAKIL, M. M.; UYEHARA, O. A.; AND MYERS, P. S.: A Theoretical Investigation of the

Heating-up Period of Injected Fuel Droplets Vaporizing in Air. NACA TN 3179, 1954.

249. El Wakil, M. M.; Priem, R. J.; Brikowski, H. J.; Myers, P. S.; and Uyehara, O. A.: Experimental and Calculated Temperature and Mass Histories of Vaporizing Fuel Drops. NACA TN 3490, 1956.

El Wakil, M. M.: See Refs. 112 and 562.

250. Engel, O. G.: Fragmentation of Waterdrops in the Zone Behind an Air Shock. J. of Res. Nat'l. Bur. Stds., Vol. 60, No. 3, March, 1958.

Ensminger, J. F.: See Ref. 94.

251. Epstein, P. S.; and Carhart, R. R.: The Absorption of Sound in Suspensions and Emulsions. I. Water fog in air. J. Acoust. Soc. Amer., Vol. 25, 1953, p. 553.

Eulner, R. N.: See Ref. 608.

252. Evans, D. D.; Stanford, H. B.; and Riebling, R. W.: The Effect of Injector-Element Scale on the Mixing and Combustion of Nitrogen Tetroxide-Hydrazine Propellants. JPL Tech. Rept. 32-1178, Nov. 1967.

Evans, D. D.: Also see Ref. 226 and 519.

Evans, H. D.: See Ref. 507.

253. Faeth, G. M.: Flame Zone Development of Monopropellant Droplets. Combustion and Flame, Vol. 12, 1968, pp. 411–416.

254. Faeth, G. M.: Monopropellant Droplet Burning at Low Reynolds Numbers. Combustion and Flame, Vol. 11, 1967, p. 167.

255. Faeth, G. M.; Dominicis, D. P.; and Olson, D. R.: An Investigation of Near Critical and Super-Critical Burning of Fuel Droplets. NASA CR-72314, Sept. 1967.

256. Faeth, G. M.; Dominicis, D. P.; Tulpinsky, J. F.; and Olson, D. R.: Supercritical Bipropellant Droplet Combustion. Twelfth Symposium (International) on Combustion, The Combustion Institute, 1969, pp. 9–18 (also see 13th Symposium).

257. Faeth, G. M.; Karhan, B. L.; and Yangecio, G. A.: Ignition and Combustion of Monopropellant Droplets. AIAA J., Vol. 6, 1968, p. 684.

258. Falk, A. Y.; Clapp, S. D.; and Nagai, C. K.: Space Storable Propellant Study–Final Report. Rocketdyne Rept. R-7677, 1968.

259. Feiler, C. E.: Effect of Combustor Parameters on the Stability of Gaseous Hydrogen-Liquid Oxygen Engine. NASA TM X-52360, 1967. (Also Fourth ICRPG Combustion Conference, CPIA Pub. No. 162, Vol. 1, Dec. 1967.)

260. Feiler, C. E.; and Heidmann, M. F.: Dynamic Response of Gaseous Hydrogen Flow System and Its Application to High Frequency Combustion Instability. NASA TN D-4040, June 1967.

Feiler, C. E.: Also see Refs. 338, 653, and 716.

261. Fendell, F. E.: Combustion in Initially Unmixed Reactants for One Step Reversible Chemical Kinetics. Astronautica Acta, Vol. 13, 1967, p. 183.

262. Fendell, F. E.: Decompositional Burning of a Droplet in a Small Peclet Number Flow. AIAA J., Vol. 6, 1968, p. 1946.

263. Fendell, F. E.: Flame Structure in Initially Unmixed Reactants Under One-Step Kinetics. Chem. Eng. Sci., Vol. 22, 1967, p. 1829.

264. Fendell, F. E.: Near-Equilibrium Decompositional Burning of Monopropellant Droplets in a Stagnant Atmosphere. Int. J. Heat Mass Transfer, Vol. 12, 1969, pp. 223–231.

265. Fendell, F. E.: Quasi-Steady Sphericosymmetric Monopropellant Decomposition in Inert and Reactive Environments. Paper P-16, 19th International Astronautical Congress, Oct. 1968, (DDC AD 680 306).

266. Fendell, F. E.; Coats, D. C.; and Smith, E. B.: Compressible Slow Viscous Flow Past a Vaporizing Droplet. AIAA J, Vol. 6, 1968, p-1953.

267. Fendell, F. E.; Sprankle, M. L.; and Dodson, D. S.: Thin Flame Theory for a Fuel Droplet in Slow Viscous Flow. J. Fluid Mech., Vol. 26, 1966, p. 267.

268. Fenwick, J. R.; and Bugler, G. J.: Oscillatory Flame Front Flow Rate Amplification Through Propellant Injection Ballistics (The Klystron Effect). Third ICRPG Combustion Conference, CPIA Pub. No. 138, Vol. 1, Feb. 1967, p. 417.

269. Ferri, A.: A Critical Review of Heterogeneous Mixing Problems. Aerospace Research Laboratories Report ARL 67-0187, Sept. 1967.

Feshbach, H.: See Ref. 504.

270. Fifer, S.: Analog Computation, Volume IV. McGraw-Hill, New York, 1961.

271. Fisher, R. A., et al.: Study of Droplet Effects on Steady-State Combustion, Vol. I: Measured Spray Parameter Analysis and Performance Correlation. Rocketdyne Tech. Rept. AFRPL-TR-66-152, Vol. I, Aug. 1966.

Florsheim, B. H.: See Ref. 725.

272. Fontaine, R. J.; Levine, R. S.; and Combs, L. P.: Secondary Non Destructive Instability in Medium Size Liquid Fuel Rocket Engines. Advances in Tactical Rocket Propulsion, AGARD Conference Proceedings No. 1, S. S. Penner, ed., Technivision Services, Maidenhead, England, 1968, pp. 383–402.

Fontaine, R. J.: See Ref. 381.

273. Ford, H. J.: A Study of the Suppression of Combustion Oscillations with Mechanical Damping Devices, Summary Report of Tasks I and II. Pratt & Whitney Aircraft PWA FR-1007, Aug. 1964.

274. Ford, H. J.: A study of the suppression of Combustion Oscillations with Mechanical Damping Devices, Summary Report of Tasks III through VI. Pratt & Whitney Aircraft PWA FR-1115, Nov. 1964.

Ford, H. J.: Also see Ref. 702.

275. Ford, W. M.; Sutton, R. D.; and Cline, G. L.: Flow Visualization in the Hydrogen-Oxygen J-2S

Engine. Research Report RR 68-3, Rocketdyne, Mar. 1968.

FORD, W. M.: Also see Ref. 155.

276. FORSYTHE, G. E.; AND WASOW, W. R.: Finite Difference Methods for Partial Difference Equations. John Wiley & Sons, New York, N. Y., 1960.

277. FOSTER, H. H.; AND HEIDMANN, M. F.: Spatial Characteristics of Water Spray Formed by Two Impinging Jets at Several Jet Velocities in Quiescent Air. NASA TN D-301, 1960.

FOSTER, H. H.: Also see Refs. 339 and 379.

278. FOX, J. C.: Preliminary Investigation of Helmholtz Resonators for Damping Pressure Oscillations in a 3.6-inch Ramjet at Mach Number 1.90. NACA RM E 51C95, 1951.

FREY, A. R.: See Ref. 407.

FRIANT, D. R.: See Ref. 300.

279. FRIEDLANDER, S. K.; AND KELLER, K. H.: The Structure of the Zone of Diffusion-Controlled Reaction. Chem. Eng. Sci., Vol. 18, 1963, p. 365.

280. FRÖSSLING, N.: Uber die Verdungtung Fallenden Tropfen. Gerlands Beitrage Zur Geophysik, Vol. 52, 1938, p. 170.

281. GABOR, D.: A New Microscope Principle. Nature, Vol. 161, May 1948, p. 777.

GALLOWAY, A. J.: See Ref. 751.

GARRETT, A. See Ref. 386.

282. GARRISON, G. D.: Absorbing Liners for Rocket Combustion Chambers—Theory and Design Techniques. Pratt & Whitney, AFRPL-TR-66-234, Aug. 1966.

283. GARRISON, G. D.: Acoustic Liners for Storable Propellant Rocket Chambers—Phase I Final Report. Pratt & Whitney, AFRPL-TR-67-205, July 1967.

284. GARRISON, G. D.: Acoustic Liners for Storable Propellant Rocket Chambers—Phase II Final Report. Pratt & Whitney Rept. PWA FR-2812, (AFRPL-TR-68-118), Aug. 1968.

285. GARRISON, G. D.: A Study of the Suppression of Combustion Oscillations with Mechanical Damping Devices—Phase II Summary Report. Pratt & Whitney Rept. FR-1922, July 1966.

286. GARRISON, G. D.; SCHNELL, A. C.; BALDWIN, C. D.; AND RUSSELL, P.R.: Suppression of Combustion Oscillations with Mechanical Damping Devices, Interim Report. Pratt & Whitney Aircraft Rept. FR-3299, Aug. 1969.

287. GARY, D. A.: A Study of Injector Spray Characteristics in a Simulated Rocket Combustion Chamber Including Longitudinal Mode Pressure Oscillations. Princeton University Dept. of Aerospace and Mechanical Sciences, Tech. Rept. No. 730, 1966.

288. GERBRACHT, F.: Injector Hydraulics. JPL Space Program Summary 37-47, Vol. III, Oct. 1967, p. 149.

GERSTEIN, M.: See Ref. 88.

GERBRACHT, F. G.: See Ref. 153.

289. GILL, G. S.; ECKEL, E. F.; WILLIAMS, F. A.; AND PENNER, S. S.: Determination of Rocket-Motor Combustion Parameters by Means of a Diverging Reactor. Seventh Symposium (International) on Combustion, Butterworths Scientific Pub., London, 1959, pp. 712–724.

GILL, G. S.: Also see Ref. 748.

289b. GINSBURG, B. R.: Flowrate Measurements for Spacecraft Thrusters. Presented at the ASME Flow Measurement Conference, Pittsburgh, Pa., Sept. 26–28, 1966 (reprints available from Ramapo Inst. Co., Inc., Bloomingdale, N. J. 07403).

GLASSMAN, I.: See Refs. 113 and 634.

GLEASON, J. L.: See Ref. 509.

290. GODSAVE, G. A. E.: Studies of the Combustion of Drops in a Fuel Spray–The Burning of Single Drops of Fuel. Fourth Symposium (International) on Combustion, Williams & Wilkins, Baltimore, 1953, pp. 818–830.

GODWIN, T. W.: See Ref. 690.

291. GOELZ, R. R.: Combustion Instability in Steel and Ablative Rocket Chambers. NASA TMX-1511, 1968.

GOELZ, R. R.: Also see Ref. 309.

292. GOLDSMITH, M.: Experiments on the Burning of Single Drops of Fuel. Jet Propulsion, Vol. 26, March 1956, p. 172.

293. GOLDSMITH, M.; AND AND PENNER, S. S.: On the Burning of Single Drops of Fuel in an Oxidizer Atmosphere. Jet Propulsion, Vol. 24, 1954, p. 245.

294. GORDEEV, V. E.; KOMOV, V. F.; AND TROSHIN, YA. K.: Concerning Detonation Combustion in Heterogeneous Systems. Proc of the Academy of Science, USSR (Physical Chemistry), Vol. 160, No. 4, 1965.

295. GORDON, C.; AND SMITH, P. W., JR.: Acoustic Losses of a Resonator with Steady Gas Flow. J. Acoust. Soc. Amer., Vol. 37, 1965, p. 257.

296. GRANT, R. P.; AND MIDDLEMAN, S.: Newtonian Jet Stability. A.I.Ch. E. J., Vol. 12, No. 4, July 1966, p. 669.

GREEN, S. A.: See Ref. 239.

297. GREENFIELD, S. P.: An Experimental Evaluation of Rocket Propellant Data. The Chemistry of Propellants, S. S. Penner and J. Ducarme, eds., Pergamon Press, 1960.

298. GREY, J.: Transient Response of the Turbine Flowmeter. Jet Propulsion, Vol. 26, No. 2, Feb. 1956, pp. 98–100.

GREY, J.: Also see Refs. 180, 181, 182, 195, and 687.

299. GROENEWEG, J. F.: The Statistical Description of a Spray in Terms of Drop Velocity, Size and Position. Ph.D. Thesis, University of Wisconsin, 1967.

GROENEWEG, J. F.: Also see Ref. 340.

GROSH, R. J.: See Ref. 675.

GUENTERT, D. C.: See Ref. 563.

300. GUNDER, D. F.; AND FRIANT, D. R.: Stability of Flow in a Rocket Motor. Journal of Applied Mechanics, Vol. 17, No. 3, 1960, pp. 327–333.

301. Gurney, R. W.: Initial Velocities of Fragments from Bombs, Shells, and Grenades. U.S. Army Ballistic Research Laboratories, Rept. No. 405, Sept. 1943.

302. Hall, A. R.: Experimental Temperature Gradients in Burning Droplet. Seventh Symposium (International) on Combustion, Butterworths Scientific Pub., London, 1959.

303. Hall, A. R.; and Diederichsen, J.: An Experimental Study of the Burning of Single Drops of Fuel at Pressures up to Twenty Atmospheres. Fourth Symposium (International) on Combustion, Williams and Wilkins, Baltimore, 1954, pp. 837–846.

304. Hall, G. W.: Analytical Determination of the Discharge Characteristics of Cylindrical-Tube Orifices. J. Mech. Engr. Sci., Vol. 5, No. 1, 1963, pp. 91–97.

305. Hammac, H. M.: An Application of the Electromagnetic Flowmeter for Analyzing Dynamic Flow Oscillations. NASA TM-53570, Jan. 1967.

306. Hammer, S. S.; and Agosta, V. D.: Longitudinal Wave Propagation in Liquid Propellant Rocket Motors. AIAA J, Vol. 2, No. 11, Nov. 1964, pp. 2042–2044.

307. Hammer, S. S.; and Agosta, V. D.: Wave Slope–Gas Dynamic Interactions in Liquid Rockets. AIAA J, Vol. 4, No. 4, April 1966, pp. 753–755.

308. Hammer, S. S.; Agosta, V. D.; and Peshke, W. T.: Combustion Instability in Liquid Propellant Rocket Engines: Bipropellant Spray Combustion. Polytechnic Institute of Brooklyn, PIBAL Rept. No. 891, AFOSR 66-0858, 1966.

Hammer, S.: Also see Refs. 55, 132, and 544.

309. Hannum, N. P.; Bloomer, H. E.; and Goelz, R. R.: Stabilizing Effects of Several Injector Face Baffle Configurations on Screech in a 20,000 Pound-Thrust Hydrogen-Oxygen Rocket. NASA TN D-4515, April 1968.

310. Hannum, N. P.; and Conrad, E. W.: Performance and Screech Characteristics of a Series of 2500-Pound Thrust Per Element Injectors for a Liquid Oxygen-Hydrogen Engine. NASA TMX-1253, 1966.

311. Hannum, N. P.; and Conrad, E. W.: Some Injection Element Detail Effects on Screech in Hydrogen Oxygen Engines. Fourth ICRPG Combustion Conference, CPIA Pub. 162, Vol. 1, Dec. 1967, p. 31, (see NASA TMX-52363).

312. Hannum, N. P.; and Scott, H. E.: The Effect of Several Injector Face Baffle Configurations on Screech in a 20,000-Pound Thrust Hydrogen-Oxygen Rocket. Third ICRPG Combustion Conference, CPIA Pub. No. 138, Vol. 1, Feb. 1967, pp. 587–595.

Hannum, N. P.: Also see Refs. 552, 624, and 717.

313. Hansen, P. D.: New Approaches to the Design of Active Filters. The Lightning Empiricist, Vol. 13, Nos. 1 and 2, published by Philbrick Researchers, Dedham, Mass., Jan.–July 1965.

314. Hanson, A. R.; and Domich, E. G.: The Effect of Liquid Viscosity on the Break-up of Droplets by Air Blasts–A Shock Tube Study, Univ. of Minnesota Institute of Technology Rept. No. 130, Eng. Res., 1956.

315. Hanson, A. R.; Domich, E. G.; and Adams, H. S., Shock Tube Investigation of the Breakup of Drops by Air Blast. The Physics of Fluids, Vol. 6, No. 8, Aug. 1963.

316. Hardacre, A.: Gas Sampling from Liquid Propellant Rocket Engines. Rocket Propulsion Establishment, Westcott, Great Britain, Tech. Memo 451, Sept. 1967.

317. Harnett, J. P.; and Eckert, E. R.: Experimental Study of the Velocity and Temperature Distribution in a High Velocity Vortex Type Flow. Transactions of the ASME, Vol. 79, May 1957.

Harris, G. H.: See Ref. 82.

Harrison, D.: See Ref. 447.

318. Harrje, D. T.: Fundamental Problems of Injector Design. Advances in Tactical Rocket Propulsion, AGARD Conference Proceedings No. 1, S. S. Penner, ed., Technivision, Maidenhead, England, Aug. 1968, pp. 267–289.

319. Harrje, D. T.: Heat Transfer in Oscillating Flow—Final Rept. Princeton University Aerospace and Mech. Sci. Rept. No. 483g, Oct. 1967.

320. Harrje, D. T.; and Condomines, A.: Combustion Instability in Liquid Propellant Rocket Motors–Twenty-Ninth Quarterly Progress Report. Princeton University Aero. Eng. Rept. No. 216-cc, Sept. 1959.

321. Harrje, D. T.; and Crocco, L.: Axial Energy Distribution Studies in a Liquid Propellant Rocket Motor. Third ICRPG Combustion Conference, CPIA Pub. No. 138, Vol. 1, Feb. 1967, pp. 523–529.

322. Harrje, D. T.; and Crocco, L.: Combustion Instability in Liquid Propellant Rocket Motors, Twenty-Sixth Quarterly Progress Report. Princeton University Aero. Eng. Rept. No. 216-z, Feb. 1959.

323. Harrje, D. T.; Reardon, F. H.; and Crocco, L.: Combustion Instability in Liquid Propellant Rocket Motors, Thirty-Fourth Quarterly Progress Report. Princeton University Aero. Eng. Rept. No. 216-hh, Nov. 1960.

324. Harrje, D. T.; Stinger, W. A.; and Sirignano, W. A.: Flow Behavior with Acoustic Liners. Fourth ICRPG Combustion Conference, CPIA Pub. No. 162, Vol. 1, Dec. 1967, pp. 103–109.

Harrje, D. T.: Also see Refs. 102, 114, 115, 180, 183, 184, 187, 188, 189, 190, 191, 192, 193, 583, 647, 694, and 766.

Hart, R. W.: See Ref. 137.

Hartnett, P. P.: See Ref. 382.

Hartsell, J. O.: See Ref. 227.

325. Harvey, D., et al.: TRW LEM Descent Engine

Characteristics. TRW Rept. 01827-6119-T000, Jan. 1969.

326. HASSON, D.; AND PECK, R. E.: Thickness Distribution in a Sheet Formed by Impinging Jets. A.I.Ch.E.J., Vol. 10, No. 5, Sept. 1964, p. 752.

327. HAVEMANN, H. A.: A Theory of Cyclone Combustion Chamber Design. National Gas Turbine Establishment, Great Britain, Rept. No. 53, May 1949.

HAWK, N. E.: See Ref. 751.

328. HEFLINGER, I. O., ET AL.: Holographic Interferometry. J. of Applied Physics, Vol. 37, Feb. 1966, pp. 642–649

329. HEFNER, R. J.: Combustion Stability Development at Aerojet-General. First ICRPG Propulsion Conference, CPIA Pub. No. 68, Vol. 1, Jan. 1965, p. 9–22.

330. HEFNER, R. J.: Diagnosis of High Frequency Combustion Stability Characteristics from Pressure Measurements. Third ICRPG Combustion Conference, CPIA Pub. No. 138, Vol. 1, Feb. 1967, pp. 375–381.

331. HEFNER, R. J.: Review of Combustion Stability Development with Storable Propellants. J. of Spacecraft and Rockets, Vol. 3, No. 7, July 1966, pp. 1046–1050.

332. HEFNER, R. J.: A Review of the Combustion Dynamics Aspects of the Gemini Stability Improvement Program. Second ICRPG Combustion Conference, CPIA Pub. 105, Vol. 1, May 1966, pp. 13–22.

333. HEFNER, R. J.; REARDON, F. H.; AND SMITH, A. J., Jr.: An Experimental Investigation of LO_2/LH_2 Combustion Stability Characteristics at High Chamber Pressure. Third ICRPG Combustion Conference, CPIA Pub. 138, Vol. 1, Feb. 1967, p. 597.

HEFNER, R. J.: Also see Refs. 473 and 347.

334. HEIDMANN, M. F.: Oscillatory Combustion of a Liquid Oxygen Jet with Gaseous Hydrogen. NASA TM D-2753, Mar. 1965.

335. HEIDMANN, M. F.: Oxygen-Jet Behavior During Combustion Instability in a Two-Dimensional Combustor. NASA TM D-2725, Mar. 1965.

336. HEIDMANN, M. F.: Propellant Vaporization as a Criterion for Rocket-Engine Design-Experimental Effects of Fuel Temperature on Liquid Oxygen–Heptane Performance. NACA RME57-E03, 1957.

337. HEIDMANN, M. F.: Visualization Studies of Combustion Instability in a Hydrogen-Oxygen Model Combustor. NASA Lewis Research Center, Film C-226.

338. HEIDMANN, M. F.; AND FEILER, C. E.: Evaluation of Tangential Velocity Effects on Spinning Transverse Combustion Instability. NASA TN D-3406, May 1966.

339. HEIDMANN, M. F.; AND FOSTER, H. H.: Effect of Impingement Angle on Drop Size Distribution and Spray Pattern of Two Impinging Water Jets. NASA TN D-872, July, 1961.

340. HEIDMANN, M. F.; AND GROENEWEG, J. F.: Analysis of the Dynamic Response of Liquid Jet Atomization to Acoustic Oscillations. NASA TN D-5339, July 1969.

341. HEIDMANN, M. F.; AND HUMPHREY, J. C.: Fluctuations in a Spray Formed by Two Impinging Jets. J.ARS, Vol. 22, No. 3, 1952, pp. 127–131.

342. HEIDMANN, M. F.; AND POVINELLI, L. A.: An Experiment on Particulate Damping in a Two-Dimensional Hydrogen-Oxygen Combustor. Fourth ICRPG Combustion Conference, CPIA Pub. No. 162, Vol. I, Dec. 1967, p. 311 (also NASA TMX-52359, 1967).

343. HEIDMANN, M. F.; AND PRIEM, R. J.: Propellant Vaporization as a Criterion for Rocket Engine Design: Relation Between Percentage of Propellant Vaporized and Engine Performance. NACA RM E57 E03, 1957.

344. HEIDMANN, M. F.; PRIEM, R. J.; AND HUMPHREY, J. C.: A Study of Sprays Formed by Two Impinging Jets. NASA TN 3855, 1957.

345. HEIDMANN, M. F.; SOKOLOWSKI, D. E.; AND DIEHL, L. A.: Study of Chugging Instability with Liquid-Oxygen and Gaseous-Hydrogen Combustors. NASA TN D-4005, June 1967.

346. HEIDMANN, M. F.; AND WIEBER, P. R.: Analysis of Frequency Response Characteristics of Propellant Vaporization. NASA TN D-3749, Dec. 1966.

347. HEIDMANN, M. F.; AND WIEBER, P. R.: Analysis of n-Heptane Vaporization in Unstable Combustor with Traveling Transverse Oscillation. NASA TN D-3424, 1966.

HEIDMANN, M. F.: Also see Refs. 260, 277, 564, and 565.

348. HERGET, W. R.; PROFFIT, R. L.; AND WITHERSPOON, J. E.: Rocket Stability Monitoring by Temporal Radiometry. AIAA Paper 60-580, 5th Propulsion Joint Specialist Conference, June 1969.

HERGET, W. F.: Also see Ref. 155.

349. HERSCH, M.: Effect of Interchaning Propellants on Rocket Combustor Performance with Coaxial Injection. NASA TN D-2169, Feb. 1964.

350. HERSCH, M.: Experimental Method of Measuring Intensity of Turbulence in a Rocket Chamber. ARS J., Vol. 31, 1961, pp. 39–45.

351. HERSCH, M.: A Mixing Model for Rocket Engine Combustion. NASA TN D-2881, June 1965.

352. HERSCH, M.; AND RICE, E. J.: Gaseous Hydrogen-Liquid Oxygen Rocket Combustion at Supercritical Chamber Pressures. NASA TN D-4172, 1967.

353. HERSH, S.; LAWVER, B. R.; HOFFMAN, R. J.; AND BREEN, B. P.: Investigation of the Flame Structure of a Thermally Unstable Fuel. Dynamic Science, NASA CR-72261, 1967.

354. HERZFELD, K. F.; AND LITOVITZ, T. A.: Absorption

and Dispersion of Ultrasonic Waves. Academic Press, New York, 1959.
HESTER, J. N.: See Ref. 168.
HEWITT, R. A.: See Ref. 473.
HILL, A. F.: See Ref. 517.
HILLIARD, F.: See Ref. 181.
355. HINDE, P. T.: Basic Aspects of Gas-Phase Mixing and Kinetics in Liquid Propellant Rocket Combustion Chambers–A Review. R.P.E., Westcott, Technical Report No. 69/1, Feb. 1969.
356. HINES, W., ET AL.: Development of Injector Chamber Compatibility Analysis. Rocketdyne Final Report, AFRPL-TR-70-12, March 1970.
357. HINZE, J. O.: Critical Speeds and Sizes of Liquid Globules. Appl. Sci. Res., Vol. A1, 1948, p. 273.
HOEHN, F. W.: See Refs. 162 and 163.
HOFFMAN, A.: See Ref. 245.
HOFFMAN, J. D.: See Ref. 169.
358. HOFFMAN, R. J.; BELTRAN, M. R.; BREEN, B. P.; AND WRIGHT, R. O.: Extension of the Priem-Guentert Annular Combustion Instability Model to a Bipropellant System. Third ICRPG Combustion Conference, CPIA Pub. No. 138, Vol. 1, Feb. 1967, p. 399.
359. HOFFMAN, R. J.; WRIGHT, R. O.; AND BREEN, B. P.: Combustion Instability Prediction Using a Non-linear Bipropellant Vaporization Model. Dynamic Science, NASA CR-920, Jan. 1968.
HOFFMAN, R. J.: Also see Refs. 89 and 353.
HOOPER, P. C.: See Ref. 229.
360. HERN, R. B.; SIDDALL, R. G.; AND THRING, M. W.: Flow Patterns in a Phase Change Rocket Combustion Model. Ninth Symposium (International) on Combustion, Academic Press, New York, 1963, pp. 965–972.
361. HORNSTEIN, B.; BUDNIK, C.; AND COURTNEY, W.: Research Study of Light Emission Caused by Pressure Fluctuations in Rocket Engines. Reaction Motors (Thiokol) RMD Rept. No. 5520-F, March 1966.
362. HOTTEL, H. C.; AND PERSON, R. A.: Heterogeneous Combustion of Gases in a Vortex System. Fourth Symposium (International) on Combustion, Williams and Wilkins Co., Baltimore, 1954.
363. HOTTEL, H. C.; WILLIAMS, G. C.; AND SIMPSON, H. C.: Combustion of Droplets of Heavy Liquid Fuels. Fifth Symposium (International) on Combustion, Reinhold, 1955, pp. 101–129.
HOTTEL, H. C.: Also see Ref. 84.
HOUPIS, C. H.: See Ref. 217.
364. HOUSEMAN, J.: Jet Separation and Optimum Mixing for an Unlike Droplet. Sixth ICRPG Combustion Conference, CPIA Pub. No. 192, Vol. 1, Dec. 1969, pp. 13–20.
HOUSEMAN, J.: Also see Refs. 415 and 416.
365. HOWELL, G. W.; AND WEATHERS, T. M.: Aerospace Fluid Component Designer's Handbook, Vol. I. Published by TRW Systems Group, Mar. 1967, (AD-809182).
HUMPHREY, J. C.: See Refs. 341 and 344.
366. HUNT, F. V.: Notes on the Exact Equations Governing the Propagation of Sound in Fluids. J. Acoust. Soc. of Amer., Vol. 27, No. 6, Nov. 1955, pp. 1019–1039.
367. HYZER, W. G.: Introduction to High-Speed Photographic Instrumentation. ISA Transactions, Vol. 5, No. 1, Jan. 1966.
368. IACABELLIS, S. F.: Liquid Rocket Engines: Their Status and Their Future. AIAA Paper No. 66-828, AIAA Third Annual Meeting, Nov.–Dec. 1966.
369. IL'YASHENKO, S. M.: Evaporation and Combustion of a Single-Component Fuel in a Chamber of a Liquid Rocket Engine. AIAA J., Vol. 1, 1963, pp. 267–271.
370. INGARD, U.: On the Theory and Design of Acoustic Resonators. J. Acoust. Soc. Amer., Vol. 25, No. 6, Nov. 1953, pp. 1037–1061.
371. INGARD, U.; AND ISING, H.: Acoustic Nonlinearity of an Orifice. J. Acoust. Soc. of Amer., Vol. 42, No. 1, July 1967, pp. 6–17.
372. INGARD, U.; AND LABATE, S.: Acoustic Circulation Effects and Nonlinear Impedance of Orifices. J. Acoust. Soc. of Amer., Vol. 22, No. 2, March 1950, pp. 211–218.
INGARD, U.: Also see Refs. 108 and 505.
373. INGEBO, R. D.: Atomization of Ethanol Jets in a Combustor with Oscillatory Combustion-Gas Flow. NASA TN D-3513, 1966.
374. INGEBO, R. D.: Drag Coefficients for Droplets and Solid Spheres in Clouds Accelerating in Air Streams. NACA TN-3762, Sept. 1956.
375. INGEBO, R. D.: Drop-Size Distribution for Impinging-Jet Breakup in Airstreams Simulating the Velocity Conditions in Rocket Combustors, NACA TN-422, March 1958.
376. INGEBO, R. D.: Maximum Drop Diameters for the Atomization of Liquid Jets Injected Concurrently into Accelerating or Decelerating Gas Streams. NASA TN D-4640, 1968.
377. INGEBO, R. D.: Photomicrographic Tracking of Ethanol Drops in a Rocket Chamber Burning Ethanol and Liquid Oxygen. NASA TN D-290, 1960.
378. INGEBO, R. D.: Vaporization Rates of Ethanol Sprays in a Combustor with Low-Frequency Fluctuations of Combustion-Gas Pressure. NASA TN D-1408, 1962.
379. INGEBO, R. D.; AND FOSTER, H. H.: Drop-Size Distribution for Cross-Current Breakup of Liquid Jets in Airstreams. NASA TN 4087, Oct. 1957.
ISING, H.: See Ref. 371.
ISODA, H.: See Ref. 413.
380. IWANICKI, L. R.; AND DYKEMA, O. W.: Effect of a Cavitating Venturi on Wave Propagation in a Duct. AIAA J., Vol. 2, No. 4, April 1964, pp. 753–755.
381. IWANICKI, L. R.; AND FONTAINE, R. J.: Sensitivity of Rocket Engine Stability to Propellant Feed

System Dynamics. AIAA Paper No. 65-558, AIAA Propulsion Joint Specialist Conference, 1965.

382. IRVINE, T. F., Jr.; AND HARTNETT, P. P.: Advances in Heat Transfer, Vol. 2. Academic Press, New York, 1965.

383. ITO, J. I.: Derivation of Orifice Hydraulic Flow Model. Aerojet-General Monthly Progress Rept. 6925-M4, Appendix A, Contract NAS 9-6925, Aug. 1967.

384. JAARSMA, F.; AND DERKSEN, W.: Shock Tube Techniques for Fuel Droplet Combustion Studies. National Aerospace Laboratory NRL, The Netherlands, Rept. MP 251, 1967.

JACKMAN, P.: See Refs. 111 and 201.

385. JACKSON, E. G.: Studies of Pump Discharge Pressure Oscillations. Rocketdyne Rept. No. R-6693-2, 1966.

386. JACKSON, E. G.; GARRETT, A.; AND TESTEN, J.: Combustion Stability Quarterly Progress Report for period 1 October to 31 December 1960. Rocketdyne Rept. CER1122-3001, Jan. 1961.

387. JAIN, V. K.: The Theory of Burning of Monopropellant Droplets in an Atmosphere of Inerts. Combustion and Flame, Vol. 7, 1963, pp. 17–27.

388. JAIN, V. K.; AND RAMANI, N.: Extinction Criterion of a Monopropellant Droplet in an Atmosphere of Inerts. AIAA J., Vol. 7, 1969, pp. 567–569.

JAIN, V. K.: Also see Ref. 663.

JAIVAN, G. I.: See Ref. 620.

JOHNS, W. R.: See Ref. 230.

389. JOHNSON, B. H.: An Experimental Investigation of the Effects of Combustion on the Mixing of Highly Reactive Liquid Propellants. JPL Tech. Rept. No. 32-689, July 1965.

390. JOHNSON, N. L.: Systems of Frequency Curves Generated by Methods of Translation. Biometrica, Vol. 36, 1949, p. 149.

391. JONES, B. A.; AND LAMBIRIS, S.: Summary Report on an Investigation of Combustion Instability for Liquid Oxygen and Liquid and Cold Gas Hydrogen Propellants. Pratt and Whitney Rept. PWA-FR-1005, June 1964.

392. JONES, D. L.: The Energy Parameter B for Strong Blast Waves. National Bureau of Standards Tech. Note 155, July 1952.

393. JONES, H. B.: Transient Pressure Transducer Design and Evaluation. Princeton University Aero. Eng. Rept. No. 595b, Feb. 1962.

394. JONES, H. B.; KNAUER, R. C.; LAYTON, J. P.; AND THOMAS, J. P.: Transient Pressure Measurements in Liquid Propellant Rocket Thrust Chambers. ISA Transactions, Vol. 4, No. 2, April 1965.

395. JONES, R. D.: Quarterly Progress Report, Advanced Engine Design Study (Aerospike). Rocketdyne, Sept. 1966.

396. JURAN, W.; AND SWICK, E. B.: The Effect of Dissolved Gas on the Stability of Pressure-Fed Rockets. Fourth ICRPG Combustion Conference, CPIA Pub. 162, Vol. I, 1967, p. 93.

KAPPL, J. J.: See Ref. 431.

KARHAN, B. L.: See Ref. 257.

397. KARLOVITZ, B.: Turbulent Flame Theory Derived from Experiments. AGARD Selected Combustion Problems: Fundamentals and Aeronautical Applications, Butterworths, London, 1954, pp. 248–262.

398. KASSOY, D. R.; AND WILLIAMS, F. A.: Liquid Droplet Combustion in Finite Rate Chemistry. Phys. Fluids, Vol. 11, 1968, pp. 1343–1351.

399. KASSOY, D. R.; AND WILLIAMS, F. A.: Variable Property Effects on Liquid Droplet Combustion. AIAA J., Vol. 6, 1968, p. 1961.

400. KATYS, G. P.: Continuous Measurement of Unsteady Flow. Pergamon Press, New York, 1965.

KELLER, K. H.: See Ref. 279.

KERSLAKE, W. R.: See Refs. 461 and 462.

401. KESSELRING, R. C.: Steady-State Streak Film Analysis in a High-Pressure Two-Dimensional Research Motor. AIAA Paper No. 66-612, Second AIAA Propulsion Joint Specialist Conference, June 1966.

402. KESSELRING, R. C.: Steady-State Streak Film Analysis in the High-Pressure Two-Dimensional Research Motor–Final Summary Report. Rocketdyne Research Rept. No. 65-19, May 1965.

403. KESSELRING, R. C.; AND OBERG, C. L.: Combustion Stability of Metallized Gelled Propellants–Final Report. Rocketdyne, AFRPL-TR-67-164, May 1967.

404. KESSELRING, R. C.; AND OBERG, C. L.: Combustion Stability of Metallized Gelled Propellants. Fourth ICRPG Combustion Conference, CPIA Pub. 162, Vol. I, 1967, p. 307.

405. KESSELRING, R. C.; AND OBERG, C. L.: Combustion Stability of Metallized Gelled Propellants. Ninth Liquid Propulsion Symposium, CPIA Pub. No. 155, Vol. II, Nov. 1967, p. 23.

KESSELRING, R. C.: Also see Refs. 167 and 170.

KIMURA, A.: See Ref. 414.

406. KINNARD, I. F.: Applied Electrical Measurements. John Wiley and Sons, New York, 1956.

407. KINSLER, L. E.; AND FREY, A. R.: Fundamentals of Acoustics, Second Edition. Jonn Wiley and Sons, New York, 1962.

KISER, H. V.: See Ref. 631.

408. KLACKING, J. M.; ADDOMS, J. F.; ARMITAGE, A. L.; AND BOYCE, R. L.: Unique Injector Concepts Development. Aerojet-General Rept. No.0518-00 (Final), AFRPL-RTD-TDR-63-1057, 1963.

KLOPOTECK, R. D.: See Refs. 728 and 729.

KNAUER, R. C.: See Ref. 394.

KNOW, R. M.: See Ref. 487.

KOMOV, V. F.: See Ref. 294.

KOSTEN, C. W.: See Ref. 778.

409. KLEIGEL, J. R.; AND QUAN, V.: Convergent-Divergent Nozzle Flows. Contract NAS 9-4358, TRW Systems Rept. 02874-6002-R000, Dec. 1966.

410. KOSVIC, T. C.; BREEN, B. P.; LEVINE, J.; AND COATS, D. E.: Combustion Instability Response

with Asymmetric Pressure Disturbances. Dynamic Science, NASA CR-72494. Jan. 1969.

KOSVIC, T. C.: Also see Refs. 89, 90, and 140.

KROMREY, E. V.: See Refs. 704 and 705.....

411. KUH, E. S.; AND PEDERSON, D. O.: Principles of Circuit Synthesis. McGraw-Hill, New York, 1959.

KULUVA, N. M.: See Refs. 167 and 523.

412. KUMAGAI, S.: Evaporation and Combustion of Droplet in Sprays. Sixth Symposium (International) on Combustion, Reinhold, New York, 1957, pp. 668–674.

413. KUMAGAI, S.; AND ISODA, H.: Combustion of Fuel Droplets in a Vibrating Air Field. Fifth Symposium (International) on Combustion, Reinhold, New York, 1955, pp. 129–132.

414. KUMAGAI, S.; AND KIMURA, A.: (Discussed on p. 289 of Ref. 536.) Science of Machine, Vol. 3, p. 431, 1951.

415. KUSHIDA, R.; AND HOUSEMAN, J.: Criteria for Separation of Impinging Streams of Hypergolic Propellants. JPL Tech. Memo. No. 33-395, July 1968.

416. KUSHIDA, R.; AND HOUSEMAN, J.: Criteria for Separation of Impinging Streams of Hypergolic Propellants. Paper WSCI-67-38, Presented at Fall Meeting of Western States Section Combustion Institute, Oct. 1967.

LABATE, S.: See Refs. 108 and 372.

LABOTZ, R. J.: See Ref. 476.

417. LAMB, H.: The Dynamical Theory of Sound. Dover Publication, Second Edition, 1960, pp. 264–269.

418. LAMBIRIS, S.: Experimental Verification of Nozzle Admittance Theory in a Simulated Rocket Chamber. Project SQUID Reprint PR-75, Sept. 1957.

419–420. LAMBIRIS, S.; AND COMBS, L. P.: Steady-State Combustion Measurements in a LOX/RP-1 Rocket Chamber and Related Spray Burning Analysis. Detonation and Two-Phase Flow, Vol. 6, Progress in Astronautics and Rocketry, Academic Press, New York, 1962, pp. 269–304 (also Rocketdyne Research Rept. No. RR 61-13 May 1961).

421. LAMBIRIS, S.; COMBS, L. P.; AND LEVINE, R. S.: Stable Combustion Processes in Liquid Propellant Rocket Engines. Combustion and Propulsion, Fifth AGARD Colloquium: High Temperature Phenomena, Macmillan, New York, 1963, pp. 596–634.

LAMBIRIS, S.: Also see Refs. 164 and 391.

422. LANDAU, H. G.: Heat Conduction in a Melting Solid. Quart. of Appl. Math, Vol. 8, 1950, pp. 81–94.

423. LAWHEAD, R. B.: Liquid Propellant Combustion Instability Research at Rocketdyne. First ICRPG Combustion Instability Conference, CPIA Pub. No. 68, Jan. 1965, p. 39.

424. LAWHEAD, R. B.: Photographic Studies of Combustion Processes in Liquid Propellant Rockets. Eighth Symposium (International) on Combustion, Williams and Wilkins Co., Baltimore, 1962, pp. 1140–1151.

425. LAWHEAD, R. B.; AND COMBS, L. P.: Modeling Techniques For Liquid Propellant Rocket Combustion Processes. Ninth Symposium (International) on Combustion, Academic Press, New York, 1963, pp. 973–981.

426. LAWHEAD, R. B.; COMBS, L. P.; AND LEVINE, R. S.: Progress in the Development of Rating Methods for Rocket Combustion Stability. AFOSR Fourth Symposium on Combustion Instability in Liquid Propellant Motors, Sunstrand-Turbo, Dec. 1957.

427. LAWHEAD, R. B.; COMBS, L. P.; AND WEBBER, W. T.: Research Studies of Combustion Instability in Large Thrust Liquid Propellant Rocket Engines. First Meeting JANAF Liquid Propellant Group, LPIA, Applied Physics Lab., Johns Hopkins University, Vol. III, Rocket Engine Research and Development, Nov. 1959, pp. 361–378.

428. LAWHEAD, R. B.; AND LEVINE, R. S.: Rocket Engine Vibration Studies. North American Aviation, RE-134, 1954.

LAWHEAD, R. B.: Also see Refs. 442 and 569.

429. LAWVER, B. R.: Some Observations on the Combustion of N_2H_4 Droplets. AIAA J, Vol. 4, 1966, p. 659.

430. LAWVER, B. R.; AND BREEN, B. P.: Hypergollic Stream Impingement Phenomena–Nitrogen Tetroxide/Hydrazine. Dynamic Science, NASA CR-7244, Oct. 1968.

431. LAWVER, B. R.; AND KAPPL, J. J.: Effects of Additives on Altitude Hypergolic Ignition. AIAA Preprint 66-608, AIAA Second Propulsion Joint Specialist Conference, June 1966.

LAWVER, B. R.: Also see Refs. 119 and 353.

432. LAYTON, J. P.: Technical Note on a Small Passage Technique for Transient Pressure Measurements in Large Rocket Motors. Princeton University, Aero. Eng. Rept. No. 595e, Oct. 1962.

433. LAYTON, J. P.; AND THOMAS, J. P.: Final Summary Technical Report on Transient Pressure Measuring Methods Research. Princeton University, Aero. Eng. Rept. No. 595t, March 1967.

LAYTON, J. P.: Also see Ref. 394.

434. LEDWELL, T. A.: The Burning of Hydrocarbon Fuel Droplets at High Pressure. Ph.D. Thesis, Dept. of Mechanical Eng., University of Waterloo, Ontario, July 1968.

LEE, D. H.: See Ref. 639.

435. LEE, K.; AND RYLEY, D. J.: The Evaporation of Water Droplets in Superheated Stream. Trans. ASME-J. Heat Transfer, Vol. 90, 1968, pp. 445–451.

436. LEEPER, C. K.: Excitation Chamber Combustion Response for Liquid Rocket Injectors, Part II–Analysis and Theory. Fourth ICRPG Combustion Conference, CPIA Pub. No. 162, Vol. 1, Dec. 1967, pp. 63–71.

437. LEFEBVRE, A. H.; AND REID, R.: The Influence

of Turbulence on the Structure and Propagation of Enclosed Flames. Combustion and Flame, Vol. 10, 1966, pp. 355–366.

438. LePage, W. R.; and Seely, S.: General Network Analysis. McGraw-Hill, New York, 1952, pp. 238–256.

439. Levich, V. G.: Physicochemical Hydrodynamics. Prentice-Hall, Inc., Englewood Cliffs, N. J., 1962.

Levine, J.: See Ref. 410.

440. Levine, R. S.: Experimental Status of High Frequency Liquid Rocket Combustion Instability. Tenth Symposium (International) on Combustion, The Combustion Institute, 1965, pp. 1083–1099.

441. Levine, R. S.; and Bambanek, R.: A Sustaining Mechanism for a Transverse Mode of Combustion Instability. Rocketdyne Rept. R-326, 1956.

442. Levine, R. S.; and Lawhead, R. B.: Rocketdyne Engine Vibration Studies–Final Summary Report. Project MX913, Contract AF33(038)-19430, July 1953.

Levine, R. S.: Also see Refs. 76, 272, 410, 421, 426, and 428.

443. Lewis, D. G.: Safer Pyrotechnics Through Laser Actuation. Space/Aeronautics, Vol. 47, No. 6, June 1967, p. 107.

444. Lewis, G. D.: Acoustic Liners for Eliminating Combustion Instability. First ICRPG Combustion Conference, CPIA No. 68, Vol. 1, Jan. 1965, pp. 251–274.

445. Lewis, J. D.: Some Basic Studies of Liquid Propellant Injection Processes. J. Roy. Aero. Soc., Vol. 68, 1964, pp. 743–750.

446. Lewis, J. D.: Studies of Atomization and Injection Processes in the Liquid Propellant Rocket Engine. Combustion and Propulsion, Fifth AGARD Colloquium: High Temperature Phenomena, Macmillan, New York, 1963, pp. 141–169.

447. Lewis, J. D.; and Harrison, D.: A Study of Combustion and Recombination Reactions During the Nozzle Expansion Process of a Liquid Propellant Rocket Engine. Eighth Symposium (International) on Combustion, Williams and Wilkins, Baltimore, 1962, pp. 366–374.

448. Lewis, J. D.; and Merrington, A. C.: Combustion of n-Heptane Spray in the Decomposition Products of Concentrated Hydrogen Peroxide. Seventh Symposium (International) on Combustion, Butterworths Sci. Pub., London, 1959, pp. 953–959.

Lewis, S. D.: See Ref. 588.

449. Li, Y. T.: Dynamic Pressure Measuring System for Jet Propulsion Research. ARS J., Vol. 23, No. 3, May 1953.

450. Lienhard, J. H.; and Meyer, P. L.: A Physical Basis for the Generalized Gamma Distributions. Quart. Appl. Math. Vol. 25, No. 3, Oct. 1967, p. 330.

Lightfoot, E. N.: See Ref. 99.

451. Lighthill, M. J.: A Technique for Rendering Approximate Solutions to Physical Problems Uniformly Valid. Phil. Mag., Ser. 7, Vol. 40, No. 311, 1949, p. 1179.

452. Linan, A.: On the Structure of Laminar Diffusion Flames. Inst. Nacional de Tecnica Aeronautics, Spain, DDC AD 432 882, June 1963.

453. Linvill, J. G.: The Approximation with Rational Functions of Prescribed Magnitude and Phase Characteristics. Proc. IRE, Vol. 40, 1952, p. 711.

Litovitz, T. A.: See Ref. 354.

Logan, S. E.: See Ref. 96.

454. Loison, R.: The Propagation of Deflagration in a Tube Covered with an Oil Film. Comptes Rendus, Vol. 234, 1952, pp. 512–513.

455. Lorell, J.; and Wise, H.: Steady State Burning of a Liquid Droplet: I. Monopropellant Flame. J. Chem. Phys., Vol. 23, 1955, p. 1928.

Lorell, J.: Also see Ref. 753.

456. Lunden, K. C.: An Analytical Investigation of the Effects of Baffles in a Liquid Propellant Rocket Combustion Chamber. Masters Thesis, Sacramento State College, Sept. 1969.

457. Luperi, M. J.; and Tick, S. J.: Vibration and Combustion Investigation of the LR99 Engine. Detonation and Two-Phase Flow, ARS Progress in Astronautics and Rocketry, Vol. 6, Academic Press, New York, 1962.

458. Mageean, J. V.: Space Storable Propellant Performance. TRW Rept. No. 09667-6001-RO-00 (NASA CR-72486), May 1969.

459. Maiman, T. H.: Stimulated Optical Emission in Fluorescent Solids. Physical Review, Vol. 123, Aug. 1961, pp. 1145–1157.

460. Maiman, T. H.: Stimulated Optical Radiation in Ruby. Nature, Vol. 187, Aug. 1960, pp. 493–494.

461. Male, T.; and Kerslake, W. R.: A Method for Prevention of Screaming in Rocket Engines. NACA RM E54F28A, Aug. 1954.

462. Male, T.; Kerslake, W. R.; and Tischler, A. O.: Photographic Study of Rotating Screaming and Other Oscillations in a Rocket Engine. NACA RM E54A29, May 1954.

463. Marble, F. E.: Dynamics of a Gas Containing Small Solid Particles. Proceedings of the Fifth AGARD Combustion and Propulsion Colloquium, Pergamon Press, New York, 1963.

464. Marks, L. S.: Mechanical Engineers Handbook, 3rd Edition. McGraw-Hill, New York, 1930, pp. 259 and 261.

465. Marshall, W. R.: Atomization and Spray Drying. Chem. Engr. Progr., Monograph Series, Vol. 50, No. 2, 1954.

Marshall, W. R.: Also see Ref. 577.

466. Maslen, S. H.; and Moore, F. K.: On Strong Transverse Waves Without Shocks in a Circular Cylinder. J. of Aero. Sci., Vol. 23, No. 6, 1956, pp. 583–593.

Maslen, S. H.; Also see Ref. 494.

467. Masters, A. I.; and Colbert, J. E.: Rocket Testing of Four Flox-Light Hydrocarbon Propellant Com-

binations. AIAA Preprint No. 66-624, AIAA Second Propulsion Joint Specialists Conference, June 1966.

468. MATTHEWS, B. J., ET AL.: Small Droplet Measuring Technique. Phase I Technical Report, TRW (Princeton) Rept. AFRPL-TR-67-295, Feb. 1968.

MATTHEWS, B. J.: Also see Refs. 764 and 765.

469. MATTHEWS, G. B.: Combustion Instability in Liquid Propellant Rocket Motors. Technical Report: Determination of Combustion Time Lag Parameters in a Liquid Bipropellant Rocket Motor. Princeton University Aero. Eng. Rept. No. 372, March 1957.

MATTHEWS, G. B.: Also see Ref. 182.

470. MAYER, E.: Theory of Liquid Atomization in High Velocity Gas Streams. ARS J., Vol. 31, No. 12, Dec. 1961, p. 1783.

MAYER, R. W.: See Ref. 138.

MAZZITELLI, D. A.: See Ref. 56.

471. MCADAMS, W. H.: Heat Transmission. McGraw-Hill, New York, 1954, pp. 444–490.

472. MCAULIFFE, C. E.: The Influence of High Speed Air Flow on the Behavior of Acoustical Elements. M.S. Thesis, M.I.T., Sept. 1950.

473. MCBRIDE, J. M.; HEWITT, R. A.; AND HEFNER, R. J.: Acoustic Techniques for Injector Baffle Development. Bulletin of the 7th Annual Liquid Propellant Symposium, ICRPG Combustion Conference, CPIA Pub. No. 72, Nov. 1967.

474. MCBRIDE, J.M.; AND VEGLIA, S. A.: Excitation Chamber-Combustion Response for Liquid Rocket Injectors, Part I: Experimental. Fourth ICRPG Combustion Conference, CPIA Pub. 162, Vol. I, Dec. 1967, p. 57.

MCBRIDE, J. M.: Also see Refs. 584 and 720.

MCCALLISTER, D. A.: See Ref. 720.

475. MCCORMACK, P. D.: A Driving Mechanism for High Frequency Combustion Instability in Liquid Fuel Rocket Engines. J. Royal Aero. Soc., Sept. 1964.

476. MCGOUGH, C. B.; LABOTZ, R. J.; AND ADDOMS, J. F.: Development of HIPERTHIN Injectors for Reaction Control Thrustor Applications. Proceedings of ASME Aviation and Space Conference, June 1968.

477. MCGOUGH, C. B.; ROUSAR, D. C.; AND VAN HUFF, N. E.: An Experimental Investigation of Heat Transfer of Cooled Injector Baffles. Bulletin of the Sixth Liquid Propulsion Symposium, CPIA Pub. 56, Vol. 1, Sept. 1964.

MCLAUGHLIN, C. W.: See Ref. 46.

MCMULLEN, E. T.: See Ref. 674.

478. MECHEL, F.; AND SCHILZ, W.: Research on Sound Propagation in Sound-Absorbent Ducts with Superimposed Air Streams. Vols. II & III, TDR No. AMRL-TDR-62-140, Dec. 1962.

479. MEISENHOLDER, S. G.; AND BICKFORD, L. L.: "POGO" Analysis of the Saturn Propulsion System. Aerojet-General Rept. AMDR 9635-037, 1967.

MERRINGTON, A. C.: See Ref. 448.

MEYER, P. L.: See Ref. 450.

MICKELSON, W. R.: See Refs. 637 and 739.

MIDDLEMAN, S.: See Ref. 296.

480. MIGDAL, D.: Continuum Gas-Particle Reacting Flow Systems. Polytechnic Institute of Brooklyn, Ph.D. Dissertation, 1968.

481. MIGDAL, D.; AND AGOSTA, V. D.: A Source Flow Model for Continuum Gas-Particle Flow. J. Appl. Mech., Vol. 34, Series E, No. 4, 1967, p. 860.

482. MILLAN, G.; AND TARIFA, C. S.: Combustion of Fuel Drops–Forced Convection and Interaction Effects. Inst. Nacional de Technica Aeronautica, Madrid, Spain, Sept. 1956.

MILLER, I.: See Ref. 82.

MILLER, J.: See Ref. 245.

483. MILLER, R. O.: A Review of Liquid Propellants. NASA TM X-1783, Apr. 1969.

484. MILLS, T. R.; AND BREEN, B. P.: A Mathematical Model of the Ignition Transient for Hypergolic Propellants. Fifth ICRPG Combustion Conference, CPIA Pub. 183, Dec. 1968, pp. 91–98.

485. MILLS, T. R.; AND SHERMAN, A.: Hydraulic Analysis of the Apollo Injector. Aerojet-General TM 183-63-29, Nov. 1963.

MILLS, T. R.: Also see Refs. 74 and 541.

486. MINORSKY, N.: Nonlinear Oscillations. D. Van Nostrand, Princeton, 1962.

487. MINTON, S. J.; AND KNOX, R. M.: Rocket Startup Transients at Low Pressures. AIAA Preprint 66-609, AIAA Second Propulsion Joint Specialist Conference, June 1966.

488. MITCHELL, C. E.: Axial Mode Shock Wave Combustion Instability in Liquid Propellant Rocket Engines. Princeton University, NASA CR-72259, 1967.

489. MITCHELL, C. E.; CROCCO, L.; AND SIRIGNANO, W. A.: Nonlinear Longitudinal Instability in Rocket Motors with Concentrated Combustion. Combustion Sci. & Tech., Vol. 1, No. 1, 1969.

MITCHELL, C. E.: Also see Ref. 194.

490. MITCHELL, J. P.: Advanced Throttling Concept Study. Pratt & Whitney, AFRPL-TR-65-98, March 1965.

491. MITCHELL, R. C.: The Effect of Nozzle Combustion on Engine Performance. Rocketdyne Rept. No. R-7103, Jan. 1968.

492. MOBERG, D. A.: Attenuation of Tangential Combustion Instability in an Ablative, Hypergolic Bipropellant 1750-lb-Thrust Rocket Engine. Fourth ICRPG Combustion Conference, CPIA Pub. 162, Vol. 1, Dec. 1967, p. 15.

493. MOLINARI, L. F.: MA-5 Baffled Injector and Uprated Test Program, Final Report, August–November 1962. Rocketdyne Rept. No. R-3322, March 1962.

MONTI, R.: See Ref. 195.

494. MOORE, F. K.; AND MASLEN, S. H.: Transverse

Oscillations in a Cylindrical Combustion Chamber. NACA TN 3152, Oct. 1954.
MOORE, F. K.: Also see Ref. 466.
495. MOORE, R. K.: Traveling-Wave Engineering. McGraw-Hill, New York, 1960, Chs. 5 and 9.
MORENO, F. G.: See Ref. 682.
496. MORETTI, G.; AND BASTIANON, R.: Three-Dimensional Effects in Intakes and Nozzles. AIAA Paper No. 67-224, AIAA 5th Aerospace Sciences Meeting, 1967.
MOREY, T. F.: See Ref. 244.
497. MORGAN, C. J.: Longitudinal Instability Limits with a Variable Length Hydrogen-Oxygen Combustor. Sixth ICRPG Liquid Propellant Combustion Instability Conference, CPIA. Pub. No. 192, Vol. 1, Dec. 1969, pp. 111–120.
MORGAN, C. J.: Also see Refs. 553, 716, and 718.
498. MORGAN, J.: Introduction to Geometrical and Physical Optics. McGraw-Hill, New York, 1953.
MORGANTE, P. J.: See Ref. 639.
499. MORRELL, G.: Critical Conditions for Drop and Jet Shattering. NASA TN D-677, Feb. 1961.
500. MORRELL, G.: Rate of Liquid Jet Breakup by a Transverse Shock Wave. NASA TN D-1728, 1963.
501. MORRELL, G.; AND POVINELLI, F. P.: Breakup of Various Liquid Jets by Shock Waves and Applications to Resonant Combustion. NASA TN D-2423, 1964.
MORRELL, G.: Also see Ref. 566.
502. MORRISON, R.: Modern Filter Theory. Dynamics Instrumentation Co., Monterey Park, California.
MORRISON, R. B.: Also see Ref. 199.
503. MORSE, P. M.: Vibration & Sound. McGraw-Hill, New York, 1948.
504. MORSE, P. M.; AND FESHBACH, H.: Methods of Theoretical Physics. McGraw-Hill, New York, 1953.
505. MORSE, P. M.; AND INGARD, K. U.: Theoretical Acoustics. McGraw-Hill, New York, 1968.
506. MUGELE, R. A.: Maximum Stable Droplets in Dispersoids. A.I.Ch.E.J., Vol. 6, No. 1, March 1960, p. 3.
507. MUGELE, R. A.; AND EVANS, H. D.: Droplet Size Distributions in Sprays. Ind. Engr. Chem., Vol. 43, No. 6, June 1951, p. 1317.
508. MULREADY, R. C.: The RL10 Oxygen-Hydrogen Rocket Engine Development Through Preliminary Flight Rating Test. 4th JANAF Liquid Propulsion Symposium, Published by APL, Johns Hopkins Univ., Doc. No. LPS 62-1, Nov. 1962, p. 367.
MYERS, P. S.: See Refs. 112, 248, and 249.
MYNCKE, H.: See Ref. 707.
NADAUD, L.: See Ref. 79.
NAGAI, C. K.: See Refs. 80, 221, and 258.
509. NESTLERODE, J. A.; CHADWICK, W. D.; AND GLEASON, J. L.: Investigation and Suppression of Rocket Feed System Oscillations. Third ICRPG Combustion Conference, CPIA Pub. No. 138, Vol. 1, Feb. 1967, p. 341.
510. NESTLERODE, J. A.; AND OBERG, C. L.: Combustion Instability in a Annular Engine. Sixth ICRPG Liquid Propellant Combustion Instability Conference, CPIA Pub. No. 192, Vol. 1, Dec. 1969, pp. 329–342.
511. NEWMAN, J. A.: A Preliminary Study of the Effects of Vaporization and Transverse Oscillations on Liquid Jet Breakup. Princeton University, NASA CR-72258, 1967.
512. NICHOLLS, J. A.; CULLEN, R. E.; AND RAGLAND, K. W.: Feasibility Studies of a Rotating Detonation Wave Rocket Motor. J. Spacecraft and Rockets, Vol. 3, June 1966, p. 893.
513. NICHOLLS, J. A.; DABORA, E. K.; AND RAGLAND, K. W.: A Study of Two-Phase Detonation as it Relates to Rocket Motor Combustion Instability. University of Michigan, NASA CR-272, 1965.
514. NICHOLLS, J. A.; RAGLAND, K. W.; AND RANGER, A. A.: Two Phase Detonations and Drop Shattering Studies. University of Michigan, NASA CR-72225, April 1967.
515. NICHOLLS, J. A.; AND RANGER, A. A.: Droplet Shattering. Fifth ICRPG Combustion Conference, CPIA Pub. No. 183, Dec. 1968, pp. 85–90.
516. NICHOLLS, J. A.; RANGER, A. A.; AND SIVIER, K. R.: Dynamics of Liquid and Solid Particles. Fourth ICRPG Combustion Conference, CPIA Pub. No. 162, Vol. I, Dec. 1967, p. 295.
NICHOLLS, J. A.: Also see Refs. 199, 207, 208, 210, 211, 572, and 576.
517. NICHOLSON, J. E.; AND HILL, A. F.: Rain Erosion on Spike Protected Supersonic Radomes. Mithas, Inc., Cambridge, Mass., MC-61-6-R3, 1963.
NICKERSON, G. R.: See Ref. 140.
518. NISHIWAKI, N.: Kinetics of Liquid Combustion Processes: Evaporation and Ignition Lag of Fuel Droplets. Fifth Symposium (International) on Combustion, Reinhold, New York, 1965, pp. 148–158.
519a. NORTHRUP, R. P.: Flow Stability in Small Orifices. Paper presented at 1951 ARS Annual Convention, Atlantic City, N. J., Nov. 1951.
NURICK, W.: See Ref. 225.
519b. NORTON, D. J.: Generalized One-Dimensional, Compound Compressible Nozzle Flow. Journal of Spacecraft and Rockets, Vol. 7, No. 3, Mar. 1970, pp. 338–341.
520. OBERG, C. L.: Final Rept.–Lunar Module Ascent Engine Acoustic Cavity Study. Rocketdyne Rept. No. R-7935, Aug. 1969.
521. OBERG, C. L.: Improved Design Techniques for Acoustic Liners. Rocketdyne Research Rept. 68-5, 1968.
522. OBERG, C. L.: LM Ascent Engine Acoustic Cavity Study. Sixth ICRPG Combustion Conference,

CPIA Pub. No. 192, Vol. 1, Dec. 1969, pp. 303–316.

523. OBERG, C. L.; AND KULUVA, N. M.: Acoustic Liners for Large Engines. Rocketdyne Rept. R-7792, March 1969.

OBERG, C. L.: Also see Refs. 403, 404, 405, 510, and 599.

524. ODGERS, I. L.; VAN DE VERG, N.; AND WICK, R. S.: Combustion Stability Research. JPL Progress Rept. 20-203, Jan. 1954.

525. O'DONNELL, J. D.: Operation and Service of Aerojet Periscope Model VI 4. Tech. Documentary Rept. No. AFPRL-TR-65-45, May 1964.

OLSON, D. R.: See Refs. 255 and 256.

OPPENHEIM, A. K.: See Ref. 701.

526. ORTON, J. W.: An Experimental Study of the Influence of Operating Conditions on Liquid Propellant Rocket Thrust Chamber Performance. R.P.E., Westcott, Gr. Britain, Technical Rept. (to be published).

527. OSBORN, J. R.; AND DAVIS, L. R.: Effects of Injection Location on Combustion Instability in Premixed Gaseous Bipropellant Rocket Motors. Purdue Univ. Rept. I-61-1, Jan. 1961.

OSBORN, J. R.: Also see Refs. 773, 774, 775, and 776.

528. OSBORN, R. H.: Liquid Rockets. Space/Aeronautics, R & D Issue 46, Vol. 2, July 1966, p. 94.

529. PADLEY, P. J.: The Origin of the Blue Continuum in the Hydrogen Flame. Faraday Society, Vol. 56, 1960.

530. PANOSIAN, J. O.: Development of a Fluorine/Hydrogen Injector. AIAA Paper No. 66-625, AIAA Second Propulsion Joint Specialists Conference, June 1966.

PARISH, H. C.: See Ref. 719.

531. PARKINSON, R. C.: Convective Heat Transfer in Rocket Engines. Heat Transfer in the Combustion Chamber. R.P.E., Westcott, Great Britain, Tech. Rpt. No. 69/5, April 1969.

532. PARKS, E. G., ET AL.: Thrust Chamber Materials and Design Concepts Evaluation. AFRPL TR-67-175, Oct. 1967.

533. PARZEN, E.: Notes on Fourier Analysis and Spectral Windows. Stanford University Applied Math Statistics Lab. Rept. No. 48, May 1963.

534. PASS, I.; AND TISCHLER, A. O.: Effect of Fuels on Screaming in a 200-Pound-Thrust Liquid Oxygen-Fuel Rocket Engine. NACA RM E56C10, 1956.

PATEL, B. R.: See Ref. 698.

PECK, R. E.: See Ref. 326.

PEDERSON, D. O.: See Ref. 411.

535. PENNER, S. S.: Chemical Rocket Propulsion and Combustion Research. Gordon & Breach Science Pub., 1962.

536. PENNER, S. S.: Chemistry Problems in Jet Propulsion. Macmillan, New York, 1957.

537. PENNER, S. S.: On the Development of Rational Scaling Procedures for Liquid-Fuel Rocket Engines. Jet Propulsion, Vol. 27, Feb. 1957, pp. 156–161.

538. PENNER, S. S.: Similarity Analysis for Chemical Reactors and the Scaling of Liquid-Fuel Rocket Engines. Combustion Researches and Reviews 1955, AGARD, Chap. 12, Butterworths Sci. Pub., London, 1955.

539. PENNER, S. S.; AND DATNER, P. P.: Combustion Problems in Liquid Fuel Rocket Engines. Fifth Symposium (International) on Combustion, Reinhold, New York, 1955, pp. 11–28.

PENNER, S. S.: Also see Refs. 63, 64, 289, 293, and 748.

540. PEOPLES, R. G.; AND BAKER, P. D.: Stability Rating Techniques. Western States Section/Combustion Institute Paper 64-11, April 1964.

541. PEOPLES, R. G.; BAKER, P. D.; AND MILLS, T. R.: Some Observations on Combustion Noise and Unstable Combustion. Aerojet-General Rept. No. 2444, Dec. 1962.

542. PEOPLES, R. G.; AND PICKFORD, R. S.: Analytical and Experimental Scaling of Thrust Chambers. Aerojet-General Rept. TN-40 (AFOSR 677), 1960.

PEOPLES, R. G.: Also see Ref. 74.

543. PERRY, J. H. (Ed.): Chemical Engineer's Handbook, 4th Edition. McGraw-Hill, New York, 1963.

PERSON, R. A.: See Ref. 362.

544. PESCHE, W. T.; AND HAMMER, S. S.: Pressure Gradients in a Liquid Propellant Rocket Motor. AIAA J., Vol. 2, No. 8, Aug. 1964, p. 1467.

PESHKE, W. T.: See Refs. 55 and 308.

545. PESKIN, R. L.; POLYMEROPOULOS, C. E.; AND YEH, P. S.: Results from a Theoretical Study of Fuel Drop Ignition and Extinction. AIAA J., Vol. 5, 1967, p. 2173, (also see Comb. Flame, Vol. 13, 1969, p. 166).

546. PESKIN, R. L.; AND WISE, H.: A Theory for Ignition and Deflagration of Fuel Drops. AIAA J., Vol. 4, 1966, p. 1646.

547. PESKIN, R. L.; AND YEH, P. S.: A Theoretical Study of the Effect of Convection on the Ignition of Single Aerosol Droplets. Edgewood Arsenal Rept. 67-10, June 1967.

PESKIN, R. L.: Also see Ref. 604.

548. PHILLIPS, B.: Acoustic Liner Studies at the Lewis Research Center. Fourth ICRPG Combustion Conference, Pub. No. 162, Vol. 1, Dec. 1967, pp. 111–122.

549. PHILLIPS, B.: Effects of High Wave Amplitude and Mean Flow on a Helmholtz Resonator. NASA TM X-1582, May 1968

550. PHILLIPS, B.: Experimental Investigation of an Acoustic Liner with Variable Cavity Depth. NASA TN D-4492, April 1968.

551. PHILLIPS, B.: Recent Advances in Acoustic Liner Technology at the Lewis Research Center. Fifth ICRPG Combustion Conference, CPIA Pub. No. 183, Dec. 1968, pp. 343–350.

552. PHILLIPS, B.; HANNUM, N. P.; AND RUSSELL, L. M.: On the Design of Acoustic Liners for Rocket Engines: Helmholtz Resonators Evaluated with a Rocket Combustor. NASA TN D-5171, April 1969.

553. PHILLIPS, B.; AND MORGAN, C. J.: Mechanical Absorption of Acoustic Oscillations in Simulated Rocket Combustion Chambers. NASA TN D-3792, Jan. 1967.

PHILLIPS, B.: Also see Ref. 710.

PICKFORD, R. S.: See Refs. 242 and 542.

554. PIEPER, J. L.; DEAN, L. E.; AND VALENTINE, R. S.: Mixture Ratio Distribution—Its Impact on Rocket Thrust Chamber Performance. J. Spacecraft & Rockets, Vol. 4, No. 6, June 1967, pp. 786–789.

PIEPER, J. L.: Also see Ref. 703.

PINCHAK, A. C.: See Ref. 776.

POLYMEROPOULOS, C. E.: See Ref. 545.

PORTER, R. N.: See Ref. 226.

555. POVINELLI, F. P.: Displacement of Disintegrating Liquid Jets in Crossflow. NASA TN D-4334, 1968.

POVINELLI, F. P.: Also see Ref. 501.

POVINELLI, L. A.: See Ref. 342.

555b. POWELL, W. B.: ICRPG Liquid Propellant Thrust Chamber Performance Evaluation Methodology. Journal of Spacecraft and Rockets, Vol. 7, No. 1, Jan. 1970, pp. 105–108.

PRICE, E. W.: See Ref. 127.

556. PRIEM, R. J.: Combustion Process Influence on Stability. Chemical Engineering Progress Symposium Series, Vol. 62, No. 61, 1966, pp. 103–112.

557. PRIEM, R. J.: Propellant Vaporization as a Criterion for Rocket Engine Design: Calculations of Chamber Length to Vaporize a Single Heptane Drop. NACA TN 3985, 1957.

558. PRIEM, R. J.: Propellant Vaporization as a Criterion for Rocket Engine Design: Calculation of Chamber Length to Vaporize Various Propellants. NACA TN 3883, 1958.

559. PRIEM, R. J.: Propellant Vaporization as a Criterion for Rocket-Engine Design: Calculations Using Various Log-Probability Distributions of Heptane Drops. NACA TN 4098, Oct. 1957.

560. PRIEM, R. J.: Theoretical and Experimental Models of Unstable Rocket Combustion. Ninth Symposium (International) on Combustion, Academic Press, New York, 1963, p. 982.

561. PRIEM, R. J.: Tutorial Seminar Paper on "L" and "J" Combustion Model. Second ICRPG Combustion Conference, CPIA Pub. No. 105, May 1966, p. 139.

562. PRIEM, R. J.; BORMAN, G. L.; EL WAKIL, M. M.; UYEHARA, O. A.; AND MYERS, P. S.: Experimental and Calculated Histories of Vaporizing Fuel Drop. NACA TN 3988, Aug. 1957.

563. PRIEM, R. J.; AND GUENTERT, D. C.: Combustion Instability Limits Determined by a Nonlinear Theory and a One-Dimensional Model. NASA TN D-1409, Oct. 1962.

564. PRIEM, R. J.; AND HEIDMANN, M. F.: Propellant Vaporization as a Design Criterion for Rocket-Engine Combustion Chambers. NASA TR R-67, 1960.

565. PRIEM, R. J.; AND HEIDMANN, M. F.: Vaporization of Propellants in Rocket Engines. ARS J., Vol. 29, 1959, p. 836.

566. PRIEM, R. J.; AND MORRELL, G.: Application of Similarity Parameters for Correlating High Frequency Instability Behavior of Liquid Propellant Combustors. Progress in Astronautics and Rocketry, Vol. 6, Academic Press, New York, 1962, pp. 305–320.

567. PRIEM, R. J.; AND RICE, E. J.: Combustion Instability with Finite Mach Number Flow and Acoustic Liners. NASA TM X-52412, 1968.

PRIEM, R. J.: Also see Refs. 249, 343, 344, and 348.

PROFFIT, R. L.: See Ref. 348.

568. PROBERT, R. P.: The Influence of Spray Particle Size and Distribution in the Combustion of Oil Droplets. Philosophical Magazine and Journal of Science, Vol. 37, p. 94, 1946.

QUAN, V.: See Ref. 409.

569. RABIN, E.; SCHALLENMULLER, A. R.; AND LAWHEAD, R. B.: Displacement and Shattering of Propellant Droplets. Rocketdyne, AFOSR TR 60-75, 1960.

570. RAGLAND, K. W.: The Propagation and Structure of Two Phase Detonations. Ph.D. Thesis, University of Michigan, 1967.

571. RAGLAND, K. W.: Solution of the Blasius Boundary Layer Equation Behind a Shock with Vaporization and Combustion at the Wall. University of Michigan, NASA CR-72235, 1967.

572. RAGLAND, K. W.; DABORA, E. K.; AND NICHOLLS, J. A.: Observed Structure of Spray Detonations. Physics of Fluids, Vol. 11, No. 11, Nov. 1968, p. 2377.

RAGLAND, K. W.: Also see Refs. 207, 208, 209, 210, 211, 512, 513, and 514.

573. RAHON, J. R.: Effects of Radial Energy Release Variations on Transverse Combustion Pressure Oscillations. MSME Thesis, Purdue University, June 1962.

RAMANI, N.: See Ref. 388.

574. RANDALL, L. N.: Rocket Applications of the Cavitating Venturi. J. ARS., Vol. 22, No. 1, Jan.–Feb. 1952, pp. 28–31.

575. RANGER, A. A.: Aerodynamic Shattering of Liquid Drops. Ph.D. Thesis, University of Michigan, 1968.

RANGER, A. A.: Also see Refs. 209, 211, 515, and 516.

576. RANGER, A. A.; AND NICHOLLS, J. A.: Aerodynamic Shattering of Liquid Drops. AIAA J., Vol. 7, No. 2, Feb. 1969.

577. RANZ, W. E.; AND MARSHALL, W. R., JR.: Evaporation From Drops. Chemical Engineering Progress, Vol. 48, 1952, pp. 141–146, 173–180.

578. RAYLEIGH, LORD: On the Instability of Jets. Proc. London Math. Soc., Vol. 10, Nov. 1878.

579. RAYLEIGH, LORD: The Theory of Sound, Vol. II, Second Edition. Dover Publication, 1945.

580. REARDON, F. H.: Application of Crocco Theory. Second ICRPG Combustion Conference, CPIA Pub. No. 105, May 1966, pp. 155–162.

581. REARDON, F. H.: Correlation of Sensitive-Time-Lag-Theory Combustion Parameters with Thrust Chamber Design and Operating Variables. Fifth ICRPG Combustion Conference, CPIA Pub. No. 183, Dec. 1968, pp. 237–244.

582. REARDON, F. H.: An Investigation of Transverse Mode Combustion Instability in Liquid Propellant Rocket Motors. Ph. D. Thesis, Princeton University Aero. Eng. Rept. No. 550, June 1961.

583. REARDON, F. H.; CROCCO, L.; AND HARRJE, D. T.: Velocity Effects in Transverse Mode Liquid Propellant Rocket Combustion Instability. AIAA J., Vol. 2, No. 9, Sept. 1964, pp. 1631–1641.

584. REARDON, F. H.; MCBRIDE, J. M.; AND SMITH, A. J., JR.: Effect of Injection Distribution on Combustion Instability. AIAA J., Vol. 4, No. 3, March 1966, pp. 506–512.

585. REARDON, F. H.; AND SMITH, A. J., JR.: An Experimental Investigation of Combustion Stability Characteristics at High Chamber Pressures. Aerojet-General Interim Rept. 11741-1, 1965.

586. REARDON, F. H.; AND WAUGH, R. E.: Feed System Effects on Combustion Instability. Aerojet-General Rept. TCR 9645-002, 1963.

REARDON, F. H.: Also see Refs. 187, 323, 333, 649, 650, and 721.

587. REBA, I.; AND COLEMAN, B.: Combustion Instability: Liquid Stream and Droplet Behavior. Aeronautical Research Lab., Wright-Patterson AFB, WADC 59-720, 1960.

REDDING, R. A.: See Ref. 732.

REETHOF, G.: See Ref. 103.

REEVES, D. F.: See Ref. 83.

REID, R.: See Ref. 437.

588. REUTENIK, J. R.; AND LEWIS, S. D.: Pressure probe and System for Measuring Large Blast Waves. Massachussetts Institute of Technology, AFFDL-TDR-65-35, June 1965.

589. RICE, E. J.: The Effect of Selected Fluid Parameters on Spatial Drop Size Distribution. Ph. D. Thesis, University of Wisconsin, 1966.

RICE, E. J.: Also see Refs. 352 and 567.

590. RIEBLING, R. W.: Controlling the Dimensions and Orientations of Impinging Propellant Sheets in Liquid Rocket Engine Injectors. J. Spacecraft and Rockets, Vol. 3, No. 11, Nov. 1966, pp. 1692–1694.

591. RIEBLING, R. W.: Criteria for Optimum Propellant Mixing in Impinging-Jet Injection Elements. J. Spacecraft Rockets, Vol. 4, No. 6, June 1967, pp. 817–819.

592. RIEBLING, R. W.: The Formation and Properties of Liquid Sheets Suitable for Use in Rocket Engine Injectors. JPL Tech. Rept. 32-1112, June 1967.

RIEBLING, R. W.: Also see Ref. 252.

593. RING, E.: Rocket Propellant and Pressurization Systems. Prentice-Hall, Englewood Cliffs, N. J., 1964.

594. RINGLEB, F. O.: Discussion of Problems Associated with Standing Vortices and Their Applications. ASME Symposium In Fully Separated Flows, 1964.

595. RIVERS, W. J., ET AL.: Effect of Rocket Chamber Combustion on Chamber Materials, Part I: One-Dimensional Computer Program–Final Report. Rocketdyne, AFRPL-TR-65-13, Jan. 1965.

ROCKOW, R.: See Ref. 245.

596. ROGERO, S.: Measurement of the High Frequency Pressure Phenomena Associated with Oscillatory Combustion in Rocket Engines. Third ICRPG Combustion Conference, CPIA Pub. No. 138, Vol. 1, Feb. 1967, pp. 361–374.

597. ROGERO, S.: Measurement of the High Frequency Pressure Phenomena Associated with Rocket Motors. JPL Tech. Rept. 32-624, May 1964.

ROGERO, R. S.: Also see Refs. 151 and 152.

598. ROJEC, E. A.: Photographic Presentation of Shear-Type Droplet Breakup. Rocketdyne Research Rept. No. 63-39, Nov. 1963.

ROOS, F. W.: See Ref. 751.

599. ROSEN, B.; AND OBERG, C. L.: Acoustic Model Studies of Baffle Configurations for the Extended Range Lance (XRL) Booster Engine. Rocketdyne Research Rept. 67-21, Dec. 1967.

600. ROSNER, D. E.: Diffusional Theory of Reactive Chemical Releases, AeroChem TP-128, Feb. 1966.

601. ROSNER, D. E.: On Liquid Droplet Combustion at High Pressures. AIAA J., Vol. 5, 1967, p. 163.

602. ROSS, C. C.: Scaling of Liquid Fuel Rocket Combustion Chambers. AGARD Selected Combustion Problems, Vol. 2, Butterworths Sci. Pub., London, 1956, pp. 444–456.

603. ROSS, C. C.; AND DATNER, P. P.: Combustion Instability in Liquid Propellant Rocket Motors–a Survey. Selected Combustion Problems, Butterworths Sci. Pub., London, 1954, pp. 352–401.

ROSS, P. S.: See Ref. 715.

604. ROSSER, W. A., JR.; AND PESKIN, R. L.: A Study of Decomposition Burning. Combustion and Flame, Vol. 10, 1966, p. 152.

ROSSER, W. A.: Also see Refs. 57, 756, and 757.

ROSSI, F. S.: See Refs. 704 and 705.

605. ROSSMAN, T. G.: Experiments on Instability in Liquid Propellant Rocket Engines. AFOSR Fourth Symposium on Rocket Combustion Instability, Sunstrand-Turbo, Pacoima, Calif., 1957.

606. ROSSMANN, T. G.: A High-Speed and High-Resolution Photographic Technique for the Observation of Propellants Injected into a Firing Combustion Chamber. Technical Note, Bell Aerosystems Rept. No. 8007-981-008, Parts I and II, May 1959,

(AFOSR Doc. No. TN59-8; ASTIA Doc. No. 208-304).

607. Rossmann, T. G.: Observation of Propellants Injected into a Firing Rocket Chamber. Bell Aerosystems Tech. Rept. No. 8007-981-011, (AFOSR TR No. 60-98), July 1960.

608. Rossman, T. G.; Eulner, R. N.; and Wood, L. M.: Photographic Investigation of Propellant Stream Behavior in a Firing Rocket Engine. Bell Aerosystems Tech. Summary Rept. No. 9136-950001, June 1966.

Rousar, D. C.: See Ref. 477.

609. Rowley, R. W.; and Tyler, W. H.: The Effect of Injector Design on Thrust-Chamber Erosion. AIAA Paper No. 65-586, 1965.

Royce, R. L.: See Ref. 408.

610. Rupe, J. H.: Bridging the Gap Between Injector Hydraulics and Combustion Phenomena in Liquid Propellant Rocket Engines. Bulletin of the First JANAF Meeting of the Liquid Propellant Group, Vol. III, Rocket Engine Research and Development, LPIA, Johns Hopkins University, Silver Spring, Md., pp. 335–360, Nov. 1959.

611. Rupe, J. H.: Bridging the Gap Between Injector Hydraulics and Combustion Phenomena in Propellant Rocket Engines. JPL Pub. No. 167, Sept. 1959.

612. Rupe, J. H.: A Correlation Between the Dynamic Properties of a Pair of Impinging Streams and the Uniformity of Mixture-Ratio Distribution in the Resulting Spray. JPL Progress Rept. No. 20-209, 1956.

613. Rupe, J. H.: An Experimental Correlation of the Nonreactive Properties of Injection Schemes and Combustion Effects in a Liquid Propellant Rocket Engine, Part I. The Application of Nonreactive Spray Properties to Rocket Motor Injector Design. JPL Tech. Rept. 32-255, July 1965.

614. Rupe, J. H.: An Experimental Correlation of the Nonreactive Properties of Injection Schemes and Combustion Effects in a Liquid-Propellant Rocket Motor, Part V. The Influence of Vanes on Combustion and Combustion Stability. JPL Tech. Rept. 32-255, Sept. 1967.

615. Rupe, J. H.: Experimental Studies of the Hydrodynamics of Liquid Propellant Injection. JPL External Pub. No. 388, June 1957.

616. Rupe, J. H.: On the Dynamic Characteristics of Free-Liquid Jets and a Partial Correlation with Orifice Geometry. JPL Tech. Rept. No. 32-207, Jan. 1962.

617. Rupe, J. H.: The Liquid Phase Mixing of a Pair of Impinging Streams. JPL Progress Rept. No. 20-195, Aug. 1953.

618. Rupe, J. H.; Dipprey, D.; Kushida, R.; and Clayton, R.: A Stability Criterion for Impinging Jets and Its Impact on Combustion. Sixth ICRPG Combustion Conference, CPIA Pub. No. 192, Vol. 1, Dec. 1969, pp. 1–12.

619. Rupe, J. H.; and Evans, D. D.: Designing for Compatibility in High Performance LP Engines. Astronautics and Aeronautics, Vol. 3, 1965, pp. 68–74.

620. Rupe, J. H.; and Jaivin, G. I.: The Effects of Injection Mass Flux Distributions and Resonant Combustion on Local Heat Transfer in a Liquid-Propellant Rocket Engine. JPL Tech. Rept. No. 32-648, Oct. 1964.

Rupe, J. H.: Also see Refs. 153 and 226.

621. Russell, G. E.: Hydraulics. Henry Holt & Co., 1937, p. 225.

Russell, L. M.: See Refs. 552 and 717.

Russell, P. R.: See Ref. 286.

Ryley, D. J.: See Ref. 435.

622. Sabersky, R. H.: Effect of Wave Propagation in Feed Lines on Low Frequency Rocket Instability. Jet Propulsion, Vol. 24, 1954, p. 172.

623. Sakurai, A.: Blast Wave Theory. Basic Developments in Fluid Dynamics, Vol. 1, M. Holt, ed., Academic Press, New York, 1965.

Salant, R. F.: See Ref. 696.

624. Salmi, R. J.; Wanhainen, J. P.; and Hannum, N. P.: Effect of Thrust-Per-Element on Combustion Stability Characteristics of a 20,000-Pound Rocket Engine, NASA TN D-4851, 1968.

625. Sanchez, J. C.: Semiconductor Strain Gage Pressure Sensors. Instruments and Control Systems, Vol. 36, No. 11, Nov. 1963, pp. 117–120.

Sanders, C. F.: See Ref. 89.

626. Satche, M.: Discussion on "Stability of Linear Oscillation Systems with Constant Time Lag." Journ. Appl. Mech., Vol. 16, 1949, p. 418.

Savell, C. T.: See Ref. 772.

627. Sawyer, R. F.: C-1 Program Special Report–Combustion Irregularity. RMD Rept. 6203-53, Aug. 1966.

628. Sawyer, R. F.: Mass Spectrometric Observation of Ignition Phenomena in a Small Rocket Combustion Chamber. Paper No. WSCI-67-39, Western States Section of the Combustion Institute Fall Meeting, 1967.

629. Sawyer, R. F.: The Hydrazine-Nitrogen Tetroxide Reaction, A Comparison of Experimental Observations. Third ICRPG Combustion Conference, CPIA Pub. No. 138, Vol. 1, Feb. 1967, p. 481.

630. Scala, S. M.: Transverse Wave and Entropy Wave Combustion Instability in Liquid Propellant Rockets. Ph.D. Thesis, Princeton University Aero Eng. Rept. No. 380, April 1957.

Schallenmuller, A. R.: See Ref. 569.

Schilz, W.: See Ref. 478.

631. Schindler, R. C.; and Kiser H. V.: Development and Demonstration of Ablative Thrust Chamber Assemblies Using LF_2/N_2H_4 Blend Propellants. Aerojet-General Rept. No. AGC-9400-14 (AFRPL-TR-69-2 and AD 395844), Jan. 1969.

632. SCHLICHTING, H.: Boundary Layer Theory, 4th Edition. McGraw-Hill, New York, 1955, p. 370.

633. SCHMIDT, E. H. W.; AND SCHOPPE, F.: Mixing and Combustion at High Turbulence in Combustion Chambers. Fifth Symposium (International) on Combustion, Reinhold, New York, 1955, pp. 343–347.

SCHNELL, A. C.: See Ref. 286.

634. SCHOB, W. J.; GLASSMAN, I.; AND WEBB, M. J.: An Experimental Investigation of Heat Transfer and Pressure Effects on Longitudinal Combustion Instability in a Rocket Motor Using Premixed Gaseous Propellants. Princeton University Aero. Eng. Rept. 649, June 1963.

635. SCHOENMAN, L.: Personal Communication. Aerojet-General Corp., Sacramento, Calif., 1968.

SCHOPPE, F.: See Ref. 633.

636. SCHOTT, G. L.: Observations of the Structure of Spinning Detonations. Physics of Fluids, Vol. 8, No. 5, 1965.

SCHUM, H. J.: See Ref. 233.

SCHUMACHER, P. E.: See Refs. 155 and 167.

SCHUMAN, M. D.: See Refs. 165, 166, and 223.

SCHUMAN, T. E. W.: See Ref. 128.

SCOTT, H. E.: See Ref. 312.

637. SCULL, W. E.; AND MICKELSON, W. R.: Flow and Mixing Processes in Combustion Chambers. NACA Rept. R-1300, 1957, pp. 32–82.

SEADER, J. D.: See Ref. 677.

638. SEEBAUGH, W. R.; AND LEE, D. H.: An Optical Method for Observing Breakup and Vaporization of Liquid Jets. Princeton University Aero. Eng. Rept. No. 647, June 1963.

SEELY, S.: See Ref. 438.

639. SENNEFF, J. M.; AND MORGANTE, P. J.: Combustion Stability Investigation of the LEM Ascent Engine. Second ICRPG Propulsion Conference, CPIA Pub. No. 105, Vol. 1, May 1966, pp. 23–46.

640. SHAFER, M. R.: Performance Characteristics of Turbine Flowmeters. Paper No. 6-WH-25, ASME, June 1961.

641. SHAPIRO, A. H.: The Dynamics and Thermodynamics of Compressible Fluid Flow, Vol. I. Ronald Press, New York, 1953.

642. SHAPIRO, A. H.: The Dynamics and Thermodynamics of Compressible Fluid Flow, Vol. II. Ronald Press, New York, 1954, Sect. 23.3.

SHEARER, J. L.: See Ref. 103.

SHEN, P. I. W.: See Ref. 48.

SHERMAN, A.: See Ref. 485.

643. SHERWOOD, C. M.: Steady-State Streak Film Analysis in the High-Pressure Two-Dimensional Research Motor. Rocketdyne Res. Rept. No. 64-34, Oct. 1964.

SIDDALL, R. G.: See Ref. 360.

SILVER, S.: See Ref. 241.

SIMPSON, H. C.: See Ref. 363.

644. SIRIGNANO, W. A.: The Nonlinearity in Acoustic Liners. To be published.

645. SIRIGNANO, W. A.: A Theoretical Study of Nonlinear Combustion Instability: Longitudinal Mode. Ph.D. Thesis, Princeton University Aerospace and Mech. Sci. Tech. Rept. No. 677, March 1964.

646. SIRIGNANO, W. A.; AND CROCCO, L.: A Shock Wave Model of Unstable Rocket Combustion. AIAA J., Vol. 2, No. 7, July 1964, p. 1285.

647. SIRIGNANO, W. A.; CROCCO, L.; AND HARRJE, D. T.: Acoustic Liner Studies. Third ICRPG Combustion Conference, CPIA Pub. No. 138, Vol. 1, Feb. 1967, pp. 581–586.

SIRIGNANO, W. A.: Also see Refs. 188, 189, 190, 191, 192, 193, 196, 197, 324, 489, 691, 693, and 694.

SIVIER, K. R.: See Ref. 516.

648. SKILLING, H. H.: Electric Transmission Lines. McGraw-Hill, New York, 1951.

SLATES, R. O.: See Refs. 126 and 127.

649. SMITH, A. J., JR.; AND REARDON, F. H.: Development of a Variable-Length Chamber for Liquid Rocket Combustion Research. Aerojet-General Rept. 212/SA3-F, Vol. 3 (BSD-TDR-64-137), Oct. 1964.

650. SMITH, A. J., JR.; REARDON, F. H., ET AL.: The Sensitive Time Lag Theory and Its Application to Liquid Rocket Combustion Instability Problems. Aerojet-General, AFRPL-TR-67-314, March, 1968.

SMITH, A. J., Jr.: Also see Refs. 333, 584, and 585.

SMITH, E. B.: See Ref. 266.

SMITH, I. E.: See Ref. 116.

SMITH, P. W., JR.: See Ref. 295.

651. SODHA, M. S.: On Internal Ballistics of Liquid Fuel Rockets. Appl. Sci. Res., Vol. 7, 1958, p. 421.

652. SOKOLOWSKI, D. E.; VINCENT, D. W.; AND CONRAD, E. W.: Characterization of Pressure Perturbations Induced in a Rocket Combustor by a Machine Gun. NASA TN D-5214, May 1969.

SOKOLOWSKI, D. E.: Also see Refs. 345 and 711.

653. SOMOGYI, D.; AND FEILER, C. E.: Mixture Ratio Distribution in the Drops of Spray Produced by Impinging Liquid Streams. ARS J., Vol. 30, 1960, p. 185.

654. SOTTER, J. G.: Nonsteady Evaporation of Liquid Propellant Drops: The Grossman Model. JPL Tech. Rept. 32-1061, 1968.

655. SOTTER, J. G.; AND CLAYTON, R. M.: Monitoring the Combustion Process in Large Engines. J. of Spacecraft and Rockets, Vol. 4, No. 5, May 1967, p. 702.

SOTTER, J. G.: Also see Refs. 152, 154 and 759.

656. SPALDING, D. B.: Combustion in Liquid-Fuel Rocket Motors. Aero. Quarterly, Vol. 10, 1959.

657. SPALDING, D. B.: Combustion of a Single Droplet and of a Fuel Spray. Selected Combustion Problems, AGARD, Butterworths, London, 1954, p. 340–351.

658. SPALDING, D. B.: Combustion of Liquid Fuel in a Gas Stream. Fuel, Vol. 29, 1950, p. 25; see also Fuel, Vol. 30, 1951, p. 121.

659. SPALDING, D. B.: The Combustion of Liquid Fuels. Fourth Symposium (International) on Combustion, Williams and Wilkins, Baltimore, 1953, pp. 847–864.

660. SPALDING, D. B.: A One-Dimensional Theory of Liquid Fuel Rocket Combustion. ARC Tech. Rept. No. 20-175, Current Paper No. 445, 1959.

661. SPALDING, D. B.: Some Fundamentals of Combustion. Gas Turbine Series, Vol. 2, Academic Press, New York, 1955.

662. SPALDING, D. B.: Theory of Particle Combustion at High Pressures. ARS J., Vol. 29, 1959, pp. 828–835.

663. SPALDING, D. B.; AND JAIN, V. K.: Theory of the Burning of Monopropellant Droplets. Combustion and Fuels Subcommittee, Great Britain, ARC-CP 447, May 1958.

SPRANKLE, M. L.: See Ref. 267.

664. SQUIRE, H. B.: The Investigation of the Instability of a Moving Liquid Film. Brit. J. Appl. Physics, Vol. 4, June 1953, p. 167.

STANFORD, H. B.: See Ref. 252.

STAUDHAMMER, P.: See Refs. 245 and 246.

STEWART, W. E.: See Ref. 99.

STINGER, W. A.: See Ref. 324.

STOPFORD, J. M.: See Ref. 696.

665. STRAHLE, W. C.: A Theoretical Study of Unsteady Droplet Burning: Transients and Periodic Solutions. Ph.D. Thesis, Princeton University Aero. Eng. Rept. No. 671, 1963.

666. STRAHLE, W. C.: High Frequency Behavior of the Laminar Jet Flame Subjected to Transverse Sound Waves. Eleventh Symposium (International) on Combustion, The Combustion Institute, Pittsburgh, 1967, p. 747.

667. STRAHLE, W. C.: Periodic Solutions to a Convective Droplet Burning Problem: The Stagnation Point. Tenth Symposium (International) on Combustion, The Combustion Institute, Pittsburgh, 1965, pp. 1315–1325.

668. STRAHLE, W. C.: The Temporal Development of a Reacting Boundary Layer Near the Stagnation Point of a Vaporizing Drop in an Oxidizing Stream. AIAA Paper No. 69-174, AIAA 7th Aerospace Sciences Meeting, New York, Jan. 1969.

669. STRAHLE, W. C.: Unsteady Laminar Jet Flame at Large Frequencies of Oscillation. AIAA J., Vol. 3, No. 5, May 1965, p. 957.

670. STRAHLE, W. C.: Unsteady Reacting Boundary Layer on a Vaporizing Flat Plate. AIAA J., Vol. 3, No. 6, June 1965, p. 1195.

671. STRAHLE, W. C.; AND CROCCO, L.: Analytical Investigation of Several Mechanisms of Combustion Instability. Bulletin of the Fifth Liquid Propulsion Symposium, CPIA Pub. No. 37, Vol. II, Dec. 1963, pp. 823–842.

672. See Ref. 579.

673. SUMMERFIELD, M.: A Theory of Unstable Propulsion in Liquid Propellant Rocket Systems. J. ARS., Vol. 21, No. 5, Sept. 1951, pp. 108–114.

674. SUMMERS, W. H.; AND MCMULLEN, E. T.: Combustion of the N_2H_4/N_2O_4 Propellant System. AIAA Paper 66-662, June 1966.

675. SUNDERLAND, J. E.; AND GROSH, R. J.: Transient Temperature in a Melting Solid. J. of Heat Transf., Vol. 83, Series C., No. 4, Nov. 1961, pp. 409–414.

676. SUTTON, G. P.: Rocket Propulsion Elements. John Wiley and Sons, New York, 1949.

677. SUTTON, G. P.; WAGNER, W. R.; AND SEADER, J. D.: Advanced Cooling Techniques for Rocket Engines. Astronautics and Aeronautics, Jan. 1966, pp. 60–71.

SUTTON, R. D.: See Ref. 275.

SWICK, E. B.: See Ref. 396.

678. SZUCH, J. R.; AND WENZEL, L. M.: Experimental Verification of a Double-Dead-Time Model Describing Chugging in Liquid-Bipropellant Rocket Engines. Fourth ICRPG Combustion Conference, CPIA Pub. No. 162, Vol. 1, Dec. 1967, pp. 175–184.

SZUCH, J. R.: Also see Ref. 731.

679. TABATA, W. K.; ANTL, R. J.; AND VINCENT, D. W.: Storable Propellant Combustion Instability Program at Lewis Research Center. AIAA Paper No. 66-602, AIAA Propulsion Joint Specialist Conference, June 1966.

TANG, P.: See Ref. 198.

680. TARIFA, C. S.: On the Influence of Chemical Kinetics on the Combustion on Fuel Droplets. Paper B9, Congres International des Machines a Combustion (CIMAC), Copenhagen, 1962; see also AFOSR TN-5, DDC AD 277 299, March 1962.

681. TARIFA, C. S.; AND DEL NOTARIO, P. P.: Some Fundamental Problems on the Combustion of Liquid Oxidizers in Hydrogen. XVIIth International Astronautical Federation Congress, Madrid, 1966.

682. TARIFA, C. S.; DEL NOTARIO, P. P.; AND MORENO, F. G.: Combustion of Liquid Monopropellants and Bipropellants in Droplets. Eighth Symposium (International) on Combustion, Williams and Wilkins, Baltimore, 1962, pp. 1035–1056.

TARIFA, C. S.: Also see Ref. 482.

TATE, K. W.: See Refs. 224 and 225.

683. TAYLOR, G.: The Dynamics of Thin Sheets of Fluid, I. Water Bells. Proc. Roy. Soc., Vol. 253A, Dec. 1959, p. 289.

TAYLOR, T. D.: See Ref. 47.

684. TEMKIN, S.; AND DOBBINS, R. A.: Attenuation and Dispersion of Sound by Particulate-Relaxation Processes. J. Acoust. Soc. Amer., Vol. 4, 1966, p. 317.

685. TEMKIN, S.; AND DOBBINS, R. A.: Measurements of Attenuation and Dispersion of Sound by an Aerosol. J. Acoust. Soc. Amer., Vol. 40, 1966, p. 1016.

TEMKIN, S.: Also see Ref. 228.
TESTEN, J.: See Ref. 386.
THOM, A. S.: See Ref. 234.
686. THOMAS, L. H.: Theory of the Explosion of Cased Charges of Simple Shape. U. S. Army Ballistic Res. Labs. Rept. No. 475, July 1944.
THOMAS, J. P.: See Refs. 394 and 433.
THOMAS, R. M.: See Ref. 227.
687. THOMPSON, R. E.; AND GREY, J.: Turbine Flowmeter Performance Model. Greyrad Corp., Rept. AMC-3, Oct. 1967.
THRING, M. W.: See Ref. 360.
TICK, S. J.: See Ref. 457.
688. TISCHLER, A. O.; AND BELLMAN, D. R.: Combustion Instability in an Acid-Heptane Rocket with a Pressurized-Gas Propellant Pumping System. NACA TN 2936, May 1953.
TISCHLER, A. O.: Also see Refs. 462 and 534.
689. TOBEY, A. C.; AND BASTRESS, E. K.: Flamè Piloting Mechanisms in Liquid Propellant Rocket Engines. A. D. Little, Scientific Rept. AFOSR 67-0938, Oct. 1966.
690. TOMAZIC, W. A.; CONRAD, E. W.; AND GODWIN, T. W.: M-1 Injector Development–Philosophy and Implementation. AIAA Paper No. 67-461, July 1967, (also NASA TMX-52289).
TOMAZIC, W. A.: Also see Ref. 215.
691. TONON, T. S.; AND SIRIGNANO, W. A.: Nonlinear Theories on Acoustic Liner Operation with Flow Effects. Princeton University, Dept. of Aerospace and Mechanical Sciences, Rept. No. 885, 1970.
692. TONON, T. S.; AND SIRIGNANO, W. A.: Near-Resonant, Off-Resonant, and Quasi-Steady Theories of Acoustic Liner Operation. Sixth ICRPG Combustion Conference, CPIA Pub. No. 192, Vol. 1, Dec. 1969, pp. 249–256.
693. TONON, T. S.; AND SIRIGNANO, W. A.: The Nonlinearity of Acoustic Liners with Flow Effects. AIAA Paper No. 70-128, AIAA Eighth Aerospace Sciences Meeting, Jan. 1970.
694. TONON, T. S.; ZAIC, G. E.; HARRJE, D. T.; AND SIRIGNANO, W. A.: Acoustic Liner Studies at Princeton University. Fifth ICRPG Combustion Conference, CPIA Pub. No. 183, Dec. 1968, pp. 351–357.
695. TOONG, T. Y.: Combustion Instability in Laminar Boundary Layers. AIAA Preprint 63-225, June 1963.
696. TOONG, T. Y.; SALANT, R. F.; STOPFORD, J. M.; AND ANDERSON, G. Y.: Mechanism of Combustion Instability. Tenth Symposium (International) on Combustion, The Combustion Institute, 1965, pp. 1301-13.
697. TORDA, T. P.; AND BURSTEIN, S. Z.: Non-linear Theory of Combustion Instability, Liquid Propellant Rocket Motors. Brooklyn Polytechnic Institute, PRL TN-58-1 (AFOSR TN 59-60), (AD-209 493), Dec. 1958.
698. TORDA, T. P.; AND PATEL, B. R.: Analytical and Experimental Investigations of Oscillations in Rocket Motor Baffle Cavities. Illinois Institute of Technology, Rept. AFOSR-68-1369, 1968.
TROSHIN, YA, K.: See Ref. 294.
699. TRUXALL, J. G.: Automatic Feedback Control System Synthesis. McGraw-Hill, New York, 1955.
700. TSUJI, H.; AND YAMAOKA, I.: The Counterflow Diffusion Flame in the Forward Stagnation Region of a Porous Cylinder. Eleventh Symposium (International) on Combustion, The Combustion Institute, 1967, pp. 979–984.
TULPINSKY, J. F.: See Ref. 256.
TYLER, W. H.: See Ref. 609.
701. URTIEW, P. A.; AND OPPENHEIM, A. K.: Experimental Observation of the Transition to Detonation in an Explosive Gas. Proc. Roy. Soc., Vol. A295, 1966, pp. 13–128.
702. UTIK, D. H.; BLACKMAN, A. W.; AND FORD, H. J.: Evaluation of Absorption Liners for Suppression of Combustion Instability in Rocket Engines. AIAA Paper No. 65-585, AIAA Propulsion Joint Specialists Conference, 1965.
UYEHARA, O. A.: See Refs. 112, 248, and 249.
703. VALENTINE, R. S.; DEAN, L. E.; AND PIEPER, J. L.: An Improved Method for Rocket Performance Prediction. J. Spacecraft and Rockets, Vol. 3, No. 9, Sept. 1966, pp. 1409–1414.
704. VALENTINE, R. S.; ROSSI, F. S.; AND KROMREY, R. V.: Effect of Fluid Dynamic Phenomena on Spontaneous Pressure Spikes in the Apollo SPS Thrust Chamber. AIAA Paper No. 67-513, AIAA Third Propulsion Joint Specialist Conference, July 1967.
705. VALENTINE, R. S.; ROSSI, F. S.; AND KROMREY, R. V.: Fluid Dynamic Effects on Apollo Engine Pressure Spikes. J. of Spacecraft and Rockets, Vol. 5, No. 1, Jan. 1968, pp. 31–35.
VALENTINE, R. S.: Also see Refs. 168 and 554.
VAN DE VERG, N.: See Ref. 524.
706. VAN DYKE, M.: Perturbation Methods in Fluid Mechanics. Academic Press, 1964.
VAN ENGELEN, H.: See Ref. 707.
VAN HUFF, N. E.: See Ref. 477.
707. VAN ITTERBEEK, A.; VAN ENGELEN, H.; AND MYNCKE, H.: Influence of the Shape of the Neck of the Helmholtz Resonator on its Absorbing Properties. Acoustica, Vol. 14, No. 4, 1964, pp. 212–215.
VARMA, A. K.: See Ref. 198.
708. VEGLIA, S. A.: Excitation Chamber-Combustion Response for Liquid Rocket Injectors, Part I Experimental Results. Fourth ICRPG Combustion Conference, CPIA Pub. No. 162, Vol. 1, Dec. 1967, pp. 57–62.
VEGLIA, S. A.: Also see Ref. 474.
709. VENNARD, J. K.: Elementary Fluid Mechanics, 4th Edition. Wiley & Sons, 1962, p. 325.
710. VINCENT, D. W.; PHILLIPS, B.; AND WANHAINEN, J. P.: Experimental Investigation of Acoustic

Liners to Suppress Screech in Storable Propellant Rocket Motors. NASA TN D-4442, March 1968.

711. VINCENT, D. W.; SOKOLOWSKI, D. E.; AND BLOOMER, H. E.: Screech Suppression Techniques for Rocket Combustors Using Earth-Storable Propellants. NASA TM X-1595, June 1968.

VINCENT, D. W.: Also see Refs. 106, 107, 652, 679 and 714.

712. VINCENT, J.: Feed System Stability Rating Program–Final Report, Phase I. Rocketdyne Rept. R-3653, June 1962.

713. VON KARMAN, T.; AND BIOT, M. A.: Mathematical Methods in Engineering. McGraw-Hill, New York, 1940, Chapter V, Sect. 9.

WAGNER, W. R.: See Ref. 677.

714. WANHAINEN, J. P.; BLOOMER, H. E.; VINCENT, D. W.; AND CURLEY, J. K.: Experimental Investigation of Acoustic Liners to Suppress Screech in Hydrogen-Oxygen Rockets. NASA TN D-3822, 1967.

715. WANHAINEN, J. P.; DEWITT, R. L.; AND ROSS, P. S.: Performance of a Low-Thrust Storable-Bipropellant Rocket at Very Low Chamber Pressure. NASA TN D-678, March 1961.

716. WANHAINEN, J. P.; FEILER, C. E.; AND MORGAN, C. J.: Effect of Chamber Pressure, Flow-per-Element and Contraction Ratio on Acoustic Mode Instability in Hydrogen-Oxygen Rockets. NASA TN D-4733, Aug. 1968.

717. WANHAINEN, J. P.; HANNUM, N. P.; AND RUSSELL, L. M.: Evaluation of Screech Suppression Concepts in a 20,000-Pound Thrust Hydrogen-Oxygen Rocket. NASA TM X-1435, 1967.

718. WANHAINEN, J. P.; AND MORGAN, C. J.: Effect of Injection Element Radial Distribution and Chamber Geometry on Acoustic Mode Instability in a Hydrogen Oxygen Rocket. NASA TN D-5375, Aug. 1969.

719. WANHAINEN, J. P.; PARISH, H. C.; AND CONRAD, E. W.: Effect of Propellant Injection Velocity on Screech in 20,000-Pound Hydrogen-Oxygen Rocket Engine. NASA TN D-3373, April 1966.

WANHAINEN, J. P.: Also see Refs. 106, 107, 624 and 710.

WASOW, W. R.: See Ref. 276.

WASSERBAUER, C. A.: See Ref. 233.

720. WAUGH, R. C.; MCCALLISTER, D. A.; AND MCBRIDE, J. M.: A Mathematical Model for Transverse Mode Instability with Feed System Coupling for Titan III. Fifth ICRPG Combustion Conference, CPIA Pub. No. 183, Dec. 1968, pp. 59–64.

721. WAUGH, R. E.; AND REARDON, F. H.: Feed System Effects on Combustion Instability. Bulletin of the Fifth Liquid Propulsion Symposium, CPIA Pub. No. 37, Vol. II, Dec. 1963, pp. 843–862.

WAUGH, R. E.: Also see Ref. 586.

WEATHERS, T. M.: See Ref. 365.

WEBB, M. J.: See Ref. 634.

WEBB, S. R.: See Ref. 163.

722. WEBBER, W. T.: Spray Combustion in the Presence of a Traveling Wave. Eighth Symposium (International) on Combustion, Williams and Wilkins, Baltimore, 1961, p. 1129.

WEBBER, W. T.: Also see Ref. 427.

723. WEBER, C.: Z. Angew. Math. Mech., Vol. 11, 1931, p. 138 (English Translation: On the Breakdown of a Fluid Jet. Ninth Progress Report, Project MX-833, Sect. II, Univ. of Colorado, Boulder, Colo.)

724. WEISS, M. A.; AND WORSHAM, C. H.: Atomization in High Velocity Air Streams. ARS J., Vol. 29, No. 4, April 1959, p. 252.

725. WEISS, R. F.; AND FLORSHEIM, B. H.: Flow in a Cavity at Low Reynolds Number. Physics of Fluids, Vol. 8, 1965, p. 1631.

726. WEISS, R. R.: An Introduction to Combustion Instability in Liquid Propellant Rocket Engines. AFRPL-TR-66-150, July 1966.

727. WEISS, R. R.: Investigation of Hyballine A14 as a Combustion Instability Suppressant in a LO_2/RP-1 Combustion System. AFRPL-TR-66-130, 1966.

728. WEISS, R. R.; CHEW, T. J. C.; AND KLOPOTEK, R. D.: A Combustion Stability Evaluation of Various Hydrazine and Hydrazine-Blend Fuels. Bulletin of the Seventh Liquid Propulsion Symposium, CPIA Pub. 72, Vol. I, Aug. 1965, pp. 343–384.

729. WEISS, R. R.; AND KLOPOTEK, R. D.: Experimental Evaluation of the Titan III Transtage Engine Combustion Stability Characteristics. AFRPL-TR-66-51, March 1966.

WEISS, R. R.: Also see Ref. 46.

730. WELLER, A. E.: Similarities in Combustion, a Review. AGARD Selected Combustion Problems, Vol. 2, Butterworths Sci. Pub., London, 1956, pp. 371–383.

731. WENZEL, L. M.; AND SZUCH, J. R.: Analysis of Chugging in Liquid Bipropellant Rocket Engines Using Propellants with Different Vaporization Rates. NASA TN D-3080, 1965.

WENZEL, L. M.: Also see Ref. 678.

732. WESLEY, R. D.; REDDING, R. A.; AND HEFNER, R. J.: Comparison of Instrumentation Techniques for High Frequency Combustion Chamber Pressure Measurements. AIAA Paper 65-360, 1965.

733. WESTERVELT, P. J.: Acoustic Impedance in Terms of Energy Functions. J. Acoust. Soc. Amer., Vol. 23, No. 3, May 1951, pp. 347-348.

WESTON, J. A.: See Ref. 240.

WHITE, D. R.: See Ref. 62.

734. WHITEHEAD, K. D.: The Generation and Development of a Viscous Vortex Ring. Ph.D. Thesis, Georgia Tech., School of Aerospace Eng. Rept. 68-4, Sept. 1968.

735. WICK, R. S.: An Analysis of Oscillatory Flow in Liquid-Propellant Rocket Systems and the Ap-

plication of the Analysis to Combustion Stability: Appendix A—Characteristics of the Cavitating Venturi, JPL Rept. 20-231, Aug. 1954.

736. WICK, R. S.: The Effect of Vehicle Structure on Propulsion System Dynamics and Stability. Jet Propulsion, Vol. 26, Oct. 1956, p. 878.

WICK, R. S.: Also see Ref. 524.

737. WIEBER, P. R.: Acoustic Decay Coefficients of Simulated Rocket Combustors. NASA TN D-3425, May 1966.

738. WIEBER, P. R.: Calculated Temperature Histories of Vaporizing Droplets to the Critical Point. AIAA J., Vol. 12, No. 12, Dec. 1963, pp. 2764–2770.

739. WIEBER, P. R.; AND MICKELSEN, W. R.: Effect of Transverse Acoustic Oscillations on the Vaporization of a Liquid Fuel Droplet. NASA TN D-287, May 1960.

WIEBER, P. R.: Also see Refs. 346 znd 347.

740. WILLIAMS, F. A.: Combustion Theory. Addison-Wesley, Reading, Mass., 1965.

741. WILLIAMS, F. A.: The Mechanism of Combustion of Droplets and Sprays of Liquid Fuels. Oxidation and Combustion Reviews, C. F. H. Tipper, ed., Vol. 3, 1968.

742. WILLIAMS, F. A.: On the Assumptions Underlying Droplet Vaporization and Combustion Theories. J. Chem. Phys., Vol. 33, 1960, p. 133.

743. WILLIAMS, F. A.: Progress in Spray Combustion Analysis. Eighth Symposium (International) on Combustion, Williams and Wilkins, Baltimore, 1962, pp. 50–69.

744. WILLIAMS, F. A.: Response of a Burning Fuel Plate to Sound Vibration. AIAA J., Vol. 3, 1965, p. 2112.

745. WILLIAMS, F. A.: A Simplified Model of Liquid Rocket Combustion. California Institute of Technology, Tech. Rept. No. 32, (Contract No. DA-04-495-ORD-1634), 1960.

746. WILLIAMS, F. A.: Structure of Detonations in Dilute Sprays. Physics of Fluids, Vol. 4, No. 11, 1961.

747. WILLIAMS, F. A.: Theory of the Burning of Monopropellant Droplets. Combustion and Flame, Vol. 3, 1959, p. 529.

748. WILLIAMS, F. A.; PENNER, S. S.; GILL, G. S.; AND ECKEL, E. F.: Combustion and Flame, Vol. 3, 1959, p. 355.

WILLIAMS, F. A.: Also see Refs. 289, 398 and 399.

WILLIAMS, G. C.: See Refs. 84 and 363.

749. WILLIAMS, R. M., JR.: Experimental Investigations of Liquid Propellant Combustion Processes Using Streak Photography. Princeton University. NASA CR 72371, 1968.

750. WILLIAMS, R. M.; AND ARNDT, F. E.: Space Storable Thrustor Investigation-Final Report. TRW, NASA CR-72495, Aug. 1969.

751. WILLMARTH, W. W.; HAWK, N. E.; GALLOWAY, A. J.; AND ROOS, F. W.: Aerodynamics of Oscillating Disks and a Right Circular Cylinder. J. of Fluid Mechanics, Vol. 27, Part 1, 1967, p. 177.

752. WISE, H.; AND AGOSTON, G. A.: Burning of a Liquid Droplet. Advances in Chemistry, No. 20, American Chemical Society, 1958, pp. 116–135.

753. WISE, H.; LORELL, J.; AND WOOD, B. J.: The Effects of Chemical and Physical Parameters on the Burning Rate of a Liquid Droplet. Fifth Symposium (International) on Combustion, Reinhold, New York, 1955, pp. 132–141.

WISE, H.: Also see Refs. 57, 58, 455, 546, 756 and 757.

754. WITHAM, G. B.: On the Propagation of Shock Waves Through Regions of Non-uniform Area or Flow. J. of Fluid Mech., Vol. 4, 1958, pp. 337–360.

WITHERSPOON, J. E.: See Ref. 348.

755. WOLFE, H. E.; AND ANDERSON, W. H.: Kinetics, Mechanism, and Resulting Droplet Sizes of the Aerodynamic Breakup of Liquid Drops. Aerojet-General Rept. No. 0395-04(18) SP, April 1964, (AD437340).

756. WOOD, B. J.; ROSSER, W. A., JR.; AND WISE, H.: Combustion of Fuel Drops. AIAA J., Vol. 1,1963, p. 1076.

757. WOOD, B. J.; WISE, H.; AND ROSSER, W. A.: Burning of a Liquid Droplet: IV. Combustion Inhibition in a Fuel-Oxidizer System. J. Chem. Phys., Vol. 27, 1957, pp. 807–808.

WOOD, B. J.: Also see Refs. 58 and 753.

WOOD, D. J.: See Ref. 232.

WOOD, L. M.: See Ref. 608.

758. WOODWARD, J. W.: Combustion Effects in Sprays. JPL Space Programs Summary No. 37-36, Vol. IV, Dec. 1965, pp. 181–183.

759. WOODWARD, J. W.; AND SOTTER, J. G.: Response of Injectors to High Amplitude Oscillations. JPL Space Programs Summary 37-41, Vol. IV, Oct. 1966, pp. 145–151.

WOODWARD, J. W.: Also see Ref. 154.

760. WORLUND, A. L.; ET AL: The Reduction of Pogo Effects by Gas Injection. AIAA Paper 66-560, AIAA Second Propulsion Joint Specialist Conference, 1966.

WORSHAM, C. H.: See Ref. 724.

761. WRIGHT, B.: Liquid Flow Characteristics of Small Diameter Unsubmerged Short Tube Orifices Discharging to Atmospheric Pressure. Rept. 610-810, Aug. 1962, Bendix Aircraft Corp., Eclipse-Pioneer Div., Teterboro, N. J.

WRIGHT, R. O.: See Refs. 91, 358 and 359.

762. WROBEL, J. R.: Some Effects of Gas Stratification on Choked Nozzle Flows. AIAA Paper 64-266, 1964.

763. WUERKER, R. F.: Q-Switched Ruby Laser Holography. Paper THF13, Spring Meeting of the Optical Society of America, 1967.

764. WUERKER, R. F.; AND MATTHEWS, B. J.: Producing Holograms of Reacting Sprays in Liquid Propellant Rocket Engines, Phase I Interim Rept.

TRW Systems Rept. No. 68—4712.2-017, Feb. 1968.

765. WUERKER, R. F.; MATTHEWS, B. J.; AND BRIONES, R. A.: Producing Holograms of Reacting Sprays in Liquid Rocket Engines–Final Report. TRW Systems Rept. No. 68.2712.2-024, July 1968.

YAMAOKA, I.: See Ref. 700.

YANGECIO, G. A.: See Ref. 257.

YEH, P. S.: See Refs. 545 and 547.

YING, S. J.: See Ref. 143.

YOUNG, A. D.: See Ref. 234.

766. ZAIC, G. F.; AND HARRJE, D. T.: Damping of Shock-Type Waves with a Helmholtz Resonator. Sixth ICRPG Combustion Conference, CPIA Pub. No. 192, Vol. 1, Dec. 1969, pp. 271–276.

ZAIC, G. F.: Also see Ref. 694.

767. ZELDOVICH, Y. B.: On the Theory of Combustion of Initially Unmixed Gases. NACA TM 1296, June 1951, Trans. from Zhurnal Tekhnicheskoi Fiziki, Vol. 19, No. 10, Oct. 1949, pp. 1199–1210.

768. ZINK, J. W.; AND DELSASSO, L. P.: Attenuation and Dispersion of Sound by Solid Particles Suspended in a Gas. J. Acoust. Soc. Amer., Vol. 39, 1958, p. 765.

769. ZINN, B. T.: A Theoretical Study of Nonlinear Combustion Instability in Liquid Propellant Rocket Engines. Third ICRPG Combustion Conference, CPIA Pub. No. 138, Vol. I, Feb. 1967, pp. 441–452.

770. ZINN, B. T.: A Theoretical Study of Nonlinear Damping by Helmholtz Resonators. AIAA Paper No. 69-481, AIAA Fifth Propulsion Specialists Meeting, June 1969.

771. ZINN, B. T.: A Theoretical Study of Nonlinear Transverse Combustion Instability in Liquid Propellant Rocket Motors. Ph. D. Thesis, Princeton University, Department of Aerospace and Mechanical Sciences Rept. No. 732, May 1966.

772. ZINN, B. T.; AND SAVELL, C. T.: A Theoretical Study of Three-Dimensional Combustion Instability in Liquid Rocket Motors. Twelfth Symposium (International) on Combustion, The Combustion Institute, 1969, pp. 139–147.

773. ZUCROW, M. J.; AND OSBORN, J. R.: An Experimental Study of High-Frequency Combustion Pressure Oscillations. Jet Propulsion, Vol. 28, 1958, pp. 654–659.

774. ZUCROW, M. J.; AND OSBORN, J. R.: Reply to Crocco's Criticism of the Zucrow-Osborn Paper. ARS J., Vol. 29, No. 3, March 1959, p. 221.

775. ZUCROW, M. J.; OSBORN, J. R.; AND BONNELL, J. M.: High Frequency Combustion Pressure Oscillations in Motors Burning Gaseous Propellants. Purdue University, Jet Propulsion Center, Rept. No. TM-65-5, 1965.

776. ZUCROW, M. J.; OSBORN, J. R.; AND PINCHAK, A. C.: Luminosity and Pressure Oscillations Observed with Longitudinal and Transverse Modes of Combustion Instability. ARS J., Vol. 30, No. 8, Aug. 1960, pp. 758–761.

777. ZUNG, L. B.: Hypergolic Impingement Mechanisms and Criteria for Mixing or Separation. Sixth ICRPG Combustion Conference, CPIA Pub. No. 192, Vol. 1, Dec. 1969, pp. 21–32.

778. ZWIKKER, C.; AND KOSTEN, C. W.: Sound Absorbing Materials. Elsevier Pub., New York, 1949.

INDEX

[The numbers refer to sections]

☆ U. S. GOVERNMENT PRINTING OFFICE : 1972 O - 428-978